

Alexander K. Tagantsev
L. Eric Cross
Jan Fousek

Domains in Ferroic Crystals and Thin Films

 Springer

Domains in Ferroic Crystals and Thin Films

Alexander K. Tagantsev • L. Eric Cross •
Jan Fousek

Domains in Ferroic Crystals and Thin Films

 Springer

Alexander K. Tagantsev
LC IMX STI Station 12
1015 Lausanne
EPFL
Switzerland
alexander.tagantsev@epfl.ch

L. Eric Cross
Department of Electrical Engineering
Pennsylvania State University
University Park PA 16802
USA
lec3@psu.edu

Jan Fousek
Department of Physics
Technical University of Liberec
Halkova 6
461 17 Liberec 1
Czech Republic

ISBN 978-1-4419-1416-3 e-ISBN 978-1-4419-1417-0
DOI 10.1007/978-1-4419-1417-0
Springer New York Dordrecht Heidelberg London

Library of Congress Control Number: 2009940898

© Springer Science+Business Media, LLC 2010
All rights reserved. This work may not be translated or copied in whole or in part without the written permission of the publisher (Springer Science+Business Media, LLC, 233 Spring Street, New York, NY 10013, USA), except for brief excerpts in connection with reviews or scholarly analysis. Use in connection with any form of information storage and retrieval, electronic adaptation, computer software, or by similar or dissimilar methodology now known or hereafter developed is forbidden. The use in this publication of trade names, trademarks, service marks, and similar terms, even if they are not identified as such, is not to be taken as an expression of opinion as to whether or not they are subject to proprietary rights.

Printed on acid-free paper

Springer is part of Springer Science+Business Media (www.springer.com)

Preface

With much excitement and great enthusiasm I introduce this thorough treatise on the major aspects of domain and domain wall phenomena in ferroics, mostly ferroelectrics, a major achievement for which there has been a long-standing need.

Ferroelectric materials possess spontaneous electrical polarization which is stable in more than one orientation and can be reoriented (switched) by an applied electric field. This property and its typical derivative characteristics, e.g., high piezoelectric response and large permittivity, make ferroelectrics exceedingly useful in diverse applications such as non-volatile memories, ultrasonic medical imaging, micro-electromechanical systems, and reconfigurable high-frequency electronics.

Typically, a ferroelectric material is divided into domains, which are regions in the material that are polarized in one of the symmetry-permitted polarization directions. The interfaces between adjacent domains, the domain walls, have a typical thickness of 1–2 unit cells. The behaviors of domains and domain walls are fundamental to ferroelectrics and dominate their properties: poling of ferroelectric ceramics, namely electrical aligning of the polar direction of ferroelectric domains, is essential for piezoelectric activity; periodically poled crystals are used as nonlinear optic materials for which the width of the inverted domains controls the desired wavelength of operation. The high permittivity of ferroelectrics widely used in capacitors is dominated by domain wall contributions, and domain wall dynamics is responsible for some 50% of the piezoelectric response in standard transducers and actuators.

Considering the vital role of domains and domain walls, the substantial body of data, and the resultant theoretical knowledge, it is surprising how limited is the space given to this subject in the classical books on ferroelectric materials. Even recent books rarely dedicate entire chapters to this topic. Meanwhile the importance of domains and domain walls is growing. Thus the study and manipulation of domain walls can be achieved with much enhanced detail using new techniques such as piezoelectric force microscopy; new thin-film growth techniques allow the control of their position, spacing, and response, and new computation methods aid in revealing their further potential.

It is therefore very timely for the ferroelectric community and for students and researchers interested in the field of ferroelectrics that the three most prominent authorities in the field have united to write this major book on ferroelectric domains in single crystals, ceramics, and thin films, covering all the important aspects of the field: basic theoretical descriptions of structural phase transitions that emphasize the symmetry and phenomenological aspects of their classifications, an overview of typical ferroic materials, a survey of experimental methods used to visualize domain patterns, aspects of domain formation and their typical shapes, and the static properties of domain walls are all addressed. A large section of the book covers theoretical and experimental aspects of switching and polarization response and overviews comprehensively domain-related properties of ferroelectric thin films.

This book will be of central importance to anyone interested in ferroelectrics and their applications: graduate students of materials science, physics, chemistry, mechanical and electrical engineering, as well as scientists and engineers, whether new to the field or simply in need of a systematic and thorough review of the vast, useful, and fascinating field of ferroic domains.

Nava Setter
7.2009, Lausanne

Acknowledgments

Our gratitude goes to people who helped us in writing this book and preparing it for publication. First of all, we would like to thank the experts who helped us in writing sections devoted to some specialized characterization techniques: Sects. 4.5 and 9.8 addressing scanning force microscopy-based techniques were written in a tight collaboration with Alexei Gruverman and Sect. 4.8 on the use of electron microscopy in domain imaging was written together with Pierre Stadelmann and Marco Cantoni. We are grateful to Yongly Wang, Victor Porokhonsky, Maxim Gureev, Alexander Tselev, Nikolay A. Pertsev, and Tatyana Volk who have read some chapters in the manuscript and provided us with their useful comments. Nikolay A. Pertsev, Xiaobing Ren, Andreas K. Roelofs, Nagarajan Valanoor, and Seungbum Hong are also kindly acknowledged for permitting us to use their figures. We are grateful to Jiri Erhart for his enormous labor of preparation of tables for the domain wall orientation (AppendixD). Our sincere gratitude goes to the draftsman of the book, Tomas Sluka.

Alexander Kirillovich Tagantsev acknowledges “Multifunctional and Integrated Piezoelectric Devices—MIND” (Network of the EU, FP6). He also likes to thank Nava Setter, the director of Ceramics Laboratory at EPFL, for providing an inspiring atmosphere in the lab that helped him a lot in writing the book.

Leslie Eric Cross is deeply grateful to Professor Rustum Roy for catalyzing his move from England to USA and for his continuing help in making the Materials Research Laboratory at Penn State a recognized center for ferroics research.

Contents

1	A Preview of Concepts and Phenomena	1
2	Fundamentals of Ferroic Domain Structures	11
2.1	Structural Phase Transitions and Domain States: Basic Concepts and Classifications	11
2.1.1	Structural Changes at Phase Transitions: Ferroics	11
2.1.2	Ferroelectric Phase Transitions	16
2.1.3	Ferroelastics and Ferrobielectrics	19
2.1.4	Higher Order Ferroics	28
2.1.5	Relation Between the Symmetries G and F: Order Parameter	32
2.1.6	Overview of Different Kinds of Phase Transitions: Species	35
2.1.7	Domain States	36
2.1.8	Ferroic Species	43
2.1.9	Ferroelectric Species	47
2.2	Coexisting Domain States	51
2.2.1	Twinning Operations	52
2.2.2	Twin Laws for Nonferroelastic Domain Pairs	53
2.2.3	Domain Wall Orientation: Electrical Compatibility	58
2.2.4	Domain Wall Orientation: Mechanical Compatibility	62
2.2.5	Ferroelastic Domains in Physical Contact	66
2.2.6	Examples of Domain Wall Orientations: Nonferroelastic Walls	69
2.2.7	Examples of Domain Wall Orientations: Ferroelastic Walls	74
2.3	Thermodynamic Approach	81
2.3.1	Single-Component Order Parameter	81
2.3.2	Uniaxial Proper Ferroelectric (Nonferroelastic)	88
2.3.3	Uniaxial Proper Ferroelectric–Ferroelastic	91

- 2.3.4 Multiaxial Proper Ferroelectric–Improper Ferroelastic 92
- 2.3.5 Uniaxial Improper Ferroelastic–Ferroelectric 97
- 2.3.6 Limitation of Traditional Thermodynamic Approach: Pseudo-proper and Weak Ferroelectricity 100
- 3 Ferroic Materials 109**
 - 3.1 Sources of Information and Statistics 109
 - 3.2 Table of Selected Ferroic Materials 110
- 4 Methods for Observation of Domains 121**
 - 4.1 Introductory Remarks 121
 - 4.2 Surface Etching Techniques 122
 - 4.3 Other Methods Based on Surface Relief 129
 - 4.4 Surface Decoration Techniques 131
 - 4.4.1 Colloidal Suspensions 132
 - 4.4.2 Decoration by Sublimation and Vacuum Evaporation 134
 - 4.4.3 Deposition in Liquids 136
 - 4.4.4 Condensation of Vapor 136
 - 4.4.5 Decoration by Liquid Crystal Layers 137
 - 4.5 Scanning Force Microscopy-Based Techniques 142
 - 4.5.1 Electrostatic Force Microscopy (EFM) 143
 - 4.5.2 Scanning Surface Potential Microscopy (SSPM) 147
 - 4.5.3 Contact Domain Imaging 149
 - 4.5.4 Lateral Force Microscopy (LFM) 150
 - 4.5.5 Domain Imaging via Surface Topography 151
 - 4.5.6 Domain Imaging via Nonlinear Dielectric Response (SNDM) 153
 - 4.5.7 Domain Imaging via Static Piezoresponse 155
 - 4.5.8 Domain Imaging via Dynamic Piezoresponse (PFM) 158
 - 4.6 Polarized Light Microscopy Based on Unperturbed Linear Optical Properties 161
 - 4.6.1 Birefringence 161
 - 4.6.2 Spatial Dispersion 169
 - 4.6.3 Optical Activity 170
 - 4.6.4 Optical Absorption and Observation in Reflected Light 172
 - 4.7 Optical Methods Based on Higher Order Optical Properties 173
 - 4.7.1 Perturbed Linear Optical Properties: Electro-optics and Elasto-optics 173
 - 4.7.2 Nonlinear Optical Properties 176
 - 4.7.3 Photorefractive Properties 179

4.8	Electron Microscopy	182
4.8.1	Scanning Electron Microscopy	182
4.8.2	Transmission Electron Microscopy	186
4.8.3	Electron Mirror Microscopy	193
4.9	Methods Based on Interactions with X-Rays	194
4.10	Pyroelectric Mapping	197
4.11	Scanning Optical Microscopy	200
4.12	Additional Methods and Concluding Remarks	203
5	Static Domain Patterns	207
5.1	Introductory Remarks and Scheme of the Chapter	207
5.2	Equilibrium 180° Domain Patterns in a Ferroelectric Plate: Theories	208
5.3	Domain Patterns Connected with Phase Boundaries.	220
5.3.1	Perfect Matching	220
5.3.2	Matching on Average	222
5.4	Selected Observations of Domains in Crystalline Ferroic Samples.	224
5.4.1	Uniaxial Ferroelectrics (Nonferroelastic) with the Second-Order Transition.	225
5.4.2	Ferroelastics with a Small Number of Domain States	235
5.4.3	Perovskite Ferroics	253
5.4.4	R Cases	262
5.4.5	Quartz	265
5.4.6	Tweed Patterns	267
6	Domain Walls at Rest	271
6.1	Thickness and Structure of Domain Walls: Methods and Data.	272
6.1.1	Direct Optical Observations	273
6.1.2	X-Ray and Neutron Scattering	278
6.1.3	X-Ray Topography	281
6.1.4	Raman Scattering	282
6.1.5	Electron Holography	283
6.1.6	Transmission Electron Microscopy.	285
6.1.7	Surface Methods	288
6.1.8	Comments on Available Data	291
6.2	Macroscopic Theories of Domain Walls	291
6.2.1	Order Parameter Profile in Domain Walls	292
6.2.2	Effects of Strain Induced by the Order Parameter	300
6.2.3	Domain Walls in Selected Ferroics	305
6.2.4	Concluding Remarks.	314
6.3	Microscopic Theories of Domain Walls.	315

- 6.4 How Flat Is the Wall? 319
 - 6.4.1 Mathematical Problem 321
 - 6.4.2 Nonferroelectric/Nonferroelastic Walls 322
 - 6.4.3 Walls in Ferroelectrics and Ferroelastics 325
 - 6.4.4 Experimental Data on Roughening of Ferroic Domain Walls and Experimental Observations 328
- 7 Switching Properties: Basic Methods and Characteristics 331**
 - 7.1 Introduction 331
 - 7.2 Ferroelectric Hysteresis Loop 332
 - 7.3 TANDEL Effect. 339
 - 7.4 Pulse Switching. 340
 - 7.5 Ferroelastic Hysteresis Loops 344
 - 7.6 More Involved Methods. 349
- 8 Switching Phenomena and Small-Signal Response 351**
 - 8.1 Introduction and Overview of Switching Mechanisms 351
 - 8.2 Basics of Domain State Reorientation 354
 - 8.2.1 Driving Force for Processes of Domain State Reorientation. 354
 - 8.2.2 Pressure Acting on a Domain Wall. 357
 - 8.3 Single Domain Wall in Motion 360
 - 8.3.1 Experimental Techniques Used to Measure Domain Wall Velocity. 360
 - 8.3.2 Motion of Ferroelectric Nonferroelastic Walls. 364
 - 8.3.3 Motion of Ferroelastic Walls in Ferroelectrics 382
 - 8.4 Theories of Single Wall Motion 391
 - 8.4.1 Two Regimes of Wall Motion. 392
 - 8.4.2 Wall Mobility in Activated Regime. Miller–Weinreich Theory 394
 - 8.4.3 Wall Mobility in Activated Regime. Advanced Theories and Present Understanding of the Problem 397
 - 8.4.4 Domain Wall Motion in Non-activated Regime. 404
 - 8.4.5 Domain Wall Motion Influenced by the Ferroelectric/Electrode Interface 410
 - 8.4.6 Motion of Curved Domain Walls 415
 - 8.5 Defect Pinning and Creep of Domain Walls 418
 - 8.5.1 Non-thermally Assisted Regime, Weak and Strong Pinning. 419
 - 8.5.2 Finite Temperatures: Weak Pinning and Creep 422
 - 8.5.3 Finite Temperatures: Strong-Pinning Regime. 426
 - 8.5.4 Weak and Strong Pinning with Flexible Defects 427
 - 8.5.5 Experimental Evidence on Weak Pinning and Creep of Ferroelectric Domain Walls 428

8.6	Switching Process in Selected Materials	429
8.6.1	BaTiO ₃	430
8.6.2	TGS and TGFB.	438
8.6.3	LiTaO ₃ and LiNbO ₃	443
8.6.4	KDP and Isomorphous Crystals	446
8.7	Theory and Modeling of Switching	448
8.7.1	Introduction.	448
8.7.2	Domain Nucleation	451
8.7.3	Domain Coalescence	457
8.7.4	Pulse Switching	459
8.7.5	Classical Polarization Hysteresis Loops.	466
8.7.6	Rayleigh Loops	470
8.7.7	Piezoelectric Hysteresis Loops.	475
8.7.8	Ferroelectric Breakdown	481
8.8	Extrinsic Contribution to Small-Signal Dielectric Response in Bulk Ferroelectrics.	483
8.8.1	Introduction.	483
8.8.2	Fully Immobile Domain Pattern	485
8.8.3	Contributions from Moving Domain Walls in Ideal Crystals.	490
8.8.4	Quasistatic Bending Contribution from “Firmly” Pinned Domain Walls	498
8.8.5	Limited Motion of Free Domain Wall	501
8.8.6	Wall Motion in Random Potential and Dispersion of the Dielectric Response (Experimental Findings and Interpretation)	504
8.8.7	Domain Freezing.	511
8.8.8	Dielectric Response Associated with Mobile Ferroelastic Domain Walls in a Clamped Multidomain Ferroelectric	515
9	Ferroelectric Thin Films	521
9.1	Introduction	521
9.2	Experimental Studies on the Static Domain Pattern in Thin Films	523
9.2.1	Domain Structure in (001) Thin Films of Tetragonal Ferroelectric Perovskites	523
9.2.2	Ferroelastic Domain Patterns in (001) Rhombohedral and (111) Tetragonal Thin Films of Ferroelectric Perovskites.	536
9.2.3	Domain Structure in Other Systems	542
9.3	Domain Pattern and Elastic Effects	544
9.3.1	Strained State of Ferroelectric Film and Dislocation-Assisted Stress Release	544

- 9.3.2 Single-Domain State in a Strained Film 553
- 9.3.3 Domain Formation Driven by Elastic Effects:
Basic Concepts 560
- 9.3.4 Domain Formation Driven by Elastic Effects:
Advanced Theoretical Results 573
- 9.3.5 Domain Formation Driven by Elastic Effects:
Theory vs. Experiment 589
- 9.4 Domain Pattern and Electrostatic Effects 599
 - 9.4.1 Equilibrium Domain Pattern in Ferroelectric/
Dielectric Sandwich Structure 599
 - 9.4.2 Equilibrium Domain Pattern in Ferroelectric
Films on Insulating Substrates 603
 - 9.4.3 Limitations of Hard-Ferroelectric Approximation
and Results Obtained Beyond
This Approximation 604
- 9.5 Switching and Polarization Hysteresis 608
 - 9.5.1 Pulse Switching 608
 - 9.5.2 Ferroelectric Hysteresis Loops; Size Effects 613
 - 9.5.3 Effects of Internal Bias and Imprint 627
- 9.6 Small-Signal Response 653
 - 9.6.1 Intrinsic Contribution—Effect of Passive
Layer 654
 - 9.6.2 Intrinsic Contribution—Depletion Effect 662
 - 9.6.3 Intrinsic Contribution—Strain Effect 664
 - 9.6.4 Extrinsic Contribution—Mechanical Effects 667
 - 9.6.5 Extrinsic Contribution—Electrostatic Effects 671
- 9.7 Polarization Fatigue in Thin Ferroelectric Films 677
 - 9.7.1 How Can Imperfections Influence
Polarization Switching in Ferroelectric
Capacitor? 678
 - 9.7.2 What Are These Imperfections and How Do They
Affect the Switching Performance of Ferroelectric
Capacitor? 686
 - 9.7.3 Overall Picture of Polarization Fatigue in PZT
Thin Films 688
- 9.8 Scanning Force Microscopy Study of Polarization
Reversal 690
 - 9.8.1 Top-Electrode-Free PFM 692
 - 9.8.2 Through-Electrode PFM 700
- 9.9 Films of Proper Ferroelectric–Ferroelastics 704
- Appendix A** 713
- Appendix B** 715

Contents	xv
Appendix C	721
Appendix D	729
Appendix E	775
Appendix F	779
Transformation Laws for Tensors	779
Voight Notations for Tensors	779
Notation for Symmetry of Tensors	780
References	783
Index	813

Chapter 1

A Preview of Concepts and Phenomena

This book covers a large area of material properties and effects connected with static and dynamic properties of domains. These are relevant to materials referred to as ferroics. In textbooks on solid state physics, one large group of ferroics is customarily covered, namely those in which magnetic properties play a dominant role: magnetically ordered materials which include ferromagnetics and antiferromagnetics. Numerous books are specifically devoted to such materials and cover a wide spectrum of magnetic domain phenomena which also incorporate essential practical aspects such as magnetic memories. In contrast, in the present monograph attention will be concentrated on domain-related phenomena in nonmagnetic ferroics. These materials are still only inadequately represented in solid state physics textbooks—even those which offer the most interesting properties, namely ferroelectrics. Therefore before starting with a systematic description of domain phenomena, in the present chapter we wish to offer the reader an introduction into what this book is all about.

Domains are a special sort of crystal twins and a few general remarks on twinning seem appropriate.

The phenomenon of growth twinning in crystals has been a subject of interest for crystallographers since crystallography started to develop as a scientific branch. The obvious reasons are the beauty of external shapes of some of the twinned crystals as well as evident and challenging symmetry relations between their constituents. Essentially, we speak about a *twin* when two or more individual crystals of the same species intergrow in a crystalline aggregate. Such parts of the aggregate are referred to as *twin components* and it is obvious that the symmetry operation (referred to as *twinning operation*) which brings one crystal into coincidence with the other cannot be a symmetry operation of the crystal itself. Twins are often just the result of an accident during crystal growth: Ions newly arriving at the surface layer of the growing crystal may have a choice of sites in which to settle, and one or more of these choices may represent the nucleus of the same crystal species growing in a different orientation. We then speak about the *growth twins* and these were often classified according to the physical appearance of the twinned crystal. The concepts of *penetration twins* (in which components may be of irregular size and shape) and *lamellar twins*

(composed of uniform alternating layers and not infrequently named *polysynthetic twins*) are almost self-explanatory. The boundary separating two constituents of the twinned crystal is referred to as the *twin boundary* or *composition plane*. Figure 1.1 shows an example of a twinned as-grown crystal. Description and understanding of growth twins presented many challenges to mineralogy and crystallography but some of them were and still are also of practical concern. A good example is offered by crystals of quartz, SiO_2 : When twinned, its useful piezoelectric properties are deteriorated. This is because the piezoelectric responses in different twin components may partly compensate each other.

Twin components may differ in the orientation of crystallographic axes. Then, their unit cell dimensions would also differ with reference to the laboratory frame. Under applied mechanical force, therefore, the energies of two neighboring twin components may differ and if this is so one of the components may grow at the expense of the other. In fact, the applied force may lead even to nucleation of the more suitably oriented twin component, that is, to the formation of a twin starting from a single homogeneous crystal. This phenomenon is called *mechanical twinning*. It has been known for a long time, especially in some metals where twins can be relatively easily formed by gliding movement of a part of the crystal against the other, under a shear stress.

Whether we deal with growth twins or mechanical twins, their crystallographic description includes two essential issues: What are the symmetry relations between the twin components and what orientations the composition

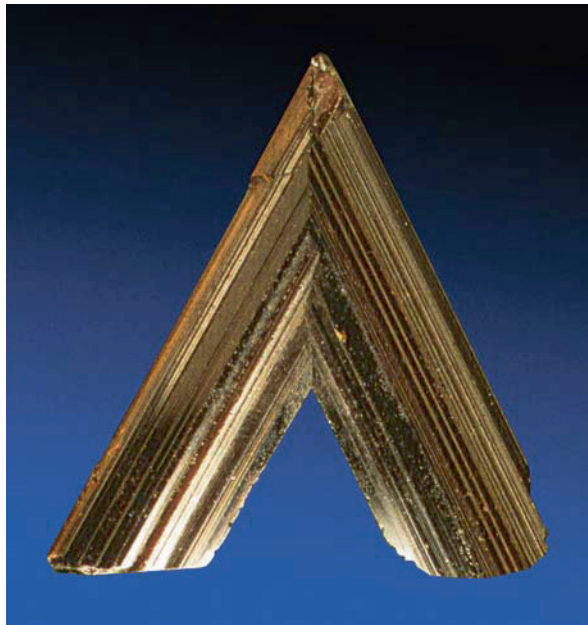


Fig. 1.1 Example of a twinned as-grown crystal (Rutil TiO_2)

plane may take. Detailed considerations lead to different classifications of twins and the topic has been treated in detail in a number of books on mineralogy and review articles (see, e.g., Cahn, 1954; Wadhawan, 1987; Shuvalov, 1988).

In this book we are concerned in the description of properties of a special kind of twins, traditionally referred to as transformation twins. Their essential feature is that the mentioned symmetry relations between their components are fully defined by specifying two crystal structures, say S_G and S_F , with two prominent properties: (i) the symmetry of S_F is *lower* than that of S_G and (ii) S_F arises from S_G by small distortions of the latter, for instance by small shifts of some of the ions. In a large number of crystalline compounds, the structure changes spontaneously from S_G to S_F at a certain *phase transition temperature* T_{TR} , simply to obey the rule that such structure is realized which, at a given temperature, corresponds to lower free energy of the material. Consider the simple example illustrated in Fig. 1.2. The structure S_G has a tetragonal unit cell. At the phase transition, this structure undergoes changes: The central ion shifts along the vertical c -axis. The actual displacements of particles may be very small (typically of the order of 10^{-2} – 10^{-3} nm, i.e., a very small fraction of the unit cell dimension), but even so they violate some of the symmetry operations of S_G and the resulting structure S_F has a *lower symmetry*. The shift of the central ion can have either sign so that two structures $S_F(A)$ and $S_F(B)$, denoted further on as S_A and S_B , can form. When no external forces are applied they have the same energy and therefore in an ideal sample it is unpredictable which of them will appear. These two structures, resulting from the *phase transformation* from a *phase* with the structure S_G to that with the structure S_F , represent *transformation twins*. Herein we will refer to these phases as G and F , respectively. The material undergoing a phase transition such as this one or similar to it is referred to as a *ferroic*. Twin components in a real sample which are formed due to a phase transformation in ferroics are called *domains*. To avoid misunderstandings, we stress already at this point that while in this hypothetic ferroic material only two *domain states* can exist, with structures S_A and S_B , in a sample of it we may have any number of twin components, i.e., any number of domains each of which represents either S_A or S_B .

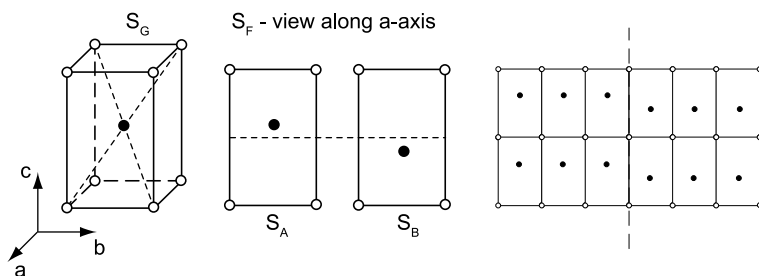


Fig. 1.2 Simple case of two ferroelectric domain states formed in a crystal lattice

Several thousands of crystalline materials are known to undergo phase transitions at which the symmetry is lowered, typically on cooling (Tomashewski, 1992a,b) or when the ambient hydrostatic pressure is changed (Tonkov, 1992). In all of them, domains may exist and there are manifold reasons for their occurrence. Static mechanical and electrical boundary conditions of a finite sample may lead to domain formation, in particular during the phase transformation process. Presence of defects incorporated into the crystal lattice during the crystal growth may prefer the coexistence of two domains next to each other. Metastable domain patterns may exist in a sample as remnants of dynamic processes which took place in it in the past. And, perhaps most important of all, domains can be formed intentionally by applying properly oriented mechanical and/or electrical forces.

Size of domains varies in wide limits, from tens of nanometers to millimeters; however, if a narrower region should be quoted as typical, linear dimension between 1 and 100 μm would seem a reasonable hint for the bulk materials, however, much smaller values are typical for thin films. While the number of domains is virtually unlimited, a very different rule applies to the count of “kinds of domains.” It is obvious from the Fig. 1.2 that, starting from a tetragonal cell, the shift of the central ion along the vertical axis can proceed in two ways only: upward or downward. This leads to just two possible structures, S_A and S_B ; these represent the only two possible *domain states*. Generally, the number of domain states may be larger than two. We shall show in the following chapter how it can be determined by simple symmetry considerations.

Compared to growth twins, domains excel in one aspect: The number of domain states and the symmetry relationship between them can be exactly formulated, knowing the symmetries of crystal structures S_G and S_F . We shall consider these symmetry aspects in some detail in the next chapter.

A phase transition between phases G and F can also be associated with a change of the form of the unit cell as illustrated in Fig. 1.3, where the unit cell in F phase becomes orthorhombic. Here the two possible structures of S_F phase,

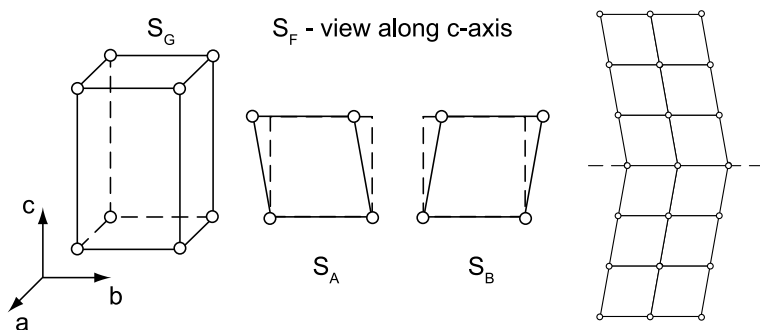


Fig. 1.3 Simple case of two ferroelastic domain states formed in a crystal lattice

S_A and S_B , differ from S_G by the sign of shear deformation in the plane normal to the fourfold axis of G phase.

What was a twin boundary or a composition plane in the general twinning narrative becomes a *domain wall* or *domain boundary* in the case of domains. But the concept of twin boundary is also frequently used, especially when speaking about two neighboring domains which differ in the shape of their unit cells, as illustrated in Fig. 1.3. Typically, having in mind nonmagnetic ferroics, the domain wall is an extremely thin region, its thickness ranging from one to several tens of lattice units. We wish to mention already at this point that, in a sample of a ferroic material, both phases (with the structures S_G and S_F) may coexist, usually within a restricted temperature interval around the phase transition temperature T_{TR} . In this book we shall reserve the term *phase boundary* for a narrow transition region separating these two structures.

Figure 1.4 shows an example of real domains. It is a microscopic image of domains in a plate of barium titanate; the sample surface was etched (Fousek and Safrankova, 1965). Here, dark and white stripes, which are several micrometers wide, correspond to domains representing two possible domain states. The photograph clearly demonstrates that domain walls are much thinner than the domain size.

It is obvious from what has been said that, under ideal conditions (perfect crystal lattice, no applied forces) the energy density of the crystal in the two domain states (or in any domain state allowed by symmetry), is the same. These are the *ground states* of the crystalline system in phase F , degenerate in energy. But within the domain wall—however thin it may be—the structure must be distorted, providing a passage between the two structures S_A and S_B . Therefore the wall is characterized by some extra energy; since the wall is very thin we consider it as a surface energy. It plays a significant role: What size and in particular what shape domains have largely depend on its magnitude and on the extent it varies with the wall orientation. If asked for a typical number, the wall energy density is usually estimated to be of the order between 1 and 10 erg/cm².

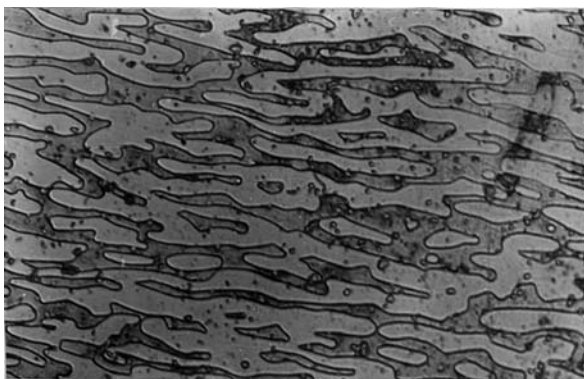


Fig. 1.4 Microscopic picture of domains in a c -plate of barium titanate; the sample surface was etched and observed in reflected light (Fousek and Safrankova, 1965)

Up to this point, domains and growth twins seem to have many similar properties. What makes domains unique are two features. First, the structural change from S_G to S_F is accompanied by fully predictable macroscopic tensor properties of the crystal. As a consequence, the difference in the tensor properties of different domain states (with structures S_A and S_B in our example) is well defined. Second, forces may be applied to the ferroic sample, which remove the energy degeneracy of domain states; again the nature and orientation of these forces are fully predictable. Often they can be easily realized and are capable of transforming the crystal from one domain state to another. This process is referred to as *domain state reorientation* but many alternative terms are employed such as *switching*.

Ferroic crystals, because of the existence of domains and possibility of reorientation, thus offer qualitatively new properties and effects which cannot be achieved with “normal” crystalline compounds that exist in one state only.

A simple and at the same time a very realistic illustration of what has been just said can be based again on the previous simple model. Assuming the central ion is positively charged, its shift is connected with formation of a dipole. Its dipole moment, when integrated over a unit volume, defines the polarization variation associated with the phase transformation. This polarization variation is customarily termed as *spontaneous polarization* \mathbf{P}_S , associated with the phase transition from S_G to S_F . Thus the structures S_A and S_B differ in the sign of \mathbf{P}_S . It is obvious that an applied electric field \mathbf{E} pointing downward prefers the structure S_A while the structure S_B is more favorable in the field of opposite sign. We expect that domains with structures preferred by the applied field, say S_A , will grow at the expense of domains with structures S_B . As a characteristic of this process, mapping average polarization vs. field results in the *hysteresis loop*. An example of such loop observed in a slowly varying field applied to a crystal of $\text{Gd}_2(\text{MoO}_4)_3$ (abbr. GMO) is shown in Fig. 1.5a (Kumada et al., 1970). It illustrates the process of *polarization reversal*. A ferroic with this property is said to be *ferroelectric*. Other ferroelectric crystals which serve as model materials for many aspects of domain properties are barium titanate, BaTiO_3 , and $(\text{CH}_2\text{NH}_2\text{COOH})_3\text{H}_2\text{SO}_4$ (triglycine sulfate — abbr. TGS).

Similarly, applying a properly oriented shear stress to the system illustrated in Fig. 1.3 we will make favorable one of the structures S_A and S_B , having different signs of the shear deformation of the unit cell. In practice, the shear stress is realized as a compressive stress along an axis making an angle of 45° with the crystal axes and its sign is reversed when compression is applied perpendicularly to the previous one. In this way we can achieve a hysteretic dependence of strain on stress, such as shown in Fig. 1.5b (Gridnev et al., 1990). A ferroic with this feature is called *ferroelastic*. Here we come very close back to the concept of mechanical twins but — since we now base our approach on the existence of the original unperturbed structure S_G — families of materials offering mechanical twins and ferroic materials are not identical. A model ferroelastic crystalline material is lead phosphate, $\text{Pb}_3(\text{PO}_4)_2$.

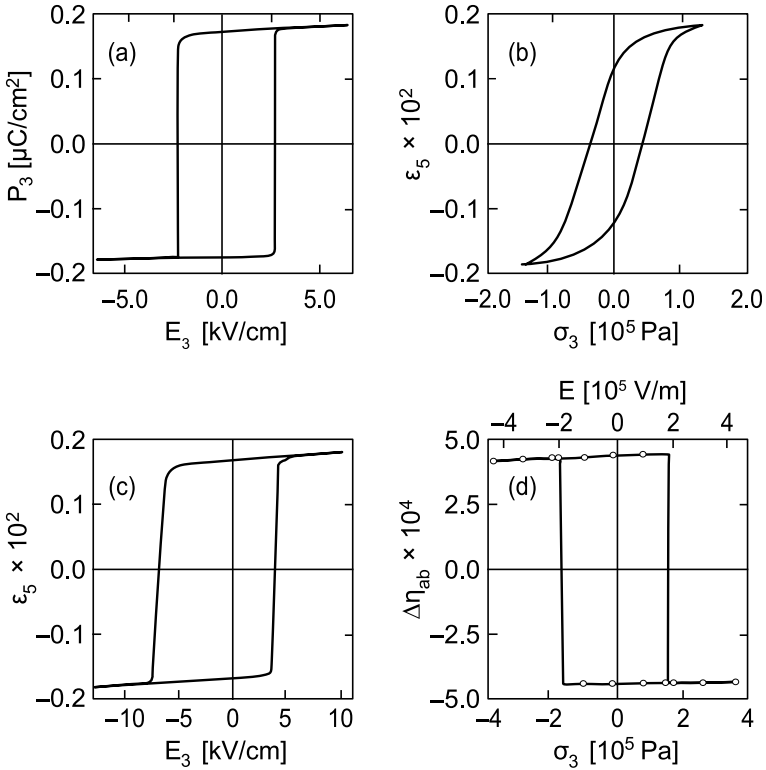


Fig. 1.5 (a) Ferroelectric hysteresis loop: hysteretic dependence of polarization on applied electric field (at a frequency of 1 mHz) in a crystal of gadolinium molybdate (GMO) (Kumada et al., 1970). (b) Ferroelastic hysteresis loop: hysteretic dependence of deformation on applied stress in a crystal of $\text{KH}_3(\text{SeO}_3)_2$ (Gridnev et al., 1990). (c) Hysteretic dependence of deformation on applied electric field in a crystal of GMO (Kumada et al., 1970). (d) Linear birefringence of a GMO crystal as a function of applied electric field or mechanical shear stress (Kumada et al., 1970)

Definitions given above are to a certain extent approximate. We shall pay more attention to this terminology in the following chapter where also other kinds of ferroics will be introduced.

The mentioned properties appear even more interesting when we look at some numerical values. In a normal dielectric like mica or rutile, with the relative permittivity value say 40, an electric field of 1 kV/cm induces polarization, equal to the surface charge density, in the amount of about $40 \mu\text{C}/\text{m}^2$. The same field can bring about polarization reversal in a ferroelectric sample with spontaneous polarization of $20 \mu\text{C}/\text{m}^2$ and this leads to the surface charge change of $40 \times 10^4 \mu\text{C}/\text{m}^2$, a value $10,000 \times$ higher. For a normal elastic material, whether sodium chloride or copper, the elastic compliance is of the order of $10^{-11} \text{m}^2/\text{N}$ so that an applied stress say $2 \times 10^4 \text{N}/\text{m}^2$ induces deformation

2×10^{-7} . The same strain can cause reversal of spontaneous strain of a ferroelastic crystal in the amount of 2×10^{-3} . For this impressive “amplification” of effects by a factor of 10^4 , however, we pay a price in terms of nonlinear and hysteretic behavior.

Appearance of the spontaneous polarization in F phase, depending on the symmetry of G phase, can lead to the deformation of the unit cell of the crystal. In the case of the structure shown in Fig. 1.2 this does not happen. However, adding more atoms to the unit cell of this structure thus lowering its symmetry, one can obtain a structure where the appearance of the spontaneous polarization along the c -axis will be entailed with a shear deformation in the perpendicular plane as shown in Fig. 1.3. It is obvious that in such structure, changing polarization by electric field may lead to reversing the shear strain at the same time. We thus observe a hysteretic dependence of strain on applied field. It is represented in Fig. 1.5c. This phenomenon can exist in ferroics which are simultaneously ferroelectric and ferroelastic. Barium titanate and GMO are well-studied representatives.

The two domain states in GMO differ also in birefringence and this fact manifests itself in yet another characteristic of domain reorientation, reproduced in Fig. 1.5d. Thus ferroics offer a large variety of characteristic macroscopic phenomena.

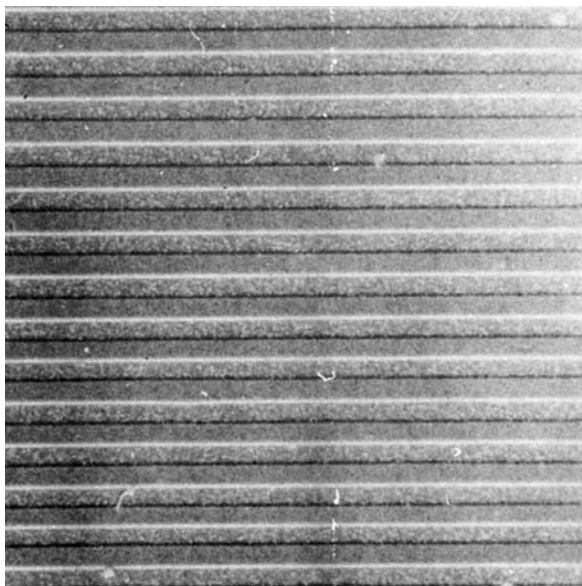
The hysteresis loop is often considered a defining feature of ferroics and of ferroelectrics in particular. The stability of either of two states when the applied force is zero is the basis of a memory device. Switching times of the order of tens or hundreds of nanoseconds are typically achieved in good single crystals at high fields. It has been established that domain walls can move faster than the velocity of sound. In thin films, switching times are not far from hitting the picosecond limit. A remarkable feature of a ferroelectric loop is that together with polarization a number of other “coupled” properties are switched, as we have just demonstrated. This opens a way to alternative methods of detecting in which state the memory device dwells at any given moment, as well as to many other application aspects. On the other hand, the polarization reversal is coupled with behavior of free charge carriers, making processes complicated; in ferromagnetics, this issue does not exist.

While the states on the hysteresis loop are transient, multidomain states can, of course, exist also in static conditions, often representing metastable states with a long lifetime. Multidomain structures which can live for very long time can also be created artificially. Figure 1.6 gives an example of an artificial regular domain pattern in a crystal of LiNbO_3 (Feisst and Koidl, 1985) “engineered” for nonlinear optical applications.

Because domain states differ in the orientation of crystallographic axes, there exist a large number of methods to observe domain structures, ranging from surface etching and decoration techniques, polarized light microscopy, and nonlinear optical scattering to high-resolution electron microscopic methods.

Domain reorientation phenomena as well as characteristics of samples in multidomain states offer manifold applications. Though, in this book, we are

Fig. 1.6 Artificially produced periodic domain pattern serves to enhance optical second harmonic generation. Etched surface of a LiNbO_3 crystal imaged by a scanning electron microscope. Reprinted with permission from Feisst and Koidl (1985). Copyright (1985), American Institute of Physics



not going to address practical applications of ferroic domain, let us shortly mention some of them. Domain reorientation is an absolutely essential process when preparing piezoelectric ceramics; note that a ceramic sample containing chaotically oriented grains of a typical piezoelectric material would reveal zero or negligible piezoelectric response. Only when grains are subject to ferroelectric poling which is just the process of domain reorientation pertinent to the $P(E)$ hysteresis loop, the sample becomes piezoelectric. Most of today's electroacoustic devices utilize such ceramics. Behavior of domain walls in low electric fields greatly enhances dielectric and piezoelectric response of multidomain systems, which allows reaching values of material coefficients like permittivity or piezoelectric constants, which cannot be realized within homogeneous samples. One of the most characteristic applications of ferroelectric hysteresis is non-volatile random access memory. Domain processes in ferroelectric ferroelastics make it possible to electrically control light propagation in the material, with a number of practical aspects. Engineered domain structures such as the one shown in Fig. 1.6 offer nonlinear optical elements with greatly enhanced efficiency of second harmonic generation. Many promising applications are in the research or development stages. For example, controlled polarization reversal makes it possible to fix holograms in photorefractive ferroelectrics. Fast switching processes are often accompanied by bursts of emitted electrons or light and these phenomena promise several practical aspects.

The goal of the preceding paragraphs was to give a qualitative and introductory overview of some of the topics to be discussed in detail in this book. In

what follows we start with introducing basic theoretical approaches to structural phase transitions, emphasizing the symmetry and phenomenological aspects of their classifications (Chapter 2) and give an overview of typical ferroic materials (Chapter 3). After a survey of experimental methods used to visualize domain patterns (Chapter 4) we shall review a number of aspects of domain formation and what their typical shapes are (Chapter 5). Chapter 6 will address the static properties of domain walls. The short Chapter 7 will be devoted to the experimental characterization of switching. The largest chapter of the book, Chapter 8, will cover the theoretical and experimental aspects of the polarization response of ferroelectrics. In Chapter 9, we have attempted to give a comprehensive overview of the domain-related properties of ferroelectric thin films. Originally, we planned to include the book chapters on domains in bulk ceramics, on domain issues in ferroics revealing an incommensurate phase and relaxors, and one which would cover practical applications of domain phenomena in ferroic; however, the time factor urged us to limit the scope of the book. These issues are only briefly mentioned in places.

This book is intended for students and researchers who are familiar with just a small part of the whole field or who are beginners. When writing it we have tried to follow a “bi-modal” approach. If something can be explained or derived in a relatively simple way, we present a detailed explanation or derivation. On the other hand, if the relevant story was, in our opinion, complicated, we present only the results referring the reader to the original papers for the explanations.

Perhaps we can end this chapter by referring to other literature, in the book form, on domain phenomena in nonmagnetic ferroics. The more recent books on ferroelectrics include works by Smolenskii et al. (1984), Xu (1991), Strukov and Levanyuk (1998), Wadhawan (2000), and by Rabe et al. (2007). In all of them the various domain issues are well treated, of course without going into details and using quite different approaches. Recently published books edited by Hong (2004), Alexe and Gruverman (2004), and Kalinin and Gruverman (2006) offer a wealth of information on domains on nanoscale and their characterization with Scanning Probe Techniques. The theoretical work of Toledano and Toledano (1988) provides the reader with the background required to analyze domain states on the basis of symmetry and thermodynamics. A small but very informative monograph on some aspects of ferroelectric domains has been published by Fesenko et al. (1990). Ferroelastic domain phenomena are treated extensively in Salje’s book (1990) on ferroelastics. A very informative book on the theory of domain-related phenomena was published by Sidorkin (2006). Close attention was paid to domain phenomena in several older monographs on ferroelectricity (Jona and Shirane, 1962; Fatuzzo and Merz, 1966; Lines and Glass, 1977; Burfoot and Taylor, 1979). There also exist a number of relevant review papers. They will be pointed out later in the corresponding chapters.

Chapter 2

Fundamentals of Ferroic Domain Structures

2.1 Structural Phase Transitions and Domain States: Basic Concepts and Classifications

2.1.1 Structural Changes at Phase Transitions: Ferroics

In this section we introduce the basic concepts required to discuss structural phase transitions in crystals on the basis of a symmetry approach. The latter is in fact closely connected with the Landau theory of phase transitions, to which we come later in this chapter. However, for the reader who is more oriented toward domain properties without studying the nature of phase transitions themselves, it may be practical to become acquainted with the symmetry approach in the first place. The analysis of domain states on the basis of symmetry gives essential information on the number of domain states and on how they can be distinguished. It is this information that forms the background of any considerations about domain reorientation processes, about domain walls, as well as about properties and applications of multidomain samples.

Speaking about a structural phase transition, we always compare two different crystal structures S_G and S_F between which the transition is realized. The difference between S_G and S_F is not trivial: We have in mind changes in the crystal structure, which cannot be described by a mere thermal expansion (due to change of temperature) or by a mere compression (due to change of hydrostatic pressure). Our structural changes are more dramatic, although they are also brought about by change of temperature or pressure. Such transitions are known to occur in several thousands of crystalline substances (Tomaszewski, 1992a,b; Tonkov, 1992). They can be classified according to a number of different criteria.

On the first level of categorization we have to distinguish between *distortive* and *reconstructive transitions* (Gränicher and Müller, 1971). In the latter case, the structures S_G and S_F have nothing in common except for chemical composition. A reconstructive transition requires indeed a complete reconstruction of the atomic structure so that chemical bonds are broken and because of that the process itself usually involves formation of dislocations and proceeds

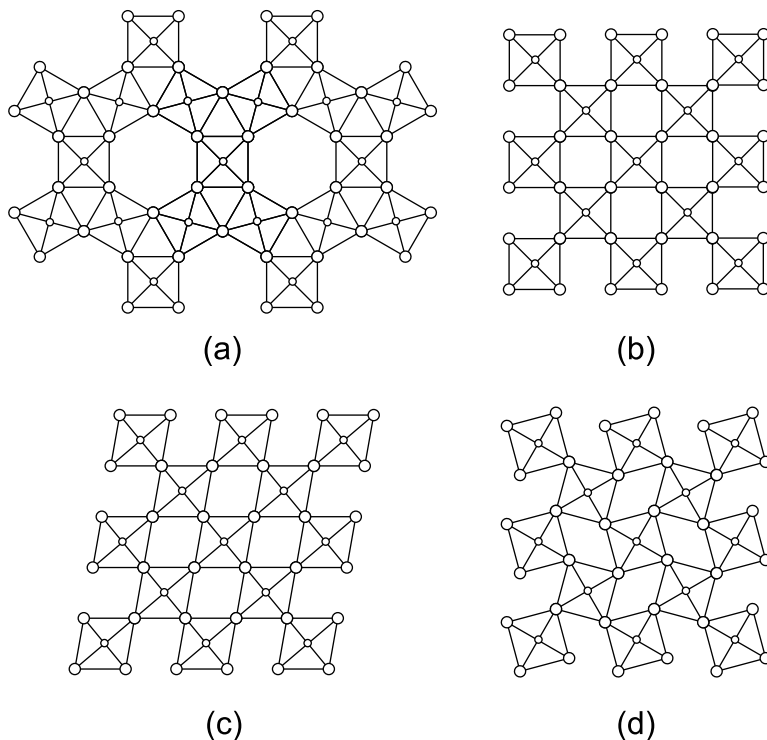


Fig. 2.1.1 Models of possible distortions of crystal structure

sluggishly. Figure 2.1.1 (in part reproduced from the book of Rao and Rao (1978)) shows schematically atomic arrangements in four different crystal structures. Transformation from the structure (a) to any of the other structures requires breaking of first coordination bonds and would represent a reconstructive transition. Well-known examples of such transitions include that between sphalerite- and wurtzite-type structures in ZnS , one between arsenolite and claudetite structures of As_2O_3 , or that between the β -phase (body-centered cubic) and hexagonal or rhombohedral modifications of titanium. Domain states as they are presented in this book do not concern reconstructive phase transitions.

In contrast, at a *distortive transition* the spatial system of crystal bonds forming the structure S_G becomes systematically distorted, without disrupting the linkage of the network. Thus, in Fig. 2.1.1, the structure (c) or (d) can be conceived as a slightly changed structure (b), due to coordinated shifts of atoms. By these distortions the crystal structure goes over into S_F and it is obvious that by doing so the crystal symmetry also changes, from symmetry group G to symmetry group F . Here G and F stand for the symbol of 32 point groups. As it is usual, we shall always use the symbol G or S_G when referring to the higher

symmetry phase and F or S_F when referring to the lower symmetry phase. Thus for distortive transition the group—subgroup relation holds, namely

$$F \subset G. \quad (2.1.1)$$

This is one of the essential features of distortive phase transitions and offers different ways for their further classifications. Logically now, the phase with the symmetry G (or shortly the phase G) is referred to as the *parent* or *prototypic* or *high-symmetry phase* while the phase with symmetry F (or shortly the phase F) is called *distorted* or *low-symmetry phase*.¹ Since the transition between the two phases is often monitored as a function of temperature (at some *transition temperature* T_{TR}) and, as a rule, the symmetry is lowered on cooling, phases G and F are often mentioned as *high-temperature* and *low-temperature phases*, respectively.

Before pursuing further the symmetry issues, however, we mention one further classification of distortive transitions. Depending on the basic type of thermal motion of the structural units related to the transition, one distinguishes *displacive* and *order–disorder transitions*. Speaking about the symmetry of a crystal, one considers the symmetry of the structure formed by the average positions of atoms involved in thermal motion. If the atoms controlling the symmetry change at the transition perform small harmonic oscillations² around their average positions, one classifies the transition as *displacive*. In this case, physically, the symmetry change at the transition is controlled by displacements of bottoms of the potential wells, where the atoms oscillate. If the atoms controlling the symmetry change at the transition perform thermally activated jumps between two or more equilibrium positions, one classifies the transition as *order–disorder*. In this case, the symmetry change is controlled by the distribution of the atoms between these positions: In the high-symmetry phase the atoms are equally distributed between them, whereas in the low-symmetry phase, this distribution becomes asymmetric resulting in a displacement of the average positions of atoms.

In real systems, both types of transitions are represented as well as more complicated cases with mixed behavior. To illustrate the modifications of a structure accompanying a real displacive phase transition, we will consider below the cubic–tetragonal transition in BaTiO_3 . Here we will follow the classical scenario of this transition; however, more complicated scenarios of it are also under discussion (Stern, 2004).

Figure 2.1.2a illustrates the perovskite-type structure of BaTiO_3 , in the cubic phase. On cooling, at $T_{\text{TR}} \cong 126^\circ\text{C}$ it transforms into the tetragonal phase. Choosing as a reference the positions of barium ions, what happens at T_{TR} (cf.

¹ Coupling a *parent* together with something *distorted* or *low symmetry* is somewhat ungraceful. Indeed Wadhawan's (1982) *daughter phase* would be more elegant.

² Since these oscillations occur around the equilibrium positions that are temperature dependent, it would be more rigorous to call such oscillation quasi-harmonic.

Fig. 2.1.2 Perovskite-type structure of BaTiO_3 : (a) unit cell in the cubic phase and (b) atomic displacements at cubic to tetragonal transition

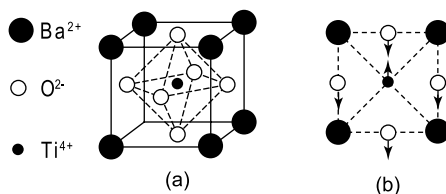
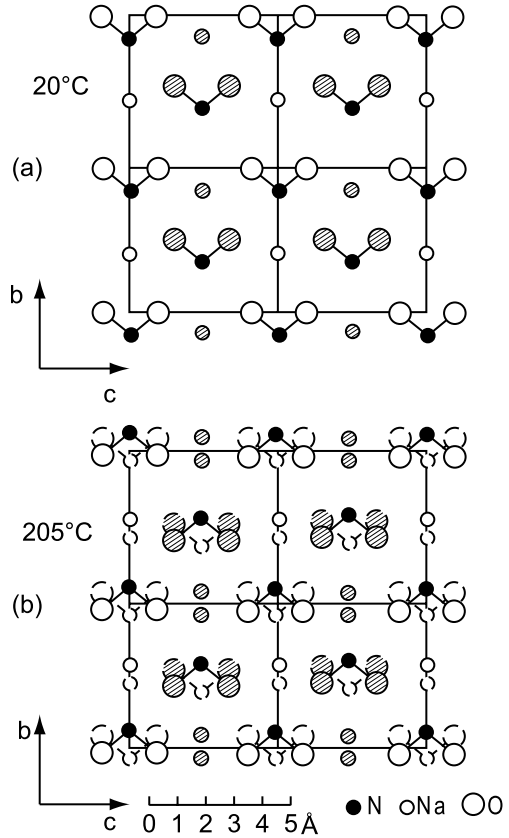


Fig. 2.1.2b) is that all titanium ions undergo a small shift along one of the cubic axes, say “upward.” There are two kinds of oxygen ions in nonequivalent positions, O_I and O_{II} ; both shift “downward,” though by different amounts. It is obvious that these shifts violate several symmetry operations of the original cell: center of symmetry, mirror plane (001), the twofold axis [010], to name a few which are obvious from this two-dimensional projection onto the (100) plane. Considering now the situation in three dimensions, as a result of these ionic displacements the point group symmetry $G = m\bar{3}m$ is lowered to $F = 4mm$ which of course is a subgroup of G .

A classical example of an order–disorder transition is provided by sodium nitrite, NaNO_2 . This crystal undergoes the order–disorder transition from $G = mmm$ to $F = mm2$ at about $T_{\text{TR}} = 163^\circ\text{C}$ (at this moment we disregard the intermediate phase which exists in a narrow temperature interval). In Fig. 2.1.3a, its unit cell is shown schematically in its ferroelectric phase. Here we assume that the NO_2 groups are fully ordered, their dipole moments all pointing along the direction of the b -axis. In fact there is partial disorder, since the probabilities of finding the NO_2 groups oriented against the b -axis is not zero so that the net dipole moment is less than maximum. Above T_{TR} the probabilities of finding the NO_2 groups in two symmetric positions become equal (Fig. 2.1.3b) so that the structure acquires an additional symmetry element — a mirror plane. Thus the net dipole moment disappears, and the average symmetry of the lattice becomes higher.

The difference between displacive and order–disorder transitions is vital when studying lattice dynamics and temperature dependences of some macroscopic properties. It does not seem to have a significant bearing on domain phenomena. On the other hand, properties of domains, their shapes, and dynamic behavior are closely related to the G – F relations. In this book, therefore, we shall base our classifications and many approaches on symmetry considerations. The symmetry approach is usually based on considering the point symmetries G , F but also on the possible change of the unit cell volume. Any phase transition fulfilling relation (2.1.1) is called a *ferroic transition* and F itself is the point group of the *ferroic* phase. Looking at the number of atoms in the unit cell, there are two possibilities. First, the number of molecular units in the primitive unit cell, or — less exactly — volume of the unit cell may not change. That is, the translational symmetry is preserved. Then we speak about a *ferrodistortive ferroic*. The phase transition from (b) to (c) in Fig. 2.1.1 obviously fulfills this requirement and the previously mentioned example of BaTiO_3 belongs to this category. Alternatively, even the translational symmetry

Fig. 2.1.3 Atomic structure of NaNO_2 . Projection along the a -axis: (a) ferroelectric phase. The NO_2 groups are planar and lying in the bc plane. The groups with the clear oxygen circles are in the plane of the figure; those with the shaded oxygen circles are displaced by a half of the lattice constant along the a -axis. The clear sodium circles are in the plane of the figure; those with the shaded sodium circles are displaced by a half of the lattice constant along the a -axis. (b) Paraelectric phase. NO_2 groups and Na ions are equally distributed between two positions shown with solid and dashed lines



may change at the phase transformation, as it is obvious in a hypothetical transition from (b) to (d) in Fig. 2.1.1. The crystal of lead zirconate PbZrO_3 provides a well-known example. In its parent phase, its cubic structure is identical with that of barium titanate shown in Fig. 2.1.2a and its unit cell contains just one formula unit. At temperature $T_{\text{TR}} \cong 230^\circ\text{C}$ the atomic structure undergoes changes primarily characterized by shifts of lead ions along one of the original $[110]$ directions which becomes the a -axis of the new orthorhombic phase of symmetry $mm2$. In neighboring cubic cells these shifts are antiparallel. This is an example of a phase transition which is referred to as *antiferrodistortive*. This type of distortion will be accompanied by an increase of the number of formula units in the primitive unit cell (from one to eight in the case of PbZrO_3). Naturally, this is the same as saying that the translational symmetry has changed. To describe the unit cell multiplication one introduces the factor

$$v = Z_G/Z_F \cong V_G/V_F, \quad (2.1.2)$$

where Z_A is the number of formula units and V_A is the volume of the primitive unit cell (neglecting the effect of thermal dilatation) in the phase of group

symmetry A . Materials are known in which the phase transition is accompanied only by a change of the translational symmetry while the point symmetry remains the same: $G = F$ but $v > 1$. These are referred to as *nonferroics* and in this book their properties will not be considered. As examples, we can mention potassium cyanide, KCN, ($v = 2$) or $\text{CH}_3\text{NH}_3\text{CdCl}_4$ ($v = 4$). In some cases, such a transition is characterized by a change of the space symmetry group but in others even that remains the same in both phases. Tolédano and Tolédano (1982) performed a symmetry analysis of all possible nonferroic phase transitions and gave a number of concrete examples.

In the following three sections we shall categorize ferroics according to macroscopic properties absent in the parent phase but newly revealed in the ferroic phase, which is the most significant aspect in understanding domain-related phenomena.

2.1.2 Ferroelectric Phase Transitions

In a way, ferroelectrics are the simplest ferroics since domain states in them differ in the orientation of a tensor of the lowest possible rank, a vector. Let us discuss the definition of a ferroelectric phase transition by which is usually meant a transition from a nonferroelectric phase G into a ferroelectric phase F . In an uncomplicated approach it is said that the *phase transition is ferroelectric* when, as a result of it, there exists *spontaneous polarization* \mathbf{P}_S in the phase F . In many cases this “ \mathbf{P}_S definition” is fully satisfactory from most points of view and we shall be using it—as almost everyone—as a shorthand. However, it does not respect the problem of determining the notion of polarization itself and fails to provide an appropriate basis for describing transitions from a phase which is already polar. We shall, therefore, discuss this point in more detail.

Polarization is customarily defined as the dipole moment per unit volume of the system of charges in the material. However, as it was recently realized (Tagantsev, 1987, 1991, 1993; Resta, 1994), for a medium with a periodic distribution of charge, the dipole moment density cannot be unambiguously introduced as a bulk property of the system. Clearly, for any finite and electro-neutral part of this structure, one can calculate, using the charge distribution, the average dipole moment density. However, the fact that the result of the calculation depends on the way in which the part was specified shows that this result does not represent a bulk property of the structure. On the other hand, a variation of the dipole moment density resulting from small changes of charge positions is defined unambiguously, not suffering from the aforementioned dependence. This enables an unambiguous definition of variation of polarization as that of the dipole moment density. Thus, any rigorous definition of the ferroelectric phase transition should deal with changes of polarization or its derivative with respect to other physical variables rather than with the polarization itself.

One possibility of such a definition is based on the *pyroelectric effect*. One considers the *pyroelectric coefficient* \mathbf{p} , a vector defined as the derivative of polarization with respect to temperature, at zero electric field in the material. Its components are

$$p_i = \left(\frac{\partial P_i}{\partial T} \right)_{E=0}. \quad (2.1.3)$$

Clearly, \mathbf{p} is a polar vector. The experimental manifestation of the pyroelectric effect is a change δQ of bound charge density on the surface of a plate-like sample cut obliquely to \mathbf{p} when its temperature is changed by δT . Since $\delta Q = \delta D_n = \varepsilon_0 \delta E_n + \delta P_n$, where δD_n , δE_n , and δP_n are changes of components (normal to the plane of plate) of the electric displacement, electric field, and polarization, respectively, the condition $E = 0$ implies $p = \delta Q / \delta T$.

The symmetry of a material puts serious restrictions on the existence and orientation of \mathbf{p} . It can only have nonzero components in samples of materials represented by one of the point symmetry groups 1, 2, m , $mm2$, 4, $4mm$, 3, $3m$, 6, $6mm$, or Curie groups ∞ and ∞m . These are referred to as *polar groups*. While point groups describe symmetries of crystalline media, the Curie groups ∞ and ∞m have been included since they play a role in nonuniform ferroelectric systems such as ceramics or polymers. If the group F is polar while G is not, we speak about a *ferroelectric phase transition*; F is then the symmetry of the *ferroelectric phase*. It may, however, happen that already G is a polar group and that on transforming from G to F the vector \mathbf{p} just acquires new components. We believe that it is reasonable to call the latter transition ferroelectric to have uniformity in the definition of all nonmagnetic phase transitions. Thus, we arrive at the following definition of a *ferroelectric transition*:

A phase transition is called ferroelectric if it results in a lower symmetry phase in which the vector of pyroelectric coefficients acquires new components which were zero, by symmetry, in the high-symmetry phase.

A convenient variable for a description of the properties of material in the ferroelectric phase is the vector of *spontaneous polarization* \mathbf{P}_S . At a given temperature T_f in the ferroelectric phase we define it as the change of polarization during cooling from a temperature in the paraelectric phase T_p down to T_f , i.e.,

$$\mathbf{P}_S(T_f) = \int_{T_p}^{T_f} \mathbf{p}(T) dT. \quad (2.1.4)$$

Concerning the accepted definition of spontaneous polarization the following remarks should be made.

First, as we will see in the section of this chapter devoted to the thermodynamic description of the phase transitions, this definition is in perfect correspondence with that accepted in phenomenological theories.³ Second, though

³ Spontaneous polarization at T_{TR} may appear discontinuously. This is so for transitions of the first order, as discussed in detail in Sect. 2.3. Then the corresponding component of \mathbf{p} at

Eq. (2.1.4) unambiguously defines the variable $\mathbf{P}_S(T_f)$ called spontaneous polarization at temperature T_f , the values of \mathbf{P}_S , in general, cannot be associated with the average dipole moment density calculated on the basis of the charge density in the material at this temperature. The reason is that it is not possible to introduce the dipole moment density unambiguously as a bulk property of the material as has been discussed at the beginning of this section. Thus, one should consider the definition given by Eq. (2.1.4) as a convention.

The magnitude of spontaneous polarization depends on temperature. In a typical case it increases with decreasing T . Several tens of degrees below T_{TR} it acquires a value which is characteristic for the given class of materials but greatly varies for different kinds of materials. For most ferroelectrics this value lies within limits 10^{-3} – 1 C/m² (0.1–100 μ C/cm²).

One should mention that the direct application of the above definition of the spontaneous polarization does not provide a convenient method of experimental determination of \mathbf{P}_S . However, based on this definition a much more practical method can be formulated. As we will see later, in principle, in the low-symmetry phase, the direction of vector \mathbf{p} can be changed by application of a pulse of electric field or mechanical stress, the absolute value of \mathbf{p} being unchanged. This procedure is called switching. In a typical case, the switching can result in changing the sign of \mathbf{p} . Then, as seen from Eq. (2.1.4), the switching will result in a change of sign of polarization \mathbf{P}_S defined according to this equation. Thus, in this case, measuring the change of polarization which accompanies the switching, one gets the values of $2\mathbf{P}_S$ and finally determines a value of \mathbf{P}_S without integration of the pyroelectric coefficient.

A definition which is very often employed states that the *phase transition is ferroelectric* when, as a result of it, there exists in the phase F spontaneous polarization \mathbf{P}_S whose direction can be reversed by applied electric field (the “reversal definition”). It is based on the fact that if the field is applied, the free energy of the material is minimum when \mathbf{P}_S directs along the field. This definition works well in many real cases. For instance, in a simple example of $G = 2/m$ and $F = 2$, it is obvious that \mathbf{P}_S may have either sign in F without changing the symmetry of this phase and can be reversed since it interacts with electric field. The “reversal definition” has two positive features. First, it stresses the fact that the medium in the phase F can exist in several states (domain states). Second, it points to the essential fact that the magnitude and direction of \mathbf{P}_S can be determined by measuring the charge, i.e., by integrating the electric current, when the direction of \mathbf{P}_S is changed by external forces. This is an alternative to the method based on pyroelectricity and if the material allows it, it represents a much more practical option.

T_{TR} is represented by a δ -function and this must be respected in integral (2.1.4). In real experiments, every component of \mathbf{P} emerges continuously, be it because of even slightly inhomogeneous distribution of temperature in the measured sample or because a phase front between the two phases travels across the sample. Thus integrating the electric current gives a correct information on \mathbf{P}_S .

However, this definition is not general enough to cover all possibilities. First, the symmetry requirements imposed by condition (2.1.1) may not allow for reversibility of \mathbf{P}_S , i.e., for the change of its sign; rather than that of \mathbf{P}_S may exist in several directions which need not include antiparallel pairs of polarization vectors, as it will be discussed later in detail. This hindrance can be easily corrected by replacing “reversibility” by “reorientability.” Second and more important, for a particular material and under given conditions, an experimentalist may not be capable of inducing the change of \mathbf{P}_S direction. This possibility is a major setback for the “reversal definition”. It would eliminate from the family of ferroelectrics many materials in which the change of \mathbf{P}_S direction has not yet been experimentally accomplished although by symmetry requirements and structural considerations it should be possible. In crystals of lithium niobate, which undergoes the $G = \bar{3}m$ to $F = 3m$, the change of \mathbf{P}_S direction was not realized for many years and yet it was clear that the material is ferroelectric; in fact in grown crystals the existence of regions with antiparallel polarization was well established. We can conclude that the “reversal definition” describes the sufficient but not necessary condition for ferroelectricity.

In view of the above discussion it appears practical to stress the symmetry aspect in the definition of a ferroelectric. The phase transition is ferroelectric if as a result of the transition the pyroelectric vector \mathbf{p} acquires new components in F which were zero, by symmetry, in G . The material in the phase of symmetry F is ferroelectric if at some temperature and pressure it undergoes a ferroelectric phase transition from G to F . In some cases, however, even this definition cannot be literally applied: Some materials, like guanidinium aluminum sulfate hexahydrate (abbr. GASH), reveal all features typical for a ferroelectric (hysteresis loop, domains) at room temperature but on heating they decompose before the temperature T_{TR} is reached. Then the phase G remains hypothetical; however, should the phase F be ferroelectric, it must be possible to construct the S_G structure of higher symmetry by small distortions of the structure S_F .

One more remark concerning the use of pyroelectric coefficient in the definition of ferroelectrics should be made. This use, besides the conceptual aspect, could be of practical interest when determination of polarization change during switching is experimentally hindered. This situation has been recently encountered in polymer–ferroelectric thin films, where switching of the sign of the pyroelectric coefficient has been used for the attribution of the materials’ ferroelectric character (Bune et al., 1998).

When treating the domain issues, symmetry considerations play an essential role. In most cases, therefore, we shall stick to the “symmetry definition”.

2.1.3 Ferroelastics and Ferrobielectrics

2.1.3.1 Ferroelastic Phase Transition

In the previous section we have seen that the change of crystal symmetry from G to F may result in a change of symmetry requirements imposed on the

pyroelectric coefficient \mathbf{p} , a polar vector, and that this leads to the definition of a ferroelectric phase. Now we shall show that changes in a second-order (symmetric) tensor can be treated in a similar way and lead to the definition of another kind of ferroic. Consider the thermal dilatation tensor which is a symmetric second-rank tensor with components α_{ij} . The requirements on its nonzero components and on possible relations between them are the same for all crystallographic classes which belong to the same system. Thus, for instance, in all tetragonal classes $\alpha_{xx} = \alpha_{yy}$ and α_{zz} are two independent nonzero components while $\alpha_{yz} = \alpha_{zx} = \alpha_{xy} = 0$; this describes thermal dilatation of a tetragonal cell characterized by two lattice parameters a , c . If, as a result of a phase transformation, the symmetry requirements on the tensor α_{ij} change, such a phase transition, as well as the resulting phase F , is referred to as *ferroelastic* (Aizu, 1969; Toledano and Toledano, 1988). The quantitative form of this definition can be given as follows: A transition is called ferroelastic if it results in a low-symmetry phase in which the thermal dilatation tensor changes the number of its independent components with respect to those in the high-symmetry phase. The low-symmetry phase is referred to as ferroelastic as well. It is obvious that the tensor α_{ij} change is connected with the change of the unit cell shape.

If this requirement is not met, the phase F and the transition are called *nonferroelastic*. It is useful to remark that, since the thermal dilatation tensor of materials belonging to different groups of the same crystalline class has the same number of independent components (Nye, 1992), no ferroelastic transition are possible between G and F belonging to the same class. The same holds for transitions from a hexagonal G phase to a trigonal phase F . Sometimes the concept of *crystal family* of a point group P is defined as including all point groups belonging to the same crystal system as P with the exception of the trigonal groups which are attributed, together with the hexagonal groups, to the hexagonal family. Using this concept, the phase transition is said to be ferroelastic if G and F belong to different crystal families.

2.1.3.2 Natural Spontaneous Strain

Considering a ferroelastic phase F , it is evident that since the shape and size of the unit cell has changed, this change can be expressed as a *deformation* impressed upon the unit cell in G . If we have in mind a uniform sample or infinite medium, rotations which are a part of the distortion tensor are not essential (Nye, 1992) and the strain we are interested in can be described by a symmetric second-rank tensor. Thus, it looks reasonable to use this strain to characterize material in the ferroelastic state by introducing the concept of *spontaneous strain* tensor. It may be defined in different ways, depending on the purpose for which it should be used. In this section we shall define *natural spontaneous strain*, ϵ_S . Its components $\epsilon_{S_{ij}}$ describe precisely how the unit cell in the parent phase has to be deformed to reach the unit cell in the ferroic phase. To make this definition exact we specify that when evaluating $\epsilon_{S_{ij}}$ at a given

temperature, the parameters of the unit cell of the parent phase are linearly extrapolated to this temperature. The natural spontaneous strain can be linked to the dilatation tensor in a similar way as spontaneous polarization was linked to the pyroelectric coefficients in the previous section, namely, for a given temperature T_f in the ferroelastic phase

$$\varepsilon_{S_{ij}}(T_f) = \int_{T_p}^{T_f} (\alpha_{ij}(T) - \alpha_{ij}(T_p)) dT, \quad (2.1.5)$$

where T_p is a temperature in the parent phase.⁴

Considering a particular transition, the task of evaluating $\varepsilon_{S_{ij}}$ is twofold. First, we wish to determine which components of ε_S are nonzero or what relations between them are fulfilled; second, we may be interested in the numerical values of the ε_S components.

Let us start with the first question. Consider a particular transition from cubic $G = m\bar{3}m$ to orthorhombic $F = mm2$. The answer, naturally, depends on the mutual orientation of the symmetry elements of G and F . Let us fix the cubic reference frame for both structures (with the z -axis parallel to a fourfold axis of G and to the twofold axis of F , respectively). Figure 2.1.4a shows the orientation of the relevant mirror planes in G . There are two possibilities for the orientation of mirror planes in F , which can be specified as $m_x m_y 2_z$ and $m_{xy} m_{\bar{xy}} 2_z$. We will use further in the book this self-evident way of notation of the orientation of the elements in F . In the first case illustrated in Fig. 2.1.4b, the spontaneous strain tensor has three independent components $\varepsilon_{S_{xx}}$, $\varepsilon_{S_{yy}}$, $\varepsilon_{S_{zz}}$. A possible temperature dependence of the unit cell parameters is shown schematically in Fig. 2.1.5a. The change of the unit cell in the second case, for $F = m_{xy} m_{\bar{xy}} 2_z$, is illustrated in Fig. 2.1.4c. In this case, clearly, the nonzero natural strain components are

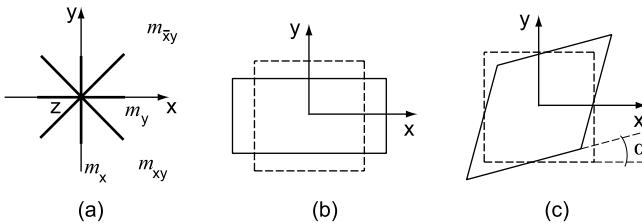


Fig. 2.1.4 Two possible transitions from $G = m\bar{3}m$ to $F = mm2$ result in different spontaneous deformation components: **(a)** orientation of mirror planes passing through the z -axis in the point group $m\bar{3}m$; **(b)** and **(c)** schematic representations of changes of the cubic unit cell (*dashed*) into the orthorhombic unit cell at transitions $m\bar{3}m - m_x m_y 2_z$ and $m\bar{3}m - m_{xy} m_{\bar{xy}} 2_z$, respectively

⁴ In case of the first-order phase transition the reader should consider a remark similar to that connected with Eq. (2.1.4).

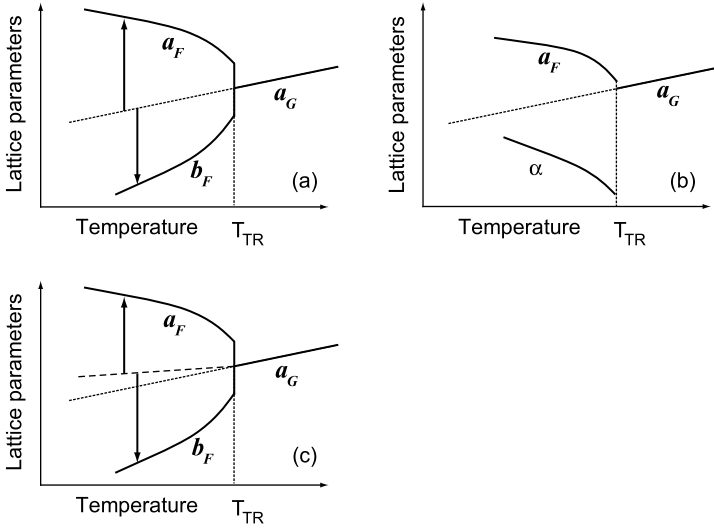


Fig. 2.1.5 Temperature dependence of unit cell parameters in the XY plane, schematically: (a) and (b) apply to (b) and (c) in Fig. 2.1.4, respectively. *Dotted lines* show the cubic lattice constant linearly extrapolated to the low-symmetry phases, a_G . Angle α measures small rotation of the cubic axis a due to the shear ε_{xy} . In (a), *arrows* show natural spontaneous strains. In (c), *arrows* show Aizu spontaneous strains for the species illustrated in (a). The *dashed line* in (c) corresponds to the center term in Aizu's definition of strain

$\varepsilon_{S_{xx}} = \varepsilon_{S_{yy}}, \varepsilon_{S_{xy}}, \varepsilon_{S_{zz}}$. In this case, a possible temperature dependence of the cell parameters is shown in Fig. 2.1.5b. These two examples are simple enough that the components of natural spontaneous strain can be guessed. In more complicated cases we have to express the dilatation tensor in the phase F in the coordinate system of G and compare the result with the dilatation tensor of G , we see immediately which new components appear in F . According to Eq. (2.1.5) these new components define the tensor of natural spontaneous strain.

Table 2.1.1 illustrates how matrices of natural spontaneous strain components are determined for the two just mentioned and two additional transitions. The symbols $\delta\varepsilon_{kl}$ or ε_{kl} stand for symmetry-allowed changes of the unit cell, induced by a change of temperature in the phase of symmetry G or F . These matrices have the same structure as that of the thermal dilatation tensors.

Table 2.1.1 Thermal strain matrices for four ferroelastic species with the $m\bar{3}m$ parent phase

$G = m\bar{3}m$	$F = m_x m_y 2_z$	$F = m_{xy} m_{xy} 2_z$	$F = m_z$	$F = m_{xy}$
$\delta\varepsilon_{xx}$	$\delta\varepsilon_{xx}$	$\delta\varepsilon_{xx}$	$\delta\varepsilon_{xx}$	$\delta\varepsilon_{xx}$
$\delta\varepsilon_{xx}$	$\delta\varepsilon_{yy}$	ε_{xy}	ε_{xy}	ε_{xy}
$\delta\varepsilon_{xx}$	$\delta\varepsilon_{zz}$	$\delta\varepsilon_{xx}$	$\delta\varepsilon_{yy}$	$\delta\varepsilon_{zz}$
		ε_{xy}	ε_{xy}	$-\varepsilon_{yz}$
		$\delta\varepsilon_{xx}$	$\delta\varepsilon_{yy}$	ε_{yz}
		$\delta\varepsilon_{zz}$	$\delta\varepsilon_{zz}$	$\delta\varepsilon_{zz}$
				$-\varepsilon_{yz}$
				ε_{yz}
				$\delta\varepsilon_{zz}$

However, compared to customary tables given in textbooks on crystal physics, for each subgroup F they are expressed in the reference frame of G . Each nonzero component for a given F represents a nonzero component of natural spontaneous strain. Let us again pay attention to the transition from $G = m\bar{3}m$ to $F = m_{xy}m_{\bar{xy}}2_z$. We see that the strain component $\varepsilon_{S_{xy}}$ appears newly in the phase F . It was forbidden by symmetry in the parent phase G and is, therefore, referred to as the *symmetry-breaking strain* component. In the table such components are given without the prefix δ . But there is one more feature in F which is new as compared to G , namely, that $\delta\varepsilon_{zz} \neq \delta\varepsilon_{xx}$. Thus, also the nonzero difference $\varepsilon_{S_{zz}} - \varepsilon_{S_{xx}}$ has the property of breaking the symmetry of G . The reader can easily recognize other symmetry-breaking components of strain for the transition from $G = m\bar{3}m$ to $F = m_{xy}$.

Later we shall present a table of all possible ferroelectric transitions in which natural spontaneous strain tensor will be given in the just described manner.

The next question is how the components of $\boldsymbol{\varepsilon}_S$ can be determined numerically. Here, the answer is easier compared to the situation we faced with the problem of determining \mathbf{P}_0 since the unit cell is well defined already in the parent phase and its shape and dimensions can be determined by X-ray diffraction. The newly appeared components of $\boldsymbol{\varepsilon}_S$, are always nondiagonal components; their real values at a temperature $T_1 < T_{TR}$ equal their spontaneous values.

Consider now strain components which when standing alone are not symmetry breaking. Obviously, what characterizes their newly acquired magnitude is the difference between the value of the unit cell dimension say a_G in the phase G and that at the considered temperature T_1 in the phase F . In order to eliminate the influence of “normal” thermal dilatation, however, the value attributed to the phase G should be extrapolated to temperature T_1 . This is schematically represented in Fig. 2.1.5a which shows the meaning of the cell parameter a_G in the cubic phase (or extrapolated to the F phase) and parameters a_F and b_F in the phase $F = m_x m_y 2_z$. In this phase, obviously, all three components of the natural spontaneous strain can be written as

$$\varepsilon_{S_{11}} = \frac{a_F - a_G}{a_G}, \quad \varepsilon_{S_{22}} = \frac{b_F - a_G}{a_G}, \quad \varepsilon_{S_{33}} = \frac{c_F - a_G}{a_G} \quad (2.1.6)$$

where c_F is the lattice constant along the Z-direction in this phase.

In a general case, the natural spontaneous strain at a given temperature T_f in the ferroelastic phase F can be defined as

$$\varepsilon_{S_{ij}}(T_f) = \varepsilon_{F_{ij}}(T_f) - \varepsilon_{G_{ij}}(T_f), \quad (2.1.7)$$

where $\varepsilon_{F_{ij}}(T_f)$ and $\varepsilon_{G_{ij}}(T_f)$ denote the strain in the phase F and the strain in the phase G extrapolated to T_f , respectively. Clearly, as defined the natural spontaneous strain is independent of the reference states employed for calculations of $\varepsilon_{F_{ij}}(T_f)$ and $\varepsilon_{G_{ij}}(T_f)$.

One can realize that, far from T_{TR} , where the linear extrapolation of thermal dilatation of the parent phase is losing its accuracy, the natural spontaneous strain cannot be unequivocally determined from the data on temperature dependence of the unit cell parameters. However, any modification of the extrapolation law for $\varepsilon_{G_{ij}}(T_{\text{f}})$ results in a variation of the natural spontaneous strain tensor by a constant symmetric second-rank tensor. As we shall see later in this book, this uncertainty by a constant tensor manifests in no measurable phenomena, since whenever the spontaneous strain is involved, it is the difference between its values in different domain states that counts.⁵

Though the uncertainty in direct experimental evaluation of the values of the natural spontaneous strain far from T_{TR} may be considered as a certain inconvenience, this definition of spontaneous strain has clear advantages compared to alternative Aizu's definition of spontaneous strain considered later in this section. First, the variable, which yields the thermodynamic theory of a structural phase transition, is exactly the natural spontaneous strain. This will be discussed in the section devoted to the thermodynamic theories. Second, as we will see later, a certain type of the ferroelastic problems can be treated in terms of the natural spontaneous strain whereas it cannot be treated in terms of Aizu's definition.

To offer an idea about the magnitude of diagonal components of natural spontaneous strain we quote values for BaTiO_3 (Wadhawan, 1982; Landolt-Börnstein, 1990). The crystal has the point symmetry $F = 4mm$ at room temperature. This phase is ferroelastic as well as ferroelectric, resulting from the parent phase $G = m\bar{3}m$. At room temperature $a = 3.992 \text{ \AA}$ and $c = 4.036 \text{ \AA}$ and natural spontaneous strain components are $\varepsilon_{S_{11}} \cong -3.64 \times 10^{-3}$ and $\varepsilon_{S_{33}} \cong 7.36 \times 10^{-3}$.

The case of the transition $m\bar{3}m - m_{xy}m_{\bar{xy}}2_z$ is slightly more complicated because the conventional axes of the two phases do not coincide and when investigating the ferroelastic phase by X-ray diffraction, orthorhombic parameters $a_F(\text{ort})$, $b_F(\text{ort})$ are determined, measured along axes which make an angle of 45° with the cubic axes. Then simple geometry gives for the symmetry-breaking shear strain the relation

$$\varepsilon_{S_{xy}} = \frac{a_F(\text{ort}) - b_F(\text{ort})}{2a_G}. \quad (2.1.8)$$

In many ferroelastic crystals a typical value for symmetry-breaking off-diagonal components of natural spontaneous strain is within the limits of 3×10^{-3} – 10^{-2} .

⁵ If the elastic compatibility problem between the parent and ferroelastic phase is considered, within the framework of natural spontaneous strain approach, zero spontaneous strain should be ascribed to the parent phase.

2.1.3.3 Aizu's Definition of Spontaneous Strain

One of the key properties of ferroelastics is that, in the low-symmetry phase, there exist at least two states of material, which differ in the orientation of the tensor of spontaneous strain. These states called domain states will be discussed later in this chapter. This property of ferroelastics has been used by Aizu (1970a) for a definition of spontaneous strain, which does not face the problem of equivocal determination from the data on the temperature dependence of the parameters of the unit cell mentioned in the previous section. He introduced a modified tensor of spontaneous strain, which we shall refer to as *Aizu strain* and denote by ε_S^{Aizu} , as follows:

$$\varepsilon_{S_{ij}}^{Aizu} = \varepsilon_{S_{ij}} - \frac{1}{q} \sum_{k=1}^q \varepsilon_{S_{ij}}(k) \quad (2.1.9)$$

where $\varepsilon_{S_{ij}}(k)$ is the natural spontaneous strain in the k 's domain state, q being the total number of the domain states in the low-symmetry phase F . As seen from Eq. (2.1.9) the Aizu strain is independent of the reference used for the calculation of the spontaneous strain since any change in the reference state results in adding the same tensor to all $\varepsilon_{S_{ij}}(k)$. This gives to the Aizu strain an advantage of being unequivocally defined from the experimental data on the temperature dependence of the parameters of the unit cell. That has determined a wide use of the Aizu strain in the literature.

It is essential to stress that, for any problems sensitive to the values of spontaneous strain when the whole sample is in the same ferroic phase F , only the difference between the spontaneous strains in different domain states matters. Since the two definitions of spontaneous strain, natural and Aizu, differ only by a constant tensor which is the same for all domain states of F , for problems of this kind, spontaneous strains introduced by them can be used in the calculations and provide the same result.

As an example of both natural and Aizu strains we consider the ferroelastic species $\bar{4}2m - Pcds - 2$ with four domain states. Table 2.1.2 shows both forms of strain; here $a = (1/2)(\delta\varepsilon_{yy} - \delta\varepsilon_{xx})$, $b = \varepsilon_{xy}$. Aizu (1970a) listed the matrices of ε_S^{AIZU} for all ferroelastic species and we show some of them in a slightly modified form in Table 2.1.3.

It is instructive to compare the physical meaning of the spontaneous strains introduced according to these definitions. Let us do it for the transition discussed above, from cubic $G = m\bar{3}m$ to orthorhombic $F = m_x m_y 2_z$ (for features of the transition, see Fig. 2.1.4). The first conclusion to be drawn is that the center term in Aizu's definition, i.e., the term $\frac{1}{q} \sum_{k=1}^q \varepsilon_{S_{ij}}(k)$, is a second-rank tensor of a cubic symmetry, which can be presented as $A\delta_{ij}$, where δ_{ij} is the Kronecker symbol. Taking the trace and comparing these two expressions one finds $A = \text{Tr}(\varepsilon_S) \equiv \sum_{m=1}^3 \varepsilon_{S_{mm}}$, we note that the subtracted term, namely $\frac{1}{3} \delta_{ij} \sum_{m=1}^3 \varepsilon_{S_{mm}}$, has the meaning of the strain in a hypothetical cubic structure, which changes with decreasing temperature with the same variation of the

Table 2.1.2 Matrices of natural spontaneous strain and Aizu strain for four domain states of species $\bar{4}2m - P\bar{6}3c2$

	$\varepsilon_S(S_i)$	$\varepsilon_{S_{\text{Aizu}}}(S_i)$
S_1	$\begin{pmatrix} \delta\varepsilon_{xx} & \varepsilon_{xy} & 0 \\ & \delta\varepsilon_{yy} & 0 \\ & & \delta\varepsilon_{zz} \end{pmatrix}$	$\begin{pmatrix} -a & b & 0 \\ & a & 0 \\ & & 0 \end{pmatrix}$
S_2	$\begin{pmatrix} \delta\varepsilon_{xx} & -\varepsilon_{xy} & 0 \\ & \delta\varepsilon_{yy} & 0 \\ & & \delta\varepsilon_{zz} \end{pmatrix}$	$\begin{pmatrix} -a & -b & 0 \\ & a & 0 \\ & & 0 \end{pmatrix}$
S_3	$\begin{pmatrix} \delta\varepsilon_{yy} & -\varepsilon_{xy} & 0 \\ & \delta\varepsilon_{xx} & 0 \\ & & \delta\varepsilon_{zz} \end{pmatrix}$	$\begin{pmatrix} a & -b & 0 \\ & -a & 0 \\ & & 0 \end{pmatrix}$
S_4	$\begin{pmatrix} \delta\varepsilon_{yy} & \varepsilon_{xy} & 0 \\ & \delta\varepsilon_{xx} & 0 \\ & & \delta\varepsilon_{zz} \end{pmatrix}$	$\begin{pmatrix} a & b & 0 \\ & -a & 0 \\ & & 0 \end{pmatrix}$

Table 2.1.3 Tensors $\varepsilon_S^{\text{Aizu}}$ for domain states S_i in selected species432-422, $3m-2m$, $m\bar{3}m-4/mmm$

$$\varepsilon_S^{\text{Aizu}}(S_1) = \begin{pmatrix} -2b & 0 & 0 \\ & b & 0 \\ & & b \end{pmatrix}, \quad \varepsilon_S^{\text{Aizu}}(S_2) = \begin{pmatrix} b & 0 & 0 \\ & -2b & 0 \\ & & b \end{pmatrix}, \quad \varepsilon_S^{\text{Aizu}}(S_3) = \begin{pmatrix} b & 0 & 0 \\ & b & 0 \\ & & -2b \end{pmatrix}$$

23- $\varepsilon ds-222$, $m\bar{3}-\varepsilon s-mmm$

$$\varepsilon_S^{\text{Aizu}}(S_1) = \begin{pmatrix} a & 0 & 0 \\ & b & 0 \\ & & c \end{pmatrix}, \quad \varepsilon_S^{\text{Aizu}}(S_2) = \begin{pmatrix} c & 0 & 0 \\ & a & 0 \\ & & b \end{pmatrix}, \quad \varepsilon_S^{\text{Aizu}}(S_3) = \begin{pmatrix} b & 0 & 0 \\ & c & 0 \\ & & a \end{pmatrix} \text{ where } a + b + c = 0$$

432- $\varepsilon ds-2_x 2_y 2_z$, $3m-\varepsilon ds-222$, $m\bar{3}m-\varepsilon s-m_x m_y m_z$

$$\varepsilon_S^{\text{Aizu}}(S_1) = \begin{pmatrix} a & 0 & 0 \\ & b & 0 \\ & & c \end{pmatrix}, \quad \varepsilon_S^{\text{Aizu}}(S_2) = \begin{pmatrix} a & 0 & 0 \\ & c & 0 \\ & & b \end{pmatrix}, \quad \varepsilon_S^{\text{Aizu}}(S_3) = \begin{pmatrix} c & 0 & 0 \\ & b & 0 \\ & & a \end{pmatrix}$$

$$\varepsilon_S^{\text{Aizu}}(S_4) = \begin{pmatrix} b & 0 & 0 \\ & a & 0 \\ & & c \end{pmatrix}, \quad \varepsilon_S^{\text{Aizu}}(S_5) = \begin{pmatrix} c & 0 & 0 \\ & a & 0 \\ & & b \end{pmatrix}, \quad \varepsilon_S^{\text{Aizu}}(S_6) = \begin{pmatrix} b & 0 & 0 \\ & c & 0 \\ & & a \end{pmatrix}$$

432- $\varepsilon ds-2_y 2_z 2_x$, $3m-P\bar{6}3c2-m_y m_z 2_x$, $m\bar{3}m-\varepsilon s-m_y m_z m_x$ Designations of these species differ in indices from those in Table B.1, because here the orthorhombic axis is taken parallel to the cubic x .

$$\varepsilon_S^{\text{Aizu}}(S_1) = \begin{pmatrix} -2b & 0 & 0 \\ & b & d \\ & & b \end{pmatrix}, \quad \varepsilon_S^{\text{Aizu}}(S_2) = \begin{pmatrix} -2b & 0 & 0 \\ & b & -d \\ & & b \end{pmatrix}, \quad \varepsilon_S^{\text{Aizu}}(S_3) = \begin{pmatrix} b & 0 & d \\ & -2b & 0 \\ & & b \end{pmatrix}$$

$$\varepsilon_S^{\text{Aizu}}(S_4) = \begin{pmatrix} b & 0 & -d \\ & -2b & 0 \\ & & b \end{pmatrix}, \quad \varepsilon_S^{\text{Aizu}}(S_5) = \begin{pmatrix} b & 0 & d \\ & b & 0 \\ & & -2b \end{pmatrix}, \quad \varepsilon_S^{\text{Aizu}}(S_6) = \begin{pmatrix} b & 0 & -d \\ & b & 0 \\ & & -2b \end{pmatrix}$$

422-222, $4mm-mm2$, $\bar{4}2m-222$, $\bar{4}2m-mm2$, $4/mmm-mmm$

$$\varepsilon_S^{\text{Aizu}}(S_1) = \begin{pmatrix} 0 & a & 0 \\ & 0 & 0 \\ & & 0 \end{pmatrix}, \quad \varepsilon_S^{\text{Aizu}}(S_2) = \begin{pmatrix} 0 & -a & 0 \\ & 0 & 0 \\ & & 0 \end{pmatrix}$$

Table 2.1.3 (continued)4-2, $\bar{4}$ -2, 4/m-2/m

$$\varepsilon_S^{\text{Aizu}}(S_1) = \begin{pmatrix} -a & b & 0 \\ & a & 0 \\ & & 0 \end{pmatrix}, \quad \varepsilon_S^{\text{Aizu}}(S_2) = \begin{pmatrix} a & -b & 0 \\ & -a & 0 \\ & & b \end{pmatrix}$$

622-222, 6mm-mm2, m2-mm2, 6/mmm-mmm

$$\varepsilon_S^{\text{Aizu}}(S_1) = \begin{pmatrix} a & 0 & 0 \\ & a & 0 \\ & & 0 \end{pmatrix}, \quad \varepsilon_S^{\text{Aizu}}(S_2) = \begin{pmatrix} a/2 & -\sqrt{3}a/2 & 0 \\ & -a/2 & 0 \\ & & 0 \end{pmatrix}, \quad \varepsilon_S^{\text{Aizu}}(S_3) = \begin{pmatrix} a/2 & \sqrt{3}a/2 & 0 \\ & -a/2 & 0 \\ & & 0 \end{pmatrix}$$

32-2, 3m-m, m-2/m

$$\varepsilon_S^{\text{Aizu}}(S_1) = \begin{pmatrix} a & 0 & c \\ & a & 0 \\ & & 0 \end{pmatrix}, \quad \varepsilon_S^{\text{Aizu}}(S_2) = \begin{pmatrix} a/2 & \sqrt{3}a/2 & -c/2 \\ & -a/2 & \sqrt{3}c/2 \\ & & 0 \end{pmatrix}, \quad \varepsilon_S^{\text{Aizu}}(S_3) = \begin{pmatrix} a/2 & -\sqrt{3}a/2 & -c/2 \\ & -a/2 & \sqrt{3}c/2 \\ & & 0 \end{pmatrix}$$

222-2, mm2-2, mm2-m, mmm-2/m

$$\varepsilon_S^{\text{Aizu}}(S_1) = \begin{pmatrix} 0 & 0 & b \\ & 0 & 0 \\ & & 0 \end{pmatrix}, \quad \varepsilon_S^{\text{Aizu}}(S_2) = \begin{pmatrix} 0 & 0 & -b \\ & 0 & 0 \\ & & 0 \end{pmatrix}$$

unit-cell volume as that which actually occurs in the F phase. Thus, the Aizu strain can be interpreted as the spontaneous strain calculated with respect to this hypothetical structure. Now we recall that, for the considered system, the natural spontaneous strain is evaluated as spontaneous strain calculated with respect to a cubic structure that evolves according to the extrapolated thermal expansion of the parent phase. This is the basis of the difference between the definitions of spontaneous strain. Thus, for the considered system, the Aizu strain can be calculated from the equation for the natural spontaneous strain, Eq. (2.1.6), in which we substitute $a_G(\text{ext})$ by $(a_F b_F c_F)^{1/3}$. The difference between these two definitions can also be seen by comparing Fig. 2.1.5a and c.

It is of importance to note that a certain convenience in using the Aizu's modified definition of spontaneous strain is not free of charge. The point is that the subtraction of the center term in Eq. (2.1.9) results in losing the information required for solving a certain class of ferroelastic problems. We have in mind, e.g., the problem of the elastic compatibility between two ferroelastic phases $F_1 \subset G$ and $F_2 \subset G$ which could coexist near the morphotropic boundary of the material, the situation of high practical importance, e.g., in $\text{Pb}(\text{Zr}, \text{Ti})\text{O}_3$ ferroelectric (Jaffe et al., 1971). This problem requires information on the difference in spontaneous strains $\varepsilon_{S_{ij}}$ in both F_1 and F_2 phases. If this difference, using definition (2.1.5), is expressed in terms of natural spontaneous strain, one finds that it need not be identical to the difference of Aizu strains in the two phases. The reason is that the center term in Eq. (2.1.9) is, in general, different in the F_1 and F_2 phases. For example, if the parent phase is cubic the difference in the spontaneous strain of these phases can be written as follows:

$$(\varepsilon_{S_{ij}})_{F_1} - (\varepsilon_{S_{ij}})_{F_2} = \left(\varepsilon_{S_{ij}}^{\text{Aizu}} \right)_{F_1} - \left(\varepsilon_{S_{ij}}^{\text{Aizu}} \right)_{F_2} - \delta_{ij} \frac{V_{F_1} - V_{F_2}}{V_G} \quad (2.1.10)$$

where V stands for the unit cell volume. We see that, since, in general, $V_{F_1} - V_{F_2} \neq 0$, the consideration of the problem of elastic compatibility between two different ferroelastic phases in terms of Aizu stress would lead to an erroneous result.

Aizu strain is not the only alternative to the natural spontaneous strain. Another definition of it, denoted here as $\varepsilon_{S_{ij}}^W$, has been proposed by Wadhawan (1982), namely

$$\varepsilon_{S_{ij}}^W = \varepsilon_{S_{ij}} - \frac{1}{3} \delta_{ij} \sum_{m=1}^3 \varepsilon_{S_{mm}}. \quad (2.1.11)$$

We just note that when discussing compatibility problems involving domain states in one phase only, the use of this definition is legitimate on the same level as the use of the Aizu strain. If the parent phase is cubic, both Aizu and Wadhawan's spontaneous strains are identical.

2.1.3.4 Ferrobielectrics

Formal aspects of describing properties of crystals by tensors do not distinguish between differences in the physical nature of phenomena. We can, therefore, expect that what was said for strain will apply also to other physical properties characterized by a second-rank symmetric tensor. In addition, the well-known precept of crystal physics states that if something is allowed by symmetry, it is there. Thus for ferroelastics we expect that, in the phase F , the spontaneous (subscript S) components $\chi_{S_{ij}}$ of susceptibility or $\kappa_{S_{ij}}$ of permittivity will also occur. To stress this point, the term *ferrobielectric* was coined (Newnham and Cross, 1974a,b) to denote such phases or phase transitions: Any ferroelastic sample which is also characterized by its dielectric properties (i.e., sample of a nonmetallic material) is also a ferrobielectric sample. The same argumentation applies to the reverse tensor of relative permittivity, namely, the tensor $\partial E_i / \partial D_j$ which is used to characterize the response of the crystal at optical frequencies. Therefore any ferroelastic phase transition is accompanied by the occurrence of spontaneous birefringence. Components of tensor properties forbidden by symmetry in the parent phase but allowed in the ferroic phase are sometimes referred to as *symmetry-breaking* properties. The designation "*morphic*" is often used in the same sense. Thus any ferroelastic material is also characterized by a *morphic birefringence*. We shall discuss it in some detail when treating methods of observing domains.

2.1.4 Higher Order Ferroics

In the previous two sections we have considered ferroelectric and ferroelastics, which are also conveniently referred to as *primary ferroics*. On the basis of this consideration, we could now easily construct tables showing phase transitions,

specified by G and F , which are ferroelectric and ferroelastic. Before doing that, however, we should finish the classification of phase transitions used in this book. After introducing vectors (polarization) and second-rank tensors (strain) as characteristic quantities for some phase transitions, we can go further up in tracking the behavior of other tensors as the symmetry changes from G to F . The reader is reminded that even if we limit ourselves to tensors of fourth-rank maximum, we know that useful and observable properties of crystals are described by more than 20 tensors differing in rank and symmetry (Sirotnin and Shaskol'skaya, 1979). So we could in fact classify phase transitions according to criteria based on the occurrence of new components of any of these tensors and invent names for them, and one might go higher as well. However, to stay practical we introduce just two more specific kinds of ferroics.

Ferroelastoelectric phase transitions are those characterized by the occurrence of new components of the piezoelectric tensor d_{ijk} in the phase F compared to the phase G . By analogy, *ferrobielastic* transitions are those characterized by the occurrence of new components of the tensor of elastic compliance tensor s_{ijkl} in the phase F compared to the phase G . Both these represent *secondary ferroics* (Newnham and Cross, 1974b) or *second-order ferroics* (Aizu, 1973b).

It can be easily seen that in any ferroelastoelectric phase also new components of the electrooptic coefficient r_{ijk} develop, as well as those of tensors describing nonlinear optical properties like second harmonic generation.

Thus, specifying point group F as a subgroup of G one can unambiguously determine to which category phase F belongs; whether this phase is ferroelectric or ferroelastic, ferroelastoelectric or ferrobielastic. All we need is to compare simple summaries of nonzero components of tensors in point groups (Sirotnin and Shaskol'skaya, 1979). At this point, a question arises. Is it possible to find such pairs G, F that the corresponding transition would not fall into any of these four categories? The answer is positive. There are four such pairs and we shall specify them in Table B.1 of ferroic species. In these cases the lowest rank of a tensor acquiring new components in phase F is higher than four. Materials that belong to any of these categories have been named *tertiary ferroics* (Amin and Newnham, 1980).

In this book we based the classification of ferroics mainly on one of their features, namely, on the genesis of new components of tensors in the phase F which were necessarily 0 in phase G . There is another significant inference, namely, that the domain states in the phase F inevitably differ in just these new tensor properties. It is on this basis that higher order ferroics can be optionally defined (Aizu, 1972; Aizu, 1973b; Newnham and Cross, 1974a,b).

It is obvious that one and the same material (one and the same phase transition) can be (but need not to be) simultaneously ferroelectric, ferroelastic, and any higher order ferroic. Actually this is rather a rule than an exception. In particular when the symmetry G is relatively high and the symmetry F is much lower, all measurable tensors may acquire new components. Then we usually ascribe the material into the category corresponding to the lowest rank tensor.

As an illustration of the tensor changes induced by a phase transition we consider the transition from $G = \bar{4}2m$ to $F = mm2$. Several well-investigated ferroic materials undergo such a transition: potassium dihydrogen phosphate (KH_2PO_4 , abbr. KDP), gadolinium molybdate ($\text{Gd}_2(\text{MoO}_4)_3$, abbr. GMO), and tanane. We have in mind macroscopic properties which are described by the following material relations:

$$\varepsilon_n = s_{nm}\sigma_m + d_{in}E_i + \alpha_n\Delta T \quad (2.1.12)$$

$$D_i = d_{im}\sigma_m + \varepsilon_0\kappa_{ij}E_j + p_i\Delta T \quad (2.1.13)$$

$$\Delta S = \alpha_m\sigma_m + p_jE_j + \left(\frac{C}{T}\right)\Delta T. \quad (2.1.14)$$

Here the Einstein summation convention was applied with i and j changing from 1 to 3, n and m changing from 1 to 6. The system of 1–6 indexing for the elastic variables can be found in Nye's book (Nye, 1992); for reference it is given in Appendix F. For the variables and material parameters in these expressions, the following notations have been accepted:

- ε_n — mechanical stress,
- D_i — electric displacement,
- ΔS — change of the entropy density,
- σ_n — elastic strain,
- E_i — electric field,
- ΔT — temperature change,
- s_{nm} — elastic compliance taken at constant electric field and temperature,
- d_{im} — piezoelectric moduli at constant temperature,
- α_n — coefficient of thermal dilatation,
- κ_{ij} — relative dielectric permittivity at zero stress and constant temperature,
- p_i — pyroelectric coefficients at constant stress,
- C — heat capacity at zero electric field and stress,
- ε_0 — permittivity of vacuum.

It is convenient to represent these coefficients as a matrix which has the general form shown in Fig. 2.1.6a (valid for the point group 1) and which is particularized for the group $\bar{4}2m$ in Fig. 2.1.6b. Figure 2.1.7a and b shows orientation of the symmetry elements for the aforementioned point groups with respect to their conventional reference frames. Figure 2.1.8a shows the matrix of nonzero components of tensors in the conventional coordinate system of F . However, this matrix cannot be directly used for characterization of the phase transition. As already mentioned to evaluate the genesis of new components of tensors when passing from phase G to F one should compare the matrices of the tensor properties in the same reference frame. Customarily one uses the reference frame of the G phase. Thus, as the next step one should transform the matrix given by Fig. 2.1.8a to reference frame of G phase to find matrix given by Fig. 2.1.8b. (The information necessary for such kind of transformation is provided in Appendix F.) Finally, comparing matrices

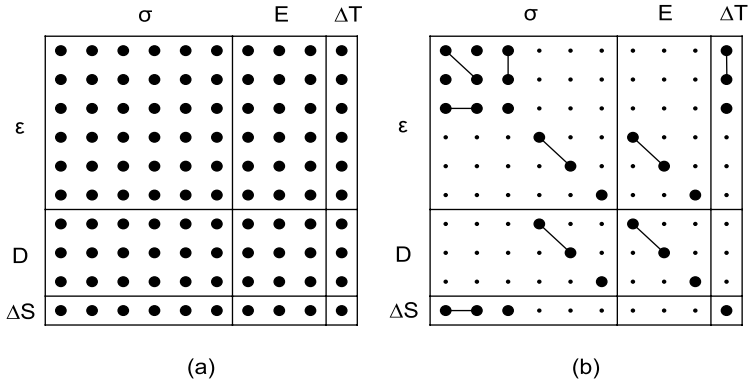


Fig. 2.1.6 Matrix of tensor properties (Nye, 1992): (a) in its general form applicable to the point group 1 and (b) for the point group $\bar{4}2m$. Here larger points show nonzero components; the values corresponding to the linked points are equal

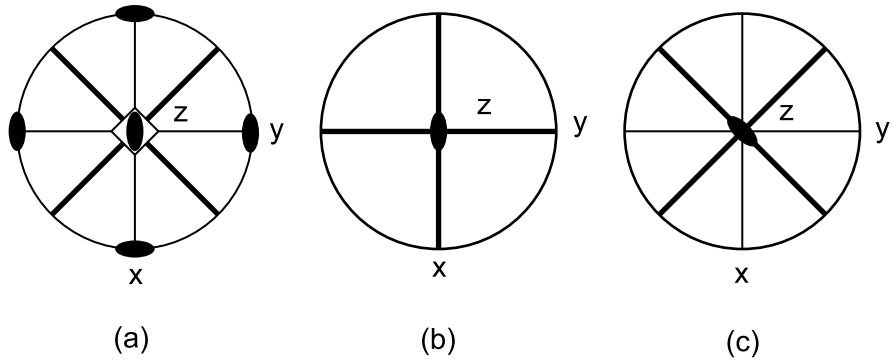


Fig. 2.1.7 (a) Symmetry elements for the group $\bar{4}2m$. Symmetry elements for the subgroup $mm2 \subset \bar{4}2m$ shown in (c) differ in orientations from those in the conventional reference frame of group $mm2$ shown in (b)

shown in Figs. 2.1.6b and 2.1.8b leads to the conclusion that in this case the phase F is ferroelectric, ferroelastic, ferroelastoelectric, as well as ferrobielastic.

Thus, the mentioned crystals of KDP and GMO and many isomorphs have attributes of both primary and secondary ferroics, but routinely they are referred to as ferroelectrics and ferroelastics.⁶

⁶ It is amusing how lavishly we throw around the prefix *ferro*, although nothing here has to do with iron. But this goes well back in history (Fousek, 1994). The Schrödinger’s proposal of the concept of a *ferroelectric* material was forgotten by the time Rochelle salt (Seignette salt) was discovered as the first ferroelectric material. Then the concept Seignette electric became common, to be later replaced first by the term ferro-dielectric and then ferroelectric. Quoting Megaw (1957) “... perhaps the real reason for its [i.e. of the term Seignette-electricity] rejection ... is its failure to fit comfortably into the English language. As an adjective,

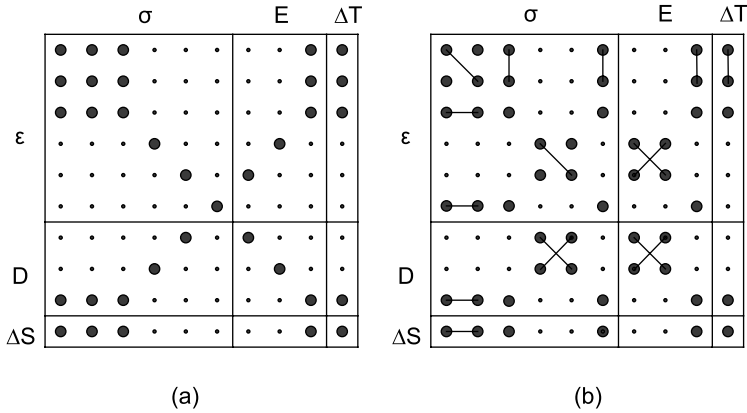


Fig. 2.1.8 (a) Matrix of tensor properties (Nye, 1992) for the group $mm2$ in its conventional orientation. (b) The same in the orientation satisfying the relation $mm2 \subset \bar{4}2m$. Here larger points show nonzero components; the values corresponding to the linked points are equal

At the end of this section we wish to remind the reader that here we did not pay attention to magnetic properties. But in fact when the concept of ferroics was coined, for both primary (Aizu, 1970) and secondary (Newnham and Cross, 1974a,b) ferroics, tensor properties related to magnetization were included in the classification.

2.1.5 Relation Between the Symmetries G and F : Order Parameter

We shall now investigate the relation between point groups G and F in more detail with the aim of introducing the concept of the order parameter of a phase transition, which will open a practical way to analyze domain states in the distorted phase.

Let us first recall the well-known Curie principle of crystal physics (Sirotnin and Shaskol'skaya, 1979). This self-evident principle states: "If certain causes end up in certain consequences, the symmetry elements of the former should manifest themselves in the latter. If some dissymmetry is observed in any phenomenon, then this dissymmetry should manifest itself also in the causes which lead to this phenomenon. Statements opposite to these are incorrect, at least on a practical level; in other words, the consequences may possess a higher symmetry than the causes which resulted in them." The present authors would like to point out that nowadays it is generally accepted that the last statement does not hold if one takes into account tensor properties of high enough order. With this reservation the Curie principle can be formulated in the following way: "If an object of certain symmetry is subjected to a perturbation, the operations of symmetry of the

>ferroelectric< is euphonius, while >Seignette-electric< grates on the ear." Here the Russians seem to stick more to facts than to sounds: their 'segniettoelektrichestvo' survives and no one pretends to deal with iron when investigating barium titanate.

resulting object are the common operations of symmetry of the original object and the perturbation.” Thus, we see that unless the perturbation is a scalar, its application should result in loss of some symmetry elements of the object. Recalling that any ferroic phase transition results in a loss of symmetry elements one can pose a reasonable question what is the perturbation which is standing behind the phase transition? The answer to this question is the objective of this section.

2.1.5.1 Transition Without Multiplication of the Unit Cell

Consider the simplest case: a ferroelectric phase transition. Suppose that the occurrence of spontaneous polarization \mathbf{P}_S can be considered as its cause. Which symmetry elements have \mathbf{P}_S , a polar vector? They are represented by the continuous Curie group ∞m ; its set of symmetry elements includes the symmetry axis of infinite order (allowing for any rotation around it) along the direction of \mathbf{P}_S and all mirror planes containing this axis. Should, therefore, the occurrence of \mathbf{P}_S be held responsible for the transition from G to F , we have to determine the symmetry operations which are common to both groups G and ∞m and check whether the relation

$$F = \infty m \cap G \quad (2.1.15)$$

holds, when the axis ∞ is properly oriented in the coordinate system of G . The symbol \cap designates the intersection of both groups on its sides. Examining the foregoing example of the transition from $G = \bar{4}2m$ to $F = mm2$ we see immediately that this relation is satisfied. Thus, in this particular case polarization can be regarded as fully responsible for the change of symmetry. Groups F satisfying relation (2.1.15) are called *maximum polar subgroups* of G . All pairs (G, F) fulfilling this condition, with specifying the orientation of F with respect to G , were found in the early stages of investigating ferroelectrics (Zheludev and Shuvalov, 1956).

In the discussed case, the physical quantity which appears in the phase F and is fully responsible for the symmetry change from G to F is called the *order parameter* of the transition. Often it is denoted by η and we shall use this designation throughout this book. We also use the notation H for the group of symmetry of the order parameter. Thus, in the foregoing case where the point group symmetry change from $G = \bar{4}2m$ to $F = mm2$ fully characterizes the transition, with $H = \infty m$, the order parameter transforms as a polar vector and we feel justified to consider it polarization.

The considered case was, in a sense, a simple one, namely, in the $G = \bar{4}2m$ group, one can find only one maximum polar subgroup of the symmetry $F = mm2$. In general this is not necessarily the case, e.g., in $G = m\bar{3}m$ group one finds three maximum polar subgroups of the type $F = 4mm$ according to the three possible orientations of the fourfold axis and three possible orientations of the order parameter (polarization) axis. To distinguish the orientations of the order parameter η and its group H , we attach to them an index i : η_i and H_i . Thus, the reduction of symmetry due to the phase transition at which η_i occurs can be described as follows:

$$F_i = H_i \cap G. \quad (2.1.16)$$

This relation states that the symmetry group F_i of the distorted phase is the maximal subgroup of the symmetry group G of the parent phase, which leaves the order parameter η_i invariant.

The situation discussed above corresponds to ferroelectrics classified as *proper ferroelectrics*⁷ (Dvorak, 1974). However, it is possible to imagine a ferroelectric transition where polarization does not play the role of the order parameter. This is, for example, the case of the transition from $G = \bar{4}2m$ down to the monoclinic phase with $F = 2_z$. In this case, the symmetry reduction is more severe than that required by the symmetry ∞m of the polarization so that the latter cannot play the order parameter role. This kind of ferroelectrics is classified as *improper ferroelectrics* (Dvorak, 1972).

It is clear that the approach used for definition of proper and improper ferroelectrics can readily be applied to the situation with the order parameter η of any symmetry. An important example of this kind is the classification into *proper and improper ferroelastics*. In this case, the approach is applied with $H = mmm$, the symmetry of the elastic deformation.

2.1.5.2 Transition with Multiplication of the Unit Cell

In the case where numbers of formula units in the unit cells of G and F phases differ as a result of the transition, i.e., $v \neq 1$ in Eq. (2.1.2), the order parameter of the transition should be introduced as a physical quantity which appears in the phase F and is fully responsible for the change in the spatial group symmetries between the phases G and F . For such transitions the F phase can be both ferroelectric and ferroelastic. However, since neither polarization vector nor deformation tensor is connected with any translational symmetry they cannot play roles of the order parameters. Thus, we again arrive at the situation of *improper ferroelectrics and ferroelastics* just discussed above where the ferroelectric or ferroelastic phases are results of the phase transition controlled by an order parameter different from polarization vector or deformation. The existence of improper ferroelectrics was predicted by Indenbom (1960) from the point of view of symmetry. A Landau theory approach for the description of improper ferroelectrics was developed by Levanyuk and Sannikov (1968). Cross et al. were the first to recognize that crystals of gadolinium molybdate (GMO) exhibit properties indicating that this material cannot fall into the category of “normal” proper ferroelectrics (Cross et al., 1968). Dvorak (1971, 1974) then determined the true symmetry of the order parameter in this material as well as in the boracite $\text{Fe}_3\text{B}_7\text{O}_{13}\text{I}$ (Dvorak, 1972). Both of them belong to the second mentioned category, undergoing transitions which are ferroelectric but not equitranslational, with $v \neq 1$.

⁷ In the chapter devoted to the thermodynamic theory we shall point out that there may be reasons for further and finer classification which includes proper ferroelectrics in contrast to pseudoproper or weak ferroelectrics. But this is of little importance for understanding domains on the basis of symmetry.

Could a material be proper ferroelectric and proper ferroelastic at the same time? Yes, it can and, in fact, the transition from $G = \bar{4}2m$ to $F = mm2$ without unit cell multiplication, i.e., with $\nu = 1$, provides us with an example. Indeed, we have already seen that the occurrence of a polar vector parallel to the z -axis in the phase $G = \bar{4}2m$ removes all symmetry elements with the exception of the twofold axis which is parallel to $\bar{4}$ and of mirror planes parallel to it; thus, according to Eq. (2.1.15), the phase $F = mm2$ is proper ferroelectric. Alternatively, we can imagine that the unit cell whose symmetry corresponds to the group $G = \bar{4}2m$ is deformed by a shear strain ε_{xy} , whose symmetry is that of a rhomb-based prism, i.e., $H = mmm$ with two mirror planes shared with G . In this case, we see from Eq. (2.1.16) that what is left are again symmetry elements representing the group $F = mm2$. If for a given material with the considered transition from $G = \bar{4}2m$ to $F = mm2$ there is no change in translational symmetry (i.e., $\nu = 1$), the transition is both proper ferroelectric and proper ferroelastic. This is the case of KDP. If $\nu > 1$, it would represent an improper ferroelectric and an improper ferroelastic; this is the case of GMO for which $\nu = 2$.

2.1.6 Overview of Different Kinds of Phase Transitions: Species

Various classifications of structural phase transitions, which we introduced in the preceding sections, proved useful in practice. Correct assignment of the category, to which a particular material (transition) belongs, makes it possible to predict a multitude of properties, including domain phenomena. Partial summary of different kinds of phase transitions, which have been described up to now, is shown in Fig. 2.1.9. Some of their designations contain symbols P , ε , d , or s . P means that this kind of transition is ferroelectric; ε , d , and s denote ferroelastic, ferroelastoelectric, and ferrobielastic transitions, respectively.

We may wish to assign a particular material a symbol which would show most of the information we have already discussed. This symbol contains the groups G and F . However, as we have seen above specifying these groups by their normal crystallographic notation may not be sufficient. Let us consider the phase transition from $G = \bar{4}2m$ to $F = 2$. Here, we should discriminate the transition where the twofold axis along z survives (this axis is parallel to the former $\bar{4}$ axis) from that where the twofold axis along x does. We distinguish these two crystallographically nonequivalent possibilities by marking them with $F = 2_z$ and $F = 2_x$, respectively. Specification of G and F , and, when necessary, with designation of their mutual orientation, defines the *species of the phase transition*. To make the notations more informative we shall include, between the symbols of G and F , also characters denoting *newly acquired properties*.

The simplest species is $\bar{1} - Pd - 1$. Here $G = \bar{1}$, $F = 1$ and on transforming from G to F within the triclinic system the crystal loses only the inversion center and acquires spontaneous polarization (symbol P) as well as the piezoelectric tensor (symbol d). Thus, the phase F is ferroelectric and ferroelastoelectric. A crystal representing the species $m\bar{3}m - d - 23$ stays cubic and becomes

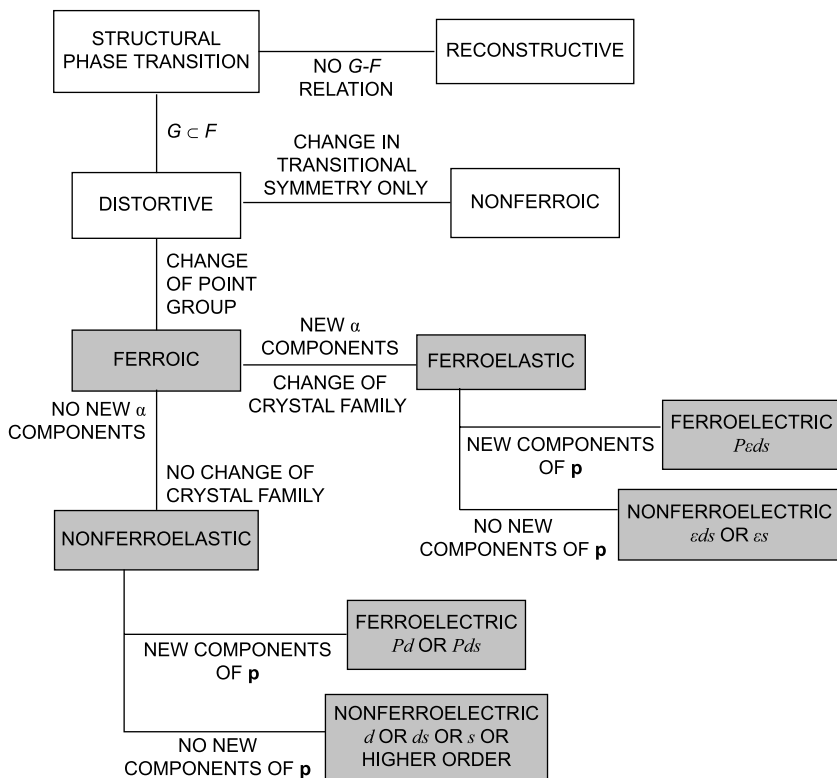


Fig. 2.1.9 Classification of structural phase transitions. *Shaded items* correspond to ferroic transitions

piezoelectric; thus the phase F of symmetry 23 and the transition itself are ferroelastoelectric. In these cases there is no need to specify the orientation of F because all of them are equivalent. The two species of the preceding paragraph are now designated as $42m - P\epsilon ds - 2_z$ and $42m - P\epsilon ds - 2_{xy}$. Both represent phase transitions which are simultaneously ferroelectric, ferroelastic, ferroelastoelectric, and ferrobielastoelectric. The symbol gives no information about the possible change of translational symmetry. We shall present a table of all species; but before doing that it is practical to introduce the concept of domain states.

2.1.7 Domain States

2.1.7.1 Basic Concepts

We have practically completed the classification of phase transitions to the degree that is useful in this book and can now proceed to its vital concept, that of domain states. Let us start with a simple example. Consider a material

classified as a proper ferroelectric and revealing a transition from $G = m\bar{3}m$ to $F = 4mm$. For this species polarization plays the role of the order parameter and the vector \mathbf{P}_S is directed along a fourfold axis of the point group F . Let it be the y -axis direction (see Fig. 2.1.10). Now, let us apply to this state of the crystal with this orientation of \mathbf{P}_S all symmetry operation of G . Clearly, the operations which are common with those of F leave the state unchanged whereas the rest of them will produce, as one can easily check, five additional states which differ in the directions of \mathbf{P}_S . The states of the crystal obtained by this procedure are called *ferroelectric domain states* of this species. Using this method we can define ferroelectric domain states of any ferroelectric species. In the considered case one can easily count the number of them (six). As it will be shown in the end of this section, the number q of domain states of a given species can be determined without performing the transformations by the symmetry operations of G , namely, it holds

$$q = |G|/|F| \quad (2.1.17)$$

where $|A|$ is the order of the point group A , defined as the number of its symmetry operations including the identity transformation. We can easily check this equation for the considered case: $|G|=48$ and $|F|=8$, implying $q=6$. For the reader's convenience, Table A.2 makes it possible to find quickly relations between point groups and their subgroups. The ratio $q = |G| / |F|$ is also called *index of F in G* .

This approach can be generalized for any kind of the order parameter η responsible for a ferroic transition. States of the crystal in the ferroic phase

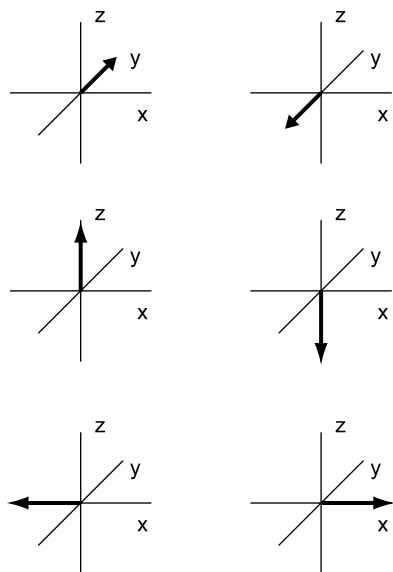


Fig. 2.1.10 Six possible orientations of \mathbf{P}_S for species $m\bar{3}m - P63c - 4mm$

differing in the orientation of η_S are referred to as *domain states*. The expression for the number of domain states in terms of the orders of point groups of the parent and low-symmetry phases, Eq. (2.1.17), applies to the general case as well, for transitions at which the number of formula units in the primitive unit cell remains constant ($v = 1$ in Eq. (2.1.2)).

A simple example demonstrating the importance of identifying the true order parameter when evaluating the number of domain states is provided by the species $\bar{4}3m - P\epsilon ds - 3_{xyz}$. This is a ferroelectric species and one may be tempted to proceed by the “geometrical” method mentioned above. This would lead to four orientations of \mathbf{P}_S and might erroneously conclude that there are four domain states. However, in fact $q = 24/3 = 8$. This is because here the order parameter transforms as a third-order tensor \mathbf{d} , so that the transition is improper ferroelectric. This is an example when all domain states can be grouped into pairs. States in each pair have the same vector \mathbf{P}_S but differ in the orientation of tensor \mathbf{d} . To describe this situation we say that the two domain states in one pair are *degenerate domain states* with respect to \mathbf{P}_S . The concept of degenerate domain states can be applied to any tensor properties. For degenerate domain states, several other terms have been proposed like that of improper domain states (Janovec, 1972) in contrast to proper domain states. A physical quantity which is newly acquired in the ferroic phase and its particular value is common to several domain states but not to all is sometimes referred to as *secondary order parameter*.

In complicated ferroics, this degeneracy of domain states is rather a rule than an exception and its understanding may be vital for practical aspects. This motivates us to consider the question of the degree of degeneracy of domain states with respect to a given tensor property, denoted here by U . We can answer this question in a simple way, using the knowledge developed when treating the problem of number of domain states which differ in the orientation of the order parameter. We recall that Eq. (2.1.17) determines the number of domain states which can be obtained from a given state by applying operations of the group G and which differ in orientations of a tensor property invariant with respect to a group $F \subset G$. Clearly, this equation is valid for any tensor property, not only for the order parameter. Thus, if we set the group F equal to the group $F_U \subset G$ that leaves the property U unchanged, then Eq. (2.1.17) will yield the number q_U of domain states differing in this property, namely,

$$q_U = |G|/|F_U|. \quad (2.1.18)$$

Let us come back to the previous example of species $\bar{4}3m - P\epsilon ds - 3_{xyz}$ and consider the number of domain states which differ in spontaneous polarization. The appropriate subgroup of G leaving polarization invariant is $F_U = 3m$. Since $|F_U| = 6$ and $|G| = 24$, Eq. (2.1.17) gives $q_U = 4$ as the number of domain states differing in the direction of \mathbf{P}_S .

The obtained results enable us to evaluate the degree of degeneracy of domain states with respect to a given tensor property U , i.e., to determine is

the number d_U of domain states differing in the order parameter but having the U property unchanged. We call d_U the *degeneracy factor*. Evidently

$$d_U = q/q_U. \quad (2.1.19)$$

By introducing the degeneracy factor we have opened the way to a very useful additional classification of ferroics which was pioneered by Aizu (1970b). If $q = q_P$ we speak about a *full ferroelectric* species, in which all domain states differ in polarization. On the contrary, when the species is ferroelectrics (i.e., $q_P > 1$) but the degeneracy factors $q/q_P > 1$, the material (or species or phase transition) is *partial ferroelectric*. Similarly, the conditions $q = q_\varepsilon$ and $q/q_\varepsilon > 1$ at $q_\varepsilon > 1$ define *full ferroelastic* and *partial ferroelastic*, respectively. The classical transition in BaTiO₃ — from $G = m\bar{3}m$ to $F = 4mm$ without unit cell multiplication — provides an example of a full ferroelectric and partial ferroelastic species. Indeed, we have checked the ferroelectric feature at the beginning of this section by finding that all six domain states differ in polarization, i.e., $q = q_P = 6$. As for strain, the subgroup of G , which keeps it invariant is $F_\varepsilon = 4/mmm$. This group contains twice as many symmetry operations as the group $4mm$. That implies $q_\varepsilon = 3$ and $q/q_\varepsilon = 2 > 1$.⁸

At this point one should notice that to give an exhaustive presentation of domain states, the equation for the number of possible domain states, Eq. (2.1.17), is to be generalized for the case of transitions with multiplication of unit cell volume ($v > 1$). Simple arguing enables us to do that. Let us recall that Eq. (2.1.17) deals with the indices of the point groups F and G , i.e., this equation takes into account only the orientation symmetry of the problem. Thus, this equation gives the number of domain states that differ in the orientation of crystallographic axes, i.e., of *orientational domain states*. If both point group and translational symmetry change at the phase transition, the crystal can transform into any of the $q_0 = |G| / |F|$ orientational domain states but each of them can be subdivided into v *translational domain states* where v is defined by Eq. (2.1.2). Thus the total number of domain states is then

$$q = q_0 v = \frac{|G| Z_G}{|F| Z_F}. \quad (2.1.20)$$

⁸ As one can notice, the pair of notions of full and partial is very close to that of proper and improper; however, a comprehensive analysis show that these pairs are not identical (Janovec et al., 1975). For equitranslational transitions proper-improper and full-partial are not exactly identical concepts: here all proper ferroelectrics (ferroelastics) are necessarily full and all partial ferroelectrics (ferroelastics) are necessarily improper. However, there exist species which are full ferroelectrics (ferroelastics) in Aizu's wording but may represent materials which must be classified as improper ferroelectrics (ferroelastics). The species no. 032 (see Table B.1 or C.1), i.e., $m\bar{3}m - P\bar{6}3c - 1$, provides an example. Here the order parameter can transform as a polar vector, as indicated by the symbol P_x, P_y, P_z in the fourth column of Table C.1. Clearly, in this case the material is proper ferroelectric. Alternatively (Janovec et al., 1975), the order parameter can transform as a third-rank tensor and polarization arises as a secondary effect, as indicated by the symbol (P_x, P_y, P_z) in Table C.1. In this case the material is an improper ferroelectric. In either case, this species is a full ferroelectric since all domain states can be distinguished by polarization.

The translational domain states are identical in the orientation of tensor properties but differ from the point of view of translational symmetry.

Let us illustrate the notions of orientational and translational domain states by an example of a simple two-dimensional hypothetical structure. In the parent phase, the structure consists of a square lattice of A atoms with B atoms in the centers of the squares (see Fig. 2.1.11a). In the low-symmetry phase, the B atoms are shifted by the same distance either in the x -direction or in the y -direction, the sign of the shifts in neighboring cell being opposite. This transition corresponds to a change of the point group symmetry from G containing eight symmetry operations (identity, rotations by 90° , 180° , and 270° , as well as mirror planes) to F containing four operations (identity, rotation by 180° and two mirror planes). The unit cell doubles at the transition, so that $\nu = 2$. Thus, using Eqs. (2.1.20) and (2.1.2) we find that within the $q = 4$ domain states one can distinguish $q_0 = 2$ orientational domain states, with $\nu = 2$ translational states in each of the latter.

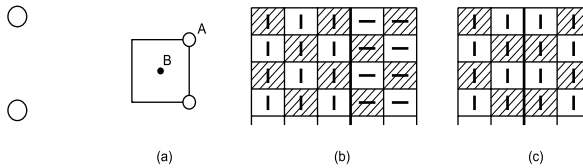


Fig. 2.1.11 (a) Parent unit cell of an imaginary two-dimensional structure. A structural transition corresponding to either vertical or horizontal shifts of B atoms is considered. (b) Low-symmetry structure containing two orientational domain states in intimate contact. (c) Low-symmetry structure containing two translational domain states in intimate contact. *Squares* in (b) and (c) represent original unit cells. *Dashes* indicate orientations of shifts of the B atoms. In *shaded squares* the signs of these shifts are opposite to those in *non-shaded squares*

As an illustration, Fig. 2.1.11b shows the lattice distortions in a two-dimensional sample containing two different orientational domain states while Fig. 2.1.11c represents the lattice distortions in a two-dimensional sample containing two translational domain states. Geometrically, the latter is a chessboard cut into two pieces along a straight line passing between the cells, shifted by one cell along the line, and glued back. Comparing these drawings we infer a key difference between the translational and orientational domain states. The orientational states can be distinguished either when being in an intimate contact as shown in the figure or by monitoring the bulk properties of the sample during a domain reorientation process. In contrast, the translational states can be distinguished only when being in an intimate contact like shown in Fig. 2.1.11c; no tensor properties of a sample offer direct information about the coexistence of translational domain states in it. Thus, although the notion of translational domains is of conceptual importance, usually it does not play a substantial role in the macroscopic properties of a multidomain sample. For

this reason, in this book we shall be mostly concerned about orientation domain states since it is these that determine, to a large extent, macroscopic properties of ferroic samples. When no confusion could arise, we shall omit the adjective orientational (and use the notation q instead of q_o) while it will be always stressed when it is the translational domain states that are addressed in the given context.

An important issue to be mentioned in this section is related to the definition of ferroics. The general definition of a ferroic adopted in this book was based on the symmetry relation (2.1.1) and definitions of particular breeds of ferroics presented above in Sects. 2.1.2, 2.1.3, 2.1.4, 2.1.5, and 2.1.6 were based on the appearance of new spontaneous quantities in the distorted phase which were, by symmetry, nonexistent in the parent phase. But there also exist widely used alternative definitions, which are based on the differences of these quantities in different domain states. Quoting Aizu (1970b), “A crystal is provisionally referred to as being ‘ferroic’ when *it has two or more orientation states in the absence of magnetic field, electric field, and mechanical stress* and can shift from one to another of these states by means of a magnetic field, an electric field, a mechanical stress or a combination of these.” A similar definition of primary and higher order ferroics was used by Newnham and Cross (1974a,b). It is a direct consequence of the symmetry arguments presented above that both of these two definitions are equivalent to that adopted in this book: If η is the order parameter responsible for the G -to- F symmetry lowering, the number of domain (orientation) states given by Eq. (2.1.17) is necessarily larger than 1. As to the “shifts” (not italicized in quoting Aizu), we shall see that in practice they may be only theoretically achievable.

For completeness, one remark can be made at this point. For a given ferroic material and in a sufficiently wide temperature range, there may exist more than one distorted phases fulfilling relation (2.1.1), of different symmetry groups F_1 , F_2 , ..., with no group-subgroup relationship between different groups F_i . Again, the classical example is the sequence of phases in barium titanate: The parent phase $m\bar{3}m$ is followed, on decreasing temperature, by phases with symmetries $4mm$, $mm2_{xy}$, and $3m$. Attempts have been made (Guymont, 1981, 1991) to analyze domain states in these cases taking into account the F_i - F_j transition but without involving the $G \subset F_i$ relationship. It was shown (Toledano and Toledano, 1988) that some evidently reconstructive transitions, with nonexistent parent phase, can be treated by group theory assuming that both phases have originated from a phase with a higher symmetry corresponding to the maximum superstructure common to both observed phases; recently an attempt has been made to introduce the concept of domains into this category (Toledano and Dmitriev, 1997).

2.1.7.2 Left Coset Approach

The considerations of the previous chapter left postponed an important point, namely, the derivation of formula for the number of orientational domain

states of ferroic species, Eq. (2.1.17). This problem can be solved by using the approach of left cosets we now discuss.

The procedure described below employing left cosets may seem superfluous for proper ferroelectrics since it is so easy to apply point group symmetry operations to vectors just by imagining. If the transition is proper ferroelastic and the deformation is simple, the number q can still be guessed. But for more complicated strains, and for order parameters corresponding to higher rank tensors, to proceed by mere geometrical visualization is hardly possible. The left coset approach has the advantage that it can be used quite generally, for any symmetry of the order parameter. It was first suggested by Aizu (1970b, 1972) and then discussed in more detail by Janovec (1972, 1976). The procedure is now routinely employed (Zikmund, 1984; Flack, 1987) and we shall give a short outline of it.

Given G and $F \subset G$, one particularly oriented subgroup F_1 is singled out. We know already that — because of the Curie principle — symmetry operations of F_1 are all those from operations in G which do not change (leave it invariant) the order parameter in its selected particular orientation η_1 . Now we choose one symmetry operation, denoted as say g_2 , which is contained in G but not in F_1 and specify the set of operations g_2F_1 . We continue by choosing an operation g_3 which is contained in G but neither in the group F_1 nor in the set g_2F_1 and form a new set g_3F_1 . This procedure goes on till all operations of G have been used up. One can show that these sets have no common elements. Thus we have divided the group G into disjoint subsets consisting of the same number of operations as they are in F ; we have *decomposed the group G into left cosets of the subgroup F_1* . Formally this is written as

$$G = F_1 + g_2F_1 + g_3F_1 + \cdots + g_qF_1. \quad (2.1.21)$$

The number q of left cosets in this decomposition is called *index of F in G* . Clearly, the index of F in G equals $|G|/|F|$, where $|A|$ is the order of the point group A , namely, the number of its symmetry operations. None of the operations of group F_1 changes one particular orientation of the order parameter, all of them leave it invariant. On the other hand, any operation in the set g_2F_1 changes it into a new orientation and each of them to the same one. This property of the set g_2F_1 holds for all remaining left cosets. Thus, we see that the number of orientational domain states q_o for the order parameter η is just equal to the index of F in G . That implies

$$q_o = |G|/|F| \quad (2.1.22)$$

and brings us back to Eq. (2.1.17). To understand the decomposition in left cosets can be rewarding since it enables one to single out symmetry operations that relate order parameters corresponding to different domain states. As an example, Table 2.1.4 shows the decomposition in left cosets for the ferroelectric species $m\bar{3}m - P\bar{6}3c - m_{xy}m_z2_{xy}$, based on the analysis of Janovec (1976). This

Table 2.1.4 Decomposition of $m\bar{3}m$ into left cosets of $m_{\bar{x}y}m_z2_{xy}$

j	Left cosets				\mathbf{P}_S direction	ϵ_S
1	1	2_{xy}	$m_{\bar{x}y}$	m_z	110	$\epsilon_{S(1)}$
2	$\bar{1}$	m_{xy}	$2_{\bar{x}y}$	2_z	$\bar{1}\bar{1}0$	$\epsilon_{S(1)}$
3	2_x	4_z^3	4_z	m_y	$\bar{1}\bar{1}0$	$\epsilon_{S(2)}$
4	2_y	4_z	4_z^3	m_x	$\bar{1}\bar{1}0$	$\epsilon_{S(2)}$
8	2_{xz}	$3_{xy\bar{z}}$	$3_{xy\bar{z}}$	4_y^3	$0\bar{1}\bar{1}$	$\epsilon_{S(3)}$
6	$2_{\bar{x}z}$	$3_{\bar{x}y\bar{z}}$	$3_{\bar{x}y\bar{z}}$	4_y^3	$0\bar{1}\bar{1}$	$\epsilon_{S(4)}$
11	2_{yz}	$3_{\bar{x}y\bar{z}}^2$	$3_{\bar{x}y\bar{z}}^5$	4_x^3	$\bar{1}0\bar{1}$	$\epsilon_{S(5)}$
10	$2_{\bar{y}z}$	$3_{xy\bar{z}}^2$	$3_{xy\bar{z}}^5$	4_x^3	$\bar{1}0\bar{1}$	$\epsilon_{S(6)}$
7	m_{xz}	$3_{xy\bar{z}}$	$3_{\bar{x}y\bar{z}}$	4_y	$0\bar{1}\bar{1}$	$\epsilon_{S(3)}$
5	$m_{\bar{x}z}$	$3_{\bar{x}y\bar{z}}$	$3_{xy\bar{z}}$	4_y^3	011	$\epsilon_{S(4)}$
12	m_{yz}	$3_{\bar{x}y\bar{z}}^5$	$3_{\bar{x}y\bar{z}}^2$	4_x^3	101	$\epsilon_{S(5)}$
9	$m_{\bar{y}z}$	$3_{xy\bar{z}}^5$	$3_{xy\bar{z}}^2$	4_x	101	$\epsilon_{S(6)}$

The number j denotes the domain state (cf. Fig. 2.3.5b). Four symmetry operations for each j define a left coset. Subscripts indicate the orientation of axes in the group G . Symmetry operations assembled on one line represent one left coset and all of them transform the vector \mathbf{P}_S chosen along [110] into one and the same alternative vector of \mathbf{P}_S , which is given in the column “ \mathbf{P}_S direction.” There are six different tensors of spontaneous deformation ϵ_S , which are not specified here; the aim is only to demonstrate how domain states defined by \mathbf{P}_S are degenerate in strain. After Janovec (1976).

is a phase transition exhibited by barium titanate and several other perovskites, with $q = 48/4 = 12$. The analysis starts by choosing \mathbf{P}_S along [110] of the cubic phase. This choice is in fact arbitrary but, since we have prescribed the subgroup $m_{\bar{x}y}m_z2_{xy} \subset G$ as the group F , it makes sense to choose this particular \mathbf{P}_S vector. Symmetry operations for this subgroup F_1 are shown in the first row. Now we choose $\bar{1}$ as the operation denoted by g_2 above. Any of symmetry operations in a left coset g_2F_1 (assembled in the following row) changes the orientation of the chosen vector [110] into $[\bar{1}\bar{1}0]$, its orientation is shown in the column “ \mathbf{P}_S direction.” Each of the following rows shows one of the left cosets whose total number is 12. We need just one operation from each left cosets to obtain all the orientations of \mathbf{P}_S vectors, i.e., all domain states, starting from the vector [110] characterizing the chosen domain state.

2.1.8 Ferroic Species

Now we are prepared to present an overview of all possible ferroics taking into account relationship (2.1.1), that is, we pay attention to point symmetries of the parent and ferroic phases only and assume that we deal with equitranslational transitions ($v = 1$). In the foregoing sections we did not go into details characterizing the symmetry of the order parameter η . The thermodynamic theories of distortive phase transitions are based on the theory of Landau who showed that the construction of a thermodynamic potential with one order parameter

puts a restriction on the possible symmetry of η , namely, that the latter transforms according to an irreducible representation of the group G . (The reader can find an excellent introduction into the concept of representations in connection with the Landau theory in the Toledanos' monograph (1988)). This requirement on the symmetry of η imposes a further restriction on the possible pairs of G and F , in addition to the simple relation (2.1.1). Aizu (1973a) was the first to come with a list of all conceivable transitions connected with order parameters transforming according to irreducible representations. However, it was pointed out (Holakovsky, 1973) that this requirement may not be absolutely essential and that in fact phase transitions can exist where η transforms according to a reducible representation. Analyses of several materials (summarized by Toledano and Toledano, 1988) showed that this is indeed the case. Lifting the condition of irreducible representation on the symmetry of the order parameter leads to an increase of the number of possible species since now the only condition is the group-subgroup relation (2.1.1).

The full list of equitranslational ferroic species, partially based on the work by Janovec et al. (1975), is presented in Table B.1. Some data concerning ferroelastoelectric and ferrobielastic domain states were completed by Litvin (*Database of ferroic species*; unpublished). We use the species assignment as it was introduced in Sect. 2.1.6. The table should enable the reader to reach the basic information on domain states once the species of a material has been established.

In this chapter we yield just a selection of the full table, to exemplify its system; see Table 2.1.5. The species are ordered according to the point groups G and, for each G , according to the point groups F , always starting at the high-symmetry end and progressing toward lower symmetries. The first column gives the sequential number of the species, which will also be used later in the table of ferroelectric species. The second column contains the symbol of the species using the above introduced pattern G -(spontaneously occurring quantities)- F . The symbol of the point group F is often provided with subscripts specifying the orientation of symmetry elements in G , which define the group F ; here we follow the notation of Janovec et al. (1975). This specification is particularly essential when components of newly acquired tensors are to be itemized, as we shall do it later for polarization and strain in the table of ferroelectric species. Another reason for indexing is that in one particular material we may have two differently oriented phases F belonging to the same species but existing at different temperature intervals. However, very often it is sufficient to specify the F group as such without indication of its orientation.

In column 3 we give the number of equivalent subgroups F . Practically, this number gives the number of possible domain states which differ in the orientation of the order parameter but not in its sign. In column 4, the total number of domain states q is shown. We stress again that on the adopted level of point groups no information is contained about translational domain states and the given number is simply the index of F in G (see Eq. (2.1.17)). Column 5 gives the number q_P of ferroelectric domain states. Here 0 means that F is nonpolar while

Table 2.1.5 Selection of ferroic species (full content see Table B.1)

1	2	3	4	5	6	7	8	9
Species no.	Species designation	n_F	q	q_P	q_ε	q_d	q_s	
001	$m\bar{3}m - d - \bar{4}3m$	1	2	0	1	2	1	
002	$m\bar{3}m - 432$	1	2	0	1	0	1	$\varepsilon[V^2]$
003	$m\bar{3}m - m\bar{3}$	1	2	0	1	0	1	$\{V^2V^2\}$
004	$m\bar{3}m - d - 23$	1	4	0	1	2	1	RR
005	$m\bar{3}m - \varepsilon s - \bar{3}_{xyz}m_{xy}$	4	4	0	4	0	4	
006	$m\bar{3}m - P\varepsilon ds - 3_{xyz}m_{xy}$	4	8	8	4	8	4	
009	$m\bar{3}m - P\varepsilon ds - 3_{xyz}$	4	16	8	4	16	8	RR
011	$m\bar{3}m - \varepsilon ds - 4_z 2_{xy} m_x$	3	6	0	3	6	3	1
012	$m\bar{3}m - \varepsilon ds - 4_z 2_x m_{xy}$	3	6	0	3	6	3	1
013	$m\bar{3}m - P\varepsilon ds - 4_z m_x m_{xy}$	3	6	6	3	6	3	
022	$m\bar{3}m - P\varepsilon ds - m_{xy} m_z 2_{xy}$	6	12	12	6	12	6	RR
025	$m\bar{3}m - \varepsilon s - 2_{xy}/m_{xy}$	6	12	0	12	0	12	2 IRs
026	$m\bar{3}m - \varepsilon s - 2_z/m_z$	3	12	0	12	0	12	RR
032	$m\bar{3}m - P\varepsilon ds - 1$	1	48	48	24	24	24	2 IRs
071	$6/mmm-6/m$	1	2	0	1	2	1	$\varepsilon V[V^2]$
082	$6/mmm-\varepsilon ds-222$	3	6	0	3	6	3	
108	$622-ds-3_z 2_x 622-ds-3_z 2_y$	1	2	0	1	2	2	
208	$2/m - \varepsilon s - \bar{1}$	1	2	0	2	0	2	
209	$2/m - P\varepsilon ds - 1$	1	4	4	2	4	2	
210	$m - P\varepsilon ds - 1$	1	2	2	2	2	2	
211	$2 - P\varepsilon ds - 1$	1	2	2	2	2	2	
212	$\bar{1} - Pd - 1$	1	2	2	1	2	1	

1 means that F is pyroelectric with only one orientation of P_S (or better to say, of the pyroelectric coefficient) and therefore nonferroelectric. Column 6 indicates the number q_ε of ferroelastic domain states. Here 0 does not appear. Number 1 means that F is nonferroelastic: the shape of the unit cell is not changed; the thermal dilatation tensor has no new components. Column 7 gives the number q_d of domain states differing in the piezoelectric tensor or, more generally, in the tensor of symmetry $V[V^2]$ or $[V^2]V$ (see text to Table 2.2.2 or Appendix F for notation of tensor symmetries). Here number 0 means that F is not piezoelectric while 1 means that F is piezoelectric but has no new components of the appropriate tensor. Column 8 shows the number q_s of ferrobielastic domain states. Here again 0 cannot occur while number 1 means that the compliance matrix has no new components in the distorted phase.

Four species have neither of the symbols P , ε , d , s in their designation meaning that they are higher order ferroics. In these cases we show in column 9 the symmetry of the lowest order tensor in which some domain states are distinguished (Amin and Newnham, 1980).

Species exist for which the group F may take two different orientations, say F' and F'' , which are *crystallographically equivalent* but once the axes in a particular material have been chosen they are clearly distinguishable. These have been named by Aizu “*minor species*.” For us it is essential that left cosets of

F' and F'' in G contain the same symmetry operations which are, however, differently oriented with respect to the coordinate system of G . Therefore domain properties are identical. In the present table minor species occupy just one row (see, e.g., the species 076).

On the other hand, some pairs of species have the same F but their elements have *crystallographically nonequivalent* orientations; an example is, for instance, the species 161 as distinguished from both minor species 160.

We have stressed that Table B.1 (as well as its selection, Table 2.1.5) is based on the analysis of equitranslational phase transitions. However, as long as we seek information on *orientational* domain states, all information remains valid even for a transition with unit cell multiplication ($v \neq 1$).

In a few cases the last column 9 contains some additional information reserved for readers familiar with the theory of presentation of point groups. As shown by Janovec et al. (1975), the phase transitions represented by some species can be achieved by two different irreducible representations and the ferroic can be either proper or improper ferroelectric (ferroelastic); these cases are indicated as “2 IRs.” This has little to say about domain states but plays an essential role in temperature dependences of material coefficients as well as of spontaneous quantities. Further, the symbol “RR” is added to those species in which the order parameter does not transform according to an irreducible representation. Its transformation properties would be given by a combination of such representations, defining a reducible representation. This fact again would reflect itself in the temperature dependences of some spontaneously acquired properties. Both symbols “2 IRs” and “RR” are included to warn the reader that materials representing these species may reveal unusual properties. We note that the information indicated by symbols “RR” or “2 IRs” becomes superfluous for transitions at which the translational symmetry also changes. Finally, the symbol “1” attached to species 011 and 012 stresses that for them the order parameter transforms according to different irreducible representations and therefore they are considered as separate species (Janovec et al., 1975).

It is obvious that this table provides straightforward information about degeneracy of domain states. The degeneracy factors defined by Eq. (2.1.19), in particular $d_p = q/q_p$, $d_\varepsilon = q/q_\varepsilon$, $d_d = q/q_d$, and $d_s = q/q_s$, can be immediately obtained from data in columns 4–8.

Let us show, on a few examples chosen from Table 3.2.1 of selected ferroic materials, how Tables 2.1.5 and B.1 can be used to obtain useful information.

Consider crystals of quartz, species no. 108, $622-ds-32$. We see that in the ferroic phase the material is nonferroelectric and nonferroelastic. The total number of domain states is 2 and the symmetry elements of both represent just one point group. These states, which in fact represent the well-known Dauphiné twins, differ in the newly acquired forms of both piezoelectric and elastic compliance tensors. We have no domain degeneracy.

Crystals of PbZrO_3 represent the species no. 005, $m\bar{3}m - \varepsilon s - \bar{3}m$. This particular material changes eight times the unit cell volume as a result of the transition and so the information available concerns orientational domain

states only. It becomes neither ferroelectric nor ferroelastoelectric, no polarization or piezoelectric effect result from the transition. The point group of each of the four domain states is differently oriented. All of these states differ in some components of spontaneous strain (or permittivity) as well as in some components of elastic compliance.

Crystals of a specific kind of BaTiO_3 which is hexagonal in its parent phase belong to the species no. 082, $6/mmm-\varepsilon ds-222$. All of the six domain states differ in the piezoelectric (or electro-optic, for this matter) tensor. They are nonferroelectric but ferroelastic and ferrobielastic. Each ferroelastic or biferroelastic domain states is doubly degenerate with respect to the domain states differing in the piezoelectric tensor. Thus, for example, a domain state which is characterized by one single permittivity tensor is degenerate with respect to states differing in their piezoelectric response.

Properties of domain states in the ferroelectric phases of “normal” barium titanate which have been discussed as examples earlier in this chapter are immediately obvious from data for species no. 013 $m\bar{3}m - P\varepsilon ds - 4mm$, no. 022 $m\bar{3}m - P\varepsilon ds - mm2$, and no. 006 $m\bar{3}m - P\varepsilon ds - 3m$.

In the adopted classification of ferroics no attention is paid to tensor properties transforming as axial tensors. The occurrence of new components of such tensors in the phase F may be of great importance for distinguishing nonferroelastic domain states. These cases will be dealt with later in connection with the so-called twin laws and listed in Tables 2.2.1 and 2.2.2.

Table B.1 offers no detailed information on the transformation properties of the order parameter and the interested reader is referred to the papers by Aizu (1973a) or Janovec et al. (1975). In the following section we shall include another table of ferroelectric transitions alone, with some additional data.

2.1.9 Ferroelectric Species

We have already defined ferroelectric phase transitions as those at which the vector describing pyroelectric properties acquires a new component which was not allowed by symmetry in the parent phase. Accordingly, such a phase transition results in the development of spontaneous polarization components. Also, some classifications have been introduced in the preceding sections: proper and improper ferroelectrics, full and partial ferroelectrics. All ferroelectric species and their full-partial attributes in accompanying ferroelastic, ferroelastoelectric, and ferrobielastic properties can be easily determined from Table B.1. However, because ferroelectrics represent the most attractive family of ferroics and one which receives considerable attention from the point of view of applications of domain properties, we shall now incorporate some additional information about their particular species.

Classifications of ferroelectrics on the basis of symmetry approach provided an attractive subject for crystallographically oriented researchers and can be

found in many original papers. The first approach to their determination offered by Zheludev and Shuvalov (1956, 1959) was based on the idea of F being the maximum polar subgroup of G , which includes proper ferroelectrics only. Aizu introduced the concept of species and worked out tables of ferroics (Aizu, 1966, 1970b, 1973a) whose later versions covered both proper and improper ferroelectrics. Shuvalov (1970) in his classification of proper ferroelectrics introduced an interesting designation for species which represents a modification of symbols proposed by Aizu (1965, 1966).

Speaking about the possible behavior of a particular ferroelectric material, the most fundamental information contains three items: the symmetry group G , direction of \mathbf{P}_S specified with respect to the symmetry elements of G , and the symmetry group F . We remind the reader again that, generally, F may not follow from the simple relation (2.1.15), because in improper ferroelectrics the symmetry reduction may be more severe.

Information on ferroelectric species is presented in Table C.1 (as well as in its selection, Table 2.1.6). The number of a species is identical with that in Table B.1, as well as its designation given in the second column. The third column indicates the total number q of orientational domain states. This is the total number of domain states if $\nu = 1$ but it is ν times smaller than the total number of domain states if $\nu \neq 1$. In the fourth column are shown nonzero components of polarization in the phase F . They are specified for the subgroup orientation shown in the symbol. Here δP_k stands for the change of polarization component which was already permitted by symmetry in the parent phase (i.e., a nonzero component p_k of the pyroelectric coefficient was permitted in G). P_k stands for the newly acquired component of spontaneous polarization. More information about polarization is included that can be obtained on the basis of analysis of order parameter transformation. P_k without brackets means that this is the “proper” component of polarization (assuming $\nu = 1$). This means that P_k serves as the order parameter (fully explaining the symmetry change). If the symbol is in brackets, (P_k) or $[P_k]$, that means that this is an “improper” polarization component, arising as a secondary effect. If both proper and improper scenarios can be responsible for the development of polarization, two lines are given in the table, indicating both possibilities. The distinction between (P_k) and $[P_k]$ is reserved for a reader familiar with the theory of representations of point groups: (P_k) means that the component of polarization transforms according to an irreducible representation whereas $[P_k]$ means that its transformation law is more complicated. From the point of view of domain crystallography there is no difference between P_k , (P_k) , and $[P_k]$. But there may be substantial differences in other physical properties, e.g., in temperature dependence of spontaneous polarization.

The following fifth column shows the number q_P of domain states differing in the direction of spontaneous polarization.

Any component P_k except that designated by δP_k is “symmetry breaking,” meaning that it is not allowed in the phase G . In most cases (nine nonpyroelectric parent phases), G does not allow for any component of polarization.

Table 2.1.6 Selection of ferroelectric phases (full content, see Table C.1) (see the main text or Table C.1 for a more detailed explanation of columns)

1 Species no.	2 Species designation	3 q	4 Data on polarization	5 qP	6 Data on strain	7 q_e	8 Shuvalov's symbol
Cubic parent phase $\delta\epsilon_{xx}, \delta\epsilon_{yy}, \delta\epsilon_{zz}, \delta\epsilon_{xy}, 0, 0, 0$							
006	$m\bar{3}m - P\epsilon ds - 3_{xyz}m_{xy}$	8	$P_x = P_y = P_z$	8	$\delta\epsilon_{xx}, \delta\epsilon_{yy}, \delta\epsilon_{zz}, \delta\epsilon_{xy}, \epsilon_{yz}, \epsilon_{yx}, \epsilon_{zy}$	4	$m\bar{3}m(4)D3F3m =$
013	$m\bar{3}m - P\epsilon ds - 4_m m_{xy}$	6	P_z	6	$\delta\epsilon_{xx}, \delta\epsilon_{yy}, \delta\epsilon_{zz}, 0, 0, 0$	3	$m\bar{3}m(3)D4F4mm =$
021	$m\bar{3}m - P\epsilon ds - m_{xy}m_{xy}2_z$	12	$[P_z]$	6	$\delta\epsilon_{xx}, \delta\epsilon_{yy}, \delta\epsilon_{zz}, 0, \epsilon_{xy}$	6	$*m\bar{3}m(3)D2Fmm2 \neq$
022	$m\bar{3}m - P\epsilon ds - m_{xy}m_z2_{xy}$	12	$P_x = P_y, (P_x = P_y)$	12	$\delta\epsilon_{xx}, \delta\epsilon_{yy}, \delta\epsilon_{zz}, 0, 0, \epsilon_{xy}$	6	$m\bar{3}m(6)D2Fmm2 =$
034	$\bar{4}3m - P\epsilon ds - 3_{xyz}m_{xy}$	4	$P_x = P_y = P_z$	4	$\delta\epsilon_{xx}, \delta\epsilon_{yy}, \delta\epsilon_{zz}, \delta\epsilon_{xy}, \epsilon_{yz}, \epsilon_{yx}, \epsilon_{zy}$	4	$4\bar{3}m(4/2)D3F3m$
035	$\bar{4}3m - P\epsilon ds - 3_{xyz}$	8	$(P_x = P_y = P_z)$	4	$\delta\epsilon_{xx}, \delta\epsilon_{yy}, \delta\epsilon_{zz}, \delta\epsilon_{xy}, \epsilon_{yz}, \epsilon_{yx}, \epsilon_{zy}$	4	$*4\bar{3}m(4/2)D3F3m$
038	$\bar{4}3m - P\epsilon ds - m_{xy}m_{xy}2_z$	6	P_z	6	$\delta\epsilon_{xx}, \delta\epsilon_{yy}, \delta\epsilon_{zz}, 0, \epsilon_{xy}$	6	$\bar{4}3m(3)D4Fmm2 \neq$
040	$\bar{4}3m - P\epsilon ds - m_{xy}$	12	$P_x = P_y, P_z (P_x = P_y, P_z)$	12	$\delta\epsilon_{xx}, \delta\epsilon_{yy}, \delta\epsilon_{zz}, \epsilon_{yz}, -\epsilon_{yx}, \epsilon_{zy}$	12	$\bar{4}3m(12/2)A * mFm$ $4\bar{3}m(12/2)A * *mFm$
Hexagonal and trigonal parent phases $\delta\epsilon_{xx}, \delta\epsilon_{yy}, \delta\epsilon_{zz}, 0, 0, 0$							
069	$6/mmm - Pd - 6mm$	2	P_z	2	$\delta\epsilon_{xx}, \delta\epsilon_{yy}, \delta\epsilon_{zz}, 0, 0, 0$	1	$6/mmm(1)D6F6mm =$
073	$6/mmm - Pd - 6$	4	$[P_z]$	2	$\delta\epsilon_{xx}, \delta\epsilon_{yy}, \delta\epsilon_{zz}, 0, 0, 0$	1	$*6/mmm(1)D6F6 =$
080	$6/mmm - P\epsilon ds - m_x m_z$	6	(P_z)	6	$\delta\epsilon_{xx}, \delta\epsilon_{yy}, \delta\epsilon_{zz}, 0, 0, 0$	3	$*6/mmm(3)D6Fmm2 =$
081	$6/mmm - P\epsilon ds - m_x m_z$	6	P_y	6	$\delta\epsilon_{xx}, \delta\epsilon_{yy}, \delta\epsilon_{zz}, 0, 0, 0$	3	$6/mmm(3)D2Fmm2 =$
	$6/mmm - P\epsilon ds - m_y m_z$		P_x		$\delta\epsilon_{xx}, \delta\epsilon_{yy}, \delta\epsilon_{zz}, 0, 0, 0$		
Tetragonal parent phase $\delta\epsilon_{xx}, \delta\epsilon_{yy}, \delta\epsilon_{zz}, 0, 0, 0$							
155	$4/mmm - P\epsilon ds - m_y m_z$	4	P_x	4	$\delta\epsilon_{xx}, \delta\epsilon_{yy}, \delta\epsilon_{zz}, 0, 0, 0$	2	$4/mmm(2)D2Fmm2 =$
	$4/mmm - P\epsilon ds - m_x m_z$		$P_x = P_y$		$\delta\epsilon_{xx}, \delta\epsilon_{yy}, \delta\epsilon_{zz}, 0, \epsilon_{xy}$		
156	$4/mmm - P\epsilon ds - m_{xy}m_z$	4	$[P_z]$	2	$\delta\epsilon_{xx}, \delta\epsilon_{yy}, \delta\epsilon_{zz}, 0, 0, 0$	2	$*4/mmm(2)D4Fmm2 \neq$
	$4/mmm - P\epsilon ds - m_x m_z$				$\delta\epsilon_{xx}, \delta\epsilon_{yy}, \delta\epsilon_{zz}, 0, 0, \epsilon_{xy}$		
170	$4\bar{2}m - P\epsilon ds - 2_x$	4	P_x	4	$\delta\epsilon_{xx}, \delta\epsilon_{yy}, \delta\epsilon_{zz}, \epsilon_{yz}, 0, 0$	4	$\bar{4}2m(2)D2F2 \neq$
171	$\bar{4}2m - P\epsilon ds - 2_z$	4	$[P_z]$	2	$\delta\epsilon_{xx}, \delta\epsilon_{yy}, \delta\epsilon_{zz}, 0, 0, \epsilon_{xy}$	4	$*\bar{4}2m(1)D4F2$
Orthorhombic parent phase $\delta\epsilon_{xx}, \delta\epsilon_{yy}, \delta\epsilon_{zz}, 0, 0, 0$							
201	$mm2 - P\epsilon ds - m_x$	2	$P_y, \delta P_z$	2	$\delta\epsilon_{xx}, \delta\epsilon_{yy}, \delta\epsilon_{zz}, \epsilon_{yz}, 0, 0$	2	$mm2(2/2)AmFm$
	$mm2 - P\epsilon ds - m_y$		$P_x, \delta P_z$		$\delta\epsilon_{xx}, \delta\epsilon_{yy}, \delta\epsilon_{zz}, 0, \epsilon_{xy}, 0$		

In Table C.1 we give information about natural spontaneous strain defined in Sect. 2.1.3. For this purpose the whole table is divided into six sections according to the crystal families (cubic, hexagonal, tetragonal, orthorhombic, monoclinic, and triclinic) of the phase G . At the top of each section we give strain components $\delta\varepsilon_{kl}$ which are compatible with the symmetry of that crystal family, in the sequence $\delta\varepsilon_{xx}$, $\delta\varepsilon_{yy}$, $\delta\varepsilon_{zz}$, $\delta\varepsilon_{yz}$, $\delta\varepsilon_{zx}$, $\delta\varepsilon_{xy}$. In fact, these can be understood as components of the thermal dilatation tensor. For each species, column 6 specifies strain components $\delta\varepsilon_{kl}$ which are compatible with the symmetry of the phase F specified in the species symbol. The sequence of components is the same as before. It should be stressed again that all these data refer to the coordinate system of G . If the particular component itself is “symmetry breaking” (not allowed in G), it is written as ε_{kl} . If it is already allowed in G , it has the prefix δ . In contrast to polarization, the situation is complicated by the fact that two components $\delta\varepsilon_{kl}$, $\delta\varepsilon_{mn}$ compatible with the symmetry of G , which are equal in G , may become different in the phase F . It is then the difference $\delta\varepsilon_{Skl} - \delta\varepsilon_{Smn}$ between them which “breaks” the symmetry, as already explained in Sect. 2.1.3. Column 7 gives the number of domain states differing in spontaneous deformation, i.e., the number of ferroelastic domain states q_ε .

The last column of the table shows the already mentioned symbol proposed by Shuvalov (1970) which has been used by some lecturers and can be found very practical. The original Shuvalov’s table included proper ferroelectrics only and for them the symbol is just reproduced here, including the original designation of cubic phases $m\bar{3}m$ and $m3$ (in keeping with the newer crystallographic standards, otherwise we employ the designation $m\bar{3}m$ and $\bar{3}m$ in this book). For species in which F is not the maximal polar subgroup as in Shuvalov’s listing, we have designed his symbol following the original rules; such a symbol is preceded by an asterisk (*). The symbol starts with the designation of point group G . This is followed by the number of axes (in the parenthesis) in the group G along which spontaneous polarization can be directed (“ferroelectric axes”). If there is just a single number in the parentheses it indicates that \mathbf{P}_S can have two orientations along each of these axes. If this number is divided by two it indicates that \mathbf{P}_S can have only one of these orientations; it is not reversible. Next is the symbol specifying the information about the orientation of the ferroelectric axis (axes). $D2$, $D3$, etc., signify that the axis is parallel to the twofold axis or threefold axis in G , respectively. Dm means that the ferroelectric axis is perpendicular to the mirror plane in G . In contrast, $A2$, $A3$, etc., indicate the ferroelectric axis to be perpendicular to the twofold or threefold axis, respectively, but otherwise with a general orientation. Am indicates an arbitrary orientation parallel to the mirror plane. The next symbol F just stands for “ferroelectric” and is followed by the symbol of the point group in the ferroelectric phase. Finally, many species are provided with either = or \neq symbol. Here = indicates that the crystal lattices for domain states with antiparallel polarization are collinear. In other words, they do not differ in spontaneous deformation. In contrast, \neq means that domain states with antiparallel \mathbf{P}_S vectors differ in ε_S . Obviously, any of these symbols is missing when \mathbf{P}_S is not reversible.

The information contained in the table also enables classification of ferroelectrics according to a scheme introduced in the very early stages of their investigations, namely, *uniaxial ferroelectrics* are those where \mathbf{P}_S can be oriented along one axis only and have two antiparallel directions; in *multiaxial ferroelectrics with reversible polarization* there are more than one such axes, along each axis \mathbf{P}_S can have either sign; in *multiaxial ferroelectrics with reorientable polarization* \mathbf{P}_S can be oriented along more than one axes of the parent phase but has no equivalent antiparallel direction.

Assigning the correct species to a ferroelectric material contains a wealth of usable information and we shall give two examples to indicate just a part of it.

Consider one of the bismuth oxide ferroelectrics with a layer structure, $\text{SrBi}_2\text{Ta}_2\text{O}_9$ (abbr. SBT), which we assume to represent the species $4/mmm-P\epsilon ds-m_y m_z 2_x$ (no. 155). We see from the table that there are four domain states, all differing in the direction of \mathbf{P}_S which is reversible. The orientation of the polar axis in the ferroelectric phase tells us that the angle between any two \mathbf{P}_S vectors is either 90° or 180° . There are only two ferroelastic domain states; changing the sign of \mathbf{P}_S does not result in any change of the unit cell shape. However, all domain states are distinguishable also in the piezoelectric and compliance tensors. Thus (using Tables B.1 and C.1), the sign of \mathbf{P}_S can be assessed indirectly by monitoring the piezoelectric response.

As another example, consider the species no. 027. The symmetry changes from cubic $m\bar{3}m$ to monoclinic m_z . The mirror in the phase F is perpendicular to the fourfold axis of the cubic lattice in the phase G . Spontaneous polarization has two components in the x, y plane of the group G and the transition can be either proper or improper. There are altogether 24 domain states and all of them differ in polarization. However, there are only 12 domain states differing in spontaneous strain, ferroelastic domain states. The species is a full ferroelectric and partial ferroelastic one: Each domain state characterized by a particular strain can have two alternative (antiparallel) directions of spontaneous polarization. For a particular domain state corresponding to the indicated subgroup F which is m_z , the symmetry-breaking deformations are ϵ_{xy} , $\delta\epsilon_{yy}-\delta\epsilon_{xx}$, and $\delta\epsilon_{zz}-\delta\epsilon_{yy}$. The latter statement follows from the comparison of $\delta\epsilon_{kl}$ tensors given for this species and those given for G at the top of the ‘‘cubic’’ section of the table.

We stress again that all these considerations are made on the level of point symmetries. More detailed classifications have been proposed based on the changes of space groups (Toledano and Toledano, 1988).

2.2 Coexisting Domain States

In Sect. 2.1.7 we have introduced the concept of domain states and treated them as independently existing states of a crystal lattice in the phase F . A crystalline sample whose total volume represents just one of the domain states is a *single domain sample*. However, there are a number of factors which make a real sample *multidomain*. In it, *domains* defined as regions whose structures

represent different symmetry-permitted domain states coexist. Their linear sizes depend on many factors but, if some often encountered number should be given, they could range (in bulk samples) between 1 and 100 μm . However, to quote just one number is misleading since in a prevailing majority of cases the domain shapes are strongly anisotropic, being close to cylinders or slabs. Domains are separated by *domain walls* whose thickness is typically much less than the linear dimensions of domains. The formation of domains may be due to a large number of factors. These are connected with the crystal growth, with the process of the phase transformation from the parent phase, with the presence of defects. We shall discuss these mechanisms in some detail later. What makes, of course, ferroics particularly attractive materials is the fact that properly designed and oriented externally applied forces can bring a ferroic sample from a domain state i to another domain state j . In practice, it is rather a rule than an exception that the reorientation is accomplished only in some parts of the sample and we end up again with a multidomain sample.

When no forces are applied or arise due to boundary conditions, a multidomain sample of an ideal crystal is not in the ground state of its energy; this is because of the existence of domain walls separating domains in which crystal lattices representing the phase F are perturbed. Thus domain walls are in fact crystal defects.

In this section we wish to discuss properties of a pair of coexisting domain states, referred to as a *domain pair*. In a sense, domain pairs actually play the role of elementary units of the polydomain states. In the following sections, based on symmetry approach, we will primarily address two questions: (i) how the elements of a domain pair (i.e., domains) can be distinguished and (ii) how these elements can coexist in physical contact. In these considerations we will not pay attention to internal properties of domain walls, which will be discussed in Chap. 6.

2.2.1 Twinning Operations

Consider two domain states resulting from a ferroic phase transition of a G - F species. Let us denote the order parameter in these states as η_i and η_j . As we have seen in Sect. 2.1, among the symmetry operations of G there are some which transform η_i into η_j . These operations are referred to as *twinning operations of the ordered pair* (η_i, η_j) . One such operation is denoted as T_{ij} . The whole ensemble of all twinning operations of an ordered pair represents the *twinning complex of the ordered pair*.⁹ Generally, it holds that the twinning complex of the ordered pair (η_i, η_j) is not identical with that of the ordered pair (η_j, η_i) .¹⁰

⁹ We remark that our twinning operations are what in Aizu's analyses of domain states (or simply states in his terminology) has been referred to as F operations (Aizu, 1969, 1970b, 1972), a term used by other authors as well (Wadhawan, 1982).

¹⁰ This interesting situation may have many practical consequences; some are connected to structures of domain walls, others relate to macroscopic phenomena.

The knowledge of a twinning operation T_{ij} of an (η_i, η_j) pair enables us to compare a given tensor property of the two domain states involved. As we already discussed in Sect. 2.1, the application of the operation T_{ij} onto a tensor property in the η_i -state determines the former in the η_j -state. This procedure makes it possible to determine those macroscopic properties which could be used for experimental distinction of the two domain states in the pair. Clearly, these properties are those which change under the application of T_{ij} .

Another utilization of the approach outlined above reveals a situation substantially different for ferroelastic domain pairs (domain states which differ in tensor properties described by a symmetric second-rank tensor) and those which are nonferroelastic.

First, domains forming ferroelastic pairs in transparent crystals can be relatively easily distinguished by optical methods, as we shall discuss in detail in Chap. 4. Observation methods are more restricted when the domain pair is nonferroelastic and there we may be interested in knowing in detail in which macroscopic properties the two domains differ. In addition, nonferroelastic domain pairs receive special attention as domain states carrying information in memory devices. We shall, therefore, consider them in more detail in the next section.

Second, when two ferroelastic domain states are in physical contact, the twinning operations as defined above describe the relative orientation of tensor properties of the two adjacent domains only approximately. This issue deserves further discussion and we shall come back to it in Sect. 2.2.5 where the necessary background will be available.

2.2.2 Twin Laws for Nonferroelastic Domain Pairs

This section is devoted to differences in tensor properties of domain states forming a nonferroelastic domain pair. As we have just mentioned, this issue is of importance for experimental distinction of such pairs which is often a difficult task. The information provided in this section enables the reader to determine tensor properties which can be used to distinguish the states forming a given pair. We present this information in Tables 2.2.1 and 2.2.2 which are based on related tables (Janovec et al., 1993; Litvin and Janovec, 1997). The approach used in these papers can be outlined as follows.

Generally, as indicated in the previous section, the twinning complex of the ordered pair (η_i, η_j) is not identical with that of the ordered pair (η_j, η_i) . When the twinning complexes of pairs (η_i, η_j) and (η_j, η_i) are identical, the pair of domain states is referred to as an *ambivalent pair* (Janovec, 1972; Janovec et al., 1993). It can be shown that the pair (η_i, η_j) is ambivalent if there exists at least one symmetry operation $g_{ij} \in G$ which serves as a twinning operation for both pairs (η_i, η_j) and (η_j, η_i) at once, i.e.,

$$T_{ij} = T_{ji} = g_{ij}. \quad (2.2.1)$$

Table 2.2.1 Twin laws for nonferroelastic and partially ferroelastic phase transitions

G	G	F	J_{ik}
$m\bar{3}m$		$\bar{4}3m$	$\bar{m}\bar{3}m$
$m\bar{3}m$		432	$\bar{m}\bar{3}m$
$m\bar{3}m$		$m\bar{3}$	$\bar{m}\bar{3}m$
$m\bar{3}m$		23	$\bar{m}\bar{3}$
			$\bar{4}32$
			$\bar{4}3m$
	$m\bar{3}m$	$\bar{3}$	$\bar{3}m$
	$m\bar{3}m$	$\bar{4}$	$\bar{4}2m$
			$4/m$
	$m\bar{3}m$	4	$4/m$
			$\bar{4}22$
			$4mm$
$\bar{4}3m$		23	$\bar{4}3m$
$\bar{4}3m$		$\bar{4}$	$\bar{4}2m$
432		23	$\bar{4}32$
432		4	$\bar{4}22$
$m\bar{3}$		23	$m\bar{3}$
$6/mmm$		$\bar{6}m2$	$6/mmm$
$6/mmm$		$6mm$	$6/mmm$
$6/mmm$		622	$6/mmm$
$6/mmm$		$6/m$	$6/mmm$
$6/mmm$		$\bar{6}$	$\bar{6}m2$
			$6/m$
$6/mmm$		6	$\bar{6}22$
			$6mm$
			$6/m$
$6/mmm$		$\bar{3}m$	$6/mmm$
$6/mmm$		$3m$	$\bar{3}m$
			$6mm$
			$\bar{6}m2$
$6/mmm$		32	$\bar{3}m$
			$\bar{6}22$
			$\bar{6}m2$
$6/mmm$		$\bar{3}$	$\bar{3}m$
			$6/m$
$6/mmm$		3	$\bar{3}$
			32
			$3m$
			$\bar{6}$
			$\bar{6}$
$\bar{6}m2$		$\bar{6}$	$\bar{6}m2$
$\bar{6}m2$		$3m$	$\bar{6}m2$
$\bar{6}m2$		32	$\bar{6}m2$
$\bar{6}m2$		3	$\bar{3}2$
			$3m$
			$\bar{6}$

Table 2.2.1 (continued)

G	G	F	J_{ik}
$6mm$		6	$\underline{6mm}$
$6mm$		$3m$	$\underline{6mm}$
$6mm$		3	$\underline{3m}$
			$\underline{6}$
622		6	$\underline{622}$
622		32	$\underline{622}$
622		3	$\underline{32}$
			$\underline{6}$
$6/m$		$\bar{6}$	$\underline{6/m}$
$6/m$		6	$\underline{6/m}$
$6/m$		3	$\underline{6/m}$
$6/m$		3	$\underline{6}$
			$\underline{\bar{3}}$
			$\underline{\bar{6}}$
$\bar{6}$		3	$\underline{\bar{6}}$
6		3	$\underline{6}$
$\bar{3}m$	$m\bar{3}m$	$3m$	$\underline{3m}$
$\bar{3}m$	$m\bar{3}m$	32	$\underline{\bar{3}m}$
$\bar{3}m$		$\bar{3}$	$\underline{\bar{3}m}$
$\bar{3}m$	$m\bar{3}m$	3	$\underline{\bar{3}}$
			$\underline{32}$
			$\underline{3m}$
$3m$	$\bar{4}3m$	3	$\underline{3m}$
32	432	3	$\underline{32}$
$\bar{3}$	$m\bar{3}$	3	$\underline{\bar{3}}$
$4/mmm$	$m\bar{3}m$	$m\bar{3}m$	$\underline{4/mmm}$
$4/mmm$	$m\bar{3}m$	$4mm$	$\underline{4/mmm}$
$4/mmm$	$m\bar{3}m$	422	$\underline{4/mmm}$
$4/mmm$	$m\bar{3}m$	$4/m$	$\underline{4/mmm}$
$4/mmm$		$\bar{4}$	$\underline{4/m}$
			$\underline{42m}$
$4/mmm$		4	$\underline{4/m}$
			$\underline{422}$
			$\underline{4mm}$
$\bar{4}2m$		$\bar{4}$	$\underline{\bar{4}2m}$
$4mm$		4	$\underline{4mm}$
422		4	$\underline{422}$
$4/m$		$\bar{4}$	$\underline{4/m}$
$4/m$		4	$\underline{4/m}$
mmm	$4/mmm, 6/mmm, m\bar{3}, m\bar{3}m$	222	\underline{mmm}
mmm	$4/mmm, 6/mmm, m\bar{3}, m\bar{3}m$	$mm2$	\underline{mmm}
$2/m$	$mmm, 4/m, 4/mmm, \bar{3}m, 6/m, 6/mmm, m\bar{3}, m\bar{3}m$	2	$\underline{2/m}$
$2/m$	$mmm, 4/m, 4/mmm, \bar{3}m, 6/m, 6/mmm, m\bar{3}, m\bar{3}m$	m	$\underline{2/m}$
$\bar{1}$	$2/m, mmm, 4/m, 4/mmm, \bar{3}, \bar{3}m, 6/m, 6/mmm, m\bar{3}, m\bar{3}m$	1	$\underline{1}$

Table 2.2.2 Numbers of distinct tensor components for nonferroelastic twin laws. The meaning of symbols is specified below the table

F	J_{ik}	ε	V	$\varepsilon[V^2]$	$V[V^2]$	$\varepsilon V[V^2]$	$[[V^2]^2]$	$[V^2]^2$	$[V^2]V^2$
1	$\bar{1}$	1	3	6	18	0	0	0	0
2	$2/m$	1	1	4	8	0	0	0	0
m	$\underline{2}/m$	0	2	2	10	0	0	0	0
222	\underline{mmm}	1	0	3	3	0	0	0	0
$mm2$	\underline{mmm}	0	1	1	5	0	0	0	0
4	$4/m$	1	1	2	4	0	0	0	0
4	$\underline{4}/m$	0	0	2	4	0	0	0	0
4	$\underline{4}22$	0	1	0	3	3	1	3	6
4	$\underline{4}mm$	1	0	2	1	3	1	3	6
4	$\underline{4}2m$	0	0	1	2	3	1	3	6
$4/m$	$4/mmm$	0	0	0	0	3	1	3	6
422	$4/mmm$	1	0	2	1	0	0	0	0
$4mm$	$4/mmm$	0	1	0	3	0	0	0	0
$\bar{4}2m$	$\underline{4}/m$	0	0	1	2	0	0	0	0
3	$\bar{3}$	1	1	2	6	0	0	0	0
3	$\underline{3}2$	0	1	0	4	4	1	4	8
3	32	0	1	0	4	4	1	4	8
3	$3m$	1	0	2	2	4	1	4	8
3	$\underline{3}m$	1	0	2	2	4	1	4	8
$\bar{3}$	$\bar{3}m$	0	0	0	0	4	1	4	8
3	$\bar{3}m$	0	0	0	0	4	1	4	8
32	$\bar{3}m$	1	0	2	2	0	0	0	0
$3m$	$\bar{3}m$	0	1	0	4	0	0	0	0
3	$\underline{6}$	0	0	0	2	2	2	4	6
3	$\bar{6}$	1	1	2	4	2	2	4	6
$\bar{3}$	$\underline{6}/m$	0	0	0	0	2	2	4	6
6	$6/m$	1	1	2	4	0	0	0	0
$\bar{6}$	$\underline{6}/m$	0	0	0	2	0	0	0	0
32	$\underline{6}22$	0	0	0	1	1	1	2	3
6	$\underline{6}22$	0	1	0	3	3	0	2	5
$3m$	$\underline{6}mm$	0	0	0	1	1	1	2	3
6	$\underline{6}mm$	1	0	2	1	3	0	2	5
32	$\underline{6}m2$	1	0	2	1	1	1	2	3
$\bar{6}$	$\underline{6}m2$	0	0	0	1	3	0	2	5
$3m$	$\underline{6}m2$	0	1	0	3	1	1	2	3
$\bar{3}m$	$\underline{6}/m$	0	0	0	0	1	1	2	3
$6/m$	$6/mmm$	0	0	0	0	3	0	2	5
622	$6/mmm$	1	0	2	1	0	0	0	0
$6mm$	$6/mmm$	0	1	0	3	0	0	0	0
$\bar{6}m2$	$\underline{6}/m$	0	0	0	1	0	0	0	0
23	$\underline{m}3$	1	0	1	1	0	0	0	0
23	$\underline{4}32$	0	0	0	1	1	0	1	2
23	$\underline{4}3m$	1	0	1	0	1	0	1	2

Table 2.2.2 (continued)

F	J_{ik}	ε	V	$\varepsilon[V^2]$	$V[V^2]$	$\varepsilon V[V^2]$	$[[V^2]^2]$	$[V^2]^2$	$[V^2]V^2$
$m\bar{3}$	$m\bar{3}m$	0	0	0	0	1	0	1	2
432	$m\bar{3}m$	1	0	1	0	0	0	0	0
$\bar{4}3m$	$m\bar{3}m$	0	0	0	1	0	0	0	0

F : symmetry of the ferroic phase; J_{ik} : twin law; ε : the structures of the two domain states are enantiomorphous; V : polar vector (spontaneous polarization); $\varepsilon[V^2]$: axial symmetric second-rank tensor describing optical activity; the tensor $V[V^2]$ describes piezoelectric effect, linear electrooptic effect, or linear photogalvanic effect; $\varepsilon V[V^2]$: describes electrogyration; $[[V^2]^2]$: stands for elastic compliance tensor; $[V^2]^2$: describes electrostriction and piezooptic (photo-elastic) effects and also the effect of spatial dispersion. The tensor of symmetry $[V^2]V^2$ characterizes the flexoelectric effect. For formal definition of the symbols used for the symmetry of tensors see Appendix F. Number 0 means that the two domain states cannot be distinguished by a tensorial property represented by the column, be it because the property is not allowed by symmetry in the ferroic phase or because the two domain states do not differ in it. Nonzero numbers stand for the count of components of the given tensor by which the two domain states can be distinguished.

It can be shown that any nonferroelastic domain pair is ambivalent. The symmetry group of such a pair can be written as

$$J_{ik} = F_{ik} + g_{ik}F_{ik} \quad (2.2.2)$$

where $F_{ik} = F_i \cap F_k$ is the intersection of groups F_i and F_k . The group J_{ik} specifies in a way the relation between the two domain states i, k and has been named *twin law of the ambivalent pair*. Now, suppose we are interested in a tensor material property \mathbf{T} . We can then easily find the number m_1 of independent components of \mathbf{T} in the group J_{ik} as well as their number m_2 in the group F . The difference $m_2 - m_1$ then gives the number of independent components that are different in domain states i and k .

Tables 2.2.1 and 2.2.2 enable one to find quickly in which tensor properties two domain states in a nonferroelastic domain pair differ. In addition, they also give the numbers of components of tensors up to the fourth rank including two axial tensors which distinguish these two states. These tables can be used in the following way. The groups G and F being given, we first determine the corresponding twin law J_{ik} in Table 2.2.1. The twinning complex of a pair is shown as underlined symmetry operation(s) in the symbol of its twinning law. When G (for the G, F pair in question) is found in the first column, the transition to F on the same line is nonferroelastic. When G is given in the second column, the species $G-F$ is a partial ferroelastic species: For this species only some domain pairs are nonferroelastic and it is these pairs that we investigate. Next, knowing J_{ik} and F we turn to Table 2.2.2 and find the numbers of components for tensors of different ranks and symmetries, in which the two domain states differ. In addition, information is added as to the possible enantiomorphism of structures representing the two domain states. Understandably, any of this information can also be found by treating each case individually and employing matrices of tensors and twinning operations.

Let us give a few examples to indicate the practical significance of the information contained in these two tables. Generally, the presence of enantiomorphism indicates a possibility of employing optically active etchants differing in handedness for distinguishing domains. In crystals of $\text{Bi}_4\text{Ti}_3\text{O}_{12}$ which is a partial ferroelastic (species $4/mmm-P\bar{6}ds-m_2$) there are eight directions of \mathbf{P}_S and domains with antiparallel polarizations have collinear lattices. This material was intensively studied in connection with ferroelectric memories and recently switching properties of thin films of this material have been of interest. Table 2.2.1 shows that domain states with antiparallel polarization differ in 10 components of the piezoelectric tensor; this points to possible importance of stresses on the polarization reversal process as well as the possibility of accomplishing domain reorientation based on ferroelastoelectric properties. Possibility of differences in electrogyration is indicated for many materials like for quartz (species $622-ds-32$) or $\text{Pb}_5\text{Ge}_3\text{O}_{11}$ (species $\bar{6}-Pd-3$). In the low-temperature monoclinic phase of $\text{NaH}_3(\text{SeO}_3)_2$ (probable species $2/m-Pd-m$) gyration might be interesting as a tool to observe domains. In CsCuCl_3 crystals (species $6/mmm-d-622$) domains, not yet observed, should be distinguished by optical activity.

These are just a few examples illustrating how the tables of twin laws can give fast useful information. Others, which, e.g., might concern nondestructive reading possibilities of ferroelectric non-volatile memories, could also be easily extracted from these tables.

2.2.3 Domain Wall Orientation: Electrical Compatibility

By introducing the concept of twinning operations in Sect. 2.2.2 we addressed one of the key problems of ferroics, namely, the question as to what are the relations between two selected domain states and how their characteristics differ when related to a single reference system. These are the essential issues when one is interested in macroscopic properties of multidomain samples. However, these properties will also be codetermined by other factors, in particular, by the size and shapes of domains, which in turn will depend on the orientation and properties of intermediate regions separating domains and domain walls.

In this and the next section we will be discussing the orientation of domain wall separating a domain pair. In general one can specify four factors controlling the orientation of a wall: (i) the state of the crystal with the wall of a given orientation should correspond at least to a local energy minimum; (ii) electrostatic energy related to differently oriented \mathbf{P}_S vectors in the neighboring domains; (iii) elastic energy related to differently oriented spontaneous strains in neighboring domains; and (iv) energy of the wall itself. In most practical situations, factors (ii) and (iii) play the decisive role. Factor (iii) is usually referred to as electrical compatibility problem. It will be discussed together with factor (i) in this section; factor (ii), usually referred to as the mechanical compatibility problem, will be treated in the next section. We postpone the discussion of factor (iv) to Chap. 6 where the necessary background will be available.

An arbitrarily oriented domain wall between ferroelectric domains, in general, carries bound charge whose density, according to the Poisson equation, equals

$$\rho_b = -\text{div } \mathbf{P} . \tag{2.2.3}$$

The existence of this charge is not energetically favorable. In principle, it can be compensated by free carriers. If this is not the case, the energetically preferable orientation of the wall corresponds to its electrically neutral state. It is determined by Eq. (2.2.3) with $\rho_b = 0$. For a wall with normal vector \mathbf{n} , which separates two domains characterized by spontaneous polarization vectors \mathbf{P}_{SA} and \mathbf{P}_{SB} , the condition of wall neutrality reads

$$(\mathbf{P}_{SA} - \mathbf{P}_{SB})\mathbf{n} = 0. \tag{2.2.4}$$

If possible compensation of the bound charge on the wall by free carriers can be neglected and if the domain pair is nonferroelastic, electrical neutrality plays the key role in the wall orientation. Two typical situations for mutual orientation of a planar wall and polarization vectors in neighboring domains apply for the species $m\bar{3}m - P\epsilon ds - 4mm$ which represents the tetragonal phase of BaTiO_3 . They are illustrated in Fig. 2.2.1a and b. The former shows the so-called 180° wall;

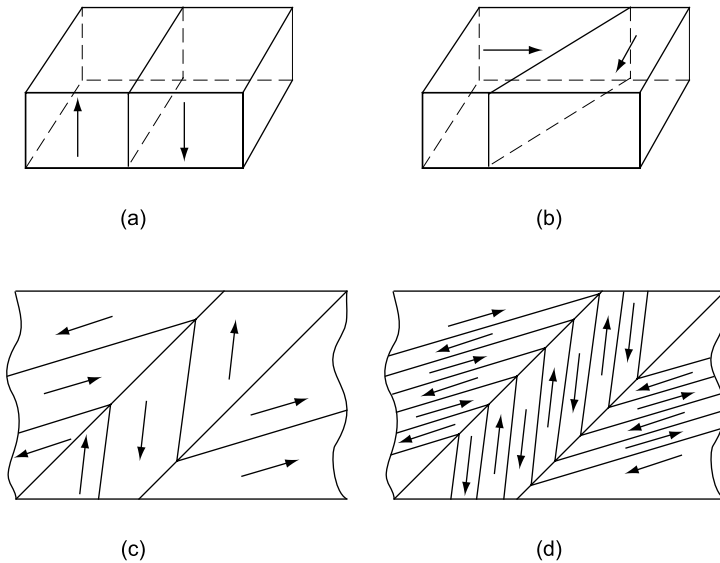


Fig. 2.2.1 (a) 180° ferroelectric domain wall. (b) 90° ferroelectric domain wall. (c) Involved domain patterns typical for multiaxial ferroelectrics. Here the 180° walls are assumed nonferroelastic so that the whole domain configuration is mechanically compatible. Head-to-tail coupling of spontaneous polarization avoids bound charge and is believed to be typical for the geometry of nonferroelastic 180° ferroelectric structures in coexistence with ferroelastic walls. (d) Electrostatic energy may also be reduced by dense antiparallel ferroelectric domains which couple head to head

its electroneutrality is maintained due to the absence of polarization component normal to the wall. The latter represents the so-called 90° wall which again is neutral because the polarization component normal to the wall is continuous on crossing the wall. It is clear that, with 180° walls, domains themselves should have the shape of slabs or cylinders. We shall see in a later chapter that this is consistent with experimental observations: It can be considered typical that ferroelectric domains tend to be elongated along the polar axis.

Domain structures in the given species containing both types of electroneutral walls are possible as well. A structure of this type is shown in Fig. 2.2.1c. Here one sees that in order to avoid the existence of bound charge we expect that 180° walls will proceed continuously throughout the 90° wall and that, on the 90° wall, \mathbf{P}_S will be coupled “head-to-tail.” Such arrangements are observed in single crystals of BaTiO_3 (Merz, 1954; Hooton and Merz, 1955). However, as it was pointed out (Arlt, 1990), it is reasonable to consider the condition of electroneutrality on the average. A configuration with head-to-head coupling where the 90° walls are electroneutral only on average is illustrated in Fig. 2.2.1d. It is worth mentioning that, being dense enough, this configuration may be realistic because of relative ease of compensation of the bound charge by free carriers.

Understandably, in many ferroelectric species domain pairs can exist in which the \mathbf{P}_S vectors make an angle γ differing from 180° or 90° ; such domain pairs are occasionally referred to as γ -pairs.¹¹

The above consideration naturally suggests another question. We have based our analysis on the fact that the uncompensated bound charge of an electrically incompatible wall substantially increases the energy of a sample. For an infinite sample containing one charged domain wall, the additional electrostatic energy when recalculated to a unit area of the wall results in an infinite increase of its surface energy density. In this situation the condition of electroneutrality should be strictly fulfilled. However, in any finite sample the violation of the wall neutrality results just in an increase of the effective wall energy and may be compensated at the expense of another contribution to the energy of the system. Thus, one could conclude that, in principle, a ferroelectric wall might carry any charge density up to its maximal possible value of $2P_S$. However, it turns out that this statement does not hold.¹² The reason is that the field created by a charged wall not only contributes to the energy of the system but also may suppress ferroelectricity in the neighboring domains. Thus, there is a limit to the maximum value of surface charge density beyond which the wall cannot exist. Applied to the problem of wall orientation, as was pointed out by Chervonobrodov and Roytburd (1988), this implies a limit to the possible deviation of the wall from its electroneutral orientation.

¹¹ In everyday language, researchers in ferroelectricity often refer to γ pairs as to γ domains. But the plural is essential; sometimes one can see that just one domain is designated as a 90° domain or 180° domain, a ridiculous specification.

¹² This relates to the case of proper ferroelectrics only; see Sect. 2.1 for definition of proper and improper ferroelectrics.

We will illustrate this problem considering a 180° wall in an infinite sample, whose plane makes an angle ψ with the direction of the ferroelectric axis Z . To check the ferroelectric stability we write down the Landau theory equation of state for the polarization components lying in the plane which contains the ferroelectric axis and perpendicular to the plane of the wall (we consider the second-order transition so that $\alpha_z < 0$ and $\beta > 0$)

$$\alpha_z P_z + \beta P_z^3 = E_z, \quad (2.2.5)$$

$$P_x = \varepsilon_0(\kappa_x - 1)E_x. \quad (2.2.6)$$

Here P_x , P_z , E_x , and E_z stand for the corresponding components of the polarization and electric field; κ_x is the relative dielectric permittivity in the direction normal to the spontaneous polarization and ε_0 is the vacuum permittivity. The electrostatic boundary conditions at the wall require the continuity of the tangential component of the electric field and the continuity of the normal component of the electric displacement ($D_i = \varepsilon_0 E_i + P_i$). Because of the symmetry of the problem, these conditions can be met only if these components are equal to zero. This requirement together with Eq. (2.2.6) enables us to find the Z -component of the electric field created by the bound charge of the wall in the form

$$E_z = -\frac{P_z}{\varepsilon_0} \frac{\sin^2 \psi}{\sin^2 \psi + \kappa_x \cos^2 \psi}. \quad (2.2.7)$$

Then Eq. (2.2.5) gives

$$\left[\alpha_z + \frac{\varepsilon_0^{-1} \sin^2 \psi}{\sin^2 \psi + \kappa_x \cos^2 \psi} \right] P_z + \beta P_z^3 = 0. \quad (2.2.8)$$

The condition to have spontaneous polarization in the sample (otherwise there is no wall!) requires that in the crystal $\alpha_z + \frac{\varepsilon_0^{-1} \sin^2 \psi}{\sin^2 \psi + \kappa_x \cos^2 \psi} < 0$. Thus, we arrive at the conclusion that the ferroelectricity can stand the field of the tilted wall only if the angle ψ meets the condition

$$\psi < \psi_0; \quad \tan \psi_0 \approx \sqrt{\varepsilon_0 \kappa_x |\alpha_z|} \approx \sqrt{\kappa_x / 2\kappa_z}. \quad (2.2.9)$$

Here $\kappa_z = 1 + 1/(\varepsilon_0 2|\alpha_z|)$ is the relative dielectric permittivity along the polar axis of the material. When deriving Eq. (2.2.9), it has been taken into account that usually $\kappa_z \gg 1$.

The walls with $\psi > \psi_0$ cannot exist. It can be shown that if a “single-standing” wall is forced to exceed the critical angle ψ_0 it will decay into a zigzag wall pattern (Chervonobrodov and Roytburd, 1988). As clear from Eq. (2.2.9), this angle is sensitive to the dielectric anisotropy of the material. In uniaxial

ferroelectrics where typically $\kappa_z \gg \kappa_x$, this criterion makes impossible any strong deviation of the walls from their electro-neutral configurations. At the same time, in materials close to the morphotropic boundary where the opposite relation takes place, $\kappa_z \ll \kappa_x$, condition (2.2.9) does not strongly limit such deviation. Qualitatively¹³ this statement applies to BaTiO₃ where at room temperature $\kappa_x/\kappa_z > 20$.

Another situation which can occur in ferroelastic ferroelectrics will become apparent in the following section. It will be seen that in a number of species domain walls satisfying the mechanical compatibility conditions are necessarily charged. And on the contrary, in these cases, the walls that are electrically neutral do not satisfy elastic requirements of compatibility. It then depends on the ratio between the enhancement of mechanical and electrical energies which wall should be realized.

2.2.4 Domain Wall Orientation: Mechanical Compatibility

For a ferroelastic domain pair the requirement of mechanical compatibility usually imposes severe restrictions on the orientation of the domain wall. A generally oriented wall between domains having different spontaneous strain tensors induces a very substantial level of additional elastic strains. The condition that the latter does not arise can be expressed as follows. Let the spontaneous strain in the domains be $\boldsymbol{\varepsilon}_S(A)$ and $\boldsymbol{\varepsilon}_S(B)$; then the transformation of any geometrical figure, which lies in the plane of the wall, due to deformations $\boldsymbol{\varepsilon}_S(A)$ and $\boldsymbol{\varepsilon}_S(B)$ should be identical up to a rigid body motion. Domain walls oriented so that this condition is met are called *permissible walls* or alternatively *stress-free walls*, since no additional elastic strains are involved. Mathematically, the mentioned condition requires (Fousek and Janovec, 1969; Sapriel, 1975) that any vector $d\mathbf{s}$ within the permissible wall fulfills the condition

$$\Delta_{ij} \cdot ds_i ds_j = 0, \quad (2.2.10)$$

where¹⁴

$$\Delta_{ij} = \varepsilon_{Sij}(A) - \varepsilon_{Sij}(B) \quad (2.2.11)$$

is a symmetric tensor with up to six independent components. Further mathematical treatment of the problem has been performed by Janovec (1976).

¹³ In BaTiO₃, the theory should be slightly modified making allowance for the first-order phase transition.

¹⁴ One comes across in the literature the use of condition (2.2.10) with matrix Δ_{ij} defined as the difference between the squares of the spontaneous strain tensors in the domains. This condition is not justified unless it leads to results identical to those derived with the use of Δ_{ij} defined by Eq. (2.2.11).

Here one can distinguish four different cases mainly controlled by the relations between the principal components of symmetric matrix Δ_{ij} : $\Delta^{(1)}$, $\Delta^{(2)}$, and $\Delta^{(3)}$. Since the volumes of the unit cell in the domains are the same, the trace of Δ_{ij} should be equal to zero, so that $\Delta^{(1)} + \Delta^{(2)} + \Delta^{(3)} = 0$.

- (A) If none of $\Delta^{(i)}$ equals zero and therefore $\det \Delta_{ij} \neq 0$, then Eq. (2.2.10) has no non-trivial solutions and the two domains cannot be separated by a stress-free wall. These situations are referred to as *R cases*.

If $\det \Delta_{ij} = 0$, permissible domain walls between the considered domain states can exist. Condition $\det \Delta_{ij} = 0$ can take place if either all principal components are zero or if only one principal component is zero.

- (B) If all principal components are zero, which means $\Delta_{ij} = 0$ for any i, j , we are dealing with a nonferroelastic domain pair so that any wall is permissible, as expected. A wall that from the point of view of mechanical compatibility conditions may acquire any orientation will be referred to as a *W_∞ wall*. The index points to the arbitrariness of the orientation.
- (C) If only one principal component of Δ_{ij} is zero, say $\Delta^{(1)} = 0$, then $\Delta^{(2)} = -\Delta^{(3)}$ and in the principal axis of the matrix Δ_{ij} , Eq. (2.2.10) reads

$$ds_2^2 = ds_3^2 \quad (2.2.12)$$

defining two permissible walls which are mutually perpendicular. Here, if, in addition, in the crystallographic reference frame matrix Δ_{ij} is already diagonal, then the wall has a crystallographically prominent orientation. This case is referred to as a *W_f wall*, the subscript “f” indicating that the orientation is *fixed* with respect to the symmetry elements of the lattice.

- (D) If the conditions of the previous case are met except for the non-diagonal form the matrix Δ_{ij} in the crystallographic reference frame, the orientation of the walls is controlled by a relation between the components of the matrix. In this case, the permissible wall has a general orientation which in fact can depend on temperature due to temperature development of spontaneous strain. Permissible walls of this kind have been denoted as *S walls*.¹⁵ At the time of their prediction (Fousek and Janovec, 1969) it was generally believed that any permissible wall must be crystallographically prominent and the prefix *S* stood for *strange*.

The situation covered by cases (C) and (D) can also be identified without diagonalizing matrix Δ_{ij} . In this situation, $\det \Delta_{ij} = 0$ coexist with the condition $I_2 \neq 0$ where I_2 is a scalar invariant of the matrix (Janovec, 1976):

$$I_2 = \begin{vmatrix} \Delta_{11} & \Delta_{12} \\ \Delta_{12} & \Delta_{22} \end{vmatrix} + \begin{vmatrix} \Delta_{11} & \Delta_{13} \\ \Delta_{13} & \Delta_{33} \end{vmatrix} + \begin{vmatrix} \Delta_{22} & \Delta_{23} \\ \Delta_{23} & \Delta_{33} \end{vmatrix}. \quad (2.2.13)$$

¹⁵ In the paper of Sapriel (1975) the *S walls* have been renamed to *W* walls. Here we shall adhere to the original notation.

We thus may encounter three different kinds of permissible walls, namely W_∞ , W_f and S . In addition, it is possible that no permissible walls may exist. In ferroelectrics, in view of Eq. (2.2.3) some of W_f - and S -type walls should be charged; sometimes we shall add the superscripts C and N to distinguish between charged and neutral walls.

Which of the cases A, B, C, or D applies to a particular domain pair can be also found on the basis of symmetry arguments (Fousek and Janovec, 1969; Janovec, 1976). For instance, if the twinning complex contains a center of symmetry, walls are of the type W_∞ ; if it contains a mirror plane, this very plane constitutes a W_f wall. Table 2.2.3 contains all symmetry criteria.

The information on domain wall orientation specified in Table D.1 will be illustrated in Sects. 2.2.6 and 2.2.7 where we will give examples of how wall orientations in particular materials are determined and we will compare the predictions based on electrical and mechanical compatibilities with the available experimental data.

The approach presented in this section has been developed and mainly used for the problem of orientation of a boundary separating two domains of a ferroic phase. However, it is quite clear that Eq. (2.2.10) can also be applied to the problem of mechanical compatibility of a boundary separating two different

Table 2.2.3 Relation between twinning operations and permissible walls

If the twinning complex $g_f F$ contains	Types of permissible walls are
Inversion $\bar{1}$	W_∞
Two non-perpendicular diads ^a	W_∞
More than two diads ^a of different directions	W_∞
Diad and rotation of higher order about the same direction as the diad	W_∞
Just two perpendicular diads; here for $F = 4, \bar{4}, 4/m, 3, \bar{3}$ the twinning complex $g_f H$ must be considered where H is the holosymmetric point group of F	W_f, W_f both perpendicular to the diads and thus also mutually perpendicular
Just one diad but no rotations about an axis perpendicular to this diad; here for $F = 4, \bar{4}, 4/m, 3, \bar{3}$ the twinning complex $g_f H$ must be considered where H is the holosymmetric point group of F	W_f, S mutually perpendicular; W_f is perpendicular to the diad
Only rotations of a order higher than 2, about the same direction; at least two of them are not related by $\bar{1}$	S, S mutually perpendicular
One operation of higher order than 2 or two such operations related by $\bar{1}$	R case
Operations of higher order than 2 about different axes	R case

^a The term diad signifies here a twofold rotation axis or a twofold inversion axis, i.e., a mirror plane with a normal parallel to the diad. The holosymmetric point group within a crystal system is one of the highest order (with the largest number of symmetry operations). After Janovec (1976).

phases of a ferroic. It could be a boundary between the parent and distorted phases in the vicinity of a ferroic first-order phase transition or it could be a boundary between two ferroic phases. The latter situation is actually of practical importance when one is dealing with a system like $\text{Pb}(\text{Zr}, \text{Ti})\text{O}_3$ in the vicinity of the tetragonal–rhombohedral morphotropic phase boundary (Jaffe et al., 1971). However, if Eq. (2.2.10) should be applied to the problem of mechanical compatibility of a heterophase boundary, an important reservation should be made. When dealing with domain walls, both natural spontaneous strain and Aizu strain can be used for calculation of the difference Δ_{ij} since, as it was stressed in Sect. 2.1.3, Δ_{ij} is the same when expressed in terms of any of these definitions. In contrast, in the case of a boundary between two different phases of a ferroic, only the natural spontaneous strains¹⁶ can be used in the calculations whereas the Aizu strain would lead to erroneous results. The point is that, in general (cf. Sect. 2.1.3), the difference Δ_{ij} is not equal to the difference between Aizu's strain of the two phases.

When applying the criterion of mechanical compatibility one should realize that how stringent it is depends on the domain pattern addressed. The point is that the additional elastic energy associated with its violation is roughly proportional to the typical domain volume in the pattern. Thus, for a single domain wall in a macroscopic sample, the criterion should be absolutely fulfilled because, in this case, the additional elastic energy can be considered as infinite. At the same time, in a fine multidomain pattern, local violations of the mechanical compatibility may take place when the possibly moderate (in this case) additional elastic energy may be compensated by other factors.

Though the above consideration has addressed only the case of mechanical matching of two domain states, it can be readily extended to the case of matching of two systems of lamella domain patterns. In this case, the average over the pattern of spontaneous strains should be used in Eq. (2.2.11) instead of the true spontaneous strains. The situations with this “mechanical matching on average” will be discussed later in the book.

Before proceeding to the next topic, we wish to add several remarks. First, coming back to walls of the W_∞ type, it has to be stressed that in this section we only considered mechanical compatibility. For this type of walls, the lattices of the two neighboring domains adhere smoothly to each other along a wall of any orientation. In contrast, the order parameter changes abruptly. The energy associated with this change may be a function of the wall orientation. This should influence the orientation of the W_∞ wall. We shall come back to this aspect in Chap. 4.

The following remark concerns the S walls. As we pointed out, the orientation of S walls specified in the reference frame of the parent phase can be temperature dependent. This rotation of S walls with temperature may involve

¹⁶ Or, obviously, any strain, which differs from it by a tensor identical for all phases of the ferroic.

a redistribution of volumes pertinent to the two domain states separated by the S wall and was termed *thermal switching* (Fousek and Janovec, 1969; Fousek, 1971). We shall give a few examples of this effect in Sect. 2.2.7.

2.2.5 Ferroelastic Domains in Physical Contact

In the preceding paragraphs we investigated mutual relations and domain wall orientations between two domain states but did not really take fully into account possible disarrangement of lattices in both neighboring domain states. For a ferroelastic domain pair, twinning operations are the operations that exactly relate the crystal structures of different domain states only if spontaneous strain is neglected. However, once one makes allowance for the spontaneous strain, these operations need not be the symmetry operations relating crystal structures of two domains which coexist in a sample and are separated by a permissible wall.

As an example, let us consider species $m\bar{3}m - P\epsilon ds - 4mm$ describing the tetragonal phase of BaTiO_3 . A particular pair of domain states with polarization vectors $[100]$ and $[0\bar{1}0]$ can be separated by any of the two crystallographically prominent walls $W_{\bar{1}10}$; Table 2.2.4 specifies their orientations as (110) and $(\bar{1}\bar{1}0)$, in the coordinate system of the parent phase. As the spontaneous strains $\Delta a/a_0$ and $\Delta c/a_0$ (see Fig. 2.2.2) develop in the distorted phase with decreasing temperature, the orientations (in the coordinate system of the parent phase) of the composition planes $(\bar{1}\bar{1}0)$ carried by two domain states depart from each other. If the c -axes were kept fixed in space parallel to the original cubic axes, the $(\bar{1}\bar{1}0)$ planes in both domains will make an angle 2φ where $\varphi = 45^\circ - \arctan(a/c)$. To keep the domains in physical contact, each of them must be rotated by an angle φ toward the other one (Fig. 2.2.2). Since spontaneous strains are small in magnitude, also the angle φ is small. From simple geometry we obtain

$$2\varphi \approx \frac{\Delta c - \Delta a}{a_0}. \quad (2.2.14)$$

In this particular case, the twinning operation for the given pair of domain states is a rotation by 90° about the $[001]$ axis. However, when we are interested in the mutual relation of tensor properties of two coexisting domains, the rotation which brings into coincidence the principal axes of the tensors is $90^\circ - 2\varphi$. The angle 2φ will be referred to as the “*clapping angle*”; it can be looked upon as the angle of mutual rotation of two physically existing single domain samples required for keeping them in physical contact. Values for the clapping angle depend on the “degree of ferroelasticity”; for BaTiO_3 at room temperature $2\varphi \cong 34'$ (Jona and Shirane, 1962), but for PbTiO_3 the value is much larger, $2\varphi \cong 3.5^\circ$ (Surowiak et al., 1993). In $\text{YBa}_2\text{Cu}_3\text{O}_7$ the clapping angle is $30'$ (Salje and Chrosch, 1996).

Table 2.2.4 Clapping angles required to keep domains in physical contact

Domain pair	Permissible walls	Clapping angles
Species with cubic parent phase and tetragonal distorted phase $432-422, \bar{4}3m - \bar{4}2m, m\bar{3}m-4/m\bar{m}m$		
$S_1 - S_2$	$x = y, x = -y$	$\varphi_3 = \pm 3b$
$S_1 - S_3$	$z = x, z = -x$	$\varphi_2 = \pm 3b$
$S_2 - S_3$	$y = z, y = -z$	$\varphi_1 = \pm 3b$
Species with tetragonal parent phase and orthorhombic distorted phase $422-222, 4mm-mm2, \bar{4}2m - 222, \bar{4}2m - mm2, 4/m\bar{m}m-nmm$		
$S_1 - S_2$	$x = 0, y = 0$	$\varphi_3 = \pm 2a$
Species with tetragonal parent phase and monoclinic distorted phase $4-2, \bar{4}-2, 4/m-2/m$		
$S_1 - S_2$	$x = py, x = -y/p$ $p = b + (a^2 + b^2)^{1/2}/a$	$\varphi = \pm (a^2 + b^2)^{1/2}$
Species with hexagonal parent phase and orthorhombic distorted phase $622-222, 6mm-mm2, \bar{6}m2 - mm2, 6/m\bar{m}m-mmm$		
$S_3 - S_2$	$x = 0, y = 0$	
$S_1 - S_2$	$x = \sqrt{3}y, y = -\sqrt{3}x$	$\varphi = \pm \sqrt{3}a$
$S_1 - S_3$	$x = -\sqrt{3}y, y = \sqrt{3}x$	
Species with trigonal parent phase and monoclinic distorted phase $32-3, 3m-m, \bar{3}m - 2/m$		
$S_2 - S_3$	$y = 0, z = -(a/c)x$	
$S_1 - S_3$	$y = \sqrt{3}x, a(\sqrt{3}y + x) - 2cz = 0$	$\varphi = \pm \sqrt{3}(a^2 + c^2)^{1/2}$
$S_1 - S_2$	$y = \sqrt{3}x, a(\sqrt{3}y + x) - 2cz = 0$	
Species with orthorhombic phase and monoclinic distorted phase $222-2, mm2-2, mm2-m, m\bar{m}m-2/m$		
$S_1 - S_2$	$x = 0, z = 0$	$\varphi = \pm 2b$

From Dudnik and Shuvalov (1989). Symbols a, b, c denote components of Aizu's strains for these species which are shown in Table 2.1.3.

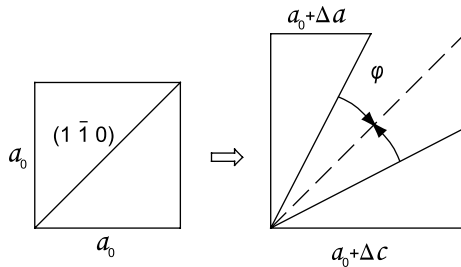


Fig. 2.2.2 If the directions of the c -axis in the domains remain parallel to fourfold axes in the parent phase then, in order to keep the domains in physical contact, each of them must be rotated by an angle φ (clapping angle) toward the other one. The clapping angle shown in this figure is strongly exaggerated

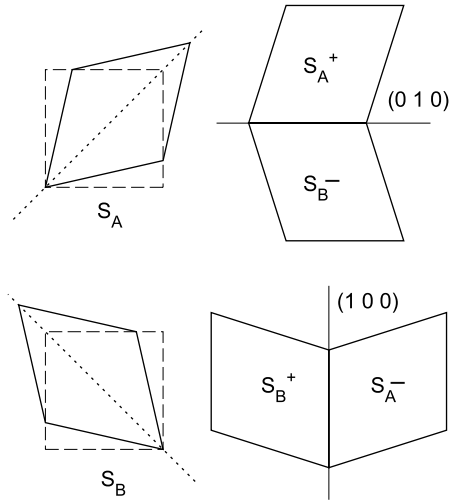
To discuss the problem of the clapping angle in the general case, Vagin and Dudnik (1983) and Shuvalov et al. (1985b), who coined a term of “spontaneous rotation” for this phenomenon, made use of a general theory of transformation twinning. The clapping angle φ was shown (in the approximation for small angles) to be given by

$$2\varphi = \pm(I_2)^{1/2} \quad (2.2.15)$$

where I_2 is defined by Eq. (2.2.13). This approach can be used for domains separated by both W_f walls and S walls. Because it is the difference tensor Δ_{ij} that is involved, both the natural and Aizu spontaneous strains can be used in these calculations. Table 2.2.4 shows results for the permissible wall orientations and clapping angles for several ferroelastic species; here the variables a , b , c are defined in Aizu strain matrices shown in Table 2.1.3. Obviously, these results can be used for a number of partially ferroelastic species as well. For instance, the rotation angle $\varphi = 3b$ for the species $m\bar{3}m-4/mmm$ agrees with that calculated above by simple geometry for BaTiO_3 which represents the species $m\bar{3}m - 4mm$ with the same spontaneous strains.

An approach where the clapping angles are neglected is called *parent clamping approximation*. Considering a real polydomain sample beyond this approximation, one can come back to the question how many domain states can be really observed in a sample? Consider the situation in a KH_2PO_4 crystal that represents species $42m - P\bar{6}3 - mm2$. We see from Tables 2.1.3 and 2.2.4 that there exist two domain states differing in spontaneous strain $\varepsilon_{S_{12}}$. Corresponding domains can be separated by permissible walls of either (100) or (010) orientation. The parent clamping approximation corresponds to the situation close below the transition temperature when spontaneous strain is negligible. The transition in this particular crystal is close to second order, but clearly discontinuous. Thus there is no reason why domain systems with walls of both permissible orientations should not be nucleated in different parts of the crystal. As the value of $\varepsilon_{S_{12}}$ grows with decreasing temperature, rotations of the two permissible walls by $\pm\varphi$ have to take place. Thus, in the sample, four different orientations of crystal lattices may develop, as shown schematically in Fig. 2.2.3. Each domain state splits into two whose lattices make an angle 2φ . Dudnik and Shuvalov (1989) suggested that such domains in ferroelastics be designated as *suborientational domains*. The effect can be easily observable when φ is not extremely small. It can be said, therefore, that due to mechanical compatibility conditions the number q_ε (real) of ferroelastic domain states observed in a real sample may exceed that given by Eq. (2.1.17) or (2.1.18), whichever is applicable; in the given example $q_\varepsilon(\text{real}) = 4$ while $q_\varepsilon = 2$. The increase of the number of observable domain states can be calculated in a general way based on the concept of the stabilizer of domain pairs, as suggested by Janovec et al. (1989). However, it is easy to see that simultaneous existence of mutually perpendicular domain walls of the W or S type is by itself not mechanically compatible: Inevitably, in a large enough sample they would

Fig. 2.2.3 Formation of four suborientational domains (S_A^+ , S_A^- , S_B^+ , S_B^-) form two domain states (S_A , S_B) with the spontaneous shears of opposite sign. The share strain shown in this figure are strongly exaggerated



intersect each other and in that region compatibility conditions would be violated. Therefore, while in a real sample domain pattern with q_ϵ (real) $> q_\epsilon$ may indeed develop, regions must simultaneously form in which the crystal lattice is highly strained and whose structure corresponds to none of the domain states of the material (Afonikova et al., 1987). An overview of theories of such additional strain fields has been given by Salje (1990).

**2.2.6 Examples of Domain Wall Orientations:
Nonferroelastic Walls**

How reliable are the predictions concerning the domain wall orientations or the nonexistence of walls in particular materials? In order not to sojourn only in abstract speculations we shall now give at least partial answers to this question. First, let us consider crystals with nonferroelastic domain pairs where mechanical compatibility plays no role and domains are to be separated by W_∞ walls. Without attempting to introduce some rigid categorization we single out three cases: W_∞ walls separating ferroelectric nonferroelastic domain pairs, W_∞ in higher order ferroics, and W_∞ representing antiphase walls between translational domain states (cf. Sect. 2.1.7).

In ferroelectrics, only 180° walls can be nonferroelastic. As already mentioned, the claim of electrical neutrality requires that these walls be parallel to the ferroelectric axis. Indeed the observations indicate this tendency of 180° walls, so that the domains themselves attain usually the form of slabs or cylinders of various cross-sections with walls parallel to \mathbf{P}_S and such *elongated domains can be considered typical for 180° walls in nonferroelastic ferroelectrics*. Figure 2.2.4 shows two opposite etched surfaces of a plate-like flux-grown

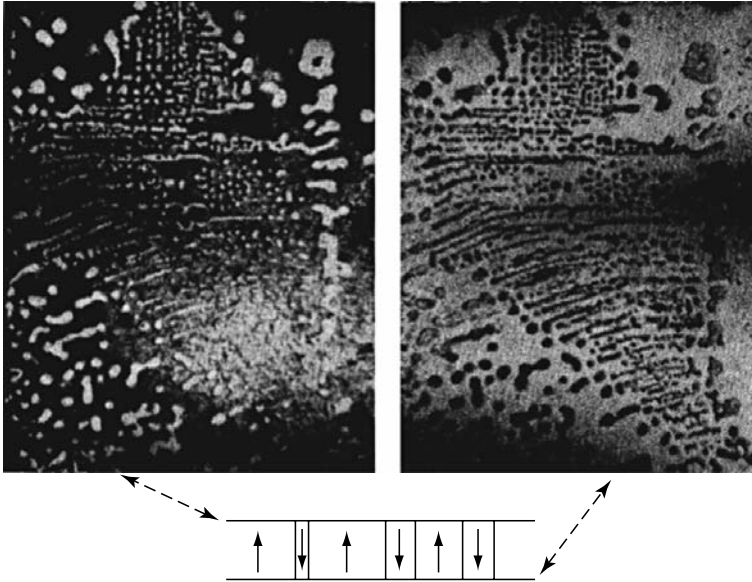


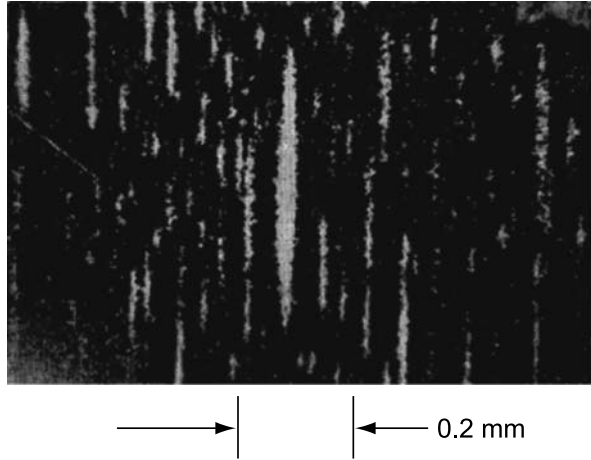
Fig. 2.2.4 Etched opposite surfaces of a BaTiO_3 plate perpendicular to the polar axis. Reprinted with permission from Hooton and Merz (1955). Copyright (1955) by the American Physical Society

BaTiO_3 crystal (Hooton and Merz, 1955). The perfect mirror image attests to the cylindrical domain shape. Figure 4.7.7 shows such cylindrical domains in large top-seeded solution-grown crystals of the same material.

However, often cylindrical-shaped domains do terminate inside the sample so that some sections of domain walls violate the condition of electrical neutrality. This may have some localized rationale (crystal defects) or it may just reflect the situation reached by a growing domain (due to applied electric field, for example). Information about such “internal” domains is not extremely rare but still rather limited since to make them visible requires either observations of surfaces parallel to the polar axis, which are rarely performed, or much more sophisticated methods allowing to see inside the sample. Internal domains were revealed in crystals of BaTiO_3 by X-ray topography (Akaba et al., 1979). Figure 2.2.5 shows the etched surface of a TGS crystal parallel to the ferroelectric b -axis; the internal domain is clearly visible. A similar observation was made for LiTaO_3 (Kuroda et al., 1996).

In a static case like this we expect that the bound charge $\rho_b = \text{div } \mathbf{P}_S$ is compensated by free carriers. Let us estimate in a simplified way the order of magnitude of free carrier density required for such a compensation. Considering a maximum value of P_S in a ferroelectric to be $50 \mu\text{C}/\text{cm}^2$ (applicable to LiTaO_3), the maximum surface charge to be compensated is $100 \mu\text{C}/\text{cm}^2$. This would require the surface density of electrons of the order of $6 \times 10^{14} \text{ cm}^{-2}$ or, taking the unit cell parameter as 4 \AA , 1 electron per unit cell area of a wall

Fig. 2.2.5 “Internal” domains revealed on the side of a single crystal of TGS parallel to the ferroelectric axis by powder decoration. Reprinted with permission from Chynoweth (1960). Copyright (1960) by the American Physical Society



perpendicular to \mathbf{P}_S . Many ferroelectrics carry P_S which is by one or two orders of magnitude lower. Compensation may be easier to achieve in crystals of semiconductive ferroelectrics like SbSI. Indeed in this material domain structures with head-to-head arrangements were frequently observed (Grekov et al., 1976; Kliya and Lyakhovitskaya, 1970b).

Domain situations with charged domain walls must necessarily occur as transient states during processes of polarization reversal. Figure 2.2.6 shows growing 180° domains in BaTiO_3 single crystal (Kobayashi, 1967); this is an optical micrograph and the origin of contrast in this case is not simple. The

Fig. 2.2.6 180° domains in BaTiO_3 crystal seen in polarized light during their growth. The polar axis is parallel to the wedges. The width of wedges at their base is about $6 \mu\text{m}$. Reprinted with permission from Kobayashi (1967). Copyright (1967), Wiley-VCH Verlag GmbH & Co. KGaA



bound charge carried by the head-to-head (tail-to-tail) 180° wall in this transient event is probably not compensated.

Because of the existence of free charge carriers the electrical neutrality need not be a decisive factor in shaping domains. Compositional inhomogeneities occurring involuntarily during the crystal growth process can lead to the formation of domain walls violating the neutrality condition. This was first realized in case of LiNbO_3 , whether as-grown doped or undoped (Nassau et al., 1965; Peuzin and Tasson, 1976). Systems of antiparallel domains with walls prevalingly perpendicular to the polar direction have been observed in several materials with growth layers connected with composition inhomogeneities. In as-grown crystals of lead germanate the existence of domain systems with charged walls was suspected on the basis of dielectric response (Cross and Cline, 1976); indeed such arrangements were visualized by cleaving (Shur et al., 1993a).

Later, in connection with producing periodic lamellar domain patterns in crystals of LiNbO_3 and LiTaO_3 methods were mastered to create 180° walls with head-to-head coupling. As an example we may mention the use of yttrium periodic doping for this purpose (Chen et al., 1989). It is understood that, during the crystal growth, the bound charge is automatically compensated by the charge associated with the modulation of concentration.

Luh et al. (1986) brought attention to yet another possible mechanism of creating charged walls. They produced crystalline fibers of LiNbO_3 in which the polar c -axis is perpendicular to the fiber. During the growth process a temperature gradient is present. It is argued that the temperature gradient leads to an appreciable electric field in the material due to the thermoelectric effect. This field is spatially oriented so that it can explain the head-to-head antiparallel domains in the fiber, which are separated by a domain wall parallel to the fiber axis. Again, compensation of ρ_b by free carriers is assumed to take place.

The condition of electrical neutrality does not limit the orientation of W_∞ walls as long as they remain parallel to the ferroelectric axis. In many cases, 180° domains with walls fulfilling this condition show a tendency to form particular characteristic shapes. Most of such observations apply to quasistatic conditions. Figure 2.2.7 shows domains of lenticular cross-sections which are typical for crystals of TGS. Figure 2.2.8 gives cross-section of domains in $\text{Pb}_5\text{Ge}_3\text{O}_{11}$ (Dougherty et al., 1972). These shapes cannot be explained on the level of the present discussion. However, it is usually observed that contours of these cross-sections do reflect the crystal symmetry in the ferroelectric phase. This points to the fact that the wall orientations forming such shapes are connected with the crystal structure rather than with macroscopic aspects of the sample. It can be expected that nonferroelastic walls with different orientations will have different internal structures. If so, the surface wall energy will depend on the wall orientation. This issue will be discussed later in Chap. 6.

It was further observed that nonferroelastic 180° domains can acquire distinctive shapes during the process of growth or shrinking under the influence of an electric field. We will discuss this effect later in Chap. 8.

Fig. 2.2.7 Cleavage surface perpendicular to the polar b -axis of TGS reveals 180° domains with lenticular shapes typical for this material, which may be seen in reflected light using a differential interference microscope. Reprinted with permission from Nakatani (1989a,b). Copyright (1989), Taylor & Francis

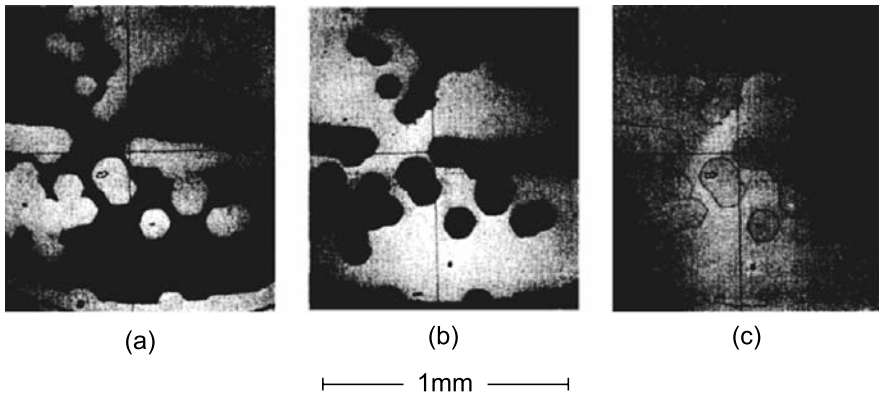
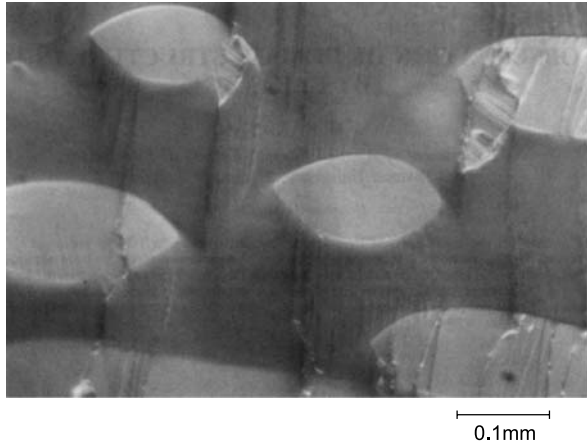


Fig. 2.2.8 180° domains in a plate of $\text{Pb}_5\text{Ge}_3\text{O}_{11}$ perpendicular to the polar c -axis viewed in polarized light: (a) and (b) analyzer rotated by 2.5° from the crossed Nichol position anticlockwise and clockwise, (c) Nichols prism precisely crossed (Dougherty et al., 1972)

Let us now turn to nonferroelectric ferroics. Table B.1 shows that there are a number of species which are nonferroelectric and nonferroelastic, so that W_∞ walls would be expected to exist. The best known representant for which abundant data are available are crystals of quartz which conform with species 622- ds -32. They may exist in two domain states which are known as electrical twins and also referred to as Dauphiné twins. Since the ferroic phase is neither ferroelectric nor ferroelastic the criteria given by Eqs. (2.2.4) and (2.2.10) pose no restrictions on wall orientations. Etching surfaces of quartz plates revealed (Willard, 1947) that in fact domain walls show large planar sections with well-defined indices. This is also true (Aizu, 1973b) when domain state reorientation is brought about by applied elastic stress; on the other hand, however, highly localized stress produced domains of very irregular shapes (Indenbom,

1979). While we may suspect again that the wall energy anisotropy plays a role, it is also possible that spatial inhomogeneity of applied stresses may be the decisive factor for determining the shape of a new ferroelastic domain and thus also for the orientation of walls.

Crystals of NH_4Cl represent higher order ferroic species $m\bar{3}m - d - \bar{4}3m$. Pique et al. (1977) found that here the W_∞ domain walls have the orientation (111). Again the interpretation was based on the wall energy anisotropy. As an alternative possibility it was suggested that wall orientation can be somehow connected with the phase boundary existing for the first-order phase transitions.

Finally we turn to the antiphase domain walls. These occur solely in materials with multiplication of the unit cell volume ($v \neq 1$) and separate domains which do not differ in any macroscopic property; for $v = 2$ they represent just a mutual shift of the distorted structures by one unit cell parameter of the parent structure. Therefore as in the preceding case, requirements (2.2.4) and (2.2.10) are ineffective. Observations made with crystals of $\text{Gd}_2(\text{MoO}_4)_3$ (abbr. GMO) (Barkley and Jeitschko, 1973) revealed that antiphase walls form irregular shapes. However, close to the intersections with W_f walls, antiphase walls show a tendency for preferential orientation. This has been interpreted by wall “reactions” (Janovec, 1976).

2.2.7 Examples of Domain Wall Orientations: Ferroelastic Walls

Now we shall discuss some real data on the orientations of domain walls of the type W_f and S , separating ferroelastic domain pairs. In most cases, their orientation was determined by polarized light microscopy.

The predictions for the orientations of W_f walls satisfying requirement (2.2.10) are unambiguous and accurate. It appears that in all known cases the predicted orientations of W_f walls agree with observations. This is true in particular when in the sample a system of only one of the two permissible walls in the conceived pair $W_f W_f$, $W_f S$, or SS is realized. Then a laminar ferroelastic domain system occurs. An example is shown in Fig. 2.2.9a; this is a micrograph of a system of domains separated by W_f walls in a ferroelastic sample of $\text{NdP}_5\text{O}_{14}$ (Huang et al., 1995). Systems of parallel walls with less regularity have been observed in many ferroelastic crystals of good quality, such as KH_2PO_4 or $\text{Gd}_2(\text{MoO}_4)_3$.

Such an ideal situation, however, does not occur very often. We shall mention two factors which often complicate the real wall orientations. First, the mechanical compatibility criterion as discussed above applies to an infinite crystal. There its nonfulfillment is impossible since it would result in an infinite elastic energy. In a finite and often defective sample, on the other hand, it can be expected that the actual W_f walls may be slightly misoriented from the predicted planes; the smaller the sample volume, the larger the possible tilt. Very often W_f walls form *wedge-shaped domains* or rather narrow domains confined by two

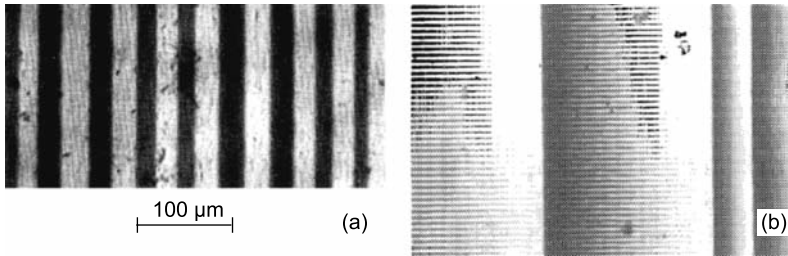


Fig. 2.2.9 (a) Ferroelastic plate-like domains, (001) oriented, in a *b*-plate of neodymium pentaphosphate seen in polarizing microscope (Huang et al., 1995). The period is about 20 μm . (b) Systems of wedge-shaped domains in the same material, with periods ranging from 6 to 20 μm . Reprinted with permission from Meeks and Auld (1985). Copyright (1985), American Institute of Physics

parallel properly oriented W_f walls which meet inside a crystalline sample to form a narrowing tip. Figure 2.2.9b shows a system of such wedges, again in neodymium pentaphosphate. The wedged domain pattern can also be induced artificially, e.g., by applying non-uniform stress. In $\text{Gd}_2(\text{MoO}_4)_3$ wedges have been formed by bending a sample (Fousek et al., 1976) and in $\text{NdP}_5\text{O}_{14}$ by repeated application of shear stress (Meeks and Auld, 1985). In ferroelectric ferroelastics the application of properly oriented electric field also produces wedge-shaped 90° domains. In common samples of ferroelectric perovskites wedge-shaped domains occur very frequently.

The application of strong electric field can also lead to local deviation on ferroelectric walls from the permissible orientation. This behavior has been documented by Fousek and Brezina (1960) in small crystals of tetragonal BaTiO_3 , where such deviation up to $22'$ has been observed. This effect has been explained by high non-uniformity of pressure acting on the wall due to dielectric anisotropy.

Let us now move on to *S* walls. The prediction of their existence in ferroelectrics (Fousek and Janovec, 1969) was believed to be confirmed by earlier observations of walls in some of the boracite crystals, in $\text{Mg}_3\text{B}_7\text{O}_{13}\text{Cl}$ in particular (Schmid, 1967). Similarly, the prediction of such walls in nonferroelectric ferroelastics (Fousek and Janovec, 1970) was substantiated by earlier research of NaNbO_3 (Wood et al., 1962). The first targeted experimental study of *S* walls in a ferroelectric ferroelastic was performed for KNbO_3 crystals (Wiesendanger, 1973). Since that time they have been observed in a number of materials. Several observations identified *S* walls of relatively large areas, with just two domain states present. This includes the study of twinning in the mineral Na-feldspar (species $2/m - \varepsilon s - \bar{1}$) (Salje, 1990) in which the W_f and *S* walls offer two types of transformation twins, albite and pericline. In other experiments *S* walls were parts of complicated domain patterns involving W_f walls as well. The latter case is represented in Fig. 2.2.10 which shows *S* walls in the orthorhombic phase of KNbO_3 (Wiesendanger, 1973), species $m\bar{3}m - P\epsilon ds - m_{\bar{x}y}m_z2_{xy}$. It is interesting

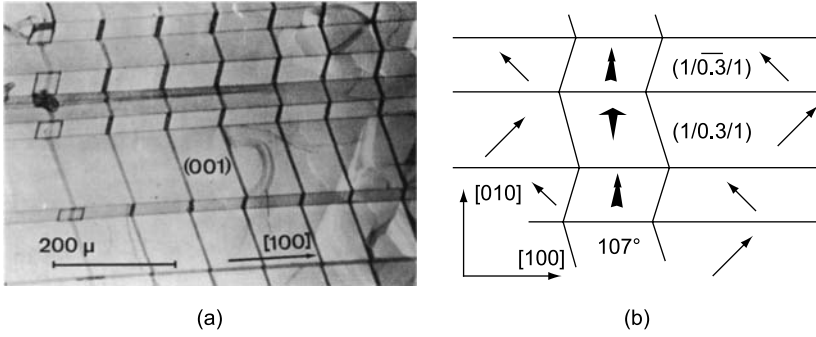


Fig. 2.2.10 Ferroelastic domains in the orthorhombic phase of KNbO_3 as seen in a (001) plate (Wiesendanger, 1973): (a) etch pattern, (b) scheme of the corresponding domain pattern. The arrows represent \mathbf{P}_S vectors. Two differently shaped vertical arrows indicate \mathbf{P}_S pointing downward and upward with respect to the plane of the drawing, respectively. The orientations of the walls are specified with Miller indices

to observe that here a system of S walls comfortably intersects a system of 90° W_f walls, although at their crossings elastically stressed regions must form.

We shall represent the procedure of determining orientations of S walls at the ferroelastic phase transition in CsHSeO_4 , following the paper of Yokota (1982). This example illustrates how determining wall orientation may help resolve symmetry of the crystal. Crystals of CsHSeO_4 at room temperature are monoclinic with the space group $P2_1/c$ and the unit cell parameters $a_m = 7.972 \text{ \AA}$, $b_m = 8.427 \text{ \AA}$, $c_m = 7.811 \text{ \AA}$, and $\beta = 101.5^\circ$. Above 128°C it becomes tetragonal with unit cell parameters $a_t = b_t = 4.18 \text{ \AA}$ and $c_t = 7.20 \text{ \AA}$. Below T_{TR} CsHSeO_4 has a structure with the cell dimensions doubled along the a - and b -axes. Thus we have $v = 4$, the transition is improper ferroelastic. For experimental reasons it was difficult to determine the symmetry of the parent phase and data were consistent with either of point groups $4/mmm$ and $4/m$. Let us investigate the species $4/mmm\text{-}\epsilon_S\text{-}2_x/m_x$. There are four ferroelastic domain states $S_1\text{-}S_4$ characterized by symmetric spontaneous strain tensors

$$\begin{aligned} \epsilon_S(S_1) &= \begin{pmatrix} \delta\epsilon_{xx} & 0 & \epsilon_{xz} \\ & \delta\epsilon_{yy} & 0 \\ & & \delta\epsilon_{zz} \end{pmatrix}, & \epsilon_S(S_2) &= \begin{pmatrix} \delta\epsilon_{yy} & 0 & 0 \\ & \delta\epsilon_{xx} & -\epsilon_{xz} \\ & & \delta\epsilon_{zz} \end{pmatrix}, \\ \epsilon_S(S_3) &= \begin{pmatrix} \delta\epsilon_{xx} & 0 & -\epsilon_{xz} \\ & \delta\epsilon_{yy} & 0 \\ & & \delta\epsilon_{zz} \end{pmatrix}, & \epsilon_S(S_4) &= \begin{pmatrix} \delta\epsilon_{yy} & 0 & 0 \\ & \delta\epsilon_{xx} & \epsilon_{xz} \\ & & \delta\epsilon_{zz} \end{pmatrix}. \end{aligned} \quad (2.2.16)$$

Using definition (2.1.9) and denoting

$$a = (\epsilon_{22} - \epsilon_{11})/2, \quad b = \epsilon_{13} \quad (2.2.17)$$

we come to Aizu's strains

$$\begin{aligned} \varepsilon_S^{\text{Aizu}}(S_1) &= \begin{pmatrix} -a & 0 & b \\ & a & 0 \\ & & 0 \end{pmatrix}, & \varepsilon_S^{\text{Aizu}}(S_2) &= \begin{pmatrix} a & 0 & 0 \\ & -a & -b \\ & & 0 \end{pmatrix}, \\ \varepsilon_S^{\text{Aizu}}(S_3) &= \begin{pmatrix} -a & 0 & -b \\ & a & 0 \\ & & 0 \end{pmatrix}, & \varepsilon_S^{\text{Aizu}}(S_4) &= \begin{pmatrix} a & 0 & 0 \\ & -a & b \\ & & 0 \end{pmatrix}. \end{aligned} \quad (2.2.18)$$

The parameters a, b are related to the monoclinic cell parameters by

$$\begin{aligned} a &= (\varepsilon_{22} - \varepsilon_{11})/2 \cong (b_m - a_m)/2b_m, \\ b &= \frac{1}{2} \tan^{-1} \frac{(a_m - 2c_m \cos \beta)}{2c_m \sin \beta}, \end{aligned} \quad (2.2.19)$$

which give

$$a = 2.40 \times 10^{-2}, \quad b = 7.94 \times 10^{-2}. \quad (2.2.20)$$

Using Eq. (2.2.10), Yokota obtained permissible wall orientations (the parent phase reference frame) listed in Table 2.2.5. Since optical study of wall orientations have been performed at room temperature and related to the monoclinic axes, it is useful to rewrite them into the coordinate system of the ferroic phase, taking into account the relation between the unit cells in both phases (Yokota, 1982; Komukae et al., 1990). The crystallographically nonequivalent permissible walls have then the following indices: W_f walls $(22\bar{1})$, $(20\bar{1})$, $(\bar{2}21)$, and (001) ; S walls $(11\bar{n})$ and $(\bar{1}1n)$. Here $n = 1/2 + (c_m/b_m)(b/a) \sin \beta$. Inserting unit cell parameters at room temperature it is found that $n = 3.04$. Optical observations of crystals confirmed the existence of four domain states which can be optically distinguished. In untreated crystalline samples walls were detected with indices (113) and $(\bar{1}13)$, which obviously correspond to the calculated S walls. By applied compressive stress new domains with boundaries $(22\bar{1})$, $(\bar{2}21)$, and $(20\bar{1})$ could be easily introduced. Thus only walls (001) were not observed.

Table 2.2.5 Permissible wall in species $4/mmm-\varepsilon S-2_x/m_x$

Domain pair	Permissible walls	
S_1, S_2	$x = -y$	$a(x - y) - bz = 0$
S_2, S_3	$x = y$	$a(x + y) + bz = 0$
S_3, S_3	$x = -y$	$a(x - y) + bz = 0$
S_4, S_1	$x = y$	$a(x + y) - bz = 0$
S_1, S_3	$x = 0$	$z = 0$
S_2, S_4	$y = 0$	$z = 0$

Analogous analysis was also performed assuming that the parent phase is of symmetry $4/m$. This leads to the prediction of only two walls which are different from any walls observed. Thus domain observations together with the analysis of their permissible orientations may help determine the correct species of the crystal. The conclusion of this analysis has been confirmed by later observations by Balagurov et al. (1986), which pointed to the space group $I4_1/amd$ for the parent phase.

PbZrO_3 is a perovskite-type material with orthorhombic symmetry mmm at room temperature and with a cubic phase above 217°C . The two phases are separated by a trigonal phase extending over a narrow temperature range only. At room temperature it represents the species $m\bar{3}m - \varepsilon_s - m_{xy}m_{\bar{x}y}m_z$. Another perovskite-type crystal is NaNbO_3 ; it is cubic above 640°C and has the orthorhombic symmetry mmm at room temperature; this phase can be treated as representing the same species as in PbZrO_3 although here the phases G, F are separated by other two, also nonpolar phases (Cross and Nicholson, 1955). Analysis of spontaneous strain in NaNbO_3 led to the prediction of S walls with indices $\{1a1\}$ where a may be temperature dependent (Fousek and Janovec, 1970). Full examination (Dec, 1988; Miga et al., 1996) is based on the Aizu strain tensor for the two domain states making the wall:

$$\varepsilon_S^{\text{Aizu}}(S_1) = \begin{pmatrix} c & d & 0 \\ & c & 0 \\ & & -2c \end{pmatrix}, \quad \varepsilon_S^{\text{Aizu}}(S_2) = \begin{pmatrix} -2c & 0 & 0 \\ & c & d \\ & & c \end{pmatrix}. \quad (2.2.21)$$

Here b, d can be evaluated from the parameters a, b, β of the monoclinic pseudoperovskite cell:

$$c = \frac{1}{3a_0}(a - b), \quad d = \tan \frac{\beta - 90^\circ}{2} \quad (2.2.22)$$

where $a_0 = [a^2b \cos(\beta - 90^\circ)]^{1/3}$. From Eq. (2.2.10) we find that in addition to W_f walls also S walls are permissible described by the relation

$$3c(x + z) + 2dy = 0. \quad (2.2.23)$$

From here we obtain data specifying the wall orientation. Dec (1988) and Miga et al. (1996) identified S walls in both PbZrO_3 and NaNbO_3 . Figure 2.2.11a shows a photograph in which an inclined S wall projects onto the (001) crystal surface. The orientation of this wall is explained in Fig. 2.2.11b. For the angle α , Eqs. (2.2.22) and (2.2.23) yield

$$\tan \alpha = 3c/2d \quad (2.2.24)$$

which can also be rewritten as

$$\alpha = \arctan \frac{a - b}{2[a^2b \cos \gamma]^{1/3} \tan(\gamma/2)}, \quad g = \beta - 90. \quad (2.2.25)$$

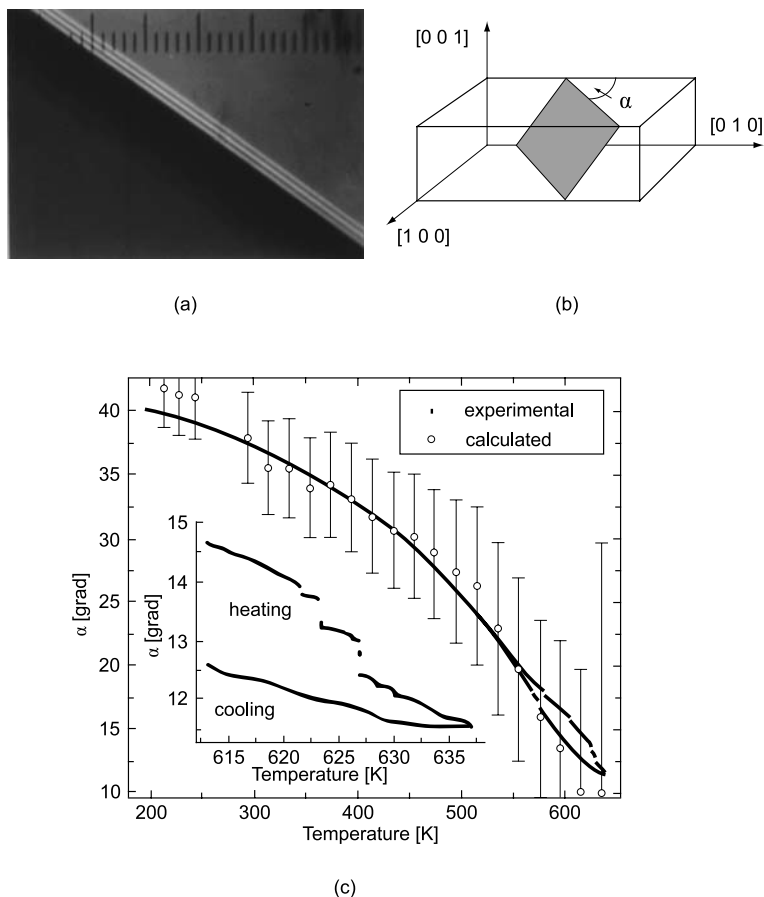


Fig. 2.2.11 An S wall in the orthorhombic phase mmm of NaNbO_3 at room temperature: photograph of the projection onto (001) plane (a) and schematic explaining its position in the sample. (b) In the photograph, the scale of one division is $1.9 \mu\text{m}$. (c) Temperature dependence of the wall orientation: the results of direct observations and calculations using Eq. (2.2.25) (Miga et al., 1996)

At room temperature, the two crystals are characterized by the following data given in Table 2.2.6. The agreement is more than satisfactory.

Now, all lattice parameters depend on temperature and so should the orientation of the S wall. The first observation of this effect in NaNbO_3 was reported by Zhelnova and Fesenko (1985). In Fig. 2.2.11c we reproduce the temperature

Table 2.2.6 Calculated and measured orientations of S walls in PbZrO_3 and NaNbO_3

	c	d	α (calcul.)	α (measured)
NaNbO_3	0.002989	0.00625	$35^\circ 20'$	$33^\circ 26' - 38^\circ 25'$
PbZrO_3	0.003982	0.0008	$82^\circ 40'$	$79^\circ 55' - 84^\circ 44'$

dependence of the angle α as calculated from Eq. (2.2.25) by Dec (1988) and Míga et al. (1996), together with their experimental data. Thus the effect of thermal switching in ferroelastics envisaged by Fousek and Janovec (1969) is real and in multidomain samples it can couple to several other phenomena. Thermal hysteresis and jumpwise behavior seen in the inset of the figure give evidence that local structure rearrangement accompanying the rotation of the domain wall may require overcoming large energy barriers.

Crystals of NaNbO_3 offer another example of interesting behavior connected with *S walls*. While the room temperature phase is nonpolar, it was found (Wood et al., 1962) that a properly oriented electric field transforms the crystal into a state which can be treated as a ferroelectric with the symmetry $mm2$; this would correspond to the species $m\bar{3}m - P\epsilon ds - m_{xy}m_{xy}2_z$. This indicates that free energies of the original mmm and field-induced $mm2$ phases are close to each other and it is one of the reasons why NaNbO_3 (and PbZrO_3 as well) is referred to as an antiferroelectric. Now let us consider a domain arrangement as shown in part (a) of Fig. 2.2.12 (Fousek and Janovec, 1970); the lines indicate the orientation of *c*-axis in the domains. Compatibility analysis shows that in the phase mmm the planes (110) and $(\bar{1}\bar{1}0)$ represent permissible walls. When the transformation into the polar phase $mm2$ is accomplished, the spontaneous polarization along the *c*-axis develops as shown by the arrows in Fig. 2.2.12b. The analysis shows that, in the ferroelectric phase, the previous domain walls are still permissible. However, the 60° W_f wall (110) does not satisfy the neutrality condition (2.2.4). The same domain states can now be separated by electrically neutral *S walls* (1a1) and $(1\bar{1}\bar{1})$ which would then form an arrangement shown in Fig. 2.2.12c. The arrangement of such zigzag walls was indeed observed by Wood et al. (1962). It can be concluded that *S walls* can result from a field-induced transition into a ferroelectric phase.

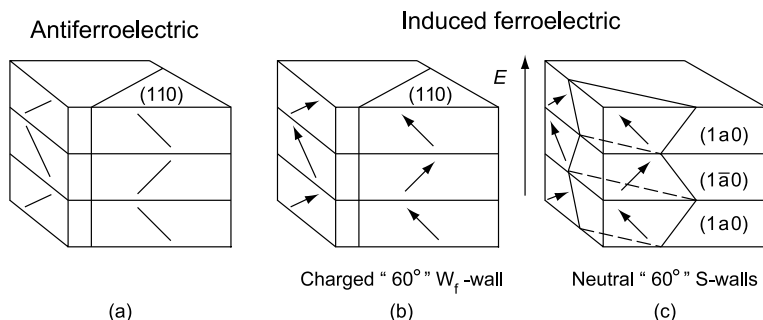


Fig. 2.2.12 Rearrangement of domain patterns (a) in antiferroelectric NaNbO_3 when a ferroelectric phase is induced by applied field (this process corresponds to an mmm to $mm2$ transformation). Formation of electrically neutral *S walls* in (c) avoids the presence of charged W_f walls shown in (b) (Fousek and Janovec, 1970). The orientations of the walls are specified with Miller indices

2.3 Thermodynamic Approach

In the previous sections, we introduced in terms of the symmetry approach the basic notions related to ferroic domains. This approach gives a very good overview of the problem and often provides the answers to various questions, actually without any calculations. On the other hand, when one is interested in quantitative manifestations of the domain structures of a ferroic, one finds that the pure symmetry arguments do not suffice. For instance, to find the orientation of an S wall, it is essential to know the temperature dependence of spontaneous strain which cannot be specified from purely symmetry considerations. Another example is domain patterns in ferroelectric thin films: In many cases even the type of the domain pattern is conditioned by the values of material parameters and here again we need more than just information on the symmetry of the system. Thus it is appropriate to combine the symmetry and thermodynamic arguments. In this approach, often referred to as the thermodynamic approach, all results of the purely symmetry consideration (though often at the expense of rather complicated calculations) are reproduced. But in addition, it enables a description of quantitative issues of the problem such as the temperature dependence of parameters of domain states, the structure of domain walls. In this book, we discuss neither conceptual aspect of this approach nor its technical aspect, referring the reader to an exhaustive coverage of this area in the books by Strukov and Levanyuk (1998) and by Toledano and Toledano (1988). In the following sections we will highlight the key points of the approach and illustrate them by using examples of some favorite ferroics. First, the basic idea of the Landau approach will be explained in terms of single-component order parameter. Then examples of Landau theory treatment will be presented for some cases which will be essentially addressed in the book, specifically uniaxial proper nonferroelastic–ferroelectric, uniaxial proper ferroelastic–ferroelectric, multiaxial proper ferroelectric–improper ferroelastic, and the uniaxial improper ferroelectric–improper ferroelastic.

2.3.1 *Single-Component Order Parameter*

In this section we outline the thermodynamic description of a phase transition in its simplest possible form. Consider a proper ferroelectric phase transition where the order parameter is a single component of dielectric polarization; in other words, we will be dealing with a uniaxial proper ferroelectric. On the basis of Landau theory of phase transitions, this transition can be described by using an expansion of a thermodynamic potential with respect to the order parameter; in our case, with respect to the mentioned component of polarization, which we specify as P_p . This expansion should be written taking into account the symmetry of the order parameter and the resulting potential should be invariant with respect to the symmetry of the parent phase. One can use

different thermodynamic potentials for this purpose. In many situations the choice is a matter of convenience. However, for a certain class of problems, which we will address later, the proper choice is mandated. Here we use a thermodynamic potential Φ , called the Gibbs energy, which is a function of polarization P_i and stress tensor σ_{ij} as independent variables. Its differential reads

$$d\Phi = E_i dP_i - \varepsilon_{ij} d\sigma_{ij}, \quad (2.3.1)$$

where E_i stands for the electric field and ε_{ij} for the strain tensor. (We recall that the differential of a potential, by definition, is a function of the differentials of its independent variables.) This expression implies the following equations, referred to as equations of state:

$$\left(\frac{\partial \Phi}{\partial P_i} \right)_\sigma = E_i \quad (2.3.2)$$

$$\left(\frac{\partial \Phi}{\partial \sigma_{ij}} \right)_P = -\varepsilon_{ij}. \quad (2.3.3)$$

The expansion of Φ with respect to the order parameter P_y , in general, reads

$$\Phi = \Phi_0 + \frac{1}{2}\alpha P_y^2 + \frac{1}{4}\beta P_y^4 + \frac{1}{6}\gamma P_y^6 + \dots, \quad (2.3.4)$$

where Φ_0 is the P_y -independent part of the potential. The expansion contains only even powers of the order parameter. This corresponds to the fact that, in the parent phase, the y -direction is nonpolar. The key point of the Landau approach is that if one assumes that the parameter α is small and changes its sign as a function of external parameters (e.g., temperature T and pressure), the equation of state related to the order parameter, Eq. (2.3.2), describes the appearance of the order parameter at the transition as well as its evolution as a function of external parameters. Let us follow this logic for a temperature-driven transition, i.e., we set

$$\alpha = \alpha_0(T - T_0), \quad \alpha_0 > 0. \quad (2.3.5)$$

For the description of the second-order phase transition not close to a tricritical point, which we are interested in at this moment, one sets $\beta > 0$ and keeps only the first two terms in this equation, putting $\gamma = 0$. Thus we have

$$\Phi = \Phi_0 + \frac{1}{2}\alpha P_y^2 + \frac{1}{4}\beta P_y^4 \quad (2.3.4a)$$

and via Eq. (2.3.2) we arrive at the equation of state for the order parameter, namely,

$$E_y = \alpha P_y + \beta P_y^3 \quad (2.3.6)$$

The solution to this equation describes the appearance of spontaneous polarization at $E_y = 0$ and $T < T_0$. Indeed, it yields

$$P_y = 0 \quad \text{at } T > T_0, \quad (2.3.7)$$

implying that the parent phase is nonpolar. For $T < T_0$, the two solutions fulfilling the stability condition are

$$P_y = \pm P_s = \pm(\alpha_0(T_0 - T)/\beta)^{1/2}. \quad (2.3.8)$$

One easily checks that at $T < T_0$ the solution $P_y = 0$ corresponds to the maximum of the Gibbs energy (see Fig. 2.3.1) and is unstable. Thus, in the distorted phase the order parameter may attain two values and these correspond to two domain states already introduced in Sect. 2.1. For both domain states the Gibbs energy in the ferroic phase is the same, namely,

$$\Phi_F = \Phi_0 - \frac{\alpha_0^2}{4\beta}(T_0 - T)^2 \quad (2.3.9)$$

so that they are degenerate in energy. Both of them correspond to the *ground state* of the system and the transition into either of them occurs with the same probability. From Eqs. (2.3.5), (2.3.6), (2.3.7), and (2.3.8) we further obtain for the dielectric susceptibility $\chi = \partial P_y / \partial E_y$

$$\chi = \frac{1}{\alpha_0(T - T_0)} \equiv \frac{\varepsilon_0 C}{T - T_0} \quad \text{for } T > T_0, \quad (2.3.10)$$

$$\chi = \frac{\varepsilon_0 C/2}{T_0 - T} \quad \text{for } T < T_0. \quad (2.3.11)$$

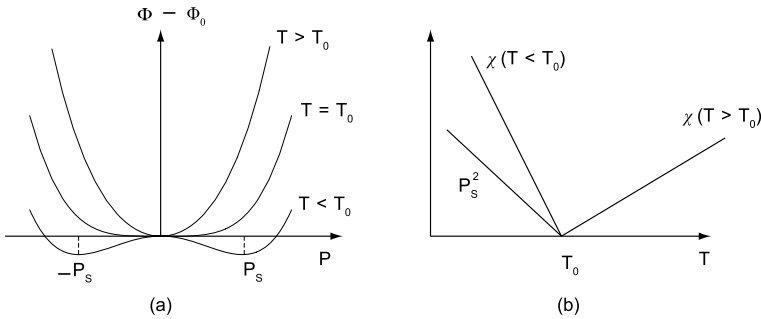


Fig. 2.3.1 Ferroelectric second-order phase transition. Schematics for the characteristic temperature dependences: (a) thermodynamic potential and (b) spontaneous value of the order parameter P_s and susceptibility χ

Figure 2.3.1 demonstrates schematically how the Gibbs energy function $\Phi(P_y)$ depends on temperature as well as the resulting dependences of P_s^2 and χ . Equation (2.3.10) is the well-known Curie–Weiss law in which C denotes the Curie–Weiss constant.¹⁷

The important feature of the considered problem is that, in the presence of electrical field coupled to the order parameter, the two domain states become energetically nonequivalent. Though it is obvious from the symmetry point of view, the thermodynamic approach makes it possible to calculate the energies of these states. At this point one should specify the thermodynamic potential used for calculations. Up to now the choice of the potential was only a matter of convenience since we have been using only the equation of state, which is independent of the thermodynamic potential used. On the basis of general thermodynamics, relations between the coefficients of different thermodynamic potentials are determined by the condition that the potentials lead to identical equations of state for given variables. However, when addressing the question which of the states (or phases) is energetically more favorable at given fixed macroscopic variables, one must use the thermodynamic potential in which these variables play the role of independent variables. Thus, to compare the “energy” of two domain states in a mechanically free sample ($\sigma_{ij} = 0$) at a fixed magnitude of electric field we should use a potential based on stress and field as independent variables. The potential $\tilde{\Phi} = \Phi - P_i E_i$ possesses this property. Indeed, one readily finds its differential as

$$d\tilde{\Phi} = -P_i dE_i - \varepsilon_{ij} d\sigma_{ij}. \quad (2.3.12)$$

Now the energies of the two domain states when a fixed field E_y is applied can be found from the expression

$$\tilde{\Phi} = \Phi_0 + \frac{1}{2}\alpha P_y^2 + \frac{1}{4}\beta P_y^4 - P_y E_y \quad (2.3.13)$$

where the two stable solutions to Eq. (2.3.6), P_+ and P_- (corresponding to the two domain states with the polarization parallel and antiparallel to the field, respectively), should be used for the values of P_y . If the applied field is small enough so that $|P_+| - P_s \ll P_s$ and $P_s - |P_-| \ll P_s$, the energies of these states can be presented as

$$\tilde{\Phi}_+ = \Phi_F - P_s E_y \quad \text{and} \quad \tilde{\Phi}_- = \Phi_F + P_s E_y \quad (2.3.14)$$

respectively, where Φ_F comes from Eq. (2.3.9). For higher values of the field one would arrive at more cumbersome expressions.

¹⁷ Note that the phenomenologically introduced quantity P_s exactly corresponds to spontaneous polarization introduced via the pyroelectric coefficient in Sect. 2.1.2 since, first, the temperature derivative of P_s defined according to Eq. (2.3.8) equals the newly acquired component of the pyroelectric coefficient (by definition), second, the value of the spontaneous polarization is opposite for two of the domain states.

We see that one of the domain states is more energetically favorable than the other. Thus, it is favorable when the volume of the former increases at the expense of that of the latter. That means that, in a poly-domain sample, a volume originally occupied by the unfavorable domain state can be, in principle, switched to that favorable. (“In principle” means that in reality this is possible if the domain wall mobility is high enough.) However, if the magnitude of the field exceeds a critical value E_{crit} , called *thermodynamic coercive field*, the switching is inevitable. The physical meaning of this situation is that, at $|E_y| > E_{\text{crit}}$, the energetically unfavorable domain state loses its stability. The magnitude of E_{crit} can be determined from the condition of infinite permittivity χ (or $1/\chi(E_y) = 0$, i.e., $dE_y/dP_y = 0$). Applying this condition to Eq. (2.3.6) one readily obtains

$$E_{\text{crit}} = \frac{2}{3\sqrt{3}} \left(\frac{\alpha_0^3}{\beta} \right)^{1/2} (T_0 - T)^{3/2} = \frac{1}{3\sqrt{3}} \frac{P_S}{\chi} \cong 0.2 \frac{P_S}{\chi} \quad (2.3.15)$$

where χ comes from Eq. (2.3.11). The meaning of the thermodynamic coercive field is also specified in Fig. 2.3.2, in terms of the $P(E)$ curve.

At this point an important feature of the considered system should be stressed: In the ferroelectric phase, there exists a certain interval of values of the field, in which the system exhibits two stable solutions. In principle this interval can be as large as from $-E_{\text{crit}}$ to $+E_{\text{crit}}$. Thus, as any bistable system the ferroelectric should exhibit hysteresis phenomena. In the case of the discussed $P(E)$ curve one speaks about *ferroelectric polarization-field hysteresis loop*. The stable parts of the $P(E)$ curve (with $\partial P/\partial E > 0$) linked by the dashed lines as shown in Fig. 2.3.2 make an example of such a loop.

All the above considerations of this section have been dealing with the case of a second-order (continuous) phase transition. However, in most ferroics the

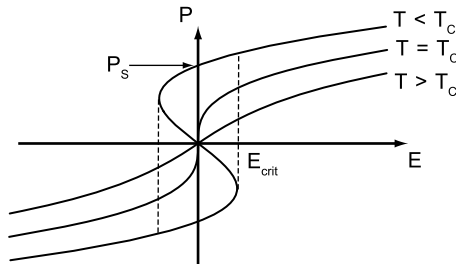


Fig. 2.3.2 Dependence of polarization on electric field at three different temperatures in a ferroelectric with the second-order transition. The stable parts of the curve (with positive slope) for $T < T_C$ together with *vertical dashed lines* represent a ferroelectric hysteresis loop. Its central part (with negative slope) corresponds to unstable states. *Dashed vertical lines* show transitions from metastable to stable states, “polarization reversal” occurring at critical fields equal to $\pm E_{\text{crit}}$

phase transition is discontinuous, i.e., the spontaneous value of the order parameter, in contrast to Eq. (2.3.8), does not grow from zero but acquires a finite value at the transition temperature. Such transitions can be well described in terms of the Gibbs function given by Eq. (2.3.4) where $\beta < 0$ and $\gamma > 0$. In this case the equation of state yields the solutions

$$P_y = 0, \quad (2.3.16)$$

$$P_y = \pm P_S \quad \text{with} \quad P_S = \sqrt{\frac{\sqrt{\beta^2 - 4\alpha\gamma} - \beta}{2\gamma}}. \quad (2.3.17)$$

Solution (2.3.16) is stable above the temperature T_0 but it is energetically favorable only at temperatures higher than T_C defined as

$$T_C = T_0 + \frac{3\beta^2}{16\alpha_0\gamma}. \quad (2.3.18)$$

The nonzero solutions (2.3.17) are energetically favorable below T_C and stable up to T_0^* defined as

$$T_0^* = T_0 + \frac{\beta^2}{4\alpha_0\gamma}. \quad (2.3.19)$$

Thus, in the temperature interval between T_0 and T_0^* the parent phase with $P_y = 0$ and the ferroic phase with $P_y \neq 0$ can coexist, one of them being metastable. The genuine transition temperature T_{TR} , therefore, may lie anywhere between T_0 and T_0^* , depending on the experimental conditions. The ideal transition point is T_C , at which the energies of solutions (2.3.16) and (2.3.17) are equal. Of importance is that at whatever temperature between T_0 and T_0^* the transition takes place, the polarization undergoes a discontinuous change between the two solutions (2.3.16) and (2.3.17). Figure 2.3.3 shows schematically temperature dependences of the Gibbs energy, polarization, and susceptibilities.

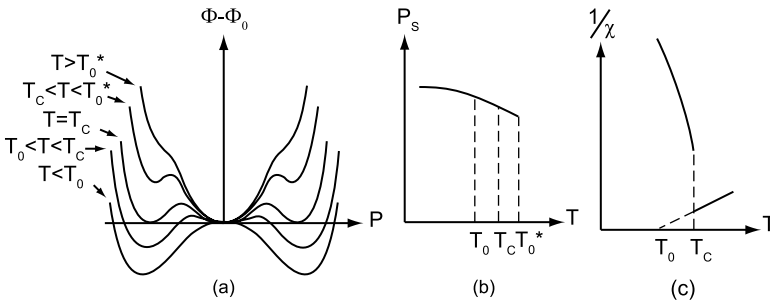


Fig. 2.3.3 Ferroelectric first-order phase transition. Schematics for the characteristic temperature dependences: (a) thermodynamic potential, (b) spontaneous value of the order parameter P_S , and (c) susceptibility χ

The dielectric anomaly above the first-order phase transition still obeys Eq. (2.3.10), whereas in the single domain ferroelectric phase, the temperature dependence of the dielectric susceptibility can be readily found in the form

$$\chi = \frac{1}{2P_S^2(\beta + 2\gamma P_S^2)}. \quad (2.3.20)$$

where P_S^2 comes from Eq. (2.3.17). Concerning this formula, two issues are worth mentioning. First, it is also applicable to the case of a second-order ferroelectric phase transition. Second, it is strictly valid only for the case of isothermal and free mechanical conditions. Typical experimental ac measurements of the dielectric susceptibility correspond to the adiabatic thermal conditions whereas the mechanical conditions depend on the measuring frequency and the dimensions of the sample. Thus, the measured susceptibility of a single-domain sample may differ from the value given by Eq. (2.3.20); depending on the parameters of the material the difference may be appreciable. This problem has been treated based on the general results of the equilibrium thermodynamic (see, e.g., book by Smolenskii et al. (1984)).

In the case of a first-order phase transition, similarly as for a second-order transition, the application of electric field which is linearly coupled to the order parameter (polarization) results in lifting the degeneracy in energy between the two domain states. The logic of calculation of their energies is straightforward. Of importance is that in the limit of small applied fields the difference between the energies of the two domain states obeys the same expression in terms of the spontaneous polarization independently of the type of the transition, namely,

$$\tilde{\Phi}_- - \tilde{\Phi}_+ = 2P_s E_y. \quad (2.3.21)$$

Similar to the case of a second-order phase transition, the hysteretic $P(E)$ dependence is expected, however, enriched with new features. Now, in a certain temperature range close to T_0 , the system has three stable states generically related to the states with $P_y = 0$, $P_y = +P_s$, and $P_y = -P_s$ at $E_y = 0$. Thus, in this range, a more complicated P – E hysteresis behavior involving three states is expected. Figure 2.3.4 illustrates this behavior in the temperature interval up to T_0^* and in the interval $T_0^* < T < T_0^{**}$

$$T_0^{**} = T_0 + \frac{9\beta^2}{20\alpha_0\gamma} \quad (2.3.22)$$

where the ferroelectric state can be induced by a large enough dc electric field. From Figure 2.3.4 one concludes that, in case of a first-order phase transition not only a simple $P(E)$ hysteresis loop in the ferroelectric phase is expected but also a double hysteresis loop in the parent phase just above the transition temperature.

Possibility of *phase coexistence* in the temperature range between T_0 and T_0^* is the most essential difference between continuous and discontinuous

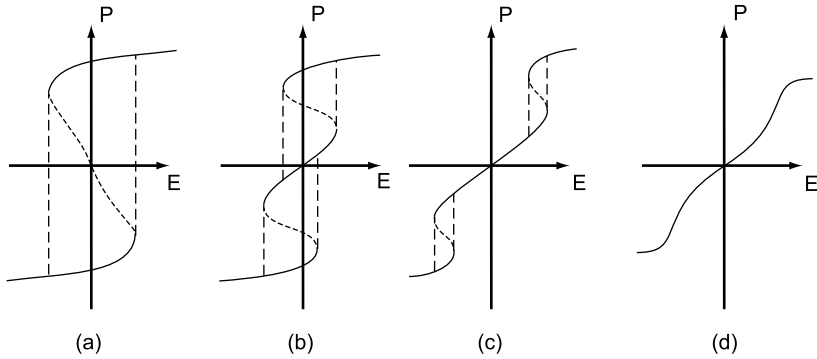


Fig. 2.3.4 Dependence of polarization on electric field at four different temperatures for a ferroelectric first-order phase transition: (a) $T < T_0$, (b) $T_0 < T < T_0^*$, (c) $T_0^* < T < T_0^{**}$, and (d) $T_0^{**} < T$

transitions. First, in ferroics with first-order phase transition, this will result in a *temperature hysteresis* of all properties of the material. Second, of importance from the point of view of domain structures is that on cooling down through a first-order phase transition on the way to a poly-domain state one can pass through an intermediate heterophase state: In the sample, both the parent and distorted phases can coexist. This intermediate state can strongly influence the resulting domain structure of the material.

At this point we stop our discussion of the general (and most simple) scheme of the thermodynamic description of ferroics. What we are missing at this moment (to have a proper overview of the problem) is, first, examples of extension of this scheme to cases of more complicated order parameters and, second, a discussion of the thermodynamic description of tensor properties, in which at least some of the domain states differ but which are not identical to the order parameter itself. In the following sections we will discuss these issues using examples of various ferroics.

2.3.2 Uniaxial Proper Ferroelectric (Nonferroelastic)

Consider the phase transition in crystals of triglycine sulfate $(\text{NH}_2\text{CH}_2\text{COOH})_3\text{H}_2\text{SO}_4$ (abbr. TGS). This transition is relatively simple and can provide an illustrative example of many aspects of domain behavior. In this book we refer to many experiments and theories concerning domains in TGS. It represents the species $2/m-Pd-2$ with $\nu = 1$ and the transition is continuous. X-ray diffraction and neutron scattering studies revealed structural details of the phase transformation (see, e.g., Xu, 1991). There are two formula units in the unit cell. Out of three glycine groups in the molecule, the glycine group II is of a non-planar type. Its nitrogen atom moves in a double potential well along

the b -axis, with a random distribution above $T_C = 49.5^\circ\text{C}$ and acquiring some degree of ordering below it. Thus the transition is of disorder–order nature and the average displacement of this atom represents the order parameter η . The value of η is found proportional to the spontaneous polarization of the crystal and therefore polarization P_y can be, alternatively, taken as the order parameter. Thus, we can apply the analysis developed in the previous section for the description of the critical dielectric behavior of TGS, i.e., the behavior related to the component of polarization taken for the order parameter. Equation (2.3.8) gives the temperature dependence of spontaneous polarization with $\alpha_0 = 3.5 \times 10^7$ m/F/K, $\beta = 7.5 \times 10^{11}$ J/C⁴m⁵ (Hoshino et al., 1957). Equation (2.3.10) describes the dielectric anomaly of χ_{yy} in the parent phase. Using Eq. (2.3.15) one can evaluate the value of the thermodynamic coercive field E_{crit} . At $T_C - T = 30$ K we find $E_{\text{crit}} = 150$ kV/cm, which is much greater than typical values (~ 0.1 kV/cm) of the experimentally observed coercive field in TGS (Pulvari and Kuebler, 1958b). Thus, we see that, in reality, the switching takes place at much smaller fields than those needed to make the unfavorable domain state unstable. This demonstrates a limitation of the considered thermodynamic approach: The switching is out of its reach and requires making allowance for the kinetics of the phenomenon. This is the basic issue for this book and we return to it later.

Looking at the notation of the species $2/m-Pd-2$ corresponding to the phase transition in TGS, we see that the thermodynamic description of this transition in terms of P_y only is not complete enough: We miss information on the piezoelectric tensor of the domain states. A simple way to get this information is to take into account in the Gibbs energy all the components of polarization and the mechanical stress σ_{ij} (or in the Voigt notation σ_n with $n = 1-6$). For the symmetry $G = 2/m$, using the results of Fousek (1967) we find

$$\begin{aligned}
 \Phi = & \Phi_0 + \frac{1}{2}\alpha P_y^2 + \frac{1}{4}\beta P_y^4 + \frac{1}{2}\alpha_x P_x^2 + \frac{1}{2}\alpha_z P_z^2 + \alpha_{xz} P_x P_z \\
 & - \frac{1}{2}s_{11}\sigma_1^2 - \frac{1}{2}s_{22}\sigma_2^2 - \frac{1}{2}s_{33}\sigma_3^2 - s_{12}\sigma_1\sigma_2 - s_{13}\sigma_1\sigma_3 - s_{23}\sigma_2\sigma_3 \\
 & - \frac{1}{2}s_{44}\sigma_4^2 - \frac{1}{2}s_{55}\sigma_5^2 - \frac{1}{2}s_{66}\sigma_6^2 - s_{15}\sigma_1\sigma_5 - s_{25}\sigma_2\sigma_5 - s_{35}\sigma_3\sigma_5 \\
 & - s_{46}\sigma_4\sigma_6 - Q_{12}\sigma_1 P_y^2 - Q_{22}\sigma_2 P_y^2 - Q_{32}\sigma_3 P_y^2 - Q_{52}\sigma_5 P_y^2 \\
 & - 2Q_{46}\sigma_4 P_x P_y - 2Q_{66}\sigma_6 P_x P_y - 2Q_{64}\sigma_6 P_z P_y - 2Q_{44}\sigma_4 P_z P_y.
 \end{aligned} \tag{2.3.23}$$

Recalling the expression of the strain in terms of the Gibbs energy one easily finds the so-called b -piezoelectric coefficients, which relate the change of polarization to the strain, ε_n , i.e., $\varepsilon_n = b_{in} P_i$ ($i = 1-3$; $n = 1-6$), as

$$b_{in} = - \frac{\partial \Phi}{\partial P_i \partial \sigma_n}. \tag{2.3.24}$$

Now, using Eqs. (2.3.23) and (2.3.24) and taking into account that in the parent phase $P_y = 0$ and in the ferroelectric phase $P_y = P_s$ or $P_y = -P_s$, depending on the domain state, we see that while the phase G is non-piezoelectric, in the ferroelectric phase all the eight piezoelectric coefficients allowed by its point symmetry 2 are formed, namely, for the domain state where $P_y = P_s$, we have $b_{21} = 2Q_{12}P_s$, $b_{22} = 2Q_{22}P_s$, $b_{23} = 2Q_{32}P_s$, $b_{25} = 2Q_{52}P_s$, $b_{14} = 2Q_{46}P_s$, $b_{16} = 2Q_{66}P_s$, $b_{36} = 2Q_{64}P_s$, and $b_{34} = 2Q_{44}P_s$. For the other domain state, the signs of b 's are opposite.

It is important to stress that the newly acquired piezoelectric coefficients b for the two domain states differ in sign and the same, of course, is true for any alternative piezoelectric coefficients coupling \mathbf{P} , \mathbf{E} , $\boldsymbol{\varepsilon}$, and $\boldsymbol{\sigma}$. Therefore TGS is a *fully ferroelastoelectric* material. We shall see later that this property can be advantageous when the sign of spontaneous polarization of a sample is to be determined in an alternative way: determining the sign of d_{21} , e.g., allows one to resolve also the sign of P_s .

According to the notation of the species $2/m-Pd-2$ TGS is not ferroelastic and this is an obvious result of the thermodynamic treatment. First, based on Eq. (2.3.3) we define the components of strain associated with the transition as

$$\varepsilon_{nS} = - \left(\frac{\partial(\Phi - \Phi_0)}{\partial\sigma_n} \right)_P. \quad (2.3.25)$$

One can easily check that the strain components defined in this way correspond to natural spontaneous strain introduced¹⁸ in Sect. 2.1.3. Second, using Eqs. (2.3.23) and (2.3.25) we find that, in TGS, the spontaneous strain components

$$\varepsilon_{1S} = Q_{12}P_s^2, \quad \varepsilon_{2S} = Q_{22}P_s^2, \quad \varepsilon_{3S} = Q_{32}P_s^2, \quad \varepsilon_{5S} = Q_{52}P_s^2 \quad (2.3.26)$$

are the same for both domains states. In addition, such deformations are consistent with the symmetry of the phase G where these occur due to thermal expansion (this can be checked by using Table C.1). In other words, there are no ‘‘symmetry breaking’’ strain components. The absence of ‘‘symmetry-breaking’’ strain components and identical spontaneous strain in both domain states shows that TGS is not ferroelastic.

¹⁸ We recall that natural spontaneous strain at a given temperature was defined as a deformation that should be imposed on the unit cell of the parent phase (real or extrapolated to this temperature) to get the unit cell of the ferroic phase. In the used thermodynamic approach the thermal expansion of the parent unit cell is described by the strain $\varepsilon_n = -(\partial\Phi_0/\partial\sigma_n)_P$. Thus one sees that the strain difference given by Eq. (2.3.25) does correspond to natural spontaneous strain.

2.3.3 Uniaxial Proper Ferroelectric–Ferroelastic

As the second example we choose the phase transition in a family of crystals of the KH_2PO_4 type (abbr. KDP) which corresponds to the species $\bar{4}2m - P\bar{6}3c - mm2$ with $\nu = 1$. This is a first-order transition occurring at 123 K, close to continuous in most members of the family. Here again the polarization, namely, its component P_z , can be considered the order parameter so that the results of Sect. 2.3.1 are applicable for the z -axis-related dielectric properties of these materials. However, the fact that the parent phase is non-centrosymmetric dramatically affects their mechanical and electromechanical properties. A full thermodynamic treatment of the phase transition in KDP-type crystals would be rather cumbersome. Since we are mainly interested in the qualitative features of phenomena distinguishing domain states we shall make several simplifying assumptions: We shall include in the Gibbs energy only two components of stress and keep only the critical component of polarization, namely, P_z . This will lead us to the following expansion of the Gibbs energy

$$\begin{aligned} \Phi = & \Phi_0 + \frac{\alpha_0}{2}(T - T_0)P_z^2 + \frac{\beta}{4}P_z^4 + \frac{\gamma}{6}P_z^6 \\ & - \frac{1}{2}s_{33}^P\sigma_3^2 - \frac{1}{2}s_{66}^P\sigma_6^2 - b_{36}P_z\sigma_6 - Q_{33}P_z^2\sigma_3. \end{aligned} \quad (2.3.27)$$

The first conclusion to be drawn from this expansion is that KDP is *ferroelastic*. Indeed, making use of the equation of state (2.3.3) we get

$$\varepsilon_6 = s_{66}^P\sigma_6 + b_{36}P_z, \quad (2.3.28)$$

$$\varepsilon_3 = s_{33}\sigma_3 + Q_{33}P_z^2. \quad (2.3.29)$$

Equation (2.3.28) implies that, in a mechanically free sample ($\sigma_n = 0$), domain states differ in the sign of the shear spontaneous strain: $\varepsilon_{6S} = b_{36}P_S$ in the domain state with $P_z = +P_S$ and $\varepsilon_{6S} = -b_{36}P_S$ in the domain state with $P_z = -P_S$, where P_S is given by Eq. (2.3.17). Then, the fact that this component of strain and P_z taken for the order parameter are linked by the linear relation (2.3.28) means that KDP is a *proper ferroelastic*, so that, in principle, this transition could be described using ε_6 as the order parameter. It is instructive to demonstrate this in another way. If ε_6 also plays a role of the order parameter, then according to the general theory of the phase transition the corresponding susceptibility, in this case the elastic compliance s_{66} , should manifest a trend to an unlimited increase for $T \rightarrow T_0$. Let us evaluate this compliance in the parent phase in the absence of electric field, which we denote as s_{66}^E . To do it we use Eq. (2.3.28) and the equation of state (2.3.2) calculated for the Gibbs energy (2.3.27)

$$\alpha_0(T - T_0)P_z - b_{36}\sigma_6 = 0. \quad (2.3.30)$$

This equation has been linearized since we are interested in a small-signal response. Eliminating P_z between Eqs. (2.3.28) and (2.3.30), we find the sought anomaly of the compliance:

$$s_{66}^E \equiv \left(\frac{\partial \varepsilon_6}{\partial \sigma_6} \right)_E = s_{66}^P + \frac{b_{36}^2}{\alpha_0(T - T_0)} \quad (2.3.31)$$

The interesting feature of KDP as proper ferroelectric–ferroelastic is that a domain state can be made unstable not only by application of the field E_z but also by application of the shear mechanical stress σ_6 . By analogy with the thermodynamic coercive field of mechanically free crystal, E_{crit} , treated in Sect. 2.3.1 one introduces *thermodynamic coercive stress* of a short-circuited sample, σ_{crit} . In the considered case, these parameters are linked by the relation $E_{\text{crit}} = b_{36}\sigma_{\text{crit}}$, which is obvious from the comparison of the equations of states corresponding to these two conditions, namely,

$$E_z = \alpha_0(T - T_0)P_z + \beta P_z^3 + \gamma P_z^5, \quad (2.3.32)$$

$$0 = \alpha_0(T - T_0)P_z + \beta P_z^3 + \gamma P_z^5 - b_{36}\sigma_6, \quad (2.3.33)$$

where we set $\sigma_3 = 0$ for simplicity.

The last thing we would like to demonstrate is that KDP is also ferroelasto-electric. This follows from Eq. (2.3.29) which shows that, in the low-symmetry phase, there appears a new piezoelectric coefficient b_{33} , which acquires in the two domain states values of $2Q_{33}P_s$ and $-2Q_{33}P_s$, respectively, depending on the orientation of spontaneous polarization. The same is true for all other newly acquired piezoelectric coefficients.

According to the notation of the species $\bar{4}2m - P\bar{6}32$ KDP-type crystals are also ferrobielastic, i.e., the domain states differ in compliance matrices. Obviously, the thermodynamic approach can reproduce this feature as well.

A practically important point is that the thermodynamic treatment always gives a description of the properties of the low-symmetry phase in the conventional reference frame of the parent phase. In the case of the species $\bar{4}2m - P\bar{6}32$, as it often happens, this frame is different from that of the low-symmetry phase: The conventional axis z of the phase $F = mm2$ is parallel to that in the phase $G = \bar{4}2m$ but the axes x, y are rotated by 45° (see Fig. 2.1.7). Thus, matrices of tensor properties of the low-symmetry phase obtained from the thermodynamic potential are, in general, different from those given in reference books where, for a given symmetry, the conventional reference frame is always used (see Fig. 2.1.8).

2.3.4 Multiaxial Proper Ferroelectric–Improper Ferroelastic

The thermodynamic theory of a particular material has probably achieved its greatest success in the treatment of BaTiO_3 developed by Devonshire (1949, 1951). The specially remarkable accomplishment was that his thermodynamic

approach provided an excellent basis for understanding the sequence of four phases. On decreasing temperature, the material transforms sequentially from the parent cubic paraelectric phase into phases of tetragonal, orthorhombic, and rhombohedral symmetry. All the three transitions are discontinuous and all the three ferroic phases are proper ferroelectric. In the symmetry-based treatments of phase transitions we just consider two phases G and F , while the transitions between ferroic phases which do not fulfill the group–subgroup symmetry relation are not dealt with. Thus in the symmetry approach discussed in the preceding chapters, we identify each of the three distorted phases of barium titanate with its own species, namely, $m\bar{3}m - P\epsilon ds - 4mm$, $m\bar{3}m - P\epsilon ds - m_{\bar{x}y}m_z 2_{xy}$, and $m\bar{3}m - P\epsilon ds - 3m$. In contrast, in the thermodynamic approach based on a properly constructed potential, one can compare the energies of all involved phases and determine which phase at a given temperature is energetically most favorable.

Conceptually, the thermodynamic treatment of perovskite ferroelectrics like BaTiO_3 is very close to those given above so that we will pay our attention mainly to the newly appearing features of the system. We consider the expansion of the Gibbs energy with respect to the polarization vector \mathbf{P} (order parameter) and stress tensor $\boldsymbol{\sigma}$. According to the $m\bar{3}m$ symmetry of the parent phase the Gibbs energy reads (Haun et al., 1987)¹⁹

$$\begin{aligned} \Phi = & \Phi_0 + \frac{1}{2}\alpha_0(T - T_0)(P_x^2 + P_y^2 + P_z^2) + \frac{\beta_{11}}{4}(P_x^4 + P_y^4 + P_z^4) + \frac{\beta_{12}}{2}(P_y^2 P_z^2 + P_z^2 P_x^2 + P_x^2 P_y^2) \\ & + \frac{\gamma_{111}}{6}(P_x^6 + P_y^6 + P_z^6) + \gamma_{112}[P_x^4(P_y^2 + P_z^2) + P_y^4(P_x^2 + P_z^2) + P_z^4(P_x^2 + P_y^2)] \\ & + \gamma_{123}P_x^2 P_y^2 P_z^2 - \frac{1}{2}s_{11}(\sigma_1^2 + \sigma_2^2 + \sigma_3^2) - s_{12}(\sigma_1\sigma_2 + \sigma_1\sigma_3 + \sigma_2\sigma_3) \\ & - \frac{1}{2}s_{44}(\sigma_4^2 + \sigma_5^2 + \sigma_6^2) - Q_{11}(\sigma_1 P_x^2 + \sigma_2 P_y^2 + \sigma_3 P_z^2) \\ & - Q_{12}[\sigma_1(P_y^2 + P_z^2) + \sigma_2(P_x^2 + P_z^2) + \sigma_3(P_y^2 + P_x^2)] - 2Q_{44}[\sigma_4 P_y P_z + \sigma_5 P_x P_z + \sigma_6 P_y P_x]. \end{aligned} \quad (2.3.34)$$

Equation of state (2.3.2) at $\mathbf{E} = 0$ gives a set of equations for the components of polarization in a mechanically free crystal. One finds that possible stable solutions²⁰ to this set of equations falls into the following four types:

¹⁹ The factor of 2 multiplying Q_{44} is introduced in this energy to respect the Voigt notation, as defined in Landolt–Bornstein (1993), where $Q_{ijkl} = Q_{mn}$ for $n = 1, 2, 3$ and $2Q_{ijkl} = Q_{mn}$ for $n = 4, 5, 6$. In many papers where this energy is used (see, e.g., Haun et al., 1987), the factor in front of Q_{44} is omitted; therefore, their Q_{44} is twice the Q_{44} defined in the textbooks.

²⁰ The stability condition in this case can be formulated as the requirement that all eigenvalues of the matrix $\frac{\partial^2 \Phi}{\partial P_i \partial P_j}$ calculated at the state be positive.

cubic phase: $P_x = P_y = P_z = 0$,

tetragonal phase: $P_x = P_y = 0$, $|P_z| = P_S$ and possible permutations of P_x , P_y , and P_z ,

orthorhombic phase: $P_z = 0$, $|P_x| = |P_y| = P_S/\sqrt{2}$ and possible permutations of P_x , P_y , and P_z ,

rhombohedral phase: $|P_x| = |P_y| = |P_z| = P_S/\sqrt{3}$.

Each type corresponds to a possible phase of the system, namely to the parent phase $m\bar{3}m$ and three ferroelectric phases, $4mm$, $mm2$, and $3m$, respectively. The constant P_S is, in general, different for different phases and has the meaning of absolute value of spontaneous polarization in the given phase. For ferroelectric phases, the solutions of each type are degenerate in energy. Solutions belonging to the same type correspond to different domain states. It is easy to count that in the three phases there exist 6, 12, and 8 domain states, respectively, differing in the direction of the polarization (see Fig. 2.3.5). For each phase, the absolute value of spontaneous polarization P_S can be found looking for the solutions to the equation of state in the corresponding form specified above. In this way Eq. (2.3.34) can be simplified down to the form identical to Eq. (2.3.4) so that Eq. (2.3.17) can be applied for calculation of P_S . As the next step we can find the energies of all stable phases. Finally, comparing these energies we find the energetically most favorable phase and finally arrive at the equilibrium phase diagram of the system.

The approach outlined above has been applied for the description of several ferroelectric perovskites, e.g., BaTiO_3 and PbTiO_3 (species $m\bar{3}m - P\epsilon ds - 4mm$). For these materials we give in Table 2.3.1, for reference, the full list of coefficients in the expansion equation (2.3.34) often employed in thermodynamic calculations.²¹

A new feature of the considered system is that it is ferroelastic though there is no linear coupling between polarization playing the role of the order parameter, and deformation, i.e., it is an improper ferroelastic. Let us illustrate this point for the $4mm$ phase which has six domain states. Using the Gibbs energy, Eq. (2.3.34), and the definition, Eq. (2.3.25), we readily find that the spontaneous strain does not “feel” the sign of polarization but it is sensitive to its orientation. Thus, we can distinguish only three ferroelastic domain states where the tensors of spontaneous strain are

$$\begin{pmatrix} Q_{11} & & \\ & Q_{12} & \\ & & Q_{12} \end{pmatrix} P_S^2, \begin{pmatrix} Q_{12} & & \\ & Q_{11} & \\ & & Q_{12} \end{pmatrix} P_S^2, \begin{pmatrix} Q_{12} & & \\ & Q_{12} & \\ & & Q_{11} \end{pmatrix} P_S^2. \quad (2.3.35)$$

²¹ The information on β and γ coefficients for BaTiO_3 available in the literature is contradictory, e.g., the coefficients given in the classical book of Jona and Shirane (1962) correspond to a situation where the $4mm$ phase is always energetically favorable compared to the $mm2$ and $3m$ phases..

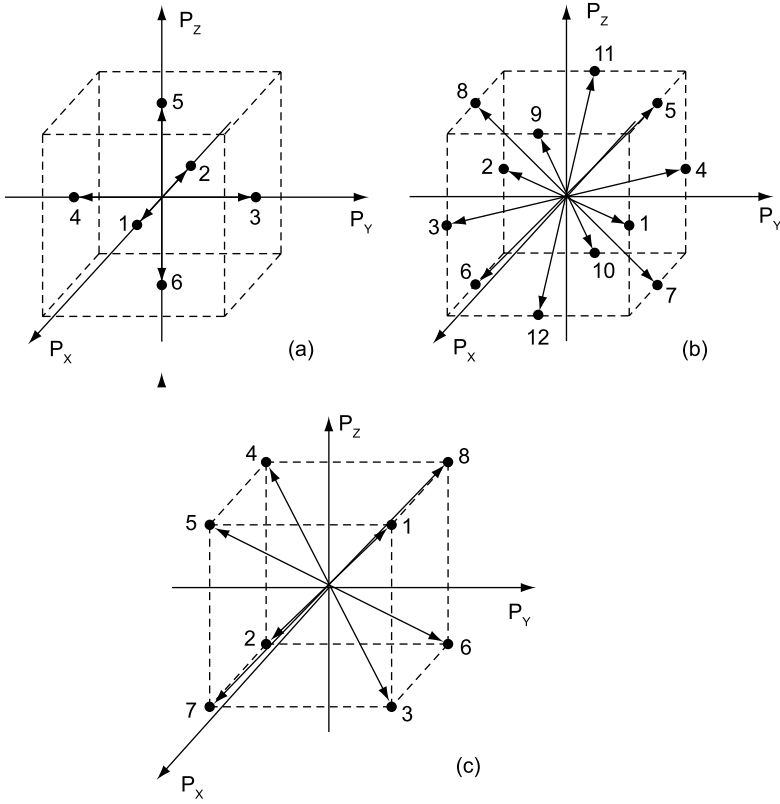


Fig. 2.3.5 Domain states of BaTiO₃ represented in the order parameter space: **(a)** tetragonal phase *4mm*, **(b)** orthorhombic phase *mm2*, and **(c)** rhombohedral phase *3m*. Vectors associated with points corresponding to domain states represent the P_S vectors. Representative domain pairs are customarily characterized by angles between the respective P_S vectors: **(a)** 180° pair (1,2), 90° pair (1,3); **(b)** 180° pair (1,2), 90° pair (1,3), 60° pair (11,5), 120° pair (11,7); and **(c)** 180° pair (1,2), 71° pair (1,3), 109° pair (1,4)

Similar situation takes place in the *mm2* and *3m* phases, where 6 and 4 ferroelastic domain states can be distinguished, respectively. Thus, we see that we are dealing with a partial ferroelastic.

Similar to all ferroelectrics discussed above perovskite ferroelectrics like BaTiO₃ are full ferroelectroelastics. For example, using Eqs. (2.3.24) and (2.3.34), we find that, in a tetragonal domain state where $P_x = P_y = 0$, $P_z = P_S$, five piezoelectric coefficients acquire nonzero values, namely, $b_{15} = b_{24} = 2Q_{44}P_S$, $b_{31} = b_{32} = 2Q_{12}P_S$, $b_{33} = 2Q_{11}P_S$. For reference we give a table of *d*-piezoelectric coefficients for all domain states of the three ferroelectric phases of BaTiO₃ (Table E.1).

Table 2.3.1 Parameters of the Gibbs energy expansion and gradient terms for BaTiO₃ and PbTiO₃. Data after Bell and Cross (1984), Haun et al. (1987), Hlinka and Marton (2006), and Hlinka (2008)

SI units	$T_c, ^\circ\text{C}$	$\alpha_0, 10^5$	$\beta_{11}, 10^8$	$\beta_{12}, 10^8$	$\gamma_{111}, 10^9$	$\gamma_{112}, 10^9$	$\gamma_{123}, 10^9$
BaTiO ₃	108	6.7	$0.19 \times (T-120) - 8.1$	6.5	$0.22 \times (T-120) + 17$	4.5	4.9
PbTiO ₃	479	7.6	-2.9	15	1.6	0.61	-3.7
SI units	$s_{11}, 10^{-12}$	$s_{12}, 10^{-12}$	$s_{44}, 10^{-12}$	$Q_{12}, 10^{-2}$	$Q_{44}, 10^{-2}$	$\delta_{12}, 10^{-11}$	$\delta_{44}, 10^{-11}$
BaTiO ₃	8.3	-2.7	9.2	-4.3	3.0	-2	2
PbTiO ₃	8.0	-2.5	9.0	-2.6	3.4	?	10

? - the value is not available or available with large uncertainty.

The P^6 -thermodynamic Landau expansion addressed above in this section is presently considered as classical. At the same time, the recent development in the field has raised a question of upgrading this expansion with the P^8 terms. Li et al. (2005) have demonstrated that the expansion modified by the P^8 terms can provide a good description of most of the thermodynamic priorities of the material, however, in contrast to the classical scheme, using a temperature independent set of anharmonic polarization coefficients. Alternatively, Wang et al. (2006, 2007b) have documented a very important role of the P^8 terms for the adequate description of the cubic–tetragonal phase transition in material.

It is worth mentioning that all perovskite ferroelectrics like BaTiO_3 exhibit first-order ferroelectric phase transitions under the free mechanical conditions. In the Gibbs thermodynamic potential, this corresponds to the negative sign of the appropriate P^4 terms. However, even a partial mechanical clamping leads to a change of the type of the transition to the second order (see Sect. 9.3.2). This implies that the negative sign of the P^4 terms controlling the order of the transition in mechanically free ferroelectric perovskites is due to a strong electrostrictive coupling between the polarization and strain.

2.3.5 Uniaxial Improper Ferroelastic–Ferroelectric

In both preceding examples only such variables were involved in thermodynamic potentials, to which the conjugate forces, namely, electrical field and mechanical stress, can be realized in the laboratory. Experimentally, this means that treating the crystal in the parent phase, one can induce a nonzero value of the order parameter either by inducing the phase transition or, without doing that, by a mere application of the mentioned “forces.” From the point of view of thermodynamic description, this means that the problem can be treated in terms of an expansion of the thermodynamic potential with respect to the macroscopic variables only (e.g., polarization and stress have been used above). However, we have already seen in this chapter that, in many materials, phase transitions occur whose order parameter η is conjugate to no macroscopical variable. In this case, a thermodynamic description of the transition requires including in the potential variables corresponding to the order parameter η and macroscopic variables. Below we will give an example of thermodynamic description of such a situation. We shall briefly discuss the thermodynamic theory of the phase transition in $\text{Gd}_2(\text{MoO}_4)_3$ (abbr. GMO), perhaps the best-known example of an improper ferroelectric.

Within the description by point group symmetries, this material can be attributed to the same species as KDP, namely, $\bar{4}2m - P\epsilon ds - mm2$. However, the number of unit cells doubles at the ferroic phase ($v = 2$). The order parameter describing this phase change has two components, η_1 and η_2 (Dvorak, 1971). They correspond to the amplitudes of two waves of atomic shifts, whose wavelengths equal to the double lattice period in the direction of

the modulation. Clearly, no macroscopic field is conjugate to this order parameter. Thus, a thermodynamic potential expansion describing this transition should contain the order parameter components (η_1 and η_2) as well as macroscopic electrical (\mathbf{P} or \mathbf{E}) and mechanical ($\boldsymbol{\varepsilon}$ or $\boldsymbol{\sigma}$) variables. The simplest mathematical description of basic properties of a mechanically free crystal of GMO can be obtained in terms of a thermodynamic potential having \mathbf{E} and $\boldsymbol{\sigma}$ as independent variables. We shall use this kind of potential. The full expansion of any thermodynamic potential of GMO is rather cumbersome (Dvorak, 1974; Smolenskii et al., 1984) and we are not going to analyze it in detail. In what follows we focus on comparison of features of proper and improper ferroelectrics corresponding to the same ferroic species. To do that we keep the minimal number of terms that make such a comparison possible and to simplify the treatment we consider the case of a second-order phase transition instead of the real first-order transition in GMO. We use the following thermodynamic potential, which is consistent with the symmetry of the order parameter (Dvorak, 1974; Smolenskii et al., 1984) and with that of the parent phase:

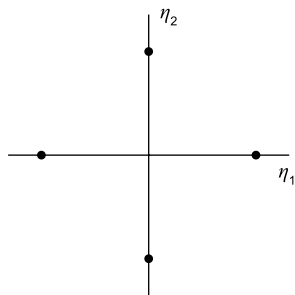
$$\begin{aligned} \tilde{\Phi} = & \tilde{\Phi}_0 + \frac{1}{2}\alpha(\eta_1^2 + \eta_2^2) + \frac{1}{4}\beta_1(\eta_1^4 + \eta_2^4) + \frac{1}{2}\beta_2\eta_1^2\eta_2^2 \\ & + \gamma(\eta_1^2 - \eta_2^2)E_z + \delta(\eta_1^2 - \eta_2^2)\sigma_6 + \lambda(\eta_1^2 - \eta_2^2)E_z\sigma_3 \\ & - \frac{\chi_{33}}{2}E_z^2 - \frac{1}{2}s_{33}\sigma_3^2 - \frac{1}{2}s_{66}\sigma_6^2 - d_{36}E_z\sigma_6. \end{aligned} \quad (2.3.36)$$

Here as usual we assume that all coefficients are temperature independent except for $\alpha = \alpha_0(T - T_0)$. We also set $\beta_1 > 0$ and $\beta_2 > \beta_1$.

We start with finding the domain states in a mechanically free and short-circuited sample. Order parameters defining the domain states can be found from the condition of minimum of $\tilde{\Phi}$. It is convenient to illustrate these states with points or vectors on the (η_1, η_2) plane (see Fig. 2.3.6). The structure of the fourth-order invariants in Eq. (2.3.36) and the condition $\beta_2 > \beta_1$ immediately suggest that minima of $\tilde{\Phi}$ belong to lines $(\eta_1 \neq 0, \eta_2 = 0)$ or $(\eta_2 \neq 0, \eta_1 = 0)$ (see the same figure). Indeed, the η terms of the expansion can be rewritten as $\frac{1}{2}\alpha(\eta_1^2 + \eta_2^2) + \frac{1}{4}\beta_1(\eta_1^2 + \eta_2^2)^2 + \frac{1}{2}(\beta_2 - \beta_1)\eta_1^2\eta_2^2$. One sees that the first two terms are independent of the orientation of the (η_1, η_2) vector, whereas the last term does make the directions $(\eta_1 \neq 0, \eta_2 = 0)$ and $(\eta_2 \neq 0, \eta_1 = 0)$ energetically favorable. The positions of the minima on these directions are controlled by conditions $\partial\tilde{\Phi}/\partial\eta_1 = 0$ and $\partial\tilde{\Phi}/\partial\eta_2 = 0$. Finally, one finds the four domain states depicted in Fig. (2.3.6): $(\eta_1 = \eta_S, \eta_2 = 0)$, $(\eta_1 = -\eta_S, \eta_2 = 0)$, $(\eta_1 = 0, \eta_2 = \eta_S)$, and $(\eta_1 = 0, \eta_2 = -\eta_S)$, where $\eta_S = (-\alpha/\beta_1)^{1/2}$.

Now, let us test the macroscopic properties of the obtained domain states. Using equations of state following from Eq. (2.3.12), $\partial\tilde{\Phi}/\partial E_i = -P_i$ and $\partial\tilde{\Phi}/\partial\sigma_n = -\varepsilon_n$, we find

Fig. 2.3.6 Order parameter plane for an improper ferroelectric of GMO symmetry. *Points* represent domain states



$$\begin{aligned}
 P_z &= \chi_{33}E_z + d_{36}\sigma_6 - \gamma(\eta_1^2 - \eta_2^2), \\
 \varepsilon_6 &= d_{36}E_z + s_{66}\sigma_6 - \delta(\eta_1^2 - \eta_2^2), \\
 \varepsilon_3 &= s_{66}\sigma_6 - \lambda(\eta_1^2 - \eta_2^2)E_z.
 \end{aligned}
 \tag{2.3.37}$$

First, from these equations we conclude that the domain states that differ only by the sign of the order parameter (like the pair of states $(\eta_1 = 0, \eta_2 = \eta_S)$ and $(\eta_1 = 0, \eta_2 = -\eta_S)$) are identical in their macroscopic properties. These are translational domain pairs discussed in Sect. 2.1.7. It is of importance to stress that, in accordance with the symmetry analysis, these states are macroscopically undistinguishable in any approximation on which the thermodynamic expansion is based.

Second, we see that the states which differ in the alignment of the (η_1, η_2) vector (like the pair $(\eta_1 = 0, \eta_2 = \eta_S)$ and $(\eta_1 = \eta_S, \eta_2 = 0)$) differ also in the sign of the spontaneous polarization P_{zS} , spontaneous strain ε_{6S} , and piezoelectric coefficient d_{33} ; for these states, Eq. (2.3.37) yields $P_{zS} = \gamma\eta_S^2$, $\varepsilon_{6S} = \gamma\eta_S^2$, $d_{33S} = \lambda\eta_S^2$ and $P_{zS} = -\gamma\eta_S^2$, $\varepsilon_{6S} = -\gamma\eta_S^2$, $d_{33S} = -\lambda\eta_S^2$, respectively. That means that these states are orientational states (according to the terminology of Sect. 2.1.7) and that GMO itself is ferroelectric, ferroelastic, and ferroelastoelectric. Comparing the set of newly acquired macroscopic properties of GMO with that of KDP (see Sect. 2.3.3) we see these are identical as one expects for two examples of the same species $42m - P\bar{c}2m - mm2$; we remind the reader that our definition of ferroic species is based on point symmetry only, not taking into account possible changes of translational symmetry.

Third, and this of course is connected with the just mentioned reminder, thermodynamics reveals a tremendous difference in the temperature dependences of the thermodynamic parameters of proper and improper ferroelectric–ferroelastics. In contrast to the properties of KDP, the equation of state (2.3.37) reveals no singularity in the temperature dependence of dielectric and elastic responses. In addition, the temperature dependence of spontaneous polarization for proper and improper ferroelectrics is basically different. According to Eq. (2.3.37), in the latter case $P_{zS} \propto \eta_S^2 \propto T_C - T$ instead of the

classical square root behavior expected for a second-order proper ferroelectric phase transition.

2.3.6 Limitation of Traditional Thermodynamic Approach: Pseudo-proper and Weak Ferroelectricity

In the presented above examples of application of Landau theory to the description of proper ferroelectric phase transitions, we have based our consideration on expansions of the thermodynamic potential in terms of a macroscopic variable — polarization. This approach is widely used providing a good qualitative description for many properties of proper ferroelectrics. However, when employing this approach, i.e., Landau theory expansion in terms of a macroscopic variable, one should keep in mind its limitations. Basically this approach suffers from two intrinsic limitations. First, the Landau theory ignores the order parameter fluctuations. This limitation is duly discussed in the literature, e.g., an excellent discussion of the issue can be found in the book of Strukov and Levanyuk (1998). In our book we are not going to touch this issue since it is basically essential for the critical behavior of ferroics, which goes out of the scope of the book. The other limitation is related to the use of a macroscopic variable as the order parameter. We will address this limitation below.

Generally speaking, the use of macroscopic polarization as a variable for the Landau expansion is not fully justified from the point of view of the microscopic theory. To evaluate the impact of this issue on the applicability of the traditional phenomenological approach we should remind the reader of the fundamentals of the microscopical approach.

On the microscopic level, the polarization of any ferroelectric can be divided into two parts. The first so-called critical part is related to the so-called critical displacements of ions, which are responsible for the enhanced dielectric response and the appearance of spontaneous polarization. In the case of perovskite ferroelectrics these are relatively simple displacements of the ions, whereas in the case of materials like KDP this is a complex distortion of the unit cell. The essential point is that these displacements are correlated so that all of them can be expressed in terms of one amplitude η_f , the so-called normal coordinate of the ferroelectric soft mode. Due to this fact, the critical contribution to polarization can be presented as

$$P_f = \frac{1}{V} e_f \eta_f, \quad (2.3.38)$$

where V stands for the unit cell volume and e_f is the so-called soft-mode effective charge. In this section, for simplicity, we consider the case of a uniaxial ferroelectric; the logic of this consideration can be readily translated to the general

case. Accordingly, Eq. (2.3.38) is written for the projection of the polarization on the ferroelectric axis of the material. We will keep only this component of polarization without specifying this further.

The second so-called non-critical part, P_r , is the contribution of the other polar distortions of the unit cell.²² This part can be presented as the sum of the contributions from the other polar optical modes (systems of correlated displacements of the ions) so that P_r can be written as a sum of terms like that given by Eq. (2.3.38) with the corresponding effective charges and normal coordinates of these modes. To further simplify the discussion we will keep only the contribution of one of these modes, which hereafter will be called the *hard mode*. This way we will arrive at the following expression for the non-critical part of polarization: $P_r = e_r \eta_r / V$, e_r and η_r being the effective charge and normal coordinate of the hard mode. Finally, the total polarization P can be written as a sum:

$$P = P_r + P_f = (e_r \eta_r + e_f \eta_f) / V. \quad (2.3.39)$$

The essential point is that the two components of the polarization and the normal coordinates are introduced as decoupled by definition so that there should be no contribution to the energy of the crystal proportional to their product.

Using Eq. (2.3.39) let us address the microscopic justification of the Landau theory. Any microscopic theory operates with microscopic variables. The microscopic theory of ferroelectrics operates with the soft-mode normal coordinate, η_f , as the order parameter and yields as a result an expansion for the free energy in terms of this variable. Clearly, in terms of the polarization, this leads to an expansion with respect to the critical part of the polarization, P_f , which is, strictly speaking, not equivalent to that in terms of the total polarization P . On the other hand, we know that the expansion with respect to the total polarization often works effectively. This disparity usually does not puzzle workers dealing with this expansion even if they realize the existence of non-critical contributions to the polarization. In this case, it is usually said that this contribution is relatively small so that neglecting this contribution does not substantially affect the results. However, this is not always the case. Thus, when dealing with the traditional “ P expansion” one should be aware of situations where the use of this expansion leads to quantitatively erroneous results. These situations will be discussed below as well as “improved” phenomenological schemes, namely, the pseudo-proper and weak ferroelectric approaches.

To prepare this discussion we will start with the analysis of two situations where one can neglect the difference between P and P_f and “safely” work with the traditional “ P expansion.” Consider the polarization response of a proper

²² For simplicity we are not discussing here the purely electronic contribution to the polarization; the incorporation of this contribution into the consideration would affect neither its logic nor the final conclusions.

ferroelectric to an external electric field. The latter couples with critical and non-critical displacements, η_f and η_r , via the corresponding effective charges, e_f and e_r . The values of the field-induced displacements are controlled by two factors: the restoring force constants of the hard and soft modes and their effective charges. In the standard situation, the values of these charges are of the same order of magnitude (about the charge of electron), whereas the restoring constant of the soft mode is much smaller than that of the hard one by definition. That implies $\eta_f \gg \eta_r$ and finally $P_f \gg P_r$ for the polarization responses to the external electric field. Thus, in this situation the difference between P and P_f can be neglected. However, we also see that this may not be justified if the effective charge of the soft mode is small compared to that of the hard mode, i.e., $e_f \ll e_r$. In this case, the smallness of the soft-mode restoring constant may be “compensated” by the smallness of its effective charge so that the polarization response may not be dominated by the critical contribution P_f , while the non-critical part P_r may be appreciable in the total polarization. A similar situation occurs for the calculation of the spontaneous polarization. If the order parameter η_f acquires a spontaneous value of η_{f_0} , the corresponding spontaneous value of the critical part of polarization, $P_{f_0} = e_f \eta_{f_0} / V$, is not, strictly speaking, equal to the produced value of the spontaneous polarization P_S . The latter differs from P_{f_0} by the contribution of the non-critical displacements. However, since the linear coupling between η_f and η_r is absent by definition, the spontaneous value of the hard mode η_{r_0} appears only due to a weak non-linear coupling and therefore it is small, i.e., $\eta_{f_0} \gg \eta_{r_0}$. In the standard situation where $e_f \cong e_r$, that clearly implies $P_{f_0} \gg P_{r_0}$ justifying the neglect of the difference between P and P_f . However, clearly this may not be justified if the effective charge of the soft mode is small compared to that of the hard mode. Thus, we have revealed a situation where not making difference between P and P_f is not justified, namely, the situations where the effective charge of the soft mode is small. However, this situation is not the only one where not differentiating between P and P_f is illegitimate. The problem of the depolarizing effect treated below is also the case.

Consider a phase transition in a plate capacitor of a proper ferroelectric. We are interested in the situation where the spontaneous polarization is normal to the electrodes, a transition into a single-domain state occurs, and the electrodes are not short circuited (no screening of the spontaneous polarization). Using the traditional approach we start with the thermodynamic potential,²³ Eq. (2.3.13),

$$\tilde{\Phi} = \Phi_0 + \frac{\alpha}{2} P^2 + \frac{\beta}{4} P^4 - PE, \quad (2.3.40)$$

where $\beta > 0$, $\alpha = \alpha_0(T - T_0)$, $\alpha_0 = (\varepsilon_0 C)^{-1} > 0$, C being the Curie–Weiss constant, and E the component of the electric field parallel to the ferroelectric axis

²³ It is useful to note that, for the considered problem, this potential does not reach the minimum at equilibrium; however, as far as we are interested in the equation of state any potential can be employed for its derivation.

of the material. This leads, via the condition $\partial\tilde{\Phi}/\partial P = 0$, to the equation of state of the ferroelectric:

$$E = \alpha P + \beta P^3. \quad (2.3.41)$$

In our system, the electric field E is not zero due to the depolarizing effect and can be determined from the Poisson equation which in our one-dimensional case implies $D = E\varepsilon_0 + P = 0$, i.e.,

$$E = -P/\varepsilon_0. \quad (2.3.42)$$

Eliminating E between Eqs. (2.3.41) and (2.3.42) we arrive at the equation of state for the polarization in the system:

$$\alpha_0(T - T_0 + \Delta T)P + \beta P^3 = 0, \quad (2.3.43)$$

where $\Delta T = C$. Thus, starting from the traditional “ P expansion,” we have found that the depolarization effect results in a shift of the transition temperature down by a value of the Curie–Weiss constant. However, one can show that this result is wrong. An adequate treatment of the problem yields a shift which is many times smaller, namely, $\Delta T = C/\kappa_b$ where κ_b is the background dielectric permittivity of the ferroelectric (in terms of our simple model κ_b is the contribution of the hard mode to the permittivity). Let us show it.

First, let us re-expand the thermodynamic potential in terms of the real order parameter η_f or, equivalently, in terms of the critical part of polarization $P_f = e\eta_f/V$, which is proportional to it:

$$\tilde{\Phi} = \Phi_0 + \frac{\alpha}{2} P_f^2 + \frac{\beta}{4} P_f^4 - PE. \quad (2.3.44)$$

Note that the last term of this equation, which is related to the electrostatic work, still contains the total polarization $P = P_f + P_r$. Then, the condition of minimality of the potential with respect to the order parameter, $\partial\tilde{\Phi}/\partial P_f = 0$, yields

$$E = \alpha P_f + \beta P_f^3 \quad (2.3.45)$$

Now attributing the background dielectric response to the hard mode, i.e., setting $P_r = (\kappa_b - 1)\varepsilon_0 E$, and using Eqs. (2.3.39) and (2.3.42) we readily arrive at the equation of states given by Eq. (2.3.43) with

$$\Delta T = C/\kappa_b. \quad (2.3.46)$$

The factor κ_b can readily be about 10. That makes a 10 times difference between the result obtained by using the “ P expansion” and that of the comprehensive consideration. One should stress that this happens even in the case where the contribution of the background susceptibility is not essential in the

overall dielectric susceptibility χ . In terms of the developed approach, the latter can be found as

$$\chi \equiv \frac{\partial P}{\partial E} = \varepsilon_0 \left(\frac{C_{\pm}}{|T - T_0|} + \kappa_b - 1 \right), \quad (2.3.47)$$

where C_{\pm} equals C at $T > T_0$ and $C/2$ at $T < T_0$.

Thus we see that in the situation where the depolarizing effect is involved the use of the total polarization in the expansion can lead to essentially wrong results. In this context it is useful to mention that in this situation the error introduced by the use of the P expansion" may vary. Here an instructive example is a realistic ferroelectric capacitor, where the regions adjacent to the ferroelectric/electrode interfaces effectively behave as layers of a low-dielectric-constant insulator. In contrast to an ideal capacitor, when short circuited in a single domain state with the spontaneous polarization normal to electrodes, such capacitor still contains some depolarizing field. This field in turn leads to a shift of the Curie–Weiss temperature down by (see, e.g., Sherman et al., 2006)

$$\Delta T = C \frac{d}{d\kappa_b + h\kappa_d}, \quad (2.3.46a)$$

where κ_d and d are the dielectric constant and thickness of the effective dielectric layer associated with the ferroelectric/electrode interfaces; h is the thickness of the ferroelectric. At $d \gg h$, the system becomes formally equivalent to an isolated ferroelectric plate and, accordingly, Eq. (2.3.46a) transforms into Eq. (2.3.46). While in the opposite case, Eq. (2.3.46a) becomes independent of the background permittivity, which means that the difference between the predictions of P and P_f expansions disappear.

The scheme presented above is not the only one that provides a description of the effects related to the background dielectric permittivity. This can also be done in terms of the so-called *pseudo-proper ferroelectric* approach introduced by Petzelt et al. (1974) and Dvorak (1970). This approach deals with the Landau expansion in terms of an order parameter η which is not the polarization but a variable linearly coupled with it. In this case instead of Eq. (2.3.44) we use the expansion

$$\tilde{\Phi} = \Phi_0 + \frac{\alpha'(T - T'_0)}{2} \eta^2 + \frac{\beta}{4} \eta^4 + fP\eta + \frac{\chi_b^{-1}}{2\varepsilon_0} P^2 - PE, \quad (2.3.48)$$

where $\chi_b = \kappa_b - 1$. Now, using the two conditions, $\partial\tilde{\Phi}/\partial P = 0$ and $\partial\tilde{\Phi}/\partial\eta = 0$, we readily arrive at the equation for the dielectric susceptibility, Eq. (2.3.47), where the Curie–Weiss constant C and the transition temperature T_0 are

$$C = \frac{f^2 \chi_b^2 \varepsilon_0}{\alpha'} \quad \text{and} \quad T_0 = T'_0 + \frac{C}{\chi_b}, \quad (2.3.49)$$

This approach also leads to the correct expression for the depolarizing-effect-induced shift of the transition temperature, Eq. (2.3.46).

Comparing the pseudo-proper phenomenological scheme with the traditional proper one, we should distinguish two situations: materials with “normal” values of the Curie–Weiss constant ($\cong 10^5$ K for the displace type ferroelectrics and $\cong 10^3$ K for those order–disorder) and material with anomalously small values of the Curie–Weiss constant. On the microscopic level these situations correspond to the case of “normal” values of the soft-mode effective charge (about the charge of an electron) and to those where this charge is anomalously small.

In the first case, the only new element introduced by the pseudo-proper approach is an adequate treatment to the background dielectric permittivity. This is the case of the KDP crystals ($C = 3,250$ K). It was argued (Dvorak, 1970) that, for this material, the pseudo-proper approach brought about qualitatively new features to the phenomenological description. However, one can be shown that as far as the value of the Curie–Weiss constant is “normal” all these features are beyond the accuracy of the Landau theory.

In the second case, we find quite a different situation. It was treated by Petzelt et al. (1974) for $(\text{NH}_4)\text{SO}_4$ ($C = 30$ K). In this case, the pseudo-proper approach enables the interpretation of a weak dielectric anomaly as a result of weak coupling between the polarization and the order parameter (small values of the f coefficient in Eq. (2.3.48)). In contrast to the first case, now this approach can also describe qualitatively new features. An example is the electrostriction effect. In terms of this approach the order parameter/stress coupling corresponds to the $\eta^2\sigma$ terms (in the thermodynamic potential) instead of the $P^2\sigma$ terms. One can show that this difference substantially affects the temperature behavior of the electrostriction coefficients of the system.

Though the pseudo-proper approach provides an adequate description of the depolarizing effect and is more advanced, than the traditional approach, in the description of the properties of the proper ferroelectrics with anomalously small value of the Curie–Weiss constant, it is still limited. It can be revealed when trying to describe the unusual features of the proper ferroelectrics with yet smaller values of $C = 2\text{--}5$ K, e.g., the change of sign of the spontaneous polarization in $\text{Li}_2\text{Ge}_7\text{O}_{15}$. The reason for that is the use of the total polarization in the expansion. As we have already pointed out in the beginning of this section, the polarization does not represent a proper variable for the expansion of the thermodynamic potential unless the polarization itself is dominated by a contribution of a single mode. Thinking in terms of microscopic justification of the Landau theory we see that the corresponding polar displacement of the ions, or, at best, the corresponding normal coordinates, should be used for the expansion. A phenomenological description which is free from the aforementioned drawback is offered by the so-called *weak ferroelectric* approach (Tagantsev, 1987, 1988; Tagantsev et al., 1987).

For the simplest case of the model introduced in the beginning of this section, the basic thermodynamic potential for such a two-mode description reads

$$\tilde{\Phi} = \Phi_0 + \frac{\alpha_f}{2}\eta_f^2 + \frac{\beta_f}{4}\eta_f^4 + \frac{\alpha_r}{2}\eta_r^2 + \gamma\eta_r\eta_f^3 - PE, \quad (2.3.50)$$

where $P = (e_r\eta_r + e_f\eta_f)/V$, $\alpha_f = \alpha_{f_0}(T - T_0) \ll \alpha_r$, and $e_f \ll e_r$. Note that the $\eta_r\eta_f$ term is absent according to the definition of η_r and η_f . Thus, the expansion is made in terms of two modes: a soft mode which carries a small charge and a hard one that carries a “normal” charge.

Comparing the weak-ferroelectric approach with two discussed above one finds that it, on one hand, reproduces all the results of those obtained in their range of applicability and, on the other hand, enables description of qualitatively new features. For the dielectric response in the paraelectric phase, via conditions $\partial\tilde{\Phi}/\partial\eta_f = 0$ and $\partial\tilde{\Phi}/\partial\eta_r = 0$, we readily arrive at the standard Curie–Weiss anomaly appended with the background dielectric susceptibility, Eq. (2.3.47), with

$$C_{\pm} = C = \frac{e_f^2}{V^2\varepsilon_0\alpha_{f_0}}, \quad \kappa_b = \frac{e_r^2}{V^2\varepsilon_0\alpha_r} + 1. \quad (2.3.51)$$

However, in the ferroelectric phase, the weak ferroelectric scheme predicts a possibility of essential deviation of the temperature dependence of the critical part of the susceptibility from the classical Curie–Weiss behavior (Tagantsev, 1987, 1988; Tagantsev et al., 1987). This temperature dependence (calculated based on Eq. (2.3.50)) can be formally described by Eq. (2.3.47) with a temperature-dependent parameter C_{\pm} :

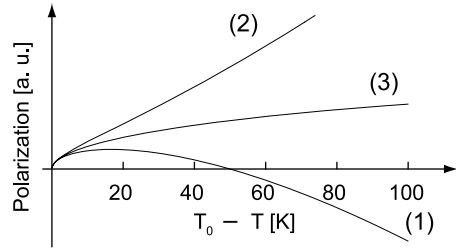
$$C_{\pm} = \frac{C}{2} \left(\frac{T - T_0 + \delta}{\delta} \right)^2, \quad (2.3.52)$$

where $\delta = \frac{1}{3} \frac{\alpha_r}{\alpha_{f_0}} \frac{e_f \beta}{e_r \gamma}$. In addition, this relation controls the temperature dependence of the oscillator strength of the soft mode. The scheme also provides an expression for the temperature dependence of the spontaneous polarization:

$$P_S = \frac{e_f}{V} \sqrt{\frac{\alpha_{f_0}(T_0 - T)}{\beta}} \left(1 - \frac{T_0 - T}{3\delta} \right). \quad (2.3.53)$$

It is seen that, in the case where the effective charge of the soft mode e_f is small enough to make the absolute value of δ comparable to $T_0 - T$, the above expression corresponds to very unusual temperature dependences of the parameters of the system. Figure 2.3.7 illustrates the temperature dependences of the spontaneous polarization expected in this case. Of special interest is the

Fig. 2.3.7 Temperature dependence of the spontaneous polarization in the weak ferroelectric model for $\delta = 50$ K(1) and $\delta = -50$ K(2). The standard square root law is also shown (3)



situation where $\delta > 0$ where the spontaneous polarization changes its sign at the temperature

$$T_p = T_0 - 3\delta. \quad (2.3.54)$$

One can show that, under the same conditions, the oscillator strength of the soft mode also vanishes but at a different temperature

$$T_{IR} = T_0 - \delta. \quad (2.3.55)$$

This means that the soft mode is expected to disappear from the infrared absorption spectrum at some temperature below the transition.

These and other predictions of the weak ferroelectric scheme are compatible with ferroelectric and dielectric properties of a number of materials in which the effective charge of the soft mode has been shown to lie in the range of 10^{-2} – 10^{-3} of an electron charge. A good example of this kind of material is $\text{Li}_2\text{Ge}_7\text{O}_{15}$, where both the change of the sign of the spontaneous polarization and the disappearance of the soft mode from the infrared spectrum have been documented (Bush and Venetsev, 1986; Kadlec et al., 1995). In addition, this approach has been extended to relate the symmetry of the parent phase with the anomalously small charge of the soft mode (Tagantsev, 1986b, 1987, 1988; Tagantsev et al., 1987).

Thus, the discussion given in this section clearly demonstrates that, though the symmetry aspect justifies the selection of the polarization for the order parameter of Landau theory of proper ferroelectrics, the theory developed this way may fail in the description of certain phenomena. At the same time, the descriptive ability of such theory can be essentially improved when using properly selected order parameters of the same symmetry.

Chapter 3

Ferroic Materials

3.1 Sources of Information and Statistics

Classifying phase transitions on the basis of point symmetry changes, Tables B.1 and C.1 show that altogether we can distinguish 212 ferroic species out of which 119 are ferroelectric. Because of the existence of domain states, they offer a huge variety of macroscopic properties and one may wonder how many of these species are really represented by presently known crystalline materials. The exact answer to this question has not and hardly could have been given, but in this chapter we wish first to give the reader some hints where to look for information on particular kinds of transitions, quote some results of Tomaszewski's research, and then present a table of ferroics whose domain properties have been extensively studied and which are mentioned in this book in different contexts.

Almost any book on ferroelectrics contains a table of crystals possessing ferroelectric phases; the contents widely vary and depend, of course, on the date when the book was written. We can refer to the monographs by Jona and Shirane (1962), Lines and Glass (1977), Smolenskii et al. (1984), and Xu (1991) as helpful sources of assembled information on materials, but of course the most valuable collection of data, including data on symmetry, is offered in the volumes III/3 (1969), III/9 (1975), III/16a (1981), III/16b (1982), III/28a and III/28b (1990) of Landolt–Börnstein New Series. An extensive table of almost 200 ferroelastics (including ferroelectric ferroelastics), specifying both space groups when known, transition temperature, and giving several references for each compound, has been included in Salje's monograph (1990). Several extremely useful tables of different kinds of ferroics are presented in the book by Toledano and Toledano (1988); their data are classified according to the symmetry of the order parameters, include space groups in both parent and ferroic phases and thus also information on basic macroscopic properties. Cummins (1990) worked out a compilation of those ferroics which reveal an incommensurate phase (a phase where the order parameter is spatially modulated) and most of them possess also a ferroic phase in the sense defined above. As for higher order ferroics, the original list was compiled by Amin and Newnham (1980).

With a few exceptions, in this book we pay attention to phase transformations occurring as a result of the change of temperature at constant ambient pressure. However, considerable attention has also been paid to transformations induced by pressure. The most complete collection of data is due to Tonkov (1992).

Speaking about ferroics in general, the most voluminous available database appears to be that presented by Tomaszewski (1992a). His compilation, published in 1992, specifies the chemical formula or name of the crystalline material, transition temperature, and both G and F symmetries in terms of space groups, if known. He also gives one basic reference for each compound. No information is included as to changes of translational symmetry, with the exception of incommensurate phases.

Tomaszewski analyzed his database in another publication (1992b) and it is worthwhile to point to some of his conclusions. Altogether 3,446 phase transitions are included which were reported to occur in 2,242 crystalline materials; out of the latter, 128 are organic. From the total number of 2,242, two transitions were reported to occur in 492 crystals, three phase transitions in 208 crystals, and more than three in 80 other crystalline materials. Available data, understandably, were not complete and only for 2,480 transitions the symmetries of both neighboring phases were known. Table 3.1.1 gives more detailed information about numbers of these well-documented transitions, as they depend on point symmetries of the high-temperature and low-temperature phases. The horizontal designation of point symmetries applies to the high-temperature phase while the vertical column of symbols applies to the low-temperature phase. Thus the field above the broken line refers to phase transitions at which the point symmetry is lowered on cooling (here represented only by the change of the crystal system, e.g., from monoclinic to triclinic). The transitions specified below the line correspond to the opposite case. The analysis presented in the previous chapter is applicable to these cases. Maximum numbers represent transitions with both G and F orthorhombic phases (255, i.e., 10.3% out of 2480) and transitions with cubic phase G and tetragonal phase F (269 cases, i.e., 10.8%). Some symmetry reductions are hardly represented at all (0 for G hexagonal and F triclinic, 0.5% for G cubic and F triclinic).

Out of the 2,480 well-described transitions, 265 are ferroelectric and a corresponding overview is included in Table 3.1.2. Here again the horizontal designation refers to the paraelectric phase. The most frequently represented ferroelectric transitions are those with tetragonal paraelectric and orthorhombic ferroelectric phase (19%) or with both G, F phases orthorhombic (18%). The meaning of the broken line in this table is the same as in Table 3.1.1

3.2 Table of Selected Ferroic Materials

Most of those ferroic materials whose domain or related properties are referred to in this book are shown in Table. 3.2.1; we also include several compounds whose domain properties might appear interesting but have not been studied

Table 3.1.1 Number of materials with well-documented phase transitions

	tricl	mon	orth	tetr	rhomb	hex	cub
tricl	22	50	21	8	26	0	13
mon	6	171	211	130	63	36	71
orth	5	43	255	176	63	69	151
tetr	0	12	33	74	6	10	269
rhomb	0	22	6	3	48	30	199
hex	2	2	11	5	11	34	65
cub	0	15	9	14	7	29	74

After Tomaszewski (1992a). Columns are specified by the crystal system of the parent phase given in the uppermost row. Rows represent crystal system of the ferroic phase, as given in the first column.

Table 3.1.2 Number of materials with well-documented ferroelectric transitions

	tricl	mon	orth	tetr	rhomb	hex	cub
tricl	2	3	1	0	1	0	2
mon	0	34	13	6	4	3	9
orth	0	5	49	51	0	0	25
tetr	0	0	0	23	0	0	17
rhomb	0	1	0	0	4	2	8
hex	0	0	0	0	0	2	0
cub	0	0	0	0	0	0	0

After Tomaszewski (1992a). Columns specify crystal system of the parent phase given in the uppermost row. Rows represent crystal system of the ferroelectric phase shown in the first column.

yet. The table is intended to give the reader a quick reference for all these crystalline materials, but at the same time its aim is to illustrate the diversity of ferroic phase transition materials from the point of view of symmetry. Materials are listed according to the symmetry of the appropriate species, with no regard of chemical composition, roughly following the sequence used in Table B.1 of ferroic species. This, of course, brings together materials of a

Table 3.2.1 Selected ferroic materials

Formula	Commonly used abbreviation; name	Species ^a	T_{TR} ^b	Order ^c	Transl. ^d
NH ₄ Cl	Ammonium chloride	$m\bar{3}m - d - 43m$	243	Second	EQ
BiF ₃	Bismuth trifluoride ^e	$m\bar{3}m - d - 43m$			NEQ
N ₂ H ₆ Cl ₂		$m\bar{3}m - m\bar{3}$			NEQ
C ₆₀	Fullerene	$m\bar{3}m - m\bar{3}$	250	First	EQ
BiFeO ₃	Bismuth ferrite	$m\bar{3}m - Peds - 3m$	1125	First	NEQ
PbZrO ₃	Lead zirconate ^f	$m\bar{3}m - Peds - 3m$	490	First	NEQ
		$-es - mmm$	481	First	NEQ
SrTiO ₃	Strontium titanate	$m\bar{3}m - es - 4/mmm$	105	Second	NEQ
CsPbCl ₃	Cesium lead chloride	$m\bar{3}m - es - 4/mmm$	318	First	NEQ
		$-es - mmm$	315	Second	NEQ
		$-es - mmm$	310	First	
		$-es - 2/m$	194	Second	
KMnF ₃	Potassium manganese fluoride	$m\bar{3}m - es - 4/mmm$	186	Second	NEQ
		$-es - 4/mmm$	88	First	NEQ
NH ₄ Br	Ammonium bromide	$m\bar{3}m - es - 4/mmm$	235	Second	NEQ
		$-d - 43m$	107		
BaTiO ₃	BT; barium titanate	$m\bar{3}m - Peds - 4mm$	399	First	EQ
		$-Peds - mm2$	278	First	EQ
		$-Peds - 3m$	183	First	EQ
		$m\bar{3}m - Peds - 4mm$	708	First	EQ
		$-Peds - mm2$	498	First	EQ
		$-Peds - 3m$	263	First	EQ
PbTiO ₃	PT; lead titanate	$m\bar{3}m - Peds - 4mm$	763	First	EQ
PbHfO ₃	Lead hafnate	$m\bar{3}m - eds - 222$	473	First	EQ
		$-Peds - mm2$	431	First	EQ
Cd ₂ Nb ₂ O ₇	Cadmium niobate ^g	$m\bar{3}m - es - mmm$	205	Second	
		$-Peds - mm2$	196	Second	
HCl	Hydrochloric acid	$m\bar{3}m - Peds - mm2$	98		
Cr ₃ B ₇ O ₁₃ Cl	Cr-Cl boracites	$43m - eds - 42m$	264	First	EQ
		$-Peds - mm2$	160	First	NEQ

Table 3.2.1 (continued)

Formula	Commonly used abbreviation; name	Species ^a	T_{TR} ^b	Order ^c	Transl. ^d
$Mg_3B_7O_{13}Cl$	Mg-Cl boracites	$43m - P\bar{e}ds - mm2$	536	First	NEQ
$Co_3B_7O_{13}Cl$	Co-Cl boracites	$43m - P\bar{e}ds - mm2$ $-P\bar{e}ds - m$ $-P\bar{e}ds - 3m$ $-P\bar{e}ds - m$	623 538 468	First First First First	NEQ NEQ EQ NEQ
$ZnO_3B_7O_{13}Cl$	Zn-Cl boracites	$43m - P\bar{e}ds - mm2$ $-P\bar{e}ds - m$ $-P\bar{e}ds - 3m$	781 564 472	First First First	NEQ NEQ NEQ
$Fe_3B_7O_{13}I$	Fe-I boracites	$43m - P\bar{e}ds - mm2$ $-P\bar{e}ds - m$ $-P\bar{e}ds - 3m$ $-P\bar{e}ds - m$	349 218 203 191	First First First First	NEQ NEQ EQ NEQ
$Ni_3B_7O_{13}I$	Ni-I boracites	$43m - P\bar{e}ds - m$	61	Second	NEQ
$K_2Cd_5(SO_4)_3$	Potassium cadmium sulfate	$23 - \bar{e}ds - 222$	432	First	EQ
$Cd_2(NH_4)_2(SO_4)_3$	CAS, cadmium diammonium sulfate;	$23 - P\bar{e}ds - 2$	92	First	NEQ
$CH_3NH_3Al(SO_4)_2 \cdot 12H_2O$	MASD, methyl ammonium sulfate hexahydrate ^b	$23 - P\bar{e}ds - 2$	177	First	
$K_3W_2Cl_9$	Potassium tungsten chloride	$6/mmm - 6/m$			EQ
$Cd_5(PO_4)_3Cl$	Cadmium chlorapatite ^e	$6/mmm - 6/m$	423	First	NEQ
$CsCuCl_3$	Cesium copper chloride	$6/mmm - d - 622$	hyp.		NEQ
$(NH_4)_2SO_4$	Ammonium sulfate	$6/mmm - \bar{e}s - mmm$ $-P\bar{e}ds - mm2$	223	First	NEQ
$Li_2Ge_7O_{15}$	LGO; lithium heptagermanate	$6/mmm - \bar{e}s - mmm$	hyp.		NEQ
$LiNH_4SO_4$	LAS; lithium ammonium sulfate	$-P\bar{e}ds - mm2$ $6/mmm - \bar{e}s - mmm$	284 hyp.	Second	NEQ NEQ
		$-P\bar{e}ds - mm2$ $- \bar{e}s - 2/m$ $-P\bar{e}ds - m$	460 283 28	First First	NEQ NEQ

Table 3.2.1 (continued)

Formula	Commonly used abbreviation; name	Species ^a	T_{TR} ^b	Order ^c	Transl. ^d
BaTiO ₃	Hexagonal barium titanate	$6/mmm-\epsilon ds-222$ $-P\epsilon ds-2$	222 74	Second First	EQ EQ NEQ
K ₂ SeO ₄	Potassium selenate	$6/mmm-\epsilon s-mmm$ $-IC$ $-Pd-mm2$	745 129 93	Second First	NEQ NEQ NEQ
(CH ₃ NHCH ₂ COOH) ₃ CaCl ₂	TSCC, tris-sarcosine calcium chloride	$6/mmm-\epsilon s-mmm$	hyp.		NEQ
KLiSO ₄	LPS, potassium lithium sulfate	$-P\epsilon ds-mm2$ $6/mmm-Pd-mm2$	130 949	Second	NEQ
SiO ₂	Quartz	$-Pd-6$ $-Pds-3m$ $-P\epsilon ds-m$ 622-IC $-ds-32$	708 205 190 849.4 848	First First First	EQ
AlPO ₄	Berlinite	622-IC $-ds-32$	853		EQ
Pb ₅ Ge ₃ O ₁₁ (NH ₄) ₃ H(SeO ₄) ₂	PGO, lead germanate ⁱ Triammonium hydrogen diselenate	$\bar{6}-Pd-3$ $3m-s-\bar{3}$	450 332	Second Second	EQ EQ
LiNbO ₃	Lithium niobate	$-\epsilon s-\bar{1}$	302	First	EQ
LiTaO ₃	Lithium tantalate	$-\epsilon s-2/m$	273	First	EQ
C(NH ₂) ₃ Al(SO ₄) ₂	GASH, guanidinium aluminum sulfate hexahydrate ⁱ	$-P\epsilon ds-m$ $3m-Pd-3m$ $3m-Pd-3m$ $3m-Pd-3m$	181 1480 958 hyp.	Second Second	EQ EQ
Pb ₃ (PO ₄) ₂	Lead phosphate	$3m-\epsilon s-2/m$ $-P\epsilon ds-2$	453 273	First First	NEQ NEQ
Pb ₃ (VO ₄) ₂	Lead vanadate	$3m-\epsilon s-2/m$ $-P\epsilon ds-2$	371 283	First First	NEQ NEQ

Table 3.2.1 (continued)

Formula	Commonly used abbreviation; name	Species ^a	T_{TR} ^b	Order ^c	Transl. ^d
$Pb_3(AsO_4)_2$	Lead arsenate	$3m - \epsilon s - 2/m$ $-\epsilon s - 2/m$ $-P\epsilon ds - 2$	601 327 100	Second First Second	
$KFe(MoO_4)_2$		$3m - \epsilon s - 2/m$ $-P\epsilon ds - 1$	311 139	Second Second	NEQ
$KIn(WO_4)_2$		$3m - \epsilon s - 2/m$	454	Second	
$KSc(MoO_4)_2$	KSM; KSc-molybdate	$3m - \epsilon s - 2/m$ $-\epsilon s - 2/m$	260 240	Second First	
$Rb_3H(SeO_4)_2$	Rubidium hydrogen selenate	$3m - \epsilon s - 2/m$ $-\epsilon s - 1$	183	First	
Ag_3AsS_3	Proustite	$3m - IC$ $-ds - 3$	447 67 43	Second First Second	NEQ
KIO_3	Potassium iodate	$-P\epsilon ds - m$ $3m - P\epsilon ds - m$ $-P\epsilon ds - 1$	28 485 343		NEQ
$CuCr_2O_4$	Copper chromate	$m\bar{3}m - \epsilon ds - \bar{4}2m$	860	First	EQ
$KSCN$	Potassium thiocyanate	$4/mmm - \epsilon s - mmm$	415	First	NEQ
Hg_2Br_2	Mercury bromide	$4/mmm - \epsilon s - mmm$	143	Second	NEQ
Hg_2Cl_2	Mercury chloride, calomel	$4/mmm - \epsilon s - mmm$	185	Second	NEQ
$YBa_2Cu_3O_7$	YBCO	$4/mmm - \epsilon s - mmm$	1023		EQ
$Ba_2NaNb_5O_{15}$	BSN or BNN; banana; barium sodium niobate	$4/mmm - Pd - 4mm$ $4mm - IC$	833 573	First First	NEQ
WO_3	Tungsten trioxide	$IC - \epsilon ds - mm2$ $-P\epsilon ds - mm2$ $-Pd - 4mm$	548 533 110		
		$4/mmm - \epsilon s - mmm$ $-\epsilon s - 2/m$ $-P\epsilon ds - \bar{1}$	1013 603 290		NEQ
$Ba_{0.4}Sr_{0.6}Nb_2O_6$	SBN; strontium barium niobate ^k	$-P\epsilon ds - m$ $4/mmm - Pd - 4mm$	233 348		

Table 3.2.1 (continued)

Formula	Commonly used abbreviation; name	Species ^a	T_{TR} ^b	Order ^c	Transl. ^d
SrBi ₂ Ta ₂ O ₉	SBT, "Y-1"; strontium bismuth tantalate	4/ <i>mmm</i> - <i>Peds</i> - <i>mm2</i>	583		
SrBi ₂ Nb ₂ O ₉	Strontium bismuth niobate	4/ <i>mmm</i> - <i>Peds</i> - <i>mm2</i>	693	Second	
Bi ₄ Ti ₃ FeO ₁₅	Bismuth titanium iron oxide	4/ <i>mmm</i> - <i>es</i> - <i>mmm</i> - <i>Peds</i> - <i>mm2</i>	1023 833	First	
K ₃ Fe ₅ F ₁₅	Tungsten bronze fluoride	4/ <i>mmm</i> - <i>Peds</i> - <i>mm2</i>	490	First	NEQ
CsHSO ₄	Cesium hydrogen sulfate	4/ <i>mmm</i> - <i>es</i> -2/ <i>m</i> - <i>es</i> -2/ <i>m</i>	414 330	First	First
CsHSeO ₄	Cesium hydrogen selenate	4/ <i>mmm</i> - <i>es</i> -2/ <i>m</i>	401	First	NEQ
Bi ₄ Ti ₃ O ₁₂	Bismuth titanate	4/ <i>mmm</i> - <i>Peds</i> - <i>m</i>	948	First	EQ
KH ₂ PO ₄	KDP; potassium dihydrogen phosphate	42 <i>m</i> - <i>Peds</i> - <i>mm2</i>	123	First	EQ
KD ₂ PO ₄	Deuterated KDP	42 <i>m</i> - <i>Peds</i> - <i>mm2</i>	223	First	EQ
RbH ₂ PO ₄	RDP; rubidium dihydrogen phosphate	42 <i>m</i> - <i>Peds</i> - <i>mm2</i>	147	Second	EQ
RbD ₂ PO ₄	Deuterated RDP, tetragonal modification	42 <i>m</i> - <i>Peds</i> - <i>mm2</i>	218	Second	EQ
KH ₂ AsO ₄	KDA, potassium dihydrogen arsenate	42 <i>m</i> - <i>Peds</i> - <i>mm2</i>	97	First	EQ
KD ₂ AsO ₄	Deuterated KDA	42 <i>m</i> - <i>Peds</i> - <i>mm2</i>	159	First	EQ
NH ₄ H ₂ PO ₄	ADP; ammonium dihydrogen phosphate	42 <i>m</i> - <i>eds</i> - 222	148	First	NEQ
ND ₄ D ₂ AsO ₄	Deuterated ammonium dihydrogen arsenate	42 <i>m</i> - <i>eds</i> - 222	299		
C ₉ H ₁₈ NO	Tanane	42 <i>m</i> - <i>Peds</i> - <i>mm2</i>	287	Second	EQ
Gd ₂ (MoO ₄) ₃	GMO; gadolinium molybdate	42 <i>m</i> - <i>Peds</i> - <i>mm2</i>	436	First	NEQ
As ₂ O ₅	Arsenic pentoxide	422- <i>eds</i> -222	578	Second	EQ
Ca ₂ Sr(C ₂ H ₅ CO ₂) ₆	DSP; dicalcium strontium propionate	422- <i>Pds</i> -4 - <i>Peds</i> -2	281 104	Second	
LaNbO ₄	Lanthanum orthoniobate	4/ <i>m</i> - <i>es</i> -2/ <i>m</i>	793	Second	EQ
BiVO ₄	Bismuth vanadate	4/ <i>m</i> - <i>es</i> -2/ <i>m</i>	518	Second	EQ
C ₄ H ₂ O ₄	H ₂ SQ; squaric acid	4/ <i>m</i> - <i>es</i> -2/ <i>m</i>	373	First	

Table 3.2.1 (continued)

Formula	Commonly used abbreviation; name	Species ^a	T_{TR} ^b	Order ^c	Transl. ^d
$Ba_2TiSi_2O_8$	Fresnoite	$4mm-\epsilon ds-mm2$	433		NEQ
NdP_5O_{14}	NPP; neodymium pentaphosphate	$mmm-\epsilon s-2/m$	413	Second	EQ
LaP_5O_{14}	Lanthanum pentaphosphate	$mmm-\epsilon s-2/m$	393	Second	EQ
$KH_3(SeO_3)_2$	KTHS; potassium trihydrogen selenate	$mmm-\epsilon s-2/m$	211	Second	EQ
$(NH_4)_2ZnCl_4$	Ammonium tetrachlorozincate	$mmm-1C$	406	Second	
		$-Pd-mm2$	364		
		$-P\epsilon ds-m$	319		
		$-P\epsilon ds-1$	268		
		$mmm-1C$	298	Second	
$[N(CH_3)_4]_2CuCl_4$	TMA-TCC; tetramethylammonium tetrachlorocuprate				
		$-\epsilon s-2/m$	292	First	NEQ
		$-\epsilon s-2/m$	263	First	
		$mmm-Pd-mm2$	1231	Second	
$KTiOPO_4$	KTP; potassium titanium phosphate				
$NaNO_2$	Sodium nitrite	$mmm-1C$	437.5	Second	
		$-Pd-mm2$	436	First	EQ
$BaMnF_4$	Barium manganese fluoride	$mmm-Pd-mm2$	hyp.		
		$-1C$	250		
		$mmm-Pd-mm2$	312	Second	
$(CH_3NH_3)_5Bi_2Br_{11}$	Alkylammonium halogenobismuthate, MAPBB				
Rb_2ZnCl_4	RZC; rubidium zinc chloride	$mmm-1C$	303	Second	NEQ
		$-Pd-mm2$	192	First	
$(NH_4)_2BeF_4$	AFB; ammonium fluoberyllate	$mmm-1C$	183	Second	
		$-Pd-mm2$	177	First	NEQ
$SC(NH_2)_2$	Thiourea	$mmm-1C$	202	Second	
		$-Pd-mm2$	171	First	EQ

Table 3.2.1 (continued)

Formula	Commonly used abbreviation; name	Species ^a	T_{TR} ^b	Order ^c	Transl. ^d
SC(ND ₂) ₂	Deuterated thiourea	$mmm-1C$ $-Pd-mm2$	216 190	Second First	EQ EQ
La ₂ Ti ₂ O ₇	Lanthanum titanate	$mm2-eds-2$	1170	Second	NEQ
NaKC ₄ H ₄ O ₆ ·4H ₂ O	Rochelle salt ^l	$222-Peds-2$	297	Second	EQ
NaNH ₄ C ₄ H ₄ O ₆ ·4H ₂ O	Ammonium Rochelle salt	$222-Peds-2$	110	First	NEQ
LiNH ₄ C ₄ H ₄ O ₆ ·H ₂ O	LAT; lithium ammonium tartrate monohydrate	$222-Peds-2$	98	Second	EQ
LiTiC ₄ H ₄ O ₆ ·H ₂ O	LTT; lithium thallium tartrate	$222-Peds-2$	11	Second	EQ
RbD ₂ PO ₄	Deuterated RDP, monoclinic modification	$2/m-2/m$	377	Second	NEQ
(CH ₃) ₃ NCH ₂ COOH ₃ PO ₄	BP; betaine phosphate ^m	$-P-$ $2/m-2/m$	317 365	Second	NEQ NEQ
(CH ₃) ₃ NCH ₂ COOCH ₃ AsO ₄	BA; betaine arsenate	$-2/m$ $mmm-es-2/m$	86 411	Second	NEQ NEQ
(CH ₂ NH ₂ COOH) ₃ H ₂ SO ₄	TGS; triglycine sulfate ⁿ	$-Pd-m$	119	Second	EQ
(CH ₂ NH ₂ COOH) ₃	TGSe; triglycine selenate	$2/m-Pd-2$ $2/m-Pd-2$	323 295	Second Second	EQ EQ
(CH ₂ NH ₂ COOH) ₃	TGFB; triglycine fluoberyllate	$2/m-Pd-2$	348	Second	EQ
Ca ₂ B ₆ O ₁₁ ·5H ₂ O	Colemanite	$2/m-Pd-2$	266	Second	EQ
CsH ₂ PO ₄	CDP, cesium dihydrogen phosphate	$2/m-Pd-2$	156	Second	EQ
Te(OH) ₆ (NH ₄ H ₂ PO ₄) ₂ (NH ₄) ₂ HPO ₄	TAAP; telluric acid ammonium phosphate	$2/m-Pd-m$	321	Second	EQ
Sn ₂ P ₂ S ₆	Tin thiohypodiphosphate	$2/m-Pd-m$	337	Second	EQ
(CH ₂ NH ₂ COOH) ₂ HNO ₃	DGN; diglycine nitrate	$2/m-Pd-m$	206	Second	EQ
PbHPO ₄	Lead hydrogen phosphate	$2/m-Pd-m$	310	Second	EQ
K ₄ Fe(CN) ₆ ·3H ₂ O	PFC; potassium ferrocyanide	$2/m-Pd-m$	249	Second	EQ
LiH ₃ (SeO ₃) ₂	LHS, lithium trihydrogen selenate	$2/m-Pd-m$	353	Second	EQ

Table 3.2.1 (continued)

Formula	Commonly used abbreviation; name	Species ^a	T_{TR} ^b	Order ^c	Transl. ^d
(K,Na)AlSi ₃ O ₈	Anorthoclase (mineral)	$2/m - \varepsilon s - 1$ $-Pd - m$	101	First	NEQ
NaH ₃ (SeO ₃) ₂	STHS, sodium trihydrogen selenate	$2/m - P\bar{c}ds - 1$ $-\varepsilon s - 1$	194 111	First First	NEQ

Symbol “hyp” means a hypothetical phase which is not reached because of decomposition of the material.

^aFor the reader’s convenience, we repeat partly the meaning of symbols used (see Sec. 2.1 for details). The last symbol denotes the point symmetry group of the ferroic phase. The preceding symbol indicates the existence of *lowest* order spontaneous quantities: P , new components of polarization, the species is ferroelectric; ε , symmetry-breaking spontaneous strain, the species is ferroelastic and ferroelectric; d , new components of the piezoelectric tensor, the species is ferroelastolectric; s , new components of elastic compliance, the species is ferrobielastic. The first symbol shows the symmetry group G ; it is omitted for materials with a sequence of phases. IC stands for a phase with incommensurate modulation

^bApproximate temperature of the transition from the *neighboring* phase at higher temperature, in K. Thus, e.g., in BaTiO₃ the crystal changes its symmetry from $4mm$ to $mm2$ at 278 K. Domain properties of the crystal in phase $mm2$ correspond to those of the species $m\bar{3}m - P\bar{c}ds - mm2$. No information on thermal hysteresis is given

^cOrder of transition from the neighboring phase at higher temperature, if known

^dSymbols “EQ” and “NEQ” stand for equitranslational ($v = 1$) and non-equitranslational ($v > 1$) phases, compared to the original parent phase of the highest symmetry. The information on whether the translational symmetry changes is not always known

^eTriferroelastic

^fTwo or more consecutive rows refer to the sequence of transitions. Each phase can be treated separately as if it arose from the parent cubic phase

^gIn this material a rich sequence of phases have been observed, some of which are of incommensurate nature. However, the final phase diagram may not have been finalized

^hAccording to some data, MASD represents the species $m\bar{3} - P\bar{c}ds - mm2$

ⁱThis material is a model ferroelectric in which two nonferroelastic domains are optically distinguishable since they differ in optical activity

^jGASH decomposes at 200°C, well before the transition temperature is reached. The most probable species is $3m - Pd - 3m$. The species $\bar{6}m2 - P\bar{c}ds - 3m$, would signify that the two domain states differ in elastic properties. The species $6/mmm - P\bar{c}ds - 3m$ connected with a reducible representation appears improbable

^kBa and Sr ions randomly occupy two α and four β positions in the lattice

^lOn cooling from the ferroelectric phase, Rochelle salt transforms back to the symmetry 222 at 255 K

^mIn the three subsequent phases of the same point symmetry, $v = 2, 4$, and 8, respectively (cf. Eq. (2.1.2))

ⁿThis is a model material for studying nonferroelastic ferroelectric domains. Almost every conceivable technique for domain visualization has been employed. Easy growth techniques and easy cleavability perpendicular to spontaneous polarization are significant advantages. In addition, the phase transition is continuous, a relatively rare case. TGS, TGSe, and TGFb are isomorphous

Published data on some of ferroics included in this table are controversial as for symmetry changes and transition temperatures. This table includes a selection “to the best of the authors’ knowledge”

very different chemical composition but, at the same time, it points to similarities we may expect in their macroscopic behavior connected with domains.

In many materials there exist a sequence of phase transitions and often each of the ferroic phases can be treated, as far as its symmetry-related domain properties are concerned, separately as if it arose from a common parent phase. Then the symmetry G is given only once; but the temperature T_{TR} indicates the approximate temperature of the transition from the neighboring phase at higher temperature, in Kelvin. BaTiO_3 offers the best known example. The three consecutive rows refer to the sequence of three ferroelectric phases as temperature is lowered. In terms of symmetry, each phase can be treated separately as if it arose from the parent cubic phase $m\bar{3}m$. The real transition from $4mm$ to $mm2$ occurs at 278 K and domain properties in phase $mm2$ correspond, symmetry-wise, to those of the species $m\bar{3}m - P\epsilon ds - mm2$.

When well established, the order (first or second) of the transition is shown but the table includes no information about thermal hysteresis if the transition is of first order; temperatures T_{TR} show approximately transition temperatures. Reported values of these temperatures often vary greatly, being dependent on crystal quality, thermal hysteresis effects, and boundary conditions. The symbol IC stands for a phase with incommensurate modulation.

When well established, information is also included on whether the translational symmetry in F differs from that in G (NEQ for non-equitranslational, $\nu \neq 1$) or it does not (EQ for equitranslational, $\nu = 1$).

Some remarks about particular materials are given in the footnotes to the table.

Chapter 4

Methods for Observation of Domains

4.1 Introductory Remarks

Splitting of a ferroic sample into domains strongly influences most of its averaged macroscopic properties. Thus by measuring these properties we can obtain indirect information about the representation of individual domain states; perhaps the simplest example is the magnitude of macroscopic polarization of a sample of a uniaxial ferroelectric crystal. In the present chapter we wish to give an overview of methods which lead to a more detailed knowledge about shapes and sizes of individual domains. The number of delineating techniques is large and continuously increases, the push behind this progress being improved spatial resolution, speed, and possibility to distinguish small domains from lattice defects which have no relation to the order parameter. We need to detect small changes in domain shapes to understand phenomena like fixing of photo-refractive holograms in ferroelectrics based on partial switching. Of particular interest are domains in ferroelectric thin films.

When imaging domain structures, the symmetry relations between domain states and real domains which are to be distinguished play a crucial role. All possible techniques are based on the differences of crystal structures in neighboring domains and can be classified into three broad categories. First, a number of methods are based on the *surface properties* of samples; they give essentially two-dimensional pictures of domains as they terminate on sample surface. Sometimes these methods can even feel the presence of domains hidden inside the sample. Surface observations may also provide useful information about domain walls. Classical etching procedures, manifold decoration methods, and observations in reflected light belong to this category. More recently, modern techniques like atomic force microscopy or environmental scanning electron microscopy are increasingly employed. Second, a large group of methods are based on the differences in *tensor properties* of domains. Polarized light microscopy is the most powerful technique of this kind, nowadays supplemented with a growing number of methods based on nonlinear optical properties. Finally, we have methods based directly on the *structural differences*, including X-ray and electron diffraction, transmission electron microscopy, and X-ray topography.

In this chapter we address most methods used for observation of ferroic domains. For some of them we present short outlines, whereas for the other, only the basic ideas are mentioned. We will not go into details which would help the reader to immediately apply any of the methods discussed. However, the material of the chapter will provide the reader with the basic knowledge and references needed to get the detailed information on the subject.

4.2 Surface Etching Techniques

Surface etching is usually used to obtain information on domains which cannot be distinguished by microscopy in polarized light, in particular to reveal ferroelectric domains with antiparallel polarization in nonferroelastics and to delineate antiphase domain boundaries. Basic domain shapes in nonferroelastic ferroelectrics were studied by etching. The method also enables the identification of centers for the reverse domain nucleation. Repeated etching of the same surface was successfully used to study shapes of growing or shrinking domains as well as velocities of advancing domain walls.

The etching process is a complex phenomenon involving interactions of ions of the etching agent with the surface structure of the ideal crystal lattice as well as with the defect structure of the sample. Etching rates may be different for neighboring domains, depending on the orientation of crystal structures with respect to the surface. We expect that two surfaces arising when a crystal is cut perpendicularly to a polar direction will have different etching rates. The polar direction is one whose two ends are not related by any symmetry operation of the point group. It may be one of several polar directions exhibited by a piezoelectric crystal or it may be unique. Etching rates are also expected to be different at crystal defects and thus to have the potential of revealing outcrops of dislocation lines, small-angle grain boundaries, impurity precipitates. Corresponding etch pits or etch hillocks are known to reflect the crystal symmetry and so again the study of their shapes can distinguish particular domain states. Domain walls are in a sense also lattice defects and indeed a sensitively engineered etching experiment can visualize walls and give information about their width at the surface. While the “art and science” of etching crystals have been reviewed (see, e.g., Heimann, 1982), it appears that particular aspects of etching multidomain ferroic crystals have not yet been thoroughly discussed from the point of view of the symmetry of the crystal and of symmetry relations (including enantiomorphism) between the etched material and the etching reagent.

Etched surfaces are usually observed in reflected light using a metallographic microscope. Much higher resolution can be achieved when the etched relief is accentuated by shadowing and replica techniques are employed for electron microscopic investigations of the patterns formed in the evaporated film. First a small quantity of metal (Cr, CrO₂, Au are often used) is evaporated onto the sample in vacuum, under an angle of 30° or less. The purpose is to emphasize details of the profile by casting shadows. The decorated surface is then covered

by an evaporated carbon layer and may be further strengthened by another layer, e.g., of a solution which after evaporation leaves a film of organic material. This combined surface film is then removed mechanically from the crystal or simply made free by dissolving the crystal. The film, now offering a replica of the crystal surface, is then observed in a transmission electron microscope. The resolving power far exceeds that of optical microscopy and details of domain shapes of size several hundred angstroms can be easily distinguished as well as exact shapes of etch pits and hillocks.

Probably the first effort when an etching technique was employed in connection with domains was to visualize twins in quartz. These crystals are usually etched in commercial 48% hydrofluoric acid for up to several hours at room temperature. In quartz, “electrical” (Dauphiné) twins can be classified as ferroelastoelectric domain pairs. In addition, quartz crystals may also contain “optical” twins which have the character of growth twins. All can be distinguished by the type of etch pits on surfaces perpendicular to the crystallographic axes, as discussed in detail by Cady (1946). A unique overview of all possible etching figures of this material was obtained by etching a hemisphere made of quartz and taking 36 pictures from various angles, showing different etching figures (Bond, 1938).

We now present a selected survey of methods used for three “model” ferroic materials and of issues which could be addressed by etching.

Barium titanate. Antiparallel ferroelectric domains were first revealed by etching in single crystals of BaTiO_3 (Hooton and Merz, 1955). As-grown plate-like samples are immersed for several minutes in concentrated HCl at room temperature, then rinsed in water, and washed in ethyl alcohol (the “dip technique”). When observed in reflected light, using magnification from $100\times$ to $200\times$, domains with antiparallel polarization vectors perpendicular to the surface are visible on both sides of the plates. (An example of the image obtained this way is shown in Fig. 2.2.4.) This is because the positive end of \mathbf{P}_S etches faster than the negative end while the etching rate of a -domains is intermediate between the two. The mechanism proposed to explain the differences in etching rates (Sawada and Abe, 1966) assumes that the ions Ba^{2+} and Ti^{4+} are decisive for the etching rate. The ion diffusing into the etchant must overcome a potential barrier which, due to electrostatic interaction, will be lower near the positive end of \mathbf{P}_S than at the negative end. Therefore, ions at the positive ends will diffuse more easily, increasing the etching rate.

Many other studies were performed using different etchants. A series of alternating steps involving the application of an electric field for a given period of time, removing the electrodes, and etching in a 0.5% aqueous solution of HF for about 10 s, made it possible to follow the growth of one particular antiparallel domain and measure domain wall velocity (Miller and Savage, 1958). Repeated etching in KCl made it possible to monitor how the shape of a domain changes when it grows or shrinks (Husimi, 1960). Alternatively, one can observe the domain pattern (Campbell, 1962) and the formation of nuclei of antiparallel domains (Stadler and Zachmanidis, 1964a) produced by incomplete poling of the sample. Etching successively first a sample with “aged” domains and then the same sample in a poled state brings up hillocks aligned along the original domain

walls and illustrates the interaction between defects and domain walls (Stadler, 1963). A sequence of etching events in a 4% solution of concentrated HCl and HF taken during a long period of time gave evidence about the coarsening of antiparallel domains (Rapoport and Dontsova, 1970). An 85% solution of H_3PO_4 was claimed to be a slow-etching agent revealing only domain boundaries and dislocations (Eknadiosyants et al., 1978).

Etching was proved useful to provide information on domains even in BaTiO_3 ceramic samples; some of the most lucid and informative pictures of domain patterns were obtained by Arlt and Sasko (1980) by etching polished surfaces in HCl and HF solutions (Kulcsar, 1956).

Etched surfaces of BaTiO_3 crystals were also studied with transmission electron microscopy (TEM). Following the etching procedure, plates were shadowed by chromium (Spivak et al., 1958) or chromium oxide (Beudon et al., 1988) and carbon replicas were made. This made it possible to observe in detail complex 180° – 90° domain structures (Spivak et al., 1958) as well as individual 180° domain walls and etched hillocks (Stadler, 1963). Direct TEM observations of domains, both ferroelastic and nonferroelastic, in very thin BaTiO_3 crystals were presented by Cameron (1957). Checkerboard patterns observed in the orthorhombic phase on both sides of thin plates testified that these domains penetrate the whole thickness of the plate. An example of such observation is shown in Fig. 4.2.1.

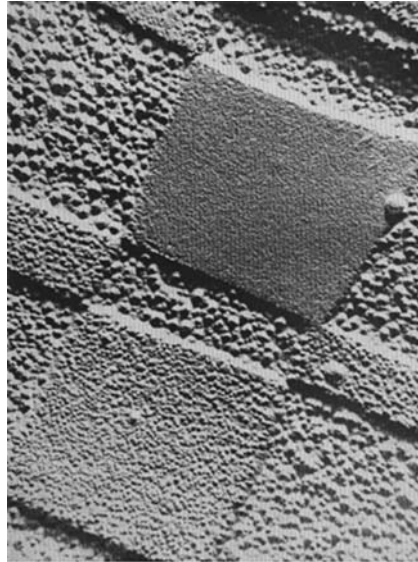


Fig. 4.2.1 Pattern of ferroelastic domains with three different directions of polarization in the orthorhombic phase of BaTiO_3 . The sample surface was etched; this is an electron microscopic picture of a replica. In the smoothest and roughest areas, the negative and positive ends of polarization are at the surface, respectively. In the area of intermediate roughness, P_S is parallel to the surface. The real horizontal dimension of the pictured area is about $4\mu\text{m}$. After Cameron (1957). Reprint courtesy of International Business Machines Corporation, copyright 1957 © International Business Machines Corporation

Triglycine sulfate. TGS is a crystal soluble in water and represents a model material for etching methods. This is a uniaxial ferroelectric exhibiting two nonferroelastic domain states. Its domain structure was visualized for the first time (Pearson and Feldmann, 1959) by a simple *rub technique*. A few drops of water were put at one corner of a thin cloth placed on a flat plane. The (010) surface of the crystal was rubbed in circular motions; a few passes suffice to delineate the domain structure. Microscopic observations in reflected light show that the positive domains have smooth surfaces while the negative domains correspond to pebbled areas. The etching rate on the positive domains is higher than on the negative domains (Nakamura and Nakamura, 1962; Sawada and Abe, 1967).

Using the *dip technique*, the sample, usually a plate with (010) major surfaces, is simply immersed in water; at the end of the required etching period it is quickly transferred to a bath of ethyl alcohol and dried (Chynoweth and Feldmann, 1960). This method has several advantages compared to the rub technique: It does not create pebbled surfaces and has a higher resolution. Even more important, it can be used even at elevated temperatures. The disadvantage is that the solubility of TGS in water is rather high and increases with temperature. Therefore, repeated etching in water with the aim to follow some kinetic domain processes would mean a considerable loss of material.

A number of alternative etchants were investigated with the aim to slow down the etching rate or to selectively reveal domains, domain walls, and dislocations; some of these experiments are included in Table 4.2.1.

Table 4.2.1 Additional information on revealing domains by etching

Compound	Method	Remark	Ref.
BaTiO ₃ , ceramics	Highly polished samples. Several drops of 48% HF to 100 ml of 5% HCl, several minutes at T_{room}	Replica technique, revealed 90° domains	Kulcsar (1956), Cook Jr (1956), and Arlt and Sasko (1980)
PbTiO ₃	HCl or H ₃ PO ₄ , at elevated T up to T_C	Thin film r.f. sputtered on MgO. Revealed 90° walls and surface relief, not 180° walls	Surowiak et al. (1993) and Sviridov et al. (1984)
PbZrO ₃ , ceramics	Polished and etched in diluted HCl. Shaded replicas observed in electron microscope	Revealed 90° domains. In poled samples dense stripe pattern believed to be antiparallel domains	Goulpeau (1969)
Ba _{1-x} Sr _x TiO ₃	HCl or H ₃ PO ₄ , in a large interval of temperatures	Films sputtered on MgO; both 180° and 90° domain pairs revealed	Surowiak et al. (1993)

Table 4.2.1 (continued)

Compound	Method	Remark	Ref.
YMnO ₃	H ₃ PO ₄ , several minutes at 130–160°C		Safrankova et al. (1967)
LiNbO ₃	See text	Shadowing with Ge and using replica technique reveals hillocks on negative surfaces (010)	Stadler (1963)
LiNbO ₃	See text	Revealed artificial domain patterns on (001) or <i>Y</i> -surfaces	Ming et al. (1982), Feisst and Koidl, (1985). Baron et al. (1996), and Nakamura (1991)
LiTaO ₃	As for LiNbO ₃		Makio et al. (1992)
KNbO ₃	Solution of KHF ₂ and HNO ₃ , 20 min at 100°C	Negative domain etches faster, 1–5 μm/min. Domains differ in characteristic etch pits	Wiesendanger (1973)
Pb(Zr _x Ti _{1-x})O ₃	15 s in 5% HCl solution with 5 drops of HF per 100 cm ³ of solution	Cleaved faces. Pt-carbon replicas. Magnification up to 14,000×	Eknadisosiants et al. (1990)
Pb ₅ Ge ₃ O ₁₁		Antiparallel domains visible on nonpolar faces	Shur et al. (1989)
BiFeO ₃	HCl and H ₂ O 1:1		Tabarez-Muñoz et al. (1985)
Bi ₄ Ti ₃ O ₁₂	HNO ₃ and HF 250:1, 3–5 min at room temperature	Polycrystalline samples	Eknadisosyants et al. (1987)
Bi ₅ (Ti ₃ Fe)O ₁₅	HCl conc. at <i>T</i> _{room} for 5 min or boiling diluted HNO ₃ , 5 min	Analysis of etch pits gives information on possible direction of P _S	Kubel and Schmid (1992)
Gd ₂ (MoO ₄) ₃	2–20% HCl	Revealed antiphase boundaries in domains of both polarities	Barkley and Jeitschko (1973) and Meleshina et al. (1974)
SbSI	HCl at 18–20°C	Etching of (110) surface probably revealed 180° domains	Kliya and Lyachovitskaya (1970)
TGS	CH ₃ COOH with addition of metallic Zn and 0.7% H ₂ O for 1.5 min	Delineates domain walls. When 0.3–0.7% of ethylene alcohol or of HNO ₃ is added, also domains are revealed	Konstantinova (1962)

Table 4.2.1 (continued)

Compound	Method	Remark	Ref.
TGS	30 ml CH ₃ COOH with 0.04 ml HNO ₃ and 0.0236 g of α -alanine	Reveals both walls and dislocations, has a good definition of etch pits. Includes a table of many etchants showing etching rates of domains and dislocations	Meleshina (1964)
TGS	CH ₃ COOH with addition of 1.4% H ₂ O and 0.7% HNO ₃	Delineates dislocations without revealing domains	Konstantinova (1962)
NaNO ₂	Ethanol with 10% of water. Rubbing on "deer's buff" gave high resolution	3D domain pattern and its field-induced changes revealed by successive etching and polishing. Observed antistriple and their development	Nomura et al. (1961)
Ca ₂ Sr (C ₂ H ₅ CO ₂) ₆	Methyl alcohol for 30 s	Cleavage steps and domain walls observed optically	Chaudhari and Krishnakumar (1989)
KTiOPO ₄	H ₃ PO ₄ plus small amount of HF, 30–60 min at 130°C	Replicas by evaporation of Pt and carbon; fixed by a gelatine solution	Ivanov et al. (1994)
KTiOPO ₄	2:1 molar mixture of KOH/KNO ₃ at 220°C for 2 s		Houé and Townsend (1995) and Gupta et al. (1993)
(NH ₄) ₂ SO ₄	H ₂ O, T_{room}	Revealed lines believed to be antiphase boundaries	Tomek et al. (1978)
La ₂ Ti ₂ O ₇	Boiling aqueous solution of nitric acid	Revealed both domains and etch pits	Nanamatsu et al. (1974)

A detailed study of etching TGS in water gave more insight into the etching mechanism (Sawada and Abe, 1967). When crystal surfaces with different orientations with respect to the polar axis were etched under identical conditions, the slope of the area representing the domain wall (i.e., the step in height divided by the apparent width of wall) was found to be constant, equal to 0.05. Changing the degree of saturation of the etchant (by adding glycine or sulfuric acid or by changing temperature) it was established that undersaturation is essential for revealing domains and high undersaturation for forming dislocation pits. Rapid removal of dissolved ions from the surface is favorable for

revealing dislocation pits but not for revealing domains. Finally, glycine ions which are positive were found to play a major role in revealing domains while negative sulfate ions play a minor one.

Based on these findings, Sawada and Abe developed a model which explains the difference in etch rates of positive and negative domains as a result of the difference in the height of the potential barrier, and therefore as consequence of the difference in rates with which positive ions are removed from the just dissolving step on the crystal surface.

Several investigators used the dip technique to investigate time changes occurring in the domain structure after the TGS sample was cooled from the paraelectric phase to room temperature (Moravec and Konstantinova, 1968; Dabrowska et al., 1977; Konstantinova and Stankowska, 1971). Repeated etching shows the time development of a particular domain. Elaborated are the studies intended to find out how the domain structure of TGS changes with temperature, which are complicated by the fact that it is often required annealing and cooling samples in a medium with defined electrical conductivity, air, or mercury being the extremes. Therefore, to etch the sample at the required time and temperature it is necessary to transfer it from this medium into the etchant. On the other hand, the domain structure in TGS was shown to be very sensitive to thermal shocks (Chynoweth and Feldmann, 1960). Care must be therefore taken to eliminate any change of sample temperature during its transfer; also it must be fast since domain patterns develop with time. These requirements could be met by sophisticated setups (Safrankova, 1970a,b; Strukov et al., 1972a). An interesting alternative solution consists of irradiating the TGS sample by X-rays in the required state (i.e., at a given temperature and time) (Gilletta, 1972). It was shown that this “freezes” the domain pattern at the time of irradiation (Chynoweth, 1959). The sample can be then cooled, shelved, and observed at one’s convenience. While in all these studies it was the (010) faces perpendicular to \mathbf{P}_S that were etched, it was shown (Chynoweth, 1960) that by etching sides of a TGS sample parallel to the polar axis it was possible to reveal “internal” domains, not intercepting the surfaces (cf. Fig. 2.2.5).

Similarly as for BaTiO_3 , etching figures of TGS are usually observed in reflected light by an optical microscope. But it is also possible to prepare shadowed negative replicas of the etched surface relief, e.g., by depositing a germanium layer (Toyoda et al., 1959).

These etching methods were used for a number of studies on equilibrium domain patterns in TGS, their spontaneous evolution with time, and even for measuring wall velocities. Some of these results will be discussed in the corresponding chapters.

Lithium niobate. LiNbO_3 is another uniaxial ferroelectric in which antiparallel domains cannot be optically distinguished by customary methods. When the polished surfaces (001) are etched for a few minutes in a mixture of one part HF and two parts HNO_3 (by volume) at the boiling point (about 110°C), adjacent domains etch at very different rates, with *negative* ends being etched much faster (Nassau et al., 1965; Niizeki et al., 1967). They also show different

surface structures. Other etchants based on alkalis gave similar etch rates. Antiparallel domains were also visualized by etching the (010) surface which is parallel to the ferroelectric axis.

Table 4.2.1 gives information on some additional experiments. Etching has proved to be powerful. It made possible to obtain information on static structures but surprisingly it was this classical method which provided data on some slow dynamic processes like domain wall velocities in barium titanate (Miller and Savage, 1959b) or the time evolution of antistripples (special kind of antiparallel domains) in crystals of NaNO_2 (Hamano et al., 1996, 1995). It has a fairly good resolution and can be employed for both transparent and nontransparent materials. It can reveal either domains or just walls including antiphase boundaries; it can selectively visualize walls or dislocations. In its basic form it is inexpensive for its simplicity, the only sophisticated instrument being a microscope suitable for observations in reflected light. The disadvantage is that it gives only surface picture and is in a sense a destructive method although it can be used repeatedly. Its limitation is the temperature range in which it can be employed since etching rates depend on temperature and generally it is difficult to etch at very different temperatures. The latter problem has been avoided by quenching the slowly evolving domain structure (Hamano et al., 1995) or by more involved methods allowing etching at elevated temperatures mentioned above.

4.3 Other Methods Based on Surface Relief

Etching is not the only way in which a relief on the surface of a crystal or ceramic grain can be achieved. It is obvious that when a domain pair is *ferroelastic*, a surface profile will be formed naturally on properly oriented surfaces when the transition temperature is passed, due to the differences in orientations of unit cells. This property has not received much attention for an obvious reason, namely that in most cases a ferroelastic domain pair can be also distinguished in polarized light. Obtaining some information about ferroelastic domains by studying surface deformations would be advantageous for nontransparent crystals or for ferroelastics in the form of films deposited on substrates. Using replica technique, very minute surface details due to domains, inaccessible by optical methods, can be visualized even for transparent crystals, but real data are scarce. The surface relief of a BaTiO_3 crystal containing 90° domains was mapped in this way (Spivak et al., 1958) and observed with magnifications up to 25,000.

There is one point to consider when preparing a sample for the observation of surface profiles due to ferroelastic domains. If the sample is polished flat in the multidomain state in the ferroic phase and then transformed—usually by heating—into the parent phase, its surface will become deformed due to the disappearance of spontaneous deformation and seemingly domains will be detected when they do not exist anymore. This could lead to erroneous conclusions. Repeated cycling through a phase transition can then lead to a superposition of “living” and “fossil” domains, both detectable on the surface at the same time (Schmid, 1993).

The depth of surface profile can be determined by evaluating stereoscopic pictures (Igras, 1959). Bhide and Bapat (1963) developed an alternative approach based on interferometric methods which offers fairly high resolution. The sample is vacuum coated with a highly reflecting Ag layer and matched against a correspondingly silvered optical flat. When illuminated by a collimated beam, multiple beam Fizeau fringes form between the crystal and the flat, which are microscopically examined. Any changes in level of the crystal surface are depicted as fringe shifts and a well-adjusted setup can distinguish level changes of several angstroms (Bhide and Chilmulgund, 1965). This multiple beam interferometry makes it possible to collect data on surface profile of a BaTiO_3 crystal due to 90° domains. Figure 4.3.1a shows schematically the profile due to one c -domain in an a -domain environment. Obviously, the angle α is related to the tetragonal lattice parameters a and c by $\tan \alpha = (c-a)/a$. At room temperature the measured value

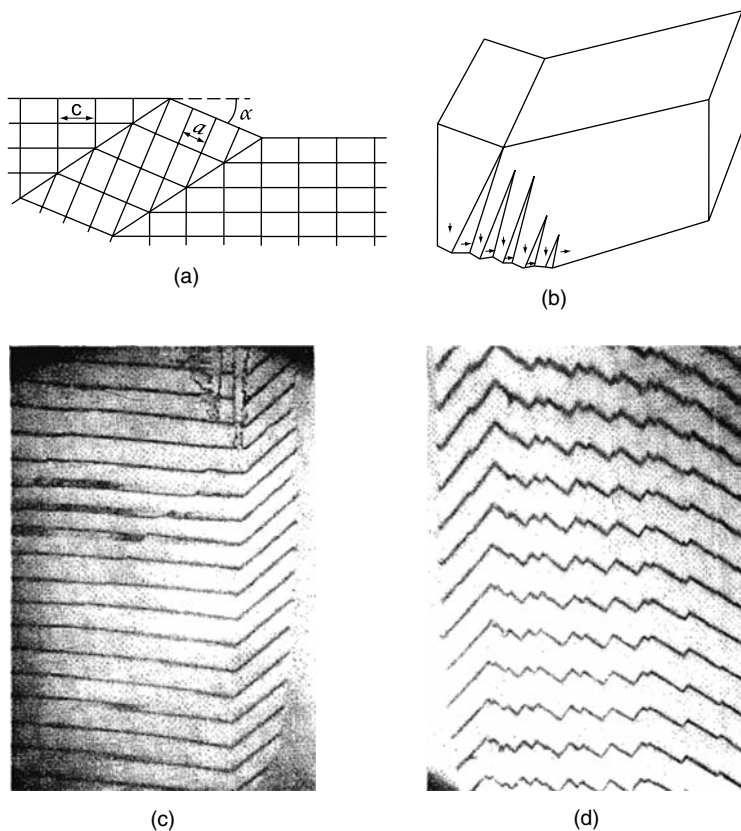


Fig. 4.3.1 (a) Surface deformation due to tetragonal spontaneous strain. (b) The domain configuration in deformed BaTiO_3 plate with 90° wedges. Interferograms of the upper (c) and lower (d) surface of the plate with the domain configuration shown in (b). Reprinted with permission from Bhide (1963). Copyright (1963), American Institute of Physics

was $\alpha = 32'$ which agrees well with the known lattice constants. Figure 4.3.1c,d shows interferograms of both surfaces of a BaTiO_3 plate. Figure 4.3.1b illustrates how the plate is deformed due to 90° wedge-shaped domains. This method makes it even possible to observe minute dynamic changes of domains induced, e.g., by electric field in real time.

Using an interference reflection microscope to observe properly oriented faces of an as-grown crystal, fringes arranged in interference patterns (giving evidence about the geometry of domain pattern) could be observed in multi-domain crystal of any ferroelastic. Weber et al. (1975) showed that domains in $\text{NdP}_5\text{O}_{14}$ differing in the sign of spontaneous shear can be well visualized in this way.

Surface relief corresponding to the geometry of *nonferroelastic* domains can be produced in some materials without etching. It was found that even by mere polishing of the *c*-face of LiNbO_3 antiparallel domains are revealed (Nassau et al., 1965), due to a slight difference in hardness.

A unique situation occurs in TGS. It is known that its most pronounced cleavage plane is perpendicular to the polar *b*-axis. However, when a TGS crystal is cleaved in a way that the cleavage crack propagates along the *c*-axis, the *cleavage planes* in neighboring domains with opposite polarization can be slightly inclined with respect to each other (Nakatani, 1989a; Konstantinova, 1962; Nakatani, 1975). Alternatively, the cleavage planes can be differently curved in different domains (Nakatani, 1979). Thus the polar surface of the crystal is spatially modulated in a way corresponding to the domain structure at the time of cleaving. When the surface is coated with evaporated silver, this pattern can be seen in reflected light or in a differential interference microscope. This method of visualizing domains in TGS can be used also at elevated temperatures and was employed to study domains close below T_C (Nakatani, 1989a) when, in an early stage of their evolution, they are too small to be delineated by liquid crystal decoration (see next sections). The smallest domains observable with this method are only 20 nm wide.

The cleavage process as a tool to delineate nonferroelastic domains was found functional also in crystals of $\text{Pb}_5\text{Ge}_3\text{O}_{11}$ (Shur et al., 1993a,b). Here the pronounced cleavage planes are $\{10\bar{1}0\}$ parallel to the polar axis. However, when the cleavage propagates under a small angle to this plane, the cleaved surfaces show a relief which can be seen in a microscope under oblique illumination and corresponds to the domain structure.

4.4 Surface Decoration Techniques

Surface decoration techniques are based on interactions between a decorating agent and the substrate which is a multidomain crystal. Differences in these interactions, leading to domain revealing, depend on the microscopic atomic surface structure and its orientation. These techniques led to many useful

observations but, with the exception of decoration with nematic liquid crystals, no theoretical attempts seem to have been undertaken to explain the interactions underlying these phenomena.

Decoration methods have a wide range of resolving power, depending on the size of decorating particles. The latter may be quite large, up to several micrometers in diameter. Most of such recipes are nondestructive and require relatively simple observation in reflected light. The other extreme is a resolution of several nanometers achieved, e.g., by evaporation of thin oriented films. These methods require that a replica is formed, to be observed in a transmission electron microscope. Often the substrate, i.e., the crystal under study, has to be dissolved to free the replica film, which makes the method fatally destructive.

Surface decoration methods usually require carefully prepared surfaces. Therefore again, as with the etching methods, the frequently studied materials are those with well-developed cleavage planes (TGS, GASH) or compounds crystallizing in the form of flat platelets (flux-grown BaTiO_3).

4.4.1 Colloidal Suspensions

Particles in a colloid may acquire a double-layer charge when brought in contact with a liquid. Depending on the orientation of their dipole layers, they may be attracted to the negatively or positively charged objects. This idea was developed into a simple decoration technique for visualization of ferroelectric domains (Pearson and Feldmann, 1959). Powders of sulfur and lead oxide were used to prepare colloidal solutions in hexane. A few drops of one colloid solution placed on a cleaved polar surface of TGS, GASH, or GUSH (guanidinium uranyl sulfate trihydrate) crystal result immediately in coloring the appropriately charged domain. The yellow powder in the sulfur colloid deposits on negative domains, leaving positive domains vacant. After the solution evaporates, positive domains may be colored red by depositing the lead oxide colloid. Colored domain pattern stays so indefinitely. The resolution in these experiments was limited by the particle size between 3 and 4 μm .

This method, often referred to as powder deposition, provided information on domain shapes in TGS, nucleation of new domains, and even on lateral growth of domains in applied field (Chynoweth and Abel, 1959a,b). It was also shown (Chynoweth, 1960) that decoration of polar faces can reveal spike-shaped domains which stop not reaching the crystal surface and, even more interesting, that such internal domains can be revealed by decorating nonpolar faces of the crystal.

Several colloidal solutions were tested to reveal domains in $\text{Ca}_2\text{Sr}(\text{C}_2\text{H}_5\text{COO})_6$ crystals (Mochizuki and Futama, 1967) but with an unsatisfactory resolution.

In the most successful reported modification of this technique a commercial liquid developer diluted by *n*-hexane was used (Hatano et al., 1973). The sample

is immersed in the diluted developer and then rinsed in *n*-hexane. Carbon particles are positively charged in the developer and deposit on negative domains. This method offers a higher spatial resolution; carbon particles about 0.1 μm in diameter coagulate to clusters with the diameter of about 0.5 μm . Figure 4.4.1 shows domains on the opposite sides of a TGS sample revealed by this method by Hatano et al. (1973). The figure indicates the presence of small domains within the large island-shaped domains. These authors also showed that the method can be employed at low temperatures by using *n*-pentane instead of *n*-hexane; domains in Rochelle salt were revealed at -20°C and in thiourea at -130°C . Suda et al. (1978a) showed, observing domains in GASH, that even large crystal areas can be visualized concurrently when the decorated surface is projected on a photographic film.

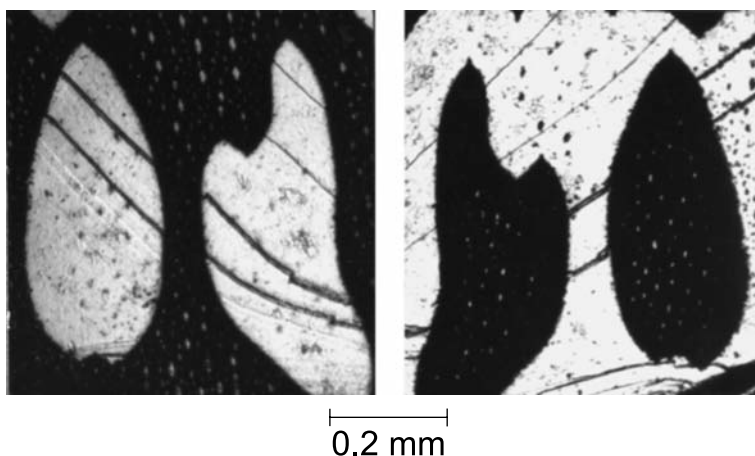


Fig. 4.4.1 The 180° domains in TGS imaged on opposite sides of a plate by powder pattern technique. Lines are scratches on the cleaved surfaces. Small dots correspond probably to a large number of small domains. After Hatano et al. (1973)

This technique was successfully employed for investigations of domain shapes in TGS (Hatano et al., 1978), even at different stages of polarization reversal (Nakatani, 1989b), and in TGS doped by alanine (Nakatani, 1991b); it served to establish that cleaving TGS may result in a domain-related surface profile (Nakatani, 1975). The method also proved useful for investigating the patterns due to screw dislocations on the polar faces of GASH crystals (Shur et al., 1982; Hatano et al., 1985b) which are also connected with charge distribution.

A remarkable alternative of decoration was proposed quite early (Pearson and Feldmann, 1959). When a colloid of fine barium titanate powder in hexane was used, particles deposit at domain boundaries. This may be understood on

the basis of high permittivity of these particles which are attracted into locations with high electric field gradient. Interestingly enough, this method does not seem to have been developed and used any further.

In addition to the just described “powder” methods, other procedures using somewhat related techniques were suggested. Thus domains on nonpolar faces of ferroelectric SbSI were visualized by selective crystallization of SbI_3 (Kliya and Lyakhovitskaya, 1970b).

Laurell et al. (1992) pointed out that liquid toners are currently available, which contain either negatively or positively charged black particles. They can be easily used for domain decoration with a resolution of several micrometers. This was demonstrated by visualizing an artificially produced domain pattern in plate-like samples of ferroelectric KTiOPO_4 . This technique was also successfully used to picture domains in TGS by Ozaki et al. (1996); their studies pointed to the important possibility the method offers in studying bound charge compensation phenomena.

4.4.2 Decoration by Sublimation and Vacuum Evaporation

We have already discussed how decoration by deposition in vacuum helps visualize the surface profile; this shadowing technique is based on the geometry of the surface. Now we wish to pay attention to decoration techniques in which the surface relief is nonexistent or not significant. They are based directly on the interaction between the multidomain sample as a target and landing particles which are formed by sublimation or vacuum evaporation. Domains are distinguished by differences in size or density of deposited particles or by the oriented epitaxial crystallites.

TGS crystals—what else!—serve to verify the usefulness of sublimation techniques. Sublimated anthraquinone (Kobzareva et al., 1970) produced needle-shaped crystals with linear dimension of 20–80 μm ; the deposited texture distinguished between the domains but with a resolution corresponding to this size. A better resolution was achieved with auramin (Shenyavskaya and Distler, 1976). Particles formed on the TGS surface have a higher density on positive domains; they even decorate domain walls. Still, their size of 2 μm in diameter is not satisfactory.

A considerably higher resolution is offered by methods employing vacuum evaporation. Particles in the evaporated decorating layer are principally of much smaller size than particles in colloids or those achieved by sublimation and the resulting patterns is worth of investigating by electron microscopy. The method was pioneered by decorating polar surfaces of TGS (Takagi and Suzuki, 1966; Takagi et al., 1967; Distler et al., 1967, 1968) and NaNO_2 (Takagi and Suzuki, 1966; Takagi et al., 1967) crystals with silver. Electron microscopic observations of replicas showed that the density of particles formed on the surface was considerably higher on negative domains (of the order of $2 \times 10^{11} \text{ cm}^{-2}$), where also their size, generally a very small fraction of a micrometer, was somewhat larger. Thus domains were revealed with a submicron resolution.

The method, often referred to as electron microscope decoration technique (Hilczer et al., 1981, 1989), has been used repeatedly to delineate nonferroelastic domains in several ferroelectric materials. Understandably, high-quality smoothness of the surface is required to avoid decoration of artifacts; for this reason, by now investigations have been reported only for cleaved surfaces or crystals growing in form of smooth plates. The method was considerably improved by cleaving the crystals when already in high vacuum to avoid contamination of surfaces, and by fine tuning of the film thickness which can be measured during the evaporation process by a quartz oscillator. The resolving power under normal conditions is about $0.1\ \mu\text{m}$ but with special care in the decoration process and using low electron densities in TEM observations of replicas a much higher resolution may be achieved, assessed to $5\ \text{nm}$ (Hilczer et al., 1981, 1989). The method was shown to be practical at both elevated and low temperatures (Distler et al., 1967; Gonzales and Serna, 1984; Hetzler and Würfel, 1978).

Very good results were reported with AgCl layers; the optimum thickness appears to be $8\ \text{nm}$ for TGS and $20\ \text{nm}$ for GASH and LAS (NH_4LiSO_4) (Szczesniak et al., 1976; Hilczer et al., 1989; Schmid et al., 1988b). The contrast revealing the domain structure appears to be in most cases due to the differences in density and size of the evaporated particles. The amount of information on the epitaxial relations of deposited particles is still scarce. The diffraction analysis (Hilczer et al., 1989) showed that, on both domains in TGS, the AgCl particles are crystallographically oriented in the same way, namely that the direction $[100]$ of AgCl is parallel to the direction $[001]$ of TGS. On the other hand, on the polar surface of GASH the epitaxial relations of the deposited particles with respect to the lattice of the substrate are very different for both domains (Meyer, 1988; Hilczer et al., 1989; Stasyuk et al., 1997); the analysis of the diffraction patterns showed that, on positive domains of GASH, the AgCl particles have the (012) plane as the contact plane while on negative domains the contact plane is (001) (Meyer, 1988). Figure 4.4.2 shows domains on the surface of a GASH crystals decorated by AgCl (Szczesniak et al., 1976), imaged soon after the crystal had been grown. The contrast deteriorates for crystals several years old.

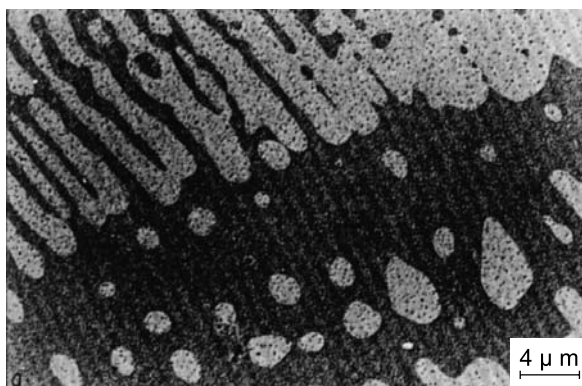


Fig. 4.4.2 TEM picture of a carbon replica of 180° domain structure on the polar face of a GASH crystal, decorated by AgCl. Reprinted with permission from Szczesniak (1976). Copyright (1976), Wiley-VCH Verlag GmbH & Co. KGaA

The mechanism of decoration is not yet well understood and there are also many controversies.

In addition to numerous experiments performed with the model and well-cleavable materials TGS (Szczeniak et al., 1995; Weidmann and Anderson, 1971; Hilczer et al., 1981) and GASH (Szczeniak et al., 1976, 1985, 1988; Hilczer et al., 1989; De Wainer et al., 1980), some other crystals were also investigated by this method. Thus antiparallel domains in BaTiO_3 can be visualized by evaporation of Cd, but only when the crystal has been “presensitized” by immersion into a solution of AgNO_3 in ethyl alcohol (Sawada and Abe, 1966). In the crystals of LAS, AgCl decoration works well on polar (010) as well as nonpolar (305) surfaces, both cleaved (Schmid et al., 1988b; Hilczer et al., 1989).

As an alternative to the evaporation of metals or alkali halides the use of polymers as decorating agents was suggested (Wicker et al., 1990, 1989); however, the achieved resolution was lower than for the decoration methods described above.

4.4.3 Deposition in Liquids

Related to the employments of colloids and having some features common with depositing epitaxial layers are methods in which the crystal is simply immersed in an appropriate liquid. This was tested for visualizing 180° domains in BaTiO_3 (Sawada and Abe, 1966): The crystal is put into concentrated HCl saturated with PbCl_2 . Fine crystals of PbCl_2 are rapidly formed whose density strongly depends on polarity of the substrate. The resolution is in the range of a few micrometers.

Another technique was used (Bhalla and Cross, 1977; Cross and Bhalla, 1978; Bhalla and Cross, 1981) for delineating ferroelectric domains in $\text{Gd}_2(\text{MoO}_4)_3$. A polished (001) plate is dipped for a few seconds into dilute HF. In reflected white light the sample now exhibits brilliant colors which are markedly different on opposite domains. The analysis showed that a closely adhering film of GdF_3 is deposited with thickness—of the order of 200 nm—differing for opposite domains. Because of large difference between refractive indices of the film and of the substrate strong interference colors occur in reflected light.

4.4.4 Condensation of Vapor

It was suggested by Toshev (1963a,b) and Strukov and Toshev (1964) that domain walls could be decorated by condensation of vapor. The technique, often referred to as solid dew method, consists of cooling down a plate-like ferroelectric sample to the temperature of liquid nitrogen; the sample is then quickly transferred onto the microscope stage and observed in reflected light. Water molecules from the air condense on the surface, preferentially decorating domain walls. The mechanism is believed (Toshev, 1966) to be connected with the dipole moment of H_2O

molecules which carries them toward the region of high electric field gradients at the intersections of domain walls with the sample surface. The method gives quickly basic information about domains in crystals with low transition temperatures and was employed to reveal domain patterns in crystals of KDP, $(\text{NH}_4)_2\text{BeF}_4$, $(\text{NH}_4)_2\text{SO}_4$, and thiourea (Koptsik and Toshev, 1965; Toshev, 1966) but is very damaging in subjecting the samples to thermal shocks.

This method of vapor condensation can be made more gentle when the condensed particles are in liquid state (Fousek et al., 1966; Safrankova et al., 1966). A ferroelectric crystal is placed in a closed chamber into which at a required moment saturated vapor of a suitable liquid is sucked, having the temperature slightly higher than the crystal temperature. On its surface condensation takes place whose intensity can be finely adjusted. The chamber is provided with a window so that the pattern of condensed droplets can be observed in a metallographic microscope. With butyl alcohol vapor domains in TGS and TGFB were visualized in this manner (Fousek et al., 1966; Safrankova et al., 1966). In some cases the condensation took place preferably on domain walls while in others the density of tiny droplets was different on antiparallel domains. The resolution of this method in its original version did not exceed 5 μm .

4.4.5 Decoration by Liquid Crystal Layers

The alignment of liquid crystals (LC) on surfaces of solids was investigated nearly a century ago when it was found (see, e.g., Mauguin, 1911) that on cleaved surfaces of various minerals nematic LCs can form homogeneous layers with distinct orientations of optical axes which are in simple relations to the symmetry of the crystalline substrate. Furuhata and Toriyama (1973) were the first to succeed in using this principle to visualize domains in a ferroelectric crystal and as so often triglycine sulfate served as the model material. The method was further developed by Tikhomirova with coworkers and its principles were discussed in detail also by Glogarová et al. (1979), Glogarová (1981), and Nakatani and Hirota (1981). For a long time it was used to study properties of domains in TGS and it was even possible to investigate some of their dynamic properties in real time. Later the technique has been shown to be applicable to a number of ferroelectrics, often under different conditions. Basically, in this method one uses optical microscopy to observe the result of surface decoration and thus it is mainly useful for domains which do not enable a contrast based on intrinsic optical properties of the crystal.

In the basic experimental arrangement, a thin layer of a nematic liquid crystal (NLC) is inserted between a plate-like sample with a cleaved upper surface and a glass cover plate. Typically, the layer thickness ranges from a few micrometers to several tens of micrometers. The NLC molecules may orient differently above different domains and this leads to an optical contrast in polarizing microscope. Obviously, the sample itself has to be transparent. More advanced setups are shown schematically in Fig. 4.4.3. In case (a) bottom

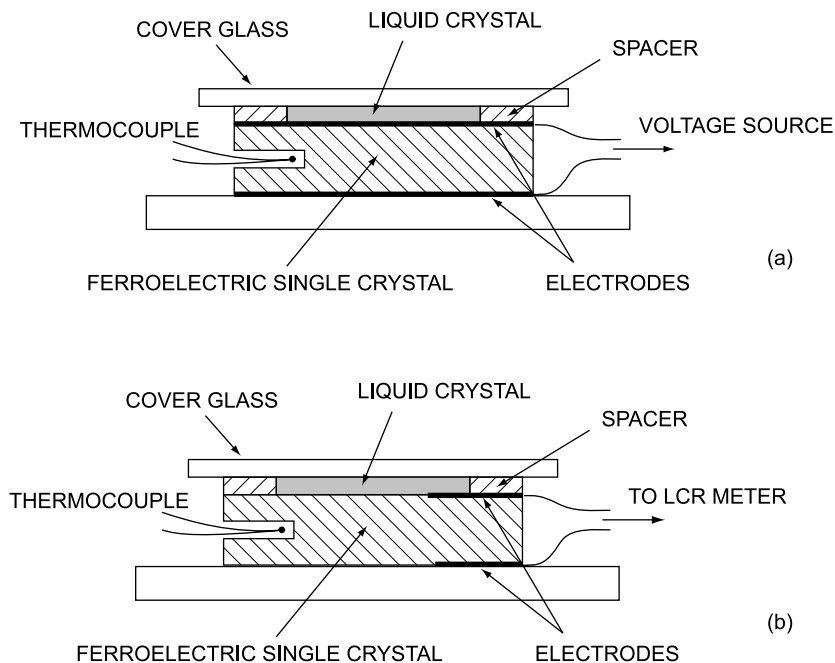


Fig. 4.4.3 Typical experimental setups for domain decoration by LC layers

surfaces of the sample and of the cover glass are provided with transparent electrodes (e.g., SnO_2 layers); thus a voltage can be applied to the system NLC + crystal and field-induced changes of domains can be observed (Tikhomirova et al., 1985a). In case (b) the upper electrode is located on a small side part of the sample so that simultaneously with optical observations in zero field, capacitance of the sample can also be measured (Nakatani, 1985). For ferroelectric sample, this makes it possible to determine with high accuracy the distance of the current temperature from the transition point. The setup is observed on a microscope stage and can be heated using an appropriate chamber. In yet another modification, NLC layers are inserted between both surfaces of the sample and glass plates so that the domain pattern corresponding to either surface of the sample can be observed by proper focusing. In all cases, typical thickness of the LC layer is a few micrometers while the sample thickness can reach the order of millimeters.

With only few exceptions, nematic LCs have been used for domain visualization. In particular, MBBA (*p*-methoxybenzylidene-*p'*-*n*-butylaniline) or a mixture of MBBA and EBBA (*p*-ethoxybenzylidene-*p'*-*n*-butylaniline) is often employed. For the ratio 1:3 of these two, the nematic phase is stable between 22 and 70°C and this makes it practical for observations of TGS crystals (Nakatani, 1985). For imaging domains in NaNbO_3 , the ratio 3:2 was employed (Hatano and Le Bihan, 1990), but also mixtures of other NLCs such

as pentyl- and heptyl-cyano-biphenyl in the ratio 59:41. For high-temperature observations of the same material alkylphenyl-cyclohexylbenzoate was used which is nematic between 90 and 185°C (Hatano et al., 1990a).

A very useful setup was designed by Tikhomirova et al. (1991a,b): In a specially developed cell the sample can be cooled and maintained at a given temperature to within $\pm 0.05^\circ\text{C}$ for a long time using the method of constant-rate evaporation of nitrogen. This made it possible to investigate domains in crystals of $\text{Li}_2\text{Ge}_7\text{O}_{15}$ whose transition temperature is 283 K. The LC used was a mixture of cyanodiphenyles which does not crystallize down to temperature of -65°C .

As an example of the possibilities this method offers, Fig. 5.4.2 shows the time development of domains in TGS (Nakatani, 1985), visualized in the setup of Fig. 4.4.3b. After keeping the specimen, a plate perpendicular to the polar direction, well above T_C for 1 h, it was slowly cooled and in the phase transition region the cooling rate was reduced to $0.006^\circ\text{C}/\text{min}$. Domain structure was observed simultaneously with measuring the capacitance and the temperature of its maximum defined T_C . Microphotographs were taken just below $T_C = 49.68^\circ\text{C}$ at intervals of 4 min. Until the temperature reaches T_C , no patterns are visible. Immediately below at $\Delta T = T_C - T = 0.02^\circ\text{C}$ lamellar patterns narrower than $0.5 \mu\text{m}$ appear. With further decreasing temperature and increasing time domains become clear and coarse. Figure 5.4.3 shows that even if T is then kept constant, the evolution of domains does not cease. Such observations are unique and hardly another method could provide similar data. Here the evolution process is rather slow; generally, several authors estimated that the LC decoration can, in the best case, offer a response time of the order of milliseconds.

To understand the alignment effect on TGS, we have to realize that NLC molecules are optically uniaxial rods, long compared to their diameter, with optic axes parallel to the long axes. They have a permanent dipole moment μ and their anisotropy leads to dielectric anisotropy $\Delta\kappa = \kappa_{\parallel} - \kappa_{\perp}$ of the material, where κ_{\parallel} and κ_{\perp} are permittivities in fields parallel and perpendicular to the long axis of the molecules, respectively. A layer formed by aligned molecules is birefringent. Since the underlying crystal is also birefringent, the analysis of optical properties of the whole system may not be simple.

The first qualitative interpretation (Furuhata and Toriyama, 1973) connected the alignment effect with the electric field above the crystal surface, whose directions may be opposite above domains of opposite polarities. However, as noticed by Tikhomirova et al. (1978), if long axes of molecules are parallel to the surface, orienting μ up and down would not result in optical differences of molecules. These authors investigated the behavior of four different NLCs with different dielectric anisotropies, $\Delta\kappa = -0.3, -5, +10, \text{ and } +0.05$. In all cases opposite domains are revealed by black/white contrast. However, changing the sign of $\Delta\kappa$ results in reversing the contrast: black domains appear white and vice versa. On freshly cleaved surfaces and on surfaces cleaved several years ago and exposed to air the contrast is the same.

On polished or etched surfaces of TGS the static domain structure is not revealed.

The authors pointed out that there are three essential factors influencing the LC orientation above the TGS surface. (1) Based on the fact that positive ends of domains dissolve much faster, it is concluded that in these regions the screening radius r_D is reduced and thus above positive domains the field extends over a smaller distance from the surface. (2) Because the van der Waals interactions between NLC molecules and crystal surface are anisotropic, NLC molecules will have the tendency to be oriented along crystallographic directions on the cleavage face of TGS. This is true particularly on “-” domains whose surfaces are poorly soluble. (3) The adsorbed water film may also have an ordered structure which in turn may induce corresponding orientation of LC.

Glogarová (1980, 1981) investigated the situation by completing the experimental setup with a cover glass on whose surface an “easy direction” was produced by rubbing; this direction tends to orient long axes of LC molecules. Perfect pictures of domains were obtained with nematics with $\Delta\kappa < 0$ (MBBA or MBBA + EBBA), while nematics with $\Delta\kappa > 0$ (a mixture of cyanobiphenyls) offered pictures disturbed by many defects and changed with time. The analysis of optical observations led to the conclusion that LC molecules make planar alignment on the surfaces of both domains, however, with different easy directions. On minus domains the director is along the [001] direction; on plus domains it is along one of the [508] or [702] directions. It is natural to assume that the observed alignment is due to anisotropic surface anchoring and one can look for easy directions provided by channels in the surface structure of the ferroelectric crystal. The analysis of TGS structure indicated (M. Glogarová, unpublished) that there exist cleavage planes whose simplified electron maps indicate the existence of structural channels clearly pronounced along the c -axis; this would explain the LC orientation on negative domains. However, no channels were found which could provide the other easy direction [508] or [702]; this orientation might originate in an anisotropic interaction between MBBA molecules and those parts of TGS molecules which change at switching, i.e., mainly NH_3 groups.

Using the mixture MBBA + EBBA, Glogarová (1981) reached a very interesting result, namely that some domains in TGS remain visible even at temperatures far above T_C where they do not exist; the contrast of some of them is fading but these remain encircled by loops. This contrast may be relevant twist disclinations in the liquid crystal. Lejcek (1983) showed theoretically that above a domain wall such objects can form, being stable when the ferroelectric is transformed into the paraelectric phase. The issue of liquid crystal molecule orientation on TGS surface has been also discussed by several authors (Nakatani and Hirota, 1981; Tikhomirova et al., 1978) who suggested alternative scenarios.

We have discussed in some detail models that have been developed to explain the mechanism of domain visualizing; all of them applied to TGS since it is for

this material that reliable data could be obtained most easily. However, the method itself was used for a number of other ferroelectric materials. Hatano et al. (1990a) applied the method to crystals of NaNO_2 . It has perfect cleavage planes (101) and $(10\bar{1})$ which are parallel to \mathbf{P}_S and on such surfaces two kinds of contrast were observed: dark-bright on domains of opposite polarities and domain wall contrast. Domains on nonpolar surfaces of ferroelectric crystals were also visualized for $\text{LiH}_3(\text{SeO}_3)_2$ by Anisimova et al. (1984) and for KTiOPO_4 by Ivanov et al. (1993, 1994).

As already mentioned, in the arrangement shown in Fig. 4.4.3a, it is possible to apply a voltage to the system crystal-LC layer and observe dynamic properties of domains. Konstantinova et al. (1978) were probably the first to perform such experiments, with MBBA layer on TGS. They observed slow switching processes and estimated that the response time of LC reorientation was less than 0.1 s. Since then a number of authors employed this method to study specific dynamic characteristics of ferroelectric switching and domain wall motion. However, it has to be borne in mind that in this regime the distribution of electric field is complicated and time dependent: We have a two-layer system and as the wall moves it creates a layer of bound charge which then is compensated in a not well understood way. Therefore, the obtained data are difficult to interpret. Indeed Dontsova et al. (1982) and Tikhomirova et al. (1985b) showed that if the gap between the electrode and sample surface is filled with an NLC layer, the velocity of sidewise motion of walls is considerably smaller if metallic electrodes are applied on the sample surface or if electrodes are made of various electrolytes. This indicates that an NLC layer with low conductivity produces intermediate conditions for compensation of the formed bound charge compared to conducting electrodes or to a dielectric gap. The layer serves as a medium for the transport of charges (its electrical resistivity is of the order of 10^8 – $10^9 \Omega\text{m}$), which are either inherent charges or charges injected from electrodes.

To mention some examples, we refer to the work of Dontsova et al. (1981, 1982, 1994) or Tikhomirova et al. (1985b, 1980b) who investigated laws of domain dynamics in polarization reversal of TGS crystals. It was at these experiments that an interesting new feature was observed. In most investigations performed in the earlier stages, TGS crystals had to be cleaved in order that domains could be visualized by the discussed technique: For cut and polished samples no contrast was observed under normal conditions, probably because of the existence of a degradation layer at the surface. However, if an ac electric field is applied to the NLC-sample system, contrast appears for any surface. Thus moving domain walls in polished deuterated TGS were visualized (Tikhomirova et al., 1985b) when in addition to the switching field also a weak high-frequency ac field was applied. The possible explanation (Tikhomirova, private communication) is that if a domain wall is moving, the impedance of the crystal in the region of the wall changes. Therefore, the voltage drop in the LC layer above the moving wall also changes and this induces local electrohydrodynamic instabilities in the LC layer. Yet the contrast origin may be different

(Tikhomirova et al., 1980a): On polished samples there is no contrast between domains but domain walls are well visible in both polarized and unpolarized light as dark lines whose thickness is of the order of the NLC layer thickness. A large amount of switching or wall velocity data have been collected by this method; however, because of the presence of the LC layer, the boundary conditions are relatively complex and evaluation of these data is complicated.

Dynamic observations are not limited to the TGS family of crystals. Hatano et al. (1990a) as well as Galtsev et al. (1990) visualized moving domain walls in crystals of NaNO_2 . Polomska and Jakubas (1990) observed the growth of 180° domains in $(\text{CH}_3\text{NH}_3)_5\text{Bi}_2\text{Br}_{11}$. Sakata and Hamano (1992, 1993) investigated plates of K_2ZnCl_4 with NLC layers on both surfaces, sandwiched between two transparent electrodes. The microscope could be focused on either surface of the sample. In zero field no domains were visible while moving domain walls when a dc field is applied became visible. Thus the polarization reversal process can be observed in situ and recorded by a video camera. Vysochanskii et al. (1992) made similar observations on crystals of ferroelectric semiconductor $\text{Sn}_2\text{P}_2\text{S}_6$.

4.5 Scanning Force Microscopy-Based Techniques

Rapid development of electronic devices based on ferroelectric thin films generated a strong need for studies of ferroelectric properties at the nanoscale. Fortunately, this need appeared at the same time as new techniques became available, which enable materials characterization which has a spatial resolution of a few nanometers. Specifically, scanning force microscopy (SFM) has emerged as a powerful tool for high-resolution characterization of virtually all types of materials, such as metals, semiconductors, dielectrics, polymers, and biomolecules. A number of papers and books on scanning probe methods have already been published, which can be used as an introduction to the principles of scanning force microscopy (see, e.g., Bonnell, 2000). In the field of ferroelectricity, the application of the SFM technique resulted in a real breakthrough providing an opportunity for nondestructive nanoscale visualization of domain structures. The employment of SFM made possible nanoscale mapping of the surface potential, evaluation of local electromechanical properties, and dielectric constant measurements. In other words, characterization by means of SFM provides crucial information on the dielectric properties of ferroelectrics with unprecedented spatial resolution.

Scanning force microscopy can be considered as a combination of a surface force apparatus and a surface profilometer as it is based on local monitoring of the interaction forces between a probing tip and a sample. The forces acting on the tip after it has approached the sample surface cause a deflection of the cantilever to which the tip is attached. This deflection can be detected optically or electrically with sub-angstrom accuracy and is controlled by a feedback

device, which regulates the vertical position of the tip as it scans the sample surface. Scanning is realized by placing the sample on a piezoelectric scanner, which allows for lateral and vertical positioning of the sample relative to the tip with nanometer precision. By keeping the cantilever deflection constant during scanning, a three-dimensional map of the surface topography can be obtained. Besides this method, called the constant force mode, many other modes have been developed. The response of the cantilever to the externally modulated force (for example, due to an applied ac bias) can be used to map such physical properties as mechanical stiffness, friction, electric fields, and density of electronic states.

Depending on the type of tip–sample force interaction—attracting or repelling—the SFM can operate in two different regimes: non-contact or contact. In the non-contact regime, the tip is scanned over the surface at a distance of 10–100 nm, which is controlled, for example, by monitoring the resonant frequency of the cantilever (Martin et al., 1987). The tip–sample interaction in this regime is dominated by the long-range electrostatic forces. Because of this feature, non-contact SFM can be used for ferroelectric domain imaging by detecting the electrostatic field of the surface polarization charges. This mode of SFM is called electrostatic force microscopy (EFM) (Stern et al., 1988). Quantitative information on local surface potential related to spontaneous polarization can be obtained by means of scanning surface potential microscopy (SSPM) (also called Kelvin probe force microscopy (KPFM) (Martin et al., 1988; Nonnenmacher et al., 1991; Barrett and Quate, 1991), a technique complementary to EFM. General disadvantages of non-contact methods include sensitivity to screening effects, sensitivity to sample surface conditions, and low resolution in ambient air.

In the contact regime, the probing tip is in mechanical contact with the sample surface and senses repulsive short-range forces. The difference in mechanical, structural, electrochemical, dielectric, and piezoelectric properties of ferroic domains can provide domain contrast in the SFM contact regime. Contact SFM methods of domain imaging include a topographic mode of atomic force microscopy (AFM), lateral (friction) force microscopy (LFM), piezoresponse force microscopy (PFM), and scanning nonlinear dielectric microscopy (SNDM).

A general feature of all scanning force microscopy-based techniques to be mentioned is their sensitivity solely to the properties of the material in interface-adjacent areas, except for the “electrode through” version of PFM.

4.5.1 Electrostatic Force Microscopy (EFM)

Imaging of ferroelectric domains in the non-contact mode is based on the detection of the modulated electrostatic interaction force between the probing tip and polarization charges. Figure 4.5.1 shows a typical setup used for this kind of imaging. Using this approach, a pioneering work on SFM domain imaging has been performed by Saurenbach and Terris (1990) in a single crystal of gadolinium molybdate. In EFM, the cantilever is made to oscillate near its

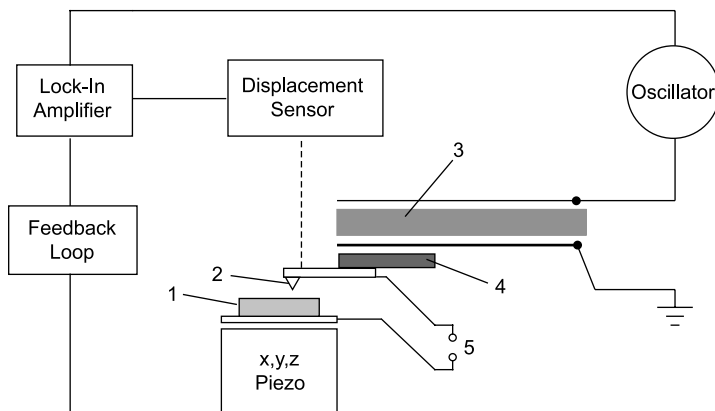


Fig. 4.5.1 Schematic of a setup for electrostatic force microscopy. 1, sample; 2, SFM tip; 3, piezoelectric bimorph actuator; 4, piece of insulator used for fixing the cantilever to the actuator; 5, input for additional voltage (used only in dual modulation scheme). After Lüthi (1993)

resonant frequency using a piezoelectric bimorph. When the tip is brought close to the surface, the attractive force gradient acting on the tip $\partial F/\partial z$ alters the force constant k_0 of the cantilever as $k' = k_0 - \partial F/\partial z$. This, in turn, leads to the change in the resonant frequency and in the vibration amplitude. This change is a key in the EFM domain imaging.

In the non-contact mode of operation two techniques can be used: amplitude modulation (AM) and frequency modulation (FM). In the AM method, the cantilever is oscillated at a fixed frequency and a change in its vibration amplitude, which is caused by the tip-sample interaction, is detected. In the FM mode, the feedback loop adjusts the tip-sample distance so as to maintain the amplitude of oscillation constant at the new frequency. In this case the frequency change, which reflects the force gradient acting on the tip, is detected. Obviously, in the case of the ferroelectric sample, there is an electrostatic contribution to the attractive force due to the Coulomb interaction between a surface polarization charge and an image charge (charge induced in the tip by the surface charge) Q_t in the probing tip. In the Saurenbach and Terris experiment, as the tip crossed the wall, it experienced a change in the force gradient and the feedback loop altered the tip-sample distance so as to keep the gradient and the vibration amplitude constant. This produced a variation of contrast in the feedback signal image, which could be interpreted as an image of the domain wall (Lüthi et al., 1993a,b; Lehnen et al., 2000). Since the Coulomb force is proportional to the product of the polarization and image charges, the force gradient signal provides information only on the polarization magnitude and not the sign. This implies that the contrast of opposite 180° domains will be the same and that only domain walls will be visible due to the spatial variation of the charge density in the vicinity of a 180° domain boundary.

A rather wide image of the domain wall (about 10 μm while the actual wall thickness is of the order of several lattice constants) obtained by Saurenbach and Terris had been attributed to the tip-sample separation and the finite size of the tip, which broadened any sharp changes in the force gradients. Later works of Lüthi et al. (1993a, 1994a,b) and of Eng et al. (1996, 1997, 1999c) demonstrated that lateral resolution in EFM can be significantly improved: In single crystals with cleaved polar surfaces, such as GASH and TGS, the width of the walls measured in EFM was in the range from 8 to 80 nm.

However, this method of domain imaging may suffer from the cross-talk with other sources of the force gradient, for example, van der Waals forces. As a result, the force gradient image is usually a superposition of domain and surface topographic features. In the case of domains of irregular shape and complex surface topography, the interpretation of the EFM images could be quite difficult. One of the ways to alleviate this problem is to use a lift-mode technique (tapping mode), which combines the contact and non-contact modes. In this approach, the tip scans each line twice: first, recording the topography in the contact regime, and second, retracing the topographic line at the predetermined height while detecting the variations in the vibration amplitude. In this case, since the tip-sample distance is kept constant during the second scan, the force gradient is related to the surface charge.

Another method to circumvent the cross-talk effect is to use a dual modulation scheme, developed for the detection of static surface charges (Terris et al., 1989; 1990). In this approach, also used by Saurenbach and Terris, the cantilever is additionally modulated by an ac voltage $V_t = V_{ac} \cos \omega t$ applied between the probing tip and the bottom electrode. The frequency of the electrostatic modulation is chosen so that it is well below the resonant frequency of the cantilever. Thus, the force gradient acting on the tip becomes modulated with frequencies ω and 2ω so that the resonance frequency of the cantilever (which is much higher than ω) also becomes modulated with these frequencies. One can show that the signal at the first harmonics is sensitive to the value and sign of the charge located at the surface. For the case where a permanent charge Q_s is located in the area which is much smaller than the tip-sample spacing, this is clear from the analysis performed by Saurenbach and Terris. In this case, the force acting on the tip can be written as

$$F = F_{\text{cap}} + F_{\text{coul}} = \frac{1}{2} \frac{\partial C}{\partial z} V_t^2 + \frac{Q_s Q_t}{4\pi\epsilon_0 z^2}, \quad (4.5.1)$$

where C is the tip-surface capacitance and z is the tip-surface separation. The total charge induced in the tip will be $Q_t = -(Q_s + Q_e) = -(Q_s + CV_t)$. Here Q_e is the charge on the surface induced by the applied voltage. The force gradient can be expressed as

$$\frac{\partial F}{\partial z} = \left[\frac{V_{ac}^2}{4} \frac{\partial^2 C}{\partial z^2} + \frac{Q_s^2}{2\pi\epsilon_0 z^3} \right] + \frac{Q_s V_{ac} \cos \omega t}{2\pi\epsilon_0 z^2} \left[\frac{C}{z} - \frac{1}{2} \frac{\partial C}{\partial z} \right] + \frac{V_{ac}^2}{4} \frac{\partial^2 C}{\partial z^2} \cos 2\omega t \quad (4.5.2)$$

Three terms in Eq. (4.5.2) represent a dc component and first and second harmonics of the force gradient. It is seen that the first harmonics component is proportional to the charge located at the surface. Such analysis when being generalized to the case of the continuous distribution of the surface charge (like in the situation with the bound charge of the spontaneous polarization) leads to the conclusion that the first harmonics amplitude (measured in the controlling circuit with a lock-in amplifies at frequency ω) reflects the sign and magnitude of the bound charge density at the sample interface under the tip. Thus, through the first harmonics monitoring, the information on the surface charge distribution becomes available. This method of domain imaging has been used by a number of groups (Blinov et al., 2001; Luo et al., 2000; Hong et al., 1999a; Eng et al., 1999a; Tsunekawa et al., 1999b; Hong et al., 1998a,b; Bluhm et al., 1997; Ahn et al., 1997; Zavala et al., 1997).

Figure 4.5.2 illustrates an application of this technique to domain imaging in a tetragonal $\text{Pb}(\text{Zr},\text{Ti})\text{O}_3$ (abbr. PZT) film. Prior to the imaging, a small part of the film was polarized by scanning with a positively biased tip and two lines were written across this area with a tip under a negative bias. The positively and negatively polarized domains appear as bright and dark areas in Fig. 4.5.2, respectively, due to uncompensated polarization charges of newly switched domains. At the same time, this image illustrates one of the limitations of the EFM method. Namely, an unwritten area shows only slight variation of the contrast, although it contains as-grown domains with polarization normal to the film surface, which was confirmed by another SFM method. Furthermore, the contrast of the written structure gradually fades and almost disappears within several hours. This behavior is due to the accumulation of surface charge on the film surface, which neutralizes polarization charges and causes a uniform contrast over the surface due to zero net charge. Therefore, although the EFM charge detection mode has the advantage of distinguishing between

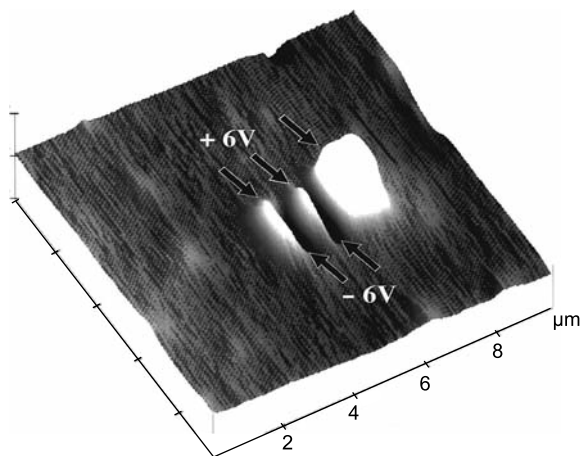


Fig. 4.5.2 EFM charge image of a PZT film. Bright and dark areas correspond to positively and negatively poled regions, respectively. Courtesy of Alexei Gruverman

topographic features and the electrostatic signal, the domain contrast in this mode can be easily obscured. In addition, a surface contamination layer always present on the sample surface under ambient conditions can change or even conceal the image of real domain structure. Conducting experiments in vacuum or in inert atmosphere can eliminate these detrimental effects and make possible detailed investigation of the spatial distribution of polarization charges and stray electric fields at ferroelectric surfaces.

4.5.2 Scanning Surface Potential Microscopy (SSPM)

In this method, in contrast to the EFM, the cantilever is not excited mechanically but a combination of an ac and a dc voltage is applied between the sample and the tip and the force acting on the tip at the modulation frequency, rather than its gradient, is monitored. The SSPM method is mainly applied to domain imaging based on detection of a surface potential associated with spontaneous polarization. Let us elucidate this method for the case where the spontaneous polarization is fully screened. Even being fully screened the bound charge of the polarization will produce a double electric layer modifying the surface potential of the sample V_s . Thus, the electrostatic force acting on the tip, which depends on difference between the tip potential $V_t = V_{dc} + V_{ac} \cos \omega t$ and the surface potential, can be written as

$$F = \frac{1}{2} (V_t - V_s)^2 \frac{\partial C}{\partial z}. \quad (4.5.3)$$

This leads to the three components of the electrostatic force:

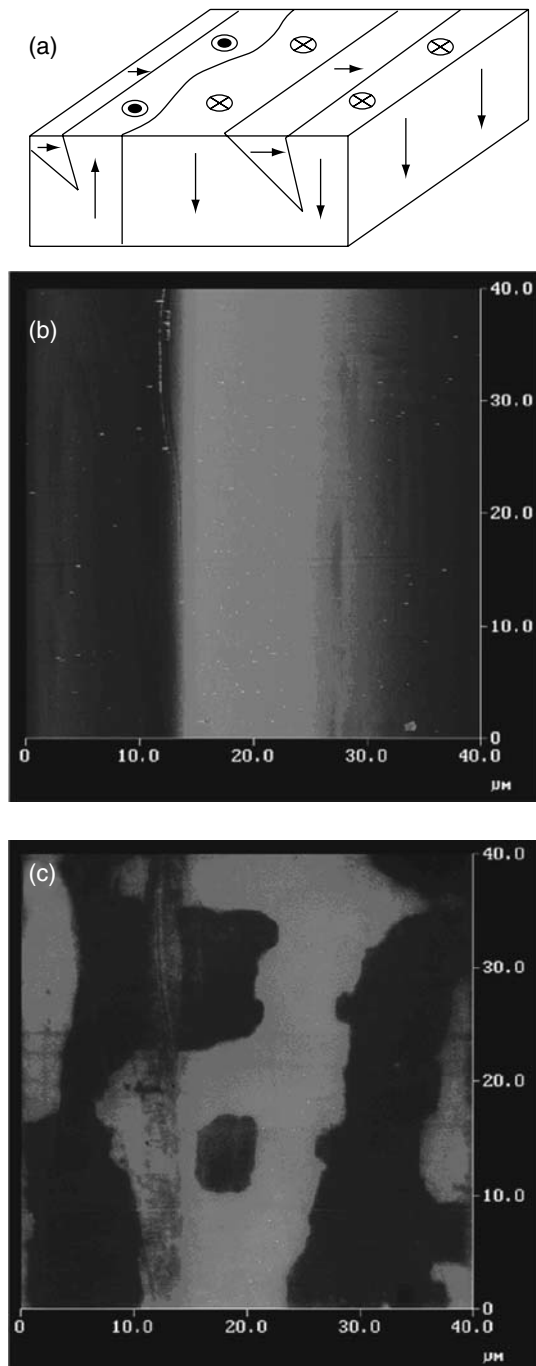
$$F_{dc} = \frac{1}{2} \left((V_{dc} - V_s)^2 + \frac{1}{2} V_{ac}^2 \right) \frac{\partial C}{\partial z}, \quad (4.5.4)$$

$$F_{1\omega} = (V_{dc} - V_s) V_{ac} \frac{\partial C}{\partial z} \cos \omega t, \quad (4.5.5)$$

$$F_{2\omega} = \frac{1}{4} V_{ac}^2 \frac{\partial C}{\partial z} \cos 2\omega t. \quad (4.5.6)$$

The absolute value of the surface potential can be measured using the so-called nulling method (Hong et al., 1998b). In this method, the first harmonic of the electrostatic force is nullified by adjusting the constant bias on the tip so that $V_{dc} = V_s$. By detecting the nullifying V_{dc} value during scanning, a surface potential image can be obtained. This approach has been extensively used by Kalinin and Bonnell to study polarization screening processes in ferroelectrics (Kalinin and Bonnell, 2001a,b; Kalinin et al., 2002). Figure 4.5.3 shows a simplified schematic diagram of domain structure (a), surface topography (b),

Fig. 4.5.3 Imaging of domain pattern in barium titanate single crystal: (a) simplified schematic diagram of domain structure; (b) surface topography image; (c) SSPM image of the same area as in (b). After Kalinin and Bonnell (2001a)



and surface potential (c) in a single crystal of barium titanate. Corrugated surface topography is an indication of *a*- and *c*-domain regions (with in-plane and out-of-plane spontaneous polarization, respectively). SSPM image provides additional information on the domain structure: Inverted potential contrast within the *c*-domain region indicates the presence of antiparallel *c*-domains (not shown in (a)).

For a comprehensive discussion of EFM and SSPM methods, we refer the reader an excellent paper by Kalinin and Bonnell (2001a).

4.5.3 Contact Domain Imaging

Figure 4.5.4 shows the block diagram of a possible setup for the *contact mode* (Eng et al., 1997). A sharp probing tip mounted on a spring-type cantilever is brought into mechanical contact with the sample surface. The interaction of the tip with the sample surface causes bending of the cantilever. In the most frequently used setup a collimated laser beam is focused on its rear side and reflected onto segment photodiode which acts as a displacement sensor. Using a four-quadrant detector one can apply this setup for detection of both vertical deflections or torsions of the cantilever. Thus, when scanning the sample surface with the tip the vertical and lateral displacements of the tip can be monitored.

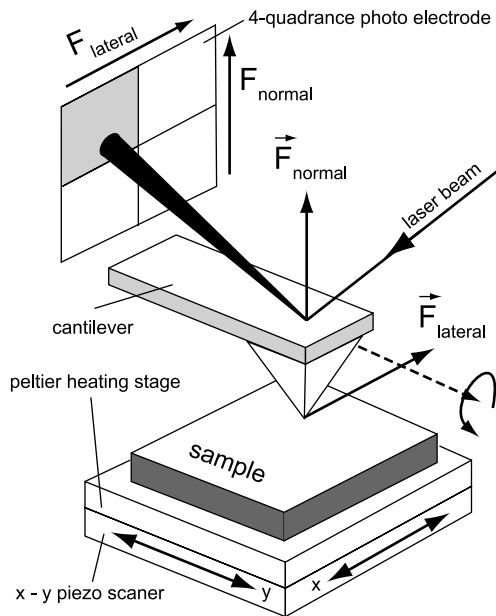


Fig. 4.5.4 Setup for the contact mode of scanning force microscopy (after Eng et al., 1997). The force F acting on the cantilever has a lateral and a normal components

Contact domain imaging can be divided into static and dynamic, or voltage-modulated, methods. Static imaging methods, such as a topographic mode of SFM and lateral force microscopy (LFM), make use of the surface domain-dependent properties of ferroelectrics, such as surface corrugations associated with the presence of different domains, difference in structure of polar faces of opposite domains, and variations in friction forces. Dynamic methods, which include PFM and SNDM, are based on voltage modulation and detection of the electrical and mechanical response of opposite ferroelectric domains to the applied ac voltage. The contact SFM imaging methods provide significant advantages, such as high lateral resolution (well below 10 nm), a possibility of the three-dimensional reconstruction of domain structure and effective control of nanodomains. However, interpretation of the domain images could be complicated by cross-talk between different mechanisms involved in the domain contrast formation.

4.5.4 Lateral Force Microscopy (LFM)

In this technique, one monitors the lateral friction force acting on the tip during scanning. The first imaging of antiparallel domains via LFM has been performed by Lüthi et al. (1993a,b). Using this approach, domain structure has been revealed on freshly cleaved surfaces of single crystals of GASH and TGS (Eng et al., 1996; 1999c; Gruverman et al., 1996; Correia et al., 1996; Bluhm et al., 1998). In most of the papers, the imaging mechanism is attributed to the permanent charging of the probing tip by a ferroelectric surface. The electrostatic tip-sample interaction causes an additional contribution to the lateral force acting on the tip and results in different torsion of the cantilever when the tip is scanning surfaces of opposite 180° domains. Consequently, electrostatic interaction results in different lateral forces acting on the tip from opposite 180° domains. The lateral resolution has been reported to be about 8 nm. The image contrast depends on the scanning direction and can be reversed by switching from forward to backward scan as illustrated in Fig. 4.5.5. This is an indication of the effect associated with the atomic structure of the surface rather than of the surface morphology. Figure 4.5.6 shows topography and friction images of a cleaved surface of TGS crystal recorded simultaneously by Eng et al. (1997). Ferroelectric domains of typical lenticular shapes are visible in the friction mode but not in topography.

A complementary mechanism of the domain contrast in LFM can be the difference in surface structure of opposite domains which gives rise to different friction coefficients of the regions occupied by these domains (Bluhm et al., 1995, 1996). One of the greatest limitations of this method is that it is extremely sensitive to the surface conditions affecting sample tribological properties: adhesion layers, interfacial wetting, contamination, and roughness. As a result, its application is mainly limited to crystals with atomically flat surfaces of

Fig. 4.5.5 Friction force micrograph of a GASH cleavage surface. An imbedded domain exhibits opposite contrast compared to the surrounding due to the difference in tip–surface friction forces. Scan direction: (a) left to right; (b) right to left. Courtesy of Alexei Gruverman

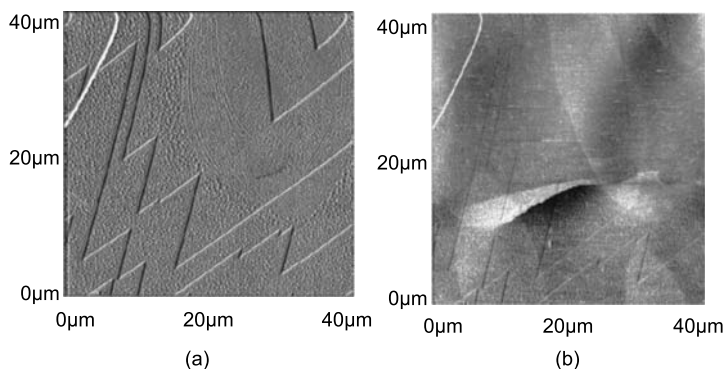
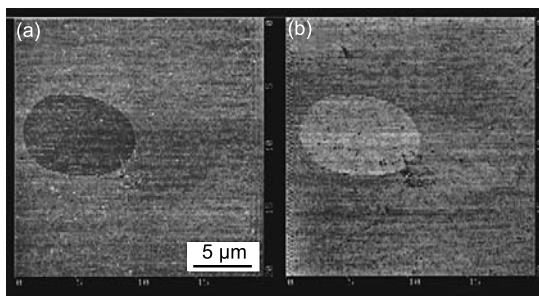


Fig. 4.5.6 Images of a TGS crystal surface simultaneously recorded in two contact modes, topography (a) and friction. (b) The covered area is $40 \times 40 \mu\text{m}^2$. Ferroelectric domains are visible in the friction mode while the topography mode emphasizes cleavage steps. After Eng et al. (1997)

cleavage planes, such as GASH and TGS. On atomically flat terraces of the freshly cleaved surfaces, even small variations in the friction forces can be easily detected. However, even in these crystals, friction images exhibit a wide diversity and should be interpreted with caution. For example, due to the different orientation of molecules on the chemically homogeneous terraces comprising the surface of individual domains, frictional contrast can occur not only between opposite domains but also inside individual domains (Bluhm et al., 1995). Long exposure to ambient environment could lead to deterioration of surface quality and to degradation of the domain contrast.

4.5.5 Domain Imaging via Surface Topography

The conventional topography mode of SFM has been used for domain studies via investigation of the domain-related surface morphology of ferroelectrics.

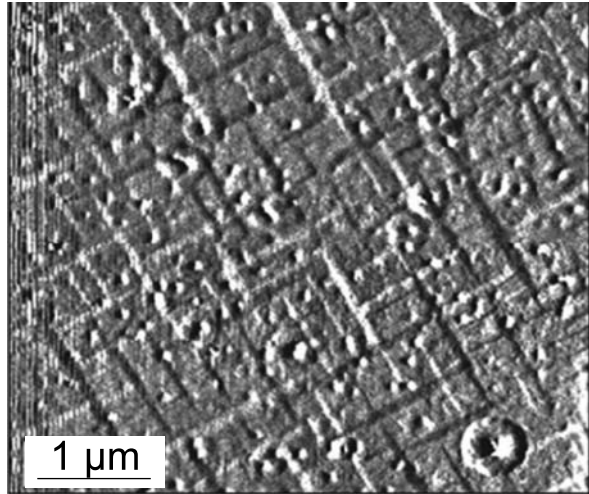
There are several mechanisms which can provide morphological contrast of ferroelectric domains: (1) topographic steps at domain boundaries due to the structural difference between positive and negative ends of domains (Nakatani, 1979); (2) inclination of the *cleaved* surfaces according to the polarity of domains and the direction of cleavage propagation (Nakatani, 1979; Shur et al., 1992, 1993b); (3) surface corrugation at the junction of *a*- and *c*-domains in perovskite ferroelectrics (Lüthi et al., 1993b; Eng et al., 1996; Jona and Shirane, 1962; Seifert et al., 1995; Munoz Saldana et al., 2001; Eng and Güntherodt, 2000; Takashige et al., 2000; Gruverman et al., 1998b; Wang et al., 1998; Ganpule et al., 2002; Gruverman et al., 1997b).

The topographic steps of several angstroms in height have been observed at the 180° domain boundaries on the cleaved surface of TGS crystals by Bluhm et al. (1996) and Eng et al. (1999a,b). This effect was explained by the relative shift of atom positions in opposite domains. An additional factor which can affect the surface topography and reveal domain structure is the different etching behavior of positive and negative domains. Selective etching with subsequent topographic imaging has been used to reveal nanoscale domains in LiNbO₃ crystals (Bluhm et al., 1997; Shur et al., 2000b). For hydrophilic materials, such as TGS and GASH, exposing a sample to humid atmosphere can reveal domains due to selective surface etching by the water vapor.

Topographic imaging of the etched surface can be used for identification of domain polarity (Lüthi et al., 1994a; Correia et al., 1996; Bluhm et al., 1996). At the same time, this feature of TGS could be a complicating factor: Fine morphological structures of ferroelectric domains on opposite cleavage faces of TGS vary strongly even for domains of equal polarity. Etching of positive domains can result both in etch hole formation and recrystallization of islands from the saturated solution at the surface, depending on which molecular layer is exposed to ambient air after the cleavage. Etch patterns can be easily confused with domain structure.

Another mechanism which can lead to domain topographic contrast is surface corrugation at the 90° domain walls separating domains with in-plane polarization (*a*-domains) and out-of-plane polarization (*c*-domains). Using this approach, *a*- to *c*-domain structure has been observed in BaTiO₃ and PbTiO₃ crystals and PZT thin films (Lüthi et al., 1993b; Wang et al., 1998; Ganpule et al., 2002; Gruverman et al., 1997b; Eng et al., 1999b; Shur et al., 2000; Wang et al., 2000b; Cho et al., 1997b; Cho et al., 1999). A difference between *a* and *c* lattice constants of the tetragonal cell produces a lattice distortion at the junction of *a*- and *c*-domains and surface inclination as was discussed above in Sect. 4.3 and illustrated in Fig. 4.3.1a. This inclination can be monitored with SFM. Thus, SFM can provide a simple and non-destructive method for studying domain patterns in epitaxial ferroelectric films by topographic imaging of their surfaces. Figure 4.5.7 shows a topographic image of a Pb(Zr_{0.20},Ti_{0.80})O₃ film deposited by laser ablation on a LaAlO₃ substrate. The *a*- to *c*-domain arrangement appears as a rectangular structure with height variations in the range of 1.5–3.5 nm, occurring as a result of twinning between *a*- and

Fig. 4.5.7 Topographic image of a PZT film on a LaAlO_3 substrate showing a rectangular structure of a - and c -domains. Courtesy of Alexei Gruverman



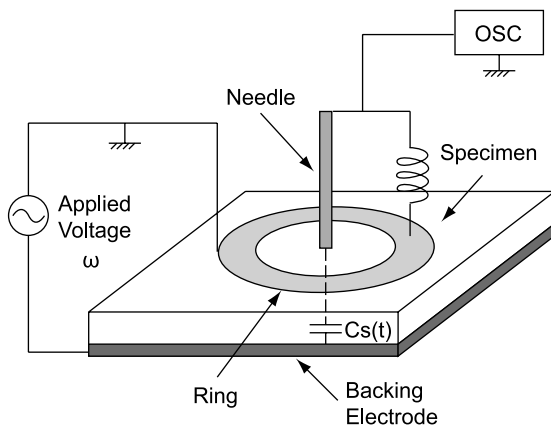
c -domains. A value of surface tilting of approximately 2° was measured at the 90° domain boundaries, which is consistent with the c/a ratio of the unit cell of the film at room temperature.

There are obvious limitations on the applicability of the SFM topographic mode for domain imaging. Any treatment of the surface during sample preparation inevitably eliminates the fine structure of morphological steps associated with domain patterns. Therefore, only crystals with cleavage planes, like TGS and GASH, are suitable for SFM topographic studies. Also, since formation of 180° domains cannot be reliably detected on the rather rough surfaces of most ferroelectric thin films (surface variations associated with the presence of the domains are much less than surface morphology variations), this method is not applicable for imaging of domain structure consisting of antiparallel c -domains, which is of direct interest for investigation of the polarization reversal processes in ferroelectrics.

4.5.6 Domain Imaging via Nonlinear Dielectric Response (SNDM)

A purely electrical dynamic method of domain delineation has been developed by Cho and his coworkers (Cho et al. 1997a,b; 1999; 2002; Odagawa and Cho, 2002). This method, termed scanning nonlinear dielectric microscopy (SNDM), is based on the detection of the capacitance variation with an alternating electric field. To measure the capacitance variation, Cho et al. developed a special lumped constant resonator probe using an electrolytically polished tungsten needle and a LC resonance circuit operating in the microwave frequency range. Figure 4.5.8 shows a setup used for SNDM imaging. Application of the modulation voltage (in the range of 100–1,000 Hz) across the sample leads to the

Fig. 4.5.8 Probe configuration in SNDM (after Cho et al., 1997). The needle makes capacitor C_s with backing electrode. The source of the microwave signal (OSC) is connected with the ring by a lumped inductance



oscillating change ΔC_s in the capacitance between the needle and the bottom electrode due to the nonlinear dielectric response of the sample with the first harmonic component proportional to the nonlinear dielectric constant κ_{333} :

$$\frac{\Delta C_s}{C_s} = \frac{\kappa_{333}}{\kappa_{33}} E_3 \cos \omega t, \quad (4.5.7)$$

where C_s and κ_{33} are a static capacitance and a linear dielectric constant, respectively; the X_3 axis is taken normal to the sample surface. The change in the capacitance is measured by detecting the modulated high-frequency signal (around 1.3 GHz) of the oscillator using a demodulator and a lock-in amplifier. The sign of an even rank tensor, such as the linear dielectric constant, does not depend on the polarization direction. On the other hand, the nonlinear dielectric constant κ_{333} is a third-rank tensor, similar to the piezoelectric constant, so the sign of κ_{333} changes with inversion of the spontaneous polarization. Therefore, a map of the polarization sign can be obtained by point-to-point detection of the field-induced changes in the nonlinear dielectric constant. This method, as it is designed, allows nanoscale detection of antiparallel 180° domains in the surface layer with a thickness much smaller than the probe size (<10 nm). According to Cho and Ohara (2001) sub-nanometer lateral resolution can be obtained by detecting the higher order nonlinear dielectric constants. However, in this case the image reflects the state of the material in a yet thinner interfacial layer. Figure 4.5.9 shows a two-dimensional SNDM image of a - to c -domain structure in barium titanate single crystal. The sign of κ_{333} in the $+c$ domain is negative, whereas it is positive in the $-c$ domain. Furthermore, the magnitude of κ_{333} is zero in the a -domain (where the spontaneous polarization has no out-of-plane component so that the κ_{333} component is not induced). It is possible to measure ferroelectric polarization parallel to the sample surface by detecting κ_{331} constant (X_1 axis is chosen and directed among the spontaneous

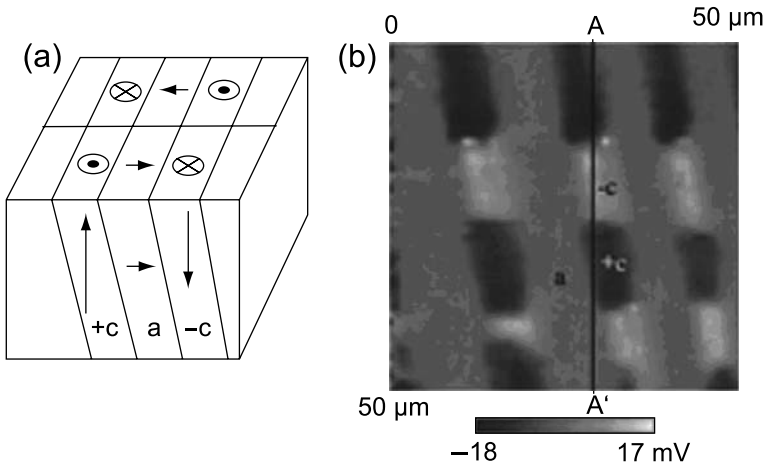


Fig. 4.5.9 SNDM image: (a) a sketch of the visualized domain structure and (b) two-dimensional image of the 90° a - c domain structure in a BaTiO_3 single crystal. Reprinted with permission from Cho et al. (1999). Copyright (1999), American Institute of Physics

polarization in the a -domain) using different configuration of electrodes, which makes SNDM suitable for three-dimensional domain structure reconstruction.

Closely related near-field scanning microwave techniques have been used for domain imaging and dielectric constant measurements in single crystals of LiNbO_3 , BaTiO_3 , and deuterated triglycine sulfate and thin films of $\text{Ba}_{0.6}\text{Sr}_{0.4}\text{TiO}_3$ (Gao et al., 1998; Lu et al., 1997; Steinhauer and Anlage, 2001; Steinhauer et al., 1999). However, the lateral resolution has been just below $1\ \mu\text{m}$ due to the size of the inner probe of the resonator.

4.5.7 Domain Imaging via Static Piezoresponse

The next domain imaging method makes use of the piezoelectric properties of ferroelectrics and therefore is often referred to as piezoresponse. It is based on the detection of local piezoelectric deformation of the ferroelectric sample induced by an external electric field. Since all ferroelectrics exhibit piezoelectric properties, application of an external voltage results in a deformation of the ferroelectric sample. Depending on the relative orientations of the applied field and the polarization vector, the sample deformation can be in the form of elongation, contraction, or shear. For the converse piezoelectric effect, the field-induced strain ε_{ij} can be expressed as:

$$\varepsilon_{ij} = d_{kij}E_k, \quad (4.5.8)$$

where d_{kij} is the piezoelectric coefficient and E_i is the applied field.

On the other hand, using the thermodynamic approach it can be shown (see Chap. 2) that the appearance of the spontaneous polarization \mathbf{P}_s induces piezoelectricity or induces new components of the piezoelectric tensor if the paraelectric phase is piezoelectric. Thus, in the ferroelectric phase, one finds

$$d_{kij} = d_{kij}^0 + 2\chi_{kn}Q_{nlj}P_{S_i}, \quad (4.5.9)$$

where χ_{kn} is the susceptibility, Q_{nlj} is the electrostriction coefficient, and d_{kij}^0 is the piezoelectric coefficient in the paraelectric phase. In the common experimental situation one deals with centrosymmetric paraelectric phase having $d_{kij}^0 = 0$. In this situation, the electric field applied normal to the sample surface (along X_3 axis) will lead to the tip displacements due to three piezoelectric coefficients d_{33} , d_{35} , and d_{34} (we use a reference frame with X_3 axis directed along the normal to the sample surface).¹ As seen from Eq. (4.5.9), for general orientation of the sample surface, all these coefficients can, in general, have contributions from all components of the spontaneous polarization. For a simple case of a BaTiO₃ type crystal of tetragonal symmetry with the surface oriented along a cubic axis of the paraelectric phase the aforementioned coefficients in the reduced matrix notation can be written as

$$d_{33} = 2\chi_{33}Q_{33}P_{S_3}, \quad (4.5.10a)$$

$$d_{35} = 2\chi_{33}Q_{55}P_{S_1}, \quad (4.5.10b)$$

$$d_{34} = 2\chi_{33}Q_{44}P_{S_2}. \quad (4.5.10c)$$

The d_{33} , or longitudinal piezoelectric coefficient, represents an expansion or contraction of the sample along the direction of the applied field (normal to the sample surface). The d_{34} and d_{35} coefficients describe field-induced shear deformations of the ferroelectric sample.

The linear relation between the values of the piezoelectric constants and spontaneous polarization infers that the domain polarity can be determined from measuring the field-induced strain. In the simple aforementioned case, the domain polarity can be associated with the sign of the latter. As it follows from Eq. (4.5.10a), the application of the electric field along the polar direction results in the elongation of the domain with polarization parallel to the applied field and in the contraction of the domain with opposite polarization, since typically $Q_{33} > 0$. The field-induced strain in this case can be written as

$$\frac{\Delta L}{L} = d_{33}E, \quad (4.5.11)$$

¹ The deformations of the sample surface due to d_{31} and d_{32} piezoelectric coefficients will not lead to any tip displacement as far as they are homogeneous in the region sensed by the electric field of the tip. In principle, these deformations may lead to tip displacements close to domain walls and grain boundaries.

where ΔL is the sample deformation and L is the sample thickness. Equation (4.5.11) can be rewritten as

$$\Delta L = -d_{33}V, \quad (4.5.12)$$

where V is an applied voltage. Note that, in this expression, the sign of the piezoelectric coefficients is correlated to that of the spontaneous polarization in the domains. Thus as we see, in the considered case of tetragonal ferroelectric, antiparallel domains with the polarization normal to the crystal surface can be visualized by monitoring their voltage-induced surface displacement. In general case, the interpretation of the field-induced surface requires a more cumbersome analysis in terms of Eq. (4.5.9). The situation can be especially complicated in the case of ferroelectrics exhibiting piezoelectric effect in the paraelectric phase. In this case, if d_{kij}^0 is appreciable, the antiparallel domain may not differ in the sign of the field-induced strain but only in its amplitude.

Due to its extremely high vertical sensitivity, nanoscale topography variations can be routinely measured in SFM. However, domain imaging based on detecting the static piezoelectric deformation is difficult to implement unless a sample has a very smooth surface. In a sample with an average surface roughness of several nanometers per square micron, the static cantilever deflection due to the piezoelectric deformation (typically of the order of several angstroms) will be superimposed on the much larger deflection signal due to the surface roughness which will make domain imaging very problematic.

From Eq. (4.5.12) it follows that increasing the imaging voltage can enhance the contrast between opposite c -domains. However, there is a strict limitation imposed on this parameter: To perform *nondestructive* visualization of domain structure, the imaging voltage should be kept below the coercive voltage of the ferroelectric sample. In addition, a high imaging voltage will lead to an increased contribution of the electrostatic signal to the tip-sample interaction, which in some cases can obscure the domain image. Given that a typical value of the coercive field in a 200 nm thick $\text{Pb}(\text{Zr},\text{Ti})\text{O}_3$ ferroelectric film is approximately 50 kV/cm, the imaging voltage should not exceed 1 V, otherwise the imaging process will change the domain structure by inducing the polarization reversal. In a PZT film with a d_{33} constant of about 200 pm/V the surface displacement induced by an external voltage of 1 V will be only 0.2 nm. Obviously, such a displacement could not be reliably detected in ferroelectric films where topographic features can be of the order of several nanometers. The static approach can be applied in some limited cases, for example, to ferroelectric samples with relatively high values of piezoelectric constants and coercive fields. Wang et al. (2000b) used this approach to delineate domains in a doped crystal of $\text{Sr}_{0.61}\text{Ba}_{0.39}\text{Nb}_2\text{O}_6$ (SBN) known for a high concentration of the pinning centers which gives rise to increased local coercive fields. Due to this feature of the SBN sample, even under an applied voltage of 200 V there exist non-switched c -domains antiparallel to the external field. At the same time, this voltage is high enough to produce surface indentation of about 2 nm due to contraction and elongation of opposite domains, which makes them discernible in the topographic mode.

4.5.8 Domain Imaging via Dynamic Piezoresponse (PFM)

A problem of low sensitivity of a static piezoresponse mode has been circumvented by employing a dynamic piezoresponse imaging method based on the voltage-modulation approach, which increases sensitivity by three orders of magnitude. In this approach, known as piezoresponse force microscopy (PFM), an ac modulation (imaging) voltage $V = V_0 \cos \omega t$ is applied to the ferroelectric sample and surface displacement is measured using a standard lock-in technique. In the simplest implementation of PFM technique, one monitors the vertical vibration of the cantilever, which follows sample surface oscillation. A domain map can be obtained by scanning the surface while detecting the first harmonic component of the normal surface vibration (vertical piezoresponse):

$$\Delta L = \Delta L_0 \cos(\omega t + \varphi) \quad (4.5.13)$$

where $\Delta L_0 = d_{33} V_0$ is a vibration amplitude and φ is a phase difference between the imaging voltage and piezoresponse. As it follows from Eq. (4.5.9), in ferroelectrics which are not piezoelectric in the paraelectric phase, the PFM signals from antiparallel domains differ in the phase by 180° . In the case of tetragonal crystal described by Eq. (4.5.10), since usually Q_{33} is positive, the signal phase can be directly related to the domain orientation. With the modulation voltage applied to the probing tip, positive domains (polarization vector oriented downward) will vibrate in phase with the applied voltage so that $\varphi(+)=0^\circ$, while vibration of negative domains (polarization vector oriented upward) will occur in counter phase because of the d_{33} sign $\varphi(-)=180^\circ$. However, as clear from Eq. (4.5.9), in ferroelectrics which exhibit the piezoelectric effect in the paraelectric phase, the sign of d_{33} may be the same in antiparallel domains. In this case, they cannot be delineated by the phase of the PFM signal, and the information on its amplitude is needed.

The dynamic piezoresponse mode has been developed for detection of polarized regions in ferroelectric copolymer films of vinylidene fluoride and trifluoroethylene (Güthner and Dransfeld, 1992) and quickly became one of the most widely used methods for nanoscale characterization of ferroelectrics. The pioneering studies performed by Franke et al. (1994), Gruverman et al. (1996, 1998a), and Hidaka et al. (1996) demonstrated the applicability of PFM for high-resolution visualization and modification of domain structure in PZT thin films.

One of the significant advantages of the PFM method is that it also allows delineation of domains with polarization parallel to the sample surface (a -domains) (Ganpule et al., 2002; Eng et al., 1999d; Roelofs et al., 2000). In the lateral PFM approach (Eng et al., 1999d) a -domains are visualized by detecting the torsional vibration of the cantilever. Application of the modulation voltage across the sample generates sample vibration in the direction parallel to its surface due to the piezoelectric shear deformation. This surface vibration,

translated via the friction forces to the torsional movement of the cantilever, can be detected in the same way as the normal cantilever oscillation in vertical PFM. The PFM amplitudes of the in-plane oscillations (lateral piezoresponse) are given by

$$\Delta X_{01} = d_{35} V_0, \quad (4.5.14a)$$

$$\Delta X_{02} = d_{34} V_0. \quad (4.5.14b)$$

As it follows from Eqs. (4.5.10b) and (4.5.10c), in the case of tetragonal crystal described by these equations, the phase of the lateral PFM signals directly provides information on the polarization direction in the a -domains. The information on the vertical and two lateral components of PFM response can be, in principle, used for the three-dimensional reconstruction of the domain arrangement. In the case of a BaTiO_3 -type crystal of tetragonal symmetry with the surface oriented normally to a cubic axis of the paraelectric phase, this can be readily done using relations Eq. (4.5.10). In this simple case, each component of PFM response controls one component of the spontaneous polarization. In a more complicated case of an arbitrary sample orientation, a more involved analysis in terms of Eq. (4.5.9) is required.

It should be noted that to obtain a complete picture of the in-plane distribution of polarization, X_1 and X_2 components of the lateral piezoresponse image should be recorded by physically in-plane rotating the sample by 90° , in addition, the quantitative analysis of the lateral piezoresponse signal is rather difficult due to the complexity of the friction mechanism involved.

Figure 4.5.10 presents experimental results on simultaneous acquisition topographical, vertical piezoresponse, and lateral piezoresponse images of a BaTiO_3 single crystal (a–c) (Abplanalp et al., 1998) and PbTiO_3 multigrain film (d–f). In both cases the surface normal of the sample is oriented parallel to a cubic axis of the paraelectric phase of the materials. In image (a), we see a shaded representation of surface topography, clearly demonstrating a system of 90° domains leading to a surface profile. Dark stripes represent c -domains (\mathbf{P}_S is perpendicular to the surface) and bright stripes correspond to a -domains (\mathbf{P}_S lies in the surface plane). The irregularly shaped regions image topographical steps in as-grown crystals but could also represent etching figures of previously existing domains. In (b) the irregular regions are antiparallel c -domains. The contrast is due to the opposite sign of the longitudinal piezoelectric coefficient. The gray stripes correspond to a -domains. In (c) dark and bright regions are a -domains with antiparallel \mathbf{P}_S vectors; here the contrast is due to the opposite sign of the shear piezoelectric coefficients. From images (d–f), it is seen that the grains of the PbTiO_3 are mainly single domain. Because of the grained structure of the film its surface is not flat enough to enable a delineation of in-plane and out-of-plane orientations of the polarization from a topographical image (d). Grains in the central part of the image exhibit a strong vertical piezoresponse signal (bright contrast in (e)), while their lateral piezoresponse signal is rather weak (gray contrast in (f)), suggesting predominantly out-of-plane orientation

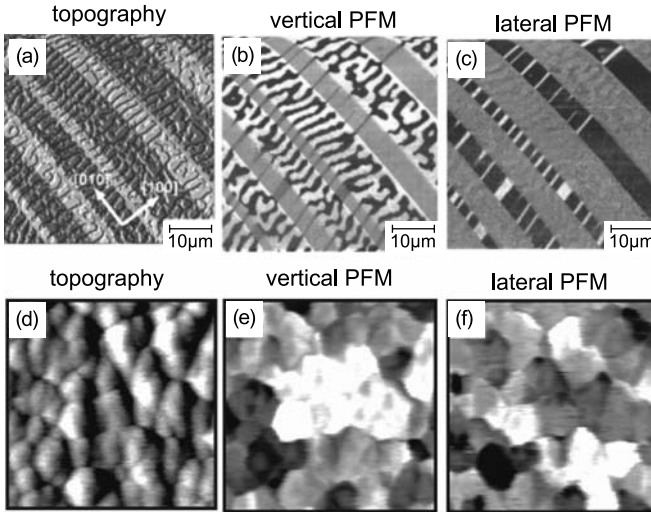


Fig. 4.5.10 Experimental results on simultaneous acquisition topographical, vertical piezoresponse, and lateral piezoresponse images of a BaTiO_3 single crystal (a–c) (after Abplanalp et al., 1998) and PbTiO_3 multigrain film (d–f). In topography image (a), *dark stripes* represent *c*-domains (\mathbf{P}_S is perpendicular to the surface), *bright stripes* correspond to *a*-domains (\mathbf{P}_S lies in the surface plane). The irregularly shaped regions image topographical steps in as-grown crystals but could also represent etching figures of previously existing domains. In (b) the irregular regions are antiparallel *c*-domains. The *gray stripes* correspond to *a*-domains. In (c) *dark* and *bright regions* are *a*-domains with antiparallel \mathbf{P}_S vectors. From images (d–f), it is seen that the grains of the PbTiO_3 are mainly single domain. The roughness of the film surface impedes observation of *a*- and *c*-domains in topographical image (d). Grains in the center have *bright contrast* in (e) and *gray contrast* in (f) suggesting out-of-plane polarization. Grains in the lower part of the image exhibit *gray contrast* in (e) and *black–white contrast* in (f), which is an indication of the in-plane polarization. The scanning area is $0.9 \times 0.9 \mu\text{m}^2$. Courtesy of A. Gruverman and B. Rodriguez

of the polarization vector. On the other hand, grains in the lower part of the image exhibit gray contrast in (e) and bright contrast in (f), which is an indication of in-plane polarization.

In terms of exciting the piezoelectric vibration of the sample, there are two main approaches in PFM. In one approach, the vibration is generated locally by applying a modulation voltage between the bottom electrode and the conductive SFM tip, which scans the bare surface of the film without a deposited top electrode. A great advantage of this approach is a possibility of establishing correlation between domain configurations and film microstructure (grain structure). In addition, this method can be used for nanoscale domain writing and direct investigation of domain wall interaction with microstructural features, such as defects and grain boundaries, for local spectroscopy measurements and investigation of electrical and mechanical coupling between adjacent grains. Furthermore, this approach offers extremely high resolution, potentially allowing investigation of the microscopic mechanism of the domain wall motion.

However, the electric field generated by the SFM tip in this configuration is highly inhomogeneous, which makes quantitative analysis of the field-dependent parameters difficult. This problem is exacerbated by the likely presence of a contamination layer at the film surface, which increases the resistance of the tip-sample electric contact. As a result, an increased time constant of the electric circuitry makes it difficult to extend the experiments on switching behavior to the micro- and nanosecond range, which is of direct application interest. In an alternative PFM approach, domain structure can be visualized through the top electrode of a ferroelectric capacitor (Auciello et al., 1997; Colla et al., 1998a; Hong et al., 1999b; Gruverman et al., 2003). In this case the piezoelectric vibration is generated in a film region underneath the deposited top electrode which is much larger than the tip-sample contact area. The modulation voltage can be applied either by using an external wire attached to the top electrode or, in the case of a micrometer size electrode, directly through the conductive SFM tip. In both cases the piezoelectric displacement is probed locally by the SFM tip. In such a configuration, a homogeneous electric field is generated throughout the ferroelectric film, which allows quantitative treatment of domain wall dynamics and investigation of polarization reversal mechanism in ferroelectric capacitors. Due to the reduced time constant, fast pulse switching and transient current measurements can be accomplished in submicron capacitors, thus making PFM suitable for memory device testing. A more detailed discussion of this technique, which is of primary interest for monitoring switching in thin film capacitors, can be found in Sect. 9.8 which is devoted to the SFM investigations of polarization reversal in ferroelectric films.

4.6 Polarized Light Microscopy Based on Unperturbed Linear Optical Properties

Now we address the question how to distinguish domains by polarized light microscopy using methods based on linear optical properties of a ferroic crystal: birefringence, optical activity, and anisotropic light absorption. It is assumed that the crystal or its parts are not subjected to any external forces or to fields arising due to the presence of the domain structure itself; these issues will be mentioned in the subsequent section.

4.6.1 Birefringence

If a ferroic material is transparent, the most natural thing to do is to place a plate-like sample on the stage of a microscope and observe it in *transmitted* polarized white light.² Parameters that can be easily changed are mutual

² Having made this statement, one has to wonder why this was not done in the earliest stages of investigations of crystalline plates of Rochelle salt—in particular when dielectric hysteresis was discovered (Valasek, 1921). The more so, that later Valasek demonstrated his very high

orientations of polarizer, analyzer, and the crystal itself. In order to obtain information on domains, the domain states must be distinguishable by their optical properties and in this section we have in mind unperturbed properties: Those determining propagation of light falling onto an ideal crystal to which no forces of mechanical or electrical character are applied—not even forces which could be generated by boundary conditions. To each domain state a symmetric polar tensor of second rank B_{ij} determining the optical indicatrix is ascribed. Distinguishing domains by their indicatrices is possible mainly for ferroelastic domain pairs only, since both strain and optical permittivity are represented by symmetric second-rank tensors with the same transformation properties. Exceptions are offered by materials which allow for the spatial dispersion effects discussed in Sect. 4.6.2. Except for these rather special cases, the number of states distinguishable by optical indicatrix in a given ferroic species equals the number of ferroelastic domain states and Tables B.1 and C.1 and tables of Appendix D can be used for its determination. The mentioned tables enable one to find quickly such cases. As always, tensors describing both the mentioned optical properties should be expressed in one coordinate system common to all domain states to be distinguished and obviously the system of the phase G is the most practical. To determine the best conditions for obtaining optical contrast delineating the domains in question is then the task of linear crystal optics. The latter is a classical topic highly developed in optical mineralogy on which there are a number of excellent monographs (see, e.g., Bloss, 1961; Wahlstrom, 1979). Here we will not go into any details but include a number of remarks specific to the task of resolving domains.

Spatial resolution is of the order of half a wavelength of visible light, and optical microscopy can successfully compete with a number of methods which may be more demanding as for conditions of sample preparation. Here we require properly oriented transparent samples with optically flat surfaces. These conditions can be usually met with single crystals but not with samples of ceramic materials. There, the presence of grain boundaries, pores, and generally a large density of ferroelastic domains are complicating factors leading to pronounced light scattering effects. The need to understand the behavior of domains under applied electric field in some ceramics used for electromechanical applications has made optical studies of ceramic samples desirable (Oh et al., 1994). One possibility is to isolate a large enough single crystalline grain in a thin sample; then the conditions come close to those for a crystal. Targeted manufacturing processes and a careful sample preparation are required (Schmid, 1993). The other possibility which has been yet very little utilized is observations in reflected light.

level in optics by many papers, as well as by his valuable book *Introduction to Theoretical and Experimental Optics* (John Wiley & Sons, 1960). Perhaps lack of equipment, or preparation of sample surfaces By performing such observations, ferroelectrics could have “beaten” ferromagnetics by 10 years (Fousek, 1994).

The basic required instrument is a good-quality optical microscope for polarized light, equipped with a calibrated compensator of either Berek or Sénarmont type to measure retardation. It may be of advantage if the stage or the sample holder is more universal, allowing for tilting of the crystal plate. Many optical studies are performed at elevated or at low temperatures, using heating stages or optical cryostats. Data can be obtained for temperatures up to several hundred degrees centigrade or down to the liquid helium temperature; then objectives are used with long working distance of up to several centimeters. Sample holders can be equipped with electrical contacts or devices which make it possible to apply electric field or uniaxial stress on the sample. Periodic dynamic domain processes can be observed using stroboscopic illumination (Fousek and Brezina, 1960; Brezina et al., 1961), and this method allows one to achieve maximum spatial resolution together with outstanding time resolution when very short light pulses are used. Instead of observations by naked eye the use of CCD cameras is now becoming widespread; a high-resolution CCD microscope (Oh et al., 1994) makes it possible to reveal details and to monitor and record dynamic domain processes and proceed later with their analysis.

In most cases the optical contrast originates from the fact that in different domains the *optical indicatrix* is differently oriented. Let us recall some basic concepts. The behavior of light propagating through a nonabsorbing medium is customarily described by the indicatrix

$$B_{ij}x_i x_j = 1, \quad (4.6.1)$$

where $B_{ij} = dE_i/dD_j$ are components of optical impermeability. In the principal coordinate system, the equation of this ellipsoid simplifies to

$$B_1 x_1^2 + B_2 x_2^2 + B_3 x_3^2 = 1, \quad (4.6.2)$$

where $B_i = 1/n_i^2$, n_i are the principal refractive indices and their differences

$$\Delta_{ij}n = n_i - n_j \quad (4.6.3)$$

define the values of principal birefringence. Polarized light microscopy is customarily performed with plate-like samples. Intersection of the indicatrix (4.6.1) with the major plane of the sample is an ellipse whose main axes are x_k , x_l ; in this coordinate system it is described by

$$B_k x_k^2 + B_l x_l^2 = 1. \quad (4.6.4)$$

Propagation of the light beam perpendicularly to the plate is governed by refractive indices n_k , n_l given by $B_i = 1/n_i^2$, $i = k, l$. The difference

$$\Delta_{kl}n = n_k - n_l, \quad (4.6.5)$$

i.e., the birefringence for the given orientation of the plate, determines the phenomenon of double refraction. Now we are interested in the case where the plate contains domains representing two domain states 1, 2 of the given ferroic crystal, whose indicatrices differ in orientation:

$$B_{ij}^{(1)} x_i x_j = 1 \quad \text{and} \quad B_{ij}^{(2)} x_i x_j = 1. \quad (4.6.6)$$

The tensor B_{ij} transforms in the same way as strain. Therefore, observation methods based on differences in birefringence can only be used for ferroelastic domain pairs. Tensor components are related by the transformation

$$B_{ij}^{(2)} = a_{ik} a_{jl} B_{kl}^{(1)}, \quad (4.6.7)$$

where a_{ik} is the matrix of direction of cosines corresponding to one of the twinning operations which brings domain state 1 into domain state 2. Intersecting both indicatrices with one plane representing the crystal plate results, in a general case, in two ellipsoidal sections differing in both the orientation of main axes as well as in the value of birefringence. Both these quantities may play a vital role in distinguishing the two domain states and this is in fact the whole essence of optical methods based on double refraction. They have two applications. If the symmetry groups G and F are known, we also know the matrix a_{ij} and our task is to design the arrangement so that these two indicatrices provide a good optical contrast. If we see domains but the information about G , F is limited, we try to analyze mutual relation of the indicatrices to determine the twinning operations.

Consider a birefringent crystal plate of thickness d whose major plane is parallel to the x_k, x_l axes placed between crossed polarizers. When illuminated by monochromatic light of wavelength λ and intensity I_0 , the transmitted intensity is

$$I = I_0 \sin^2 2\theta \sin^2(\pi d \Delta n_{kl} / \lambda), \quad (4.6.8)$$

where θ is the angle between the vibration plane of the polarizer and the vibration direction of the larger of refractive indices n_k, n_l . If the crystal plate contains domains representing a ferroelastic domain pair, the optical contrast, i.e., the difference in intensities I , may be of one or more of several origins. The domains may differ in their extinction directions (i.e., angles θ), in the values of Δn_{kl} or in the sign of the latter. Rotating the sample between crossed polarizers is usually sufficient to establish contrast in the two first-mentioned cases while a compensator, adding a path difference, is required in the last case. Which of these cases are realized depends on the first place on the transformation (4.6.7). However, we have to recall that when the ferroelastic species is given, the transformation matrices a_{ij} are defined in the parent clamping approximation; to ensure coexistence of two domains representing two ferroelastic domain states, a small rotation given by the clamping angle must be added. We shall illuminate this point on two examples discussed below.

What has been said in the preceding paragraph refers to the bulk of neighboring domains. If they are separated by a wall which is inclined with respect to

the plate normal, the light beam hitting the wall propagates successively through the two domains. In this case in the region on which the inclined wall projects, we may observe interference effects connected with the wedge-shaped form of both domains above each other. But sometimes a ferroelastic wall perpendicular to the plate is often visible by itself, even in nonpolarized light. The apparent thickness of a 90° wall in tetragonal BaTiO_3 is several tenths of a micrometer (Little, 1955). Theoretically, there is a possibility to distinguish optically domain boundaries themselves since obviously because of the deformed crystal lattice they differ in optical permittivity from the surrounding domains. However, most data indicate that domain walls have thickness far below optical resolution. Thus the direct visibility of a ferroelastic wall has little to do with its real width. It is mediated by reflection and refraction of light beam which is not perfectly parallel to the wall. Corresponding refraction phenomena have been studied for several materials (Tsukamoto et al., 1982, 1984; Koralewski and Szafranski, 1989).

Before giving several examples of typical situations, we wish to discuss the so-called *spontaneous birefringence*, a very often used concept. Let the indicatrix in the parent phase be

$$B_{ij}^{(p)} x_i x_j = 1 \quad (4.6.9)$$

and that in domain state 1 of the ferroelastic phase be

$$B_{ij}^{(1)} x_i x_j = 1, \quad (4.6.10)$$

which can be considered as the indicatrix in the parent phase which has been “deformed” due to the phase transition. This deformation can be described by the spontaneous changes of impermittivity, namely

$$\delta_S B_{ij}^{(1)}(T) = B_{ij}^{(1)}(T) - B_{ij}^{(p)}(\text{extrap.}), \quad (4.6.11)$$

where the last term denotes the value extrapolated to temperature T . It is easy to realize that $\delta_S B_{ij}^{(1)}(T)$ is in fact the exact analogue of natural spontaneous strain $\varepsilon_{S_{ij}}$. Since B_{ij} and ε_{ij} transform in the same way, Table C.1 and Appendix D, which provide information on ε_{ij} , can be used to specify components of $\delta_S B_{ij}$ for all ferroic species. Some components $B_{ij}^{(p)}$ can equal zero by symmetry; then the components $\delta_S B_{ij}^{(1)}(T)$ are newly acquired in the ferroic phase and we call them “morphic” components. It can be shown (Fousek and Petzelt, 1979) that there are five different possible types of how the indicatrix of the parent phase is deformed due to the phase transformation. They fall into three categories:

1. The indicatrix equation contains only diagonal terms in both phases so that $\delta_S B_{ij}^{(1)} = 0$ for $i \neq j$. Both phases belong to cubic, optically uniaxial, or orthorhombic systems. Changes $\delta_S B_{ij}^{(1)}$ in diagonal components lead to the

changes of refractive indices $\delta_S n_i = -(1/2)n_i^3 \delta_S B_{ii}$ and corresponding change of birefringence

$$\delta_S \Delta_{ij} u = \delta_S u_i - \delta_S u_j \quad (4.6.12)$$

is referred to as the *spontaneous birefringence*. Note that because of relation (4.6.11) it may only represent the difference between the actual birefringence at the given T and the extrapolated birefringence. If in the parent phase the given component is zero, we speak about the *morphic birefringence*.

2. One of the nondiagonal components $\delta_S B_{ij}^{(1)} \neq 0$ ($i \neq j$). To be specific, let us take $\delta_S B_{12}^{(1)} \neq 0$; other choices would lead to analogous conclusions. Now, three cases are possible. (2a) $n_1 = n_2$ and $\delta_S B_{11}^{(1)} = \delta_S B_{22}^{(1)}$. Then the main indicatrix axes in the ferroic phase make a fixed angle of 45° with the old axes. In this new coordinate system we have three different morphic principal birefringence values for cubic to orthorhombic transitions ($n_1 = n_2 = n_3$ in the parent phase) and one principal morphic birefringence $\delta_S \Delta n_{12}$ for the tetragonal to orthorhombic transition ($n_1 = n_2$ in the parent phase). (2b) $n_1 = n_2$ and $\delta_S B_{11}^{(1)} \neq \delta_S B_{22}^{(1)}$. Now the indicatrix rotates about the axis 3. For cubic to monoclinic transitions three morphic principal birefringence values occur; for tetragonal to monoclinic transition only $\delta_S \Delta n_{12}$ is nonzero. (2c) $n_1 \neq n_2$. Since only one nondiagonal $\delta_S B_{12}^{(1)} \neq 0$, this is the case of orthorhombic to monoclinic or monoclinic to monoclinic transitions. No birefringence is morphic; the indicatrix rotates about the c -axis. For monoclinic to monoclinic transitions, this rotation is already allowed by symmetry in the parent phase and the definition of “spontaneous” rotation is similar to that given by Eq. (4.6.11).
3. In the general case all $\delta_S B_{ij}$ are nonzero. This would correspond either to transitions into a triclinic ferroic phase or to transformations in which the indicatrix axes rotate by a fixed spatial angle, changing, e.g., into body diagonals of the parent cubic cell.

It should be pointed out that since transformation properties of strain ε_{ij} and optical impermeability B_{ij} are the same, most of what was said about spontaneous strain can be transferred into the realm of optics. However, in practice the two tensor properties are dealt with in a different way. This is true in particular when the concept of spontaneous birefringence is used, since it refers to the coordinate system of the phase F .

We now give several examples of typical situations illustrating how optical contrast can be achieved between two domain states based on Eq. (4.6.8). Let us first consider the species $m\bar{3}m - 4mm$. The spontaneous changes of B_{ij} can be extracted from Table C.1 for the subgroup $4_z mm$. We have in mind a crystal plate perpendicular to the cubic z -axis of the parent phase, in which two domain states S_A, S_B represent equivalent subgroups $4_x mm$ and $4_y mm$, respectively. For the domain state S_A the nonzero spontaneous changes of the B_{ij} tensor are obviously $\delta B_{xx} \equiv a$ and $\delta B_{yy} = \delta B_{zz} \equiv b$. The twinning operation is a rotation by 90° about the c -axis so that for the domain state S_B we have $\delta B_{xx} = \delta B_{zz} \equiv b$ and

$\delta B_{yy} \equiv a$. While in the cubic phase the equation of the indicatrix was $B_0(x^2 + y^2 + z^2) = 1$, for the two domain states we now have the following cross-sections of the indicatrices:

$$S_A : (B_0 + b)x^2 + (B_0 + a)y^2 = 1, \tag{4.6.13a}$$

$$S_B : (B_0 + a)x^2 + (B_0 + b)y^2 = 1. \tag{4.6.13b}$$

The principal axes for both domain states will be identical with the cubic axes while the birefringence values

$$\Delta n_{xy}(S_A) = n_x - n_y = -(1/2)n_0^3(b - a), \tag{4.6.14a}$$

$$\Delta n_{xy}(S_B) = n_x - n_y = (1/2)n_0^3(b - a) \tag{4.6.14b}$$

differ only in sign. Because of this and since the principal axes are the same, the transmitted light intensity given by Eq. (4.6.8) will be the same for both domain states. This is, of course, only true in the parent clamping approximation. In fact the extinction orientations differ by the clapping angle φ . The geometry of this case is shown schematically in Fig. 4.6.1a. The clapping angle is usually too small to become essential in standard observations. The situation changes when an additional birefringent plate is inserted adding the value Δ to the optical paths for both domain states. Then the total optical paths will be $\Delta + [(1/2)n_0^3(b - a)]t$ and $\Delta - [(1/2)n_0^3(b - a)]t$, respectively, where t is the thickness of the sample and a high contrast in intensity of the transmitted light will be achieved. This is how 90° domains in BaTiO_3 and other tetragonal perovskites can be easily distinguished.

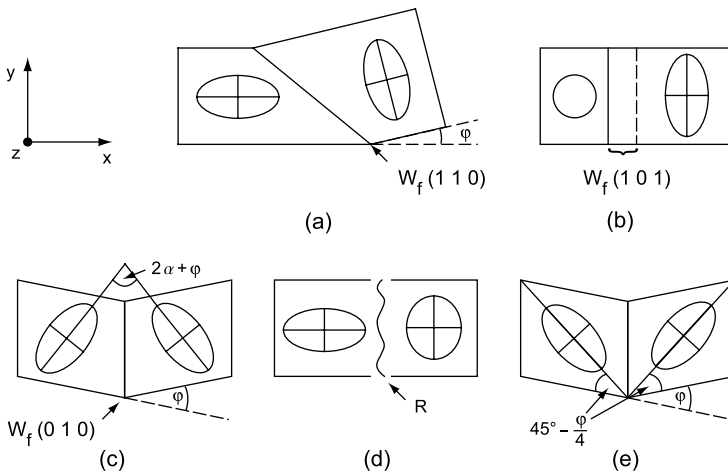


Fig. 4.6.1 Schematic representation of indicatrix sections for different domain pairs. See text. The sections of the indicatrix ellipsoids specify the symmetry of the observed planes of neighboring domains. φ is the clapping angle, α is the extinction angle

When in the given crystal plate one of the domain states is S_C corresponding to the subgroup 4_2mm , the domains will be easily distinguishable as shown in the Fig. 4.6.1b.

As a second example we consider the species 23-2, the case of lagbeinites. We start again with the isotropic indicatrix $B_0 (x^2 + y^2 + z^2) = 1$ of the parent phase. Consider two domain states S_A , S_B corresponding to positive and negative spontaneous polarization along the z -axis, i.e., the subgroup 2_z . Here the twinning operation is the twofold axis along x . From the form of spontaneous strain specified in Table C.1 we easily deduce that for both domain states $\delta B_{xx} \equiv a$, $\delta B_{yy} \equiv b$, $\delta B_{zz} \equiv c$ while $\delta B_{xy} \equiv d$ for the state S_A but $\delta B_{xy} = -d$ for the state S_B . Their indicatrices now read

$$S_A : (B_0 + a)x^2 + (B_0 + b)y^2 + (B_0 + c)z^2 + 2dxy = 1, \quad (4.6.15)$$

$$S_B : (B_0 + a)x^2 + (B_0 + b)y^2 + (B_0 + c)z^2 - 2dxy = 1.$$

We now have in mind a plate perpendicular to the z -axis. Principal axes of the indicatrix sections for the two domain states make an angle α with the original axes x , y given by

$$\tan \alpha = \pm \frac{2d}{a - b}. \quad (4.6.16)$$

Thus the difference in extinction angles is 2α and both domain states can be easily distinguished between crossed polarizers. The clapping angle φ adds to the value of α , as shown in Fig. 4.6.1c.

Spontaneous birefringence is given by (Glogarová and Fousek, 1972)

$$\Delta n'_{12} = -n_o^3 \left(d + \frac{a^2 - b^2}{8d} \right) = -n_o^3 |d| \left[1 + \frac{1}{2(\tan 2\alpha)^2} \right], \quad (4.6.17)$$

where the prime symbol emphasizes that birefringence is measured with respect to the new principal axes. Plates perpendicular to the z -axis containing other pairs of domain states in this species which involve subgroups 2_z , 2_x or 2_z , 2_y differ in the value of birefringence only. These pairs actually correspond to the R cases defined in Sect. 2.2.4. Figure 4.6.1d portrays this situation.

It is essential to note that in this case mutual rotation of the two indicatrices is independent of the clapping angle which is determined by spontaneous strain. Both effects may add up. This situation occurs often and by measuring the angle between extinction positions alone the shear component of spontaneous strain cannot be reliably determined. The problem was addressed by Koralewski and Szafranski (1989) who specified the angles between extinction positions as well as the clapping angles for two materials. In Rochelle salt (species 222- 2_x) at $T = 280$ K $\varphi = 3'$, $2\alpha = 2^\circ 30'$. In lithium ammonium tartrate (species (222- 2_y)) at about 80 K $\varphi = 2^\circ 18'$, $2\alpha = 6^\circ$.

Let us finally inspect the species $\bar{4}2m - mm2$, the case of KH_2PO_4 or $\text{Gd}_2(\text{MoO}_4)_3$ crystals. Using the designation of the previous example, we have in this case $a = b$ so that in the parent clamping approximation the principal axes of both indicatrices make an angle of 45° with the tetragonal axes. In this approximation the extinction orientations of both domain states coincide but again as in the first quoted example, the indicatrix cross-sections are rotated by 90° with respect to each other. To achieve a good contrast a compensator adding an optical path has to be used. In addition, the clamping angle may also contribute to the contrast. The situation is depicted in Fig. 4.6.1e.

Analysis of birefringent properties of individual domain states and orientational relations between the indicatrices together with the orientations of domain walls represent powerful methods for determining the species of a particular ferroic, even before a thorough X-ray structural analysis could be performed. Out of many available examples we mention the determination of the species pertinent to $\text{Bi}_4\text{Ti}_3\text{O}_{12}$. It was the optical analysis (Cummins and Cross, 1967, 1968) of coexisting domain states observed in two mutually perpendicular plates that led to the recognition of the species $4/mmm - P\epsilon ds - m_{xy}$.

All that has been said in this section was formulated as if we had in mind static observations. Very often the most valuable information about domains can be obtained by monitoring the differences in domain structures when external forces are or are not applied. Fast kinetic domain processes induced by periodic forces are conveniently investigated by microscopic observations in polarized light with a stroboscopic illumination. Motion of ferroelectric-ferroelastic domain walls in an ac electric field (Stadler, 1966; Fousek and Brezina, 1960; Shur et al., 1989a) was studied in this way. The method makes it easily possible to attribute particular domain events to their macroscopic manifestations such as Barkhausen pulses (Brezina et al., 1961). An alternative to stroboscopy is a CCD microscope (Mulvihill et al., 1997).

Optical distinction of domains based on birefringent properties may have a number of practical applications in displays, optical valves, or as a background for nondestructive reading of ferroelectric memories.

4.6.2 Spatial Dispersion

In short we wish to mention a special case where domain states can be distinguished also by a linear optical property which is different from the simple linear birefringence discussed above. Additional possibilities for optical delineation of domains occur when the effect of spatial dispersion is taken into account, i.e., when one takes into account that the optical polarization at a given point of the crystal depends not only on the local electric field at that point but also on its value in the surroundings, i.e., on its spatial derivatives:

$$P_i(\mathbf{r}) = \alpha_{ij}E_j(\mathbf{r}) + \gamma_{ijk}\frac{\partial E_j(\mathbf{r})}{\partial x_k} + \beta_{ijkl}\frac{\partial^2 E_j(\mathbf{r})}{\partial x_k \partial x_l}. \quad (4.6.18)$$

Here the term containing the first derivatives is responsible for the phenomenon of *optical activity*, which will be addressed in detail in the next section. The term containing the second derivatives describes an effect of spatial dispersion different from optical activity (often shortly called *spatial dispersion*). The tensor controlling this effect, β_{ijlm} , is of the same symmetry $[V^2]^2$ as the tensor of photoelastic constants. This effect contributes to optical permittivity of the material with a term proportional to $\beta_{ijlm}k_jk_m$, where k_i are the components of the light wavevector. This means that, in some experimental situations, the natural birefringence can be observed in cubic crystals, which is induced by effect of spatial dispersion.

From the point of view of domain observation, this effect can enable delineation of the domains which differ by a tensor of $[V^2]^2$ symmetry. Species where this effect could become essential are evident from Tables 2.2.1 and 2.2.2. Crystals undergoing a phase transition within the cubic system, e.g., those representing species 432–23 are the best candidates. We know of no cases where the spontaneous birefringence based on spatial dispersion has been used for domain observation. However, low-angle twins in cubic crystals of $\text{Ni}_3\text{B}_7\text{O}_{13}\text{I}$ with the symmetry $\bar{4}3m$ have been delineated on the basis of this effect (Pastrnak and Cross, 1971).

4.6.3 Optical Activity

We now come to one additional tensor property which may serve for distinguishing domains in a polarizing microscope, namely *optical activity*. As was mentioned in the previous section, in terms of the constitutive equation, the effect of *optical activity* is associated with the lowest gradient term in it. Taking into account this effect results in a modification of the evolution of polarization of light when it travels across a crystal. Customarily, this effect is treated in terms of the so-called gyration tensor g_{ij} that can be expressed in terms of the third-rank tensor γ_{ijk} from Eq. (4.6.18) (see, e.g., Nye, 1992; Agranovich and Ginzburg, 1979). The gyration tensor is an axial one. Therefore, its components in two domain states (A), (B) are related by the transformation

$$g_{ij}^{(B)} = \pm a_{ik}a_{jl}g_{kl}^{(A)} \quad (4.6.19)$$

in which the sign depends on whether the hand of the axial systems is retained (sign +) or changed (sign –). In fact, the sign depends on whether the twinning operation contains reflection or if it is a pure rotation. Gyration tensor has nonzero components in 15 crystal classes, and in ferroic phases with these symmetries the optical activity might be useful for optical distinction of domains if the corresponding domain states differ in g_{ij} . For species of proper ferroelectrics, Shuvalov and Ivanov (1964) performed a crystallographic analysis of effects connected with gyration.

It is important to realize that if, in a crystal, light propagates in a general direction with respect to the principal indicatrix axes, the effects of optical activity are superimposed onto the effects of birefringence and can be regarded as a small perturbation of the latter (Nye, 1992). The task of determining the gyration tensor components for such propagation directions is difficult and in fact there are many controversies in literature concerning the validity of published data for a number of ferroelectrics. Therefore, in practice, when we face the task to optically distinguish domains in a ferroelastic domain pair, obviously the simple method will be based on differences in the indicatrices, even if the two domains differ also in the tensor g_{ij} .

If the domain pair is *nonferroelastic*, optical activity may become important. Tables 2.2.1 and 2.2.2 enable one to see immediately in which ferroic species nonferroelastic domain pairs can be distinguished by optical activity and to show how many components of the gyration tensor can be used. Note that if the two domain states differ in enantiomorphism, they also differ in the optical activity tensor, but not vice versa. Again, however, for a general propagation vector the birefringence effects will be overwhelming. We shall see later that changes of optical activity due to domain reorientation have been observed for a number of biaxial crystals (see, e.g., Kobayashi, 1991) but the effect is not suitable for imaging domains, being overshadowed by birefringence effects. A qualitatively different situation arises when the light propagates along an optic axis for which birefringence is zero, i.e., we have in mind a crystal plate oriented so that $n_k = n_l$ in Eq. (4.6.5). Then the incident linearly polarized light wave splits into two circularly polarized waves, one right-handed and the other left-handed (see Heising, 1947 for definitions of handedness and Otko et al., 1989 for more general discussion of optical activity), which propagate with velocities c/n_{right} and c/n_{left} , respectively. On leaving the crystal plate of thickness t they combine in a linearly polarized wave whose vibration plane is rotated with respect to that of the incident plane by the angle

$$\phi = \frac{\pi t}{\lambda_0} (n_{\text{left}} - n_{\text{right}}) \quad (4.6.20a)$$

or

$$\phi = \frac{\pi t}{\lambda_0 n} G_0, \quad (4.6.20b)$$

where λ_0 is the wavelength in vacuum and n is the refractive index that the crystal would have in the absence of optical activity. The ratio of ϕ/t is often referred to as the rotatory power ρ for the given orientation. The value of G_0 depends on the direction cosines l_k of the optical wave normal. It is defined by

$$G_0 = g_{ij} l_i l_j, \quad (4.6.21)$$

where $g_{ij} = g_{ji}$ is the gyration tensor.

While optic axes with general orientations can be found even for optically biaxial phases, the real strength of the effect will manifest itself in cases of optically uniaxial crystals when plates with crystallographic prominent orientations are not birefringent but can be optically active.

Crystals of $\text{Pb}_5\text{Ge}_3\text{O}_{11}$ representing the species $\bar{6} - Pd - 3$ offer the best known example of the effect. The two domain states have the same uniaxial indicatrix with the optical axis z but differ in sign of the gyration tensor components $g_{11} = g_{22}$ and g_{33} and can be easily distinguished in polarizing microscope on the basis of Eqs. (4.6.20) and (4.6.21). The effect can be observed for crystals of good quality (Dougherty et al., 1972; Shur et al., 1985b); an example is shown in Fig. 2.2.8.

Related observations were made even earlier for crystals of quartz. However, there it is not domains (“electrical twins”) which can be distinguished by optical activity but rather growth twins (“optical twins”) existing already in the parent phase.

4.6.4 Optical Absorption and Observation in Reflected Light

In the preceding discussion the concept of optical absorption has not been mentioned at all. But in fact the optical permittivities are complex quantities whose imaginary parts reflect absorption phenomena. Strictly speaking, a complex refractive index $n^* = n - ik$ should be used to characterize a material. Here k is the extinction coefficient which determines the ratio of intensities I and I_0 of transmitted and incident light, respectively:

$$k = \frac{\lambda}{4\pi t} \ln \left(\frac{I_0}{I} \right). \quad (4.6.22)$$

Here λ and t are the light wavelength and the sample thickness, respectively. In some materials and depending on the light wavelength, the extinction coefficient and thus optical absorption may be strongly anisotropic, the phenomenon of linear dichroism. Turmaline provides a well-known example of linear dichroism. In some ferroics—for instance in those containing transition metal ions with incomplete d -shells—the effect of anisotropic dichroism is superimposed on the effect of linear birefringence and may contribute to optical distinguishability of ferroelastic domains. Propagation of light in such a system has been discussed by Rivera (1993). The effect was found to give a contribution to domain distinction in ferroelastic $\text{K}_3\text{Fe}_5\text{F}_{15}$ (Ishihara et al., 1993).

Domains can also be observed in reflected light. The real strength of these observations manifests itself when ferroelastic domains in nontransparent materials are investigated. Ferroelastic domains in crystals of $\text{YBa}_2\text{Cu}_3\text{O}_{7-x}$ were investigated in this way by Schmid et al. (1988) and others (Vlasko-Vlasov et al., 1988; Rabe et al., 1989); particularly appealing color plates of domain patterns in this material have been published (Rabe et al., 1993). It was observed that for complexes of small domains the analysis of reflected patterns may not

be simple. When investigating stacks of lamellar domains with a high density of domain walls such that the domain width is close to or below the resolution of the microscope, the reflectivity may mimic a symmetry inconsistent with the X-ray results. One of possible interpretations refers to the possibility that the domain wall itself is characterized by a complex refractive index which is slightly different from that of the bulk crystal (Rabe et al., 1990; Schmid, 1993).

4.7 Optical Methods Based on Higher Order Optical Properties

In the previous section we dealt with optical differences of domains, most of which could be observed under a microscope using linearly polarized light. It was assumed that the employed optical properties were such as given by basic tensor properties of individual domain states, the only exception being the existence of the clapping angle to bring domains into physical contact. No external forces were assumed to be applied. Therefore, the choice of tensor properties available to distinguish domains was relatively narrow. If, however, domains are placed into an electric field or are mechanically stressed, additional properties may lead to optical contrast if the two domain states differ in some components of electro- or elasto-optic tensors. Such fields may be applied intentionally but very often they may be present due to boundary conditions of the sample or due to defects. The basic information—which fields can be helpful to image domains—is subject to a similar analysis as for unperturbed properties. We ask, for example, how the electro- or elasto-optic tensors are transformed from one domain state to the other and which field component, when applied, would cause differences in induced birefringence. Twinning operations are helpful in performing this task. Methods based on perturbed optical properties can be very useful and in the following paragraph we mention several examples of such approaches.

Still other optical methods for domain visualization rely on nonlinear optical characteristics. Even more involved optical attributes represent photorefractive properties of crystals. Both of them require fairly advanced experimental setups and will be treated in the subsequent sections.

4.7.1 *Perturbed Linear Optical Properties: Electro-optics and Elasto-optics*

An illustrative example of the approach based on linear electro-optic effect was given by Pique et al. (1977). In crystals of NH_4Cl (species $m\bar{3}m - d - \bar{4}3m$) the two domain states differ in the sign of the electro-optic coefficient r_{63} . When an electric field is applied along the [001] direction, the B_{ij} tensor is modified as

$$\delta B_6 = \pm r_{63} E_3, \quad (4.7.1)$$

where the sign depends on the domain state. A laser beam propagating along [110] direction experiences optical retardation which is of opposite sign in the

two domains. This produces optical contrast similarly as if the domains would differ in spontaneous birefringence. Clear pictures of domain patterns were obtained in fields of 20 kV/cm.

The application of properly oriented electric field was used to visualize domains also in several classical ferroelectrics. Borodina and Kuznetsov (1984) applied the field normally to the c -axis of tetragonal BaTiO₃ crystals. This leads to an inclination of the indicatrix by an angle whose sign differs for domains with antiparallel \mathbf{P}_S . In crossed polarizers, domains cannot be distinguished when the light beam is strictly parallel to the c -axis. However, inclining the sample so that the beam propagates along the optical axis in domains of one sign, the indicatrix of the other domain becomes inclined with respect to the beam and optical contrast is obtained. Otko et al. (1993a) used the same method to image domains in LiNbO₃. These authors have also shown that the required electric fields can also arise due to the pyroelectric effect. Domain walls which are not parallel to \mathbf{P}_S carry bound charge which can be expected to be compensated by trapped free carriers. A fairly quick cooling of lithium niobate sample results in an increase of \mathbf{P}_S so that compensation is violated and the excess bound charge induces strong internal field. This in turn reduces the symmetry of optical indicatrix (“pyroelectrooptical effect”) and domains become visible in polarized light. In lithium niobate, these internal fields can survive for several days. These observations show several characteristic features. The distribution of visible anomalies is extremely uneven, dependent on the domain shape and observation conditions. Induced optical anomalies are strongly concentrated in the close vicinity of domain walls so that one can see the visualized domains as shining transparent envelopes. Superimposed on these images are complicated interference patterns. Otko and coworkers (Otko and Stasyuk 1995; Otko et al., 1997) worked out a theoretical analysis and computer simulation of such domain images based on the assumption that all refractive index anomalies are concentrated within a thin layer near domain walls while the bulk of the domains remains in an undisturbed optically uniaxial state.

The electro-optical method was also employed to map domain patterns in KTiOPO₄ (Bierlein and Ahmed, 1987; Ivanov et al., 1994); while such studies do not offer a very high resolution compared to surface techniques used for this material (etching, LC decoration), they have the advantage of providing some information about the representation of domain states along the optical path of the propagating light beam.

Another remarkable example of employing perturbed linear optical properties was offered by Aizu (1973b) for quartz. In the species 622- ds -32, the two domain states (we have in mind Dauphiné twins) differ in components of the elastic compliance matrix and therefore also in components of the elasto-optic tensor π_{mn} defined by

$$\delta B_m = \pi_{mn} \sigma_n, \quad (4.7.2)$$

which is of the same rank but of lower symmetry. The component π_{42} is of opposite sign for different domains. This makes possible the delineation of

domains. A crystal plate with (011) faces is observed in polarized light. The uniaxial pressure applied along [011] causes rotation of the indicatrix whose sign differs for the two domains, leading to a pronounced optical contrast. Dolino (1975) employed a similar technique and described in detail the experimental setup which could also be combined with observing domains on the basis of their electro-optical properties.

It is obvious that in addition to these engineered experiments, fields in a multidomain sample may be present due to a number of natural causes. In the early stages of domain investigations it was frequently noticed that domains were seen in polarized light when they should not have been. The most often encountered examples are those of 180° domains in tetragonal BaTiO_3 . Merz (1952, 1954) observed dense patterns of them contained between parallel 90° walls, in light propagating nearly perpendicular to the polar c -axis. There are many possible sources of such effects. Even slight changes of temperature may produce an enormous electric field in an isolated ferroelectric crystal if pyroelectric coefficients of the particular material are high. Alternatively, the field may result from freshly formed domain patterns containing walls with uncompensated bound charge or simply from the charge $-\text{div}\mathbf{P}_S$ located at the crystal surface. Similarly, complicated ferroelastic domain patterns necessarily result in stress fields. All these fields may lead to an optical contrast between domains which is not compatible with their unperturbed properties.

We now mention observations of domains or domain walls under dynamic conditions. The real breakthrough in studying polarization reversal process in BaTiO_3 was the discovery made by Miller and Savage (1959a) who found that 180° domains produce an optical contrast when placed between crossed polarizers and viewed *along* the polar direction in white light. These and the later data (Merz, 1956; Miller and Savage, 1961; Brezina and Fotcenkov, 1964) relate to observations of domains which have been recently formed or modified by an applied electric field. Being observed through transparent thin evaporated gold or liquid electrolyte, the reversed domains generally appeared darker than the surrounding regions. Nakamura et al. (1963) obtained very distinct pictures of antiparallel domains in the same geometry; again, these were only visible for a short time after they had been formed by applied field. Similarly, Kobayashi (1967) observed narrow 180° domains during their growth process in an applied electric field in a crystal free of 90° domains, in light propagating nearly perpendicular to the c -axis. Later, similar observations were reported by Sinyakov et al. (1972) in samples about $2\ \mu\text{m}$ thick. All these observations corroborates with the X-ray diffraction data for BaTiO_3 , which suggest that the freshly switch areas are optically biaxial, probably of monoclinic symmetry (Kobayashi et al., 1963).

The lesson that can be deduced from the described experiments is that even if the simple symmetry analysis indicates that domain pairs in a particular material could not be optically observed directly, there may be many ways how to circumvent this obstacle and still use the basic optical equipment.

4.7.2 Nonlinear Optical Properties

We have seen that restricting ourselves to “unperturbed” optical properties, linear optics can give information on nonferroelastic domains only in rare cases when spatial dispersion effects can be applied. New possibilities are offered by nonlinear optical properties and we first give a very brief introduction to the topic. Noncentrosymmetric classes allow the existence of nonzero components of the nonlinear susceptibility χ_{ijk}^{NL} in the relation

$$P_i^{\text{NL}} = \chi_{ijk}^{\text{NL}} E_j E_k. \quad (4.7.3)$$

Considering electric field at optical frequencies, this nonlinear dependence leads to a number of phenomena depending on the frequencies of the fields. Here we are interested in just one of them, generation of the second optical harmonics (SH). It is governed by tensor $\chi_{ijk}^{\text{NL}}(2\omega)$ which is symmetric in the indices j, k so that its symmetry is the same as that of the piezoelectric coefficient d_{ijk} . Assume that the incident light beam propagates along the z -axis, i.e.,

$$E(\omega) = E_0 \cos(\omega t - q_1 z), \quad (4.7.4)$$

with velocity $\omega/q_1 = \omega n/c$. For simplicity we omit indices. To avoid diffraction from the edges, the beam cross-section must be smaller than the entrance face of the sample; in turn, the thickness of the latter must be small enough to avoid broadening of the beam due to diffraction. By virtue of nonlinear properties of the material at each location the second harmonic polarization wave (“source wave”)

$$P = \chi^{\text{NL}}(2\omega) E_0^2 \cos(2\omega t - 2q_1 z) \quad (4.7.5)$$

is generated. It serves as a source of a field wave at a frequency 2ω

$$E(2\omega) = E_1 \cos(2\omega t - q_2 z), \quad (4.7.6)$$

whose amplitude E_1 is proportional to χ^{NL} . Because of the dispersion, $n(2\omega) \neq n(\omega)$ this wave propagates with a velocity different from the source term, i.e., $q_2 \neq 2q_1$. Harmonics generated at different parts of the crystal interfere. This interference is destructive when the propagating wave covers a distance which is an even multiple of the *coherence length*

$$l_c = \frac{\pi}{q_2 - 2q_1} = \frac{\lambda}{4[n(2\omega) - n(\omega)]}, \quad (4.7.7)$$

while after an odd number of coherence lengths the second harmonic intensity is maximum. Here λ is the free-space wavelength of the fundamental wave. Typical values of l_c are between 1 and 20 μm . Since the crystalline medium is anisotropic, in many cases a propagation direction of the fundamental wave can be found for which $n(2\omega) = n(\omega)$ so that l_c becomes infinite; it is understood that the fundamental and second harmonic waves can be differently polarized. This

situation is referred to as *phase matching*. Understandably, the *phase matching direction* depends on the wavelength of the fundamental wave.

Consider crystals of TGS, species $2/m-Pd-2$. It is apparent from this symbol or from Tables 2.2.1 and 2.2.2 that domains with opposite \mathbf{P}_S directions differ in the sign of their nonlinear optical coefficients. This fact was used by Dolino (1973) for their imaging. A plate-like crystal cut perpendicular to the ferroelectric axis and provided with transparent liquid electrodes is illuminated by a laser beam along the phase-matching direction. The cross-section of the beam scans the whole area of the plate. Figure 4.7.1 shows schematically the situation with two domains present. Rays such as AB or CD are in phase. But if a ray such as EG crosses a domain wall there is a destructive interference between the rays produced in the EF and FG sections since they are of opposite phase. Thus in projection the wall will appear black. Rotating the sample away from the phase-matching direction reverses the contrast. This is because the interference of second harmonic waves is more destructive in the single domain regions than across the boundary.

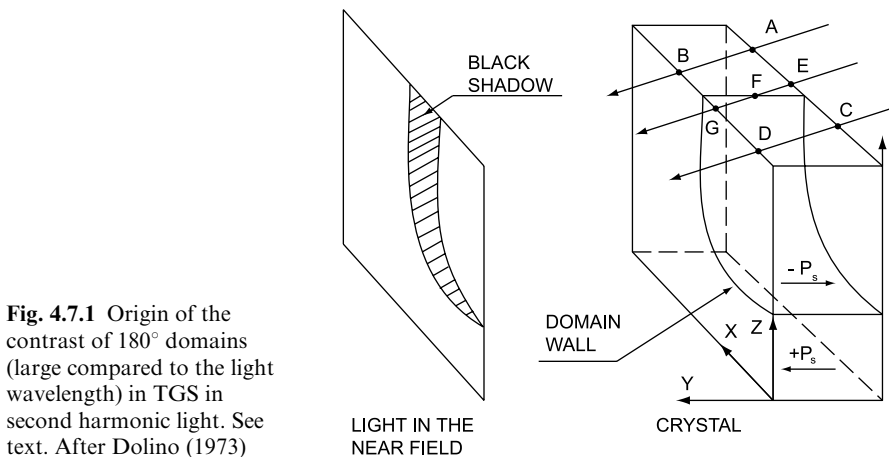


Fig. 4.7.1 Origin of the contrast of 180° domains (large compared to the light wavelength) in TGS in second harmonic light. See text. After Dolino (1973)

The same method was used to image the topography of Dauphiné twins in quartz (Dolino et al., 1973), based on the same symmetry arguments. The resolution is not high; domains are supposed to be large compared to the wavelength and complicated situations arise when the beam is crossing more than one domain wall.

Data on scattering of a SH wave provide an alternative indirect tool for obtaining data on domain shapes and sizes. Dolino et al. (1969) were the first to investigate the case where the fundamental wave hits many domains differing in the sign of the susceptibility χ^{NL} and is scattered. A laser beam hits a TGS plate with ferroelectric axis b in the major plane. The angular dependence of the SH scattered light intensity is measured in a plane perpendicular to b . The scattering

curve narrows when domains are removed by an applied field. If the fundamental wave propagates in the phase-matching direction, formation of domains decreases the SH intensity for reasons apparent from the preceding paragraph. In a later work (Dolino et al., 1970) the situation was theoretically analyzed in detail and further generalization of the theory (Dolino, 1972) offered analysis of scattering patterns in TGS so that the presence of domains of different shapes can be identified.

Weinmann and Vogt (1974) measured the angular distribution of the scattered SH intensity for different wave vectors of the incident wave, analyzing the situation in crystals of NaNO_2 where similar arguments apply. In both cases pronounced maxima of $I_{2\omega}$ are found in multidomain crystals. With T approaching T_C these maxima disappear. Theoretical analysis was done based on the previous knowledge that domains are lamellae perpendicular to a . It is concluded that with rising T the lamellar geometry stays but domains become narrower, from 30 to 50 μm at room temperature (showed by etching and being consistent with scattering data) down to 2 μm near the transition point.

An alternative study was performed by Cudney et al. (1997) for crystals of tetragonal BaTiO_3 containing only antiparallel domains. Figure 4.7.2a shows the experimental setup; the sample is oriented with its c -axis perpendicular to the plane of the drawing. The polarizer blocks the fundamental laser beam but lets the perpendicularly polarized SH wave through. The crystal is first poled and then depolarized by an applied field; the degree of depolarization is monitored by measuring the charge. Figure 4.7.2b shows scattering patterns for poled and 40% depoled sample. The scattered line is structured along the y -direction while the width along z -direction remains the same; this gives evidence that domains stretch from one surface to the other. As in the case of TGS, the nonlinear susceptibility tensor in antiparallel domains differs in sign. The SH field amplitude $E_i(2\omega)$ is a function of the wave vector mismatch $2\mathbf{q}_1 - \mathbf{q}_2$

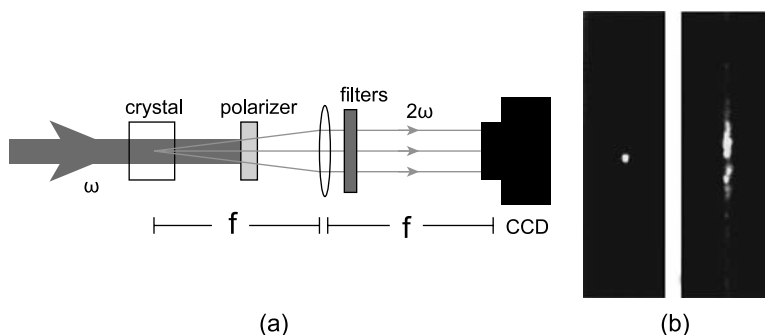


Fig. 4.7.2 (a) Experimental setup for the analysis of domains by second harmonic scattering. $f=100$ mm, pulse intensity 3 MW/cm^2 , sample dimensions $\sim 2.5 \times 5 \times 5$ mm. (b) Far-field scattering patterns for a single domain crystal (*left*) and for a crystal depoled by 40% (*right*). After Cudney et al. (1997)

where \mathbf{q}_1 is the wave vector of the first harmonics and \mathbf{q}_2 stands for that of the second harmonics. An involved analysis of the situation results in a formula for the total SGH intensity $I_{2\omega}(2\mathbf{q}_1-\mathbf{q}_2)$ which is a function of the number of domains of width a and which predicts the angular variation of the intensity of the scattered SH wave for a given distribution of domain width $g(a)$. Thus the latter can be obtained by fitting the scattering profile. The result for a sample with 80% volume of positive and 20% of negative polarization is shown in Fig. 4.7.3.

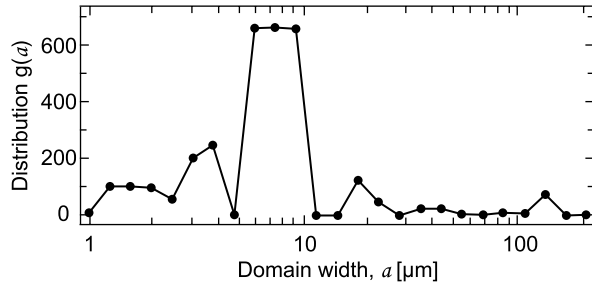


Fig. 4.7.3 Example of the analysis of SH scattering experiment with a BaTiO_3 sample doped by 20%: number $g(a)$ of 180° domains (assumed to have square cross-sections) vs. domain width a . After Cudney et al. (1997)

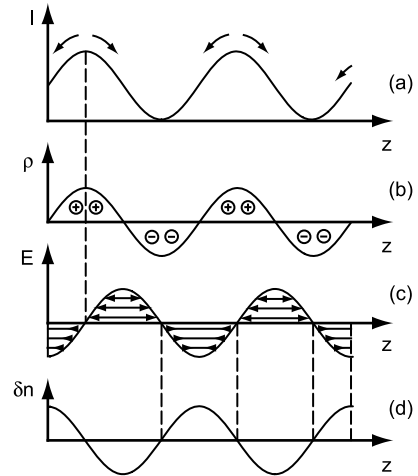
To summarize, direct observations using SH are limited to very simple domain structures. Second harmonic scattering may be a useful method where others fail. However, to analyze data correctly, the domain geometry has to be assumed or already known from other studies. Then SH scattering may give additional information on what the domain size distribution is or how it depends in such factors as temperature. Understandably, the resolution of the method is limited by the wavelength.

4.7.3 Photorefractive Properties

Some of the ferroelectric materials exhibit photorefractive properties; BaTiO_3 , LiNbO_3 and KNbO_3 represent well-investigated examples. The photorefractive may serve as an auxiliary tool for imaging domain structures. Here we briefly address its basic principles. Photorefractive has been covered in detail in several monographs (Sturman and Fridkin, 1992; Günter and Huignard, 1988).

Photorefractive effects can occur in crystals which contain suitable impurities and exhibit electro-optic properties. A sample is nonuniformly illuminated; the electrons or holes which are excited from the impurity centers by light of suitable wavelength migrate and are trapped at other locations. They will be reexcited and retrapped until they drift out of the illuminated region. Together with the ionized impurities they form a spatial distribution of charge, which results in a spatially nonuniform electric field. Via the electro-optic effect, refractive indices of the material are spatially modulated. Figure 4.7.4 illustrates this phenomenon for the case where the spatial modulation of the light intensity is sinusoidal. Since in many ferroics (whenever the species designation contains

Fig. 4.7.4 Basic scheme of the photorefractive effect. Non-uniform illumination causes charge transport (a). This results in charge redistribution $\rho(z)$ (b); it is assumed that the phase of $\rho(z)$ corresponds to diffusion as the prevailing transport mechanism. Resulting electric field (c) modulates the refractive index (d)



the symbol $-\dots Pd. \dots$) the electro-optic tensor can be different in different domains, the photorefractive pattern can provide information on the domain pattern in the material.

The idea of implementation of this technique is as follows. When a single domain crystal is exposed to spatially modulated light intensity (e.g., created by two interfering beams of light), a homogeneous grating of the refractive index is formed due to the photorefractive effect. If a ferroic sample contains domains differing in electro-optical coefficient, the grating becomes spatially modulated according to the domain pattern revealing it.

Kahmann et al. (1990) have suggested the use of this phenomenon for imaging antiparallel domains in ferroelectrics by a method named *beam coupling topography*. This method is based on the self-diffraction effect when the two incident interfering beams cross in a crystal, i.e., diffraction of the beams on the grating that they have created. The photorefractive grating results in energy transfer from one beam to the other. In a single domain sample, the sense of the energy transfer is controlled by the sign of a certain linear combination r_{eff} of electro-optic coefficients of the medium. Thus, in a multidomain sample, the antiparallel domains can be delineated by the sense of the energy transfer as it is illustrated in Fig. 4.7.5. The method was first applied to crystals of $\text{Ba}_x\text{Sr}_{1-x}\text{Nb}_2\text{O}_6:\text{Ce}$ (Kahmann et al., 1990, 1992, 1994). It is obvious that if the beam mixing takes place in two or more domains located behind each other, the contrast would become diffuse or lost. This feature was overcome by Grubsky et al. (1996). Figure 4.7.6 shows their experimental arrangement. A sample consisting of antiparallel domains is illuminated with one beam (signal beam) along its polar axis whereas the second beam (pump beam) is focused to a thin slice which is perpendicular to it. As a result only within this slice the energy transfer occurs so that the domain geometry in this slice only is represented in the intensity pattern of the transmitted signal beam, which is resisted by a CCD camera. When the

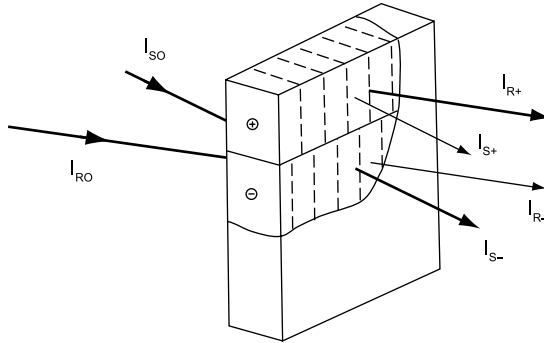


Fig. 4.7.5 Domain contrast formation by beam-coupling topography. A space charge grating is generated by interfering beams I_{R_0} and I_{S_0} , independent of domains. In antiparallel domains (denoted \oplus and \ominus), the refractive index grating is shifted by $\lambda/2$. The interference of transmitted and refracted beams amplify the intensity I_{R^\oplus} and diminish the intensity I_{S^\oplus} . The opposite holds for the domain \ominus . After Kahmann et al. (1992)

slice is scanned across the crystal along the polar axis, a three-dimensional picture of antiparallel domains can be constructed. The idea was applied to top-seeded solution-grown crystals of BaTiO_3 . Figure 4.7.7 shows an example of domain pattern in a crystal 6.6 mm long (in this picture the polar-axis length has been artificially compressed to make the distant domains visible). The resemblance of the pictures in individual slices to slices of “Emmentaler” tempted some researchers to refer to the method as the Swiss cheese technique (Grubsky et al., 1996). Independently, Grabar et al. (1997) used the same method to image domains in crystals of $\text{Sn}_2\text{P}_2\text{S}_6$. Such pictures are unique in their 3D character but the resolution is limited as in any other optical method. In its present form the method is suitable for visualizing static patterns.

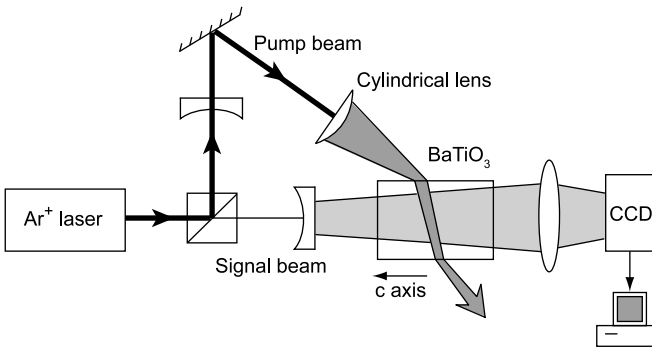
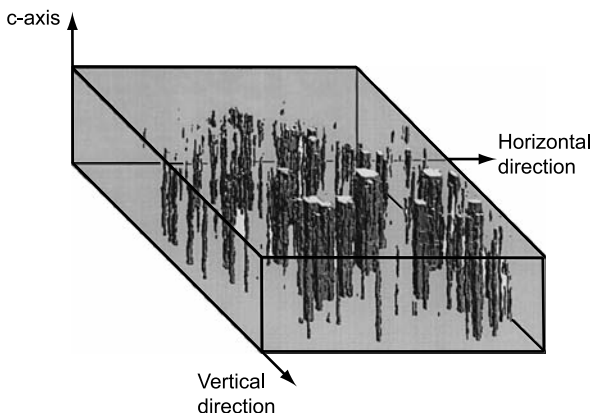


Fig. 4.7.6 Experimental setup for 3D imaging of domains using the Swiss cheese technique. After Grubsky et al. (1996)

Fig. 4.7.7 Antiparallel domains in tetragonal BaTiO_3 imaged by the Swiss cheese technique. Optical slices spaced $250\ \mu\text{m}$ apart. After Grubsky et al. (1996)



4.8 Electron Microscopy

The present section gives an overview of several methods used for studying domains in ferroics based on the interaction of electron beams with a multidomain ferroic sample. These techniques may differ essentially in their principles as well as in the required equipment. It is beyond the scope of this book to go into a detailed description of the techniques used and rather we shall restrict ourselves to a discussion of the basic principles of domain imaging in these techniques, the information they offer, and their limitations.

In any electron microscope, the sample is exposed to an electron beam. There are two principal imaging techniques in electron microscopy corresponding to the detection of the electrons emitted back from the sample surface and the detection of the electrons that have passed through the sample. The first technique is called *scanning electron microscopy* (SEM), the second—*transmission electron microscopy* (TEM). The application of these techniques for domain imaging will be addressed in the two following sections. Later we will briefly discuss one more using electron beam for domain imaging, namely *electron mirror microscopy*.

4.8.1 Scanning Electron Microscopy

We have already mentioned that scanning electron microscopy (SEM) is being used to visualize domains on surfaces of decorated multidomain crystals. There its advantage is high resolution in distinguishing the density or arrangement of decorating particles. However, a considerable effort was made to employ SEM for direct domain observations. After the examination in a scanning electron microscope the sample may be used again in another experiment since its

surface has not been damaged. Further, SEM allows for direct observations at different temperatures as well as for observing slow kinetic processes.

There is a fact that next to all these promising features the method has as its major setback: Most of the ferroic crystals of interest are good insulators and samples may get charged during a SEM observation. This charging may impact the domain pattern of the sample. This was documented by observations such as of polarization reversal (Sogr and Kopylova, 1995), domain growth (Nakatani, 1973), or domain nucleation (Abboud et al., 1993) in crystals of TGS due to the electron beam itself. In addition, the accumulation of charge may deflect the electron beam on subsequent scans and so negatively influence the method itself.

For observation of ferroic domains, two basic modes of operation can be used. One of them is associated with the *secondary electrons* and the other with *backscattered electrons*. These modes can be elucidated as follows. The cathode which is the electron source is on a high negative potential $-V_0$ relative to the grounded anode; V_0 is typically between 1 and 50 kV. The electrons of the incoming beam accelerated to the energy eV_0 hit the sample surface. As a result of inelastic scattering processes *secondary electrons* are produced, with energy much lower than that of the electrons in the primary beam, typically below 50 eV. As a result of multiple elastic scattering of the incoming electrons, *backscattered electrons* emerge from the sample, with a wide distribution of energies below that of the primary beam. By choosing the electron detector and its potential, secondary or backscattered mode of observation can be selected. In a typical SEM setup the sample is in vacuum 10^{-5} – 10^{-6} Torr.

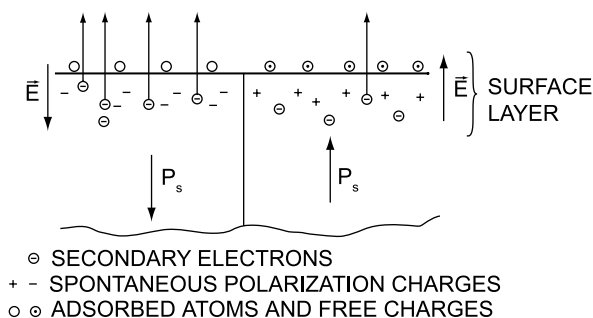
For nonmagnetic dielectrics there are two principally different sources of contrast: spatial variations of topography and surface electrical potential. Both these factors will influence the number of detected electrons and in general we may expect that both of them also lead to contrast between domains. We have already discussed in detail in connection with other methods that surface topography relief can be expected to exist for ferroelastic domains and, as a result of sample preparation, for nonferroelastic domains as well. In fact one of the earliest observations of ferroelastic domains by SEM was performed for etched crystals of BaTiO_3 (Robinson and White, 1967), the contrast being purely of topographic origin. However, for all ferroelastic domain pairs one can also expect that contrast arises due to the channeling effect (Unruh, 1963; Sogr and Kopylova, 1996); the latter reflects the fact that the mutual orientation of the primary electron beam and the crystal lattice is different in neighboring ferroelastic domains. On the other hand, for nonferroelastic–ferroelectric domains the surface relief in the electric potential and the topographic relief can be expected to control imaging rather than the channeling effect.

For ferroelectrics in particular the problem of charge accumulation is serious. This was why the first attempt to observe ferroelectric domains was performed with WO_3 crystals which are semiconductive. Le Bihan and Cella

(1970) succeeded to observe both 180° and 90° domains as well as surface topography due to hillocks and found that the domain contrast was the same in both modes, e.g., with secondary and backscattered electrons, respectively. However, for a metallized sample the domain contrast disappeared, a clear indication that domains were visible not due to topography but rather due to differences in surface potential. This can be understood as differences in the work function. In fact the difference of work function for antiparallel domains in TGS was later measured and found to be about 1 eV in samples aged for a few days after preparation (Le Bihan and Abboud, 1989).

Later experiments with crystals of TGS and other ferroelectrics (Maussion and Le Bihan, 1976; Le Bihan and Maussion, 1974) showed that the contrast is always seen in the secondary mode and this mode is now generally employed with rare exceptions (Oleinik and Bokov, 1975). In fact, when the detector is typically at a potential of +10 kV all emitted electrons are detected, but the secondary electrons constitute the main part of the detected current. The simplest model of contrast formation is shown schematically in Fig. 4.8.1 (Le Bihan, 1989). A surface layer is formed at antiparallel domains in which adsorbed molecules also play a role. It is assumed that in this layer electric field exists correlated with the direction of \mathbf{P}_s underneath. This field controls the intensity of emitted secondary electrons. The layer thickness is usually estimated to be of the order of nanometer to tens of nanometers (Kokhanchik, 1993).

Fig. 4.8.1 Scheme of secondary electron emission from ferroelectric antiparallel domains as suggested by Le Bihan (1989). The detection of the field E in the surface layer controls the intensity of emitted electrons



It has thus become customary to investigate ferroelectric domain structures with nonmetallized samples. As was mentioned above, since few ferroelectrics are appreciably conductive the surface charging may pose a problem with domain delineating based on the surface bound charge of the spontaneous polarization. The problem of surface charging of weakly conductive samples was addressed by Le Bihan and Maussion (1971) and by Le Bihan (1989); they demonstrated possibility of essential suppression of this effect. This possibility is based on the observation that the ratio of the electron current emitted back by

the sample to the electron current received by it, the so-called yield δ , can be larger than unity in a certain range of the accelerating potential. Thus there exist two values V_1 and V_2 of the acceleration potential ($V_2 > V_1$), at which $\delta = 1$ so that at these values the electron beam does not charge the sample surface. The analysis, taking into account the capacitance and the resistance of the sample, shows that the value V_2 of the accelerating potential can correspond to a stable state of the system (Le Bihan, 1989). Thus working close to this value enables a substantial suppression of the sample charging, which makes it possible to successfully read the surface bound charge of ferroelectric domains. In practice, the condition $\delta = 1$ is not exactly met. In this case, as follows from the approach developed by Le Bihan and Maussion (1971) and by Le Bihan (1989), in the stationary state the sample surface will carry the charge density associated with the incident electron beam

$$\sigma_{\text{sur}} = J_p t_M (\delta - 1), \quad (4.8.1)$$

where J_p is the current density of the primary electrons reaching the sample and t_M is the Maxwell relaxation time. Thus, at long exposition time the surface charging leading to a loss of the contrast between domains typically occurs. However, even in this regime, domain walls are still contrasted as was reported for TGS (Le Bihan, 1989), NaNO_2 (Hatano and Le Bihan, 1990), and Mn-I boracite (Castellanos-Guzmán et al., 1995). This is believed (Le Bihan, 1989) to be connected with the fact that there is a large potential drop across the wall creating an intense electric field above it, of the order of 10^5 V/cm, which deviates both primary and secondary electrons; thus domain walls remain uncharged and retain their contrast. However, Aristov et al. (1983, 1984) have proposed another interpretation suggesting that domain boundaries might have excess electrical conductivity, whereas Sogr (1989) connected the wall contrast with the small shifts of domain walls due to the incoming beam.

As an example, Fig. 4.8.2 reproduces the SEM picture of 180° domain walls in a crystal of GASH (Szczesniak et al., 1995).

While it is generally accepted that the contrast in domains is connected with the surface potential, observations are available indicating that other mechanisms may be involved. It was established (Aristov et al., 1984) that antiparallel domains in LiNbO_3 can be made visible even on the Y -planes which are parallel to the polarization vector. On repeated irradiation the contrast first inverts but finally disappears.

In fact, most of the published data on ferroelectric domains obtained by SEM at non-metallized sample do not excel in spatial resolution. Typically, pictures of areas are presented with linear dimension of one to several hundreds of micrometers. This is related to the limitation on the accelerating voltage, which, in turn, limits the achievable level of magnification. Applying conductive coatings makes it possible to reach higher magnifications and at the same time to apply external electric field to the sample in order to influence its domain

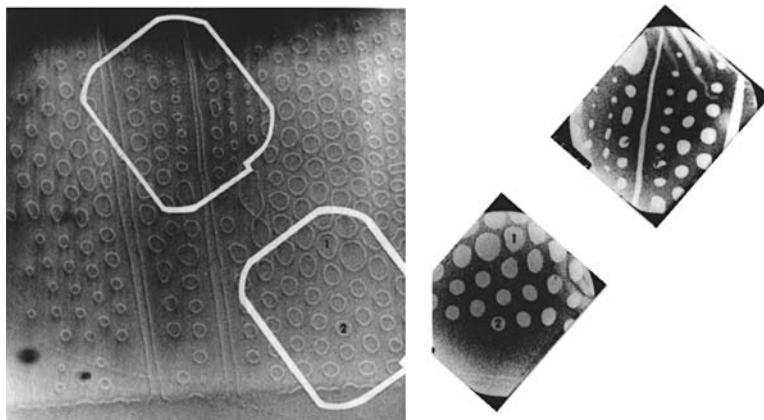


Fig. 4.8.2 *Left:* SEM picture of domain walls surrounding egg-shaped domains on (0001) surface of GASH crystal taken in the secondary electron mode at an accelerating voltage of 1 kV (Szczesniak et al., 1995). *Right:* the same areas, domains decorated by AgCl. Courtesy of L. Szczesniak. Magnification 440 \times

structure. The growth of domains in TGS crystals was observed in such a way (Grandet et al.; 1981). Some other interesting results obtained by SEM include the influence of pyroelectric charge produced by a small temperature change on the domain contrast (Averty and Le Bihan, 1993; Ozaki et al., 1996), simultaneous observations of domains on perpendicular crystal faces (Maussion et al., 1986), and higher resolution observations of etched domains (topographic contrast) formed in LiNbO_3 due to the pyroelectric effect (Pendergrass, 1987).

The SEM method has found increasing applications in evaluating periodic domain structures for optical applications in crystals of KTiOPO_4 (Skliar et al., 1997) and LiNbO_3 (Ishigame et al., 1991; Le Bihan et al., 1995). Of practical importance is the use of environmental SEM which operates at pressures by four orders of magnitude higher than conventional SEM (Zhu and Cao, 1998). It was reported that, by using this technique, domains were delineated in LiTaO_3 crystals while the images were found stable with no contrast change over a period of several hours.

4.8.2 Transmission Electron Microscopy

A transmission electron microscope (TEM) is an electron-optical device where the electrons passed through the sample are used to obtain the information on its structure. The focusability and short wavelength of electron beams are responsible for the high resolving power of the TEM. The principles of generation of the electron beam are the same as for SEM. The electrons are emitted from the cathode by either thermal emission or field emission and focused on the sample by electromagnetic lenses. The vacuum (that permits the propagation of the

electron beam) at the sample is in the range of 10^{-6} Torr. Specially designed sample holders allow not only tilting the sample in order to control the diffraction conditions but also to heat or cool the sample for in situ observation of phase transitions. Modern TEM allow the observation of the atom columns and have a resolution which has just recently broken the 1 Å barrier (O’Keefe et al., 2001).

In this section we introduce the basic principles of TEM and describe the concepts of *bright field imaging*, *dark field imaging*, *weak beam dark field imaging*, and *high-resolution transmission electron microscopy* (HRTEM). We will also illustrate the application of these methods to visualize ferroic- and compositional-ordering domains and domain walls. For a complete introduction to transmission electron microscopy, the reader is referred to specialized books (e.g., Williams and Carter, 2004).

In a conventional transmission electron microscope, a thin specimen is irradiated with an electron beam of uniform current density. For HRTEM, 5–20 nm thick samples are used, for other TEM method sample thinness may be up to 100 nm. The electron energy is most commonly in the range between 100 and 300 keV. Electrons are extracted from a tip or filament in the electron gun by thermoelectronic or field effect emission. A condenser–lens system permits variations of the illumination and the area of the specimen illuminated. The electrons travel through the specimen where they are scattered by various elastic and inelastic scattering processes. The electrons passed through the sample are focused by the objective lens and a diffraction pattern is produced in its back focal plane. This diffraction pattern, where the diffraction spot corresponds to differently diffracted beams, is the base for different imaging techniques. The diffraction pattern can be projected onto a viewing screen with further recording on a CCD camera or by direct exposure of a photographic emulsion. Alternatively, one or all of the transmitted and diffracted beams can be selected by an aperture introduced in the diffraction plane (back focal plane of the objective lens) to form an image of the sample. If only one of the beams (spots of the diffraction pattern) is used, then bright field, dark field, and weak beam dark field images are obtained. The HRTEM image is obtained when the result of the interference of many (ideally all) diffracting beams with the transmitted one is observed at high magnifications.

4.8.2.1 Bright Field Imaging, Dark Field Imaging, Weak Beam Dark Field Imaging, and Selected Area Electron Diffraction

Figure 4.8.3 explains the selection of the spots of the diffracting pattern to obtain bright field, dark field, and weak beam dark field images. Diffraction conditions are best illustrated using the Ewald sphere (locus of all elastically scattered beams) shown in this figure. The intensity of diffracted beams is maximal for all reciprocal lattice points that are intersected by the sphere, i.e., for which the Bragg condition is satisfied:

$$\vec{k}_g = \vec{k}_0 + \vec{g} \quad (4.8.2)$$

\vec{k}_g and \vec{k}_0 are, respectively, the wave vectors of the diffracted and the transmitted beam and \vec{g} is a reciprocal lattice vector. Due to the particularly small thickness of TEM samples, the reciprocal lattice points appear as small rods oriented in the direction of the foil normal. This makes the intersection between the Ewald sphere and the reciprocal lattice points readily achievable.

The *bright field image* is obtained by using the transmitted beam (Figs. 4.8.3a and 4.8.4b). In this case, the image contrast is formed on a uniformly bright background (therefore bright field). A perfect crystalline lattice produces a uniform image contrast depending on the diffraction conditions (diffracted beams are stopped by the objective aperture). Any lattice imperfection will modify the local diffraction conditions and change the diffracted intensity resulting in a change of image contrast.

In the case of *dark field image*, only one diffraction spot is used corresponding to a certain well-chosen orientation of the crystalline lattice (Figs. 4.8.3b and 4.8.4b), e.g., corresponding to the orientation of one domain when two (or many) domains with different orientations are in view. Then only areas which are in diffraction condition for the selected diffraction spot contribute to the image formation. They will be seen as bright objects on a dark background (therefore dark field).

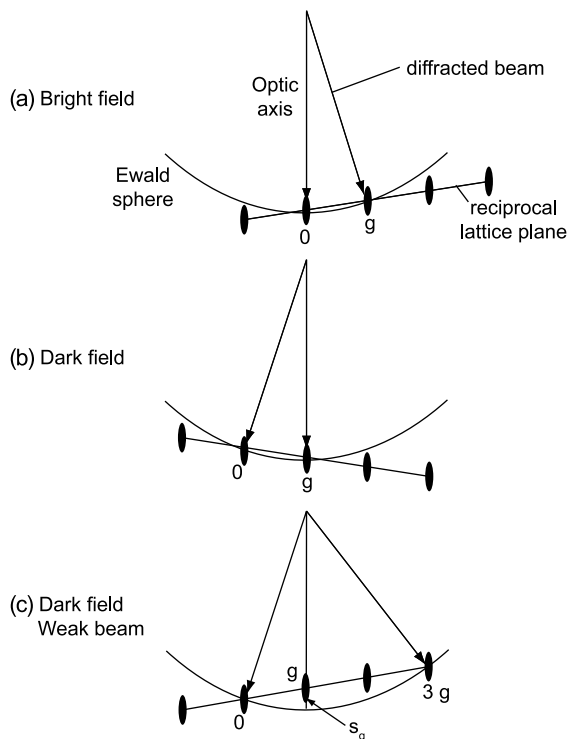


Fig. 4.8.3 The selection of the spots of the diffracting pattern to obtain bright field, dark field, and weak beam dark field images. Due to the small thickness of TEM samples, the reciprocal lattice points appear as small rods oriented in the direction of the foil normal. The directions of the transmitted beams are shown with arrows pointing at 0. For getting images, the electrons propagating along the optical axis are collected

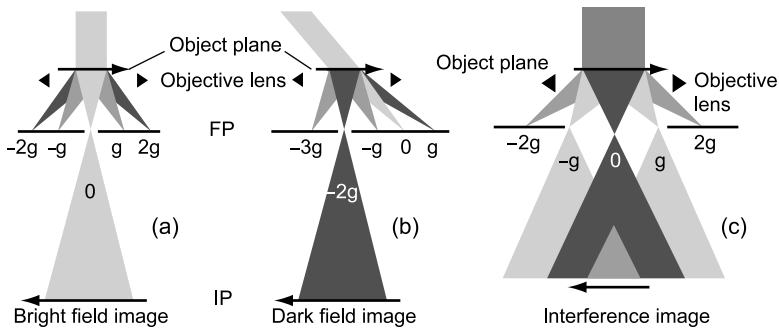


Fig. 4.8.4 The selection of the spots of the diffracting pattern to obtain bright field, dark field, and high-resolution (interference) images. FP, focus plane of the objective lens; IP, image plane of the objective length

For getting a *weak beam dark field image*, a diffraction direction is chosen that is slightly out (a well-defined amount) of the exact Bragg condition for a given reciprocal lattice vector \vec{g} (Fig. 4.8.3c). This configuration where the Bragg condition is exactly fulfilled for a farther ($3\vec{g}$ in this figure) lattice point and the selected diffraction spot is weakly (therefore weak beam) excited is favorable for the comprehensive and quantitative study of lattice defects and interfaces. Because of the involvement of the two Bragg points, the method is often referred to as *two-beam diffraction conditions*.

In the case of the dark field imaging in contrast to the bright field imaging, the incident electron beam is inclined with the respect to the optical axis of the electron microscope as shown in Fig. 4.8.4b so that the diffracted beam is centered on the optical axis of the microscope after diffraction.

The area of which an electron diffraction pattern is obtained with a parallel illumination can be selected using an aperture in the image plane of the objective lens. This technique is called *selected area electron diffraction (SAED)*. The diffraction pattern is then obtained by the electrons passing through this area only. SAED pattern enables the identification and analyzes crystallographic orientations of objects (domain or grains) in the selected area.

Figure 4.8.5 shows the bright field image (a) and SAED pattern (b) taken from a thin (010) PbTiO_3 film containing of 90° domains with the spontaneous polarization lying in the plane of the film (the so-called *a/a* domain pattern). The SAED pattern observed is the superposition of the diffraction patterns of the two domains separated with a $(\bar{1}01)$ domain wall seen in the selected area in Fig. 4.8.5a. The splitting of the spots in the image is caused by the misalignment of the crystalline planes (100) and (001) in the neighboring domains. At the same time there is no splitting for (202) spots as expected from the mechanical compatibility conditions.

Figure 4.8.6 shows the dark field and weak beam dark field images taken from an area of a PbTiO_3 film containing of 90° domains with the spontaneous

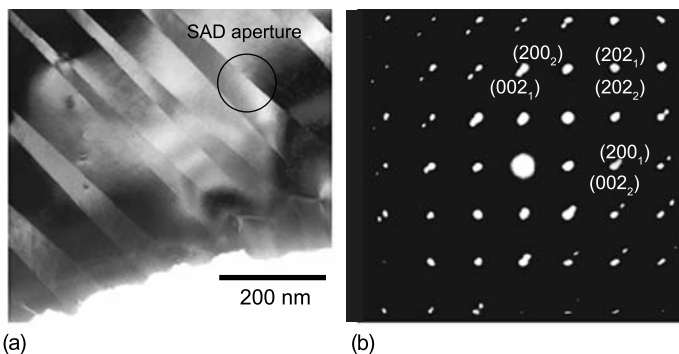


Fig. 4.8.5 Bright field image (a) and SAED pattern (b) taken from a thin (010) PbTiO_3 film containing 90° domains with the spontaneous polarization lying in the plane of the film. Reprinted with permission from Foeth et al. (1999a). Copyright (1999), Oxford University Press

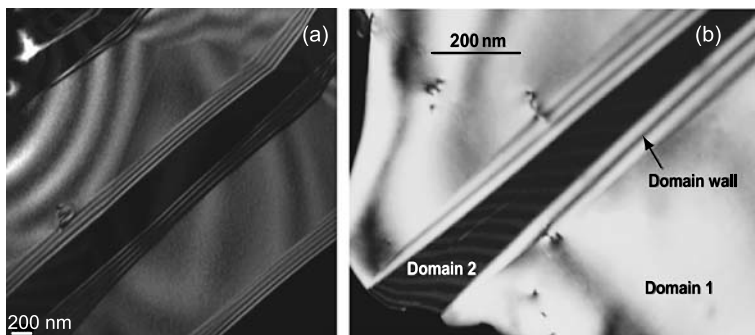


Fig. 4.8.6 Dark field (a) and weak beam dark field (b) images taken from an area of a PbTiO_3 film containing 90° domains with the spontaneous polarization either normal or parallel to the plane of the film. Reprinted with permission from Foeth et al. (1999a). Copyright (1999), Elsevier

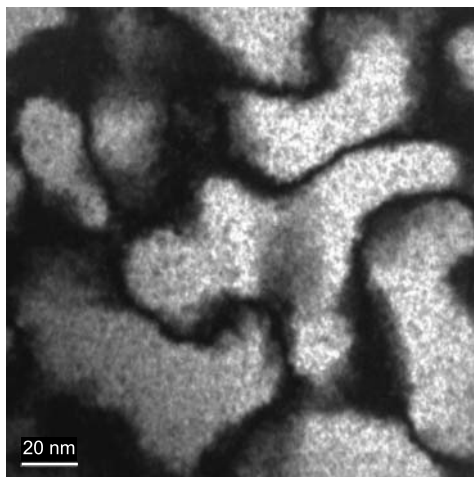
polarization either normal or parallel to the plane of the film (the so-called c/a domain pattern). Only one set of domains is close to Bragg conditions and appears bright in the dark field image, the other set of domains remains dark (Fig. 4.8.6a). At the domain boundary, which is slightly inclined with respect to the viewing direction a fringe pattern is observed. This is the result of multiple scattering at the inclined walls. In the weak beam dark field image (Fig. 4.8.6b) multiple scattering is reduced and the well-defined diffraction conditions can be used to numerically simulate the interference pattern. From comparison of the images with the result of image simulations one can evaluate the domain wall thickness.

In general, the weak beam dark field imaging (two-beam diffraction conditions) makes a very important tool of domain imaging. It has been extensively

used from starting the first studies of domain walls in ferroelectrics. We will address this topic in detail when discussing the experimental investigations of domain walls in Sect. 6.1.6.

The dark field imaging technique can also be used for detection of domains of chemical ordering in disordered ferroelectrics. Such work has been performed (Akbas and Davies, 1997) for mixed perovskite $\text{Pb}(\text{Mg}_{1/3}\text{Ta}_{2/3})_{0.95}\text{Zr}_{0.05}\text{O}_3$ where the occupation of the B-site with Mg or Ta can be progressively tuned from fully disordered to ordered with the doubling of the lattice parameter. The ordered areas can be visualized by dark field imaging which is produced for the diffraction spot $3/2(111)$ specific for the structure with the doubled period (Fig. 4.8.7). Only the ordered regions which scatter the electrons into the $1/2(111)$ direction contribute to the image contrast. It is seen that the ordered regions form domains of up to 100 nm in size separated by the disordered matrix (dark contrast).

Fig. 4.8.7 B-site ordered areas in $\text{Pb}(\text{Mg}_{1/3}\text{Ta}_{2/3})_{0.95}\text{Zr}_{0.05}\text{O}_3$ visualized by dark field imaging which is produced for the diffraction spot $3/2(111)$, specific for the structure with the doubled period. Reprinted with permission from Cantoni et al. (2004). Copyright (2004), American Institute of Physics

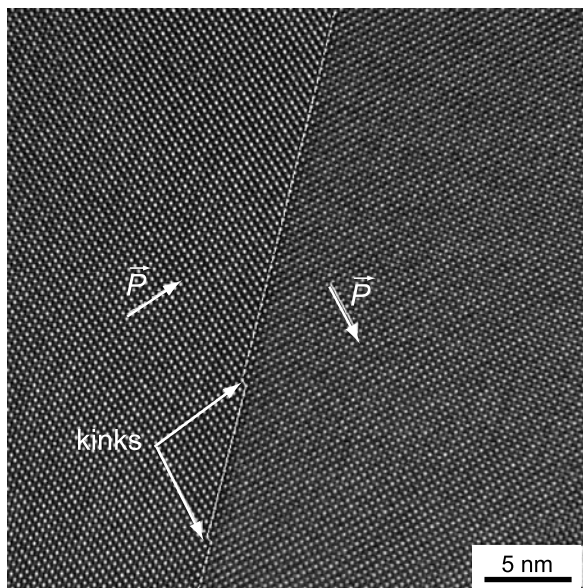


4.8.2.2 High-Resolution Transmission Electron Microscopy

In *high-resolution transmission electron microscopy* (HRTEM) many diffracted beams are used to get the image. Technically this is done by selecting many diffraction spots in the back focal plane of the objective lens using a suitable objective aperture. The image contrast is formed by the interference of the selected reflections. Figure 4.8.4 illustrates the difference in the selection of the diffraction spots in the bright field imaging, dark field imaging, and HRTEM.

HRTEM readily provides atomic level resolution. Figure 4.8.8 shows a typical high-resolution micrograph of a 90° domain wall in PbTiO_3 taken using a Philips CM-300 FEG microscope with a point-to-point resolution of 0.17 nm.

Fig. 4.8.8 Typical high-resolution micrograph of a 90° domain wall in PbTiO_3 taken using a Philips CM-300 FEG microscope with a point-to-point resolution of 0.17 nm. Reprinted with permission from Foeth et al. (1999a,b). Copyright (1999), Oxford University Press



The theory of the HRTEM imaging is quite involved and goes out of the scope of this book. Here, we would like to comment the point that it is not obvious to determine the position of the atomic columns just by contemplating the experimental micrographs. It can be understood in the simplest approximation where the electron absorption in the sample is neglected. In this approximation, the diffracted electron wave exhibits only a phase shift after passing through the sample. The phase shift reflects the crystal potential of the material, $V(x, y)$, where x and y are the Cartesian coordinates in the plane of the thin sample. However, the former does not affect the intensity of the diffracted wave in the $x - y$ plane of the image. The information hidden in the phase of the diffracted electron wave can be developed after the interference of the diffracted wave with the un-scattered wave. However, in a real TEM the correspondence between the crystal potential of the material, $V(x, y)$, and the intensity of the sum of the diffracted and un-scattered wave, $I_{\text{tot}}(x, y)$, is not straightforward because of additional phase shifts acquired by the diffracted wave in the device (defocusing, spherical aberration of the magnetic lens being the most important ones). This implies that additional tuning, which compensated these shifts is needed to get the HRTEM which reproduce truly the crystal potential of the material (specifically the atomic arrays in it). The situation becomes more complicated when multiple scattering occurs and when the electron absorption cannot be neglected (for thicker crystals or for crystals containing heavy atoms). In this case one has to make use of the full dynamical theory of electron diffraction and imaging in order to quantify the experimental micrographs (Cowley, 1975; Ishizuka and Uyeda, 1977).

HRTEM observations have been used for characterization of domain walls in various ferroelectrics, the structure, thickness, and roughness of the walls being addressed. Useful information of this kind has been reported for KNbO_3 (Bursill et al., 1983), BaTiO_3 (Shiojiri et al., 1992; Floquet et al., 1997), and PbTiO_3 (Stemmer, 1995; Foeth et al., 1999b).

HRTEM has also been applied of the identification of the type of chemical ordering in mixed perovskite ferroelectric $\text{Pb}(\text{Mg}_{1/3}\text{Ta}_{2/3})_{0.95}\text{Zr}_{0.05}\text{O}_3$ already discussed above in the context of the dark field imaging. The latter method, as was mentioned, enables the detection of the B-cite ordered domains in the disordered matrix. However, the information provided by this technique is not enough to determine the microscopical type of ordering. This delicate identification has been performed by Cantoni et al. (2004) by comparing the HRTEM images taken for a specially selected setting with the results of computer simulations. Because of its nature (interference contrast) the contrast in HRTEM images varies strongly with the imaging conditions (focus) and the specimen thickness. Therefore, an unambiguous identification of the occupation of atom columns and the measurement of the column spacing is only possible for special cases where all of the parameters are known and can be taken into simulations. In these cases, however, HRTEM is a very powerful tool of direct verification of the microstructure on an atomic level.

4.8.3 Electron Mirror Microscopy

Electron mirror microscopy like SEM provides information on the surface potential of the material but in contrast to the latter, in this technique the electrons do not enter the sample but are just reflected by its surface potential. To achieve this in an electron mirror microscope the sample is kept at a potential which is slightly more negative than the cathode. The reflected electrons carrying information on the surface potential are collected by the anode.

For visualization of ferroic domains, this method was first used by Spivak et al. (1959) and theoretically analyzed by Someya et al. (1970). It allowed the observation of 90° domains in partially electroded BaTiO_3 crystal plates as well as their nucleation in an applied field (English, 1968a). English (1968b) showed that the method can also be used at elevated temperatures and employed for observations of boundaries between paraelectric and ferroelectric phases in grains of PZT ceramics. Maffit (1968) performed interesting experiments when observing the same spot of a multidomain BaTiO_3 crystal grown by the Remeika method, which was either bare or covered with an electrically conducting layer. In the former case both surface topography and surface potential contribute to image contrast. In the latter case only the surface topography is visualized.

The method can be used to observe domain wall motion. This was shown by Kobayashi et al. (1972) who investigated motion of domain walls in GMO in real time. The domain observation was relied on the surface topography.

The spatial resolution as judged by available data is not high. Perhaps one of the most rewarding ways of utilizing this method was suggested by Le Bihan and Chartier (1977) and by Le Bihan et al. (1977). In a modified arrangement, the quantitative electron mirror microscope allowed to determine the difference in the surface potential of two antiparallel domains; for TGS crystals the value of about 1 V was obtained.

4.9 Methods Based on Interactions with X-Rays

One can distinguish two principal ways of getting information on ferroic domains using X-ray radiation: X-ray topography and X-ray diffraction. In this section we will address the conventional X-ray topography as well as the synchrotron radiation topography. The X-ray diffraction-based methods will be discussed in Chap. 9 in the context of domains in ferroelectric thin films.

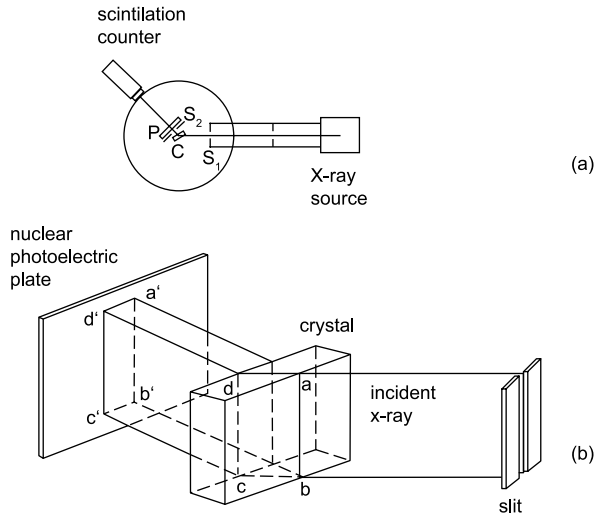
The concept of X-ray topography covers a number of methods which make it possible to use the diffraction of X-rays with the aim of imaging a crystal in such a way that a particular spot in the crystal is assigned a location on its image—topogram. In X-ray topograms, one distinguished *domain bulk contrast* and *domain wall contrast*. In the first case, different domains are imaged with different intensities. In the second, alternatively, only domain walls are imaged with intensity, which is different from those identical for the domains. Topograms represent crystal images which are not magnified; magnification has to be performed in a photographic manner.

There are a number of topographic methods which differ in experimental arrangements. The incident X-ray beam may be parallel or divergent, monochromatic or continuous. The diffracted beam can be observed in transmission or reflection geometries. Sometimes transmission topographs are taken to observe domains inside the specimen while surface reflection topographs serve to observe domains near the surface.

The most common technique for the observation of domains is the Lang's method. A typical setup is shown in Fig. 4.9.1. By choosing the angle of incidence of the monochromatic beam the required reflecting plane in the crystal is selected. The main slit S1 is narrow, adjusted so that the horizontal divergence of the incident beam is smaller than the difference in Bragg angles of the chosen reflecting plane (hkl) for the radiation used. The height of the incident beam allows that the whole vertical dimension of the sample be irradiated. The receiving slit S2 blocks the primary beam. The crystal and the photographic plate, usually a nuclear emulsion, can be shifted to obtain the image of the whole sample.

The spatial resolution of the method is not high, typically 1–3 μm . Dense lamellae of thickness even far above this limit (say 20 μm) can only be separated under optimal projection conditions. Overlapping of lamellae and walls leads to complicated contrast patterns which are difficult to interpret. Combining

Fig. 4.9.1 (a) Experimental arrangement for X-ray topography. S_1 , main slit; S_2 , receiving slit; P , nuclear photographic plate; C , crystalline sample. (b) Correspondence between the crystal section ($abcd$) and its image (a', b', c', d') on the photographic plate (Suzuki and Takagi, 1971)



transmission topographs with observations in reflection in which the penetration depth may be only several micrometers (Kawata et al., 1981) may allow for deciphering some details in domain shapes.

The use of X-ray topography to image domains in ferroics was pioneered by Čáslavský and Polcarová (1964) who investigated the contrast of ferroelastic domains in BaTiO_3 and by Lang (1965) who succeeded to image both Dauphiné (ferroelastoelectric) and Brazil (growth) twins in quartz crystals. Possible mechanisms of the origin of contrast were discussed in detail by a number of researchers (see, e.g., Petroff, 1969; Parpia, 1982a,b; Takahashi and Takagi, 1978b; Suzuki and Takagi, 1971; Capelle et al., 1982) and reviewed by Klapper (1987).

One distinguishes three situations where the *domain bulk contrast* appears (Klapper, 1987): (i) *orientational contrast*, (ii) *structure factor contrast*, (iii) and *anomalous dispersion contrast*.

In the case of *orientational contrast*, crystal lattices of the two domains are not parallel to each other. This is the case of ferroelastic domains. Here the crystal is imaged in the corresponding reflection, the contrast depends on the angular divergence of the primary beam; in the Lang's method, the radiation with a primary beam divergence of typically 2–5 min is used. If the tilt between the reflecting planes of the two domains is larger than the beam divergence, only one domain reflects and we have full-and-zero contrast. In this way domains in $\text{GdDy}(\text{MoO}_4)_3$ were imaged (Capelle and Malgrange, 1982). However, if the tilt angle is comparable or smaller than the primary beam divergence, a faint domain image is obtained or the contrast is completely lost.

If the lattices of the two domains are parallel, the reciprocal lattice points coincide but generally they differ in the moduli of structure factors. Because of

that the two domains reflect with different intensities and appear by *structure factor contrast*. On this mechanism was based imaging of Dauphiné twins in quartz (Lang, 1965; McLaren and Phakey, 1969).

Finally, if the domains do not differ in the structure factors either, they still can be distinguished due to the so-called effect of anomalous dispersion. This is the case of the *anomalous dispersion contrast*. Imaging of antiparallel domains in BaTiO_3 (Niizeki and Hasegawa, 1964; Akaba et al., 1979; Takagi et al., 1979), NaNO_2 (Suzuki and Takagi, 1971), and CsH_2PO_4 (Ozaki et al., 1997) were based on this mechanism. Figure 4.9.2 shows antiparallel domains in NaNO_2 as imaged in two different $0kl$ reflections: (011) and (031) (Suzuki and Takagi, 1971).

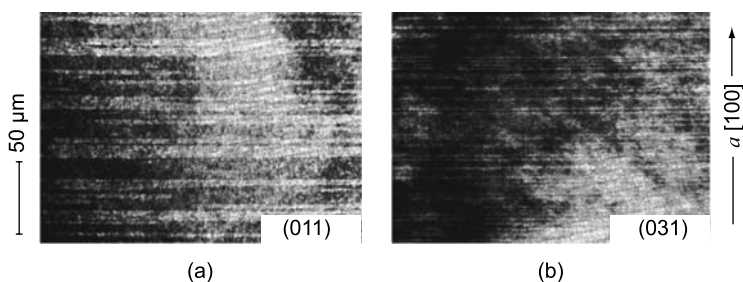


Fig. 4.9.2 X-ray sectional topographs of a NaNO_2 crystal taken by $\text{CuK}\alpha$ radiation with two of several $0kl$ reflections which give the best domain contrast (Suzuki and Takagi, 1971)

Klapper (1987) has formulated a set of practical rules for the selection of reflections to achieve good domain contrast in case of domains with parallel lattices.

In real crystals, the domain contrast can be also due to lattice distortions in the interface adjacent layers. Thus the visibility of 180° domains in thin plates of BaTiO_3 was attributed to slight misorientations of polarization vectors near the surfaces (Kawata et al., 1981).

In many cases the domain bulk contrast is absent and it is the domain walls which are imaged by X-ray topography. Much effort was devoted to the *domain wall contrast* with the aim to obtain data on domain wall thicknesses and structures. This will be discussed in some detail in Chap. 6.

X-ray topography makes it possible to easily recognize changes in domain structures induced by applied electric field or stress; such observations were performed for instance for BaTiO_3 (Takagi et al., 1979) and NaNO_2 (Suzuki and Takagi, 1972). However, the limited spatial resolution makes it difficult to use this method for solving sensitive issues like nucleation or small modulation of ferroelectric domain walls due to the presence of free charges. In general, the significance of X-ray topography is not so much in mapping of domains but in the investigation of domain walls and the lattice distortions in their neighborhood.

It may be pointed out that X-ray topographical observations may not be totally harmless. It is known that irradiating some ferroelectrics by even small X-ray radiation doses may lead to profound changes in their switching behavior, indicating a different response of domain walls. Petroff (1969) indicated a loss of contrast during topographical observations of TGS crystals and Polcarová et al. (1970) detected changes of lattice parameters.

Synchrotron radiation sources are characterized by a high-intensity X-ray beam with continuous distribution of wavelengths and natural collimation. When used for topography they offer several advantages as compared to classical X-ray methods (Robert and Lefaucheux, 1983; Schlenker and Baruchel, 1994). Exposure times can be greatly reduced, allowing for rapid sequences of topographs to be taken, which makes it possible to record changes in domain structures and phase transformations in real time. Because the beam divergence is small, precise measurements with a quasi-plane wave can be performed. The synchrotron technique allows one to select, from the white spectrum, a more suitable range of wavelengths or even a monochromatic radiation with the chosen wavelength. This may be found useful for materials with high absorption at wavelengths of conventional X-ray sources but also for selecting the origin of contrast.

The method was used to image ferroelastic domains (Aleshko-Ozhevskij et al., 1985; Aleshko-Ozhevskij, 1983; Jiang et al., 1993; Zhao et al., 1991; Scherf et al., 1997) and also phase boundaries between parent and ferroic phases, in wide temperature ranges. Both static imaging and dynamic imaging have been demonstrated. Studies of ferroelastic domain pairs in the monoclinic phase of $\text{NdP}_5\text{O}_{14}$ and other pentaphosphates performed by the Nanjing group (Huang et al., 1994a,b; Jiang et al., 1993; Hu et al., 1994) offer typical examples of the orientational bulk and domain wall contrasts.

Because ferroelastic domains can be observed optically with higher resolution, the real strength of synchrotron radiation topography might rather be in the area of nonferroelastic domain pairs where the contrast will be based on anomalous dispersion. Crystals of CsH_2PO_4 were studied in this way (Ozaki et al., 1997). Nonferroelastic domains have also been imaged in other ferroelectrics like KTiOPO_4 (Wang et al., 1993), KNbO_3 , and BSN (Jiang et al., 1993).

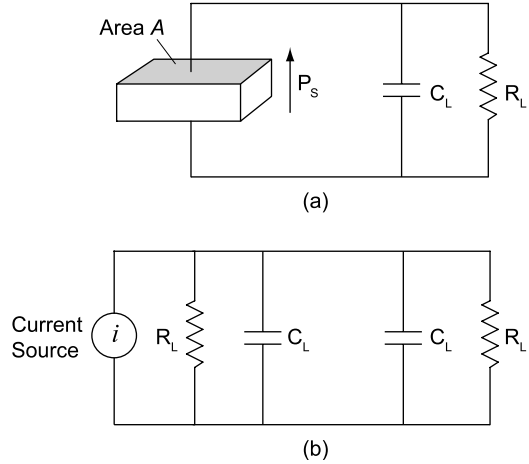
4.10 Pyroelectric Mapping

Domain imaging method utilizing pyroelectric effect is based on the relation

$$\Delta D_i = \kappa_0 \kappa_{ij}^{\sigma} \Delta E_i + p_i^{E,\sigma} \Delta T, \quad (4.10.1)$$

where $\mathbf{p}^{E,\sigma}$ is the pyroelectric coefficient at constant field and stress. It is applicable to ferroelectrics since domain states can differ in components of $\mathbf{p}^{E,\sigma}$ in them. This equation is to be considered a relation describing the situation at a certain point in the sample. Local change of temperature causes a local change of \mathbf{P}_S due to the pyroelectric effect; redistribution of polarization leads

Fig. 4.10.1 Basic scheme for detecting the pyroelectric response (a) and its equivalent circuit (b). After Lines and Glass (1977)



to the change of electric field which again influences polarization. Figure 4.10.1 shows the very basic arrangement for measuring the pyroelectric properties (Hadni et al., 1976). Assuming low-level thermal excitation, the sample itself can be ascribed a linear capacitance C_x and resistance R_x . In a real experiment it is connected to an external circuit with input impedance C_L , R_L . The sample temperature is changed by ΔT . The magnitude of time constant $\tau = RC$ where $C = C_x + C_L$ and $1/R = 1/R_x + 1/R_L$ determines the value of the pyroelectric voltage ΔV (Hadni et al., 1976). In the simplest case of a single domain sample the situation is homogeneous, described by a certain value of $\mathbf{p}^{E,\sigma}$. If the temperature change is fast compared to τ

$$\Delta V = \frac{Ap\Delta T}{C} \exp\left(-\frac{t}{RC}\right), \quad (4.10.2)$$

while for slow rate of change of temperature

$$\Delta V = -ApR \frac{dT}{dt} \left\{ 1 - \exp\left(-\frac{t}{RC}\right) \right\}. \quad (4.10.3)$$

Here A denotes the illuminated area of the sample and p is the component of $\mathbf{p}^{E,\sigma}$ normal to the electroded surface of the sample. This voltage leads to an electric current flowing through the external resistor R_L , with the corresponding time constant. Its sign is determined by the sign of p ; for a single domain ferroelectric sample $p \propto d\mathbf{P}_S/dT$ and correspondingly its sign depends on the polarity of \mathbf{P}_S . Chynoweth (1956) was the first to demonstrate that the pyroelectric signal in barium titanate reveals the sign of \mathbf{P}_S .

If the sample is multidomain, the contributions from volume elements to the change of the surface charge have to be summed up. The total charge is obtained

by integrating over the sample volume, accounting for the temperature gradient and depolarizing field. Thus measuring the pyroelectric effect of the whole sample gives evidence on the average value of spontaneous polarization; it can be used even in the dynamic regime to investigate slow processes of \mathbf{P}_S reversal (Latham, 1967).

The same principle can be employed to obtain information about spatial distribution of \mathbf{P}_S , i.e., about the domain structure. The sample surface is heated only locally and the size of the region of elevated temperature determines the spatial resolution of the method. Scanning the sample surface gives evidence on the geometry of domains. In the first experiments of Burfoot and Latham (1963), local heating of barium titanate crystals was produced by a focused electron beam of 4 μm radius. Pyroelectric voltage showed peaks related to optically visible 90° domain walls.

The method was then fully developed by Hadni et al. (1965) and brought to a high level in speed, resolution, and insight into the sample. Some of the results obtained for TGS crystals are unique such as data on nucleation processes and domain wall velocity (Hadni and Thomas, 1975), domain maps during slow switching processes (Hadni and Thomas, 1976), or writing microdomains by heated spots (Hadni et al., 1973).

One of the successful setups of the method, which is often referred to as the *pyroelectric probe technique*, was described by Hadni et al. (1976). A He–Ne laser spot is focused on the crystal plate and displaced in successive lines. The sweeping device is essentially made of two fast galvanometers with their mirrors oscillating around two perpendicular axes; the driving frequencies are 3 kHz for the vertical axis mirror and 20 Hz for the horizontal axis mirror. Both polar surfaces of the sample are gold plated and connected through a resistor R_L . The laser beam is modulated by a Pockels cell and gives a sine wave illumination at frequencies from 10^4 Hz to 2×10^5 Hz. Due to the pyroelectric effect, a sine-wave current flows through R_L . A phase detector measures the signal whose amplitude is proportional to the pyroelectric coefficient. It modifies the intensity of a spot on the oscilloscope. The spot is swept in synchronization with the laser beam. Phase detection determines the sign of the response. Up to 20 images per second could be taken (Hadni and Thomas, 1976; Tran et al., 1981) and with an Argon blue laser surface resolution of 1 μm was achieved (Hadni, 1993). Figure 4.10.2 offers an example of pyroelectric domain map (Hadni et al., 1976). The process has been analyzed theoretically, partly analytically, and partly by simulation (Hadni et al., 1976; Kirpichnikova et al., 1993). Experiment and modeling have also covered complex situations, for example, where repeated illumination leads to nucleation—on the opposite crystal surface—and growth of domains with opposite polarity.

The pyroelectric mapping method was used to visualize domains in crystal-line plates of TGS, BaTiO_3 (Clay et al., 1974), KTiOPO_4 (Bierlein and Ahmed, 1987; Ivanov et al., 1994), and also in NaNO_2 (Tran et al., 1981; Krug et al., 1993b). For TGS and sodium nitrate, data about domain wall velocities were also obtained (Tran et al., 1981) by measuring wall positions repeatedly after

Fig. 4.10.2 Pyroelectric image of domains in a TGS plate 10 μm thick. The size of the image is 130 μm . Reprinted with permission from Hadni and Thomas (1976). Copyright (1976), Taylor and Francis



successive application of a dc field. An interesting modification of this method was offered by Ungar et al. (1981) and Pradhan et al. (1984) who showed that it can also be used to visualize domains in plates parallel to the ferroelectric axis.

It was shown by Krug et al. (1993b) that the same experimental approach can also be used to visualize domains in nonpyroelectric materials. The response in the alternatively named “laser scanning microscope” is then due to photoelectricity or thermoelectricity. Krug et al. (1993a,b) described in detail also another modification of such experimental system. The apparatus was completed with an optical system allowing monitoring simultaneously the image of the optical reflection of the sample surface.

4.11 Scanning Optical Microscopy

Discovery of tunneling/atomic force microscopy which is essentially based on high precise positioning of the sample has also resulted in the development of scanning optical microscopy. In this technique an optical signal is collected from a small spot on the surface of the sample, the position of the spot being scanned with the help of a micro-positioning device. The yield is a map of the scattering intensity of the sample surface. In this method, as in the classical optical techniques, the domain contrast is mainly due to the difference of the optical indicatrices in the domains. In the case of nonferroelastic domains, where their optical indicatrices are the same, such difference is induced by application of additional dc electric field. Customary, the informative optical signal is additionally modulated and lock-in technique is used to increase the sensitivity of the method and to suppress the unwanted background. In this section, not going into detail of technical implementations of the method, we will outline the ideas of its different modifications, illustrate its performance

with some images, and indicate its limitations. We will discuss *confocal scanning optical microscopy* (CSOM), *near-field scanning optical microscopy* (SNOM³), and one more relevant technique.

In confocal scanning optical microscopy (CSOM) a laser light is focused to a diffraction-limited spot on the sample surface, the light reflected back from this spot is detected using conventional optics. This method has been used for imaging natural domain patterns in (Ba,Sr)TiO₃ films (Hubert et al., 1997) and artificial domain patterns in LiNbO₃ crystals (Tikhomirov et al., 2000). The submicron spatial resolution is readily achievable with this method.

Near-field scanning optical microscopy (SNOM) (Betzig and Trautman, 1992) goes beyond the diffraction limit of the $\lambda/2 \cong 200$ nm where λ is the wavelength of the visible light. This method is based on the fact that the classical diffraction limit of optical resolution is applicable if the detection element or the light source are located at a distance many wavelengths from the observed object. If, however, the detector is scanned laterally across the sample surface in its close proximity, an image of the surface can be created at a resolution which depends on the size of the light source or the detector and the distance from them to the surface. The subwavelength resolution can be achieved if the source having the size smaller than λ is placed closer than λ to the surface or, alternatively, if the equally small detector is placed as close to the surface. This happens due to the so-called near-field effects. SNOM is used in two modifications: with aperture (a-SNOM) and *apertureless* (s-SNOM⁴). The latter modification is also called *scattering* SNOM.

A-SNOM itself can function in two modes: excitation mode and collection mode. In the excitation mode, a metal-coated optical fiber with an open tip is used to make a light spot on the sample surface and the classical far-field optics is used for the detection of the scattered light.

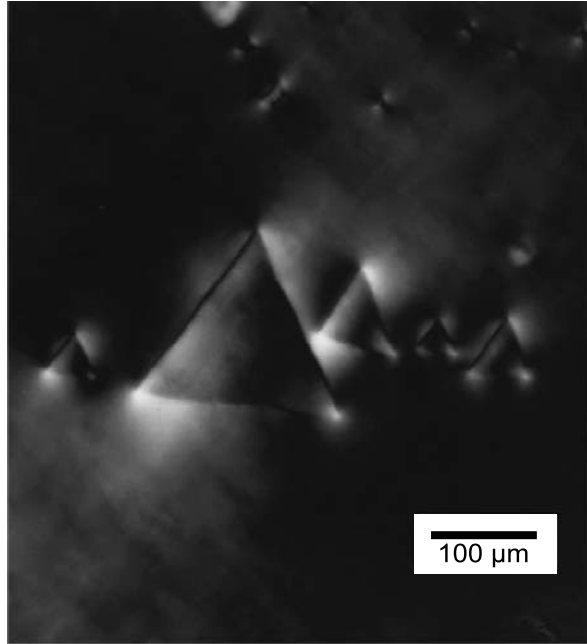
In the collection mode, the sample is illuminated with a classical optics source but a metal-coated optical fiber with an open tip is used for the detection of the scattered light. In both modes, the spatial resolution of 100 nm is routinely obtained, which in principle may be improved up to 20 nm (Levy et al., 2000). The resolution of a-SNOM is fully controlled by the apertures diameter at the tip, which, for several reasons, cannot be made smaller than 50 nm (Levy et al., 2000; Setter et al., 2006). This technique has been applied for imaging of domain patterns in BaTiO₃, PZT (Smolyaninov et al., 1999, 2001), and LiTaO₃ (Smolyaninov et al., 1999, 2001; Yang et al., 1997). Figure 4.11.1 shows an example of a-SNOM image of a domain pattern in a LiTaO₃ crystal.

The apertureless SNOM circumvents the problem of the aperture diameter and opens a way to further improvement of the resolution. The idea of this technique is, while using classical optics light source and detector, to introduce a subwavelength scatter (e.g., an AMF tip) in the light spot in the close vicinity of

³ NSOM is also used as abbreviation.

⁴ Abbreviation ANSOM is also in use.

Fig. 4.11.1 SNOM (aperture 60 nm) image 180° domains in Z-cut of LiTaO_3 after domain inversion at room temperature. Resolution of the image 200 nm. Reprinted with permission from Yang et al. (1997). Copyright (1997), American Institute of Physics



the surface. Now if the light, which passes through the scatter, can be distinguished from the unwanted background, the scatter itself can play a role of the light source or detector of a subwavelength size. This technique has been successfully applied to domain imaging in the samples $(\text{Ba}, \text{Sr})\text{TiO}_3$ (Hubert and Levy, 1998; Levy et al., 2000) and TGS (Orlik et al., 2000), the spatial resolution up to 30 nm being reported. Figure 4.11.2 shows an example of s-SNOM image of 180° domain pattern in a TGS sample plate cleaved perpendicular to the polar axis.

An optical scanning technique conceptually close to s-SNOM has been recently developed by Eng and coworkers (Otto et al., 2004). In this technique,

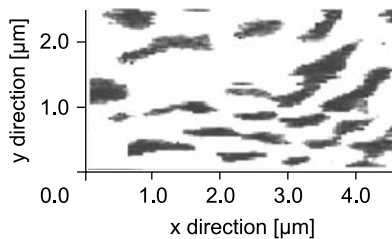


Fig. 4.11.2 Apertureless SNOM image of 180° domain pattern in a TGS sample plate cleaved perpendicular to the polar axis. Image pixel size is 35 nm. Reprinted with permission from Orlik et al. (2000). Copyright (2000), American Institute of Physics

the optical properties of the sample are affected via the electro-optic effect produced by the electric field of a fully metal-coated AFM tip. If the tip radius is small and positioned close enough to the surface, the optical properties of the sample will be modified only in a small area. Thus, if the signal from this area can be distinguished from the background, by scanning the tip, one gets the map of the electro-optical coefficient of the sample surface. This information, as in standard optical techniques, can provide an image of the domain pattern in the material. This technique has been applied to domain visualization in BaTiO_3 with a 250 nm spatial resolution controlled by the confinement of the electric field of the tip.

4.12 Additional Methods and Concluding Remarks

In the preceding sections we attempted to offer a fairly comprehensive survey of methods used to visualize ferroic domains or to obtain some information concerning the distribution of their sizes and shapes. But the list is not and cannot be complete: new techniques are constantly appearing based either on improved technical methods or on new physical principles. We shall mention very shortly some of those which have not yet been mentioned.

When a laser beam propagates through a multidomain ferroic crystal, a diffraction pattern can be observed bringing information of the domain structure in the material. This has been demonstrated for KDP (Salomon, 1981), LiNbO_3 (Blistanov et al., 1984), and TGS (Shapiro et al., 1966) crystals. A somewhat related technique, named “laser tomography” by Ratcliffe (1982), consists essentially of scanning, with an extremely fine beam of light from a laser, through the specimen and viewing the scattered light in a perpendicular direction, the specimen being immersed in a fluid chosen so as to match the appropriate refractive index. A theoretical model relevant to these observations was addressed by Laikhtman and Petrov (1977a,b).

Scanning acoustic microscopy is customarily applied as a method to study elastic nonhomogeneities. In this method, leaky surface acoustic waves which propagate along the interface between a specimen and a liquid coupler are excited. The reflection of the waves at any texture gives information both on the location of the latter and on the variation of acoustic impedance. Kojima (1989, 1983) showed that a commercial scanning acoustic microscope can be used to obtain some information about ferroelastic domains. When reflected acoustic waves are analyzed, evidence about the geometry of ferroelastic domains in $\text{Gd}_2(\text{MoO}_4)_3$ and $\text{NdP}_5\text{O}_{14}$ crystals was obtained.

The scanning electron acoustic microscopy is a method designed specifically to observe ferroic domains. The apparatus by Zhang et al. (1996) was based on a commercial scanning electron microscope. The electron beam injected into the sample is intensity modulated, typically at a frequency of 40–400 kHz. The resulting acoustic signal is detected by a piezoelectric transducer, coupled to the

rear surface of the sample. The obtained acoustic signal is processed to form electron-acoustic image on an oscilloscope. Yin et al. (1998) succeeded in using the method to observe domains in BaTiO₃ ceramics and PMN–PT single crystals. Liao et al. (1999a,b) observed simultaneously a secondary electron image and succeeded in using the method to identify changes in domain structures of BaTiO₃ crystals due to the application of electric field. Jiang et al. (1999) applied this method to crystals of NdP₅O₁₄ and Bi₄Ti₃O₁₂ and discussed the phenomena involved in generating and detecting acoustic waves due to the interaction between the primary electron beam and the sample. Different mechanisms such as thermo-elastic effect, piezoelectric, and electrostrictive effect as well as excess carrier coupling may contribute to the acoustic signal generation depending on the specimen under investigation. Spatial variations of these properties influence the reflected signal and give rise to image contrast. Yin et al. (1999) pointed out that the “thermal wave coupling mechanism,” i.e., local heating leading to acoustic waves, could also play a role at low-modulation frequencies.

Considerable attention had been paid by the Grenoble group to the γ -ray diffractometry method. Bastie et al. (1976) and Bastie and Bornarel (1979) used the following system to study domains in ferroelectric–ferroelastic KDP: A collimated beam of γ -rays ($\lambda = 0.03 \text{ \AA}$) from a radioactive source enters the investigated crystal and is diffracted; the transmitted beam is eliminated by a lead stop. Rotating the sample makes it possible to obtain rocking curves, i.e., intensity of the diffracted beam plotted against the angle ω corresponding to a Bragg peak. The integrated reflecting power of each Bragg peak is proportional to the corresponding diffracted region of the sample. Scanning the sample and taking rocking curves at different positions give information about the domain distribution in the sample. This may be proved useful, e.g., for opaque crystals. At a particular spot of the sample and applying successively electric field, hysteresis curve can be obtained showing how the two domain states are represented in the diffracting region during the hysteresis cycle. An improved version is the differential γ -ray diffractometry offered by Bornarel and Bastie (1980). It permits a study of the effects of applied electric field, which result in deformations of different sign in domains of opposite polarity.

Some information on ferroelectric domain pattern can be obtained using the electron emission effect. The mechanism was discussed in some detail by Kugel et al. (1995), Kugel and Rosenman (1996), Rosenman (1993), and Rosenman and Rez (1993). The spatial distribution of the emitted electron flux reflects the domain pattern. Electron flux generated from the sample is amplified and transferred to a luminescent screen. The spatial resolution of the method is low, about 10 lines per millimeter. The method was applied to LiNbO₃, TGS, and LiTaO₃ crystals.

Several authors studied electron paramagnetic resonance (EPR) spectra of selected ferroic crystals, paying attention to the influence of domains. Hartmann and Windsch (1972) were probably the first to observe domain-related EPR phenomena: They showed that changing the domain pattern of vanadyle-doped TGS by a thermal shock or electric field application, which results in an

expected increase of permittivity due to domain wall contribution, is also reflected by an additional EPR spectrum whose intensity decreases with time. Up to now this effect was not utilized to reach some new information on changes in domain patterns. Fujimoto and Sinha (1983) studied EPR spectra of impurity ions VO^{2+} embedded in $(\text{NH}_4)_3\text{H}(\text{SO}_4)_2$ crystals (species $\bar{3}m - \epsilon s - 2/m$) and showed how the three domain states can be identified. Interesting results were obtained by Zapart et al. (1997) for crystals of $\text{KSc}(\text{MoO}_4)_2$ (at low temperatures, species $\bar{3}m - \epsilon s - 2/m$). By measuring EPR spectra and their line shapes, it was deduced that the domain width is just twice the domain wall thickness so that the relative volumes of domain walls and domains are comparable.

Li et al. (1992) showed that the micro-Raman spectroscopy can be used to identify ferroelastic switching. The changes of spectra due to compression of PbTiO_3 and BaTiO_3 crystals were interpreted as due to 90° domain reorientation.

Nuclear magnetic resonance (NMR) spectra can also be used to obtain some information about domain states represented in ferroic crystals containing ions with corresponding properties. As an example we mention the study of CsPbCl_3 (species $m\bar{3}m - \epsilon s - 2/m$) by Lim and Jeong (1999); the presence of domains was detected on the basis of NMR signals of ^{133}Cs .

It is obvious that neutron diffraction and X-ray diffraction can be used to obtain data on the relative volumes occupied by different ferroelastic domain states. Jex et al. (1982) studied crystals of RbCaF_3 (species $m\bar{3}m - 4/mmm$) by neutron diffraction, using a four-circle diffractometer. The full set of (311) and (331) superlattice points was observed as a function of temperature and it was shown how from their intensities the relative volumes of the three ferroelastic domain states can be determined. Tietze et al. (1981) solved the same problem by X-ray diffraction for crystals of KMnF_3 (the same species). The method employed utilized the intensity distribution from symmetrically equivalent superlattice Bragg peaks. Measured were intensities of properly selected Bragg reflections from which relative volumes of the three domain states are calculated.⁵

From the preceding sections of this chapter as well as from the above paragraphs it is evident that the number of domain observation methods is very large; and new methods are still being offered, one a year at least. For a ferroic species of any symmetry several experimental approaches are available to obtain information about domains in a particular sample. Yet we could not state that the extent of this information is always satisfactory. Many of available methods do not offer a high enough spatial resolution. In addition, a prevailing number of methods are those which provide information just about domains which reach the sample surface. Thus shapes and sizes of domains embedded inside a sample are mostly unknown, especially when domains in question are nonferroelastic. In particular, the question of built-in nuclei

⁵ Interestingly enough, in both cases it was found that the relative volumes of the three ferroelastic domain states differ substantially well below the transition temperature but approach 1/3 close to the transition temperature.

remains an important unsolved problem of ferroelectric switching. Similarly, available information on domains inside ceramic grains is rather incomplete, for obvious reasons. Methods offering the highest and fully satisfactory resolution are limited to samples of unrealistic thickness, where domain properties may significantly differ from those in bulk samples.

A very unsatisfactory situation is in the field of dynamic processes. While classical methods described above can give information about single domain wall velocities, we have still no reliable way to obtain direct information about particular dynamic processes which take place during switching of nonferroelastic ferroelectrics or higher order ferroics.

Chapter 5

Static Domain Patterns

5.1 Introductory Remarks and Scheme of the Chapter

After discussing in some detail the theoretical aspects of properties of domain states and after describing a number of methods to observe domains, we now wish to deal with some real domain structures in single crystals. Several thousands of papers have been published on observations of domain patterns in different kinds of ferroics,¹ offering a large amount of interesting data for materials listed in Chap. 3 and many others. Some of them are just observations as it stands, others were performed with the aim to create situations corresponding to theoretically defined conditions.

When treating properties of domain patterns in real ferroic samples, it is necessary to distinguish features of stable domain structures from those of dynamic domain phenomena. In the present chapter we have primarily in mind static and quasistatic domain patterns which can be observed in the absence of intentionally applied external forces that would tend to change their geometry or sizes. We define static or quasistatic domain patterns arbitrarily as those which do not appreciably change on the time scale of hours. These are the patterns which may correspond to the thermodynamic equilibrium of the sample or which are metastable with long lifetimes because of large energy barriers that would have to be overcome to reach more stable configuration.

Available data on domain patterns can be, in some approximation, classified into three categories. First, we can observe domains in a sample as it stands, meaning that its history (sample preparation, thermal record, applied forces) is not known. Second, and perhaps most often, the sample has been treated in a way which has been planned or which at least is known. Third, the sample quality and the external conditions (e.g., thermal history) are well defined and carefully prepared so that we may expect the resulting domain structure to correspond to minimum energy harmonizing with its intrinsic properties and external conditions; this is often referred to as the “equilibrium domain pattern.”

¹ We have in mind nonmagnetic ferroics; in the authors' catalogue of references some 6000 papers are listed. Surely the number of publications dealing with ferromagnetic domains would be higher by a factor between 50 and 100.

In the present chapter we first discuss, in Sect. 5.2, theoretical aspects of the last mentioned case, paying attention to the simplest example of equilibrium domain pattern in ferroelectric samples containing only domains with antiparallel orientation of \mathbf{P}_S vectors (“180° domains”). Such patterns have been studied extensively in ferroelectrics, both nonferroelastic and ferroelastic, with the aim to obtain regular patterns corresponding to thermodynamic equilibrium. This research was, in its early stages, inspired by successful treatments of equilibrium domain structures in ferromagnets. The role of the energy of demagnetizing field has its electrical counterpart treated in some detail in the following section. However, in ferroelectrics the situation is different because of the existence of free charge carriers that may contribute in a decisive way to the reduction of depolarization energy. This issue will be addressed in Sect. 5.2 as well.

In Sect. 5.3 we shall discuss another factor influencing the domain patterns: Formation of the latter during a first-order transition, when the boundary separating the parent and ferroic phases, may strongly influence the formation of domains. The origin of this effect is connected with the elastic and electric compatibility conditions.

In the most extensive Sect. 5.4, some real domain patterns will be described, which have been observed in different kinds of ferroics. In fact, compared with the vast amount of available data, this selection is—due to the lack of space—rather short. Here we restrict ourselves to single crystals representing different kinds of species; some observations of domains in thin films will be given in Chap. 9. In Sects. 5.4.1, 5.4.2, and 5.4.3, we will give examples of patterns in some “typical” ferroics. In Sect. 5.4.4 we shall present some examples of R cases, those when no ideal elastically compatible domain walls exist, and will show how in samples representing such species the problem of multidomain states is solved in reality. Only marginal attention will be paid to domains in ferroelastoelectrics, in the Sect. 5.4.5, while the so-called tweed pattern will be shortly discussed in Sect. 5.4.6.

The present chapter will not address elastic effects on formation of ferroic domain patterns. This issue will be discussed in Chap. 9 devoted to thin films, the systems where these effects are often of crucial importance.

5.2 Equilibrium 180° Domain Patterns in a Ferroelectric Plate: Theories

In this section we deal with theoretical approaches to equilibrium domain patterns, considering the classical situation of 180° domain structures: A sample of uniaxial ferroelectric or of a multiaxial ferroelectric in which only domains with antiparallel polarization exist. Here we will address this problem for the ideal case where no external means (like short-circuited electrodes) are used to set the electric field in the sample to zero. In the case of a ferroelectric in a

short-circuited capacitor, in the first approximation, the splitting into domain of the sample is not expected. However, more rigorous analysis reveals that this may not be always the case, especially in ferroelectric thin films. This special problem will be addressed later in Sect. 9.4.

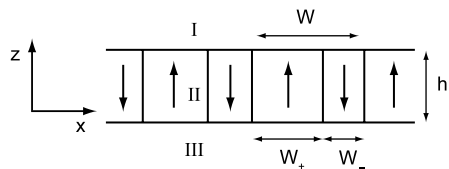
In Sect. 2.3, the thermodynamic theory considers ferroelectrics for a specified value of the macroscopic electric field and, in the absence of the latter, a uniform single-domain state was found energetically favorable. However, such state can readily cease to be energetically favorable as far as a finite free-standing piece of the ferroelectric is considered. In this case, the bound charges of the spontaneous polarization on the surface of the sample will create the depolarizing electric field which will increase the energy of the system. The energy of depolarizing electric field can be reduced, if the sample is split into domains. At the same time, the domain formation will increase the energy of the system by the energy of the appeared domain walls. All in all, the balance between these two contributions to the energy will decide whether the material splits into domains or not and determines the parameters of the domain pattern if its formation is favorable. It is clear from electrostatic arguments that if the sample is elongated along the polarization direction, the energy of the depolarizing field can be rather small and a single-domain state may be readily favorable whereas in a plate—like a sample with the polarization normal to the plate—the energy of the depolarizing field is larger and a multidomain state is expected.

In this section we will discuss the latter case. We have in mind a plate of thickness h of a ferroelectric cut perpendicularly to the ferroelectric axis z ; the plate thickness is assumed to be much smaller than its linear dimensions. The simplest domain pattern expected in such a system (and often experimentally observed) is schematically shown in Fig. 5.2.1. In real system, this pattern usually possesses no net polarization, i.e., the fractions of the opposite domains are equal, and it is dense, i.e., its period W is much smaller than the plate thickness h . When corresponding to energy minimum, the period of the pattern W follows the square root law of h :

$$W \propto \sqrt{h}, \quad (5.2.1)$$

which is known as the Kittel law in magnetic system; for ferroelectrics, this law has been obtained by Mitsui and Furuichi (1953). We will come across this law again in Chap. 9, when discussing the elastic effect on domain formation in ferroelectric thin films. Below in this section we present the analysis by Mitsui

Fig. 5.2.1 Schematics of a ferroelectric plate with lamella domain structure. I and III—free space, II—ferroelectric



and Furuichi and discuss different aspects of 180° domain structures as well as different theories dealing with these structures. However, before doing so we would like first to elucidate the basic origin of the Kittel–Mitsui–Furuichi law.

The Kittel–Mitsui–Furuichi law results from the balance between the energy of the created domain walls F_W and the electrostatic energy F_{dep} . The former is evidently proportional to the plate thickness and domain density ($\propto 1/W$), thus

$$F_W \propto h/W. \quad (5.2.2)$$

At the same time, the electrostatic energy obeys a relation

$$F_{\text{dep}} \propto W. \quad (5.2.3)$$

This relation is due to the fact that, in the dense domain pattern, there is a strong reduction of the electric field at the distances larger than W from the sample surface; at such distances the contributions from the stripes of positive and negative bound charges on the surface efficiently compensate each other. Thus, only the approximately W -thick surface-adjacent layers contribute to the electrostatic energy of the system. Minimizing the sum of the contributions given by Eqs. (5.2.2) and (5.2.3) readily leads to the sought law. One can check that similar reasoning can be applied to magnetic and elastic systems leading to the same law for the domain period. From the above arguments, one can also conclude that the Kittel–Mitsui–Furuichi law should fail at the point when it starts predicting the domain period larger than the plate thickness since at this point the arguments justifying Eq. (5.2.3) fails. This issue will be addressed later in this section and in Sect. 9.4.

Let us now address the Mitsui and Furuichi theory. To determine equilibrium domain structures the thermodynamic potential of the plate-like sample should be minimized, taking into account all electrical and mechanical boundary conditions. This is a complicated task which in the Mitsui and Furuichi approach is simplified by assuming that the sample behaves as a “hard” ferroelectric, its dielectric properties being adequately described by the following linear relations:

$$\begin{aligned} P_z(x, y, z) &= \pm P_S(x, y) + \varepsilon_0(\kappa_c - 1)E_z(x, y, z), \\ P_x &= \varepsilon_0(\kappa_a - 1)E_x(x, y, z), \\ P_y &= \varepsilon_0(\kappa_a - 1)E_y(x, y, z), \end{aligned} \quad (5.2.4)$$

where \mathbf{E} is the local macroscopic field and $\kappa_{a,c}$ denotes the diagonal component of the permittivity tensor. Thus we assume the existence of spontaneous polarization with a given magnitude and with two possible orientations along the z -axis, but neglect nonlinear effects. The plate (medium II) is surrounded by vacuum (media I and III) as shown in Fig. 5.2.1. This approach is equally applicable to both proper and improper ferroelectrics although it is approximate

only and we shall discuss its limitations later. The Maxwell equations require for the dielectric displacement \mathbf{D} in medium II

$$\operatorname{div} \mathbf{D}_{\text{II}} = \rho_f; \quad (5.2.5)$$

here ρ_f is the density of *free* charge in the dielectric. The boundary conditions for the interface I/II read

$$(\mathbf{D}_{\text{I}} - \mathbf{D}_{\text{II}})\mathbf{n} = \sigma_f, \quad (5.2.6a)$$

$$(\mathbf{E}_{\text{I}} - \mathbf{E}_{\text{II}})\mathbf{t} = 0, \quad (5.2.6b)$$

where \mathbf{n} is the unit vector along the normal pointing from II to I and \mathbf{t} denotes the unit tangential vector; σ_f stands for the surface free charge density. Similar conditions hold for the interface II/III. At this stage, we do not allow for the existence of any free charge carriers so that $\rho_f = \sigma_f = 0$.

Let us first assume that the crystal is single domain with positive spontaneous polarization. Then, by symmetry, the involved quantities can depend on z only. From Eqs. (5.2.5) and (5.2.6a) we find that an electric field \mathbf{E}_{dep} exists in the plate, of magnitude

$$E_{\text{dep}} = -P_0/\kappa_c \varepsilon_0, \quad (5.2.7)$$

which is directed against spontaneous polarization and is therefore called *depolarizing field*. In general this field can be very large. For a crystalline BaTiO₃ plate at room temperature, e.g., with $P_S \cong 0.26 \text{ cm}^{-2}$ and $\kappa_c \cong 150$ one readily finds $E_{\text{dep}} \cong 2 \times 10^8 \text{ V/m}$. The electrostatic energy of this field is referred to as *depolarization energy*, which can also be substantial. Its *spatial* density is generally given by the relation

$$\Phi_{\text{dep}} = \frac{1}{2} \mathbf{E}(\mathbf{D} - \mathbf{P}_S) = \frac{1}{2} \varepsilon_0 \kappa_{ij} E_j E_i. \quad (5.2.8)$$

For our purpose it is useful to integrate it so as to obtain the depolarization energy U_{dep} *per unit area* of the plate. From the two preceding relations we obtain

$$U_{\text{dep}} = P_S^2 h / 2 \varepsilon_0 \kappa_c. \quad (5.2.9)$$

By formation of domain structure this value can be essentially reduced. Let us find the depolarizing energy for a periodic domain pattern (W is its period), in which domains of alternating polarization are lamellae of the width W_+ and W_- ($W_+ + W_- = W$), with walls perpendicular to the x -axis, as shown in Fig. 5.2.1. For this geometry, the spontaneous polarization in medium II can be written in the form of Fourier series

$$P_S(x) = P_S \frac{W_+ - W_-}{W_+ + W_-} + \sum_{n=1}^{\infty} \frac{4P_S}{\pi n} \sin \frac{\pi n W_+}{W_+ + W_-} \cos nkx. \quad (5.2.10)$$

It is useful to introduce the following abbreviations:

$$c \equiv \sqrt{\kappa_a/\kappa_c}, \quad g \equiv \sqrt{\kappa_a\kappa_c} = c\kappa_c, \quad (5.2.11a)$$

$$k = 2\pi/W, \quad A = (W_+ - W_-)/W, \quad (5.2.11b)$$

$$R = \pi ch/W. \quad (5.2.11c)$$

To calculate the depolarization energy for this case we first have to determine the spatial field distribution. In region II, the potential $\phi_{\text{II}}(x, z)$ must satisfy the Laplace equation:

$$\kappa_a \frac{\partial^2 \phi_{\text{II}}}{\partial x^2} + \kappa_c \frac{\partial^2 \phi_{\text{II}}}{\partial z^2} = 0. \quad (5.2.12)$$

Similar equations hold for ϕ_{I} and ϕ_{III} in regions I and III, however, with the permittivity equal to 1. The boundary conditions include the potential continuity

$$\phi_{\text{I}}(z = 0) = \phi_{\text{II}}(z = 0), \quad \phi_{\text{II}}(z = -h) = \phi_{\text{III}}(z = -h), \quad (5.2.13)$$

and the continuity of tangential components of the field which can be written as

$$\frac{\partial \phi_{\text{I}}}{\partial x}(z = 0) = \frac{\partial \phi_{\text{II}}}{\partial x}(z = 0), \quad (5.2.14a)$$

$$\frac{\partial \phi_{\text{II}}}{\partial x}(z = -h) = \frac{\partial \phi_{\text{III}}}{\partial x}(z = -h). \quad (5.2.14b)$$

The potentials fulfilling these requirements are

$$\phi_{\text{I}} = \frac{1}{4\pi\epsilon_0} \sum_{n=1}^{\infty} \frac{1}{n^2} \frac{8P_S ch}{R} \sin n\pi \frac{A+1}{2} \frac{1}{1+g \coth nR} \cos nkx \exp(-nkz), \quad (5.2.15a)$$

$$\phi_{\text{II}} = \frac{P_S A}{\epsilon_0 \kappa_c} z + \frac{1}{4\pi\epsilon_0} \sum_{n=1}^{\infty} \frac{1}{n^2} \frac{8P_S ch}{R} \sin n\pi \frac{A+1}{2} \frac{\sinh(nR + nkc z)}{\sinh nR + g \cosh nR}, \quad (5.2.15b)$$

$$\phi_{\text{III}} = -\frac{P_S Ah}{\epsilon_0 \kappa_c} - \frac{1}{4\pi\epsilon_0} \sum_{n=1}^{\infty} \frac{1}{n^2} \frac{8P_S ch}{R} \sin n\pi \frac{A+1}{2} \frac{\cos nkx \exp[nk(z+h)]}{1+g \coth nR}. \quad (5.2.15c)$$

Using these results one can calculate the electrostatic energy of the system, which comprises the energy of the field inside the plate, given by Eq. (5.2.8), and the energy of the field outside it. Thus, for the domain pattern one finds for the electrostatic energy per unit area of the plate

$$U_{\text{dep}} = \frac{1}{2} \frac{P_S^2 h}{\epsilon_0 \kappa_c} \left(A^2 + \frac{8g}{\pi^2 R} \sum_{n=1}^{\infty} \frac{1}{n^3} \sin^2 \left(n\pi \frac{A+1}{2} \right) \frac{1}{1+g \coth nR} \right). \quad (5.2.16)$$

When looking for domain pattern which minimizes the total energy, one readily checks that the structures with zero net polarization, i.e., with $A = 0$, are always more advantageous than electrically unbalanced structures with $A \neq 0$. Thus, we continue consideration for the case where $W_+ = W_- = W/2$. In the approximation where the electrostatic interaction between the plate surfaces can be neglected, expression (5.2.16) can be simplified down to the form

$$U_{\text{dep}} = \frac{0.13P_S^2 W}{\varepsilon_0(1 + \sqrt{\kappa_c \kappa_a})}. \quad (5.2.17)$$

As can be shown from analysis of series (5.2.16), this approximation is valid if

$$W < h \sqrt{\frac{\kappa_a}{\kappa_c}}. \quad (5.2.18)$$

We will call this situation dense domain pattern. This can be considered as generalization of the notion of dense domain pattern (defined above by the relation $W < h$) to the case of materials with strong dielectric anisotropy.

Now the period of the equilibrium domain structure can be found by minimizing the total energy of the system per unit area of the plate

$$U_{\text{tot}} = U_{\text{dep}} + U_{\text{w}}, \quad (5.2.19)$$

where U_{w} denotes the energy of domain walls per unit surface of the plate, which relates to the wall energy per unit area σ_{w} as

$$U_{\text{w}} = 2\sigma_{\text{w}} \frac{h}{W}. \quad (5.2.20)$$

Now, minimizing total energy with respect to W we obtain for the equilibrium domain width

$$W_{\text{eq}}/2 = \sqrt{h_{\text{M}}h}, \quad (5.2.21)$$

where the characteristic length reads

$$h_{\text{M}} = 3.7\varepsilon_0(1 + \sqrt{\kappa_a \kappa_c})\sigma_{\text{w}}/P_S^2. \quad (5.2.22)$$

This result was first obtained by Mitsui and Furuichi who discussed domain patterns in Rochelle salt crystals. With this domain structure, the total energy per unit area of the plate attains the value

$$U_{\text{min}} = 2 \left[\frac{0.26\sigma_{\text{w}}}{\varepsilon_0(1 + \sqrt{\kappa_c \kappa_a})} \right]^{1/2} P_S h^{1/2}. \quad (5.2.23)$$

Using relations (5.2.18) and (5.2.21) one finds the obtained results are valid for sample thicker than the critical thickness²

$$h_{\text{crit}} = 4\sqrt{\frac{\kappa_c}{\kappa_a}}h_M. \quad (5.2.24)$$

Some estimates for h_{crit} for a number of ferroelectrics have been performed by Kopal et al. (1997). Taking $\sigma_w = 10 \text{ erg/cm}^2 = 10^{-2} \text{ J/m}^2$ it is found that at room temperature for TGS $h_{\text{crit}} \cong 10^{-5} \text{ cm}$, for BaTiO₃ $h_{\text{crit}} \cong 10^{-8} \text{ cm}$, for Pb₅Ge₃O₁₁ $h_{\text{crit}} = 6 \times 10^{-7} \text{ cm}$, for Gd₂(MoO₄)₃ $h_{\text{crit}} = 4 \times 10^{-5} \text{ cm}$, for KH₂PO₄ (at 100 K) $h_{\text{crit}} = 10^{-6} \text{ cm}$, and for Rochelle salt (at 273 K) $h_{\text{crit}} = 3 \times 10^{-5} \text{ cm}$. Common single crystalline ferroelectric samples prepared in the laboratory by cutting and polishing have usually thicknesses 100–500 μm ; for these, the dense pattern approximation is fully justified.

These estimates apply to temperatures rather far below the phase transition points. One might argue that domain structures are usually formed on cooling at temperatures T_C . It is therefore interesting to estimate how h_{crit} may depend on temperature (Kopal et al., 1997). Let us consider ferroelectrics with a second-order phase transition. For a proper uniaxial ferroelectric material we expect $P_S^2 \propto (T_0 - T)$, $\kappa_z \propto (T_0 - T)^{-1}$, and we recall that $\sigma_w \propto (T_0 - T)^{3/2}$ (see Sect. 6.2.1). Thus h_{crit} scales like $(T_0 - T)^{-1}$. For an improper ferroelectric, on the other hand, we expect $P_S \propto (T_0 - T)$, $\kappa_z = \text{const.}$, and again $\sigma_w \propto (T_0 - T)^{3/2}$ so that h_{crit} scales like $(T_0 - T)^{-1/2}$. For the case of cubic ferroelectrics, one can readily check that h_{crit} also scales like $(T_0 - T)^{-1/2}$. Thus, the value of h_{crit} may be quite large close to the phase transition point. Also for ferroelectric transitions which are discontinuous but close to second order, we may expect that h_{crit} will increase as T_C is approached from below. However, it practically occurs that it is in ferroelectric thin films where the dense pattern approximation may not be valid. This situation will be discussed in Sect. 9.4.

One should note that Eqs. (5.2.21), (5.2.22), and (5.2.23) have been repeatedly used to discuss observed domain patterns and their time developments. In particular, many estimates for the energy densities σ_w were based on observations of quasi-regular lamellar domain structures and Eqs. (5.2.21) and (5.2.22).

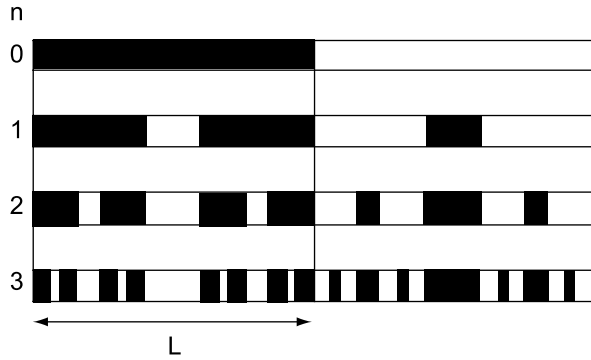
The conclusions obtained above on the structure of the equilibrium domain pattern have been drawn using several assumptions. One of these was that regarding the periodicity of the resulting equilibrium pattern. A possibility of alternative more complicated equilibrium structure has also been discussed in the literature by Ozaki et al. (1993) who claimed that in crystals of KH₂PO₄ the antiparallel domain pattern has the form of lamellae, as reported before (Mitsui and Furuichi, 1953), but that as the crystal plate thickness d increases, the periodicity... $W_+/W_-/W_+/W_-$... with $W_+ = W_-$ becomes broken and more

² The given expression for the critical thickness is very close to that given by Kopal et al. (1997).

complicated yet still periodical sequences of positive and negative domains occur, falling into the category of fractal patterns. They were interpreted as periodic patterns representing the so-called prefractals of the pentad Cantor sets (Ozaki, 1995). The first four prefractal structures, $n = 0, 1, 2, 3$ are shown in Fig. 5.2.2 (Ozaki and Ohgami, 1995). In the left half-period L we have N domain stripes of width W_+ of positive polarity. The $n(n+1)$ th prefractal structure is obtained from the previous one by reversing the polarity of a central fifth part of every negative domain in the right half-period in the n th structure. Ozaki and Ohgami calculated the depolarization energy of such patterns, assuming the equation of state (5.2.4) and working in the dense pattern approximation, to find for the total energy of the system

$$U_{\text{tot}} = \frac{4P_S^2 L}{\pi^3 \epsilon_0 (1 + \sqrt{\kappa_c \kappa_a})} \alpha(n) + (2^{n+1} - 1) \frac{\sigma_w h}{L}. \quad (5.2.25)$$

Fig. 5.2.2 Schematic drawing of the ‘prefractal’ domain patterns of period $2L$ with $n = 0, 1, 2, 3$ (see text). \mathbf{P}_S is perpendicular to paper. *White* and *black* correspond to the directions of polarization up and down. After Ozaki and Ohgami (1995)



Here numerical factors are $\alpha(0) \cong 1.052$, $\alpha(1) \cong 0.435$, $\alpha(2) \cong 0.183$, $\alpha(3) \cong 0.117$, etc. For $n = 0$ we obtain the situation described by Eqs. (5.2.17), (5.2.19), and (5.2.20). U_{dep} as a function of n exhibits a minimum for $n = 3$. At this configuration the ratio of plus/minus domains is 1.05 in the left half-period and 0.95 in the right half-period; the structure as a whole, of course, is neutral. The half-period L_{eq} minimizing U_{tot} is

$$L_{\text{eq}} = \sqrt{(2^{n+1} - 1) \frac{\sigma_w \pi^3 \epsilon_0 (1 + \sqrt{\kappa_c \kappa_a}) h}{8P_S^2 \alpha(n)}} \quad (5.2.26)$$

and the corresponding energy is

$$U_{\text{min}} = 2 \left[\frac{8\alpha(n)\sigma_w(2^{n+1} - 1)}{\pi^3 \epsilon_0 (1 + \sqrt{\kappa_c \kappa_a})} \right]^{1/2} P_S h^{1/2}, \quad (5.2.27)$$

which exhibits minimum value for $n = 0$, as given by Eq. (5.2.22) for the previously considered structure with the simple periodicity. Thus, we see that prefractal structure does not provide us with a deeper energy minimum for the system.

All the lamella domain patterns considered above can be called “one dimensional” since they are characterized by just one parameter, their width. The appearance of such patterns can be expected in ferroelectric ferroelastics where domain wall orientations are strictly limited. At the same time, in the case of nonferroelastic domain patterns, where the domains are separated with W_∞ walls parallel to \mathbf{P}_S , other “two-dimensional” patterns can occur. Indeed, observations of 180° domain patterns in such crystals show very often domains of one polarity in the form of prolonged islands in the sea of the domain state with opposite polarity of \mathbf{P}_S . The question what are equilibrium parameters of two-dimensional domain patterns was addressed by Fousek and Safrankova (1966). Several types of two-dimensional domain patterns have been considered; however, no configuration giving the minimal energy lower than that of the simple lamella structure has been found. One of the considered types is explained in Fig. 5.2.3 where the “unit cell” of this pattern is shown. Figure 5.2.4 shows the dependence of the minimal energy of the system as the function of the aspect ratio of the cell. It demonstrates that the lamella structure corresponds to the energy minimum.

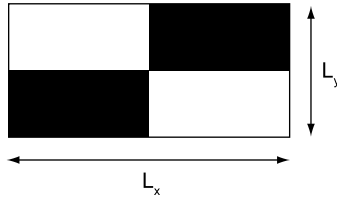


Fig. 5.2.3 ‘Unit cell’ of a simple two-dimensional domain pattern. \mathbf{P}_S is perpendicular to paper. *White* and *black* correspond to the directions of polarization up and down. After Fousek and Safrankova (1966)

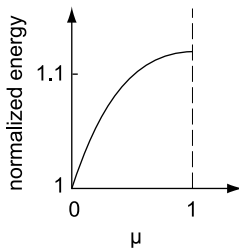


Fig. 5.2.4 Energy per unit area of the equilibrium patterns showed in Fig. 5.2.3 (normalized to that of the equilibrium lamella structure with the same material parameters of the ferroelectric) plotted as a function of the aspect ratio μ of the ‘unit cell’. After Fousek and Safrankova (1966)

Now we draw the reader's attention to an implicit assumption behind the above whole analysis; specifically, the use of the hard-ferroelectric approximation has implied that the ferroelectric state in the domains remains stable under the action of the depolarizing field. For the considered case of dense domain structures, this assumption can be readily justified far from the surface of the plate where the field is much smaller than the value given by Eq. (5.2.7). At the same time, at distances smaller than the domain period, the field remains strong so that the stability of the ferroelectric state in these regions to be checked.

Let us evaluate the impact of the depolarizing field on the ferroelectric state in a dense domain pattern of typical proper ferroelectrics. As is clear from the result, Eq. (2.3.46), obtained in Sect. 2.3.6, the depolarizing field in a homogeneously polarized plate shifts the transition temperature down by C/κ_b where C is the Curie–Weiss constant and κ_b is background dielectric permittivity. This shift is the results of the depolarizing field created by two layers of the bound charge (of the spontaneous polarization) on the faces of the plate. In the dense domain pattern close to the surface of the plate, the field is created only by one layer of this kind. Thus, in this case, the field and the shift of the transition temperature are expected to be twice as small. Since for proper ferroelectrics the magnitude of C is typically 10^3 – 10^5 K and κ_b can be considered to be of the order of 10, the transition temperature at the surface of the dense domain pattern should be shifted to lower temperatures by 100–10,000 K and may become totally unrealistic. This implies that, strictly speaking, in typical proper ferroelectrics the Mitsui and Furuichi model may readily fail (e.g., for displacive ferroelectrics where the Curie–Weiss constant is about 10^5 K) except for materials with very small value of C , like in weak or pseudo-proper ferroelectrics. This is actually the failure of the hard-ferroelectric approximation, Eq. (5.2.4), close to the surface of the ferroelectric plate.

However, in improper ferroelectrics the situation is different. In these systems, ferroelectricity is not suppressed by depolarizing field, as noted by Levanyuk and Sannikov (1968). The point is that the depolarizing effect has only slight influence on the temperature of the first-order transition and none at all on that of the second order. Let us explain the latter case in some detail. The simplified thermodynamic potential of an improper ferroelectric (it can be obtained from Eq. (2.3.36) after a change of the variables and the minimization with respect to the phase of the order parameter) can be written as

$$\Phi = \Phi_0 + \frac{1}{2}\alpha\eta^2 + \frac{1}{4}\beta\eta^4 + \gamma\eta^2 P + \frac{1}{2}aP^2, \quad (5.2.28)$$

where only $\alpha = \alpha_0(T - T_0)$ is a temperature-dependent coefficient, $\beta > 0$, and $a > 0$. Setting $\partial\Phi/\partial\eta = 0$, $\partial\Phi/\partial P = E$, and depolarizing field $E = E_{\text{dep}} = -P/\epsilon_0$, we find

$$P = -\frac{\gamma}{a + 1/\epsilon_0}\eta^2. \quad (5.2.29)$$

Thus, the equation of state for the order parameter reads

$$\frac{\partial \Phi}{\partial \eta} = 0 = \alpha \eta + \left(\beta - \frac{2\gamma^2}{a + 1/\epsilon_0} \right) \eta^3, \quad (5.2.30)$$

leading to the spontaneous values

$$\eta_S^2 = -\frac{\alpha}{\beta - (2\gamma^2/a + 1/\epsilon_0)} \quad P_S = \sqrt{\frac{\alpha\gamma}{\beta(a + 1/\epsilon_0) - 2\gamma^2}}. \quad (5.2.30a)$$

From these equations we see that, in an improper ferroelectric, the depolarizing effect does not affect the transition temperature resulting only in a decrease in the magnitude of spontaneous polarization compared to its value

$$P_S = \sqrt{\frac{\alpha\gamma}{\beta a - 2\gamma^2}} \quad (5.2.30b)$$

for the short-circuited conditions.

All in all, the above analysis shows that the Mitsui and Furuichi model is fully justified in the cases of improper and weak ferroelectrics whereas, in the case of typical proper ferroelectrics, formally, this approach fails. However, on the practical level, this model (for the dense domain pattern) can be viewed as a reasonable approximation because in the main part of the sample it is fairly self-consistent. Here one should stress that if the domain wall spacing is larger than or comparable to the thickness of the sample, in typical proper ferroelectrics, the hard-ferroelectric approximation may readily fail everywhere so that the Mitsui–Furuichi-type calculations cannot be used at all for the description of domain patterns.

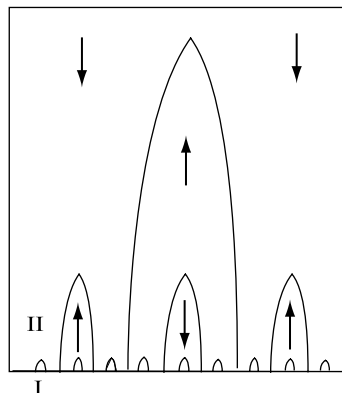
One can go beyond the Mitsui–Furuichi approach. At present, there are three ways to do it: (i) consideration of a “branching” scenario, (ii) abandoning the hard-ferroelectric approximation, and (iii) taking into account the finite conduction of the material.

The first possibility to avoid too high electric field at the plate surface has been suggested by Marchenko (1979). In his model, still working in the hard-ferroelectric approximation, it is assumed that half-lens-shaped domains exist at the sample surface, forming a quasifractal structure shown in Fig. 5.2.5. They are embedded in each other with alternating direction of P_S . There are no domain walls crossing the whole sample. Calculations lead to the maximum length L of these domains in a plate of thickness h as follows:

$$L = \frac{3^{1/2} - 1}{5 \cdot 3^{1/2} - 1} h \cong 0.1 h. \quad (5.2.31)$$

The formation of embedded domains (the so-called *branching*) stops where the domain width becomes comparable with the domain wall thickness. It is

Fig. 5.2.5 Elements of the branching domain pattern in the vicinity of the ferroelectric/free space border. I—free space, II—ferroelectric. Arrows show directions of spontaneous polarization. After Marchenko (1979)



believed that at this point the electric fields near the plate surface become small enough not to destabilize ferroelectricity.

The second possibility to avoid too high electric field at the plate surface is to abandon the hard-ferroelectric approximation (at least in the surface-adjacent areas of the sample). Unfortunately, this approach cannot be implemented purely analytically requiring numerical solution of Ginzburg–Landau equation for the polarization (Wang et al., 1995). It has been shown that, in this approach, the square root law for the thickness dependence of the domain period can also be reproduced. An advanced analysis performed by De Guerville et al. (2005) has also revealed some elements of branching in the equilibrium domain pattern found. We will address these results in more detail later in Sect. 9.4. Discussing the approach to the equilibrium domain pattern based on the Ginzburg–Landau equation, one should mention the treatment of the domain formation when crossing the phase transition from the paraelectric phase (Chenskii, 1972; Chenskii and Tarasenko, 1982). In this case, the domain pattern appears as a sinusoidal modulation of polarization. Remarkably, the period of this modulation also changes with the plate thickness as \sqrt{h} . We will address the results from the aforementioned papers in more detail later in Sect. 9.4.

The third approach to the problem is to take into account the possibility of screening of the bound polarization charge with free carriers. In most of the previous formulae, the quantity P_S was used as a *material* parameter defined by Eq. (5.2.4) but in fact it played only a role of *surface* density of the bound charge. Ferroelectric samples were considered of zero electrical conductivity. This may be a good approximation for many real materials, in particular for those with low transition temperatures. It is obvious that free charge may significantly reduce the total surface charge which is the source of depolarizing field and energy. In fact the high electric field near the surface can be reduced to an acceptable level due to the surface charge transport. When discussing phenomena connected with compensation of the bound charge by free carriers, in the simplest approach, the magnitude of P_0 can be replaced by ρP_0 where the factor ρ is the degree of compensation and $0 < \rho \leq 1$.

More involved theories to address this problem have been developed (Chenskii, 1972; Darinskii et al., 1991; Selyuk, 1971). Not going into details of these papers we just mention that all these theories predict an increase in the domain period with increasing free carrier concentration, with a transition to a single-domain state a high enough level of screening. This behavior is intuitively expected since the free carrier screening decreases the energy of the depolarizing field and does not affect the domain wall energy. An essential new feature brought about by the screening effects is the conclusion that the period of the domain pattern can essentially deviate from the \sqrt{h} law in system where without screening this dependence is expected. According to Darinskii et al. (1991), for the case of the screening with non-degenerated free carriers, the period of appeared polarization modulation should follow the relations

$$W \propto \frac{1}{\sqrt{\frac{1}{h} - \frac{h_0}{\lambda_D^2}}}, \quad (5.2.32)$$

$$h_\delta = 2\pi \sqrt{\frac{\varepsilon_0 \delta}{\kappa_a}}, \quad (5.2.33)$$

where λ_D is the Debye screening length and δ is the correlation coefficient defined in Eq. (6.2.1).

5.3 Domain Patterns Connected with Phase Boundaries

Considering ferroics with ferroelastic properties one has to take into account also mechanical aspects of the problem. These issues play a significant role at the phase transitions of the first order: Mechanical compatibility must be ensured between the part of a sample in the parent phase and that which has already transformed into the ferroelastic phase. The problems involved will be discussed in the following two sections. The approaches discussed below are also applicable to the problem of mechanical compatibility at a phase boundary, which can appear at the first-order phase transition between two ferroelectric phases (e.g., between tetragonal and orthorhombic phases in BaTiO_3). We will also discuss this situation at the end of this section.

5.3.1 Perfect Matching

A discontinuous phase transition involves the problem of mechanical compatibility of the parent G and ferroelastic phase F . When a sample passes through the temperature T_{TR} , new phase usually nucleates in a corner or at an edge. On decreasing temperature, the volume of F phase increases and the two phases

become separated by a boundary, often of a planar character. Its existence and orientation are influenced by the conditions of electrical and mechanical compatibility, a problem similar to the compatibility of domain states discussed in Sects. 2.2.3 and 2.2.4. Here we pay attention to the mechanical aspect.

If the parent phase and the domain state A of the ferroic phase, characterized by spontaneous strain $\epsilon_{S_{ij}}^{(A)}$, should be separated by a mechanically compatible phase boundary, the latter must satisfy the condition that the following equation has a nontrivial solution:

$$\epsilon_{S_{ij}}^{(A)} x_i x_j = 0. \tag{5.3.1}$$

If this is so, this equation in fact determines the orientation of the phase boundary itself. The analogy with the domain compatibility condition (2.2.10) is obvious.

For a limited number of ferroelastic species the mechanically compatible phase boundaries do exist. They were determined by Shuvalov et al. (1985a) on the basis of the condition just specified. Table 5.3.1 gives examples of their results; the original table presented the full list of mechanically compatible boundaries includes orientations of boundaries in the following species: 422–222, 4mm–mm2, 42m – mm2, 4/mmm–mmm; 622–222, 6mm–mm2, 6m2 – mm2, 6/mmm–mmm; 4–2, 4 – 2, 4/m–2/m; 622–2, 6mm–2, 6m2 – m, 6/mmm–2/m; 6–2, 6–m, 6/m–2/m. To ensure physical contact of both phases, one of them must be rotated by an angle φ also specified in the table. Understandably, this is in direct analogy with the clapping angle ensuring the physical contact of two ferroelastic domains. In a similar approach, the problem of phase boundary orientation was addressed also by Boulesteix et al. (1986).

Thus in all species listed above the two phases can coexist in the way that on the ferroic side of the boundary a single-domain state is realized. However, in

Table 5.3.1 Phase boundaries and clapping angles for selected ferroelastic species

Species	Phase boundary	Clapping angle between the parent and ferroic phases ^a	Note
422–222, 4mm–mm2, 42m – mm2, 4/mmm–mmm	$x = +y' \quad x = -y'$	$\varphi_3 = a$	The x', y' axes are rotated by 45° with respect to x, y
422–2, 4mm–2, 42m – 2, 4/mmm–2/m	$x = +y' \quad x = -y'$	$\varphi_3 = [(\sin^2\theta - \cos^2\theta)a - (2\sin\theta \cos\theta)b]$	The x', y' axes are rotated around z by $\theta = (1/2) \arctan(-b/a)$ with respect to x, y
222–2, mm2–2, mm2–m, mmm–2/m	$x' = z' \quad x' = -z'$	$\varphi_3 = b$	The x', z' axes are rotated by 45° with respect to x, y

^a a, b are components of the natural spontaneous strain.

calculations leading to these results only linear relations between spontaneous strain and the order parameter have been taken into account, neglecting higher order terms. From here it follows that these results are only applicable for first-order phase transitions close to second order. On the other hand, Shuvalov's results can be applied even for phase interfaces of species not listed above if accidentally the decisive component of spontaneous strain is relatively small. As an example we refer to the case of $\text{Pb}_3(\text{PO}_4)_2$ whose species $\bar{3}m - 2/m$ is not included in the list (Shuvalov, 1985a). The diagonalized tensor of its spontaneous strain has three components, ε_{11} , ε_{22} , and ε_{33} of which the last is by an order of magnitude smaller than the previous two. If we set this component equal to zero, we reach the conclusion that the stress-free phase boundary exists whose normal \mathbf{n} makes an angle of $\pm 46,65^\circ$ with the x -axis and $\pm 43,35^\circ$ with the y -axis. Taking into account the additional rotation of the ferroelastic phase with respect to the parent phase the conclusion has been reached that for $\text{Pb}_3(\text{PO}_4)_2$ the angle of the phase boundary with the y -axis should be $\pm 49,07^\circ$ compared to the experimental value $49 \pm 0.5^\circ$.

5.3.2 Matching on Average

In many cases, the spontaneous strain tensor is such that phase compatibility relation (5.3.1) cannot be fulfilled. However, at a discontinuous transition, the ferroelastic phases may be nucleated in different parts of a sample, grow, and finally meet inside it. If the elastic misfit is too large, this process may result in breaking the sample. However, this misfit can be significantly reduced by splitting the part of the sample in the ferroic phase into ferroelastic domains. The compatibility conditions can then be satisfied for the averaged spontaneous strain.

In a general theoretical way the problem was discussed by Wechsler et al. (1953) and their approach is often addressed when martensitic transformations are treated. Here we will present a simplified approach (cf. DiDomenico and Wemple, 1967), following the calculations of Dec (1993). As an example, we wish to investigate conditions for matching a parent cubic phase with the lattice constant a_0 with tetragonal phase with cell parameters a , c . Natural spontaneous strains in the three ferroelastic domain states are

$$\varepsilon_S^{(1)} = \begin{bmatrix} \varepsilon_a & 0 & 0 \\ 0 & \varepsilon_a & 0 \\ 0 & 0 & \varepsilon_c \end{bmatrix}, \quad \varepsilon_S^{(2)} = \begin{bmatrix} \varepsilon_a & 0 & 0 \\ 0 & \varepsilon_c & 0 \\ 0 & 0 & \varepsilon_a \end{bmatrix}, \quad \varepsilon_S^{(3)} = \begin{bmatrix} \varepsilon_c & 0 & 0 \\ 0 & \varepsilon_a & 0 \\ 0 & 0 & \varepsilon_a \end{bmatrix}, \quad (5.3.2)$$

where $\varepsilon_c = (c - a_0)/a_0 > 0$ and $\varepsilon_a = (a - a_0)/a_0 < 0$. Discussing possible coexistence of any of these domain states with the parent phase, one can easily check that the compatibility condition is not satisfied. However, it can be fulfilled if we consider an interface between the parent phase and a multidomain state. Let us

check this possibility for two domain states 1 and 2. The average spontaneous strain of the system of coexisting domains can be written as

$$\bar{\varepsilon}_{S_{ij}} = (1 - \alpha)\varepsilon_{S_{ij}}^{(1)} + \alpha\varepsilon_{S_{ij}}^{(2)}, \quad (5.3.3)$$

where α is the volume fraction of domain state 2. To check the possibility of mechanical compatibility of this mixture with the parent phase we apply the condition (5.3.1) to this average spontaneous strain. It results in an equation for α with the solution $\alpha = \varepsilon_c / (\varepsilon_c - \varepsilon_a)$. We can easily check that, for this value of α , the average spontaneous strain has the form

$$\bar{\varepsilon}_S = \begin{bmatrix} \varepsilon_a & 0 & 0 \\ 0 & \varepsilon_a + \varepsilon_c & 0 \\ 0 & 0 & 0 \end{bmatrix}, \quad (5.3.4)$$

which indeed does satisfy the compatibility condition. The orientation of phase boundary is given by Eq. (5.3.1) with ε_{ij} defined by the preceding matrix. That determines the direction cosines $\{hkl\}$ of the normal \mathbf{n} to the interface in the form

$$h = \left(\frac{\varepsilon_a}{-\varepsilon_c} \right)^{1/2}, \quad k = \left(\frac{\varepsilon_a + \varepsilon_c}{\varepsilon_c} \right)^{1/2}, \quad l = 0. \quad (5.3.5)$$

From here we obtain the angles α, β, γ between the normal \mathbf{n} and the axes of the cubic phase.

This theoretical approach provides an explanation to the experimental data on the $m\bar{3}m - 4mm$ phase boundary orientations in several perovskites reported by Fesenko et al. (1975, 1990). These orientations were found to be (650) for crystals of BaTiO_3 and (320) for crystals of PbTiO_3 . In fact, in the latter case actually there exist 32 crystallographically equivalent boundaries. Only eight of them were realized in a sample if there was no temperature gradient while in a properly engineered gradient any of these 32 boundaries could be realized. The phase front was accompanied by a periodic 90° domain pattern. If there was only one phase front, this 90° pattern did not depend on temperature. If there were more phase fronts, the 90° domain pattern is complicated and changed with temperature. The orientations of stable boundary planes are compared in Table 5.3.2 with the results of calculations according to the above formulae, where excellent agreement between the theory and experiment is evident.

The discussed theoretical approach can also be applied to phase boundaries that can appear at the first-order phase transition between two ferroelectric phases (e.g., between tetragonal and orthorhombic phases in BaTiO_3). In this case, however, in general, to both phases the average spontaneous strain can be ascribed. In this case, the difference in the average spontaneous strain between both phases (A and B) can be written as

$$\Delta_{ij} = \sum_{\alpha} \alpha_{\alpha}^A \varepsilon_{S_{ij}}^{A,\alpha} - \sum_{\beta} \alpha_{\beta}^B \varepsilon_{S_{ij}}^{B,\beta}, \quad (5.3.6)$$

Table 5.3.2 Orientation of phase boundaries between cubic and multi-domain tetragonal phases

	Boundary orientation		Ratio of domain volumes	
	Theory	Experiment	Theory	Experiment
BaTiO ₃	$\alpha = 49^\circ 40'$	$\alpha = 50^\circ \pm 1^\circ$	2.2	$\cong 2$
	$\beta = 40^\circ 20'$	$\beta = 40^\circ \pm 1^\circ$		
	$\gamma = 90^\circ 00'$	$\gamma = 90^\circ \pm 1^\circ$		
PbTiO ₃	$\alpha = 53^\circ 56'$	$\alpha = 55^\circ \pm 1^\circ$	2.89	$\cong 3$
	$\beta = 36^\circ 04'$	$\beta = 35^\circ \pm 1^\circ$		
	$\gamma = 90^\circ 00'$	$\gamma = 90^\circ \pm 1^\circ$		

where $\varepsilon_{S_{ij}}^{A,\alpha}$ and $\varepsilon_{S_{ij}}^{B,\beta}$ are the natural spontaneous strains³ in the domain states of the phases A and B, respectively, indexes α and β numerating these states; α_α^A and α_β^B are the fractions of the domain states obeying the normalization conditions. $\sum_\alpha \alpha_\alpha^A = 1$ and $\sum_\beta \alpha_\beta^B = 1$. The information on the orientation of the phase boundary can now be obtained for Eq. (2.2.10) with Δ_{ij} coming from (5.3.6). An approach conceptually close to that presented above has been applied to the tetragonal–orthorhombic phase transition in KNbO₃ (Metrat, 1980). However, the validity of the results obtained is questionable since a non-justified criterion of the mechanical compatibility (see the first footnote in Sect. 2.2.4) was used in the calculations.

5.4 Selected Observations of Domains in Crystalline Ferroic Samples

We now wish to present a representative selection of experimental observations of domain patterns in selected kinds of ferroics. For several crystalline ferroelectrics—TGS, barium titanate, KH₂PO₄, and Rochelle salt in particular—numerous experiments were performed with the aim to reach and visualize equilibrium domain patterns in the sense of Sect. 5.2. These will be covered in some detail. But in addition there is an enormous amount of interesting data on static observations of domains not dealing with these idealized patterns, which have never been summed up and could cover almost the full volume of this book. In this section we present a very limited selection of data with the aim to demonstrate some of either typical or challenging domain configurations in different kinds of ferroics. When comparing any of these data we have to bear in mind that in most observations the sample quality is not fully defined, and yet crystal growth conditions and defects play important roles. Often the boundary conditions, another essential factor, are not properly specified either. While we do not wish to describe here effects induced by intentionally applied external forces, in selected cases we find it

³ In this case the Aizu strain, in general, cannot be used in this equation (see Sect. 2.1.3).

indispensable to describe domain patterns formed after the application of such forces. Reported observations are sorted into several categories of ferroics which—as it follows from the considerations in Sect. 2.3—differ in their basic properties. In each of them, only a few of the most studied materials are covered in some detail.

5.4.1 Uniaxial Ferroelectrics (Nonferroelastic) with the Second-Order Transition

5.4.1.1 TGS, Triglycine Sulfate

Triglycine sulfate and isomorphous ferroelectric crystals representing the species $2/m-Pd-2$ have served as model materials for domain studies and their domain structures have been described and discussed in about 500 papers. There are a number of reasons for this popularity. A crystal of TGS can be relatively easily grown from water solution in a good quality and with the linear size of several centimeters. Its cleavage plane is perpendicular to the polar axis which makes it possible to prepare excellent plates of the required orientation. Also, it is chemically stable and not hygroscopic, although it is soluble in water. The other incentives for studying this material are the favorable location of $T_C = 49.5^\circ\text{C}$ and the fact that there are several methods to observe domains: Easy etching, as described in Chap. 4, as well as a number of decoration methods of which liquid crystal decoration proved to be very effective. In previous chapters we have already referred to domains in TGS, in particular in connection with methods for domain observations. Investigations of domain shapes in TGS will also be mentioned in Chap. 6.

Now let us briefly summarize some selected data on domains in TGS. This is not a straightforward task since, in the observations, several factors combine and cannot be well distinguished: sample quality, boundary conditions, temperature, and time.

Although single TGS crystals grown in many laboratories have been of large size, good quality, and comparable macroscopic properties, it is known that they contain segments, often referred to as growth pyramids, which strongly differ in domain patterns and in the response of domains to applied electric fields. The TGS crystal is grown from a seed and the growth pyramid (hkl) can be defined as a locus of the natural plane having indices (hkl) throughout the growing process (Furuhata, 1970). Several authors (Stankowska and Czarnecka, 1989; Konstantinova and Stankovskaya, 1970; Dontsova et al., 1988; Konstantinova and Stankowska, 1971) demonstrated the differences of domain patterns in distinct pyramids. Obviously, these phenomena may be closely connected with the distribution of additives in different growth pyramids, but the exact character of defects responsible for this effect is not known. Konstantinova and Stankowska (1971) pointed out that the domain geometry, domain size, as well as their time development strongly depend on the concentration of Cu^{+2} additives as well as on the growth pyramid from which the

sample is cut. Dontsova et al. (1988) managed to particularize how these additives are distributed in various growth pyramids and studied the density of domain nuclei in growth sectors of TGS crystals doped by various well-specified admixtures. Although none of these observations have been yet treated theoretically, we can conclude that the very existence of growth pyramids represents a warning that some of the obtained results cannot be generalized and that proper consideration of the influence of defects on the static domain pattern is essential even in a nonferroelastic material like TGS.

Let us first state that in “as-prepared”—meaning no programmed temperature–time treatment has been involved—plate-like electrically isolated samples of TGS, at room temperature, domains of one polarity of \mathbf{P}_S form irregular islands in the sea of the other polarity (see Fig. 4.4.1). Sometimes domain walls show a preference to be aligned along the a -axis, resulting in lenticular domains extended along this axis for which their average width can be measured and specified. Typically, as shown by etching both surfaces (see Fig. 4.4.1), domains are formed by domain walls parallel to the polar b -axis which ensures their electroneutrality. Occasionally, however, etching surfaces parallel to the polar axis may reveal “internal” domains which do not reach the polar surfaces (Chynoweth, 1960) (see Fig. 2.2.5).

In targeted experiments, first the question if the depolarizing field indeed plays the expected role is asked. Moravec and Konstantinova (1968) examined plates of TGS which were short-circuited by applying a layer of silver paste, then annealed above T_C , and subsequently cooled to room temperature. By etching, they were found almost in single domain, in strong contrast to the on average nonpolar pattern found in insulated samples. This appears to prove unambiguously the role of depolarization energy when the domain pattern is formed at the phase transition. These results were later confirmed by Stankowska and Czarnecka (1989). The experiments of Gilletta (1972), however, indicated a more involved—although not controversial—situation. TGS plates were cooled alternatively in mercury and in vacuum (or paraffin oil, with the same result). A few minutes after passing through, T_C samples were irradiated by X-rays which, on the basis of previous experience, was believed to freeze, at that temperature, the domain structure. The latter was then revealed by etching at room temperature. Domain patterns were similar in both cases except that in the short-circuited samples domains were of larger size. Gilletta explained these results by the presence of a surface layer (see Sect. 9.4.1). Indeed, he presented dielectric data which point to the existence of an intrinsic surface layer on insulated TGS plates and a much thicker (1 μm) surface layer in samples with evaporated Ag electrodes. The nature of the former may be structural perturbations, the latter could be due to chemical interaction with silver. In alternative experiments, in which domains were revealed by etching, Gilletta showed that, after shelving the insulated plates for several weeks, large domains developed, while plates that were immersed in mercury became single domain within hours or days. We include these observations to indicate the difficulties faced when obtaining possibly reliable data.

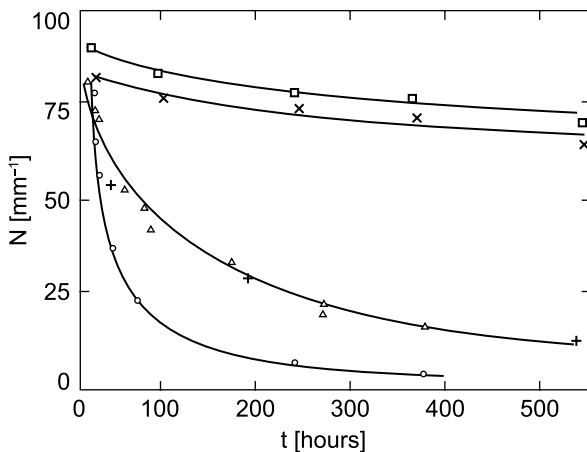
More distinctive information can be specified for samples which went through a defined cooling process. Hatano et al. (1977) observed that after annealing a TGS plate above T_C and cooling it down to room temperature, first a fairly periodical stripe structure occurs with well-defined orientations of domain walls, perpendicular to the crystallographic c -axis. With time the stripes change into lenticular or elliptical domains. These authors observed an analogical process in TGSe, where fairly regular plate domains reached after cooling, parallel to the crystallographic (001) planes, change with time into lenticular domains whose tips are restricted by walls with the $(\bar{2}01)$ orientation. The shapes of domains in both these materials have been successfully discussed on the basis of wall energy anisotropy and we shall come back to this point in Sect. 8.4.6.

Valuable evidence of the influence of crystal quality and the time factor was obtained by Moravec and Konstantinova (1968). They prepared plates 3–4 mm thick from four crystals of different degrees of purity: TGS1 (three times recrystallized TGS synthesized from three times recrystallized glycolol); TGS2 (one time recrystallized TGS synthesized from non-recrystallized glycolol); TGS3(Cu) and TGS3(Fe) (grown from TGS2 with addition of Cu and Fe, respectively). After annealing at 96°C, plates were cooled at a rate of 0.3 K/min down to room temperature. After a waiting time t_{shelf} , up to 500 h, the sample was etched and photographed. The preferred wall orientation was specified as perpendicular to the direction $[\bar{1}, 0, 2]$. Then the number N of walls per millimeter was counted along this direction. Figure 5.4.1 shows their results. The value of N was found to depend on t_{shelf} , obeying the equation

$$\frac{1}{N} - \frac{1}{N_0} = K(t_{\text{shelf}} - t_0). \quad (5.4.1)$$

This behavior demonstrates the aging process of insulated samples. This result clearly represents the role of crystal quality on the observed domain

Fig. 5.4.1 Time dependence of the number of domain walls per 1 mm along the direction perpendicular to the wall preferred orientation. o—TGS1; Δ —TGS2; +—TGS2, short-circuited; \square —TGS3(Cu⁺⁺); \times —TGS3(Fe⁺⁺⁺). After Moravec and Konstantinova (1968). The roles of the crystal purity and of electrical boundary conditions are clearly demonstrated



pattern at a given time: The presence of defects has a profound effect on the rate of the process with which the domain system changes. The aging process itself was interpreted as corresponding to a slow compensation of the surface bound charge by free carriers. This trend can be compared to that expected for an equilibrium domain pattern, though, the domain patterns observed are not equilibrium. Namely, the compensation of the surface bound charge should lead to a reduction of the effective value of P_S in Eq. (5.2.22) and to the corresponding growth of W_{eq} . Now, a curve is also included in Fig. 5.4.1, showing the same type of dependence for samples of TGS2, which were short-circuited after having been cooled to room temperature and then again after each etching step. We see that the aging process $N(t_{shelf})$ was not influenced and proceeded as for the insulated sample. There is an analogy with the above-mentioned Gilletta's observations, and while we lack an exact interpretation of this finding one can again deliberate about the influence of a passive surface layer. Alternatively, it could be that the process of reaching equilibrium at room temperature is already too slow because well below T_C the wall mobility is correspondingly sluggish. While we have already pointed out that there is no doubt about the role of depolarization energy, we now have to conclude that once the neutral structure has been reached there is little incentive for proceeding to reach states with further reduced energy.

Considering all complicating factors involved, the differences in data obtained by different authors are not surprising. Konstantinova and Stankowska (1971) further extended previous study of Moravec and Konstantinova. While the law of Eq. (5.4.1) was confirmed, they showed that not only the coefficient K , i.e., the aging rate but also the domain geometry is strongly affected by the crystal growth temperature and by the location of growth pyramid from which the sample had been prepared. Aging effects were also studied by Dabrowska et al. (1977) and the role of defects was in particular demonstrated by Stankowska and Czarnecka (1989). Thus the role of crystal quality is being repeatedly confirmed. Another elegant demonstration was offered by Szczesniak and Szczepanska (1990): They showed that the length of the rejuvenation period (during which the sample is kept above T_C) has a profound effect on the distribution function of domain width, for samples which are otherwise identical.

It is evident that even in the carefully performed experiments just mentioned, there are two essential factors—temperature and time. In this context, unique observations made by Nakatani (1985) using liquid crystal decoration technique deserve special attention. In these experiments, after rejuvenation, the TGS plate was cooled through T_C at a rate of 0.006 K/m; capacitance of a small electroded part made it possible to determine, with a precision and reproducibility of 0.01 K, the moment when T_C is passed. A series of photographs shown in Figs. 5.4.2 and 5.4.3 seem to be at present the best available demonstration of how domains form and develop in a nonferroelastic material with a continuous transition. In Fig. 5.4.2, the domain patterns have been imaged during step cooling every 4 min down to $T_C - 0.26$ K. A continuous increase with time of the mean domain

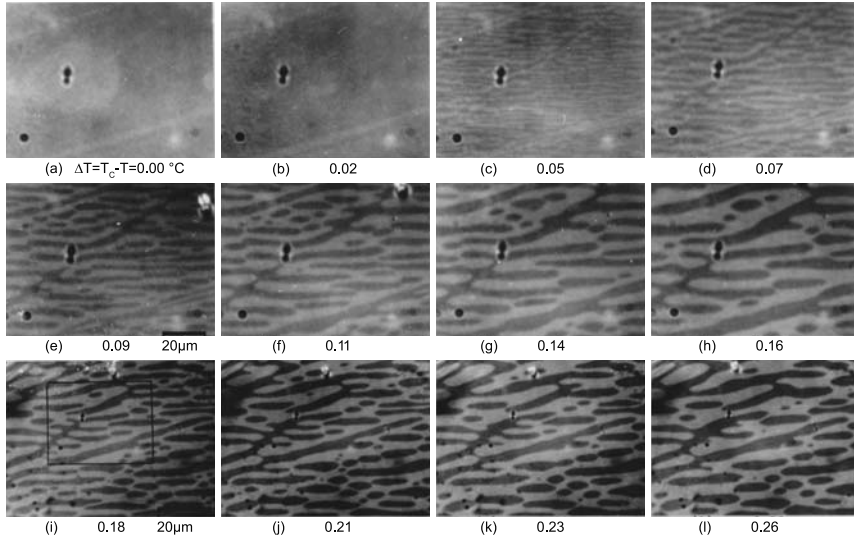


Fig. 5.4.2 Time evolution of domain pattern in TGS on cooling just below $T_C = 49.68^\circ\text{C}$ imaged by LC decoration. Microphotographs are taken on slow cooling at intervals of 4 min; temperatures are given. After Nakatani (1985)

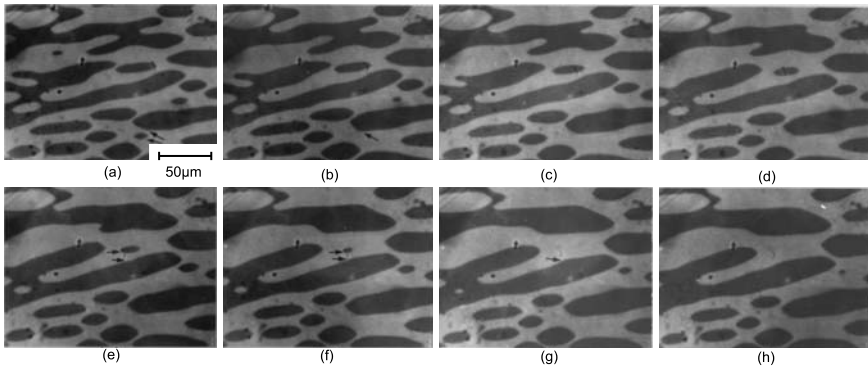


Fig. 5.4.3 Time evolution of domain pattern in TGS at fixed temperature $T = T_C - 0.39^\circ\text{C}$ imaged by LC decoration. Microphotographs are taken at intervals of 4 min. Frames (a)–(h) correspond to the window shown in Fig. 5.4.2i. *Small arrows* indicate the shrinking domains and the protruding boundary. After Nakatani (1985)

width is seen. This dependence, $W(t)$, is linear as documented in Fig. 5.4.4a. The cooling was stopped at $T_C - 0.39\text{ K}$; however, the domain growth continues (see Fig. 5.4.3) with the same rate (see Fig. 5.4.4b). These results indicate that it is the time which is the decisive factor for the domain development rather than temperature. The linear $W(t)$ dependence starts to saturate only after about 10 h (Fig. 5.4.4c).

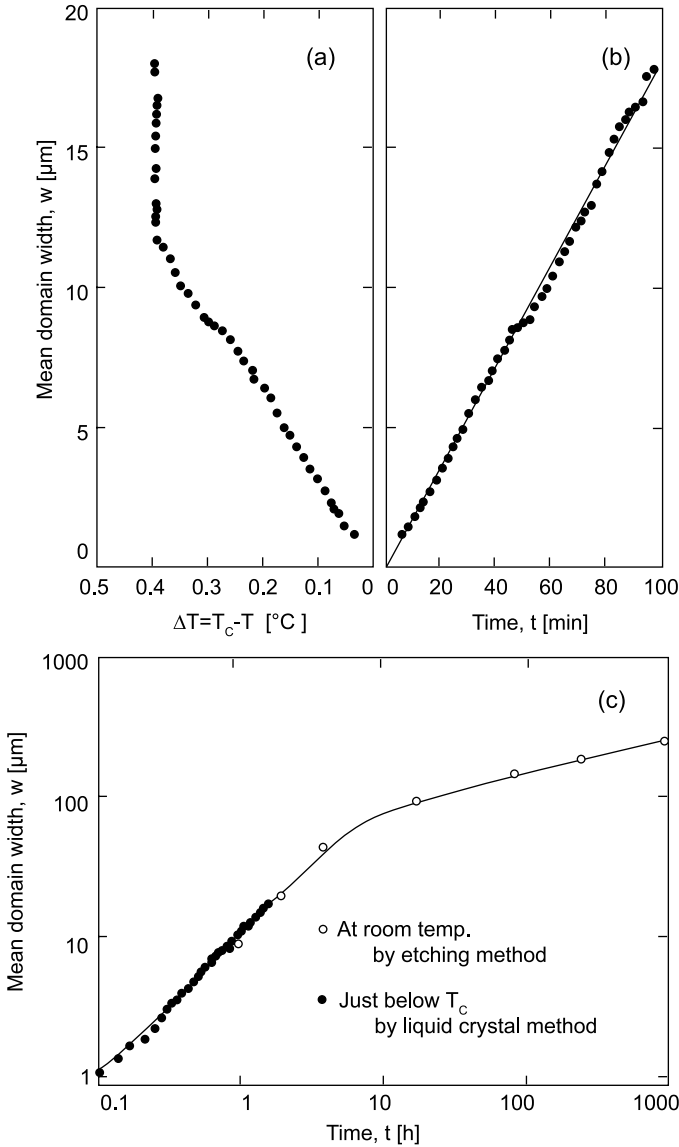


Fig. 5.4.4 Temperature/time (a) and purely time (b) dependences of the mean domain width w . These data were obtained from microphotographs such as in Fig. 5.4.2, taken at intervals of 2 min. (c) Time dependence of w taken at room temperature and just below T_c . After Nakatani (1985)

While in the just described experiment the crystal is gently pulled through the transition point, Tomita et al. (1989) employed the decoration technique to study the time development of domains in TGS after quenching, a fast cooling process from above T_c down to room temperature. Figure 5.4.5 shows some of

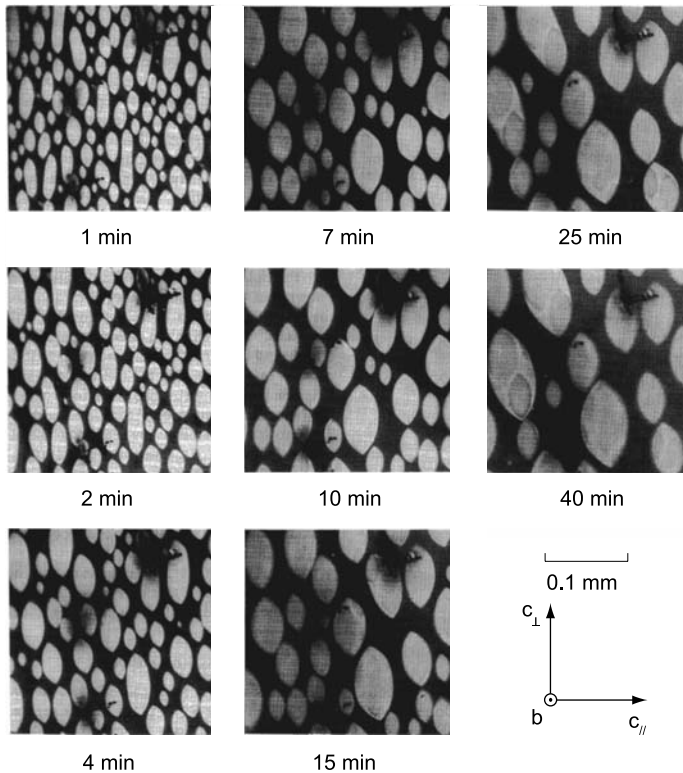


Fig. 5.4.5 Time evolution of domain pattern in TGS quenched down to room temperature. After Tomita et al. (1989)

their data. Comparing the domain evolution for the case of slow cooling and quenching, one distinguishes the same general trend—increases in the mean domain width with time. As for the difference, it is in the domain shape (in the quenching case the domains are mainly lenticular) and in the time dependence of the domain width. According to Tomita et al. (1989), in the quenching regime, this dependence is much slower than linear: the power law with the exponent about 0.3.

Among qualitative result related to the domain pattern in TGS one can mention SFM data obtained in the friction mode (Correia et al., 1996), attesting to the presence of “domain structure branching” in the material.

All the observation mentioned above can be rationalized in terms of the general theoretical approach to the domain formation on ferroelectrics: competition between the depolarizing-field and domain wall energies under additional influence of defects pinning the walls and free charges screening the surface bound charge. At the same time, quantitative interpretation of these results in terms of the theory of the equilibrium domain pattern does not seem

realistic. Here we can mention experimental attempts to quantify the parameters of the close-to-equilibrium domain patterns. Safrankova (1970a,b) and later Strukov et al. (1972a) have investigated the equilibrium domain size W_{eq} on temperature and sample thickness. Figure 5.5.6 shows the ratio W_{eq}^2/h calculated by Strukov et al. (1972a) from their experimental data on 200 samples of thicknesses from 0.25 to 2.5 mm. According to Eqs. (5.2.22) and (5.2.23), for this material, this ratio should be independent⁴ of sample, temperature, and sample thickness. At the same time Fig. 5.5.6 demonstrates an essential spread and thickness dependence of this parameter, suggesting that the observed domain patterns are not close to real equilibrium. The data by Safrankova (1970a) corroborate this point.

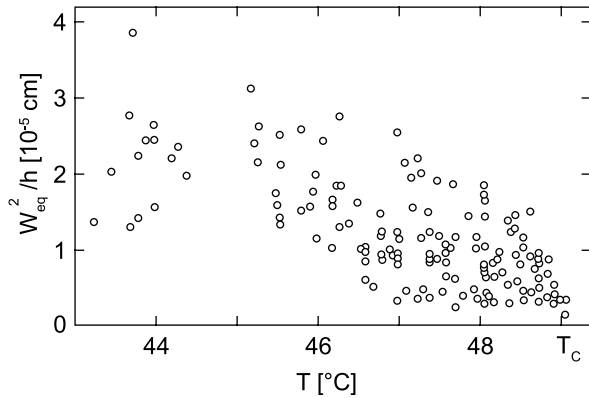


Fig. 5.4.6 Experimental data on W_{eq}^2/h collected from TGS samples of thicknesses from 0.25 to 2.5 mm. After Strukov et al. (1972a)

These and other numerous results on domains in TGS represent some 50% of all available data on domain patterns in ferroelectrics. Let us briefly summarize them. (1) There is a profound tendency that neutral structures are formed. (2) Samples prepared for domain observations may carry a passive surface layer which imitates an “isolated sample” even if it is provided with short-circuited electrodes. (3) Both lenticular and stripe shapes are characteristic but intermediate patterns occur most often. (4) On cooling, a fine domain structure appears at T_C and coarsens with time. On slow cooling, it is time rather than temperature that determines the instantaneous structure. (5) The speed of this coarsening process depends critically on crystal quality. (6) In good-quality samples the speed of this process slows down at lower temperatures, requiring hundreds of hours. (7) The distribution function of domain sizes becomes sharper for samples annealed above T_C . (8) In TGS, the theoretically substantiated dependence of the characteristic domain size on plate thickness has not been clearly demonstrated.

⁴ This follows from the relations valid for TGS: $h_M \propto \sqrt{\kappa_c} \sigma_W / P_S^2$, $\sqrt{\kappa_c} \propto 1/P_S$, and $\sigma_W \propto P_S^3$. Here the latter relation follows from Eq. (6.2.10b).

In short, we may state that in high-quality crystals of TGS we do not really observe equilibrium domain structures but some which are not far from conditions of theoretical equilibrium.

Closing the discussion of domains in TGS we wish to point out that, in some of the observation methods, it is difficult to avoid temperature gradients in the sample or even thermal shocks. Chynoweth and Feldmann (1960) paid special attention to these two factors. They showed that a warming shock results in a very regular domain pattern in which domains of one polarity have the shape of cylinders with lens-shaped cross-sections. A cooling shock resulted in arrays of very narrow circular domains. A simple model was suggested in explanation of this effect.

For lack of space, we do not include data on domains in isomorphous crystals TGFB and TGSe. There are no qualitative differences, although different wall anisotropy leads to other domain shapes (Hatano et al., 1977).

5.4.1.2 Other Representatives

TGS and its isomorphs are the most studied uniaxial nonferroelastic ferroelectrics from the point of view of domain properties. In this section we shall now mention only in passing some other materials from this group.

Lead germanate, $\text{Pb}_5\text{Ge}_3\text{O}_{11}$, is a good candidate for static observations of domains. It undergoes a continuous transition at 177°C , representing the species $\bar{6} - Pd - 3$, whose interesting property is that domains with antiparallel polarization differ in the sign of optical activity. This fact (cf. Sect. 4.6.3) makes it possible to observe nonferroelastic domains in a polarizing microscope. However, Iwasaki et al. (1972) and Blumberg and Kürsten (1979) pointed out that in freshly grown crystals of lead germanate domains cannot be visualized. Dougherty et al. (1972) were the first to visualize domains in *c*-cuts of this material, by means of optical rotation (see Fig. 2.2.8). Hexagonal-shaped islands with walls of $\{1\bar{1}00\}$ orientations were found to be preferred.

Considerable attention to domain properties of this material was paid by Shur et al. (1982). They showed that, in a fresh sample, domains become visible only when an ac field is applied, first with diffuse walls but gradually acquiring a strong contrast. This was explained by assuming that fresh untrained samples contain head-to-head domains which are screened by free carriers; these domains mutually compensate the rotation of polarization. The applied ac field destabilize this compensation and makes domains penetrate the whole thickness of a sample and become optically distinguishable. The sample can be again thermally depolarized which leads to the previous situation, namely to a large number of antiparallel and head-to-head domains (Shur et al., 1988). In a later paper, Shur et al. (1985b) studied domain shapes in more detail. They showed that when the mentioned switching process advances in fields exceeding $2.5 \times 10^5 \text{ V/cm}$, domains of irregular shapes are created. If fields are below this

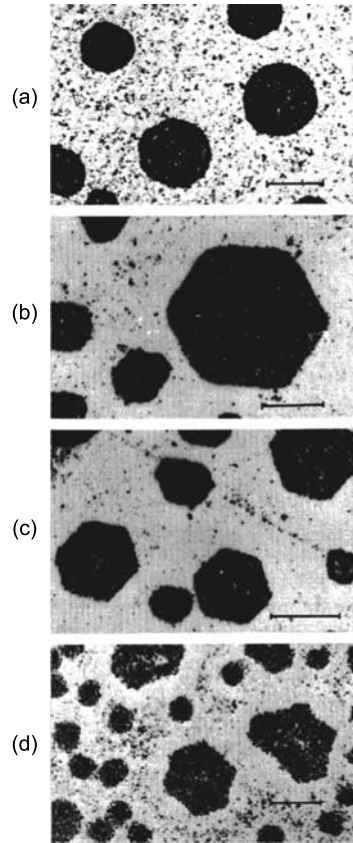
value, domains have regular shapes, with walls of defined orientation, and domains of hexagonal or triangular shapes can be deliberately formed.

Seemingly, these facts go beyond the scope of this section in which we discuss domain shapes without considering changes in domain patterns by external forces. However, these observations may give the reader a suggestion how to cope with situations when no domains can be observed although their presence can be expected on the basis of other considerations.

The last ferroic we wish to mention here is GASH, one of the most investigated materials within the category of uniaxial ferroelectrics. In contrast with the previous two, its transition temperature cannot be reached since the decomposition process takes place already at about 200°C, still within the ferroelectric phase. Available data suggest that this material can be treated as representing the species $\bar{3}m - Pd - 3m$. Its attractiveness is due to the relative easiness of the growing process and also since several decoration techniques as well as atomic force microscopy can be applied to observe domains on its well-defined cleavage planes perpendicular to \mathbf{P}_S . Cleaved plates reveal a central part of hexagonal shape and six outer parts; Le Bihan (1990) showed that they are in fact growth pyramids, extending from the center of the crystal.

We give a short overview of selected domain observations, with the aim to show the diversity of data, demonstrating again the unspecified role of crystal defects. Hilczer et al. (1975), Szczesniak et al. (1976), and Suda et al. (1978a) were the first to investigate domain shapes. They found that the central region is usually single domain while in the outer segments a large number of small domains occur, both plate like and circular. With decreasing temperature many new small domains appear and have the tendency to change from circular to hexagonal cross-sections; this is demonstrated in Fig. 5.4.7. Tikhomirova et al. (1979) observed a different kind of domains, in the form of narrow loops and considerable lengths of 10^2 – 10^3 μm . They begin and terminate at the edges of the crystal or form close configuration of arbitrary shape. The patterns on opposite surfaces of a sample 0.2–3 mm thick are absolutely identical; the fact that these patterns are related to domains is proved by the fact that in an applied field they expand, symmetrically in both directions. While several authors, e.g., Le Bihan et al. (1984) and Szczesniak et al. (1985) confirm that in as-grown crystals domains exist only outside the central hexagonal zone, Hatano et al. (1985a,b) observed peculiar spiral domains in this zone and connected them with the spiral growth theory of the crystal. Galiyarova and Dontsova (1999) investigated domain shapes with the intention to determine the relation between their perimeter and area, in connection with the idea of fractal features of domains. All of the mentioned observations were performed with solution-grown crystals. Hatano et al. (1990b) prepared gel-grown crystals of GASH. He showed that in this case the outer six growth sectors are single domain of alternating polarity, unlike in solution-grown crystals where they are subdivided into domains.

Fig. 5.4.7 Variation of the small domain shape with temperature decrease in a GASH crystal. (a) 75, (b) 100, (c) 120, and (d) 130°C. The edges of the hexagonal domains are parallel to the mirror planes. Bar signs in each figure indicate length of 20 μm . After Suda et al. (1978a)



5.4.2 Ferroelastics with a Small Number of Domain States

In this section we present examples of domain patterns in materials exhibiting two and three ferroelastic domain states. From the latter category, however, we will not address here perovskite materials; these will be addressed later in Sect. 5.4.3. Giving credit to the historical importance of KDP, this ferroelastic with two domain states will be discussed separately either.

5.4.2.1 Ferroelastics with Two Ferroelastic Domain States

Let us first discuss simple representatives of proper ferroelastics with two domain states, neodymium or lanthanum phosphate, $\text{NdP}_5\text{O}_{14}$ or $\text{LaP}_5\text{O}_{14}$. They exemplify the species $mmm-\epsilon s-2/m$ and undergo continuous transitions at 413 and 393 K, respectively. The spontaneous shear in the two domain states is $\pm\epsilon_{S_{13}}$, and the corresponding component $\delta_S B_{13}$ of optical indicatrix is large enough so that domains differing in its sign can be observed optically in samples of b -cut (normal to the twofold axis). Mechanically compatible domain walls

are parallel either to the a -axis, i.e., perpendicular to the c -axis of the parent phase; these are called a -type walls, separating a -type domains (often referred to as a -type twins). Alternatively, the walls are parallel to the c -axis of the parent phase; these are called b -type walls, separating b -type twins (Weber et al., 1975; Huang et al., 1994b).

First optical observations of domains were reported by Weber et al. (1975) who gave an accurate crystallographic representation of domain pairs and proved ferroelasticity by switching under applied stress. Indirect domain-induced effects were reported by several investigators; e.g., Errandonea (1981) found that the intensity of the Rayleigh line, i.e., of the elastically scattered beam, is strongly dominated by reflections on a -type walls. Attention to domain phenomena was inspired in particular by investigations of Meeks and Auld (1985), who showed that regular domain patterns can be induced in these crystals.

Huang et al. (1994b) studied static domain properties in crystals of $\text{NdP}_5\text{O}_{14}$ optically. In plates perpendicular to the b -axis, both orientations of domain walls were observed, often forming wedge-shaped domains. However, most observed walls were of the a -type; the b -type walls (parallel to (100) of the parent phase) are usually formed in the fields of local stress, at elevated temperatures. This was explained by a higher surface tension of the b -walls. Indeed, symmetry considerations point to nonequivalency of the two walls.

By both optical microscopy and synchrotron radiation topography it was found (Huang et al., 1994b) that at elevated temperature the density of domains increases, sometimes forming a nearly periodic structure. Close to T_C numerous microdomains fill the crystal, frequently altering from one state to another. When T_C is determined from the temperature dependence of spontaneous strain, microdomains disappear at this temperature while large domains may still be visible above T_C , probably due to local stress in the sample.

While the basic data on domains were obtained by microscopic observations, other methods provided additional information. Studies by synchrotron X-ray topography (Hu et al., 1994) in Er-doped $\text{LaP}_5\text{O}_{14}$ crystals also recorded fluctuations of the number of domains at T_C . A simple thermodynamic treatment of the transition shows that the energy barrier between the two domain states varies with temperature as $|T - T_C|^2$ while the wall energy decreases as $|T - T_C|^{3/2}$. Based on these facts, it can be argued that as T_C is approached, the probability of creating new domains by thermal fluctuations increases. In crystals of this composition, only a -type domains are observed, b -type domains are not (Huang et al., 1995).

As discussed in Chap. 4, on samples with properly oriented surfaces, ferroelastic domains will form a surface relief. This was demonstrated by Hamazaki et al. (1996, 1998) for $\text{NdP}_5\text{O}_{14}$, whose as-grown (100) surface was observed by SFM in topographical mode. At the (001) domain walls the surface bends by an angle of 0.48° . The same method was also used by Takashige et al. (1998). These crystals, typical ferroelastics, have received attention for investigations also by other methods based on elastic differences between domains. For example,

Jiang et al. (1999) used a scanning electron acoustic microscope and Kojima (1989) used a kind of acoustic microscope.

To summarize, crystals of pentaphosphates represent a classical example of ferroelastic ferroics of simple symmetry: The phase transition is equitranslational and there are just two orientational domain states. Basic domain properties are known. However, because these materials undergo the second-order transition, it appears that they offer an extremely interesting subject for further research of how the transition proceeds, how ferroelastic domains are formed, and what—if any—are pretransitional phenomena.

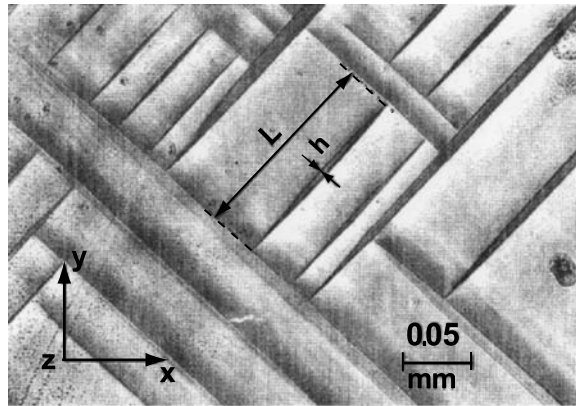
The second ferroelastic material we include in this section is bismuth vanadate, BiVO_4 . It is a proper ferroelastic, customarily considered to represent the species $4/m-\epsilon s-2/m$ in which the symmetry-breaking component of natural spontaneous strain is ϵ_{12} . In contrast to pentaphosphates, here we expect only S walls to exist, of orientations $(p, 1, 0)$ and $(1, -p, 0)$. This was realized by Manolikas and Amelinckx (1980a); indeed they observed sets of mutually perpendicular walls, both passing through the c -axis and forming wedges. From the values of spontaneous strain components they determined the value of p ; for the angle $\varphi = \arctan(-1/p)$ which the two walls make with the x - and y -axes, respectively, they obtained $\varphi = 31.4^\circ$, in good agreement with the observed value of $\varphi \approx 32^\circ$.

Obviously, the value of p is expected to depend on temperature. This problem was addressed by David and Wood (1983) who measured the temperature dependence of the orientation of walls, i.e., of the parameter p . Calculations of p using data on spontaneous strain led to a good agreement between theory and experimental data, for temperatures between T_{room} and 220°C . Here p decreases linearly with T , within the range of about 0.72–0.65. Later, bismuth vanadate was investigated by Avakyants et al. (1985) with similar results. In addition, these authors studied the surface profile of a rod-like sample produced by perpendicular (nearly perpendicular because the parent clamping approximation is lifted) S walls; the planar surface is rippled by changes of the order of 1° .

More recently, however, the fairly consistent observations of S walls in this material have been questioned by Moon et al. (1987) who observed, by X-ray diffraction and NMR, walls of a new orientation (110). This was confirmed by Lim et al. (1989) who reported its coexistence with an S wall of indices $(1p0)$ where $p = 0.724$. Based on these observations it was suggested that in fact BiVO_4 represents the species $4/mmm-\epsilon s-2/m$ with four domain states rather than $4/m-\epsilon-2/m$. This was supported by additional studies of domain walls in this material by Lim et al. (1995) which resulted in the conclusion that in the samples used only W_f walls were seen and no S walls. Thus bismuth vanadate, despite the large number of high-quality papers already published, still offers a lively area of research.

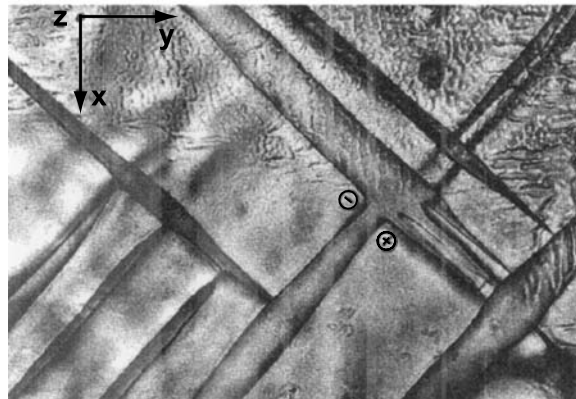
Another ferroelastic material we would like to discuss is KSCN, representing species $4/mmm-\epsilon s-mmm$. At $T_{\text{TR}} = 415\text{ K}$ it undergoes the transition (of order–disorder type) which is of first order, although the discontinuity is very small (Kroupa et al., 1988). This is an improper ferroelastic, its order parameter

η is connected with ordering of the SCN^- groups. Again, there are two ferroelastic domain states but in contrast to the two previous materials, here the transition is non-equitranslational: the primitive unit cell doubles. The two ferroelastic domain states differ in sign of the newly acquired strain component $\varepsilon_{S_{xy}} \propto \eta_S^2$. Compatibility conditions predict ferroelastic domain walls of W_f type with the orientations (110) and $(\bar{1}10)$, and in c -oriented plate-like samples these are indeed observed in a polarization microscope (Schranz et al., 1988). Typically, just below T_{TR} , dense patterns of narrow domains terminating within the sample are formed on cooling (Fig. 5.4.8a). Lens-shaped domains occur frequently while planar walls crossing the whole sample are very rare (Schranz and Rychetsky, 1993). From about 1°C below T_{TR} down to room temperature no significant changes in the domain pattern are observed (Schranz et al., 1988). Perpendicular domain systems, obviously situated above each other in a plate-like sample, can be seen.



(a)

Fig. 5.4.8 Domain pattern in KSCN. (a) Typical pattern not too close to T_{TR} . (b) Domain pattern at $T_{\text{TR}} - 0.05$ K. On cooling, junctions '+' and '-' merge and lens-shaped domains such as shown in (a) form. Reprinted with permission from Schranz, W., Static and dynamic properties of the order-disorder phase transition in KSCN and related crystals, *Phase Transitions*, **51**, 1 (1994). Copyright (1994), Taylor and Francis



(b)

Schranz and Rychetsky (1993) performed an aimed study of two aspects of ferroelastic domain patterns in KSCN. First, they paid attention to narrow lens-shaped domains. On cooling a single-domain sample, they raise a few degrees below T_{TR} and show characteristic temperature dependences of their dimensions—length L and width h . Changes of temperature and waiting times were arranged so that the obtained data would correspond to the states close to equilibrium. Reproducible results for temperature dependences of L and h were obtained, shown in Fig. 5.4.9. These dependences have been successfully modeled using twinning dislocation approach (cf. the end on this section devoted to domains in KH_2PO_4), specifically it has been shown that for $h/L < 1$

$$L \propto \exp[A/\varepsilon_{S_{xy}}(T)], \quad h \propto \ln L \propto B/\varepsilon_{S_{xy}}(T), \quad (5.4.2)$$

where A and B are constants. Figure 5.4.9 demonstrates a good agreement between the theory and experiment.

The second interesting aspect of ferroelastic domains in KSCN is the coexistence of mutually perpendicular wedges. The prevailing wall orientations of perpendicular wedges are (110) and $(\bar{1}10)$. Any of them are mechanically permissible but if they meet, a strongly deformed region is formed. The interesting property of KSCN is that since the phase transition is very close to the second order, near T_{TR} the spontaneous strain is small. Then the right-angled walls meet relatively often and an unusual domain pattern is formed as shown in Fig. 5.4.8b. On cooling, it transforms into a pattern such as that in Fig. 5.4.8a. Schranz (1994) and Schranz et al. (1993) offered an explanation for this effect.

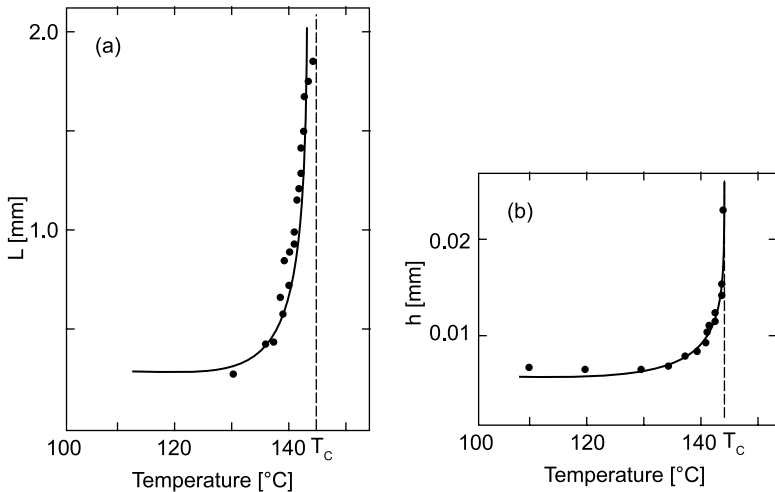


Fig. 5.4.9 Temperature dependence of the length (a) and width (b) of lens-shaped domains in KSCN. *Dots* are experimental data, *curves* represent fits to relations (5.4.2). After Schranz and Rychetsky (1993)

At the two junctions (“+” and “-” in Fig. 5.4.8b) a strain field is formed leading to an attractive force F_r between them. This force was calculated as

$$F(r) = -2\mu\varepsilon_{xy}^2 r \ln(R/r)/\pi(1 - \nu), \quad (5.4.3)$$

where μ is the shear elastic modulus, ν stands for the Poisson ratio, and R is the dislocation core radius. Near T_{TR} the magnitude of F_r is not high enough to move the junctions. With decreasing temperature spontaneous strain and thus also F_r increase and the two junctions move to each other until they finally merge to form lens-shaped domains shown in Fig. 5.4.8a.

The doubling of the unit cell at the transition in KSCN makes possible the existence of the orientational domains divided with antiphase boundaries (see Sect. 2.1.7). Such domains have been detected with etching technique (Schranz and Rychetsky, 1993). The antiphase boundaries have been found to make an angle of 45° with those ferroelastic. It has been demonstrated that the orientation of the antiphase boundaries consists of the anisotropy of the surface tension of the boundaries, calculated based on the known parameters of the Landau energy of the material (Rychetsky and Schranz, 1993).

An example of a two-domain-state ferroelastic is the famous improper ferroelectric–ferroelastic $\text{Gd}_2(\text{MoO}_4)_3$ (abbr. GMO) with the first-order phase transition at $T_{TR} = 160^\circ\text{C}$. It corresponds to species $\bar{4}2m - Peds - nm2$, which allows W_f walls of two orientations ((100) and (010) in the crystallographic frame of the parent phase), which at the same time are parallel to the direction of the spontaneous polarization and for this reason are neutral. Because of the improper character of the transition (unit cell multiplication), antiphase boundaries can also form. Barkley and Jeitschko (1973) and Meleshina et al. (1974) have offered detailed description of the domain patterns in GMO. In contrast to the just discussed improper ferroelastic KSCN no regular dense domain pattern is formed after the cooling through the transition. The domain size can be comparable to the sample size. As for the antiphase boundaries, they seem to exhibit a little anisotropy of the surface tension and, when far from the ferroelastic walls, they acquire arbitrary shapes, making loops or ending at dislocations (Fig. 5.4.10). According to Meleshina et al. (1974) there exists a strong attraction between the antiphase and ferroelastic boundaries. When a ferroelastic wall passes through an antiphase boundary it straightens the latter. When an antiphase boundary ends at a ferroelastic wall, the angle between them acquires a definite temperature-dependent value. The possibility of ending of antiphase boundaries at dislocations is its important feature. As can be understood using Fig. 2.1.11 as the definition of the antiphase boundary, any edge dislocation with the proper Burgers vector should give rise to an antiphase boundary in the low-symmetry phase: The dislocation provides a missing (or extra) lattice constant of the parent phase to form the phase shift of the order parameter across the antiphase boundary. Not all features of the domain pattern in GMO are rationalized; for example, the temperature dependence of

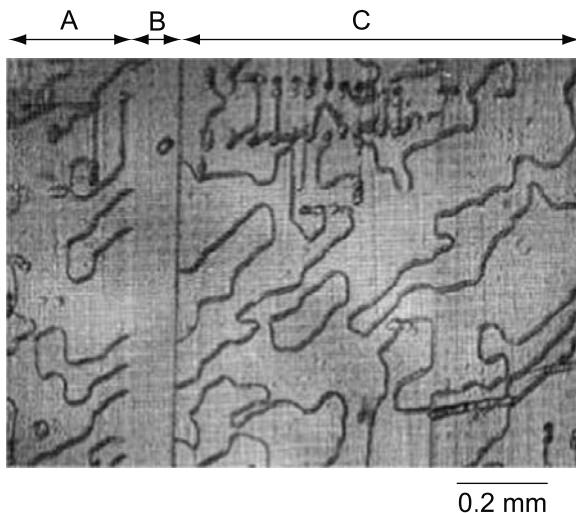


Fig. 5.4.10 Domain pattern revealed by etching on c -cut of $\text{Gd}_2(\text{MoO}_4)_3$ crystal. A and C denote domains with the polarization directed into the plane of the image, B denotes a domain with the opposite direction of polarization. The domain and antiphase boundaries are seen as *straight* (dividing A, B, and C areas) and *curved lines*, respectively. The antiphase boundaries are imaged by etching only in A and C domains (the etchant is not active at positive domains). Such distribution of antiphase boundaries is typical in crystals cooled through T_{TR} when very little wall movement occurs. Reprinted with permission from Barkley, J.R., Jeitschko, W., *J. Appl. Phys.*, **44**, 938 (1973). Copyright (1973), American Institute of Physics

the angle between the ferroelastic and antiphase boundaries (Barkley and Jeitschko, 1973) has not yet received its theoretical explanation.

The last example of a two-domain-state ferroelastic we would like to mention here is Rochelle salt, historically the first ferroelectric compound. It belongs to the category of proper ferroelectric ferroelastics with two domain states (species $222\text{-}P\epsilon ds\text{-}2$, $T_C = 297\text{ K}$). In their classical work, Mitsui and Furuichi (1953) were the first to pay attention to basically periodical domain patterns in a ferroelectric. A typical domain pattern imaged by the birefringence technique is shown in Fig. 5.4.11. The lamellar domains shown in this figure are parallel to the b - and c -axes (the a -axis is taken parallel to the spontaneous polarization) according to the mechanical compatibility conditions specific for this species. As a function of the sample thickness, the period of the lamella pattern was reported to be in compatible with the square root law however with a large scatter as shown in Fig. 5.4.12. The short-circuiting of the sample (e.g., keeping for 2 h in an electrolytic solution) was found to reduce the domain density (Mitsui and Furuichi, 1953), however, only for plates thinner than $400\ \mu\text{m}$. For Rochelle salt again the complicating time-versus-temperature aspect plays a role. It was reported (Dabrowska et al., 1977) that in samples that have been kept below T_C for 2 h, the domain widths remain constant while in samples that

Fig. 5.4.11 A typical domain pattern in Rochelle salt imaged by the birefringence technique. View in the direction of the spontaneous polarization. Reprinted with permission from Mitsui, T., Furuichi, J., *Phys. Res.*, **90**, 193 (1953). Copyright (1953) by the American Physical Society

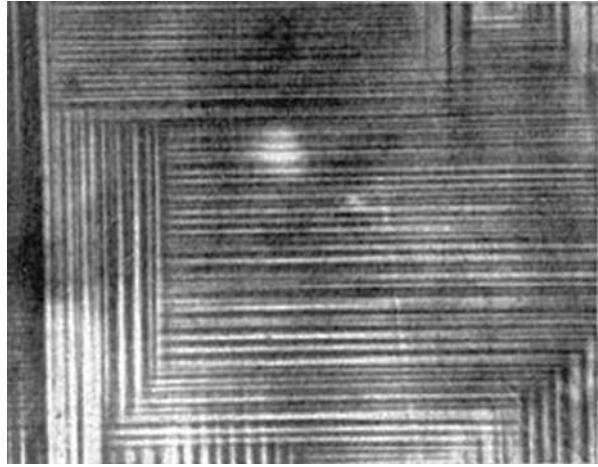
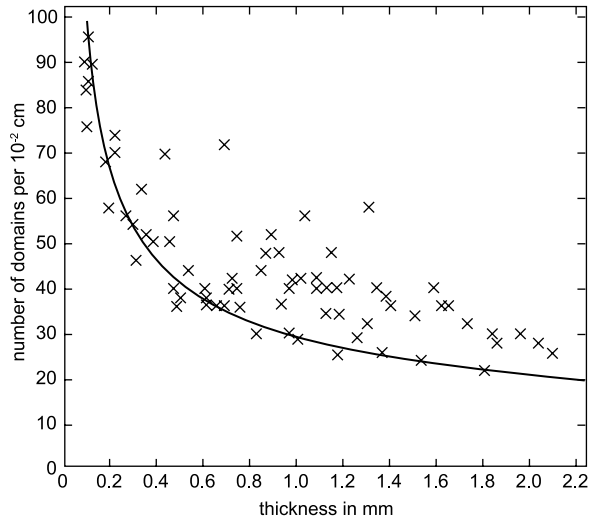


Fig. 5.4.12 Domain density in Rochelle salt as a function of the plate thickness h . x —experimental data; the line corresponds to the domain spacing $W/2 = 1.1 \times 10^{-3} \sqrt{h}$. W and h are in cm. After Mitsui and Furuichi (1953)



were slowly cooled through T_C till room temperature, the domain widths continue to increase for several hours.

5.4.2.2 Ferroelastics with Three Domain States (Not Including Perovskite Material)

All preceding materials in this section were characterized by just two ferroelastic domain states. Now we shall shortly mention crystals offering three domain states, namely $\text{Pb}_3(\text{PO}_4)_2$ and $\text{KFe}(\text{MoO}_4)_2$ and their isomorphs. Both represent the ferroelastic species no. 133, $\bar{3}m - \epsilon s - 2/m$.

$\text{Pb}_3(\text{PO}_4)_2$ undergoes a discontinuous transition from $\bar{3}m$ to $2/m$, at $T_{\text{TR}} = 180^\circ\text{C}$; in Sect. 5.3 we have already discussed the orientation of its phase boundary. Brixner et al. (1973) reported the basic domain properties of this material. The twofold axes of the three ferroelastic domain states lie in the (001) plane of the parent phase and make angles of 120° . The newly acquired shear components of spontaneous strain are the origin of a relatively involved situation with elastic compatibility. Any two domain states can be separated either by a W_f wall or by an S wall. Thus there are three permissible walls of the W_f type, namely $W_3 = (010)$, $W_1 = (\sqrt{3}\bar{1}0)$, and $W_2 = (\sqrt{3}10)$, and three permissible S walls perpendicular to the W_f walls. The unit cells, symmetry elements, and domain walls are schematically shown in Fig. 5.4.13 (Otko et al., 1983). Real domains in single crystals of $\text{Pb}_3(\text{PO}_4)_2$ create fairly complicated patterns but all predicted walls have been actually optically observed and their orientations were found to fulfill mechanical compatibility conditions (Chabin et al., 1976, 1977; Vagin et al., 1979; Ayroles et al., 1979). Figure 5.4.14 shows an example of a domain pattern as seen in a (001) plate in polarizing microscope (Chabin et al., 1977). Here all three domain states D_1 , D_2 , and D_3 are represented and can be easily identified by extinction positions. The double arrows indicate the twofold axes. The domains representing D_2 and D_3 are separated by the W_1 wall or by the S_1 wall. Ideally, all W_f walls should be perpendicular to the (001) plane while orientation of the S_1 wall is determined by the values of spontaneous strain components; at room temperature, this wall makes an angle of 73° with the (001) sample surface. In fact, the extinction directions in neighboring domains do not make exactly the angle 60 or 120° , because in reality the domain clamping approximation is lifted. For the same reason,

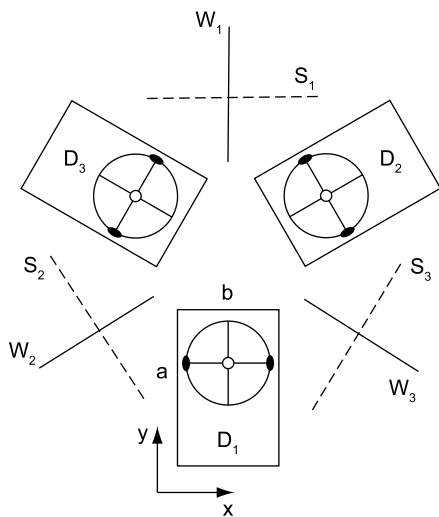


Fig. 5.4.13 Unit cells and symmetry elements in the three domain states of $\text{Pb}_3(\text{PO}_4)_2$, schematically. Orientations of the intersections of W_f and S walls with XY plane (shown with *solid* and *dashed lines*, respectively). W_f walls are perpendicular to this plane, S walls are inclined. From Otko et al. (1983)

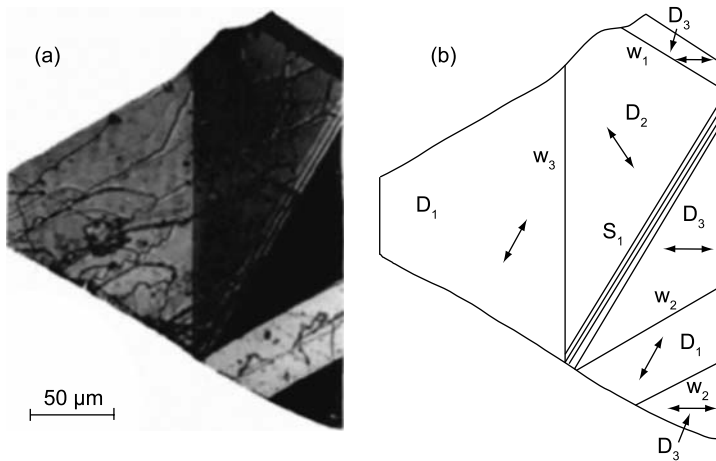


Fig. 5.4.14 Example of domain pattern in $\text{Pb}_3(\text{PO}_4)_2$ as seen in a (001) plate in polarizing microscope (b) and its assignment (a). After Chabin et al. (1977). All three domain states D_1 , D_2 , and D_3 are represented. W_f walls are perpendicular to the plate, the S wall is oblique (thickness fringes are seen in (b)). Double-headed lines show the orientations of the twofold axes in the domains

obviously, it was observed that the surfaces of neighboring domains make a small angle of the order of 1° .

Manolikas and Amelinckx (1980b) investigated domains in isomorphous crystals of $\text{Pb}_3(\text{VO}_4)_2$ ($T_{\text{TR}} = 120^\circ\text{C}$) by electron microscopy. In addition to the analysis of wall orientations they presented interesting observations of unusual regular local domain configurations. Figure 5.4.15a shows an image of one of such configurations. The identification of the walls and domain states making this image is given in Fig. 5.4.15b. An infesting feature of this configuration is the presence of a triangular area possibly corresponding to the metastable parent phase ($\bar{3}m$ symmetry).

For another isomorph, $\text{Pb}_3(\text{AsO}_4)_2$, detailed observations of domains were reported by Dudnik et al. (1983). These authors also discussed in detail the orientations of S walls and found a good agreement with theory. No involved studies seem to have been made of the temperature dependence of real domain patterns. It was reported that they change on heating only when T_{TR} is approached (Bolshakova et al., 1989).

The same species, namely $\bar{3}m - \epsilon s - 2/m$, is represented also by a family of molybdates and tungstates. Otko and his coworkers (Otko et al., 1983, 1993b) investigated domain properties in crystals of $\text{KFe}(\text{MoO}_4)_2$ and $\text{KIn}(\text{WO}_4)_2$. In unstressed samples of the molybdate, domains are commonly separated by W_f walls. On the contrary, in tungstate samples of good-quality tilted S walls prevail and W_f walls are observed only exceptionally. The suggested interpretation is the difference in wall energy densities of the two kinds of walls in the two

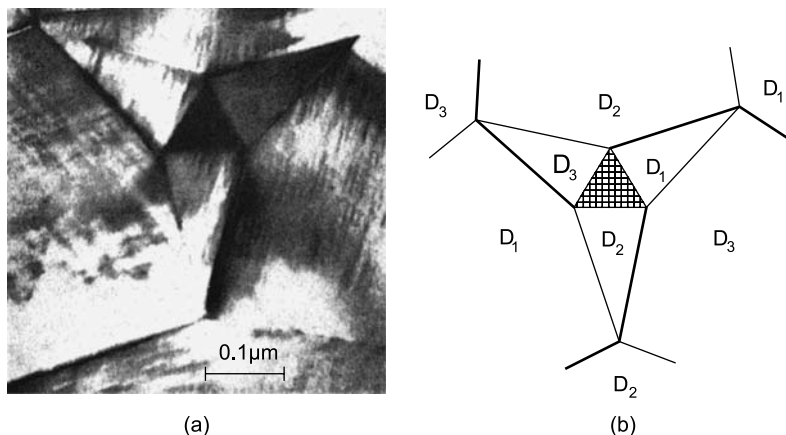


Fig. 5.4.15 A domain pattern observed in $\text{Pb}_3(\text{VO}_4)_2$ by electron microscopy (a), the plane of the image is XY plane, and its assignment (b). Domain states are marked as D_1 , D_2 , and D_3 . Thick lines— S walls. Thin lines— W walls. The central region, shown as cross-hatched in (b), is believed to be metastable parent phase. After Manolikas and Amelinckx (1980a,b)

materials: for the molybdate, $\sigma_w(W_f) < \sigma_w(S)$ while for the tungstate the opposite inequality should hold.

As seen in Figs. 5.4.14 and 5.4.15, for this species, situations often occur where more than two domain states meet along a line. Understandably, such intersections are not elastically compatible and these geometries are paid for by additional elastic energy. Otko et al. (1983) studied which domains occur at the phase boundary at the transition to the ferroelastic phase and why some of them disappear on cooling. The authors have specified a series of often occurring domain geometry transformations which avoid the contact of three domain states.

5.4.2.3 KH_2PO_4 , A Ferroelectric Ferroelastic

Domain patterns in KH_2PO_4 (abbr. KDP) have been the first ferroelectric domain patterns intensively studied and the researchers are still active in the field. Despite this, the physics behind these patterns is not yet fully understood. Below, in this section, we will give a brief overview of the observation of the domain patterns in this material, though, in many cases, we will not be able to provide adequate interpretations for the experimental material.

Potassium dihydrogen phosphate, KDP, represents species $\bar{4}2m - Pcds - mm2$. This material was actually the second discovered ferroelectric, in 1935 by Busch and Scherrer (1935). The transition occurring at $T_{\text{TR}} = 123$ K is of first order. The discontinuity in P_S , however, is quite small (Zeyen and Meister, 1976) and KDP represents one of those discontinuous transitions which are very close to the second order. Thermal hysteresis of T_{TR} amounts only to several tenths of a degree.

The alternative material whose domain properties are expected to be very much the same as those of KDP is its deuterated relative KD_2PO_4 (abbr. DKDP). Its phase transition occurring at $T_{\text{TR}} = 210 \text{ K}$ is also of first order, with thermal hysteresis 0.2 K .

KDP crystals are grown from water solution, are transparent, and generally of very high quality. Figure 5.4.16 shows its typical shape and growth sectors (Abe, 1987); untreated samples prepared from different pyramids of an as-grown crystal differ in their domain patterns. The pyramidal sector is usually selected for sample preparations since it is known to be less defective than the prismatic sector.

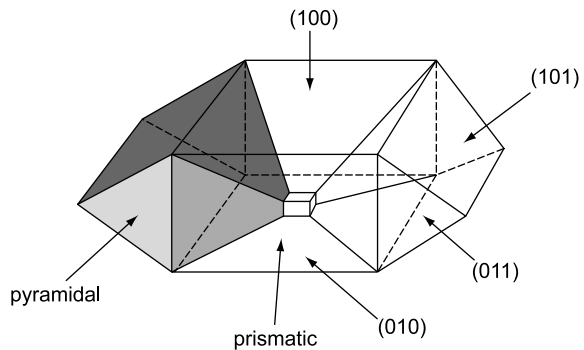


Fig. 5.4.16 Growth sectors in a single crystal of KDP. After Abe (1987)

Spices $\bar{4}2m - P6cds - mm2$ exhibits two ferroelectric domain states which can be joined with domain walls oriented perpendicular to a - and b -axes of the parent phase. Probably the first evidence of the existence of domains in KDP was indicated by Zwicker and Scherrer (1944): They found that the effective birefringence of a c -plate in the ferroelectric phase was zero without biasing field and nonzero with a biasing field, with the same temperature dependence as P_S . This was an indirect evidence for the existence of domains while Ubbelohde and Woodward (1945) demonstrated their presence by X-ray measurements. Mitsui and Furuichi (1953) were probably the first to observe domains in KDP in a microscope but only more than 10 years later. Fomichev (1965), Fouskova et al. (1966), Bornarel et al. (1966), and Toshev (1966) presented pictures of characteristic patterns and analyzed the basic domain geometry.

Typically, pairs of domain walls several micrometers apart meet inside a c -oriented plate-like sample, obviously forming a wedge-like closure; near their tips the two walls cannot be distinguished any longer. Often a system of such parallel domains forms a quasiperiodic pattern. Two perpendicular systems may coexist, their boundary having an irregular shape, which may take a different form on subsequent cooling. Alternatively, the two systems can be parallel but mutually shifted by about one-half of their period, as reported by Toshev (1966). Sometimes such systems can be located, when viewing along the

c-axis, above each other; seemingly a square-like pattern can then be detected (Koptsik and Toshev, 1965). All these data indicate that the narrow domain systems are initiated independently in different parts of a sample and meet only afterwards. Domain geometries known as currently occurring in other ferroelectric ferroelastics, e.g., $\text{Gd}_2(\text{MoO}_4)_3$, namely the existence of only several parallel domain walls quite apart from each other, are rare in KDP and if they occur, only so at temperatures well below the transition point. Studies of side-wise motion of individual ferroelastic–ferroelectric walls, performed for BaTiO_3 (Fousek and Brezina, 1964) or GMO (Flippen, 1975; Kumada, 1970), have never been realized for KDP family of ferroics.

Let us now describe in some detail the most essential or the mostly investigated properties of domain patterns in KDP. Most of available information is based on microscopic observations of *c*-plates. At low temperature, a chamber has to be used in which the requirement of zero temperature gradient is often violated. Information obtained by X-ray diffraction or by γ -diffractometry is indirect and does not offer data on real geometry of domains. Scanning electron microscopy was shown to be applicable (Antoshin and Spivak, 1972; Maussion and Le Bihan, 1976) but it was found that the electron beam may interact with the domain structure, leading to changes or even to complete disappearance of domains.

In a *c*-oriented plate-like sample cooled below T_{TR} , the most typical domain arrangements are sets of parallel domain walls of orientations (100) or (010) in accordance with the criterion of the mechanical compatibility. The thickness dependence of the domain spacing of such patterns has been addressed by many authors, mainly with the aim to check whether the Mitsui–Furuichi square root law, Eq. (5.2.1), holds. For KDP samples with thickness of a few mm, this law was confirmed by Toshev (1966) and Ha and Kim (1985). By contrast, the observations of Abe (1987) showed an extremely large scatter of the domain spacing. Figure 5.4.17 summarizes all the mentioned data.

An essential feature of the domain formation in KDP is that, typically, it is not crucially sensitive to whether the sample is open- or short-circuited. The problem was first identified by Bjorkstam and Oettel (1967). Contrary to expectations, they found that, at the transition, a dense domain structure appears which is identical for an isolated and a short-circuited crystal. Similar observations were later reported by Nakamura et al. (1984) and by Bornarel et al. (1972). These observations may be explained by assuming that there is a non-switchable “passive” layer on surfaces of the plate-like sample. X-ray diffraction data in favor of such layer have been reported by Afonikova et al. (1987). However, taking into account the results of the theory for domain formation in the presence of the passive layer (see Sect. 9.4) so little effect of short-circuiting is difficult to explain. Alternatively, Nakamura et al. (1984) attributed the domain formation to the effect close to spinodal decomposition known from binary mixtures.

It is worth mentioning the experiments revealing the importance of the electrostatic boundary conditions. Bornarel et al. (1972), though reporting identical domain patterns for open- or short-circuited condition, has found

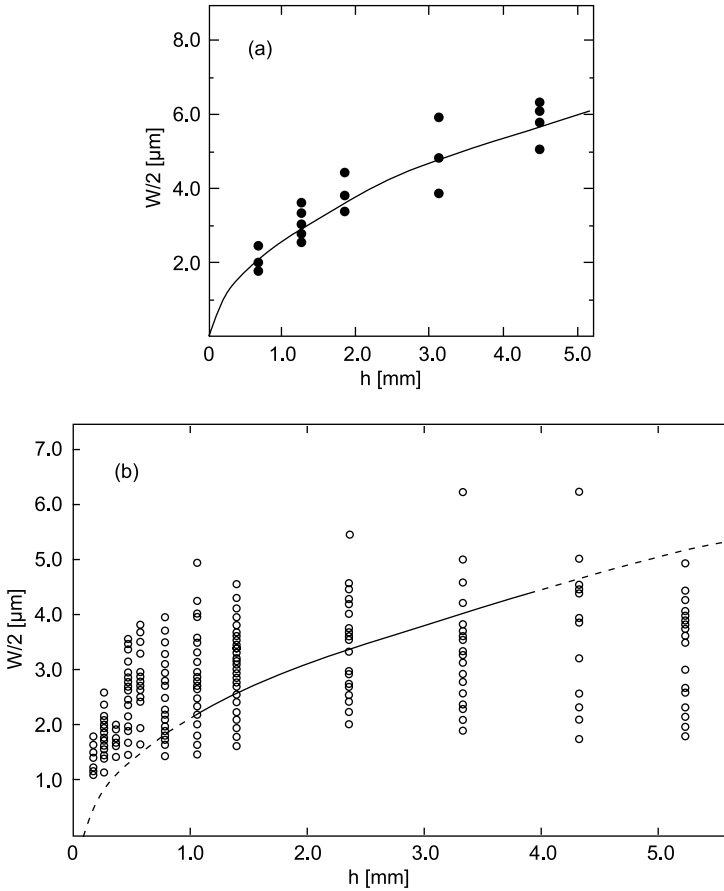


Fig. 5.4.17 Domain spacing, $W/2$, as a function of the thickness of KDP plate, h . (a) Circles—data by Ha and Kim (1985), line—the $W \propto \sqrt{h}$ law. (b) Circles—data by Abe (1987); line—the $W \propto \sqrt{h}$ law corresponding to data by Toshev (1966)

that the in-plane shear stress σ_{12} needed to remove the formed domain pattern⁵ is much larger in the open-circuited case. The impact of depolarizing effects of completely different types has been reported by Ozaki et al. (1993, 1994) and by Ozaki (1995). These authors calmed that manipulating with electrostatic boundary conditions one can induce in KDP crystals periodic domain patterns, which are more complicated than the simple lamella structure, specifically, the so-called prefractals of the pentad Cantor sets discussed in Sect. 5.2.

Another essential feature of the domain patterns in KDP is that a simple count of the number of ferroelectric domain state, e.g., using polarization microscopy

⁵ In KDP σ_{12} and P_3 are linearly coupled in the parent phase (see Eq. (2.3.27)), which enables mechanical switching.

or a diffraction technique (Afonikova et al., 1979; Shekhtman et al., 1973; Aknazarov et al., 1975; Bornarel and Bastie, 1980), will yield four states instead of two expected. This phenomenon is explained by the clapping-angle effect addressed above in Sect. 2.2.5. Figure 2.2.3 shows the orientation of the crystalline lattice in four suborientational domain states appeared due to this effect. The existence, in reality, of four domain states which differ in the orientation of the spontaneous strain tensor poses additional problems with the mechanical compatibility inside a multidomain KDP sample. This problem is illustrated in Fig. 5.4.18a, where the matching of two perpendicular systems of lamella domain patterns is schematically depicted. The boundaries between such domains have been addressed by Afonikova et al. (1987) using both X-ray diffraction and angular scanning topography. Samples prepared by rapid cooling from the paraelectric phase contain a large number of such boundaries. Diffraction patterns showed a continuous sequence of states between the two domain complexes. This indicates that the orthorhombic cell angle varies continuously. The data were interpreted as evidence that a layer of the paraelectric phase exists in the transitory region. The width of this layer was estimated as 1 μm and was found to increase as T_{TR} is approached. These layers were found to be easily mobile at small changes of temperature. Analysis of mechanical matching at the boundary between the sets of domains enabled description of geometrical features of the system. It was shown that if a system of domains meets with a perpendicular wall, the deviation angle α shown in Fig. 5.4.18b depends on the relative volume of the domain states V_{I} and V_{II} and the angle β . It holds that (Abe, 1987)

$$\alpha' = \frac{|V_{\text{I}} - V_{\text{II}}|}{V_{\text{I}} + V_{\text{II}}} \left(\frac{\pi}{2} - \beta \right). \tag{5.4.4}$$

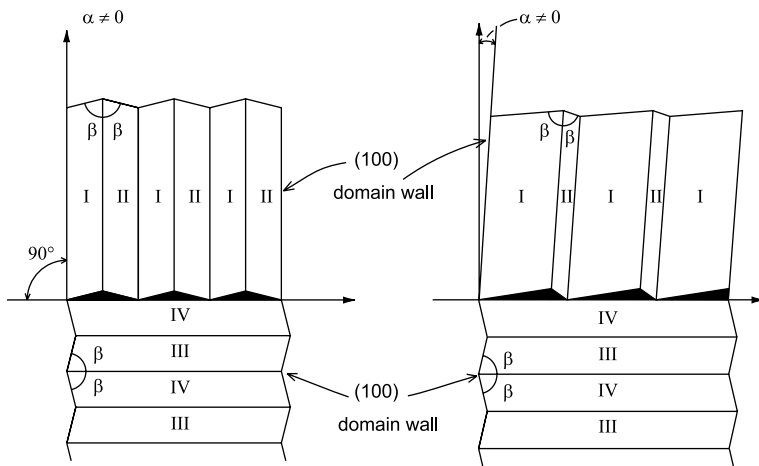


Fig. 5.4.18 Mechanical matching of four (I–IV) suborientational domain states in KDP. After Abe (1987)

Here $\pi/2 - \beta$ is the spontaneous shear strain. For a particular sample, from the integrated intensities of X-ray reflections the value of the factor was determined as $|V_I - V_{II}|/(V_I + V_{II}) = 0.38$ which gives $\alpha = 9.5'$. This agreed well with the observed value.

A problem with perfect mechanical matching also evidently occurs when a plate-like domain ends inside another domain of opposite polarity. The strain fields induced by the domain tip has been extensively addressed by Bornarel with coworkers (Bornarel and Lajzerowicz, 1968, 1972; Bornarel, 1972, 1987) using the approach of twinning dislocations. Figure 5.4.19 explains how a deviation of a ferroelastic wall from the permitted orientation can be presented as system of pieces of the permissible wall shifted by one lattice constant and interconnected with twinning dislocations. The Burgers vector of the dislocation is a function of spontaneous shear $\varepsilon_{S_{12}}$ and of the lateral displacement a of the wall. As seen from Fig. 5.4.19b, a step displacement by the lattice spacing gives the order of magnitude of the smallest Burgers vector: $b = 2a \tan \varepsilon_{S_{12}} \approx 2a\varepsilon_{S_{12}}$. At 100 K, inserting $a = 7.42 \text{ \AA}$ and $\varepsilon_{S_{12}} = 0.008$ we get $b \cong 0.12 \text{ \AA}$. In this framework an effective Burgers vector $B = 2L\varepsilon_{S_{12}}$ can be ascribed to the whole domain tip where L is the domain width. The coupling between the domain tips has been modeled as that between effective dislocations with such Burgers vector to

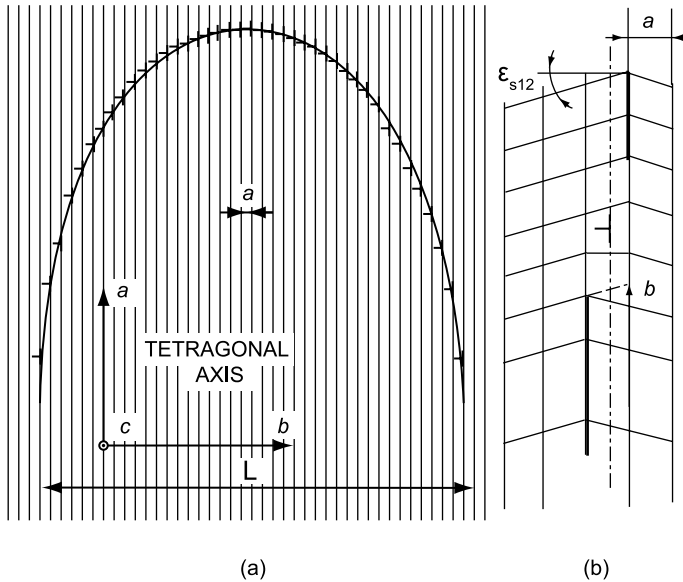
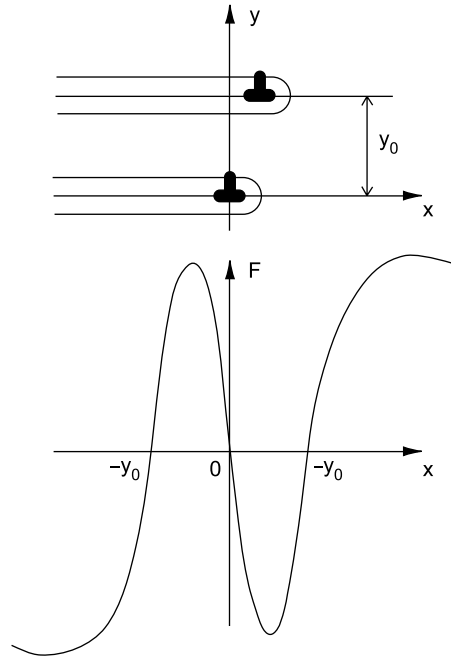


Fig. 5.4.19 Dislocation description of a domain tip in KDP. (a) Distribution of the dislocations along the tip. (b) Drawing for the calculation of the Burger vector for the dislocation which provides a one unit cell shift of the wall. By using these shifts, a wall inclined with respect to the permitted orientation can be presented as that consisting of steps of the mechanically permitted wall. The dislocations needed for such description of the domain tip are shown in (b). After Bornarel (1972)

Fig. 5.4.20 Force acting between the domain tips, F , in KDP crystal as a function of the x -coordinate of the upper tip in the drawing. After Bornarel and Lajzerowicz (1972b)



show a non-monotonic character of this coupling (Fig. 5.4.20). This result enables explanation of the specific domain configurations. For example, the attraction between the tips at small distances explains the formation of the flat front of the tips shown in Fig. 5.4.21a, whereas the repulsion between them helps rationalize formation of the pattern shown in Fig. 5.4.21b.

Appreciable attention of researchers has been paid to the phase front formation and domain development just at the phase transition in KDP crystals. For a detailed discussion of this problem we refer the reader to the work of Bornarel and coworkers (Bastie et al., 1980; Bornarel, 1991; Bornarel and Cach, 1993; Kvitek and Bornarel, 1995, 1997; Bornarel et al., 2000). Here we would like to give one example of observation of the ferroelectric phase formation in a DKDP sample with minimal temperature gradient (of the order of 10^{-3} K/mm) schematically shown in Fig. 5.4.22. Here on cooling the ferroelectric phase is initiated in the corners of a cube-like sample and the phase fronts are quasi-planar. It was also observed that under these conditions, at the beginning, the ferroelectric phase contains only a few domains, but rapid formation of domains begins when both fronts meet in the sample center. Domains traverse the whole sample and then the phase front disappears. The resulting dense domain texture is usually dominated by just one of the two domain states.

Concluding presentation on the material of domain issues of KDP we would like to stress that though an appreciable part of the experimental data can be at least rationalized in terms of existing theoretical approaches, there exists a body

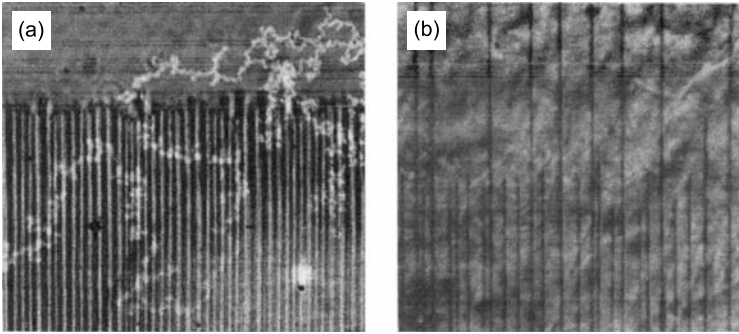


Fig. 5.4.21 Patterns consisting of wedged domains in KDP. Reprinted with permission from Bornarel and Lajzerowicz (1972b). Copyright (1972), Taylor and Francis

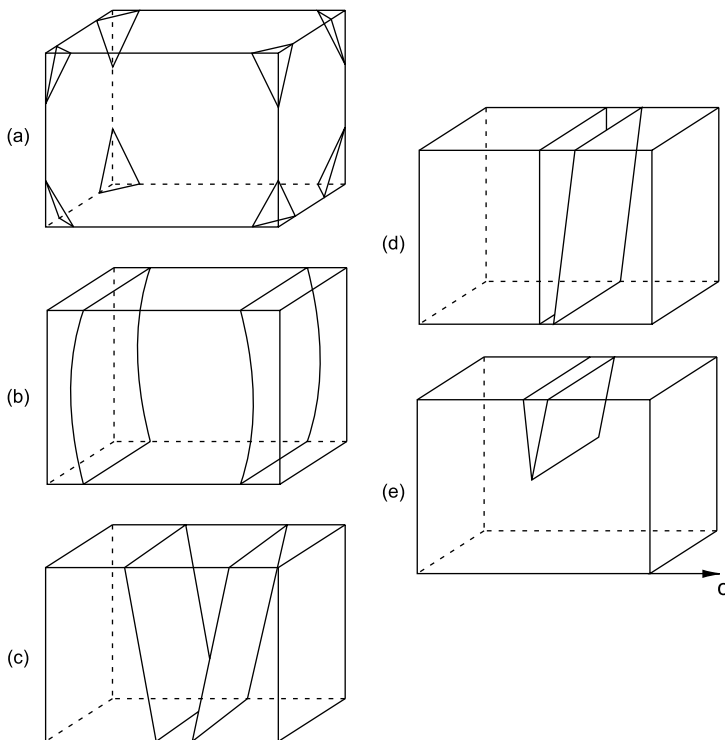


Fig. 5.4.22 Evolution of the phase front during the phase transition in DKDP at homogeneous thermal condition (temperature gradient is about 10^{-3} K/mm). Arrow shows the direction of polar c -axis. After Bornarel et al. (2000)

of experimental information which is not reasonably interpreted. An example of the question that still waits for the answer is “Why does GMO, belonging to the same species as KDP, exhibit so different domain patterns?”

5.4.3 Perovskite Ferroics

The ideal cubic perovskite structure (Fig. 2.1.2) is usually unstable on cooling with respect to polar or nonpolar lattice distortions. Among widely studied materials only KTaO_3 remains cubic at very low temperatures. In the case of the instability-associated polar distortion, which we term as ferroelectric instability, one deals with multiaxial ferroelectrics like BaTiO_3 , PbTiO_3 , and KNbO_3 . As for the instability associated with nonpolar distortion, which we term here as structural instability, in perovskites, it is inevitably associated with a transition with the unit cell multiplication. Such instabilities are very common in these materials. If the temperatures of the ferroelectric and structural instabilities are close to each other, the structural transition may strongly affect the dielectric properties of the material. When the structural transition is slightly above the temperature of the ferroelectric instability, the so-called antiferroelectric behavior may occur with double P - E hysteresis loops and strong dielectric anomaly.⁶ Good examples of the antiferroelectric behavior are provided by PbZrO_3 and of NaNbO_3 , which correspond to species $m\bar{3}m - \epsilon s - mmm$. If, however, the ferroelectric and structural instabilities are far from each other in temperature, the structural transition has a little impact on the dielectric properties of the material. A well-studied material with such behavior is SrTiO_3 (species $m\bar{3}m - \epsilon s - 4/mmm$). In this section, we will concentrate on the domain features of *single crystals* of multiaxial ferroelectric, giving only a few remarks on the case with the unit cell multiplication. Domain properties of the corresponding thin films will be addressed in Chap.9.

As we know, any multiaxial ferroelectric must be at least a partial ferroelastic and this is the case of BaTiO_3 . It represents, on decreasing temperature, three species: $m\bar{3}m - P\epsilon ds - 4mm$, $m\bar{3}m - P\epsilon ds - mm2$, and $m\bar{3}m - P\epsilon ds - 3m$. We shall be mostly interested in its tetragonal phase $4mm$ which results from the parent phase by a first-order transition and for which the amount of collected data on domains makes the material competitive with TGS. This may have two factual reasons: practical applicability of BaTiO_3 and some isomorphs, like KNbO_3 , and suitably located transition temperatures. Barium titanate has been so thoroughly investigated also for historical reasons: Its ferroelectric properties

⁶ Historically such behavior was attributed to a manifestation of the anti-polar ordering (in anomaly with antiferromagnets) (Kittel, 1951). However, further analysis has shown that such behavior can occur at any structural ordering (Balashova and Tagantsev, 1993; Strukov and Levanyuk, 1998). At the same time, the introduction of the anti-polar ordering itself becomes ill-defined in the context of the conceptual problem with the notion of polarization (see Sect. 2.1.2).

were discovered already in the 1940s, independently in three laboratories in the Soviet Union, USA, and Japan.

First a historical remark: Probably the first observations of domains in BaTiO_3 were presented by Matthias and von Hippel (1948). They offered microscopic photographs of wedge-shaped domains, discussed optical effects caused by crossing perpendicular systems of such domains, and explained the optical appearance of a multidomain crystal cube when it is viewed from three sides. We can state that the basic domain features were understood since this paper was published.

It was this material that inspired the nomenclature so often used for simple labeling of observed domains. Merz (1954) considered a plate-like crystal—at that time the only available geometry for this material—and referred to a domain with the vector \mathbf{P}_S parallel with the sample surface as to an *a*-domain while to domain with \mathbf{P}_S perpendicular to the surface as to a *c*-domain. This description, related to the sample shape, is unambiguous. In contrast, the very often used designation “180° domains” or “90° domains” is meaningful only when one describes a domain pair or a system of domains and its usage in singular is meaningless.

Possible directions of \mathbf{P}_S in the discussed species are obvious (see Fig. 2.3.5) and permissible walls separating any pair of domains can be found in tables of Appendix D. Let us give an overview of the relatively simplest domain patterns occurring in plate-like samples of tetragonal barium titanate. Figure 5.4.23 shows a partial selection of observed domain configurations. Compared to the previous cases of TGS or of ferroelastics with two or three domain states,

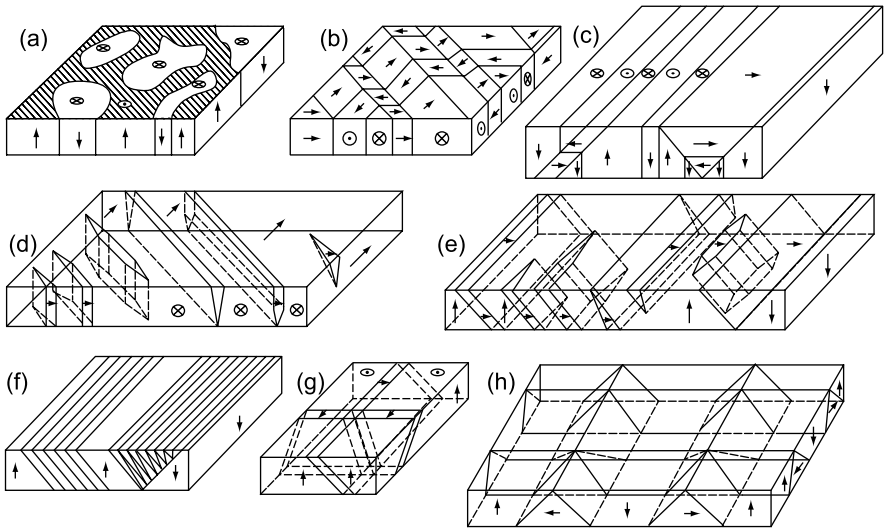


Fig. 5.4.23 Some of domain configurations in species $m\bar{3}m - P_6ds - 4\text{mm}$. Arrows specify the \mathbf{P}_S vectors. After Eknadosyants et al. (1997) and Fousek and Brezina (1961)

we have a large variety of possible geometries and one can speak about “domains within domains.” Tetragonal BaTiO_3 is a model phase for the coexistence of W_f and W_∞ walls (see Fig. 5.4.23). One can expect that in basic domain geometries we have only head-to-tail coupling of \mathbf{P}_S vectors at 90° walls which ensures the electroneutrality of the latter. However, in samples which went through some more complicated history, e.g., having been observed by the TEM method, “head-to-head” and “tail-to-tail” geometries are realized (Tanaka and Honjo, 1964). We should note that the energy of electrostatic field due to bound charges of density $\sqrt{2}P_S$ would be fairly high unless the compensation by free charges takes place; this issue was treated in detail by Yudin et al. (1978).

It may be mentioned that compared to BaTiO_3 , in freshly grown crystals of PbTiO_3 domain patterns have been found to be less involved (Eknadiosyants et al., 1997), probably because of higher tetragonality.

We now shortly enumerate factors which seem to be most important in determining what domain pattern is realized; we have in mind samples which were not intentionally treated thermally or by application of electrical or mechanical forces.

Barium titanate crystals are grown at temperatures well above T_{TR} . If the Remeika method is employed, plate-like samples are formed in the growth process and then cooled through T_{TR} . If the top-seeded solution growth (TSSG) method is used, the as-grown crystals are bulky. In either case, during the cooling process the temperature gradient is not controlled and complicated domain patterns may be formed in as-grown crystals, as a result of elastic compatibility aspects at the paraelectric–ferroelectric phase boundary as already pointed out in Sect. 5.3. Obviously, crystal purity and intentional doping are other factors influencing the domain patterns: Impurities can prefer specific domain states in different parts of the crystal or induce the presence of a domain wall in a particular location. Growth pyramids (Park and Chung, 1994) represent an illustration of this effect. Čáslavský and Polcarová (1965) reported observations, in *c*-plates, of stripes making an angle $\pm 6^\circ$ with the [010] or [100] directions. Made visible by X-ray topography or in polarizing microscope, they disappear above T_C but reappear after subsequent cooling. It was suggested that their formation is due to defects which enforce rotation of \mathbf{P}_S .

We note in passing that growth pyramids, as well as ferroelastic domains, have to be strictly distinguished from growth twins. In the latter, the crystal lattices are mutually disoriented in a way which has nothing to do with ferroic twinning operations.

The next factor which may strongly influence the domain pattern in a particular sample is the way it was prepared. Normally, the sample is cut from an as-grown or larger crystal and polished. The influence of polishing a BaTiO_3 sample is well known to experimentalists and has been described by several authors (Beudon et al., 1988; Park et al., 1998). Beudon et al. (1988) discussed in some detail how polishing a BaTiO_3 plate in different ways results in different kinds of domain patterns.

Müser et al. (1978) observed that, when a rectangular block is cut from a BaTiO₃ crystal prepared by TSSG method, close to its surfaces domains are seen in a polarizing microscope even at temperatures above T_{TR} . Interestingly, the thickness x of this ferroelectric layer is a function of temperature, namely $1/x = g(T - T_1)$ where $T_1 \cong T_{TR}$. The effect disappeared when a layer about 1 μm thick was etched off from the sample. However, if the cube faces are polished again, the phenomenon reappears. The conclusion can be drawn that plastically distorted surface layers, about 1 μm thick, result from the polishing process. They exhibit an increased transition temperature. Park and Chung (1994) and later Park et al. (1998) investigated plate-like samples cut from crystals grown by the same method. They observed that 90° domain patterns depend on the way a plate-like sample is prepared; also, after polishing its surfaces, domain patterns were changing in the time scale of minutes. We note in passing that these authors, in addition to a number of already known domain shapes, observed a regular zigzag domain wall pattern, attributed to a 90° domain pair. Domain patterns in BaTiO₃ above T_{TR} have also been observed by Bursill and Peng (1984, 1986) using electron microscopy.

Comparing these and other observations (Beudon and Le Bihan, 1985; Biedrzycki et al., 1993) it becomes obvious that all mentioned factors, i.e., growth method, crystal purity, the way the sample is prepared, its history, but also the observation method itself, may combine to essentially affect the domain pattern. As a result, contradictory information on domain pattern can be reported and its general validity must be taken with caution.

In Sect. 5.4.1 we described some experiments performed with crystalline plates of TGS, with the aim to prove the role of depolarization energy and reach domain pattern corresponding to the minimum total energy. Similar attempts have been made with plates of BaTiO₃ grown by the flux (Remeika) method, by Fousek and Safrankova (1965). Plate-like crystals were first etched above the Curie point to remove any possible surface layer. Three alternative procedures were employed to study a large number of samples 20–140 μm thick: (I) Slow cooling at a rate of 1 K/min through the transition point to room temperature, (Ia) in oil (conductivity at room temperature $\eta = 10^{-6}\Omega^{-1}\text{cm}^{-1}$), or (Ib) in glycerine with admixture of NaCl ($\eta = 10^{-3}\Omega^{-1}\text{cm}^{-1}$); (II) fast cooling at a rate of 1 K/s in these two media (IIa, IIb). Afterward the samples were etched to reveal domains and in the regions (which were always larger in slowly cooled samples) with the c -axis perpendicular to the plane of the plate, the areas, S_+ , S_- , of positive and negative domains, respectively, were measured. Results can be summarized in the following ways: (a) Procedures Ib, IIb, and IIa led to non-neutral structures, S_+ , S_- differing by several tens of percents; domains had the form of chaotically distributed irregular islets. (b) Experiment Ia gave nearly neutral domain states with $S_+/S_- = 1 \pm 0.03$ and with islet domains prolonged along the a -axis (Fig. 5.4.24a); in 25% of the cases, the average width of stripes could be well defined and lay between 1 and 4 μm (Fig. 5.4.24b).

The influence of electrical conductivity of the surrounding medium testifies unambiguously to the role of depolarization energy. On the other hand, the

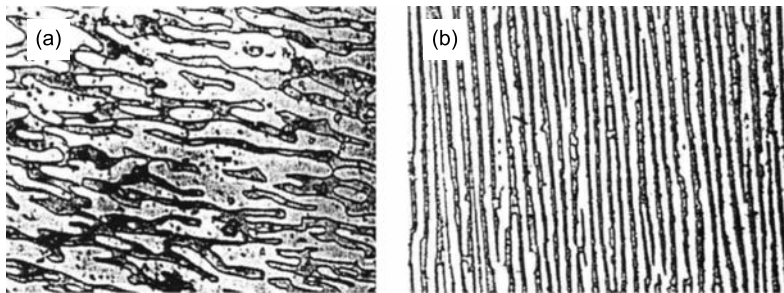


Fig. 5.4.24 Neutral 180° domain structures in slowly cooled plates of BaTiO_3 , perpendicular to the c -axis. (a) Islet-shaped domains prolonged in the direction of the a -axis; (b) domain pattern close to periodic lamellae. After Fousek and Safrankova (1965)

possibility of reaching non-neutral states by fast cooling has no simple explanation. To interpret the latter result as being due to the time required to reach a neutral domain pattern does not seem to be acceptable since, in such configurations, the magnitude of depolarizing field is capable to suppress completely the phase transition.

We now come back to domain patterns connected with the compatibility of the phase front, discussed in general terms in Sect. 5.3. Meyerhofer (1958) observed the formation of domains at the phase boundary of BaTiO_3 and, as already mentioned, the problem was addressed in detail by the Rostov-on-Don group (Fesenko et al., 1973, 1975, 1985; Surowiak et al., 1978), for crystals of PbTiO_3 , BaTiO_3 , and $\text{K}(\text{Ta},\text{Nb})\text{O}_3$. Most of the results have been summarized in the monograph (Fesenko et al., 1990). Let us pay attention to the first two materials. They differ in T_{TR} (490 and 126°C , respectively), in jump of spontaneous strain $(c/a - 1)_{\text{TR}}$ (0.012 and 0.0032), in the jump of polarization (40 and $20 \mu\text{C}/\text{cm}^2$), and also in electrical conductivity at T_{TR} (10^{-1} and $10^{-8} \Omega^{-1}\text{cm}^{-1}$). These numbers suggest that, in lead titanate, the elastic compatibility may strongly influence the phase boundary orientation than in barium titanate while for the electric compatibility the situation is opposite. The given values are fixed; what can be chosen are conditions of the transition, i.e., temperature gradient orientation with respect to crystal axes, its magnitude, and the phase front velocity.

The orientation of the phase boundary is, as already mentioned in Sect. 5.3.2, of the type (320) for PbTiO_3 and of the type (056) for BaTiO_3 . Figure 5.4.25 shows schematically a ferroelastic domain pattern as it forms at the phase boundary and specifies kinds of domain patterns observed in differently oriented plates. Relative domain volumes which ensure mechanical compatibility for the two materials have been given in Table 5.3.2. To achieve these well-defined configurations, the sample must be cooled through T_{TR} in a temperature gradient directed along the normal to the respective phase boundary. If there is only one phase front, this 90° pattern stays permanently. If, for a

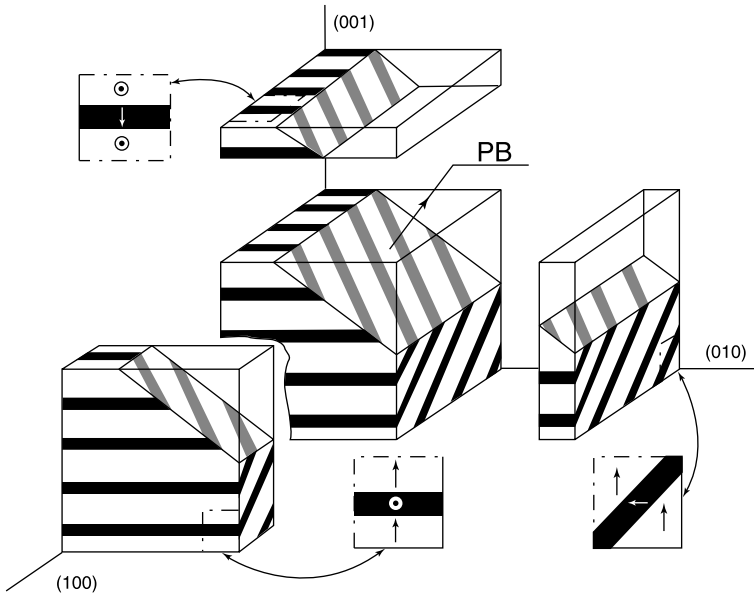


Fig. 5.4.25 Ferroelastic (90°) domain patterns formed at the phase boundary $m\bar{3}m - 4mm$, in plates differently oriented with respect to the phase front. Arrow indicates the orientation of the spontaneous polarization. PB indicate the phase boundary and its normal. Reprinted with permission from Fesenko et al. (1985). Copyright (1985), Taylor and Francis

more general temperature gradient orientation, there are more phase fronts, the 90° domain pattern is complicated and changes with temperature.

Consider now the formation of 180° domain systems imbedded into a system of 90° walls formed at the transition. Here two factors play a role: the electric conductivity and the phase boundary velocity v . In PbTiO_3 with large conductivity, for low values of v , domains with antiparallel polarization are absent. At v exceeding some critical value, which is a function of the sample thickness and varies in the range $5 \times 10^{-5} - 10^{-6}$ m/s, such domains are nucleated at the phase boundary. During the motion of the latter they reach a conical shape and form a periodical pattern of systems of islands on the sample surface. These systems have the shape of a stripe parallel to the phase front. Figure 5.4.26a shows schematically such a pattern in a c -domain. (This pattern itself is an element of a twin pattern like shown in Fig. 5.4.25.) An essential feature of the bulk domain structure, revealing itself in this pattern, is the predominance of head-to-head configuration, which is possible because of a pronounced conductivity of PbTiO_3 . In BaTiO_3 , though the formation of ferroelastic patterns by the phase front is similar to that in PbTiO_3 , the formation of 180° domains differs a lot. First, they form at any velocity of the front. Second, they have a shape of continuous “though” domains crossing the whole ferroelastic domain instead of systems of islands. The details of the final pattern depend of the conditions of

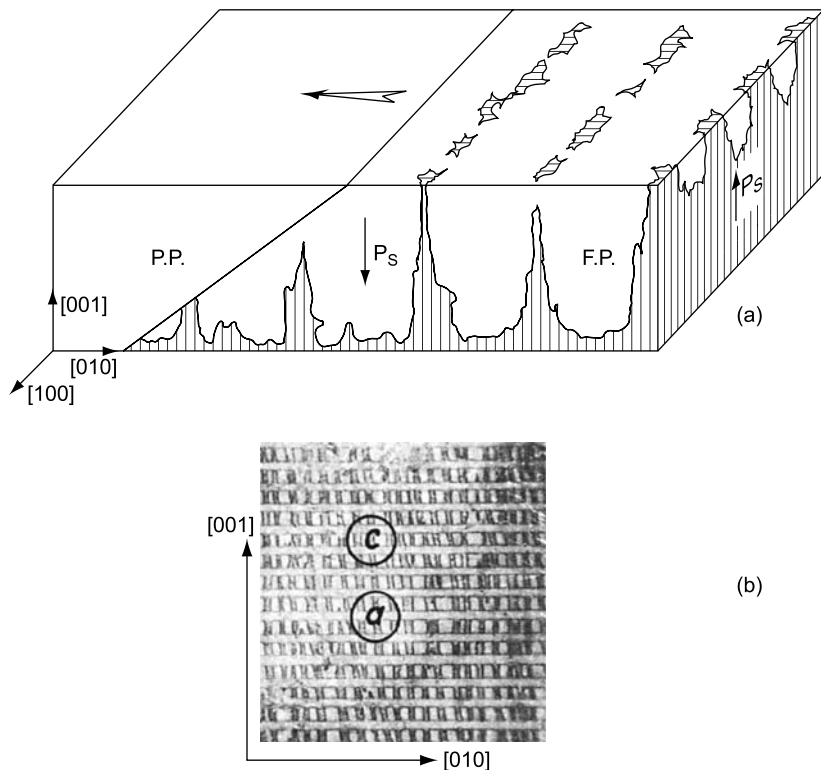
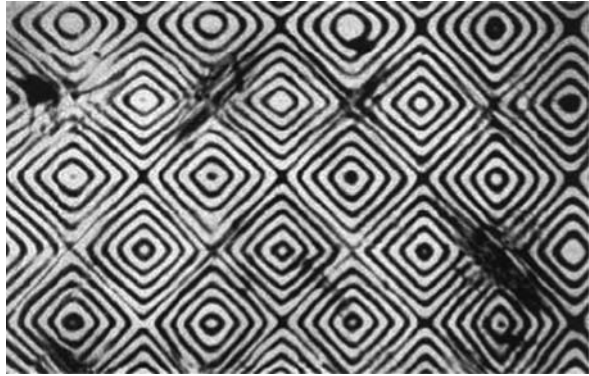


Fig. 5.4.26 (a) Spatial distribution of the polarization in a c -oriented region formed by motion of a phase boundary in PbTiO_3 . The direction of motion is shown with *black arrow*. The paraelectric and ferroelectric phases are denoted as PP and FP. The region with the ferroelectric phase consists of two domains predominantly separated with a head-to-head wall. Direction of the spontaneous polarization is shown with *arrows*. (b) Etch patterns of the combined 90° and 180° domain system in BaTiO_3 , formed as a result of the phase boundary motion. Symbols c and a denote c - and a -domains, respectively. It is seen that the former is split into 180° domains. The imaged area is about $70 \times 70 (\mu\text{m})^2$. Reprinted with permission from Surowiak et al. (1978). Copyright (1978), Taylor and Francis

the phase transformation. It may be fairly regular as illustrated in Fig. 5.4.26b. The shape of 180° boundaries can be also rather irregular. Surowiak et al. (1978) has reported images of the domain patterns with irregular shape of 180° boundaries, which are very similar to that shown in Fig. 4.5.23a–c. The difference in the domain formation in PbTiO_3 and BaTiO_3 is evidently related to the difference in the conductivity of these materials. In BaTiO_3 , the low conductivity makes impossible both single-domain twins and head-to-head configurations.

In the tetragonal phase of BaTiO_3 , an interesting complex square-net domain pattern composed of 90° domain walls, here referred to as Forsbergh

Fig. 5.4.27 Forsbergh pattern in a BaTiO_3 plate. Reprinted with permission from Forsbergh (1949). Copyright (1949) by the American Physical Society



pattern, was reported by Forsbergh (1949) and other authors (Nakamura et al., 1979; Kirpichnikova et al., 1995). It may arise in plate-like crystalline BaTiO_3 samples during slow cooling through the transition point. Figure 5.4.27 shows such pattern observed in crossed polarizers. The appearance of this kind of patterns has been linked to crossing of groups of laminar domains; however, no theory for the formations of such patterns is presently available.

We have shortly described some of the domain observations in the tetragonal phase of BaTiO_3 . Much less effort was put on the low-temperature phases $mm2$ and $3m$ of this material. One of the most interesting observations was made by Cameron (1957). He found that crystals etched in the orthorhombic phase reveal “checkerboard pattern.” Its etched surface relief was visualized by electron microscopy and is reproduced in Fig. 4.2.1. The pattern on the opposite side of the sample is similar but displaced along one of the primitive crystal axes, the displacement being equal to the thickness of the sample. It seems that exact assignment of visualized domain states is not available but since domain walls are planar, we probably see a mechanically non-compatible system of mutually perpendicular W_f walls.

Barium and lead titanates are probably the most studied examples of multi-axial ferroelectrics. Another candidate is potassium niobate, having the same sequence of phases as BaTiO_3 . However, at room temperature it represents the species $m\bar{3}m - P6ds - mm2$ and a systematic study of coexistence of 180, 90, and 60° domain pairs would be of interest. The truth is, however, that more effort has been put on making these crystals ideally single domain because of important applications of their nonlinear optical properties. Remarkable observations of intersecting W_f and S walls in the $mm2$ phase, made by Wiesendanger (1973), were mentioned already in Sect. 2.2.7. Jun et al. (1988) reported very complicated domain patterns in surface layers of Czochralski-grown crystals and mutually crossing systems of 60 and 90° domain pairs. Lian et al. (1996) investigated domains in plates of pseudo-cubic orientation, cut from TSS-grown crystals, at room temperature. Perpendicular systems of 90° lamellar domains were observed but also 90 and 60° domain walls crossing each other. It

should be mentioned that here by intersecting walls we mean a situation different from that analyzed by Yamamoto et al (1977a,b) and discussed by Salje (1990). In the latter case, e.g., in crystals of $\text{Gd}_2(\text{MoO}_4)_3$, two mutually perpendicular W_f walls meet in the crystal and form a rounded junction whose radius depends on the elastic stiffness coefficients. This case requires only two domain states to be represented in the sample. By contrast, the situations observed in the orthorhombic phase of KNbO_3 involve four domain states meeting, in a planar projection, in one point.

Concluding this section we will make some remarks on domain patterns in perovskites with a phase transition associated with the unit cell multiplication. An essential feature of these materials is the expected occurrence of antiphase boundaries because of the cell multiplication at the transition. In practice this feature has received little attention. However, judging from the diffraction data on SrTiO_3 , these kinds of walls can be quite abundant in perovskites (Wang et al., 2000a). Between two groups of the material mentioned in the beginning of this section (with antiferroelectric behavior and without it), in the latter, the ferroelastic domain patterns have been of very little interest for research, being typically addressed when these interfere with measurements of other physical properties. For example, Müller et al. (1970) polished plates of SrTiO_3 , to avoid undesirable twinning. At the same time, in perovskites with antiferroelectric behavior, the ferroelastic twinning has been intensively addressed. In Sect. 2.2.7 we have already given examples of studies on the orientations of S domain walls in $m\bar{3}m - \epsilon s - mmm$ species realized in PbZrO_3 and NaNbO_3 crystals (Dec, 1988; Miga et al., 1996). Investigations of domain patterns in this species have been reported by several groups (Tanaka et al., 1982; Dec and Kwapulinski, 1989; Balyunis et al., 1993; Jona et al., 1955; Fesenko and Smotrakov, 1976). The observed patterns have been termed as 60 and 90° structures. Concerning this terminology, one should be aware that, strictly speaking, it is appropriate to species $m\bar{3}m - Peds - mm2$, but not $m\bar{3}m - \epsilon s - mmm$ where already in the parent clamping approximation (see Sect. 2.2.5) the angles between the indicatrices in the different domain states are not exactly equal to 60 and 90°. The domain patterns in PbZrO_3 can be very involved containing boundaries where the mechanical matching between two groups of the twins is possible only on average. Orientation of such boundaries has been theoretically addressed in Balyunis et al. (1993); however, the results reported may not be correct as they were obtained using an unjustified criterion of mechanical compatibility (Metrat, 1980) (see footnote 14). An interesting feature of PbZrO_3 is that, depending on the stoichiometry, the transition from the cubic to the orthorhombic phase can be direct or passing through an intermediate ferroelectric rhombohedral phase (Dec and Kwapulinski, 1989; Ujma et al., 1988). Observations of domain patterns in the rhombohedral phase as well as the phase boundaries between the rhombohedral and orthorhombic phases have been reported by Dec and Kwapulinski (1989), Balyunis et al. (1993), and Bah et al. (1994).

5.4.4 *R Cases*

By now we have discussed two motives which can result in regular but often complicated domain patterns: depolarizing fields in ferroelectrics, elastic matching at phase boundaries in ferroelastics. Situations related to the last one may occur in ferroic species in which *R* cases may occur, i.e., in which domain pairs can be formed with no mechanically compatible walls.

Table D.1 shows that there are a considerable number of species in which no permissible walls are allowed between some particular domain states. A general analysis of ferroelastics leads to the conclusion that in the seven following species no permissible walls between ferroelastic domain states exist at all: $23-222$, $m\bar{3} - mmm$, $m\bar{3} - mm2$, $m\bar{3} - 222$, $3-1$, $\bar{3} - 1$, and $\bar{3} - \bar{1}$. It may be expected that when the phase transition is continuous, non-compatible domain pairs will not occur at all. No examples of such materials seem to be known. However, if the phase transition is discontinuous, various domain states can be nucleated independently in different parts of the sample, and when the transition is completed the corresponding domains will inevitably face each other. Then the question arises of how such domains will mutually conform. Obviously the answer depends on the magnitude of elastic energy that has to be involved in matching the two domains together. This additional energy will strongly depend on the values of spontaneous strain components and also on the area of the domain wall. However, in addition to elastic deformation of the two domain states, another possibility can be considered, namely that matching on average will take place, similar to that discussed in Sect. 5.3. One or both incompatible regions will be subdivided into ferroelastic domain states in a way that the average spontaneous strain will meet the compatibility condition with the other region, along a defined boundary.

Let us shortly discuss real situations in three ferroelastic materials in which *R* cases are envisaged. Crystals of MASD were reported to represent the species $23-Peds-2$. Spontaneous polarization directs along the cubic axes so that in principle we may have 180° and 90° domain pairs like in the often studied tetragonal barium titanate. Unlike in $BaTiO_3$, however, antiparallel domains represent ferroelastic pairs and can be separated by W_f walls of the type $[100]$. It was realized already by Jona and Shirane (1962) that here 90° walls are prohibited in a stress-free crystals. However, microscopic observations of samples which were cemented to a microscope slide before cooling ($T_{TR} \cong 177$ K) testified to the fact that three ferroelastic domains corresponding to three mutually perpendicular directions of \mathbf{P}_S did form. Their boundary orientations were close to either (111)- or (110)-type planes. No movements of these boundaries were observed in applied electric field which, however, resulted in some polarization reversal due to antiparallel processes (Jona and Shirane, 1962). Such behavior can be rationalized by assuming that the position of the 90° walls corresponds to deep minimum of the total mechanical energy of the fully stressed sample. Frozen position of these ferroelastic walls can also be

attributed to the effect of cementing the sample (see Sect. 9.3 for a discussion of similar effect in ferroelectric thin films). Bearing in mind the clamping effects of the microscope slide, the problem, actually, must be treated in terms of compatibility conditions in a partially clamped sample; relevant theoretical treatments have been offered by Shuvalov with coworkers (Shuvalov et al., 1987; Dudnik and Shuvalov, 1989).

In contrast to the species assignment made above, later studies (Glushkov et al., 1987) of MASD indicated that in fact this crystal belongs to the species $m\bar{3} - P\bar{6}3c - mm2$. However, even in this case the 180° walls are not permissible. Measurement of their dielectric properties performed by Glushkov et al. (1987) provided interesting domain-related information. It was found that the thinner the multidomain samples, the larger the permittivity value in a considerable range below the transition temperature. This could be explained well by assuming that “not perfectly permissible,” i.e., somewhat strained walls indeed do exist in thinner samples and due to their high mobility considerably enhance the dielectric response.

A comprehensive study of domains was performed for crystals of $\text{Cd}_2(\text{NH}_4)_2(\text{SO}_4)_3$ (abbr. CAS) (Glogarová and Fousek, 1972). Here, we would like to go into detail since, in this crystal, we are dealing with a piece of instructive information, which however is not fully understood. CAS is an improper ferroelectric belonging to species $23-P\bar{6}3c-2$ ($T_{\text{TR}} \cong 92$ K). Ferroelectric domains correspond to six polarization directions along the cubic axes. While antiparallel domains are separated by permissible walls of the (100) type, no walls are permitted for 90° domain pairs (Table D.20). Domains representing all six domain states can be optically distinguished (Glogarová and Fousek, 1972). Despite a very low value of the spontaneous polarization (≈ 0.7 $\mu\text{C}/\text{cm}^2$), the domain formation was found very sensitive to the electrical conditions. Figure 5.4.28 schematically shows typical patterns observed with polarized microscope in an (001) plate. Figure 5.4.28a images an insulated sample. Here the stripes with double arrows correspond to a -domains (or 180° patterns of these domains, which cannot be resolved in this orientation). These stripes are separated with those containing dense 180° patterns of c -domains. Figure 5.4.28b shows a short-circuited plate. Here, much large c -domains are seen. In both images, neighboring 90° domains are observed indeed. Despite the fact that this neighborhood corresponds to the R case, it was found that the domain states are divided with two sets of mutually perpendicular domain walls (like in the case of permitted matching). For domain pairs with \mathbf{P}_S vectors [001], [100] or [001], $[\bar{1}00]$ the wall takes one of two orientations (570) or (7 $\bar{5}$ 0) while for domain pairs [00 $\bar{1}$], [100] or [00 $\bar{1}$], $[\bar{1}00]$ the wall orientations (750) or ($\bar{5}$ 70) were indicated. (In all these cases the last index 0 is taken with some uncertainty.) It could have been guessed that they represent *on average* permissible walls between the [001] domain and a dense domain pattern of a -domains. However, according to Glogarová and Fousek (1972), the strain analysis shows that even in this case permissible walls would not exist. Thus (570) and analogical walls must indeed be only non-coherent, accompanied by elastic stress. If we assume that a -domains do not

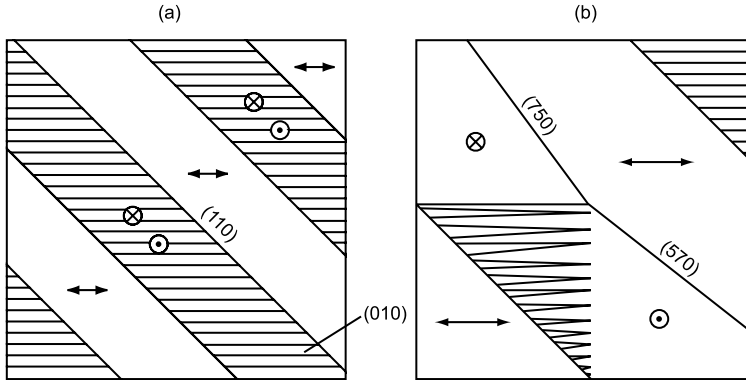


Fig. 5.4.28 Domains in $(\text{NH}_4)_2\text{Cd}_2(\text{SO}_4)_3$, representing the ferroelectric and ferroelastic species 23-*Peds*-2 where no 90° permissible walls are allowed; schematic drawings of polarized microscope images. (a) Typical domain patterns as observed in an insulated (001) plate. The stripes with double arrows correspond to *a*-domains (or 180° patterns of these domains, which cannot be resolved in this orientation). These stripes are separated with those containing dense 180° patterns of *c*-domains. (b) Typical part of domain patterns in a short-circuited (001) plate. In contrast to (a), two large *c*-domains separated with a zigzag wall are seen. In both images, forbidden 90° permissible walls are seen. After Glogarová and Fousek (1972)

represent 180° patterns, one concludes that these non-coherent walls are also charged, which is difficult to expect in view of the aforementioned strong sensitivity of the domain pattern to the electric boundary conditions. The feature, which can be readily rationalized in this complicated system, is the presence of (110) walls in the insulated sample (Fig. 5.4.8a). This wall can be viewed, in a good approximation, as the “average” of the sequence of (750) and (570) walls.

Crystals of $\text{K}_2\text{Cd}_2(\text{SO}_4)_3$ have been reported to represent the species 23-*eds*-222 ($T_{\text{TR}} \cong 432 \text{ K}$). Here again, no walls strictly comply with mechanical compatibility conditions. However, optical microscopic observations of Biletskii et al. (1988) and of Vlokh et al. (1997) revealed that in mechanically free and fairly thick (0.6 mm or more) samples, ferroelastic domain structure can be observed in a narrow temperature interval below the transition temperature, both on cooling and on heating. It disappears further down in the ferroelastic phase. When occasionally the domain pattern stayed until room temperature, microcracks could be observed near the frontier between the polydomain and single-domain regions, indicating an increase in the mismatch elastic energy, as the magnitude of spontaneous strain increases on cooling. The mentioned walls can take one of four well-defined orientations. A more detailed discussion of Vlokh et al. (1998) indicated that what appears to be domain walls might be in fact regions several tens of micrometers thick whose optical properties suggest that they represent slabs of the cubic phase.

We can conclude this section by stating that mechanical contacts of mechanically incompatible domains have been documented. As we have already

mentioned, the existence of such contacts in finite crystals is not absolutely impossible since in a finite sample a price of *finite* additional energy (though bulk energy) should be paid. However, when an R case is realized, a natural question of why this energy is acceptably low is to be posed. Is it a particular relation between the components of the spontaneous strains or is it rather a feature of the particular domain geometry? Unfortunately, for all of the discussed materials this question has not been clearly answered. An especially intriguing situation with CAS is worth mentioning. The mechanically incompatible walls increase the energy of the system by an additionally *bulk* elastic energy of the domains. For this reason one expects that the favorable orientation of the non-coherent walls should be different in different domain configurations, which is clearly not consistent with the experimental observations in CAS.

5.4.5 Quartz

Crystal quartz (SiO_2) is a secondary ferroic which has met with very wide success in the marketplace. The world's secondary timing standards and many clocks and watches depend upon quartz crystal piezoelectric resonators. In single crystals of quartz, the presence of domains is unwanted since they reduce the effective piezoelectric response and, even worse, they change completely the resonance modes. Thus quartz is historically the first material in which the presence of ferroic domains plays an essential practical role, though a negative one.

Quartz represents the ferroelastoelectric and ferrobielastic species 622-*ds*-32, with the transition temperature 848 K. The transition is equitranslational. In fact, in a narrow temperature range of about 1.4 K between the two phases of this crystal, there exists an incommensurate phase.

Let us shortly discuss domain properties of quartz as they follow from the indicated 622 to 32 transition. In both phases there are nonzero piezoelectric coefficients $d_{14} = -d_{25}$. In the ferroic phase additional (morphic) coefficients are newly acquired, namely $d_{11} = -d_{12} = -(1/2)d_{26}$. The two domain states are related by the twofold axis directed along z -axis and differ in sign of the morphic coefficients. Domain pattern corresponding to this symmetry relation is referred to as *Dauphiné twinning* or *electrical twinning*. Since the given species is not ferroelastic, mechanical compatibility conditions do not impose any restriction on the orientation of domain walls.

Both phases of quartz exhibit two enantiomorphic modifications, referred to as right- or left-handed quartz. These modifications can be obtained one from the other by a reflection in the mirror plane perpendicular to the x -axis of the structure. When these modifications coexist in the trigonal phase of a single crystal, they are separated by $(11\bar{2}0)$ twin boundaries and their structures are related by a reflection in this plane. Such twins are commonly referred to as *Brazilian twins*. They differ in

sign of all piezoelectric coefficients and of optical gyration. It is essential to realize that these twins do not represent ferroic domains.

The fact that domain states of quartz (Dauphiné twins) differ in the sign of piezoelectric coefficients specified above attracted great attention to domain phenomena in this material. For applications in classical resonators, homogeneous (single-domain) samples are required. Quartz crystals are found in nature or “synthetic” single crystals are grown from an aqueous solution at high pressure and high temperature. They may contain both Dauphiné and Brazilian twins. Crystals with regions containing the latter are avoided since such twins cannot be influenced by applied forces. Contrary to that, Dauphiné twins represent domain pairs of ferroelastoelectric or ferrobielastic label and can be influenced by simultaneously applied electric field and mechanical force or just by the latter, properly oriented.

Boundary conditions are not expected to play an essential role in domain patterns in this family of ferroics. Reported observations of domains in not specially treated samples of quartz agree upon the fact that as-found crystals contain rather complicated domain geometries; this was demonstrated, e.g., by Bond (1938) who observed the etched surface of a sphere-shaped sample. By X-ray topography, Lang (1965) detected domains of irregular shapes with planar sections of domain walls, including those totally enclosed within the specimen. McLaren and Phakey (1969) studied Dauphiné twin boundaries by electron and X-ray diffraction and stressed that the Dauphiné domains were never observed to cross Brazil twin boundaries. A short overview of domain patterns was summarized in the monograph of Klassen-Neklyudova (1964), based on the observations of etched samples. Generally, the contours of Dauphiné twins can be wavy, curvilinear, or straight. A detailed study of thermally twinned crystals showed that Dauphiné twins are sensitive to structural defects; twinning often follows the growth zones and twin boundaries frequently reveal minute defects connected with local residual stress. If stress is applied to a quartz plate to reach the single-domain state (ferrobielastic switching), after its removal, the detwinned plate restores the twinned regions precisely as before. This clearly demonstrates the influence of defects on the domain pattern.

In addition to etching and X-ray topography, ferroelastoelectric domains in quartz can be made visible in crossed polarizers when properly oriented either electric field or mechanical stress is applied. Aizu (1973a,b) was the first to point out that if the domain states in quartz are ferrobielastic and differ in elastic compliances, they must differ also in the corresponding components of other tensors of the fourth rank, including the tensor describing elasto-optic properties. His analysis led to the conclusion that if a uniaxial pressure p is applied along the (011) or $(01\bar{1})$ axis, the indicatrices of the two domain states rotate around the x -axis in such a way that they finally make an angle proportional to the product $\pi_{2322}p$ where π_{2322} is the elasto-optic coefficient. This will lead to a clear contrast of domains in polarized light, which Aizu confirmed by microscopic observations. In fact, domains with clearly defined planar geometry, which he observed optically, demonstrate ferrobielastic switching and cannot

be considered typical for as-grown crystals. But in principle, with small applied stresses the method could be used to observe the original domain patterns.

Laughner et al. (1981) paid more attention to the situation in quartz under applied stress. Because the two domain states differ in some components of elastic compliance, when stress is applied they differ in total strain although the material is not ferroelastic. These differences, being induced, are small but in principle one can apply the same elastic compatibility conditions for the orientation of domain walls under applied stress as for ferroelastic crystals. However, the reported observations of domains formed by stresses applied for differently oriented cuts showed that the walls did not fulfill these relations, probably because defects in the used crystals played an essential role.

Domain optical distinction can also be based on the fact that since the two domain states are ferroelastoelectric, they differ also in some coefficients of the electro-optic tensor. A general analysis of optical visibility of Dauphiné twins in crossed polarizers, in applied field or stress, was offered by Dolino (1975). When the electric field is applied along the x -axis, the two indicatrix ellipsoids rotate and domains become visible. However, since the involved electro-optic coefficients are small, a fairly high field of 40 kV/cm has to be used to reach a satisfactory contrast. Alternatively, Dolino et al. (1973) showed that domain observations can be based also on nonlinear optical properties. It should be noted that if quartz samples are irradiated by a laser beam, attention must be paid to keep the absorbed energy low since, as shown by Anderson et al. (1976), the thermal stresses can result in nucleating new domains, obviously due to ferrobielasticity.

Discussing domains in quartz one should indicate that large-scale domain patterns in the ferroelastoelectric phase of quartz can be related to the dense domain patterns existing in the narrow temperature range of the aforementioned incommensurate phase. However, because of the space problem, we do not address this interesting issue in the book as well as other issues related to the incommensurate phase.

While considerable attention was paid to domain patterns in quartz little is known about domains in an isostructural crystal of AlPO_4 . Zvereva et al. (1992) investigated the surface of this crystal by etching to find both right- and left-handed parts as well as Dauphiné twins.

5.4.6 Tweed Patterns

In the introductory theoretical parts of this book we defined domain states on the basis of symmetry approach as well as on the basis of thermodynamic treatments of phase transitions. Domains as we have understood them by now “have the right” to be formed only when the symmetry of the material changes, i.e., at and below the transition temperature (pressure may play an analogical role).

In a number of materials, below some temperature—not sharply specified—small regions, often referred to as microdomains, can be observed. Among the

methods used are polarized microscopy, X-ray diffraction, and transmission electron microscopy. They form quasi-regular patterns which on the first sight do not exactly correspond to the basic symmetry approach to ferroics. In some cases they are referred to as tweeds. We mention the topic only in short, giving several references to more involved treatments. In fact, the concept of tweed patterns is used in more than one meaning. As remarked by Putnis and Salje (1994), it happens frequently in the study of materials that observations made in one field are not directly compared with observations in another until each has evolved its own set of terminologies and interpretations. This statement applies very well to the studies of tweed microstructures in minerals and metals as compared to the studies of domains in ferroelastics (whether ferroelectric or not) with clearly defined phase transformations.

One family of microstructures referred to as tweed texture is connected with spinodal decomposition in a solid solution (Putnis and Salje, 1994). It results in modulation of the chemical composition along clearly defined crystallographic directions. Its wavelength is of the order of 10^2 Å, leading to satellite reflections around the Bragg peaks. If the process takes place in a structure of high symmetry, there exist equivalent directions for such a modulation and a microstructure can be observed, referred to as tweed pattern.

The concept of tweed patterns is frequently used in connection with structural phase transitions (Putnis and Salje, 1994). In some minerals, representing in fact ferroelastic crystalline materials, and below a temperature not sharply specified, small regions, often referred to as microdomains, have been observed. These regions differ in their macroscopic symmetry from the average symmetry of the whole sample. Their typical linear dimension is of the order of 10^2 – 10^4 Å. Often the whole sample is split into microdomains of lower symmetry, spatially arranged to form a quasi-regular system and it is such a system which is referred to as the tweed pattern.

One classical example of real observations of tweed patterns is offered by the mineral KAlSi_3O_8 , referred to as K-feldspar. It undergoes the order–disorder phase transition representing the species $2/m - \epsilon s - \bar{1}$ (Putnis and Salje, 1994). The equilibrium transition temperature is about 500 K and the phase transformation is governed by ordering of the Si and Al ions, the process which is rather slow so that direct experiments on the ordering transition are not possible. The intermediate states of Si and Al order are represented by “tweed microstructures,” meaning that the sample is split into small regions, tweeds. They are observable by polarized microscopy and their boundaries are of two prevailing mutually perpendicular orientations. On average, the crystal symmetry remains monoclinic but within tweeds some degree of ordering is already reached, with the corresponding lowering of symmetry. To interpret these observations, two possibilities can be considered. First, the observed tweed structure can be recognized as a stable periodically modulated strain pattern which minimizes the free energy (the latter of course includes the strain gradient terms). Second, the tweeds could represent a metastable pattern allowing for local Si/Al ordering without the need for a macroscopic change of symmetry. In the vocabulary

of the present book, the first possibility corresponds to spatial modulation of the strain but not of the ordering while the second one to a dense classical ferroelastic domain pattern. According to Putnis and Salje, the available phonon spectra point to the first interpretation.

In some minerals undergoing a phase transition, the latter is “smeared out” and it is difficult to define exactly the transition temperature. Then in many interpretations it is accepted that the tweed pattern is formed already in the parent phase and that it represents long-lived fluctuations of the order parameter (Salje, 1990). Microregions of low symmetry embedded in the higher symmetry crystal lattice are sometimes referred to as “embryos.” Their occurrence in the higher symmetry phase of a material which undergoes a structural phase transition is sometimes defined as the “precursor regime.”

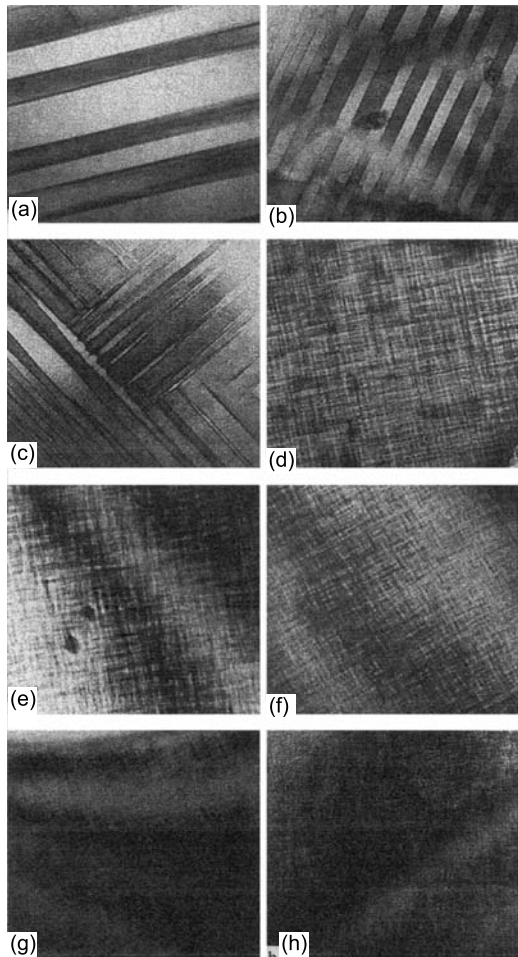


Fig. 5.4.29 Domain patterns in $\text{YBa}_2\text{Cu}_3\text{O}_7$ doped with Co. Concentrations of Co are (a) 0, (b) 1, (c) 2, (d) 2.5, (e) 2.8, (f) 3, (g) 5, (h) 7%. For concentrations higher than 2.4% the material is expected to be in the parent phase. Patterns shown in images (d)–(f) represent the so-called tweed patterns. Reprinted with permission from Schmahl et al. (1989). Copyright (1989), Taylor and Francis

As discussed in detail by Salje (1990), it is the possibility of this kind of long-lived fluctuations that may explain the formation of tweed patterns such as observed optically in the mineral cordierite. Even in the temperature region where there is still no spontaneous strain present and the crystal must be considered in the parent phase, the diffraction patterns in some materials have shown diffuse signals which can be indexed in the low-temperature phase and interpreted as the tweed structure. At the same time, the superlattice reflections are not necessarily compatible with the lattice of either phase.

The problem of tweed patterns has been theoretically addressed by Bratkovsky et al. (1994). They indicate that the anisotropy of observed patterns can be linked to the anisotropy of order parameter fluctuations in the parent phase. Such anisotropic fluctuation patterns were computer simulated.

To summarize, some approaches treat the observed tweed patterns as small-size quasiperiodic ferroelastic domain structure while the others assume a coexistence of regions with the parent and ferroelastic symmetry.

Shortly after the discovery of high-temperature superconductivity, a considerable attention was paid to domains and tweed microstructures in crystals of superconducting $\text{YBa}_2\text{Cu}_3\text{O}_{7-x}$ ($x \cong 0.1$). It represents the species $4/mmm-\epsilon_s-mmm$. The transition can be driven by either temperature ($T_C \cong 700^\circ\text{C}$ in the pure material) or by doping with Co (the critical concentration is about 2.4% at room temperature) (Schmahl et al., 1989). Figure 5.4.29 (a–h) shows electron micrographs by Schmahl et al. of domain patterns in $\text{YBa}_2(\text{Cu}_{1-y}\text{Co}_y)\text{O}_{7-x}$ at different Co concentrations, y . For $y < 2.4\%$ (Fig. 5.4.29a–c), we see classical ferroelastic domain patterns. At the concentration 2.4% of Co, we pass through the transition point; therefore Fig. 5.4.29d–h should correspond to tweed patterns in the parent phase. The microstructure whose period is obviously decreasing with increasing x corresponds to lattice modulation along two directions (110) and $(1\bar{1}0)$ in the parent phase. It appears that in this material the existence of tweeds has been proved beyond any doubt.

Chapter 6

Domain Walls at Rest

This chapter is devoted to the properties of domain walls and let us stress first that here we have in mind a *static* situation in a ferroic sample. Problems connected with domain walls which are not in static or quasistatic equilibrium will be dealt with separately in Chap. 8. An important aspect of walls has been already discussed in Chap. 2, namely their orientation from the point of view of electrical and mechanical compatibilities of neighboring domains. There we considered walls as infinitely thin two-dimensional objects. Now we focus on its internal structure and properties governed by this structure. In Chap. 4 we have pointed out that several domain-imaging methods provided information about the wall thickness; in Sect. 6.1 we wish to describe some of these observations in more detail. In this section, we will also present available experimental data on thickness and surface tension of domain walls.

To address the problem of crystal structure inside the domain wall, the simplest and most widely used approach is based on thermodynamic theories. As we have seen in Chap. 2, these theories of ferroic transitions predict that an ideal crystal in the ferroic phase represents just one of the domain states with spatially homogeneous value of order parameter. But thermodynamic theories can also be used to describe multidomain states when the order parameter is considered as continuous function of the spatial coordinates. In the simplest situation we prescribe boundary conditions in the two opposite parts of a sample as representing different domain states S_A and S_B , respectively, characterized by values η_{SA} and η_{SB} of the order parameter η . Because of the transition region between these states, which is the domain wall, the energy of the system is necessarily enhanced.¹ The thermodynamic approach can be used to look for the spatial distribution of the order parameter for which this increase of total energy is minimal. This distribution represents the structure of the domain wall. Historically, addressing the domain wall structure researches were interested in its type, especially in the case where the order parameter can be easily visualized. Thus, in proper ferroelectrics, the question raised

¹ This is not the case for the materials where the minimal energy of the crystal corresponds to a spatially modulated state. These materials are not considered in this book.

already in the early states of research was the following: Does the vector \mathbf{P}_S rotate in space when it has to change, within the domain wall, from say $+P_S$ to $-P_S$, which would constitute an electric analogy of the ferromagnetic Bloch wall? Or does it first diminish to zero and then increase in the opposite direction? Different answers may be obtained for different kinds of phase transitions, depending on the order parameter and crystal structure. The obtained spatial distribution of order parameter makes it possible to express the wall thickness and its excess energy in terms of coefficients of the free energy function. Considering a domain wall as a two-dimensional object, the excess energy is represented as surface energy density (or surface tension) σ_w measured in J/m^2 . This kind of theories, where continuous spatial variations of the order parameter are treated, we will call *macroscopic* (or continuous) theories. Such theories have been developed for several kinds of ferroics and we shall pursue this subject in some detail in Sect. 6.2.

The domain wall structure can also be addressed on the atomistic level. The first attempts in this direction have been performed in terms of very simplified discrete models. However, presently, supported with new numerical methods of quantum chemistry and the immense progress in informatics, quite advanced modeling of domain walls on atomistic level becomes possible. Section 6.3 will address this kind of models which we will call *microscopic* models.

Since, the presence of the wall increases the energy of the system, one may expect that the energetically favorable walls will be flat. This is true in an ideal (defect-free) crystal when the thermal fluctuations are neglected. However, in a real crystal at finite temperature, it is not a priori clear whether the flat wall configuration is energetically favorable. We devote Sect. 6.4 to this problem. In this section, we will overview the relevant theoretical results and experimental findings.

6.1 Thickness and Structure of Domain Walls: Methods and Data

Numerous experimental methods have been employed to obtain data on domain wall width. Some of them are identical with those used for observing domain patterns but others have been developed specifically to address the problem of wall thickness. Most of them are real observation methods but attempts have also been made to obtain information based on models related to the measurements of macroscopic properties of the sample. We shall now briefly describe several of the methods which have been used. Attention will also be paid to the methods which provide some information on the internal wall structures.

The domain wall thickness, in simple terms, is conceived as the width of the region where significant departures of the order parameter from its values deep inside the two domains, η_{SA} and η_{SB} , occur. There are two obvious difficulties connected with this definition. First, how large these departures have to be in

order that the corresponding distorted region still belongs to the domain wall. Second, a particular method may enable one to observe some properties coupled to $\eta(x)$, not the order parameter itself; the changes of these properties may extend over regions having a different width. What is included in this chapter are data and methods concerning domain walls at rest. As an exception, we also include the paragraph on Raman scattering, a method that by now has been used only to estimate the thickness of a moving domain wall.

In Table 6.1.1 some of the available data are collected on domain wall thickness in different ferroic materials.

6.1.1 *Direct Optical Observations*

As we have already pointed out, in ferroelastics, domain patterns are customarily observed in a polarizing microscope and this is usually the first thing an experimentalist does with a transparent crystal. Hundreds of photographs have been published. Alternatively, also isolated domain walls themselves can often be observed. As an example we refer to observations of single crystals of gadolinium molybdate (abbr. GMO) (Shepherd and Barkley, 1972) performed with a high-quality plate-like specimen of GMO cut perpendicular to the ferroelectric c -axis and well polished. By applying a properly oriented stress and/or electric field it is relatively easy to prepare a sample containing just two domains separated by one of the permissible (100) or (010) walls. Sections of the two indicatrices are apparent from Fig. 6.1.1. Viewing along the c -axis in convergent white light whose polarization plane is aligned parallel to the wall, the wall appears as a well-defined bright or dark line, depending on the orientation of the analyzer. With monochromatic and collimated light the width of the wall in GMO appears larger, presumably due to a combination of refractive-diffractive effects. Such direct observations were used to give some crude estimations of the wall thickness, being interpreted as the maximum width of the transition region for which the lattice distortion produces birefringence different from that in the bulk of the domains. Based on such observations, Shepherd and Barkley (1972) estimated the apparent thickness of the 180° wall in GMO to be $3 \mu\text{m}$; Little (1955), based on similar observations, quoted $0.4 \mu\text{m}$ as the thickness of the 90° domain wall in tetragonal barium titanate. These data, however, cannot be considered reliable. They can be influenced by effects like light deflection on domain walls which was investigated in detail by Tsukamoto et al. (1980, 1984) in GMO and other ferroelastics.

If the sample is thick, interference pattern in the region surrounding the wall can be observed. For a 1 cm thick GMO sample and in crossed nichols a large number of fringes are observed in the microscope on both sides of the wall when the incident beam is polarized parallel to the wall (Fig. 6.1.1). When its polarization plane makes an angle $+45^\circ$ or -45° , fringes appear on the left-hand or right-hand side of the wall, respectively. This can be interpreted by the existence

Table 6.1.1 Data on thickness of domain walls in selected ferroites

Material	Type of wall ^a	Method	Wall thickness ^b	Remark	Ref.
TGS	180° nonferroelastic	Epitaxial crystallization of polymers evaluated by electron diffraction	0–1 μm	On the crystal surface	Wicker et al. (1989)
		Decoration with AgCl, TEM of replicas	120 Å	On the crystal surface	Hilzer et al. (1981)
		Atomic force microscopy	80 Å	At the crystal surface	Eng et al. (1997)
			600–800 Å		Ohgami et al. (1996)
		Data of thermal diffusivity	500 Å	Deduced from macroscopic data	Krajewski and Jaroszyk, (1973)
		Data of longitudinal acoustic wave propagation	400–1,500 Å	Deduced from macroscopic data	Tyliczynski (1977)
		X-ray topography	0.5 μm		Petroff (1969)
			0.75 μm		Petroff (1969)
			5 μm		Parpia (1982a)
			1 μm		Takagi and Suzuki (1994), Suzuki and Takagi (1971)
NaNO ₂	180° nonferroelastic	X-ray topography			
		EM of replica films	0.3–1 μm	On the crystal surface	Suzuki and Takagi (1971)

Table 6.1.1 (continued)

Material	Type of wall ^a	Method	Wall thickness ^b	Remark	Ref.
Pb ₅ Ge ₃ O ₁₁	180° nonferroelastic	Neutron scattering	20–30 Å	For all temperatures below $T_c \approx 450$ K	Cowley et al. (1976)
LiTaO ₃	180° nonferroelastic	SNOM	0.2–0.6 μm	On the crystal surface	Yang et al. (1997)
		HREM, resolution 2.7 Å	Virtually zero	Zero thickness is evidenced by images as well as by structural models together with computer modeling	Peng and Bursill (1982)
BaTiO ₃	180° nonferroelastic	Observation in polarized light along a TEM	Optic axes are rotated by 1° in a region 1 μm thick ≤ 50 Å	Walls visible only during switching and a short time afterward	Nakamura et al. (1963)
	180° inclined to c -axis	X-ray topography	2–3 μm	Samples thinned down 1,000 Å; no surface layer found	Tanaka and Honjo (1964)
	90° ferroelastic	TEM	72–116 Å	Depending on crystal growth technique	Dennis and Bradt (1974)
		TEM	≤ 200 Å	Samples thinned down up to 1,000 Å	Tanaka and Honjo (1964)
		TEM	< 100 Å	Thinned-down sample	Blank and Amelinckx (1963)
		TEM	≤ 100 Å when $E = 35$ kV/ cm is applied	Sample thinned down to 1000–3,000 Å	Fuchs and Liesk (1964)
		Electron holography	10–50 Å	Sample thinned down for TEM operation at 200 kV	Zhang et al. (1993), (1994), (1992)
		TEM	50 ± 10 Å	Sample thinned down to 500–2,000 Å	Yakunin et al. (1972)

Table 6.1.1 (continued)

Material	Type of wall ^a	Method	Wall thickness ^b	Remark	Ref.
PbTiO ₃	90° ferroelastic	HRTEM	10 ± 3 Å	Energy 50 m J/m ² ; a/c, wall in (001) films	Stemmer et al. (1995)
Ba _{0.82} Pb _{0.18} TiO ₃	90° ferroelastic	HRTEM	Virtually zero	a/c wall in (001) films	Foeth et al. (1999)
			8 ± 3 Å ^c	sample thinned down to 100 Å	Foeth et al. (2007)
			11 ± 7 Å ^c	Samples thicker than 300 Å	Dennis and Bradt (1974)
			10–50 Å ^c	From T _{TR} –500 K to T _{TR}	Peng Ju Lin and Bursill (1983); Bursill and Peng (1992)
KNbO ₃	60° or 120° ferroelastic (110)-type walls	HRTEM	90 Å increasing to 150 Å	For T increasing from –190° to +30°C	Peng Ju Lin and Bursill (1983); Bursill and Peng (1992)
			Ionic displacements within 15 Å, changes in electron density within 50 Å	Operation at 200 kV; walls claimed to carry bound charge connected with the observed diffused electronic charge	Kanzig and Sommerhalder (1953)
KH ₂ PO ₄	180° ferroelastic	Indirect conclusion based on behavior of small particles	A few lattice constants a ₀		Andrews and Cowley (1986)
			4a ₀ well below		Bruce (1981)
			T _{TR} , 10a ₀ at T _{TR}		Bhalla and Cross (1981)
			2a ₀ , 120 K below T _{TR}		Flippen (1975)
KD ₂ PO ₄	180° ferroelastic	Neutron scattering	5 μm		Suzuki, (1972)
			8 μm		Shepherd and Barkley (1972)
Gd ₂ (MoO ₄) ₃	180° ferroelastic	Surface decoration	< 1 μm		
			Polarized microscopy		

Table 6.1.1 (continued)

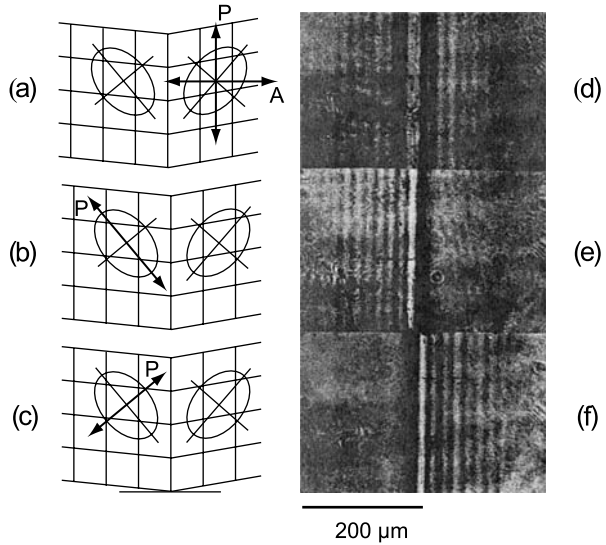
Material	Type of wall ^a	Method	Wall thickness ^b	Remark	Ref.
		Raman scattering	> 0.8 μm		Shepherd and Barkley (1972)
		Light diffraction	1.3 μm		Suzuki, (1972)
		TEM	10 μm		Esayan et al. (1974)
		TEM	$\leq 100 \text{ \AA}$	Thinned samples covered with a carbon film to avoid charging	Yamamoto et al. (1977a)
	antiphase	TEM	30–70 \AA		Yamamoto et al. (1977b)
SC(NH ₂) ₂	180° nonferroelastic	X-ray topography	1 μm	At $T = 149 \text{ K}$	Aoyama et al. (1992)
Ba ₂ NaNb ₅ O ₁₅	180° nonferroelastic	HRTEM	Virtually zero		Bursill and Peng (1992)
Pb ₃ (PO ₄) ₂	Ferroelastic	X-ray diffraction	70 \AA		Wruck et al. (1994)
YBa ₂ Cu ₃ O ₇	Ferroelastic	X-ray diffraction	7 \AA		Salje (1995); Salje and Chrosch (1996)
LaAlO ₃	Ferroelastic	X-ray diffraction	20 \AA increasing to 250 \AA	For T increasing from 295 to 900 K	Chrosch and Salje (1999)

^a The angle is that between polarization vectors of a ferroelectric material

^b The exact meaning of the measured thickness depends on the model used to evaluate data. For instance in Petroff (1969) the observed images were attributed to strain field around the wall; the wall thickness was evaluated as the width of departure from Bragg's law in reflections 011, 140, 002, and 102. This interpretation was challenged, e.g., in Takahashi and Takagi (1978) the contrast is explained by the dynamical theory of X-ray diffraction

^c These value are corrected by a factor of 2 to make allowance for the non-standard definition of the wall thickness adopted in Foeth et al. (1999a,b, 2007) Unless otherwise specified, measurements were performed at room temperature

Fig. 6.1.1 Light intensity distribution near an isolated domain wall in GMO (d)–(f) and the corresponding orientations of nichols (marked with A) and of polarizer (marked with P) with respect to crystal axes (a)–(c). Light propagates along the c -axis



of a region near the wall where the indicatrix is perturbed. The beam propagating in this region is deviated toward the higher refractive index region. It interferes with non-deviated beams which cross the sample in the non-perturbed region and gives rise to fringes parallel to the domain wall.

When properly analyzed, interference patterns could be in principle used for estimating the wall thickness or, more exactly, thickness of the region in which the refractive index is perturbed. The problem was discussed theoretically by Laikhtman and Petrov (1977b). Analyses of the angular intensity distribution of light diffracted at a domain wall were performed by Suzuki and Takagi (1971, 1972) and by Esayan et al. (1974).

6.1.2 X-Ray and Neutron Scattering

Neutron and X-ray scattering due to the presence of domain walls has been analyzed theoretically by Bruce (1981) for both ferroelastic and nonferroelastic domain walls. A cube-like sample of N^3 unit cells is considered, consisting of two domains separated by a wall perpendicular to the y -axis. It has been shown that if the domain wall were of zero thickness the scattered neutrons would form lines in reciprocal space, extending from the Bragg points perpendicular to the plane of the wall. The scattered neutrons are expected to form a set of sharply peaked ridges in this direction. If the domain pair is ferroelastic, each Bragg point within these ridges will split into two separate components originating from the two domains. The essential part of Bruce's analysis concerns the model

of a ferroelastic domain wall with finite thickness t_w . The wall perpendicular to the y -axis is modeled by a layer $n = t_w/a$ unit cells thick, which has the unperturbed structure of the paraelectric phase, where a is the corresponding lattice constant of the material. In this case, the shape of the intensity of scattered neutrons as a function of the transferred wave vector has been shown to consist of a broad wing on either side of the Bragg peak as before; in addition, now the wing is modulated by an oscillatory term. These oscillations of scattered intensity have two sources: cells in the wall itself, plus the interference effect between the contributions from the two domains. The first effect is spurious, connected with the “sharpness” of the wall model used here while the second effect is real. However, the intensity scattered by one single wall is expected to be proportional to N^2 and would be masked by other processes like Bragg scattering, thermal diffuse scattering, and incoherent scattering which are proportional to N^3 . Should the wall effect be observable, a large number of walls must be present in the scattering volume. For typical parameters of KDP crystals, the wall scattered intensity has been estimated to be a factor of 10^5 weaker than the Bragg scattering.

The neutron scattering experiment (Bruce, 1981) was performed using a triple-axis neutron spectrometer with a single crystal of KD_2PO_4 at a temperature 100 K (the transition temperature is 222 K). Comparison of the observed intensities of scattered neutrons with the results of modeling in terms of the above approach showed that the maximum allowed domain wall width in this crystal is 4 unit cells; the best fit is obtained for $n = 2$.

By means of a two-axis X-ray diffractometer and $\text{CuK}\alpha_1$ radiation, Andrews and Cowley (1986) investigated scattering of X-rays from crystals of KH_2PO_4 and KD_2PO_4 . The setup made it possible to investigate scattering as a function of temperature. A strongly temperature-dependent scattering intensity was found above the transition points and attributed to critical fluctuations. In the ferroelectric phase, the scattering is expected due to the presence of the domain walls with perturbed structures. The scattered intensity was theoretically analyzed for a more realistic model than the “sharp” model used above, namely, the lattice distortions u within a wall perpendicular to the y -axis are taken as being described by the formula resulting from macroscopic theories of walls in ferroics with the continuous transition

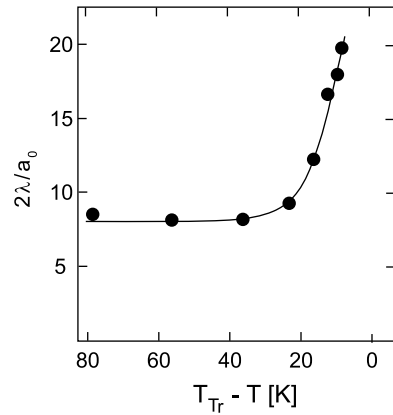
$$u(y) = u_0 \tanh(y/\lambda), \quad (6.1.1)$$

and it is assumed that displacements of all atoms are governed by this relation. The scattering intensity distribution in k_y direction near the Bragg points has been evaluated as

$$I(k_y) = \frac{A\lambda^2}{\sinh^2(\pi\lambda k_y/2)}, \quad (6.1.2)$$

where A is the coefficient proportional to the number of domain walls and u_0^2 . In order to maximize this number, crystals of KDP and DKDP were cooled in zero field. Scattering from walls consisted of streaks extending from the Bragg reflections along the [100] and [010] directions in agreement with the orientations of permissible domain walls. No differences in shape were observed of the scattering around different Bragg points in the $(h0l)$ plane and this gives evidence that the pattern of displacements remains reasonably constant through the domain wall. The scattering intensity could be well fitted to Eq. (6.1.2) over three orders of intensity. The domain wall width 2λ in units of the lattice constant resulting from these data is shown in Fig. 6.1.2 as a function of temperature.

Fig. 6.1.2 Temperature dependence of the domain wall thickness in KH_2PO_4 as deduced from X-ray scattering data (Andrews and Cowley, 1986). The wall thickness, 2λ , normalized to the lattice constant $a_0 \cong 7.4 \text{ \AA}$ is plotted. Data above $T = T_C - 2 \text{ K}$ could not be evaluated because of the background caused by scattering due to fluctuations



Chrosch and Salje (1994) and Salje and Chrosch (1996) used high-resolution X-ray diffractometry to investigate the wall thickness in single crystals of high- T_C superconductor $\text{YBa}_2\text{Cu}_3\text{O}_{7-x}$. These crystals represent ferroelastic species $4/mmm\text{-}es\text{-}mmm$. Using $\text{CuK}\alpha_1$ radiation, suitable Bragg peaks like (029) and (209) were chosen to register rocking curves, i.e., diffraction intensity in dependence on the angle of incidence of the X-ray beam. The diffraction pattern was analyzed assuming again that the spontaneous strain profile corresponds to Eq. (6.1.1). Obtained data led to the conclusion that at room temperature the domain wall is $7 \pm 2 \text{ \AA}$ thick which is the order of just one lattice constant. It should be stressed that these data also indicated a very high wall density, that is, a small inter-wall distance of about 230 \AA . Thus the ratio of the scattering intensity from the walls to the total scattering intensity has been found very high compared to that in other ferroelastic or ferroelectric materials.

X-ray diffraction has also been used to investigate wall thickness t_w in ferroelastically twinned LaAlO_3 (Chrosch and Salje, 1999). In the interval of 300–900 K, the wall thickness has been found to change in the range 2–25 nm,

following the law $t_w \propto (T_C - T)^{-1}$, which, however, is hard to explain in terms of the continuous theory (see Sect.6.2).

6.1.3 X-Ray Topography

Using X-ray topography, considerable effort was devoted to observations of domain walls and to the analysis of domain wall contrast with the aim to obtain data on domain wall thicknesses and structures. Klapper (1987) distinguishes two mechanisms which make the wall appear on an X-ray topograph: *kinematical contrast* due to lattice strain within the wall, and *dynamical contrast* due to scattering caused by the fact that the dynamical X-ray wave fields are out of phase in the two domains and a phase shift occurs at the wall (interbranch scattering). In this case a fringe pattern may be observed. The effect is connected with the fault vector describing the displacement of the two parallel domain lattices and can be described as a consequence of the phase shift of the structure factor.

Detailed studies of domain wall contrast for 180° walls in TGS have been performed by a number of authors (Petroff, 1969; Takahashi and Takagi, 1978a,b; Parpia, 1982a,b) with appreciable difference in the results and interpretation. The majority of authors, however, share the opinion that wall images can be interpreted as being due to the kinematical contrast. The evaluation of spatial distribution of strain in the domain wall indicated that the wall thickness in this material is rather large, of the order of a micrometer. The X-ray topography estimates for the width of 180° domain walls in tetragonal BaTiO_3 have also yielded values in the micron range (Kawata et al., 1981), the values that are orders of magnitude different from those obtained by other methods (see Table 6.1.1).

One should mention that X-ray topography estimates for the wall width are quite indirect. Suzuki and Takagi (1971) pointed out that even the sharpest observed width D of a wall image does not give direct information on the actual wall thickness d , because the topographic image is spread out by the diffraction effect and angular divergence of the beam. To give an idea of the role of different effect in the formation of the wall image, we will give, without derivation, the relation used by Suzuki and Takagi in their wall width estimates for NaNO_2 :

$$D = d + \lambda L/d + \omega L - \delta, \quad (6.1.3)$$

where λ is wavelength of the X-ray beam with angular divergence ω , L is the distance between the crystal and the photographic plate, and δ is the distributed range of developed silver nuclei along the track of the X-ray photon in the emulsion. Under the experimental conditions chosen for the study of NaNO_2 these quantities were $\lambda = 1.54 \text{ \AA}$, $\delta \cong 0.5 \text{ \mu m}$, $L = 0.7 \text{ cm}$, and $\omega = 1.6 \times 10^{-4} \text{ rad}$

which give $D = d + 1/d + 0.1 \mu\text{m}$. The value of D observed on the topographs of this material was $2\text{--}3 \mu\text{m}$, which limits the allowed range for the wall thickness d to $0.35 \mu\text{m} \leq d \leq 2.7 \mu\text{m}$.

A detailed analysis of the topographic contrast was also performed for nonferroelastic walls in NaNO_2 (Suzuki and Takagi, 1971, 1972; Takagi and Suzuki, 1994) and thiourea (Aoyama et al., 1992); results obtained for wall thicknesses are included in Table 6.1.1.

As for the interpretation of fringe patterns which are sometimes observed, different opinions have been expressed but it appears that conclusions about mutual shift of domain lattices along the wall by a fraction of unit cell parameter in crystals like TGS or LiNH_4SO_4 have to be taken with caution. On the other hand, a detailed analysis of sectional topographs of $\text{GdDy}(\text{MoO}_4)_3$ crystals containing antiphase domain walls led to the conclusion (Capelle et al., 1982) that, in addition to the expected translation of crystalline lattices of the domains neighboring such a wall, a small additional translation takes place. This is in qualitative agreement with the evaluation of electron microscopic images (Yamamoto et al., 1977a,b).

6.1.4 Raman Scattering

As evident from Table 6.1.1, one additional method which led to a surprisingly large value of the wall thickness is Raman scattering. Such a value has been obtained by Shepherd and Barkley (1972). In their setup, a GMO crystal containing just one domain wall was provided with electrodes; thus an ac square-wave field ($\omega = 400 \text{ Hz}$) can be applied along the c -axis so that the wall oscillates over a distance of 0.4 mm . An Ar-laser beam parallel to the domain wall was focused in the center of the region traversed by it and the light scattered at 90° is detected. Polarizations are chosen such that only phonons of A_1 symmetry propagating along the (001) plane contribute to the signal. Three scattering experiments recording phonon spectra were performed: (a) in both paraelectric and ferroelectric phases, without the wall; (b) with the moving wall, detecting spectra at the frequency ω in a phase which can be adjusted; and (c) with the moving wall, detecting spectra at the frequency 2ω . Due to the fact that the laser beam is focused exactly in the middle of the region where the wall travels, experiment (b) gives information on the difference between the domains whereas experiment (c) makes it possible to see the difference between scattering from the wall and that from the homogeneous orthorhombic phase. Three peaks were observed exactly where the differences between scattering of tetragonal and orthorhombic phases were seen in experiment (a).

The interpretation of observed data was based on the assumption that the wall structure has a tetragonal component corresponding to the paraelectric phase. The ratio of the signals at 820 cm^{-1} in experiments (a) and (c) gives information on the thickness of this tetragonal part of the wall. However, the time must be known for which the wall is exposed to the laser beam; this was

estimated by assuming a constant velocity during the wall motion. The obtained data (Sheperd and Barkley, 1972) led to the conclusion that the wall thickness (or rather the thickness of the tetragonally distorted region) is $0.8 \mu\text{m} \pm 10\%$.

It just appears that all optical data point to a very thick domain wall in GMO. This contrasts strongly with data obtained by transmission electron microscopy (cf. Table 6.1.1). In view of this controversy it might be worthwhile to perform a new detailed analysis of light diffraction data. In the Raman scattering experiment one might suspect that the assumption of the tetragonal character of the wall is too simplistic.

6.1.5 Electron Holography

Generally, holographic methods permit that both amplitude and phase distribution of a wave front are recorded in terms of intensity only. A transmission electron microscope can be used to perform electron holography so that changes in both amplitude and phase of the transmitted wave front are made visible. In particular, if electrons are not scattered so that the amplitude of the transmitted wave is not changed, the alteration of the phase of the wave front can be visualized, with a high resolution. This change can be brought about by slight modifications of the crystalline structure through which the wave propagates as well as by electric fields which may be present.

Zhang et al. (1992) utilized this idea to produce a hologram of a 90° domain wall in tetragonal BaTiO_3 . The incident electron beam is split so that one half travels outside the sample and the other half passes through it parallel to the domain wall. They interfere and produce a hologram (Fig. 6.1.3a). The

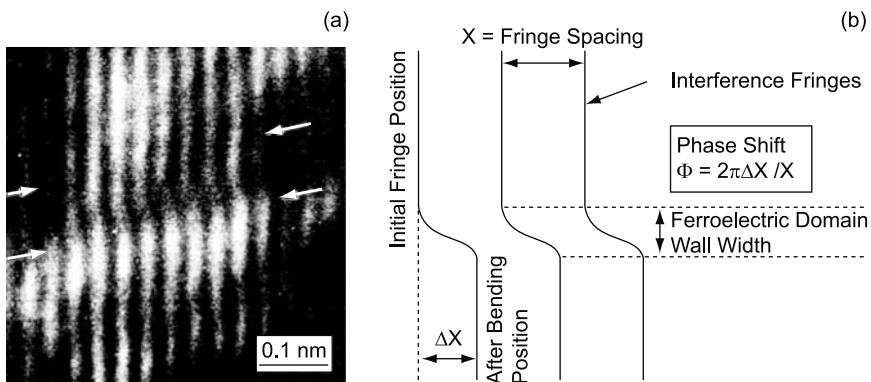
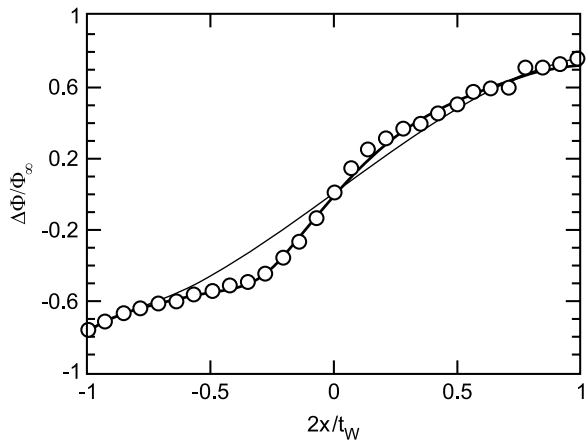


Fig. 6.1.3 (a) Electron hologram taken over an area of a 90° domain wall in BaTiO_3 . The fringe spacing is 3.6 \AA ; pairs of arrows indicate the “edges” of the wall. (b) Schematic representation of the fringe bending and explanation of the phase shift of the electron wave. Reprinted with permission from Zhang et al. (1992). Copyright (1992), American Institute of Physics

interference fringes are straight on both sides of the wall but mutually shifted; this shift is seen as bending of fringes within a stripe representing the domain wall. The width of the stripe with bent fringes, shown in Fig. 6.1.3a with arrows, is related directly to the domain wall thickness. The observed interference pattern is also schematically shown in Fig. 6.1.3b. The quantitative analysis of the interference pattern is carried out in terms of the phase change of the electron wave which travels through the sample (Zhang et al., 1992, 1993; Cao and Randall, 1993). The two neighboring fringes correspond to the phase shift of 2π . Thus, the relative fringe bending can be directly translated into the phase change caused by the wall, $\Delta\Phi$, as explained in Fig. 6.1.3b. It has been suggested by Cao and Randall (1993) that this change is mainly due to depolarizing field produced by bound charges on the sample surface. If the latter were fully compensated by free charges, the phase change would tend to zero and no potential contrast could be formed. Assuming that the compensation is only partial, leading to a proportional reduction of the net polarization, the phase profile of the wall can be found proportional to that of the spontaneous polarization, $P_S(x)$. According to Cao and Randall, an additional strain-related contribution to the phase change, which is proportional to $P_S^2(x)$, can also be incorporated into the model. Figure 6.1.4 (Cao and Randall, 1993) shows the experimental data of Zhang et al. (1992) together with fits which were calculated without and with the correction for strain, assuming the simplest tanh-type polarization profile in the wall.

Fig. 6.1.4 The phase shift of the electron wave, $\Delta\Phi(x)$, (normalized to Φ_∞ , the half of total phase shift across the wall) corresponding to the image shown in Fig. 6.1.3a (circles). *Thin line* is a fit to $\tanh(z)$ function. *Thick line* is a fit where a strain-related contribution, which is proportional to $\tanh^2(z)$, is also accounted for. After Cao and Randall (1993)



The detailed interpretation of the phase profile may be subject to further modifications (Ravikumar et al., 1997). For instance, the interpretation of the interference pattern could be further complicated when strong dynamic diffraction occurs: Pronounced electron channeling conditions may lead to a strong excitation for some of the diffracted beams which then act as independent

object waves and produce multiple interference regions. A 90° domain wall in PbTiO_3 was visualized under such conditions (Ravikumar et al., 1997). Thus, as with any other method, the data of wall thickness by means of electron holography have to be considered with caution. In addition, one has to keep in mind the extreme requirements on the sample thickness when TEM is used. Under such conditions domain walls may acquire profiles which differ from those in bulk samples.

6.1.6 Transmission Electron Microscopy

As was already mentioned in Sect. 4.8, transmission electron microscopy (TEM) in its different modifications has been successfully used for investigation of domain wall in ferroics.

The weak-beam dark-field imaging (two-beam diffraction conditions) makes a very important tool of domain imaging. A typical image obtained using this technique is shown in Fig. 4.8.6. This technique has been extensively used starting from the first electron microscopy studies of domain walls in ferroelectrics, mostly focusing on BaTiO_3 and PbTiO_3 single crystals (Blank and Amelinckx, 1963; Tanaka and Honjo, 1964; Bradt and Ansell, 1967; Shakmanov and Spivak, 1968; Yakunin et al., 1972; Hu et al., 1986). The main problems that were addressed by the first TEM observations of the domain walls in barium titanate were their type, structure, and thickness. Two types of domain walls (90° and 180°) were readily identified. A better stability of the 90° walls during the TEM observations was noticed (Bradt and Ansell, 1969). The domain wall thickness in BaTiO_3 was first evaluated as about 20 nm by Tanaka and Honjo (1964) and later as 8 nm in $(\text{Ba,Pb})\text{TiO}_3$ by Dennis and Bradt (1974). The direct TEM observations of the temperature dependence of the domain wall thickness were performed for the first time in $(\text{Ba, Pb})\text{TiO}_3$ from -190 to 30°C (Dennis and Bradt, 1974). The temperature dependence of the 90° domain wall thickness of PbTiO_3 has also been evaluated from the analysis of the thickness fringes in weak-beam dark-field images (Foeth et al., 1999a,b; 2007). Figure 6.1.5 demonstrates the temperature evolution of such images. The temperature dependence of the wall thickness calculated from these images is shown in Fig. 6.1.6. Comparing the values on the wall thickness in PbTiO_3 estimated in the mentioned papers of Foeth et al. with other data, one should divide these values by a factor of two to account for the nonstandard definition of the wall thickness adopted in these papers.

As mentioned above in Sect. 4.8.2 high-resolution transmission electron microscopy (HRTEM) has been used for observations of domain walls in various ferroics. Images and other information on domain walls (often the wall thickness) have been reported for many materials. For example, such data are available for KNbO_3 (Bursill et al., 1983; Bursill and Peng, 1986), LiTaO_3 and $\text{Ba}_2\text{NaNb}_3\text{O}_{15}$ (Bursill and Peng, 1986), BaTiO_3

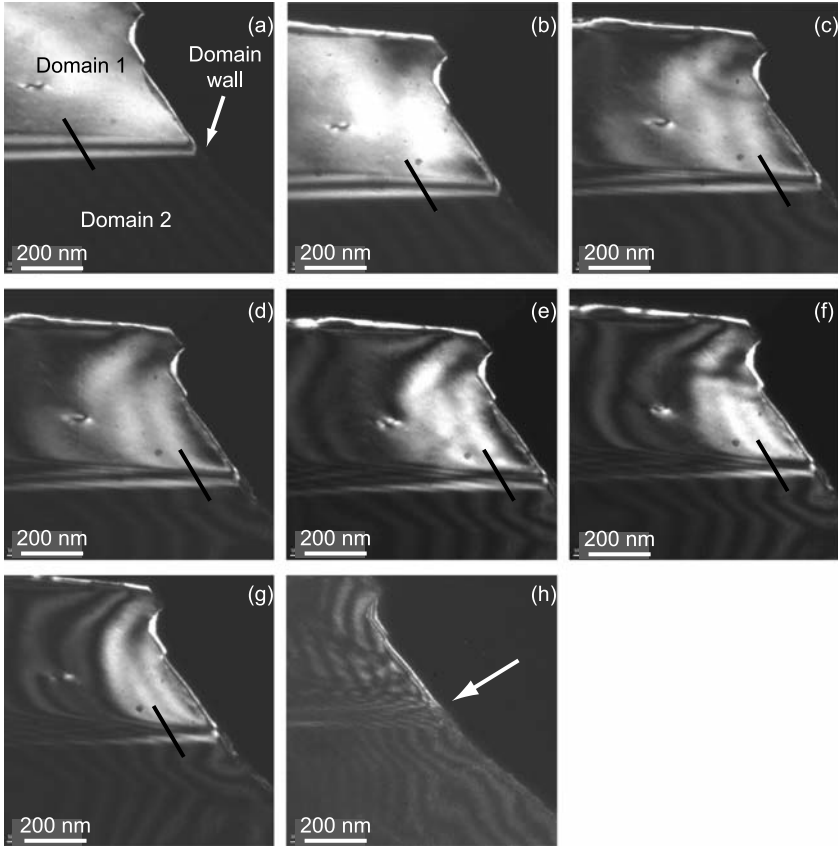


Fig. 6.1.5 Weak-beam dark-field images of 90° domain wall in PbTiO_3 taken at different temperatures. The temperature differences from the transition point T_{TR} are 332 K (a), 132 K (b), 37 K (c), 27 K (d), 12 K (e), 7 K (f), 2 K (g), and 0 K (h). T_{TR} is fixed by image (h). Along the bars shown in images (a)–(f), the analysis of the signal has been performed. Foeth et al. (2007)

(Shiojiri et al., 1992; Floquet et al., 1997; Bursill and Peng, 1986; Tsai et al., 1992), $\text{Pb}(\text{Zr}, \text{Ti})\text{O}_3$ (Tsai et al., 1992), PbTiO_3 (Stemmer, 1995; Foeth et al., 1999a,b), AgNbO_3 (Verwerft et al., 1989), and $\text{YBa}_2\text{Cu}_3\text{O}_{7-x}$ (Zhu and Suenaga, 1992). Apart from typical non-charged walls in well-insulating ferroelectrics, in quite conductive PbTiO_3 , the head-to-tail arrangement of the domains has been directly observable by HRTEM (Spycher et al., 1987). The domain wall thickness evaluated from HRTEM data is typically in good agreement with that obtained from dark and weak-beam dark-field TEM. An explicit comparison of this kind has been offered by Foeth et al. (1999a,b) for 90° domain walls in PbTiO_3 . Instructive results on the same system have been reported by Stemmer et al. (1995). In this study, the lattice displacement profiles

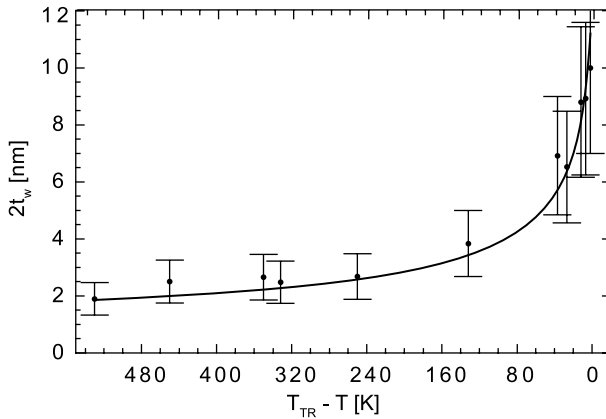


Fig. 6.1.6 Domain wall thickness evaluated from the analysis of the intensity distribution shown in Fig. 6.1.5 (dots) fitted to the result of continuous theory for the first-order phase transitions, Eq. (6.2.12) (curve). All thermodynamic parameters entering Eq. (6.2.13) have been taken from an independent source, only the correlation coefficient being used as the fitting parameter. Compared to the original here the y-axis scale is corrected by a factor of 2 to make allowance for the non-standard definition of the wall thickness adopted in papers by Foeth et al., (1999a,b; 2007)

for the walls of the same type, which were differently oriented with respect to the plane of the ferroelectric film, have been investigated (the so-called *a/a* and *c/a* walls). Figure 6.1.7 shows these profiles where an appreciable difference in the profile abruptness is seen. This clearly shows that the information on formally the same type of walls can be sensitive to the condition to which these are exposed. In the considered case, the difference may be related to mechanical anisotropy of the film deposited onto a substrate.

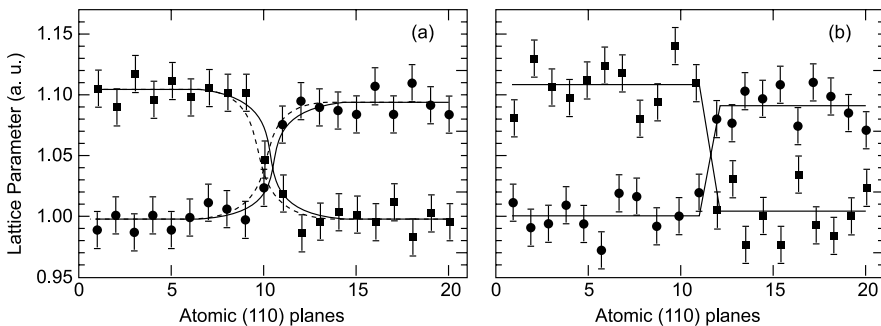


Fig. 6.1.7 Variation in lattice parameters *a* and *c* across 90° domain walls in PbTiO_3 obtained from HRTEM data: (a) *a/c* wall and (b) *a/a* wall. Data are plotted as a function of position in units of the (101) inter-plane distance. The solid line in (a) is a fit to $\tanh(z)$ function assuming that the wall is centered at a Pb–Ti–O plane; the broken line assumes a central O-only plane. It is seen that the *a/a* wall is appreciably narrower than the *c/a* wall. After Stemmer et al. (1995)

6.1.7 Surface Methods

In Chap. 4 we have addressed various surface-based methods of imaging of domains and domain walls. In this section we briefly discuss the application of these methods to getting information on the thickness and structure of domain walls in ferroics.

Some of these surface methods are based on surface decoration. The resolving power then depends on the decorating agent and on the observation method. An approach relying on optical observations with correspondingly low resolution was used for crystals of GMO (Bhalla and Cross, 1981). Films of uniform layer of GdF_3 were produced on the sample surface. When observed in reflected light, the underlying domain structure was clearly distinguished. This made it possible to estimate the maximum wall thickness as $1 \mu\text{m}$.

Much higher resolution can be reached when observations are made by electron microscopy. Again, the surface of a sample containing domains is decorated and the width of the transient region between two neighboring domains which are covered by decorating agents is measured. Hilczer et al. (1981, 1989) used AgCl as epitaxial decorating layers of thickness 8–20 nm, evaporated on cleaved polar surfaces of ferroelectric crystals. Then carbon replicas were made and observed in a transmission electron microscope. The width of the transition region between two domains decorated with different density or orientation of particles can be considered to be the maximum width of the domain wall. Figure 6.1.8 shows an example of a wall separating two decorated domains. Experiments performed with TGS crystals led to the value of 12 nm. Another material investigated by this method was NaNO_2 (Suzuki and Takagi, 1971). Domain contrast was achieved by evaporating silver particles and the resulting film was backed by evaporated carbon replica film. Domain walls were found to be of thickness ranging between 0.3 and $1 \mu\text{m}$.

A method which promises an extremely high resolution is the scanning force microscopy (SFM). As we have discussed in the preceding chapter, this

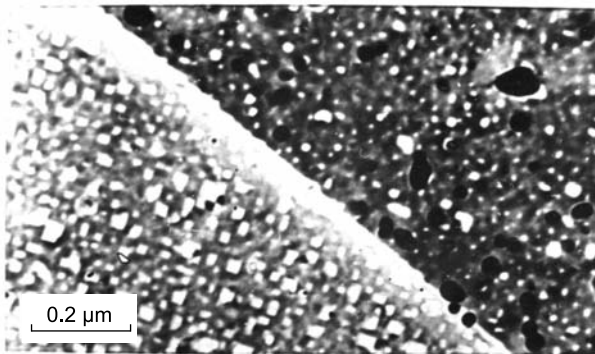


Fig. 6.1.8 TEM picture of a replica of the surface of a TGS sample with antiparallel domains decorated by AgCl layers of thickness about 2 nm. Reprinted with permission of Politechnika Wroclawska. After Hilczer et al. (1981)

technique can be used for imaging domains in ferroelectric and ferroelastic crystals provided that the sample has a correspondingly flat surface in the area where domain walls are located. Observations of domains in cleaved samples of TGS crystals made it possible to zoom in on domain boundaries (Eng et al., 1997). Scanning between two domains of opposite polarities led to the conclusion that the width of the 180° wall at the surface is below 80 \AA . This value was found in the friction mode and, interestingly enough, confirmed in the non-contact mode where the contrast originates from the electric field close above the sample surface. Similar experiments with the same material were performed by Ohgami et al. (1996), both in the contact and non-contact modes. The wall thickness estimated in this paper is $60\text{--}80 \text{ nm}$. Similarly as in the paper by Eng et al. (1997), it was concluded that along the wall there is a step in height, estimated to be $2\text{--}3 \text{ \AA}$ high. Such a step, if it always accompanied a domain wall in this material, would influence a number of phenomena connected with wall motion.

SFM techniques have been successfully applied to domain wall imaging in GASH by Lüthi et al. (1993b). Figure 6.1.9 demonstrates the image obtained in non-contact dynamic mode from a GASH crystal and the signal-intensity profiles for two cross-sections of this image. Here, domain walls with a thickness of $50\text{--}100 \text{ nm}$ are seen. This result is not affected by the instrumental lateral resolution of the method, which has been evaluated as 1 nm .

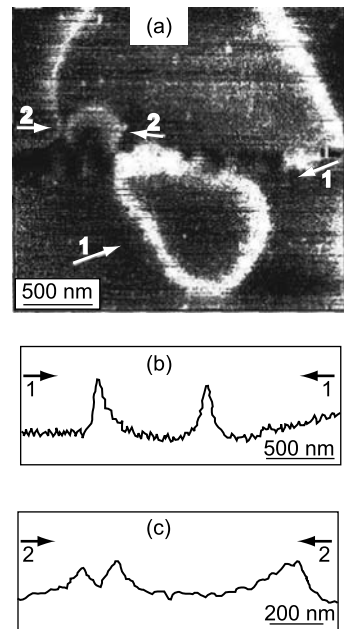
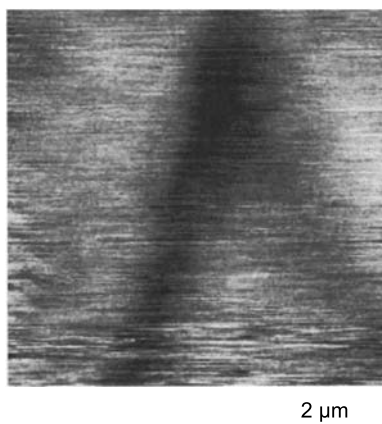


Fig. 6.1.9 SFM image obtained in non-contact dynamic mode from a GASH crystal (a) and the signal-intensity profiles for two cross-sections (shown with *arrows*) of this image (b) and (c). Domain walls with a thickness of $50\text{--}100 \text{ nm}$ are seen. The instrumental lateral resolution is 1 nm . After Lüthi et al. (1993b)

Concerning complications related to SMF investigations of domain walls, one can mention the problem with the identification of a domain wall with complete certainty. There may exist other linear artifacts on the crystal surface which in fact do not represent surface intersections of domain walls. Perhaps the best possibility will be to identify domains in a low-resolution mode, in which the wall may be reliably recognized by their characteristic shapes, and then successively zoom in on the domain wall. The alternative unmistakable method to identify a 180° domain wall is based on distinguishing the sign of electric charge on both sides of the wall (Ohgami et al., 1996). Another complication is that the cleavage process, for instance, in TGS, itself may produce a surface step at the domain wall (Suda et al., 1978b; Nakatani, 1979) and its width can be mistakenly considered the domain wall width.

Scanning near-field optical microscopy (SNOM), especially in its apertureless modification (s-SNOM), can exhibit resolution sufficient for investigation of the thickness and structure of not too thin domain walls. SNOM with aperture (a-SNOM) has been used for investigation of domain wall issues in LiTaO_3 (Yang et al., 1999, 1997). A wall vertex in this material imaged with a-SNOM is shown in Fig. 6.1.10, the reported resolution being 200 nm. Here the wall thickness is about 1,000 nm, which is orders of magnitude larger than the value documented with HRTEM (Peng and Bursill, 1982).

Fig. 6.1.10 A wall vertex of a triangular domain in LiTaO_3 imaged with SNOM with aperture of 60 nm; the reported resolution is 200 nm. Reprinted with permission from Yang et al. (1997). Copyright (1997), American Institute of Physics



Several other methods useful for observing domains on surfaces of samples, like laser scanning microscopy based on pyroelectric signal, offer only limited resolution and have not yet been proved suitable for domain wall studies.

6.1.8 Comments on Available Data

The summary of available data on domain wall thickness in different ferroelectric and ferroelastic materials as collected in Table 6.1.1 shows that even for the same material values obtained by different methods vary widely. Generally speaking, optical and X-ray topography methods have given much larger values than transmission electron microscopy or electron holography. To some extent this may be related to the fact that samples prepared for TEM have to be extremely thin so that boundary conditions for walls strongly differ from those for a bulk sample. One could contemplate that this may have a direct effect on the crystal lattice connecting neighboring domains. But large discrepancies exist even in data obtained by different surface methods applied to bulk samples. Here it appears that to obtain really reliable information, one cannot rely on a few scanning events but many data have to be statistically evaluated to avoid accidental artifacts. Also, the surface topographic profile may be seriously affected by the way the sample was prepared. But first of all, an unambiguous proof must be available that the object studied is really a domain wall.

It is evident that very few data are available on the temperature dependence of the wall thickness. Data obtained with scattering techniques and TEM gave evidence for a substantial increase of the wall thickness (e.g., in DKDP, PbTiO_3 , and LaAlO_3) when the transition temperatures are approached. On the other hand, data on $\text{Pb}_5\text{Ge}_3\text{O}_{11}$ (Cowley et al., 1976) based on neutron scattering indicate only a small increase.

6.2 Macroscopic Theories of Domain Walls

The treatment of phase transitions based on thermodynamic potentials as discussed in Chap. 2 referred to spatially homogeneous states: No quantity was considered that would depend on the coordinates. This approach is obviously inadequate when domains are present. Two generalizations are possible. The first one tends to explain the occurrence of a domain pattern as a whole. This has been discussed in some detail in Chap 5. In an alternative approach only one domain pair is considered and the aim of the theory is to describe the domain wall separating the two domains. This section deals with the latter case, treated in terms of thermodynamic approach where the order parameter is considered as a continuous function of the spatial coordinates in the system. For ferroelectrics, this kind of treatment was pioneered by Zhirnov (1958), Bulaevskii (1964), and Bulaevskii and Ginzburg (1964). The main points of thermodynamic theory of domain walls in ferroics can be discussed by taking into account only the energy related to the order parameter itself, not making explicit allowance for elastic effects. The latter can be of importance, as will be

discussed later. However, full treatment of domain wall structure can be reduced, at the price of certain assumptions, to a problem that deals only with the order parameter itself. This makes it reasonable to address the main issues of the theory in terms of the order parameter only. This will be done in the following section. In the subsequent section we will discuss the effect related to the order parameter/stress coupling. To conclude this section we will overview the application of the general theory to selected kinds of ferroics.

6.2.1 Order Parameter Profile in Domain Walls

6.2.1.1 Single-Component Order Parameter

Let us outline the basic features of the theory in terms of a single-component order parameter η . The ground states defined by thermodynamic theories treated in Sect. 2.3 are spatially uniform; therefore any domain wall as a transition region where the order parameter is necessarily nonhomogeneous increases the energy of the crystal. The lowest order term representing this increase is proportional to a bilinear term of components of the order parameter gradient. For the moment, for simplicity we keep only the $(\nabla\eta)^2$ term so that the free energy density in its simplest form now reads

$$\Phi(T, \eta) = \Phi_0 + \frac{1}{2}\alpha\eta^2 + \frac{1}{4}\beta\eta^4 + \frac{1}{2}\delta(\nabla\eta)^2, \quad (6.2.1)$$

with $\alpha = \alpha_0(T - T_0)$, $\delta > 0$, and $\beta > 0$; we have in mind the second-order transition. Solutions $\pm\eta_S$ for homogeneous domain states remain unaffected by the gradient term. The latter is sometimes referred to as the *correlation energy* (Smolenskii et al., 1984) and the coefficient δ as the *correlation coefficient*. Other names like gradient energy, gradient coefficient, or Ginzburg coefficient are also used. This energy plays an essential role when thermal fluctuations of the order parameter are investigated; since $\delta > 0$, this term tends to reduce such fluctuations. Within a domain wall between the two domain states the values of order parameter change from $+\eta_S$ to $-\eta_S$. We assume that the wall is planar and perpendicular to x . To find the solution $\eta(x)$ corresponding to minimum total energy of the sample we prescribe the boundary conditions: $\eta \rightarrow \eta_S$ for $x \rightarrow \infty$ and $\eta \rightarrow -\eta_S$ for $x \rightarrow -\infty$. The spatial distributions $\eta(x)$ should minimize the free energy of the sample

$$\Phi(T) = A \int_{-\infty}^{+\infty} \Phi[T, \eta(x)] dx, \quad (6.2.2)$$

where A is the cross-sectional area of the sample. The function $\eta(x)$ satisfies the requirement of minimum given by the Euler equation

$$\frac{d}{dx} \left(\frac{\partial \Phi}{\partial (\partial \eta / \partial x)} \right) - \frac{\partial \Phi}{\partial \eta} = 0, \quad (6.2.3)$$

which leads to a nonlinear differential equation of the second order

$$\delta \frac{d^2 \eta}{dx^2} = \alpha \eta + \beta \eta^3. \quad (6.2.4)$$

The solution to this equation satisfying the above boundary conditions reads (Zhirnov, 1958)

$$\eta(x) = \eta_S \tanh \left(\frac{x}{\sqrt{2\delta / -\alpha}} \right) \equiv \eta_S \tanh \left(\frac{x}{t_{th}} \right), \quad (6.2.5)$$

where

$$t_{th} = \sqrt{-2\delta / \alpha} \quad (6.2.6)$$

has the meaning of a spatial scale of the wall. The double of this value is customarily taken as the wall thickness

$$t_w = 2t_{th}. \quad (6.2.6a)$$

This type of the domain wall profile, shown in Fig. 6.2.1 (curve a), will be referred to as the tanh-type solution; “kink solution” is also a term often used. In the middle of the domain wall $\eta = 0$, which corresponds to the parent phase. Therefore we expect that within some central region the structure is close to that of the phase G . As we have seen in the previous section, some techniques for the measurements of domain wall thickness are based on modeling the wall by a layer whose structure is exactly that of the parent phase.

The quantity t_w expressed in terms of coefficients of the free energy can be ascribed a more general meaning (Smolenskii et al., 1984). It can be related to the *correlation radius* (correlation length) for the ordered phase, which is customarily defined as

$$r_c = t_w / 4 = \sqrt{\delta / (-2\alpha)} = \sqrt{\frac{\delta / 2\alpha_0}{T_0 - T}} \quad (6.2.7)$$

and represents a quantity characterizing the spatial changes of the order parameter in the ferroic phase. Its physical meaning can be illustrated by a simple

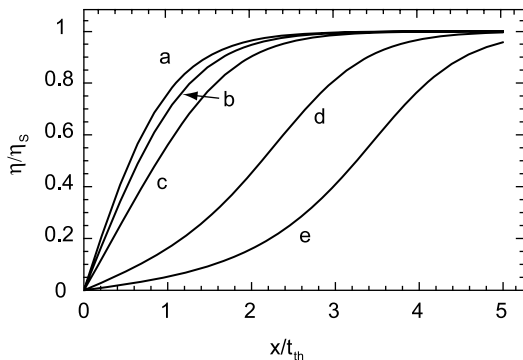


Fig. 6.2.1 Normalized profile of a half of a domain wall for different values of parameter A defined by Eq. (6.2.13): **(a)** $A = 0$, a material with the “pure” second-order phase transition, $\gamma = 0$; **(b)** $A = 1/2$, a material with the tricritical point, $\beta = 0$; **(c)** $A = 2$, a material with the first-order phase transition at $T = T_0$; **(d)** $A = 50$ and **(e)** $A = 500$ correspond to a material with the first-order phase transition at the temperatures very close to the transition, $(T_C - T)/(T_C - T_0) = 0.02$ and $(T_C - T)/(T_C - T_0) = 0.002$, respectively

model (Strukov and Levanyuk, 1998). Imagine that by some localized applied force the order parameter on the plane $x = x_0$ is kept at a value $\eta(x_0) = \eta_0$ which is close to η_S . Because of the correlation energy term, η cannot change discontinuously and therefore it gradually tends to its normal equilibrium value η_S . The calculation leads to the spatial dependence

$$\eta(x) = (\eta_0 - \eta_S) \exp(-|x - x_0|/r_c) + \eta_S. \quad (6.2.8)$$

This dependence is sometimes referred to as the Ornstein–Zernicke function for a one-dimensional case. It is obvious that the correlation length is closely connected with the spatial relaxation of the order parameter in the vicinity of a lattice defect. As such it plays an important role when discussing the interaction between domain walls and defects or between domain walls themselves. In addition, it determines the spatial scale of thermal fluctuations of the order parameter around its equilibrium value. In the parent phase, a one-dimensional decay of the order parameter can also be described by Eq. (6.2.8) where $\eta_S = 0$ and $r_c = [\delta/\alpha_0 (T - T_0)]^{1/2}$. This corresponds to introduction of the correlation length in the parent phase as $[\delta/\alpha_0 (T - T_0)]^{1/2}$.

The spatially dependent solution (6.2.5) necessarily increases the energy of the crystal compared to the energy of a single domain state. This extra energy can be ascribed to the domain wall and expressed as the surface energy density σ_w per unit wall area:

$$\sigma_w = \int_{-\infty}^{+\infty} [\Phi(\eta(x)) - \Phi(\eta_S(x))] dx. \quad (6.2.9)$$

From Eqs. (6.2.5) and (6.2.9) one readily finds

$$\sigma_w = \frac{2\sqrt{2}}{3} \frac{\delta^{1/2}}{\beta} |\alpha|^{3/2} = \frac{2\sqrt{2}}{3} \alpha_0^{3/2} \frac{\delta^{1/2}}{\beta} (T_0 - T)^{3/2} \quad (6.2.10a)$$

or alternatively

$$\sigma_w = \frac{2\sqrt{2}}{3} \eta_S^3 (\beta\delta)^{1/2}. \quad (6.2.10b)$$

It follows from the preceding formulae that as the temperature of a second-order transition is approached, the wall thickness t_{th} is expected to increase as $1/(T_0 - T)^{1/2}$ while its energy density decreases as $(T_0 - T)^{3/2}$. For the case of proper ferroelectric, it is also convenient to express σ_w in terms of the spontaneous polarization, lattice permittivity, thermodynamic coercive field (see Eq. (2.3.15)), and the wall thickness:

$$\sigma_w = \frac{P_S^2 t_w}{6 \chi} = \frac{\sqrt{3}}{2} P_S E_{crit} t_w. \quad (6.2.10c)$$

There is another important feature of domain walls that can be specified at this point. When writing the free energy (6.2.1) we have neglected the anisotropy of the gradient term. In reality it represents a sum of several terms proportional to $\frac{\partial \eta}{\partial x_i} \frac{\partial \eta}{\partial x_j}$. When taken into account, the anisotropy of the gradient term will obviously result in a dependence of the coefficient δ [in Eq. (6.2.4)] on the orientation of domain wall. In turn, via Eqs. (6.2.6) and (6.2.10b), it results in orientational dependence of wall thickness and energy density. Normalizing t_w , σ_w , and δ to their values for a certain orientation of the wall, t_{w0} , σ_{w0} , and δ_0 , one obtains

$$\frac{\sigma_w}{\sigma_{w0}} = \frac{t_w}{t_{w0}} = \sqrt{\frac{\delta}{\delta_0}}. \quad (6.2.10d)$$

This anisotropy of the wall energy can play a role in the wall orientation. In reality this role is of importance only for the walls whose orientation is not fixed by the elastic effects (W_∞ walls in terms of the classification introduced in Chap. 2). We will illustrate this point later by an example of walls in TGS crystals.

If the transition is of the first order, the simplest potential reads

$$\Phi(T, \eta) = \Phi_0 + \frac{1}{2} \alpha \eta^2 + \frac{1}{4} \beta \eta^4 + \frac{1}{6} \gamma \eta^6 + \frac{1}{2} \delta \left(\frac{d\eta}{dx} \right)^2, \quad (6.2.11)$$

with $\beta < 0$ and $\gamma > 0$. Instead of solution (6.2.5) the wall is now described by

$$\eta(x) = \eta_s \frac{\sinh(x/t_{th})}{\sqrt{A + \cosh^2(x/t_{th})}}, \quad (6.2.12)$$

where

$$t_{\text{th}} = \sqrt{\frac{2\delta}{\eta_S^2(\beta + 2\gamma\eta_S^2)}}, \quad A = \frac{\gamma}{2\gamma + (3\beta/2\eta_S^2)}. \quad (6.2.13)$$

Written this way Eqs. (6.2.12) and (6.2.13) are also valid for the case of $\beta \geq 0$, thus also covering the cases of the “pure” second-order phase transition ($\beta > 0$ and $\gamma = 0$) where $A = 0$ and the tricritical point ($\beta = 0$ and $\gamma > 0$) where $A = 1/2$. The profile given by Eq. (6.2.12) is not very different from the tanh shape unless the temperature is not too close to the transition temperature T_c where A is larger than or of the order of unity. Figure 6.2.1 (curves a–c) shows this profile for $A = 0$, $A = 1/2$, and $A = 2$; the latter value is reached at the temperature equal to the Curie–Weiss temperature (at $T = T_0$). At $T \rightarrow T_c$, A diverges according to the law

$$A \approx \frac{T_c - T_0}{T_c - T}. \quad (6.2.14)$$

Very close to the transition temperature (where $A \gg 1$) the wall profile depends strongly on temperature, as illustrated in Fig. 6.2.1 (curves d and e). Here the central part of the curve *e* can be interpreted as an onset of appearance of the parent phase in the wall center (Lajzerowicz, 1981). This actually means that the domain walls can serve as perfect seeds of the parent phase when passing T_c on heating. In the region where the low-temperature phase is metastable, i.e., at $T_c < T < T_0^*$ (cf. Eq. (2.3.19)), the domain wall between the two domain states in question does not exist. In this case, two domains with the opposite signs of the order parameter can be linked only via a finite-thickness layer of the parent phase. It is useful to note that the thickness parameter t_{th} given by Eqs. (6.2.6) and (6.2.13) can be written in a generic form

$$t_{\text{th}} = \sqrt{4\delta\chi} = 2r_c, \quad (6.2.15)$$

which is valid for either orders of the phase transition. Here χ is the permittivity with respect to the field conjugated to the order parameter and r_c is the correlation length.

6.2.1.2 Multi-component Order Parameter

Now we will highlight the features of domain walls separating domain states in ferroics with multi-component order parameter by using a simple example of a transition which is driven by a two-component order parameter (η_1, η_2). Let us consider a transition described by the free energy expansion which formally corresponds to that used in Chap. 2 for discussion of thermodynamics of improper ferroelectrics:

$$\begin{aligned} \Phi = \Phi_0 + \frac{1}{2}\alpha(\eta_1^2 + \eta_2^2) + \frac{1}{4}\beta_1(\eta_1^4 + \eta_2^4) + \frac{1}{2}\beta_2\eta_1^2\eta_2^2 \\ + \frac{1}{2}\delta \left[\left(\frac{\partial\eta_1}{\partial x} \right)^2 + \left(\frac{\partial\eta_2}{\partial x} \right)^2 \right], \end{aligned} \quad (6.2.16)$$

where $\alpha = \alpha_0(T - T_0)$, $\beta_2 > \beta_1 > 0$, and $\delta > 0$. As we have seen in Sect. 2.3.5, such a transition results in four domain states represented in Fig. 6.2.2: $(\eta_1 = \eta_S, \eta_2 = 0)$, $(\eta_1 = -\eta_S, \eta_2 = 0)$, $(\eta_1 = 0, \eta_2 = \eta_S)$, and $(\eta_1 = 0, \eta_2 = -\eta_S)$, where $\eta_S = (-\alpha/\beta)^{1/2}$. Two types of domain walls, corresponding to order parameter rotations in the (η_1, η_2) plane by 180° and 90° , are possible in this system. We shall refer to them as to 180° and 90° walls, respectively. They are illustrated in Fig. 6.2.2 by lines connecting points that represent domain states. The structure of the walls, i.e., the coordinate dependence of the order parameter, can be derived from the Euler equation (6.2.3) written for both components of the order parameter, namely,

$$\begin{aligned} -\delta \frac{\partial^2 \eta_1}{\partial x^2} + \alpha \eta_1 + \beta_1 \eta_1^3 + \beta_2 \eta_1 \eta_2^2 &= 0, \\ -\delta \frac{\partial^2 \eta_2}{\partial x^2} + \alpha \eta_2 + \beta_1 \eta_2^3 + \beta_2 \eta_2 \eta_1^2 &= 0. \end{aligned} \tag{6.2.17}$$

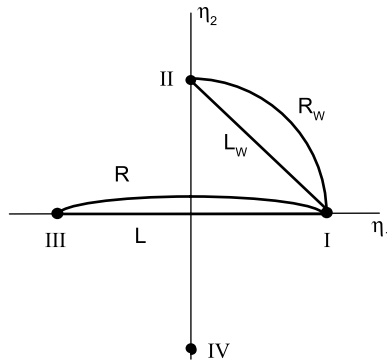


Fig. 6.2.2 Mapping on the order parameter plane of domain states (points I–IV) and domain walls (curves). Mapping R is shown schematically. The mappings of the walls are labeled as follows: L, linear solution for the 180° wall; L_w, linear solution for the 90° wall; R, rotational solution for the 180° wall; R_w, purely rotational solution for the 90° wall

For the 180° wall, e.g., corresponding to a curve connecting points III and I, the solution of this equation should also meet boundary conditions: $(\eta_1 \rightarrow \eta_S, \eta_2 \rightarrow 0)$ for $x \rightarrow \infty$ and $(\eta_1 \rightarrow -\eta_S, \eta_2 \rightarrow 0)$ for $x \rightarrow -\infty$. For the 90° wall, e.g., one corresponding to a curve connecting points II and I, the boundary conditions are $(\eta_1 \rightarrow \eta_S, \eta_2 \rightarrow 0)$ for $x \rightarrow \infty$ and $(\eta_1 \rightarrow 0, \eta_2 \rightarrow \eta_S)$ for $x \rightarrow -\infty$.

Let us start with the analysis of the 180° wall. One distinguishes two types of solutions for this kind of wall: The so-called linear solution (line L in Fig. 6.2.2), where only one order parameter component changes with the coordinate whereas the other component stays zero, and the so-called rotational solution, in which both components change in the wall (curve R in Fig. 6.2.2). In the case

of linear solution, the problem is obviously reduced to the single-component case with a tanh-type solution for η_1 , given by Eq. (6.2.5). However, in contrast to the single-component case, this solution does not always describe a stable 180° wall since under certain condition it is unstable with respect to the appearance of the nonzero second component in the wall. The limit of stability of the linear solution can be found using the technique developed for this kind of problems (Bulaevskii and Vekhter, 1986). We look for the minimum eigenvalue of the functional obtained from the second of Eqs. (6.2.17) where we put $\eta_1(x) = \eta_S \tanh(x/t_{th})$ and linearize it with respect to η_2 . If it is negative the linear solution is unstable. One readily finds this functional in the form

$$\left(-\frac{\partial^2}{\partial x^2} + B + U \tanh^2(x/t_{th}) \right) \eta_2, \quad (6.2.18)$$

where $B = \alpha/\delta$; $U = \beta_2 \eta_S^2/\delta$. Its smallest eigenvalue can be found in the form (see, e.g., Tagantsev et al., 2001a)

$$\lambda = \left(\sqrt{4Ut_{th}^2 + 1} - 1 + 2Bt_{th}^2 \right) / (2t_{th}^2). \quad (6.2.19)$$

Finally, using Eqs. (6.2.6) and (6.2.19) we find that the linear solution is stable if $\beta_2 > 3\beta_1$. When this is not the case, the linear wall is not stable. In principle, that means either a rotation type of the 180° wall is stable or the 180° wall is unstable with respect to a decay into two 90° walls. For the case described by free energy equation (6.2.16), as was shown by Sonin and Tagantsev (1988, 1989), the latter possibility takes place. However, once high-order invariants, i.e., $\gamma(\eta_1^2 + \eta_2^2)^3/6$, are taken into account in the free energy, the rotation type of 180° wall can be stable (curve R in Fig. 6.2.2). The phase diagram of the states of the 180° wall in terms of $\beta_2 - 3\beta_1$ and γ has been developed by the same authors.

As it has been shown by Ishibashi and Dvorak (1976), the situation when $\beta_2 = 3\beta_1$ corresponds to a special state of the system in which the set of involved equations reduces to two decoupled equations in terms of the following variables:

$$\begin{aligned} \eta_+ &= \eta_1 + \eta_2, \\ \eta_- &= \eta_1 - \eta_2. \end{aligned} \quad (6.2.20)$$

This is clearly seen if one rewrites Eq. (6.2.17) in terms of these variables:

$$\begin{aligned} -\delta \frac{\partial^2 \eta_+}{\partial x^2} + \alpha \eta_+ + \frac{\beta_1 + \beta_2}{4} \eta_+^3 - \frac{\beta_2 - 3\beta_1}{4} \eta_+ \eta_-^2 &= 0, \\ -\delta \frac{\partial^2 \eta_-}{\partial x^2} + \alpha \eta_- + \frac{\beta_1 + \beta_2}{4} \eta_-^3 - \frac{\beta_2 - 3\beta_1}{4} \eta_- \eta_+^2 &= 0. \end{aligned} \quad (6.2.21)$$

Thus, the problem of the domain walls structure for small $|\beta_2 - 3\beta_1|/\beta_1$ becomes analytically tractable. The tanh-type solutions of these equations at

$\beta_2 = 3\beta_1$ were actually used in the aforementioned analysis of the stability phase diagram for the 180° wall.

The analysis of the 90° wall structure is more complex. For arbitrary values of the free energy coefficient no full analytical solutions of the problem is available. A certain progress in analytical description of the problem has been achieved by Bulaevskii and Ginzburg (1964) and by Bulaevskii (1964). Later, Cao et al. (1990) offered a discussion of a numerical analysis of the problem. The full analytical solution is available if either $|\beta_2 - 3\beta_1|/\beta_1 \ll 1$ or $|\beta_2 - \beta_1|/\beta_1 \ll 1$. For the case $|\beta_2 - 3\beta_1|/\beta_1 \ll 1$, neglecting weak coupling between the variables in Eqs. (6.2.21), one finds for the spatial dependence of the order parameter in the wall

$$\begin{aligned}\eta_1 &= \frac{\eta_s}{2} [1 + \tanh(x/t_{\text{th}})], \\ \eta_2 &= \frac{\eta_s}{2} [1 - \tanh(x/t_{\text{th}})].\end{aligned}\tag{6.2.22}$$

This solution corresponds to a straight line connecting the points I and II in the order parameter plane (line L_w in Fig. 6.2.2).

If, however, $|\beta_2 - \beta_1|/\beta_1 \ll 1$, the solution corresponds to a curve which is very close to an arc linking the points representing the aforementioned domain states (curve R_w in Fig. 6.2.2). This solution has been treated by Fousková and Fousek (1975) and by Laikhtman and Tagantsev (1975). They considered the situation of the first-order phase transition setting $\beta_1 < 0$ and taking into account the $\gamma(\eta_1^2 + \eta_2^2)^3/6$, invariant in the free energy. It turned out that the situation for the first-order and second-order phase transitions is conceptually close. The condition $|\beta_2 - \beta_1|/\beta_1 \ll 1$ corresponds to weak anisotropy in the order parameter plane, the situation where the potential Φ is only weakly dependent on the angle φ characterizing the order parameter. It is clearly seen when, rewriting the free energy in terms of polar variables

$$\begin{aligned}\eta_1 &= r \cos \varphi, \\ \eta_2 &= r \sin \varphi,\end{aligned}\tag{6.2.23}$$

we obtain

$$\begin{aligned}\Phi &= \Phi_0 + \frac{1}{2}\alpha r^2 + \frac{1}{16}(3\beta_1 + \beta_2)r^4 + \frac{1}{16}(\beta_1 - \beta_2)r^4 \cos 4\varphi \\ &+ \frac{1}{2}\delta \left(\left(\frac{\partial r}{\partial x} \right)^2 + r^2 \left(\frac{\partial \varphi}{\partial x} \right)^2 \right)\end{aligned}\tag{6.2.24}$$

instead of Eq. (6.2.16). In polar variables the equations of state for the wall read

$$\begin{aligned}\delta \left[\frac{\partial^2 r}{\partial x^2} - \gamma \left(\frac{\partial \varphi}{\partial x} \right)^2 \right] &= r \left[\alpha + \frac{1}{4}(3\beta_1 + \beta_2)r^2 + \frac{1}{4}(\beta_1 - \beta_2)r^4 \cos 4\varphi \right], \\ \delta \frac{\partial}{\partial x} r^2 \frac{\partial \varphi}{\partial x} &= \frac{1}{4}(\beta_2 - \beta_1)r^4 \sin 4\varphi.\end{aligned}\tag{6.2.25}$$

The 90° wall corresponds to a solution to Eq. (6.2.25) with boundary conditions $r = \eta_S$, $\varphi = \pi/2$ for $x \rightarrow \infty$ and $r = \eta_S$, $\varphi = 0$ for $x \rightarrow -\infty$. To within a small parameter $|\beta_2 - \beta_1|/\beta_1 \ll 1$, the purely rotating solution, i.e.,

$$r = \eta_S, \quad \varphi = \tan^{-1}[\exp(x/t_R)], \quad t_R = t_{th} \sqrt{\beta_1/2(\beta_2 - \beta_1)}, \quad (6.2.26)$$

satisfies Eqs. (6.2.25). The rotational structure of this wall is reminiscent of the Bloch wall in magnets. As one can see from Eq. (6.2.26), in the range of applicability of this solution, the thickness of rotational wall t_R will be much greater than that of the linear 180° wall t_{th} . It is worth mentioning that for the range of parameters where the purely rotational solution gives a good approximation for the structure of the 90° wall, i.e., $|\beta_2 - \beta_1|/\beta_1 \ll 1$, the stability condition for the 180° wall, $\beta_2 > 3\beta_1$, is not met. Thus, in this range of parameters the 90° wall is the only stable one.

One remark should be made for completeness. In the above analysis we have been dealing with the free energy containing actually only one anisotropic invariant $\eta_1^2 \eta_2^2$ and with the coefficients fulfilling the specific condition $\beta_2 > \beta_1 > 0$. In the literature, however, the problems of domain wall structure have been treated for a range of parameters different from $\beta_1 > \beta_2 > 0$ as well as for free energy having an additional invariant $(\eta_1^2 - \eta_2^2)^2$. One can show that the latter problems can be reduced to that treated in this section by rotating the reference frame in the order parameter plane.

6.2.2 Effects of Strain Induced by the Order Parameter

Above we have treated the structure of a domain wall taking into account the energy associated with the order parameter only. The results obtained correspond to a problem of domain wall structure when mechanical stresses are formally set to zero. In reality, one should take into account the energy of mechanical stresses induced by spatial variation of the order parameter. This complicates the problem and introduces new features into the phenomenon. They can be summarized as follows. (i) One-dimensional solution for a domain wall is impossible in a mechanically free sample (Cao and Barsch, 1990). To get such a solution one should adopt spatially inhomogeneous mechanical boundary conditions. (ii) Once these conditions are set, the problem can be reduced to a one-dimensional problem dealing with the order parameter only. Coefficients in the resulting equation are sensitive to elastic properties of the material and to crystallographic orientation of the domain wall. (iii) Mechanical effects essentially contribute to the orientational dependences of thickness and energy of the wall.

In this section we will illustrate all these features considering a simple example of the 180° wall in the tetragonal phase of a BaTiO₃-like structure. For simplicity we will treat the case of the second-order transition. Let the

nonzero component of polarization P_z be a function of the coordinate x_1 . We write down the Euler equation (6.2.3) for this component, using Eq. (2.3.34), where the P^6 terms are neglected and which is appended with the correlation term $[(\partial P_z/\partial x_1)^2 + (\partial P_z/\partial x_2)^2]\delta/2$. This leads to the following equation:

$$-\delta \frac{\partial^2 P_z}{\partial x_1^2} + \alpha P_z + \beta_{11} P_z^3 - 2P_z[Q_{11}\sigma_3 + Q_{12}(\sigma_1 + \sigma_2)] = 0, \quad (6.2.27)$$

where the components of stress tensor can be determined using the elastic equations of state:

$$\begin{aligned} \varepsilon_1 &= s_{11}\sigma_1 + s_{12}(\sigma_3 + \sigma_2) + Q_{12}P_z^2, & \varepsilon_4 &= s_{44}\sigma_4, \\ \varepsilon_2 &= s_{11}\sigma_2 + s_{12}(\sigma_3 + \sigma_1) + Q_{12}P_z^2, & \varepsilon_5 &= s_{55}\sigma_5, \\ \varepsilon_3 &= s_{11}\sigma_3 + s_{12}(\sigma_1 + \sigma_2) + Q_{11}P_z^2, & \varepsilon_6 &= s_{66}\sigma_6 \end{aligned} \quad (6.2.28)$$

provided that the components of the strain tensor satisfy conditions of mechanical compatibility (Love, 1944), namely,

$$\frac{\partial^2 \varepsilon_2}{\partial x_3^2} + \frac{\partial^2 \varepsilon_3}{\partial x_2^2} = \frac{\partial^2 \varepsilon_4}{\partial x_2 \partial x_3}, \quad \frac{\partial^2 \varepsilon_1}{\partial x_3^2} + \frac{\partial^2 \varepsilon_3}{\partial x_1^2} = \frac{\partial^2 \varepsilon_5}{\partial x_1 \partial x_3}, \quad \frac{\partial^2 \varepsilon_1}{\partial x_2^2} + \frac{\partial^2 \varepsilon_2}{\partial x_1^2} = \frac{\partial^2 \varepsilon_6}{\partial x_2 \partial x_1}, \quad (6.2.29a)$$

$$\begin{aligned} \frac{\partial^2 \varepsilon_1}{\partial x_2 \partial x_3} + \frac{1}{2} \frac{\partial^2 \varepsilon_4}{\partial x_1^2} &= \frac{1}{2} \left(\frac{\partial^2 \varepsilon_6}{\partial x_1 \partial x_3} + \frac{\partial^2 \varepsilon_5}{\partial x_2 \partial x_1} \right), \\ \frac{\partial^2 \varepsilon_2}{\partial x_1 \partial x_3} + \frac{1}{2} \frac{\partial^2 \varepsilon_5}{\partial x_2^2} &= \frac{1}{2} \left(\frac{\partial^2 \varepsilon_6}{\partial x_2 \partial x_3} + \frac{\partial^2 \varepsilon_4}{\partial x_2 \partial x_1} \right), \\ \frac{\partial^2 \varepsilon_3}{\partial x_2 \partial x_1} + \frac{1}{2} \frac{\partial^2 \varepsilon_6}{\partial x_3^2} &= \frac{1}{2} \left(\frac{\partial^2 \varepsilon_5}{\partial x_2 \partial x_3} + \frac{\partial^2 \varepsilon_4}{\partial x_3 \partial x_1} \right). \end{aligned} \quad (6.2.29b)$$

One can easily check that a one-dimensional solution of this set of equations for a mechanically free sample, i.e., all $\sigma_i = 0$, is impossible. Specifically, there is a problem with ε_3 and ε_2 . According to Eqs. (6.2.28), in a mechanically free crystal these components should depend on x_1 . On the other hand, x_1 -dependent components ε_3 and ε_2 are incompatible with the second and third of Eqs. (6.2.29a). However, if one sets these components of strain equal to their spontaneous values inside the domains, i.e.,

$$\varepsilon_2 = Q_{12}P_s^2, \quad \varepsilon_3 = Q_{11}P_s^2, \quad (6.2.30)$$

the problem can be reduced to a one-dimensional one by setting

$$\sigma_1 = \sigma_4 = \sigma_5 = \sigma_6 = 0. \quad (6.2.31)$$

Eliminating σ_2 and σ_3 between Eqs. (6.2.27) and (6.2.28) and making use of Eqs. (6.2.30) and (6.2.31) we arrive at the following equation for polarization (Dvorak and Janovec, 1965):

$$-\delta \frac{\partial^2 P_z}{\partial x_1^2} + B(\alpha P_z + \beta_{11} P_z^3) = 0, \quad (6.2.32)$$

where

$$B = 1 + \frac{1}{\beta_{11}} \left[\frac{(Q_{12} + Q_{11})^2}{s_{11} + s_{12}} + \frac{(Q_{12} - Q_{11})^2}{s_{11} - s_{12}} \right]. \quad (6.2.33)$$

(Attention, Eqs. (6.2.32) and (6.2.33), strictly speaking do not hold for a mechanically free sample with the domain wall! See the further discussion.) Thus, the problem is reduced to the basic equation for the 180° domain wall profile, Eq. (6.2.4), which yields the tanh-type solution:

$$P_z(x) = P_s \tanh\left(\frac{x}{t_{\text{th}}}\right), \quad t_{\text{th}} = \frac{t_{\text{th}0}}{\sqrt{B}}, \quad (6.2.34)$$

where $t_{\text{th}0} = \sqrt{-2\delta/\alpha}$ is the wall thickness calculated without taking into account the stresses induced by the order parameter nonhomogeneity. Thus, we see that taking into account the stress effect results in a change of the spatial scale of the wall profile.

Another manifestation of the stress effects is a change of the surface energy density of the wall. Using relations (2.3.34), (6.2.28), (6.2.30), and (6.2.31) one can rewrite the thermodynamic potential of the problem in terms of P_z only (Dvorak and Janovec, 1965; Tagantsev et al., 2001a):

$$\Phi_{\text{eff}} = \frac{\delta}{2} \left(\frac{\partial P_z}{\partial x_1} \right)^2 + B \left(\frac{\alpha}{2} P_z^2 + \frac{\beta_{11}}{4} P_z^4 \right). \quad (6.2.35)$$

The surface energy density σ_w of the wall calculated with the aid of Eqs. (6.2.9), (6.2.34), and (6.2.35) also scales with a factor of \sqrt{B} :

$$\sigma_w = \sqrt{B} \sigma_{w0}. \quad (6.2.36)$$

The above treatment has been dealing with one specified orientation of the wall. The same approach can be applied for the description of a wall of any orientation that is allowed by the conditions of mechanical and electrostatic compatibilities of domains discussed in Chap. 2. To do this, one changes the crystallographic reference frame (X_1, X_2, X_3) to a new one (X'_1, X'_2, X'_3) , where X'_1 is normal to the wall. Although the calculation is mathematically rather cumbersome, the scheme of the above treatment can be followed. It results in

Eqs. (6.2.32), (6.2.34), (6.2.35), and (6.2.36) where the B -parameter is a function of the wall orientation. For instance, for a wall making an angle of 45° with the axes X_1 and X_2 one finds

$$B = 1 + \frac{1}{\beta_{11}} \frac{Q_{11}^2(s_{11} + s_{12} + s_{44}/2) + 2Q_{12}^2s_{11} - 4s_{12}Q_{11}Q_{12}}{s_{11}(s_{11} + s_{12} + s_{44}/2)/2 - s_{12}^2}. \quad (6.2.37)$$

The orientational dependence of B is a consequence of elastic anisotropy in the (X_1, X_2) , plane. One can check that if this anisotropy is absent, i.e., $2(s_{11} - s_{12}) - s_{44} = 0$, Eqs. (6.2.33) and (6.2.37) give the same value of B . It is worth mentioning that in the considered case, the orientational dependence of B is the only source of anisotropy of thickness and energy of the wall, since, in this case, the correlation energy is isotropic in the (X_1, X_2) plane so that the mechanism of orientational dependence discussed in Sect. 6.2.1 cannot be applied. If the correlation energy is anisotropic we can generalize the equation for the orientational dependence of wall energy and thickness (6.2.10d) by including elastic effects, to obtain

$$\frac{\sigma_w}{\sigma_{w0}} = \sqrt{\frac{\delta}{\delta_0}} \sqrt{\frac{B}{B_0}}, \quad \frac{t_{th}}{t_{th0}} = \sqrt{\frac{\delta}{\delta_0}} \sqrt{\frac{B_0}{B}} \quad (6.2.38)$$

where B_0 and δ_0 are the values of parameters of B and δ for a certain orientation of the wall. The main result of this section, i.e., that it is possible to simplify the problem involving the stress effects to that dealing with order parameter only, holds in the case of the first-order phase transition. However, the renormalization of the equations for the wall profile and the expressions for the wall thickness and energy are more complicated than the simple scaling transformation represented by Eqs. (6.2.34), (6.2.36), and (6.2.38). In more complicated problems, e.g., stability of a domain wall in the case of a multi-component order parameter (like that discussed above in this section) the elastic effects, in general, can qualitatively change the situation. A discussion of such situation in SrTiO_3 can be found in the paper by Tagantsev et al. (2001a).

Concerning the above consideration we would like to stress some important issues. First, as one can expect, the aforementioned procedure which eliminated elastic variable is possible only for walls which satisfy the condition of mechanical compatibility of the adjacent domains. Second, though the elastic variables can be eliminated from the equations, the price of nonzero stress components σ_{22} and σ_{33} in the area of domain wall still has to be paid. For a sample having the shape of a bar elongated along x_1 , this requires non-uniform mechanical boundary conditions on the lateral (elongated) faces of the sample. To satisfy these conditions, an x_1 -dependent pressure should be applied to these surfaces. Clearly, in no real experiments this pressure is applied so that the question arises of how the result of this section can be applied to any real situation. This question has been recently addressed by Lee et al. (2003) for a special case of

a wall in a proper two-dimensional ferroelastic. Being translated into the language of our consideration the obtained answer to this question is as follows. Far from lateral faces inside the sample, Eqs. (6.2.30) are strictly valid. Therefore ε_3 and ε_2 are equal to their bulk spontaneous values. However, close to these faces Eqs. (6.2.30) are violated in a way which ensures free mechanical boundary conditions on the lateral surfaces of the sample. This will result in deformation of the lateral surfaces of the bar which lose their planar shape in the vicinity of the wall, unless plastic deformations occur.

Concluding this section we will discuss one more effect related to the so-called flexoelectric coupling that plays an appreciable role in description of phenomena associated with spatial inhomogeneity of the polarization and strain. In terms of Helmholtz free energy it is described by a bilinear coupling between the polarization and strain gradient (see, e.g., Tagantsev (1991)), like shown in the following example where only P_3 and $\varepsilon_5 = 2\varepsilon_{13}$ variables are kept:

$$F = \frac{\chi_{33}^{-1}}{2} P_3^2 + \frac{s_{44}^{-1}}{2} \varepsilon_5 + f_{44} \frac{\partial \varepsilon_5}{\partial x_1} P_3. \quad (6.2.39)$$

As clear from the minimization of this expression, this coupling leads to the flexoelectric effect, i.e., the linear response of the polarization to the strain gradient:

$$P_3 = -\chi_{33} f_{44} \frac{\partial \varepsilon_5}{\partial x_1}. \quad (6.2.40)$$

In the mechanically free situation, expansion (6.2.39) also implies the occurrence of the linear strain response to the polarization gradient:

$$\frac{\partial u_3}{\partial x_1} + \frac{\partial u_1}{\partial x_3} = \varepsilon_5 = s_{44} f_{44} \frac{\partial P_3}{\partial x_1}. \quad (6.2.41)$$

Integration of this equation across a 180° domain wall normal to X_3 -axis leads to an offset of mechanical displacement u_3 between two domains:

$$\delta u_3 = 2s_{44} f_{44} P_S. \quad (6.2.42)$$

It is instructive to evaluate the strength of this effect. We will do this for a material with high P_S . We take $P_S \cong 0.9 \text{ C/m}^2$ (Meyer and Vanderbilt, 2002) for PbTiO_3 at low temperatures and $s_{44} = 9 \times 10^{-12} \text{ m}^3/\text{J}$ (see Table 2.3.1). Following atomic “estimates,” f -coefficients should be of the order of a few volts (Tagantsev, 1991). This leads us to an appreciable value of a few tenths of angstrom for the expected mechanical offset between the domains. We will be back to this effect when discussing the microscopic theories of domain walls.

6.2.3 Domain Walls in Selected Ferroics

The method of treating domain wall structures outlined above has been widely applied for the description of walls in different ferroics. In this section we will present a few examples.

6.2.3.1 Domain Walls in Uniaxial Nonferroelastic–Ferroelectrics

Uniaxial ferroelectric triglycine sulfate (TGS) provides a simple example of the second-order phase transition driven by a single-component order parameter. It represents the species $2/m-Pd-2$ with \mathbf{P}_S directed along the y -axis. Electrically neutral walls in TGS should be parallel to the y -direction. Since the material is not ferroelastic, conditions of mechanical compatibility impose no restrictions on the wall orientation. In this situation, the energetically favorable orientation of domain walls is controlled by anisotropy of their surface energy density. Related calculations (Fousek, 1967; Hatano et al., 1976) have been performed following the approach formulated in the previous sections. Dependences of thickness and surface energy densities on the angle φ between the normal to the wall and the crystallographic x -direction have been determined. It has been shown that, after elimination of elastic variables, the problem reduces to Eq. (6.2.35) with φ -dependent δ and B parameters:

$$\delta(\varphi) = \delta_{2121} \cos^2 \varphi + \delta_{2323} \sin^2 \varphi - \delta_{2123} \sin 2\varphi, \quad (6.2.43)$$

$$B(\varphi) = 1 + 2(c'_{11}k_3^2 + 4c'_{55}k_1^2 + 4c'_{15}k_1k_3 + 2q'_{12}k_3 + 4q'_{52}k_1)/\beta',$$

$$k_1 = (c'_{15}q'_{12} - c'_{11}q'_{52})/2(c'_{11}c'_{55} - c'^2_{15}), \quad (6.2.44)$$

$$k_3 = (c'_{15}q'_{52} - c'_{55}q'_{12})/(c'_{11}c'_{55} - c'^2_{15}).$$

where c'_{ij} and q'_{ij} are the elastic constants and “charge/stress” electrostriction coefficients in the reference frame rotated by angle φ with respect to the crystallographic axes²; β' is the coefficient of dielectric non-linearity at constant strain; the δ -coefficients correspond to the correlation energy taken in the form (Fousek, 1969)

$$\Phi_{\text{corr}} = \frac{1}{2} \delta_{2121} \left(\frac{\partial P_y}{\partial x} \right)^2 + \frac{1}{2} \delta_{3232} \left(\frac{\partial P_y}{\partial z} \right)^2 + \delta_{2321} \frac{\partial P_y}{\partial x} \frac{\partial P_y}{\partial z} \quad (6.2.45)$$

Equation (6.2.35) implies a tanh shape of the polarization profile in the wall, whose thickness and energy are given by Eq.(6.2.38) where B and δ come from Eq. (6.2.43).

² Explicit expressions for c'_{ij} and q'_{ij} can be found in the paper by Fouskova and Fousek (1975).

This theory enables one to estimate numerically parameters of the wall in TGS and to determine its most favorable orientation. Using an order-of-magnitude estimate for the correlation parameter, $\delta = 5 \times 10^{-14}$ – 5×10^{-13} cm² (in CGS units) and neglecting its anisotropy, Fousek (1967) obtained $t_{\text{th}} = 1 \times 10^{-8}$ – 3.5×10^{-8} cm and $\sigma_w = 4$ – 12 erg/cm². Hatano et al. (1976) discussed the anisotropy of σ_w taking into account both angular dependences $B(\varphi)$ and $\delta(\varphi)$. The function $B(\varphi)$ can be determined (Hatano et al., 1977) since elastic properties of TGS are well known. As for the $\delta(\varphi)$ dependence, it reflects the anisotropy of the correlation length which can be measured by X-ray critical scattering. From scattering data the value $\delta(20.4^\circ) = 3.6 \times 10^{-15}$ cm² can be deduced. It was further assumed (Hatano et al., 1976) that the correlation lengths along the crystallographic directions [001], [100], and [101] are proportional to the Wigner–Seitz cell dimensions in these directions. This then leads to the values $\delta_{2121} = 3.71 \times 10^{-15}$ cm², $\delta_{2323} = 1.33 \times 10^{-15}$ cm², and $\delta_{2321} = -0.27 \times 10^{-15}$ cm². With these data the anisotropy of the energy and thickness of the 180° wall in TGS was evaluated at room temperature (Hatano et al., 1977). The results for the wall energy are shown in Fig. 6.2.3. The wall thickness was found changing in the interval 20–35 Å. This figure also contains analogous information for isostructural triglycine selenate (TGSe). For TGS, the value of σ_w lies between 0.6 and 1.0 erg/cm² with a minimum at $\varphi \cong 97^\circ$. This seems to explain the observations which suggest that domain walls in TGS show a clear tendency to be oriented with $\varphi = 90^\circ$. A similar approach was employed to discuss wall energy anisotropy in NaNO₂ (Hatano and Le Bihan, 1990).

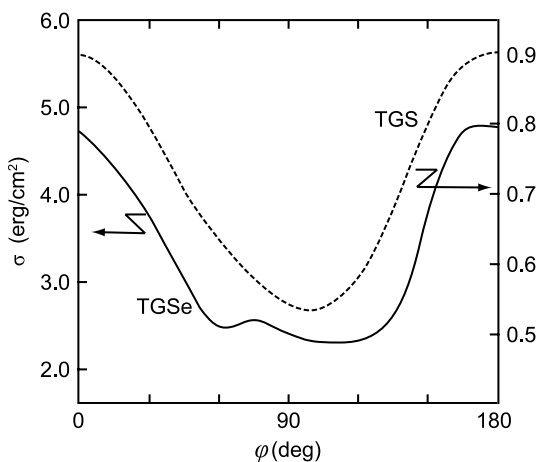


Fig. 6.2.3 Calculated orientational dependence of the wall-energy densities of TGSe at 0°C and of TGS at room temperature. After Hatano et al. (1977)

One should note that all estimates for the coefficient δ are very approximate and conclusions regarding the magnitudes of wall energy and thickness must be taken with caution. However, they all point to the fact that the wall thickness in TGS is rather small, just several unit cell parameters.

6.2.3.2 Domain Wall in a Multiaxial Ferroelectric: Barium Titanate

The problem of the structure of 180° and 90° domain walls in tetragonal BaTiO_3 (species $m\bar{3}m - P\epsilon ds - 4mm$) has been addressed repeatedly by a number of authors (Zhirnov, 1958; Kholodenko, 1962; Bulaevskii, 1964; Bulaevskii and Ginzburg, 1964; Kittel, 1972; Cao and Cross, 1991), the most comprehensive treatment being recently offered by Hlinka and Marton (2006). The starting point of the theory is the Gibbs energy for the single domain BaTiO_3 given by Eq. (2.3.34) and the correlation energy (Cao and Cross, 1991):

$$\begin{aligned} \Phi_{\text{corr}} = & \frac{1}{2} \delta_{1111} \left[\left(\frac{\partial P_1}{\partial x_1} \right)^2 + \left(\frac{\partial P_2}{\partial x_2} \right)^2 + \left(\frac{\partial P_3}{\partial x_3} \right)^2 \right] \\ & + \delta_{1122} \left[\left(\frac{\partial P_1}{\partial x_1} \right) \left(\frac{\partial P_2}{\partial x_2} \right) + \left(\frac{\partial P_1}{\partial x_1} \right) \left(\frac{\partial P_3}{\partial x_3} \right) + \left(\frac{\partial P_2}{\partial x_2} \right) \left(\frac{\partial P_3}{\partial x_3} \right) \right] \quad (6.2.46) \\ & + \frac{1}{2} \delta_{1212} \left[\left(\frac{\partial P_1}{\partial x_2} + \frac{\partial P_2}{\partial x_1} \right)^2 + \left(\frac{\partial P_1}{\partial x_3} + \frac{\partial P_3}{\partial x_1} \right)^2 + \left(\frac{\partial P_2}{\partial x_3} + \frac{\partial P_3}{\partial x_2} \right)^2 \right]. \end{aligned}$$

The recently undated values of the correlation parameters are given in Table 2.3.1. The problem is conceptually identical with that presented in Sects. 6.2.1 and 6.2.2. Let us highlight only the most essential points of its treatment.

We start with a 180° wall which is perpendicular to the x_1 -axis and links the domain states $P_3 = -P_s$, $P_1 = 0$, $P_2 = 0$ for $x_1 \rightarrow -\infty$ and $P_3 = P_s$, $P_1 = 0$, $P_2 = 0$ for $x_1 \rightarrow \infty$. We assume that the wall carries no bound charge, which is equivalent to the requirement that $P_1 = 0$ for any x_1 . That reduces the number of involved components of polarization to two and makes possible only solutions of two types: (i) the “linear” solution where only $P_3 \neq 0$ and (ii) the “rotational” solution where P_2 also changes on crossing the wall. Bulaevskii (1964) has shown that in BaTiO_3 the rotational solution is energetically unfavorable. As for the linear solution, it can be readily treated on the lines of Sect. (6.2.2) resulting (after elimination of the mechanical variables) in Eq. (6.2.11) (Bulaevskii, 1964; Cao and Cross, 1991). That leads finally to the wall with polarization profile typical for systems with the first-order phase transition, Eq. (6.2.12). The orientational dependence of the wall energy was evaluated by Dvorak and Janovec (1965) to find extremely small anisotropy of 0.13%. These authors have taken into account only the “elastic” effect described by B factor from Eq. (6.2.35). This probably explains the disagreement between their results and the experimental data (Fousek and Safrankova, 1965). As clear from the very anisotropic correlation energy (see Table 2.3.1), the phenomenological theory, in fact, may predict an appreciable anisotropy of the energy of 180° walls in BaTiO_3 .

Consider now a 90° wall separating domain states $P_1 = P_s$, $P_2 = P_3 = 0$ and $P_3 = P_1 = 0$, $P_2 = P_s$. This wall is a ferroelastic W_{Γ} -type wall, its plane is

fixed normal to a $\langle 110 \rangle$ direction. The formation of bound charge due to polarization inhomogeneity is very unfavorable in ferroelectric. This decides the head-to-tail configuration of the wall. Considering the material as insulator and using the Poisson equation, one concludes that the projection of the electrical displacement onto the wall normal should be constant throughout the crystal. This condition can be properly approximated with the condition of the constancy of the corresponding component of the polarization.³ Treating the problem in the reference frame (X_L, X_T, X_3) , where the axis X_L is directed along the wall normal, implies that $P_L = P_S/\sqrt{2}$ throughout the crystal and the problem reduces to that dealing with a single component of polarization P_T and mechanical variables.⁴ After elimination of the elastic variables (cf. Sect. 6.2.2) one arrives at the effective free energy equation (6.2.11) written in terms of P_T and at the solution given by Eq. (6.2.12). The latter can be rewritten in the cubic reference frame and describes the polarization profile in the 90° wall as

$$\begin{aligned} P_1(x) &= \frac{P_s}{2} \left[1 - \frac{\sinh(x/t_{th})}{[A + \cosh^2(x/t_{th})]^{1/2}} \right], \\ P_2(x) &= \frac{P_s}{2} \left[1 + \frac{\sinh(x/t_{th})}{[A + \cosh^2(x/t_{th})]^{1/2}} \right]. \end{aligned} \quad (6.2.47)$$

The expressions for parameters controlling this profile in terms of the coefficients of the free energy expansion have been deduced by Bulaevskii (1964); the correlation coefficient δ introduced in this paper should be set equal to $(\delta_{1111} - \delta_{1122})/2$ (Cao and Cross, 1991).

Solution (6.2.47) is not exact because it is the component electrical displacement not of the polarization that is fixed by the electrostatics. However, one can show that inaccuracy associated with this fact is about $1/\kappa_c$ where κ_c is the relative dielectric constant along the polar direction of the ferroelectric. According to Darinskii and Fedosov (1971), at room temperature the difference between wall energies for the exact and approximate solutions is smaller than 1%. However, the approximate solution misses an important qualitative feature, namely, it keeps the value of P_L component of polarization exactly constant, equal to $P_L = P_S/\sqrt{2}$, whereas in reality P_L slightly deviates from this value when crossing the wall. The same authors evaluated the spatial variation of P_L (roughly P_S/κ_c) the related bound charge, and the profile of the imposed electrostatic potential. They found that the resulting bound charge forms two back-to-back

³ This is a good approximation in materials with ‘normal’ values of the soft-mode effective charge (of the order of the charge electronic). In ferroelectrics with anomalously small values of this charge, like weak ferroelectrics (see Sect. 2.3.6), this approximation fails.

⁴ Actually, the P_z component may also appear in the wall. The stability of the available solutions for 90° walls with respect to the appearance of this component can be investigated following the approach outlined in Sect. 6.2.1.

double electric layers. This kind of charge distribution does not lead to a jump of electrostatic potential at the wall. However, this distribution was shown to create a potential well of about 0.5 eV in the wall for a particle having the charge of an electron. This conclusion may be of importance for mobility and pinning of the wall by charged defects. The results of recent calculations by Hlinka and Marton (2006) are in good agreement with these conclusions.

It is worth mentioning that, if the conductivity of the material is not negligible, free carriers could compensate the internal field in the 90° wall. If the Debye screening length λ_D is comparable to the wall thickness t_w , this compensation can be substantial. In this situation the condition of constant P_L can be strongly violated and solution (6.2.47) is no longer applicable. Problem of the 90° wall structure in BaTiO_3 under the condition of complete screening of P_L has been in fact addressed by Cao and Cross (1991); they used an implicit assumption that the bound charges related to the inhomogeneity of the polarization does not create any electric field in the wall. In their approach the problem has been reduced to that dealing with two components of the polarization for which, in general, in contrast to the aforementioned “no-compensated” situation, we do not have a good analytical approximation to the solution. It has been shown that, for a special set of material parameters, a solution of type (6.2.47) is also possible in their case. This problem has also been treated recently by Hlinka and Marton (2006) who obtained its numerical solution for the realistic set of the thermodynamic parameters of BaTiO_3 . They have also performed the comparison of the solutions for “compensated” ($\lambda_D \ll t_w$) and “non-compensated” ($\lambda_D \gg t_w$) situations. The derived polarization profiles are shown in Fig. 6.2.4. An appreciable difference between these solutions is seen.

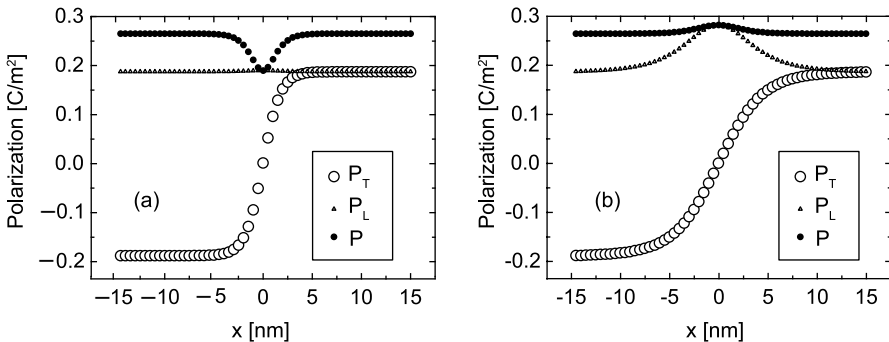


Fig. 6.2.4 Polarization profiles in a 90° domain wall calculated for BaTiO_3 at room temperature: P_T , transversal component of the polarization; P_L , longitudinal component of the polarization; P , absolute value of the polarization; (a) the case of insulating crystal where the long-range electrostatic interaction suppresses variations of P_L , (b) the hypothetical case of highly conductive crystal with the Debye screening length smaller than the wall thickness where the depolarizing electric field in the crystal is suppressed. After Hlinka and Marton (2006)

The principal difference between these situations is that the long-range electrostatic coupling lets the development of the longitudinal component of the polarization only for about $0.01P_S$ whereas, in the compensated case, it is about $0.3P_S$. It is also seen that the long-range electrostatic coupling adequately taken into account in the non-compensated case leads to an essential shrinkage of the wall. One should note that, for BaTiO_3 , the compensated situation looks very hypothetical.

To finish the discussion of the application of the continuous thermodynamic approach to domain walls in this crystal, we will present Table 6.2.1 where theoretical estimates obtained for the wall energy σ_w and its wall width $t_w = 2t_{th}$ (normalized to the lattice constant) are summarized.

Table 6.2.1 Results of continuous theories of domain walls in tetragonal phase of BaTiO_3

	$\sigma_w, \text{mJ/m}^2$	t_w/a_0	Ref.
180° wall	10	2.5–10	Zhirnov (1958)
	6	1.5	Hlinka and Marton (2006)
	11	3.3	Bulaevskii (1964)
90° wall	2–4	12–50	Zhirnov (1958)
	5	5.5	Bulaevskii (1964)
	–	250	Kittel (1972)
	–	9	Hlinka and Marton (2006)
	7	10	Darinskii and Fedosov (1971)

6.2.3.3 Domain Wall in an Improper Uniaxial Ferroelastic Ferroelectric: Gadolinium Molybdate

Gadolinium molybdate was the first discovered improper ferroelectric (Cross et al., 1968; Dvorak, 1974). It represents the species $\bar{4}2m - Pcds - mm2$ with $\nu = 2$ (the unit cell volume is doubled in the ferroic phase), the total number of domain states is four. We have discussed its properties in Chap. 2 in terms of a two-component order parameter (η_1, η_2) , using the Landau theory. Figure 6.2.2 shows the mapping of the four domain states on the order parameter plane. The description of domain walls linking any two of these states requires the knowledge of the correlation energy that can be presented in the form (Laikhtman and Tagantsev, 1975)

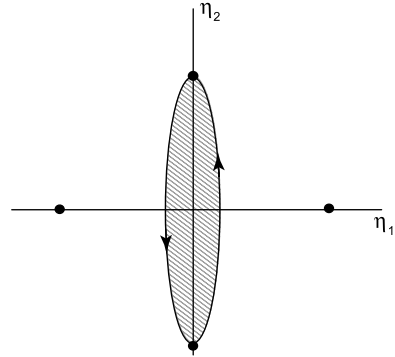
$$\begin{aligned}
 \Phi_{\text{corr}} = & \frac{1}{2} \delta_1 \left[\left(\frac{\partial \eta_1}{\partial x_1} \right)^2 + \left(\frac{\partial \eta_1}{\partial x_2} \right)^2 + \left(\frac{\partial \eta_2}{\partial x_1} \right)^2 + \left(\frac{\partial \eta_2}{\partial x_2} \right)^2 \right] \\
 & + \delta_2 \left[\left(\frac{\partial \eta_1}{\partial x_1} \right) \left(\frac{\partial \eta_1}{\partial x_2} \right) \left(\frac{\partial \eta_2}{\partial x_1} \right) \left(\frac{\partial \eta_2}{\partial x_2} \right) \right] + 2\delta_3 \left(\frac{\partial \eta_1}{\partial x_1} \right) \left(\frac{\partial \eta_2}{\partial x_2} \right) \quad (6.2.48) \\
 & + \frac{1}{2} \delta_4 \left[\left(\frac{\partial \eta_1}{\partial x_3} \right)^2 + \left(\frac{\partial \eta_2}{\partial x_3} \right)^2 \right].
 \end{aligned}$$

One distinguishes two categories of domain walls. Walls of the first category link domain pairs which differ in orientation of the order parameter in the order parameter plane by 90° as well as in sign of spontaneous polarization and spontaneous strain; to be short, we shall call them polarization walls. Walls of the second category, referred to as antiphase boundaries, link domain pairs identical in polarization and strain but differing in sign of the order parameter; in terminology of Chap. 2, these walls link the translational domains. Both categories of domain walls in GMO have been discussed by a number of authors (Fousek, 1967; Ishibashi and Dvorak, 1976; Sonin and Tagantsev, 1988, 1989; Tagantsev and Sonin, 1989; Rychetsky et al., 1992).

Let us start with the polarization wall. The conditions of mechanical compatibility fix its orientation as perpendicular to either the X_1 or the X_2 axis of the parent phase. For this orientation, after eliminating the elastic variables and making use of the correlation energy given by Eq. (6.2.48) and the Landau expansion of the thermodynamic potential (Dvorak, 1971) (a simplified version of the latter being given by Eq. (2.3.36)), one obtains the effective free energy in terms of the order parameter only. The resulting effective energy has the structure identical to that of the free energy written neglecting stress effect. After rotation of coordinates in the order parameter plane the resulting effective free energy can be presented in the form given by Eq. (6.2.16) to which the isotropic six-order invariant $\gamma(n_1^2 + n_2^2)^3/6$ should be added. In terms of this effective free energy the problem has been addressed by Fousková and Fousek (1975) and Laikhtman and Tagantsev (1975). Both groups of authors have argued that the evolution of the order parameter in the wall is close to a pure rotation, its spatial dependence being given by Eq. (6.2.26). Fousková and Fousek based their conclusion on the comparison of the energy corresponding to the arc-type trajectory (R_w in Fig. 6.2.2) linking the domain states in the order parameter plane and that of the trajectory passing through the point $(\eta_1 = 0, \eta_2 = 0)$. Laikhtman and Tagantsev have shown that the purely rotational solution, i.e., Eq. (6.2.26), gives a good approximation for the exact solution of the problem in the case of a weak anisotropy in the order parameter plane. They argue that indeed in GMO this anisotropy is weak, supporting their hypothesis by data on ultrasonic scattering on the wall. It has been pointed out that if a purely rotational profile of the wall takes place, the wall should be anomalously thick.

Antiphase boundaries of two types may exist in GMO, the so-called linear wall and rotational wall; corresponding trajectories in the order parameter plane are shown in Fig. 6.2.2 and marked L and R , respectively. The antiphase boundary has been treated in terms of the aforementioned effective free energy employed for the treatment of the polarization wall (Fousková and Fousek, 1975; Ishibashi and Dvorak, 1976; Sonin and Tagantsev, 1989, 1988), though this is fully justified only when it is oriented perpendicular to the crystallographic axes of the parent phase. Analyses close to that outlined in Sect. 6.2.1.2 have been offered. It has been established that, close to phase transition, the linear type of the wall is the only stable one (Sonin and Tagantsev, 1989, 1988). The profile of the order parameter modulus in the wall was found typical for the case of the first-order phase

Fig. 6.2.5 The so-called circulation line—topological defect of the order parameter, analogue of the Bloch line in ferromagnetic domain walls. Mapping onto the order parameter plane. *Arrows* show the change of the order parameter corresponding to walking around the defect in the real space. After Tagantsev and Sonin (1989)



transition (Fousková and Fousek, 1975); see Eq. (6.2.12). According to Sonin and Tagantsev (1989) the parameter $G = |\beta_1 - \beta_2|/(\alpha|\gamma|)^{1/2}$ plays the decisive role in the stability criteria of the wall. Just below the phase transition (large G) a linear solution is advantageous while, as G decreases with falling temperature, the boundary changes into a rotational one or splits into two polarization boundaries. At a certain temperature, therefore, we may expect a *phase transition in the wall structure*. Discussions of this kind of phase transition can be found in papers by Ishibashi and Dvořák (1976), Lajzerowicz and Niez (1979), Bullbich and Gufan (1989), and the aforementioned authors (Sonin and Tagantsev, 1989, 1988). The transition has been found very peculiar, namely, its phase diagram in terms of coefficients of the free energy expansion contains a multicritical point of the infinite order (Sonin and Tagantsev, 1989, 1988).

An additional interesting aspect of antiphase walls was pointed out by Tagantsev and Sonin (1989). It is obvious that antiphase walls of rotational character can be represented in the order parameter space by two different paths with the opposite sense of rotation, clockwise and anticlockwise. It can be shown that their energies are equal (Fousková and Fousek, 1975; Tagantsev and Sonin, 1989). In different sections of one domain wall the different solutions may occur, meeting along a line termed *circulation line*. This object can also be classified as an order parameter vortex. Such a line represents an additional, the so-called topological “defect” within the domain wall. It can be illustrated by the closed contour in the order parameter plane shown in Fig. 6.2.5. To some extent the circulation lines are an analogy of the Bloch line in ferromagnetic domain walls. Within antiphase walls, strain components ε_{xz} and ε_{yz} may be induced due to energy-invariant coupling order parameter gradients with the strain tensor, such as $\varepsilon_{yz}[\eta_1 (\partial\eta_2/\partial x) - \eta_2 (\partial\eta_1/\partial x)]$. The two wall sections with opposite sense of rotation differ in the sign of this invariant. Therefore an applied shear stress σ_{yz} prefers one of the wall paths, clockwise *or* anticlockwise, and thus it would exert a pressure on the circulation line. It has been shown that, as one expects for topological defects, this pressure is proportional to the area of the corresponding contour in the order parameter plane (Fig. 6.2.3).

6.2.3.4 Domain Wall in Nonferroelectrics

We now consider examples of nonferroelectric ferroics with three- and two-component order parameter. A continuum theory of domain walls in *proper ferroelastics* corresponding to species $m\bar{3}m - \epsilon s - 4/mmm$ with the first-order transition, driven by a three-component order parameter, was developed by Barsch and Krumhansl (1984). This theory is applicable to ferroelastics BiVO_4 and $\text{Pb}_3(\text{PO}_4)_2$. Domain walls in an *improper ferroelastic* with a three-component order parameter (η_1, η_2, η_3) corresponding to the same species have been treated by Cao and Barsch (1990) and the theory was applied to SrTiO_3 . Further detailed theoretical analysis of domain walls in this crystal has been performed by Tagantsev et al. (2001a). The situation has been found typical for a system with a multi-component order parameter (see Sect. 6.2.1.2) and to a certain extent similar to that in BaTiO_3 where the three-component order parameter is polar, however, much more complicated in several aspects.

First, as we have seen above, in BaTiO_3 the electrostatic effects do not allow for “longitudinal” linear 180° walls, i.e., walls where the i -component of polarization changes with the i -component of the coordinate. In the case of SrTiO_3 , this limitation is absent and, actually, the boundaries of this type are the most energetically favorable. This type of boundaries, which are antiphase and “ 180° walls” in the order parameter plane, exhibits the traditional tanh-type profile (Cao and Barsch, 1990). At 40 K the wall thickness, t_w , have been evaluated as some two lattice constants⁵ (Tagantsev et al., 2001a). Another type of antiphase boundary links the domain states which differ in sign of the i -component of the order parameter whereas the plane of boundary is parallel to the i -component of the coordinate. According to Tagantsev et al. (2001a), the properties of these walls are very different from those of the longitudinal walls. These are expected to be much thicker (20–25 lattice constants at 40 K), having the Néel-type structure (with nonzero longitudinal component of the order parameter in the wall). In addition, at a temperature of about 40 K the nonpolar SrTiO_3 becomes unstable with respect to the appearance of spontaneous polarization in the body of the wall, which according to the authors may reach a value of $4 \mu\text{C}/\text{cm}^2$.

In addition, the situation with ferroelastic (90°) walls in SrTiO_3 is more complicated than in BaTiO_3 , since the condition of electroneutrality $\partial P_i / \partial x_i = 0$ that made the problem effectively one component (analytically solvable) is here not applicable. Therefore, in contrast to BaTiO_3 , the problem does not have a general analytical solution. Cao and Barsch (1990) offered an analytical solution for the case when a special relation between the parameters of the problem is satisfied. The result obtained actually corresponds to the special case originally discussed by Ishibashi and Dvorak (1976) (cf. Eqs. (6.2.20), (6.2.21), and (6.2.22)).

Among systems with a two-component order parameter, great attention has been paid to compounds KSCN and Hg_2Br_2 . Both represent the species

⁵ Cao and Barsch (1990) give a much smaller value for t_w because of a lost numerical factor (Tagantsev et al., 2001a).

$4/mmm$ – es – mmm with $v = 2$ although the microscopic mechanisms of their transitions are very different (Rychetsky and Schranz, 1993). The situation in this system is similar to GMO: four domain states that can be linked either by ferroelastic walls (“90°” walls) or by antiphase boundaries (“180°” walls). For the ferroelastic walls and antiphase boundaries oriented perpendicular to either X_1 or X_2 axes of the parent phase, after elimination of the elastic variables, the problem reduces to that treated in detail in Sect. 6.2.1.2 (see Eqs. (6.2.17)). For an antiphase boundary with the normal arbitrarily oriented in the (X_1, X_2) plane, the coefficients δ , α , and β in these equations should be renormalized, the renormalizing factor being different for the first and second equations and depending on the orientation of the wall. Quantitative analysis of properties of both types of domain walls in the mentioned materials has been performed by Rychetsky and Schranz (1993, 1994) and by Rychetsky (1995). For ferroelastic walls, these authors found that the solution is close to the exact solution of Ishibashi and Dvorak (1976) (see Eqs. (6.2.20), (6.2.21), and (6.2.22)). For this type of walls, their numerical estimations led to the following values: at 5 K below T_C , for KSCN $\sigma_w \cong 0.26$ erg/cm² and $t_w \cong 26$ Å, i.e., about 4 lattice constants; for Hg₂Br₂ $\sigma_w \cong 0.008$ erg/cm² and $t_{th} \cong 320$ Å, i.e., about 70 lattice constants. As for the antiphase boundary, Rychetsky and Schranz (1993), using the results of a more general analysis by Bullbich and Gufan (1989) and by Sonin and Tagantsev (1989), reached the conclusion that, for Hg₂Br₂, the linear solution (L-curve in Fig. 6.2.2) is unstable whereas, for KSCN, the wall of this type is stable for any orientation.

6.2.4 Concluding Remarks

Continuum theories of domain walls provide an attractive issue for theoretical activities and the subject was treated in a large number of papers. We have demonstrated on several examples that the general approach is the same, as it was outlined in Sects. 6.2.1 and 6.2.2. It should be noted that, the case of the multi-component order parameter, the theory often results in coupled Euler equations which have no analytical solution. Most of the published theories avoid this problem by choosing particular relations between involved coefficients by which these equations are decoupled; this then leads to well-known kink-type solutions. A more accurate approach, however, is to resort to numerical solutions (Cao and Cross, 1994; Hlinka and Marton, 2006).

One can ask the general question to what extent the continuum approach is justified. We can assume that continuum treatment of inhomogeneities will be acceptable when the local changes of η across the unit cell distance a_0 are much smaller than its spontaneous value in the domains η_S . Roughly speaking, we expect the theory to give a good approximation when the wall thickness t_{th} is larger than at least a few lattice constants a_0 (better $10a_0$). The overview of data on domain wall thicknesses presented in Table 6.1.1, which are rather contradictory, allows for the possibility that in some materials this condition is

fulfilled although the truly high-resolution methods suggest that $10a_0$ is often above the upper limit. For example, neutron scattering data (Bruce, 1981) for KH_2PO_4 led to an outright rejection of any continuum approach in this material. In any case, predictions based on continuum theories have proved useful in several aspects. First, they themselves point out that ferroic walls are very thin; we have quoted a number of estimates which typically predict $t_{\text{th}} \leq 10a_0$. Second, the thermodynamic approach shows which material parameters control domain wall structure and thickness and this may give some guidelines for assessing domain-conditioned properties of different materials.

An issue in reach of the continuum approach is the behavior of the domain walls which are close to the sample surface or inside ultra thin films (free standing or deposited onto thick substrates). It was pointed out above that even the condition for permissible walls, Eq. (2.2.10), will be influenced by sample thickness (Shuvalov et al., 1987; Glushkov et al., 1987) so that some domain pairs can exist, which otherwise represent the R cases. Thus, one can clearly expect an appreciable impact of the aforementioned factors on the domain wall structure. This effect may be even of practical importance in view of increasing applications of ferroelectric thin films. However, because of the lack of space, in this book, we restrict ourselves only to referring the reader to some relevant publications (Darinskii et al., 1989a; Novak and Salje, 1998; Lee et al., 2002; Conti and Salje, 2001).

6.3 Microscopic Theories of Domain Walls

In the previous section we have discussed the main issues of theories of domain walls in ferroics, which are based on the Landau expansions in terms of a continuous order parameter appended with terms containing the order parameter gradient. Though such theories make a convenient tool for theoretical description of domain walls, their application to real systems is often limited. First, the value of the gradient term is usually difficult to evaluate. Second, the domain wall thickness obtained in these theories often occurs to be of the order of lattice constants of the material. This makes the results obtained in the continuum theory, at best, marginally justified. All these facts make important theories of domain walls dealing with atomic displacements rather than with a continuous order parameter. We will call these theories *microscopic* in contrast to the first of theories, which we call *macroscopic*. In this section we discuss microscopic theories of domain walls focusing on the most addressed in the literature examples of BaTiO_3 and PbTiO_3 ferroelectrics.

It was the microscopic approach that was used in the first theoretical studies of domain walls in ferroelectrics (Kinase and Takahasi, 1957). In early papers treating the problem on the microscopical level (Kinase and Takahasi, 1957; Kinase et al., 1970; Lawless, 1968), the authors addressed domain walls in tetragonal BaTiO_3 in terms of refinements of the classical Slater model (Slater,

1950). In these papers, the Ti displacements were treated as the main bearer of the ferroelectric polarization whereas the ferroelectric instability was described in terms of an interplay between the short range ionic repulsion and destabilizing “finite range” part of dipole–dipole interaction (with the contribution of the macroscopic electric field eliminated). In its original version formulated for the bulk material, the Slater model provided a reasonable description for the tetragonal phase in BaTiO_3 . When adapted to the problem of domain walls, the new element of the model was the necessity to evaluate the dipole–dipole interaction in the case of an inhomogeneous distribution of “ferroelectric” dipoles. All calculations performed using this method yielded “essentially zero thickness” for 180° walls in tetragonal BaTiO_3 . That is compatible with the prediction of the phenomenological theory which gives the wall thickness close to the lattice constant. For such thin walls, the wall energy naturally becomes sensitive to its position in the crystalline lattice. The energies of differently oriented and centered 180° walls in tetragonal BaTiO_3 have been evaluated by Lawless (1968). He found that the wall preferable orientation is (100) with the perovskite A-site (i.e., Ba) in its center (see Fig. 6.3.1 and Table 6.3.1 for explanation and more information). The B-site (i.e., Ti)-centered (100) wall was found to have a much higher energy. The evaluated energy of 180° walls of (110) orientation was also found to be a few times larger than that of the A-site-centered (100) wall. This result is very different from a very small (0.13%) anisotropy of the energy of this kind of wall predicted by the macroscopic theory (Dvorak and Janovec, 1965). At the same time, an appreciable anisotropy of the 180° -walls predicted by the microscopic theory is compatible with the experimental observations of Fousek and Safrankova (1965) who reported preferable (100) orientation for walls of this kind.

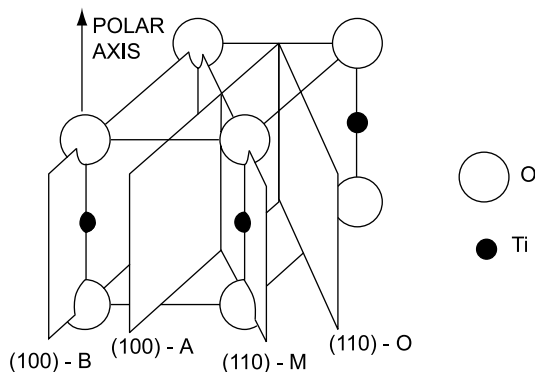


Fig. 6.3.1 Schematic drawing of different orientations and positions of a 180° wall in a tetragonal BaTiO_3 -like perovskite ferroelectric. Only the B-site (Ti) and oxygen ions lying just above and below the B-sites are shown. Notations of the planes correspond to those of Table 6.3.1. Reprinted with permission from Lawless (1968). Copyright (1968) by the American Physical Society

Table 6.3.1 Results of microscopic theories of domain walls

	(100)-A	(100)-B	(110)-M	(110)-O	Barr.	t_w/a	Temp.	Ref.
BaTiO ₃ 180°	1.4					~1	RT	Kinase and Takahasi (1957)
	1.52	47.9	45.3	10.3	46	~1	RT	Lawless (1968)
	16					1.4	RT	Padilla et al. (1996)
BaTiO ₃ 90°			22.5	36.4	14	9–10	RT	Kinase et al., (1970)
PbTiO ₃ 180°	100	220			120	~1	0 K	Poykko and Chadi (1999)
	132	169			37	~1	0 K	Meyer and Vanderbilt (2002)
PbTiO ₃ 90°			35		1.6	1.3	0 K	Meyer and Vanderbilt (2002)

Columns 2–4 give the energy of the walls as a function of their orientation and the position of their central plane: A and B indicate the planes passing through A and B perovskite sites; M indicates a plane passing through the ions of metals; O indicates a plane passing through the oxygen ions only. Column “Barr.” gives the height of the Peierls barrier. All energies are given in mJ/m². The rest of the columns give the wall thickness normalized to the lattice constant, temperature, and the references

The refined Slater model has also been used for the description of 90° walls in tetragonal BaTiO₃ by Kinase et al. (1970). They have evaluated the energy and thickness for the walls centered on (110) plane containing metals and (110) plane containing only oxygens. The wall of the later type was found to be more energetically favorable. The theory predicted rather thick 90° walls (about 10 lattice constants).

Recent developments of ab initio calculations of crystalline solids make possible more involved considerations of domain wall in ferroelectrics. Two approaches have been employed in these considerations, which can be called true ab initio approach and method of effective Hamiltonian.

The ab initio approach is readily applicable in the case where the ferroelectric phase of interest is favorable at zero temperature. In this approach, the parameters of the wall at zero temperature are calculated using the first-principle pseudo-potential method based on density functional theory (Payne et al., 1992). The structure of the wall is determined by minimizing (with respect to ionic displacements) the total energy of the system containing the wall; the wall energy is found by comparing the energy of the system with the wall and without it. The computer facilities typically enable calculations for systems (supercell) containing up to 15 unit cells of the material with periodically boundary conditions. This technique has been employed for modeling domain walls in PbTiO₃ by Poykko and Chadi (1999) and by Meyer and Vanderbilt (2002). Both groups found that, for (100) 180° walls have minimal energy if they are A-site centered (see Table 6.3.1). This preferable position of the wall is the same as in the aforementioned calculations for BaTiO₃. On the same basis, 90° walls in PbTiO₃ have been addressed by Meyer and Vanderbilt (2002). The wall energy has been found some four times smaller than

for the 180° wall. The activation barrier for the wall motion (the Peierls barrier) was calculated to be much smaller than the wall energy (1.6 compared to 35 mJ/m^2). Both kinds of walls have been found atomically thin. The results of calculations by Meyer and Vanderbilt for the 180° wall are illustrated in Fig. 6.3.2 where the ferroelectric polarization is presented as a function of the distance across the wall. The offset of the Pb position shown in this figure has been estimated as 0.6 \AA . This result is compatible with that conditioned by the flexoelectric effect in the continuum theory (Sect. 6.2.2). However, at present, it is not clear how quantitative comparison of these results can be done.⁶

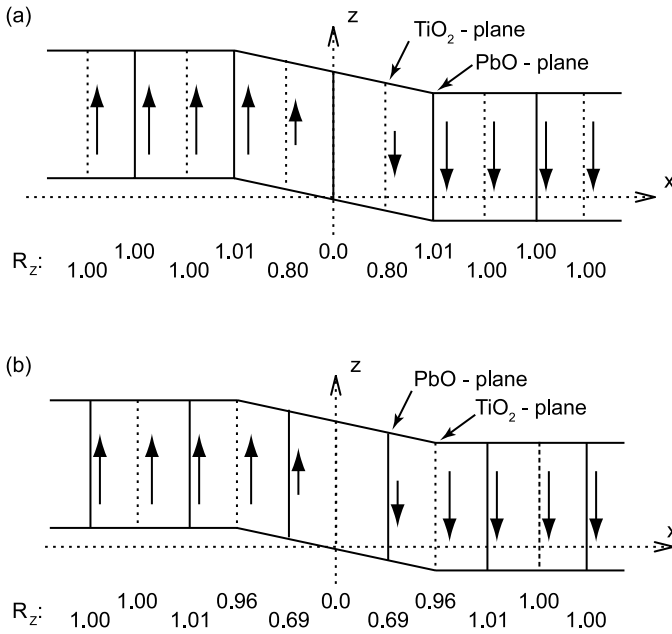


Fig. 6.3.2 Change of polarization across the Pb-centered (a) and Ti-centered (b) 180° walls calculated for PbTiO_3 at 0 K . R_z denotes the polar distortions of each lattice plane in the z -direction, in the units of the distortion associated with the bulk spontaneous polarization. The arrows indicate the sense of these distortions in the metal-oxide planes. The lengths of the arrows are proportional to the magnitudes of the distortions. Reprinted with permission from Meyer and Vanderbilt (2002). Copyright (2002) by the American Physical Society

⁶ The problem is that the optical displacements of the ions (or internal strains) are by definition defined to within an arbitrary constant (see, e.g., a detailed discussion of Tagantsev, 1991). This makes difficult separation between the optical and acoustical displacements (which enter the deformation tensor) on the two sides of the wall. Without this separation, one cannot tell what mechanical off-set corresponds to a given profile of atomic displacements. In Meyer and Vanderbilt (2002), this separation has been postulated and mechanical offset of 0.04 \AA across the wall has been calculated. However, the interpretation of this result is not clear because of the apparent ambiguity of the aforementioned separation.

Another prediction of the *ab initio* calculations (Meyer and Vanderbilt, 2002) is the offset of the electrostatic potential at 90° walls associated with nonzero longitudinal component of the polarization in the wall. This prediction is qualitatively different from that of the continuum theory (mentioned in Sect. 6.2.3 in the context of 90° walls in BaTiO_3). According to the continuum theory (Darinskii and Fedosov, 1971) the bound charge related to the nonzero longitudinal component of the polarization forms two back-to-back double electric layers which do not create a potential offset at the wall (cf. Sect. 6.2.3).

The second *ab initio* technique, the method of effective Hamiltonian, is summoned when the ferroelectric phase of interest exists only at finite temperatures, which is the case of tetragonal phase in BaTiO_3 . The idea of this method is to calculate the energy of the crystalline structure as an expansion in terms of a limited number of atomic displacements in a unit cell (counted from the parent cubic structure) and components of the strain tensor. The coefficients of this expansion are calculated by using the first-principle approach mentioned above. The equilibrium state of the system is further determined by using Monte-Carlo simulations with the Hamiltonian obtained. This method has been successfully applied to modeling the sequence of the phase transition in the single domain BaTiO_3 (Zhong et al., 1995). Using this method, the structure and energy not only of the ground state but also that of a metastable state containing a domain wall can be determined. Calculations performed in terms of this approach (Padilla et al., 1996) gives for the energy of 180° walls in BaTiO_3 a value of 16 mJ/m^2 which is some 10 times larger than those of the earlier calculations (see Table 6.3.1). The same authors have found the (100) walls are atomically thin and have lower energy when centered on A-site plane. These results agree with those of the earlier calculations in terms of the refined Slater model.

6.4 How Flat Is the Wall?

Considering a ferroic domain wall one reasonably poses a question of how far is its real shape from an ideally flat surface. It is clear that a flat domain wall which crosses an ideal crystalline ferroic can adjust its orientation and position with respect to the crystalline lattice to correspond to the absolute energy minimum of the system “crystal with a wall.” This means that, at zero temperature and in a defect-free crystalline material, domain walls in ferroics should be perfectly flat. However, at finite temperature and in a real crystal containing defects, this may not be true. Actually, strictly speaking this is never true since both temperature fluctuations and defects situated close to the wall will inevitably locally bend it. When domain wall deviates from its ideally flat state one speaks about wall *roughening*.

To describe the roughening effect, one uses the scheme that we explain in terms of a two-dimensional model. In this model, the two adjacent domains correspond to two areas on the plane and the domain wall dividing the domains

corresponds to a linear boundary dividing the areas. The finite surface energy of the wall in this case corresponds to a finite linear tension of this boundary. At 0 K in a defect-free crystal, because of this linear tension the straight “state” of the boundary is energetically favorable. The temperature and defects will roughen the boundary, i.e., make it to deviate from the straight “state.” The notions of the *rough* and *flat* walls can be introduced by considering a segment of the boundary of the length L and look for a rectangle of this length which in a symmetric way covers an essential fraction (e.g., 50%) of this segment (see Fig. 6.4.1). The width of the found rectangle is denoted as w . Clearly, for very small L , the width w will somehow increase with increasing L . However, with further increase of L two cases are possible: (i) w tends to a finite limit and (ii) w keeps increasing at $L \rightarrow \infty$. The boundary is called *flat*, when it corresponds to the first case and *rough* in the second case. This scheme can be readily generalized to the three-dimensional situation corresponding to a wall in a ferroic crystal. In this case, to characterize the wall roughening, the domain wall is to be essentially covered by a parallelepiped. The above definition of the roughening effect does not exactly correspond to its strict mathematical definition, which we will give below in the text, though it is practically equivalent to it.

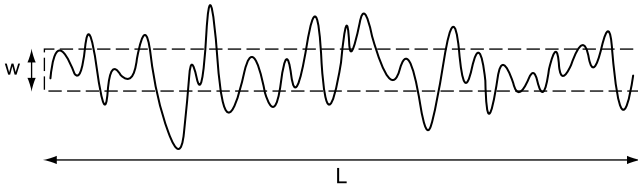


Fig. 6.4.1 Schematic drawing of a segment of length L of a one-dimensional domain wall which deviates from its flat (straight) state. The width of the rectangle which covers some 50% of the curved length of this segment is denoted as w

The problem of ferroic domain wall roughening makes a special case of the problem of interface roughening. More general, it is the problem of roughening of the so-called topological defects (Chaikin and Lubensky, 1995). This problem covers the behavior of different systems. The roughening issues of liquid/vapor interfaces, dislocations, crystal facets, and magnetic flux vortices in superconductors have been intensively studied by theoreticians and experimentalists (see, e.g., Brazovskii and Nattermann, 2004). The general theoretical approach to the problem is readily applicable to the case of ferroic domain wall, however, its implication in this case have been rarely discussed (Kolomeisky et al., 1990; Nattermann, 1983). The experimental studies of the ferroic walls in the context of roughening phenomena are also very limited. However, we believe that the basic knowledge on the roughening phenomena may be useful for the researches working in the field of ferroic domains. This has motivated the inclusion of this

section in the book. In this section, we will summarize the implication of the general theory of the interface roughening to the case of ferroic domain wall, elucidate some of the results in terms of simple scaling arguments, and discuss the experimental situation. More detailed and advanced discussion of the matter can be found, e.g., in the review paper by Brazovskii and Nattermann (2004).

To finish this introductory text to this section we would like to mention that, in application to ferroic domain wall at rest, the roughening problem appears to be rather academic. At the same time, a treatment essentially based on the roughening approach has been found extremely fruitful for the problems of domain pinning and creep. In this context this section makes a basis for the discussion of an issue of high practical importance, namely, the role of defects in switching, which will be addressed in Chap. 8.

6.4.1 Mathematical Problem

For the mathematical description of roughening effect, the following scheme is used (Chaikin and Lubensky, 1995). One considers the deviation $w(x_1, x_2)$ of the wall from its flat position, with (x_1, x_2) being the in-plane Cartesian coordinates of the considered point on the wall. If the mean square of the difference $w(x_1, x_2) - w(0, 0)$ increases without saturation with increasing $|x_1|$ or/and $|x_2|$, then one says that the wall is rough, otherwise one says that the wall is flat. To mathematically quantify the roughness of the wall one introduces the notion of *roughness* or wandering exponent ζ . For the case of an in-plane isotropic wall, it is introduced by the relation

$$w^2(L) \equiv \left\langle [w(x_1, x_2) - w(0, 0)]^2 \right\rangle \propto L^{2\zeta} \quad \text{at } L \rightarrow \infty, \quad (6.4.1)$$

where L is the length of the (x_1, x_2) vector and $\langle \dots \rangle$ stands with thermodynamic averaging or averaging over defect configurations. If $\zeta \geq 0$, the wall is rough, the case of $\zeta = 0$ formally corresponding to the case of logarithmic dependence. In the case of in-plane wall anisotropy, in a similar way, one can introduce the exponents ζ_1 and ζ_2 corresponding to the limits $|x_1| \rightarrow \infty$ at $x_2 = 0$ and $|x_2| \rightarrow \infty$ at $x_1 = 0$, respectively.

The absolute value of the typical wall wandering and the wall roughness exponent are contorted by many factors. These are the temperature, local surface energy of the wall, additional electrostatic and/or elastic energy arising when the local orientation of the wall deviates for that permissible (electrically and mechanically), Peierls potential (see Sect. 8.4), and defects.

In the following, when discussing the impact of defects we will consider only the case of point defects. Two types of defects are commonly distinguished: random field (RF) defects and random bond (RB) defects (see, e.g., Levanyuk and Sigov, 1988). The energy of an RF defect is different for different domain

states whereas the energy of an RB defect is the same for all domain states but it is different when the defect is in the bulk of a domain and in a domain wall. When an RF defect is crossing the plane of a domain wall, the variation of the energy of the system is step-like, whereas in the case of an RB defect it is a variation having the form of a smeared δ function. This is illustrated in Fig. 6.4.2.

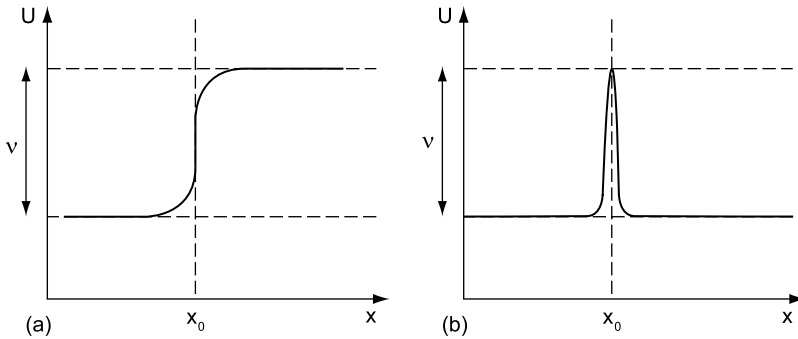


Fig. 6.4.2 Schematic plot of the energy of a domain wall $U(x)$ as function of the distance $x - x_0$ between the wall and a defect: (a) random field (RF) defect and (b) random bond (RB) defect

Examples of RF defects are well known for perovskite ferroelectrics (e.g., BaTiO_3 and $\text{Pb}(\text{Zr},\text{Ti})\text{O}_3$). In these materials, a B-site substitution with an ion of smaller valence (e.g., Mn^{+3} for Ti^{+4} in BaTiO_3 ; see Sect. 8.6.1) when compensated with an oxygen vacancy creates an electrical dipole serving as an RF defect. The examples of RB defects have not been discussed for ferroelectrics though one may expect appearance of this kind of defects as a result of isovalent substitutions.

6.4.2 Nonferroelectric/Nonferroelastic Walls

We start from the simplest case of the wall separating domains which cannot be distinguished neither by spontaneous polarization nor by spontaneous strain. Examples of such walls are provided by domain wall in high-order ferroics and by antiphase boundaries in materials exhibiting a transition with unit cell multiplication. A change of orientation of such walls is not associated with the appearance of macroscopic electric or elastic fields, in other words, they are electrically and mechanically permissible for any orientation. Walls of this kind are “flattened” by the surface tension and the Peierls crystalline potential. According to existing theories (see, e.g., Chaikin and Lubensky, 1995), in a defect-free crystal, the competition between thermal fluctuations and the flattening factor leads to the so-called roughening phase transition: At low

temperatures the wall is localized in one potential minimum of the Peierls potential whereas above a certain transition temperature the wall becomes “logarithmically” rough. Well above the transition, the average (6.4.1) characterizing roughness can be found as

$$w^2(L) = \frac{k_B T}{\pi \sigma_w} \ln(L/a), \quad (6.4.2)$$

where a is the lattice constant and σ_w is the surface energy of the wall per unit area, which is taken isotropic so that the energy of the bent wall can be written as the following integral over the wall area:

$$U = \sigma_w \int \left[1 + \frac{1}{2} (\Delta w)^2 \right] dS \quad (6.4.3)$$

This situation corresponds to the roughness exponent $\zeta = 0$.

A wall in an ultra thin film where only the in-plane roughness matters corresponds to an effectively one-dimensional problem. In this case, the integral in Eq. (6.4.3) can be treated as one dimensional. The change of the effective dimension of the problem strongly changes the situation; now the wall is rough at any temperature with the roughness exponent $\zeta = 1/2$. Specifically, one finds

$$w^2(L) = \frac{k_B T L}{\pi \sigma_w h}, \quad (6.4.4)$$

where h is the film thickness.

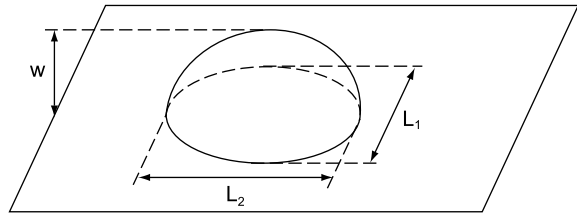
The derivation of the above relations is out of the scope of this book. However, to give the physical idea behind the trends controlling the roughening phenomena, we will obtain the roughness exponents using the so-called “Fluery-type” or “Imry–Ma” scaling arguments (Kardar, 1987). In this approach, one evaluates the energy, U_b , associated with a small bulge on a wall. Such a bulge is schematically shown in Fig. 6.4.3. In one-dimensional case, simple geometrical arguments yield⁷

$$U_b \cong \sigma_w \frac{h}{L} w^2. \quad (6.4.5)$$

From this relation, it is seen that for the same energy, larger displacements of the wall w can be obtained with a larger in-plane size of the bulge L . This expresses the trend of the wall to roughening. The roughening law is fairly

⁷ Here and thereafter the use of sign ‘ \cong ’ means that we are dealing with rough order-of-magnitude estimates. The exact relations can contain numerical factors varying from a few tenths to a few units.

Fig. 6.4.3 Schematic drawing of a bulge on a domain wall



reproduced by the relation between w and L for a typical thermal fluctuation with the energy $k_B T$. Indeed, the relation $U_b \cong k_B T$ yields

$$w^2 \cong \frac{k_B T L}{\sigma_w h} \quad (6.4.6)$$

in qualitative agreement with Eq. (6.4.4).

For a normal two-dimensional wall in a three-dimensional sample the energy of the bulge (shown in Fig. 6.4.3 with $L_1 = L_2 = L$) can be evaluated as⁸

$$U_b \cong \sigma_w w^2. \quad (6.4.7)$$

In this case, the relation $U_b \cong k_B T$ gives $w^2 \cong k_B T / \sigma_w$ which, being interpreted as an indication to the absence of the “power law” roughening, is also compatible to Eq. (6.4.2).

The above results for the exponents of thermal roughening, ζ_{th} , can be presented by the formula

$$\zeta_{th} = \frac{2-d}{2}. \quad (6.4.8)$$

where d stands with the effective dimension of the wall, i.e., $d = 2$ for a normal wall and $d = 1$ for the effectively one-dimensional situation in ultra thin films.

Investigations of systems with defects showed that the thermal roughening effect discussed above is substantially weaker than that due to the defects. Let us show this for the case of RF defects using the scaling arguments. Consider a flat two-dimensional wall in a material with point defects, the average distance between them being D . The energy of such a wall may be reduced by making a bulge on it. The reason for it is as follows. By making on the wall a bulge with dimensions w and L (see Fig. 6.4.3 with $L_1 = L_2 = L$), one changes the energy of $N \cong L^2 w / D^3$ defects. Because of the randomness of their orientations, on average, the variation of the energy of the defects is zero to within $\pm v \sqrt{N}$, where

⁸ Here, for simplicity, we consider the case of a domain wall with the isotropic surface tension. If the surface tension is anisotropic, obviously for the optimal bulges $L_1 \neq L_2$. In this case, however, $L_1 \propto L_2$ and one can readily show that the roughness exponent will be the same as in the case of the isotropic surface tension.

v is the coupling energy per defect. Thus, by bulging the wall may reduce the energy of the defects in the crystal by a value of

$$U_{\text{RF}} \cong v \left(\frac{L^2 w}{D^3} \right)^{1/2}. \quad (6.4.9)$$

However, this reduction is limited by the extra surface energy of the bulge, which is given by Eq. (6.4.7). The relation between the dimensions of the optimal bulge can be found by minimizing the sum of the surface and defect energy, Eqs. (6.4.7) and (6.4.9). This relation reads

$$w \cong \frac{1}{D} \left(\frac{v}{\sigma_w} \right)^{2/3} L^{2/3}. \quad (6.4.10)$$

According to this relation, a deviation of the wall from its flat state is energetically favorable and the larger the wall segment, the stronger this deviation. This relation is also interpreted as the roughening law with the exponent $\zeta = 2/3$. Thus, we see that the roughening effect of defects is stronger than that of thermal fluctuations.

Similar consideration gives for the one-dimensional case $\zeta = 1$. These results for the case of RF defects are confirmed by a rigorous analysis. They can be written in the general form

$$\zeta_{\text{RF}} = \frac{4-d}{3}, \quad (6.4.11)$$

where d stands for the dimension of the wall ($d = 2$ for the wall in a bulk crystal and $d = 1$ for the effectively one-dimensional situation).

Random bond (RB) defects are also more efficient in roughening than thermal fluctuations. In this case, the roughness exponent is linked to the dimension of the wall as

$$\zeta_{\text{RB}} = \frac{4-d}{b}. \quad (6.4.12)$$

The value of parameter $b = 4.5$ has been rigorously established only for the one-dimensional case. For the case of a wall in a bulk crystal ($d = 2$), there is no consensus on the value of b : Values between 4 and 5 have been obtained in different approaches (Brazovskii and Nattermann, 2004; Kardar, 1987; Nattermann et al., 1990).

6.4.3 Walls in Ferroelectrics and Ferroelastics

The key feature of ferroelectric and ferroelastic domain walls is that their bending is associated with the appearance of macroscopic (electric and elastic)

fields. This effect makes an additional flattening factor. Let us illustrate this point in terms of the scaling arguments for the case of RF defects interacting with ferroelectric and ferroelastic walls.

Consider the roughening of a 180° ferroelectric/nonferroelastic wall. Bearing in mind the experience with macroscopic bulging of this type of wall, which is known to be strongly anisotropic, we assume for the moment that the optimal bulge should be elongated in the direction of the spontaneous polarization to reduce the depolarizing energy. Thus it should be characterized with three spatial scales, L_1 , L_2 , and w ($L_2 \gg L_1 \gg w$), as shown in Fig. 6.4.3. For this configuration, the expression for the surface and RF energies, Eqs. (6.4.7) and (6.4.9), can be generalized to the following forms:

$$U_b \cong \sigma_w w^2 \frac{L_2}{L_1} \quad (6.4.13)$$

and

$$U_{\text{RF}} \cong v \left(\frac{L_1 L_2 w}{D^3} \right)^{1/2}. \quad (6.4.14)$$

The electrostatic energy associated with the depolarizing field can be roughly estimated as that of an elongated ellipsoid with the semi-axes L_1 , L_2 , and w ($L_2 \gg L_1 \gg w$):

$$U_{\text{dep}} \cong g \frac{L_1^2 w^2}{L_2} \quad \text{with} \quad g = \frac{P_S^2}{\epsilon_0 \kappa_a}, \quad (6.4.15)$$

where P_S and κ_a are the spontaneous polarization and relative permittivity of ferroelectrics in the direction normal to the spontaneous polarization.⁹ Optimizing the sum of the surface and depolarizing energy one finds that L_2 scales as $L_1^{3/2}$. Further optimization which takes into account the RF energy leads to the relations between the height of the bulge and its in-plane dimensions: $w \propto L_1^{1/2}$ and $w \propto L_2^{1/3}$. Thus, following the arguments used in the previous consideration we conclude that, in the case of ferroelectric wall, the roughening is anisotropic with the exponents $\varsigma_1 = 1/2$ and $\varsigma_2 = 1/3$. This implies, as one can expect, a stronger roughening in the direction normal to the spontaneous polarization.

The above analysis, however, has been performed under the assumption that the optimal bulge is essentially elongated, i.e., $L_2 \gg L_1$. This is valid only for distances which are large enough, specifically for

$$L_2, L_1 \gg L_{\text{dip}} = \sigma_w / g. \quad (6.4.16)$$

⁹ Estimate (6.4.15) corresponds to the estimate of the depolarizing energy associated with a bulge on the wall used by Miller and Weinreih (1960).

For distances smaller than L_{dip} the depolarizing energy is not essential in the total energy balance so that the result for nonferroelectric/nonferroelastic wall, Eq. (6.4.10), becomes valid. This can be checked, e.g., by comparing the surface and electrostatic contribution to the energy, Eqs. (6.4.13) and (6.4.15), at $L_2 \propto L_1^{3/2}$. Thus, in general, ferroelectric/nonferroelastic walls can exhibit a crossover in the roughness exponents from $\zeta = 2/3$ at $L \ll L_{\text{dip}}$ to $\zeta_1 = 1/2$ and $\zeta_2 = 1/3$ at $L \gg L_{\text{dip}}$.

A ferroelastic wall is yet more rigid than the purely ferroelectric one because the orientation of the former, when it is homogeneously flat, is fully controlled by conditions of mechanical domain compatibility whereas the conditions of domain compatibility only partially controls the orientation of the ferroelectric wall (keeps it parallel to the direction of the spontaneous polarization). To evaluate the flattening effect due to the elastic energy, one should incorporate it into the total energy balance. For an isotropic bulge (shown in Fig. 6.4.3 with $L_1 = L_2 = L$), this energy can be estimated as¹⁰

$$U_{\text{el}} \cong c\varepsilon_s^2 Lw^2, \quad (6.4.17)$$

where ε_s and c stand for typical values of the spontaneous deformation and elastic modulus. If L is large enough, i.e.,

$$L \gg L_{\text{el}} = \sigma_w / (c\varepsilon_s^2), \quad (6.4.18)$$

the surface energy given by Eq. (6.4.7) can be neglected comparing to this contribution. Now, the relation between w and L for an optimal bulge can be found by equating U_{el} and U_{RF} , Eq. (6.4.9), to find w independent of L . This implies $\zeta = 0$. Thus, we see that the “power law” roughening effect of RF is suppressed by the ferroelastic nature of the wall. Thus, similar to the previous case, one finds a crossover in the roughness exponents from $\zeta = 2/3$ at $L \ll L_{\text{el}}$ to $\zeta = 0$ at $L \gg L_{\text{el}}$.

The theoretical results obtained on the roughening of ferroelectric and ferroelastic domain walls can be summarized as follows. The long-range interactions contributing to the energy of the bent walls make roughening of this kind of walls weaker or suppress it. In the case of thermal roughening it is fully suppressed (Lajzerowicz, 1980)¹¹ for both ferroelastic and ferroelectric walls. For both the thermal and defect-driven roughening of ferroelectric–nonferroelastic walls in the direction normal to the spontaneous polarization, the roughness exponents formally correspond to a change of the dimension of the interface from $d = 2$ to $d = 2.5$ in Eqs. (6.4.8), (6.4.11), and (6.4.12).¹² In the case of ferroelastic wall, $\zeta = 0$

¹⁰ This estimate can be obtained, for example, using the results on the oscillation spectrum of ferroelastic walls (Nechaev and Roshchupkin, 1989).

¹¹ The conclusion about suppression of thermal roughening for ferroelastic wall obtained in this paper is correct; however, the calculations have been performed for the correlation function qualitatively corresponding to a wall in a ferroelectric/nonferroelastic.

¹² The result for the RB case is not rigorously justified.

for both RF and RB cases, which formally correspond to a change of the dimension of the interface from $d = 2$ to $d = 4$ in Eqs. (6.4.11) and (6.4.12). All these conclusions are valid when the roughening is considered at distances larger than certain spatial scales L_{dip} and L_{el} ; at smaller distances the long-range interactions do not essentially affect the results obtained without these interactions taken into account.

The above results can be applied to both bulk ferroics and ferroic thin films. However, in the case of thin films, the roughening of ferroelectric and ferroelastic domain walls can be affected by the electrostatic and mechanical boundary conditions. Here, different roughening regimes are possible depending on the relation between the typical spatial scales of the problem. We will not discuss these regimes though the aforementioned boundary conditions can be readily incorporated in the above analysis.

6.4.4 Experimental Data on Roughening of Ferroic Domain Walls and Experimental Observations

Experimental data which may be related to roughening of ferroic domain walls are very scarce.

First attempt to analyze data on ferroic domain walls in terms of the roughening effect has been done by Bruce (1981). He developed a theory of elastic (e.g., X-ray or neutron) scattering from a wall exhibiting the thermal “logarithmic” roughening (see Eq. (6.4.2)). The theoretical prediction on the angular dependence of the scattering intensity has been compared to the data on the neutron scattering from a domain wall in $\text{Pb}_5\text{Ge}_3\text{O}_{11}$. The qualitative similarity between the theoretical prediction and experimental data has been interpreted as a possible evidence of a roughening phase transition occurring at the domain wall.

A possibility of the direct observation of domain wall bending on nanometer scale with piezoelectric force microscope (PFM) inspired experimental investigation of domain wall roughness in PZT thin films in the group of Triscone (Paruch et al., 2005). In tetragonal epitaxial films of thickness 50–100 nm, ferroelectric 180° domains of area of 10–20 μm^2 have been written with an AFM tip loaded with a dc voltage. The profile of the domain boundaries has been imaged using a PFM. The mean square deviation of the boundary from the flat position w has been evaluated to find it an increasing function of the length L of the wall segment tested for $L < 100$ nm; for larger L , a saturation of w has been observed. The w – L relation, obtained at $L < 100$ nm, has been considered as a manifestation of the roughening effect, whereas the saturation at larger L has been attributed by the authors to the incapability of the large wall segments to reach the true energy minimum. From the analysis of $w(L)$ dependence at $L < 100$ nm, a roughness exponent

of ≈ 0.26 has been estimated. This value has been interpreted as a fingerprint of the roughening caused by RB defects. Rationalizing this value in terms of Eq. (6.4.12), one sets $d = 2.5$ (because of ferroelectric/nonferroelastic nature of the wall) to find $b \approx 5.8$ which is not far from the theoretical estimate.

Chapter 7

Switching Properties: Basic Methods and Characteristics

7.1 Introduction

We approach one of the main issues of the investigations of ferroics: their properties conditioned by dynamic domain phenomena. It is these properties that play the decisive role in many recent applications. But before entering this subject in Chap. 8, we wish to describe experimental methods used for obtaining integral data about such phenomena. We have in mind the data that reflect domain wall motion and other mechanisms involved in the processes in which a ferroic sample changes its domain state under the action of external forces. These mechanisms involve possible nucleation of new domains, growth of nucleated or of already existing domains, and their coalescence. Such integral data provide the basic information on characteristics of the switching process as a whole, like its speed, its dependence on the applied force, on the boundary conditions, or on temperature. In this chapter we describe the basic methods to obtain such data. We will mainly concentrate on the basic characteristics: $P(E)$ dependences for ferroelectrics and $\varepsilon(\sigma)$ dependences for ferroelastics or alternatively $\varepsilon(E)$ dependences for ferroics which exhibit simultaneously ferroelastic and ferroelectric properties.

In some cases it may be difficult to measure the primary order parameter as a function of the conjugate force, such as the $P(E)$ dependence for ferroelectrics. Then to obtain some information on the switching process one may rely on measuring other properties which can be believed to be linearly related to the order parameter. As an example we may mention the measurements of the pyroelectric coefficient dependence on the applied electric field, in the form of a hysteresis loop, for ultrathin films of ferroelectric polymers (Ducharme et al., 1997). There it was difficult to detect directly the small switched charge while the pyroelectric coefficient was of a large enough magnitude to be detected. This method of material characterization by measuring properties which are linearly coupled to the order parameter has become popular since the very beginning of the research of ferroics. Such data may be useful from the point of view of applications. In many cases it is relatively easy to measure macroscopic quantities which are coupled to a higher power of the order parameter η . If they are proportional to η^2 we obtain the so-called butterfly hysteresis loops.

We stress that this chapter covers selected aspects of measuring switching characteristics of a considerable part or of the whole sample. Here we discuss neither “local switching” phenomena such as creating a new small domain by local application of electric field or mechanical stress nor methods for observing motion of individual domain walls.

7.2 Ferroelectric Hysteresis Loop

In Fig. 7.2.1 the basic circuit is shown for recording the switching process in a ferroelectric sample. It is often referred to as the Sawyer–Tower circuit, after the authors who were the first to use this system (Sawyer and Tower, 1930) when investigating polarization reversal in Rochelle salt crystals. Here the applied ac voltage U is divided between the sample and the capacitor C connected in series. On the horizontal axis of the oscilloscope we wish to record the magnitude of electric field applied to the sample alone. To fulfill this requirement the value of C has to be large compared to the effective capacitance (the ratio “the maximum charge over the maximum voltage applied”) of the sample. On the vertical axis, the recorded voltage corresponds to the instantaneous value of charge Q_P representing the dielectric displacement $D = \varepsilon_0 E + P$. In most ferroelectric materials, the first term is negligible compared to induced polarization. For this reason, the recorded hysteresis loop is interpreted as the dependence $P(E)$ rather than $D(E)$.

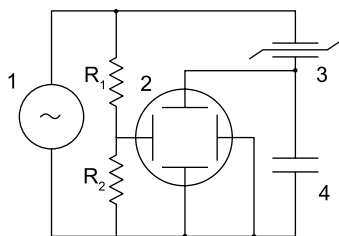


Fig. 7.2.1 The Sawyer–Tower circuit: 1, source of ac voltage; 2, oscilloscope; 3, capacitor with ferroelectric sample; 4, additional capacitor. $R_1 > R_2$ —resistors of the voltage divider

It is obvious that if the sample is lossy, the conductive current flowing through it has a component which when integrated on the capacitance C produces charge Q_{con} such that an ellipse $Q_{\text{con}}(E)$ is superimposed on the recorded hysteresis loop. This ellipse, in addition, is influenced (rotated in the charge–voltage coordinate system) by stray capacitances of the experimental setup. These effects may distort the recorded data on the $D(E)$ loop of the ferroelectric and are unwanted; therefore, the ellipse of proper shape and orientation is to be subtracted from the total hysteretic response. Modified circuits which allow for such compensations were proposed by a number of authors (see, e.g., Roetschi, 1962; Gadkari et al., 1986; Sinha, 1965; Hatano et al., 1992; Diamant et al., 1957).

The classical Sawyer–Tower technique and its modifications still offer very effective and inexpensive tools for examining polarization reversal processes in ac fields. In recent years, in addition to these classical methods, alternative electronic schemes have been developed. This is the so-called virtual ground method which, for the first time, was suggested by Glazer et al. (1984). Nowadays, this method is widely used in connection with the expanding activities in the area of ferroelectric thin film memories. As an example, we mention the setup used by the Radiant Technologies, Inc. Systems and represented schematically in Fig. 7.2.2. In this configuration, the transimpedance amplifier maintains the terminal A at a virtual ground potential. Thus the sample is effectively “grounded” during the switching process. All charge that flows through it as a result of the applied voltage is collected by an integrator circuit. The voltage generated on the output of the integrator is then measured and displayed as a function of the applied voltage. The system makes it possible to measure accurately a large range of capacitance values at a large range of speeds. The capacitor in series with the sample required in the Sawyer–Tower circuit is abolished and thus the effects of possible parasitic impedances are eliminated. Probably the most important advantage of the system becomes effective when only one period of ac field is applied. In this case, in the classical Sawyer–Tower system, after the voltage returns to zero the charge that has been collected in the sense capacitor generates a voltage V_{back} which is in fact applied to the sample in the direction opposite to the last applied voltage. This can lead to “back-switching”: In part of the sample polarization can return back to its previous orientation. In contrast, in the virtual ground measuring system the V_{back} voltage is not generated: In the interval between the two subsequent periods of applied voltage, typically several seconds long, the sample is virtually short circuited and backswitching could only be initiated by an internal bias in the sample.

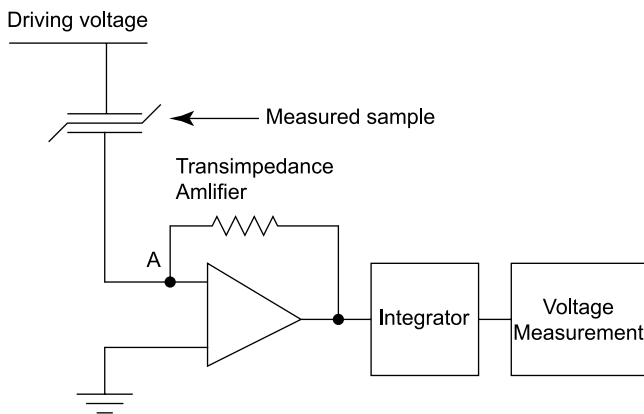


Fig. 7.2.2 The virtual ground measuring system (Radiant Technologies, RT6000HVS)

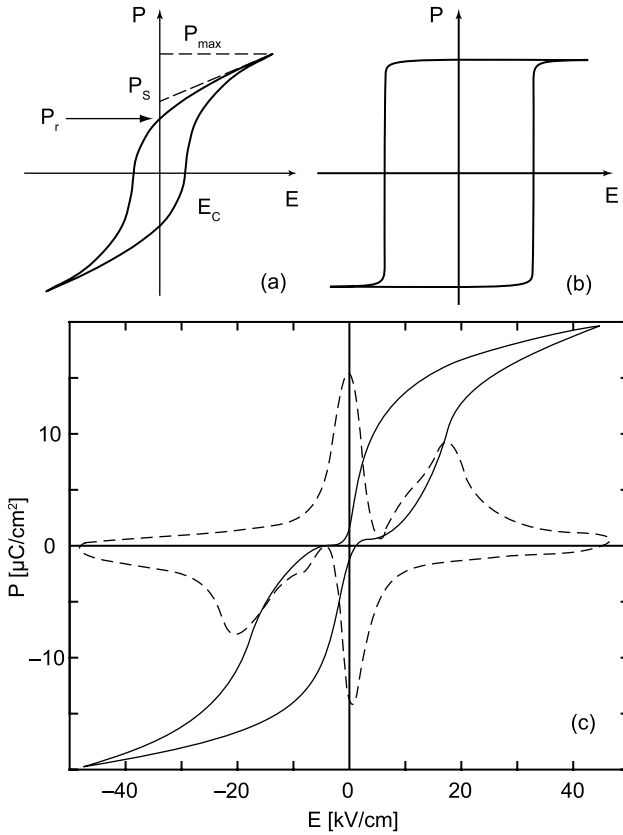


Fig. 7.2.3 (a) Conventional P - E hysteresis loop of a ferroelectric (schematically); (b) ideal hysteresis loop; and (c) double hysteresis loop and its derivative

It is now appropriate to specify the definitions of basic quantities used to characterize a ferroelectric hysteresis loop. A typical customarily observed $P(E)$ loop is represented in Fig. 7.2.3a when driven by a continuous ac field. It defines maximum and remanent polarizations P_{\max} and P_r as well as the coercive field E_c which corresponds to the points where $P \cong D = 0$. In general, the values of P_{\max} and P_r do not suffice to determine the value of spontaneous polarization P_s . However, if the loop is saturated, i.e., the branches of the loop merge before the tip of the loop, and if the driving field is not too high, the intersection of a tangent of the loop taken at its tip yields the value of P_s . The meaning of “not too high” is that the field does not result in appreciable nonlinearity of the lattice dielectric permittivity. This condition is not always met for characterization of thin films. There exist materials where P_s can be determined directly from the hysteresis loop. This is usually the situation of high-quality single crystals when the $P(E)$ loop is measured far below the phase transition. Such an “ideal loop” is shown in Fig. 7.2.3b and there is no doubt that the intersection with the vertical axis

defines the value¹ of P_S which equals both P_{\max} and P_r . Connecting the extreme points (i.e. $P_{\max}(E_m)$) of the curves taken at different field amplitudes, we obtain what is sometimes referred to, not quite logically, as the virgin curve.

As an example, we refer to the delightful hysteresis loops taken for TGS crystals by Nakatani (1972) and shown in Fig. 7.2.4. As the amplitude E_m of the applied field $E = E_m \sin \omega t$ increases, the shape of the $P(E)$ dependence changes from an oblong-like dependence to an ideal hysteresis loop.

The classical Sawyer–Tower method and its analogies have been customarily used to record hysteresis loops in the frequency region between 1 Hz and 1 kHz (see, e.g., Campbell, 1957; Shil’nikov et al., 1999a). It may be of interest to perform measurements at even lower frequencies. Unruh (1965) obtained reliable data for hysteresis characteristics of Rochelle salt and triglycine sulfate, based essentially on the classical method, at frequencies down to 10^{-2} Hz. In the same way, Shil’nikov et al. (1999b) measured hysteresis loops of TGS at frequencies between 0.05 and 90 Hz, for several field amplitudes; their data are reproduced in Fig. 7.2.5. At these frequencies, the experimentalists may face the problems connected with surface and bulk electrical conductivity of the specimen. Then the integral switching process at frequencies below 1 Hz may be investigated by measuring, instead of polarization itself, some quantities which are coupled to polarization in a known way and which are not affected by the electric current due to conductivity. As an example, we refer here to Abe’s (1964) measurements performed in *ac* fields of frequencies down to 4 mHz; the quantity measured as a function of applied field was the integrated intensity of polarized light passing through a sample. In the case of Rochelle salt this intensity can be shown to be proportional to the areas of reversed domains and thus to the average polarization.

Often, the registration of the $P(E)$ dependence offers information not only on the basic ferroelectric switching process but also on some more involved phenomena. Deformation of the hysteresis loop may give evidence of internal

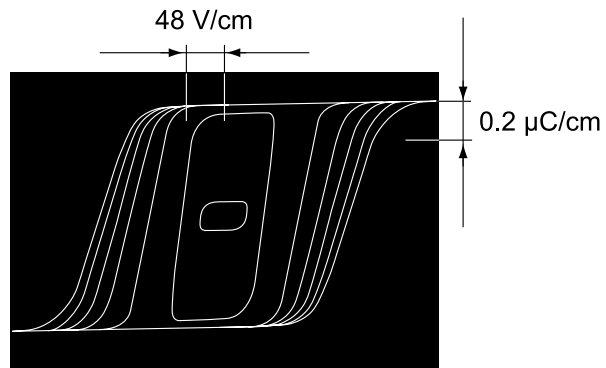


Fig. 7.2.4 Dependence of 60 Hz hysteresis loop shape of TGS on applied field, its amplitude being $E_m = 160, 320, 800, 1,600,$ and $3,200$ V/cm, successively from the internal one. Temperature -24.5°C . After Nakatani (1972)

¹ Or its projection, if the normal of a plate-like sample is not parallel to the ferroelectric axis.

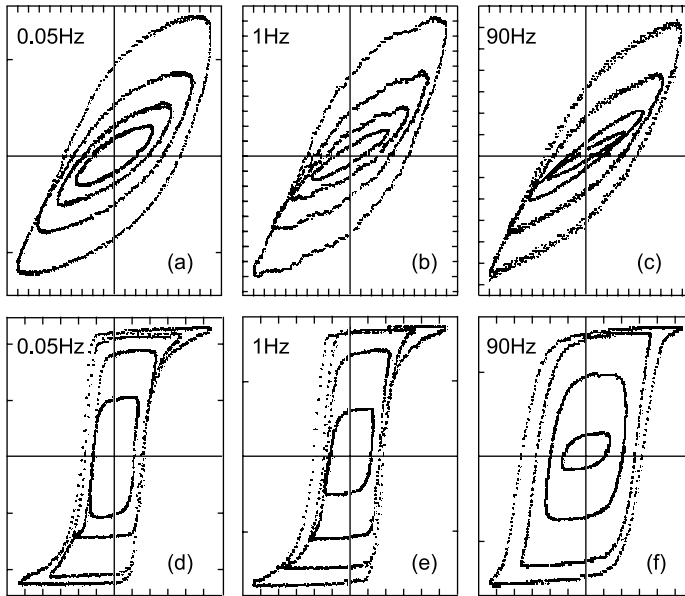


Fig. 7.2.5 Hysteresis loops of TGS crystals at 18°C demonstrating the influence of field amplitude and frequency. $E_m = 35, 55, 74,$ and 92 V/cm (a)–(c) and $E_m = 140, 230, 370,$ and 550 V/cm (d)–(f). Horizontal axes units: 10 V/cm (a)–(c) and 100 V/cm (d)–(f). Vertical axes units: 10^{-4} (a), 10^{-5} (b,c) and 10^{-2} C/m² (d)–(f). Reprinted with permission from [Shil'nikov, A.V., Pozdnyakov, A.P., Nesterov, V.N., Fedorikhin, V.A., Uzakov, R.E., The analysis of domain boundaries dynamics of TGS single crystals under the ac-Fields of low and ultralow frequencies, *Ferroelectrics*, **223**, 149 (1999)]. Copyright (1999), Taylor and Francis

biasing field and time changes of the loop shape demonstrate different kinds of ageing effects. Frequently the so-called double hysteresis loop is observed. It can be connected with the influence of lattice defects whose presence prefers a domain pattern with zero average polarization. As an example, Fig. 7.2.2c shows such loops for ceramic samples of BaTiO₃ doped with Fe (Hagemann, 1978). Alternatively, double hysteresis $P(E)$ loops are observed at temperatures just above T_{TR} in ferroelectrics with the first-order phase transition; they arise from inducing the ferroelectric phase by ac biasing field (Merz, 1953, Hatano et al., 1985a). This is a mechanism analogue to that responsible for the double ferroelectric loops in antiferroelectrics; it is not defect related.

In connection with the development of ferroelectric thin films it becomes usual to use just one period of a triangular ac voltage wave for switching characterization. Figure 7.2.6 shows an example of this kind of data recorded with an RT-6600S setup (Radiant Technology Inc.). It portrays the switching processes in PLZT thin films, annealed at different temperatures (Hirano et al., 1999). Here the triangular-shaped voltage consists of a number of short intervals during which the voltage is constant and the charge is integrated and

displayed in form of points. The discontinuous jump at zero voltage images the process taking place during the period between two subsequent cycles. Typically, the duration of the triangular pulse is 10 ms (corresponding to the frequency of 100 Hz) with 200 sampling points.

In the classical Sawyer–Tower circuit the capacitor C can be replaced by a resistor R . In this configuration, what is detected as a function of applied ac field $E = E_m \sin \omega t$ is the electric current

$$i = \frac{dD}{dt} = \frac{\partial D}{\partial E} \frac{\partial E}{\partial t} = \omega \frac{\partial D}{\partial E} \sqrt{E_m^2 - E^2} \tag{7.2.1}$$

Here the slope $\partial D/\partial E$ of the hysteresis loop is multiplied by the function $\omega\sqrt{E_m^2 - E^2}$, which is an ellipse. Thus, depending on the shape of the hysteresis loop and on the applied amplitude, the maximum current may not correspond to the maximum $\partial D/\partial E$. If the data are taken applying a triangular voltage wave so that within one half-period the derivative $\partial E/\partial t$ is constant, then the curve of $i(E)$ corresponds to the real derivative of hysteresis loop. In this case and for a typical unconstricted loop the positions of its maxima are sometimes considered to represent the coercive fields. Since the slope $\partial D/\partial E$ may not reach its maximum exactly at $P = 0$, the value of the coercive field defined in this way can slightly differ from that defined above (Fig. 7.2.3).

It is useful to point out that the area of the hysteresis loop $D(E)$ determines the effective dielectric losses. Obviously, the density of energy lost in the sample during one cycle of period T is

$$\int_0^T iE dt = \int_0^T \frac{dD}{dt} E dt = \oint E dD \tag{7.2.2}$$

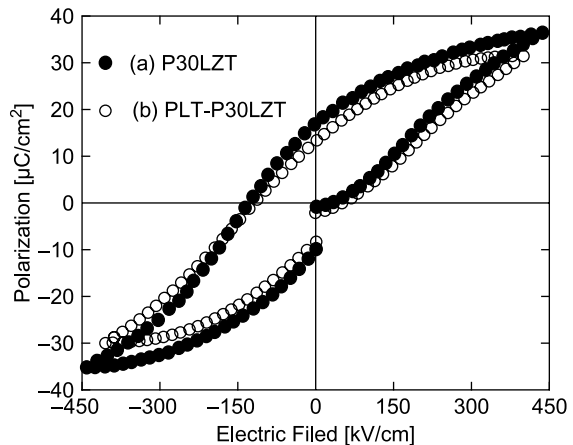


Fig. 7.2.6 Hysteresis loop of PLZT thin films obtained with the system shown in Fig. 7.2.2. After Harano et al. 1999

and the energy lost (or heat developed) in 1 s equals

$$Q = f \oint E dD. \quad (7.2.3)$$

At the same time, this loss of energy can be conveniently written in terms of the imaginary part κ'' of permittivity as

$$Q = \pi f \kappa'' E_m^2, \quad (7.2.4)$$

where E_m is the amplitude of ac field of frequency $f = 1/T$. Thus the imaginary part of effective permittivity can be related to the area of the loop:

$$\kappa'' = (1/\pi E_m^2) \oint E dD. \quad (7.2.5)$$

This equation implies the possibility of a cross-check of the hysteresis loop itself and the dielectric loss data.

At the end of this section we wish to discuss several artifacts and possible factors not related to the intrinsic properties of the ferroelectric material itself.

First, the surface conditions can seriously influence the obtained data. Thus the polarization reversal process can strongly depend on the coupling of the sample with electrodes. Janovec et al. (1960) showed that a BaTiO_3 crystal plate with two identical liquid electrodes showed a symmetric hysteresis loop with fast switching. With two identical indium electrodes the loop was also symmetric but switching was slower. The use of different materials for different electrodes led to an asymmetric loop, showing that a liquid electrode provided more favorable conditions for switching starting at that electrode. The existence of a surface layer located between the homogeneous sample and electrode has a tremendous effect on the switching properties, as demonstrated by Brezina and Fotchenkov (1964) and discussed by Drougard and Landauer (1959). Rosenman and Kugel (1994) showed experimentally that a vacuum gap or a thin teflon layer located between the sample and the electrode can seriously influence or fully suppress the switching process. These and similar factors have to be considered when interpreting experimental data on switching and we will come back to this problem in Chaps. 8 and 9.

Second, in a specific device, it may happen that the source of the applied voltage may not be able to provide the current required for the switching process to proceed fast enough as determined by its natural domain processes. This situation can be modeled by a resistor in series with the ac power supply. As a result, the large slope $\partial D/\partial E$ may be reduced so that the hysteresis loop is deformed.

Third, we wish to note that in exceptional cases, a hysteresis curve of the typical shape may be observed and yet the material could turn out not to be ferroelectric at all. If the dielectric response of a material is strongly nonlinear but non-

hysteretic and at the same time the sample is lossy, one obtains the $D(E)$ curve strongly resembling a hysteresis loop. This was, e.g., the case of $\text{LiN}_2\text{H}_5\text{SO}_4$ where seemingly properly shaped loops (Schmidt and Parker, 1972) were explained in terms of intrinsic protonic conductivity of this material. A similar situation was recognized for ceramic samples of TiTaO_3 and some other materials (Le Bihan et al., 1978). As pointed out by Scott et al. (1993), another example of “false” hysteresis curves is provided by polymeric electrets. Charges originating in mobile ions diffusing under applied voltage can slowly accumulate at the surfaces of plate-like samples of electrets, resulting in a bistable state whose orientation depends on the polarity of applied voltage. Thus seemingly the electrets can also be switched in polarity; however, the processes resulting in a measurable hysteresis curve are very slow (Sessler et al., 1980).

Fourth, one has to realize that, when studying the frequency dependences of the mentioned quantities E_C , P_{\max} , etc., at higher frequencies, the experimentalist may face the problem of self-heating. This is discussed in some detail in the following section.

7.3 TANDEL Effect

When studying the frequency dependence of coercive field, it was observed (see, e.g., Campbell, 1957) that E_C first increases but then, with further increasing frequency, it starts to decrease again. The explanation was based on the assumption that due to hysteresis losses (cf. Eq. 7.2.3) the sample heats up and approaches the Curie point so that the area of the transversed loop decreases. Later it was found by Shuvalov (1960) that at some critical frequency of the field applied to the Y -cut of triglycine sulfate crystal the sample increases its temperature with a jump.

Glanc et al. (1964) studied these effects in detail and found that when an ac voltage of high enough frequency is applied to the Y -cut of a TGS crystal, the specimen is heated to a temperature T_S close to T_C and the value of T_S is stabilized with respect to the ambient temperature T_A of the surroundings. This was explained by Dvorak et al. (1964) in general terms as the consequence of negative temperature coefficient of losses. The crystal is in a state of temperature autostabilization and since it reveals nonlinear properties it can be referred to as “temperature autostabilized nonlinear dielectric element” (TANDEL). In addition to TGS, the effect was later observed in a number of other ferroelectrics. We give a schematic insight into the phenomenon.

We know (Eq. (7.2.3)) that the rate of heat production Q_1 in the ferroelectric is proportional to the area of the $D - E$ hysteresis loop. It is also known the both height and width of the loop decrease on increasing temperature so that the loop area and Q_1 are decreasing functions of temperature. In the stationary state, the rate heat production Q_1 should be balanced by the heat dissipation into the ambient Q_2 , which is proportional to the difference $T_S - T_A$. The cycling of the

sample leads to an increase in its temperature but the negative temperature coefficient of losses (decrease of the loop area with increasing temperature) will result in temperature stabilization. The final temperature of the system is given by a solution to the equation satisfying the stability condition (Dvorak et al., 1964)

$$Q_1 = Q_2, \quad \partial Q_1 / \partial T < \partial Q_2 / \partial T. \quad (7.3.1)$$

This phenomenon was simulated by Fousek (1965a) in the approximation of rectangular polarization loop. In this approximation, the rate heat production $Q_1 \propto P_0 E_c$ where P_0 and E_c are the half-height and half-width of the loop, respectively. It was also assumed that depending on the amplitude of the driving field E_0 three regimes are possible: (i) for small fields ($E_0 < E_{0k}$), the loss is negligibly small and one sets $P_0 = 0$; (ii) for intermediate fields ($E_{0k} < E_0 < E_{0c}$), $P_0 \propto E_0 - E_{0k}$ and $E_c = E_0$; and (iii) for large fields ($E_{0c} < E_0$), $P_0 = P_s$ and $E_c = E_{0c} + g(E_0 - E_{0c})$, where P_s is the spontaneous polarization. The simulation has been performed for the experimental situation close to that in TGS. This defines the choice of the temperature dependences of the parameters controlling the problem: $E_{0k} \propto E_{0c} \propto g \propto \sqrt{T_C - T}$ where T_C is the transition temperature.

Novák and Hrdlička (1968) confirmed the validity of this model experimentally, for TGS samples. The TANDEL effect was observed in a number of ferroelectric materials (Malek et al., 1964) as well as in glass ceramics (Lawless, 1987). It represents some danger when data on hysteresis loops are interpreted without taking the process of self-heating into account.

7.4 Pulse Switching

An ac voltage applied to a ferroelectric sample drives a switching process whose time development is in some correspondence with the time-dependent magnitude of the applied field. It is obvious that when the applied field during the whole operation remains constant, we obtain more straightforward information about the polarization reversal process. This was for the first time realized by Merz (1956) who investigated the switching process in barium titanate crystals by applying rectangular voltage pulses of alternate polarity and detecting the switching current flowing through the ferroelectric sample. Often a pause with zero field is inserted between the pulses of opposite polarity. Figure 7.4.1 shows the basic scheme of the circuit employed and also the typical profiles of the current $i(t)$ monitored. The first sharp current peak corresponds to the linear capacitance of the sample, not connected to any domain phenomena. When the polarization reversal takes place in the whole volume of the sample, obviously

$$\int_0^{\infty} i(t) dt = 2P_s \quad (7.4.1)$$

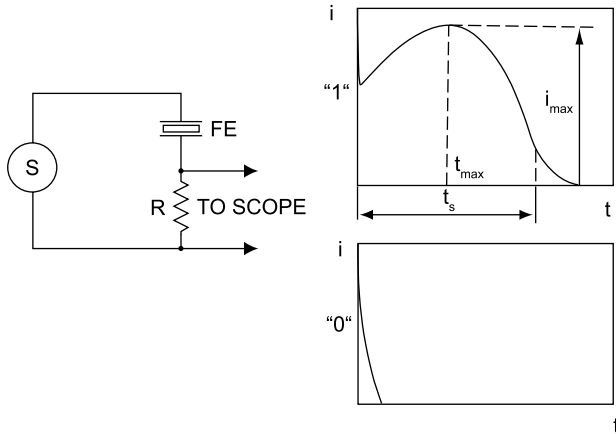


Fig. 7.4.1 *Left*: Basic scheme for pulse switching; the source S applies voltage pulses of prescribed polarity. *Right*: The curve “1” shows the switching current density i which is typically characterized by the values of i_{\max} , t_{\max} , and t_s . The curve “0” shows the response when the applied field is parallel to spontaneous polarization; it corresponds to linear capacitance of the sample

In reality, the value of polarization determined in this way may be smaller than P_S because of certain backswitching after the previous polarization reversal process. It is essential that the output impedance of the current source is low enough so that the voltage would not drop even when the switching current reaches its maximum value i_{\max} .²

Three quantities characterizing the switching process are defined unambiguously, namely, the applied field E , the maximum value i_{\max} of the current, and the time t_{\max} at which it occurs. For practical purposes, the time required to complete the switching process is an important attribute. In customary measurements, the length t_{appl} of the applied field pulse should be long enough to virtually complete the switching process so that integral (7.4.1) taken from 0 to t_{appl} would be very close to $2P_S$. Otherwise the switching process is completed only partially. As another characteristic of switching a notion of switching time t_s is introduced. This time is often defined as that necessary to reverse \mathbf{P}_S in a certain fraction, e.g., 95%, of the sample volume (Fatuzzo and Merz, 1966). For convenience, however, the switching time t_s is defined in another way, as the time necessary for the switching current to drop to a certain fraction, e.g., 5% of its maximum value i_{\max} .

It is this method, when the processes proceed at constant applied field, that allows for well formulated theoretical discussions. The dependences $t_s(E)$ and $i_{\max}(E)$ for BaTiO_3 and other materials provide the core information on which

² A number of researchers constructed their own pulse generators; as an example we may mention the ‘economical’ apparatus designed by Ravi et al. (1980): a bipolar square pulse generator with a low output impedance, short rise time, variable pulse amplitude, and repetition frequency. A number of convenient sources are now commercially available.

theoretical interpretations of switching are based. It is obvious that to obtain reliable results, again the power of the current source is of importance to provide the rising time of the applied pulse considerably shorter than t_{\max} . In practice, it is required that the value of t_{\max} should be independent of the capacitance (area of electrodes, in fact) of the sample.

Apart from the classical *transient current* method just discussed above an alternative technique, which can be called *poling back* technique, has been suggested by the group of Waser (Grossmann et al., 2000). This technique comprises an application of the pulse sequence shown in Fig. 7.4.2. In this sequence, the first, the second, and the fourth pulses have the same amplitudes and durations large enough to perform the full polarization reversal whereas the amplitude, V_3 , and length, t_3 , of the third pulse are variable. The amount of the polarization switched by the third pulse is determined by switching it back by the fourth pulse. This method was shown to have a clear advantage compared to the classical one in the case where the switching is stretched for many decades in time. The reason for that is an increasing difficulty with reliable monitoring of very small currents that are typical for the stretched switching. Usually, the transient current method enables us to cover no more than two decades in time (Merz 1956; DeVilbiss and DeVilbiss, 1999; Song et al., 1997), whereas the poling back technique can readily cover a six to eight decade interval (Lohse et al., 2001; Tagantsev et al., 2002a,b). An example of the plot of time dependence of switched polarization for PZT thin films is shown in Fig. 7.4.3.

It is worth mentioning that the application of both techniques requires considerable precaution in order not to take the RC-controlled dynamics of the measuring setup for a manifestation of the real switching dynamics of the material (Larsen et al., 1991; DeVilbiss and DeVilbiss, 1999; Seike et al., 2000). A simple reliable test excluding the RC artifact is to check that the switching current kinetics is independent of the capacitor area.

The switching times, understandably, depend strongly on the applied field. To give an example of their magnitude, for bulk ferroelectric crystals, in which 180° polarization reversal process is not accompanied by a change of spontaneous strain (BaTiO₃, TGS), typical switching times are of the order of 10–0.1

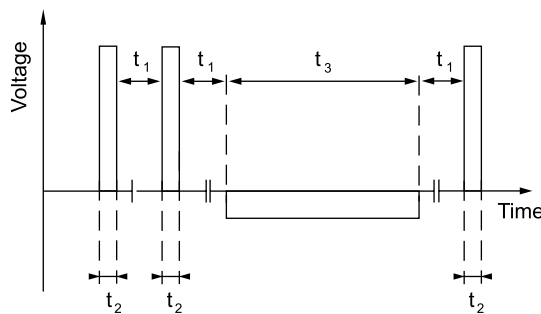
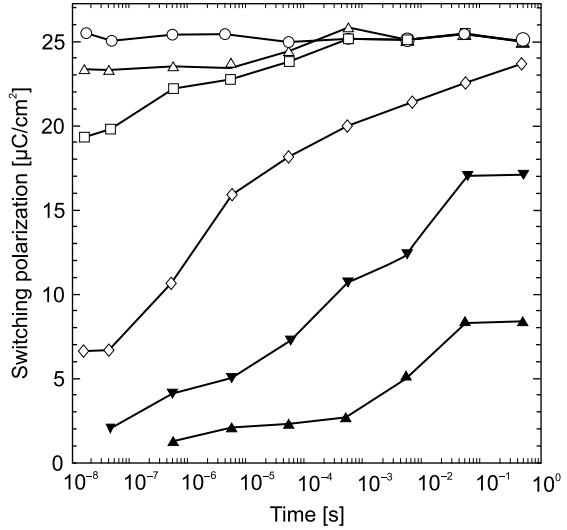


Fig. 7.4.2 Sequence of voltage pulses used for measurements of the switching polarization with the poling back technique

Fig. 7.4.3 Switching polarization as a function of the switching time, for different voltages measured with the poling back technique on a capacitor containing 135 nm thick film of PZT. After Tagantsev et al. (2002b)



μs in fields of several kilovolts per centimeter. However, we shall see in Chap. 9 that in thin ferroelectric films switching times below 1 ns have been reached, though for much higher fields.

Concerning ferroelectric switching produced by short- and low-voltage pulses the observations of Fatuzzo and Merz (1959) are worth mentioning. They showed that if a series of voltage pulses much shorter than t_s are applied to a TGS crystal, there is no net reversal of \mathbf{P}_S . There exists a critical pulse length t^* at which the crystal begins to switch and if a series of pulses, each longer than t^* , is applied, \mathbf{P}_S will be completely reversed. Both phenomena are represented schematically in Fig. 7.4.4. This kind of behavior is called “ t^* effect.” It is

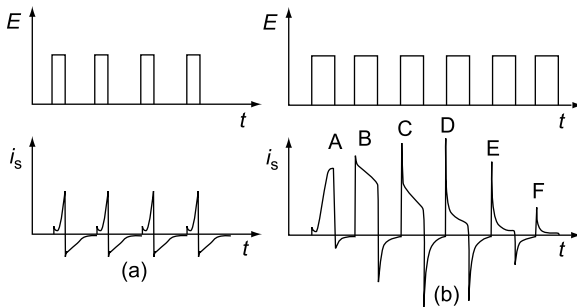


Fig. 7.4.4 Pulses of applied electric field and of the switching current in a TGS crystal (a) for field pulses shorter than a critical duration ($t_{\text{pulse}} < t^*$) no switching was observed and (b) for a series of longer pulses ($t^* < t_{\text{pulse}} < t_s$) the switching process is completed. Reprinted with permission from [Fatuzzo, E., Merz, W.J., *Phys. Rev.*, **116**, 61 (1959)]. Copyright (1959) by the American Physical Society

interesting that in the latter case the shapes of the individual small current pulses fit together yielding the “regular” pulse, except for the initial peaks A , B , C , D , E , F . The critical time t^* depends on the amplitude of the applied pulse; for very low fields it is a very small fraction of t_s while for high fields it can approach the magnitude of t_s . Taylor (1965) pointed out that the “ t^* effect” could be used for non-destructive readout from a memory matrix as well as for its successive addressing. He also showed (Taylor, 1966) that the value of t^* depends on the applied field and sample thickness and in particular that the ratio t^*/t_s depends on the quality of the sample surface. While in this chapter we pay attention to the methods only, it can be noted in passing that partial switching phenomena have not received corresponding attention of theorist. Here the work by Burfoot (1959) can only be mentioned.

7.5 Ferroelastic Hysteresis Loops

Ferroelastic hysteresis loops show the strain induced by an applied mechanical stress of alternating polarity, i.e., the $\varepsilon(\sigma)$ dependence. In principle, what is to be measured—in the simplest correspondence to the symmetry change induced by the phase transition—is the deformation of the sample subjected to a homogeneous mechanical stress. In ferroelastics which are simultaneously ferroelectric, we can also get information about the behavior of strain by applying an electric field, i.e., from the $\varepsilon(E)$ dependence. Alternatively, we could also measure the $P(\sigma)$ as well as the $P(E)$ dependences, which all would have the characteristics of hysteresis loops. It might appear possible that these dependences could be easily converted into each other since we know the $P(\varepsilon)$ or $\varepsilon(P)$ relations “dictated” by the symmetry of the parent phase. However, in general, different kinds of loops do not bring identical information and such conversions should include a number of rather complicated factors; for instance, the shape of the $P(\sigma)$ hysteretic dependence may not conform with the shape of the $P(E)$ hysteresis loop since customarily the two are taken at different boundary conditions. We remind the reader that except for 180° nonferroelastic ferroelectric switching, ferroelastic aspects are always present even in ferroelectric hysteresis loops.

In this section we concentrate on the basic ferroelastic $\varepsilon(\sigma)$ hysteresis loops. Their main characteristics are defined in analogy with ferroelectric loops. The meanings of spontaneous strain, remanent strain, maximum strain, and coercive stress are self-evident and these concepts are routinely used.

Basically, we are interested in measuring a strain component as a function of the conjugated stress component. In principle, the application of “axial” stress, i.e., tension and compression, is required for a properly oriented sample. Ferroelastic hysteresis loops have been investigated in several laboratories for a number of ferroelastics, but the methods employed significantly differ. We mention several examples. Pakulski et al. (1987) used an apparatus shown in

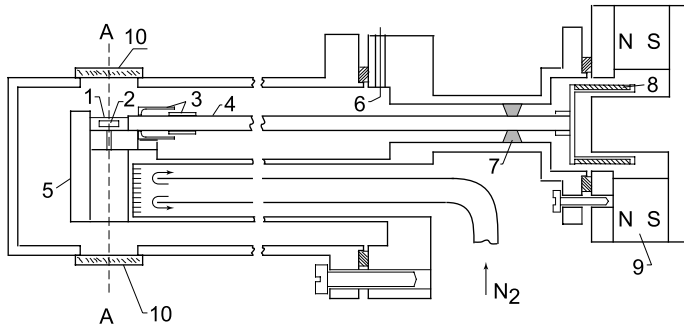


Fig. 7.5.1 Stress apparatus (Pakulski et al., 1987): 1, sample; 2, electrodes for permittivity measurement; 3, capacitor displacement sensor; 4, ceramic rod; 5, cold finger; 6, electrical feedthrough; 7, teflon ring; 8, coil; 9, permanent magnet; 10, glass window; A–A optical axes of the microscope

Fig. 7.5.1 which allows one to measure directly $\epsilon(\sigma)$ loops, revealing components of the spontaneous strain. Its notable features are that the sample can be simultaneously observed in a microscope and the whole setup allows the measurements at low temperatures. The specimen has the form of a rectangular bar. Its lateral faces are polished to allow optical observations and then it is glued into the apparatus. The force is transmitted to it through a ceramic rod; it is proportional to the current flowing through the coil placed in a magnetic field, with the proportionality coefficient $p = 5 \text{ N/A}$. The deformation induced by this force is monitored with a displacement sensor. The sample slot makes it possible to measure capacitance of the sample, however, with gaps 0.2 mm thick between the electrodes and the sample. Figure 7.5.2a gives examples of data obtained with this apparatus. Ferroelastic loops $\epsilon_{12}(\sigma_{12})$ were measured for the LiCsO_4 crystal, representing the species $mmm-\epsilon_s-2/m$, by monitoring the elongation and contraction of a $z-45^\circ$ cut with dimensions $10 \times 2 \times 0.5 \text{ mm}^3$. Loops of permittivity vs. stress, also shown in the figure, demonstrate the ferroelectric features of the phase transition in this material. The change in the polarity of the $\kappa(\sigma)$ loop, when passing from 197 to 172 K is surprising and we include this data to demonstrate what interesting features such studies can offer. Several explanations have been proposed (Pakulski et al., 1987) for this effect.

In some cases “double loops” were observed (Pakulski et al., 1983; Shuvalov et al., 1984). Such loops are probably connected with a strong tendency of the sample for backswitching and after repeated cycling they often change into standard hysteresis loops (Kudryash et al., 1989).

Often tensile testing commercial apparatus is used to demonstrate ferroelastic hysteresis, such as Instron-type machines constructed for testing mechanical properties of metals. Prasad and Subbarao (1977) and Tsunekawa and Takei (1976) employed this technique for BaTiO_3 and LaNbO_4 , respectively. In this case, only a partial loop corresponding to one sign of the stress is available. This

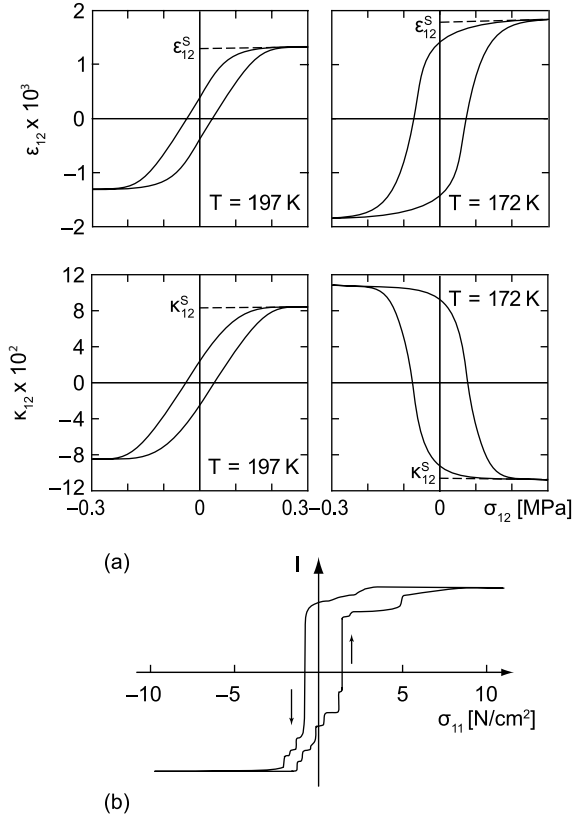


Fig. 7.5.2 (a) Stress–strain and stress–permittivity loops of LiCsO_4 ; the stress frequency is 0.05 Hz (Pakulski et al., 1987). (b) Ferroelastic hysteresis loop of $\text{KFe}(\text{MoO}_4)_2$ recorded using the current proportional to the light flux through the sample as a measure of the strain (Krainyuk et al., 1983b). Elastic analogues of Barkhausen jumps are seen

is a strong disadvantage since no information about the shape of the full switching curve is available. The reliable information is just one quarter of the loop corresponding to the backswitching.

Information on ferroelastic switching can also be obtained in more involved geometries. Some authors offer data obtained for the torsion stress which involve twisting of the sample. In the torsion geometry, a rod-shaped sample is fixed at one end and a torque is applied to its face at the opposite side, with the rotation axis parallel to the rod. If z is the rod axis, the strain components which are induced are ε_{xz} and ε_{yz} . They are roughly independent of z but inhomogeneous along the radius of the rod. Alternative experiments have been performed in the bending geometry. Here again the bar-like sample is fixed at one end and force is applied to the opposite end, directing along x , perpendicular to the bar. The sample bends and the induced strain ε_{zz} is inhomogeneous, changing

linearly with x , passing through zero in the middle of the bar. Torsion and bending can be used to obtain some information about the hysteretic behavior of strain but generally do not provide data about the order parameter dependence on the conjugate force. No complete analysis of response of samples of materials representing different ferroelastic species to such applied forces seems to be available.

In most cases, experimental data on ferroelastic hysteresis are usually based on measurements performed with frequencies in the range from 10 to 10^{-4} Hz. These rates are much lower than in the case of ferroelectric switching, including that in ferroelastic ferroelectrics. This fact is connected with technical aspects of the experiments rather than with the speed of ferroelastic switching: We know that polarization reversal in ferroelectric ferroelastics, when driven by electric fields, can be quite fast and ferroelectric hysteresis loops in these materials are often taken at frequencies above 10^2 Hz.

For the above-mentioned torsion and bending geometry, Krainyuk et al. (1983a,b) used an apparatus in which a rod-shaped sample is fixed at one end and provided with a magnet clamped to the other end. Helmholtz coils excite magnetic field of chosen orientation which acts on the magnet and the developed force results in deformation of the sample. A light beam reflects at a mirror attached to the magnet and its reflection angle is a measure for strain at the end of the rod. The setup allows also for simultaneous optical observations of the sample. Depending on the direction of magnetic field excited by Helmholtz coils, bending or torsion can be induced; this is obvious from Fig. 7.5.3a,b which shows the sample, S and N poles of the magnet, direction of the magnetic field \mathbf{H} , direction of the mechanical moment \mathbf{M} , as well as the small mirror and reflected beam; in (a) the bending and in (b) the torsion are induced. Data obtained by this apparatus clearly demonstrate nonlinear and hysteretic elastic responses of the sample. However, it may be difficult to obtain information about spontaneous strain and basic switching properties because of the inhomogeneity of strain in the sample.

Gridnev and co-workers used a method with several similar features for studying strains of prevalingly torsion character (Gridnev and Shuvalov, 1983). The sample is glued into the metallic main axis of rotational pendulum; the torsion of the axis is determined by torsion deformation of the sample and

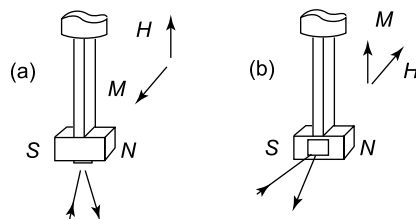


Fig. 7.5.3 Basic geometry of the apparatus for measuring bending (a) and torsion (b) (Krainyuk et al., 1983a,b). The detections of the applied magnetic field (H) and angular momentum produced (M) are shown

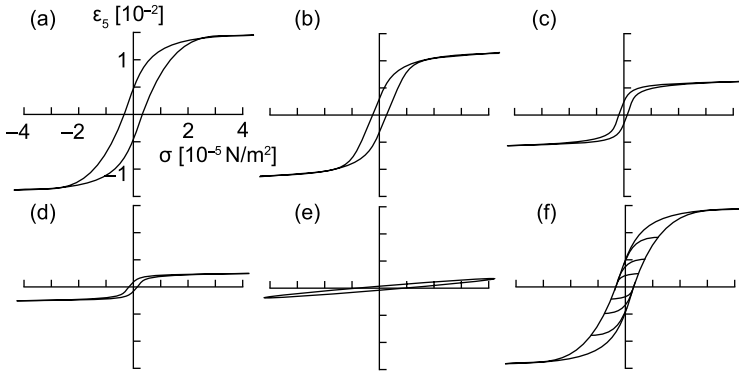


Fig. 7.5.4 Ferroelastic hysteresis in $\text{KH}_3(\text{SeO}_3)_2$ at different temperatures (Gridnev et al., 1979): (a) -178°C ; (b) -100°C ; (c) -67.5°C ; (d) -62.4°C ; (e) -59.6°C ; and (f) shows the loops for different stress amplitudes at $T = -178^\circ\text{C}$

detected by capacitor detectors mounted on a rod fixed perpendicular to the main axis. A number of ferroelastic materials were investigated by this method. Figure 7.5.4 shows ferroelastic loops of $\text{KH}_3(\text{SeO}_3)_2$, at different temperatures and amplitudes, where the hysteretic dependence of ε_5 is plotted vs. applied stress (Gridnev et al., 1979).

All methods for studying macroscopic characteristics of ferroelastic switching mentioned above were based on quasistatic processes: the applied mechanical forces were changing slowly, in correspondence with the frequency range specified above. Vagin et al. (1979) offered data for switching times measured when applying mechanical pulses, in analogy with the ferroelectric pulse methods; however, no technical details seem to have been offered. For single crystals of $\text{Pb}_3(\text{PO}_4)_2$ and applied stresses between 2×10^2 and $9 \times 10^2 \text{ N/cm}^2$, reported switching times amounted to 3–0.3 ms.

At the end of this section it is to be pointed out that here we have concentrated mainly on the methods of measurements of “true” ferroelastic switching phenomena. There are, however, many other methods to obtain indirect information on ferroelastic switching. For Rochelle salt crystals, Abe (1958) concluded that the average rotation angle of polarized light is nearly proportional to the change of average strain. This method, instead of recording true strain–stress hysteresis loops, can give more easily information about the frequency and temperature dependences of the coercive field (Abe, 1964). Salje and Hoppmann (1976) (see also Salje, 1990) studied ferroelastic loops in $\text{Pb}_3(\text{P}_x\text{V}_{1-x}\text{O}_4)_2$ crystals using two approaches: direct information about the average value of strain measured by the angle of laser beam reflected from the surface of strained sample and indirect information obtained by measuring the averaged birefringence. The shapes of the two loops were found slightly different and this was attributed to the non-linear relationship between strain and birefringence. Similar approach, namely, recording the change in light flux through the sample located between crossed

polarizers, was used for detecting ferroelastic loops of $\text{KFe}(\text{MoO}_4)_2$ (Krinsky et al., 1983), obtained under rigorous uniaxial loading of proper orientation. With the appropriate orientation of the crystal, the photosensor signal is proportional to the relative volume of one of the orientational states in the sample. One of the observed loops is shown in Fig. 7.5.2b. Here the elastic analogy of huge Barkhausen jumps is evident, an effect very often accompanying ferroelastic switching (see data on BaTiO_3 from Sect. 8.6).

7.6 More Involved Methods

In the last section of this chapter we wish to mention, in passing, switching characteristics which can be achieved by methods other than those mentioned above or which are important for ferroics with more involved switching properties.

In ferroelectrics, one method could be found useful to characterize some features of polarization reversal in ac fields, namely, Fourier analysis of the switching current. Little attention seems to have been paid to this possibility. Karpov and Poplavko (1984) offered Fourier analysis of the hysteresis loop in TGS. In addition to the information itself, this experimental approach, when proper characteristics would be assigned to the spectrum, could provide a tool for specifying some particular aspects of switching, e.g., basic features of the ageing processes without observing the whole loop.

In the above sections we concentrated on ferroelectric and ferroelastic switching processes. Have hysteresis loops been observed also for higher order ferroics, ferroelastoelectrics, and ferrobielastics in particular? Many attempts have been made along this line, which unambiguously demonstrated domain reversal processes; however, the resulting data have not been presented in the form of hysteresis loops. In ferroelastoelectrics, switching should be driven by applying simultaneously electric field and elastic stress, based on the energy term $d_{ijk}E_i\sigma_{jk}$ with the value of d_{ijk} differing in different domain states. An obvious candidate for this phenomenon is quartz, representing the species 622-*ds*-32. Its two domain states differ in sign of the piezoelectric coefficients $d_{111} = -d_{122} = -(1/2)d_{212}$, but also in sign of the elastic compliances $s_{1123} = -s_{2223} = (1/2)s_{1213}$. Thus when an electric field with nonzero components E_1 and E_2 is applied together with the stress of nonzero components σ_{11} , σ_{22} , σ_{12} , σ_{13} , and σ_{23} , the free energy densities of the two domain states differ by

$$\Delta\Phi = 2d_{111}(E_1\sigma_{11} - E_1\sigma_{22} - 2E_2\sigma_{12}) + 4s_{1123}(\sigma_{11}\sigma_{23} - \sigma_{22}\sigma_{23} + 2\sigma_{12}\sigma_{13}). \quad (7.6.1)$$

The first term in this formula provides the driving force for elastoelectric switching: Concurrent application of E_1 and σ_{11} or of E_1 and σ_{22} or of E_2 and σ_{12} makes favorable one of the two domain states and any of these couples of applied fields could be used as the switching force. Careful experiments were performed by Laughner et al. (1979) which at temperatures close to T_C resulted

in domain state reorientation in limited volume parts of a quartz crystal. No changes in the spatially averaged piezoelectric response of the whole sample were recorded which would remind a hysteretic dependence of, e.g., d_{111} on the product $E_1\sigma_{11}$. Ammonium chloride ($m\bar{3}m - d - \bar{4}3m$) provides another alternative for the observation of $d(E\sigma)$ hysteresis loops. Mohler and Pitka (1974) applied uniaxial stress along the [011] axis, together with an electric field along the axis [100]. Since the two domain states differ in sign of the d_{123} coefficient, the domain pattern was really strongly influenced as demonstrated by the change of d_{123} from zero to a maximum value of 3×10^{-12} C/N. Another candidate for ferroelastoelectric switching is CsCuCl₃ ($6/mmm-d-622$) but attempts to induce ferroelastoelectric switching were not successful (Fousek et al., 1980).

In ferrobilastics, the switching process would be driven by the difference in the $s_{ijk}\sigma_{ij}\sigma_{kl}$ energy terms for different domain states. In other words, the anisotropy of elastic response is the driving force for the phenomenon. The ferrobilastic hysteresis curve would then be represented by the dependence of s_{ijkl} on the product $\sigma_{ij}\sigma_{kl}$ of the applied stress components.³ As in the previous case, quartz crystals are good candidates for observing this phenomenon. In fact this field of investigations was driven by the fact that quartz plays the leading role in the area of utilization of crystalline piezoelectrics and domains (Dauphiné twinning), since they differ in the sign of piezoelectric coefficients d_{111} , d_{122} , and d_{212} , representing an obstruction in applications. The source of driving force for the ferrobilastic switching in quartz is the last term in Eq. (7.6.1). Wooster and Wooster (1946) were probably the first to use this effect for controlling twins. Applying torque they succeeded in bringing multidomain samples into single-domain states and could even propose a spatial diagram demonstrating the magnitudes of differently oriented torques required to complete the switching process. Bertagnolli et al. (1979) investigated ferrobilastic switching in quartz by applying uniaxial stress in the [011] direction, which leads to nonzero stress components $\sigma_{22} = \sigma_{33} = \sigma_{23}$. A part of the hysteresis loop (for compressive stress) was detected by recording the piezoelectric charge, instead of measuring the quantity which defines ferrobilasticity, namely, elastic compliances. Shiau et al. (1984) described ferrobilastic switching in quartz in detail: Compressive stress was applied onto faces of a bar-shaped sample whose normal made angles of 90° and 55° with the crystallographic axes x_1 and x_3 , respectively. Again, instead of measuring one of the components s_{1123} , s_{2223} , or s_{1213} which define the ferrobilasticity of quartz, the density of charge on the (001) faces of the sample was recorded. The ferrobilastic switching was unambiguously registered; however, using an instrument with unipolar loading (the Instron machine), the complete hysteresis loop with both signs of applied stress was not recorded.

³ We may note that in the original paper of Newnham and Cross (1974b), ferrobilastics were characterized by the dependence of strain vs. stress in form of a 'butterfly' loop.

Chapter 8

Switching Phenomena and Small-Signal Response

8.1 Introduction and Overview of Switching Mechanisms

This chapter is devoted to phenomena associated with a change in time of the domain state of a ferroic. Locally, such change corresponds to *transitions between domain states* at least in a small fraction of the sample volume. When the major part of a sample changes its domain state one speaks about a *switching process* or simply switching. The most characteristic macroscopic phenomenon representing this process is the hysteresis loop, often used as a logo for ferromagnetics, ferroelectrics, or ferroelastics. Such hysteretic dependence of the order parameter on the conjugate force is an integral effect; it is the macroscopic portrayal of numerous microscopic processes taking place in a ferroic sample. Most of this chapter will be dealing with switching and switching-related phenomena. At the end of the chapter we will also address the situation where the change of the domain state of a ferroic is associated with transitions between domain states in a small volume fraction of the sample. This situation is typical when the ferroic is probed with an external perturbation of small amplitude, it can be termed as *small-signal response*.

It is appropriate to mention that if it were not for polarization switching phenomena, ferroelectrics would never have attracted so much attention in basic and applied research areas. The possibility to make a Rochelle salt crystal single domain supported utilization of the material in piezoelectric sensors (including those in classical gramophones) and in fact led to the discovery of ferroelectricity. The possibility to make a ceramic sample—originally isotropic, since it contains millions of chaotically oriented grains—piezoelectric involves domain aspects and resulted in extended industrial activities. The possibility to reverse spontaneous polarization very fast in thin samples opened a new territory in memory elements and provides one of the driving forces for research in this area. As a secondary impact, research of polarization reversal effects led to similar activities in the field of ferroelastics.

In a simple case of the switching process, only two domain states are involved—the original and the final one. While this is typical for switching in ferroics with just two domain states, it can be realized—by properly chosen conditions—even in ferroic sample which allows, by symmetry, more than two

domain states. A well-known example is 180° switching, i.e., reversal of sign of the \mathbf{P}_S vector, in tetragonal barium titanate. In more complex cases, several domain states are involved in the process which then becomes rather complicated; these situations are difficult to realize in a defined way and are, therefore, little understood. Switching phenomena include a number of processes; in fact, still not all of them are well understood. In this chapter we wish to approach macroscopic characteristics of these effects as well as the involved processes themselves. Let us first give a schematic overview of them. To have a simple case in mind, we consider a crystalline plate of a uniaxial ferroelectric nonferroelastic material, cut perpendicularly to the ferroelectric axis. It is provided with electrodes so that an electric field can be applied along this axis. In an ideal case the original state is homogeneous and single domain. In practice, it is usually “almost single domain” since some minute (residual) domains with opposite polarization could be present either as metastable remnants of the foregoing processes or as stable regions with fixed polarization resulting from crystal lattice interaction with local defects. Figure 8.1.1a illustrates such situation; here the prevailing direction of the polarization is taken positive. After the application of the field directed against this direction several processes take place. First, all or some of the mentioned metastable or stable “frozen-in” nuclei will start to grow (Fig. 8.1.1b). In order to reduce the area of walls carrying an appreciable bound charge of density $\text{div}\mathbf{P}_S$ which produces electrostatic energy, we anticipate that these nuclei will grow preferably *along* the ferroelectric axis and in typical cases this expectation is indeed confirmed by observations. A separate process is the formation of new nuclei (Fig. 8.1.1b). Typically, a small domain—nucleus—representing the preferred domain state is formed and in fact such nucleation occurs independently in many spots of the sample. The

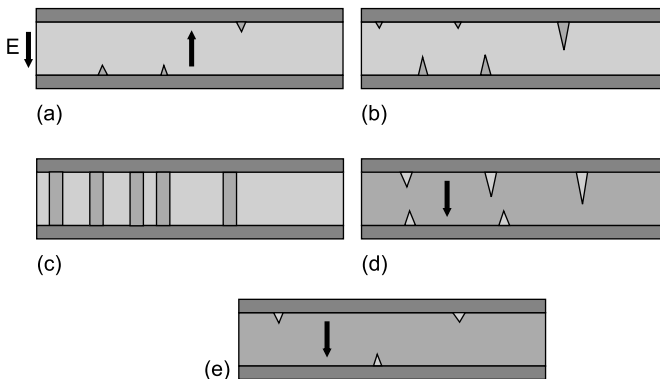


Fig. 8.1.1 (a) to (e) Nucleation and growth of nonferroelastic ferroelectric domains in a parallel plate capacitor (electrodes are shown with the darkest shading)—schematic representation of the switching process. *Arrows* show the directions of the spontaneous polarization and of the applied electric field. The polarity of domains is also shown with the intensity of shading

issues involved in this process are the energy of the nucleus and its shape and size. As in the case of any first-order phase transition (switching is actually an electric-field-driven first-order phase transition) the nuclei can grow, giving rise to macroscopic domains, only when their energy exceeds a certain critical value. The growth of such supercritical nuclei reduces total energy of the sample. This growth is primarily characterized by the domain wall velocity, including its anisotropy. When the grown-up nucleus has reached both electrodes it usually represents a narrow domain which no longer carries a bound charge on its walls. In the Russian literature these domains are practically referred to as “skvoznye domeny,” often translated as “through domains.” The following phase of the process is then the sidewise motion of walls of the through domains (Fig. 8.1.1c). It is characterized by the sidewise velocity of domain walls. However, as walls of neighboring through domains approach each other the problem becomes geometrically very complex and velocities can now be ascribed to shrinking domains of the original domain state rather than to growing domains of the resulting domain state. In other words, a wall loses its identity as belonging to one or another particular domain. This final stage of the switching process is sometimes referred to as domain coalescence (Fig. 8.1.1d). The whole process results in a sample with almost homogeneous polarization oriented along the field; however, some small long-live metastable domains or frozen-in nuclei of the original polarization direction may remain in the sample (Fig. 8.1.1e). Note that in Fig. 8.1.1 the remnants and nuclei of reverse domains are always shown close to the ferroelectric electrode interfaces. This does not mean that these are possible only at these locations; however, ferroelectric electrode interfaces are often the preferable locations. This issue will be discussed later in this chapter and in Chap. 9.

A related picture could be drafted for a uniaxial ferroelastic ferroelectric. However, since now domain walls have to comply fully or almost fully with severe requirements implied by mechanical compatibility conditions, some stages of the switching process will be very different. The concepts of nuclei and their forward growth could be preserved. These will have the shape of narrow wedges. The sidewise growth of the through domains will proceed by the motion of ferroelastic walls of only two compatible orientations, leading to an elastically complex domain pattern which only “with great difficulties” will harmonize into a single-domain state with opposite polarization. In ferroelastics where no mechanically compatible walls are allowed the process is expected to proceed in a similar way, with walls taking orientations minimizing the unavoidable elastic energy.

The driving forces responsible for domain reorientation processes originate from the difference of free energies of different domain states in the applied electric and/or elastic fields. In the following Sec. 8.8.2 we shall specify these forces for different kinds of ferroics and pay attention to mechanisms involved in these processes.

In Sect. 8.8.3 we shall discuss in some detail the motion of single-domain walls in nonferroelastic ferroelectrics, from the experimental point of view. The

theory of this phenomenon will be addressed in Sect. 8.4. Sect. 8.5 is devoted to phenomena of pinning and creeps of domain walls. Sects. 8.6 and 8.7 will be devoted to the presentation of experimental results and theories of switching treated as a macroscopic phenomenon. Finally, in Sects. 8.8 and 8.9 we shall address the problem of dielectric response of multidomain crystalline samples when measured in small applied fields. Domain walls may respond to low-level electric or mechanical forces by very small displacements which, however, may result in large values of dielectric susceptibility, piezoelectric, and elastic coefficients measured in small applied fields.

In this chapter, the discussed properties are related to bulk crystalline samples. Dynamic domain characteristics which are specific for thin films will be treated in Chap. 9.

8.2 Basics of Domain State Reorientation

8.2.1 Driving Force for Processes of Domain State Reorientation

Switching processes mentioned in the preceding section are initiated and driven by applying macroscopic (electric and/or mechanical) external fields. In the present section we shall formulate in an explicit way the basic macroscopic aspects of these driving forces.

In an ideal sample of a ferroic material and in the absence of external fields, the transition from the phase G can result in *any* of the q domain states of the phase F allowed by symmetry: These states are degenerate in energy. The degeneracy can be lifted when an external field of proper physical character and orientation is applied. When the G -to- F phase transition itself proceeds in such a field, one or more of the q domain states may be energetically preferred. When the field is applied in the phase F , the ferroic sample may undergo a domain reorientation process between two states; say from state q_A to state q_B . There are two possible reasons for this. First, the field may be high enough to make state q_A unstable. In such a situation the sample “leaves” state q_A simply because the latter does not exist for the given magnitude and orientation of the applied field. However, this situation is of minor practical interest since the domain state reorientation usually takes place at smaller values of the field, at which both of the two states are still locally stable but one of them is already more energetically favorable. Thus, one can say that the energy criterion governs any reorientation of domain structure in ferroics. Let us address this criterion.

To decide which of the domain states is more favorable under the condition of fixed external fields (electric field \mathbf{E} and stress σ_{ij}), one should compare the total free energy of the crystal and the external sources of the fields. That means that it is not the free energy of the ferroic only that should be compared to tell

the favorable domain state but rather the properly chosen thermodynamic potential, which takes into account the work performed by the external sources. According to classical thermodynamics, for the case of fixed field \mathbf{E} and stress σ_{ij} , the density $\tilde{\Phi}$ of this potential is linked to the free energy density F of the ferroic by the following relation:

$$\tilde{\Phi} = F - \varepsilon_{ij}\sigma_{ij} - P_i E_i. \quad (8.2.1)$$

In terms of the Gibbs energy Φ introduced already in Chap. 2, this potential can also be written as

$$\tilde{\Phi} = \Phi - P_i E_i. \quad (8.2.2)$$

Thus, the difference between the values of this potential for two domain states represents the driving force for the transition between them. Having in mind domain states denoted by q_A and q_B , this difference will be written as $\Delta\tilde{\Phi}_{AB} = \tilde{\Phi}_A - \tilde{\Phi}_B$.

Let us consider two domain states in the simplest case that of a uniaxial proper ferroelectric of the TGS type. For the corresponding species only two domain states are possible, which differ in the sign of spontaneous polarization. An external perturbation which lifts the energy degeneracy of these states is the electric field. Let us determine $\Delta\tilde{\Phi}$ for these states when the field is directed along the ferroelectric axis of the crystal. In this case, according to Sect. 2.3 the density of the appropriate potential reads (see Eq. (2.3.13))

$$\tilde{\Phi} = \Phi_0 + \frac{1}{2}\alpha P^2 + \frac{1}{4}\beta P^4 - PE. \quad (8.2.3)$$

To calculate $\Delta\tilde{\Phi}$ one should, first, find the values of polarization in the domain states where it is parallel or antiparallel to the field, P_+ and P_- , respectively. Second, one finds $\Delta\tilde{\Phi}$ by using Eq. (8.2.3). If the applied field is small enough so that $|P_+| - P_S \ll P_S$ and $P_S - |P_-| \ll P_S$ (P_S is the absolute value of spontaneous polarization), we can use the result of Chap. 2, namely Eq. (2.3.14), and arrive at the commonly used expression

$$\Delta\tilde{\Phi}_{+-} = -2P_S E. \quad (8.2.4)$$

Clearly, close enough to the transition temperature the aforementioned conditions for P_+ and P_- do not hold, so that a more precise treatment is needed. Making use of Eq. (8.2.3) and of the equation of state $\partial\tilde{\Phi}_+/\partial P = 0$, the exact expression for this difference can be readily found in the form

$$\Delta\tilde{\Phi}_{+-} = -(P_+ - P_-) \frac{3E - \alpha(P_+ + P_-)}{4}. \quad (8.2.5)$$

As it should be, this equation reduces to Eq. (8.2.4) in the limit of small fields. For higher fields, the energy difference between the domain states given by the exact formula is smaller than that given by Eq. (8.2.4). However, it turns out that this reduction is rather small; it can reach a few percent when the applied

field reaches a value comparable to that of the thermodynamic coercive field given by Eq. (2.3.15).

In the above example, we have profited from the relative simplicity of the problem and presented the exact solution to the latter. In the case of an arbitrary ferroic the situation is more complicated, so that the most constructive way is to present the difference $\Delta\tilde{\Phi}$ as the Taylor expansion in terms of the external fields \mathbf{E} and σ_{ij} . Taking into account the basic properties of the potential $\tilde{\Phi}$ (cf. Eq. (2.3.12))

$$\frac{\partial\tilde{\Phi}}{\partial E_i} = -P_i \quad \text{and} \quad \frac{\partial\tilde{\Phi}}{\partial\sigma_{ij}} = -\varepsilon_{ij}, \quad (8.2.6)$$

we can present the difference between the thermodynamic potentials of ferroic domain states “2” and “1” as

$$\begin{aligned} \Delta\tilde{\Phi}_{21} = & \left(P_{S_i}^{(1)} - P_{S_i}^{(2)}\right)E_i + \left(\varepsilon_{S_n}^{(1)} - \varepsilon_{S_n}^{(2)}\right)\sigma_n + \left(d_{in}^{(1)} - d_{in}^{(2)}\right)E_i\sigma_n \\ & + \frac{1}{2}\left(\kappa_{ij}^{(1)} - \kappa_{ij}^{(2)}\right)E_iE_j + \frac{1}{2}\left(s_{mn}^{(1)} - s_{mn}^{(2)}\right)\sigma_m\sigma_n + \dots \end{aligned}, \quad (8.2.7)$$

where $d_{in}^{(v)}$, $\kappa_{ij}^{(v)}$, and $s_{mn}^{(v)}$ stand for the morphic components of piezoelectric coefficients, permittivity, and elastic compliance, respectively, in the domain state v . Here $i, j = 1, 2, 3$ while $m, n = 1, 2, 3, 4, 5, 6$. (We remind the reader that morphic tensor components are those which are newly acquired in the ferroic phase.) The terms kept in this expansion provide us with the expressions for the energy difference driving the domain reorientation in ferroelectric, ferroelastic, ferroelastoelectric, ferrobielectric, and ferrobielastic materials, respectively.

In principle, this expansion can be continued. The higher order terms proportional to E^3 , $E^2\sigma$, σ^2E , and σ^3 terms are essential for domain reorientation in tertiary ferroics. The latter can be easily identified from Table B.1. The switching forces in them have been analyzed by Amin and Newnham (1980). A concrete example of the species $m\bar{3}m - m\bar{3}$ is cadmium chlorapatite $\text{Cd}_5(\text{PO}_4)_3\text{Cl}$. It can be called *triferroelastic* since a term proportional to σ^3 differentiates the two domain states. Elpasolite, K_2NaAlF_6 , represents the species $6/mmm - 6/m$ which is also a triferroelastic. The remaining tertiary species are $m\bar{3}m - 432$ and $m\bar{3}m - 23$.

Higher order coefficients are usually very small. So we generally expect that, for realistic stresses and fields, the energy differences given by the higher order terms will be small, making domain state reorientation difficult to achieve before electrical or mechanical breakdown takes place. Indeed we have very little data on this kind of reorientation.

Applying a switching force defines the equilibrium state with one or more domain states corresponding to minimum free energy. Now the *domain reorientation process* or *switching process* is to take place and in principle it is only a matter of time when the equilibrium state will be reached. It depends on the time profile of the applied forces and on energy barriers involved in the actual

process. The energy terms given by Eq. (8.2.7) provide the primary sources driving the switching process but in real experiments the energy balance is usually more complicated because of additional contributions to the energy. These include the energy of the electric fields existing outside the sample and also of fields and stresses connected with simultaneous coexistence of domain state during the reorientation process. Some of these aspects will be also mentioned later in this Chapter.

8.2.2 Pressure Acting on a Domain Wall

The difference in the thermodynamic potentials between two domain states exposed to the action of external perturbations results in a pressure acting on the domain wall separating these states. This pressure is an important factor controlling switching in ferroics. It can be calculated using the principle of virtual displacements. Specifically, one can relate the pressure f acting on a wall in a ferroic to the change of the proper thermodynamic potential of the ferroic ΔW induced by a displacement of the wall Δx . Consider an element of the wall of area ΔS . The work needed to shift this element by distance Δx is equal to $\Delta x \cdot f \cdot \Delta S$. On the other hand, according to the classical thermodynamics, this work should be equal to ΔW . That leads us to the expression for the pressure acting on the element of the wall

$$f = \frac{\Delta W}{\Delta S \cdot \Delta x}. \quad (8.2.8)$$

Thus, the calculation of the pressure acting on a wall reduces to the calculation of the variation of thermodynamic potential of the system.

The sought pressure can be readily found in the case where the macroscopic fields (E_i and σ_{ij}) are fixed and homogeneous in the sample. In this case, the ferroic is characterized by the density of thermodynamic potential, $\tilde{\Phi}$ (see Sect. 8.2.1), so that ΔW can be found as $\Delta W = \Delta x \cdot \Delta S \cdot \Delta \tilde{\Phi}_{12}$ where $\Delta \tilde{\Phi}_{12}$ is the difference between the values of $\tilde{\Phi}$ for the domain states “1” and “2.” This implies (via Eq. (8.2.8)) that, in the considered situation, the pressure acting on the wall is merely equal to the difference between the densities of the thermodynamic potential on the two sides of the wall. It is instructive to express this pressure in terms of macroscopic tensor properties of the domains and, by using the expansion of $\Delta \tilde{\Phi}_{12}$, Eq. (8.2.7), to find

$$\begin{aligned} f = & \left(P_{Si}^{(1)} - P_{Si}^{(2)} \right) E_i + \left(\varepsilon_{Sn}^{(1)} - \varepsilon_{Sn}^{(2)} \right) \sigma_n + \left(d_{in}^{(1)} - d_{in}^{(2)} \right) E_i \sigma_n \\ & + \frac{1}{2} \left(\kappa_{ij}^{(1)} - \kappa_{ij}^{(2)} \right) E_i E_j + \frac{1}{2} \left(s_{nm}^{(1)} - s_{nm}^{(2)} \right) \sigma_n \sigma_m + \dots \end{aligned} \quad (8.2.9)$$

Here and therein, the pressure is considered as positive when acting from domain “2” to “1.”

In real ferroics the values of the pressure acting on a wall can be very different. Let us evaluate the pressure acting on a 180° wall parallel to the direction of the electric field (like that in the parallel plate capacitor shown in Fig. 8.2.1(a) in two classical ferroelectric systems, TGS single crystal and $\text{Pb}(\text{Zr},\text{Ti})\text{O}_3$ (abbr. PZT) thin film, at the electric field of the order of the coercive field. Taking into account the first term from Eq. (8.2.9) we find the sought pressure equal to $2P_S E$. This implies values of the pressure equal to 5.6 N/m^2 for TGS and $2.4 \times 10^6 \text{ N/m}^2$ for PZT. These estimates have been obtained using the values $P_S = 2.8 \mu\text{C/cm}^2$ and $E = 1 \text{ V/cm}$ for TGS and $P_S = 30 \mu\text{C/cm}^2$ and $E = 40 \text{ kV/cm}$ for PZT film.

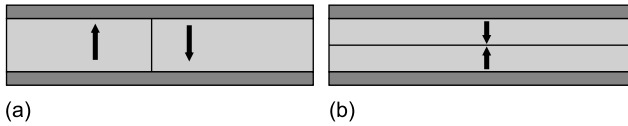


Fig. 8.2.1 Parallel plate capacitors (electrodes are shown with the darkest shading) containing 180° ferroelectric walls. *Arrows* show the directions of the spontaneous polarization: **(a)** wall perpendicular to the electrodes bearing no bound charge, **(b)** head-to-head wall parallel to the electrodes bearing bound charge

There are two limitations for applicability of the above results: (i) The “fields” E_i and σ_{ij} are assumed to be homogeneous throughout the sample; (ii) no free charges except those on the electrode are admitted in the system. A more involved theory (Roitburd, 1971; Nechaev and Roschupkin, 1988) offers a treatment of the problem in the case where the first limitation is lifted. This theory gives a generalized version of Eq. (8.2.9) as

$$\begin{aligned}
 f = & \left(P_{Si}^{(1)} - P_{Si}^{(2)} \right) \frac{E_i^{(1)} + E_i^{(2)}}{2} + \left(\varepsilon_{Sn}^{(1)} - \varepsilon_{Sn}^{(2)} \right) \frac{\sigma_n^{(1)} + \sigma_n^{(2)}}{2} \\
 & \left(d_{in}^{(1)} - d_{in}^{(2)} \right) \frac{E_i^{(1)} \sigma_n^{(2)} + E_i^{(2)} \sigma_n^{(1)}}{2} + \left(\kappa_{ij}^{(1)} - \kappa_{ij}^{(2)} \right) \frac{E_i^{(1)} E_j^{(2)}}{2} \\
 & + \left(s_{mn}^{(1)} - s_{mn}^{(2)} \right) \frac{\sigma_n^{(2)} \sigma_m^{(1)}}{2} + \dots
 \end{aligned} \tag{8.2.10}$$

It is seen that this expression can give values of the pressure substantially different from those given by the simple difference of thermodynamic $\tilde{\Phi}$ potential on the two sides of the wall.

The result given by Eq. (8.2.10) also holds when free charges are present in the ferroic, except the case where the domain wall is carrying some free charge on it. Such situation readily occurs when the domain wall is charged (i.e., $\text{div}\mathbf{P} \neq 0$ at the wall) and the bound charge is fully or partially compensated

with free charge. For such situation, a relation for the polarization-related force acting on a wall carrying free charge has been obtained by Mokry et al. (2007) as follows:

$$f = \Phi^{(2)} - \Phi^{(1)} - \frac{1}{2} \left(E_i^{(1)} + E_i^{(2)} \right) \left(P_i^{(2)} - P_i^{(1)} - \sigma_f n_i \right). \quad (8.2.11)$$

Here Φ is the Gibbs energy density (see the previous section), σ_f is the free charge density per unit area of the wall, and n_i is the normal to the wall plane directed inside domain “2.”

Analysis performed using this relation has shown that the force acting on a charge domain wall can be strongly reduced when it is free-charge compensated (Mokry et al., 2007). Such result is consistent with a statement by Landauer (1957) who pointed out that the bound charge screening at domain walls not only reduces the energy of the depolarizing field but may also reduce the pressure acting on the wall.

It is instructive to illustrate this effect with a simple example. Consider a capacitor containing a “head-to-head” nonferroelastic 180° domain wall parallel to its plates, the bound charge of the wall being fully compensated by free carriers (see Fig. 8.2.1b) so that the electric field E is homogeneous throughout the capacitor. It readily follows from Eq. (8.2.11) that, in the hard-ferroelectric approximation (i.e., when the polarization in the domain can be presented in the form: $P = \pm P_S + \kappa_c \varepsilon_0 E$; cf. Eq. (5.2.4)), no pressure is applied to the wall. Indeed, in this approximation, the Gibbs potential Φ of the two domains can be considered as equal and $P^{(2)} - P^{(1)} = \sigma_f = 2P_S$. Calculations beyond this approximation yield the value of the pressure, which is much smaller than the classical $2P_S E$ value. For the simplest form of the potential Φ given by Eq. (2.3.4a) according to Mokry et al. (2007) with a good accuracy one finds

$$f = -\frac{\chi^2 E^3}{P_S}. \quad (8.2.12)$$

Here χ is the lattice contribution to the susceptibility of the ferroelectric and the negative sign indicates that the pressure is applied in the opposite direction to that related to the $2P_S E$ term. The origin of this small contribution to the pressure is the difference in the nonlinear dielectric response of the two domains.

It is worth mentioning that vanishing the pressure on the wall in the hard-ferroelectric approximation can be concluded directly from the explicit form of the thermodynamic potential of the system. Consider the above system for a fixed potential difference between the electrodes. In this system, because of the full screening of the bound charge on the wall, in the hard-ferroelectric approximation, the electric field is homogeneous and fixed. Thus, the corresponding thermodynamic potential of the ferroelectric in the capacitor can be written as

$$W = \int_{V_c} \left(\Phi(P) + \frac{\varepsilon_0 E^2}{2} \right) dV - (\phi_1 q_1 + \phi_2 q_2) \quad (8.2.13)$$

where q_1 , q_2 and φ_1 , φ_2 are the charges and electrostatic potentials on the electrodes, respectively; integration over the capacitor volume V_c is implied. One readily sees that, in the accepted approximation, a wall displacement does not result in any change of W since, in this approximation, Φ is the same in both domains, E is constant, and the charges on the plates do not change because the fully screened domain wall is neutral. This implies no pressure applied to the wall.

8.3 Single Domain Wall in Motion

8.3.1 Experimental Techniques Used to Measure Domain Wall Velocity

Domain wall velocities can be determined from direct observations or from indirect data on some macroscopic phenomenon accompanying the wall motion, when the domain geometry is known. The method used must fulfill two requirements. First, it is to allow application of the force acting on the wall, i.e., of electric field, mechanical stress, or of a combination of both, without imposing unwanted boundary conditions. Second, it must offer a satisfactory resolution in determining the wall positions.

Optical methods appear to be ideal. To measure the velocity of single-domain walls by direct optical observations, crystals which are simultaneously ferroelectric and ferroelastic are preferred since wall motion can be easily induced by applied electric field, and direct determination of wall velocity in a polarizing microscope is relatively easy. In an ideal case, a domain wall is singled out in a sample of high quality and, depending on the crystal symmetry and sample geometry, the field is applied (i) using transparent electrodes on the sample surfaces used for the optical observations or (ii) using common electrodes deposited on the side surfaces of the sample. When a ferroelastic wall moves through the sample, the shape of the latter changes; thus it has to be ensured in the experimental setup that this is not hindered by any kind of external clamping such as cementing the sample on a glass plate or using an unsuitable sample holder. If electric field of alternating polarity is used, stroboscopic illumination allows one to observe the wall position as a function of time. Since very short and intensive light pulses can be easily produced, the technique allows high time resolution. The stroboscopic technique was employed first for studying wall motion in Rochelle salt (Mitsui and Furuichi, 1953) (in this pioneering work a rotating disk with brushes and a window were employed to control the applied field and the phase at which the wall was observed) and later fully electronic devices with light pulses of duration below 1 μ s were exploited to study 90° wall motion in BaTiO₃ (Fousek and Brezina, 1960) and gadolinium molybdate (Shur et al., 1985a, 1989b). Nowadays, much higher time resolution could be achieved with suitable laser light pulses as short as 100 ns at a repetition rate up to 10 kHz.

Nonferroelastic 180° domains in some ferroic species can also be optically distinguishable due to optical activity. Then the stroboscopic technique could also be used to measure wall velocity. A well-known example is lead germanate (Dougherty et al., 1972) where in high-quality crystals the domain wall velocity was investigated stroboscopically (Shur et al., 1985c).

Another optical technique of measuring wall motion in alternating fields is based on the detection of a photoinduced signal (Tikhomirov, 1996). The image of vibrating wall is transmitted onto the cathode of a photomultiplier through a slit diaphragm so that the wall displacement modulates the light intensity passed to the detector. Variations in the output signal reflect the wall motion.

Velocities of some domain wall may strongly depend on temperature. Then care must be taken in microscopic observations for which the intensity of the light can be quite high and leads to a considerable increase in the sample temperature. For instance, the experiments with BaTiO_3 plates (Miller and Savage, 1959c) indicated that the high and low light levels resulted in a substantial temperature difference of about 8 K.

Domain walls whose positions cannot be directly determined optically are more difficult to study. In the early stages of research, the basic data on dynamics of 180° walls in BaTiO_3 were obtained (Miller, 1958; Miller and Savage, 1958) by subsequent etching of the sample after the application of electric field for a given period of time. This is in a way a destructive process; however, it provided the essential data later confirmed by other methods.

The liquid crystal decoration technique offers another method for optical observations of walls which cannot be observed directly. Data on wall velocity in nonferroelastic ferroelectrics TGS and GASH were obtained by this method. In these materials, domains are not visible in a polarizing microscope but the decoration technique offers sharp pictures and allows direct optical measurements of wall velocities in a polarizing microscope. Tikhomirova et al. (1985a, 1986a) and Dontsova et al. (1982) used a cell representing a sandwich in which the upper surface of the crystal plate was in contact with nematic layer, 1–10 μm thick. This was followed by a glass plate provided with an SnO_2 electrode. Thus the crystal surface faced a thin insulating layer, namely the nematic. Therefore the electrical conditions under which the domain walls move may not be exactly defined. The domain wall motion could be influenced by the rate of the process in which the bound charge produced by the motion of domain wall was compensated by electrical conductivity of the liquid crystal layer or perhaps of the crystal under investigation.

This disadvantage does not apply to another method used for ferroelectric walls which do not provide optical contrast, namely the pyroelectric probe technique (Hadni, 1970; Hadni and Thomas, 1975). In this system the sample is necessarily electroded to detect the pyroelectric charge induced by a modulated laser beam so that a voltage can be applied which causes the walls to move. Analyzing subsequent scans gives information about wall velocities.

Indirect methods of measuring wall velocity are based on Landauer's formula for the switching current (Landauer, 1957). We have in mind an

electroded crystal plate of thickness d , perpendicular to the ferroelectric axis. The current i_s flowing through the electrodes is related to the volume V_{sw} in which spontaneous polarization is reversed by 180° and equals

$$i_s = \frac{2P_S}{d} \frac{dV_{sw}}{dt}. \quad (8.3.1)$$

Knowing the values of P_S and d as well as the geometry of growing domains and their instantaneous size, data for wall velocities can be deduced from the analysis of the switching current $i_s(t)$.

This indirect method of measuring wall velocity was first used by Miller and Savage for 180° walls in the tetragonal phase of BaTiO_3 . These walls are not expected to be visible in a microscope. (We shall see later in this chapter that, in fact, optical methods can be and were used for this material.) In one of their first studies Miller and Savage (1958) used the sample holder shown in Fig. 8.3.1. Here, sand blasting a dimple (250 μm in diameter) in the plate-like sample was made, which predetermined the location where a domain would form and electrolyte electrodes (aqueous solution of LiCl) were used for the application of the field to the ferroelectric. With the liquid electrodes, the sample could be easily extracted from the sample holder to perform direct observations of the domain pattern at the different stages of switching. It was found that the reverse domain grew around the dimple having the shape close to a perfect square (see Fig. 8.3.12a). The simple geometry of the growing domain enabled linking (using Eq. (8.3.1)) the switching current $i_s(t)$ and the domain wall velocity as

$$v = \frac{i_s}{8P_S a}, \quad (8.3.2)$$

where a is the length of side of the square domain. The latter can be determined from the integrated switching current

$$a = \left[\frac{1}{2P_S} \int_0^t i_s(t) dt \right]^{1/2}. \quad (8.3.3)$$

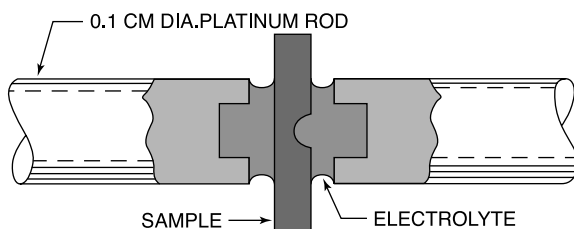


Fig. 8.3.1 Liquid electrode holder with a dimpled sample of BaTiO_3 mounted between the electrodes used by Miller and Savage (1958). Reprinted with permission from Miller and Savage (1958). Copyright (1958) by the American Physical Society

It was this technique that was used to establish the basic law of motion of a nonferroelastic wall in BaTiO_3 . It was also used by Taylor (1962) for determination of the velocity of the walls of square-like and circular-like domains in BaTiO_3 . In these experiments, some discontinuities in switching currents were detected; these were interpreted by domain coalescence, an assumption confirmed by powder patterning.

However, later (Miller and Savage, 1959a,c) it was found that 180° domain walls in BaTiO_3 can be optically distinguished; this applies in particular to freshly formed domains or to moving domain walls. Direct optical observations then allowed one to widen the field interval in which walls in BaTiO_3 were investigated, using semitransparent metallic electrodes. Here one should mention that the nature of the visibility of 180° domain walls in BaTiO_3 is still not clear. There is an explanation offered by Kobayashi (1967), which is connected with the rotation of principal optical axes in domain walls, however, its application to the very thin domain walls typical to this crystal (see Chap. 4) seems to be problematic.

Bittel et al. (1968) studied 180° wall velocities in Rochelle salt, by analyzing the switching current. This is a ferroelastic material and therefore, in contrast to the studies of BaTiO_3 crystals, samples were chosen with regular stripe systems consisting of parallel domain walls. It was found by stroboscopic observations that, under the applied field, all walls in such a system moved almost in the same way. If the number of walls per unit length is n , l is the length, and b is the width of the sample, then the displacement of all walls by x causes a charge $q_w = 2P_S l b n x$ on the electrodes to develop. This charge can be easily measured as a voltage U_w on a capacitor C in series (in fact using the classical Sawyer–Tower circuit). Using an obvious relation

$$U_w(t) = \frac{2P_S l b n}{C} x(t), \quad (8.3.4)$$

voltage U_w can be used to determine $x(t)$ and its time derivative.

In contrast, Kumada (1970) found that polarization reversal in the ferroelectric ferroelastic crystal of gadolinium molybdate may proceed by the motion of a single-domain wall only. The switching in a sample of the square cross-section with the only wall parallel to the side or the diagonal of the square was experimentally addressed. The wall velocity was determined from the time dependence of the switching current taking into account a possible dependence of the wall length on its position in the sample.

To obtain meaningful data giving information on the basic laws of wall motion not influenced by the presence of undefined defects or by boundary conditions, crystals must be grown and samples were prepared with extreme caution. Till now only few of the available data seem to fulfill these requirements. In particular, in experiments where the electric field is homogeneous throughout the sample, any data showing that the wall velocity depends on its instantaneous position and especially on the distance from its original position cannot be taken as a generally valid law of the wall motion.

8.3.2 *Motion of Ferroelectric Nonferroelastic Walls*

After having discussed the methods used for measuring domain wall velocities we now wish to give a brief overview of experimental data. We shall concentrate on wall motion in ferroelectrics for which there have been many attempts to obtain reliable data. In the present section we will discuss the behavior of nonferroelastic ferroelectric domain walls.

Several decades ago much effort was devoted to attempts to devise digital memories based on 180° polarization reversal in ferroelectric crystals. It was realized that the switching not connected with changes of strain would be advantageous from the point of view of reliability of the device and therefore understanding reversal processes in nonferroelastic ferroelectrics was of primary importance. Among the investigated materials, BaTiO_3 played the leading role.

Having in mind the 180° wall motion, the situation in ferroelectrics which are not proper ferroelastics is simpler from one point of view: Elastic stresses can be expected to have little influence. However, it can also be more complicated because while severe restrictions of wall orientation due to spontaneous strain do not apply, the anisotropy of wall energy density may determine the shape of growing or shrinking domains. In Sect. 8.3.2.1 we shall discuss the situation where the curvature, energy anisotropy, and shape of the wall have little impact on its motion. Some features of shapes of growing domains related to wall energy anisotropy or to the specific mechanisms of wall motion will be discussed in Sect. 8.3.2.2.

8.3.2.1 Planar Walls

Below we will address experimental data on the motion of nonferroelastic ferroelectric walls that have been obtained for a few materials, the most attention being paid to ferroelectrics classical for this kind of experiments, namely to BaTiO_3 and TGS.

The earliest and still the most fundamental studies were performed by Miller and Savage long time ago and the law of motion of 180° walls in the tetragonal phase of BaTiO_3 deduced from their data is still widely used when discussing a number of phenomena. In fact, it is often considered to be of general validity for nonferroelastic ferroelectrics. This assumption, however, has to be taken with some caution.

As it was mentioned above in Sect. 8.3.1, Miller and Savage (1958) observed the expansion of a square-like domain in the tetragonal phase of BaTiO_3 at room temperature. One essential remark has to be made here. While the wall velocity v at a given field can be undoubtedly determined using Eqs. (8.3.2) and (8.3.3), one has to bear in mind that during the domain growth process also the area of domain walls increases. Therefore, the value of v determined in this way need not only be a function of the applied field (due to which the total energy decreases as the domain grows) but also be a function of the rate at which the energy of the wall surrounding the domain increases. For a square-shaped domain, the impact of the increasing wall area on its velocity is controlled by

a factor $\sigma_w/(aEP_S)$ (Miller and Savage, 1958) where a is the length of one side of the domain and σ_w is the surface energy per unit area of the wall. The effect of increasing wall area can be neglected if $\sigma_w/(aEP_S) \ll 1$. For typical values of the parameters of Miller and Savage's experiments $\sigma_w/(aEP_S) \cong 10^{-2}$ so that increasing wall energy seemed to have been minute and the motion of walls could be considered to represent the motion of an isolated wall.

Taking, therefore, v as a function of E only, data for a number of samples were shown (Miller and Savage, 1958) to be well fitted, in the range between 150 and 500 V/cm, to the expression of Eq. (8.3.5) in which v_∞ and δ are independent of the applied field.

$$v = v_\infty \exp(-\delta/E). \quad (8.3.5)$$

These data apply to crystal plates grown by the Remeika method, i.e., from the flux, from which the surface layer produced during the growth process was first removed by etching above the Curie point. For samples of thickness 100–200 μm the value of δ ranged between 1.9×10^3 and 3.9×10^3 V/cm. The value of v_∞ depended strongly on the way crystals were grown. Thus, for samples grown from the melt which contained 0.1 mol% AgNO_3 , the magnitude of v_∞ (0.7–9.1 cm/s) was repeatedly smaller than that for samples grown from the melt which contained 0.02 mol% Fe_2O_3 (7.8–68 cm/s). Changing iron concentration in the melt from 0.00 to 0.25 atomic percent led to a decrease in wall velocity by more than an order of magnitude (Miller and Savage, 1959c). These findings demonstrated clearly that the impurity content and defect structure have an essential influence on domain wall velocity.

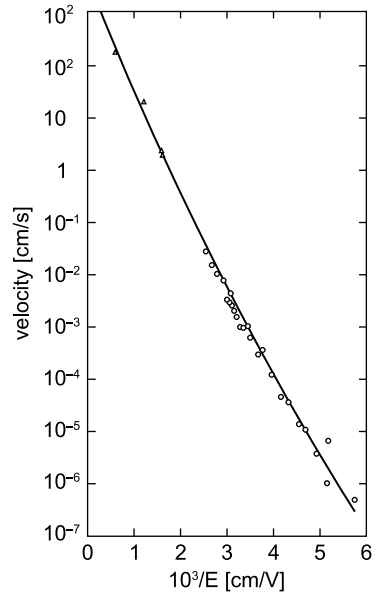
It is essential that, unless v_∞ and δ vary with E in some drastic manner, none of these data can be fitted to the law $v = \mu(E - E_0)$ which, as we shall see below, was found to be valid for lead germanate and in particular for ferroelastic ferroelectrics.

Further measurements (Miller and Savage, 1959b) were extended to the range of applied fields up to 1500 V/cm. In the higher field range, data were obtained by etching the sample after a field pulse was applied for a given time. Final results covering eight orders of velocity magnitude, which are summarized in Fig. 8.3.2, show that Eq. (8.3.5) with δ and v_∞ strictly field independent does not accurately describe the data over the entire measured range. However, within limited intervals this relation is a good approximation.

Independent experiments with BaTiO_3 plates, performed by Taylor (1962) at room temperature, confirmed the equation of motion (8.3.5). His values of coefficients $v_\infty = 2.8 \times 10^4$ cm/s and $\delta = 7.8$ kV/cm were found applicable for velocities between 10^3 and 10^4 cm/s, for the range of fields 2.6–6 kV/cm. Rather than by straight domain observations, these data were obtained by analyzing the shape of the switching current, similar to that described by Eq. (8.3.1).

All mentioned data by Miller and Savage were obtained with liquid electrodes. After the direct visibility of moving domain walls in BaTiO_3 had been established (Miller and Savage, 1959a), these authors continued their studies with semitransparent evaporated gold electrodes (Miller and Savage, 1959c). The field

Fig. 8.3.2 Logarithm of 180° wall velocity in tetragonal BaTiO_3 vs. the inverse of the applied field. After Miller and Savage (1959b)



dependence was found to be the same as with liquid electrodes; data covering four decades of velocity (10^{-6} – 3×10^{-2} cm/s) fulfill Eq. (8.3.5) with a change of slope, in the $\log v$ vs. $1/E$ plot, at 10^{-4} cm/s. These studies revealed a profound influence of several factors on wall velocities. First, for plates of the same thickness, wall velocity in samples with liquid electrodes is more than an order of magnitude higher than that in samples with metal electrodes. Second, the sample thickness itself plays an essential role. Thus, for instance, the field E_1 required to reach a velocity of 10^{-3} cm/s fulfills the relation $E_1 = 400(1 + d_0/d)$, where d is the sample thickness and $d_0 = 5 \times 10^{-3}$ cm. The analysis of data showed that it is the value of δ rather than that of v_∞ which depends on d . Third, the wall velocity of metal-electroded samples is affected by water vapor. Samples measured in dry winter days have higher wall velocities. And finally, a pronounced “memory effect” was observed for motion of 180° walls. When the crystal was kept in one \mathbf{P}_S direction for 16 h, in the field pulses applied afterwards in the opposite direction the wall moves first very unwillingly, but at subsequent pulses more easily. Also, the areas polarized in the direction of the measuring field for the longest time are the easiest to polarize in that same direction in the subsequent reversals. This is another fact showing that charge distributions left from previous reversals have an effect on wall motion, which persists for many minutes. It indicates that some slow relaxation process take place as the field is applied.

The experimental data presented above and, specifically, the discovered wall mobility law, Eq. (8.3.5), and a pronounced impact of the sample thickness on the parameters of this law stimulated theoretical activity which yielded a nucleation-controlled model for the wall motion (Miller and Weinreich, 1960) (see Sect. 8.4.2)

and a surface layer model (Drougard and Landauer, 1959) where the depolarizing field interferes with the wall motion (see Sect. 8.4.5). In turn, these models motivated more detailed investigation of the phenomenon. Here, remarkably is a paper by Miller and Savage (1961), where several seminal features of 180° domain wall dynamics in BaTiO_3 have been established. Some results from this paper are shown in Fig. 8.3.3. Figure 8.3.3a demonstrates that the wall velocity is not constant during application of a voltage pulse of a fixed amplitude. In this context it was established that the wall velocity saturated after it passes some 200 nm distance, independently of a value of the driving voltage. Figure 8.3.3b reveals a kind of memory effect. Namely when pretreated with a voltage pulse, the impact of the second identical pulse is sensitive to the delay time between the pulses. Finally, Fig. 8.3.3c demonstrates a sensitivity of the wall velocity to the length of the voltage pulse applied. Some these features of the wall dynamics can be rationalized in terms of the aforementioned theories; see Sects. 8.4.2 and 8.4.5.

Until now we referred only to the data taken at room temperature. The inverse exponential form of the law (8.3.5) suggests that the motion of a domain wall of this kind cannot be compared to pulling an object characterized by friction but

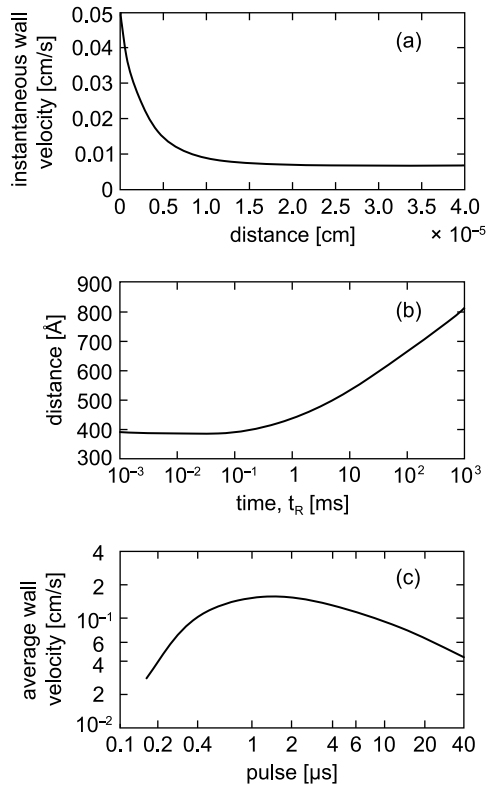


Fig. 8.3.3 Data on 180° wall dynamics in tetragonal BaTiO_3 . After Miller and Savage (1961).
 (a) Instantaneous wall velocity vs. wall displacement from its position at rest; (b) distance of wall displacement after the application of a single voltage pulse vs. the time interval t_R between two subsequent pulses; (c) average wall velocity vs. pulse length

rather suggests a nucleation mechanism. Then it can be expected that the velocity would be strongly temperature dependent. Thus the influence of temperature on wall velocity could provide a key factor for understanding the involved mechanisms. Indeed, already the first observations (Miller and Savage, 1958) showed that the increase in temperature by about 10 K above room temperature had a profound effect on v , increasing its value by about two orders of magnitude. In the later study Miller and Savage (1959b) showed, using liquid electrodes, that within the temperature range between 20 and 30°C the wall velocity vs. field dependence can be still described by the inverse exponential law, Eq. (8.3.5), and that the temperature dependence lies primarily in δ and not in v_∞ . In this region, they found that δ decreases by 1% per °C. Savage and Miller (1960) covered a wider temperature region using metal-electroded samples. They pointed out that the obtained data depend strongly on relative humidity. The increase in the latter from 17 to 30% resulted in the wall velocity higher by a factor of about three, in the applied fields between 400 and 550 V/cm. In pure BaTiO₃ samples, the temperature increase from 25 to 100°C resulted in the reduction of δ by a factor of 3.

The data on direct wall observations in BaTiO₃ discussed above were taken for fields 0.1–2.0 kV/cm. The upper half of this interval covers the region of fields usually used to study hysteresis loops in barium titanate. Stadler and Zachmanidis (1963) significantly extended this region, up to 450 kV/cm. Short voltage pulses were applied using liquid electrodes and domain structure was revealed by etching after each step. The velocity data reproduced in Fig. 8.3.4a show a considerable scatter but can be reasonably well fitted to the equation

$$v = v_0 E^{1.4}. \quad (8.3.6)$$

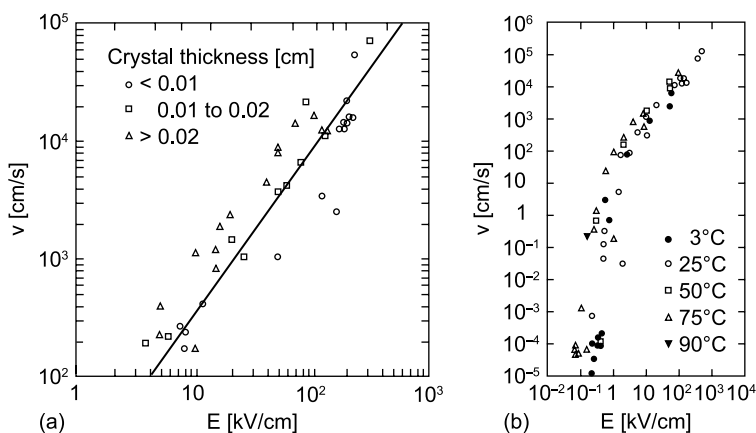


Fig. 8.3.4 Velocity of 180° walls in tetragonal BaTiO₃ measured at high fields. (a) In samples of different thicknesses. After Stadler and Zachmanidis (1963). (b) At different temperatures. After Stadler and Zachmanidis (1964)

At the highest applied fields the wall velocity reaches the value of 10^5 cm/s which amounts to half of the speed of longitudinal sound waves. In fact in a longer field pulse the speed may be even higher since the data by Zen'iti et al. (1958) shows that switching is slower when it proceeds in frequently interrupted voltage pulses than in a single step function. In an additional study (Stadler and Zachmanidis, 1964a,b), an involved investigation of temperature dependence of 180° wall velocity in BaTiO_3 was offered. Again liquid electrodes (water solution of NaCl) were used since they were found to give simpler domain shapes than metal electrodes. Starting from a single-domain state, samples were partially switched by applying pulses of electric field. After each partial switching process the plate-like sample was etched and photographed; the velocity was simply calculated by dividing the wall displacement by the pulse duration; the role of finite size of the growing domain was not considered; in fact the authors observed even a characteristic change of domain shapes. In this study, the authors have also addressed the impact of the temperature on the $v(E)$ dependence, which is summarized in Fig. 8.3.4b. Though, here the scatter is somewhat disturbing, the authors concluded that the temperature increase leads to some shift of the $v(E)$ curve in this plot to the left.

Experimental data which we have discussed up to now concern the tetragonal phase of BaTiO_3 . Additional information about wall behavior in this material was obtained by Callaby (1965) who studied their properties in the orthorhombic phase, stable at temperatures below about 5°C . Here \mathbf{P}_S is parallel to $\langle 110 \rangle$ directions of the cubic parent system so that $\{110\}$ slices can be poled perpendicularly to the major surfaces. It turned out that, similarly as in the tetragonal phase, antiparallel domains could again be distinguished optically in a polarizing microscope. They have square-like cross-sections with two walls of the (100) type and the other two of the (110)-type orientation. At low fields the motion can be followed by eye; at higher fields the wall positions were measured before and after the application of a field pulse. It turned out that the law of motion given by Eq. (8.3.5) was well satisfied for velocities in the range between 10^{-5} and 10^4 cm/s. Data which are reproduced in Fig. 8.3.5a were taken at $T = -15^\circ\text{C}$. They demonstrate also the anisotropy of the wall velocity; the inverse exponential law, Eq. (8.3.5), is well satisfied, with $v_\infty = 3 \times 10^4$ cm/s and $\delta = 5.7 \times 10^3$ V/cm for the (100) wall, and with $v_\infty = 5.5 \times 10^2$ cm/s and $\delta = 4.1 \times 10^3$ V/cm for the wall of (110) orientation. At a field of approximately 400 V/cm the two velocities were the same, the growing domain was square in shape. In this figure data are not included for the field interval from 300 to 700 V/cm where direct observation of the wall was no longer possible. In keeping with the measurements of Miller and Savage, the wall velocity was found to decrease as the wall moves, following the relation $v \propto 1/x^{1.5}$ where x is the displacement of the wall. After some distance d_{ss} the wall reaches steady-state velocity. At 160 V/cm d_{ss} is 70 Å, but at 550 V/cm it exceeds 7×10^4 Å.

Similarly as in the tetragonal phase, temperature was found to play an essential role in nonferroelastic wall motion also in the orthorhombic phase

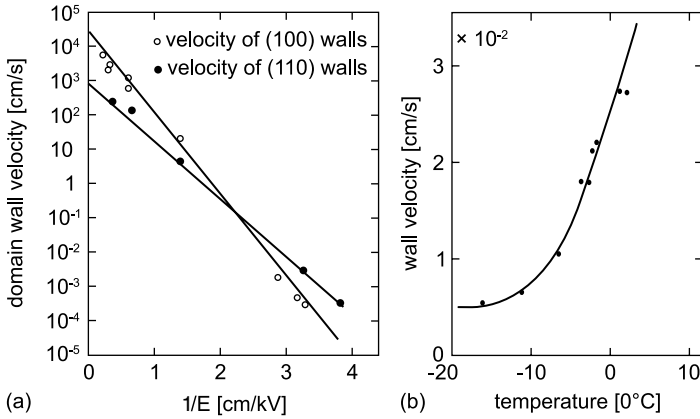


Fig. 8.3.5 A 180° wall velocity in the orthorhombic phase of BaTiO_3 . After Callaby (1965). (a) Dependence on applied field at -15°C . (b) Temperature dependence of (110)-oriented 180° wall velocity at an applied field of 300 V/cm

of barium titanate. Callaby's (1965) data are shown in Fig. 8.3.5b. In the same study, experiments similar to those by Miller and Savage (1961) for tetragonal BaTiO_3 have been performed. Some differences in the domain wall dynamics in orthorhombic and tetragonal phases have been established. For explanation of this difference a surface layer model, different from that by Drougard and Landauer (1959), has been developed Callaby's (1965).

Till now we have referred to some data and proposed models which concerned crystals of BaTiO_3 . It is appropriate to point out that all these investigations were performed using flux-grown samples and that some discrepancies or even basic features of observed dynamic domain properties might be related either to specific lattice defects or to surface layers of plate-like samples. Only when this research area was to a large extent abandoned, the top-seeded pulling method was successfully introduced to grow large and high-quality crystals of this material (cf., e.g., the book by Xu (1991)). Therefore, repeating some of the previous experiments might be interesting.

Next to barium titanate, the other model ferroelectric material with non-ferroelastic antiparallel domain pairs is triglycine sulfate. Large crystals of TGS, when grown with proper care from water solution, are free of optically detectable defects. As we have already discussed, domains are usually visualized by etching or decoration techniques.

In good-quality crystals of TGS and its isomorphs, domains tend to have lenticular shapes. It is appropriate to point out that some researchers have neglected the problem of the shape of a growing domain, investigating the wall velocity in one chosen direction, that is, observing a particular side of a domain of two-dimensional cross-section. Another remark of general character is that since results of Miller and Savage for BaTiO_3 were already known when

the investigations of TGS were initiated, a certain degree of inclination to fit the obtained data to Eq. (8.3.5) could be assumed.

Here we shall refer to only some of the available data. In one of the first attempts to address this subject, Hayashi and Mishima (1969) applied mercury electrodes (which are easily removable) to a TGS plate and after a partial switching process revealed the new positions of domain walls by etching, repeating this process for given values of the applied field a number of times. Results were shown to fulfill the inverse exponential law, Eq. (8.3.5), with $v_\infty = 39$ cm/s and $\delta = 150$ V/cm. In more detail, domain wall motion in TGS at room temperature was studied by Hadni and Thomas (1975) who used the pyroelectric probe technique for imaging domains in a plate 20 μm thick. As the first step, velocity was measured for walls of domains already existing in the sample; in an applied field of 200 V/cm the average speed amounted to 1×10^{-2} to 1.4×10^{-2} $\mu\text{m}/\text{s}$, depending on the direction of the wall propagation. However, more informative are the data for domains which were first nucleated by the applied field since their walls can be supposed to be less influenced by pinning effects. These data are summarized, for walls moving in the slowest direction, in Fig. 8.3.6 which shows the plot of the average wall velocity vs. field. For a sample 20 μm thick it can again be well fitted by the inverse exponential law, Eq. (8.3.5), with $v_\infty = 475$ cm/s and $\delta = 1.15 \times 10^4$ V/cm. This figure also shows the data for a sample of smaller thickness of 6 μm . Similarly as in BaTiO_3 , wall velocities were found to depend strongly on sample thickness: A reduction of sample thickness from 20 to 6 μm leads to a three-orders-of-magnitude reduction of the wall velocity. In a narrower interval of

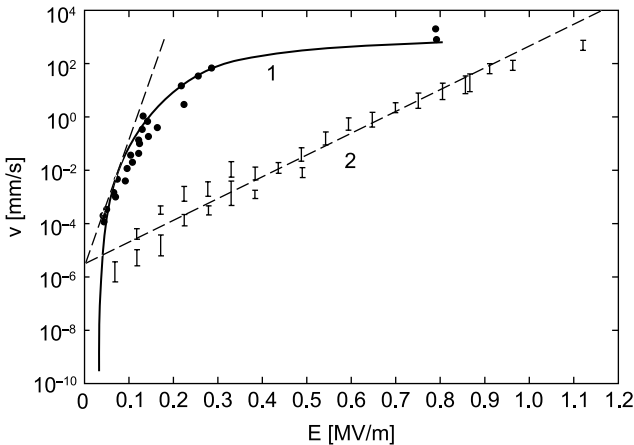


Fig. 8.3.6 Wall velocity vs. applied field for TGS. After Hadni and Thomas (1965). Curve 1: sample 20 μm thick. Curve 2: sample 6 μm thick. *Solid line* corresponds to a fit to Eq. (8.3.5), *dashed lines* represent fits to the $v = v_0 \exp(\alpha E)$ law

velocities, Hadni and Thomas (1975) have also fitted their data to the simple exponential law

$$v = v_0 \exp(\alpha E) \quad (8.3.7)$$

as shown in Fig. 8.3.6.

The alternative technique of liquid crystal decoration for studying wall velocities in TGS was employed by a number of Russian investigators; as already emphasized, the boundary conditions involved in this method can complicate the interpretation of obtained data. Results were presented in the form of plots $\ln v$ vs. $1/E$ at temperatures between 28 and 45.5°C and in the field range 30 V/cm to 1.3 kV/cm (Dontsova et al., 1982; Tikhomirova et al., 1986ab; Dontsova et al., 1989). The authors found that their data can be fitted to the inverse exponential law, Eq. (8.3.5), however with the different values of the fitting parameters in three field regions. In the three field regions domains differ in form, their cross-sections changing from circular to lenticular and to rhombic. The wall velocity was found to fulfill the relation

$$v \propto \exp(-U_0/kT) \quad (8.3.8)$$

with the activation energy U_0 changing stepwise at 43°C from 0.6 to 0.7 eV below this temperature to 6–7 eV above this temperature. The same visualization method made it also possible to measure the amplitude of a wall oscillating in applied ac field. The obtained data (Dontzova et al., 1989) demonstrated a pronounced relaxation effect, already at frequencies below 0.1 Hz. In an aged sample the wall amplitudes are generally smaller than in a sample which was annealed above the transition temperature. Dontsova and Popov (1975), in connection with their study of spontaneous changes of domain shapes in TGS, measured also wall velocities for fields between 0.1 and 1 kV/cm; here they found Eq. (8.3.5) to be satisfied, with $v_\infty = 0.4$ cm/s, $\delta = 670$ V/cm. Later, however, it was pointed out (Dontsova et al. 1981) that in the field interval up to 1000 V/cm three linear sections in the dependences $\ln v$ vs. $1/E$ are observed, differing in the activation fields: For one of the investigated crystals, $\delta = 110$, 530, and 2000 V/cm in three field regions.

Using the same decoration technique, the wall velocities were investigated also in crystals of guanidine aluminum sulfate hexahydrate (GASH) (Dontzova et al., 1989). Similarly as for TGS, the authors claim that relation (8.3.5) was fulfilled, with different values of the coefficients v_∞ and δ in three different ranges of the applied field.

It is obvious that the most reliable data on the wall velocity dependence on applied field are those based on direct domain observations, and with one exception (Taylor, 1962) all data mentioned above were of this character. However, attempts have also been made to obtain information on wall velocities by elaborate interpretation of the switching current $i_s(t)$, which represents the current flowing through the sample after the application of a pulse-shaped

electric field. Perez et al. (1987) used this indirect method for determining sidewise wall velocities. They applied square-like electrical field pulses of alternating polarity, which normally would lead to the well-known time-dependent switching current. However, on pulses of one polarity of the applied field E an additional field increase $\Delta E = E/10$ was superimposed, for a time period short compared with the total switching time. This resulted in an instantaneous increase Δi in the switching current i . Based on a simple model of switching geometry primarily characterized by sidewise expansion of domains with velocity v , it was argued that $\Delta i/i = \Delta v/v = \Delta \ln(v)$. The analysis of experimental data for TGS crystals at room temperature and for fields in a limited range $0.3 < E < 1.1$ kV/cm led to the relation

$$v = cE^2; \quad (8.3.9)$$

the indirect method, however, did not allow to determine the magnitude of the constant c .

Tikhomirova et al. (1980a) paid attention to the velocity anisotropy as well as to the influence of temperature. Lens-shaped domains always grow much faster along their long axis in the $[\bar{1}02]$ direction than along the c -axis; at $E = 150$ V/cm and $T = 27^\circ\text{C}$, for instance, the respective velocities are $v_{\parallel} \cong 4 \times 10^{-3}$ cm/s $\cong 2v_{\perp}$. In the $\ln v_{\parallel}$ vs. $1/E$ dependence two linear sections are observed for four different temperatures and the $v_{\perp}(1/E)$ dependences were found to be similar. Thus these sections correspond to law (8.3.5), differing in the values of δ and v_{∞} . When T changes from 23 to 47°C , for different crystals v_{∞} increases by a factor of 2–2.5 while δ decreases by a factor of 5–10. We have to stress again that while these results are presented as domain wall velocities, it is not isolated planar walls which are moving.

When measuring domain wall velocities, surface boundary conditions—such as the mentioned surface layers—can play an essential role. However, well-defined experimental studies devoted to this problem are very limited. For TGS, interesting data were offered by Tikhomirova et al. (1985b). Their aim was to investigate the influence of nonuniform boundary conditions on motion of 180° walls in TGS in the sandwich NLC–TGS–NLC where NLC stands for the nematic liquid crystal layer. In their experimental arrangement shown in Fig. 8.3.7, the inserted glass plate provides different boundary conditions in the different parts of the sample. Starting with a single-domain state, after the application of the field, domains are nucleated in region I (no glass); they grow

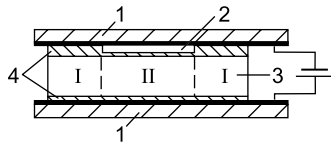


Fig. 8.3.7 Experimental setup by Tikhomirova et al. (1985b). 1, glass plates with conductive SnO_2 layers; 2, glass plate; 3, TGS plate; 4, layers of nematic liquid crystal

with sidewise velocity v_1 till their fronts reach the border of region II (glass). When the domain front acquires the shape of this border, the wall continues to move under glass into region II, with velocity $v_2 < v_1$ which continuously decreases. Now, that the field of opposite polarity is applied, this wall, say wall A , does not move backwards. Instead, polarization reversal proceeds again in region I and finally new wall B is formed which penetrates into region II. This can be continued with a wall C . When the latter reaches the already standing wall B , they annihilate and the standing wall A starts to move with the velocity which had the wall C when it reached the wall B .

The authors offered an interesting interpretation of this behavior. In region I, for a sufficiently strong field E the switching time is limited by the conductivity of NLC. When a wall enters region II, its velocity is limited from above by diffusion of free carriers into the thin NLC layer. The distance x covered in the time interval t by the wall entering region II is of the order of \sqrt{Dt} where D is the diffusion coefficient in the NLC. The proportionality $x \propto \sqrt{t}$ has been experimentally confirmed. The fact that the last-but-one introduced domain wall is immobile in the presence of the last moving wall was explained in the following way: Its motion is practically impossible due to the small concentration of compensating charges, since the diffusion of free charges takes place prevalingly between the edge of region II and the last introduced (and moving) wall.

It was suggested that the described method could be used not only to produce domain patterns of a required configuration in uniaxial ferroelectrics but also to estimate electrical conductivity, viscosity, diffusion coefficient, and other parameters of NLC, using the data on time dependence of velocity of domain walls.

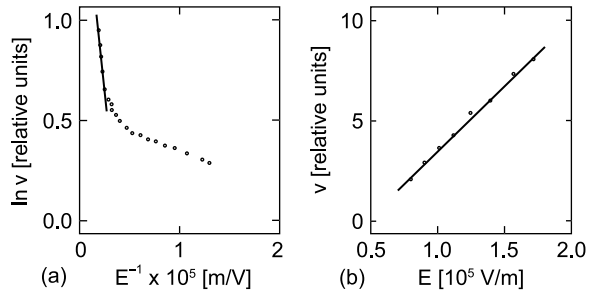
It has to be pointed out that while law (8.3.5) has been repeatedly used to interpret data on TGS, the values of δ obtained by different authors strongly differ. They depend on boundary conditions employed in the method used to determine δ , and also on the applied fields. In addition, different samples may behave differently, due to crystal lattice imperfections. Systematic investigations in this field are still missing. For ferroelastic domain walls, it is generally accepted that lattice imperfections such as dislocations can influence the wall motion induced by applied field. However, it was shown by several authors that this is the case even for nonferroelastic domain walls such as those in TGS crystals. By etching technique, Nakamura and Nakamura (1962) observed that moving walls in TGS are caught by dislocations and that their interactions depend on the applied field: In the field of 30 V/cm, a domain wall was caught in dislocation which resulted in zigzag shape of the wall. However, in the field of 350 V/cm it passed smoothly through the dislocation. These results were later confirmed by Meleshina (1971, 1970) who observed etch patterns showing successive positions of domain boundaries and dislocation emergence points. Theoretically, the issue was discussed by Suda (1979).

The third nonferroelastic ferroelectric material we wish to include in this overview of wall velocity data is lead germanate, $\text{Pb}_5\text{Ge}_3\text{O}_{11}$. In fact this material is especially suitable for studies of wall velocities. The reason is that it represents the species $\bar{6} - Pd - 3$ in which domains are directly distinguishable in a

polarizing microscope, due to optical activity which is a morphic effect for this species. The problem was addressed by Shur et al. (1984b, 1985d, 1990). Polarization of crystal plates provided with transparent electrodes was reversed by applying rectangular ac field pulses and, during the reversal process, the domain wall positions were measured in a polarizing microscope, using stroboscopic illumination. Walls penetrating the whole sample thickness (2 mm) were selected. Before the actual measurements, the samples were “rejuvenated” by switching in a 50 Hz field until a symmetric hysteresis loop was observed. In this way unwanted effects of “unipolarity” due to defects preferring a particular orientation of \mathbf{P}_s are largely avoided; these, as it was shown in an independent study (Shur et al., 1984a), lead to backswitching phenomena which would greatly influence data on domain wall velocity. Some of the results are shown in Fig. 8.3.8 (Shur et al., 1985c). Here, for applied fields exceeding the threshold field $E_0 = 470$ V/cm but smaller than 2.5×10^3 V/cm, the wall velocity was found to be a linear function of the electric field

$$v = \mu(E - E_0) \quad (8.3.10)$$

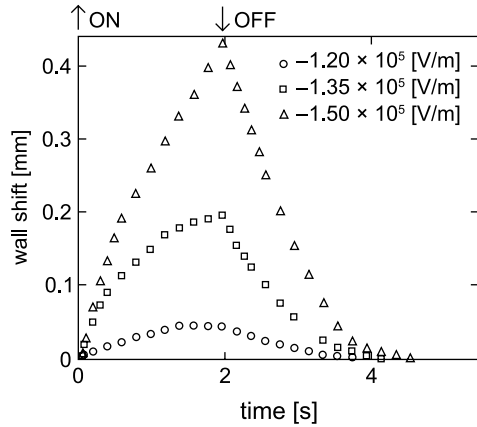
Fig. 8.3.8 Wall velocity in lead germanate. (a) Solid line corresponds to $v \propto \exp(-\delta/E)$; (b) solid line corresponds to $v \propto (E - E_0)$. After Shur et al. (1985c)



while for fields exceeding this value relation (8.3.5) is fulfilled. It is essential to realize that these data refer to average velocities calculated from the time required for the wall to cover a given distance under the assumption that the velocity is constant. Later experiments of Shur et al. (1990), however, showed that similar to other materials the wall is slowing down as it travels from its original position. In analogy to the earlier investigations of barium titanate, the effect was interpreted in terms of the interface-related depolarizing phenomenon (see Sect. 8.4.5). Figure 8.3.9 illustrates such effect. Here it is seen that, for smaller values of the applied field (e.g., $E = 1.2$ kV/cm), the wall virtually stops after 2 s and it still keeps moving at higher fields. At the same time, in the whole field range addressed, there is observed the full backswitching when the field is off.

The problem of domain wall velocity in nonferroelastic ferroelectrics was of extensive interest several decades ago, in particular because it was connected with the widely addressed issue of ferroelectric memories based on single

Fig. 8.3.9 Time dependences of domain wall shifts in lead germinate during and after the application of a 2 s pulse of an electric field of three indicated values. After Shur et al. (1990)



crystals. More recently, it disappeared from the family of research issues of high preference, despite the fact that now a number of new materials falling into this category are known. It has to be admitted, however, that the selection of efficient methods with well-defined boundary conditions is still quite limited. One of the few studies of wall velocity in relatively new materials has been performed by Matyjasek and Jakubas (1997), on single crystals of alkylammonium halogenobismuthate, $(\text{CH}_3\text{NH}_3)_5\text{Bi}_2\text{Br}_{11}$ (species *mmm-Pd-mm2*). The investigated crystals showed a high built-in bias field E_b . Thus the macroscopic characteristics like switching time and wall velocity were found dependent on the sign of the applied field. Intensive backswitching was observed, in particular close to $T_C = 312$ K. This phenomenon may be connected with a surface layer due to which a depolarizing field is formed for a quickly moving domain wall. Figure 8.3.10 demonstrates the field dependence of the velocity at different temperatures, when the applied field was of polarity opposite to that of E_b . Two straight sections correspond to the inverse exponential law (8.3.5) with different values of δ . These two sections are related to different shapes of domains: lenticular in region I and zigzag in region II. Such data were found not to be well reproducible since the process of nucleation is not the same in every cycle. With increasing T , the value of δ decreases, e.g., $\delta = 2400$ V/cm at 293 K while $\delta = 850$ V/cm at 307 K.

As it is clear from data included in this section, the classical barium titanate studies of Miller and Savage still represent the most complete set of data on wall motion, for any nonferroelastic ferroelectric material. These authors also showed the role of crystal quality or perhaps of particular additives. This factor is often completely forgotten when discussing some experimental results on switching. However, up to now no data seem to be available, which would specify these effects in detail and allow an involved analysis. In particular, practically nothing is known on the influence of specified crystal quality or particular additives on the values of v_∞ and δ coefficients or even on the validity of Eq. (8.3.5) and the retardation effects (slowing-down of the wall under a fixed

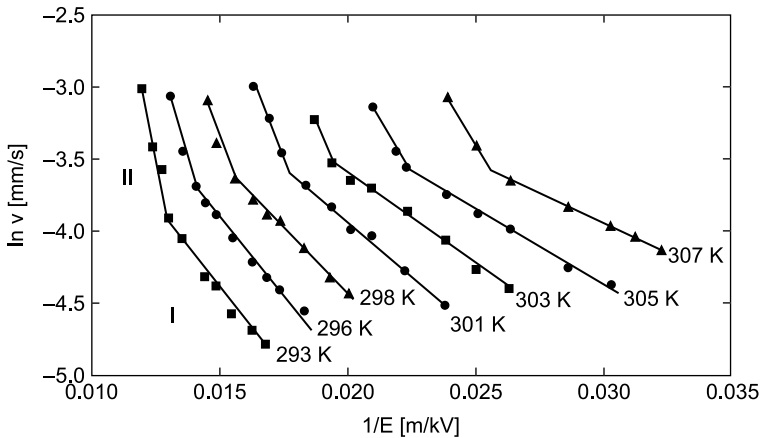


Fig. 8.3.10 Field dependence of velocity of nonferroelastic 180° domain walls in alkylammonium halogenobismuthate at different temperatures. After Matyjasek and Jakubas (1997)

applied field). Similarly, in triglycine sulfate it was shown clearly by Dontsova et al. (1982) that the velocity of lateral motion of domain walls is strongly affected by the growth conditions and previous history of a sample. In an aged crystal it is by two orders of magnitude less than that in a crystal annealed for 2 h at 80°C . Crystals grown in the paraelectric phase have a more labile domain structure than those grown in the ferroelectric phase. All these phenomena remain unexplained.

8.3.2.2 Growing Domains

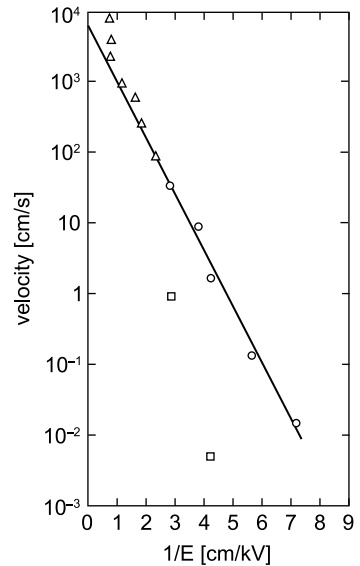
In the previous this section we had in mind the motion of those nonferroelastic walls in ferroelectrics which are parallel with the polar axis; in other words, we considered the “sidewise” wall motion. In addition, we concentrated on cases where the shape of the growing domain did not — or was supposed not to — essentially influence domain wall velocity. Now we shall lift these two limitations and offer some additional experimental data. It is again assumed that an electric field is applied whose polarity supports the \mathbf{P}_S orientation in the growing domain. First, we will discuss the growth of long narrow domains along the polar direction; this phenomenon follows the formation of a small nucleus with antiparallel orientation of \mathbf{P}_S . When such a narrow domain reaches both surfaces of a plate-like sample, the switching process continues by its sidewise growth. This phenomenon can be expected to be anisotropic on the two-dimensional level, depending on the anisotropy of domain wall velocity, and we shall present some relevant data at the end of this section.

The time required for a narrow domain nucleated at one electrode to reach the opposite electrode may play a role in the speed of the whole switching process. However, we have no systematic and confirmed data addressing this

problem, primarily because of difficulty of the direct observation of nucleated domains which are very small.

The problem of the forward growth velocity of narrow nonferroelastic 180° domains was addressed by Stadler (1966). He claimed that in a -oriented plates of barium titanate (i.e., the c -axis lies in the plane of the sample), domain walls were visible as dark regions $2\text{--}4\ \mu\text{m}$ wide, separated from the dark field by bright-colored lines $0.5\text{--}1\ \mu\text{m}$ wide. This allowed applying stroboscopic method for measuring speed above $50\ \text{cm/s}$. For lower velocities the successive positions of the wall after each short pulse of applied field were directly determined. While some walls speeded up on approaching the far side, others slowed to an abrupt stop inside the crystal. It was established that for domains which were first to be seen during reversal, the data could be fitted to the inverse exponential law, Eq. (8.3.5), with $v_\infty = 5500\ \text{cm/s}$ and $\delta = 1.8\ \text{kV/cm}$. These data are shown in Fig. 8.3.11. However, domains which appeared somewhat later moved considerably slower while domains appearing much later were impossible to follow in the complicated picture the author saw.

Fig. 8.3.11 Velocity of forward growth of narrow 180° domains in BaTiO_3 . Circles are measurements of one domain wall and triangles represent several other walls moved after voltage was applied. Squares represent walls which moved after the polarization had already been partially reversed. After Stadler (1966)



Stadler's effort to measure directly the forward velocity of a narrow growing domain seems to be quite solitary. However, several attempts have been made to obtain information on wall velocities by an elaborate interpretation of the switching current $i_s(t)$, which represents the current flowing through the sample after the application of pulse-shaped electric field. Binggeli and Fatuzzo (1965) were the first to rely on this indirect method. They based their approach on the assertion that in TGS, for fields above $20\ \text{kV/cm}$, the time required for the

formation of nuclei with opposite polarization is much shorter than the domain transit time. If this were so, then from the data on switching time the forward wall velocity v_{forw} could be determined. The latter was found to increase linearly with the applied field till it reached a critical value of the order of the sound velocity in the material. For further increasing field, v_{forw} was found to increase with an even higher slope. In this interpretation approach, however, sidewise growth of domains was not considered and thus it appears questionable. A more involved interpretation approach to determine wall velocities from the analysis of switching current was offered by López and González (1973). They introduced five quantities characterizing $i_s(t)$, namely i_{max} , t_{max} (see Sect. 7.4), and three additional parameters characterizing the shape of switching current. The $i_s(t)$ function was modeled as a function of the transit time t_d (needed for a nucleus to reach the opposite electrode), sample thickness d , sidewise wall velocity, total number of formed nuclei, and probability of formation of an isolated nucleus. Based on this model, the forward wall velocity $v_d = d/t_d$ was found to satisfy the inverse exponential law, Eq. (8.3.5) dependent on the sample thickness. The highest velocities obtained for the highest applied fields of 10 kV/cm were found to be $v_d = 24,000$ cm/s.

We can summarize that the efforts devoted to the issue of forward velocity were rather limited and it still represents an open problem.

When a growing nucleus reaches both surfaces of a ferroelectric plate, it starts to expand sidewise and it is this process that we are now going to discuss. Typically, nonferroelastic domain walls are not planar and do not extend over the whole surface of a sample. The problem of shapes of growing domains was addressed a long time ago; however, our knowledge is rather limited since only a few classical ferroelectrics were investigated in some detail. Below we present some experimental data on this matter whereas we shall consider the theoretical approaches to the shape of growing domain in the Sect. 8.4.6. Here it may be useful to point out that these shapes are primarily determined by the wall velocity anisotropy.

The most involved data concern BaTiO₃ in its tetragonal phase and it is appropriate to start with the classical Miller–Savage investigations (Miller, 1958; Miller and Savage, 1959b). They used plate-like samples etched down to the thickness of about 50 μm , with liquid electrodes; domains were visualized by etching. A previously poled single-domain sample was first partially switched by a short application of a dc field. Then a distribution of domain sizes was observed, with the smallest ones which are circular in cross-section at one side of the crystal and cannot be seen on the other side. With a strong preference, the domains start growing from the electrode biased with a negative voltage. These domains are of the conical shape with the estimated apex angle of 1° . They grow sidewise and by the time the base is about 10 μm in diameter, the truncated cone is nearly a cylinder. In further expansion of a domain, there is a strong preference to form a square-like cross-section, whose edges make 45° with the crystallographic a -axes (Fig. 8.3.12a). The same was observed for metal-electroded samples. As the applied field is increased, the growing domains become octagonal in shape (Fig. 8.3.12b). Finally for higher fields they

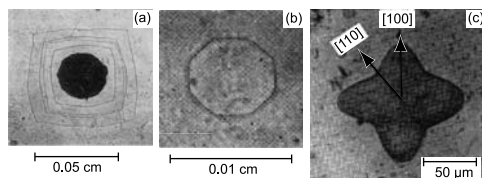


Fig. 8.3.12 Shapes of isolated growing 180° domains in tetragonal BaTiO_3 ; see text. After Lee et al. (1984) and Miller and Savage (1958); Reprinted with permission from Miller and Savage (1958). Copyright (1958) by the American Physical Society

become square-like again but now with sides parallel to the a -axes. It should be mentioned that the basic wall velocity data (Fig. 8.3.2) refer to the first stage: walls of the approximate (110) orientation.

In the investigations of other authors, most of these observations were confirmed and some additional data were presented. Husimi (1960) found that when the primary squares shrink due to the application of field of opposite polarity, they become octagonal and then again square like, but with diagonals along $[110]$. Stadler and Zachmanidis (1963) observed that when a domain grows in the primary stage, its velocities along the two a -directions are sometimes different, leading to an oblong-shaped cross-section. When studying the temperature dependence of 180° domain wall velocity, these authors observed that the originally square-like growing domains become very rounded at temperatures from 50 to 75°C ; at 75°C they are almost perfect circles (Stadler and Zachmanidis, 1963). This was explained by assuming that at these temperatures, the energy of such a wall is independent of its orientation.

Much later, Lee et al. (1984) revisited the issue of dynamic domain behavior in BaTiO_3 crystals. They used saturated aqueous solution of LiCl as electrodes as in some of the papers by Miller and Savage. When the field of 187 V/cm was repeatedly applied, each time for 15 s , small round-shaped nuclei grew into square-shaped domains with $[100]$ diagonals as reported before. However, when the total time of applied field exceeded 45 s , the domain shape developed such as that shown in Fig. 8.12c. The authors brought attention to the fact that the sequence of domain shapes corresponds to the sequence of (001) cross-sections of velocity surfaces of elastic waves in this material.

It would be difficult to summarize the known facts of BaTiO_3 and connect them with some consistent theoretical approach (see Sect. 8.4.6 for a limited discussion). Here we are to stress that all mentioned data were collected several decades ago and, though the dynamics of domain growth in barium titanate was not fully understood, little attention was paid to this field of research since that time. With presently available high-quality crystals, the issue seems to be worth of further investigations.

We now pay some attention to the studies of growing domains in crystals of triglycine sulfate and its isomorphs. It was already pointed out above that domain wall velocities in this material were repeatedly studied, without clearly

specifying the domain shapes or the wall orientations. The usefulness of such data is somewhat limited. It is known that after the application of electric field small domains are nucleated; then they start to expand sidewise, usually acquiring a lenticular shape (Hayashi and Mishima, 1969). According to Dontsova et al. (1982), at high fields, domains can acquire a rhomboidal shape.

The most involved study of shapes of growing domains in TGS and TGSe crystals was performed by Suda et al. (1978b). They initiated the switching process by applying low field for a given period of time, using liquid electrodes. Shapes of growing domains were determined by the powder pattern decoration method. In TGS, the authors claimed to have observed two typical shapes of growing domains: lenticular and elliptical, in both cases with the long axes perpendicular to the crystallographic c -axis; this is in some contradiction with the above-mentioned results. In TGSe, “restricted lenticular” domains are formed. These observations, illustrated in Fig. 8.3.13, were successfully related to a theoretical approach, as discussed in the Sect. 8.4.6. This figure also contains the modeled domain shapes (Suda et al., 1978b).

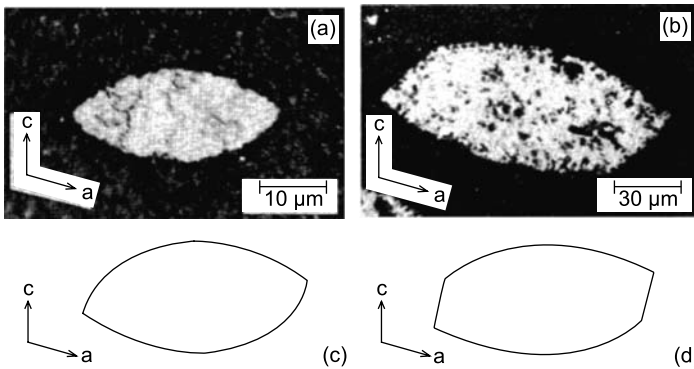


Fig. 8.3.13 Shapes of growing domains: experiment and theory after Suda et al. (1978b). (a) Powder pattern in TGS at room temperature, under applied field of 2.4 kV/cm; (b) powder pattern in TGSe at 0°C, under applied field of 2.1 kV/cm. Calculated domain shapes for TGS (c) and TGSe (d)

All in all despite a large number of published observations, we do not have an unambiguous description of domain shapes in TGS or isomorphous materials, a fact which is related to unspecified sample qualities and their histories as well as to not satisfactorily specified boundary conditions when domains are visualized.

Till now, it appears that barium titanate and TGS-type crystals have been the only candidates of nonferroelastic ferroelectrics for involved investigations of the shapes of growing domains. Only very few other attempts to address this issue seem have been undertaken, which led to some preliminary results. For

example, when studying polarization reversal behavior in lead germanate, $\text{Pb}_5\text{Ge}_3\text{O}_{11}$, Shur et al. (1985b) observed that domains growing in applied fields below 3 kV/cm are typically of regular hexagonal shape (cf. Fig. 2.2.8); however, when field pulses of opposite polarity but different duration are applied, domains acquire triangular shapes.

8.3.3 Motion of Ferroelastic Walls in Ferroelectrics

In ferroelectrics, any pair of domain states which differ in spontaneous strain, differ also in the direction of \mathbf{P}_s . As a consequence, motion of ferroelastic walls in ferroelectrics can always be induced by applying electric field of proper orientation. Experimentally, this is a relatively easy task; in particular, the observed domain wall can be made to move in any required direction by choosing polarity of the applied field while to apply alternatively a compressive and expansive stress would require rather involved experimental setups. In the present section, we concentrate on ferroelastic domain walls in ferroelectrics. First, we discuss the “sidewise” motion of planar walls; next, dynamic properties of narrow ferroelastic domains terminating inside a sample will be considered.

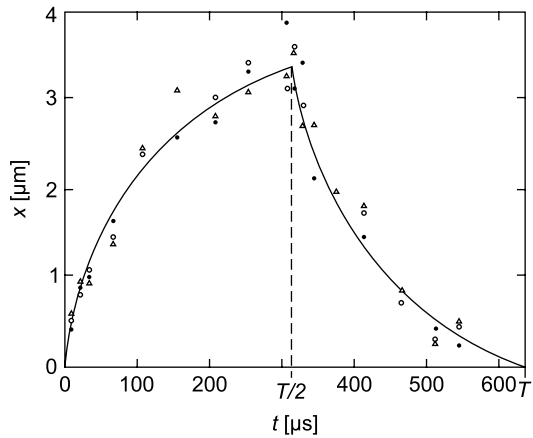
8.3.3.1 Planar Walls

The orientation of ferroelastic domain walls is severely limited by the conditions of mechanical compatibility. Serious orientation departures violating these conditions cannot be expected even for moving domain walls. However, small deviations do occur and result usually in the formation of wedge-shaped domains. The motion of wedges has several specific features and will be discussed in a separate section. At present we shall have in mind ferroelastic walls which on a macroscopic scale are planar, fulfilling the mechanical compatibility conditions.

The first domain walls in nonmagnetic ferroics whose dynamic properties were investigated were ferroelastic walls in the earliest known ferroelectric crystal, Rochelle salt. Mitsui and Furuichi (1953) applied square-wave voltage of alternating polarity with frequency 22 Hz and measured stroboscopically domain wall position as a function of time. They found that some threshold field amplitude E_0 must be applied to make the wall move and that the wall velocity slows down as it departs from the original position by 1 or more micrometers, giving evidence of the existence of a built-in restoring force. In the temperature interval between 11 and 22°C the velocity at the original position follows the linear law (8.3.10) in the field interval 70–300 V/cm (Mitsui and Furuichi, 1954). In this temperature range μ is roughly constant but E_0 decreases from ~ 80 to ~ 40 V/cm with increasing temperature between 11 and 22°C. To have a feeling about the real magnitudes of velocities we give just one value: $v = 0.25$ cm/s at $E \cong 200$ V/cm.

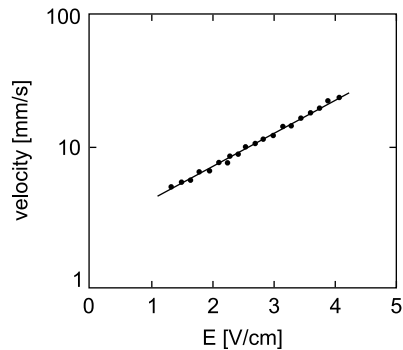
Very similar measurements on Rochelle salt were performed by Bittel et al. (1968). Their data obtained both stroboscopically and by electrical measurements

Fig. 8.3.14 Time dependence of domain wall position in Rochelle salt during one period of *ac* square-shaped field (amplitude 360 V/cm, frequency 1600 Hz). Points, optical observation; solid line, electrical measurement. After Bittel et al. (1968)



(using Eq. 8.3.4) clearly demonstrated slowing-down and backswitching effects, illustrated in Fig. 8.3.14, similar to those reported for lead germanate (cf. Fig. 8.3.9). However, in contrast to the previous investigators they fit their velocity data for the field interval 120–400 V/cm (at the original position of the wall) to the simple exponential law, Eq. (8.3.7), with $v_0 = 0.24$ cm/s and $\alpha = 5.5$ cm/kV (Fig. 8.3.15). At room temperature and for $E = 200$ V/cm this gives $v \cong 0.7$ cm/s. Understandably, it would be meaningless to extrapolate this equation down to $E = 0$. In the same series of experiments a strong influence of humidity on the wall mobility was observed.

Fig. 8.3.15 Wall velocity in Rochelle salt, measured at the original position of the wall, as a function of applied field. After Bittel et al. (1968)



Another ferroelectric–ferroelastic crystalline material, gadolinium molybdate (abbr. GMO), has the advantage that its crystalline plates can be relatively easily prepared with only one or very few domain walls. This makes the wall velocity measurements more reliable since interaction between domain walls can be avoided. Kumada’s data (1969, 1970) (see Sect. 8.3.1 for the method) showed that the wall motion satisfies well the linear mobility law, Eq. (8.3.10),

with $\mu = 2 \times 10^{-2} \text{ cm}^2/\text{Vs}$ which is independent of temperature between 20 and 80°C ; at higher temperatures the appearance of new walls prevented to perform meaningful measurements. The author did not specify the value of E_0 .

Shur et al. (1985a, 1989b, 1990) studied wall motion in GMO in detail, in a square-wave ac electric field. Similarly as for Rochelle salt they found that the slowing-down and backswitching effects are very similar to those for lead germanate and Rochelle salt as shown in Figs. 8.3.9 and 8.3.14. When velocity is evaluated from the time required to cover the first $25 \mu\text{m}$ from the initial position, the linear mobility law, Eq. (8.3.10), is well satisfied with $\mu = (2.0 - 2.5) \times 10^{-2} \text{ cm}^2/\text{V}\cdot\text{s}$ (Shur et al., 1989b) and the mobility is independent of temperature, up to 150°C . This is in a good agreement with Kumada's measurements. An example of data is shown in Fig. 8.3.16. Measurements were made only for fields not exceeding some 12 kV/cm since at higher fields new domains nucleated and the behavior of a single wall could not be followed. The threshold field $E_0 = (1.0 - 1.7) \times 10^3 \text{ V/cm}$ (Shur et al., 1985a, 1989b) depends on the history of the sample. This is also true for the maximum displacement of the wall within one period. Figure 8.3.17 is a demonstration of the aging and rejuvenation effects.

In KH_2PO_4 the validity of the linear mobility law, Eq. (8.3.10), was also confirmed by Bornarel (1987). He found that distant walls move with a constant velocity and independently of each other, provided they are further apart than the sample thickness. Coupling between domain walls was documented up to a distance of $850 \mu\text{m}$. When two walls approach each other and their distance d nears $10\text{--}20 \mu\text{m}$, its further decrease becomes a very long process; a strong

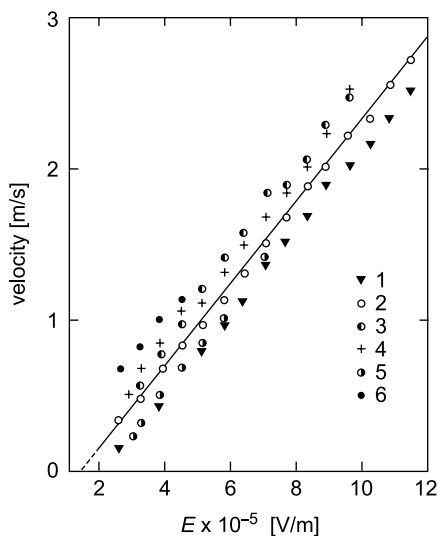
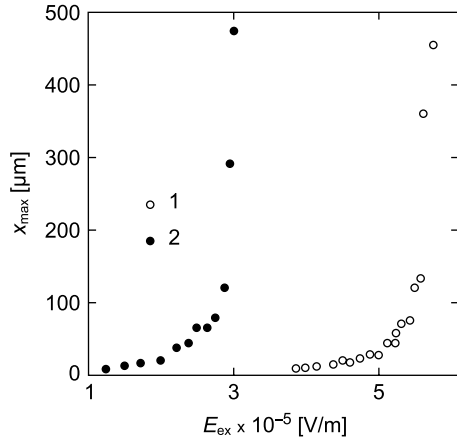


Fig. 8.3.16 Wall velocity in GMO at different temperatures. 1— 30°C ; 2— 100°C ; 3— 126°C ; 4— 126°C ; 5— 137°C ; 6— 150°C . After Shur et al. (1985a)

Fig. 8.3.17 Maximum displacement of a domain wall in GMO as a function of applied field. (1) Specimen was held without field applied for 18 h; (2) specimen subjected to preliminary switching for 3 h. After Shur et al. (1989b)



repulsive wall interaction takes place. The final value of d equals the width w of a needle-shaped domain which can exist in the sample at a given sample thickness and temperature.

Another material for which experimental data are available is one of the few organic ferroelectrics, namely tanane, $C_9H_{18}NO$. It represents the same species as KDP, $\bar{4}2m - P\bar{e}ds - mm2$. It was found (Bornarel and Legrand, 1981) that the linear mobility law, Eq. (8.3.10), applies to the motion of an isolated wall. A few degrees below $T_C = 287$ K, μ lies between 10^{-7} and 10^{-5} $\text{cm}^2/\text{V}\cdot\text{s}$ while the limits for E_0 are 100 V/cm and 2 kV/cm. The observations of domain behavior in tanane, though scarce, revealed two interesting features. For obvious reasons, two neighboring domain walls, in an applied dc field, move in opposite directions. Their velocities were found to depend on their instantaneous distance d ; this is demonstrated in Fig. 8.3.18a. This suggests that an additional pressure due to a repulsive interaction between the walls acts on them. The presented data enable evaluation of this pressure which we denote as p_{rep} . Using the linear mobility law $v = \mu(p - p_0)$ and taking into account this additional pressure, the wall velocity when the wall distance increases, v_a , and that when the wall distance decreases, v_b , can be written as

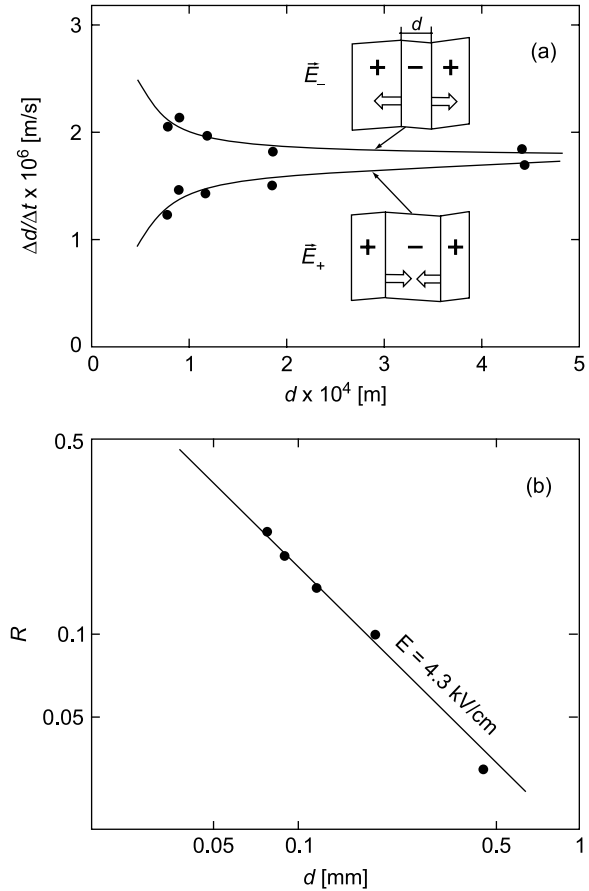
$$v_a = \mu(p_E + p_{rep}), \quad v_b = \mu(p_E - p_{rep}), \quad (8.3.11)$$

where p_E is the pressure due to the applied field. From this, for a fixed value of the applied field, one readily finds

$$R = (v_a - v_b)/(v_a + v_b) \propto p_{rep} \quad (8.3.12)$$

Using this relation, the data shown in Fig. 8.3.18a make it possible to plot p_{rep} as a function of wall distance d . This is shown in Fig. 8.3.18b which

Fig. 8.3.18 (a) Relative velocity $\Delta d/\Delta t$ vs. wall spacing d , for two moving walls in tanane at 9°C. (b) The ratio R vs. d , in logarithmic scale. The line has the slope -1 . After Bornarel and Legrand (1981)



demonstrates that the repulsive interaction between two planar domain walls varies as the inverse of their distance. In tanane, for a sample 1 mm thick, the repulsive effect is detectable for distances up to 300 μm .

Motion of ferroelastic domain walls separating domains with a noncollinear orientation of the spontaneous polarization has also been experimentally studied. 90° domain walls in BaTiO_3 is a classical example of such kind of walls. The motion of these walls has been mainly addressed for the situation where these form wedge-shaped domains. (We will discuss this situation later in this section.) At the same time the experimental studies of motion of individual planar 90° walls have been rather limited. Here one can mention the work by Fousek and Brezina who reported results of direct optical observations of oscillations of individual $\{011\}$ walls driven by a 50 Hz ac electric field in an electroded $\{001\}$ plate of BaTiO_3 . It was found that the walls exhibit visible oscillations as a whole only at field amplitudes exceeding a certain critical value

E_0 which, however, appreciably varies (0.3–3 kV/cm) from sample to sample and also as a function of the sample prehistory. The amplitude of the wall oscillation d_0 increases with increasing E_0 . The d_0 vs. E_0 dependence also exhibits an essential sample-to-sample variation. Being approximated as a linear function this dependence can be characterized with a typical slope of $0.3 \mu\text{m}^2/\text{V}$. All these data suggest that conditions for the wall motion can be very different in different parts of the sample. This can be taken as an indication of an appreciable coupling between the walls and defects. To rationalize this variance of the parameters of the wall motion one should assume that distribution of the defects is strongly inhomogeneous at least in the typical volume covered by the oscillating wall ($\cong 10^{-4} \text{mm}^3$). The same suggestion can be drawn from the variance of the shapes of the “wall-displacement-field” hysteresis loops reported in this paper (Fig. 8.3.19).

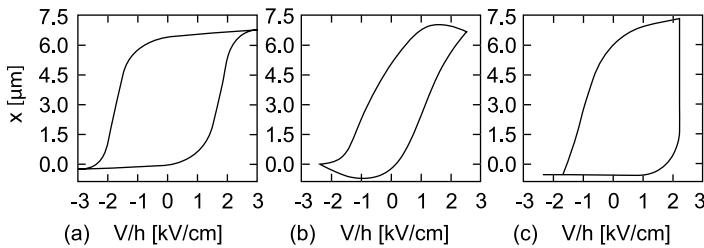


Fig. 8.3.19 Hysteresis loops “wall displacement, x ”—“average electric field, V/h ” recorded on different samples of BaTiO_3 (or after different pretreatments of one sample); V and h are the voltage applied to the sample and its thickness, respectively. After Fousek and Brezina (1960)

Motion of ferroelastic 90° walls in ac electric field exhibits a new qualitative feature compared to that of 180° walls; namely, in the former case, one finds a kind of dc effect. In other words, the oscillatory motion of the wall is accompanied with its drift. Fousek and Brezina in their experiment with inclined ferroelastic 90° walls in BaTiO_3 have reported such a drift in the direction corresponding to the increase in the volume of the domain with the polarization collinear to the applied electric field. This effect has been attributed to a manifestation of a high-order contribution to the pressure acting on the wall. This contribution is described by the fourth term in Eq. (8.2.9) and driven by the difference in the dielectric energy in the domains. Its sign is independent of the direction of the field, thus providing a dc effect in the oscillatory motion of the wall. In the case of BaTiO_3 , where at room temperature the anisotropy of the dielectric permittivity κ_a/κ_c is about 25, this contribution has been shown to be appreciable with the sign of the wall drift corresponding to the type of the dielectric anisotropy. Interestingly, it has been found that the aforementioned drift effect can lead to a removal of the wall from the sample.

8.3.3.2 Needle-Shaped and Wedge-Shaped Domains

Needle-shaped and wedge-shaped domains¹ are observed very frequently in the majority of ferroelastic crystals. The term “needle-shaped” is used for domains schematically shown in Fig. 8.3.20 (a) and (b) whereas domains schematically shown in Fig. 8.3.20c are called wedge shaped. These two types of domains have in common their wedge-shaped terminations. Hereafter we will use the term wedge-shaped domains for both types. Dynamic properties of this kind of domains can be most easily studied when the domain pair is ferroelectric at the same time, making it possible to apply a force acting on domain walls in an easy way, without any mechanical constraints. We can expect that the growth of narrow domains with wedge-shaped terminations will have kinetic characteristics different from those of planar walls, because a substantially different geometry will result in different elastic conditions. The principal feature of wedge-shaped ferroelastic domains is that the walls making these domains are not fully mechanically compatible.

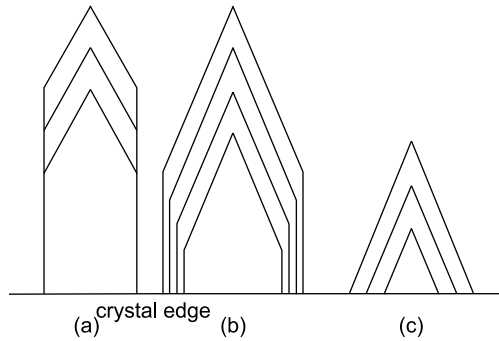


Fig. 8.3.20 Growth of needle-shaped and wedge-shaped domains may grow

In many papers two kinds of such domains were studied, schematically shown in Fig. 8.3.21. Figure 8.3.21a shows a situation typical for KDP where the wedge is made of two ferroelectric 180° domain walls parallel to the direction of the spontaneous polarization. Even the inclined sections at the ends these walls are electrically neutral. Figure 8.3.21b shows another situation typical for ferroelectric 90° pairs in BaTiO_3 . Here, the walls are necessarily charged in the area of the tip since, there, the wall is rotated with respect to the ideal orientation with $\text{div}\mathbf{P}_s = 0$. However, if the ferroelastic domains are divided into 180° domains, the boundaries limiting the wedge-shaped domain can be electrically neutral on average. Another distinguishing feature is that while, in the case of 180° wedge-shaped domains (like in KDP; see Fig. 8.3.21a), the domain geometry does not essentially influence the homogeneity of applied electric field, in BaTiO_3 the spatial distribution of the field is strongly affected by 90° domains because of

¹ The term ‘spike-shaped domains’ is also in use.

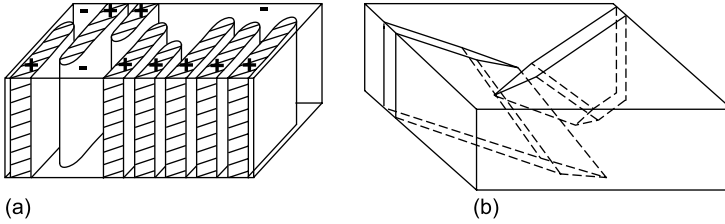


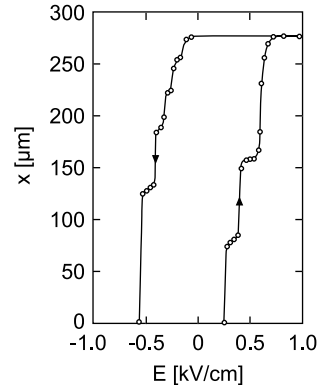
Fig. 8.3.21 Needle-shaped and wedge-shaped domains: (a) -180° domain textures in orthorhombic KH_2PO_4 . The signs of the polarization in the domains are shown with “+” and “-.” Reprinted with permission from Bornarel, J., *Domains in KH_2PO_4 , Ferroelectrics* **71**, 255 (1987). Copyright (1987), Taylor and Francis. (b) Crossing 90° a -domains in a plate of tetragonal BaTiO_3 . The directions of the polarization in the wedge-shaped domains are perpendicular to that in the rest of the sample. After Fousek and Brezina (1961)

the anisotropy of permittivity. In both cases, however, the tip of the needle forms a region of inhomogeneous strain. It is obvious that the lattice structure at the tip is strongly deformed but no direct structural data seem to be available. The growth of a wedge-shaped domain may be but need not be accompanied by an increase in its width; all possibilities shown schematically in Fig. 8.3.20 were observed in BaTiO_3 (Fousek and Brezina, 1961). For KDP, geometry a seems to be the rule although geometry b has also been considered to explain some domain properties. In both materials these domains are easily observable in a polarizing microscope; the contrast is due to walls rather than due to domains.

Little (1955) was the first to study wedges, in single crystals of BaTiO_3 . In the tetragonal phase of this material wedge-shaped domains, of typical width $10\text{--}30\ \mu\text{m}$, represent 90° domains and, in an a -oriented plate, a system of wedges can easily be introduced by the application of a field perpendicular to the existing polarization. A detailed study of the dynamic properties of wedges which occur spontaneously in plate-like samples was made by Fousek and Brezina (1961). Such a wedge usually requires a critical field to move and, for a sample containing several wedges, its typical value is of the order of several hundreds V/cm. In an ac field of frequency 50 Hz the wedge tip travels over large distances, leading to a substantial increase in the total domain wall area. Often the tip moves by jerks; examples of such characteristics are shown in Fig. 8.3.22. When a growing needle-like domain reaches the surface of the sample it separates into two parallel mechanically compatible walls. This transformation manifests itself in a huge jump of the switching current (a huge Barkhausen pulse). It is essential that 90° domain pairs in BaTiO_3 represent degenerate (in the “domain meaning”) systems since each neighboring region can contain a number of 180° domains, and antiparallel reversal processes may have an essential influence on the dynamic characteristics of the 90° wall. These hidden phenomena make it difficult to obtain data specifying the law of motion for such wedges in a dc field.

The aspect of domain degeneracy is absent for needle-like domains in KH_2PO_4 and mechanisms involved in their motion are simpler. Our knowledge

Fig. 8.3.22 Length of a 90° wedge-shaped domain in tetragonal BaTiO_3 : wedge length vs. applied field, at 50 Hz. A jerky character of motion is seen. After Fousek and Brezina (1961)



of their behavior is mainly based on the extensive research performed by Bornarel and Lajzerowicz. They used plate-like samples perpendicular to the polar c -axis, provided with transparent electrodes, and photographed the domain structures after the application of electric field.

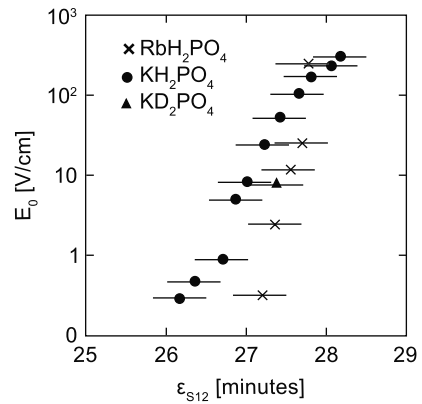
Typically, KDP single crystalline plates contain, in addition to regions incorporating systems of lamellar domains, also regions with dense systems of needle-like domains whose tips are terminating in the sample forming a front perpendicular to their lengths (see Fig. 5.4.21). Their characteristic width is of the order of $10\ \mu\text{m}$ and while their separation varies, a value of $150\ \mu\text{m}$ can be considered as typical (Bornarel and Lajzerowicz, 1968). In addition, isolated “needles” also exist. It was found (Bornarel and Lajzerowicz, 1970) that the dynamic characteristics of the latter differ from those of systems of needle-like domains which perform an orchestrated motion. When a series of electric pulses several kV/cm strong and several tens of nanoseconds long are applied, the average velocity of domain tips representing the growth of domain lengths can be measured. While the distribution of velocities is quite wide, two maxima are evident. For say $E = 1600\ \text{V/cm}$ and at $T = 100\ \text{K}$, most of the isolated tips move with $v \cong 900\ \text{m/s}$ while most of the fronts of the systems of needles move with $v \cong 100\ \text{m/s}$. This difference gives evidence of a long-range mechanical interaction between wedge-shaped tips of needle-like domains.

Later the velocity of isolated tips was studied in detail (Bornarel, 1975) and it was found to fulfill the linear mobility law (8.3.10). However, even for domains within one sample, the distribution limits of the coefficients are rather wide: at $T = 89\ \text{K}$, E_0 ranges from 0.5 to $3.3\ \text{kV/cm}$ and μ from 150 to 910 CGS units. The maximum of the velocity distribution for a given field seems to increase exponentially with the applied field, from $10^3\ \text{cm/s}$ for $1\ \text{kV/cm}$ to $10^5\ \text{cm/s}$ for $6\ \text{kV/cm}$; the latter value is not far from the velocity of sound. Often the tip motion is not smooth: Visible imperfections are seen to block the tip motion. Sometimes the presence of another tip in the neighborhood accelerates the observed motion. It is essential that the threshold field E_0 does not fully describe

the “willingness” of the domain tip to begin moving. In addition, the field pulses must be applied for a period longer than some critical length τ^* . It seems to suggest that it is some thermally activated process that is responsible for wall motion. As the length of the wall increases, the tip finally comes to a stop and the field has to be slightly increased to make it move again. Thus, effectively, E_0 increases with the domain length.

The magnitude of the critical field E_0 varies with temperature and also with composition of materials undergoing the same kind of transition as KH_2PO_4 , namely KD_2PO_4 and RbH_2PO_4 (Bornarel and Lajzerowicz, 1972). For instance, $E_0 \cong 10$ V/cm applies to KH_2PO_4 and KD_2PO_4 for temperatures 98 and 153 K, respectively. It was found that the value of the critical field strongly correlates with that value of spontaneous shear ε_{xy} . This correlation is documented in Fig. 8.3.23.

Fig. 8.3.23 Critical field E_0 required to move wedge-shaped domains in KDP-like ferroics vs. spontaneous shear strain $\varepsilon_{S_{12}}$. *Points* represent three materials at different temperatures. After Bornarel and Lajzerowicz (1972a)



It should also be mentioned that, similarly as in BaTiO_3 , the presence of the sample edge may have a profound effect on the tip velocity which greatly increases as the growing needle approaches the sample boundary (Bornarel and Lajzerowicz, 1972a). The range of this attractive force is about $300 \mu\text{m}$.

Bornarel (1972) interpreted most of these observed properties by a model in which the tip of a needle-like domain is characterized by an assembly of twinning dislocations. The use of twinning dislocations for description of the static domain pattern in KDP-type crystals has been already mentioned in Sect. 5.4.2 (see Fig. 5.4.19). For description of the dynamics of needle-like domain, the static framework has been extended by incorporation of elements of the Peierls dislocation model.

8.4 Theories of Single Wall Motion

In the present section we will give an overview of the theories contributing to understanding of the experimental finding on motion of single-domain wall in ferroics discussed in the previous sections. Though these theories have been

developed for the case of nonferroelastic domain wall in ferroelectrics, many of the ideas employed in these theories are applicable to domain walls of other types, e.g., ferroelastic walls or walls in nonferroelectrics. We will comment on this issue in the conclusion to the present section.

The main part of this section (Sects. 8.4.1, 8.4.2, 8.4.3, 8.4.4, 8.4.5 and 8.4.6) is devoted to a discussion ignoring the impact of defects on the wall motion; the role of the defects will be addressed in Sect. 8.5.

8.4.1 Two Regimes of Wall Motion

As we know (see Sect. 8.2.2) the application of an external macroscopic field conjugated to the order parameter of a ferroic, in general, results in a pressure f applied to domain walls existing in the ferroic. This pressure in the final run will result in a motion of the domain walls. Roughly one can distinguish two regimes of wall motion, depending on the relation between this pressure and the strength of the interaction between the wall and the crystalline lattice. The difference between these regimes can be explained as follows.

As we have discussed in the section devoted to the microscopic theory of domain walls (Sect. 6.3) the energy of a domain wall depends, among many other factors, also on the position of the wall center with respect to the sites of crystalline lattice of the material. In general, this dependence can be characterized by the so-called *Peierls potential* $V_P(z)$ which describes the variations of the wall energy (per unit area) when the wall is displaced as whole by a distance z in the direction of its normal. Obviously, $V_P(z)$ depends on the crystallographic orientation of the wall and it is a periodic function of z with the period, c , equal to the lattice period in the considered direction. Figure 8.4.1 (curve a) schematically illustrates the profile of such a potential; we introduce the amplitude V_{P0} to characterize its strength. The application of the external field modifies this profile. Taking into account the pressure induced by the field, f , and the Peierls potential one finds the spatial dependence of the wall energy $W(z)$ in the form

$$U(z) = S_0(V_P(z) - fz), \quad (8.4.1)$$

where S_0 is the area of the wall. As illustrated in Fig. 8.4.1 (curves b and c) the resulting energy profile for the wall motion can either possess minima and maxima (b) or be monotonical (c), depending on the value of the pressure f . One clearly sees that, in the first case, the application of pressure does not lead to the motion of the wall, unless thermal fluctuations are intensive enough to help the wall to overcome the potential barriers. In this situation, the motion of the wall can be presented as a sequence of “waitings” at the potential minima and thermoactivated “jumps” over the maxima. We will call this regime of motion *activated regime*. The situation illustrated in 8.4.1 (curve c) is very different from that just discussed above: Here the wall can move without assistance of the thermal fluctuation. For this reason, we will call this regime of motion *non-activated regime*. Mathematically,

these two regimes can be distinguished by comparison the pressure f and the maximal steepness of the potential $f^* = \max[dV_P/dz]$: the activated regime corresponds to $f < f^*$, the non-activated regime to $f > f^*$. As clear from Fig. 8.4.1 (curve a) we can roughly evaluate $f^* \sim 2V_{P0}/c$. For ferroelectrics, clearly the regime of the wall motion is determined by the relation between the applied electric field E and a critical field E^* . For a 180° ferroelectric wall [at which $f = 2E P_S$], the critical field can be written as

$$E^* = 0.5f^*/P_S \sim V_{P0}/(cP_S), \quad (8.4.2)$$

where P_S is the spontaneous polarization.

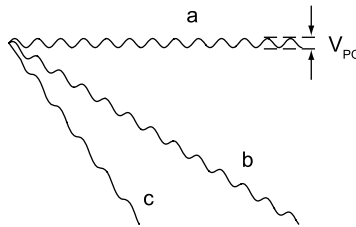


Fig. 8.4.1 Schematic drawing of the dependence of the wall energy on its position in an ideal crystal. (a) No external pressure is applied (Peierls potential); (b) the external pressure f is smaller than the critical value f^* ; (c) $f > f^*$

To give an idea of the values of the Peierls potential and the critical field E^* we will cite the estimates by Burtsev and Chervonobrodov (1982) for 180° ferroelectric walls in BaTiO_3 at room temperature: $V_{P0} \sim 0.05\text{--}0.07 \text{ erg/cm}^2$ and $E^* \sim 10 \text{ kV/cm}$. It is instructive to comment on these values. First, comparing the value of V_{P0} to the estimates for the surface energy of the wall ($\sim 10 \text{ erg/cm}^2$; see Sects. 6.2–6.3) we see that the Peierls potential represents light ripples on the background of the total wall energy. Second, comparing the value of E^* to the field range where the wall mobility in BaTiO_3 has been studied (0.15–450 kV/cm; cf. Sect. 8.3), we see that this range includes this value. That means that the understanding to the behavior of the wall motion in both regimes is crucial for the interpretation of the experimental data. It is clear that the physical processes which control the wall motion in these two regimes are quite different. For this reason, we will be treating these regimes in separate sections. The next section is devoted to the theories applicable to the activated regime.

At this point, we would like to make a terminological remark. When discussing in the above consideration the dynamics of the wall in a fixed external field we have called the variable used “energy,” implying that its spatial derivative gives the force acting on the wall. However, as the reader can conclude from the Sect. 8.2, this variable is actually the thermodynamic potential chosen in accordance with the conditions of the experiment. Though being aware of this terminological disparity, we will continue to use in this section the term “energy” for the thermodynamic potential as shorthand.

8.4.2 Wall Mobility in Activated Regime. Miller–Weinreich Theory

The theory of sideways motion of ferroelectric domain wall in activated regime has been pioneered by Miller and Weinreich (1960) in their classical paper. In this paper, the authors formulated the principal idea of the mechanism of the wall motion in this regime and, based on this idea, showed that the field dependence of the wall velocity $v(E)$ of the type

$$v(E) \propto e^{-(\delta/E)} \quad (8.4.3)$$

is expected for this kind of wall motion. This dependence was in good agreement with the experimental data on the low-field mobility in BaTiO₃. That provided a wide recognition for the theory. However, a more detailed analysis reveals a serious disparity between results of the original Miller–Weinreich (MW) theory and the totality of the experimental data. It became clear later that, though the authors had incorporated in their theory a very important feature of the phenomenon, a self-consistent description of the latter should also take into account a couple more of its features. In the current section, we will present MW theory in its original form. In the next section, we will discuss the shortcoming of this theory and outline the ways in which it has been improved and revised.

Consider motion of a wall in the activated regime but not too close to the border to the non-activated regime, i.e., we do not consider the situation where to $E^* - E \ll E^*$. By definition, the motion in this regime is possible if the thermal fluctuations help the wall to overcome the potential barrier on its way.

The simplest scenario of wall motion is its motion as a hole. In this case, the wall of area S_0 should overcome barriers of the order of $U_p = S_0 V_{p0}$ (see Eq. (8.4.1)). As it is easy to check, for any macroscopic size of the sample, this energy is many orders of magnitude greater than the thermal energy kT . This means a vanishing provability, $\propto \exp(-U_p/kT)$, of a thermally activated jump of the wall as a whole over the barriers and rules out this scenario.

Clearly the thermoactivated jump of the wall over the Peierls barriers as a whole is not the only possibility; one can consider jumps of small pieces of the wall. In this case, we can substantially reduce the associated Peierls energy. On the other hand, now we should also pay the price for the reduction of the “jumping” area: the total area of the wall increases. That will contribute to the total energy of the system via an enhanced contribution of the surface energy of the wall. However, it is easy to understand that provided the jumping pieces, which actually can be considered as two-dimensional nuclei of the reverse domains on the domain wall, are small enough, the probability of the jumps can be appreciable even when both contributions to the activation energy are taken into account. The reasonable probability to have such nuclei opens a realistic possibility for macroscopic motion of the wall in the activated regime. However, to realize this possibility one should satisfy an additional condition. Namely, when a piece of the wall has overcome the potential barrier to arrive at

a position separated by the lattice spacing from its initial position, the formed nucleus should be unstable with respect to increase in its area. If it is so, a single jump of a piece of the wall will finally result in a shift of the domain wall by one lattice spacing.

The scenario described above makes the leading idea of MW theory whose scheme contains the following steps: (i) One calculated the energy of a nucleus on the wall as a function of their shape and dimensions. (ii) One determines the parameters of unstable nucleus whose energy is the smallest among all unstable nuclei; we called this the *critical nucleus* and denote its energy as U_c . (iii) One determines the nucleation rate of critical nuclei, I_c , as proportional to the Gibbs factor

$$I_c \propto \exp(-U_c/kT). \quad (8.4.4)$$

(iv) Since one critical nucleus can give rise in a shift of the wall by one lattice constant, the velocity $v(E)$ of the sideway wall motion is assumed to be proportional to the nucleation rate I_c , i.e.,

$$v(E) \propto I_c. \quad (8.4.5)$$

Let us outline the derivations by Miller and Weinreich (1960). The above scheme of calculation has been performed for nuclei having the shape of triangular steps terminating at the electrode, as shown in Fig. 8.4.2a. The energy of such a nucleus can be presented as consisted in three parts

$$U = -2P_S E V_n + \sigma_w A_n + U_d. \quad (8.4.6)$$

Here the first term give the gain in the bulk energy on the ferroelectric, which is calculated under the assumption that the electric field is homogeneous in the capacitor, V_n stands for the volume of the nucleus. The second one gives the energy paid for the increase in the area of the wall A_n , σ_w being the surface energy density of the wall. U_d , referred to as the depolarizing energy, is the energy of the electric field produced by bound charges on the new oblique sections of domain wall. In other words, the last term takes into account that in the presence of the nucleus the electric field in the capacitor is not any more homogeneous everywhere. Note that the lateral sides of the nucleus cross perpendicularly the Peierls barrier, which is situated at a distance of $c/2$ from the plane of the wall. For this reason, the contribution of the Peierls energy to U is expected to be small and hence neglected in Eq. (8.4.6). For the geometrical parameters of the nucleus explained in Fig. 8.4.2a, the energy U can be presented in the following explicit form:

$$U = -2P_S Ealc + 2\sigma_w c(a^2 + l^2)^{1/2} + 8P_S^2 \frac{c^2 a^2}{\kappa_a l} \left(\ln \frac{2a}{c} - 1 \right), \quad (8.4.7)$$

where κ_a is the dielectric constant in the direction perpendicular to the direction of the spontaneous polarization. It is seen that the energy of the triangular

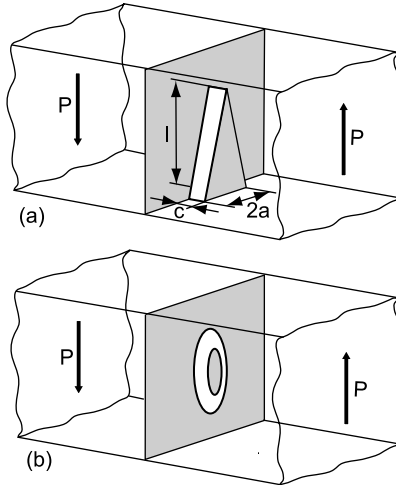


Fig. 8.4.2 Shape of critical nucleolus in theories of activated motion of domain walls. **(a)** Miller–Weinreich theory (1960). **(b)** Burtsev and Chervonobrodov theory (1982). The difference between the shapes in the in-plane geometry (*triangular* or *ellipse*, respectively) and in the orientation of the lateral side of the nucleus (normal to the plane of the wall or inclined, respectively). In Miller–Weinreich theory the nucleation occurs at the electrode (lower horizontal plane in the figure). In Burtsev and Chervonobrodov theory the nucleation occurs everywhere on the wall

nucleus is controlled by two geometrically parameters: its half-width a and height l . As it is usually done in nucleation problems, the dimensions of the critical nucleus (a^* and l^*) are to be determined by the conditions

$$\partial U/\partial a = 0, \quad \partial U/\partial l = 0. \tag{8.4.8}$$

These conditions lead Miller and Weinreich to

$$a^* \cong \frac{2}{3} \frac{\sigma_w}{P_S E}, \quad l^* \cong \frac{2\sigma_w^{1/2} \sigma_p^{1/2}}{\sqrt{3} P_S E}, \tag{8.4.9}$$

where $\sigma_p = (4P_S^2 b/\kappa_a)(\ln(2a/c) - 1)$, and finally to the expression for the energy of the critical nucleus

$$U_c \cong \frac{8}{3\sqrt{3}} \frac{c\sigma_w^{3/2} \sigma_p^{1/2}}{P_S E}. \tag{8.4.10}$$

The physical situation standing behind the above calculation is as follows. In contrast to the simplest situation (like in the case of a boiling liquid) where the dimensions of the critical nucleus are determined by competition of the bulk and surface energies solely, in the considered case the third contribution—depolarizing energy—enters the game. The latter compete with the surface

energy. Namely, for a fixed half-width of the nucleus, to decrease the surface contribution one should obviously decrease the height l of the nucleus whereas from the point of view of the depolarizing contribution a needle-type shape is favorable, i.e., large l 's. Depending on which of the trends win, the nucleus will be elongated, i.e., $l/a \gg 1$, or flat, i.e., $l/a \ll 1$. Miller and Weinreich performed their calculations for the case of elongated critical nuclei (the formulae (8.4.9) and (8.4.10) are valid only for this case), which they found consistent with the set of material parameters of BaTiO_3 they used for testing their theory.

Using the basic relation (8.4.4) and assuming the validity of Eq. (8.4.5), Miller and Weinreich arrived at the sought equation for the sideway motion (8.4.3), a value of the activation field δ being equal to

$$\delta_{\text{MW}} = \frac{U_c}{kT} = \frac{8}{3\sqrt{3}} \frac{c\sigma_w^{3/2}\sigma_p^{1/2}}{P_S kT} = \frac{16}{3\sqrt{3}} \frac{c^{3/2}\sigma_w^{3/2}}{\kappa_a^{1/2}kT} \left(\ln \frac{2a^*}{c} - 1 \right)^{1/2}. \quad (8.4.11)$$

Thus, the theory gives an explanation for a rather peculiar field dependence of the velocity of sideway motion documented for some ferroelectric (see Sect. 8.3). As for quantitative comparison with the experiment, it has been performed only for 180° wall in BaTiO_3 . It was shown (Miller and Weinreich, 1960) that using the known thermodynamic parameters of the material and taking $\sigma_w = 0.42 \text{ erg/cm}^2$, which should be considered substantially lower than the main theoretical estimates (cf. Tables. 6.2.1 and 6.3.1), a reasonable values of $\delta = 4 \text{ kV/cm}$ can be evaluated from Eq. (8.4.11). Concerning the temperature dependence of the activation field predicted by Eq. (8.4.11), it has been found qualitatively different from that measured experimentally (Savage and Miller, 1960).

8.4.3 Wall Mobility in Activated Regime. Advanced Theories and Present Understanding of the Problem

It is clear from the previous section that MW theory enabled substantial progress in understanding the nature of the motion of domain walls. However, as was recognized later, this theory left quite a lot of open questions and did not stand the test on quantitative self-consistency (see the previous section). Let us list these questions.

- (i) The shape of the critical nuclei was not optimized in MW theory. Could the optimization of the nucleus shape essentially affect the final result?
- (ii) Does the assumption that the wall velocity is proportional to the nucleation rate, Eq. (8.4.5), always hold?
- (iii) What physical mechanism is standing behind the departure of the $v(E)$ law from the exponential dependences?
- (iv) Is the pre-exponential factor in the $v(E)$ law always just a field-independent constant?

All these questions have been treated by Stadler and Zachmanidis (1963), Nettleton (1967), Hayashi (1972a,b, 1973), Burtsev and Chervonobrodov (1982), and Sidorkin (1993). In this book we are going to discuss the first three questions since these occur to be of primary importance for the subject. As for the fourth question, we will refer the reader to the original papers of Hayashi (1972a) where the theoretical results on the pre-exponential factor in the $\nu(E)$ law are available.

8.4.3.1 The Role of Shape of Critical Nuclei

Looking wider at the problem of the domain wall motion one finds it close to that treated by the well-developed theory of two-dimensional nucleation at phase transformations in solids (Cahn, 1960). Burtsev and Chervonobrodov (1982) modified this theory for the case of the domain wall motion in ferroelectrics. One of their principal results states that, in general, the shape of the critical nucleus suggested by Miller and Weinreich is far from optimal and that by optimizing its shape one can decrease that value of the activation field for the nucleation rate by one to two orders of magnitude. Clearly, this modification is essential for the theory.

Burtsev and Chervonobrodov indicated two ways for the optimization of the critical nucleus shape. First, they consider oval shape of the nuclei instead of triangular. Second and of crucial importance for the problem, they found that the oblique lateral sides of the nuclei ensure an essential gain in the energy, provided the Peierls barrier amplitude is much smaller than the surface energy density of the wall, i.e.,

$$V_{p0} \ll \sigma_w, \quad (8.4.12)$$

the property which is expected for domain walls and interphase boundaries (Cahn, 1960). The shape of this kind of the critical nucleus is illustrated in Fig. 8.4.2b. It has been shown (Burtsev and Chervonobrodov, 1982) that, for this type of nuclei, the activation field for the nucleation rate, δ_{BC} , is related to the activation rate calculated by Miller and Weinreich, δ_{MW} , Eq. (8.4.11), as

$$\delta_{BC} = \zeta \left(\frac{V_{p0}}{\sigma_w} \right)^{3/4} \delta_{MW}, \quad (8.4.13)$$

where the factor ζ is of the order of unity; it is weakly dependent upon the parameters of the problem and the model of the Peierls barrier accepted for the calculations. The physical interpretation of this result is rather transparent. By making the lateral sides of the nucleus oblique we gain in the surface energy. On the other hand, now the wall does not cross the Peierls barrier perpendicularly, as was in the case of MW nucleus, thus the price of an appreciable contribution of the Peierls energy should be paid. Since the Peierls barrier amplitude is small compared to the surface energy density of the wall, Eq. (8.4.12), an oblique configuration of the lateral sides of the critical nucleus provides some decrease in its energy. Using for 180° domain wall in BaTiO_3 the estimates

$V_{p0} \cong 0.05 - 0.07 \text{ erg/cm}^2$ and $\sigma_w \cong 10 \text{ erg/cm}^2$ (cf. Tables 6.2.1 and 6.3.1) we conclude from Eq. (8.4.13) that optimizing the nucleus shape can provide indeed a reduction of energy barrier for nucleation by one to two orders of magnitude.

8.4.3.2 The Nucleation Rate vs. Wall Velocity Relation

The problem of the relation between the rate of formation of critical nuclei and the velocity of domain wall motion has been addressed by Hayashi (1972a,b) and by Burtsev and Chervonobrodov (1982). Hayashi considered this problem for the situation of electrode-adjacent nucleation of triangular steps on the wall shown in Fig. 8.4.3 whereas Burtsev and Chervonobrodov treated the case of the two-dimensional nucleation all over the wall area. Here, similar to the Hayashi model, the nucleation can take place both on the originally flat surface of the wall and on the already formed nuclei. Qualitatively identical results have been reported for both situations. It has been shown that, depending on the relation between the applied field and some critical field, E^{**} , which depends on the material parameters and temperature, one can distinguish two regimes with a crossover region between them. For $E > E^{**}$, there is a linear relation between the wall velocity $v(E)$ and the nucleation rate I_c

$$v(E) \propto I_c \tag{8.4.14}$$

in accord with the assumption of Miller and Weinreich, Eq. (8.4.3). In contrast, for $E < E^{**}$, the wall velocity is proportional to a fractional power of I_c

$$v(E) \propto I_c^\xi, \tag{8.4.15}$$

where the exponent ξ varies from 1/3 to 1/2 depending on the nucleation scenario. The picture of wall motion has been found very different in the two regimes. In the low-field regime, a layer-by-layer growth of virtually flat walls takes place. In contrast, in the high-field range the critical nuclei pile on each other, as shown in Fig. 8.4.3, and the surface of moving wall appears to be essentially rough.

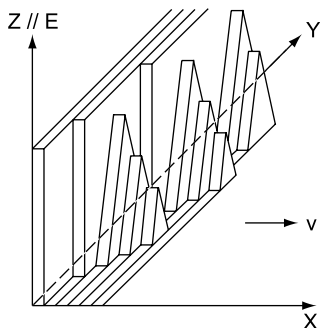


Fig. 8.4.3 Schematic drawing of nucleation and expansion of nucleus controlling the domain wall motion. After Hayashi (1972b). A 180° wall parallel to ZY -plane moves in X -direction. The polarization and applied field are parallel to Z -direction. Nucleation of reverse domain takes place at the electrode (XY -plane)

It is interesting to note that the assumption made by Miller and Weinreich that, for layer-by-layer growth, the wall velocity is proportional to the nucleation rate has not been justified whereas it has been justified for the regime where the piling up of the nuclei takes place, the situation not implied by these authors.

The values $1/2$ (Hayashi, 1972a,b) and $1/3$ (Burtsev and Chervonobrodov, 1982) for the exponent ξ have been obtained for the case of electrode-adjacent nucleation and for that of two-dimensional nucleation. In the first case, the reverse domains are assumed to nucleate at the electrodes (like that in the Miller and Weinreich model; see Fig. 8.4.2a), whereas in the second case, the nucleation with the same probability all over the wall is assumed (see Fig. 8.4.2b).

The above finding essentially influences the results of the calculations. It actually implies that the activation field for the wall motion δ is not always equal to the activation field for the nucleation rate, the latter we denote now as δ_n . Specifically, in low-field regime, δ should be two to three times smaller than δ_n . This result has been found relevant to the experimental situation in BaTiO_3 . According to Hayashi (1972a,b) and Burtsev and Chervonobrodov (1982) it is the regime where $E < E^{**}$ that takes place at the lowest fields in BaTiO_3 at room temperature. One can easily check that, in this case, taking into account the proper relation between the wall velocity and the nucleation rate, i.e., the use $\delta_n/2$ or $\delta_n/3$ instead of δ_n for the activation field for the wall motion will change a value of the wall velocity by many orders of magnitude. Another prediction of the presented approach is that, if the studied field interval contains the crossover field E^{**} , an appreciable increase in the activation field for the wall velocity, from $\delta_n/2$ or $\delta_n/3$ to δ_n , with increasing field is expected. According to Hayashi (1972a,b) this crossover can explain the deviation from pure MW law illustrated in Fig.8.3.2.

Referring the reader to the original papers (Hayashi, 1972a,b; Burtsev and Chervonobrodov, 1982) we are not going to discuss in this book the calculation resulting in the aforementioned findings. However, we find it instructive to present semi-quantitative arguments which can elucidate the physics behind the relations between the nucleation rate and the wall velocity. We address the case of two-dimensional nucleation treated by Burtsev and Chervonobrodov (1982). Let us denote Δt —the time needed for the wall to shift by one lattice constant, u_l —the linear velocity of lateral expansion of the nuclei, I_{2D} —the rate of nucleation per unit area, and r_0 —the linear dimension of the critical nuclei (we neglect for simplicity the elongation of nuclei). Consider the kinetics of the wall motion. Any growing layer should be in dynamical equilibrium; we mean that on the area of the wall that was moved forward due to the appearance and further growth of one nucleus there should be on average one nucleation during the time Δt . This condition can be obviously written as

$$\Delta t(r_0 + u_l \Delta t)^2 I_{2D} = 1. \quad (8.4.16)$$

In terms of this equation, the two regimes of wall growth discussed above correspond to the following two conditions: (i) The size of a critical nucleus can

be neglected compared to the displacement of its lateral sides during the time Δt , that is $r_0 \ll u_l \Delta t$. (ii) The critical nuclei do not substantially grow during the time Δt , that is $r_0 \gg u_l \Delta t$. The time needed for displacement of the wall by one lattice constant in these two cases, Δt_i and Δt_{ii} , can be found from Eq. (8.4.16) as

$$\Delta t_i = (u_l^2 I_{2D})^{-1/3} \quad \text{and} \quad \Delta t_{ii} = (r_0^2 I_{2D})^{-1} \quad (8.4.17)$$

that leads to the relations between the corresponding wall velocity and the nucleation rate

$$v_i = c(u_l^2 I_{2D})^{1/3} \quad \text{and} \quad v_{ii} = cr_0^2 I_{2D}. \quad (8.4.18)$$

We see that Eq. (8.4.18) does reproduce relations (8.4.14) and (8.4.15) stated above for the regimes where $E < E^{**}$ and $E > E^{**}$, respectively. Using Eq. (8.4.17) we also find that the nucleation rate in these regimes meets inequalities $r_0^3 I_{2D}/u_l \ll 1$ and $r_0^3 I_{2D}/u_l \gg 1$, respectively. In these inequalities, the strongest (exponential) field dependence exhibits the nucleation rate I_{2D} ; this determines the correspondence between the wall motion regimes and the field intervals.

The important feature of the high-field regime—essential roughness of the growing wall—also can be elucidated. In this regime, the growing structure “is made” of slowly growing nuclei. For this reason, the first layer made of the nuclei by the time Δt_{ii} contains “holes” of the linear dimensions about r_0 . Filling these holes by the lateral expansion of the nuclei will take time about $\Delta t_f = r_0/u_l$. During this time the front of the growing structure will advance by the distance $\Delta t_f v_{ii} = cr_0^3 I_{2D}/u_l$. This means that the growing front is rough with a deepness of modulation about $r_0^3 I_{2D}/u_l$ times the lattice constant.

Similar reasoning can qualitatively explain the results obtain by Hayashi for the case of the nearby-electrode (actually one-dimensional) nucleation.

8.4.3.3 Departure from the Exponential Law and Temperature Dependence of the Velocity

As we know from the results of the experiments, the field dependence of velocity of domain wall in ferroelectrics is not always exponential. For example, in most studies of the 180° wall in BaTiO₃ at room temperature, the exponential law was clearly observed at fields below 1 kV/cm. At higher fields (10–450 kV/cm), this law transforms into a power law with the exponent rather close to one. Since the time this result was published by Stadler and Zachmanidis (1963) three very different interpretations of this phenomenon have been offered.

First, Stadler and Zachmanidis themselves offered a modification of the MW theory. Miller and Weinreich (1960) had shown that the energy of the critical nucleus which is n -lattice-constant thick is $n^{3/2}$ times the energy of the “ordinary,” one-lattice-constant-thick nucleus U_c . Naturally, assuming that an n -lattice-constant thick nucleus provides a shift of the wall by n lattice

constants, Stadler and Zachmanidis presented the contribution from the nuclei of different thicknesses to the wall velocity in the form

$$v(E) \propto \sum_{n=1}^{\infty} n \exp\left(-\frac{U_c(E)}{kT} n^{3/2}\right). \quad (8.4.19)$$

It was shown that in the high-field limit Eq. (8.4.19) yields $v(E) \propto E^{1.4}$ in a close agreement with the experimental data. Thus, the power law for the wall mobility was interpreted as a result of interference of contributions of nuclei of different thicknesses.

The second scenario has been proposed by Hayashi (1972a,b). He pointed out that according to the MW theory, for fields at which the power law field dependence of the wall mobility had been observed, the width of critical nuclei becomes smaller than the lattice spacing. This means that, for this case, the theory requires revision. According to Hayashi, in the case of very strong fields, chains of unit cells parallel to the direction of the spontaneous polarization should be considered as critical nuclei. The theory developed for this kind of nucleation yielded a field dependence of the velocity close to $v(E) \propto E^n$, provided the field is high enough. For a 180° wall in BaTiO_3 at room temperature, he obtained $n \approx 1.54$ in close agreement with the experimental data. Thus, the power law for the wall mobility was interpreted as a result of an essential change of the geometry of the nucleation.

Though formally the two above scenarios could be considered as possible explanations for the experimental finding, according to Burtsev and Chervonobrodov (1982) there exists a reason to rule them out at least in the case of BaTiO_3 . The point is that the activation approach of the type used in MW theory corresponds to the physical situation in the material only if the field is smaller than E^* , the critical field of the activated regime given by Eq. (8.4.2). For higher fields, in the non-activated regime, as we discussed in Sect. 8.4.1, the motion of the wall as a rigid plain is possible since the field is high enough to suppress the Peierls barriers (see Fig. 8.4.1c) so that the nucleation is not needed at all to promote the wall motion. According to estimates (Burtsev and Chervonobrodov, 1982), for a 180° wall in BaTiO_3 at room temperature, $E^* \sim 10$ kV/cm. Thus, the field interval, where the field dependence of the wall velocity is a power law, corresponds to the non-activated regime of motion. In this regime as we will discuss later, a power law field dependence of the wall velocity is naturally expected. Thus, the transition from the exponential to the power law field dependence of the wall velocity was explained as a crossover from the activated to non-activated regimes of wall motion. At present, this scenario looks to be the most justified, at least for the case of BaTiO_3 .

At this point we would like to address an issue which seems to be of the key importance for the experimental verification of the whole theory on activated motion of domain wall in ideal (defect-free) material, namely the temperature dependence of the Peierls barrier V_{P0} . It has been theoretically established that the Peierls barrier of an interphase boundary or a domain wall is strongly

dependent on their thickness (Cahn, 1960; Suzuki and Ishibashi, 1985). The result obtained in the continuous approximation reads (Cahn, 1960)

$$V_{P0} = 4\pi^4 \sigma_w \left(\frac{t_{th}}{c}\right)^3 \exp\left(-\pi^2 \frac{t_{th}}{c}\right), \quad (8.4.20)$$

where σ_w and t_{th} are the surface energy density of the wall and its half thickness, respectively. This is really a fast function of the wall thickness, e.g., a change of t_{th}/c from 1 to 2 results in a change of V_{P0}/σ_w from 0.02 to 0.8×10^{-5} . This has important implications.

First, the critical field E^* , which according to Eq. (8.4.2) is proportional to the Peierls barrier, should dramatically decrease with increasing wall thickness. This field divides the activated and non-activated regimes of wall motion. Thus, in the material with relatively thick walls, the non-activated regime should take place where no MW type theories are applicable. For instance, in a material where the activated regime occurs in a certain temperature range, in a view of temperature dependence $t_{th} \propto (T_c - T)^{-1/2}$, a crossover to the non-activated regime should be inevitably expected on approaching the transition temperature.

Second, if, in a certain temperature range, the wall motion does correspond to the activation scenario, the activation field δ should exhibit a complex temperature dependence that is basically an exponential function of $T_c - T$. This can be shown as follows. We have discussed above in this section that due to the fact that the Peierls barrier for a wall, V_{P0} , is expected to be much smaller than its surface energy density, σ_w , an optimization of the shape of the critical nuclei is possible. According to Eq. (8.4.13) this leads to a reduction of the activation field δ by a factor of about $(V_{P0}/\sigma_w)^{3/4}$. Thus, taking into account Eq. (8.4.11) and the temperature dependences $\sigma_w \propto (T_c - T)^{3/2}$ and $t_{th} \propto (T_c - T)^{-1/2}$ (see Sect. 6.2) we find

$$\delta \propto \frac{\sigma_w^{3/2} t_{th}^{9/4}}{T} \exp\left(-0.75\pi^2 \frac{t_{th}}{c}\right) \propto (T_c - T)^{8/9} e^{-(M/\sqrt{T_c - T})}, \quad (8.4.21)$$

where M is a constant. It is useful to note that this result actually implies a double exponential temperature dependence for the wall velocity. In our opinion, such dependence can be considered as reliable fingerprints of the activated MW regime of wall motion.

To conclude the above discussion, we would like to note that very limited relevant experimental information is available for the moment. As an example of application of the aforementioned approach, we can refer to a paper by Sidorkin (1993). He explained a deuteration-induced increase in the domain wall mobility in KDP (10^6 times) (Bjorkstam and Oettel, 1966) as a result of deuteration-induced increase in the wall thickness. According to Sidorkin a slight change of the wall thickness can provide a 10^6 times variation of the velocity since the dependence is actually double exponential (cf. Eqs. (8.4.13) and (8.4.20)).

8.4.4 Domain Wall Motion in Non-activated Regime

In Sect. 8.4.1 we have introduced two types of domain wall motion: activated and non-activated. The former has been discussed in the previous section, now we proceed to the discussion of the latter. The principal difference between these regimes already expressed in their names relates to the assistance of thermal fluctuations needed for the wall motion. This assistance is required in the activated and it is not required in the non-activated regime. This difference implies an essential difference in the physical mechanisms limiting the wall velocity in these regimes. We have seen in the previous sections that, in the activated regime, the nucleation rate of critical nuclei controls the wall mobility. In the non-activated regime, this factor is irrelevant and the limiting factors are the energy dissipation resulting from the polarization reversal in the wall and the inertia of the ions carrying the ferroelectric polarization. As we will see below, the former directly controls the wall mobility whereas the latter controls the thickness of the moving wall. In the following sections we will address these two issues mainly in terms of the continuous Ginzburg–Landau theory. The consideration will be performed in terms of the simplest model: 180° wall in a uniaxial ferroelectric with elastic effects being neglected. The below presentation will be based on papers by Sannikov (1962), Laikhtman (1973), and Collins et al. (1979). More theoretical results on domain motion in non-activated regime can be found in papers by Wang and Xiao (2000) and by Loge and Suo (1996).

8.4.4.1 Low-Field Wall Mobility in Non-activated Regime

Consider a moving domain wall in a uniaxial ferroelectric in terms of the Ginzburg–Landau theory. Neglecting for simplicity the elastic effects we start from the thermodynamic potential given by Eq. (2.3.13) appended with the gradient terms like in Eq. (6.2.1)

$$\tilde{\Phi} = \Phi_0 + \frac{1}{2}\alpha P^2 + \frac{1}{4}\beta P^4 + \frac{1}{2}\delta \left(\frac{\partial P}{\partial x} \right)^2 - PE. \quad (8.4.22)$$

The equation of motion for the polarization can be obtained by generalizing the static Euler equation (like (6.2.3)) by adding terms that describe the energy dissipation during the polarization reversal and the inertia of the ions carrying the ferroelectric polarization. Such an equation of motion reads

$$\frac{\partial}{\partial x} \left(\frac{\partial \tilde{\Phi}}{\partial (\partial P / \partial x)} \right) - \frac{\partial \tilde{\Phi}}{\partial P} = \eta \dot{P} + \zeta \ddot{P}, \quad (8.4.23)$$

where the dots mean the time derivatives. Equations (8.4.22) and (8.4.23) readily imply

$$\zeta \ddot{P} + \eta \dot{P} - \delta \frac{\partial^2 P}{\partial x^2} + \alpha P + \beta P^3 = E. \quad (8.4.24)$$

The polarization profile corresponding to the 180° domain wall at rest

$$P_0(x) = P_S \tanh(x/t_{\text{th}}) \quad (8.4.25)$$

(where $P_S^2 = -\alpha/\beta$ and $t_{\text{th}}^2 = -2\delta/\alpha$) satisfies this equation (see Sect. 6.2.1); however, the moving domain wall described by the function

$$P = P_{\text{tr}} \equiv P_0(x - vt) \quad (8.4.26)$$

(where v is the wall velocity) is not an exact solution to it. On the other hand, expecting that the function (8.4.26) can be a good approximation for a slowly moving wall, we are looking for a solution to Eq. (8.4.24) in the form $P = P_{\text{tr}} + p$, where $p \ll P_{\text{tr}}$. Inserting this form into Eq. (8.4.24) and considering the dynamic terms and E in it as small perturbations we arrive at the following first-order perturbation theory equation for p :

$$\hat{L}p = E - \eta \dot{P}_{\text{tr}} - \zeta \ddot{P}_{\text{tr}}, \quad (8.4.27)$$

where the differential operator \hat{L} reads

$$\hat{L} = -\delta \frac{\partial^2}{\partial x^2} + \alpha + 3\beta P_{\text{tr}}^2. \quad (8.4.28)$$

At this point, for further progress one usually enjoys the results of theory of differential operators. First, one checks that this operator is Hermitian and that

$$f(x) = \partial P_{\text{tr}}/\partial x = P_S \cosh^{-2}[(x - vt)/t_{\text{th}}]/t_{\text{th}}$$

is a bounded solution of the homogeneous equation $\hat{L}f = 0$. Second, one takes into account that inhomogeneous equation (8.4.27) has a bounded solution for p under a condition that its r.h.s. is orthogonal to a bounded solution of the corresponding homogeneous equation, i.e., to $\partial P_{\text{tr}}/\partial x$. It is this condition of orthogonality that ensures that, in the limit of small wall velocities, p is small compared to P_{tr} . Inserting Eq. (8.4.26) into Eq. (8.4.27) we find this condition in the form

$$\int_{-\infty}^{\infty} \left(E - \gamma \frac{d^2 P_0(z)}{dz^2} v^2 - \eta \frac{dP_0(z)}{dz} v \right) \frac{dP_0(z)}{dz} dz = 0. \quad (8.4.29)$$

Integrating this expression and taking into account that $\int_{-\infty}^{\infty} \cosh^{-4}(z) dz = 4/3$ and $\int_{-\infty}^{\infty} \cosh^{-2}(z) \frac{d}{dz} \cosh^{-2}(z) dz = 0$ we readily arrive at the following mobility law for the wall:

$$v = \frac{3t_{\text{th}}}{2\eta P_S} E. \quad (8.4.30)$$

In other words, a constant mobility

$$\mu_0 = \frac{3t_{\text{th}}}{2\eta P_S} \quad (8.4.31)$$

can be attributed to the wall.

It is instructive to evaluate the maximal velocity v_m that the wall can acquire in the low-field regime. This velocity corresponds to a driving field equal to the thermodynamic coercive field.² Using Eqs. (2.3.15) and (8.4.30) one finds

$$v_m = \frac{t_{\text{th}}}{2\sqrt{3}\eta\chi}. \quad (8.4.32)$$

Here $\chi = 1/(-2\alpha)$ is the lattice dielectric permittivity.

Clearly the above results hold in the case where the shape of the moving wall is close to the static one (given by Eq. (8.4.25)). This imposes a limitation on the value of the driving electric field. However, since the problem of the wall mobility has physical meaning only for the driving fields smaller than the thermodynamic coercive field, there may be situations where the linear mobility law Eq. (8.4.30) provides a good approximation to the exact result for any physically meaningful values of the field. We will discuss this issue later using the exact solution of the problem.

8.4.4.2 Exact Solution for a Moving Wall; Modification of the Profile of Moving Wall

The problem of moving domain wall written in the form of Eq. (8.4.24) was shown to have an exact stable solution (Collins et al., 1979). This solution reveals qualitatively new features of the phenomena. In this book, we will not address the way how this solution has been found, referring the interested reader to the original paper. We will present only this solution and discuss its main features.

For a wall in a field $E > 0$ which divides domains with $P = P_- < 0$ at $x \rightarrow -\infty$ and $P = P_+ > 0$ at $x \rightarrow +\infty$ ($|P_-| < P_S$ and $P_+ > P_S$; P_- and P_+ are the solutions to the static problem), the exact solution to Eq. (8.4.24) reads

$$P = P_{\text{ex}} \left(\frac{x - vt}{t_{\text{ex}}} \right), \quad P_{\text{ex}}(z) = \frac{P_+ e^Z + P_- e^{-Z}}{e^Z + e^{-Z}}, \quad (8.4.33)$$

where

$$t_{\text{ex}} = t_{\text{th}} \frac{2P_S}{P_+ + |P_-|} \sqrt{1 - \frac{v^2}{v_0^2}}, \quad (8.4.34)$$

$$v = \mu_{\text{ex}} E, \quad (8.4.35)$$

² For higher fields, the antiparallel to the field orientation of the polarization is absolutely unstable so that the polarization reversal will take place through the bulk switching.

$$\mu_{\text{ex}} = \frac{3t_{\text{ex}}}{2\eta P_S} \frac{P_S(P_+ + |P_-|)}{2P_+|P_-|}. \quad (8.4.36a)$$

Here the critical velocity $v_0 = \sqrt{\delta/\zeta}$. The wall mobility can also be written in the form

$$\mu_{\text{ex}} = \frac{3t_{\text{th}}}{2\eta P_S} \frac{P_S^2}{|P_+ P_-|} \sqrt{1 - \frac{v^2}{v_0^2}}. \quad (8.4.36b)$$

Comparing the solution given by Eqs. (8.4.33), (8.4.34), (8.4.35), and (8.4.36) with the low-field solution, Eqs. (8.4.26), (8.4.30), and (8.4.31), we find (i) a deviation from the tanh shape of the distribution of the polarization in the wall, (ii) a change in the effective thickness of the wall (t_{ex} instead of t_{th}), and (iii) a change in the wall mobility (μ_{ex} instead of μ_0).

In the modification of the wall thickness, one can distinguish two trends. First, there is the “relativistic” correction $\sqrt{1 - v^2/v_0^2}$ which arises due to the $\zeta\dot{P}$ in Eq. (8.4.24). The physical origin of this correction is the inertia of the ions carrying the ferroelectric polarization. This correction formally results in unlimited “thinning” of the wall when the velocity approaches the critical velocity v_0 . Second, there is a factor of $2P_S/(P_+ + |P_-|)$ related to the dielectric nonlinearity of the ferroelectric. Due to this factor the wall under the field becomes thicker.

Clearly, the predictions of the exact theory look richer than those of the linear theory; however, the interpretation of the results of the exact theory requires an analysis which takes into account realistic parameters of the system and the limitations of the continuous theory. Such an analysis is given below.

8.4.4.3 Interpretation of the Theoretical Results for Wall Motion in Non-activated Regime. Additional Factors Influencing the Phenomenon

Here we are going to address the relevance of the theoretical result presented above to a realistic experimental situation and to give the reader an idea on possible experimental manifestation of the phenomena discussed.

First, let us note that, depending on the relation between the critical velocity $v_0 = \sqrt{\delta/\zeta}$ and the velocity v_m which is the maximal that the wall can reach in terms of low-velocity approximation, Eq. (8.4.32), one can single out two quantitatively different situations where (i) $v_m < v_0$ and (ii) $v_m > v_0$. Writing the ratio v_m/v_0 explicitly

$$\frac{v_m}{v_0} = \sqrt{\frac{|\alpha|\zeta}{12\eta^2}} = \frac{1}{2\sqrt{3}} \frac{\Omega_0}{\Gamma_0} \quad (8.4.37)$$

(where $\Omega_0 = \sqrt{2|\alpha|\zeta}$ and $\Gamma_0 = \eta/\zeta$ are the resonance frequency and damping for the spatially homogeneous linear polarization dynamics governed by

Eq. (8.4.24)) we see that these regimes roughly correspond to the case of over-damped and under-damped polarization dynamics, respectively. It is instructive also to note that, according to simple order-of-magnitude estimates, the critical velocity $v_0 = \sqrt{\delta/\zeta}$ is expected to be of the order of the sound velocity in the material.

Let us discuss these situations “deep inside” the two regimes, i.e., at (i) $v_m \ll v_0$ and (ii) $v_m \gg v_0$.

In the over-damped regime, the “relativistic” factor $\sqrt{1 - v^2/v_0^2}$ in the expression for the wall thickness (8.4.34) can be neglected. Thus, we find that, in this regime, the moving wall is a factor $2P_s/(P_+ + |P_-|)$ thicker than that when at rest. However, this correction appears to be insignificant. For the second-order phase transition, one shows that the value of $2P_s/(P_+ + |P_-|)$ always lies between 1 and $2/\sqrt{3} \approx 1.15$. Thus, this “thickening” effect is small and hardly of any experimental interest. The same is true for the difference in the polarization profiles given by Eqs. (8.4.25) and (8.4.33).

The wall mobility appears to be more sensitive to the high-field regime of motion. In the over-damped regime, from Eqs. (8.4.31) and (8.4.36) we readily find

$$\mu_{\text{ex}} = \left(\frac{P_s^2}{P_+ |P_-|} \right) \mu_0. \quad (8.4.38)$$

One easily checks that as E increases from 0 to thermodynamic coercive field (given by Eq. (2.3.15)) the factor $P_s^2/(P_+ |P_-|)$ changes from 1 to $3/2$. Thus, in the over-damped regime a slightly *superlinear* mobility law is expected. In Fig. 8.4.4, curves (a) and (c) illustrate the field dependence of the wall thickness and velocity as predicted by the theory for the over-damped regime.

For the under-damped situation we are facing a totally different behavior; now the “relativistic” factor $\sqrt{1 - v^2/v_0^2}$ fully controls both the thickness and the mobility of the wall. The theory predicts that the wall thickness tends to zero at $v \rightarrow v_0$ (see Eq. (8.4.34)). One easily checks that this readily implies that the wall velocity saturates on the level of the critical velocity v_0 and the wall motion with $v > v_0$ is impossible. This behavior is illustrated with curves (b) and (d) in Fig. 8.4.4. As seen from this figure, the characteristic feature of the wall motion in the case of under-damped polarization dynamics is a *sublinear* (with saturation) mobility law.

Concluding the discussion of the relevance of the model results to the real situation we would like to make a few remarks concerning factors neglected in the above model.

First, the model ignores the elastic effects. However, according to the results available in the literature, at least for nonferroelastic domain walls, these effects do not qualitatively change the situation. An exact solution for a moving wall, which takes into account rotation of molecular groups associated with the ferroelectric polarization and elastic stresses, has been offered by Pouget and Maugin (1985). These authors reported a modified (compared to the discussed

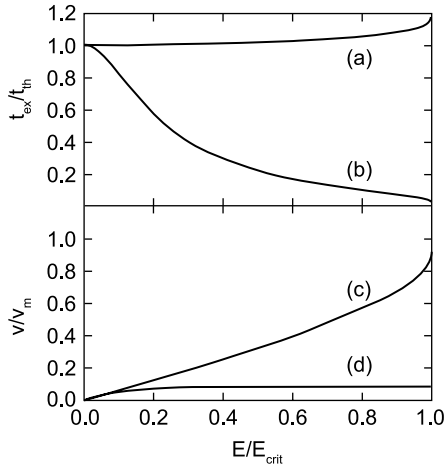


Fig. 8.4.4 Thickness (a, b) and velocity (c, d) of a 180° ferroelectric wall as functions of the applied electric field according to the continuous theory, Eqs. (8.4.33), (8.4.34), (8.4.35), and (8.4.36). The velocity is normalized to the velocity v_m given by Eq. (8.4.32). The field is normalized to the thermodynamic coercive field given by Eq. (2.3.15). The wall thickness is normalized to its thickness at rest, $t_{th} = \sqrt{-2\delta/\alpha}$. Curves (a) and (c) are plotted for the case of over-damped polarization dynamics ($v_0/v_m = 10$). Curves (b) and (d) are plotted for the case of under-damped polarization dynamics ($v_0/v_m = 0.1$)

above) polarization profile in the moving wall. However, since the authors have neglected the dissipation phenomena, it is difficult to appreciate the relevance of this result to the situation in real systems.

A generalization of the theory for the low-field mobility can be found in the paper by Laikhtman (1973). In the limit of small E , this is an exact phenomenological theory that takes into account the moving polarization kink and also the elastic and thermal perturbation induced by this kink. It has been shown that the energy dissipation related to the heat transport across the moving wall can be essential for the wall dynamics. Taking into account this effect the wall-mobility law (8.4.30) can be rewritten as the following balance-of-force equation

$$G \cdot v = (G_P + G_t) \cdot v = 2P_S E, \tag{8.4.39}$$

where the r.h.s. stands for the force acting on the wall owing to the applied field (cf. Sect. 8.2.2) whereas the l.h.s. has the meaning of the friction force acting on the wall. Here two contributions to the “wet friction” coefficient G can be distinguished: G_P is the contribution to the wall friction controlled by the relaxation of the polarization ($\eta\dot{P}$ in Eq. (8.4.24)) while G_t is the contribution controlled by the heat transport. Equation (8.4.30) corresponds to $G_P = (4/3)\eta P_S^2/t_{th} \propto 1/t_{th}$. Laikhtman addressed the second contribution to find $G_t \propto t_{th}$. Thus, we see that the relation between these two contributions to

the wall friction is very sensitive to the wall thickness. Laikhtman has evaluated these contributions for TGS at room temperature to conclude that the contribution controlled by the heat transport can be essential; e.g., using, however, a somehow too large value of the wall thickness $t_{\text{th}} \cong 10^{-5}\text{cm}$, he has found $G_P/G_t \cong 0.25 \times 10^{-3}$.

Concerning the equation of wall motion (8.4.39) one more remark can be made. Several authors (see, e.g., Gentner et al., 1978) have developed a microscopic theory of the G friction coefficient considering the scattering of the acoustical phonons against the wall as an origin of the friction. These theories are directly applicable for the case where the wall velocity is smaller than the typical velocities of the acoustical waves. For higher velocities, a modified theory is needed. In general, such a theory, though not presently available, should give a value of the G constant different from that obtained for the low-velocity regime. Thus, in terms of the microscopic theory of wall friction, a change of slope on the $v(E)$ curve at a velocity of the order of the sound velocity might also be expected.

To the best of our knowledge, the theoretical results presented above have not been compared to the available experimental data on the wall mobility in ferroelectrics. In this book, not attempting a systematic comparison of this kind, we would like to make just one remark. The superlinear type of wall-mobility law reported by Stadler and Zachmanidis (1963) (shown in Fig. 8.3.4) for BaTiO_3 at for $E = 10\text{--}450\text{ kV/cm}$ might be relevant to the theoretical prediction for the over-damped case. This interpretation is supported by the over-damped nature of the soft mode in this material; in addition the value of 450 kV/cm is of the order of the thermodynamic coercive field in BaTiO_3 at room temperature.

8.4.5 Domain Wall Motion Influenced by the Ferroelectric/ Electrode Interface

In the above sections devoted to the theories of domain wall motion we have addressed an idealized situation where the electric field in the sample is not disturbed by the presence of the wall and equal to the applied field. In these sections, we have derived relations between the applied field and the wall velocity. The application of these relations to the situation in a real capacitor requires, however, taking into account the fact that the field seen by the domain wall can differ from the applied field and be sensitive to the position of the wall and its velocity. The existence of such a difference has been suggested by experimental results reported by several authors, e.g., by Merz (1956) and Callaby (1967) for BaTiO_3 and by Shur et al. (1990) for $\text{Gd}_2(\text{MoO}_4)_3$ and $\text{Pb}_5\text{Ge}_4\text{O}_{11}$. Presently, it is generally believed that a special thin layer at the ferroelectric/electrode interface is responsible for this difference. Three models for such a layer have been offered by Merz (1956), Drougard and Landauer

(1959), and Callaby (1965). Though none of these models are able to give an exhaustive quantitative description of the totality of the observed features, they offer a realistic qualitative interpretation of them. The present section is devoted to discussion of these models and their implications.

The models are schematically illustrated in Fig. 8.4.5. All the models contain a modified surface layer³ of thickness d . The Merz’s model, illustrated in Fig. 8.4.5a, contains a nearby-electrode layer with the dielectric permittivity, κ_d , which is much smaller than that in the bulk one, κ_c , but which, however, can be switched like the bulk of the ferroelectric. The surface layer in the model by Drougard and Landauer, illustrated in Fig. 8.4.5b, (i) is non-switchable, (ii) has a low dielectric permittivity, and (iii) exhibits an appreciable conduction (lossy). In the model by Callaby, illustrated in Fig. 8.4.5c, the material of the capacitor is homogeneous in all the properties except the wall mobility, which is assumed to be much smaller inside the surface layer.

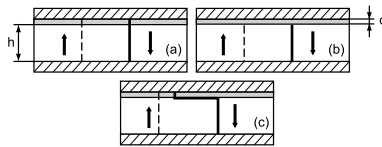


Fig. 8.4.5 Schematics of surface layer models. Two electrodes (*hatched*), ferroelectric (*no shading*), and surface layer (*shaded*) are shown. *Dashed lines* show the original positions of the wall. *Solid lines* show the position of the wall after the application of the electric field directed upwards. **(a)** Merz model, where the surface layer is perfectly switchable but has a smaller permittivity than the bulk material. **(b)** Drougard–Landauer model, where the surface layer is non-switchable. **(c)** Callaby model, where the surface layer is identical to the bulk except for a reduced value of the wall mobility. In the latter model a step on the moving wall (as shown in the figures) is expected

In the model by Merz, the impact of the surface layer on the wall motion is evident: The field seen by the wall in the bulk, E_f , is reduced compared to the value of the applied field, $E = V/h$ (V is the potential difference between the electrodes and h is the thickness of the ferroelectric). For the case of interest where $d \ll h$, one readily arrives at the well-known expression

$$E_f = \frac{E}{1 + (d\kappa_c/h\kappa_d)}. \tag{8.4.40}$$

This expression provides a difference between the applied field and the field seen by the wall, which depends on the thickness of the ferroelectric and that of the surface layer. Naturally assuming that, for a series of the samples with

³ In all three models, the authors consider the impact of the two layers of thickness $d/2$ at each electrode, which is roughly equivalent to the impact of one layer of thickness d . We will be discussing the situation with one layer.

different thickness, the thickness of the surface layer is independent of h , Eq. (8.4.40) leads to higher wall mobility in thicker samples. Specifically, for the wall motion in the activated regime with the mobility law $v \propto \exp(-\delta/E)$, the reduction of the field given by Eq. (8.4.40) implies the dependence $v \propto \exp(-\delta_{\text{eff}}/E)$ with $\delta_{\text{eff}} = \delta(1 + h_0/h)$ (h_0 is a constant). For Remeika-grown BaTiO₃ crystals this kind of $\delta_{\text{eff}}(h)$ dependence has been found in good agreement with the experiment (Merz, 1956).

In the model of Drougard and Landauer illustrated in Fig. 8.4.5b, the surface layer is just a dielectric one with a finite conduction and it is assumed that due to this conduction the free charge transport from the electrode to the layer/ferroelectric interface is possible; it is also assumed that a certain surface charge density σ can exist at this interface. Let us discuss this model starting from the single-domain situation. In this situation for the case of interest (where $d \ll h$), one easily finds that the difference between the field seen by the ferroelectric and the applied field, the so-called depolarizing field ΔE_{dep} , reads

$$\Delta E_{\text{dep}} = -\frac{d}{h\epsilon_0\kappa_d}(P + \sigma). \quad (8.4.41)$$

This field depends on the state of the ferroelectric and the prehistory of the capacitor. After staying for a long enough time in the single-domain state (with $P = -P_S$) under short-circuited conditions ($E = 0$), the field in the capacitor vanishes ($E_f = 0$) and so the depolarizing field does, since $E_f = E + \Delta E_{\text{dep}}$. This requires $\sigma = P_S$ which means a full screening of the ferroelectric polarization by the free charges delivered by the conduction across the layer. If we then switch the capacitor to the positively poled single-domain state (with $P = P_S$) and do it fast (compared to the relaxation time of the charge at the layer/ferroelectric interface, τ) we will find the depolarizing field

$$\Delta E_{\text{dep}} = -\frac{d}{h\epsilon_0\kappa_d}2P_S. \quad (8.4.42)$$

This field is created⁴ by a sheet of charge of density $2P_S$ at the layer/ferroelectric interface. Keeping the capacitor in the positively poled state for a time substantially exceeding τ obviously results in vanishing the depolarizing field again and developing negative screening charge: $\sigma = -P_S$.

For the case of two-domain state illustrated in Fig. 8.4.5b, a more involved consideration is needed. Like in the preceding case, after being in the same state for a long time the depolarizing field is absent in the system. If then the wall is displaced by a distance s , the depolarizing field appears. It is created by a stripe of charge of density $2P_S$ and width s located at the layer/ferroelectric interface. In this case, the average depolarizing field $\langle \Delta E_{\text{dep}} \rangle$ acting on the wall depends on the relation between d , s , and h . It is obvious that, for $s \gg h \gg d$, the

⁴ The depolarizing field is actually the sum of the field directly produced by these charges and the field produced by the charges induced by this charge in the electrodes.

depolarizing field is equal to that in the case of semi-infinite sheet of charges. For the symmetry reason it is equal to a half of the value given by Eq. (8.4.42), i.e., in this case,

$$\langle \Delta E_{\text{dep}} \rangle = -\frac{d}{h\epsilon_0\kappa_d} P_S. \quad (8.4.43)$$

It can be shown (Drougard and Landauer, 1959; Shur et al., 1990), though it is less obvious, that this result holds under much less restrictive condition $h, s \gg d$. That means that the Eq. (8.4.43) is valid even for $h \geq s$ if only $s \gg d$. For s tending to zero obviously the depolarizing field tends to zero as well. The formula describing the development of the depolarizing field as one increases s can be found in the form (Drougard and Landauer, 1959; Shur et al., 1990)

$$\langle \Delta E_{\text{dep}} \rangle \approx -\frac{dP_S}{h\epsilon_0\kappa_d} \frac{2}{\pi} \left[\tan^{-1} \frac{s}{2d} + \frac{s}{4d} \ln \left[1 + \left(\frac{2d}{s} \right)^2 \right] \right]. \quad (8.4.44)$$

Thus, in the Drougard–Landauer model, this equation gives the average depolarizing field that acts when the domain wall is displaced fast enough from its original position. This field is screened down by the charge transport across the layer after the time exceeding the relaxation time τ .

The third model, the model of Callaby (1965), though being physically different from that of Drougard and Landauer, phenomenologically, is quite similar to the latter. According to Callaby, the small part of the wall, which belongs to the surface layer, is assumed to be less mobile. This difference in the mobility will result in lagging behind the lateral part of the wall and in the formation of a stripe of the charged head-to-head domain wall as shown in Fig. 8.4.5c. This stripe creates a depolarizing field in the same way as the charged stripe in the Drougard–Landauer model does so that Eq. (8.4.44) for the field holds with s standing for the width of the stripe. The configuration with the head-to-head stripe is not energetically favorable. Thus, being left at rest in the zero external field for a long time, the stripe will shrink its width down to zero. This process is analogous to the conduction-driven screening of the bound charge in the Drougard–Landauer model. The phenomenological similarity between the two models results in virtually identical qualitative predictions of these.⁵

Let us have a look at the predictions of the Drougard–Landauer and Callaby (DLC) models. First of all, clearly, the DLC models predict a thickness dependence of the wall mobility as the Merz model does. The difference between the DLC and Merz models is that, in the former case, the field seen by the wall is smaller than the applied field by a field-independent term (e.g., given by Eq. (8.4.44)) while, in the Merz model, the applied field is reduced by a scaling factor. A qualitative new feature of the DLC models is that the relation between

⁵ In the original paper, Callaby has compared his model with that by Drougard and Landauer, arguing that there is essential difference between predictions of the two models. However, looking at the models more fully as it is done in this book, one finds a strong similarity between these predictions.

the field seen by the wall and the applied field is sensitive to the prehistory of the system. We would like to mention two nontrivial implications of this feature: “stop” effect and backswitching.

“Stop” effect. Consider the situation where during the time of the experiment the screening effect can be neglected. Then, the wall motion will be accompanied by a reduction of the field acting on it due to a growth of $\langle \Delta E_{\text{dep}} \rangle$ with growing wall displacement. This will result in slowing down of the wall moving under the action of constant applied field. If the difference between applied field and the maximal value of $\langle \Delta E_{\text{dep}} \rangle$ (given by Eq. (8.4.43)) is smaller than the threshold field for the wall motion, the wall will stop at a certain distance from its original position.

Backswitching effect. Consider wall motion from its original position where it has been for a long time. Let us turn off the applied field, so that the wall will see only the depolarizing field whose sign is opposite to that of the originally applied external field. This can induce a backward displacement of the wall. If the screening of the depolarizing field is negligible and the maximal depolarizing field substantially exceeds the threshold field for the wall motion, the wall will return to its position where it was before the application of the external field.

Both the above effects have been experimentally identified and investigated in a number of ferroelectrics (see Sect. 8.3).

The DLC models predict and explain several more interesting phenomena. We refer the interested reader to the original paper by Callaby (1965).

To conclude this section, we would like to discuss to what extent the above three models are realistic and what their limitations are. The Merz model, as was realized by Drougard and Landauer (1959), requires much lower dielectric permittivity in the layer than in the bulk, however, with the same switching performance. This is a very strong requirement for a real system, so that this model seems to be of purely academic interest. The main assumption of the Callaby model—a much lower nearby-electrode wall mobility—could be realized, e.g., due to the defect-induced reduction of the wall mobility near the electrode. However, this model faces a serious problem: The field between the head-to-head stripe and the electrode will jeopardize the ferroelectricity in this layer. One can easily check that, in the case of a proper ferroelectric, this field will suppress the ferroelectricity, except for the case of anomalously small values of P_S (weak ferroelectrics). Thus, the Callaby model is applicable only for weak and improper ferroelectrics. The Drougard–Landauer model causes basically no objections; it can be considered as a reasonable approximation for a real situation where both the bound and screening charges occupy sheets of a finite thickness. It has been pointed out by Shur et al. (1990) that the screening charge should be distributed over a distance of the Debye screening length from the electrode. The same authors have modified the Drougard–Landauer model taking into account this issue and offered a quantitative description for wall dynamics in $\text{Gd}_2(\text{MoO}_4)_3$ and $\text{Pb}_5\text{Ge}_4\text{O}_{11}$. However, it is difficult to judge to what extent these results are conclusive because of the additional assumptions and parameters introduced by the authors into the original framework.

8.4.6 Motion of Curved Domain Walls

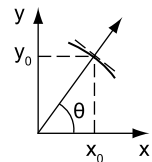
The results of the previous sections are the mobility laws derived for domain walls traveling in different regimes. All these results have been obtained for the case of a planar wall. In reality, the domain walls are often curved. A typical situation is the formation of a macroscopical domain from a cylindrical nucleus. Description of motion of a curved domain wall is trivial for the special case where the wall mobility does not depend on the wall orientation. Evidently, in this case, the wall will travel keeping its original shape. In general case, where the wall mobility is a function of its orientation, the wall changes its shape when traveling. In this section, we will address the theory of this phenomenon. Its elegant description that is based on the result of the theory of shock waves and crystalline optics has been offered by Nakamura (1960). The developed theory has been applied to the interpretation of evolution of domain shapes in BaTiO_3 (Nakamura, 1960) and in TGS and TGSe (Suda et al., 1978b). In what follows we will present the key points of this theory and its applications.

The problem of motion of a wall with anisotropic mobility is basically a special case of the problem of propagation of the wave front in an anisotropic medium. A well-known example of such a problem is offered in the crystalline optics, where the theory of propagation of the front of an electromagnetic wave has been developing from the times of Huygens. Actually, the mathematical scheme developed in optics can be directly applied to the problem of the wall motion. For this reason, we will mainly skip the mathematical derivation and focus on the final results and their interpretation; the interested reader is referred to textbooks on crystalline optics and the original paper by Nakamura (1960).

Consider the motion of a small element of the curved wall of a given orientation with respect to the reference frame XY (see Fig. 8.4.6). As shorthand, we will say that the orientation of the element is θ when its normal makes angle θ with the X -axis. Let the angular dependence of velocity of the plane wall be $v(\theta)$. According to Nakamura (1960), the motion of the considered element can be described by the following relation:

$$\begin{aligned} x &= x_0 + \left(v(\theta) \cos \theta - \frac{dv(\theta)}{d\theta} \sin \theta \right) \delta t \\ y &= y_0 + \left(v(\theta) \sin \theta + \frac{dv(\theta)}{d\theta} \cos \theta \right) \delta t \end{aligned}, \quad (8.4.45)$$

Fig. 8.4.6 Orientation of domain boundary surface (for Eq. (8.4.45))



where (x_0, y_0) is the original position of the element and (x, y) is its position after a small interval of time δt . This is the basic relation describing motion of curved domain walls.

The physical meaning of relation (8.4.45) is simple. The terms containing $v(\theta)$ evidently describe a displacement of the element along its normal. The origin of the terms containing $dv/d\theta$ can be elucidated as follows. Because of non-vanishing angular dependence of wall velocity and nonzero curvature of the element, there is a gradient of the velocity along the element. That means that the displacement $v\delta t$ of the element along its normal is accompanied by its rotation by a certain angle $\delta\theta$. Thus, the new position of the element with orientation θ should be looked for as a result of the normal displacement of an element with original orientation $\theta - \delta\theta$. For the motion of the element with a fixed orientation, that implies an additional displacement $(dv/d\theta)\delta t$ in the direction perpendicular to the normal to the element. This explains the origin of the terms containing $dv/d\theta$.

Equations (8.4.45) enable a parametric description of the shape of growing and shrinking domains. Essential implications of these relations for the situation of anisotropic domain growth are as follows: (i) Starting from a domain having a smooth shape one can arrive, after a growth or shrinkage of the domain, at a shape containing “corners” (discontinuities of the derivative). (ii) For growing domains, the corners form in the directions where $v(\theta)$ is maximal whereas, for shrinking domains, they form in the directions where $v(\theta)$ is minimal.

Figures 8.4.7 and 8.4.8 exemplify the above issues for the case of a hypothetical dependence $v(\theta)$. Figure 8.4.7 shows the polar diagram for $1/v(\theta)$. The growth of a circular domain to a side-rounded square is illustrated in Fig. 8.4.8a. The backward shrinkage of the side-rounded square is illustrated in Fig. 8.4.8b. The result of the latter is a square rotated by 45° with respect to the original side-rounded square. Inspecting Figs. 8.4.7 and 8.4.8 we find the aforementioned correspondence between the orientation of the corners, sense of the domain evolution, and positions of maxima and minima of the $v(\theta)$. The trajectories of the elements with a fixed orientation are also shown. We can conclude from this figure that the corners form due to the crossing (converging) of different trajectories. Analysis of this situation in terms of the wave approach can be found in the original paper by Nakamura (1960).

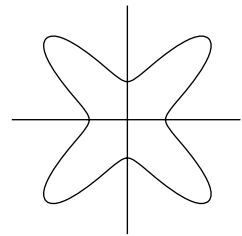


Fig. 8.4.7 Example of polar diagram of reciprocal rate of domain growth $1/v(\theta)$. After Nakamura (1960)

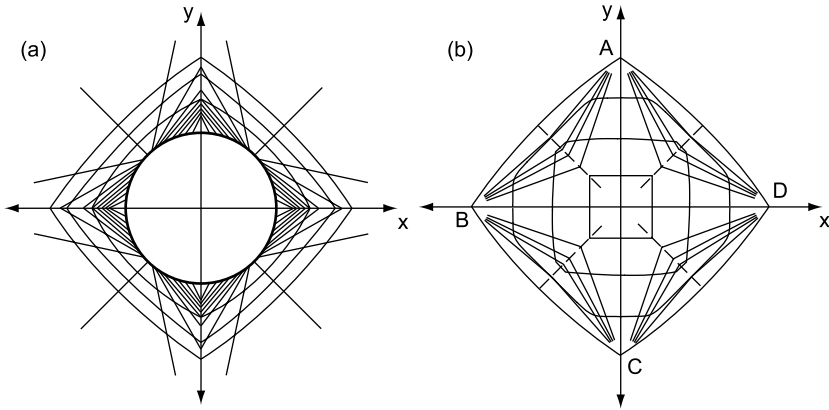


Fig. 8.4.8 Evolution of the shape of growing and shrinking domains for the growth anisotropy illustrated in Fig. 8.4.7. (a) Growth of a circular domain. (b) Shrinkage of ABCD square domain. Trajectories of elements of the wall with different orientation are shown. After Nakamura (1960)

Nakamura (1960) has compared the above theoretical prediction with the experimental data on the field-induced evolution of the shape of 180° domain in BaTiO_3 crystals (Miller, 1958; Miller and Savage, 1958; Husimi, 1960); see Sect. 8.3.2. The theory has been found in a perfect agreement with the experiment.

Suda et al. (1978b) applied the Nakamura's theory to the analysis of the applied-field-induced evolution of domain shape in TGS and TGSe. These authors use the Miller–Weinreich theory to obtain the $v(\theta)$ dependence for these materials. They also assume that the anisotropy of the wall velocity is solely governed by the anisotropy of the activation field $\delta(\theta)$, which in turn is controlled by the anisotropy of the wall surface energy σ_w and by that of the dielectric permittivity in the direction of the wall normal, κ_a . Accordingly, in this modeling

$$v(\theta) = v_\infty \exp(-\delta/E), \quad \delta(\theta) = K\sigma_w^{3/2}\kappa_a^{-1/2}, \quad (8.4.46)$$

where K is a constant independent of θ . The authors numerically simulated the evolution of the domain shape using Eqs. (8.4.45) and (8.4.46) with $\sigma_w(\theta)$ obtained from the results of theoretical calculations (shown in Fig. 6.2.3) and the $\kappa_a(\theta)$ dependence evaluated from the experimental data. It was shown that depending on the value of the applied field a growing circular domain could acquire the shape with two angles (“lenticular”), four angles (“restricted lenticular”), or could keep a corner-free (“elliptical”) shape. An essential quantitative result of the theory is the prediction of restricted lenticular domains for TGSe and lenticular domains for TGS, in accordance with the presence of four and two maxima in their $\sigma_w(\theta)$ dependences, respectively. This prediction has been found in perfect agreement with the experiment. A comparison of the calculated and experimentally observed domain shapes is presented in Fig. 8.3.13.

8.5 Defect Pinning and Creep of Domain Walls

In the previous section we have discussed the domain wall motion neglecting the impact of the structural defects. Though the models developed in this context are relevant to some experiments carried out in pure materials, one can readily come across situations where the role of structural defects in the domain wall motion is not negligible. These situations will be discussed below. This issue actually makes a special case of an extended area of theoretical condensed matter physics—interaction of structural disorder with the so-called topological defects. In this chapter we will present a “projection” of the results obtained in this area onto the problem of domain wall motion in ferroics. We have presented such kind of consideration in Sect. 6.4 when treating a ferroic domain wall at rest. Similar to the consideration from that section, below we will restrict ourselves to a brief discussion of the basic ideas appended with simple model illustrations.

The presence of structural defects in a ferroic obviously impedes the domain wall motion. One says that the wall is *pinned* by defects when, under an external pressure, the wall does not move because of its coupling with defects of the crystal. The potential imposed by the defects onto the wall is called *pinning potential*. In this context, one also introduces a notion of *pinning pressure* defined as external pressure needed to cause *depinning*—the macroscopic motion of the wall through the pinning potential. The depinning can occur either without the assistance of thermal fluctuations or with such assistance. In the former case, the application of the external pressure leads to the full suppression of the potential barriers that pin the wall. In the thermally assisted regime, the applied pressure determines the direction for the wall motion and only partially reduces the potential barrier that pins the wall, while thermal fluctuations essentially help to overcome it. In the following we will first consider the non-thermally activated regime. We denote calculated pinning pressure in this case as f_{pin} . Then, we consider a realistic situation taking place at finite temperatures where both regimes are possible. In this case, to introduce pinning pressure unambiguously, one should also specify the time interval within which the macroscopic wall displacement is expected. Clearly, since now the depinning is fluctuation assisted, the longer the waiting time, the smaller the pinning pressure. The maximal pinning pressure corresponding to the microscopic times (about the period of lattice vibrations) we denote as $f_{\text{pin},T}$. The pinning pressure at macroscopic time t we denote as $f_{\text{pin},T,t}$. When the applied pressure f is smaller than $f_{\text{pin},T}$, the only exponentially slow wall motion is possible, a situation similar to the activated regime of wall motion in defect-free material (see Sect. 8.4.2). This phenomenon is customarily called *creep*.

In the following discussion we will address the pinning pressures f_{pin} , $f_{\text{pin},T}$, and $f_{\text{pin},T,t}$ as well as the dependence of the wall velocity on the applied pressure f in the creep regime of motion.

Considering the impact of defects on the motion of a domain wall one should also take into account the ability of defects to move and change their orientation.

In this section we will mainly deal with the situation where the defects do not change their state during the observation time. This is the situation of the so-called *frozen disorder*. The opposite situation of “flexible defects” (i.e., where the distribution and orientation of defects is appreciably affected by their coupling with the order parameter) we will only briefly comment. For simplicity we will treat only the case of one-component order parameter and, in the case of ferroelectric, 180° non-charged walls will be considered.

In the following four sections, we will address the situation where the coupling of the wall with the crystalline potential (the Peierls potential, see Sect. 8.4.1) plays a minor role compared to the defect/wall coupling and thus can be neglected.

8.5.1 *Non-thermally Assisted Regime, Weak and Strong Pinning*

Consider a domain wall of thickness t_w in a ferroic with the density of defects $n = 1/D^3$, where D is the average distance between them. The defects may be of random field (RF) or random bond (RB) types (see Sect. 6.4, Fig. 6.4.2). We will be interested in the pinning pressure f_{pin} created by these defects in the situation where the depinning effect of thermal fluctuations can be neglected. To get a good insight into this problem it is instructive to start with the treatments within two naive approaches which lead to formally contradicting results.

The first method, which was widely used at the early stages of investigation of pinning, can be outlined as follows. Consider an individual defect. The maximal force that can be applied from it to the wall can be evaluated as the energy of the wall/defect interaction v (see Sect. 6.4, Fig. 6.4.2) divided by the domain wall width t_w , i.e., as v/t_w . On the other hand, a piece of the wall of area S can be naively viewed as pinned by the number of defects $N = S t_w/D^3$ contained in the volume of the wall of this area. This gives for the pinning pressure⁶

$$f_{\text{pin}} = f_0 \equiv (v/t_w)N/S = vn. \quad (8.5.1)$$

The alternative method treats a wall having very high surface energy so that it stays flat when interacting with defects. To illustrate it we address, for simplicity, the case of RF defects which may have two orientations and contribute $+v$ or $-v$ to the energy depending on the mutual orientation of the defect and the order parameter. We again consider a piece of the wall of area S (containing $N = S t_w/D^3$ defects). The contributions to energy from differently oriented defects essentially compensate each other as well as the pinning forces.

⁶ This is a rough estimate valid for both RB and RF defects. In the latter case, the number of defects impeding the wall motion is obviously $N/2$ not N as set in this estimate. One can neglect the factor of $1/2$ to within the estimate accuracy.

According to the laws of statistics, their total contribution can be evaluated as that from \sqrt{N} defects of the same orientation. This gives for the pinning pressure

$$f_{\text{pin}} = (v/t_w)\sqrt{N}/S = \frac{f_0}{\sqrt{N}}. \quad (8.5.2)$$

We see that the difference between the results of Eqs. (8.5.2) and (8.5.1) can be very big. It is due to the fact that, in the derivation of (8.5.1), it was implicitly assumed that the wall was soft enough to “hang” over unfavorable defects collecting the forces from them, whereas in the second method, the wall was assumed not bending at all. It is instructive to note that the result obtained by the second method appears to be unphysical since it predicts the pinning pressure for macroscopically large pieces of the domain wall to vanish, since $f_{\text{pin}} \propto 1/\sqrt{N} \propto 1/\sqrt{S}$.

The above discussion suggests that the pinning pressure created by the defects, in general, should be essentially dependent on the surface tension of the wall. Conceptually, the problem of finding f_{pin} is to find the maximal area, S_{fl} , of the wall, on which it behaves as flat. In other words, the problem is to find the maximal area, S_{fl} , on which the wall “averages” the negative and positive contributions to the pinning pressure. From S_{fl} , the number of defects participating in averaging $N = S_{\text{fl}} t_w/D^3$ can be found, which finally determines the pinning pressure through Eq. (8.5.2). One should mention that the concept of the “averaging” scale is one of the recent breakthroughs of the physics of disordered systems. For the first time this concept was introduced for the superconducting systems by Larkin and Ovchinnikov (1979).

Let us outline the solution to the problem for the case of nonferroelectric/nonferroelastic wall interacting with RF defects. First, one introduces the length L_e on which the wall wanders for a distance equal to the wall thickness by rewriting Eq. (6.4.10) as

$$w \cong t_w \left(\frac{L}{L_e} \right)^{2/3} \quad \text{with} \quad L_e = \frac{\sigma_w (t_w D)^{3/2}}{v}. \quad (8.5.3)$$

The length L_e can be considered as maximal spatial scale on which the wall behaves as flat (Nattermann et al., 1990). This can be rationalized, since the typical scale of the random potential, which the wall is exposed to, is about t_w so that for scales $L < L_e$ the wall stays in one potential minimum and can be considered as flat. Thus, S_{fl} can be evaluated as L_e^2 giving

$$N_b = \left(\frac{\sigma_w t_w^2}{v} \right)^2 \quad (8.5.4)$$

for the number of the defects, N_b , which is averaged by a flat segment of the wall and

$$f_{\text{pin}} = f_0 \frac{v}{\sigma_w t_w^2}. \quad (8.5.5)$$

for the pinning pressure. From Eq. (8.5.5), we see that if the energy of the coupling with defects is small enough (or the wall is stiff enough) so that

$$\frac{v}{\sigma_w t_w^2} \ll 1, \quad (8.5.6)$$

the pinning pressure is reduced compared to the estimate Eq. (8.5.1) where the defects were treated as acting independently. Condition (8.5.6) also guarantees that the number of impurities averaged by a flat segment of the wall is large thus justifying the application of the statistical approach. At the same time, if condition (8.5.6) is not met, the statistical approach fails and the impurities should be considered independently. These two situations are called *weak-pinning* and *strong-pinning* regimes, respectively. The existence of such regimes is common for the problems where the coupling of topological defects with frozen disorder is considered (like order parameter vortices and waves of charge density; see, e.g., Blatter et al., 1994).

The strong-pinning regime where a condition opposite to Eq. (8.5.6) occurs, i.e., $\sigma_w t_w^2 < v$, exhibits an additional feature. Now it is favorable for the wall to be captured by the defects spaced by the distance larger than the wall thickness—at such capture, the gain from the pinning v would be more than the extra surface energy $\sigma_w t_w^2$ (cf. Eq. (6.4.7)). Specifically, it is favorable for the wall to be captured by the defect spaced from its flat position up to the distance $w_{\text{cap}} = \sqrt{v/\sigma_w}$. This will influence the number of defects interacting with the wall. For the wall of area S this number can be now found as $N_{\text{st}} = S w_{\text{cap}}/D^3 = S\sqrt{v/\sigma_w}/D^3$ (instead of $N = S t_w/D^3$ used for getting the estimate for the pinning pressure, Eq. (8.5.1)). Accordingly, the pinning pressure for the strong-pinning regime reads (cf. Eq. (8.5.1))

$$f_{\text{pin}} = f_{\text{st}} \equiv (v/t_w) N_{\text{st}}/S = v n \sqrt{\frac{v}{\sigma_w t_w^2}}. \quad (8.5.1a)$$

The above results for the weak-pinning regime can be readily generalized to the case of nonferroelastic walls in ferroelectrics. In the context of the developed approach it is clear that the additional electrostatic energy associated with the bending of the ferroelectric domain wall should result in further increase in the difference between the pinning pressures calculated in the strong- and weak-pinning regimes since this energy leads to an additional stiffening of the wall. As was shown in Sect. 6.4.3, the wandering of such wall is anisotropic. Therefore it should be characterized by two spatial scales, L_{e1} and L_{e2} , instead of the single length L_e . On the lines of the analysis from Sect. 6.4.2, one can show that

$$L_{1e} = L_e m^{1/2} \quad \text{and} \quad L_{2e} = L_e m^{3/2}, \quad (8.5.7)$$

where

$$m = t_w D \left(\frac{g}{v} \right)^{2/3}, \quad (8.5.8)$$

with g being defined by Eq. (6.4.15). Parameter m controls the importance of the depolarizing energy on the scale where the wall can be considered as flat. If $m \gg 1$, then this contribution to the total energy balance is important and the relations (8.5.7) apply. In the opposite case, the depolarizing energy can be neglected and only one spatial scale, L_e , controls the problem. Thus, in the former case, the number of impurities over which the pinning forces should be averaged can be evaluated as

$$N_b = \frac{L_{1\varepsilon} L_{2\varepsilon} t_w}{D^3} = \left(\frac{\sigma_w t_w^2}{v} m \right)^2 = \left[\frac{\sigma_w t_w^2 D}{v} \left(\frac{g}{v} \right)^{2/3} \right]^2, \quad (8.5.9)$$

leading according to Eq. (8.5.2) to

$$f_{\text{pin}} = f_0 \frac{v}{\sigma_w t_w^2} \frac{1}{m}. \quad (8.5.10)$$

In the latter case, at $m \ll 1$ the previous result, Eq. (8.5.5), holds.

Two features of the situation with the ferroelectric wall are worth mentioning. First, the condition of the weak-pinning regime can be milder than Eq. (8.5.6), specifically

$$\frac{v}{\sigma_w t_w^2 m} \ll 1 \quad (8.5.11)$$

at $m > 1$. Second, by varying the defect concentration one can switch between the pinning regimes given by Eqs. (8.5.5) and (8.5.10). A remarkable difference between these regimes lies in the concentration dependence of the pinning pressure. Specifically, as clear from Eqs. (8.5.1), (8.5.5), (8.5.8), and (8.5.10), in these regimes $f_{\text{pin}} \propto n$ (according to the naive logic the pinning pressure should be proportional to the defect concentration) and $f_{\text{pin}} \propto n/D \propto n^{4/3}$, respectively.

Restricting our discussion of the non-thermally activated regime to the above analysis we would like to make two further remarks. First, this analysis can be readily generalized to the case where the sample thickness h is smaller than the spatial scales on which the wall can be considered as flat. This would yield various size effects for the pinning pressure with $f_{\text{pin}} \propto h^{-\alpha}$ with $\alpha > 0$. Second, in the situation with ferroelastic walls, where the long-range elastic forces additionally contribute to the wall stiffness, one reasonably expects a further reduction of the pinning pressure compared to the strong-pinning regime. However, a straightforward application of the above approach fails in this case and a more rigorous treatment of the problem is missing.

8.5.2 Finite Temperatures: Weak Pinning and Creep

In the energy terms, the above consideration corresponds to the full suppression of the pinning barrier (for either weak- or strong-pinning regime) by applied external pressure. To make a realistic description of the pinning pressure one should also take into account the thermoactivated regime of depinning, which

becomes important when the pressure applied to a wall f is smaller than the pinning pressure f_{pin} calculated above. The pinning pressure in this regime, $f_{\text{pin,T}}$, is determined from the condition that the typical height of the barriers $\Delta U(f)$, which the wall should overcome to move at given $f = f_{\text{pin,T}}$, equals the thermal energy $k_{\text{B}}T$. This pressure corresponds to depinning of the wall on the microscopic time scale (about the period of lattice vibrations). This approach can equally be applied to the cases where the potential barrier is formed by the coupling of the wall with many impurities (weak-pinning regime) and with a single impurity (strong-pinning regime). In this section we consider the latter regime, the former regime being considered in the next section.

Let us first estimate $f_{\text{pin,T}}$ for the case of nonferroelectric/nonferroelastic wall. Here, under an external pressure, the wall motion is controlled by the balance between the energy of the domain wall surface, Eq. (6.4.7), the energy of the defects⁷, and the gain in energy due to displacement of the wall in the presence of the external pressure. To estimate $f_{\text{pin,T}}$, one should find the shape of the optimized bulges on the wall promoting its thermally activated motion through the pinning potential. For such a bulge, the first two contributions are of the same order. This condition, as was shown in Sect. 6.4, leads to a relation

$$w \cong t_{\text{w}} \left(\frac{L}{L_{\varepsilon}} \right)^{\zeta} \quad (8.5.12)$$

between the bulge parameters L and w ; the corresponding sum of these contributions can be evaluated using Eq. (6.4.7) as

$$U_{\text{b+d}} \cong \sigma_{\text{w}} t_{\text{w}}^2 \left(\frac{L}{L_{\varepsilon}} \right)^{2\zeta}. \quad (8.5.13)$$

Under the external pressure this contribution competes with the third contribution which is equal to the product of the bulge volume and the pressure. Using Eq. (8.5.12), this contribution can be evaluated as

$$U_f \cong fL^2w = t_{\text{w}}L_{\varepsilon}^2f \left(\frac{L}{L_{\varepsilon}} \right)^{2+\zeta} = k_{\text{B}}T_{\varepsilon} \frac{f}{f_{\text{pin}}} \left(\frac{L}{L_{\varepsilon}} \right)^{2+\zeta} \quad (8.5.14)$$

where f_{pin} is explicitly defined by Eq. (8.5.5) and $k_{\text{B}}T_{\varepsilon} \equiv \sigma_{\text{w}}t_{\text{w}}^2$. The fully optimized bulge corresponds to the minimum of the sum $U_{\text{b+d}} + U_f$. Using Eqs. (8.5.13) and (8.5.14) we readily estimate its dimensions

$$L \cong L_{\varepsilon} \left(\frac{f_{\text{pin}}}{f} \right)^{1/(2-\zeta)}, \quad (8.5.15)$$

$$w \cong t_{\text{w}} \left(\frac{f_{\text{pin}}}{f} \right)^{\zeta/(2-\zeta)}, \quad (8.5.16)$$

⁷ For the RF case, this contribution to the energy is given by Eq. (6.4.9).

and energy

$$\Delta U \cong k_B T_\varepsilon \left(\frac{f_{\text{pin}}}{f} \right)^\mu, \quad (8.5.17)$$

$$\mu = \frac{2\zeta}{2 - \zeta}. \quad (8.5.18)$$

Equation (8.5.17) defines the typical height of the barriers that the wall should overcome to move at a given external pressure. Thus, the condition $\Delta U(f) = k_B T$ leads to the expression for the temperature-dependent pinning pressure

$$f_{\text{pin},T} \cong f_{\text{pin}} \left(\frac{T_\varepsilon}{T} \right)^{1/\mu}. \quad (8.5.19)$$

According to the logic of the previous consideration, this equation yields the value of the pinning pressure as far as it defines the pinning pressure smaller than f_{pin} , i.e., at $T > T_\varepsilon$. For lower temperatures the thermal fluctuations do not substantially affect the pinning pressure and $f_{\text{pin},T} \cong f_{\text{pin}}$.

The obtained result for the pinning pressure at finite temperature corresponds to the wall depinning on the microscopic time scale $1/\omega_0$ where ω_0 is a typical frequency of ionic vibration in the solid. If we consider the depinning at macroscopic times t , then making allowance for the Gibbs statistics of thermal fluctuations the condition for depinning can be written as

$$\frac{1}{t} \cong \omega_0 \exp \left[-\frac{\Delta U(f)}{k_B T} \right]. \quad (8.5.20)$$

This leads us to a generalization of Eq. (8.5.19) in the form

$$f_{\text{pin},T,t} \cong f_{\text{pin}} \left(\frac{T_\varepsilon}{T \ln \omega_0 t} \right)^{1/\mu}. \quad (8.5.21)$$

The above results for the pinning pressure, Eqs. (8.5.5) and (8.5.21), can be expressed by a single extrapolating formula (Nattermann et al., 1990)

$$f_{\text{pin},T,t} \cong \frac{f_{\text{pin}}}{\left(1 + \frac{T}{T_\varepsilon} \ln \omega_0 t \right)^{1/\mu}}. \quad (8.5.22)$$

The phenomenon behind the time-dependent pinning pressure can be viewed alternatively. The fact that, for an external pressure f , the time needed for the wall to overcome the pinning barriers is defined by Eq. (8.5.20) can be translated into the wall velocity $v_w(f)$. Taking into account that during the waiting time given by this equation the wall on average moves for a distance equal to the height of the optimal bulge given by (8.5.16) we find

$$v_w(f) \propto \left(\frac{f_{\text{pin}}}{f} \right)^{\mu/2} \exp \left[-\frac{T_\varepsilon}{T} \left(\frac{f_{\text{pin}}}{f} \right)^\mu \right]. \quad (8.5.23)$$

This basically exponential dependence, which is valid for $f < f_{\text{pin},T} \equiv f_{\text{pin}}(T_\varepsilon/T)^{1/\mu}$, corresponds to the so-called creep motion of the wall, the exponent μ being called *creep exponent*. We have come across a dependence of such kind while considering the wall motion over the Peierls potential barriers in terms of Miller–Weinreich mechanism (see Sect. 8.4.2), which is conceptually close to the above consideration.

The above approach can be equally applied to the description of pinning and creep of nonferroelastic domain walls in a ferroelectric. Here, two situations can be identified depending of the value of parameter m (defined by Eq. (8.5.8)).

As was discussed above, at $m > 1$ in the non-activated regime the optimal bulge is large enough (its dimensions meet the inequality (6.4.16)) so that the depolarizing energy on its spatial scale is important and makes it elongated. In the thermally activated regime, as clear from the above consideration, the optimal bulge size increases. This means that, at $m > 1$, when calculating the pinning pressure in thermally activated regime the above analysis should be modified so that it takes into account the elongation of the optimal bulge. Such analysis leads to the pinning pressure and creep law in the forms (8.5.22) and (8.5.23) where f_{pin} should be taken according to Eq. (8.5.10) and T_ε and μ redefined as

$$k_B T_\varepsilon = \sigma_w t_w^2 m, \quad (8.5.24)$$

$$\mu = \frac{2\varsigma_1 + 1/2}{2 - \varsigma_1}, \quad (8.5.25)$$

where ς_1 is the roughness exponent of the system. In this regime, the smallest dimension of the optimal bulge, L_1 , is given by a relation similar to (8.5.15)

$$L_1 \cong L_{1\varepsilon} \left(\frac{f_{\text{pin}}}{f} \right)^{1/(2-\varsigma_1)}, \quad (8.5.26)$$

where f_{pin} and $L_{1\varepsilon}$ are defined by Eqs. (8.5.10) and (8.5.7), respectively.

For $m < 1$ the situation is different. This condition means that on the scale, where the wall can be considered as flat, the depolarizing energy becomes smaller than the surface energy and can be neglected. Thus, in this case, in the non-activated regime, the optimal bulge is not essentially elongated. In the thermally activated regime, i.e., with T growing above T_ε , the bulges of larger energy and therefore of larger size come into play. For the pinning pressure at longer times, the bulge size further increases. Physically, this is clear from the whole logic of the consideration of the thermally activated regime. Formally the aforementioned dependence can be obtained by inserting $f = f_{\text{pin},T,t}$ into Eq. (8.5.15) with $f_{\text{pin},T,t}$ coming from Eq. (8.5.21) to find for the size of the relevant (not elongated) bulge as a function of t and T :

$$L \cong L_\varepsilon \left(\frac{T \ln \omega_0 t}{T_\varepsilon} \right)^{1/2\varsigma}. \quad (8.5.27)$$

Now, at large enough values of the parameter $T \ln \omega_0 t$, the bulge size becomes sufficiently large to make the depolarizing energy contribution important and the bulge elongated. This corresponds to the regime where relations (8.5.24), (8.5.25), and (8.5.26) apply. Thus, at $m < 1$ we are dealing with the situation where the characteristics of pinning and creep will depend on the relation between the value of parameter $T \ln \omega_0 t$ and a certain critical value.

The aforementioned crossover becomes really interesting when being translated into the creep law for the wall velocity. In this case, as seen from (8.5.15), the smaller the pressure, the larger the relevant bulges. The crossover in the pinning regime corresponds to condition $L_e = L_{\text{dip}}$ (the characteristic length L_{dip} is introduced by Eq. (6.4.16)). The crossover pressure evaluated from this condition reads

$$f_{\text{cross}} = f_0 \frac{v}{\sigma_w t_w^2} m^{3-3\zeta/2}. \quad (8.5.28)$$

This crossover may manifest itself in the creep exponents which are different at $f > f_{\text{cross}}$ and $f < f_{\text{cross}}$. However it occurs that it is not observable for the RF case. In this case, in both regimes the creep exponents (calculated according to Eqs. (8.5.18) and (8.5.25)) are the same $\mu = 1$.

8.5.3 Finite Temperatures: Strong-Pinning Regime

In the case of strong pinning the thermal fluctuation can also reduce the pinning pressure. To estimate it, one should evaluate the height of the typical potential barriers, $\Delta U(f)$, which pin the wall at a given value of the applied pressure. In the strong-pinning regime, these are associated with the motion of pieces of the wall across individual impurities and can be evaluated as

$$\Delta U(f) = v - V_{\text{ac}} f, \quad (8.5.29)$$

where V_{ac} is the change of the volume of the favorable domain when the wall “climbs” on the impurity. V_{ac} can be estimated as $S_i t_w$ where S_i is the area per impurity in the wall. Now, calculating S_i like for the derivation Eq. (8.5.1.a), one finds $S_i = D^3 / \sqrt{v/\sigma_w}$, $V_{\text{ac}} = D^3 \sqrt{\sigma_w^2 t_w^2 / v}$, and

$$\Delta U(f) = v(1 - f/f_{\text{st}}), \quad (8.5.30)$$

where f_{st} is the pinning in the strong-pinning regime given Eq. (8.5.1.a). Now, on the lines of the consideration from the previous section, the temperature- and time-dependent pinning pressures in the strong-pinning regime can be presented in the form

$$f_{\text{pin,T,t}} \cong f_{\text{st}} \left(1 - \frac{k_B T}{v} \ln \omega_0 t \right). \quad (8.5.31)$$

Similarly, the wall mobility law for $f < f_{st}$ can be written as

$$v_w \propto \exp \left[-\frac{v}{k_B T} \left(1 - \frac{f}{f_{st}} \right) \right]. \quad (8.5.32)$$

This expression is readily applicable at $k_B T < v$. If it is not the case, when calculating the wall velocity one should also take into account the thermally activated jumps of the wall against the applied pressure. In this case, one finds essentially linear mobility law

$$v_w \propto \exp \left[-\frac{v}{k_B T} \left(1 - \frac{f}{f_{st}} \right) \right] - \exp \left[-\frac{v}{k_B T} \left(1 + \frac{f}{f_{st}} \right) \right] \approx 2 \frac{v}{k_B T} \frac{f}{f_{st}}. \quad (8.5.33)$$

It is instructive to note that, if the thermal fluctuations substantially influence the behavior of the wall, the difference between the weak- and strong-pinning regimes is yet more pronounced than that in the non-thermally activated regime. For instance, the wall mobility laws, being considered in a wide enough interval of the applied pressure, are very different.

8.5.4 Weak and Strong Pinning with Flexible Defects

In the previous sections we addressed the pinning and creep of domain walls which couple with defects whose position and state (e.g., orientation of RF defects) do not change in time. It is clear that such description may not be a good approximation for real systems especially for long observation times. The ability of defect to adjust themselves to the local values of the order parameter can essentially affect the behavior of the system. As a result of such rearrangement the defect distribution becomes correlated leading to an increase in the pinning barriers. This is known to lead to aging and imprint effects (see 9.5.3) which are harmful to many applications of ferroelectrics. In this section we would like to comment on the impact of the defect flexibility on the pinning and creep effects. We will discuss the situation of flexible (reorientable) RF defects. However, similar conclusion can be drawn for RB defects as well.

Let us compare the impact of defect reorientation on the weak and strong (individual) pinning. Consider a piece of the wall of area S pushed by some external pressure in the individual pinning regime. This piece interacts with $N_{st} \cong S \sqrt{v/\sigma_w}/D^3$ defects (see Sect. 8.5.1). In the case of random distribution of their orientation, approximately $N/2$ defects oppose the wall displacement (it is spanned on them) whereas the rest $N/2$ defects can be freely passed by the wall. If we let defects fully relax to their energetically favorable state (locally align with the order parameter), the orientation of the defects will be homogeneous throughout any domain. Clearly in this case, all N defects will oppose the wall displacement. This will lead to doubling of the pinning pressure.

In the weak-pinning regime, the same system will behave differently. In the case of random distribution of the defect orientation, according to Eq. (8.5.2), the pinning pressure is $\sqrt{N_b}$ times smaller than the value f_0 given by Eq. (8.5.1), where $\sqrt{N_b}$ is the number of the defects interacting with the wall on the scale on which the wall can be considered as flat. This reduction is associated with the fact that, on this scale, the actions of favorable and unfavorable defects strongly compensate each other. In the case of the fully relaxed defects, in an attempt to move, all defects encountered by the wall will be unfavorable. That implies no room for the aforementioned compensation, no reduction of the pinning pressure due to the averaging effect, and therefore the pinning pressure will correspond to estimate Eq. (8.5.1), i.e., $\sqrt{N_b}$ times larger than before the defect relaxation.

The above consideration shows that the strong- and weak-pinning regimes can be additionally distinguished if the RF system can be subjected to aging which leads to the alignment of the defects according to the local orientation of the order parameter. In the strong-pinning regime, an aging-induced increase in the pinning pressure up to two times is possible. (The factor of 2 corresponds to the case of the 100% defect alignment; in principle the alignment may not be full.) At the same time, in the weak-pinning regime, a much stronger increase in pinning pressure is possible. Though the above consideration has addressed the non-thermally activated depinning, it is clear that the above reasoning can be also applied to the case of pinning at finite temperatures and creep.

8.5.5 Experimental Evidence on Weak Pinning and Creep of Ferroelectric Domain Walls

Only a limited attention has been paid to focused experimental studies of the weak pinning and creep phenomena. Here we can mention only atomic force microscopy measurements of the field dependence of the velocity of 180° domain walls in thin films of $\text{Pb}(\text{Zr}_{0.2}\text{Ti}_{0.8})\text{O}_3$ performed by Triscone and coworkers (Tybell et al., 2002; Paruch et al., 2005, 2006). One should mention that it is a difficult experimental task to distinguish the creep mobility law $v \propto \exp(-\text{const.}/E^\mu)$ from that expected in the case of individual pinning, $v \propto \exp(\text{const.} \times E)$.

In the earlier publication (Tybell et al., 2002) this group reported the creep law with the creep exponent μ in the interval 1.01–1.21, which to within the experimental accuracy was interpreted as $\mu = 1$. The experimental data used for the calculation of these values of the creep exponent are presented in the chapter devoted to ferroelectric thin films (Fig. 9.8.2). The obtained values of the creep exponent were regarded as an indication that the wall moves in the weak-pinning regime with RF defects. As we pointed out above, in RF systems, the relation $\mu = 1$ always holds. In the case of a ferroelectric–nonferroelastic domain wall, this means that this relation holds independently of whether the additional electrostatic rigidity of the wall is relevant in the creep process or not.

In the further work (Paruch et al., 2005) on the same system, the creep exponent μ was found to be in the interval 0.51–0.59. Additional information of the pinning mechanism was obtained from the measurements of the roughness exponent ζ , whose value was found to lie in the interval 0.22–0.26 (see for more discussion Sect. 6.4.4). These two sets of exponents were interpreted as an indication that the wall moves in the weak-pinning regime with RB defects and that the additional electrostatic rigidity of the wall is relevant in the creep process. This conclusion was supported by the following observations. First, the reported values of μ and ζ are close to those obtained for this system in different theoretical approaches. Second, the μ and ζ pairs of the exponent for the same sample satisfy with a good accuracy Eq. (8.5.25).

A recent work (Paruch et al., 2006) of the same group on the same system experimentally addressed the impact of artificially introduced defects on the values of the creep exponent μ . It was found that the defect introduction leads to an appreciable reduction of μ , from values of 0.62–0.69 for the nominally pure systems down to the intervals 0.30–0.5 or 0.19–0.31 depending on the defect type.

8.6 Switching Process in Selected Materials

The change of a domain state under the application of an external perturbation conjugated to the order parameter, customarily called switching, is the key property of ferroics. In the previous sections we have focused on the situation where the change of the domain state in the whole crystal or its part occurs as a result of displacement of a single-domain wall. For the general situation, the experimental data and theory will be addressed in this section and the following one. Another special situation where a small ac perturbation leads to a basically linear response of the domain state of the sample will be treated separately in Sect. 8.8.

At this point, it is proper to clarify the terminology. The term “switching” can be used in the wide and narrow senses. In the wide sense it has been just introduced above. When used in the narrow sense, it means a change of the domain state in most parts of the sample. In the narrow sense, the term switching is often used in order to distinguish the situation where the application of an ac perturbation results in the change of the domain state virtually in the whole sample (switching regime) from that where such perturbation affects only the domain states in the close vicinity of the domain walls (non-switching regime). In this and the following sections we will discuss switching in the narrow sense (in this sense this term will be used hereafter) as well as the Rayleigh domain wall dynamics, which formally cannot be classified as switching in the narrow sense. These sections will be mainly dealing with the situations occurring in bulk single crystals; the cases of thin films will be treated separately in Chap. 9.

As a general remark on switching one should mention that it is always very sensitive to the imperfections of the material, which very often are not under

proper control. For this reason, the switching behavior of crystals of the same material but which are not identical in processing, thermal prehistory, electrical prehistory, and aging may be essentially different. For the same reason, a comprehensive presentation of the experimental data on switching in a material that has been already for 60 years under the consideration (like BaTiO_3) can readily provide material for a small book. In this section we are not aiming at such comprehensive description. What we are rather going to present is a selection of the experimental data on widely investigated ferroics chosen to give the reader an idea of how the switching may happen.

8.6.1 BaTiO_3

Perovskite barium titanate is a classical ferroelectric exhibiting a sequence of phase transitions on cooling from the centrosymmetric paraelectric phase. The stoichiometry of this compound also allows another crystalline modification which is also ferroelectric, however, with a hexagonal paraelectric phase. Below we will discuss the switching behavior of the perovskite BaTiO_3 .

The first detailed information of switching behavior of BaTiO_3 was obtained by Merz (1954) from the direct optical observations and pulse switching measurements in the tetragonal ferroelectric phase. The principal conclusion drawn for the polarized light microscopy observations (in additionally strained crystals) was that the switching primarily occurs via a forward growth of 180° wedge-type domains appearing first at the electrodes. This suggests that the nucleation of new domains is more favorable than the sideways motion of those already existing. The switching current (see Sect. 7.4) was found to be very sensitive to the value of the applied field. The maximal switching current, i_{\max} , monitored as a function of the applied field is shown in Fig. 8.6.1b. Figure 8.6.1a shows the switching time (see Sect. 7.4) measured in the same experiment, t_S . The product $t_S i_{\max}$ was found virtually independent of the value of the applied field, E . For $E \geq 7 \text{ kV/cm}$, the $i_{\max}(E)$ dependence shown in Fig. 8.6.1b is close to a linear law. The temperature dependence of the “differential resistance” corresponding to this linear law is shown in Fig. 8.6.2b. The initial part of the $i_{\max}(E)$ curve, for $E < 5 \text{ kV/cm}$, can be fitted to the exponential law

$$i_{\max}(E) \propto \exp[-\delta/E]. \quad (8.6.1)$$

The temperature dependence of the activation field δ is shown in Fig. 8.6.2a. The exponential $i_{\max}(E)$ dependence (at small fields) was interpreted as an indication that, at these fields, the switching current is controlled by the nucleation of new domains, whereas the linear $i_{\max}(E)$ dependence was treated as a fingerprint of the regime where, due to high values of the field, the nucleation is relatively easy and the switching current is controlled by the forward growth of the wedged domains. Metz has related the multiple domain nucleation at a

Fig. 8.6.1 Parameters of pulse switching for a Remeika-grown crystal of BaTiO₃ as functions of the applied field. Sample thickness 50 μm. Electrode area 10⁻⁴ cm². *Upper panel*—switching time. *Lower panel*—maximal switching current. After Merz (1954)

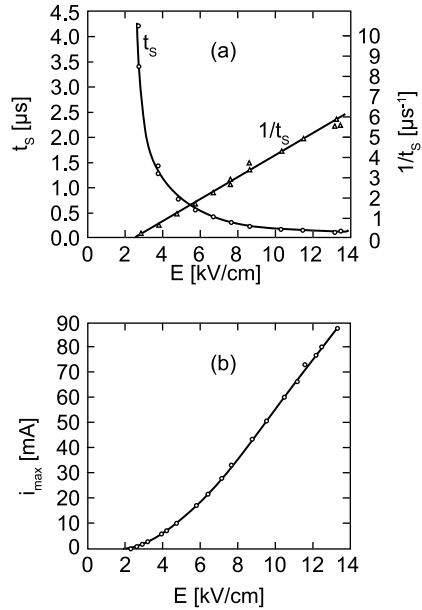
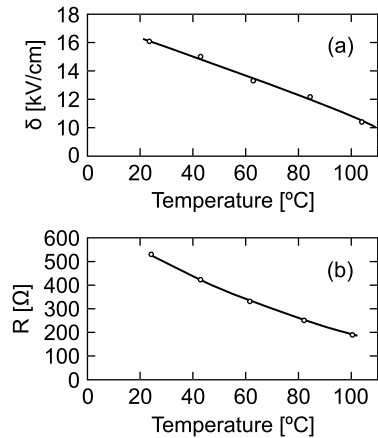


Fig. 8.6.2 Temperature dependences of parameters of pulse switching. The parameters of the sample are given in the caption for Fig. 8.6.1. *Upper panel*— δ from Eq. (8.6.1). *Lower panel*—differential resistance of the sample corresponding to the linear regime of $i_{\max}(E)$ in Fig. 8.6.1. After Merz (1954)



certain field level (optically observed) with a sharp “low-field-corner” typical for the P - E hysteresis loops typical for BaTiO₃ (see Fig. 8.6.3b and c).

For description of pulse switching dynamics of BaTiO₃, Pulvari and Kuebler (1958a) successfully used the following system of phenomenological relations:

$$\frac{P(t)}{P_S} = 1 - 2 \exp[-0.5(t/t_{\max})^2], \tag{8.6.2}$$

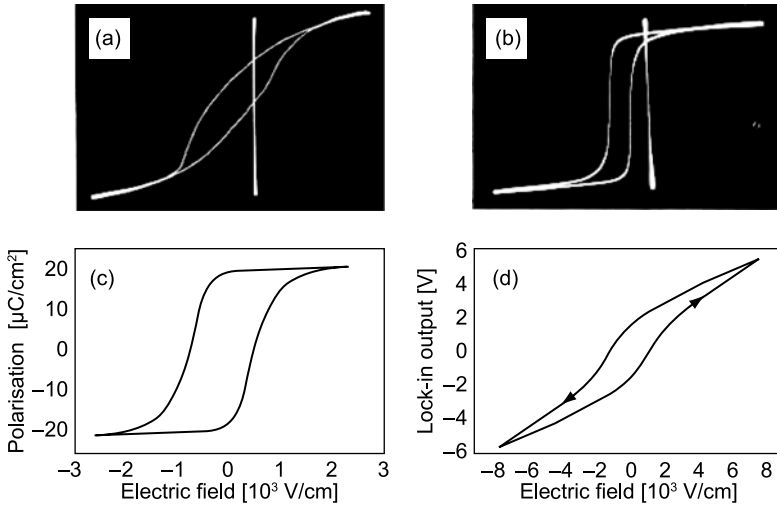


Fig. 8.6.3 Room temperature P - E hysteresis loops of a Remeika-grown crystal of BaTiO_3 . (a) and (b) Loops taken with a Sawyer-Tower circuit before and after heat treatment, respectively. (In (b) the remanent polarization is $\cong 25 \mu\text{C}/\text{cm}^2$ and the coercive field is $\cong 1 \text{ kV}/\text{cm}$). Reprinted with permission from von Hippel, A., *Rev. Mod. Phys.* **22**, 221 (1950) by the American Physical Society. (c) Loop taken with a Sawyer-Tower circuit. (d) Nanoscale loop taken with a scanning force microscope. Reprinted from Eng, L.M.: *Nanoscale domain engineering and characterization of ferroelectric domains*. *Nanotechnology* **10**, 405 (1999) with permission by IOP Publishing Ltd

$$\frac{1}{t_{\max}} = \gamma E \exp[-\delta/E], \quad (8.6.3)$$

where γ is a constant. These relations also provide a good description for the aforementioned data by Metz.

The most common way to study switching in BaTiO_3 was monitoring P - E hysteresis loops. Strain-field (Pan et al., 1988) and birefringence-field (Meyhofer, 1958) hysteresis loops have been also used for characterization of switching in this crystal but to a much less extent. Figure 8.6.3 shows examples of the P - E loops: Figure 8.6.3a and b presents one of the first loops reported in 1950 (von Hippel, 1950) for Remeika-grown single crystals; figure c and d shows recently reported loops (Eng, 1999) for single crystals grown with the same technique.

It was found already in the early stages of BaTiO_3 studies that its coercive field, E_c , is not a constant (as it was sometimes expected, based on the knowledge of classical ferromagnets) but depends significantly on frequency, ω , and amplitude of the applied field, E_m . As the frequency grows, the field changes faster and the domain processes characterized by the loop increase their

“delay”; thus we expect an increase in the field at which the average polarization of the sample reaches zero, i.e., of the coercive field. This was shown by Wieder (1957) for both tetragonal and orthorhombic phases of BaTiO₃ and later studied by Campbell (1957) and Pulvari and Kuebler (1958a) at room temperature. Figure 8.6.4a shows the function $E_C(\omega)$ measured with field amplitudes $E_m = 2E_C(\omega)$. The cross points represent data obtained with continuous ac field; circles correspond to data taken with pulsed sine waves, to avoid the heating effects. The same authors (Pulvari and Kuebler, 1958a) investigated also the dependence $E_C(E_m)$, shown in Fig. 8.6.4b for $\omega = 200$ Hz. These dependences are compatible with the above data on the field and time dependence of the switching current. Specifically, the phenomenological relations for switching dynamics Eqs. (8.6.2) and (8.6.3) can be translated into the logarithmic frequency dependence of the coercive field and near proportionality of E_C to the activation field for pulse switching δ (Pulvari and Kuebler, 1958a). For the case of sine wave driving field the corresponding relation reads

$$1.3\omega E_m - \gamma E_C^2 \exp[-\delta/E_C] = 0. \tag{8.6.4}$$

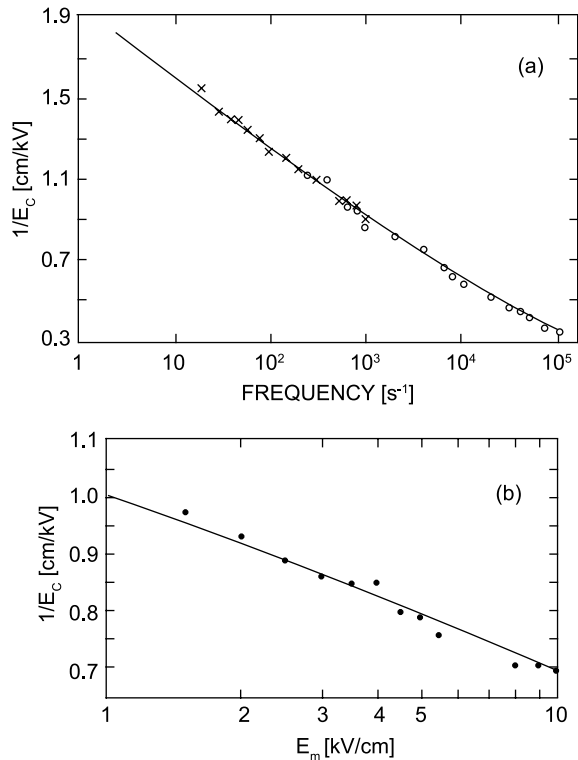


Fig. 8.6.4 Coercive field E_C of P - E hysteresis loops of a Remeika-grown crystal of BaTiO₃. (a) Dependence on the frequency of the sine wave driving field under condition $E_m = 2E_C$; crosses—continuous sine wave, circles—pulsed sine wave. (b) Dependence on the amplitude of the driving field E_m measured at a frequency of 200 Hz. After Pulvari and Kuebler (1958a)

This equation provides a good description for the data presented in Fig. 8.6.4. Parameters E_c and δ were found to be a linear function of the inverse thickness of the sample for the range 20–70 μm , δ being approximately eight times larger than E_c . Concerning this thickness dependence, it is useful to note that the authors did not mention any etching procedure and since obviously “Remeika-type” crystals were used, their samples could have carried a surface layer which, according to many workers, can play an essential role of the switching performance of ferroelectric crystals. Discussing the coercivity in BaTiO_3 crystals one should indicate that, as usual in ferroelectrics, the experimentally determined value of E_c (about 1 kV/cm at room temperature) is much smaller than the value of the thermodynamic coercive field E_{crit} (about few hundreds of kV/cm at room temperature).

An important feature of the switching process is that, on a small enough time scale, the switching current is not a monotonic function of time and the corresponding $P - E$ hysteresis loop is not smooth. Being motivated by the magnetic analogy, this problem was addressed on the very early stage of investigation of BaTiO_3 by Newton et al. (1949) followed by later systematic studies by Chynoweth (1958) and Brezina et al. (1961). The pulses of current superimposed on the smooth background, called in analogy with magnetic systems *Barkhausen pulses*, were readily identified. Figure 8.6.5 shows oscilloscope photographs of typical Barkhausen pulses observed by Chynoweth (1958). However, the available experimental data are contradictory. For example, Newton et al. (1949) reported that the total number of the pulses at a switching event is a linear function of the applied field, Fig. 8.6.6, whereas according to Chynoweth (1958) the total number of pulses in a given sample is

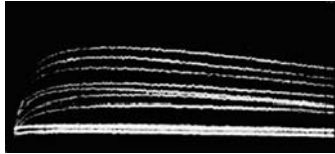


Fig. 8.6.5 Oscilloscope photographs of typical Barkhausen pulses in BaTiO_3 . The total length of the trace is 100 μs . Reprinted with permission from Chynoweth (1958). Copyright (1958) by the American Physical Society

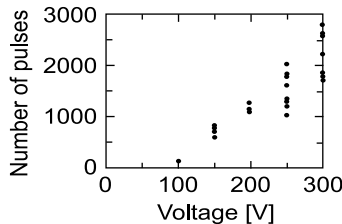


Fig. 8.6.6 Number of Barkhausen pulses given by a BaTiO_3 sample as a function of applied voltage. Distance between the electrodes is 0.15 cm. Volume of the sample is $5.6 \times 10^{-4} \text{ cm}^3$. After Newton et al. (1949)

independent of the applied field. In this detailed work, the author revealed several clearly pronounced trends. Based on the totality of the obtained results it was concluded that the origin of the observed Barkhausen pulses is the nucleation and initial stages of growth of new wedge-shaped 180° domain extending along the polar axis of the material. In this context, the fixed number of pulses given by a crystal implies a definite number of nucleation sites on the crystal surface. It is worth mentioning that such interpretation of the Barkhausen pulses is principally different from the traditional scenario in magnetic system, where the Barkhausen pulses are attributed to jerky domain wall motion. However, the current pulses related to this kind of domain wall motion can also be observed in BaTiO_3 crystals. Brezina et al. (1961) reported giant Barkhausen pulses which accompany switching associated with the jerky motion of 90° domain walls. We have already discussed this effect in Sect. 8.3.3. Another argument in favor of Barkhausen pulses associated with the jerky motion of domain wall in BaTiO_3 was presented by Rudyak et al. (1973) who distinguished in their experimental data two kinds of pulses strongly different in their shape; these two types were attributed to pulses resulting from the nucleation and from the jerky domain motion.

Polarization-field hysteresis loops of BaTiO_3 crystals were found to be affected by UV illumination. Warren and Dimos (1994) demonstrated that the illumination combined with application of a dc bias field can essentially (by 90%) suppress the height of the loop taken from Remeika-grown crystals. The suppressed state is stable (the reduced loop remains unchanged at least after a 2 week sample storage at room temperature). However, this state can be erased using the same illumination combined with application of a dc bias of the polarity opposite to that applied for the loop suppression. The suppression of the loop was maximized for band-gap illumination, i.e., $\lambda = 404 \text{ nm}$ ($h\nu = 3.075 \text{ eV}$; BaTiO_3 band-gap $E_g = 3.1 \text{ eV}$). Results, quite different from the above, were reported by Cudney et al. (1994) for the crystals obtained with a top-seeded solution technique. It was found that, the continuous illumination during electrical cycling with light ($\lambda = 488 \text{ nm}$) leads to an appreciable increase in the loop height and a reduction of the backswitching (the top of loop becomes flatter under illumination), Fig. 8.6.7.

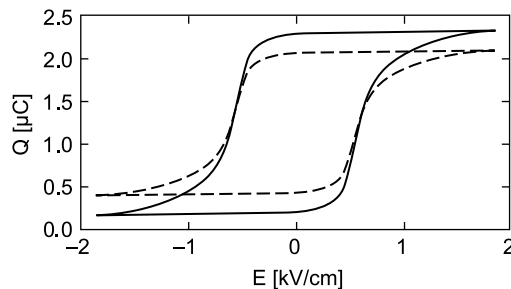


Fig. 8.6.7 Impact of continuous illumination ($\lambda = 488 \text{ nm}$) on charge/electric field, $Q-E$, hysteresis loop of a BaTiO_3 crystal grown by a top-seeded technique. The electrode area is 8 mm^2 . *Solid line*—with illumination. *Dashed line*—without illumination. After Cudney et al. (1994)

Already in the early stages of investigations it was pointed out that the kind of electrodes can seriously influence the shape of a hysteresis loop (Janovec et al., 1960). A BaTiO_3 crystal plate with two identical liquid (aqueous solution of LiCl) electrodes showed a symmetric hysteresis loop with fast switching. With two identical indium electrodes the loop was also symmetric but the switching was slower. Combined electrodes lead to an asymmetric loop, showing that a liquid electrode provides more favorable conditions for switching starting at that electrode. The loop asymmetry due to non-equivalent electrodes is the evidence of the role of surface conditions in switching. The effect of the humidity of the ambience on the shape of the hysteresis loops in BaTiO_3 crystals reported by Anderson et al. (1955) also indicates the role of the surface conditions in switching.

The electric-field-driven switching discussed above is related to the field-induced change of the domain state. In BaTiO_3 , exhibiting three first-order structural phase transitions, the electric field not only can switch the domain state but also can “switch” the phase, resulting in “double hysteresis loops” shown already in Fig. 2.3.4. The appearance of the double hysteresis loops in the vicinity of a ferroelectric first-order phase transition is clear from a schematic field–temperature phase diagrams as illustrated in Fig. 8.6.8c and d (for

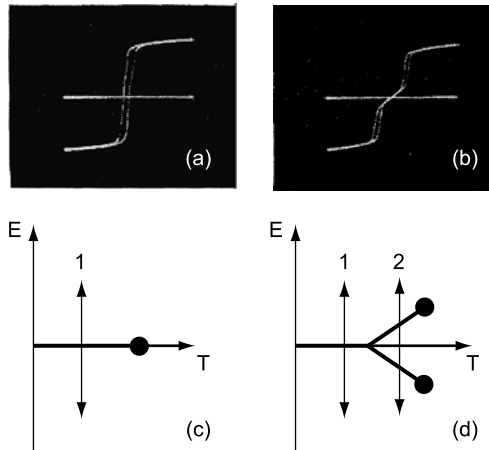


Fig. 8.6.8 Single (a) and double (b) $P - E$ hysteresis loops taken from a BaTiO_3 sample at temperatures $T_C - 1 \text{ K}$ and $T_C + 3.5 \text{ K}$, respectively. Reprinted with permission from Merz (1953). Copyright (1953) by the American Physical Society. Schematic temperature/electric field phase diagram of a ferroelectric phase transition; (c) the case where at $E = 0$ the transition is of the second order; (d) the case where at $E = 0$ the transition is of the first order. Direction of the field is parallel to that of the spontaneous polarization. *Solid lines* correspond to the lines of first-order phase transitions. *Points* correspond to the isolated critical points. Field variation according to the *double-headed line* marked with “1” corresponds to simple $P - E$ hysteresis loops. Field variation according to the *double-headed line* marked with “2” corresponds to a double $P - E$ hysteresis loop

more information see Sect. 2.3.1). For the cubic–tetragonal phase transition the double hysteresis loops were observed and interpreted by Merz (1953). Figure 8.6.8a and b shows regular and double hysteresis loops taken from a BaTiO₃ crystal at temperatures $T_C - 1$ K and $T_C + 3.5$ K, respectively. Triple hysteresis loops related to the tetragonal–orthorhombic phase transition were reported by Huijbregtse and Young (1956). The mechanism of the formation of such loop is similar to that of the double loops; however, it is more complicated because in this case both phases have several domain states.

Viewing the polarization switching as an electric-field-driven phase transition happening much before the “unfavorable phase” becomes absolutely unstable at $E = E_{\text{crit}}$, it is clear that crystalline imperfections must play a decisive role in this process. Despite the obvious importance of this issue, the focused work on the impact of imperfections on switching in BaTiO₃ is quite limited. As an early work on this issue one can indicate a work by Kudzin et al. (1964). This work documents formation of double $P - E$ loops induced by impurities that make the polydomain state with zero net polarization energetically favorable. This effect was recently revisited in illuminating studies by Zhang and Ren (2005, 2006) where the impact of Mn doping (0.3 mol%) on switching in BaTiO₃ crystals was addressed by simultaneous monitoring of the polarization, domain pattern, and strain. In BaTiO₃, Mn⁺³ ions substitute for B-site Ti⁺⁴ ions. In a rough approximation, every substituted ion can be considered as electrically compensated with an oxygen vacancy which can occupy one of the six neighboring positions (see Fig. 2.1.2). The resulting dipole (substitution–vacancy) represents an RF defect for the polarization, which due to appreciable mobility of oxygen vacancies can change its orientation. In the cubic phase or in the tetragonal phase reached by fast cooling through the transition, the distribution of the oxygen vacancies between the six positions is homogeneous. However, after a long stay in the tetragonal phase, this distribution acquires the $4mm$ symmetry between one (the most favorable), four (the second-best), and one (the most unfavorable) positions of the vacancy. Obviously, the orientations of this distribution in different domains follow the orientations of the spontaneous polarization in them. Zhang and Ren (2005) demonstrated that, in properly aged tetragonal phase crystals, the coupling between the polarization and redistributed impurities is so strong that the domain pattern, in which the aging was performed, is practically fully restored after cycling with the switching electric field. Figure 8.6.9 shows that this is the case in the aged crystals, whereas in non-aged crystals, the domain pattern is significantly affected by the cycling. In the same paper it was also shown, using the strain-field hysteresis loop, that the aging results in a substantial increase in the amplitude of the induced strain. In turn this attests to enhancement of the 90° switching in the aged sample, which is consistent with the distribution of the impurities making the 90° rotation more favorable than the 180° rotation. The same effect was also demonstrated from the experiments with aging in a single-domain state (Zhang and Ren, 2006). Here, the crystal was aged in a single-domain state and then was switched further

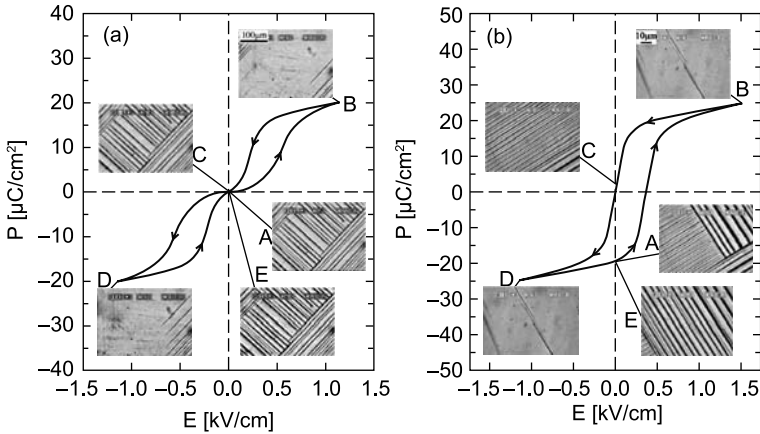


Fig. 8.6.9 Polarization-field hysteresis loops of BaTiO_3 crystals doped with 0.3 mol % of Mn and micrographs illustrating 90° domain patterns corresponding to different stages of switching. (a) Crystal aged at 80°C for 2 weeks. (b) Crystal heated above T_C and kept for 4–5 h. It is seen that in the first case the domain pattern is fully reproduced after a switching cycle. After Zhang and Ren (2005). Courtesy of Prof. Xiaobing Ren

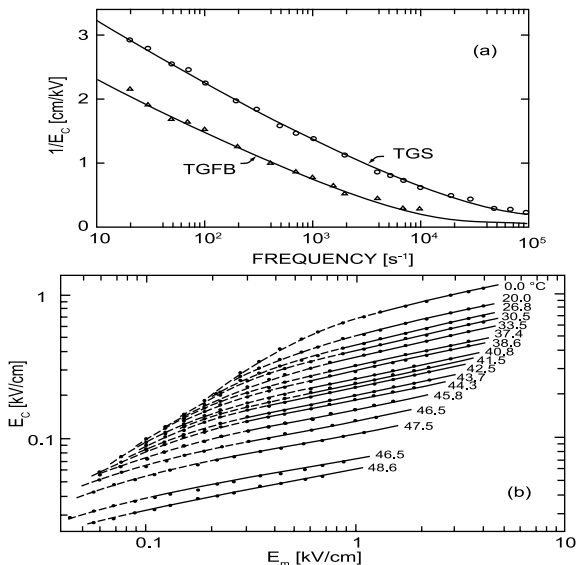
in a field perpendicular to the initial direction of the polarization; this yielded double $P - E$ hysteresis loops.

8.6.2 TGS and TGFB

Triglycine sulfate (TGS) and its isomorph triglycine fluoberyllate (TGFB) are considered as model uniaxial ferroelectric–nonferroelastics. Despite intensive investigations, the switching data on these materials obtained by different authors are not free from contradictions.

Some data on switching in TGS have been presented above in the book. Figure 7.2.4 shows that, at high enough amplitudes of the driving field, TGS exhibits exemplary rectangular saturated $P - E$ hysteresis loop. However, at smaller amplitudes, as shown in Fig. 7.2.5, the shape of the loops transforms toward the Rayleigh shape. An important feature of the $P - E$ loops is that their coercive field does not show any trend to the saturation on increasing amplitudes of the driving field, as shown in Fig. 8.6.10b. Pulvari and Kuebler (1958) successfully applied the phenomenological framework given by Eqs. (8.6.2) and (8.6.3), originally used for BaTiO_3 , to the description of the switching dynamics in TGS and TGFB. Figure 8.6.10a shows the frequency dependence of the coercive field E_c of these crystals measured at the driving field amplitude $E_m = 2E_c$, demonstrating good agreement with the prediction of Eq. (8.6.4). However, in contrast to BaTiO_3 , no thickness dependence of E_c was reported in the range 0.15–0.45 mm at room temperature; the corresponding data are

Fig. 8.6.10 (a) Frequency dependence of $1/E_c$ for TGS and TGFB. After Pulvari and Kuebler (1958). (b) Driving-field amplitude and temperature dependence of E_c for TGS, measured at 60 Hz. Temperature is indicated at the plots. After Nakatani (1972)



shown in Fig. 8.6.11. The pulse switching experiments revealed that the activation field δ is also thickness independent, the ratio δ/E_c being 3 for TGS and 1.5 for TGFB.

The above data by Pulvari and Kuebler clearly contradict those by Kay and Dunn (1962). The latter found that the coercive field of TGS is frequency independent in the range 40–4 KHz. At the same time these authors reported a pronounced thickness dependence of the coercive field which can be fit to the law $E_c \propto h^{-2/3}$ as shown in Fig. 8.6.12. An alternative thickness dependence of the coercive field, $E_c \propto 1 + h_0/h$, was reported for TGS by Hadni et al. (1983) for the thickness range 1.3–5,000 μm .

Fig. 8.6.11 Thickness dependence of E_c and of the activation field δ for TGS and TGFB. Circles represent E_c from hysteresis loop measurements. Crosses give δ obtained from pulse measurements. After Pulvari and Kuebler (1958)

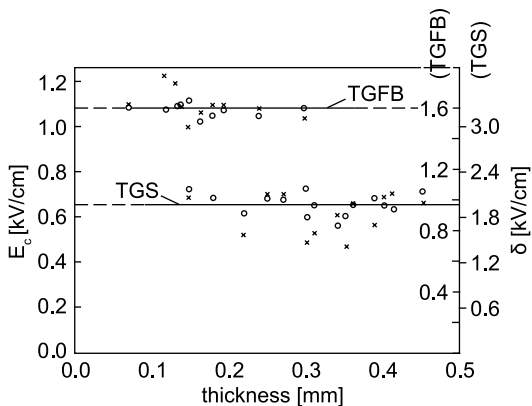
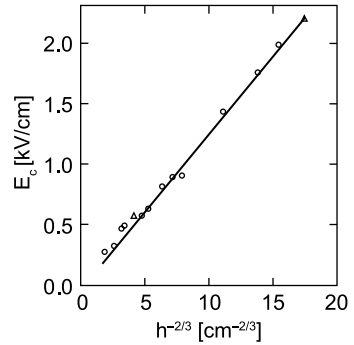
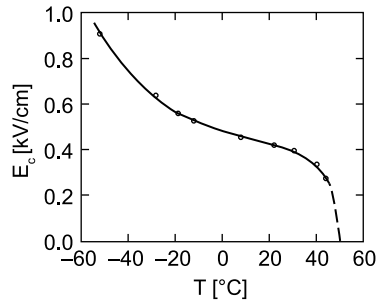


Fig. 8.6.12 Thickness dependence of E_c for TGS. Circles and triangles represent data taken from slices cleaved from different samples. After Kay and Dann (1962)



The temperature dependence of the coercive field in a wide temperature range was addressed by Domanski (1958). His data for the driving field with frequency 50 Hz and amplitude 1.5 kV/cm are presented in Fig. 8.6.13. As usual in ferroelectrics, the experimentally determined value of E_c is much smaller than the value of the thermodynamic coercive field E_{crit} ; in the case of TGS, the Landau theory predicts $E_{\text{crit}} \propto (T_c - T)^{3/2}$ with $E_{\text{crit}} \cong 1$ kV/cm at $T_c - T \approx 1$ K. Interestingly, Martinez and Gonzalo (1982) found that close to the transition temperature, $T_c - T = 0.03 - 0.2$ K, the relation $E_c \propto (T_c - T)^{3/2}$ is consistent with the experimental data. However, the determined proportionality coefficient was some 200 times smaller than the thermodynamic coercive field in the Landau theory. The authors also compare their experimental data with their original model for the coercivity to find disagreement in the proportionality coefficient in some 20 times. Another temperature dependence of the coercive field in TGS in the vicinity of T_c , $E_c \propto T_c - T$, was documented by Okada et al. (1980). However, according to Martinez and Gonzalo (1982) this discrepancy was due to a difference in the used definitions of the coercive field.

Fig. 8.6.13 Temperature dependence of E_c for TGS at frequency 50 Hz and driving field 1.5 kV/cm. After Domanski (1958)



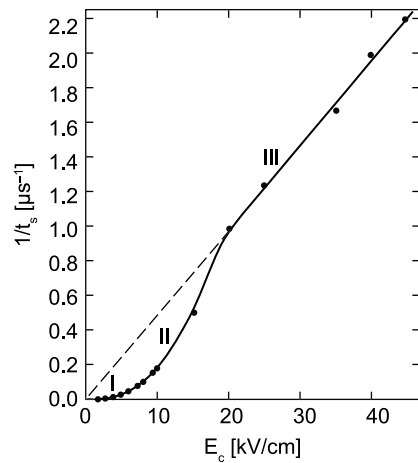
A comprehensive investigation of switching dynamics in TGS by pulse switching technique in very wide interval of driving fields was done by Fatuzzo and Mertz (1959) (up to 50 vs. 3 kV/cm in experiments by Pulvari and Kuebler).

Based on a body of experimental data these authors concluded that the switching scenario in TGS is basically the same as in BaTiO_3 . Namely, at small applied fields the bottleneck of switching is the nucleation of new domains at the electrodes, whereas at high fields the switching is governed by the forward growth of the needle-shaped domains, the sideway expansion of the through domains not playing essential role. Figure 8.6.14 shows field dependence of the inverse switching time reported by Fatuzzo and Merz (1959). In this figure, the nucleation-controlled regime is marked with I and the regime controlled by the forward growth of the needle-shaped domains is marked with III. In these regimes, the switching time can be fit to the relations $1/t_s \propto \exp(-\delta/E)$ and

$$1/t_s = kE, \quad (8.6.5)$$

respectively. Similar to the case of BaTiO_3 , the validity of this relation was considered as an argument for the switching scenario proposed. Another feature of the switching dynamics revealed by Fatuzzo and Merz, which supports the forward growth scenario for high-field regime, is the thickness dependence of the k coefficient from Eq. (8.6.5). Specifically, it was found that k is inversely proportional to the sample thickness. This is clearly possible in the case of forward growth mechanism whereas it cannot be rationalized in the case where the sideway expansion of the through domains plays an essential role. Analyzing partial switching in this crystal, these authors also found that too short pulses do not lead to a change of the polarization of the crystal; this, the so-called t^* effect, is discussed above at the end of Sect. 7.4. The simplest interpretation of this effect is that the needle-shaped domains become stable only once they reach the opposite electrode of the sample, otherwise, in the absence of the applied field, they shrink back and disappear (Fatuzzo and Merz, 1959; Taylor, 1966).

Fig. 8.6.14 Field dependence of the inverse switching time in TGS at room temperature. After Fatuzzo and Merz (1959). According to Fatuzzo and Merz (1959), the field intervals marked with symbols “I” and “III” correspond to the switching regimes primarily controlled by the domain nucleation and the forward growth of need-shaped domains, respectively



The nucleation-controlled nature of the low-field regime of switching in TGS (I regime) is also indirectly supported by a three —times change of the activation field δ at the field of about 1 kV/cm, which was reported by many authors, e.g., in the paper by Jaskiewicz and Przeslawski (1979). These authors indicated that such crossover is typical for a phase transformation driven by two-dimensional nucleation. We have addressed the theory of this effect in Sect. 8.4.3.2 in the context of the relation between the nucleation rate and the wall velocity (the rate of the phase transformation).

Discussing switching dynamics in TGS one should mention a work by Hashimoto et al. (1994) where $P - E$ hysteresis loops exhibited by a TGS crystal were reported and analyzed in terms of a Kolmogorov–Avrami-type model which primarily deals with sideway motion of the domain walls (see Sect. 8.7.5). These authors demonstrated that several features of the measured loops can be described in terms of this model. This may be considered as an indication to a decisive role of the sideway domain motion in this material. However, the model provides a good description only if the domain growth dimension is taken as non-integer. Since, in this problem, the non-integer growth dimension has no clear physical meaning, this logic cannot be taken for granted as conclusive. We will return to the discussion of the switching data on TGFB in terms of a Kolmogorov–Avrami-type model in Sect. 8.7.4

Impact of defects on the switching performance of TGS crystals has been addressed by many workers. Here one should distinguish two principally different situations. *First*, it is the situation similar to that we have discussed above for BaTiO₃ where the defects “memorize” during aging the domain state in a region of the crystal. In this case, if by the application of an electric field the domain state in the region is changed, once the field is turned off, the original domain state in the region is restored. Here of importance is that one can memorize any domain pattern that can be created in the crystal. This kind of treatment can lead to double $P - E$ hysteresis loops as well as to a voltage offset of single $P - E$ hysteresis loops (if the crystal was aged in a single-domain state and further switched in an electric field parallel to the original direction of the polarization). For TGS, this kind of defect impact has been documented for Cu-doped (see, e.g., (Eisner, 1974)) and radiation damaged material (Chynoweth, 1959). The *second* situation occurs when TGS is doped with chiral molecules. Specifically, the substitution of α -alanine molecule for glycine was used (Brezina and Havránková, 1985). This kind of doping makes favorable one of the two crystallographic orientations of the spontaneous polarization. That means that one direction of the polarization becomes preferable throughout the whole crystal when it is grown in the ferroelectric phase. It was also demonstrated that, by using the right (*D*- α -alanine) or the left (*L*- α -alanine) modifications of α -alanine, one can select the preferable detection of the spontaneous polarization. Such doping results in a voltage offset of the $P - E$ hysteresis loops corresponding to the internal bias field in the range 0.3–5 kV/cm (Nakatani, 1991). A theory-group-based interpretation of this effect was offered by Zikmund and Fousek (1988, 1989).

8.6.3 LiTaO_3 and LiNbO_3

Lithium tantalate (LT) and lithium niobate (LN) are uniaxial ferroelectrics with non-piezoelectric paraelectric phase thus exhibiting nonferroelastic domain states. In this aspect these crystals are similar to TGS. However, they differ much from TGS in many aspects. These are displacive ferroelectrics exhibiting high transition temperatures (about 1,200°C for LN and 620°C for LT), high room temperature values of the spontaneous polarization, and they can stand an appreciable degree of non-stoichiometry that dramatically influences their switching properties. These materials are of high interest for many practical applications based on their optical, piezoelectric, and pyroelectric properties (Volk and Woehlecke, 2008). Since the domain structure of LT and LN matters for all these applications, polarization reversal in these materials has been extensively investigated, sometimes using non-common poling techniques, e.g., with involvement of element diffusion (Rosenman et al., 1995), proton exchange (Nakamura and Tourlog, 1993), and electron beam impact (Nutt et al., 1992). Here in the book we will discuss only the classical situation of switching in a homogeneous electric field (in a parallel plate capacitor). For the experimental data on switching in LT and LN driven by an inhomogeneous electric field we refer the reader, e.g., to original papers (Agronin et al., 2004; Shur et al., 1999; Yamada et al., 1993).

At the early stages of investigation, it was recognized that full polarization reversal at room temperature in LT and LN requires application of very high electric fields (more than 300 kV/cm) (Wemple et al., 1968). However, partial polarization reversal was reported, for pure LN, starting from 100 kV/cm and for Fe-doped—from 10 kV/cm (Kovalevich et al., 1978; Kamentsev and Rudyak, 1984).

LT and LN provide a classical example of the impact of crystalline imperfections on the switching performance of ferroelectrics. These materials can be grown with appreciable deficiency of Li and corresponding excess of Nb or Ta. According to Gopalan and Gupta (1997) defects associated with this non-stoichiometry may make polar (RF) defects which strongly couple with the ferroelectric polarization. The impact of the stoichiometry on switching in LT is illustrated in Fig. 8.6.15 where the $P - E$ hysteresis loops reported by Kitamura et al. (1998) for stoichiometric and the so-called congruent (with 1.5% Li deficit) composition of LiTaO_3 are shown. The strongly reduced coercive field and voltage offset are clearly seen for the stoichiometric composition. For LN such effect was traced for three concentrations of the Li deficit as shown in Fig. 8.6.16. The variation of stoichiometry also leads to a qualitative change of some features of polarization switching like the shape of the growing domains and the shape of switching current. According to the results obtained by Shur and coworkers (Shur et al., 2002), for congruent LT, columnar domains with triangular cross-section are typical whereas growing domains with more complicated cross-sections (e.g., hexagonal) are typical for stoichiometric LT. The same group (Shur et al., 2001b) reported results suggesting an appreciable

Fig. 8.6.15 Room temperature polarization-field hysteresis loops of congruent and stoichiometric lithium tantalate crystals. After Kitamura et al. (1998)

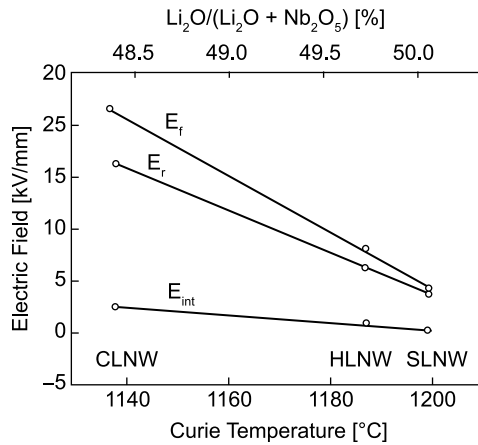
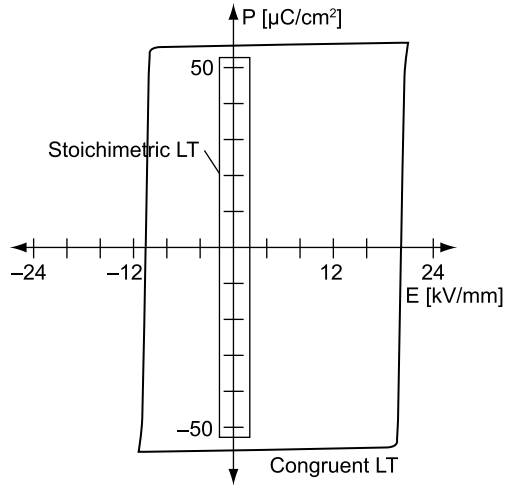


Fig. 8.6.16 Dependence of switching parameters of lithium niobate crystals, determined at room temperature, on its composition: E_f —field needed for switching from a virgin single-domain state, E_r —field needed for switching from the once-reversed polarization state, $E_{int} = (E_f - E_r)/2$ —field corresponding to the voltage offset of switching. The sample compositions were evaluated from the values of the transition temperature, which are also shown. Abbreviations: CLNW, SLNW, and HLNW denote the near-stoichiometric, the congruent, and the intermediate compositions of lithium niobate with high hydrogen content. Reprinted with permission from Gopalan et al. (1998). Copyright (1998), American Institute of Physics

difference in the shape of switching current in materials with different stoichiometry: For stoichiometric LT it mainly consists of individual spikes, whereas for congruent LT, the current contains an appreciable smooth component. These features are illustrated in Fig. 8.6.17. This figure also shows that, in the

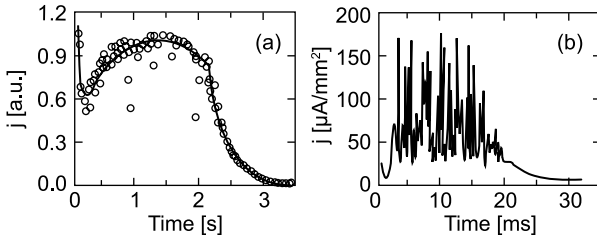


Fig. 8.6.17 Shapes of switching currents in lithium tantalate at room temperature. **(a)** Congruent composition, driving field of 190 kV/cm, **(b)** stoichiometric composition, driving field of 33 kV/cm. Reprinted with permission from Shur et al. (2001a). Copyright (2001), American Institute of Physics

stoichiometric material, a much smaller electric field produces much faster switching. A specific shape of transient current (consisting of very sharp (< 1 ms) spikes spread over 50–100 ms depending on the applied field) was indicated by Gopalan et al. (1998) as typical for LN in general.

The spike-like components of the transient current reported for LN and LT suggest that, in these crystals, the polarization reversal is mainly controlled by forward growth of the needle-like domains whereas the merging of expanding columnar domains seems to be of minor importance. The direct observation by Kuroda et al. (1996) of the side view of dynamical domain patterns in MgO-doped LN supported such suggestion. Figure 8.6.18 shows the side views (normal to the polar axis) of different stages of the polarization reversal in

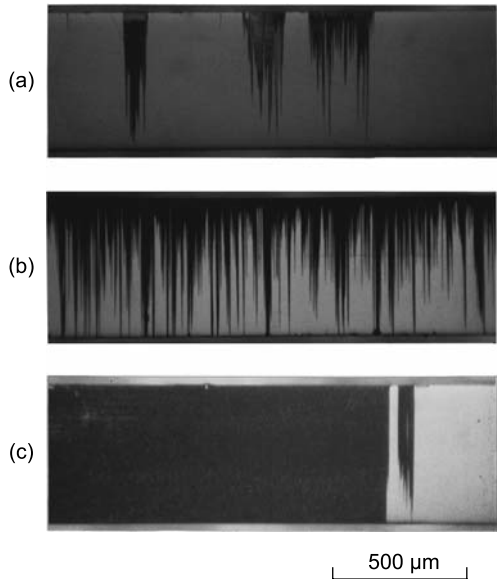


Fig. 8.6.18 Domain patterns at different stages of switching in MgO-doped lithium niobate, revealed by etching of + Y surface of a Z-cut crystal. The applied field is 4.45 kV/mm. **(a)** After 5.6 s. **(b)** After 160.2 s. **(c)** After more than 1 h. Reprinted with permission from Kuroda et al. (1996). Copyright (1996), American Institute of Physics

this system, which clearly illustrate the predominant role of the forward growth. One should mention that such switching scenario, where most of the inverse domains end in the bulk of the crystal, implies a presence of appreciable bound electric charge distributed in the crystal, the situation unfavorable from the electrostatic point of view. A comprehensive characterization of the charged domain walls was performed by Shur and coworkers (Shur et al., 2000a) who demonstrated that, in congruent LN, zigzag configurations of the charged domain wall stay in the sample even after the applied field is turned off. As an unexpected observation, which also attests to the dominant role of charged domain walls in this system, we mention the behavior of LN plate heated from room temperature (at which it was single domain) to 1,110°C and kept in air for over 5 h. Such treatment led to the formation of two head-to-head domains of equal volumes separated by a rather flat charged domain walls. At the same time, the exposition to 1,110°C in flowing Ar gas resulted in the formation of the same type of domains, however, with a much smaller volume of the reverse one.

8.6.4 KDP and Isomorphous Crystals

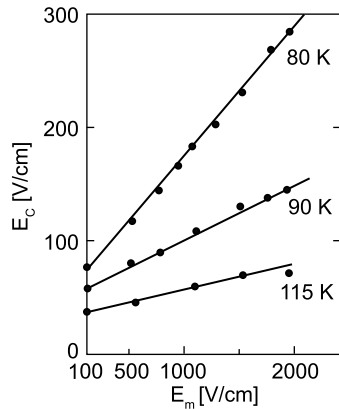
Potassium dihydrogen phosphate (KDP), the second discovered ferroelectric, is an example of uniaxial ferroelectric with a piezoelectric coupling between the order parameter and deformation in the paraelectric phase. Thus, this material exhibits two domain states which differ both in the spontaneous polarization and in the strain. As we have discussed above in this book, the ferroelastic nature of the domain states essentially influences the static domain pattern and domain wall motion in this crystal. Some features of switching in KDP were found unique; however, in most of the aspects of switching on macroscopical level, the behavior of KDP-type crystals is comparable to that of BaTiO₃ and TGS.

Peculiar direct information of the switching mechanism in DKDP (deuterated isomorph of KDP) was offered by Aleshko-Ozhevskij et al. (1985) who monitored the polarization reversal driven by an applied electric field by using synchrotron radiation topography. It was found that, in poly-domain samples, the polarization reversal is strongly correlated. According to these authors, in areas 10–100 μm thick containing many thin lamella domains, all unfavorable domains switch at the same time. At some 60 K below the transition temperature, switching in correlated areas starts at a field of 0.1–0.2 kV/cm and it is complete at 1 kV/cm. The specifics of the polarization reversal in KDP was repeatedly stressed in works by Bornarel and coworkers. As a unique feature of KDP, for example, the time dependence of switching current with two maxima reported by Guyon and Lajzerowicz (1966) was indicated.

At the same time, the phenomenological description of switching in KDP can be successfully done using the framework tested on BaTiO₃ and TGS.

According to Guyon and Lajzerowicz, for pulse switching at small fields, the inverse switching time follows the exponential law $\exp(-\delta/E)$ (with $\delta = 0.2$ kV/cm at temperature 20 K below the transition temperature) followed with a linear field dependence at higher fields (cf. Sects. 8.6.1 and 8.6.2). Moreover, the logarithmic dependence of the coercive field on the amplitude of the driving field reported for KDP by Bornarel (1995) (Fig. 8.6.19) is comparable to the Pulvari–Kuebler (1958a) phenomenological framework and with the data for BaTiO₃ shown in Fig. 8.6.4. The time dependence of the switching current in KDP was monitored by Usher et al. (1990) for the applied fields 0.05–1 kV/cm in the temperature interval of some 35 K below the transition temperature. These authors typically did not observe the two-maxima profile reported by Guyon and Lajzerowicz (1966) except for the case of a cracked crystal. The obtained, thus, one-maximum traditional profiles were fitted to that predicted by the Kolmogorov–Avrami-type model (see Sect. 8.7.3). Obtained from this fit values of the growth dimensions were found non-integer and close to those determined from the frequency dependence of the hysteresis loops in TGS (Hashimoto et al., 1994).

Fig. 8.6.19 Dependence of the coercive field, E_c , on the amplitude E_m of the driving field at different temperatures in a KDP crystal. The driving field frequency is 50 Hz. After Bornarel (1995)



The temperature dependence of the coercive field in KDP was reported by several authors (Guyon and Lajzerowicz, 1966; Bornarel, 1995; Barkla and Finlayson, 1953). Though these data differ much, one common qualitative feature may be distinguished. Specifically, after a rise of E_c on cooling just below the phase transition there comes a kind of saturation followed by the second sharp rise on cooling at a temperature that is some 50–60 K below the transition temperature. Such anomaly as documented by Barkla and Finlayson (1953) is shown in Fig. 8.6.20a. This behavior reminds that reported for TGS and shown in Fig. 8.6.13. The same authors reported a very strong drop of the domain contribution to the permittivity occurring at the temperature of the second rise of E_c (Fig. 8.6.20b). The latter effect was later called “domain freezing” (Huang et al., 1997) and it was also identified in TGS. Thus, the

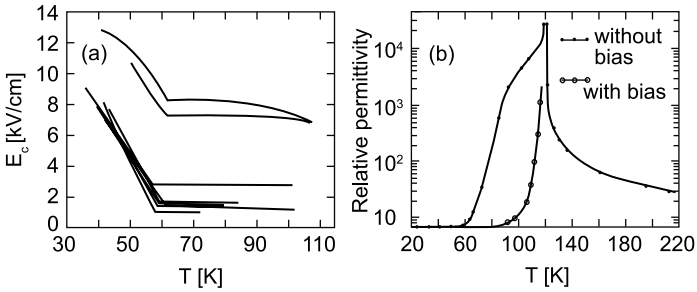


Fig. 8.6.20 (a) Temperature dependence of the coercive field of different KDP samples. The driving field frequency is about 10^{-2} Hz. (b) Temperature dependence of the dielectric constant of a mechanically free KDP crystal, i.e., measured at the frequency of the driving field which is smaller than the piezoelectric resonance frequency of the sample. The data presented for the cases where dc bias is absent and under a dc bias of 3 kV/cm. After Barkla and Finlayson (1953)

similarity in the temperature dependence of the coercive field in KDP and TGS may be rationalized as a manifestation of the domain freezing effect (see Sect. 8.8.7 for more information).

8.7 Theory and Modeling of Switching

8.7.1 Introduction

Ferroelectric switching is an example of a first-order phase transition which is driven by the application of an external electric field. This is clearly seen from the phase diagrams for a homogeneous state of a ferroelectric in a fixed electric field shown in Fig. 8.7.1. These diagrams illustrate the situation in the simplest

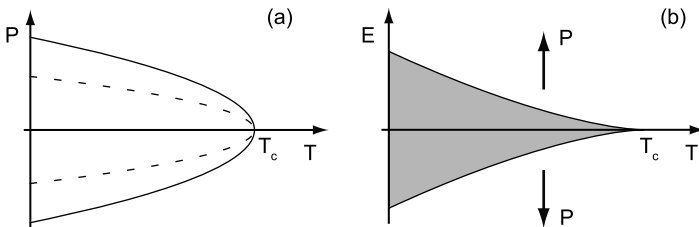


Fig. 8.7.1 Schematic phase diagrams of a uniaxial ferroelectric with the second-order phase transition. (a) Polarization–temperature ($P - T$) diagram: *Solid line* shows the state in the absence of the electric field; under the field all values on the polarization are achievable except for the area limited with the parabola shown with *dashed line*. (b) Field–temperature ($E - T$) diagram: the areas where only one (indicated by *arrows*) direction of the polarization are shown; in the *shaded area* two polarization states are possible. The boundary of the *shaded area* corresponds to the values of the thermodynamic coercive field

case of a uniaxial ferroelectric whose behavior is controlled by the thermodynamic potential as given by Eq. (2.3.13). The solid lines in Fig. 8.7.1a correspond to the equilibrium values of the polarization in the absence of the electric field $P_s(T)$. The application of an electric field changes the polarization. However, its variation is limited, i.e., there exist values of the polarization which cannot be achieved for a given temperature. These values belong to the area in Fig. 8.7.1a, which is limited by the so-called spinodals of the system shown with the dashed lines. These lines correspond to the condition $(\partial E/\partial P)_T = 0$ and, for the considered system, the absolute value of the polarization on these lines is equal to $P_s(T)/\sqrt{3}$. The electric field applied along the direction of the spontaneous polarization increases the polarization; by increasing the field one can, in principle, increase it unlimitedly. On the other hand, the application of an electric field opposing the direction of the spontaneous polarization reduces the polarization of a single-domain ferroelectric; however, it cannot be reduced below a value of $P_s(T)/\sqrt{3}$. The value of field required to get $P = P_s(T)/\sqrt{3}$ is called thermodynamic coercive field E_{crit} . For the considered system it is given by Eq. (2.3.15). Thus, for $|E| > |E_{\text{crit}}|$, only one orientation of the polarization is possible, whereas for $|E| < |E_{\text{crit}}|$, there exist two possible polarization states of the system, one of these being metastable. This is illustrated in Fig. 8.7.1b. Considering in this context the ferroelectric switching we distinguish two cases. The first case, which can be called spinodal switching, corresponds to the switching that happens homogeneously throughout the crystal when the applied field reaches a value of E_{crit} . This situation has never been experimentally documented (except maybe in ultrathin polymer films); we will not address it in our book at all. The second case corresponds to the real experimental situation where the switching takes place at fields that are much smaller than E_{crit} . The typical feature of this situation is that the polarization reversal takes place inhomogeneously via formation of nuclei of reverse domain or formation of macroscopic domains from the remnants of reverse domains left after the previous polarization reversal. Only this situation will be addressed in this book and it is this situation that we mean in using the term “switching”

As was discussed in the preceding sections the process of domain reorientation or switching of a ferroelectric can be separated into several stages. In the case of switching from a single-domain state, one usually distinguishes three stages: (i) the formation of nuclei of reverse domains, (ii) the growth of the nuclei to form through domains, and (iii) the sideways growth of the through domains (see Fig. 8.1.1). Theoretical studies of switching in ferroelectrics have been focused on the first and the third of the aforementioned stages. It was typically assumed that the second stage is very fast and that the polarization variation during this stage does not essentially contribute to the switchable polarization. Though the high (compared to the wall sideways motion) speed of the forward domain growth is supported by theoretical analysis by Molotskii (2003a), the neglect of the second stage of switching does not seem to be generally justified. Clearly that, at a certain high enough rate of the reverse domain nucleation, both the time of the forward domain propagation and the

corresponding contribution to the switching polarization can play an appreciable role in switching. The experimental data presented in the preceding section suggest that this situation is relevant to switching in classical ferroelectric crystals. However, to the best of our knowledge, this situation has not received a proper theoretical treatment. Thus, below in this section we will discuss the switching theories exclusively dealing with the nucleation and sideway wall motion. Such approach requires the following considerations: A treatment of the rate of nucleation of reverse domains, a description of the sideway motion of the domain walls, and a calculation of the volume of reversed part of the crystal, which is not a trivial task because of the overlapping of the growing domains. One of these problems, namely the dynamics of the sideway wall motion, has been treated above in Sect. 8.4. The other two problems, i.e., those related to the nucleation and coalescence of the growing domains, will be considered below in Sects. 8.7.2 and 8.7.3. Based on these results we will address the problem of pulse switching (the polarization response to a step of the applied voltage) in Sect. 8.7.4. On the same basis, a theoretical treatment of the classical polarization hysteresis loops (we mean well-shaped saturated or subsaturated loops) will be offered in Sect. 8.7.5.

The classical situation of the ferroelectric switching covered in Sects. 8.7.2, 8.7.3, 8.7.4, and 8.7.5 is relevant to polarization reversal accompanied by macroscopic displacements of the domain walls. However, there exists a common situation where the amplitude of the driving field is very low and one can come across the so-called Rayleigh hysteresis loops. These loops correspond to a situation where the driving field is not strong enough to initiate the nucleation of reversed domains or/and to induce macroscopical displacements of the domain walls. The hysteretic polarization response observed in this regime corresponds to mesoscopical irreversible displacements of the small areas of the domain walls. A theory for this regime of the polarization response will be addressed in Sect. 8.7.6. Until recently, the classical and the aforementioned “Rayleigh” scenarios seem to cover properly the experimentally observed situation in polarization reversal. However, the recent experimental results on the switching kinetics in ferroelectric thin films have demonstrated an essentially new type of polarization reversal which requires an alternative theoretical approach to the problem. Since the present chapter does not address the behavior of the thin ferroelectric films, the discussion of this approach is postponed to Chap. 9.

One more phenomenon related to the problem of ferroelectric switching will also be addressed in Sect. 8.7.7 where a simple theory of the so-called piezoelectric hysteresis loop will be presented.

The situation of switching in a homogeneous electric field treated in Sects. 8.7.2, 8.7.3, 8.7.4, 8.7.5, 8.7.6, and 8.7.7 is true to the common case of a parallel plate capacitor. In the case of switching driven by the scanning force microscope, whose tip is loaded with electrostatic potential, the applied electric field is strongly inhomogeneous. In Sect. 8.8.8, we will present a theory of domain generation in this situation.

To conclude this introductory section we would like to make some remarks on the scope of this section. It addresses mainly well-developed and widely discussed issues of ferroelectric switching covering the switching between two domain states driven by homogeneous electric field. The problem of switching involving more than two domain state has received little theoretical treatment; however, this kind of switching can make a realistic scenario in perovskite ferroelectric in the vicinity of morphotropic phase boundary. Discussion of this problem can be found in a paper by Ishibashi and Iwata (1999), where an essential reduction of the thermodynamic coercive field is predicted close to the vicinity of morphotropic phase boundary. The results presented in this section have been obtained using classical analytical methods. As for the results of numerical simulation of switching we restrict ourselves to referring the reader to original papers (Ahluwalia and Cao, 2001; Ahluwalia and Cao, 2003; Cao et al., 1999). There is an issue that we have also left out of the scope of our consideration, namely random-system effects on integral switching in ferroelectrics (e.g., $P - E$ hysteresis), though we have briefly addressed random-system effects on domain wall motion in Sect. 8.5. For the case of magnetic hysteresis, the corresponding theoretical analysis is available (see, e.g., Nattermann et al., 2001 and references therein). Some of the results obtained for magnetic hysteresis may be adjusted to the situation in ferroelectrics; however, the corresponding results are still missing in the literature.

8.7.2 Domain Nucleation

The nucleation of new domains in fields much smaller than the thermodynamic coercive field is a key problem of the theory of ferroelectric switching. This problem was first qualitatively addressed by Merz (1956); a further quantitative consideration was offered by Landauer (1957). These considerations were performed on the lines of the standard nucleation theory at the first-order phase transition. In the case of the ferroelectric switching, the new feature is the necessity of taking into account the energy of the depolarizing field in addition to the bulk and surface energy of the nucleus. Following the usual logic of the nucleation problem, the energy, U_c , of the critical nucleus (i.e., the nucleus having the minimal energy from all nuclei which are unstable with respect to further expansion) was calculated and the nucleation rate was evaluated as proportional to the Gibbs factor $\exp(-U_c/kT)$. In its original form, the Landauer theory encounters a serious problem, namely the values of the critical nucleus energy U_c turned out to be unrealistically large ($U_c = 10^8$ kT for BaTiO_3 at room temperature and $E = 0.5$ kV/cm (Landauer, 1957)). Even at much higher applied fields routinely used in ferroelectric thin film capacitors, this energy remains too big to provide realistic nucleation rates ($U_c = 10^3$ kT for PZT film at room temperature and $E = 100$ kV/cm, which makes the Gibbs factor to be $\exp(-U_c/kT) \cong 10^{-430}$ (Tagantsev, 1996). All these estimates have

been obtained for the case of the nucleation in an ideal insulating crystal, i.e., for the nucleation that is not assisted by the presence of defects or free carriers in the material. Since the switching from the single-domain states always experimentally takes place at fields essentially smaller than the thermodynamic coercive field, it was commonly assumed that, in real crystals, the nucleation of new domains is always defect assisted. For the first time this kind of nucleation scenario was theoretically addressed by Janovec (1959) who modeled nucleation stimulated by the space charge field at the ferroelectric/electrode interface. Revision of the Landauer theory on the lines of defect-stimulated nucleation has been recently undertaken by Molotskii et al. (2000) and Gerra et al. (2005). Molotskii and his coworkers have shown that formation of a Landauer nucleus simultaneously with an electron droplet may be energetically favorable; however, the results of the papers cannot be reliably translated into an estimate for the nucleation rate. Gerra and his coworkers revisited the interface-stimulated scenario by Janovec; the Landauer model has been generalized by incorporation of the energy of the ferroelectric/electrode interface, which is dependent on the sign of the polarization at this interface. The latter model has been found to provide a realistic description of reverse domain nucleation.

Below in this section, we will present the Landauer model and its version modified by the incorporation of polarization-dependent surface term (Gerra et al., 2005).

Landauer (1957) has treated a nucleus of reversed domain having the form of a half prolate spheroid of radius r and length l terminating on one electrode (Fig. 8.7.2). Its energy (actually thermodynamic potential in a capacitor kept under a fixed voltage) can be written as⁸

$$U = -ar^2 l + brl + c \frac{r^4}{l}; \quad (8.7.1)$$

$$a = \frac{4\pi P_S E}{3}, \quad b = \frac{\pi^2 \sigma_w}{2}, \quad c = \frac{4\pi P_S^2}{3\kappa_a \epsilon_0} \left(\ln \left(\frac{2l}{r} \sqrt{\frac{\kappa_a}{\kappa_c}} \right) - 1 \right). \quad (8.7.2)$$

Here σ_w , κ_c , and κ_a are the surface energy of 180° wall and the relative lattice dielectric constants in the direction of the spontaneous polarization and

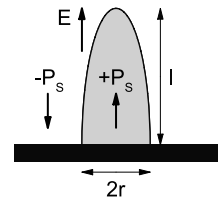


Fig. 8.7.2 Nucleus of reverse domain in the Landauer model. Electrode is shown as black rectangular

⁸ The following expression for c is written for the case where the argument of the logarithmic function is much greater than unity, which is usually the case for this problem.

perpendicular to this direction, respectively. The parameters r and l of the critical nucleus, r_L and l_L , and its energy U_L were routinely determined from minimization of U . The condition $\partial U/\partial l = 0$ yields that U has a global minimum with respect to l at

$$l = \sqrt{\frac{cr^3}{b-ar}}. \quad (8.7.3)$$

This result together with condition $\partial U/\partial r = 0$ gives

$$r_L = 5A/6, \quad l_L = r_L \sqrt{5c/a}, \quad U_L = 0.4ar_L^2 l_L, \quad (8.7.4)$$

where $A = b/a$. Using these expressions one readily arrives at the above estimates for the energy of the critical nucleus, which are typically by orders of magnitude exceeding the thermal energy. For instance, the above estimate for a (PbZr_xTi_{1-x}O₃) PZT film at $E = 100$ kV/cm can be obtained when setting $P_S = 30 \mu\text{C/cm}^2$, $\sigma_w = 0.01 \text{ J/m}^2$, and $\epsilon_a = \epsilon_c = 200$.

The activation energy of nucleation can be essentially reduced by assuming that energy of the ferroelectric/electrode interface is substantially dependent on the sign of the polarization pointing to the electrode. This asymmetry can be due to electronic or mechanical properties of the interface and/or the presence of impurities or dislocations. This ferroelectric/electrode coupling can be related to an interface energy density γ that changes its sign according to the polarization direction. In the simplest case, it will be linear in the polarization P_S : $\gamma = \zeta P_S$ where ζ plays the role of a surface field conjugate to the order parameter P_S . One incorporates this phenomenon into Landauer model by adding a new term

$$U_{\text{sur}} = dr^2, \quad d = \gamma\pi \quad (8.7.5)$$

to the energy given by Eq. (8.7.1). With this term taken into account, the energy of the nucleolus as a function of its normalized radius $x = r/r_L$ has the form (Gerra et al., 2005)

$$\frac{U(x)}{U_L} = \sqrt{6}x^2 \left[\sqrt{x \left(1 - \frac{5}{6}x\right)} - \sqrt{\frac{5}{6}}\sqrt{AD} \right], \quad D \equiv \frac{d}{2\sqrt{bc}}. \quad (8.7.6)$$

Figure 8.7.2 shows a plot of $U(x)$ for different values of the parameter \sqrt{AD} . In the original Landauer model, where $D = 0$, we have a local minimum at $r = l = 0$ and a saddle point at $r = r_L$. For nonzero values of D , the point $x = 0$ becomes unstable, the local minimum U_{min} is shifted to the right and the local maximum U_{max} —to the left, while the activation energy, $\Delta U = U_{\text{max}} - U_{\text{min}}$ is decreased. Here, $U_{\text{min}} = U(x_{\text{min}})$ and $U_{\text{max}} = U(x_{\text{max}})$, where x_{min} and x_{max} are the positive roots of the following equation:

$$\frac{5\sqrt{5x}(1-x)}{4\sqrt{6-5x}} = \sqrt{AD}. \quad (8.7.7)$$

When the parameter \sqrt{AD} exceeds its critical value, $(\sqrt{AD})_c \approx 0.553$, Eq. (8.7.7) has no positive roots and the activation barrier disappears (Fig. 8.7.3c and d). Unlike the classical Landauer model, we arrive at the situation where at applied fields corresponding to the condition $\sqrt{AD} > (\sqrt{AD})_c$ the nucleation barrier is completely suppressed.

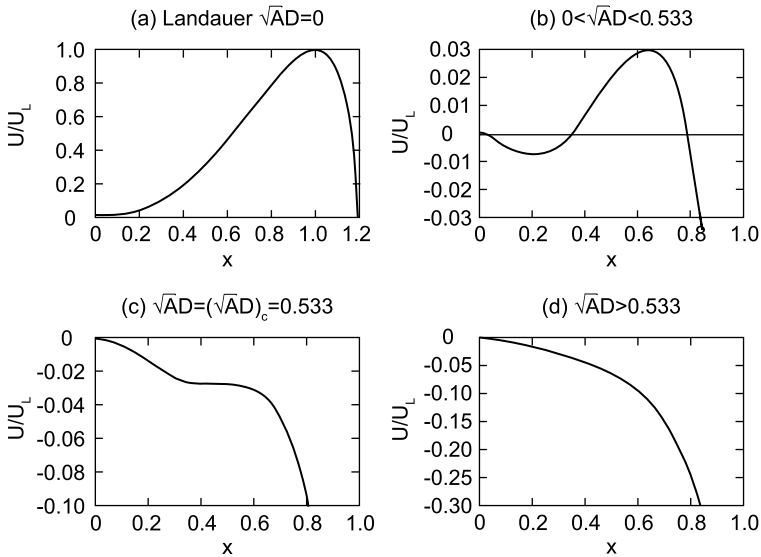


Fig. 8.7.3 The effect of parameter \sqrt{AD} on the dependence of energy of the nucleus (normalized to the Landauer activation energy U_L) on its radius (normalized to the radius of the Landauer nucleus r_L)

It is instructive to express \sqrt{AD} in terms of the anisotropy factor $\eta = \kappa_a/\kappa_c$ and the thermodynamic coercive field $E_{crit} = P_S/(3\sqrt{3}\kappa_c\epsilon_0)$ introduced by Eq. (2.3.15)⁹

$$\sqrt{AD} = k \frac{\gamma}{\sigma_w} \sqrt{\eta \frac{E}{E_{crit}}}, \quad k \approx 0.04. \tag{8.7.8}$$

Figure 8.7.4 shows a plot of the activation energy $\Delta U = U_{max} - U_{min}$ as a function of the physical quantities appearing in Eq. (8.7.8). It is evident that as well as by the external electric field, nucleation is favored by high values of the ratio γ/σ and the anisotropy factor η . The latter less evident effect is related to a reduction of the electrostatic energy which is inversely

⁹ One should note that this type of thermodynamic coercive field may not be the real thermodynamic coercive field of the system if more than two antiparallel domain states are involved in switching (see the paper by Ishibashi and Iwata, 1999).

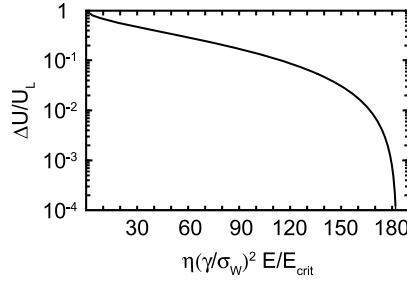


Fig. 8.7.4 Nucleation barrier ΔU (normalized to the Landauer activation energy U_L) as a function of the dielectric anisotropy factor $\eta = \kappa_a/\kappa_c$, the applied electric field E , and the ratio between the energy of polarization/electrode coupling (per unit area) γ and the surface tension of the domain wall σ_w

proportional to the transverse permittivity κ_a (cf. Eq. (8.7.2)). From condition $\sqrt{AD} > (\sqrt{AD})_c$ and Eq. (8.7.8) one obtains the applied field needed for total suppression of the nucleation barrier, which we will call *zero-temperature critical field* $E_c^{T=0}$:

$$\frac{E_c^{T=0}}{E_{\text{crit}}} \approx \frac{183}{\eta} \left(\frac{\sigma_w}{\gamma} \right)^2. \quad (8.7.9)$$

In Fig. 8.7.4, we note that the nucleation barrier drops to zero abruptly as the applied field approaches $E_c^{T=0}$. For fields less than 70% of the critical value, $\Delta U \geq 0.1 U_L$, implying, for typical values of the relevant parameters, unrealistically low nucleation rates. This means that, in the modified model, the finite-temperature critical field is within 30% of $E_c^{T=0}$. Moreover, if the nucleation is the limiting factor of switching, then the coercive field of hysteresis loops is close to this finite-temperature critical field and thus only moderately, non-exponentially temperature dependent (through the temperature dependence of the parameters of the material).

Two more features following from the above analysis are worth mentioning. First, the nucleation has been found to be favored by a high value of the anisotropy factor η . This implies that the switching can be facilitated in perovskite-type ferroelectrics near morphotropic phase boundaries, where this factor is anomalously high. This prediction may be relevant to the coercive field reduction in PZT at the tetragonal side of the morphotropic phase boundary reported by Yamamoto (1996). Second, the model readily provides an exponentially wide spectrum of waiting times for nucleation. It is clear from Fig. 8.7.4 that, in the steep part of the curve (corresponding to a realistic thermally activated regime), small variations of the system parameters readily lead to orders-of-magnitude variations of the activation barrier, on which the waiting time is exponentially dependent. This result is important in the context

of the data on the switching kinetics in ferroelectric thin films, which have been interpreted in terms of this kind of spectrum. We will discuss this problem below in Sect. 9.5.1.

For the moment, the absence of experimental data and result of first principal calculations of the energy of the ferroelectric/electrode interface make difficult quantitative estimates for the strength of the effects discussed above. However, according to Gerra et al. (2005), the rough order-of-magnitude estimates suggest that the ferroelectric/electrode interaction can significantly facilitate the switching. Based on the Landau theory result for the wall energy $\sigma_w = t_w P_S E_{\text{crit}} \sqrt{3}/2$ (see Eq. (6.2.10c)) where t_w is the wall thickness and the so-called “atomic” estimate for the effective surface field $\zeta \cong E_{\text{at}} l_{\text{at}}$ where $E_{\text{at}} \cong 100$ MV/cm is a typical atomic electric field and l_{at} is the lattice constant, one gets $\sigma_w/\gamma = \sigma_w/(P_S \zeta) \cong (E_{\text{crit}}/E_{\text{at}})(t_w/l_{\text{at}})$. Bearing in mind parameters of perovskite ferroelectrics like BaTiO₃ we find that the ratio σ_w/γ may be as small as 10^{-2} . Thus, according to Eq. (8.7.9), the model can yield a coercive field two orders of magnitude smaller than E_{crit} . For a numerical estimate, taking room temperature parameters of BaTiO₃ ($P_s = 26$ $\mu\text{C}/\text{cm}^2$, $\kappa_a = 2000$, $\kappa_c = 120$, and $\sigma_w \cong 7 \times 10^{-7}$ J/cm²) and $\sigma_w/\gamma = 0.02$ one obtains $E_c^{T=0} \cong 2$ kV/cm. These estimates show that the model may provide reduction of the coercive field down to the values typical for BaTiO₃ single crystals (about 1 kV/cm).

The above model has considered a situation where the surface field ζ is homogeneous in sign, which may not be a realistic situation. From Eq. (8.7.3), we see that unrestricted growth of the nucleus is possible only when $r \rightarrow r^* \equiv b/a$. So if the average linear size of the regions where ζ is homogeneous, r_0 , is larger than r^* , nucleation will not be affected by the variations of ζ . On the other hand, when $r_0 < r^*$, fluctuations in the sign of ζ will result in opposite contributions to the energy, i.e., different parts of the interface support different orientations of the polarization. The latter situation requires a more involved consideration. The case of small-scale inhomogeneity of ζ where $r_0 \ll r^*$ has been treated by Gerra et al. (2005) on the lines of the statistical approach of Imry and Ma (1975). Results similar to presented above have been obtained, however, with higher values of the zero-temperature critical field.

At this point it is instructive to compare the nucleation problem treated in terms of original Landauer model with the problem which one encounters when treating the thermally activated sideways motion of a 180° domain wall (see Sect. 8.4.2). In both cases the parameters of the critical nucleus are determined from finding extremum of the expressions for nucleus energy, which have an identical structure, specifically, consisting of the bulk and surface contributions and that of the depolarizing field (cf. Eqs. (8.7.1) and (8.4.7)). However, the comparison of the above results to those of the Sect. (8.4.2) reveals for the same material a few-order-of-magnitude difference between the evaluated critical nucleus energies in these two situations. This difference can be readily understood. In the case of the nucleation of a new domain, a new interface boundary is formed, whereas in the case of the wall motion, an existing interface boundary just deforms to make the nucleus needed for a displacement of the wall to the

next minimum of the Peierls potential. A much smaller surface energy is typical for the nuclei in the latter case. The difference in the depolarizing energy for these two cases also contributes to the total difference in the critical nucleus energies. However, as was pointed out by Molotskii et al. (2000) this is an effect of the secondary importance compared to the problem with excessive surface energy. The above arguments also rationalize the reduction of the nucleation energy in the modified Landauer model, where the excessive energy of the newly formed interface is compensated by a decrease in the ferroelectric/electrode energy. In this context, a paper by Kukushkin and Osipov (2002) is worth mentioning. In this paper, an exhaustive analysis of the kinetics of the “phase transformation” corresponding to the switching in a uniaxial ferroelectric is offered; however, the results and conclusions of the paper turn out to be inapplicable to the real situation in ferroelectrics because of the authors’ neglect of the aforementioned excessive interface and depolarizing energy.

Concluding the discussion of reverse domain nucleation, an important general note is to be made. The introduction of the defect energy into the consideration not only makes it possible to reduce the nucleation energy but also introduces a nucleation mechanism which does not freeze out at $T \rightarrow 0$. Thus in this case one can speak about *cold-field nucleation*, where the nucleation barrier is fully suppressed by the applied electric field, in contrast to *thermally activated nucleation*, where thermal fluctuations assist in overcoming this barrier. These situations also differ in the moment for the appearance of the nuclei. If the cold-field nucleation dominates the polarization reversal, then the nucleation is not delayed in time after the variation of the applied field. For pulse switching, for example, this means that all nuclei will form at the moment of the pulse application. At the same time, in the thermally activated regime, the nucleation is delayed leading, in general, to more complicated switching dynamics. We will be back to this point in Sect. 8.7.4.

8.7.3 Domain Coalescence

The knowledge on the nucleation rate of reverse domains combined with that on the applied-field-driven motion of ferroelectric domain walls can be used for calculations of the switched polarization P_{sw} . In the general case, it is a complicated problem that comprises taking into account three factors: the impact of the evolving domain pattern on the polarization in the domains, the interaction between domains, and overlapping of growing domains. The first two issues are very difficult for treatment so that, by now, they have not been actually addressed theoretically. In contrast, overlapping of domains can readily be described by a theory. This theory makes the subject of this section where we address it for the case of 180° switching.

Consider switching from a single-domain state, which starts with nucleation of reversed domains from randomly distributed nucleation sites followed by the

further domain growth. At the early stages of switching where the overlapping of growing domains is negligible, the switched polarization can be obviously found as

$$P_{sw} = \Delta P \frac{V_{tot}}{V_0} = \Delta P \frac{S_{tot}}{S_0}, \quad (8.7.10)$$

where ΔP is the difference between the polarization of the final and initial states of the system, V_0 is the volume of the sample, and V_{tot} is the sum of the volumes of the newly appeared domains.¹⁰ The last equality of Eq. (8.7.10) is written for the situation where the switching in a plate capacitor is controlled by the sideways motion of 180° domain walls passing throughout the thickness of the capacitor; here S_0 and S_{tot} stand for the intersection of the volumes V_0 and V_{tot} with the ferroelectric/electrode interface. This is actually the situation to which the present theory can be primarily applied since, in this case, the electrostatic coupling between the domains is absent so that the geometrical effect of the domain coalescence taken into account by the theory dominates the phenomenon. Equation (8.7.10) starts to fail as far as the overlapping among the domains becomes essential. This happens once S_{tot} becomes comparable to S_0 . This is illustrated in Fig. 8.7.5. Here the sum of the areas of the circles gives S_{tot} whereas the switched polarization is controlled by the area covered by the totality of the circles S so that the normalized switched polarization $q(t) = P_{sw}/\Delta P$ can be written as

$$q(t) = \frac{S}{S_0}. \quad (8.7.11)$$

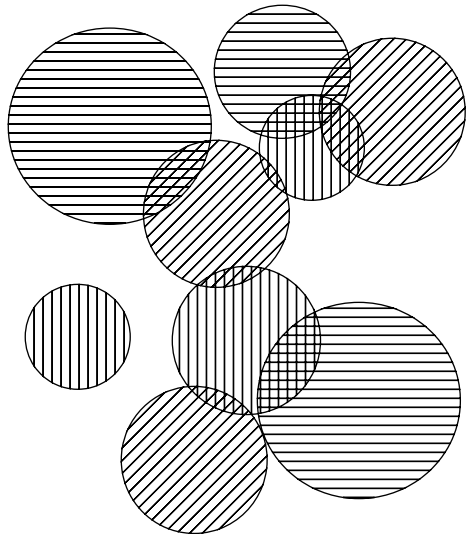


Fig. 8.7.5 Illustration of overlap of domains growing from different nuclei

¹⁰ When discussing the switching phenomena in this and the two following sections we will focus on the domain contribution to the switched polarization neglecting the lattice contribution to it. If needed, the latter can be taken into account by adding a proper term.

The calculation of S makes a mathematical problem, which, in the case of random distribution of big number of the nuclei, can be exactly solved. An exact solution of this problem has been offered by Kolmogorov (1937) and Avrami (1940). They have shown that, in this case, S , S_{tot} , and S_0 are linked by a simple relation

$$S = S_0(1 - \exp(-S_{\text{tot}}/S_0)). \quad (8.7.12)$$

This equation, which we call Kolmogorov–Avrami theorem, is valid for the problem of overlapping coverage of space of an arbitrary dimension. For example, in the three-dimensional case, this relation can be evidently rewritten in terms of V_0 and V_{tot} .

Let us derive Eq. (8.7.12) following the idea by Kolmogorov (1937). The variable proper for calculations is not S but $1 - S/S_0$. For a random coverage of the surface with circles, it has the mathematical meaning of probability p_{non} that a given point was not covered by any of the circles. Indeed, the uncovered area can be found as $p_{\text{non}}S_0$ which makes $S - S_0$. On the other hand, the probability that a point is not covered by any of the N circles equals the product of the probabilities that the point is not covered by each circle, $1 - S_i/S_0$, where S_i is the area of the i th circle. Thus, we have

$$1 - S/S_0 = (1 - S_1/S_0)(1 - S_2/S_0)(1 - S_3/S_0)(1 - S_4/S_0)\dots(1 - S_N/S_0). \quad (8.7.13)$$

Taking the logarithm of Eq. (8.7.13) we arrive at the following relation:

$$\ln(1 - S/S_0) = \sum_i \ln(1 - S_i/S_0) \approx - \sum_i S_i/S_0 = -S_{\text{tot}}/S_0, \quad (8.7.14)$$

which readily leads us to Eq. (8.7.12).

It is seen that the above calculations are justified on the assumption that $S_i/S_0 \ll 1$, i.e., the area of each circle is small compared to S_0 . Applying formula (8.7.12) to the problem of the coalescence of growing domains in a finite sample, we will inevitable violate this condition at the final stage of switching once $S_i \cong S_0$. However, if the number of nucleolus in the sample N_n is large, this stage corresponds to an exponentially small non-switched area (according to Eq. (8.7.12) it can be evaluated as $S_0 \exp(-N_n)$). Thus, being interested in measurable amounts of switching polarization, the use of the Kolmogorov–Avrami theorem is justified as far as the number of nuclei in the sample is large.

8.7.4 Pulse Switching

The theoretical analysis of the ferroelectric switching in crystals has been mostly performed for the case of the 180° switching, which involves reorientation of nonferroelastic domains. In this case, only two orientations of the spontaneous polarization are considered and the elastic aspect of the problem can be

legitimately ignored. In the present section we consider this situation, addressing the switching caused by an abrupt application of a step of electric field to a ferroelectric originally poled in the direction antiparallel to the field. The application of the field will result in formation of supercritical nuclei which give rise to expanding macroscopic domains of reverse polarization, in brief reverse domains. Affected by the depolarization effect the supercritical nuclei are elongated in the direction of the spontaneous polarization. As mentioned above in this section, the first stage of their growth is their fast expansion along the direction of the spontaneous polarization to form the through domains. In theories of switching (e.g., Fatuzzo, 1962; Ishibashi and Takagi, 1971), the time taken by this stage is typically neglected. We will neglect it as well and comment a possible impact of this neglect later in this section. Thus, in the adopted model, the description of the polarization reversal is reduced to the growth and coalescence of the appeared through domains. This kind of theory for the ferroelectric switching was first developed by Fatuzzo (1962) and further generalized by Ishibashi and Takagi (1971). The following presentation is mainly based on the work by Fatuzzo.

Let us address this problem basing on the results of Sects. 8.7.2 and 8.7.3, starting from the case of *cold-field nucleation*. In this case, the moment the field is applied all seeds which become critical at this value of the field yield supercritical nuclei which, in turn, instantly provide the initial through domains. In the considered nucleation regime no new supercritical nuclei and through domains will later appear in the system. According to Eq. (8.7.12) the calculation of the switched volume of the sample requires the knowledge of the bare sum of the areas of the reverse domains, S_{tot} . Assuming the circular shape of the initial and growing domains (the latter also implies that the velocity of the sideway motion of the domain wall v is isotropic in the plane of the domain growth), the area S_{tot} evidently reads

$$S_{\text{tot}} = N\pi(r_0 + vt)^2, \quad (8.7.15)$$

where N and r_0 are the number and the radius of the initial through domains, respectively. Though N , v , and r_0 are, in general, field dependent, for the case of pulse switching these can be considered as constants. Equations (8.7.11), (8.7.12), and (8.7.15) lead us to the expression for the time dependence for the normalized switched polarization

$$q(t) = 1 - \exp\left[-\left(\frac{t_0 + t}{t_{\text{col}}}\right)^2\right], \quad (8.7.16)$$

where

$$t_0 = \frac{r_0}{v} \quad \text{and} \quad t_{\text{col}} = \frac{1}{v\sqrt{\pi n_0}}. \quad (8.7.17)$$

and $n_0 = N/S_0$ is the density of the critical seed in the sample. Following Kolmogorov, the above discussed regime is sometimes called “ β -model”.

In the case of *thermally activated nucleation*, the calculation can be performed on the same lines. The difference is that since now the nucleation occurs with a certain probability all the time, the calculation of S_{tot} requires the summation of the areas of circles of different sizes existing at the given moments, i.e.,

$$S_{\text{tot}} = \pi \sum_i [r_0 + v(t - \tau_i)]^2, \quad (8.7.18)$$

where τ_i stands for the nucleation time of the i th through domain. For the considered situation where the number of appearing domains is big, one can pass in Eq. (8.7.18) from the summation over the domains to the integration over the nucleation time (via introduction the nucleation rate per unit volume in the sample $R(t) = S_0^{-1}dN/dt$) to get

$$S_{\text{tot}} = S_0 \pi \int_0^t R(\tau) [r_0 + v(t - \tau)]^2 d\tau. \quad (8.7.19)$$

If the reservoir of the seeds is not substantially exhausted during the observation time of the switching, the nucleation rate can be reasonably assumed to be constant: $R(t) = R_0$. Following Kolmogorov, the regime with the constant nucleation rate is sometimes called “ α -model.” In this regime, calculations can readily lead us to the following expression for the time dependence for the normalized switched polarization:

$$q(t) = 1 - \exp \left[-\frac{(t_0 + t)^3 - t_0^3}{t_{\text{act}}^3} \right], \quad (8.7.20)$$

where

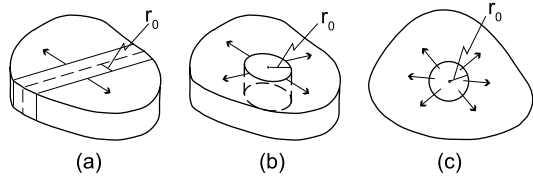
$$t_{\text{act}} = \sqrt{\frac{3}{\pi R_0 v^2}}. \quad (8.7.21)$$

Equations (8.7.20) and (8.7.16) can be readily generalized from the case of n -dimensional switching (Ishibashi and Takagi, 1971), which are illustrated in Fig. 8.7.6. The one-dimensional situation may be of interest for ferroelectrics corresponding to the switching via formation of a random lamella pattern. However, the three-dimensional case is not relevant to the ferroelectric switching, at least in the simple isotropic growth version currently considered. The n -dimensional generalizations of these equations read

$$q(t) = 1 - \exp \left[-\left(\frac{t_0 + t}{t_{\text{col}}} \right)^n \right], \quad (8.7.22)$$

$$q(t) = 1 - \exp \left[-\frac{(t_0 + t)^{n+1} - t_0^{n+1}}{t_{\text{act}}^{n+1}} \right], \quad (8.7.23)$$

Fig. 8.7.6 Schematic drawing of n -dimensional isotropic domain growth: (a) $n = 1$, (b) $n = 2$, and (c) $n = 3$



where the parameters now are also functions of n (see Ishibashi and Takagi (1971) for the explicit expressions). Essential feature of the generalized model is that the parameters that govern the speed of switching, t_{col} and t_{act} , are always decreasing functions of the wall velocity: $t_{\text{col}} \propto v^{-1}$ and $t_{\text{act}} \propto v^{-(n-1)/n}$.

In the situation where taking into account the initial areas of the growing through domains is of minor importance for the switching dynamics, i.e., when $t_{\text{col}}, t_{\text{act}} \gg t_0$, all the above results can be covered by a unified relation that reads

$$q(t) \approx 1 - \exp \left[- \left(\frac{t}{t_{\text{sw}}} \right)^k \right], \quad (8.7.24)$$

where the exponent k can acquire the integer values from 1 to 4 depending on the dimensionality of the domain growth and the scenario of nucleation. The effect of value of the exponent k on the switching dynamics is illustrated in Fig. 8.7.7a. It is seen that, qualitatively, this effect is not strong. An important feature of the unified relation (8.7.24) is illustrated in Fig. 8.7.7b. Namely, in the semi-logarithmic scale, any variation of the time parameter t_{sw} shifts only the plot q vs. $\log t$ along the $\log t$ axis but does not change its form. This is a characteristic feature of the Kolmogorov–Avrami switching dynamics in this regime. This feature can be used for the identification of this type of switching dynamics in real systems, e.g., in semi-logarithmic plots the switching curves taken at different applied fields should differ only in the time offset but not in the shape. An example of such behavior in a crystal of TGFB is shown in Fig. 8.7.8.

The switching behavior of the considered models for the case where taking into account the initial areas of the reversed domains is essential, i.e., $t_{\text{col}}, t_{\text{act}} \cong t_0$ or $t_{\text{col}}, t_{\text{act}} < t_0$ is illustrated in Fig. 8.7.7c and d. It is seen from this figure that now, in the case of cold-field nucleation scenario, the model describe a special case of two-stage polarization reversal¹¹ (Fig. 8.7.7c). This means a switching current profile with two maxima; the existence of such kind of profile was disputed for KDP crystals (see Sect. 8.6.4). In the case of the activation nucleation scenario (Fig. 8.7.7d), an increase in the size of the initial domains (effectively an increase in t_0)

¹¹ Formally, in this situation, the first stage of the switching occurs infinitely fast. The finite rate of the polarization reversal at this stage is evidently controlled by the time taken by the through growth of the nuclei, which was neglected in the theory.

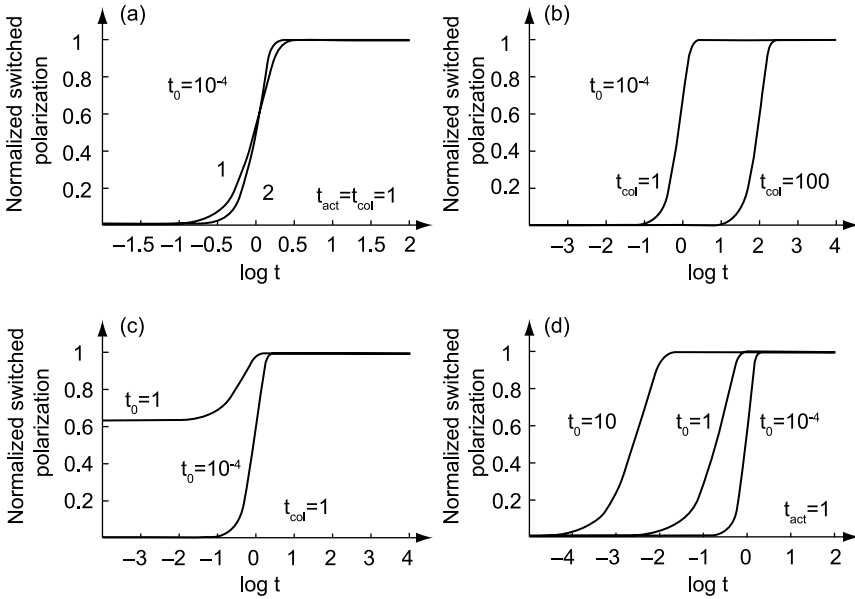


Fig. 8.7.7 Kinetics of pulse switching in α - and β -models for the isotropic two-dimensional domain growth according to Eqs. (8.7.20) and (8.7.16), respectively. (a) Curve 1 corresponds to β -model, curve 2 corresponds to α -model; the curves are very close to those obtained from Eq. (8.7.24) with $k = 2$ and 3, respectively. (b) The results of β -model for two values of parameter t_{col} ; the curves are very close to those obtained Eq. (8.7.24) with two, 100 times different, values of parameter t_{SW} . (c) The results of β -model for two values of parameter t_0 . (d) The results of α -model for three values of parameter t_{col} . The values of all parameters are indicated in the figures

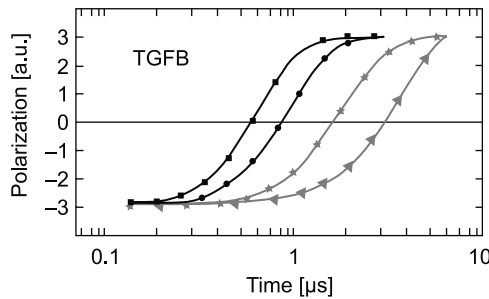


Fig. 8.7.8 Kinetics of pulse switching in TGFB crystals for four values of the applied field. The higher the field, the larger the shift of the switching curves to the left. Reprinted with permission from Lohse et al. (2001). Copyright (2001), American Institute of Physics

can result in an essential acceleration of switching, however, with a lower logarithmic slope in the transitory interval of time. In the limit $t \ll t_0$, this behavior is close to that given by Eq. (8.7.24) with $k = 1$, as can be concluded from Eq. (8.7.20).

One should mention that the α - and β -models by no means cover possible switching kinetics controlled by domain coalescence. In reality, these models are the limiting cases. As realistic “intermediate” case, one can consider a situation where there exists a typical activation energy for the nucleation and therefore a typical waiting time for nucleation τ_0 can be introduced. As a simple function of modeling the nucleation rate in this case we set

$$R(t) = \frac{n_0}{\tau_0} \exp\left[-\frac{t}{\tau_0}\right]. \quad (8.7.25)$$

In the case of two-dimensional domain growth with the negligible initial size of the nucleus, such nucleation rate leads (via Eq. (8.7.19) with $r_0 = 0$) to the following expression for the normalized switching polarization (Fatuzzo, 1962):

$$q(t) = 1 - \exp\left[-\left(\frac{\tau_0}{t_{\text{col}}}\right)^2 2\left(\frac{m^2}{2} - m + 1 - e^{-m}\right)\right], \quad (8.7.26)$$

where $m = t/\tau_0$. It is seen that this expression describes a crossover between the α -model at $t < \tau_0$ to the β -model at $t > \tau_0$. One readily checks that, for the domain growth of other dimensions, the nucleation rate Eq. (8.7.25) leads to a similar “ $\alpha - \beta$ ” crossover.

Thus, we see that switching kinetics, controlled by the domain coalescence and treated using the Kolmogorov–Avrami approach, results in an exponential time dependence of the normalized switching polarization. In some limiting cases, it is the “pure” dependence with a unique k given by Eq. (8.7.24). However, taking into account more realistic features of the phenomenon results in a crossover behavior corresponding to different values of the exponent k for the beginning and end stages of the switching. Remarkably the crossover due to the finite area of the nucleus (see Eqs. (8.7.22) and (8.7.23)) manifests itself in an increase in k with the time, whereas for the crossover related to the proper description of the nucleation rate (see Eq. (8.7.26)), an opposite behavior of this exponent is expected. To complete the crossover issue, one can mention the crossover with a reduction of k with time for the α -model in granular ferroelectrics, where domain walls are not allowed to cross the grain boundaries (Duiker and Beale, 1990).

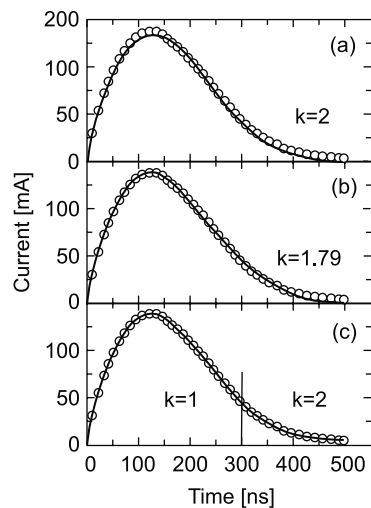
When applying that above result to the description of the switching kinetics in real system one should bear in mind that all above expressions are dealing with the domain contribution to the switching polarization. The total polarization P_{sw} switched by a voltage step should be calculated taking into account the lattice contribution to the polarization P_{lat} as well. Thus the following relation should be used

$$P_{\text{sw}} = \Delta P q(t) + P_{\text{lat}}, \quad (8.7.27)$$

where P_{lat} is time independent and can be found from the equation of state of the ferroelectric, e.g., Eq. (2.3.6).

The theoretical results for the switched polarization presented in this section enable the calculation of the switching current. There are many examples where the time dependences of the switching current calculated in this way are in qualitative agreement with the experimental data in ferroelectrics. An example of such agreement is illustrated in Fig. 8.7.9a. However, the quantitative description of the profiles of the switching currents does not seem to be usually possible in terms of appealingly universal relation (8.7.24) whereas the aforementioned crossover regimes have not been addressed, at least in the numerous recent studies. To reach a better quantitative description of the experimental data, a further modification of the classical approach was done. First, non-integer values of the k -parameter in relation (8.7.24) were used when fitting the experimental data (Usher et al., 1990). Second, a change of the dimensionality of the domain growth during switching was assumed. Accordingly, different parts of the experimental curve were fitted to relation (8.7.24) with different values of the k -parameter. Examples of such fit are shown in Fig. 8.7.9b and c. A better quality of the fits is seen, which however is obtained at the price of the additional fitting parameter(s). It should be mentioned that the physical interpretation of the modified models does not seem to be clear. For instance, the origin of fractional dimensionality of switching is not clear. As for the change of the dimensionality of the domain growth during switching, its justification is not always evident. For example, according to Shur and coworkers (Shur et al., 1998) it can occur when the typical scale of the domain pattern *increases* to reach the typical distance between the objects limiting free domain growth, e.g., the grain size. The fit shown in Fig. 8.7.9c was justified by these authors on the lines of this approach applied to the case of elongated grains. This justification can be questioned bearing in mind that the decreasing part of the curve, where the presumed crossover is indicated, corresponds to *decrease* in the

Fig. 8.7.9 Different fits of the same time dependence of the switching current in a PZT thin film. (a) Fit to Eq. (8.7.24) with $k = 2$, (b) fit to Eq. (8.7.24) with $k = 1.79$, (c) fit to a crossover formula corresponding to $k = 2$ for the first part of the curve and to $k = 1$ for its tail. Reprinted with permission from Shur et al. (1998). Copyright (1998), American Institute of Physics



typical scale of the domain pattern (i.e., the average diameter of non-switched areas) not to its increase.

The above reviewed theory of the pulse switching based on the Kolmogorov–Avrami approach also enables a modeling of the electric field and temperature dependences of the switched polarization and switching current (once one uses the theoretical results on the field and temperature dependences of velocity of the wall sideways motion (see Sect. 8.4)). However, one should mention that this modeling is severely limited by the lack of information on the field and temperature dependences of the density of the critical seeds and nucleation rate entering the basic relations of the theory.

8.7.5 Classical Polarization Hysteresis Loops

In the previous section, we have addressed a Kolmogorov–Avrami approach-based description of polarization pulse switching. This approach can equally be applied to the description of switching driven by a periodical electric field, the case where the polarization plotted as a function of the field traces a hysteresis loop. In principle, such loop can be obtained using thermodynamic theory as was discussed in Sect. 2.3.1 (see Fig. 2.3.2). However, the loop predicted by thermodynamic theory (“thermodynamic hysteresis loop”) is not relevant to those observed in real ferroelectrics (possibly except for some special situation in ultrathin ferroelectric films) because switching always starts at fields much smaller than the thermodynamic coercive field. A principal difference between the physical situations behind the thermodynamic hysteresis loop and a real $P-E$ hysteresis loop is that the former is controlled by a distinct threshold field whereas behind the latter there may be no threshold field. At the same time, a real ferroelectric loop (with the coercive field orders-of-magnitudes smaller than the thermodynamic coercive field) can be extremely “square” (see Sect. 8.6), creating appearance of threshold-controlled switching. Below in this section we will demonstrate how Kolmogorov–Avrami approach-based models, being “threshold free,” can yield quite square hysteresis loops. At the end of this section we will also make remarks on the problem of ferroelectric hysteresis loops in view of the modern theory of hysteresis phenomena.

We will start with the model developed by Janta (1970, 1971) who addressed the cases of the two- and one-dimensional domain growth yielding similar qualitative picture of the phenomenon. Below we present the results obtained for the case of the two-dimensional domain growth. The basic assumption of the model is that, even in the nominally fully poled state, the ferroelectric contains a certain amount of small remnants of the inverse domains which (after the application of the switching electric field) give rise to larger domains just as a result of their growth without any threshold to be exceeded by the applied field. In Janta’s model with the two-dimensional domain growth, the case of the in-plane isotropic domain growth is considered and the remnants are supposed to have the forms of circular cylinders

(through domains) of the same radius r_r , which are randomly distributed with the density n_r (per unit area). Thus, at the early stages of the evolution from a poled state, the domain pattern represents a system of circular cylinders parallel to the direction of the applied field. Mathematically this situation is similar to the β -model treated in the previous section. The difference is that now the wall velocity is time dependent. For the switching from a state with the aforementioned domain remnants, Eq. (8.7.15) can be rewritten as

$$\frac{S_{\text{tot}}}{S_0} = n_r \pi \left(r_r + \int_0^t v[E(t')] dt' \right)^2. \quad (8.7.28)$$

In the case of periodical $E(t)$, this equation holds from a moment when $E = 0$ through the next moment where the field equals zero again, i.e., from the negative to the positive remanence. Setting $E(t) = E_m \sin \omega t$ and $v(E) = v_\infty \exp(-\delta/E)$ (cf. Eq. (8.3.5)) and using Eqs. (8.7.10), (8.7.11) and (8.7.12) we obtain for the “domain part” of the normalized polarization P/P_S

$$\frac{P(\varphi)}{P_S} = 1 - 2 \exp \left[- \left(\theta + \gamma \int_0^\varphi \exp \left(- \frac{1}{\beta_0 \sin \varphi'} \right) d\varphi' \right)^2 \right], \quad (8.7.29)$$

where $\beta = E_m/\delta$ is the normalized amplitude of the driving field and $\gamma = v_\infty (\pi n_r)^{1/2} / \omega$ is the normalized period of this field. Here, parameter $\theta = r_r (\pi n_r)^{1/2}$ controls the degree of poling of the ferroelectric at remanence. It can be determined from the condition

$$P(0) = -P(\pi), \quad (8.7.30)$$

reflecting the symmetry of the loop, which can be rewritten as

$$\exp \left[- \left(\theta + \gamma \int_0^\pi \exp \left(- \frac{1}{\beta_0 \sin \varphi'} \right) d\varphi' \right)^2 \right] + \exp[-\theta^2] = 1. \quad (8.7.31)$$

The polarization loops derived by using Eqs. (8.7.29) and (8.7.30) are presented in Fig. 8.7.10. According to Janta (1970) the shape of these loops as well as their evolution caused by variations of the amplitude and frequency of the driving field are in a good qualitative agreement with experimental data on BaTiO₃ and TGS crystals (see Sects. 8.6).

In the limit of strongly saturated loops where $\theta \ll 1$, neglecting θ in Eq. (8.7.29) one arrives at a simple expression for the frequency dependence of the hysteresis loops as follows:

$$\frac{P_S - P(E, \omega)}{2P_S} = \exp \left(- \frac{B(E)}{\omega^2} \right), \quad (8.7.32)$$

where $B(E)$ is a function of the field only.

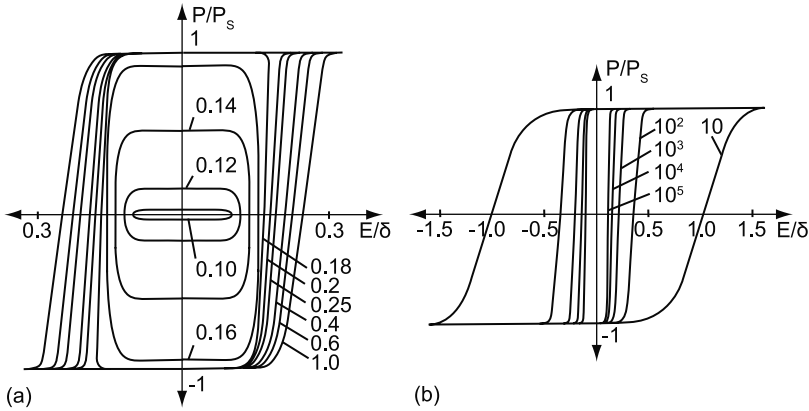


Fig. 8.7.10 Hysteresis $P - E$ loops derived from Janta’s model with the isotropic two-dimensional domain growth (Janta, 1970). **(a)** Loops for different values of normalized amplitude of the driving field $\beta = E_m/\delta$, which are given in the figure; the normalized period of the field $\gamma = 10^3$. **(b)** Loops for different values of the normalized period, which are given in the figure; the amplitude of the driving field is set as twice the coercive field

The results by Janta can be generalized by considering the domain nuclei instead of remnants as the seeds of the polarization reversal. We will give an example of such generalization for the case of d -dimensional isotropic domain growth initiated by the d -dimensional isotropic nuclei. In this case, Eq. (8.7.19) should be replaced with the following:

$$\frac{V_{\text{tot}}(t)}{V_0} = C_d \int_0^t R[E(t_1), t_1] \left[r_0[E(t_1)] + \int_{t_1}^t v[E(t_2)] dt_2 \right]^d dt_1, \quad (8.7.33)$$

where $R(E, t)$ is the nucleation rate which, in general, is a function of the electric field and an explicit function of time. The factor C_d depends on the geometry and dimension of the domain growth, for one-, two-, and three-dimensional situations illustrated in Fig. 8.7.6, it acquires values of 1, π , and $4\pi/3$, respectively. Starting from Eq. (8.7.33), Orihara et al. (1994) addressed the saturated loops for two models which allow obtaining analytical results. These models can be considered as generalizations of the Kolmogorov α - and β -models. Like the α - and β -models these considerations do not cover all situations described by the Kolmogorov–Avrami description of $P - E$ hysteresis loops (via Eq. (8.7.33)).

In the first model, the initial domain radius r_0 is neglected and the nucleation rate is set as

$$R(E, t) = R(E). \quad (8.7.34)$$

This substitution via Eqs. (8.7.10), (8.7.11), and (8.7.12) readily leads to an analytical expression for the frequency dependence of the polarization loop.

For the case of an arbitrary periodic driving signal $E = E_0\Psi(\omega t)$ where $\Psi(\varphi) = \Psi(\varphi + 2\pi)$, one finds

$$\frac{P_S - P(E, \omega)}{2P_S} = \exp\left(-\frac{A(E)}{\omega^{d+1}}\right) \quad (8.7.35)$$

and

$$A(E) = C_d \int_0^E R(E_1) \left[\int_{E_1}^E \frac{v(E_2)}{E_0} \frac{dE_2}{G(E_2)} \right]^d \frac{dE_1}{G(E_1)}. \quad (8.7.36)$$

Here $G(E) = d\Psi/d\varphi$ calculated at $\varphi = \Psi^{-1}(E/E_0)$ where $\Psi^{-1}(x)$ is the inverse function of $\Psi(x)$.

In the second model, the initial domain radius r_0 was also neglected and the nucleation rate was set as¹²

$$R(E, t) = \int_0^E n_{00}(E_1) \delta(t - t_0(E_1)) dE_1. \quad (8.7.37)$$

Inserting (8.7.37) into (8.7.33) leads through simple mathematics to a generalization of the result of the Janta model (8.7.32) as follows:

$$\frac{P_S - P(E, \omega)}{2P_S} = \exp\left(-\frac{B(E)}{\omega^d}\right), \quad (8.7.38)$$

where

$$B(E) = C_d \int_0^E n_{00}(E_1) \left[\int_{E_1}^E \frac{v(E_2)}{E_0} \frac{dE_2}{G(E_2)} \right]^d dE_1. \quad (8.7.39)$$

It is instructive to notice that, for these two models, the frequency dependence of the hysteresis loops can be presented in a unified form¹³

$$\ln \frac{P_S - P}{2P_S} = -\frac{\text{const.}}{\omega^k}, \quad (8.7.40)$$

where k is an integer (from 1 to 3 for the situations of the two- and one-dimensional domain growth, which are of interest for ferroelectrics). To the

¹² This functional dependence of the nucleation rate can be reduced to that corresponding to β -model by setting $t_0(E) = 0$ and $n_{00}(E) = n_0\delta(E)$.

¹³ We would like to remind readers that in this section only the ‘domain part’ of the polarization is addressed, i.e., the polarization with the lattice contribution being subtracted.

best of our knowledge this equation has never been documented for integer values of the exponent k , though sometimes experimental data were successfully fitted to it with non-integer k . For example, Hashimoto et al. (1994) found that their data on TGS fitted to Eq. (8.7.40) with $k \approx 1.3$.

It is clear that the analysis discussed above can hardly provide quantitative description of $P - E$ hysteresis loops in real ferroelectrics; however, as is common for simple models, the results of such analysis are useful as providing illustrations for the trends experimentally documented. In this context it is indispensable to be aware of the situation where the analysis may readily fail. In the presented analysis, the weak point is the assumption that the hysteresis loop is symmetric, with the average over the period value of the polarization equal zero. In the above analysis, this assumption was essentially used in condition (8.7.30). As was recently realized for other kinds of hysteretic phenomena, this kind of seemingly self-evident condition can be violated for small amplitudes or/and high frequencies of the driving field. In this case, the polarization starts oscillating about a nonzero average value. When a system, under the impact of changing amplitude or/and frequency of the driving field, changes its mode of cycling (from “symmetric” to “asymmetric”) one speaks of *dynamic transition*. Thus, one can arrive at a situation qualitatively different from that described by Eqs. (8.7.35) and (8.7.38). For magnetic systems, such situation has been intensively studied theoretically and experimentally (Chakrabarti and Acharyya, 1999; Lyuksyutov et al., 1999; Nattermann et al., 2001). Though the obtained theoretical results make a good starting point for a discussion of this issue in application to the ferroelectrics, such discussion is not presently available in the literature. The review paper by Chakrabarti and Acharyya (1999) provides a simple introduction to the problem of dynamic transition in hysteresis.

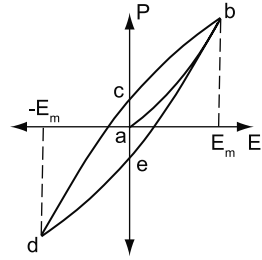
8.7.6 Rayleigh Loops

In this section we will consider a description of ferroelectric loops for the situation where the motion of domain walls as a whole under the action of the driving field is suppressed by defects and only a small fraction them can be displaced by distances comparable to the size of the sample or the domain wall spacing. In this situation, the driving field can produce only a partial switching of the sample, which often corresponds to the so-called Rayleigh hysteresis loops schematically shown in Fig. 8.7.11. Loops of this shape were first observed in magnetics by Rayleigh (1887) who also offered simple empirical expressions for their analytical description. In the case of ferroelectrics, these relations can be applied to the “domain part” of the polarization. Using Rayleigh’s relations the curves shown in Fig. 8.7.11 can be described as

$$P = \alpha E^2, \quad (8.7.41)$$

for the “initial magnetization curve,” $a-b$, and

Fig. 8.7.11 Rayleigh $P - E$ hysteresis loop



$$P = \alpha E E_m \pm \frac{\alpha}{2} (E_m^2 - E^2) \tag{8.7.42}$$

for the two branches of the loop where “+” should be used for the $b-c-d$ branch and “-” for the $d-e-b$ branch. Simple relations (8.7.41) and (8.7.42) can be interpreted in a frame of a simple phenomenological approach put forward by Preisach (1935). Let us outline this approach.

Consider a domain wall coupling with the defects of the crystal. As was discussed in Sect. 4.4 this coupling makes the wall essentially non-flat with its segments lying in the local minima of the random potential of the defects. It is clear that, due to the randomness of the potential, the local energy minimum a segment of the wall is lying in is not its only possible position and, by a small displacement, it can be brought to other local minima. This situation is schematically illustrated in Fig. 8.7.12. The application of an electric field will result in a redistribution of the segments of the wall among the minima of the random potential. If the field is weak enough, it cannot depin the whole wall but it will rather produce short jumps of weakly pinned wall segments between the neighboring minima of the random potential. The variation of polarization accompanying these jumps is considered as the source of the polarization response corresponding to the Rayleigh hysteresis loops. The simplest model which successfully simulates this kind of response corresponds to the following mathematical scheme.

- (i) An ensemble of double-well potentials (systems) is considered.
- (ii) Each system contains one particle; a jump of the particle between the wells of the potential corresponds to a displacement of a weakly pinned segment of a domain wall.
- (iii) The position of the particles describes the polarization states of the ferroelectric: Each particle in the right-hand well of the potential contributes a dipole moment p_0 to that of the total dipole moment of the ferroelectric whereas each particle in the left-hand well contributes $-p_0$. All dipoles are considered to be aligned in the same direction, say z -direction. Thus, the domain contribution to the polarization of the ferroelectric can be written as

$$P = \frac{p_0}{V} (N_R - N_L), \tag{8.7.43}$$

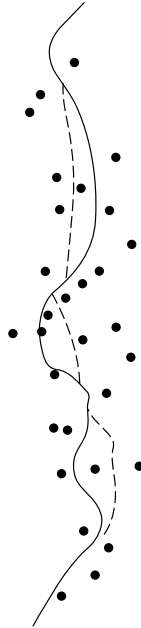


Fig. 8.7.12 Schematic drawing of domain wall interacting with defects (shown with *dots*). *Solid and dashed lines* illustrate possible positions of the wall in the local minima of the potential created by the defects

where N_R and N_L are the numbers of the particles in the right- and left-hand wells, respectively; V is the volume of the sample.

- (iv) Each double-well potential is characterized by two parameters: the barrier height W_C and the asymmetry W_A as illustrated in Fig. 8.7.13. Thus, each double-well potential can be presented as a point on the (W_C, W_A) plane. For

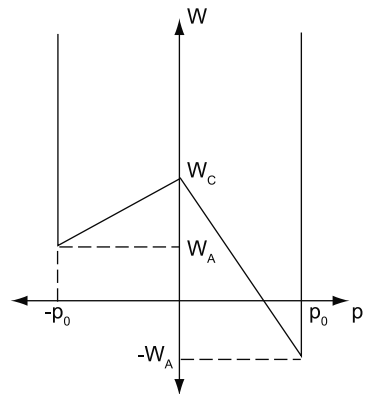


Fig. 8.7.13 Energy of a weakly pinned segment of domain wall as a function of the dipole moment associated with flips of this segment between its two equilibrium positions as defined in the Preisach model

further consideration, it is more convenient to use variables $e_C = W_C/p_0$ and $e_A = W_A/p_0$ and the (e_C, e_A) plane. The electric field in z -direction E changes the energy of the right- and left-hand wells by values of $-Ep_0$ and Ep_0 , respectively. Thus, the field can induce “switching” between the wells.

- (v) The thermal activation effects in switching are neglected, i.e., it is considered that the switching in a double well takes place only when the applied field completely suppresses the barrier between the wells. This means that the switching from the left well to the right one takes place at $E = e_C + e_A$ and back at $E = -e_C + e_A$. This local switching can be described by a loop shown in Figure 8.7.14. This figure elucidates the physical meaning of parameters e_C and e_A as the half-width of the local loop and its field offset.

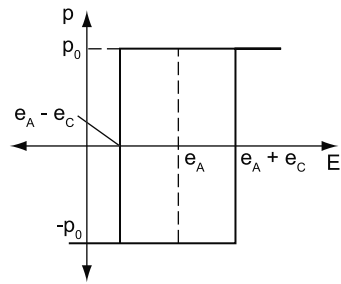
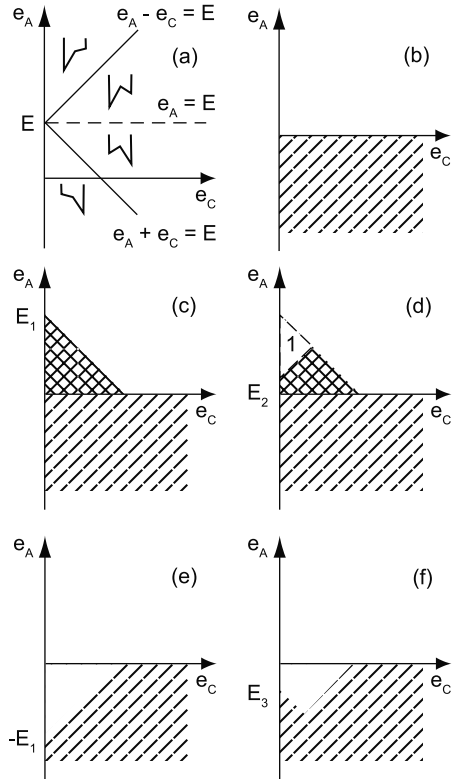


Fig. 8.7.14 Dipole moment-field hysteresis loop associated with flips of the weakly pinned segment of the domain wall, whose energy is given in Fig. 8.7.13

The (e_C, e_A) plane is convenient for the classification of the double-well potentials for a given value of the applied field. As shown in Fig. 8.7.15a, the lines $e_A + e_C = E$, $e_A - e_C = E$, and $e_A = E$ divide the (e_C, e_A) plane into areas corresponding to the four types of the local potential: (i) where the only minimum is on the right, (ii) where the only minimum is on the left, (iii) where there are two minima, the deepest one being on the right, and (iv) where there are two minima, the deepest one being on the left.

Using this classification, one readily describes the switching of the ensemble of the double wells simulating the partial switching of the ferroelectric. Let us start from the equilibrium state of our system in the absence of the applied field where each particle occupies the deepest minimum. In this case, clearly, the systems with $e_A < 0$ are poled positively (up) and those with $e_A > 0$ are poled negatively (down) as illustrated in Fig. 8.7.15b. Consider the switching caused by an applied field $E_1 > 0$. To find the corresponding variation of the polarization, one should count the number of systems flipped by the field. In the graphical representation, these systems belong to the cross-hatched triangular area in Fig. 8.7.15c. If then we decrease the field down to a positive value E_2 , the contribution of the systems belonging to the triangle marked with “1” in Fig. 8.7.15d should be subtracted from the result obtained at $E = E_1$. On the same line one can find the (e_C, e_A) mapping of the state with $E = -E_1$ obtained with a further reduction of the field (shown in Fig. 8.7.15e) as well as the mapping

Fig. 8.7.15 Preisach model: mapping of the state of the system of weakly pinned segments of domain wall onto the (e_C, e_A) plane. See the text



shown in Fig. 8.7.15 f. The latter corresponds to an increase in the field from $-E_1$ to E_3 . It is clear that, in this model, to calculate the field-induced variation of the polarization, one should be able to count the number of the representative points covered by geometrical figures discussed above. In the simplest version of the Preisach model two additional assumptions are made: (i) the density of representative points, n , set fixed over the whole (e_C, e_A) plane; (ii) this density is set high enough so that a typical variation of the electric field will flip many double potentials. These two assumptions make it possible to link the variation of the polarization ΔP to the change of the mapping area corresponding to the systems poled up, ΔS , namely $\Delta P = \Delta S \times n \times 2p_0/V$. Using this relation and the geometrical considerations presented above one readily arrives at the following $P - E$ dependences for the description of the loop shown in Fig. 8.7.11:

$$P = \frac{np_0}{V} E^2 \tag{8.7.44}$$

for the “initial magnetization curve,”

$$P = \frac{np_0}{V} \left[E_m^2 - \frac{1}{2}(E_m - E)^2 \right] = \frac{np_0}{V} \left[EE_m + \frac{E_m^2 - E^2}{2} \right] \tag{8.7.45}$$

for the descending branch, and

$$P = \frac{np_0}{V} \left[-E_m^2 + \frac{1}{2}(E_m + E)^2 \right] = \frac{np_0}{V} \left[EE_m - \frac{E_m^2 - E^2}{2} \right] \quad (8.7.46)$$

for the ascending branch. One sees that Eqs. (8.7.44), (8.7.45), and (8.7.46) readily reproduce the Rayleigh relations, Eqs. (8.7.41) and (8.7.42), with $\alpha = np_0/V$.

The basic version of the Preisach model presented above, where jumps of the wall segments are replaced by jumps of the particles in the double-well systems and where the change of the dipole moment per jump is the same for all systems, is rather simplified. Clearly, the dipole moments in question are not the same for different jumps of different wall segments. Another simplification is the constancy of the density of the representative points. For large mapping areas this may not be true. In principle, this apparent drawback of the model can be fixed by introducing the density of representative point dependent on e_C and e_A . This gives a way to a generalization of the Preisach model, which is well mathematically developed and can be applied to the description of the hysteresis loops of any kind not only of the Rayleigh loops. The mathematical aspect of the problem is comprehensively discussed in the book by Mayergoyz (1991). The generalized Preisach model was first applied to ferroelectrics by Turik (1963, 1964). Other examples of application of this model to ferroelectrics can be found in papers of other authors (Jiang et al., 1997; Robert et al., 2001; Bartic et al., 2001; Damjanovic, 2005).

Another aspect of the Preisach description of the hysteresis loops is its microscopic justification. This problem was addressed, first, for the case of magnetics (Néel, 1942; Kronmüller, 1970) and further on for ferroelectrics (Boser, 1987). The statistical consideration of the problem showed that polarization (magnetic) response of the ensemble of domain walls in a random pinning potential is consistent with the basic Preisach model.

8.7.7 Piezoelectric Hysteresis Loops

As discussed above in this chapter cycling a ferroelectric with an ac electric field induces not only $P - E$ loops but also hysteretic curves actually of all its parameters. Among these curves the hysteretic loops of the piezoelectric coefficient, $d - E$ loops, are usually considered as those that are most close to the primary $P - E$ loops. Experimentally, the shapes of the $P - E$ and $d - E$ loops are sometimes similar but the cases where there exists a qualitative difference between these are not rare. This applies to the case of crystalline samples (Schmidt et al., 1982; von Cieminski and Schmidt, 1988), thin films (Hiboux et al., 1999; Chen, 2003), and ceramics (Uchida and Ikeda, 1965; von Cieminski et al., 1990). Below in this section we will address the relation between these two

kinds of hysteresis loops for two simple situations: (i) a saturated square $P - E$ hysteresis loop where the switching occurs in a narrow interval of applied field close to a well-defined coercive field; (ii) a real hysteresis $P - E$, non-saturated and/or affected by backswitching; part of the sample may be non-switchable.

8.7.7.1 Thermodynamic Piezoelectric Loops and the Case of Abrupt Switching

In the situation where the switching occurs in a narrow interval of applied field close to a well-defined coercive field, the shape of both the $P - E$ and $d - E$ loops can be found from the Landau theory. We will consider, for simplicity, the case of the second-order phase transition in a uniaxial ferroelectric (the polar axis is directed along z -axis). We will also consider the behavior of the longitudinal d piezoelectric coefficient defined as

$$d = d_{333} = \frac{\partial \varepsilon_{33}}{\partial E_3}. \quad (8.7.47)$$

Below, the indices for all variables entering this equation and the polarization will be omitted. The experimental situation addressed corresponds to applying to a sample a combination of (i) an ac electric field slowly changing in symmetric limits with the amplitude large enough to produce polarization switching and (ii) a weak ac field used to measure the d coefficient. Starting from Eqs. (2.3.3) and (2.3.23) the relation between the strain ε and the polarization P reads $\varepsilon = QP^2$ where $Q = Q_{33}$. Inserting this relation into Eq. (8.7.47) and taking into account the equation of state for the ferroelectric, $E = \alpha P + \beta P^3$, we find the following expression for d as a function of the polarization:

$$d = 2QP \frac{\partial P}{\partial E} = \frac{2QP}{\alpha + 3\beta P^2}. \quad (8.7.48)$$

This result leads us to an important conclusion, namely, that, in contrast to the polarization, the piezoelectric coefficient is *always a decreasing function of the field* (in the interval where it is continuous). That can be readily shown by checking the sign of the derivative $\partial d / \partial E = 2Q(\alpha - 3\beta P^2) / (\alpha + 3\beta P^2)^3$, which is clearly negative. One can show that this statement holds for the case of the first-order phase transition, except maybe for a narrow temperature interval between T_0 and T_C .

It is instructive to compare the shapes of the piezoelectric loop corresponding to Eq. (8.7.48) and the corresponding polarization loop. These loops are shown in Fig. 8.7.16. The solid lines correspond to the idealized case where the thermodynamic coercive field is reached on the loop. In this case a strong growth of $|d|$ at $E \rightarrow E_{\text{crit}}$ is seen. In a realistic situation where the antiparallel configuration of the polarization and field becomes unstable at $E = E_c \ll E_{\text{crit}}$ (the jumps at E_c in the figure are shown with the dashed lines), this growth is essentially limited; however the trend holds.

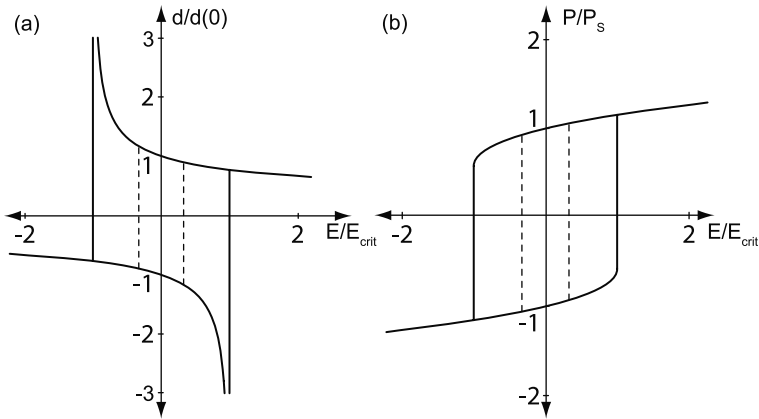


Fig. 8.7.16 Piezoelectric (a) and polarization (b) hysteresis loops simulated in terms of the Landau theory for the second-order phase transition described with the free energy expansion up to the P^4 terms (solid lines). The loops formed with two dashed lines correspond to the case of abrupt polarization switching at a field smaller than the thermodynamic coercive field

8.7.7.2 Piezoelectric Loops Affected by Non-saturation, Backswitching, and Partial Switching

Very often the remanent polarization of a $P - E$ loop is smaller than the spontaneous polarization of the material. The reasons for that are (i) the so-called backswitching, i.e., the appearance of domains when the field decreases from the tip of a saturated polarization loop to the remanence and (ii) partial switching of the sample. Below we will address the relation between the $P - E$ and $d - E$ loops for the situation where these effects are essential and/or the polarization switching is not abrupt taking place in an interval of the applied field. This problem has been theoretically addressed by Tagantsev et al. (2004a). The oncoming consideration is mainly based on the results from this paper. As above we will consider the longitudinal d piezoelectric coefficient for the case where the polarization is collinear to an ac electric field driving the $P - E$ and $d - E$ hysteresis loops in symmetric field limits. As well we restrict our consideration to the case where the 180° nonferroelastic switching takes place at moderate values of the applied field so that the nonlinearity of the lattice contribution to the ac dielectric susceptibility, χ_{lat} , can be neglected. In this case, the polarization of the ferroelectric P can be divided into the domain and lattice contributions

$$P = P_{dom} + P_{lat} \equiv P_S(2\alpha - 1) + \chi_{lat}E, \tag{8.7.49}$$

where α is the volume fraction of the positively oriented domains. Now the description of the $P - E$ loop reduces to setting a hysteretic function $\alpha(E)$ describing the evolution of the domain population during the cycling. The

same separation can be done for the ac susceptibility measured at a given point of the loop

$$\chi = \chi_{\text{dom}} + \chi_{\text{lat}} = 2P_S \frac{\overline{\partial\alpha}}{\partial E} + \chi_{\text{lat}}. \quad (8.7.50)$$

Here we have used the notation $\frac{\overline{\partial\alpha}}{\partial E}$ for what we call *ac derivative* of $\alpha(E)$. We define it as the amplitude of the first harmonics of $\alpha(E + E_{\text{ac}} \cos \omega t)/E_{\text{ac}}$. Because of the hysteretic nature of the function $\alpha(E)$, in general, the ac derivative differs from the normal derivative of $\alpha(E)$ calculated from the corresponding branch of the $P - E$ hysteresis loop.¹⁴

Using again the relation $\varepsilon = QP^2$ we find the strain in the positively poled material as follows:

$$\varepsilon_+ = QP^2 = Q[P_S^2 + 2P_S\chi_{\text{lat}}E + (\chi_{\text{lat}}E)^2] \quad (8.7.51a)$$

whereas for the negatively poled material we have

$$\varepsilon_- = QP^2 = Q[P_S^2 - 2P_S\chi_{\text{lat}}E + (\chi_{\text{lat}}E)^2]. \quad (8.7.51b)$$

We determine the strain in the polydomain state as the weighted average of the strains in the fully poled states. This enables us to calculate the piezoelectric coefficient as

$$\begin{aligned} d &= \frac{\overline{\partial}}{\partial E} [\alpha\varepsilon_+ + (1 - \alpha)\varepsilon_-] = Q \frac{\overline{\partial}}{\partial E} [P_S^2 + (2\alpha - 1)2P_S\chi_{\text{lat}}E + (\chi_{\text{lat}}E)^2] \\ &= 2Q \left[P_S(2\alpha - 1)\chi_{\text{lat}} + \chi_{\text{lat}}E \cdot 2P_S \frac{\overline{\partial\alpha}}{\partial E} + \chi_{\text{lat}}^2 E \right]. \end{aligned} \quad (8.7.52)$$

This expression acquires a simple form when rewritten in terms of lattice and domain contributions to the polarization and small-signal susceptibility:

$$d = 2Q(P\chi_{\text{lat}} + P_{\text{lat}}\chi_{\text{dom}}). \quad (8.7.53)$$

Equation (8.7.53) makes it possible to specify a number of conclusions concerning the shape of the piezoelectric loop. The structures of the terms entering this formula are familiar: electrostriction coefficient \times polarization \times susceptibility. The contribution to the piezoelectric loop controlled by the first term, $d_0 = 2QP\chi_{\text{lat}}$, has the shape of the $P(E)$ loop (Fig. 8.7.17a). The shape of the contribution of the second term, $\Delta d = 2QP_{\text{lat}}\chi_{\text{dom}}$, is very different from that of the first contribution. This term vanishes at the saturated tips of the loop

¹⁴ Like the measured $C-V$ curve of a ferroelectric capacitor very often does not correspond to the field derivative of its polarization loop.

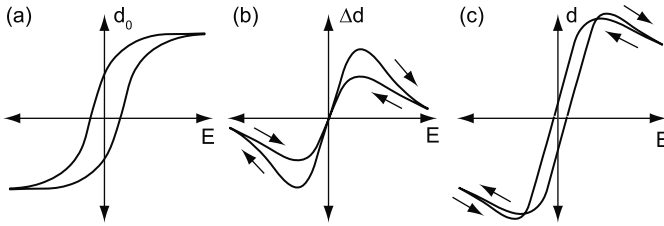


Fig. 8.7.17 (a) and (b) Schematics of two contributions to piezoelectric loop, $d_0 = 2QP\chi_{lat}$ and $\Delta d = 2QP_{lat}\chi_{dom}$, which are predicted by the theory according to Eq. (8.7.53). (c) Piezoelectric loop $d(E) = d_0(E) + \Delta d(E)$ corresponding to the contributions shown in (a) and (b). After Tagantsev et al. (2004a)

where $\chi_{dom} = 0$ because of the absence of domain walls at saturation. It also vanishes at the remanence where $P_{lat} = \chi_{lat}E = 0$. Thus, the absolute value of Δd passes through a maximum between the tip of the loop and the remanence. Since the domain contribution to the permittivity χ_{dom} is proportional to the domain population, which is a hysteretic function of the field, the term $\Delta d = 2QP_{lat}\chi_{dom}$ will also exhibit a hysteresis schematically shown in Fig. 8.7.17b. Its remarkable feature is that it is clockwise like the $\chi - E$ hysteresis at $E > 0$. Finally we see that the piezoelectric hysteresis loop can be presented as a sum of a loop having the shape of regular anticlockwise $P(E)$ loops and a clockwise $\Delta d(E)$ loop with “humps.” If the contribution Δd is appreciable, the $d(E)$ loop may exhibit humps and clockwise rotating tips (noses). This is schematically illustrated in Fig. 8.7.17c. For comparison, Fig. 8.7.18 shows a piezoelectric loop obtained from a (111) tetragonal PZT thin film¹⁵ where a clear nose and two humps are seen.

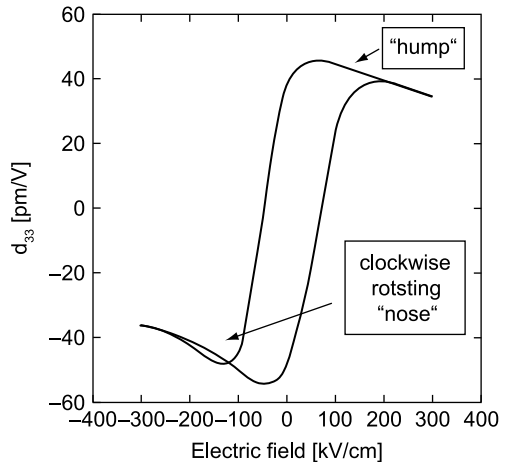


Fig. 8.7.18 A $d_{33} - E$ hysteresis loop obtained from a 300 nm thick PZT45/55 (tetragonal) film of (111) orientation. After Hiboux et al. (1999)

¹⁵ Though such film may contain ferroelastic domains these are not piezoelectric active for the considered settings.

It is instructive to evaluate the importance of Δd for a realistic set of the material parameters. A suitable for this purpose relation

$$\frac{\Delta d}{d - \Delta d} = \frac{\chi_{\text{dom}} E}{P} \quad (8.7.54)$$

can be readily obtained from Eq. (8.7.53). We will obtain this estimate for the values of the parameters typical for characterization of $\text{Pb}(\text{Zr},\text{Ti})\text{O}_3$ thin films. Thus, taking $\chi_{\text{dom}}/\epsilon_0 = 700$, $P \cong P_s \cong 30 \mu\text{C}/\text{cm}^2$, and $E = 100 \text{ kV}/\text{cm}$ we estimate this ratio as 0.2. This means that the effects predicted by this theory can be appreciable.

One can relate the nose and hump with features of the polarization switching. The hump can appear if χ_{dom} is appreciable when the applied field decreases from the tip of the loop down to zero. This implies that intensive domain formation takes place at this phase of the hysteresis loop. Thus, we conclude that the appearance of hump attests to strong backswitching in the system in the corresponding field interval. Following similar reasoning, a pronounced nose of a piezoelectric loop can be related to weak backswitching. It is in this case where the difference in domain population (and in turn in χ_{dom}) is significant for the “from-remanence-to-tip” and “from-tip-to-remanence” phases of the loop.

Equation (8.7.53) also clearly shows that the piezoelectric loops should be slimmer than the polarization loops (i.e., the coercive field of the polarization loop should be always larger than that of the piezoelectric loop) since at $P = 0$ the piezoelectric coefficient has already changed its sign.

Now let us consider the situation where, in addition, a volume fraction γ of the sample is non-switchable, exhibiting, at $E = 0$, the net frozen polarization P_N . The frozen polarization will differently affect the $P - E$ and $d - E$ loops. For the $P - E$ loop (customarily symmetrized along the P -axis) this will in general lead to a reduction of the swing of the measured polarization, whereas for the $d - E$ loop, in addition to a reduction of its swing, an offset of the loop along the d -axis is expected. Let us illustrate this effect in the approximation employed above, where the measured polarization and strain of the sample are calculated as the weighted averages.

Now the average polarization of the whole system defined in accordance with the “ P -axis-symmetrized” way of its measurement, i.e., satisfying the condition $\max[P] = -\min[P]$, can be written as

$$P = (1 - \gamma)P_1 + \gamma\chi_{\text{lat}}E, \quad (8.7.55)$$

where P_1 is the polarization in the switchable part of the crystal, given by Eq. (8.7.49) with γ having meaning of the fraction of this part. For the average differential permittivity and piezoelectric coefficient, applying Eqs. (8.7.50) and (8.7.53) to the switchable part, one finds

$$\chi = (1 - \gamma)\chi_{\text{dom}} + \chi_{\text{lat}} \quad (8.7.56)$$

and

$$d = (1 - \gamma)2Q(P_1\chi_{\text{lat}} + P_{\text{lat}}\chi_{\text{dom}}) + \gamma 2Q(\chi_{\text{lat}}P_N + \chi_{\text{lat}}^2 E). \quad (8.7.57)$$

Now using the extrinsic contribution to the susceptibility of the system, $\chi_{\text{extr}} = \chi - \chi_{\text{lat}}$, as a variable we arrive at a form of the piezoelectric coefficient

$$d = 2Q(P\chi_{\text{lat}} + P_{\text{lat}}\chi_{\text{extr}}) + \gamma 2QP_N\chi_{\text{lat}}, \quad (8.7.58)$$

where the first term is actually identical to the result for the system without the frozen polarization whereas the second one is a constant offset conditioned by the frozen polarization.

Thus, we see that, in terms of the polarization P traced by the standard symmetrized $P - E$ loop, and permittivities χ_{extr} and χ_{lat} , which can be in principle evaluated from the $C - V$ curves of the sample, the presence of the areas with frozen spontaneous polarization manifests itself in an offset of the $d - E$ loop along the d -axis.

8.7.8 Ferroelectric Breakdown

In the previous sections we have discussed the switching caused by a homogeneous applied electric field. For a long time this situation was the only typical experimental situation (in parallel plate capacitors). The recent use of scanning force microscopes (SFM) has brought about another situation. The switching caused by an SFM whose tip is loaded with a high electric potential occurs in a very inhomogeneous electric field. The theory of this special kind of switching has been recently developed by Molotskii (2003b) and Molotskii et al. (2003). These authors have shown that, in this case, the polarization reversal can take place inside regions elongated normally to the sample surface having a length that can exceed the tip radius by many orders of magnitude. If the sample is thin enough, the resulting regions of reverse polarization can have the shape of narrow cylindrical domains. The authors have called this phenomenon *ferroelectric breakdown*. The predictions of this theory have been found compatible with the experimental observations. Below we will discuss this phenomenon following the aforementioned papers.

In the context of polarization switching, the field inhomogeneity in SFM reveals itself in two aspects. First, close to the tip, the field can be very strong. Its normal component reaches a value of about $V/(R\epsilon_0\kappa_c)$ where R , V , and κ_c are the tip radius, the voltage applied to the tip, and the normal component of the permittivity of the ferroelectric (lattice contribution), respectively. This field may readily be strong enough to provide local polarization reversal at the tip. Second, this field strongly decreases with increasing distance from the tip. Thus far in the bulk of the sample, the applied field is expected to be too small to cause any switching.

However, the mathematical analysis of the problem has shown that the polarization reversal is possible far from the tip being driven by the decreasing depolarization energy of the expanding domain. Let us outline the key points of this analysis.

The formation of reverse domain under the field created by an SFM tip of radius R spaced by a distance δ from the surface of the ferroelectric is considered as shown in Fig. 8.7.19. It is assumed that the reverse domain has the shape of a half prolate spheroid (like in the Landauer model; see Sect. 8.7.2). Also like in the Landauer model, the hard-ferroelectric approximation is adopted, where the ferroelectric is characterized with its spontaneous polarization P_S and its lattice dielectric permittivity having two independent components κ_c (along P_S) and κ_a (perpendicular to P_S). It is shown that along this approach, the equilibrium dimensions of the reverse domain (length l and radius r) can be found from the minimization of its energy (Molotskii, 2003b)

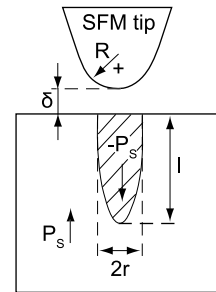


Fig. 8.7.19 Schematic drawing of SFM tip and the reverse domain induced by the application of positive potential to the tip

$$U = brl + c \frac{r^4}{l} - f(\sqrt{r^2 + s^2} - s), \quad s = R + \delta, \quad (8.7.59)$$

$$f = \frac{2C_t V P_S}{\epsilon_0 (1 + \sqrt{\kappa_a \kappa_c})}, \quad (8.7.60)$$

where the first two terms are the energy related to the creation of the domain wall and that of the depolarizing field. The explicit expressions for parameters b and c are defined by Eq. (8.7.2). The third term (written for the case of practical interest where $l \gg r, s$), is related to the gain of the bulk energy due to the polarization reversal in the domain. Here C_t is the tip capacitance. In general, C_t is a complicated function of the parameters of the problem (Molotskii, 2003b), which in the case where the gap δ is very small, $\delta/R \ll 4/(1 + \sqrt{\kappa_a \kappa_c})^2$, can be approximated as $C_t \approx 4\pi\epsilon_0 R \frac{\sqrt{\kappa_a \kappa_c} + 1}{\sqrt{\kappa_a \kappa_c} - 1} \ln \frac{\sqrt{\kappa_a \kappa_c} + 1}{2}$. Typically, the ratio $\delta/R \cong 10^{-3}$, so that this inequality is not met as a strong one. In this case this formula may be used as a rough estimate.

The analysis of Eq. (8.7.59) shows that (i) the formation of the reverse domain is energetically favorable at any value of the applied voltage and (ii) the reverse domain tends to acquire certain dimensions instead of growing

unrestrictedly, unlike in the Landauer model. If the applied voltage is high enough, the length of the reverse domain can be comparable to the thickness of a “bulk” sample (fraction of mm). Thus, using SFM tip loaded with high voltage, cylindrical “through” domains can be created in bulk samples.

It is instructive to present an estimate for the situation where the generation of such “through” domains has been documented (Molotskii et al., 2003): a LiNbO_3 crystal with application of 3.2 kV to tip with $R = 50$ nm and $\delta \cong 0.1$ nm. Taking for parameters of this system: $\sigma_W = 10 - 35$ mJ/m², $\kappa_a = 30$, $\kappa_c = 84$ $P_S = 75 - 80$ $\mu\text{C/cm}^2$, and $C_t \approx 1.7 \times 10^{-17}$ F, the minimization of Eq. (8.7.59) gives for equilibrium dimensions (radius r_m and length l_m) of the reverse domain (Molotskii et al., 2003):

$$2r_m \approx 2 \left(\frac{f}{5\sqrt{bc}} \right)^{2/3} \approx 1 - 1.5 \mu\text{m}, \quad (8.7.61)$$

$$l_m \approx \frac{f}{5b} \approx 200 - 700 \mu\text{m}. \quad (8.7.62)$$

This estimate for the length of the reverse domain is consistent with the observation of “through” domains under these conditions in a 150 μm thick sample of LiNbO_3 : The sample thickness smaller than the estimated domains length can be interpreted as the condition for the formation of through domains. The theoretical estimate (8.7.61) for the domains radius has been found to be comparable to the effective diameter of the observed through domains. However, the theory discussed above is inapplicable for the description of the “through” domain radius so that the reason for this theory–experiment agreement remains unclear.

Qualitatively, the physical mechanism behind the described phenomenon can be elucidated as follows. The strong field near the SFM tip leads to the local switching in the tip-adjacent region. This switched region stretches out from the strong-field region to decrease the depolarizing energy which decreases with the domain elongation (see the second term in Eq. (8.7.59)). Thus, the applied field does not directly influence the forward growth of the domain (only indirectly through the polarization reversal at the tip). This explains the propagation of the elongated domain through the regions of crystal far from the tip where the applied field is actually vanishing.

8.8 Extrinsic Contribution to Small-Signal Dielectric Response in Bulk Ferroelectrics

8.8.1 Introduction

The dielectric response of a multidomain ferroelectric is traditionally divided into two parts. The first part, the so-called *intrinsic contribution*, can be

determined as the weighted average of the lattice contributions of the ferroelectric domains to the response. The second part, the so-called *extrinsic contribution*, comprises the contribution associated with the presence of the domain pattern in the ferroelectric. Even, an immobile domain pattern can affect the dielectric response of a ferroelectric as will be discussed in Sect. 8.8.2. However, the most important mechanisms of the extrinsic contribution are associated with the domain wall motion. The main part of this section will be devoted to these mechanisms.

Displacement of a ferroelectric domain wall is a very efficient method to change the average polarization of a crystal. When such displacements are induced by an electric field, they contribute to the dielectric permittivity of the material. We will denote the corresponding contribution as κ_w and refer to it as the *domain* contribution. Its reference value can be obtained evaluating the average permittivity which the material exhibits at switching, i.e.,

$$\kappa_w \cong \frac{P_S}{\epsilon_0 E_c}. \quad (8.8.1)$$

Here P_S and E_c are the spontaneous polarization and the coercive field of the ferroelectric, respectively. Bearing in mind a BaTiO₃ crystal, we take $P_S = 25 \mu\text{C}/\text{cm}^2$ and $E_c = 1 \text{ kV}/\text{cm}$ to find a value of $\kappa_w \cong 250,000$, which is large compared to the typical values of the lattice contribution to the permittivity. In this section we will be mainly dealing with the *small-signal dielectric response* which we specify as the polarization response to the electric fields which are much smaller than E_c . In this case, the above estimate, Eq. (8.8.1), can be considered as an upper bound. This estimate actually correctly suggests that the extrinsic contribution to permittivity can be comparable or even larger than the lattice one. Below we will give examples where the experimental value of the domain contribution is less than one order of magnitude smaller than this estimate.

In the present section we will mainly address the situations typical for ferroelectric single crystals where the domain walls are not objected to the impact of external, mechanical, or/and electrostatic, constraints. As an exception, in Sect. 8.8.8 we will discuss the extrinsic contribution from ferroelastic domain walls of a ferroelectric grain in ceramics, which is clamped by the “neighbors.” The effects of mechanical clamping by the substrate and that of the so-called passive layer, typical for thin films, will be dealt with in Chap. 9.

An essential feature of the extrinsic contribution to the dielectric permittivity of ferroelectrics is that it is strongly influenced by the defects of the material. This poses problems on the experimental and theoretical levels.

For focused experimental investigation of this contribution, one should be able to reproduce the same domain pattern and, in the ideal case, to get some information on its microstructure. Since the domain pattern is often far from the equilibrium, this is not an easy task (even when dealing with identically processed samples). The conclusive comparison of the experimental data

obtained from differently processed sample is yet more difficult, since, in this case, we need information both on the domain pattern and on the population and type of defects in the sample.

For theoretical treatment, the description of the extrinsic contribution to the permittivity requires modeling of the domain wall motion in the random potential of the defects, the information on which is usually hardly available. This is a tough theoretical task which is typically treated in terms of substantially simplified models. Despite such simplifications, the results with controllable inaccuracy are rare. For this reason, an experimentalist has often to be content with theoretically predicted trends for comparison with the experimental data.

Discussing the dielectric response we will use the notions of the real, κ'_{ij} , and imaginary, κ''_{ij} , parts of the dielectric permittivity, which control the in-phase and out-of-phase components of the induced electrical displacement. Specifically, for the applied field $E_i = E_{mi} \cos \omega t$, these components can be written as

$$D_i^{\text{in}} = \kappa'_{ij} \varepsilon_0 E_{mj} \cos \omega t, \quad D_i^{\text{out}} = \kappa''_{ij} \varepsilon_0 E_{mj} \sin \omega t, \quad (8.8.2)$$

respectively. The real and imaginary parts of the susceptibility χ_{ij} can also be introduced according to the relation $\varepsilon_0(\kappa_{ij} - \delta_{ij}) = \chi_{ij}$.

Concerning the content of this section one more remark is to be made. For the moment, the available experimental information on the domain contribution to the permittivity of ferroelectrics and the available relevant theories do not suffice to outline a comprehensive big picture of the problem. What is actually available is a collection of various experimental and theoretical results, which is far from being complete. For this reason, we will not be able to present a systematic discussion of the subject but rather a discussion of selected issues.

8.8.2 Fully Immobile Domain Pattern

One readily expects that, in a ferroelectric, it is the driving-field-induced motion of domain walls that controls the extrinsic contribution to the permittivity. However, in the literature, a number of mechanisms of the extrinsic contribution have been considered, which are present even in the absence of such motion. Specifically, these mechanisms are as follows: excessive polarizability of domain walls (Lawless and Fousek, 1970), the electrocaloric effect inducing heat transport across the domain walls (Marvan, 1969), and the piezoelectric clamping effect (Drougard and Young, 1954). The manifestation of these mechanisms can be in principle detected or has been detected provided the contribution to the permittivity associated with wall motion is not too large.

8.8.2.1 Excessive Polarizability of Domain Walls

Lawless and Fousek (1970) evaluated the dielectric response of the distorted materials “inside” a 180° domain wall in BaTiO_3 . Since in such wall the

polarization passes through zero, the “material inside it” can be viewed as being closer to the phase transition than in the bulk of the domains. The calculations performed in terms of a refinement of the Slatter model showed that, indeed, the domain wall contributes to the permittivity as a material with 6.5-times larger permittivity than in bulk BaTiO₃. For a lamellar domain pattern with 1 μm spacing typical for static 180° domain patterns of bulk BaTiO₃ this effect would lead to quite small extrinsic contribution to the permittivity with $\kappa_w \cong 1$. However, according to Lawless and Fousek, at switching in strong fields (where numerous nucleation of reverse domain is expected), much larger domain densities are expected. As a result, under such condition, this contribution can become comparable to a value of $\kappa_w \cong 20$ reported for the extrinsic contribution to the permittivity in Remeika BaTiO₃ crystals at room temperature (Fousek, 1965a).

8.8.2.2 Electrocaloric Effect

The characteristic feature of ferroelectric domain states is their distinction in the pyroelectric coefficients. According to thermodynamics, these coefficients also control the electrocaloric effect. Both the pyroelectric and electrocaloric effects can be described by the following constitutive equations:

$$\begin{aligned} dP_i &= \chi_{ij}^T dE_j + p_i dT \\ dS &= p_i dE_i + \frac{c_E}{T} dT, \end{aligned} \quad (8.8.3)$$

where dS , χ_{ij}^T , p_i , and c_E are the variation of entropy, isothermal dielectric susceptibility, pyroelectric coefficient, and the heat capacity per unit volume at constant electric field, respectively. From the second equation of Eq. (8.8.3), the electrocaloric effect that consists in a temperature change caused by the adiabatic application of an electric field reads

$$dT = -\frac{T}{c_E} p_i dE_i. \quad (8.8.4)$$

Since all ferroelectric domain states differ in p_i , the application of an ac electric field to a polydomain sample should result in a spatial modulation of its temperature. The dielectric susceptibility measured with such field will be sensitive to the relationship between its frequency ω and the time of thermal relaxation of the system $\tau_h \cong W^2 c_E / \lambda$ where W is the period of the domain pattern and λ is the coefficient of thermal conductivity of the material. At $\omega\tau_h \ll 1$, the isothermal susceptibility χ_{ij} will be measured, whereas at $\omega\tau_h \gg 1$ it will be its adiabatic value

$$\chi_{ij}^S = \chi_{ij}^T - \frac{T}{c_E} p_i p_j. \quad (8.8.5)$$

Thus, the presence of a domain pattern in a ferroelectric should result in a frequency dispersion of its dielectric susceptibility at frequency $\cong 1/\tau_h$ and in a loss maximum at the same frequency (in view of the Kramers–Kronig relation).

For a lamellar pattern of 180° domains of period W and the ac field parallel to the direction of the spontaneous polarization, this mechanism was modeled by Marvan (1969). He found the time-dependent stationary spatial distribution of the temperature in the system by solving the heat transport equation. In this equation the heat source changes its sign at the domain wall whose thickness was neglected. From this solution, using Eq. (8.8.3) the average polarization of the domain pattern was determined leading to the following contributions to the corresponding components of the susceptibility

$$\chi' = \chi^T + \frac{Tp^2}{c_E} \beta_1(\omega), \quad (8.8.6)$$

$$\chi'' = \frac{Tp^2}{c_E} \beta_2(\omega), \quad (8.8.7)$$

where

$$\beta_1 = \frac{1}{A} \frac{\sinh A + \sin A}{\cosh A + \cos A}, \quad (8.8.8)$$

$$\beta_2 = \frac{1}{A} \frac{\sinh A - \sin A}{\cosh A + \cos A}, \quad (8.8.9)$$

$$A = \frac{W}{2} \sqrt{\frac{\omega c_E}{2\lambda}} \approx 2.3 \sqrt{\frac{\omega}{\omega_{\max}}}. \quad (8.8.10)$$

Functions $\beta_1(A)$ and $\beta_2(A)$ are shown in Fig. 8.8.1. The dispersion described by Eqs. (8.8.6), (8.8.7), (8.8.8), (8.8.9) and (8.8.10) is of non-Debye type. The essential difference from the Debye relaxation is evident in the high

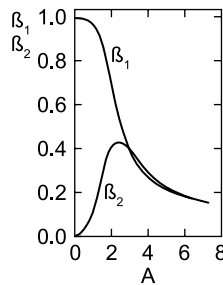


Fig. 8.8.1 Functions $\beta_1(A)$ and $\beta_2(A)$ where $A \approx 2.3\sqrt{\omega/\omega_{\max}}$, which control the contributions of the electrocaloric mechanism to the real and imaginary parts of the permittivity. See Eqs. (8.8.6) and (8.8.7). After Marvan (1969)

frequency limit where $\beta_1(\omega) \approx \beta_2(\omega) \propto 1/\sqrt{\omega}$. The loss associated with this mechanism passes a maximum of

$$\chi''_{\max} \approx 0.42 \frac{Tp^2}{c_E} \quad (8.8.11)$$

at frequency

$$\omega_{\max} \approx 41 \frac{\lambda}{c_E} \frac{1}{W^2}. \quad (8.8.12)$$

Taking $W/2 = 1 \mu\text{m}$ as a typical domain wall spacing and an estimate $\lambda/c_E \cong 10^{-2} \text{ cm}^2/\text{s}$, which are close to the corresponding values for TGS and BaTiO₃ (Maier et al., 1980; Marvan, 1969), we find $\omega_{\max}/2\pi \cong 1 \text{ MHz}$. Thus, in polydomain ferroelectrics, this mechanism is expected to cause frequency dispersion of the susceptibility and a loss maximum in the radio frequency range.

The strength of the effect can be characterized by the parameter $Tp^2/\chi^T c_E$. In a ferroelectric undergoing the phase transition close to the second order this parameter does not exhibit strong critical (i.e., as a function of $T_C - T$) temperature dependence (in terms of the P^4 -Landau expansion $p^2/\chi^T = \text{const.}$) For TGS and BaTiO₃ at room temperature, it has a value of the order of 0.1. Thus for the real part of the susceptibility the effect is small. On the other hand, for the loss tangent, the expected contribution of a few percent in the maximum can be appreciable. According to Maier et al. (1980), who treated the problem in the Debye approximation, this loss mechanism can be relevant to the experimental situation in KDP, TGS, and BaTiO₃.

8.8.2.3 Piezoelectric Clamping

An important feature of ferroelectrics is the piezoelectric effect providing a linear coupling between the polarization and deformation. In view of this coupling the mechanical conditions can affect the value of the dielectric permittivity. One can readily show that the full or partial mechanical clamping leads to a reduction of the permittivity. Such clamping effect can manifest itself in a reduction of the permittivity of a single-domain ferroelectric when it breaks into domains. In this case, the mechanical clamping is conditioned by the difference in the tensors of the piezoelectric coefficients of neighboring domains. Such difference leads to that in the piezoelectric strains induced by the measuring electric field in the neighboring domains. Since the latter are in physical contact, this leads to their partial mechanical clamping.

The effect of this kind of clamping on the permittivity of a ferroelectric was first documented and explained by Drougard and Young (1954) for BaTiO₃ crystals. They monitored the permittivity of a Remeika-grown *c*-domain crystal as a function of the additional slowly changing electric field (with a rate of 30 V/cm/min). This field was large enough to reverse its spontaneous polarization. The crystal exhibited very abrupt switching so that at any field, except for the narrow intervals around the coercive field, it was always in a single-domain

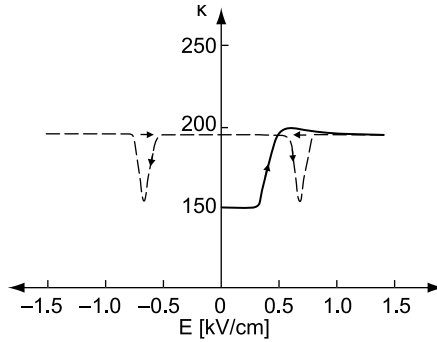


Fig. 8.8.2 Dielectric permittivity of a *c*-domain BaTiO₃ crystal (measured with an ac electric field with amplitude 1.45 V/cm and frequency 20 KHz) as a function of quasistatic additional strong ac field (amplitude 1.5 kV/cm and frequency 10⁻⁵ Hz); the aspect of experimentally obtained plots. Room temperature. The sense of the variation of the strong field is shown with *arrows*. In the original state, the sample was depoled by 60 Hz cycling with decreasing field amplitude. After Drougard and Young (1954)

state. An appreciable reduction of the permittivity within these field intervals was documented as shown in Fig. 8.8.2. The effect was attributed to a manifestation of a dense 180° domain pattern existing in the crystal during the polarization reversal. In such pattern, the neighboring domains differ in the sign of the ϵ_{33} component of the piezoelectric strain (X_3 -axis is set parallel to both the polar axis of the crystal and to the direction of the applied field). In the dense domain pattern this leads to the clamping of this strain component. The impact of such clamping on the permittivity can be evaluated from the following constitutive equations:

$$\begin{aligned} D_3 &= \epsilon_0 \kappa_{33}^{\text{free}} E_3 + d_{333} \sigma_{33} \\ \epsilon_{33} &= d_{333} E_3 + s_{3333} \sigma_{33}, \end{aligned} \tag{8.8.13}$$

where $\kappa_{33}^{\text{free}}$, d_{333} , and s_{3333} are the corresponding components of the dielectric permittivity at constant stress, the piezoelectric coefficient, and the elastic compliance at constant field. Using condition $\epsilon_{33} = 0$, the value of the clamped permittivity can be found from Eq. (8.8.13) as

$$\kappa_{33}^{\text{cl}} = \kappa_{33}^{\text{free}} \left(1 - \frac{d_{333}^2}{\epsilon_0 s_{3333} \kappa_{33}^{\text{free}}} \right). \tag{8.8.14}$$

The reduction of the permittivity in a polydomain sample described by this equation can be observed at ac frequencies lower than the frequency of the piezoelectric resonance. At such frequencies the measured permittivity of single-domain crystal should be equal to $\kappa_{33}^{\text{free}}$. At frequencies higher than the piezoelectric resonance, already the single-domain sample will exhibit the

clamped value of the permittivity. Thus, at these frequencies the effect on polydomain clamping of the permittivity will be absent. This behavior was experimentally confirmed by Fousek (1965a,b) who measured the permittivity of a polydomain BaTiO₃ crystal below and above the piezoelectric resonance. In this experiment, the domain population of the crystal was stepwise changed by the application of dc-field pulses and the permittivity was measured between the pulses (in the absence of the dc field). Below the resonance Fousek documented a decrease in the permittivity with increasing domain population, in agreement with the results by Drougard and Young. Whereas, above the resonance, it was found that the introduction of new domain into the system leads to an increase in the permittivity. The latter effect was attributed to the contribution of the wall motion to the permittivity.¹⁶

The experimental data shown in Fig. 8.8.2 are in good agreement with Eq. (8.8.14). For BaTiO₃ at room temperature using the material parameters $s_{3333} = 16 \times 10^{-12} \text{ m}^2/\text{N}$, $d_{333} = 90 \times 10^{-12} \text{ C}/\text{N}$, and $\kappa_{33}^{\text{free}} = 185$, one finds $d_{333}^2 / \epsilon_0 s_{3333} \kappa_{33}^{\text{free}} = 0.31$. This implies a clamping reduction of the permittivity close to that observed experimentally.

It should be mentioned that the experimental situation reported by Drougard and Young, where a decrease in the permittivity at the coercivity is observed, is rare. It seems to take place due to very slow switching. Typically, the C - V curves (the differential capacitance vs. the applied voltage) driven by a field of much higher frequency demonstrate maxima instead of minima at the coercive voltage. This behavior will be discussed in the next section.

8.8.3 Contributions from Moving Domain Walls in Ideal Crystals

As was discussed in Sect. 8.4 the macroscopic displacements of domain wall are possible in the two regimes: thermally activated and non-activated. In the former, the wall motion from one minimum of the Peierls potential to another is assisted by thermal fluctuations. Whereas, in the latter, the applied field is strong enough to suppress the barriers of the Peierls potential and the motion can take place without the assistance of thermal fluctuations. When treating the small-signal dielectric response associated with the wall displacements, one should also take into account that wall displacements are also possible inside one minimum of the Peierls potential. Thus, there exist three situations (activated, non-activated, and “inside-one-minimum” regimes) to be addressed in the context of the domain wall contribution to small-signal dielectric response. In this section we will treat these situations for the case where domain walls remain on average flat while moving. Here we do not exclude the case of local wall bending by thermal fluctuations like in the Miller–Weinreich model. The moving wall within this model we consider as flat on average. The assumption that a wall remains flat on average when moving sounds realistic for domain walls in an ideal (defect-free) crystal.

¹⁶ See discussion in the next section.

8.8.3.1 Wall Near the Bottom of Peierls Potential

Consider motion of a ferroelectric domain wall in a minimum of the Peierls potential staying close to its bottom. The wall is treated as a hard interface. For simplicity, let it be a 180° wall. The potential energy (per unit area) of such wall counted from its equilibrium position can be evidently written as

$$W_w = \frac{1}{2} Kx^2, \quad (8.8.15)$$

where x is the wall displacement from its equilibrium position. The “rigidity constant” K can be evaluated if the barrier height of the Peierls potential, V_{P_0} , is known. Assuming that $W_w \cong V_{P_0}/2^{17}$ at $x = c/4$ (where c is the lattice constant in the direction of the wall motion) we find

$$K \cong 4V_{P_0}/c^2. \quad (8.8.16)$$

In a small electric field E , a pressure of $2P_S E$ is applied to the wall. Using Eq. (8.8.15) one readily finds the field-induced displacement of the wall $x = 2P_S E/K$. If the sample contains many domain walls with the typical wall spacing L , their displacements by a distance x will lead to a polarization variation of the sample $P = 2P_S x/L$. All in all, one finds the contribution of this system of walls to the dielectric permittivity in the following form:

$$\kappa_w \cong \frac{P_S^2 c^2}{V_{P_0} L \epsilon_0}. \quad (8.8.17)$$

It is instructive to evaluate this value for tetragonal BaTiO_3 crystal for the typical domain wall spacing $L = 1 \mu\text{m}$. Using the following values of the material parameters: $P_S = 0.25 \text{ C/m}^2$, $c = 0.4 \text{ nm}$, and $V_{P_0} = 0.05 - 0.07 \text{ mJ/m}^2$ (Burtsev and Chervonobrodov, 1982) we find $\kappa_w = 16 - 23$. This is close to the values of $\kappa_w = 15 - 30$ reported by Fousek for the domain contribution in this crystal at room temperature (Fousek, 1965a,b). In this study the permittivity was measured at frequencies above the piezoelectric resonance so that the domain clamping effect was suppressed (see discussion in the previous section).

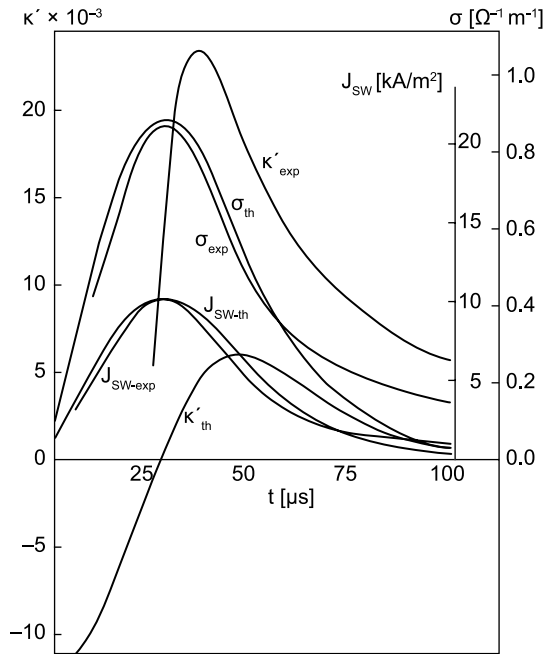
8.8.3.2 Dielectric Response of Moving Domain Walls and $C-V$ Curves

It was found already in early works on BaTiO_3 that during not too slow switching the small-signal dielectric permittivity can be strongly enhanced (Drougard et al., 1954). Nowadays, monitoring the small-signal dielectric response as a function of changing bias is often used for characterization of ferroelectric thin films. The result of such monitoring is customarily called $C-V$ curve (differential capacitance vs. applied voltage). In such experiments, in contrast to the situation discussed in Sect. 8.8.2.3, the dielectric response of

¹⁷ This is an exact relation for a model for the potential made of segments of parabolas “ x^2 ” and “ $-x^2$.”

moving walls is monitored. This makes an essential difference. In this aspect, a very similar situation occurs when the small-signal dielectric permittivity is monitored during pulse switching. However here, the analysis of the experimental data is simpler since the walls move in a virtually constant electric field. For the case of the pulse switching, an appreciable increase in the permittivity was documented for TGS and $\text{LiH}_3(\text{SeO}_3)_2$ by Fatuzzo (1961) while a comprehensive set of data for BaTiO_3 and TGS was reported by Fousková and Janousek (1965). Some of the data on BaTiO_3 by Fousková and Janousek are shown in Fig. 8.8.3. Here, the real part of the permittivity, κ' , the ac conductivity, $\sigma = \omega\epsilon_0\kappa''$, and the switching current are plotted as functions of time. An enormous increase in κ' up to 20,000 is clearly seen.

Fig. 8.8.3 Experimental curves (indexed with “exp”) of time dependence of the switching current density (J_{SW}), relative permittivity (κ') measured at 100 kHz, and equivalent parallel conductivity ($\sigma = \omega\epsilon_0\kappa''$) measured at 2 MHz during switching in a BaTiO_3 crystal and the results of the calculations (indexed with “th”) according to Eqs. (8.8.24), (8.8.29), and (8.8.23b). After Fouskova (1965)



This phenomenon was modeled in terms of a Kolmogorov–Avrami-type model for the two-dimensional domain growth by Fousková (1965). In this theory, one calculates the switching current induced by the combined action of a large dc and small ac components of the electric field

$$E = E_{\text{dc}} + E_m \cos \omega t. \tag{8.8.18}$$

The ac component of the current density, which is calculated to within the linear terms in E_m , is interpreted as

$$J_{\text{ac}} = \omega E_m \epsilon_0 (-\kappa' \sin \omega t + \kappa'' \cos \omega t), \tag{8.8.19}$$

where κ' and κ'' are the real and imaginary parts of the permittivity. Such determination of κ' and κ'' is fully consistent with the customary experimental measurement technique. Below we will explain the basic idea of this theory. In addition, we will demonstrate that, calculated or/and measured κ' and κ'' in this way may not give the true value of the permittivity but an apparent value. For the theory by Fousková (1965), for example, the calculated value of κ' is apparent while its true value is zero.

Consider domain walls in a crystal under the combined action of a large dc and small ac components of the electric field given by Eq. (8.8.18). Since the switching is addressed, the field E_{dc} is supposed to be large enough to free the wall from the minima of the Peierls potential during its application, the wall velocity being a function of the applied field, $v(E)$.¹⁸ Thus, the walls are moving with a slightly time-modulated velocity

$$v(E) \approx v(E_{dc}) + \frac{\partial v}{\partial E} E_m \cos \omega t \equiv v_0(1 + \gamma E_m \cos \omega t), \quad (8.8.20)$$

where $\gamma = (\partial v / \partial E) / v(E)$ at $E = E_{dc}$ and $v_0 = v(E_{dc})$. The contribution of such motion to the permittivity depends on the domain growth geometry at switching.

It is instructive to start with the simplest situation. We consider the initial stage of switching controlled by the one-dimensional 180° domain growth (see Fig. 8.7.6a) from N planar nuclei (of zero width) spread over the distance B . By the initial stage we mean the stage where the domain overlapping can be neglected. Here, the polarization as a function of time can be written as

$$P = \frac{2P_S}{B} 2N \int_0^t v(E) dt - P_S. \quad (8.8.21)$$

This leads to the amplitude of the ac current

$$J_{ac} = J_{SW} \gamma E_m \cos \omega t \quad (8.8.22)$$

expressed in terms of the switching current

$$J_{SW} = 4P_S v_0 N / B. \quad (8.8.23)$$

Now using Eq. (8.8.19) we find that $\kappa' = 0$ and

$$\kappa'' = J_{SW} \frac{\gamma}{\omega \epsilon_0}. \quad (8.8.24)$$

This is a naturally expected result: The real part of the permittivity is absent since there is no “restoring force” in the system and the contribution to the imaginary part is as from the pure conduction.

¹⁸ This dependence can correspond to any regime of wall motion (activated or non-activated).

Now let us address as the next step the initial stage of switching controlled by the two-dimensional domain growth (see Fig. 8.7.6b) from N nuclei (of zero area) spread over the area A . Here, the polarization as a function of time reads

$$P = \frac{2P_S}{A} N\pi \left(\int_0^t v(E) dt \right)^2 - P_S. \quad (8.8.25)$$

From this equation one readily finds for the total current

$$J = \frac{4P_S}{A} N\pi v_0^2 (1 + \gamma E_m \cos \omega t) \left(t + \int_0^t \gamma E_m \cos \omega t dt \right) \quad (8.8.26)$$

and the amplitude of the ac current

$$J_{ac} = J_{SW} \gamma E_m \left(\cos \omega t + \frac{1}{\omega t} \sin \omega t \right) \quad (8.8.27)$$

expressed in terms of the switching current, which now has the form

$$J_{SW} = \frac{4P_S \pi N v_0^2 t}{A}. \quad (8.8.23a)$$

For the two-dimensional domain growth like for the one-dimensional one, there is no “restoring force” so that $\kappa' = 0$ is expected. However this is not the case. From Eq. (8.8.27) we see that the imaginary part of the permittivity is still given by Eq. (8.8.24) with the switching current coming from Eq. (8.8.23a). At the same time, now there appears a nonzero real part of the permittivity

$$\kappa' = -J_{SW} \frac{\gamma}{\omega^2 t \epsilon_0}. \quad (8.8.28)$$

The presented calculations for the two-dimensional domain growth illustrate the concept of the calculations for the switching-stimulated permittivity enhancement performed by Fouskova (1965). She considered the problem in terms of two models: the β -model (no additional nucleation during switching) with the nucleus radius r_0 (see Sect. 8.7.4) and the Fatuzzo model with the nucleation rate given by Eq. (8.7.25). For the β -model, it was found that

$$\kappa' = -J_{SW} \frac{\gamma}{\omega^2 t \epsilon_0} \left[1 - \frac{2\pi N}{A} (v_0 t + r_0)^2 \right] \frac{1}{1 + r_0/v_0 t} \quad (8.8.29)$$

with

$$J_{SW} = \frac{4P_S \pi N v_0^2 t}{A} (1 + r_0/v_0 t) \exp \left[-\frac{\pi N v_0^2 t^2}{A} (1 + r_0/2v_0 t) \right] \quad (8.8.23b)$$

while for κ'' Eq. (8.8.24) holds. One readily checks that Eqs. (8.8.29) and (8.8.23b) are consistent with Eqs. (8.8.28) and (8.8.23a) in the limit $r_0 \rightarrow 0$ and $t \rightarrow 0$. For the Fatuzzo model, more complicated relations were obtained.

The comparison of the theoretical predictions given by Eqs. (8.8.24), (8.8.29), and (8.8.23b) to the experimental data for BaTiO₃ is shown in Fig. 8.8.3. Here the parameters of the theory are determined from the fit of the switching current to Eq. (8.8.23b) and then the curves for κ' and κ'' are plotted according to Eqs. (8.8.24), (8.8.29), and (8.8.23b). Here a good quantitative agreement is seen for κ'' , while for κ' one can speak only of qualitative agreement. The fit to the Fatuzzo-model-based calculations is qualitatively similar but quantitatively better (less pronounced area with $\kappa' < 0$).¹⁹ When applied to TGS, the approach by Fouskova leads to a similar quality description.

Concerning the theory presented above one can naturally raise the following questions. What is the “restoring force” behind the large κ' in the case of the two-dimensional switching in contrast to the one-dimensional case where $\kappa' = 0$? How the domain wall contribution to the permittivity can be negative (see Eq. (8.8.28))? The single answer to these two questions is that, in a sense, the calculated nonzero κ' is not the “true” real part of the permittivity as it is defined by Eq. (8.8.2) and there is no “restoring force” behind it in the case of the two-dimensional switching like that in the one-dimensional case. This is clear from the following simple example.

Let us consider a domain having the boundary area S and let the boundary oscillate under the action of an ac electric field $E = E_m \cos \omega t$ with velocity $v(E)$ proportional to the instant value of the field. The contribution of such motion to the total polarization obviously obeys the following relation:

$$P_{ac} \propto S \int_0^t v(E) dt' \propto S \sin \omega t \quad (8.8.30)$$

that leads to $\kappa'' \neq 0$ and $\kappa' = 0$. This situation corresponds to the one-dimensional case. Now let S slowly grow with time. This would lead to a slow growth of the amplitude of P_{ac} . If $S \propto t$, we find

$$P_{ac} \propto t \sin \omega t. \quad (8.8.31)$$

Physically this relation should be interpreted as $\kappa'' \propto t$ and $\kappa' = 0$. However, formally calculating the ac current (as $J \propto \partial P / \partial t$) we find

$$J_{ac} \propto \sin \omega t + t \omega \cos \omega t. \quad (8.8.32)$$

Comparing this relation with Eq. (8.8.19), one finds that κ' is nonzero and negative. Thus, the “current” method of determination of κ' “takes” the linearly increasing loss for time independent and negative κ' . The value of the apparent

¹⁹ A negative contribution to the permittivity at switching was also found in calculations by Landauer et al. (1956).

κ' can also be positive. For example, at the end of switching, when the domain wall area decreases with time, on the same line one finds $\kappa' > 0$. The change of the sign of κ' during the switching predicted by Eq. (8.8.29) actually corresponds to the crossover from growing to decreasing total domain wall area.

It is worth to indicate one more aspect in which the just discussed contribution to κ' is not a “true” contribution: For a static domain pattern corresponding to a snapshot of an evolving in time domain pattern this contribution vanishes.

Concluding the discussion of the small-signal response at switching the following remarks should be made. When κ' is determined from the ac component of the switching current (as customarily done) it clearly contains a spurious contribution that does not correspond to the in-phase component of the electric displacement. However, this contribution does not seem to be the only contribution to κ' at switching. The point is that, according to the modeling, a time interval at the beginning of switching is expected, where this contribution must be negative while this has not been experimentally observed. The additional true contribution, which would explain the increase in κ' at the beginning of switching, may be attributed to a real restoring-force-controlled motion of domain walls. Here, in an ideal defect-free crystal, such motion is possible at the bottom of the Peierls potential, where a domain wall resides between the jumps of the Miller–Weinreich scenario. In terms of such mechanism, the increase in κ' can be interpreted as a result of an increasing number of the walls participating in switching. Another scenario associated with the restoring-force-controlled wall motion was developed by Fatuzzo (1961).

In the context of the aforementioned spurious contribution to κ' at switching, it becomes clear that the information delivered on the domain pattern by C – V measurements can be essentially different when such measurements are done in the continuous and step modes. In the latter method, which is nowadays often used, the driving voltage is applied stepwise and the permittivity is measured at the ends of the steps when the walls can be in motion or immobile, depending on the step length. This, may imply an appreciable impact of the step length on the results of the measurement.

8.8.3.3 Dispersion of the Dielectric Response Due to Free Domain Walls

Any domain wall motion is associated with motion of the atoms of the crystal at the moments when the wall passes through them. This atomic motion in turn is associated with relaxation processes and some acceleration of the atoms. For this reason the wet friction coefficient and effective mass can be ascribed to the wall. These parameters of the wall can be readily introduced in terms of the Ginzburg–Landau theory. In Sect. 8.4.4, devoted to the motion of a 180° domain wall with a constant velocity, we have demonstrated a derivation of the friction coefficient starting from the equation of motion for the polarization

$$\zeta \ddot{P} + \eta \dot{P} - \delta \frac{\partial^2 P}{\partial x^2} + \alpha P + \beta P^3 = E. \quad (8.8.33)$$

On the same line, the equation for the accelerated wall motion can be obtained (Sannikov, 1962). Here, the calculations are virtually identical to those given by Eqs. (8.4.25), (8.4.26), (8.4.27), (8.4.28), (8.4.29), and (8.4.30) except for the polarization profile for the moving wall, which should be taken in a more general form, namely $P = P_0(x - x_0(t))$ where $x_0(t)$ is the position of the center of the wall. Such calculations readily lead to the equation of wall motion

$$M_w \ddot{x}_0(t) + \beta_w \dot{x}_0(t) = 2P_S E \quad (8.8.34)$$

which generalizes Eq. (8.4.30). Here

$$M_w = \frac{4P_S^2}{3t_{th}} \zeta \quad \text{and} \quad \beta_w = \frac{4P_S^2}{3t_{th}} \eta \quad (8.8.35)$$

are the effective mass and wet friction coefficient of the wall per unit area, respectively, with t_{th} being the half thickness of the domain wall defined by Eq. (6.2.6). For a ferroelectric containing walls spaced by the distance L , the corresponding complex permittivity (actually its complex conjugated) can be found in the form

$$\kappa^* = \frac{3t_{th}}{L\zeta} \frac{1}{i\omega\Gamma_0 - \omega^2}. \quad (8.8.36)$$

$$\Gamma_0 = \frac{\eta}{\zeta}. \quad (8.8.37)$$

Here Γ_0 is the damping for the linear polarization dynamics governed by Eq. (8.8.33), which typically lies in the THz range. Thus, in radio frequency range the dielectric response is strongly dominated by the friction, which is equivalent to a shunting conduction

$$\sigma = 3 \frac{t_{th}}{L\eta}, \quad (8.8.38)$$

where, for BaTiO₃, with 1 μm spacing between the walls, taking $\Gamma_0 = 10^{13} \text{ s}^{-1}$ and $\zeta\epsilon_0 = 10^{-29} \text{ s}^2$ (Vaks, 1973) we find $\sigma = 300 \text{ m}^{-1}\Omega^{-1}$. Such conductivity is comparable to the room temperature conductivity in doped Si. Thus, we see that the continuous Ginzburg–Landau description of the wall motion corresponds to an extremely lossy material. However, this result may correspond to a realistic experimental situation when the effect of the Peierls potential can be neglected. For instance, such situation takes place at ac field amplitudes larger than 10 kV/cm (see Sect. 8.4.1). For smaller amplitudes, the wall in principle can be considered as free if the ac field frequency is low enough so that, during its period, the thermal fluctuations can essentially help the wall in overcoming the Peierls potential barriers. However, in this case, the above approach should be modified to incorporate the effect of thermal fluctuations. To the best of our knowledge, such description is not presently available in the literature.

At the same time, the problem can be addressed for the situation where the wall moves inside a single minimum of the Peierls potential. In this case the appropriate restoring force can be incorporated in the equation. As a result, the equation for the wall motion becomes (cf. Eqs. (8.8.15) and (8.8.16))

$$M_w \ddot{x}_0(t) + \beta_w \dot{x}_0(t) + Kx_0(t) = 2P_S E, \quad (8.8.39)$$

where the rigidity constant K is coming from Eq. (8.8.16). This equation describes the dielectric response of a damped oscillator so that the equation for the complex permittivity becomes

$$\kappa^* = \frac{3t_{th}}{L\zeta} \frac{1}{\Omega_W^2 - \omega^2 + i\omega\Gamma_0}, \quad (8.8.40)$$

$$\Omega_w = \sqrt{\frac{3t_{th} V_{P0}}{\zeta P_S^2 c^2}} = \Omega_0 \sqrt{\frac{V_{P0} t_{th}}{\sigma_w c}}. \quad (8.8.41)$$

Here $\Omega_0 = \sqrt{2|\alpha|/\zeta}$ is the resonance frequency of the linear polarization dynamics governed by Eq. (8.8.33); $\sigma_w = 2|\alpha|P_S^2 t_{th}/3$ is the surface wall energy per unit area in the Ginzburg–Landau theory (see Eq. (6.2.10c)).

Let us evaluate the dielectric response described by Eq. (8.8.40) for the case of BaTiO₃. Using for the Peierls barrier, as before, $V_{P0} = 0.05 - 0.07$ mJ/m² and taking $t_w = 2t_{th} \cong 2c$ for the wall thickness and $\sigma_w \cong 10$ mJ/m² for its energy, we find $\sqrt{V_{P0}/\sigma_w} t_{th}/c \cong 1/10$. This means that the resonance frequency Ω_w associated with the wall oscillations at the bottom of the Peierls potential is expected to be one order of magnitude lower than the soft-mode frequency Ω_0 . At the same time, in BaTiO₃, the soft-mode is over-damped, i.e., $\Gamma_0 > \Omega_0$. Thus, the obtained dielectric response corresponds to an over-damped oscillator. This also means that the inertia of the wall (i.e., its effective mass) plays a negligible role in the response. It is virtually of the Debye type, with a rather high relaxation frequency $\sigma/(2\pi\kappa_w\epsilon_0) \cong 0.25$ THz. At this frequency the imaginary part of the permittivity reaches a modest value of $\kappa_w/2 \cong 10$.

8.8.4 Quasistatic Bending Contribution from “Firmly” Pinned Domain Walls

Let us address the dielectric response of a domain wall coupling with the imperfections of a crystal. Typically this coupling is much stronger than the Peierls potential so that we will neglect the latter in the further consideration. The wall–defect coupling, as was discussed in Sects. 6.4 and 8.5, leads to the wall roughening and can strongly affect its coercivity. For the small-signal dielectric response, i.e., for the fields much smaller than the coercive field, this coupling provides a restoring force for the wall motion. This force is due to an energy

increase associated with the bending of the wall from its position in the absence of the applied field. In contrast to the above treatment, the problem becomes essentially multidimensional so that the Ginzburg–Landau description of the problem requires incorporation of all spatial derivatives in the equation of motion for the polarization (z -component), i.e., Eq. (8.8.33) should be generalized to the form

$$\zeta \ddot{P} + \eta \dot{P} - \delta_{33ij} \frac{\partial^2 P}{\partial x_i \partial x_j} + \alpha P + \beta P^3 = E. \quad (8.8.42)$$

In this case, the equation of motion (and bending) of the wall can be obtained with the calculations which are similar to those given by Eqs. (8.4.25), (8.4.26), (8.4.27), (8.4.28), (8.4.29), and (8.4.30). The difference is that now the polarization profile should be taken in a yet more general form, namely $P = P_0(x - x_0(y, z, t))$, where $x_0(y, z, t)$ is the x -coordinate of the wall center counted from a reference YZ -plane. Such calculations readily lead to the following equation of wall motion (Laikhtman, 1973):

$$M_w \ddot{x}_0 + \beta_w \dot{x}_0 + g_{\alpha\beta} \frac{\partial^2 x_0}{\partial x_\alpha \partial x_\beta} = 2P_S E, \quad (8.8.43)$$

$$g_{\alpha\beta} = \frac{4P_S^2}{3t_{th}} \delta_{33\alpha\beta}, \quad (8.8.44)$$

where α and β can acquire values 2 and 3. This equation is actually the equation of motion for an anisotropic membrane with the surface tension tensor $g_{\alpha\beta}$. If the in-plane wall anisotropy is neglected, this tensor can be expressed in terms of the surface wall energy per unit area: $g_{\alpha\beta} = \sigma_w \delta_{\alpha\beta}$ (attention, $\delta_{\alpha\beta}$ is the Kronecker δ). However, the wall dynamics is, in general, different from that of a membrane since E entering Eq. (8.8.43) is not just the applied field. It also contains the depolarizing component caused by the bound charges which can appear at the wall bending. This effect provides additional “non-local” stiffness to the wall. To complete the description of the wall motion, the coupling with the defects should also be incorporated in the equation of motion to find

$$M_w \ddot{x}_0 + \beta_w \dot{x}_0 + g_{\alpha\beta} \frac{\partial^2 x_0}{\partial x_\alpha \partial x_\beta} + \sum_i \frac{\partial U_i(x_0)}{\partial x_0} = 2P_S E, \quad (8.8.45)$$

where $U_i(x_0)$ is the energy of the wall interaction with the i th defects of the system. For the case of random bond and random field defects this energy was introduced in Sect. 6.4.1 (see Fig. 6.4.2).

The contribution of a domain wall to the dielectric permittivity in terms of Eq. (8.8.45) has been addressed by many authors. In the present section we consider the quasistatic response (all time derivatives are neglected) of a domain wall which is “firmly” pinned by the defects, i.e., the applied ac field does not

cause any depinning (even local) so that under the field the wall just bulges between the pinning centers. First, to clarify the approach, we will roughly estimate such dielectric response in the simplest approximation where the depolarizing effect is neglected. Later we will consider the results of calculations for more realistic situations.

Consider a wall pinned by defect with spatial separation l_p so that the defect breaks it into segments of area $S_p \cong l_p^2$, which can freely bend. Let the applied field induce the segment bowing with the maximal deflection w . The value of this deflection is controlled by the balance between the work done by the external pressure $2P_S E$, which is about $2P_S E w S_p$, and the variation of the surface energy of the wall $\sigma_w w^2$ (cf. Eq. (6.4.7)). This yields $2P_S E S_p / \sigma_w$ and $4P_S^2 E S_p^2 / \sigma_w$ for the maximal wall deflection and the dipole moment produced by this deflection. Taking into account that the number of movable segments per unit area of the wall is inversely proportional to S_p , the contribution to the dielectric permittivity of a multidomain sample with the typical wall spacing L can be found in the form

$$\kappa_w \cong S_p \frac{4P_S^2}{\sigma_w L \varepsilon_0}. \quad (8.8.46)$$

The spatial separation of the pinning defect in the wall l_p , which essentially controls this contribution (since $S_p \cong l_p^2$), is sensitive to the pinning regime. The treated case of the “firmly” pinned wall corresponds to the strong pinning which, according to Sect. 8.5, occurs when the energy of defect-wall coupling v is large enough to satisfy the condition

$$v \gg \sigma_w t_w^2. \quad (8.5.47)$$

This inequality means that it is favorable for the wall to be captured by the defects spaced from its flat position by the distance larger than the wall thickness. At such capture, the gain from the pinning v would be more than the extra surface energy $\sigma_w t_w^2$. Specifically, it is favorable for the wall to be captured by the defects spaced from its flat position up to the distance

$$w_{\text{cap}} = \sqrt{v / \sigma_w}. \quad (8.8.48)$$

For a wall segment deflected by such distance, the two competing contributions to its energy are equal. Then, the number of the pinning defects per unit area of the wall, $1/S_p$, can be found from the evident relation $S_p w_{\text{cap}} = 1/n$. This finally leads to $1/S_p = n w_{\text{cap}} = n \sqrt{v / \sigma_w}$ and

$$\kappa_w \cong \frac{4P_S^2}{\varepsilon_0 \sigma_w L n t_w} \sqrt{\frac{\sigma_w t_w^2}{v}} = \frac{4P_S^2}{\varepsilon_0 L n \sqrt{v \sigma_w}}. \quad (8.8.49)$$

The approach outlined above has been applied by Darinskii et al. (1989b) to the analysis of the dielectric response associated with ferroelectric wall in the strong-pinning regime but without the neglect of the depolarizing effect. In addition, the analysis was performed in a more quantitative manner. The result obtained for the extrinsic contribution to the permittivity

$$\kappa_w = \frac{8P_S^2}{\varepsilon_0 L n \sqrt{v\sigma_w}} \left(\frac{L_{\text{dip}}}{t_w} \right)^{1/4}, \quad (8.8.50)$$

$$L_{\text{dip}} = \frac{\sigma_w \varepsilon_0 \kappa_{\text{lat}}}{P_S^2} \quad (8.8.51)$$

inherits from Eq. (8.8.49) the concentration dependence and the dependence on v . Here L_{dip} is the spatial scale introduced in Sect. 6.4.3 and κ_{lat} is the lattice contribution to the permittivity of the ferroelectric. The depolarizing effect taken into account in Eq. (8.8.50) influences the dielectric response via two competing trends. This effect makes the wall stiffer—this should lead to a reduction of the response. At the same time, the stiffer wall should be captured by less defects—this should enhance the response. This competition is reflected in the extra factor $2(L_{\text{dip}}/t_w)^{1/4}$ in Eq. (8.8.50) compared to Eq. (8.8.49). What trend wins depends on the relation between the spatial scales L_{dip} and t_w .

The same authors (Darinskii et al., 1989b) have also analyzed the case of 180° ferroelectric/ferroelastic wall separating domains which differ in the sign of the spontaneous shear strain. This situation required taking into account the long-range elastic forces which affect both the wall stiffness (cf. Sect. 8.4.3) and the capture of the wall by defects. The contribution to the permittivity in the strong-pinning regime was found in the following form:

$$\kappa_w = \frac{4\sqrt{2}}{\varepsilon_0 L n} \left(\frac{\pi^3 \kappa_{\text{lat}} P_S^3}{\mu \varepsilon_S^2 v^2 t_w} \right)^{1/4}, \quad (8.8.52)$$

where ε_S and μ are the absolute value of the spontaneous strain and the shear modulus, respectively (the elastic effect were taken into account in the isotropic approximation). Though this result essentially differs from (8.8.49) to (8.8.50) it shares their common feature, namely $1/\kappa_w \propto n\sqrt{v}$.

8.8.5 Limited Motion of Free Domain Wall

The discussions from the preceding sections outline a clear picture of how ferroelectric domain walls contribute to the dielectric response. A ferroelectric domain wall not restrained in its motion by pinning against the Peierls barriers and/or crystalline defects contributes only to the imaginary part of the permittivity so that

$$\kappa_w \propto \frac{1}{i\omega}. \quad (8.8.53)$$

However, in the presence of the pinning, the restoring forces appear together with real part κ_w . Putting aside the Peierls potential effect, one clearly sees the origin of the latter in the wall bending which provides a quasi-harmonic restoring force. However, it occurs that even without wall bending the wall-defect interaction can lead to the appearance of a contribution to the real part of κ_w . Such situation takes place when the displacement of the wall is limited by some obstacles, e.g., by strong repulsive random bond defects. This situation can be illustrated with a simple model. Consider a wall moving as a hard surface so that the bending contribution is excluded. If, during the cycle of the measuring ac field, the wall does not meet any obstacle then the dielectric response is purely dissipative. This holds for *any wall mobility law* $v = v(E)$. However, if the distance, which the wall has for its free motion, is smaller than the swing of the wall displacement (in the unlimited motion for the given field amplitude and frequency), the wall will spend some time standing by the obstacle. During this period of time, the wall is “waiting” when the field changes its sign, only then it will leave the obstacle. The direct calculations of the first polarization harmonics show the appearance of the contribution to the real part of the permittivity once the wall motion is limited. For a system of domain walls distributed with the linear density L^{-1} whose motion is confined by the distance L_{free} , the extrinsic contribution to the permittivity reads²⁰ (Tagantsev and Fousek, 1999)

$$\kappa'_w = \frac{2}{\omega \pi L \varepsilon_0 E_m} \int_0^{\phi_0} v(E_m \sin \phi) \cos \phi \, d\phi, \quad (8.8.54)$$

$$\kappa''_w = \frac{2}{\omega \pi L \varepsilon_0 E_m} \int_0^{\phi_0} v(E_m \sin \phi) \sin \phi \, d\phi, \quad (8.8.55)$$

where E_m is the amplitude of the probing ac field. Here ϕ_0 is the width of the phase interval during which the wall moves between the stuck positions at the obstacles. Obviously $0 < \phi_0 < \pi$; it can be found as the corresponding root to the equation

$$\int_0^{\phi_0} v(E_m \sin \phi) \, d\phi = \omega L_{\text{free}}. \quad (8.8.56)$$

One can readily check that, formally, the non-restricted wall motion is described by Eqs. (8.8.54) and (8.8.55) with $\phi_0 = \pi$. Noting that, at $\phi_0 = \pi$, the integral from Eq. (8.8.54) is zero for *any mobility law* $v = v(E)$ we see that, indeed, for the not restricted wall motion always $\kappa'_w = 0$.²¹

²⁰ In the original paper in these equations a factor of ‘ $2/\omega$ ’ is missing. Further in this paper, there are factors of ‘2’ missing in the definition of the normalizing constants χ_ω , ζ_ω , and χ_M .

²¹ The above derivation proves that $\kappa'_w = 0$ for any arbitrary non-hysteretic dependence $v = v(E)$. On the same lines, one readily shows that this also holds for an arbitrary hysteretic dependence $v = v(E)$.

Tagantsev and Fousek (1999) have applied relations (8.8.54) and (8.8.56) to the cases of the exponential and linear wall mobility laws. Here we present the results for the latter case, i.e., $v(E) = \mu E$. The results obtained for the exponential wall mobility law, though being quantitatively different, are qualitatively similar to those obtained for the linear mobility law. For $v(E) = \mu E$, the expressions for the components of complex permittivity were found in the following form:

$$\kappa'_w = \frac{\kappa_0(\omega)}{\pi} \sin^2 \phi_0, \tag{8.8.57}$$

$$\kappa''_w = \frac{\kappa_0(\omega)}{2\pi} (2\phi_0 - \sin 2\phi_0), \tag{8.8.58}$$

$$\cos \phi_0 = 1 - \frac{2\omega}{\omega_E}, \tag{8.8.59}$$

where $\kappa_0(\omega) = \frac{2\mu P_s}{\omega L \epsilon_0}$ and $\omega_E = \frac{2\mu E_m}{L_{free}}$. Equations (8.8.57), (8.8.58), and (8.8.59) are applicable on condition that $\omega < \omega_E$. The situation, where $\omega > \omega_E$ and Eq. (8.8.59) has no solution, corresponds to the wall motion without reaching the obstacles, i.e., to the purely dissipative dielectric response: $\kappa''_w \propto 1/\omega$ and $\kappa'_w = 0$.

The frequency and amplitude dependences of the dielectric response described by Eqs. (8.8.57), (8.8.58), and (8.8.59) are shown in Fig. 8.8.4a and b. Figure 8.8.4c shows the corresponding Cole–Cole plot. In Fig. 8.8.4b and c, the components of the permittivity are shown normalized to the value

$$\kappa_E = \kappa_0(\omega_E) = \frac{L_{free}}{L} \frac{P_s}{E_m \epsilon_0}. \tag{8.8.60}$$

One should note the following features of this kind of extrinsic dielectric response. First, the Cole–Cole plot is similar to a part of that for the Debye response with a distribution of the relaxation times, while, physically, no

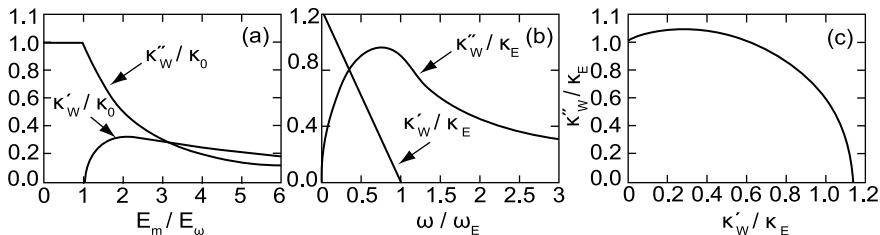


Fig. 8.8.4 Amplitude (a) and frequency (b) dependences of the contributions to the dielectric permittivity according to Eqs. (8.8.57), (8.8.56), (8.8.57), (8.8.58), (8.8.59) and (8.8.60) and the corresponding Cole–Cole plot (c). $E_w = 0.5\omega L_{free}/\mu$. After Tagantsev and Fousek (1999)

spectrum of the relaxation times can be attributed to the system. Second, as seen from Fig. 8.8.4a, an increase in E_m beyond the threshold leads to a reduction of κ_w'' . Such behavior is opposite to that expected in the case where the amplitude increase leads to depinning of the walls.

The results of the above analysis can be qualitatively applied to a description of the first harmonics polarization response taken from a ferroelectric in *switching regime*, i.e., when that amplitude of the driving field is essentially larger than the coercive field of the system. In this case the displacements of the walls are limited by the wall spacing in the multidomain state or by the size of the sample. For a simple model of switching these results can be applied quantitatively. In this model the switching is conducted by a lamella pattern of 180° domains. In a single-domain state, once the applied field changes its sign, the reverse domains appear as very thin plates and grow until the domain walls annihilate yielding the oppositely poled single-domain state. These nuclei plates are assumed to be distributed with a spacing L_N . This implies that the domain walls of the pattern will cover a distance of $L_N/2$ before the annihilation. It is clear that the results obtained above can be quantitatively applied to this switching model once we set $L = L_{\text{free}} = L_N/2$. Though this switching model is oversimplified, one can expect that it provides a qualitatively correct description of the first harmonic polarization response in the switching regime in general. Specifically, when a ferroelectric sample is cycled with an ac field essentially exceeding its coercive field, the measured effective permittivity (real and imaginary parts) should qualitatively comply with the Cole–Cole plot shown in Fig. 8.8.4c.

8.8.6 Wall Motion in Random Potential and Dispersion of the Dielectric Response (Experimental Findings and Interpretation)

Extrinsic contribution to the dielectric permittivity in ferroelectrics typically exhibits a complex frequency dispersion. Customarily, this dispersion is attributed to the coupling of domain wall with the random potential of crystalline imperfections which are believed to be present even in high purity materials. The decomposition of this contribution into the parts associated with different mechanisms and/or different regimes of the wall motion is usually a difficult task which does not always yield unequivocal results. The interpretation of the experimental data is also complicated by a limited progress presently achieved in the relevant theory. The theoretical results available usually deal with special limiting cases being obtained in terms of semi-quantitative and scaling arguments. The application of these results to real ferroelectric systems is not straightforward. For example, the developed theories usually consider the wall motion without taking into account the long-range electric and elastic effects which are important for “purely” ferroelectric and ferroelectric/ferroelastic domain boundaries. At best, when applying these results to a “purely”

ferroelectric wall, one modifies them by changing the effective interface dimension from 2 to 2.5 (cf. Sect. 6.4.3). However, strictly speaking, the validity of such substitution should be checked for every problem under consideration. Bearing in mind all stated above, we do not believe that a comprehensive discussion of the issue is presently feasible. For this reason, in this section, we will present some experimental information on the dispersion of the dielectric response in polydomain ferroelectric, which we will be appended with a discussion of main theoretical approaches used for the interpretation.

Experimental data on the frequency dispersion of the extrinsic contribution to the complex permittivity are available for many ferroelectrics, including “regular” ferroelectrics like TGS (Fousek and Janousek, 1966), relaxors, and exotic systems like the O¹⁸-substituted SrTiO₃ (Dec et al., 2004) (see also data used for the discussion of the domain freezing in Sect. 8.8.7). However, the focused studies on the problem in “regular” ferroelectrics are rare. Here we will present the recent results obtained by Park (2000) on Pb(Fe_{1/2}Nb_{1/2})O₃ and by Kleemann and coworkers (Kleemann et al., 2006; Braun et al., 2005) on KTiOPO₄. These are shown in Figs. 8.8.5 and 8.8.6. In both cases, the data have been obtained on single crystals. In the former material, a 180° domain pattern with the walls parallel to the direction of the applied field was expected from the geometry of the experiment. In the latter, an artificial 180° domain pattern of a period of 9 μm was introduced using lithographic methods. The situation in KTiOPO₄ was complicated by the super-ionic conduction of the material. To avoid effects related to it, the difference between the dielectric response of single-domain and polydomain crystals was always analyzed.

A distinct feature of the Cole–Cole plots shown in Figs. 8.8.5 and 8.8.6. is a crossover from a Debye-type relaxation at the high-frequency side to a relaxation corresponding to the Jonscher universal relaxation law (Jonscher, 1996) corresponding to the following relation:

$$\Delta\kappa^* \propto \left(\frac{1}{i\omega}\right)^\beta, \quad (8.8.61)$$

($0 < \beta < 1$) which also implies

$$\frac{\Delta\kappa''}{\Delta\kappa'} = \tan\left(\frac{\beta\pi}{2}\right). \quad (8.8.62)$$

The data on Pb(Fe_{1/2}Nb_{1/2})O₃ (Park, 2000) yield $\beta = 0.15 - 0.4$ in the temperature interval²² $T = 350 - 400$ K. The data on KTiOPO₄ (Braun et al., 2005) correspond to $\beta = 0.35$ at $T = 233$ K. Another important feature of the crossover in the relaxation mechanism is that the dielectric nonlinearity is much

²² This interval contains the transition temperature. The domain contribution to the permittivity is believed to exist above the transition because of some residual domains present in the paraelectric phase.

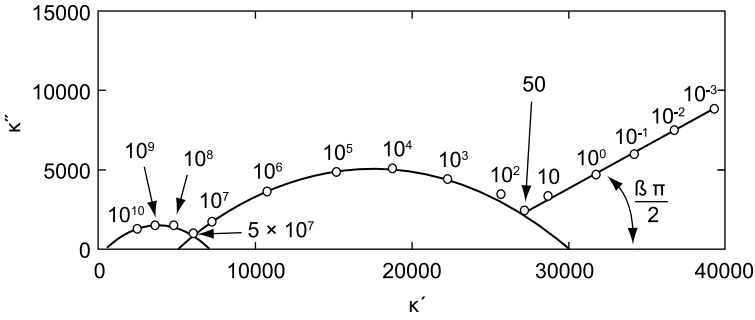


Fig. 8.8.5 The Cole–Cole plot for the permittivity of single crystal of $\text{Pb}(\text{Fe}_{1/2}\text{Nb}_{1/2})\text{O}_3$. The measuring frequency indicated in Hz. After Park (2000)

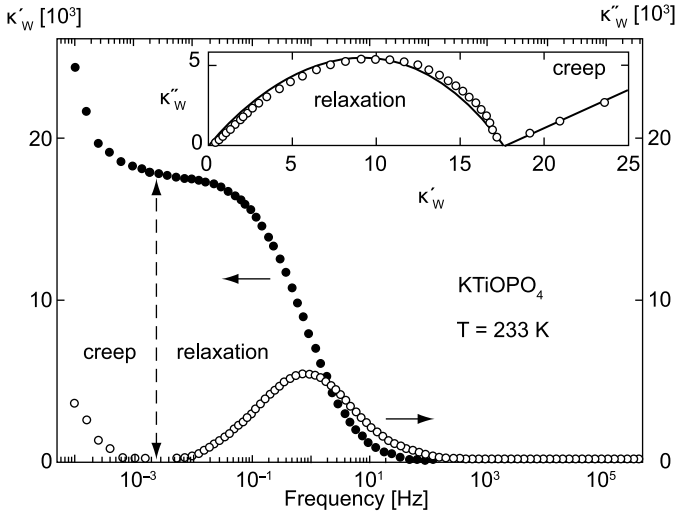


Fig. 8.8.6 Frequency dependence of the extrinsic contribution (difference between the data for polydomain and single-domain crystals) to dielectric permittivity and the Cole–Cole plot for KTiOPO_4 . After Kleemann et al. (2006)

stronger in the low-frequency regime (Kleemann et al., 2006). Most of the aforementioned features of the dielectric response of polydomain ferroelectrics are in qualitative agreement with data reported by Fousek and Janousek (1966) for the “classical” ferroelectric of TGS.

The presently available literature interpretation of the dispersion of permittivity of polydomain ferroelectric can be summarized as follows.

At very high frequencies, segments of the domain walls are moving (under the action of the ac field) inside the valleys of the random potential of crystalline imperfections. This regime is called *relaxation*. The potential of imperfections

provides some quasi-harmonic restoring force for the wall segments. This restoring force taken into account together with some wet friction leads to a Debye-type contribution to the permittivity from the segment

$$\kappa_w^* \propto \frac{1}{1 + i\omega\tau}, \quad (8.8.63)$$

where τ is the relaxation time constant. The distribution of the relaxation times of different segments, natural in random systems, will modify the dielectric response. Then, for its description, the so-called poly-dispersive Debye formula is often used

$$\kappa_w^* \propto \frac{1}{1 + (i\omega\tau)^\alpha} \quad (8.8.64)$$

with $0 < \alpha < 1$. Arcs in the Cole–Cole plots in Figs. 8.8.5 and 8.8.6 can be modeled with this relation. Accordingly, the corresponding contribution to the permittivity is attributed to the *relaxation* mechanisms, i.e., to the motion of the wall segments inside the valley of the random potential of crystalline imperfections.

On frequency lowering, say below a certain threshold frequency ω_c , it is supposed (Kleemann et al., 2006; Fedorenko et al., 2004) that, during the period of ac field, there is an appreciable probability that the wall segments will leave their “original” valleys of the pinning potential. The wall motion in this regime is viewed and termed differently by different authors.

According to Fedorenko et al. (2004) here, one can distinguish two sub-regimes. For frequency ω just below ω_c , the wall segment leaves its original valley and travels between metastable minima of the potential; however, the ac field period is not long enough to let it reach the true minimum.²³ This happens in the frequency range $\omega^* < \omega < \omega_c$ whose lower bond, ω^* , being an exponential function of $-1/E_m$ is determined by Eqs. (8.5.20) and (8.5.17). The physical meaning of ω^* is that, for the times longer than $1/\omega^*$, the wall is involved in the macroscopic motion as a whole. The regimes of the oscillatory wall motion corresponding to the frequency ranges $\omega^* < \omega < \omega_c$ and $\omega < \omega^*$, in terminology by Fedorenko et al. (2004), are called *stochastic* and *creep* regimes, respectively.

In such defined creep regime, at $\omega < \omega^*$, the walls are expected to move according to a certain mobility law, i.e., $v = v(E)$. In this case, unless the wall motion is restricted by some obstacles, the polarization response is purely dissipative, i.e., $\kappa_w'' \propto 1/\omega$ and $\kappa_w' = 0$, no matter if the mobility law is exponential (creep law) or linear (see Sect. 8.8.5). The term “creep regime” is probably conditioned by the fact that, at small fields, in the traditional “weak-pinning” model it is the creep law that controls the wall motion.

²³ In terms of consideration from Sect. 8.5.2, such minimum corresponds to the optimal bulge for the given value of the applied field.

In the *stochastic* regime, at $\omega^* < \omega < \omega_c$, where the macroscopic wall motion is impossible, according to Fedorenko et al. (2004) the dielectric response should follow the law given by Eq. (8.8.61), thus exhibiting $\kappa'_w \neq 0$. In terms of involved calculations, the validity of this law was demonstrated using the analogy between the considered problem and that of the stochastic motion of a particle in the random field environment. The values of the exponent β were found to be an increasing function of the amplitude of the driving field E_m . The exact result, $\beta \propto \sqrt{E_m}$, was obtained only for the one-dimensional case. One should mention that the increasing field dependence of β matches well with the physical picture of the phenomenon. Namely, on increasing E_m one approaches regime $\omega < \omega^*$ where $\beta = 1$.

An alternative terminology was used by Kleemann and coworkers (Kleemann et al., 2006; Braun et al., 2005). Though using the same terminology for the very high-frequency range, the regime where the Jonscher law holds was termed *creep* regime whereas the regime with the purely dissipative wall motion (at lower frequencies) was termed *sliding* regime. The conflict in the terminology is summarized in Table 8.8.1. Hereafter in the book we will use the Kleemann's terminology as already widely employed, though it is somehow contradictory. Specifically, in the *sliding regime*, the creep wall motion is possible while there is no creep wall motion in the *creep regime*.

Discussing the dispersion of the dielectric response in polydomain crystals, one should mention an approach which enables modeling of the extrinsic contributions to the permittivity whose frequency dependences are essentially different from the trivial Debye-and conductivity-type relations. The starting point of this approach is an observation that the contribution from a pinned domain wall to the complex permittivity is, on one hand, proportional to the Debye factor (cf. Eq. (8.8.63)) and, on the other hand, to the area of the typical movable segment S_p of the wall (see Eq. (8.8.46)). Thus one can present the contribution associated with the segment in the form

$$\Delta\kappa_w^* \propto \frac{S_p}{1 + i\omega\tau}. \quad (8.8.65)$$

When the motion of the segment is limited to a single valley only, the segment-to-segment variations of S_p and τ are not expected to be large leading to the Debye-type response (relaxation regime). However, if the ac field frequency is low enough, there appears an appreciable probability that, during time $1/\omega$, the wall will jump out of the valley. Here two situations, of strong and weak pinning, can be distinguished.

Table 8.8.1 Terminology for the regimes of frequency dispersion of the extrinsic contributions to the complex permittivity (see the text)

Complex permittivity	Fedorenko	Kleemann
$\propto \frac{1}{1+(i\omega\tau)^\alpha}$	Relaxation	Relaxation
$\propto \left(\frac{1}{i\omega}\right)^\beta$	Stochastic	Creep
$\propto \frac{1}{i\omega}$	Creep	Sliding

In the case of the individual coupling between the wall and defects (strong pinning), the segment can hop over a single impurity. The height of the barrier associated with this jump will control the relaxation time of dielectric response. Of importance is that, in this situation, the barrier height is basically controlled by the average distance between the impurities.²⁴ For this reason, no essential segment-to-segment variation of the barrier (and of relaxation time) is expected. Passing to these regimes from the relaxation one, the movable segment area S_p will clearly change. However, no essential spread of S_p will be expected either. All these clearly leads to a Debye-type response.

In the weak-pinning regime the situation is different. Here a wide spectrum of the sizes and hopping barriers is available leading to wide spread of S_p and τ and finally to an essentially non-Debye dielectric response. Let us address this point in the widely used approximation of isotropic elastic membrane (the electrostatic contribution to the bending energy is neglected). In this case, the energy barrier U_L separating the equilibrium states of the segments of the size L can be found from Eq. (8.5.13). Then according to the Gibbs statistics, the relaxation time of the segment can be written as

$$\tau(L) \cong \omega_0^{-1} \exp\left[\frac{U_L}{k_B T}\right] \cong \omega_0^{-1} \exp\left[\left(\frac{L}{L_\varepsilon}\right)^{2\zeta} \frac{T_\varepsilon}{T}\right], \quad (8.8.66)$$

where ζ is the roughness exponent; the rest of the parameters are introduced in Sect.8.5.2. Now, in principle, the segments of any length can contribute to the polarization response. The key assumption of the approach (Nattermann et al., 1990) is that, since $\Delta\kappa_w \propto S_p$, the polarization response is dominated by the segments that have the maximal size from those following the ac field. In other words, the polarization response is dominated by the segments whose size satisfies the resonance condition $\omega\tau(L) \cong 1$. Using Eq. (8.8.66) one finds for the length of such segments

$$L(\omega) = L_\varepsilon \left(\frac{T}{T_\varepsilon} \ln \frac{\omega_0}{\omega}\right)^{1/2\zeta}. \quad (8.8.67)$$

Then, after Nattermann, evaluating the real part of the permittivity as proportional to the area of the resonance segment (cf. Eq. (8.8.65)) one finds

$$\kappa'_w \propto L(\omega)^2 \propto \left(\ln \frac{\omega_0}{\omega}\right)^\gamma \quad (8.8.69)$$

with $\gamma = 1/\zeta$. To restore the imaginary part, one uses the Kramers–Kronig relation in the form of the “ $\pi/2$ rule” (see e.g., (Courten, 1986))

²⁴ This is actually an assumption. However, when comparing the weak and strong pinning regimes it looks qualitatively correct.

$$\kappa''(\omega) = -\frac{\pi}{2} \frac{\partial \kappa'(\omega)}{\partial \ln \omega}, \quad (8.8.70)$$

to find

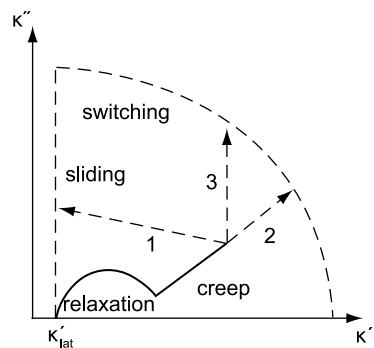
$$\kappa_w'' \propto \left(\ln \frac{\omega_0}{\omega} \right)^{\gamma-1}. \quad (8.8.71)$$

The results given by Eqs. (8.8.69) and (8.8.71) are identical to those obtained by Fedorenko et al. (2004) in the approximation of isotropic elastic membrane.²⁵ If the electrostatic stiffness of the wall is taken into account, on the same line one arrives at Eqs. (8.8.69) and (8.8.71) however with $\gamma = 5/(4\zeta_1 + 1)$ where ζ_1 is the roughness exponent for this case.

One readily checks that assuming that the size of the resonance segments scales as a power law of the ac field frequency, i.e., $L(\omega) \propto \omega^{-\phi}$, the above arguments lead to the Jonscher law, Eq. (8.8.61) with $\beta = 2\phi$. Based on this assumption Kleemann et al. (2006) derived the Jonscher law in terms of similar arguments.

To finish this section which is primarily dealing with the small-signal response, i.e., for the driving fields E_m smaller that the coercive field, we would like to give an outlook at the whole frequency range including the situation where on frequency lowering this condition is violated. Here we should recognize that one has a relatively clear picture only for the two limiting cases as shown in the Cole–Cole plot in Fig. 8.8.7. At the high-frequency end, one finds the relaxation and creep regimes (shown with solid lines). At the low-frequency end, assuming that the condition $E_m > E_c(\omega)$ is reached, the wall motion is expected to be purely dissipative with $\kappa_w'' \propto 1/\omega$ and $\kappa_w' = 0$ (sliding regime) unless the wall motion is limited by some obstacles and/or the full switching of the sample occurs. The later regime is

Fig. 8.8.7 Schematic of the Cole–Cole plot for complex permittivity of a polydomain ferroelectric. See the text. The lattice contribution to the real part of the permittivity is denoted as κ'_{lat} . The lattice contribution to the imaginary part of the permittivity is neglected



²⁵ The above derivation, though expressing idea of the approach, is oversimplified. For a more rigorous consideration see the original papers (Nattermann et al., 1990; Fedorenko et al., 2004).

the *switching regime* discussed in Sect. 8.8.5, with the Cole–Cole plot of the type shown in Fig. 8.8.4c.

As for the intermediate frequency range, to the best of our knowledge, no model is available to its description. The trajectories in the Cole–Cole plot corresponding to conceivable scenarios of the intermediate frequency crossover are shown as arrowed dotted lines.

The first option labeled with “1” corresponds to the case where in a certain frequency range *all domain walls* of the sample participate in the purely dissipative motion. In this regime the real part of the permittivity must be equal to the lattice permittivity. Independent of the physical mechanism behind the intermediate frequency crossover, it must be associated with some reduction of κ' on frequency lowering as clear from Fig. 8.8.7. The second option labeled with “2” corresponds to the case where the creep regime directly converts into the switching regime; symbol “3” labels the crossover scenario favored by Kleemann et al. (2006).

8.8.7 Domain Freezing

Domain freezing is one of the first effects documented in ferroelectrics and it is definitely the oldest from those not properly understood in this system. This effect was actually reported in 1935 in the first publication on the second discovered ferroelectric KDP. Figure 8.8.8 shows the first reported temperature dependence of the permittivity of a KDP crystal. Busch and Scherrer (1935) reported it as an evidence for the ferroelectricity in this crystal. The two characteristic temperatures θ_1 and θ_2 marked in this figure were interpreted as two transition temperatures in analogy with the Rochelle salt, the only known ferroelectric by that time. In reality, in KDP there is only one ferroelectric phase transition corresponding to temperature θ_1 . As for the behavior of the permittivity between θ_1 and θ_2 , it is controlled by the domain wall dynamics. Since 1935 such kind of plateau in the temperature dependence of the permittivity below the transition temperature was repeatedly reproduced for KDP and other ferroelectrics. This phenomenon has been named *domain freezing*. This term implies

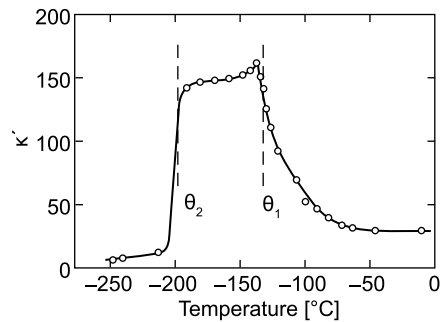


Fig. 8.8.8 Temperature dependence of the real part of the permittivity of KDP crystals. Measuring field amplitude -1 kV/cm, frequency -50 Hz. First evidence for the ferroelectricity in KDP. After Busch and Scherrer (1935)

the existence of a contribution of the domain walls to the permittivity, which vanishes below a certain temperature where the domain wall motion freezes out.

This phenomenon has been well documented for the ferroelectrics of KDP family (see, e.g., Bornarel et al., 1966; Strukov et al., 1972b; Gladkii et al., 1973; Magataev et al., 1975; Peercy and Samara, 1973; Nakamura et al., 1989), TGS (Huang et al., 1997), and BaTiO₃ (Wang et al., 2007a). All experimental data reported are qualitatively consistent in describing the same physical phenomenon in all these materials. Here one should stress that all features of the domain freezing correspond to the amplitudes of the measuring field much smaller than the coercive field. Though there have been a number of attempts to model this phenomenon or rationalize its mechanism (Bornarel, 1972; Fedosov and Sidorkin, 1977; Kuramoto, 1987; Huang et al., 1977), the microscopic scenario which would be able to explain the whole body of experimental data is not presently available in the literature. For this reason, in this book, we restrict ourselves to the presentation of experimental data illustrating the characteristic features of domain freezing in aforementioned materials.

In the context of the domain freezing, the most investigated are the ferroelectrics of the KDP family. For these materials, it was established that the value of the permittivity at the plateau is very sensitive to the crystal quality and the amplitude and frequency of the measuring field; the dc bias exceeding the value of the coercive field was also found to essentially affect (reduce) the value of the permittivity at the plateau (see, e.g., Bornarel et al., 1966; Nakamura et al., 1989; Fally et al., 2001) or remove it completely as shown in Fig. 8.6.20. Figure 8.8.9 shows the dielectric data for a high-purity KDP crystal: Here a two-orders-of-magnitude difference in the permittivity at the plateau compared to Fig. 8.8.8 is seen as well as the impact of the ac field frequency. The impact of the ac field amplitude on the complex dielectric permittivity of a KDP crystal is illustrated in Fig. 8.8.10. Higher permittivity for higher field amplitudes or/and lower

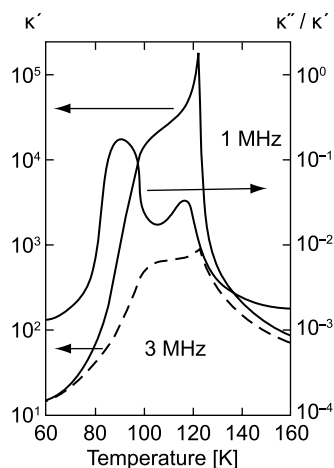
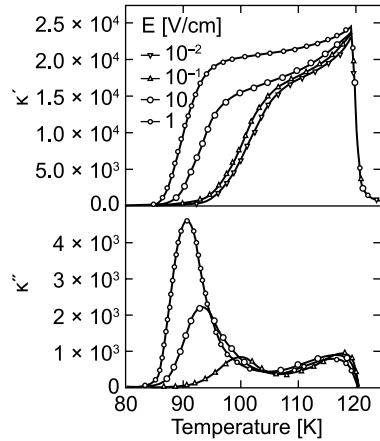


Fig. 8.8.9 Temperature dependence of real part of the dielectric permittivity and loss factor of a high-quality KDP crystals measured at different frequencies of the ac field. After Bornarel et al. (1966)

Fig. 8.8.10 Temperature dependence of the real and imaginary parts of the dielectric permittivity of high-quality KDP crystals measured at different amplitudes of the ac field and frequency 1 Hz. Reprinted with permission from Fally, M., Fuith, A., Müller, V., *Phys. Rev. B* **64**, 026101 (2001). Copyright (2001) by the American Physical Society



frequencies documented in these figures clearly suggest some kind of depinning mechanisms behind the effect. Analysis of the loss spectrum has revealed a very strong slowing down of the dielectric relaxation on approaching the low-temperature end of the plateau. The temperature dependence of the characteristics relaxation time τ was found compatible with the Vogel–Fulcher law (Nakamura et al., 1989; Huang et al., 1997):

$$\tau = \tau_0 \exp\left(\frac{A}{T - T_f}\right), \quad (8.8.72)$$

where the constants τ_0 , T_f , and A were found sensitive to the purity of the sample.

In TGS, the domain freezing exhibits basically the same features as in KDP. Here, using α -alanine-doped samples, the dielectric response in poly- and nominally mono-domain samples has been compared to find a very strong suppression of the effect in the latter (Huang et al., 1997).

In the classical ferroelectric of BaTiO_3 , the domain freezing was recently discovered in the rhombohedral phase (Wang et al., 2007a). Figure 8.8.11 shows the comparison of the measured temperature dependence of real part of the dielectric permittivity of (111) oriented BaTiO_3 single crystals to the Landau theory prediction for a single-domain crystal. It is seen that in all phases but the low-temperature rhombohedral one, the dielectric response is mainly controlled by lattice contribution whereas in the latter a very large extrinsic contribution appears. The effect was found strong in the depoled samples. In general, the impact of the thermal and electrical pretreatment on the dielectric response in the rhombohedral phase was found to be very complicated. Of interest are the results on the dielectric nonlinearity in the plateau region. The data shown in Fig. 8.8.12 suggest a kind of ac-field-amplitude-driven dynamical phase transition occurring in this region.

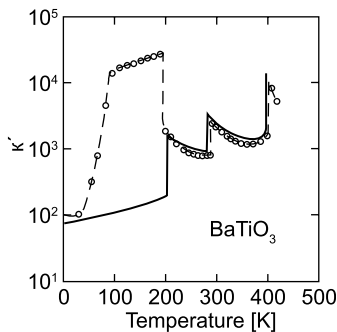
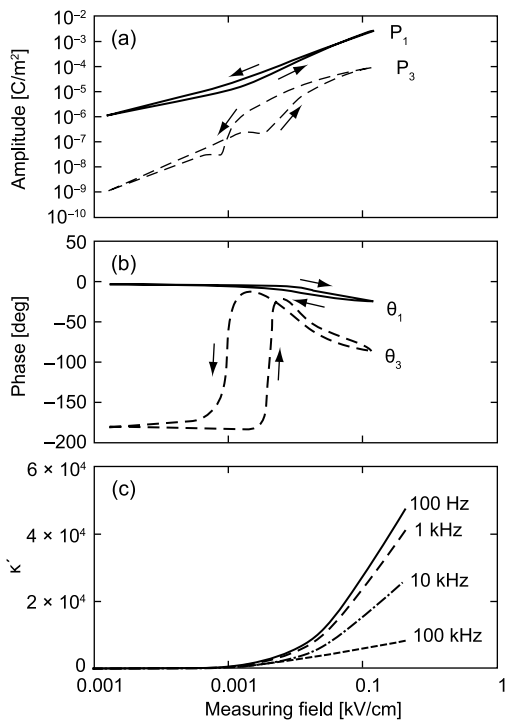


Fig. 8.8.11 Temperature dependence of real part of the dielectric permittivity of (111)-oriented BaTiO₃ single crystals. *Open circles and dashed line* represent the experimental values measured using a small ac signal (100 Hz, 0.05 kV/cm) upon heating under zero bias electrical field and mechanical stress. Before the measurement, the crystal was annealed at 473 K overnight, then cooled down to 250 K, and depoled with a fast decayed (from 1 kV/cm to zero within five periods) low-frequency ac field, and finally cooled down to 15 K. The *solid line* shows the prediction of the Landau theory for the temperature dependence of the permittivity in a $\langle 111 \rangle$ single-domain crystal. In the orthorhombic phase, the *solid line* corresponds to the contribution of a (110) domain. After Wang et al (2007a)

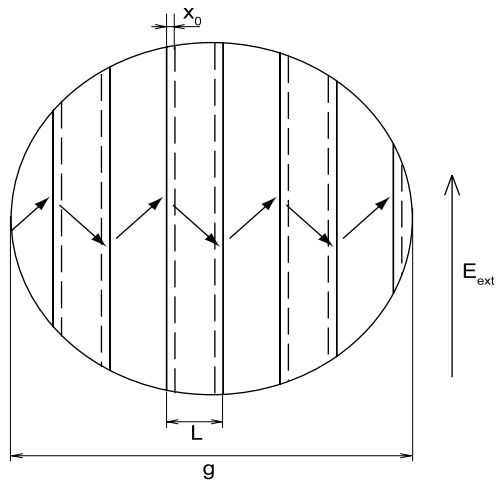
Fig. 8.8.12 Dielectric response of a BaTiO₃ single crystal monitored at 140 K. Before measurements the crystal was first cooled to 140 K and then electrically depoled (as described in the caption of Fig. 8.8.11). *Panels (a) and (b)* show the amplitude and phase angles of the first and third polarization harmonics ($P_1 \sin(\omega t + \theta_1)$ and $P_3 \sin(3\omega t + \theta_3)$, respectively.) vs. the amplitude of the ac driving field ($E \sin \omega t$) at the frequency 1 kHz. *Panel (c)* shows the amplitude dependence of the real part of dielectric permittivity measured at various frequencies. After Wang et al. (2007)



8.8.8 Dielectric Response Associated with Mobile Ferroelastic Domain Walls in a Clamped Multidomain Ferroelectric

In this section we have already addressed a few scenarios for the dielectric response associated with domain walls. These scenarios can be distinguished based on the mechanisms controlling the restoring force, effective mass, and friction force associated with the wall motion. In the present section we will address the situation taking place in grains of ferroelectric ceramics split into ferroelastic domains. In this system, where the grain is mechanically clamped by the “matrix” of neighboring grains, one comes across new mechanisms for the aforementioned features of the domain wall dynamics. Below we will outline the theory of the dielectric response in such system to highlight these mechanisms. In general, the theory of the dynamics of ferroelastic domain walls is quite involved; for a comprehensive theoretical treatment of the matter we can refer the reader to a book by Sidorkin (2006). A very instructive paper on the dielectric response controlled by the motion of ferroelastic walls was published by Pertsev and Arlt (1993). In this paper, the authors have developed a rather general theory of the phenomenon and demonstrated the application of their theory to a model where both the calculations and the interpretation of the results obtained can be readily done. In this section we will basically follow the treatment of this model given by Pertsev and Arlt. In this model, a spherical grain in a sample of ferroelectric ceramics, which contains 90° domain walls not interacting with structural defects, is considered. The domain pattern in the grain is shown in Fig. 8.8.13. In the absence of the applied electric field, the grain contains a periodic pattern of flat walls. The domain pattern is dense, i.e., the grain size g is assumed to be much larger than the domain wall spacing L :

Fig. 8.8.13 Spherical grain with a lamellar 90° domain structure. The *dashed lines* designate 90° domain walls displaced by an amount x_0 from their equilibrium positions. g is the grain diameter. L is the domain wall spacing. The direction of the applied field is indicated. *Arrows* inside domains show the directions of the spontaneous polarization



$$g > L \quad (8.8.73)$$

The general form of the equation for a displacement of the wall from its position in the initial domain pattern, x_0 , can be written by generalizing Eq. (8.8.39) as follows:

$$M_W \ddot{x}_0 + \beta_W \dot{x}_0 + Kx_0 = (P_{Si}^{(1)} - P_{Si}^{(2)})E_i + (\varepsilon_{Sn}^{(1)} - \varepsilon_{Sn}^{(2)})\sigma_n, \quad (8.8.74)$$

where M_W , β_W , and K are effective mass, friction constant, and the Peierls barrier restoring force constant of the wall, respectively, as they were introduced for an ideal crystal in Sect. 8.8.3. The r.h.s. of this equation corresponds to the pressure acting on a ferroelectric/ferroelectric wall as it was introduced in Sect. 8.2.2. We would like to stress that the electric field and mechanical stress entering the r.h.s. of Eq. (8.8.74) are the actual fields in the grain comprising the external and internal components, e.g., the applied and depolarizing electric fields. In the absence of the applied electric field, we assume that the electric and elastic fields are fully relaxed and this pressure vanishes. For a dense domain pattern, this is a good approximation.

Application of an external ac electric field, according to Eq. (8.8.74), will cause displacements of the walls in the pattern as shown in Fig. 8.8.13. In turn these displacements will bring about some “internal” electric field and strain. The internal electric field created, E^{int} , is just the depolarizing electric field appeared in the grain, which, once the walls are displaced from their initial position, will exhibit a nonzero net polarization. This field is proportional to x_0 as being proportional to the net polarization which, in turn, is proportional to x_0 . The internal stress caused by the displacements of the walls, σ^{int} , is linked to x_0 , in general, in a complicated manner. (An advanced theory of this effect can be found in the paper by Pertsev and Arlt (1993).) However, this link can be rationalized in the case where the grain size is smaller than the acoustic wavelength at the frequency of the external ac electric field. In this case, one can distinguish three contributions to σ^{int} , which are proportional to x_0 , \ddot{x}_0 , and x_0 (Pertsev and Arlt, 1993). The first is associated with the elastic energy of the clamped grain with displaced walls (this is actually a mechanical analog of the depolarizing-field-driven effect just discussed above). The second is associated with the kinetic energy of motion of the grain material. The third term, proportional to the third derivative of the wall displacement with respect to time, is due to the emission of the acoustic waves by the moving walls. For this model, explicit expressions for E^{int} and σ^{int} have been derived in the approximation of elastically isotropic medium (the same elastic constants for the grain and “matrix”) neglecting the piezoelectric effect in the material. Under these approximations, making use of these expressions and taking into account the orientation of the spontaneous polarization, one can present Eq. (8.8.74) in the following form (the details of calculations can be found in the paper by Pertsev and Arlt (1993)):

$$(M_w + M_d)\ddot{x}_0 + (K + K_d)x_0 - \Psi\ddot{x}_0 + \beta_w\dot{x}_0 = \sqrt{2}P_S E^{\text{ext}}, \quad (8.8.75)$$

where

$$K_d = \frac{2P_S^2}{\varepsilon_0(\kappa_{33} + 2\kappa_{\text{matr}})L} + \frac{4(7 - 5\nu)G\varepsilon_S^2}{15(1 - \eta)L}, \quad (8.8.76)$$

$$M_d = \frac{4}{75} \left[3 + 2 \left(\frac{1 - 2\nu}{2 - 2\nu} \right)^2 \right] \frac{G\varepsilon_S^2}{L} \tau_g^2, \quad (8.8.77)$$

$$\Psi = \frac{1}{45} \left[3 + 2 \left(\frac{1 - 2\nu}{2 - 2\nu} \right)^{2.5} \right] \frac{G\varepsilon_S^2}{L} \tau_g^3, \quad (8.8.78)$$

$$\tau_g = g/c_t. \quad (8.8.79)$$

Here G and ν are the shear modulus and the Poisson ratio of the material; P_S and ε_S are the absolute values of the spontaneous polarization and spontaneous shear strain in the domains, κ_{33} and κ_{matr} are a component of the effective dielectric constant in the grain (in the direction of the applied field) (Turik, 1970) and that of the ceramics. The parameter $\tau_g = g/c_t$ is the time needed for the transverse sound to cross the grain, c_t being its velocity. When deriving these equations, it has been taken into account that the electric field entering equation of motion of the wall can be presented in the form

$$E_i = E_i^{\text{int}} + AE_i^{\text{ext}}, \quad (8.8.80)$$

where E_i^{ext} is the external electric field in the matrix far from the grain and the factor A links this field with that inside the grain. At the same time, since the piezoelectric effect has been neglected, the stress in the grain was taken equal to the internal that associated with the wall motion, σ_{int} .

Let us discuss the role of the new effects introduced by Eq. (8.8.75).

The contribution to the restoring constant K_d is controlled by the two terms, which originate from the electrostatic and elastic effects, respectively. According to the order-of-magnitude estimates these contributions are expected to be of the same order. Using the set of parameters typical for $\text{PbZr}_{0.49}\text{Ti}_{0.51}\text{O}_3$ given in the paper by Pertsev and Arlt (1993) ($\varepsilon_S = 0.029$, $P_S = 0.6 \text{ C/m}^2$, $G = 1.26 \times 10^{10} \text{ N/m}^2$, $\kappa_{33} = \kappa_{\text{matr}} = 500$, $\nu = 0.4$) one finds similar values for these terms. According to the calculations of these authors these values lead to the domain wall contribution of 350 to the dielectric constant of the ceramics in the static limit. This value is compatible with the experimental estimates for this contribution. A remarkable feature of this contribution is that it is predicted independent of the domain wall spacing. This can be readily concluded from the knowledge developed in this section. Indeed, as clear from the derivation of Eq. (8.8.17), in general, the contribution of a domain wall to the static dielectric constant is inversely proportional to the product “domain wall spacing times

restoring force constant.” Since in the above theory the restoring force constant, given by Eq. (8.8.76), is itself inversely proportional to the domain wall spacing, the aforementioned contribution occurs to be independent of the latter. It is worth noting that this often happens in the case where the restoring force is related to the energy of macroscopic electric or/and elastic fields (cf. the results for thin films in Sects. 9.6.4 and 9.6.5). In calculations of the dielectric response in the above model, the effect of the Peierls barriers was neglected. Such neglect cannot be always justified. If we take the estimate for the Peierls barriers for a 180° wall BaTiO_3 used in Sect. 8.4.3, $\nu = 0.4$, we readily find comparable values of $V_{P_0} \approx (5 - 7) \times 10^{-5} \text{ J/m}^2$ and K_d . At the same time, the Peierls barrier height decays very fast with increasing wall thickness (see Eq. (8.4.20)). Thus, this neglect can be justified if the wall is not “very thin,” as seems to be the case of 90° walls.

Another remarkable feature of the model considered is that it yields an appreciable effective mass for the wall. The order-of-magnitude estimates and numerical estimates using typical values of the material parameters of perovskites readily show that the initial mass of the wall, M_0 , is at least two orders of magnitude smaller than the additional mass M_d , acquired due to the elastic effects.

The dynamical effects associated with the “elastic” effective mass and the sound emission by the domain walls can be substantial at common microwave frequencies. This is readily concluded from Eqs. (8.8.75), (8.8.76), (8.8.77), (8.8.78), and (8.8.79). Specifically, one sees that, at the angular frequency $\omega \cong \tau_{\text{eg}}^{-1}$, the terms in Eq. (8.8.75) related to the elastic contribution to the restoring force, to the “elastic” effective mass, and to the sound emission become comparable. This implies a strong dispersion of the dielectric response at this frequency. For $\text{PbZr}_{0.49}\text{Ti}_{0.51}\text{O}_3$ with the grain size $g = 2 \mu\text{m}$ and density $\rho = 7.6 \text{ g/cm}^3$ one finds about 100 MHz for the frequency corresponding to the time τ_{eg} . Modeling performed by Pertsev and Arlt (1993) for this system on the lines of Eqs. (8.8.75), (8.8.76), (8.8.77), (8.8.78), and (8.8.79) clearly illustrates such behavior (see Fig. 8.8.14).

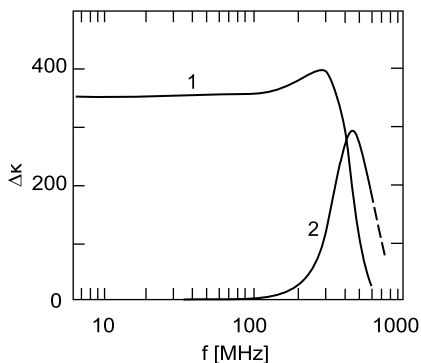


Fig. 8.8.14 The frequency dependence of the domain wall contributions to the real (*curve 1*) and imaginary (*curve 2*) parts of the dielectric constant calculated on the lines of Eqs. (8.8.76), (8.8.77), (8.8.78), and (8.8.79) for unpolarized $\text{Pb}(\text{Zr}_{0.49}\text{Ti}_{0.51})\text{O}_3$ ceramics with the grain size $2 \mu\text{m}$. After Pertsev and Arlt (1993)

One should make the following remarks concerning the model discussed above. It definitely reveals some important qualitative features of the dielectric response of the ferroelastic domains in a clamped grain. At the same time, Eq. (8.8.75) cannot be used for the quantitative description of the frequency dispersion of the system at $\omega \cong \tau_g^{-1}$ since it has been derived under the assumption $\omega \ll \tau_g^{-1}$. Such quantitative description can be obtained numerically using the general results derived by Pertsev and Arlt (1993), which, however, are to be complemented with the incorporation of the piezoelectric response of the material into the model.

Chapter 9

Ferroelectric Thin Films

9.1 Introduction

Ferroelectric thin films presently are the object of intensive fundamental and applied studies, which to a great extent have been stimulated by the horizons of their applications as functional materials in non-volatile memories in microelectronics, mechanical sensors, actuators in micromechanics, pyroelectric detectors, and in tunable microwave and electro-optical devices. When speaking of ferroelectric thin films, one usually means films of thicknesses ranging from a few tens to hundreds of nanometers deposited on a thick (typically 0.5 mm or thicker) substrate. This determines mixed mechanical boundary conditions with the fixed in-plane components of the deformation while the film is free in the out-of-plane direction. The anisotropy of these conditions plays a decisive role in many properties of ferroelectric thin films.

For description of the microstructure of ferroelectric films one customarily uses the terms “epitaxial,” “textured,” and “polycrystalline”. When the orientation of the crystallographic axes of the films is the same throughout the film, one speaks about an epitaxial film. Practically this may be achieved when the film is deposited on a crystalline substrate of the structure that is very close to that of the ferroelectric, and the crystalline lattice of the latter can be viewed as a continuation of that of the substrate. “Epitaxial” is actually used as a synonym of “single crystalline”. A polycrystalline film is usually called “polycrystalline” when the orientation of its grains is fully random. When this orientation is not fully random, one speaks about polycrystalline films with a mixed or preferable orientation. The term “textured films” is applied to the case where the orientation of the out-of-plane crystallographic axis is the same in all grains of the film whereas the in-plane orientation is random. To describe the orientation of a film, hereafter we will use the Miller indices (ijk) to indicate the orientation of the surface of the films in the reference frame of the paraelectric phase of the ferroelectric. For example, the notation “(001) BaTiO₃ film” means a film with the surface normal to a fourfold axis of the paraelectric phase of the material. In such film, in the ferroelectric tetragonal phase, in principle, both the in-plane and out-of-plane orientations of the spontaneous polarization are possible.

The most intensively investigated are perovskite thin films (e.g., $\text{Pb}(\text{Zr},\text{Ti})\text{O}_3$ (PZT), BaTiO_3 , SrTiO_3 , and $(\text{Ba},\text{Sr})\text{TiO}_3$, $\text{Pb}(\text{Mg}_{1/3}\text{Nb}_{2/3})\text{O}_3$ (PMN)). Among other materials special attention is paid to Aurivillius structure ferroelectrics like pure or modified $\text{SrBi}_2\text{Ta}_2\text{O}_9$ and $\text{Bi}_4\text{Ti}_3\text{O}_{12}$ which are considered as good candidates for ferroelectric memory devices. Extended investigation of ferroelectric thin films reveals that their properties can substantially differ from those of the bulk form of the same material. As an example of this difference one can indicate substantially elevated (compared to the bulk samples) values of coercive fields in the films (e.g., in PZT films). Another typical feature of films is strongly reduced values of the dielectric constant in the case where the dielectric constant of the bulk material is very high (reaches values of a few tens of thousands like in SrTiO_3 and PMN).

Discussing the difference in the properties of bulk ferroelectrics and thin films, one distinguishes two groups of factors.

The first group covers the factors related to the difference in the processing condition. The deposition temperature of thin films (or crystallization temperature in case of low-temperature deposition), usually ranging from 500 to 800°C, is considerably lower than the fabrication temperature of single crystals and bulk ceramics. Another remarkable feature of thin film processing is a big surface-to-volume ratio. All these factors can substantially influence the stoichiometry, microstructure, and defectness of the thin films. The big surface-to-volume ratio can also lead to a certain degree of compositional inhomogeneity across the film thickness.

The second group covers the factors related to the physical phenomena that become important in the films due to their small thickness.

- (i) The mechanical interaction between a film and the substrate results in stressed and strained states of the film. Since the thickness of the substrate is usually much greater than that of the film, the substrate is only slightly deformed whereas the lattice parameters of the ferroelectric film can substantially differ from those of the bulk material. When a misfit-dislocation-assisted stress release takes place at the ferroelectric/substrate interfaces, the strain and stress at the interface become inhomogeneous.
- (ii) Properties of a ferroelectric near its free surface or a ferroelectric/substrate interface are, in general, different from those in the bulk. If the film thickness is comparable to the width of such a “disturbed” layer, the properties of the film as a whole can be affected, e.g., its average dielectric response. If, in addition, the polarization in the films has a component normal to the plane of the film, the depolarizing effect enters the game. As a result, the bulk of the films become sensitive to the presence of the disturbed layer leading to yet more pronounced thickness dependence of the film properties. The origin of the “disturbed” layer may be both intrinsic (e.g., the presence of misfit dislocation or coupling between the ferroelectric polarization and the substrate) and extrinsic (e.g., the presence of a layer of a secondary phase).

- (iii) The electrochemical interaction between the electrodes and the ferroelectric is also a possible source of the thickness size effect. This interaction can result in the formation of the so-called depletion space charge in an appreciable fraction of film volume. The field and polarization induced by this charge can substantially influence the properties of ferroelectric films.

Not underestimating the importance of the first group of factors, in this chapter we will mainly focus on the domain-related issues of ferroelectric thin films in the context of the second group of factors. The goal of this chapter is to review the basic theoretical concepts and experimental findings in this field, trying to cover most of the important issues. When reading this chapter the reader should realize that the field is relatively young so that the theoretical understanding is quite “inhomogeneous” (we mean advanced theories are available on some issues whereas only non-developed concepts are available on others) and the experimental findings are sometimes contradictory (or at least look so). Such situation urged us to make a choice between the presentations of only accomplished theory and fully understood experimental finding on the one hand and, on the other hand, of more open big picture of the activity in the field. We have chosen the latter option. In its spirit, we devoted Sect. 9.2 to a review of nearly raw experimental data on domain patterns in ferroelectric thin films. Some of these data will be discussed later in the context of the available theories. In general, in this chapter, as was said, trying to cover important problems, we combine in our presentation properly understood issues with issues that, though being important, are still less understood.

9.2 Experimental Studies on the Static Domain Pattern in Thin Films

Domain pattern in ferroic thin films became an issue of interest during the past two decades, the main focus being on ferroelectric thin films. This section will mainly address the experimental data on static domain patterns in thin films of classical perovskite ferroelectrics such as PbTiO_3 , BaTiO_3 , as well as solid solutions based on these materials. In addition, we will review briefly the experimental results on less investigated systems like films of $\text{SrBi}_2\text{Ta}_2\text{O}_9$, $\text{Bi}_4\text{Ti}_3\text{O}_{12}$, and KNbO_3 .

9.2.1 Domain Structure in (001) Thin Films of Tetragonal Ferroelectric Perovskites

Domain features of thin films of ferroelectric perovskites with a cubic–tetragonal phase transition have been attracting much attention of workers since the early 1990s, though some observations of domain patterns in this kind of films have been reported in yet earlier papers (Sviridov et al., 1984). This activity has mainly

addressed PbTiO_3 , and to a lesser extent films of $\text{Pb}(\text{Zr,Ti})\text{O}_3$ (PZT), $(\text{Pb,L a})\text{-TiO}_3$ (PLT), BaTiO_3 , and $(\text{Ba,Sr})\text{TiO}_3$ (BST). To date, most of studies have been performed on epitaxial films deposited onto crystalline substrates of (001) or pseudo-(001)¹ orientations (MgO , KTaO_3 , SrTiO_3 , and LaAlO_3) using a wide variety of deposition techniques (magnetron sputtering, pulse laser deposition (PLD), metal-organic chemical-vapor deposition (MOCVD), molecular-beam epitaxy (MBE), and chemical solution deposition (CSD)). The domain patterns in films are visualized by using different techniques. The most conventional techniques are scanning force microscopy (SFM) pioneered in ferroelectric thin films by Franke et al. (1994) and transmission electron microscopy (TEM). In earlier papers a good domain contrast was achieved by using a method which included a chemical etching followed by making platinum-carbon replicas, the latter being visualized using an electron microscope (Sviridov et al., 1984; 1992). A high resolution of 180° domains was recently demonstrated by using scanning nonlinear dielectric microscopy (SNDM) (Odagawa and Cho, 2001). An important parameter of domain patterns—fraction of domains making the pattern—can also be reliably determined by comparing intensities of XRD peaks corresponding to different domain states. Using all these techniques a large body of experimental data, sometimes contradictory, has been collected on the domain features of (001) thin films of tetragonal ferroelectric perovskites. In what follows we will try to overview the main trends revealed, without going into details of fabrication and characterization techniques.

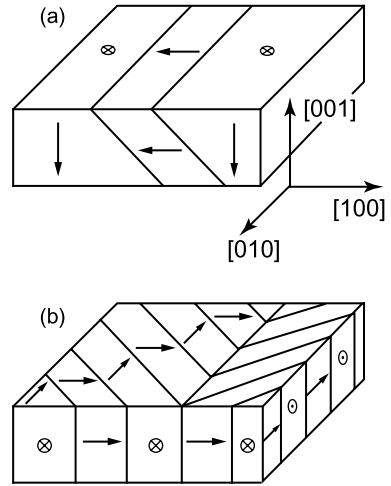
9.2.1.1 Configuration of Ferroelastic Domain Patterns

One reasonably expects that domain patterns of a ferroic film should be formed by the walls that meet the conditions of mechanical compatibility for the bulk material². Accordingly, in the case of ferroelastic domains in tetragonal ferroelectric perovskites, only walls of $\{110\}$ orientations are expected. In a (001) film (the X_3 -axis is defined perpendicular to the plane of the film), this determines two types of simplest ferroelastic patterns made of c - and a -domains (domain states) where the c - or a -axis is normal or nearly normal to the plane of the film, respectively. These are the so-called a/c - and a_1/a_2 -variants. In the a/c -variant, the domain walls are parallel to one of the (101), (011), ($\bar{1}01$), and ($0\bar{1}1$) planes, making approximately angles of 45° with the plane of the film. In the a_1/a_2 -variant, the walls are parallel either to (110) or to ($1\bar{1}0$) planes, being perpendicular to the plane of the film. According to the possible orientation of the domain walls in these variants, four a/c -variants and two a_1/a_2 -variants are distinguished. The orientations of the walls and spontaneous polarization in the

¹ In the case where the substrate is pseudocubic.

² Actually, this may not always be the case; see papers by Shuvalov et al. (1987) and Dudnik and Shuvalov (1989).

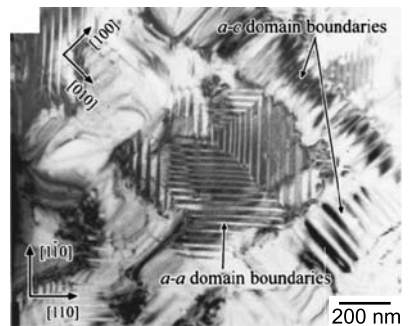
Fig. 9.2.1 Domain patterns in (001) tetragonal ferroelectric thin films: a/c -pattern (a) and a_1/a_2 -pattern (b). Arrows show the directions of the spontaneous polarization



a/c - and a_1/a_2 -variants are illustrated in Fig. 9.2.1. A general feature of experimentally observed patterns is that a_1/a_2 -variants contain equal fractions of a_1 - and a_2 -domains in accordance with simple theoretical arguments (see Sect. 9.3.3) whereas the fraction of c -domains in a/c -domain patterns is very sensitive to many parameters of the film/substrate system.

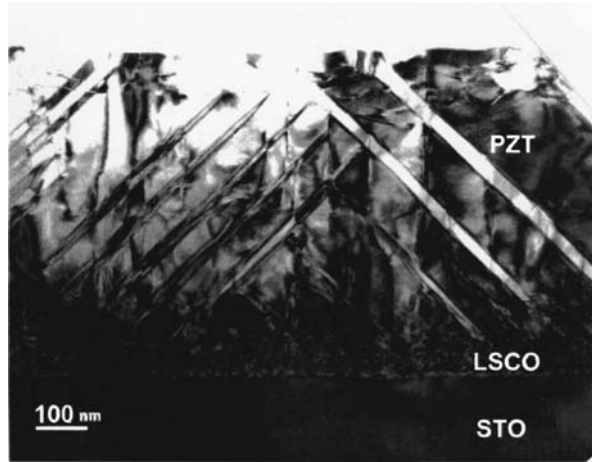
The domain patterns experimentally observed in (001) thin films of tetragonal ferroelectric perovskites are a/c - and a_1/a_2 -variants as well as their superpositions. Below we will give examples of such structures. Figure 9.2.2 shows a plan-view TEM image of 200 nm thick PbTiO_3 (PLD film on KTaO_3 substrate), where two a_1/a_2 -variants and at least two a/c -variants are seen.³ The coexistence

Fig. 9.2.2 Coexistence of different types of domain patterns in (001) tetragonal ferroelectric thin films. Plan-view TEM image of an epitaxial PbTiO_3 films on (001) KTaO_3 substrate. Reprinted with permission from Lee et al. (2001b). Copyright (2000), American Institute of Physics



³ From this type of image one cannot distinguish the variants that have identical orientation of the intersection between their domain walls and the free surface of the film.

Fig. 9.2.3 Cross-section TEM image of a $\text{Pb}(\text{Zr}_{0.2}\text{Ti}_{0.8})\text{O}_3$ epitaxial film on (001) SrTiO_3 substrate. Reprinted with permission from Ganpule et al. (2000a). Copyright (2000), American Institute of Physics



of a_1/a_2 - and a/c -variants is a rare situation; more typical is the coexistence of only a/c -variants (two or more). An example of such coexistence is illustrated in Fig. 9.2.3. Here a cross-section TEM image of a 400 nm thick PZT (20/80) film (PLD film on SrTiO_3 substrate) shows two a/c -variants with the walls parallel to (101) and $(\bar{1}01)$ planes (Ganpule et al., 2000a). An SFM image obtained from an identically processed film is shown in Fig. 9.2.4. A cross-hatched pattern

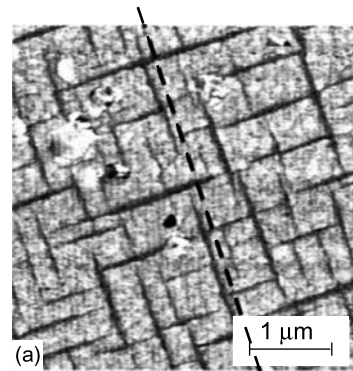
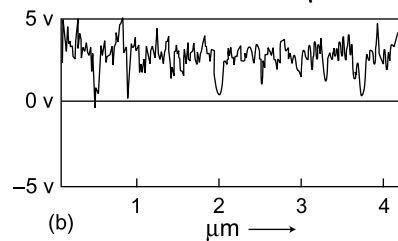


Fig. 9.2.4 (a) Typical piezoelectric image of a $\text{Pb}(\text{Zr}_{0.2}\text{Ti}_{0.8})\text{O}_3$ epitaxial film. (b) The amplitude of the electric signal corresponding to the vibration intensity as a function of the distance along the line drawn in (a). Reprinted with permission from Ganpule et al. (2000a). Copyright (2000), American Institute of Physics



shown in this figure corresponds to interpenetrating a/c -variants having walls parallel to (101) and (011) planes, the black stripes visualizing the intersections of a -domains with the free surface of the film. Similar images were obtained by different authors using various visualizing techniques: SFM in the height mode (Seifert et al., 1995), SFM in the piezoelectric mode (Maruyama et al., 1998), TEM (Ganpule et al., 2000a), and chemical etching followed by making platinum–carbon replicas (Sviridov et al., 1992). Actually these structures should be considered as made of all three possible ferroelastic domain states. According to Roytburd et al. (2001) two types of three-domain-state regular structures are possible: the so-called “second-order polydomain” and “cellular polydomain” structures schematically shown in Fig. 9.2.5. The cross-hatched patterns typically observed correspond to the “cellular polydomain” type structure, which, however, are not as regular as that shown in Fig. 9.2.5. Independently of whether an a/c -domain pattern corresponds to a three-domain-state structure or the film consists of non-overlapping areas containing different types of a/c -variant, the films usually contain nearly equal fractions of four possible a -domain states. If the film is not too thin, these states can be distinguished by using the XRD intensity reciprocal space mapping (Foster et al., 1995; Lee and Baik, 2000). The result of such analysis offered by Lee and Baik (2000) is shown in Fig. 9.2.6 where the XRD contour maps for HK-reciprocal space of PbTiO_3 (100) reflections are shown for films of different thicknesses (PLD film on MgO substrate). In thinner films, Fig. 9.2.6a and b, the (100) Bragg point is not split, which means that, in all four a -domain states, the vertical a -axes are strictly normal to the substrate. In thicker films, Fig. 9.2.6c and d, the (100) Bragg point is split into four points, showing that now all four a -domain states are misoriented with respect to the substrate. The cause of this misorientation is the clapping angles between a - and c -domains, the latter being oriented normally to

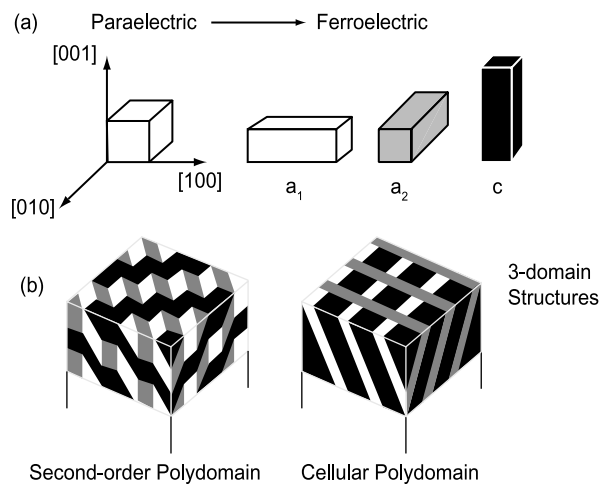


Fig. 9.2.5 Possible three-domain-state regular structures in (001) tetragonal ferroelectric thin films. After Roytburd et al. (2001)

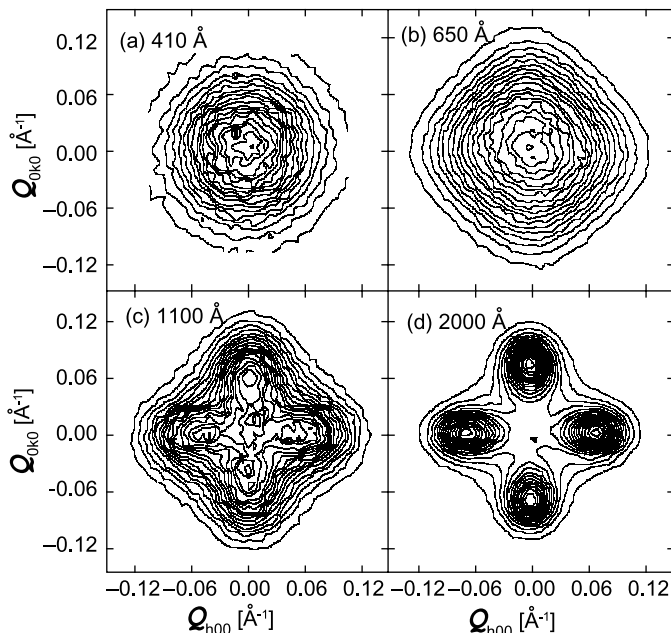
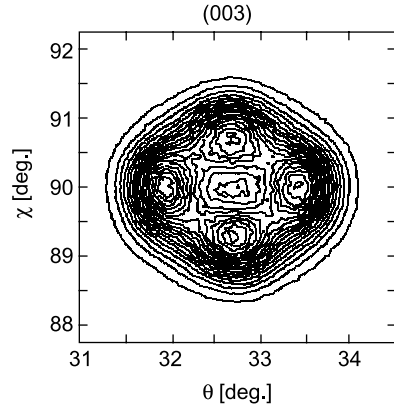


Fig. 9.2.6 XRD counter maps for HK-reciprocal space of PbTiO_3 (100) reflection intensity shown for films of different thicknesses. Reprinted with permission from Lee and Baik (2000). Copyright (2000), American Institute of Physics

the substrate (Lee et al., 2001b). It was, however, found that the tilt φ_a of a -domains is smaller than that of the bulk value of the clapping angle $2\arctan(c/a) - 90^\circ$ (see Sect. 2.2.5), c and a being the lattice parameters of the bulk material. For example, according to two groups of authors (Foster et al., 1995; Lee and Choi, 2001), for $\text{PbTiO}_3/\text{MgO}$ films, $\varphi_a \sim 2.6^\circ$, that is smaller than the bulk value of the clapping angle 3.6° . For the same system, yet smaller values of φ_a have also been obtained (Lin et al., 1999): in the range 1.9 – 2.15° , depending on the cooling rate. The c -domains of a/c -variant also can be misoriented with respect to the substrate. Figure 9.2.7 shows an area map of XRD intensity of (003) peak of a 790 nm thick PbTiO_3 film (MOCVD film on MgO substrate) (Foster et al., 1995); the splitting of the peak corresponds to a 0.6° misorientation of c -domains in the film.

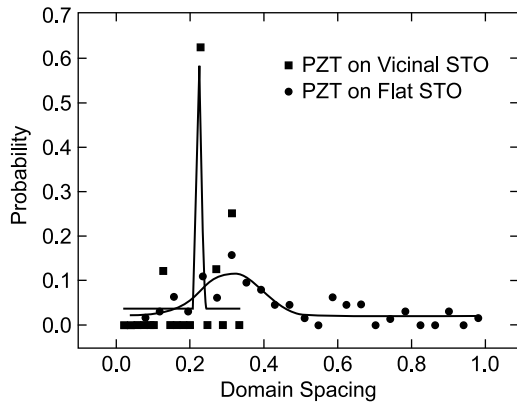
The images shown in Figs. 9.2.2, 9.2.3, and 9.2.4 suggest that the domain patterns in the films can be characterized by a certain value of the a -domain spacing. However, it is seen from these figures that, in different regions of the same film, this value can readily differ by a factor of 2. Despite this scatter of the data a clear trend can be traced: The average spacing in ferroelastic domain patterns in films of a given material increases with increasing film thickness. These two statements are illustrated with the experimental data

Fig. 9.2.7 XRD counter map of XRD intensity of (003) reflection of a 790 nm thick PbTiO_3 film. Reprinted with permission from Foster et al. (1995). Copyright (1995), American Institute of Physics



given in Table 9.3.2 later in this chapter. A systematic analysis of periodicity of ferroelastic domain patterns in $\text{PZT}/\text{SrTiO}_3$ films has been reported by Nagarajan et al. (2001). The obtained statistics of the a -domain spacing is illustrated in Fig. 9.2.8. It is seen that the periodicity in the film deposited onto a flat SrTiO_3 substrate is rather poor; at the same time, it can be strongly improved by using a vicinal substrate, i.e., a crystalline substrate having the orientation which is very close to a certain high-symmetry orientation, e.g., (001). Such substrates exhibit a system of small steps on the surface spaced by many lattice constant distance. This effect is illustrated in Fig. 9.2.8 showing a very narrow distribution of the domain spacing in a film grown on a vicinal SrTiO_3 substrate having 7–10 nm steps every 200 nm. In this system the steps fix the positions of narrow a -domains. Natural defects in the substrate also often provoke nucleation of ferroelastic domains in the film (Foster et al., 1997).

Fig. 9.2.8 Probability of a -domain spacing in (100) $\text{PbZr}_{0.2}\text{Ti}_{0.8}\text{O}_3$ epitaxial thin films on (100) SrTiO_3 substrates for the exact (100) orientation (Flat STO) and for 3° vicinal cut toward (010) (Vicinal STO). Reprinted with permission from Nagarajan et al. (2001). Copyright (2001), American Institute of Physics



9.2.1.2 Composition of Ferroelastic Domain Patterns

The most clearly determined characteristic of a/c -domain patterns in films is the fraction of different domain states. A convenient parameter describing the composition of the pattern is the volume fraction of c -domains, which we denote as α . It can be evaluated from TEM or SFM images. For instance, using the TEM image shown in Fig. 9.2.3 one can evaluate $\alpha = 0.7\text{--}0.9$ from the ratio of the volumes of the a - and c -domains shown in this image. Another way of evaluation of the average fraction of domain states in a pattern is to analyze the intensities of XRD peaks. In terms of total intensities of the (001) and (100) reflections, $\Sigma I(001)$ and $\Sigma I(100)$, the fraction of c -domain states can be evaluated as

$$\alpha = \frac{\Sigma I(001)}{\Sigma I(100) + \Sigma I(001)}. \quad (9.2.1)$$

Reliable information on the XRD intensity peaks can be obtained from maps of XRD intensities (or rocking curves) like those shown in Figs. 9.2.6 and 9.2.7. For a common situation the (001) point is not split and the (100) point is so that $\Sigma I(001) = I(001)$ and $\Sigma I(100) = 4I(100)$. Just the use of areas of the corresponding maxima of θ - 2θ curves can lead to wrong values of α . A detailed discussion of this point has been offered by Foster et al. (1995).

For PbTiO_3 and tetragonal PZT films, the fraction α has been evaluated as a function of film thickness h by many authors. It has been found that the $\alpha(h)$ dependence is sensitive to the substrate material and film composition. Available experimental data reveal both increasing and decreasing types of the $\alpha(h)$ dependence as it is shown in Fig. 9.2.9. This figure suggests a correlation between sense of this dependence and the sign of the in-plane strain imposed by the substrate on the film at the processing temperature (typically some 700°C). Namely, the positive sign of this strain corresponds to $\alpha(h)$ increasing as a function of h and vice versa. In the case of MgO and KTaO_3 substrates (Fig. 9.2.9a and b), at the processing temperature, the lattice constants of the substrates a_s (4.351 and 4.004 Å) are greater than that of the bulk ferroelectric in the paraelectric phase $a_c = 3.979$ Å. Via the effect of epitaxy this leads to tensile stresses in the film. In the case of $\text{PbTiO}_3/\text{SrTiO}_3$ ($a_c = 3.979$ Å and $a_s = 3.934$ Å) and $\text{Pb}(\text{Zr}_{0.2}\text{Ti}_{0.8})\text{O}_3/\text{LaAlO}_3$ ($a_c = 4.02$ Å and $a_s = 3.821$ Å) the inverse relation between a_s and a_c takes place so that, in the paraelectric phase, the film is under compression. Results for $\text{PbTiO}_3/\text{MgO}$ system, similar to those shown in Fig. 9.2.9a, have been reported by Choi et al. (1998). The trend illustrated for the $\text{PbTiO}_3/\text{SrTiO}_3$ system in Fig. 9.2.9c, namely the thinner the film, the higher the fraction of c -domains, is in qualitative agreement with results reported by Forster et al. (1995) and Theis and Schlom (1997). However, for this system, several authors have reported the pure c -domain state for quite thick (up to 250 nm) films (Lee et al., 2001b; Kwak et al., 1994; Gan et al., 1998).

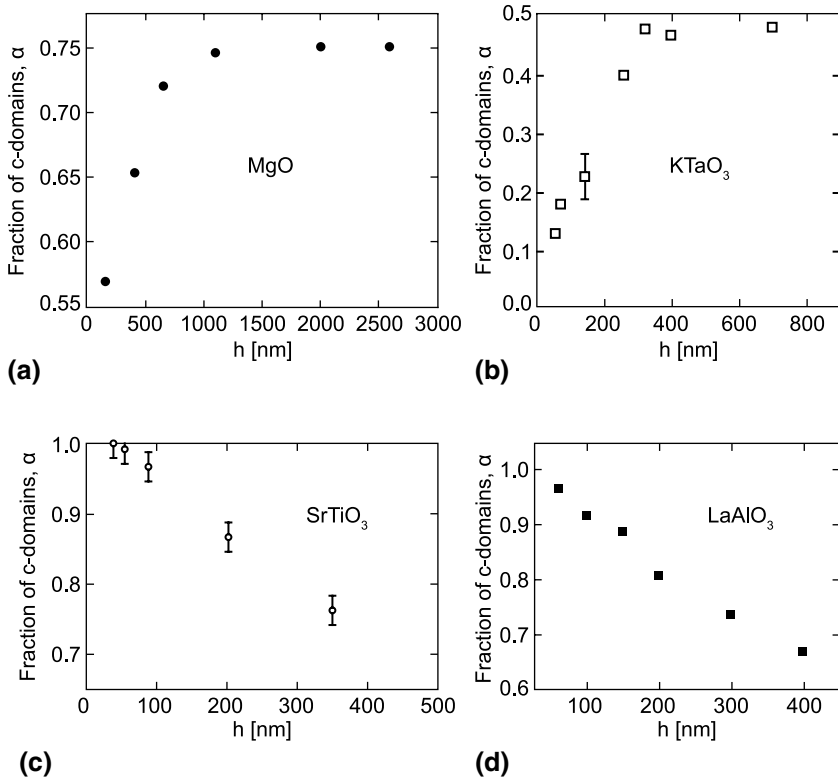


Fig. 9.2.9 Fraction of *c*-domains in of PbTiO_3 films on different substrates as a function of the film thickness. (a) MgO, (b) KTaO_3 , (c) SrTiO_3 , (d) LaAlO_3 . After Lee and Baik (2000), Kwak et al. (1992), Hsu and Raj (1995), and Nagarajan et al. (1999)

The temperature dependence of α was experimentally addressed for films of PbTiO_3 and PLT on MgO (Lee and Baik, 1999; Kwak et al., 1994; Alpay et al., 1998; Kang and Baik, 1997) and for $\text{PbTiO}_3/\text{KTaO}_3$ films (Kwak et al., 1994). The same trend, namely a reduction of α with increasing temperature, was obtained. The results by Lee and Baik (1999) on $\text{PbTiO}_3/\text{MgO}$ films (PLD; $h = 300$ nm) are shown in Fig. 9.2.10a, the results of Kwak et al. (1994) being very close to those shown. Figure 9.2.10b shows the $\alpha(T)$ dependence obtained by Kwak et al. (1994) for $\text{PbTiO}_3/\text{KTaO}_3$ (MOCVD, $h = 250$ nm).

Data on the concentration dependence of the fraction of *c*-domains α in PZT/MgO system (magnetron sputtering) were reported by Lee et al. (1997b). The ratio of integrated intensities of rocking curves for (001) and (100) was used for the evaluation of this parameter. It was found that, both at room and phase transition temperatures, α increased with increasing Zr concentration (see Fig. 9.2.11), the effect being better pronounced at the transition temperature.

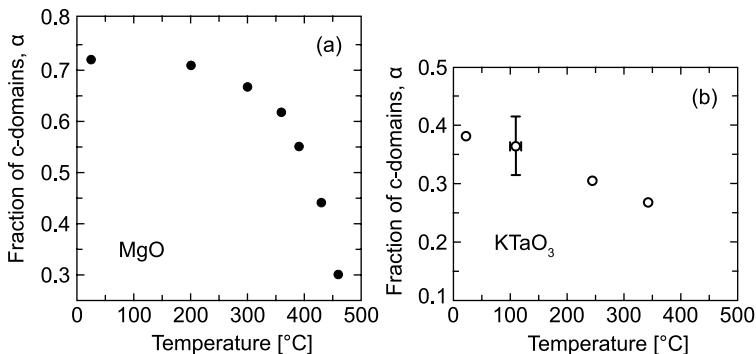
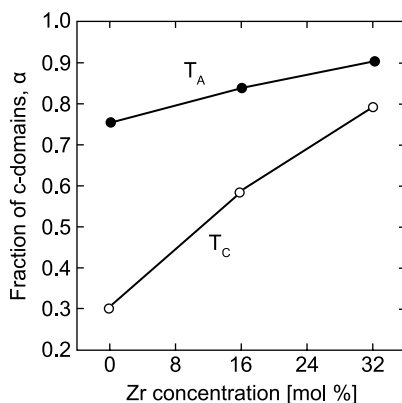


Fig. 9.2.10 Fraction of *c*-domains in PbTiO₃ films on different substrates as a function of temperature. (a) MgO; (b) KTaO₃. After Lee and Baik (1999) and Kwak et al. (1992)

Fig. 9.2.11 Fraction of *c*-domains in of Pb(Zr,Ti)O₃ films on MgO substrate as a function of Zr concentration at room temperature (marked T_A) and close to the phase transition (marked T_C). After Lee et al. (1997b)



Similar behavior has been reported for the La-concentration dependence of α in PLT/MgO films (Kang and Baik, 1997).

All experimental data on *a/c*-patterns in (001) films presented above have been obtained for PbTiO₃ (pure or modified) films which attracted the most attention of workers. Much less information is available on *a/c*-patterns from ferroelectric thin films of BaTiO₃. Despite considerable amount of publications on (001) BaTiO₃ films, the information on ferroelastic domain patterns in these is virtually absent since most of the works report on *a*- or *c*-monovariant states. A correlation between the type of the monovariant and thermal expansion coefficient of the substrate has been reported for MgO, GaAs, and fused quartz substrates (Ogawa et al., 1991; Srikant et al., 1995). For MgO substrate, which has a higher coefficient of thermal expansion than that of BaTiO₃ in the paraelectric phase, one observed the *c*-domain state, whereas for GaAs and fused quartz having smaller expansion coefficients, it was the *a*-domain state. As for

the a/c -pattern, it has been only observed in the peripheral regions of BaTiO₃ (001) films (MBE, $h = 20$ nm) (Tsunekawa et al., 1999a,b). According to SFM image, this pattern exhibits a period of some 70 nm and the c -domain fraction $\alpha \cong 0.5$. The a_1/a_2 -pattern was reported for BaTiO₃ (001) films (MOCVD, $h = 500\text{--}600$ nm) by Kaiser et al. (1995).

9.2.1.3 Antiparallel Domain Patterns

Antiparallel domain patterns have been observed in (001) perovskite thin films by using different experimental techniques. Probably the first information on 180° domains in these systems has been reported by Surowiak et al. (1993) who employed a method with a chemical etching followed by making platinum–carbon replicas. These authors monitored antiparallel c -domains in (Ba_{1-x}Sr_x)TiO₃/MgO ($x = 0 - 0.3$) films obtained by sputtering covering the thickness range $h = 20 - 5000$ nm. The films were purely c -domain oriented. The temperature evolution of the domain pattern observed in a (Ba_{0.7}Sr_{0.3})TiO₃ film is illustrated in Fig. 9.2.12. This film was found to be under a strong in-plane compression which resulted in a 90 K shift of the transition temperature in the film compared to its value for the target (310 K). The mean width of the observed domains was reported to increase as $\approx 0.28h$ with increasing film thickness h .

Thickness-dependent 180° domain patterns in MBE deposited BaTiO₃/SrTiO₃ films has been reported by Tsunekawa et al. (1997, 1998) for film thicknesses of 4, 20, 1000 nm. The information was obtained by using SFM. A correlation between the sign of polarization in domains and their height, which enabled the visualization of the pattern, was attributed by the authors to dry etching effects. The end shape of the 180° cylindrical domain was found regular (almost round) in thinner films becoming irregular with increasing thickness. In thicker films, the coexistence of 180 and 90° domains was observed. The determined thickness dependence of the average diameter of the domain ends D is shown in Fig. 9.2.13, where the data on bulk BaTiO₃ crystals obtained by the same authors are also incorporated. As the best fit for this dependence a relation $D = 3.2h^{0.51}$ (D and h are in nm) was suggested.

Similar correlation between the domain height and their sign was reported by Odagawa and Cho (2001) who used a combination of height-mode SMF technique with scanning nonlinear dielectric microscopy (see Sect. 4.5.6). In their experiments, the polarity of the domains was determined from the phase of the second polarization harmonics taken simultaneously with surface topology images. For PZT/SrTiO₃ films, the positively poled domains were reported to be 1 nm higher than those poled negatively. An example of a cross-section of the second harmonics phase image containing 180° domains is shown in Fig. 9.2.14, here 1–3 nm domains separated with 0.3–0.5 nm transient regions. The latter should be interpreted as conditioned by the finite instrumental resolution not by the wall thickness since the phase of the second harmonics can be related to the *sign* of the polarization, which changes abruptly in the wall of any thickness.

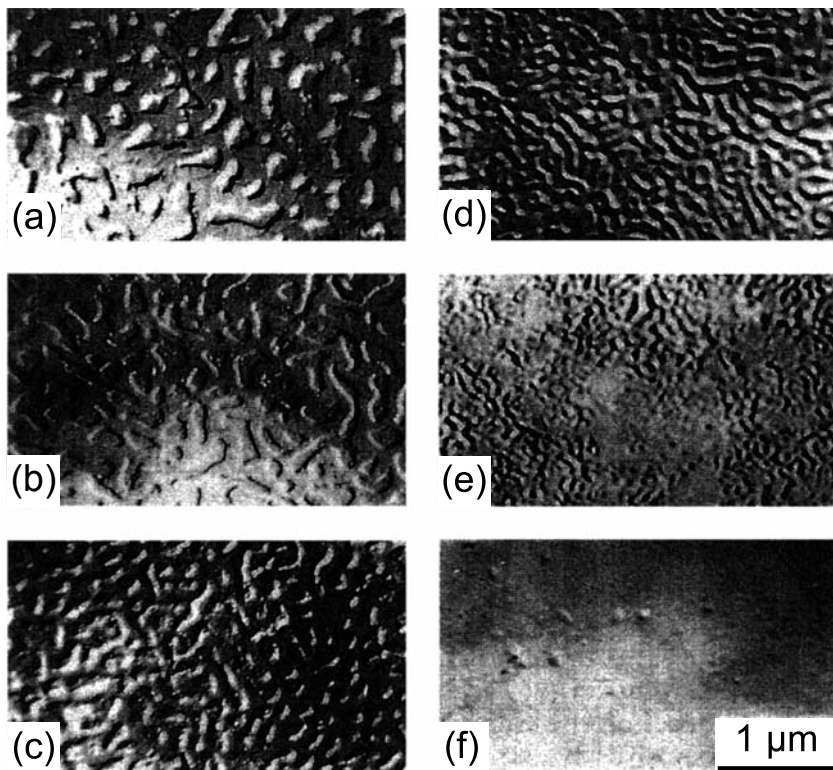


Fig. 9.2.12 Evolution of *c*-domain structure in (001) films of $\text{Ba}_{0.7}\text{Sr}_{0.3}\text{TiO}_3$ on MgO substrate as a function of temperature (a) 293 K, (b) 333 K, (c) 353 K, (d) 369 K, (e) 383 K, (f) 403 K. Reprinted with permission from Surowiak, Z., Mukhortov, V.M., Dudkevich, V.P. Phase transitions and domain structure in heteroepitaxial ferroelectric $(\text{Ba}_{1-x}\text{Sr}_x)\text{TiO}_3/(100)\text{MgO}$ and $\text{PbTiO}_3/(100)\text{MgO}$ thin films, *Ferroelectrics* **139**, 1 (1993). Copyright (1993), Taylor and Francis

Fig. 9.2.13 Geometrically averaged diameter of the ends of *c*-domains vs. the thickness of an epitaxial BaTiO_3 film on SrTiO_3 substrate. After Tsunekawa et al. (1997)

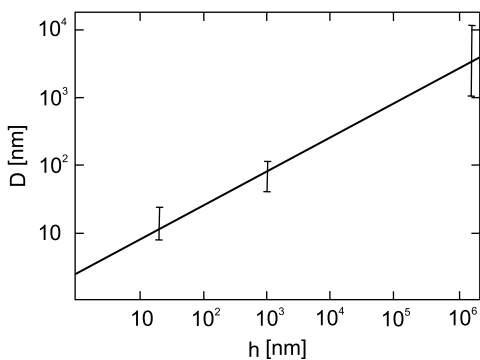
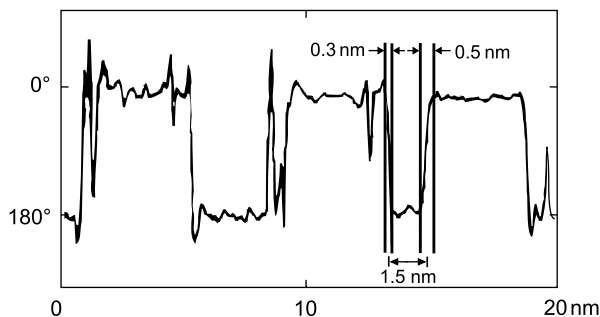


Fig. 9.2.14 A cross-section of the second harmonics phase image containing 180° domains. $\text{Pb}(\text{Zr},\text{Ti})\text{O}_3$ films on SrTiO_3 substrate. Reprinted with permission from Odagawa and Cho (2001). Copyright (2001), Taylor and Francis



All the experiments discussed above are dealing with information obtained from the interface or from a thin interfacial layer of the films. To obtain the direct information on the 180° domain patterns in the “bulk” of the film one should test the sample using a kind of radiation that can penetrate into it. An example of such a study has been offered by Streiffer and coworkers (2002). In this work, epitaxial $\text{PbTiO}_3/\text{SrTiO}_3$ films of thicknesses $h = 1.6 - 42$ nm were studied using X-ray scattering. Upon cooling below the transition temperature, satellites appeared around Bragg peaks indicating the presence of 180° stripe domain patterns of period $W = 3.7 - 24$ nm, the thickness dependence of period of the patterns (shown in Fig. 9.2.15) being consistent with the square root law $W = 3.2 h^{0.5}$ (W and h are in nm). Another interesting finding of this chapter is the observation of three types of the domain structures depending on the temperature and the thickness of the film. It was reported that on progressive cooling from the paraelectric state the system exhibits, first, a pattern where the domain width is comparable to the domain wall thickness, second, a pattern with relatively narrow domain walls, and finally, a single-domain state.

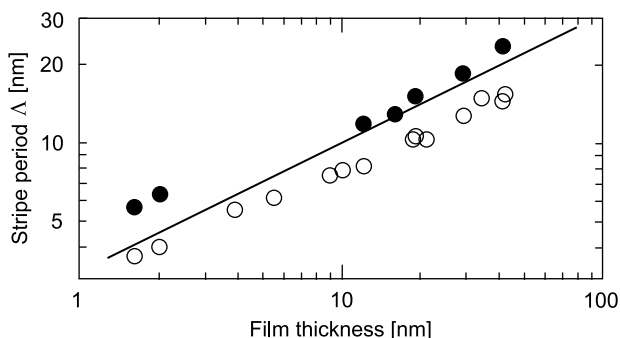


Fig. 9.2.15 Period of a striped c -domain pattern vs. thickness of PbTiO_3 films on SrTiO_3 substrate. *Solid symbols*: $T = T_c - 250$ K. *Open symbols*: $T = T_c - 50$ K. *Line*: theory at $T = T_c - 250$ K (the square root law with the parameters taken from independent sources, see Sect. 9.4). After Streiffer et al. (2002)

9.2.2 Ferroelastic Domain Patterns in (001) Rhombohedral and (111) Tetragonal Thin Films of Ferroelectric Perovskites

In this section we will discuss the theoretically expected and experimentally observed structures of ferroelastic domain patterns in (001)-oriented rhombohedral and (111)-oriented tetragonal ferroelectric thin films. Specifically, we will address the case of perovskite ferroelectrics with the cubic $m\bar{3}m$ paraelectric phase and tetragonal $4mm$ and/or rhombohedral $3m$ ferroelectric phases. The common feature of these systems is that none of their domain states have spontaneous polarization purely normal to the plane of the film whereas the vectors of spontaneous polarization in these domain states are arranged in a symmetric manner with respect to the film normal. We will see that a certain similarity is also expected between the ferroelastic domain patterns in these systems.

The geometry of domain patterns in these systems has been treated by Streiffer et al. (1998) and Romanov et al. (1999) based on the conditions of mechanical and electrical compatibilities (see Sects. 2.2.3 and 2.2.4). Specifically, it has been found that in these systems, in all domains, the components of the spontaneous polarization normal to the plane of the film are equal in the absolute value whereas its in-plane components are equal in absolute value but differ in orientation.

For the case of the cubic–rhombohedral ferroelectric phase transition ($m\bar{3}m \Rightarrow 3m$), four possible ferroelastic states (or variants) are shown in Fig. 9.2.16. Orientations of elastically permissible domain walls separating these variants are given in Table 9.2.1 (see also tables in Appendix D). The walls are of $\{100\}$ and $\{110\}$ orientations. The symmetric arrangement of the vectors of spontaneous polarization of the variants with respect to the film normal implies that the in-plane spontaneous strain in the variants can differ only in their orientations, i.e., the tensors of the spontaneous deformation of the domains are related by in-plane rotations of the reference frame. This situation is similar to the a_1/a_2 -pattern in tetragonal (001) films discussed in the previous section. Like in the a_1/a_2 -pattern, in (001) rhombohedral films, the width of the domains making a ferroelastic pattern is expected to be the same. However, two types of patterns are possible.

Domain patterns of the first type contain walls that are perpendicular to the plane of the film. The structure of such patterns is shown in Fig. 9.2.17a and b; they contain walls of (100) and (010) orientations. As clear from Fig. 9.2.17b, the net polarization of this pattern possesses only the in-plane component. Domain patterns of the second type contain oblique walls that make angles of about 45° with the plane of the film (Fig. 9.2.17c and d). As clear from Fig. 9.2.17d, the net polarization of this pattern possesses a nonzero out-of-plane component. Thus, the domain structure with vertical walls is nonpolar in the out-of-plane direction whereas the structure with oblique walls is “perfectly poled” in this direction, i.e., it exhibits the maximal vertical projection of the net

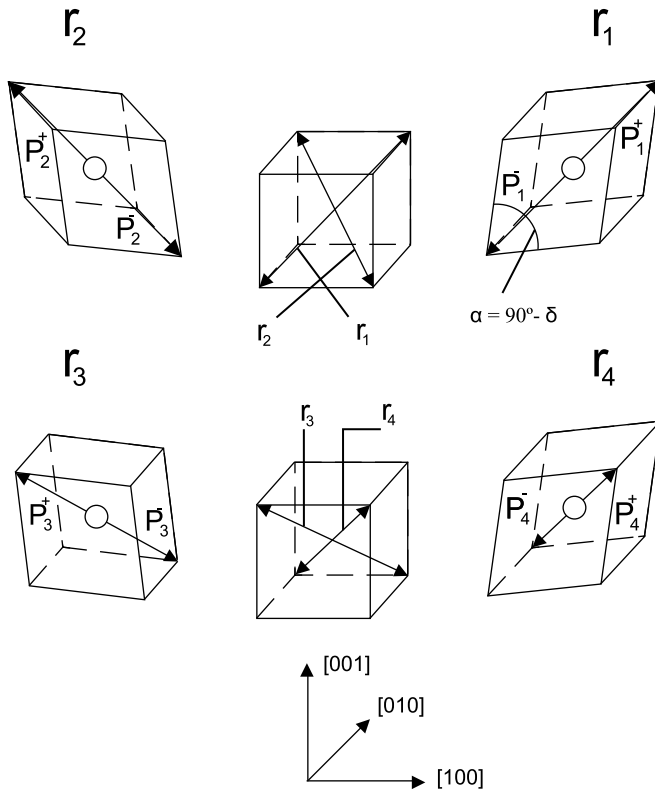


Fig. 9.2.16 Elementary cell transformations resulting from cubic-rhombohedral ferroelectric phase transition showing four structural variants of the rhombohedral phase (r_1, r_2, r_3, r_4) and eight polarization variants ($P_1^+, P_1^-, P_2^+, P_2^-, P_3^+, P_3^-, P_4^+, P_4^-$) corresponding to eight domain states allowed at this transition. Reprinted with permission from Streiffer et al. (1998). Copyright (1998), American Institute of Physics

Table 9.2.1 Coherent domain boundaries between different variants (defined in Fig. 9.2.16). The asterisks denote variants that are not expected in epitaxial (001) films. After Streiffer et al. (1998)

Variant	r_1	r_2	r_3	r_4
r_1		(100)	(001)*	(010)
		(011)	(110)*	(101)
r_2			(010)	(001)*
			($\bar{1}01$)	($\bar{1}10$)*
r_3				(100)
				($0\bar{1}1$)

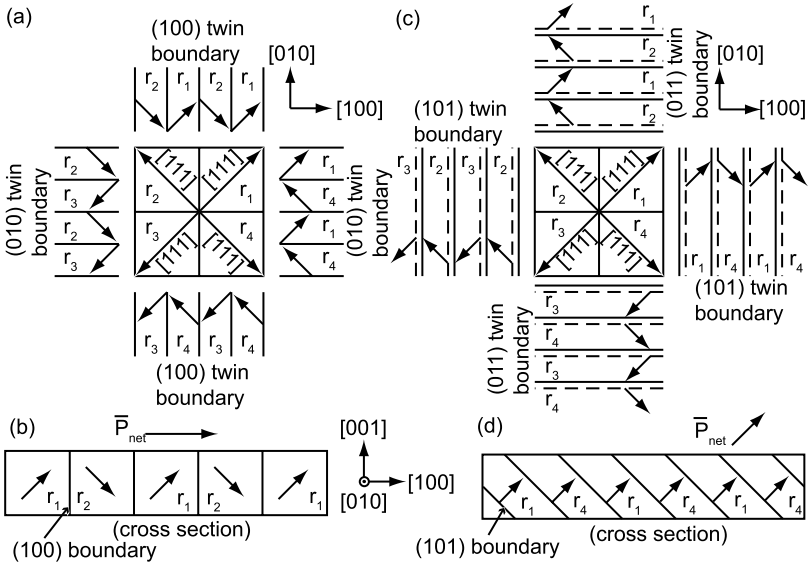


Fig. 9.2.17 Schematic plan views (a) and (c) and cross-sections (b) and (d) of possible domain parents in (001) ferroelectric films exhibiting a cubic–rhombohedral ferroelectric phase transition. *Arrows* show the directions of spontaneous polarization in the domains and of the net polarization of the pattern. For the definition of the structural variants of the rhombohedral phase (r_1, r_2, r_3, r_4) see Fig. 9.2.16. Reprinted with permission from Streiffer et al. (1998). Copyright (1998), American Institute of Physics

spontaneous polarization. One should mention that not all ferroelastic patterns permitted in the bulk material are expected in (100) rhombohedral films. The reason is as follows. The driving force of the formation of ferroelastic domain patterns is a stress release. In the case of ceramics, it is a three-dimensional stress release in grains clamped on average by the rest of the material. In films on a substrate, it is a release of the two-dimensional stress imposed by the substrate. If the in-plane spontaneous strains in two ferroelastic variants are the same, a pattern made of these variants cannot obviously contribute to the above two-dimensional stress release and, thus, is not favored. This is the case of a domain structure containing r_1/r_3 or r_2/r_4 pairs which are not expected to occur in the considered system (see Sect. 9.3.4 for a more detailed discussion).

In the case of (111) tetragonal films, one finds a situation similar to that discussed above for (001) rhombohedral films. Here, also two types of domain patterns are possible. One is nonpolar in the out-of-plane direction and contains vertical walls, which can be parallel either to $(\bar{1}01)$, or to $(0\bar{1}1)$, or to $(\bar{1}10)$ crystallographic planes. This pattern is explained in Fig. 9.2.18a and b. The patterns of the second type are “perfectly poled” in the out-of-plane direction and contain oblique walls of either (101), or (011), or (110) orientations as shown in Fig. 9.2.18c and d.

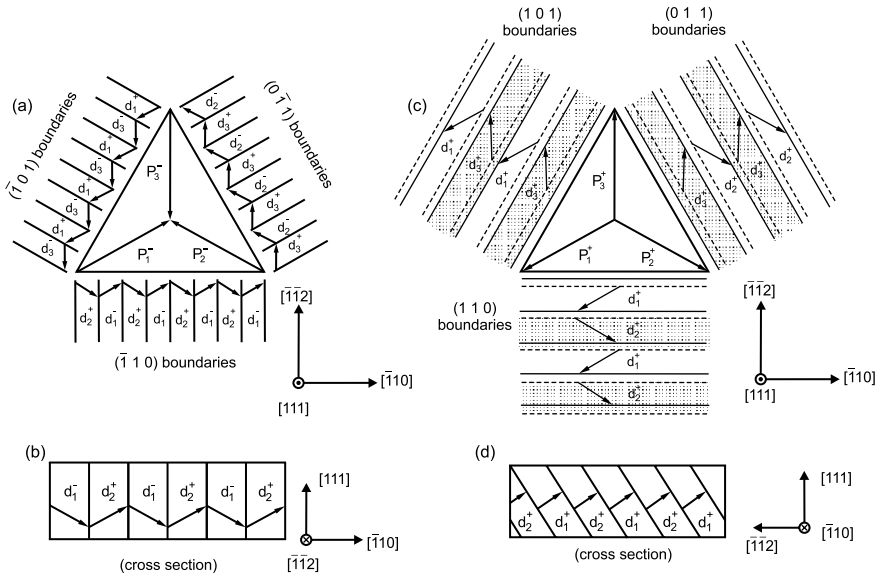


Fig. 9.2.18 Schematic plan views (a) and (c) and cross-sections (b) and (d) of possible domain parents on (111) ferroelectric films exhibiting a cubic–tetragonal ferroelectric phase transition. Arrows show the directions of spontaneous polarization in the domains. Symbols d_i^\pm denotes six possible domain states allowed at this transition. After Romanov et al. (1999)

Comparing the two types of the domain patterns in rhombohedral and tetragonal systems discussed above an essential qualitative difference between these systems can be pointed out. In (001) rhombohedral films, the intersection lines between domain walls and the upper film surface are oriented either along [100] or along [010] directions disregarding the type of the pattern. These directions are equivalent in terms of the cubic symmetry of the paraelectric phase. For this reason, one cannot distinguish the “nonpolar” and “perfectly poled” patterns merely judging from the orientation of these lines (cf. Fig. 9.2.17). In contrast, in (111) tetragonal films, for the “nonpolar” and “perfectly poled” patterns, the orientations of the intersection lines are non-equivalent in the aforementioned sense (see Fig. 9.2.18). Thus, the information on the cross-section of a domain pattern with the film surface enables identification of the pattern type.

A comprehensive investigation of domain structure of (100) rhombohedral PZT thin films was performed by Streiffer et al. (1998). The results of plan-view TEM and SEM studies were reported for MOCVD non-electroded films of two compositions: 80/20 and 65/35 deposited on SrRuO₃-buffered SrTiO₃. Using the information from the δ -fringe contrast, plan-view TEM tilting experiments, and arcing of higher order diffraction spots in selected area electron diffraction pattern, it was shown that the domain structure of the films contains exclusively “nonpolar” patterns having walls of (100) and (010) orientations. The vertical

orientation of the wall was also confirmed by TEM images taken from 200–400 nm thick foils, which are shown in Fig. 9.2.19. Here, the domain pattern consists of orthogonal groups of the order of 10 parallel twin lamellae with traces, with the length of up to some 20 μm and the wall spacing of the order of 200–500 nm. The projected width of the walls is approximately 30 nm, which is consistent with a small ($\sim 5^\circ$) tilt of the foil. SEM images of the films also reveal cross-hatched domain patterns of the same orientation, however, with much smaller domain wall spacing. For 520 nm thick PZT 80/20 films it was found to be 80–120 nm, and for 700 nm thick PZT 65/35 films 50–100 nm. The vertical orientation of the domain walls in non-electroded (100) rhombohedral PZT films was also documented with TEM cross-section images by Lin et al. (1999). As was pointed out by Streiffer et al. (1998) the nonpolar domain configuration can be anticipated for non-electroded films since it is more electrostatically favorable than the “perfectly poled” pattern.

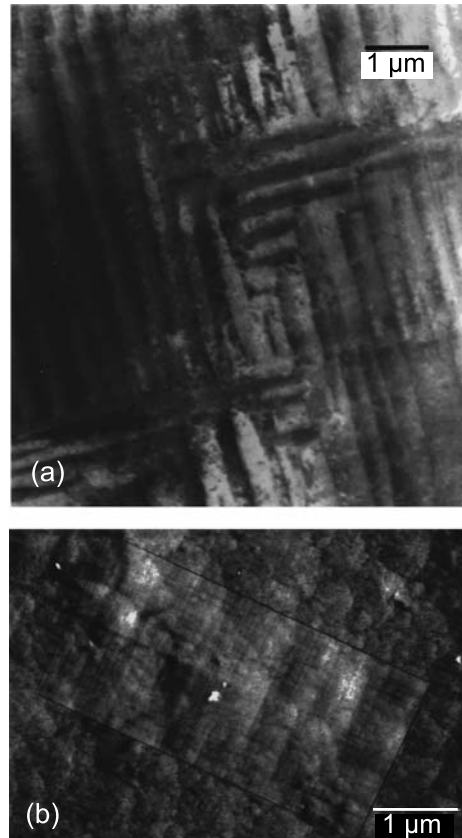


Fig. 9.2.19 (001) film of tetragonal $\text{PbZr}_{0.65}\text{Ti}_{0.35}\text{O}_3$. Plan-view TEM (a) and SEM (b) images of domain patterns. In the rectangular, the voltage contrast is enhanced by applying a Fourier filter. Reprinted with permission from Streiffer et al. (1998). Copyright (1998), American Institute of Physics

The experimental data on domain patterns in (111) tetragonal ferroelectric thin films are limited though PZT films of this type are actually used in non-volatile memory devices.

Results of SFM (topography mode) studies of sputtered (111) PZT (25/75) films deposited on Si covered with different sublayers (Pt, IrO_2 , and Al_2O_3) have been reported by Zybill et al. (1999, 2000). For 700 nm films, the patterns visualized have typical domain wall spacing about 20 nm. For films on Pt sublayer, the spacing increases with increasing film thickness h : $h = 300, 500,$ and 700 nm correspond to spacings of 12, 16, and 19 nm, respectively (Zybill et al., 2000). An example of height-mode SFM image of the surface of a film revealing a domain pattern is shown in Fig. 9.2.20 (after Zybill et al., 1999). This image enables also an evaluation of the width of 90° -domain wall as ~ 1 nm. The investigated films were found to be spontaneously poled during the deposition. This suggests that the film contains “perfectly poled” patterns with oblique domain walls.

An example of nonpolar domain pattern in a (111) PZT tetragonal ferroelectric film has been reported by Romanov et al. (1999). In this paper, the conclusion about the presence and type of the domain pattern was drawn from the SEM images shown in Fig. 9.2.21, where the contrast was related to the sign of the normal component of the polarization in the domains. This image was interpreted as a superposition of three types of nonpolar domain patterns illustrated in Fig. 9.2.18b.

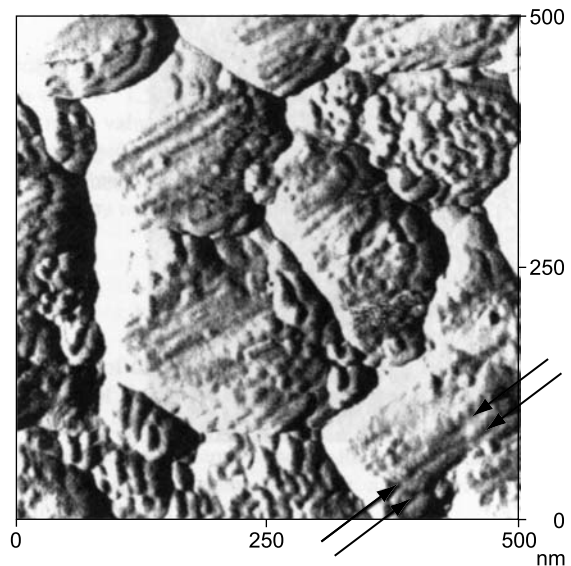
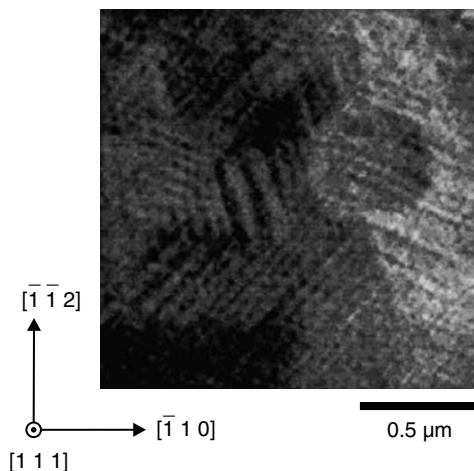


Fig. 9.2.20 An example of height-mode SFM image of the surface of a (111) tetragonal $\text{PbZr}_{0.25}\text{Ti}_{0.75}\text{O}_3$. Domain walls are shown with *arrows*. After Zybill et al. (1999)

Fig. 9.2.21 SEM image of a domain pattern in tetragonal (111) PZT film. Reprinted with permission from Romanov et al. (1998). Copyright (1998), Wiley-VCH Verlag GmbH & Co. KGaA



9.2.3 Domain Structure in Other Systems

Experimental information available in the literature on domain patterns in systems different from tetragonal and rhombohedral perovskite films is very limited as well as the relevant theoretical work. This impedes conclusive discussion of this matter. For this reason in the present section we restrict ourselves to brief mentioning of some publications and findings.

Room temperature domain structure of orthorhombic (with the cubic paraelectric phase) KNbO_3 films has been experimentally addressed by Gopalan and Raj (1996, 1997). The studied films had a thickness of about 350 nm and were laser ablated onto a SrTiO_3 (100) substrate or onto a MgO (100) substrate with a 12 nm SrTiO_3 sub-layer. The films exhibit excellent cube-on-cube epitaxy. TEM investigations reveal that among 12 possible ferroelectric domain states (see Fig. 2.3.5b) only 8, which have nonzero out-of-plane component of the spontaneous polarization, participate in the domain patterns. Judging from plan-view TEM micrographs, the films were found to contain a domain pattern made of 60° and 120° domain walls whose traces on the (001) plane are parallel to the $[011]$ and $[0\bar{1}1]$ pseudo-cubic directions (Fig. 9.2.22), a typical domain wall spacing being about 100 nm. Area fractions of four domain pairs (with the same in-plane component of the spontaneous polarization within any pair) were evaluated from the result of the second optical harmonics generation measurements. For some 30 mm^2 area of as-deposited films tested, the fractions of the pairs were found virtually equal (to within a 2–3% accuracy).

Similar characterization of monoclinic $\text{Bi}_4\text{Ti}_3\text{O}_{12}$ films has been offered by Barad et al. (2001). $\text{Bi}_4\text{Ti}_3\text{O}_{12}$ films of 100 nm thickness were MBE deposited onto SrTiO_3 with the epitaxial orientation relationship SrTiO_3 (001)[110]/ $\text{Bi}_4\text{Ti}_3\text{O}_{12}$ (001)[100]. The symmetry of the bulk material allows eight ferroelectric domain states. The plan-view TEM analysis revealed a network of 90°

Fig. 9.2.22 Plan-view TEM micrograph of a domain pattern in orthorhombic (100) film of KNbO_3 . Reprinted with permission from Gopalan and Raj (1997). Copyright (1997), American Institute of Physics

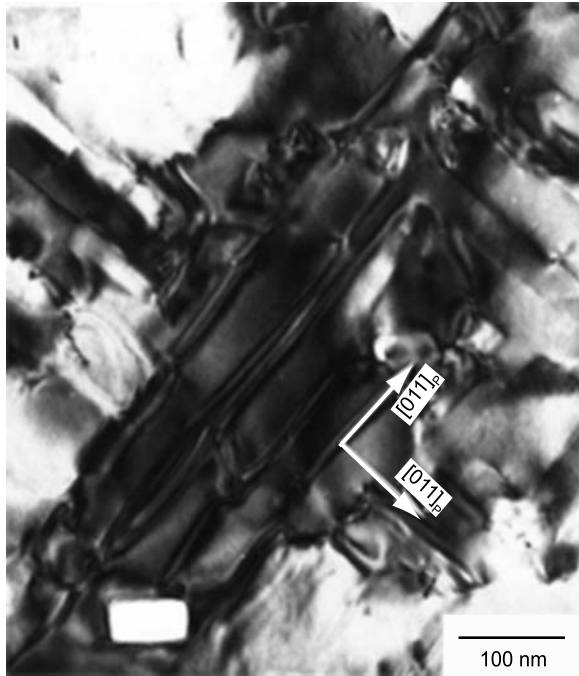
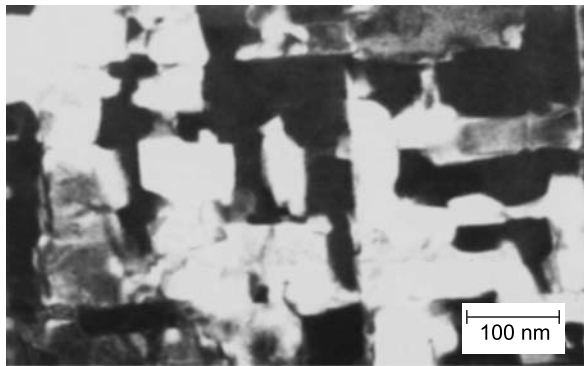


Fig. 9.2.23 Network of 90° domain walls as seen in the plan-view dark-field TEM image of a monoclinic (001) $\text{Bi}_4\text{Ti}_3\text{O}_{12}$ thin film. Reprinted with permission from Barad et al. (2001). Copyright (2001), American Institute of Physics



domain walls approximately parallel to $\text{SrTiO}_3\langle 100 \rangle$ directions (Fig. 9.2.23), the typical domain wall spacing being about 100–200 nm. Area fractions of four domain pairs A_x^+ , A_x^- , A_y^+ , and A_y^- (with the same in-plane component of the spontaneous polarization within any pair; here the suffix and index denote its orientation and sign of polarization in the pair, respectively) were evaluated from the results of the second optical harmonics generation measurements. For some 1 mm^2 area of as-deposited films tested, a point-to-point variation of the ratio $\frac{|A_x^+ - A_x^-|}{|A_y^+ - A_y^-|}$ was found to be 15–20% about the value of 1.

Films of isostructural Aurivillius phase $\text{SrBi}_2\text{Ta}_2\text{O}_9$ and $\text{SrBi}_2\text{Nb}_2\text{O}_9$ have been drawing attention of researcher because of the use of these materials for memory application; however, the information on domain patterns in these films is very limited. Weak piezoelectric response and very small ferroelastic distortion make difficult standard TEM and SFM visualization of domain pattern in these materials. The results obtained by using optimized SFM (Gruverman and Ikeda, 1998) and Fourier transform HRTEM (Zurbuchen et al., 2002) suggest the presence of quite irregular domain patterns with typical spatial scale of some 10–100 nm. According to these results, in films of these materials, both 180 and 90° domain walls are strongly curved.

9.3 Domain Pattern and Elastic Effects

9.3.1 Strained State of Ferroelectric Film and Dislocation-Assisted Stress Release

The key difference between a mechanically free bulk material and a thin film made of the same material, which is deposited on a dissimilar substrate, is that the film is strained, i.e., the film has the lattice parameters different from those of the bulk material. In this situation one speaks about the presence of misfit strain in the film. This notion plays an essential role in the treatment of elastic effects in ferroelectric thin films. The objective of this section is to discuss the factors controlling the misfit strain and its typical distribution in the films. Let us start with the terminology we are going to use.

Unfortunately, the terminology presently used for the description of strains in ferroelectric films is quite confusing. Namely, the researchers working in the field use the term “misfit strain” in two meanings that can be essentially different when one deals with the low-symmetry phase of the material. This problem is related to the use of two different approaches: the approach based on the Landau theory and that where the purely mechanical aspect of the problem is addressed. In our book, we are going to present both approaches, thus we are to develop below a unified terminology, which will enable us to avoid the aforementioned ambiguity.

We start with the notion of *misfit strain*. When a ferroelectric film, being deposited onto a substrate, exhibits the in-plane lattice constant(s) different from that (those) of the bulk material, one says that the film experiences misfit strain. Thus, formally the misfit strain is defined as the two-dimensional deformation (in the plane of the film) that is required to transform *the unit cell of the non-strained material* into that of the film and we denote it as $\varepsilon_{M\alpha\beta}$ (Here $\alpha, \beta = 1, 2$; we use the Cartesian reference frame with X_3 axis perpendicular to the film/substrate interface). This definition is currently used when one deals with the mechanical aspect of polydomain state of ferroelectric films. However, workers dealing with the Landau theory of ferroelectric thin films define the misfit strain as the two-dimensional deformation that is required to transform *the unit cell of*

the parent phase of the non-strained material into that of the film, for temperatures below the transition point, the extrapolated values of the parameters of the parent unit cell being used. In the parent phase, these definitions are clearly identical; however, in the ferroelectric phase they are essentially different. We use the term *parent misfit strain* for the quantity defined in the latter way and denote it as $\varepsilon_{P\alpha\beta}$. The difference between misfit strain and parent misfit strain is illustrated in Fig. 9.3.1. This figure addresses the case of the cubic/tetragonal phase transition in a (001) epitaxial film of a BaTiO₃-type ferroelectric deposited on an elastically isotropic substrate. Here, the misfit strains are shown with arrow “1” for the paraelectric phase and with arrows “2” and “3” for the ferroelectric phase. The parent misfit strain is shown with arrow “1” for the paraelectric phase and with arrow “4” for the ferroelectric phase. In the same figure the *natural spontaneous strain* already introduced in Chap. 2 is also shown (arrows “5” and “6”). We denote the in-plane components of the latter as $\varepsilon_{S\alpha\beta}$. One easily checks that the tensors of natural spontaneous strain, misfit strain, and parent misfit strain are linked by the following relation:

$$\varepsilon_{M\alpha\beta} = \varepsilon_{P\alpha\beta} - \varepsilon_{S\alpha\beta}. \tag{9.3.1}$$

To clarify the introduced system of definitions we give below expressions for the misfit strains and parent misfit strains for the aforementioned system (illustrated in Fig. 9.3.1). For this system, at any temperature the parent misfit strain tensor can be written as

$$\varepsilon_{P\alpha\beta} = \varepsilon_P \begin{pmatrix} 1 & 0 \\ 0 & 1 \end{pmatrix}, \quad \varepsilon_P = \frac{a_s(T) - a_c(T)}{a_s(T)}, \tag{9.3.2}$$

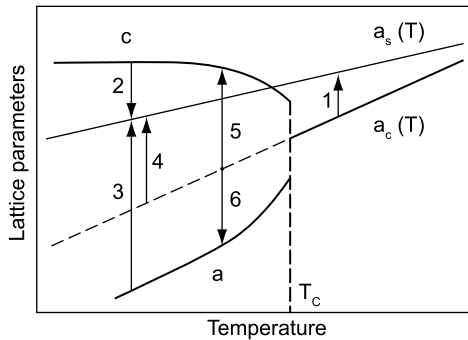


Fig. 9.3.1 Illustration for the concepts of misfit and parent misfit strains. A ferroelectric (like in PbTiO₃) with a cubic/tetragonal ferroelectric phase transition at temperature T_C is considered. The temperature dependences of its lattice constants are shown: $a_c(T)$ —for the cubic phase, a and c —for the tetragonal phase. An epitaxial (001) film of this ferroelectric deposited onto a (001) cubic substrate without formation of misfit dislocations is considered. The temperature dependence of the substrate lattice constant is shown as $a_s(T)$. The variation of the lattice constants corresponding to the natural spontaneous strain (5,6), misfit strain (1, 2, and 3), and parent misfit strain (1,4) are shown with *arrows*

where $a_s(T)$ is the actual in-plane lattice constant of the films and $a_c(T)$ is the value of the in-plane lattice constant (real or extrapolated to the given temperature as shown in Fig. 9.3.1) of the films in the paraelectric phase if they were free standing. The misfit strain in the paraelectric phase is also given by Eq. (9.3.2). In the ferroelectric phase, the tensors of misfit strain for the two a - and c -domain states can be written as

$$\varepsilon_{Mz\beta}^{(1)} = \begin{pmatrix} \varepsilon_c & 0 \\ 0 & \varepsilon_a \end{pmatrix}, \quad \varepsilon_{Mz\beta}^{(2)} = \begin{pmatrix} \varepsilon_a & 0 \\ 0 & \varepsilon_c \end{pmatrix}, \quad \varepsilon_{Mz\beta}^{(3)} = \begin{pmatrix} \varepsilon_a & 0 \\ 0 & \varepsilon_a \end{pmatrix}, \quad (9.3.3)$$

where $\varepsilon_a = \frac{a_s - a}{a_s}$, $\varepsilon_c = \frac{a_s - c}{a_s}$; a and c stand for the parameters of the tetragonal unit cell of the bulk material. The difference

$$\varepsilon_T = \varepsilon_c - \varepsilon_a = \frac{c - a}{a_s}, \quad (9.3.4)$$

which is often called *tetragonality strain*, characterizes the degree of the tetragonal distortion in the bulk material.

For the following discussions, two more parameters related to the misfit strain will be useful, namely *tetragonality ratio*

$$\chi = -\frac{\varepsilon_c}{\varepsilon_a} = \frac{c - a_s}{a_s - a} \quad (9.3.5)$$

and relative coherency strain

$$\phi = \frac{\varepsilon_a}{\varepsilon_a - \varepsilon_c} = \frac{a - a_s}{a - c} = \frac{1}{1 + \chi}. \quad (9.3.6)$$

At this point we would also like to specify that in this chapter, we will be treating only situations where the strains are small. Accordingly, the terms proportional to higher powers of strain will be neglected everywhere. For example, we do not distinguish the difference between the following expressions: $\varepsilon_a = (a_s - a)/a_s$ and $\varepsilon_a = (a_s - a)/a$.

Let us now discuss the factors controlling the strains in the films. We will start from the situation at the deposition temperature.⁴ In general, the in-plane crystalline periodicity of a mechanically free ferroelectric differs from the in-plane periodicity of the substrate. As a result, during the deposition the film “tries” and, under a certain condition, “succeeds” to adjust its in-plane periodicity to that of the substrate. Though this adjustment is favorable from the point of view of the film/substrate interface energy, the price of an additional elastic

⁴ In the case for low-temperature deposition in amorphous phase with subsequent crystallization at a high temperature one should speak about the crystallization temperature. In the book, as shorthand, we will use the term ‘deposition temperature’ instead of the crystallization temperature.

energy should be paid for it. However, one can reduce this energy by formation of misfit dislocations. By introducing a high enough dislocation density, one, in principle, could satisfy at once two conditions: the epitaxy relation (matching of unit cells of the film and substrate) at the interface and the absence of stresses in the body of the films. We illustrate the two aforementioned limiting cases in terms of the model shown in Fig. 9.3.2. In this schematic drawing, the thin lines show the rows of atoms of the film whereas the thick lines show the rows of atoms of the substrate. For simplicity, we consider the situation where the x_1 -direction period of the material of the film, a , is different from that of the substrate, a_s , but close to it, as shown in Fig. 9.3.2a, whereas the periods in the direction perpendicular to the plane of the figure are equal. Figure 9.3.2b illustrates a dislocation-free adjustment of the film to the surface potential of the substrate. A hypothetical situation where the dislocations provide a complete stress release in the body of the film is illustrated in Fig. 9.3.2c.

The strain states of the films shown in Fig. 9.3.2b and c can be characterized with values of the misfit strain. In the case of 9.3.2b, the misfit strain obviously reads $\epsilon_M = (a_s - a)/a_s$. In the case of 9.3.2c, the film is inhomogeneously strained thus, strictly speaking, its strain state cannot be characterized with a single value of the misfit strain. However, dealing with a similar situation in practice, one customarily uses two values. One indicates $\epsilon_M = (a_s - a)/a_s$ as the misfit strain implying its value expected when there is no dislocation-assisted strain release. In this case, the misfit strain is considered as a characteristic of the pair of materials used in the heterostructure. Alternatively, one indicates $\epsilon_M = 0$ as the misfit strain implying that far from the interface the film is not strained. Thus, using the notion of the misfit strained one should be aware of possible confusions associated either with the aforementioned ambiguity or with the difference in the notion of “misfit strain” and “parent misfit strain.”

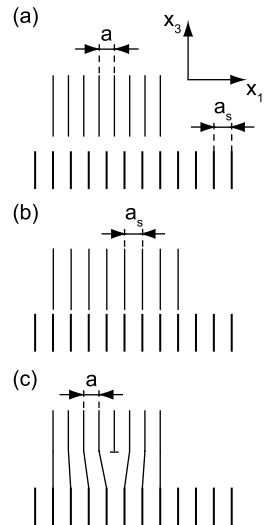


Fig. 9.3.2 Model used for explanation of the dislocation-assisted stress release (see the text)

The dislocation density (number per unit length) ρ corresponding to this situation illustrated in Fig. 9.3.2c can be evidently related to the misfit strain $\varepsilon_M = (a_s - a)/a_s$ as

$$\rho = \rho_{\text{relax}} = \varepsilon_M/a. \quad (9.3.7)$$

In a real situation, since the creation of dislocation costs some energy, the dislocation density ρ will be smaller than ρ_{relax} and the film still sustains the misfit strain $\varepsilon_r = \varepsilon_M - a\rho$ called *residual misfit strain*. When the dislocation density ρ is equal to its equilibrium value ρ_{eq} , the corresponding value of the residual misfit strain $\varepsilon_{r_0} = \varepsilon_M - a\rho_{\text{eq}}$ will be called *equilibrium residual misfit strain*. It is this situation that we will mainly address in this section.

We readily see that, from the point of view of the “bulk” of the film, the film/substrate contact with the equilibrium concentration of the dislocations is equivalent to a non-relaxed contact of the film with a substrate with the lattice constant

$$a_s^* = a_s(1 - a\rho_{\text{eq}}). \quad (9.3.8)$$

Thus, following Speck and Pompe (1994) one can say that after an equilibrium array of misfit dislocations has developed at the interface, the film no longer “sees” the potential of substrate, but it rather experiences the potential of the substrate modified by the array, residual misfit strain in the films being controlled by the effective substrate lattice constant a_s^* . Residual stress determined in this way corresponds to the equilibrium situation. In reality, the equilibrium concentration of the dislocation may not be achieved. That corresponds to a smaller strain release in the body of the film. In terms of our model that leads to a value of the effective substrate lattice constant lying between a_s and a_s^* . The logic of this model consideration can be readily translated to any real situation.

The quantitative description of the dislocation-controlled stress release in ferroic thin films requires consideration of the energetics and kinetics of the problem. For the equilibrium situation, i.e., where the dislocation mobility is high enough to provide their equilibrium concentration, the general theory of the phenomenon is well developed (see book by Tsao (1993)) for an excellent review and paper by Speck and Pompe (1994) for an example of application of this theory to ferroelectric films). The principal result of this theory, the Matthews–Blakeslee criterion⁵ (Matthews and Blakeslee, 1974), can be formulated as follows. The strain state of the films is determined by the relation between the film thickness h and a certain critical thickness h_c . The critical thickness and the equilibrium dislocation density in films thicker than h_c are functions of the original misfit strain and film thickness.

⁵ Presently, the Matthews–Blakeslee theory is not the only one available on the dislocation-assisted stress release in thin films (see, e.g., papers by People and Bean (1985) and Holec et al (2008)). To the best of our knowledge the results of these theories have never been applied to the description of ferroelectric thin films, though they may be relevant.

Let us address the basic points of this theory. One considers the energy of the whole system (films + substrate). It contains three contributions: elastic energy of the substrate, elastic energy of the films, and the energy of creation of the dislocations. The film and substrate apply equal and opposite tractions $F_{\text{film}} = -F_{\text{sub}}$ upon one another. That implies that the in-plane stresses in the film and substrate are inversely proportional to their thicknesses h and h_{sub} : $\sigma_{\text{film}} = F_{\text{film}}/h$ and $\sigma_{\text{sub}} = -F_{\text{film}}/h_{\text{sub}}$, and that the elastic energies of these are also inversely proportional to their thicknesses: $U_{\text{el}} \propto h(\sigma_{\text{film}})^2 \propto 1/h$ and $U_{\text{sub}} \propto h_{\text{sub}}(\sigma_{\text{sub}})^2 \propto 1/h_{\text{sub}}$. Because the substrate thickness is usually a few orders of magnitude larger than the film thickness, the elastic energy of the substrate can be neglected compared to that of the films. Thus, the equilibrium dislocation density in the film corresponds to a trade-off between its elastic energy and the energy of creation of dislocations.

We will illustrate the further development of the theory in terms of the simple model that we treated above. The elastic energy of the film can be found using the result of the elasticity theory for a biaxially strained body (see, e.g., Pompe et al., 1993). We consider the films as an elastically isotropic medium having Young modulus E and the Poisson ratio ν . (This assumption will not affect the basic conclusion of this consideration.) It is clear that, in the situation illustrated in Fig. 9.3.2b, film sustains the in-plane deformation with the components $\varepsilon_{11} = \varepsilon_{\text{M}} - \rho a$, $\varepsilon_{22} = 0$, and $\varepsilon_{12} = 0$. The corresponding elastic energy per unit area of the film, u_{el} , is a decreasing function of ρ and can be written as

$$u_{\text{el}} = \frac{Eh}{1-\nu} (\varepsilon_{\text{M}} - \rho a)^2. \quad (9.3.9)$$

On the other hand, the energy of creation of dislocations per unit area of the film u_{dis} is obviously proportional to the dislocation density ρ

$$u_{\text{dis}} = \Lambda_{\text{dis}} \rho; \quad \Lambda_{\text{dis}} = \frac{1}{2} \frac{Ea^2}{1-\nu^2} \frac{\ln(\alpha h/a)}{2\pi}. \quad (9.3.10)$$

Here Λ_{dis} is the dislocation energy per unit length given by the standard dislocation theory (see, e.g., Speck and Pompe, 1994) and α is a numerical parameter of the order of unity.⁶ The equilibrium dislocation density corresponds to a minimum of the total energy of the system $u_{\text{el}} + u_{\text{dis}}$. One readily finds that, for film thickness h smaller than some critical value h_{c} , the dislocation-free state is favorable, parameter h_{c} being defined as the solution to the equation

$$h_{\text{c}} = \frac{L(h_{\text{c}})}{|\varepsilon_{\text{M}}|}, \quad (9.3.11)$$

⁶ For h larger than the distance between the dislocations $1/\rho$, strictly speaking, Eq. (9.3.10) should be modified: h under “ln” should be replaced with $1/\rho$. The impact of this replacement on the final results is small. Hereafter, for simplicity, in this and similar “ln” factors we will ignore the difference between h and $1/\rho$, keeping h for any film thicknesses.

where

$$L(h) = a \frac{\ln(xh/a)}{8\pi(1+\nu)}, \quad (9.3.12)$$

while at $h > h_c$ the equilibrium dislocation density is

$$\rho = \rho_{\text{eq}} \equiv \frac{\varepsilon_M}{a} \left(1 - \frac{L(h)}{\varepsilon_M h} \right). \quad (9.3.13)$$

Equations (9.3.8), (9.3.12), and (9.3.13) lead to the following expression⁷ for the effective substrate lattice constant a_s^* as a function of the film thickness:

$$a_s^* = a \left(1 + \frac{L(h)}{h} \right) \quad (9.3.14)$$

for $h > h_c$ and $a_s^* = a_s$ for $h < h_c$. This expression is valid for the above considered case where the substrate imposes tensile stress to the films, i.e., $a < a_s$. The expression, which is also applicable to the case where $a > a_s$, should take into account that the sense of the deformation accompanying the stress release is controlled by the sign of the difference $a - a_s$. Such expression can be written as

$$a_s^* = a \left(1 + \text{sign}(a_s - a) \frac{L(h)}{h} \right). \quad (9.3.15)$$

The above results enable us to arrive at an important conclusion, namely, that the effective substrate lattice constant a_s^* (corresponding to the equilibrium density of dislocations) is sensitive to the value of the misfit strain ε_M only when the film thickness is smaller than the critical thickness and $a_s^* = a_s$. In the case of the partial stress release, i.e., for greater film thickness, the effective substrate lattice constant a_s^* is independent of the absolute value of ε_M , being sensitive only to the sign of the latter. The dependence given by Eq. (9.3.15) is schematically depicted in Fig. 9.3.3.

The results obtained above are qualitatively valid for real epitaxial thin films. To apply these results quantitatively one should take into account such factors as the mutual orientation of the Burgers vector \vec{b} , the dislocation lines, and the plane of the film. This leads to the modification of the expression for function $L(h)$ that now reads (Speck and Pompe, 1994)

$$L(h) = \frac{|\vec{b}|}{8\pi \cos \lambda} \frac{1 - \nu \cos^2 \beta}{1 + \nu} \ln(xh/|\vec{b}|). \quad (9.3.16)$$

⁷ According to the accepted accuracy of our calculations, in the obtained expression, the ratio $aL(h)/h$ has been substituted for $a_s L(h)/h$.

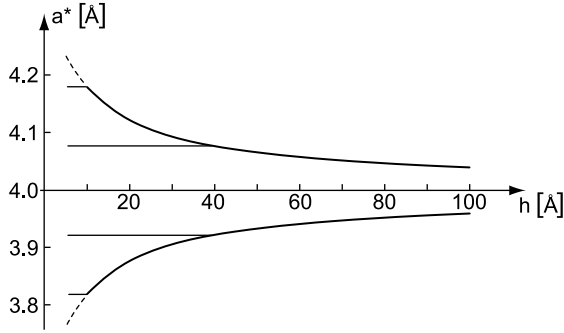


Fig. 9.3.3 Results of the Matthews–Blakeslee Lattice theory. The in-plane lattice constant vs. thickness of epitaxial (001) films of a cubic material with the stress-free value of the lattice constant 4.00 Å, which is deposited onto (001) cubic substrates with the lattice constants 3.82, 3.92, 4.08, and 4.18 Å. The cusps on the curves correspond to the critical thickness h_c . See the text. It is seen that, for films thicker than h_c , the lattice constant of the film is not sensitive to the absolute value of the misfit strain

Here β is the angle between the dislocation and the Burgers vector and λ is the angle between the Burgers vector, a line which lies within the interface and in a plane normal to the dislocation line. With this definition of $L(h)$ one can still use Eqs. (9.3.11) and (9.3.15) in the real situation.

An example of the results of calculations of dislocation-assisted stress release is given in Fig. 9.3.4. The calculations have been performed by Speck and Pompe (1994) for a (001) PbTiO_3 epitaxial film grown on a (001) SrTiO_3 substrate. Figure 9.3.4a shows the calculated dependence h_c on the misfit strain. The features of this system are illustrated in 9.3.4b. The values $|\vec{b}| = \sqrt{2} \times 4 \text{ \AA}$, $\beta = 90^\circ$, $\lambda = 45^\circ$, $\alpha = 4$, and $\nu = 0.3$ were used in the calculations. For these

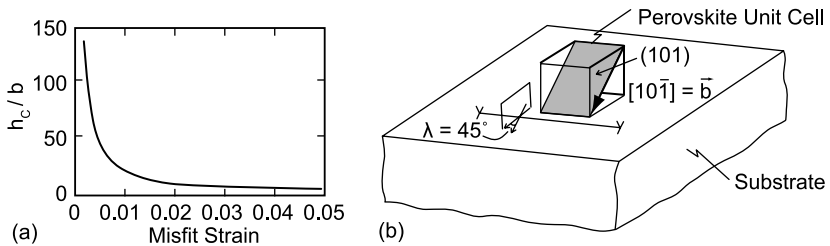


Fig. 9.3.4 (a) Normalized critical thickness, h_c/b , for perovskite epitaxial thin films with the dislocation-assisted stress release according to Eqs. (9.3.11), (9.3.16), and (9.3.17). **(b)** Parameters of misfit dislocations providing the stress release in perovskite epitaxial thin films. β is the angle between the dislocation and the Burgers vector and λ is the angle between the Burgers vector a line which lies within the interface and in a plane normal to the dislocation line. Reprinted with permission from Speck and Pompe (1994). Copyright (1994), American Institute of Physics

values that are typical for perovskite thin films of interest, function $L(h)$ can be evaluated as

$$L(h) = 0.24 \ln(0.7h), \quad (9.3.17)$$

where $L(h)$ and h are measured in \AA .

The above theory enables us to make an important conclusion on the strain state of the film. From the point of view of the strains in the films, we can distinguish the three following situations.

- (i) For $h < h_c$, the strain is homogeneous throughout the films and equals the value of the original misfit strain.
- (ii) If h exceeds h_c but remains of the order of h_c , the distance between the dislocations, $1/\rho_{\text{eq}}$, exceeds the film thickness. This is clear from a rough estimate

$$\frac{1}{\rho_{\text{eq}}} \cong h \frac{5h_c}{h - h_c}, \quad (9.3.18)$$

which follows from Eqs. (9.3.13) and (9.3.17) for typical values of the problem parameters. This implies that, in this case, the strain in the film is strongly inhomogeneous.

- (iii) Finally, for $h \gg h_c$ when $1/\rho_{\text{eq}} \ll h$, we arrive at a situation where, outside the substrate adjacent layer of a thickness of few h_c , the strain distribution can be considered as homogeneous with its magnitude reduced compared to its original value.

The above consideration of the strain state of the film was actually dealing with a film just deposited onto a substrate. For a real experimental situation, this corresponds to films just deposited at rather high temperature in the paraelectric phase. On cooling down, still in the paraelectric phase, the misfit strain changes. If the film is in the dislocation-free regime or if the misfit dislocation density does not follow the temperature variation, the misfit strain changes strictly according to the difference in thermal expansion coefficients of the film and the substrate. If the formation of new dislocation occurs during cooling, the effective substrate lattice constant should be, respectively, corrected.

The three factors discussed above—the *epitaxy relation*, *dislocation formation*, and *difference in thermal expansion coefficients of the film and the substrate*—exhaustively control the strained state of the film in the paraelectric phase. On cooling down to the ferroelectric phase, another powerful factor—*formation of ferroelastic domains*—enters the game. The role of this factor in the strain control of the film is actually obvious. We will illustrate this point by using an earlier discussed example of the cubic/tetragonal phase transition in a (001) film BaTiO_3 deposited onto an elastically isotropic substrate. In this system, three ferroelastic domain states being in the epitaxial contact with substrate experience misfit strains given by Eq. (9.3.3). For single-domain states, this is correct without

reservations. However, for a multidomain state, this holds only close to the film/substrate interface (at distances much smaller than those to the nearest ferroelectric domain wall). Farther from the interface, the strains in domains level off approaching the average value of the strain in the film. The latter in turn is controlled by the volume fraction of different ferroelastic domain states. This way the domain structure of the film can essentially influence the strain in it.

9.3.2 *Single-Domain State in a Strained Film*

This section addresses the thermodynamics of single-domain state as affected by the strain imposed by the substrate upon the ferroelectric film. The results presented below are applicable to the description of true single-domain states as well as to that of the ferroelectric features of the material “inside” domains of multidomain patterns with the domain width much larger than the film thickness. This extension is possible because, under this condition, the strain “inside” any domain is identical to that in the corresponding single-domain film.

The presence of a misfit strain in a ferroelectric film can strongly influence the thermodynamics of its single-domain state. To a certain extent the situation is similar to that in bulk crystals under hydrostatic pressure p , but it is not identical. In the case of a bulk ferroelectric, one controls two external parameters, temperature T and pressure p , so that a two-dimensional (p - T) phase diagram suffices for the description of the state of the material. In the case of a ferroelectric film on a substrate, one controls the temperature and three components of the in-plane strain, ε_1 , ε_2 , ε_6 , and, in principle, σ_3 component of stress (we use the Voigt matrix notations, with the X_3 -axis of the Cartesian reference frame normal to the plane of the film). Thus, because of the mechanical boundary conditions, unlike in a crystal under hydrostatical pressure, for the films, in general, the phase diagram should be specified in more than two axes.

There is also an essential difference in the thermodynamic description of the bulk ferroelectrics and thin films. Namely, the thermodynamic Gibbs function $\Phi(T, P_i, \sigma_i)$, which has the polarization P_i and stress σ_i as independent variables, is not an appropriate⁸ thermodynamic potential for strained thin films. We mean that, for thin films clamped by the substrate, Φ does not reach its minimum at the thermodynamic equilibrium. Appropriate for thin films thermodynamic function G can be obtained via the following Legendre transformation (Pertsev et al., 1998):

$$G = \Phi + \varepsilon_1 \sigma_1 + \varepsilon_2 \sigma_2 + \varepsilon_6 \sigma_6. \quad (9.3.19)$$

⁸ One should mention that the choice of the appropriate potential matters for derivation of the phase diagram of a system only in the case where the phase diagram contains lines of first-order phase transitions. If it is not the case, all treatments based on different thermodynamic potentials will result in the same phase diagram. This relates to the fact that all the potentials result in equivalent equations of state.

The thermodynamic function G reaches the minimum at equilibrium in the system where the strain components $\varepsilon_1, \varepsilon_2, \varepsilon_6$ and the stress components $\sigma_3, \sigma_4, \sigma_5$ are fixed. If the film is much thinner than the substrate, these conditions are often met with good accuracy. (We will be back to this issue at the end of this section.) It is useful to mention that, in the common experimental situation where upper surface of the film is mechanically free, G coincides with the Helmholtz free energy $F = \Phi + \varepsilon_1\sigma_1 + \varepsilon_2\sigma_2 + \varepsilon_3\sigma_3 + \varepsilon_4\sigma_4 + \varepsilon_5\sigma_5 + \varepsilon_6\sigma_6$ since in this case $\sigma_3, \sigma_4, \sigma_5$ are identically equal to zero. An important issue for the thermodynamics of the system is that the fixed strain components $\varepsilon_1, \varepsilon_2,$ and ε_6 are equal to those of the two-dimensional tensor $\varepsilon_{P\alpha\beta}$ of the parent misfit strain⁹ introduced in the previous section. This is a direct consequence of the fact that, in the standard Landau theory of ferroelectrics, the spontaneous strains are always “counted” from the unit cell of the parent phase extrapolated down to a given temperature. Thus, starting from the thermodynamic Gibbs function Φ and using transformation (9.3.19) one can eliminate the elastic variables $\sigma_1, \sigma_2,$ and σ_6 with the help of the equations of state

$$\partial G/\partial\sigma_1 = -\varepsilon_1, \quad \partial G/\partial\sigma_2 = -\varepsilon_2, \quad \text{and} \quad \partial G/\partial\sigma_6 = -\varepsilon_6. \quad (9.3.20)$$

For the typical situation where $\sigma_3, \sigma_4,$ and σ_5 are identically equal to zero, this leads us to the thermodynamic function G defined as a function of the temperature T , the tensor $\varepsilon_{P\alpha\beta}$, and the polarization vector \mathbf{P} . The minimization of G with respect to the polarization provides us with the $(\varepsilon_{P\alpha\beta} - T)$ diagram for single-domain states of the film. In such calculations, the macroscopic electric field in the ferroelectric is automatically set zero; thus, the obtained diagrams correspond to the situation in a short-circuited capacitor containing the film.¹⁰

Let us discuss the result of the calculations outlined above in application to BaTiO₃-type perovskite films of (001) and (111) orientations grown on substrates with the isotropic in-plane thermal expansion. In this case, the parent misfit strain tensor can be written in the form given by Eq. (9.3.2) and thus controlled by only one independent parameter ε_P . The calculations using Eqs. (2.3.34), (9.3.19), and (9.3.20) lead to the thermodynamic function G dependent on $T, \varepsilon_P,$ and \vec{P} . For the film of (001) orientation it reads (Pertsev et al., 1998)

$$\begin{aligned} G = & a_1(P_1^2 + P_2^2) + a_3P_3^2 + a_{11}(P_1^2 + P_2^2)^2 + a_{33}P_3^4 + a_{13}P_3^2(P_1^2 + P_2^2) \\ & + a_{12}P_1^2P_2^2 + \frac{\gamma_{111}}{6}(P_1^6 + P_2^6 + P_3^6) + \\ & \gamma_{112}[P_1^4(P_3^2 + P_2^2) + P_2^4(P_1^2 + P_3^2) + P_3^4(P_1^2 + P_2^2)] + \gamma_{123}P_1^2P_2^2P_3^2, \end{aligned} \quad (9.3.21)$$

⁹ In the cited papers, the term ‘misfit strain’ was used for this quantity. We had to change the original terminology to avoid confusion.

¹⁰ The condition that the electric field in the film is zero, strictly speaking, is not satisfied in a short-circuited capacitor because of incomplete screening of the bond charge with the free charges in the electrodes. This effect, which may be of importance for ultrathin films, will be discussed in Sect. 9.4.

where the coefficients can be expressed in terms of those of the Gibbs function (2.3.34)

$$\begin{aligned}
 a_1 &= \frac{\alpha_0(T-T_0)}{2} - \varepsilon_P \frac{Q_{11}+Q_{12}}{s_{11}+s_{12}}, \quad a_3 = \frac{\alpha_0(T-T_0)}{2} - \varepsilon_P \frac{2Q_{12}}{s_{11}+s_{12}}, \\
 a_{11} &= \frac{\beta_{11}}{4} + \frac{(Q_{11}^2+Q_{12}^2)s_{11}-2Q_{11}Q_{12}s_{12}}{2(s_{11}^2-s_{12}^2)}, \quad a_{33} = \frac{\beta_{11}}{4} + \frac{Q_{12}^2}{s_{11}+s_{12}}, \\
 a_{12} &= \frac{\beta_{12}}{2} - \frac{(Q_{11}^2+Q_{12}^2)s_{12}-2Q_{11}Q_{12}s_{11}}{s_{11}^2-s_{12}^2} + \frac{2Q_{44}^2}{s_{44}}, \quad \text{and } a_{13} = \frac{\beta_{12}}{2} + \frac{Q_{12}(Q_{11}+Q_{12})}{s_{11}+s_{12}}.
 \end{aligned} \tag{9.3.22}$$

For the film of (111) orientation in the reference frame of the film (where the X_3 -axis is normal to the plane of the film and the X_1 -axis is taken to be parallel to the $[1\bar{1}0]$ twofold axis of the cubic paraelectric phase), the G function can be written as (Tagantsev et al., 2002a)

$$\begin{aligned}
 G_{\text{eff}} &= a_1^*(P_1^2+P_2^2) + a_3^*P_3^2 + \\
 & a_{11}^*(P_1^2+P_2^2)^2 + a_{33}^*P_3^4 + a_{13}^*P_3^2(P_1^2+P_2^2) + a_{2223}P_2P_3(P_2^2-3P_1^2) + G^{(6)},
 \end{aligned} \tag{9.3.23}$$

where

$$\begin{aligned}
 a_3^* &= \frac{\alpha_0(T-T_0)}{2} - \varepsilon_P \frac{2(2Q_{11}+4Q_{12}-2Q_{44})}{4s_{11}+8s_{12}+s_{44}}, \quad a_1^* = \frac{\alpha_0(T-T_0)}{2} - \varepsilon_P \frac{2(2Q_{11}+4Q_{12}+Q_{44})}{4s_{11}+8s_{12}+s_{44}}, \\
 a_{11}^* &= \frac{\beta_{11}+\beta_{12}}{8} + \frac{Q_{11}^2(4s_{11}+3s_{44})+Q_{12}^2(12s_{11}-8s_{12}+11s_{44})+2Q_{44}^2(3s_{11}+5s_{12}+s_{44})}{4(s_{11}-s_{12}+s_{44})(4s_{11}+8s_{12}+s_{44})} \\
 & + \frac{2Q_{11}Q_{12}(4s_{11}-8s_{12}+5s_{44})+2Q_{11}Q_{44}(2s_{11}+2s_{12}+s_{44})+4Q_{12}Q_{44}(-4s_{12}+s_{44})}{4(s_{11}-s_{12}+s_{44})(4s_{11}+8s_{12}+s_{44})}, \\
 a_{33}^* &= \frac{\beta_{11}+2\beta_{12}}{12} + \frac{2Q_{11}^2+8Q_{12}^2+2Q_{44}^2+8Q_{11}Q_{12}-4Q_{11}Q_{44}-8Q_{12}Q_{44}}{3(4s_{11}+8s_{12}+s_{44})}, \\
 a_{13}^* &= \frac{\beta_{11}}{2} + \frac{2Q_{11}^2(2s_{11}+2s_{12}+s_{44})+2Q_{12}^2(4s_{11}+3s_{44})+2Q_{44}^2(s_{11}+3s_{12})}{(s_{11}-s_{12}+s_{44})(4s_{11}+8s_{12}+s_{44})} \\
 & + \frac{4Q_{11}Q_{12}(4s_{12}-s_{44})+2Q_{11}Q_{44}(3s_{11}+5s_{12}+s_{44})+4Q_{12}Q_{44}(s_{11}+3s_{12})}{(s_{11}-s_{12}+s_{44})(4s_{11}+8s_{12}+s_{44})}, \\
 a_{2223} &= -\frac{\sqrt{2}}{6} \left(\beta_{11}-\beta_{12} + 2 \frac{Q_{11}^2+Q_{12}^2-2Q_{44}^2-2Q_{11}Q_{12}+Q_{11}Q_{44}-Q_{12}Q_{44}}{s_{11}-s_{12}+s_{44}} \right).
 \end{aligned} \tag{9.3.24}$$

For the six-order polarization terms

$$G^{(6)} = \frac{\gamma_{123}}{6} P^6 + \frac{2\gamma_{112}-\gamma_{123}}{2} P^2 I_1(\vec{P}) + \frac{\gamma_{111}-6\gamma_{112}+2\gamma_{123}}{6} I_2(\vec{P}), \tag{9.3.25}$$

where¹¹

$$I_1(\vec{P}) = \frac{1}{2}(P_1^4 + P_2^4) + \frac{1}{3}P_3^4 + P_1^2P_2^2 + 2P_3^2(P_1^2 + P_2^2) + \frac{2\sqrt{2}}{3}P_2P_3(3P_1^2 - P_2^2), \quad (9.3.26)$$

$$I_2(\vec{P}) = \frac{1}{36}(9P_1^6 + 11P_2^6 + 4P_3^6) + \frac{5}{2}P_3^2(P_1^4 + P_2^4) + \frac{5}{3}P_3^4(P_1^2 + P_2^2) + 5P_1^2P_2^2P_3^2 \\ + \frac{5}{12}P_1^2P_2^2(3P_1^2 + P_2^2) + \frac{5\sqrt{2}}{18}P_2P_3(9P_1^4 - 3P_2^4 - 4P_2^2P_3^2 + 6P_1^2P_2^2 + 12P_1^2P_3^2) \quad (9.3.27)$$

The calculations performed for (001) films of PbTiO_3 (Pertsev et al., 1998), BaTiO_3 (Pertsev et al., 1999b), and $\text{Pb}(\text{Zr},\text{Ti})\text{O}_3$ (Pertsev et al., 2003b) have led to (ϵ_p, T) phase diagrams for single-domain states of these films,¹² which are shown in Figs. 9.3.5 and 9.3.6. Results corresponding to a number of cross-sections of the diagram for the BaTiO_3 film have also been obtained by Desu et al. (1996). The (ϵ_p, T) phase diagram for (111) films of PbTiO_3 (Tagantsev et al., 2002a) based on expression (9.3.23) is shown in Fig. 9.3.7. Similar analysis for

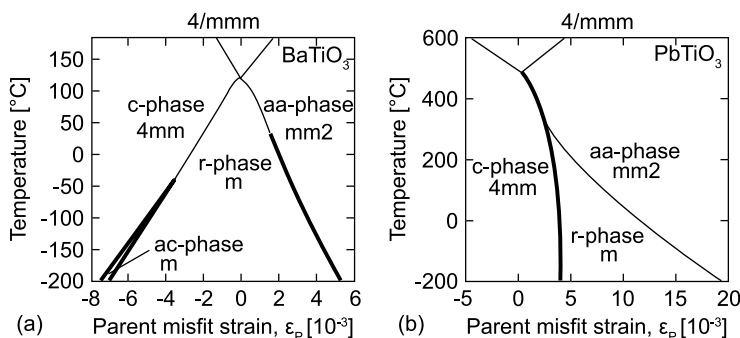


Fig. 9.3.5 Parent misfit strain vs. temperature phase diagrams of (001) single-domain BaTiO_3 (a) and PbTiO_3 (b) thin films epitaxially grown on (001) cubic substrates. The second- and first-order phase transitions are shown with *thin* and *thick* lines, respectively. The quadruple and triple points at $\epsilon_p = 0$ correspond to the Curie–Weiss temperatures of these materials in the bulk form. The point symmetries of the phases are indicated. The spontaneous polarization in the phases has the following components: *c*-phase, $(P_1 = 0, P_2 = 0, P_3 \neq 0)$; *aa*-phase, $(|P_1| = |P_2| \neq 0, P_3 = 0)$; *ac*-phase, $(P_3 \neq 0 \text{ and } P_1 \neq 0, P_2 = 0 \text{ or } P_2 \neq 0, P_1 = 0)$; *r*-phase, $(|P_1| = |P_2| \neq 0, P_3 \neq 0)$. After Pertsev et al. (1999)

¹¹ This result can also be presented in terms of invariant tensors of the cubic symmetry $g_{ijkl}^{(4)}$ and $g_{ijklmn}^{(6)}$ whose components in the cubic reference frame equal ‘1’ when all their indices are equal, otherwise the components equals ‘0’. Namely $I_1 = g_{ijkl}^{(4)}P_iP_jP_kP_l$ and $I_2 = g_{ijklmn}^{(6)}P_iP_jP_kP_lP_mP_n$ calculated in the film reference frame.

¹² An (ϵ_p, T) diagram for (001) BaTiO_3 , which is different from that shown in Fig. 9.3.5a was given in the paper of Pertsev et al. (1998). This diagram should be neglected as obtained based on a set of thermodynamic parameters of bulk BaTiO_3 , which did not properly correspond to the system.

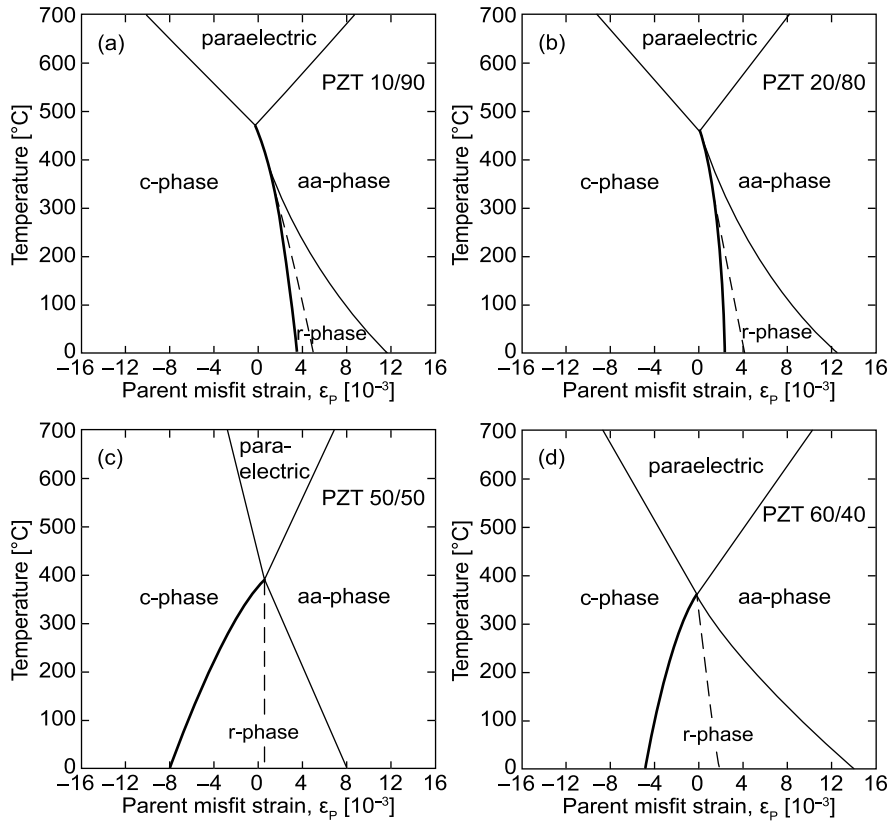


Fig. 9.3.6 Parent misfit strain vs. temperature phase diagrams of (001) single-domain $\text{Pb}(\text{Zr},\text{Ti})\text{O}_3$ films epitaxially grown on (001) cubic substrates. The Zr/Ti ratios are indicated. The phase notations are identical to those from Fig. 9.3.5. The second- and first-order phase transitions are shown with *thin* and *thick lines*, respectively. The triple or quadruple point at $\epsilon_p = 0$ corresponds to the Curie–Weiss temperature of the stress-free bulk material. The *dashed line* indicates the (ϵ_p, T) conditions, at which the polarization in the *r*-phase becomes oriented along the body diagonal of the prototypic cubic unit cell ($P_1 = P_2 = P_3$). After Pertsev et al. (2003b)

(001) films of SrTiO_3 , which was however complicated by the presence of additional nonferroelectric ordering, was performed by Pertsev et al. (2000, 2002). The main result of this work is the prediction of strain-induced ferroelectricity in (001) films of SrTiO_3 , which in the bulk form is only an incipient ferroelectric (it exhibits a strong increase in the permittivity without passing to the ferroelectric phase down to absolute zero of temperature). This prediction has been experimentally confirmed by Haeni et al. (2004).

The inspection of the phase diagrams shown in Figs. 9.3.5, 9.3.6, and 9.3.7 reveals a strong impact of the films/substrate mechanical coupling on the

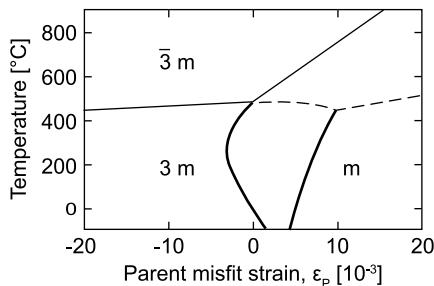


Fig. 9.3.7 Parent misfit strain vs. temperature phase diagram for (111) single-domain PbTiO_3 thin film epitaxially grown on (111) cubic substrates. The second- and first-order phase transitions are shown with *thin* and *thick lines*, respectively. The line on which the out-of-plane component of the dielectric permittivity passes through a maximum is shown with the *dashed line*. The point group symmetries of the phases are indicated (Tagantsev et al., 2002a)

single-domain state of ferroelectrics.¹³ First, the ferroelectric phase transitions change their order from the first to the second. Second, in the films, there appear phases of the type forbidden in the bulk crystals of the same material. For instance, in bulk PbTiO_3 , only a phase with one nonzero component of the polarization (with respect to the cubic reference frame) is allowed whereas, in the (001) and (111) films, domain states with two and three nonzero components of the polarization are also possible. Third, in thin films, lowering the symmetry of the problem (owing to the biaxial strain imposed by the substrate on the ferroelectric) makes stable substrate phases which have the number of domain states different from those possible in the bulk material. For example, one sees from these diagrams that, in the case where the substrate compresses the ferroelectric in the parent phase, i.e., $\varepsilon_p < 0$, in all considered cases, one deals with transitions to phases having only two domain states, specifically, $\frac{4}{m}mm \Rightarrow 4mm$ and $\bar{3}m \Rightarrow 3m$ transitions occur, like in uniaxial ferroelectrics. The change of the number of domain states in the ferroelectric phases should have implications on the features of domain structures in the films.

The presented phase diagrams and other diagrams of this type can be employed for analysis of sequences of the expected single-domain states in a ferroelectric film on a given substrate. This sequence is given by the cross-section of the (ε_p, T) phase diagram with the curve $\varepsilon_p = \varepsilon_p(T)$ representing the temperature dependence of the parent misfit strain, which can be determined experimentally from the data on the in-plane lattice constant of the ferroelectric. For simple cases, the $\varepsilon_p(T)$ dependence can also be evaluated theoretically. For example, in the case of ideal dislocation-free epitaxy, one readily finds

$$\varepsilon_p(T) = \varepsilon_r + (a_{TS} - a_{TF})(T - T_G), \quad (9.3.28)$$

¹³ Let us recall, that, in the bulk BaTiO_3 , a sequence of the first-order phase transitions separating four (cubic–tetragonal–orthorhombic–rhombohedral) phases occurs whereas, in PbTiO_3 , only one cubic–tetragonal first-order phase transition does.

where a_{TS} , a_{TF} , T_{G} , and ε_r are the thermal expansion coefficient of the substrate, that of the cubic parent phase of the ferroelectric, the deposition temperature, and the misfit strain at this temperature, respectively.

Concluding this section we would like to discuss the limitations and range of applicability of the theory discussed above.

First, the described procedure of calculations contains an implicit approximation, which could influence the obtained phase diagrams. The point is that the standard expression for the Gibbs function of a BaTiO₃-type ferroelectric, e.g., Eq. (2.3.34), does not contain the electromechanical terms of the type $P_i^4 \sigma_j$ whose coefficients are not available in the literature. Though these terms play negligible role for the properties of the bulk single crystal, they can significantly influence the thermodynamics of thin films. It is easy to show that, passing (via elimination of the elastic variable) from Φ to the effective thermodynamics function $G(T, \mathbf{P}, \varepsilon_{\text{P}})$, the $P_i^4 \sigma_j$ -type terms will manifest themselves in a renormalization of the coefficient for the P_i^6 terms in $G(T, \mathbf{P}, \varepsilon_{\text{P}})$. Though the coefficients for the $P_i^4 \sigma_j$ -type terms are not known, there is no reason to believe that aforementioned renormalization is insignificant (Tagantsev et al., 2002a). This renormalization can modify the positions of the line of first-order phase transitions in the phase diagrams and even alter the symmetry of the ferroelectric phase. For example, in the case of (111) PbTiO₃ films under positive parent misfit strain, it can alter the point group of ferroelectric phase from “ m ” (as shown in Fig. 9.3.7) to “2” (Tagantsev et al., 2002a).

Second, the whole approach is based on the assumption that the strain in the film is homogeneous. This assumption is fully justified only for the case of thin enough epitaxial films where no misfit dislocations form neither during deposition nor during cooling down to the ferroelectric phase, i.e., for $h < h_c$. If the film thickness h is about the critical thickness for misfit-dislocation formation h_c , the strain in the films is strongly inhomogeneous and the results of the theory are quantitatively inapplicable. For yet thicker films, i.e., for $h \gg h_c$, the strain is homogeneous in the main part of the films. That makes the theory applicable again, however, with a reservation. The situation where the out-of plane component of the spontaneous polarization is not zero requires further treatment. In this case, the inhomogeneity of the in-plane strain in a substrate adjacent layer of thickness h_c implies an x_3 -dependent polarization component P_3 . This, in turn, implies the appearance of depolarizing field, which being taken into account, may influence predictions of the theory. Another issue of concern is a possible (via the flexoelectric effect) poling effect of the strain gradient. This issue will be addressed later in this chapter (in Sect. 9.5.3).

Third, up to this point we have considered only limitations on the applicability of the results of the theory of the single-domain state of the films. These limitations should be appended with one more important limitation. To apply the result of this theory to the real situation, the films should be in a state where the domain width is much larger than the film thickness. Only in this case the basic assumption of the theory, that the strain components ε_1 , ε_2 , and ε_6 are

solely fixed by mechanical coupling between the films and the substrate, can be satisfied in the majority of the volume of every domain. Otherwise a domain-assisted strain release should be taken into account. This extremely important issue will be discussed in the following sections.

9.3.3 Domain Formation Driven by Elastic Effects: Basic Concepts

The problem of domain (twin) formation driven by elastic effects in thin films of ferroics was pioneered by Roytburd (Roitburd, 1976) and later treated by many workers. These studies have made available a good qualitative and, in many cases, quantitative mathematical description of the phenomenon. The progress has been achieved in terms of a number of approaches such as follows: (i) consideration of dense periodical domain structures (the domain period smaller than the film thickness) using the average mechanical energy of the systems as the basic approximation, which we will hereafter call *mean-strain approach* (e.g., Roitburd, 1976); (ii) calculations based on the analytical results for elastic Green functions (e.g., Pompe et al., 1993); (iii) calculations using the fictitious dislocations for the description of the deformation fields (e.g., Pertsev and Zembilgotov, 1995 and Romanov et al., 1996); (iv) Landau theory of the dense domain pattern (e.g., Koukhar et al., 2001); and (v) the phase-field calculations based on Ginzburg–Landau theory (Li et al., 2002, 2001). In the present section we address the fundamentals of domain formation driven by elastic effects in terms of the Roytburd’s mean-strain approach which, though being mathematically rather simple, provides a good insight into the phenomenon and, in most cases, its adequate quantitative description. The results of more involved theories will be discussed in Sect. 9.3.4.

9.3.3.1 Factors Governing Domain Formation Driven by Elastic Effects

Let us compare the energy of multi- and single-domain states of ferroelectric films and readily check that, under certain conditions, the multidomain state can be energetically favorable. A simple example of such a situation provides a (001) film¹⁴ of tetragonal BaTiO₃ deposited onto a substrate in a way that its in-plane unit cell remains square and its lattice constant a_s meets a condition that $a < a_s < c$ (a and c are the parameters of the tetragonal unit cell of mechanically free BaTiO₃). This can take place when the film is epitaxially deposited onto a cubic substrate (with the lattice constant a_s) without dislocation formation. It is intuitively clear from simple geometrical arguments that a multidomain state with the average in-plane lattice constant close to a_s can be more energetically favorable than either of the single-domain states. To check whether it is so and

¹⁴ As was specified in Sect. 9.1, when indicating the (001) orientation of a tetragonal ferroelectric film we imply the orientation of the film in the paraelectric cubic phase. Thus, the films of such orientation being in the ferroelectric phase can contain both a - and c domains.

to find the parameters of the energetically favorable domain pattern (if any) one should take into account a number of different contributions to the energy of the system. For the case of a dense domain structure, i.e., when the domain period W is smaller than the film thickness h , one can distinguish the following four contributions¹⁵ to energy of the film per unit area (thereafter as a shorthand we will refer to it as “energy”)

$$U_{\text{tot}} = U_{\text{mac}} + U_{\text{mic}} + U_{\text{W}} + U_{\text{S}}, \tag{9.3.29}$$

where U_{mac} , U_{mic} , U_{W} , and U_{S} are the elastic energy corresponding to the average (macroscopic) strain in the system, the energy of microstresses at the film/substrate interface, the energy of the domain walls, and the contribution related to the difference in the energy of the film/substrate interface for the different domain states. These contributions are illustrated in Fig. 9.3.8. Some information on the relative importance and role of these contributions can be obtained from simple qualitative arguments.

Let us start from the factors controlling the period of the domain structure W . Among the contribution entering Eq. (9.3.29) only U_{mic} and U_{W} are W dependent.

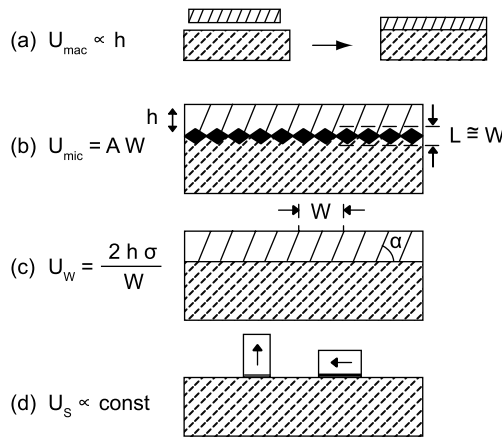


Fig. 9.3.8 Schematic representation of the contributions to the electric energy of a dense periodic ferroelectric domain pattern. (a) Energy of the average (macroscopic) strain. (b) Energy of microstresses at the film/substrate interface. (c) Energy of the domain walls. (d) Contribution related to the difference in the energy of the film/substrate interface for the domain states involved in the pattern. *Dashed line-hatched areas* show substrate. *Open areas* show ferroelectric film. Systems of parallel lines show ferroelectric domain walls. *Arrows* in (d) show the orientation of a crystallographic direction of the material in the different ferroelectric domain states

¹⁵ In this and ongoing sections we are not taking into account the contribution of the macroscopic electric field that can arise in ferroelectric multidomain structures (depolarizing field). We will address the impact of this contribution later on in this chapter.

The contribution of energy of domain walls is proportional to the domain pattern density thus it is inversely proportional to the period W :

$$U_W = 2\sigma h/W. \quad (9.3.30)$$

(Here σ equals the surface tension of the domain wall σ_W , if it is perpendicular to the plane of the film; in the case of oblique walls, σ should be taken as equal to $\sigma_W/\sin \alpha$ where α is the angle between the wall and the plane of the substrate; see Fig. 9.3.8). The U_{mic} contribution originates from the inhomogeneous stresses in the ferroelectric and substrate. These stresses are due to the difference of the spontaneous deformations of neighboring domains. They are mainly concentrated close to the ferroelectric/substrate interface in a stripe of a thickness L about W . Thus, one expects $U_{\text{mic}} \propto W$. (This situation is similar to the contribution of inhomogeneous electric fields in 180° ferroelectric domain structures in a non-electroded sample.) Thus, the W -dependent contribution to the energy of the domain system can be written as

$$U_{\text{mic}} + U_W = AW + 2\sigma h/W, \quad (9.3.31)$$

where parameter A can be considered as a constant if the domain structure is dense enough. The period of the equilibrium domain structure can be found from minimizing (9.3.31) with respect to W , which leads us to the classical square root thickness dependence of the domain period:

$$W = (2\sigma h/A)^{1/2}. \quad (9.3.32)$$

This period corresponds to an equilibrium value of $U_{\text{mic}} + U_W$ equal to

$$U_{W_{\text{eq}}} = 2(2\sigma hA)^{1/2}. \quad (9.3.33)$$

Thus, the energy of the equilibrium domain system can be reduced to the sum of three contributions, $U_{\text{mac}} + U_{W_{\text{eq}}} + U_S$, the dependences of these contributions on the film thickness being different: $U_{\text{mac}} \propto h$, $U_{W_{\text{eq}}} \propto (h)^{1/2}$, and U_S is thickness independent. This implies that, in thick enough films, it is the contribution of the macroscopic stresses, U_{mac} , that govern the energetics of the system. Let us address this contribution.

9.3.3.2 Domain Formation Driven by the Energy of Macroscopic Stress

The energy of macroscopic stress makes the main driving force for the domain formation in ferroelectric films, and to a great extent it is this energy that controls the type of their equilibrium domain structure. The goal of this section is to explain the basic features of this mechanism of domain formation. We will do that following the simple mean-strain approach offered by Roytburd. To make the presentation more transparent we will address a simple case of a (001) film of a tetragonal BaTiO_3 -type ferroelastic and neglect the elastic anisotropy of the material (but not the anisotropy of the spontaneous strain!). However, the consideration can be readily extended to an elastically anisotropic situation (see Sect. 9.4).

Let us start from the elastic energy of single-domain ferroelastic states. There are three ferroelastic states in the considered system. They correspond to one state with the out-of-plane (normal to the film) orientation of the tetragonal axis (*c*-domain) and two states with its in-plane orientation (*a*-domains). In these states, the material is strained in the plane of the film and it is mechanically free in the direction of the film normal. The in-plane component of the deformation is given by the matrices of the misfit strain Eq. (9.3.3). (We keep the reference frame accepted above in this section with X_3 -axis normal to the plane of the film.) The elastic energy of these states can be evaluated using the result of the elasticity theory for the energy density, u_{el} , of a biaxially strained body (Pompe et al., 1993):

$$u_{el} = \frac{1}{2} \frac{E}{1 - \nu^2} (\varepsilon_{11}^2 + \varepsilon_{22}^2 + 2\nu\varepsilon_{11}\varepsilon_{22}), \quad (9.3.34)$$

where E and ν are the Young modulus and the Poisson ratio, respectively.¹⁶ From Eqs. (9.3.3), (9.3.5), and (9.3.34) we readily find for the elastic energy of *c*- and *a*-domains, u_c and u_a , respectively:

$$u_c = \frac{E}{1 - \nu} \varepsilon_a^2 = 2u_0(1 + \nu), \quad (9.3.35)$$

$$u_a = \frac{1}{2} \frac{E}{1 - \nu^2} (\varepsilon_a^2 + \varepsilon_c^2 + 2\nu\varepsilon_a\varepsilon_c) = u_0(1 + \chi^2 - 2\nu\chi), \quad (9.3.36)$$

where χ is the tetragonality ratio defined by (9.3.5) and

$$u_0 = \frac{1}{2} \frac{E}{1 - \nu^2} \varepsilon_a^2. \quad (9.3.37)$$

At this point it is instructive to note that according to Eqs. (9.3.35) and (9.3.36) the *a*- and *c*-domain states have the same elastic energy at $\chi = 1 + 2\nu$, i.e., at

$$a_s = \frac{a + c}{2} - \nu \frac{c - a}{2(1 + \nu)}, \quad (9.3.38)$$

This means that the intuitive geometrical reasoning that the mechanical energy of the *a*- and *c*-domain states should be equal when the actual in-plane lattice constant of the film a_s equals $(a + c)/2$ does not work because of a nonzero value of the Poisson ratio. The above result also means that if one considers the competition of single-domain states only, the *c*-monovariant is more favorable at $\chi > 1 + 2\nu$ whereas, at $\chi < 1 + 2\nu$, the *a*-monovariant is. In the diagram given in Fig. 9.3.9 (#1), this is illustrated in terms of relative coherency strain $\phi = 1/(1 + \chi)$.

¹⁶ The elastic energy of the substrate can be neglected. See Sect. 9.3.1 for the justification.

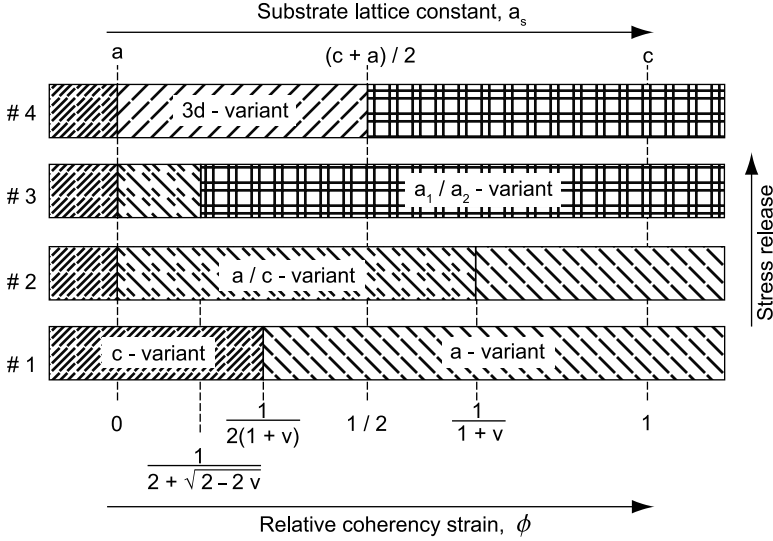


Fig. 9.3.9 Diagram shows the domain states or domain patterns having the minimal average (macroscopical) elastic energy in a (001) tetragonal ferroelectric film as functions of the relative coherency strain, ϕ . The corresponding values of the substrate lattice constants are also shown. The “3d-variant” stands for the three-domain-state structure. See text for details

Now let us evaluate a possible energy gain due to domain formation. We start from the a/c -variant structure introduced in Sect. 9.2.1. Since there exist two a -domain states (with the tetragonal axis parallel to the X_1 and X_2 in-plane directions), two types of this structure is possible. However, energetically these are identical, so that we will consider only one type. This structure is made of two domain states (of c - and a -domains with the tetragonal axis parallel to the X_1 -direction). This provides some one-dimensional stress release in the X_1 -direction. The volume fraction of c - and a -domains in this structure we denote as α and $1 - \alpha$, respectively, $0 < \alpha < 1$. The elastic energy corresponding to the average stress in the structure, U_{mac} , can be found using Eq. (9.3.34) with the strain equal to the weighted average of the misfit strains in the domains, i.e.,

$$\varepsilon_{\gamma\beta}^{(1,3)} = \alpha \varepsilon_{M\gamma\beta}^{(3)} + (1 - \alpha) \varepsilon_{M\gamma\beta}^{(1)}. \quad (9.3.39)$$

The calculations give

$$U_{\text{mac}}(\alpha) = [\alpha u_c + (1 - \alpha) u_a - \alpha(1 - \alpha) u_{\text{ac}}] h, \quad (9.3.40)$$

where

$$u_{\text{ac}} = \frac{1}{2} \frac{E}{1 - \nu^2} (\varepsilon_a - \varepsilon_c)^2 = \frac{1}{2} \frac{E}{1 - \nu^2} \varepsilon_{\text{T}}^2 = u_0 (1 + \chi)^2. \quad (9.3.41)$$

The last r.h.s. term in (9.3.40) is always negative; it corresponds to the energy gain due to the partial stress release driven by domain formation. It can also be interpreted as the energy of the indirect long-range interaction between domains through the substrate (Roytburd, 1997). We will call the coefficient controlling this interaction, u_{ac} , therein as normalized energy density of inter-domain interaction.

Minimizing (9.3.40) with respect to α we find the equilibrium fraction of c -domains for the equilibrium state of the system

$$\alpha_{eq} = \frac{1}{2} + \frac{u_a - u_c}{2u_{ac}} = \frac{\chi - \nu}{1 + \chi} = 1 - (1 + \nu)\phi \quad (9.3.42)$$

corresponding to the total elastic energy of the film:

$$U_{eq}^{(a/c)} = \left[u_a - \frac{(u_a - u_c + u_{ac})^2}{4u_{ac}} \right] h = u_0(1 - \nu^2)h. \quad (9.3.43)$$

The multidomain state exists if ($0 < \alpha_{eq} < 1$). This condition corresponds to the relation between the energies

$$-u_{ac} < u_c - u_a < u_{ac}. \quad (9.3.44)$$

In terms of the relative coherency strain, it can be rewritten as $0 < \phi < 1/(1 + \nu)$, using Eqs. (9.3.35), (9.3.36), (9.3.41), and (9.3.6). Thus, for the system with ϕ lying inside this interval, the ac -variant is favorable, outside of it, the a - and c -monovariants are. The resulting phase diagram for the domain states of the film is shown in Fig. 9.3.9 (#2).

The above treatment shows that the domain-assisted stress release can lower the energy of the ferroelastic film. However, it is clear that the domain structure considered above may not provide the ultimate solution to the problem, since other domain structures may offer further lowering of the mechanical film energy. One easily checks that, under certain conditions, the structure containing the two a -domain states is favorable; it is the so-called a_1/a_2 -variant shown in Fig. 9.2.1b. For this structure, the average deformation reads

$$\varepsilon_{\gamma\beta}^{(1,2)} = \alpha\varepsilon_{M\gamma\beta}^{(1)} + (1 - \alpha)\varepsilon_{M\gamma\beta}^{(2)}, \quad (9.3.45)$$

where the matrices of misfit strain come from Eq. (9.3.3). Via Eq. (9.3.34) we arrive at the elastic energy of this variant

$$U_{mac}(\alpha) = [u_a - \alpha(1 - \alpha)u_{aa}]h, \quad (9.3.46)$$

where α stands for the volume fraction of one type of the domains and

$$u_{aa} = \frac{E}{1 + \nu} (\varepsilon_a - \varepsilon_c)^2 = \frac{E}{1 + \nu} \varepsilon_T^2 = 2u_0(1 + \chi)^2(1 - \nu). \quad (9.3.47)$$

We readily find that this energy reaches its minimum

$$U_{\text{eq}}^{(a/a)} = \left(u_a - \frac{u_{aa}}{4} \right) h = u_0 \frac{(1+v)(\chi-1)^2}{2} h \quad (9.3.48)$$

at $\alpha = 1/2$, i.e., as one can expect from the symmetry arguments, the 1:1 mixture of the two domain states minimizes the energy of the a_1/a_2 -variant. Comparing the energy of this variant with that of the two monovariants and with the energy of the optimized a/c -variant we find that the a_1/a_2 -variant provides a further lowering of the mechanical energy of the film for $\chi < 1 + \sqrt{2-2v}$, i.e., for $\phi > 1/(2 + \sqrt{2-2v})$. The phase diagram taking into account this fact is shown in Fig. 9.3.9 (#3). An interesting feature of this diagram is that it does not contain the a -monovariant at all, since the a_1/a_2 -variant is always more favorable than either of a -variants. This is a general feature of a system containing two domain states with equal elastic energies. We will comment more on this point below in Sect. 9.3.4.

The above analysis demonstrates a possibility of lowering the elastic energy of the film via the formation of two-component ferroelastic domain structures. However, we see that the release of the average stress has never been complete except for the points $\phi = 0$ and $\phi = 1/2$ (i.e., at $a_s = a$ and $a_s = (a + c)/2$, respectively) where obviously, on average, the c -monovariant and a_1/a_2 -variant are not stressed, respectively. According to Roytburd (1997) a further energy lowering (for an interval of ϕ) is possible if all the three domain states are involved in the structure.

Two kinds of these structures, the so-called three-domain-state structures introduced in Sect. 9.2.1, are shown in Fig. 9.2.5. These are domain structures where the three domain states mixed in a way where all domain walls involved in the structure are mechanically compatible, so that no additional microstresses are brought about with the complication of the structure. The average deformation in this structure can be written as

$$\varepsilon_{\gamma\beta}^{(12,3)} = \alpha_3 \cdot \left[\alpha_1 \varepsilon_{M\gamma\beta}^{(3)} + (1 - \alpha_1) \varepsilon_{M\gamma\beta}^{(1)} \right] + [1 - \alpha_3] \cdot \left[\alpha_2 \varepsilon_{M\gamma\beta}^{(3)} + (1 - \alpha_2) \varepsilon_{M\gamma\beta}^{(2)} \right], \quad (9.3.49)$$

where α_1 , α_2 , and α_3 are the fraction of c -domain state in the a_1/c -variant, that in the a_2/c -variant, and the fraction of the a_1/c -variant layers in the three-domain structure, respectively. Insertion of Eq. (9.3.48) into Eq. (9.3.34) yields the energy of the average mechanical stress in the system. It is clear from the symmetry arguments that the minimum of this energy should be looked for at $\alpha_1 = \alpha_2$ and $\alpha_3 = 1/2$. These conditions simplify the energy of the system down to the following form:

$$U_{\text{eq}}^{(3d)} = u_c \frac{[\alpha_1(1 + \chi) + 1 - \chi]^2}{4} h \quad (9.3.50)$$

which reaches zero at its minimum when

$$\alpha_1 = (\chi - 1)/(\chi + 1) = 1 - 2\phi. \quad (9.3.51)$$

This minimum is physically meaningful if $0 < \alpha_1 < 1$. In terms of the relative coherency strain ϕ this implies that, for $0 < \phi < 1/2$, the three-domain-state structures provide the full average stress release in the film. The phase diagram that takes into account this kind of domain pattern is shown in Fig. 9.3.9 (#4).

9.3.3.3 Effect of Film Thickness on the Stress-Driven Formation of Domain Structure

The effect of film thickness on the stress-driven formation of domain structure is an issue whose exact treatment is, in general, possible only numerically. We will give a number of examples of such considerations in Sect. 9.3.4. In this section we will treat this problem in terms of a relatively simple approximation offered by Roytburd (1997, 1998b), which provides an adequate mathematical treatment in many cases of practical interest.

We address this effect for the case of domain patterns containing two domain states. In addition, we consider the situation of a dense domain structure, i.e., the situation where the domain period W is smaller than the film thickness h . In this case, as we have discussed above, the energy of the film can be presented as a sum of energy of macroscopic internal stress U_{mac} , the optimized (with respect to W) sum of the energies of microstresses and domain walls, $U_{W_{\text{eq}}}$ (see Eq. (9.3.33)), and the contribution related to the difference in the energy of the film/substrate interface for the two kinds of domain states making the domain pattern, U_S . Following the results of the preceding section we express the U_{mac} contribution in terms of the elastic energy density of the two domain states, u_1 and u_2 , their volume fractions, $(1 - \alpha)$ and α , and the normalized energy density of their long-range coupling through the substrate,¹⁷ u_{12} , to get

$$U_{\text{mac}}(\alpha) = [(1 - \alpha)u_1 + \alpha u_2 - \alpha(1 - \alpha)u_{12}]h. \quad (9.3.52)$$

The U_S can also be easily obtained in the following form:

$$U_S = (1 - \alpha)U_{S_1} + \alpha U_{S_2}, \quad (9.3.53)$$

where U_{S_1} and U_{S_2} are the energies of the film/substrate interface for the two domain states. As for the $U_{W_{\text{eq}}}$ contribution, Eq. (9.3.33), it is much more involved. Though its thickness dependence is clear from the scaling arguments as we have shown above, getting information on the dependence of $U_{W_{\text{eq}}}$ on the misfit strain and α requires the knowledge of the coefficient A in the expression for the energy of internal microstresses, $U_{\text{mic}} = AW$. An approximation for

¹⁷ For the moment Eq. (9.52) is written in analogy with Eq. (9.40), a general proof for it will be given in Sect. 9.3.4.

U_{mic} , which essentially simplifies further calculation, has been offered by Roytburd (1997, 1998b):

$$U_{\text{mic}}(\alpha) = (1 - \alpha)^2 \alpha^2 u_{12} W, \quad (9.3.54)$$

where ζ is a constant of the order of unity. For the domain patterns in question when α is not too close to 1 or 0, Eq. (9.3.54) with $\zeta = 0.27$ provides a good approximation¹⁸ to the exact values of U_{mic} when $W/h < 1$. At α close to 1/2, it works even for $W/h \approx 2$. We will employ this approximation in our analysis, i.e., setting $A = \zeta(1 - \alpha)^2 \alpha^2 u_{12}$, and return to discussion of its accuracy in Sect. 9.3.4. Thus, following the derivation of Eq. (9.3.33), the optimized sum of U_{mic} and the energy of the domain walls can be presented in the form

$$U_{W_{\text{eq}}}(\alpha) = (1 - \alpha) \alpha u_{12} (h \cdot h_0)^{1/2}, \quad (9.3.55)$$

where

$$h_0 = 8\zeta\sigma/u_{12} \quad (9.3.56)$$

is a characteristic length. As clear from comparing Eqs. (9.3.52) with (9.3.55), the physical meaning of h_0 is the film thickness at which the gain in energy of the pattern due to the long-range coupling through the substrate is compensated by energy of the microstresses and domain walls. At $h = h_0$, domain period is a few times greater than the film thickness as it is seen from the expression for the domain period, Eq. (9.3.32), rewritten in terms of h_0 :

$$W = \frac{\sqrt{h_0 h}}{2\zeta\alpha(1 - \alpha)}. \quad (9.3.57)$$

Now combining Eqs. (9.3.52), (9.3.53), and (9.3.55) we can present the total energy of the system in a form identical to that of the $U_{\text{mac}}(\alpha)$ contribution, Eq. (9.3.40):

$$U_{\text{tot}} = [(1 - \alpha)\tilde{u}_1 + \alpha\tilde{u}_2 - \alpha(1 - \alpha)\tilde{u}_{12}]h, \quad (9.3.58)$$

$$\tilde{u}_1 = u_1 + \frac{U_{s_1}}{h}; \quad \tilde{u}_2 = u_2 + \frac{U_{s_2}}{h}, \quad (9.3.59)$$

$$\tilde{u}_{12} = u_{12} \left(1 - \sqrt{\frac{h_0}{h}} \right). \quad (9.3.60)$$

¹⁸ The approximation addresses the case where the elastic properties of the substrate are identical to that of the film. For this reason, elastic parameters of the substrate do not enter Eq. (9.3.54).

Thus, the problem of the domain formation in the film of a finite thickness has been formally reduced to that considered above for a thick enough film, however, with the parameters that are thickness dependent. This enables us to use a mathematical result from the previous section, namely the expression for the equilibrium fraction of the domain state α

$$\alpha_{\text{eq}} = \frac{1}{2} + \frac{\tilde{u}_1 - \tilde{u}_2}{2\tilde{u}_{12}}, \quad (9.3.61)$$

cf. Eq. (9.3.42), and the condition for the stability of the multidomain state

$$-\tilde{u}_{12} < \tilde{u}_1 - \tilde{u}_2 < \tilde{u}_{12}, \quad (9.3.62)$$

cf. Eq. (9.3.44).

We can distinguish two kinds of size effects in our problem: one is related to the difference in surface (films/substrate) energies of the two domain state and the other to the combined action of microstresses and the wall energy. The impact of these effects is different since the former results in a thickness dependence of the effective energy densities of the domain states whereas the latter introduces a thickness dependence of the effective energy densities of their coupling. This is seen from Eqs. (9.3.59) and (9.3.60). We will consider these effects separately.

Let us start from the size effect related to the combined action of microstresses and the wall energy. It manifests itself via reduction of the effective coupling energy \tilde{u}_{12} , which makes the driving force for the domain formation. At $h = h_0$ the effective coupling energy vanishes and the theory predicts no polydomain states in films thinner than h_0 . At $h > h_0$, the polydomain state is possible but its stability window shrinks compared to that obtained taking into account only the energy of the macroscopic stress. As an example of such a behavior we will consider the thickness dependence of the parameters of the a/c -pattern, which was treated in the preceding section. Equations (9.3.60) and (9.3.61) provide us with an expression for the c -domain fraction α_{eq} as a function of the relative coherency strain ϕ and the normalized film thickness $h/h_{0a/c}$ ($h_{0a/c}$ is the characteristic length the a/c -pattern calculated according Eq. (9.3.56)):

$$\alpha_{\text{eq}} = \frac{1}{2} + \frac{u_a - u_c}{2u_{ac}} \frac{1}{1 - \sqrt{\frac{h_{0a/c}}{h}}} = \frac{1}{2} + \frac{1/2 - (1 + \nu)\phi}{1 - \sqrt{\frac{h_{0a/c}}{h}}}. \quad (9.3.63)$$

Figure 9.3.10a shows α_{eq} plotted as a function of ϕ for $\nu=0.3$ calculated for different values of the normalized film thickness. Another instructive example of this size effect is the thickness dependences of the borders between a/c -variant and monovariants (a or c) for this system. These dependences can be readily obtained from the two limits of condition (9.3.62). In terms of the relative coherence strain, they read

$$\phi_{a,a/c} = \frac{1}{1 + \nu} - \frac{1}{2(1 + \nu)} \sqrt{\frac{h_{0a/c}}{h}}, \quad (9.3.64)$$

$$\phi_{c,a/c} = \frac{1}{2(1 + \nu)} \sqrt{\frac{h_{0a/c}}{h}}. \tag{9.3.65}$$

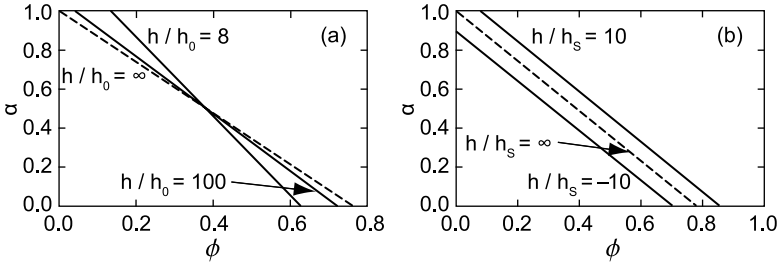


Fig. 9.3.10 Effect of the film thickness on the dependence of volume fraction of the *c*-domain state, α , on the relative coherence strain, ϕ (according to Eqs. (9.3.58), (9.3.59), and (9.3.60)). The *a/c*-domain pattern in a (001) tetragonal ferroelectric film with the Poisson ratio $\nu = 0.3$. **(a)** The impact of microstresses located at the film/substrate interface. **(b)** The impact of the interface (ferroelectric/substrate) energy. $h_0 = h_{0c/a}$ See the text

Here and therein the lower indices for ϕ indicate the variants that meet in the diagram at this value of the relative coherence strain. The thickness dependence of the border between the *a/c*- and a_1/a_2 -variants can be found from comparing their energies. The characteristic lengths given by Eq. (9.3.56) for these two variants, $h_{0a/c}$ and $h_{0a/a}$, are, in general, different. For this reason, the general equation for the border between these invariants is very cumbersome. In a compact form, this equation can be found for the case where the characteristic lengths for these two variants are set equal:

$$\phi_{a/a,a/c} = \frac{1}{2 + \sqrt{2 - 2\nu}} + \frac{\sqrt{2 - 2\nu} - 1}{2(1 + \nu)} \sqrt{\frac{h_{0a/c}}{h}}. \tag{9.3.66}$$

For this situation, the phase diagram for the single- and for bi-domain-state structures as predicted by the considered framework is shown in Fig. 9.3.11. In

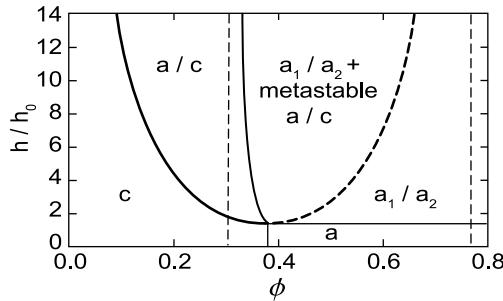


Fig. 9.3.11 Effect of the film thickness, h , on the energetically favorable type of the domain variant (according to the Roytburd theory of the size effect, Eqs. (9.3.63), (9.3.64), (9.3.65), and (9.3.66)). Results of the calculations for domain structures involving not more than two domain states in a (001) tetragonal ferroelectric film with the Poisson ratio $\nu = 0.3$. In the limit $h \rightarrow \infty$ and neglecting the metastable state, the diagram transforms into line #3 in the diagram shown in Fig. 9.3.9. Here $h_0 = h_{0c/a} = h_{0a/a}$

the limit $h \rightarrow \infty$ this diagram corresponds to the diagrams (#2) and (#3) from Fig. 9.3.9. Interesting feature of these diagrams is a wide region of possible coexistence of the a/c - and a_1/a_2 -variants where the former variant is metastable. Actually, the a_1/a_2 -variants should also be metastable in the area marked “ a/c ”; however, we have not shown that in the diagram since no relevant calculations are available for the moment.

The case of the surface energy-related effect can also be treated using the stability condition (9.3.62) which now reduces to

$$-u_{12} < u_1 - u_2 + \frac{U_{S_1} - U_{S_2}}{h} < u_{12}. \quad (9.3.67)$$

We see that the decrease in the film thickness impedes the satisfaction of one of the inequalities in Eq. (9.3.67) whereas it facilitates the satisfaction of the other. These inequalities correspond to the borders between the poly- and single-domain states. Thus, the variation of thickness will just shift the window of the stability of the polydomain state rather than shrink it. Evidently, the window shifts to favor the domain state with the smaller surface energy. To illustrate this point, we will present an expression for the c -domain fraction, α_{eq} , as a function of the relative coherency strain ϕ and the film thickness, which takes into account only the surface-energy-related effect. Using Eqs. (9.3.59) and (9.3.61) we readily find

$$\alpha_{\text{eq}} = \frac{1}{2} + \frac{u_a - u_c}{2u_{ac}} + \frac{h_s}{h} = 1 - (1 + \nu)\phi + \frac{h_s}{h}, \quad (9.3.68)$$

$$h_s = \frac{U_{S_a} - U_{S_c}}{2u_{ac}}, \quad (9.3.69)$$

where U_{S_c} and U_{S_a} are the surface (films/substrate) energies of c - and a -domain states and the characteristic length h_s that governs the strength of the size effect. The latter can be compared to the characteristic length for the first size effect, h_0 (introduced by Eq. (9.3.56), via an obvious relation

$$\frac{h_s}{h_{0a/c}} = \frac{1}{16\zeta} \frac{U_{S_a} - U_{S_c}}{\sigma}. \quad (9.3.70)$$

For the surface energy-related effect, the c -domain fraction, α_{eq} , as a function of ϕ for different values of the normalized film thickness h/h_s is given in Fig. 9.3.10b. The qualitative difference in the manifestations of the considered size effects is clearly seen by comparing Fig. 9.3.10a and b.

Let us now address the range of applicability of the above results. The key point of the “mean-strain” theory, namely the separation of the mechanical energy into the contributions of macro- and micro-internal stresses, is justified, as we already mentioned, only for dense domain structures. According to Roytburd (1998b), mathematically this theory is quantitatively applicable at

$W < h$ in general case and at $W < 2h$ for the most favorable case of symmetric domain patterns with $\alpha \approx 1/2$. Using Eq. (9.3.57) with $\xi = 0.27$ we find for the condition of applicability of the “mean-strain” theory $h > 56h_0 \left(\frac{1/4}{\alpha(1-\alpha)} \right)^2$ and $h > 14h_0$ for the two aforementioned situations, respectively. Checking the validity of this criterion we immediately find out that there are situations where the theory runs out away from its range of applicability. It takes place, first, in the vicinity of the bounds of the stability regions for polydomain states, i.e., at $\alpha \rightarrow 0$ and $\alpha \rightarrow 1$, and second, in films thinner than some $30h_0$. The latter finding is clear of great importance for the whole consideration. Namely, the conclusion of the theory that at $h < h_0$ the single-domain state is always favorable becomes non-justified. However, the theory still provides useful information on this thickness interval since the theory actually states that, at $h < h_0$, no dense domain structure is possible in the system. From this we can conclude that at $h < h_0$, the film should be either in the single-domain state or in a multidomain state with the period that is much greater than the film thickness.¹⁹ These two possible states of the films correspond to the same stress state for the main part of the systems. Thermodynamically both these states are actually single domain. For example, the thermodynamics of the single-domain ferroelectric films (see Sect. 9.3.2) is directly applicable to domains making a pattern with $W \gg h$. Thus, we can formulate an important result of the above theory: in ferroelectric films thinner than the characteristic thickness h_0 the physically single-domain state is energetically favorable.

To conclude this section we present estimates for the characteristic lengths h_0 and h_S . For the a/c -pattern, the walls are inclined by 45° to the plane of the film that implies $\sigma = \sqrt{2}\sigma_W$. Aiming at order-of-magnitude estimates, we will use the result of the continuous theory of domain walls for the wall energy, Eq. (6.2.10c). Then with the help of Eqs. (9.3.56) and (9.3.41) we arrive at the following relation between $h_{0a/c}$ and the wall thickness t_w :

$$h_{0a/c} = B_{a/c} t_w; \quad B_{a/c} = \frac{8\sqrt{2}\xi}{3} P_s^2 \chi^{-1} \frac{1 - \nu^2}{E\epsilon_T^2}. \quad (9.3.71)$$

Let us evaluate the coefficient $B_{a/c}$ entering this expression for PbTiO_3 films at room temperature. Using $\xi = 0.27$ and the values of material parameters of PbTiO_3 ($P_s = 0.52 \text{ C/m}^2$, $1/E \cong 8 \times 10^{-12}$, $\chi \cong 200\epsilon_0$, $\nu \cong 0.31$, $\epsilon_T^2 = 0.063$) we find $B_{a/c} \cong 0.3$. For the a_1/a_2 -variant, similar calculations give for its characteristic lengths $h_{0a/a}$

$$h_{0a/a} = B_{a/a} t_w; \quad B_{a/a} = \frac{4\xi}{3} P_s^2 \chi^{-1} \frac{1 + \nu}{E\epsilon_T^2} \quad (9.3.72)$$

¹⁹ The third hypothetical possibility that, for $h < h_0$, the domain period always stays of the order of the film thickness we exclude as containing an excessive density of domain walls.

with $B_{a/a} \cong 0.15$. It is worth mentioning that the combination of thermodynamic parameters entering the expressions for B 's is expected to be weakly temperature dependent so that the temperature dependence of the critical thickness should roughly follow that of the domain wall thickness.

To evaluate the characteristic length for the second size effect, h_s , we need information of the difference between the surface (film/substrate) energies (per unit area) of the two domain states. Though these energies themselves can hardly be evaluated without knowledge of the chemistry of the interface, their difference, as governed by the electrode-adjacent variation of the order parameter, can be roughly estimated as being about the domain wall energy (per unit area), i.e., $|U_{Sc} - U_{Sa}| \cong \sigma_w$. Based on this and using Eq. (9.3.70) we find $|h_s| \cong 0.06t_w$.

Despite the roughness of these estimates we can conclude that the characteristic thickness h_0 should be of the order of the domain wall thickness, actually a few times smaller, whereas h_s is yet smaller. The estimates obtained enable us to tell the range of theoretical parameters corresponding to the typical experimental situation where the thickness of thin films investigated is at least one to two orders of magnitude larger than the domain wall thickness. We readily conclude that in this situation $h \gg h_0$ ($h > 30 h_0$ in the evaluated case of PbTiO_3). This means that, in experiments, one usually deals with dense domain patterns, which can be adequately described by the Roytburd "mean-strain" approach, except maybe for the case of record thin films and strongly asymmetric domain patterns, where $\alpha \rightarrow 0$ or $\alpha \rightarrow 1$.

9.3.4 Domain Formation Driven by Elastic Effects: Advanced Theoretical Results

In the previous section we have addressed the fundamentals of the mechanical effects on the domain states and domain pattern in ferroic thin films. The material selected for that section introduces the basic notions and gives ideas about the physics behind the considered phenomena in terms of simple and mathematically transparent approaches. The goal of this section is to complement the aforementioned material with the results of more involved theoretical treatments of the problem. In contrast to the previous section we will only overview the obtained results mainly skipping derivations. We will address (i) the application of mean-strain Roytburd's approach to the elastically anisotropic situation and to the case of polydomain heterostructures, (ii) the treatment of domain structures by using the methods of fictitious dislocations and elastic Green's functions, (iii) the consideration of dense domain structures taking into account the stress dependence of the order parameters in domains, and (iv) theory of domain patterns in (001) rhombohedral and (111) tetragonal films of ferroelectric perovskites.

9.3.4.1 Results of the Mean-Strain Approach

The mean-strain approach outlined in the previous section can be applied to situations more complex than those treated there. Relevant results can be found in the original papers by Roytburd and coworkers (Roytburd, 1998a,b; Alpay and Roytburd, 1998). Here we will address only two issues, which are of the most practical interest.

The treatment presented in Sect. 9.3.3 is valid in the case of an arbitrary elastic anisotropy. Namely, the expression derived above for the case of elastically isotropic ferroelectric (e.g., Eq. (9.3.58)) can be used in the anisotropic situation with the elastic energy (density) of the domain states and the energy (density) of inter-domain through-substrate interaction, which are adequately calculated. When the elastic anisotropy of the ferroelectric is taken into account, the elastic energy u_1 of the strained domain state “1” should be written as (Roytburd, 1976)

$$u_1 = \frac{1}{2} \varepsilon_{M\alpha\beta}^{(1)} G_{\alpha\beta\gamma\delta}(\vec{n}) \varepsilon_{M\gamma\delta}^{(1)}, \quad (9.3.73)$$

where $\alpha, \beta = 1 - 2$, $\varepsilon_{M\alpha\beta}^{(1)}$ is the misfit strain of domain state “1,” $\vec{n} = (0, 0, 1)$ is the normal to the film interface, and $G_{ijlm}(\vec{n})$ is the so-called planar elastic modulus tensor:

$$G_{ijlm}(\vec{n}) = c_{ijlm} + c_{ijkp} n_p U_{kr} n_l c_{rilm}; \quad (U^{-1})_{kr} = n_i c_{ikrp} n_p. \quad (9.3.74)$$

The normalized energy (density) of inter-domain through-substrate interaction (cf. Eq. (9.3.41)) between domains “1” and “2,” in this case, reads

$$u_{12} = \frac{1}{2} \left(\varepsilon_{M\alpha\beta}^{(1)} - \varepsilon_{M\alpha\beta}^{(2)} \right) G_{\alpha\beta\gamma\delta}(\vec{n}) \left(\varepsilon_{M\gamma\delta}^{(1)} - \varepsilon_{M\gamma\delta}^{(2)} \right). \quad (9.3.75)$$

Using these expressions in the basic Eqs. (9.3.58), (9.3.59), (9.3.60), and (9.3.61) generalizes the results of the preceding section to the elastically anisotropic situation. For example, now Eq. (9.3.61) provides information on the impact of elastic anisotropy of the ferroelectric on the fractions of the domain states in the film. One can show that u_{12} calculated according to Eq. (9.3.75) is always positive. This implies, as is clear from Eq. (9.3.52), an important result already mentioned above: In systems containing two domain states with equal elastic energies, $u_1 = u_2$, the domain patterning is always favorable as far as the energy of the microscopic mechanical energy plays the decisive role.

The results of Sect. 9.3.3 address the situation of infinitely thick substrate, in other words, the situation where an infinitely thick layer of “passive material” is attached to the ferroelectric film. In this case, the macroscopic elastic energy of the passive material can be neglected. The situation conceptually close to this is a periodical heterostructure made of ferroic layers of thickness h and passive layer of thickness h' with the same elastic properties. It has been shown that

this situation can be readily described in terms of the developed approach (Roytburd, 1998a,b; Alpay and Roytburd, 1998). An instructive result of the theory is the expression for the equilibrium fraction of one of the domain states in a bi-domain structure. Being a generalization of (9.3.63), it reads (Alpay and Roytburd, 1998)

$$\alpha_{\text{eq}}^{(2)} = \frac{1}{2} + \frac{u_1 - u_2}{2u_{12} \left[1 - \sqrt{\frac{h_0}{h} \left(1 + \frac{h}{h'} \right)} \right]}. \quad (9.3.76)$$

Equation (9.3.76) demonstrated a non-trivial interplay between the effects of the partial stress release in the passive layers and microstresses.

9.3.4.2 Theory of Domain Pattern of Arbitrary Density for Cubic–Tetragonal Transition in (001) Films

The problem of the equilibrium domain pattern resulting from a cubic–tetragonal transition in (001) films of perovskite ferroelectrics like PbTiO_3 , $\text{Pb}(\text{Zr},\text{Ti})\text{O}_3$, and BaTiO_3 has been extensively treated in Sect. 9.3.3 in terms of the mean-strain approach. Though the results obtained there provide a good coverage of the typical experimental situations, they are still limited since the approach itself is applicable only if the domain structure of the film is dense, i.e., if the period of the structure W is smaller than the film thickness h . As we have mentioned this condition is always violated when the film thickness is smaller than some 20 critical thicknesses h_0 or when the fraction of one of the domain states tends to zero, $\alpha \rightarrow 0$ or $1 - \alpha \rightarrow 0$ (see Sect. 9.3.3). Description of the domains in these situations as well as the evaluation of the accuracy of the mean-strain approach calls for a more precise treatment of the problem. Such treatments have been offered by several authors who used different advanced methods of the elasticity theory. In this section we will overview the theoretical results on bi-domain state structures, i.e., the a/c - and a_1/a_2 -variants illustrated in Fig. 9.2.1.

Three kinds of problems have been addressed: (i) calculation of elastic energy of the a/c -variant (Pompe et al., 1993; Pertsev and Zembilgotov, 1995), (ii) calculation of elastic energy of the a_1/a_2 -variant (Pompe et al., 1993; Pertsev and Zembilgotov, 1995; Romanov et al., 1996), and (iii) calculation of elastic energy of an a -domain band inserted in a large c -domain (Pompe et al., 1993). All the problems were addressed in the approximation of elastic isotropy of both the ferroelectric and the substrate, whose elastic constants were taken identical. These quite involved calculations have been performed by Pompe and coworkers using elastic Green functions approach (Pompe et al., 1993), by Pertsev and Zembilgotov (1995) and by Romanov with coworkers (1996) using method of fictitious dislocations and disclinations. For the case of a film of an arbitrary thickness the rigorous results can be derived only numerically. For the a_1/a_2 -pattern, Romanov and coworkers (1996) offered an approximate, but fully analytical, treatment of the problem, which yields qualitatively correct results. We will not discuss the technical aspect of all these calculations,

referring the interested reader to the original papers, and address the most important of the results obtained.

The rigorously calculated total elastic energy of the a/c - and a_1/a_2 -periodic patterns (Pertsev and Zembilgotov, 1995) can be written in the form identical to that of the total elastic energy, $U_{\text{mac}}(\alpha) + U_{\text{mic}}(\alpha)$, used in the mean-strain approach (see Eqs. (9.3.52) and (9.3.54)):

$$U_{\text{tot}}(\alpha) = [(1 - \alpha)u_1 + \alpha u_2 - \alpha(1 - \alpha)u_{12}]h + u_{12}W\Pi_{12}(W/h, \alpha), \quad (9.3.77)$$

where u_1 , u_2 , and u_{12} are the elastic energy densities of the two domain states making the pattern and the normalized energy of their interaction introduced according to Eqs. (9.3.35), (9.3.36), (9.3.41), and (9.3.47). The function $\Pi_{12}(W/h, \alpha)$, being, in general, different for different pairs of the domain states, vanishes at $\alpha = 0$ and $\alpha = 1$. In the limit of dense domain structure, $W/h \rightarrow 0$, and at $\alpha = 1/2$, it acquires a value of $7\zeta(3)/16\pi^3 \approx 0.017$. (Here $\zeta(x)$ is the zeta function.) As one expects, in the dense structure limit, the results of rigorous calculations are very close to those of the mean-strain approach. The first r.h.s. term from Eq. (9.3.77) is identical to the energy of macrostresses $U_{\text{mac}}(\alpha)$. The second r.h.s. term from Eq. (9.3.77) can be compared to the contribution of microstresses in the mean-strain approach $U_{\text{mic}}(\alpha) = \xi(1 - \alpha)^2\alpha^2u_{12}W$, Eq. (9.3.54). The identical dependences of these expressions on the period of the structure and the material parameters of the system (entering in u_{12}) are seen. The difference is that, in the mean-strain theory, the function $\Pi_{12}(W/h, \alpha)$ is approximated by $\xi(1 - \alpha)^2\alpha^2$. In the limit $W/h \rightarrow 0$ and with $\xi = 7\zeta(3)/\pi^3 \approx 0.27$, these functions coincide at $\alpha = 0$, $\alpha = 1/2$, and $\alpha = 1$, having, according to Roytburd (1998b), very similar symmetric bell-like forms.

Once the function $\Pi_{12}(W/h, \alpha)$ is available (for arbitrary W/h it is available only in a numerical form, see Pertsev and Zembilgotov, 1995), the scheme described in the Sect. 9.3.3, where $\xi(1 - \alpha)^2\alpha^2$ in the expression for $U_{\text{mic}}(\alpha)$ is replaced by $\Pi_{12}(W/h, \alpha)$, can be employed for determining the parameters of the domain patterns as functions of the film thickness, material parameters of the ferroelectric, and the clamping condition imposed by the substrate. A program equivalent to that aforementioned has been numerically implemented by Pertsev and Zembilgotov (1995); the obtained results are illustrated in Figs. 9.3.12, 9.3.13, 9.3.14, and 9.3.15.

Figure 9.3.12 shows the fraction of c -domains in a/c -variant, $\alpha_{\text{ec}}(\phi)$, numerically calculated (Pertsev and Zembilgotov, 1995) as a function of the relative coherency strain ϕ for the Poisson ratio $\nu = 0.3$ and different values of the normalized film thickness: $h/h_{0c/a} = 3.3, 6.6, 10.0, 13.3, \text{ and } 16.7$ (solid lines). For $h/h_{0c/a} = 16.7$, the curve can be compared to the prediction of the mean-strain approximation (straight solid line) since, at this value of the normalized thickness, we are entering the range of applicability of this approximation. We see that, for $\phi > 0.15$, this approximation yields the results that are very close to those of the exact theory. It fails for smaller values of ϕ where, however, as one can check using Eqs. (9.3.57) and (9.3.42), the domain period is quite large ($W > 3h$). It is clear that on increasing thickness the range of applicability of the mean-strain

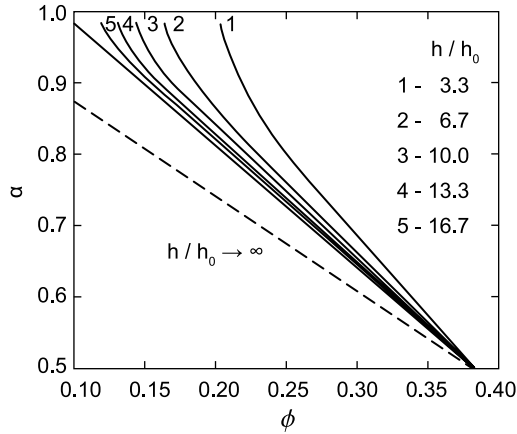


Fig. 9.3.12 Effect of the film thickness on the dependence of the volume fraction of the *c*-domain state, α , on the relative coherence strain, ϕ . The *a/c*-domain pattern in a (001) tetragonal ferroelectric film with the Poisson ratio $\nu = 0.3$. Curves 1–5 show the results of numerical calculations by Pertsev and Zembilgotov (1995) for the normalized thicknesses $h/h_0 = 3.3, 6.7, 10, 13.3,$ and 16.7 , respectively. Solid straight line—the result of the mean-strain approach for $h/h_0 = 16.7$. Dashed line—the $\alpha(\phi)$ dependence in the limit $h/h_0 \rightarrow \infty$. Here $h_0 = h_{0c/a}$

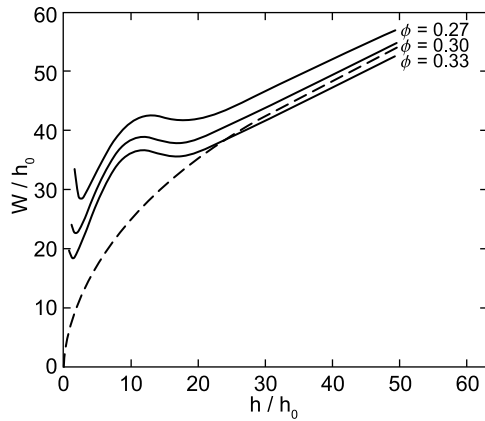


Fig. 9.3.13 Normalized period of the *a/c*-domain pattern in a (001) tetragonal ferroelectric film with the Poisson ratio $\nu = 0.3$. Solid curves—the results of the numerical calculations by Pertsev and Zembilgotov (1995) for different values of the relative coherence strain, ϕ . Dashed line—the ‘square root law’ which, in the limit of large film thickness, is consistent with the results the mean-strain approach for $\phi = 0.3$. Here $h_0 = h_{0c/a}$. See the text

theory increases. In the limit $h/h_{0c/a} \rightarrow \infty$, the exact and approximate theories yield the same $\alpha_{eq}(\phi)$ dependence, which is shown with the dashed line.

The thickness dependence of the period of the *a/c*-variant calculated numerically (Pertsev and Zembilgotov, 1995) is presented in Fig. 9.3.13 for three values of the relative coherency strain $\phi = 0.27, 0.30,$ and 0.33 . At small h the curves

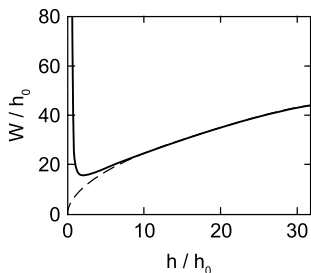


Fig. 9.3.14 Normalized period of the a_1/a_2 -domain pattern in a (001) tetragonal ferroelectric film. *Solid curves*—the results of the numerical calculations by Pertsev and Zembilgotov (1995), which take into account the exact strain distribution in the film. *Dashed line*—the ‘square root law’ which, in the limit of large film thickness, is consistent with the results the mean-strain approach. Here $h_0 = h_{0a/a}$. See the text

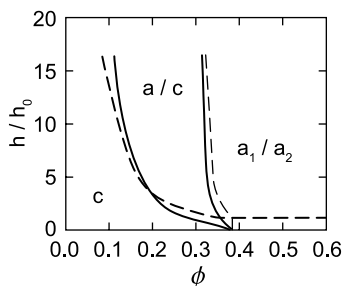


Fig. 9.3.15 Effect of the film thickness, h , on the energetically favorable type of the domain variant. Results of the calculations for domain structures involving not more than two domain states in a (001) tetragonal ferroelectric film with the Poisson ratio $\nu = 0.3$. *Solid curves*—the results of the numerical calculations by Pertsev and Zembilgotov (1995) taking into account the exact strain distribution in the film. *Dashed lines* show, for comparison, the predictions of the mean-strain theory already presented in Fig. 9.3.11 (the area of metastability of the a/c -variant is not shown for simplicity of the figure). Here $h_0 = h_{0c/a} = h_{0a/a}$

end up at the values of h corresponding to the minimal thickness below which the c -monovariant is preferable to the a/c -variant. The curve for the case of $\phi = 0.30$ is compared to the square root dependence predicted by the mean-strain theory, Eq. (9.3.57). For $\xi = 0.27$ and α coming from Eq. (9.3.42) with $\phi = 0.30$, the result of the mean-strain theory is shown in this figure with the dashed line. It is seen that for the normalized thicknesses $h/h_{0c/a} > 25$ the mean-strain approximation perfectly reproduces the result of the exact theory.²⁰

²⁰ One should note that for smaller thicknesses, where the situation is on the limit or out of the limit of applicability of the mean-strain approximation, its predictions are still qualitatively correct. First, like in the exact theory, it is predicted that the a/c pattern becomes unstable for the film thicknesses below a certain critical value. Second, at small $h/h_{0c/a}$, taking into account the thickness dependence of α (given by Eq. (9.3.63)) in Eq. (9.3.57), one arrives at a $W(h)$ curve deviating up from the square-root law similar to the numerically calculated curves in Fig. 9.3.12 do.

The investigations (Pompe et al., 1993; Pertsev and Zembilgotov, 1995; Romanov et al., 1996) of the energetics of the a_1/a_2 -variant reveal a qualitative difference in the thickness evolution of the a_1/a_2 - and a/c -variants: the former, in contrast to the latter, remains energetically favorable for an arbitrary small film thickness. These investigations have also predicted a formally unlimited increase in the period of a_1/a_2 -pattern for the film thickness tending zero. This is illustrated in Fig. 9.3.14 where the results of the numerical calculation by Pertsev and Zembilgotov (1995) are shown. The thickness dependence of the domain period of the a_1/a_2 -variant has also been treated analytically in the so-called Somigliana dislocation quadrupole approximation by Romanov and coworkers (1996). The curve obtained analytically is close to that shown in Fig. 9.3.14 to within 20% accuracy. In the limit of very thin films $h/h_{0_{a/a}} \ll 1$, these calculations provide an analytical description of the thickness dependence of the domain period

$$W \propto h \exp(1.9h_{0_{a/a}}/h), \quad (9.3.78)$$

where $h_{0_{a/a}}$ is defined by Eqs. (9.3.56) and (9.3.47). Comparing the result obtained numerically with that of the mean-strain approximation (shown as the dashed line in the same graph), one sees that at $h/h_{0_{a/a}} > 15$, as one expects, this approximation perfectly reproduces the result of the exact theory. On the other hand, the quantitative description of the steep rise of the domain period with decreasing thickness at small $h/h_{0_{a/a}}$ is left out of the reach of this approximation. However, as was mentioned in Sect. 9.3.3.3, in a sense, the qualitative prediction of this approximation is correct: for $h/h_{0_{a/a}} < 1$, it predicts the single state, which is physically very close to a polydomain states with very large domains.

Combining the result of Pompe and coworkers (1993) and Pertsev and Zembilgotov (1995) one can derive the “ h - ϕ ” diagram for the single- and for bi-domain-state structures. This diagram is shown in Fig. 9.3.15. It should be considered as a revised version of the diagram developed in terms of mean-strain approximation and shown in Fig. 9.3.11. (In Fig. 9.3.15 for simplicity the region of the metastability of the a/c -variant is not shown.) For comparison, the curves corresponding to this approximation are also incorporated in Fig. 9.3.15. It is seen that, except for very small thicknesses $h/h_{co} < 2-3$, the results of the exact and mean-strain theories are rather close.

9.3.4.3 Theories Taking into Account the Stress Dependence of the Order Parameter

The approaches applied above for the description of equilibrium domain patterns do not make allowance for the variation of the order parameter in the film caused by the substrate-induced stress. This variation always takes place because of the coupling between the deformation and the order parameter complicating the problem. However, for the case of dense domain pattern, the problem can still be treated analytically as was recently shown by Pertsev with

coworkers (Pertsev and Koukhar, 2000; Koukhar et al., 2001; 2006). An alternative approach, the so-called phase-field numerical approach, has been also recently applied to this problem by Li et al. (2001, 2002, 2003). Below we briefly outline these approaches and discuss the results obtained with their help.

The basic idea by Koukhar et al. is to consider the distribution of the polarization, electric field, and strain in a dense domain pattern as piecewise homogeneous with mechanical and electrical boundary conditions satisfied. At the same time, the mechanical stress in the film is set homogeneous. This approximation, whose accuracy is better the denser the pattern, readily yields the energy of the film as a function of the above variables and the fractions of domain states making the pattern. The minimization of the obtained energy with respect to all these variables enables the authors to determine the type and parameters of the energetically favorable domain pattern. This approach has been implemented for the consideration of dense 90° bi-domain-state structures in BaTiO_3 and PbTiO_3 (001) films. The authors based their calculations on the Gibbs function phenomenological expansion (see Eq. (2.3.34)). The result of calculations is the parameters of the equilibrium domain patterns of the system as functions of the temperature and parent misfit strain.

To illustrate the link between the approach of Koukhar et al. (2001) and that of Roytburd (1998a,b) we will compare the predictions of these theories concerning the fraction of c -domains in the a/c -domain pattern in a (001) PbTiO_3 film, α_{eq} . According to Koukhar et al. (2001), α_{eq} reads

$$\alpha_{\text{eq}} = 1 - \left(1 - \frac{s_{12}}{s_{11}}\right) \frac{\varepsilon_{\text{P}} - Q_{12}P_{\text{S}}^{*2}}{(Q_{11} - Q_{12})P_{\text{S}}^{*2}}, \quad (9.3.79)$$

$$P_{\text{S}}^{*2} = \frac{-\beta_{11}^* + \sqrt{\beta_{11}^{*2} - 4\gamma_{111}\alpha^*}}{2\gamma_{111}}, \quad (9.3.80)$$

$$\alpha^* = \alpha_0(T - T_0) - \frac{2Q_{12}}{s_{11}}\varepsilon_{\text{P}}, \quad \text{and} \quad \beta_{11}^* = \beta_{11} + \frac{2Q_{12}^2}{s_{11}}. \quad (9.3.81)$$

Here P_{S}^* is the spontaneous polarization in the polydomain pattern expressed in terms of the parent misfit strain ε_{P} and the thermodynamic parameters of the material (see Eq. (2.3.34)). In the considered approximation as a result of the homogeneity of the stress, the spontaneous polarization P_{S}^* is the same in both a - and c -domains; however, it is different from its value in the bulk material P_{S} .²¹

²¹ It is proper to indicate that Eqs. (9.3.80) and (9.3.81) give actually the results of the third modification of Landau theory for this kind of materials. Speaking about three modifications we mean the versions of Landau theory for (i) mechanically free material (Sect. 2.3.4), (ii) single-domain film clamped by a thick substrate (Sect. 9.3.2), and (iii) film clamped by a thick substrate but containing a dense ferroelectric domain pattern. Similar to cases (i) and (ii), in case (iii), the stresses are mainly homogeneous throughout the sample. In terms of the stress level, case (iii) is intermediate between (i) and (ii).

The result given by Eqs. (9.3.79), (9.3.80) and (9.3.81) can be readily compared to the corresponding result of the Roytburd’s mean-strain approach, i.e., $\alpha_{eq} = 1 - (1 + \nu)\phi$ (see Eq. (9.3.42)). Taking into account that for the considered orientation of the film the Poisson ratio $\nu = -s_{12}/s_{11}$ and the relative coherency strain ϕ can be presented as $(\epsilon_P - Q_{12}P_S^2)/(Q_{11} - Q_{12})P_S^2$, we readily rewrite the result of Roytburd’s theory as

$$\alpha_{eq} = 1 - \left(1 - \frac{s_{12}}{s_{11}}\right) \frac{\epsilon_P - Q_{12}P_S^2}{(Q_{11} - Q_{12})P_S^2}. \tag{9.3.82}$$

Thus we see that, in the considered aspect, the difference between the results of the two theories is the use of the modified (by the stresses in the film) value of spontaneous polarization P_S^* instead P_S .

To illustrate the effect of the stress-induced variation of the order parameter taken into account by the theory by Koukhar et al. (2001), let us compare the α vs. ϵ_P dependences predicted by the two theories (i.e., Eqs. (9.3.79) and (9.3.82)) for the case of PbTiO_3 at $T = 25$ and 440°C .²² The result of this comparison is shown in Fig. 9.3.16. One concludes from this figure that far from the transition (at $T = 25^\circ\text{C}$) this effect is of minor importance whereas relatively close to the transition (at $T = 440^\circ\text{C}$) its impact can be considerable. Another important feature seen is that, at the border between c - and a/c -variants (i.e., at $\alpha = 1$ and $\phi = 0$), the theories give the identical results, as one can expect, since at $\phi = 0$ the c -variant is not strained.²³

The theory by Koukhar et al. (2001) enables the development of the $(T - \epsilon_P)$ phase diagram for the domain pattern of the film, which makes allowance for single- and bi-domain-state structures. Such diagrams for PbTiO_3 and BaTiO_3 (001) films are shown in Fig. 9.3.17a and c, respectively.

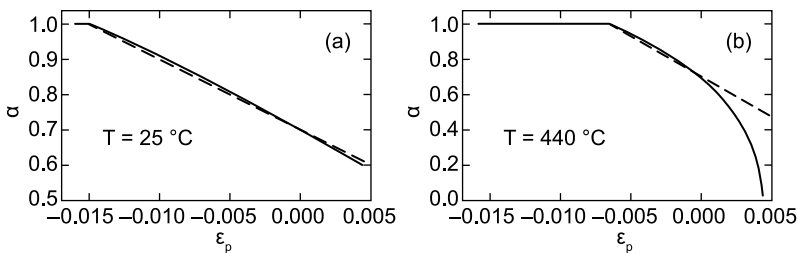


Fig. 9.3.16 The dependence of the volume fraction of the c -domain state, α , on the parent misfit strain, ϵ_P , in a (001) tetragonal PbTiO_3 film with the a/c -domain pattern calculated according to the mean-strain approach (*dashed lines*) and the theory by Koukhar et al. (2001) (*solid lines*). Results of calculations are presented for two temperatures indicated in the graphs

²² The materials parameters used in these calculations are listed in Table 2.3.1.

²³ One readily checks that at $\phi = 0$, i.e., at $\epsilon_P = Q_{12}P_S^2$, $P_S^* = P_S$.

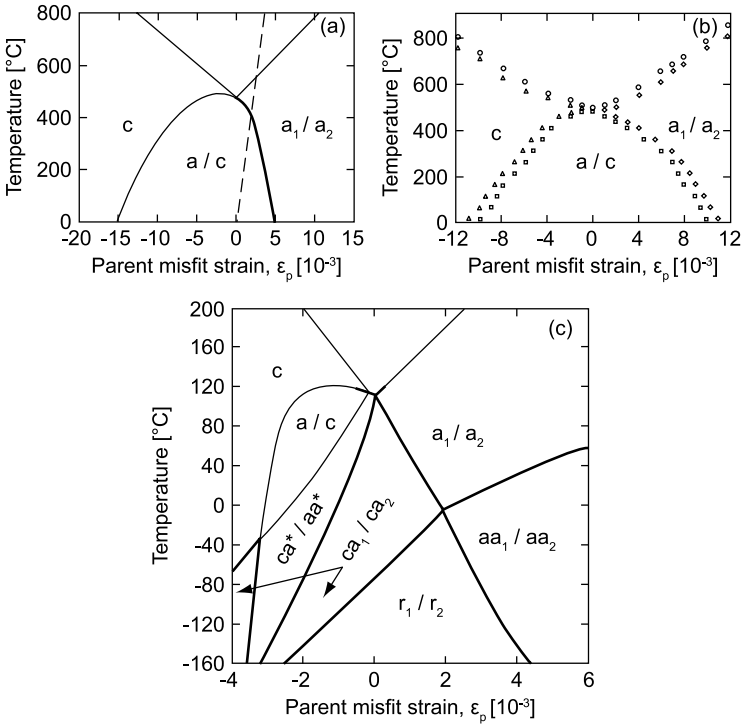


Fig. 9.3.17 Calculated 'temperature–parent misfit strain (ϵ_p)' diagrams for the (multi)domain states in (001) tetragonal films of PbTiO₃ (a, b) and BaTiO₃ (c). (a) and (c)—the results by Koukhar et al. (2001); here *thin lines* show the second-order phase transitions, the *thick lines*—the first-order phase transitions. Reprinted with permission from Koukhar et al. (2001). Copyright (2001) by the American Physical Society. (b) The results of the phase-field calculations by Li et al. (2001); here the *symbols* limit the areas on the diagram where the given domain pattern is favorable. 'c' indicates the c-domain monovariant. The nomenclature of the domain patterns is explained in Fig. 9.3.18. *Dashed line* shows the temperature dependence of the parent misfit strain expected in the case of MgO substrate and the formation of equilibrium density of misfit dislocations at the crystallization temperature (but without further dislocation formation at lower temperatures)

It is instructive to compare these diagrams with the predictions of Roytburd's mean-strain approach (line #3 in Fig. 9.3.9). For the case of PbTiO₃ and far below the phase transition, the difference between the predictions of the two approaches is rather small. The theories give the identical position of the c- to a/c-variant border, as was stated above, and very close positions of the a₁/a₂- to a/c-variant borders (at room temperature its position in the diagram shown in Fig. 9.17a to within 5% corresponds to the value of the relative coherency strain equal to $1/(2 + \sqrt{2 - 2\nu})$ predicted by Roytburd's theory). However, we find a very different situation for BaTiO₃. Here the theory by Koukhar et al. predicts a qualitatively new effect—appearance of the domain

patterns made of domain states unknown for the bulk BaTiO₃. For instance, at room temperature in addition to the “known” *c*-, *a*₁/*a*₂-, and *a/c*-variants, there appear new ones (*ca*^{*}/*aa*^{*}, *ca*₁/*ca*₂, and *aa*₁/*aa*₂) having orientations of the spontaneous polarization shown in Fig. 9.3.18. Such complex diagram containing new phases can be considered as a typical feature of systems where in the bulk form the energy of different ferroelectric phases is close to each other. This point is supported by the results obtained for Pb(Zr_{*x*}Ti_{*1-x*})O₃ films by Koukhar et al. (2006). The ε_P-*T* diagrams developed in this chapter are relatively simple for the end members of this solid solution whereas close to the morphotropic boundary at *x*≈0.5 the diagram is quite complex.

A comparison of the diagrams shown in Fig. 9.3.17a and c with those for the single-domain state of these films (Fig. 9.3.5) reveals an essential difference between these. The only feature of the single-domain phase diagram that is shared by the diagrams shown in Fig. 9.3.17a and c is the temperature and the order of the

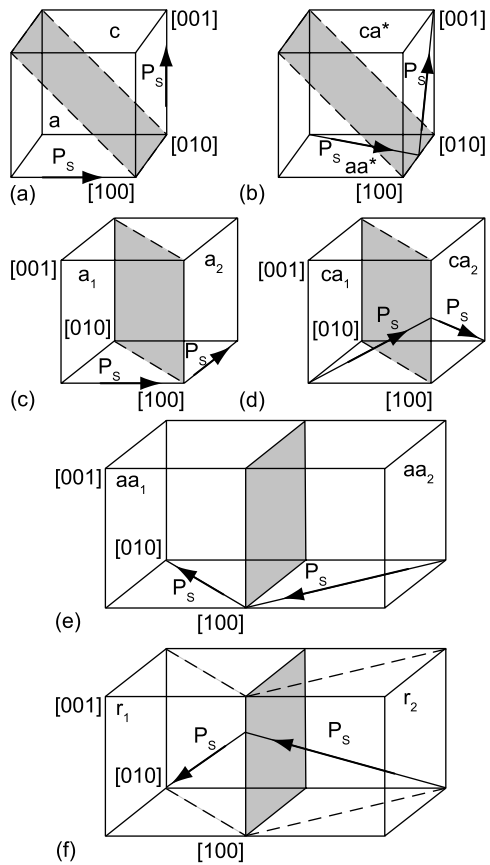


Fig. 9.3.18 Orientations of domain walls separating domains in the domain patterns addressed in the diagrams shown in Fig. 9.3.17. Orientations of the spontaneous polarization are shown with arrows. (a) *ac*, (b) *ca*^{*}/*aa*^{*}, (c) *a*₁/*a*₂, (d) *ca*₁/*ca*₂, (e) *aa*₁/*aa*₂, and (f) *r*₁/*r*₂. Koukhar et al. (2001). Copyright (2001) by the American Physical Society

ferroelectric phase transition forms the parent phase (except for a narrow interval of small ε_p). Of interest is the behavior of the system at the transition from the paraelectric phase to that with the in-plane orientation of the spontaneous polarization. In the dense domain structure, the low-symmetry phase is the a_1/a_2 -variant whereas the predicted single-domain state is the aa -variant with $\langle 110 \rangle$ directions of the polarization. Thus, in these situations, the orientation of the polarization differs by an angle of 45° . This may manifest itself in a change of the orientation of the polarization of the film on increasing thickness. In thicker films with the dense domain pattern, the $\langle 100 \rangle$ directions of the polarization are favorable. On the other hand, in very thin films, where the domain period is expected to be greater than the film thickness, the elastic state of the film approaches that in the single-domain state, where the diagonal $\langle 110 \rangle$ directions of polarization are favorable.

Let us now outline the so-called phase-field approach (Li et al., 2001; 2002) and the results obtained within it. The basic idea of this approach is to simulate the relaxation of the polarization to its equilibrium spatial distribution using the time-dependent Ginzburg–Landau equations. Specifically, the polarization kinetics is described by equation

$$\frac{\partial P_i(\vec{x}, t)}{\partial t} = -L \frac{\delta F}{\delta P_i(\vec{x}, t)}, \quad (9.3.83)$$

where the variational derivative is taken from the free energy density of the ferroelectric F written with the gradient terms taken into account (for more information on these terms see Sect. 6.2) and L is the kinetic coefficient. The relaxation of mechanical degree of freedom is assumed to be instantaneous, i.e., the condition of the local mechanical equilibrium

$$\frac{\partial \sigma_{ji}}{\partial x_i} = \frac{\partial}{\partial x_i} \frac{\partial F}{\partial \varepsilon_{ji}} = 0 \quad (9.3.84)$$

is applied. The values of the spatial average strain and stress components are fixed according to the mechanical boundary conditions and the aspect ratio of the film mechanically clamped on a thick substrate, i.e., $\langle \varepsilon_1 \rangle = \langle \varepsilon_2 \rangle = \varepsilon_p$, $\langle \varepsilon_6 \rangle = 0$, and $\langle \sigma_3 \rangle = \langle \sigma_4 \rangle = \langle \sigma_5 \rangle = 0$ (cf. Sect. 9.3.2). The spatially inhomogeneous contribution to the strain is set zero at a plane lying in the substrate at a certain distance from the film/substrate interface. The equilibrium domain pattern is determined from the time-dependent solution to Eqs. (9.3.83) and (9.3.84) (result of the polarization relaxation) by using the so-called semi-implicit Fourier-spectral method and numerical simulations with $128 \times 128 \times 36$ grid points. The $(T - \varepsilon_p)$ diagram developed for PbTiO_3 film, using the same set of the thermodynamic parameters as Koukhar et al. (2001) used, is shown in Fig. 9.3.17b. This diagram is rather close to that obtained by Koukhar et al. in the limit of the dense domain pattern. A certain difference between the diagrams obtained by these methods can be attributed to the finite-thickness effect in the case of the phase-field calculations. In these calculations, the X_3 grid

spacing is set about one-fourth of the domain wall width. For a PbTiO_3 film, this is about the critical thickness h_0 introduced for this problem in Sect. 9.3.3. Thus, the film thickness addressed in these calculations is about $36h_0$. According to Sect. 9.3.3, films of this thickness correspond to the limit of the range of applicability of Roytburd's dense-domain-pattern theory. The dense-domain-pattern theory developed by Koukhar et al. is not expected to have milder limits of applicability. Thus, the results of phase-field simulations for the $36h_0$ thick film may essentially deviate from those of the dense-domain-pattern theory.

A remark on the reliability of the results discussed in this section should be made. In general, the frameworks discussed above can provide treatments of domain patterns in ferroelectric thin films, whose accuracy can be controlled. However, the results presented above for BaTiO_3 and PbTiO_3 films are not, strictly speaking, the case. The reason is that corresponding calculations are based on traditional expansion of the Gibbs function, which does not contain the σP^4 -type terms. As mentioned in Sect. 9.3.2 these terms may essentially alter the obtained value of the film energy. Thus, the results in question should be taken with some reservation.

9.3.4.4 Theory of Domain Patterns in (001) Rhombohedral and (111) Tetragonal Films of Ferroelectric Perovskites

Let us now discuss the theoretical results on ferroelectric domain patterns in (001) rhombohedral and in (111) tetragonal ferroelectric thin films. Specifically, we will address the case of perovskite ferroelectrics with a cubic $m\bar{3}m$ paraelectric phase and tetragonal $4mm$ and/or rhombohedral $3m$ ferroelectric phases. The common obvious feature of these systems is that no domain state has spontaneous polarization purely normal to the plane of the film whereas the vectors of spontaneous polarization in the domain states are arranged in a symmetric manner with respect to the film normal (see Sect. 9.2.2). This situation is distinguished with respect to the relation between the in-plane components of the tensor's spontaneous deformation of the variant, $\varepsilon_{S\alpha\beta}(\alpha, \beta = 1, 2)$. Namely, the principal values of these matrices are equal so that the variants differ only by the orientation of the principal axes of the tensors. Less rigorously, one can say that the in-plane spontaneous deformation of the variants differ only in its orientation. Actually, such a situation was already treated above for the a_1/a_2 -pattern. We will see that the results obtained for the a_1/a_2 -pattern can readily be translated to the systems addressed in this section.

First let us address the implication of the mean-strain theory for the problem. The basic information required for its application is the knowledge of the matrices of misfit strains of the variants, $\varepsilon_{M\alpha\beta}$, which are controlled by the matrices of the parent misfit strain, $\varepsilon_{P\alpha\beta}$, and the matrices of the natural spontaneous strain, $\varepsilon_{S\alpha\beta}$. For the domain patterns under

consideration, this information is readily available. The matrices of the in-plane components of the tensor's spontaneous deformation, $\varepsilon_{S\alpha\beta}$, can be readily presented as

$$\begin{aligned}\varepsilon_{S\alpha\beta}^{(d_1)} &= \varepsilon_{is} \begin{pmatrix} 1 & 0 \\ 0 & 1 \end{pmatrix} + \varepsilon_T \frac{\sqrt{3}}{6} \begin{pmatrix} 1/\sqrt{3} & 1 \\ 1 & -1/\sqrt{3} \end{pmatrix}, \\ \varepsilon_{S\alpha\beta}^{(d_2)} &= \varepsilon_{is} \begin{pmatrix} 1 & 0 \\ 0 & 1 \end{pmatrix} + \varepsilon_T \frac{\sqrt{3}}{6} \begin{pmatrix} 1/\sqrt{3} & -1 \\ -1 & -1/\sqrt{3} \end{pmatrix}, \\ \varepsilon_{S\alpha\beta}^{(d_3)} &= \varepsilon_{is} \begin{pmatrix} 1 & 0 \\ 0 & 1 \end{pmatrix} + \varepsilon_T \frac{\sqrt{3}}{6} \begin{pmatrix} -1 & 0 \\ 0 & 1 \end{pmatrix},\end{aligned}\tag{9.3.85}$$

for d_1 - d_3 variants of the (111) tetragonal films and

$$\begin{aligned}\varepsilon_{S\alpha\beta}^{(r_1, r_3)} &= \varepsilon_{is} \begin{pmatrix} 1 & 0 \\ 0 & 1 \end{pmatrix} + \frac{\delta}{2} \begin{pmatrix} 0 & 1 \\ 1 & 0 \end{pmatrix}, \\ \varepsilon_{S\alpha\beta}^{(r_2, r_4)} &= \varepsilon_{is} \begin{pmatrix} 1 & 0 \\ 0 & 1 \end{pmatrix} - \frac{\delta}{2} \begin{pmatrix} 0 & 1 \\ 1 & 0 \end{pmatrix},\end{aligned}\tag{9.3.86}$$

for r_1 - r_4 variants of the (001) rhombohedral films, the variants being explained in Figs. (9.2.16), (9.2.17), and (9.2.18). Here ε_{is} is one-third of the relative change of the unit cell volume resulted from the phase transition, ε_T is the tetragonality strain (see Eq. (9.3.4)), and δ (see Fig. (9.2.16)) is the angle of rhombohedral distortion.²⁴ For the tetragonal case, the matrices are written in the origin where “ X_1 ”-axis is parallel to the trace of the d_1/d_2 inclined domain wall on the (111) plane and “ X_2 ”-axis is perpendicular to this trace (see Fig. 9.2.18c). For the rhombohedral case, the standard cubic reference frame is used. One can readily check that the matrices, Eq. (9.3.85), transform into each other upon the 120° rotations of the origin and the matrices, Eq. (9.3.86), transform into each other upon the 90° rotations. This implies equal elastic energies of the single-domain variants.²⁵ For a binary domain pattern, this degeneracy leads to the equal volumes of the variants in the pattern. Thus, the only two questions related to the domain structure are left: (i) Under what conditions the multidomain state is more favorable than the single-domain one? (ii) What is the period of the equilibrium domain pattern?

As follows from Sect. 9.3.3 (see Eqs. (9.3.56) and (9.3.57) with $\alpha = 1/2$), in the mean-strain approach, the domain period is controlled by the surface energy of domain walls and the so-called normalized energy density of the long-range

²⁴ Equations (9.3.85) and (9.3.86) are written to within the approximation of small ε_T and δ .

²⁵ In principle it may not be the case when the thermal expansion of the substrate is not isotropic in the plane of the film or the epitaxy relation in the cubic phase lowers the in-plane symmetry of the film. We will not cover these situations which have not been addressed in the literature.

inter-domain coupling between two variants (“1” and “2”) through the substrate u_{12} . The latter is a function of the difference $\varepsilon_{M\alpha\beta}^{(1)} - \varepsilon_{M\alpha\beta}^{(2)}$ of the misfit strains of the variants (see Eqs. (9.3.75)). Using relation (9.3.1) one readily finds that this difference is equal to $\varepsilon_{S\alpha\beta}^{(2)} - \varepsilon_{S\alpha\beta}^{(1)}$. Thus, it is the difference of the in-plane components of the spontaneous strains of the variants that should be determined to characterize the pattern. One readily finds from Eqs. (9.3.85) and (9.3.86) that, for the discussed domain systems, this difference is always a pure shear:

$$\varepsilon_{S\alpha\beta}^{(r_1)} - \varepsilon_{S\alpha\beta}^{(r_2)} = \delta \begin{pmatrix} 0 & 1 \\ 1 & 0 \end{pmatrix}. \quad (9.3.87)$$

$$\varepsilon_{S\alpha\beta}^{(r_1)} - \varepsilon_{S\alpha\beta}^{(r_2)} = \delta \begin{pmatrix} 0 & 1 \\ 1 & 0 \end{pmatrix}. \quad (9.3.88)$$

This is a situation identical to that in the a_1/a_2 -pattern in (001) tetragonal films where this difference written in the proper reference frame reads

$$\hat{\varepsilon}_s^{(a_1)} - \hat{\varepsilon}_s^{(a_2)} = \varepsilon_T \begin{pmatrix} 0 & 1 \\ 1 & 0 \end{pmatrix}. \quad (9.3.89)$$

Thus, we see that, to within the mean-strain approach, the problem of the energetics of the domain pattern in (001) rhombohedral and (111) tetragonal films is equivalent to that of the a_1/a_2 -pattern. Specifically, the relations derived for the equilibrium period of the a_1/a_2 -pattern are applicable to the two systems under the consideration.²⁶

For future analysis, it is proper, using Eqs. (9.3.47), (9.3.56), and (9.3.57), to present the relations for the period W and the critical thickness of the a_1/a_2 -pattern in the form

$$W = \frac{2}{\xi} \sqrt{hh_0}, \quad (9.3.90)$$

$$h_0 = \frac{4\xi\sigma}{G\omega_s^2}, \quad (9.3.91)$$

where $G = 0.5E/(1 + \nu)$ is the shear modulus, $\omega_s = \varepsilon_T$ is the values of the shear strain relating the crystalline lattices of the two domain states involved in the a_1/a_2 -pattern, and $\sigma = \sigma_W / \sin \alpha = \sqrt{2}\sigma_W$. Here α and σ_W are the angle between the domain walls and the substrate and the energy density (per unit area) of the wall, respectively. In this form, the relations for the domain period and the

²⁶ In the approximation of elastic isotropy of the material of the film and the substrate, which is currently used in the problems of this kind.

critical thickness can be applied to the domain patterns in (111) tetragonal and (001) rhombohedral films once the proper relations for ω_s and σ are used. Based on Eqs. (9.3.87) and (9.3.88) and the information on the geometry of the domain patterns (see Sect. 9.2.2) these relations are as follows. For the domain patterns in the (111) tetragonal films $\omega_s = \varepsilon_T/\sqrt{3}$, $\sigma = \sqrt{3/2}\sigma_W$ (inclined pattern), and $\sigma = \sigma_W$ (the walls are normal to the substrate). For the domain patterns in the (001) rhombohedral films $\omega_s = \delta$, $\sigma = \sqrt{2}\sigma_W$ (inclined pattern), and $\sigma = \sigma_W$ (the walls are normal to the substrate). As for the parameter ξ , for the a_1/a_2 -pattern, from numerical calculations (Pertsev and Zembilgotov, 1995) it can be evaluated as 0.27. The same value can be used for the cases where the walls making the pattern are oblique. This can be decided based upon the treatment by Romanov et al. (1998, 1999) where it was shown that the cases of oblique walls in (111) tetragonal and (001) rhombohedral films are elastically equivalent to the situation in the a_1/a_2 -pattern. In the case of vertical walls in the former systems, the situation is more complicated (Romanov et al., 1998; 1999) and no exact treatment of the problem is available. However, based on the analytical results by Romanov et al. a value of $0.27(2-\nu)/(1-\nu)$ can be used as a reasonable estimate for ξ in this case.

Despite its appealing simplicity the mean-strain approach is limited to the films essentially thicker than the critical thickness h_0 . For this reason, the prediction of this approach that at $h < h_0$ the multidomain state is not energetically favorable (see Sect. 9.3.3) cannot be trusted. For the a_1/a_2 -pattern, we have already seen that this prediction is not valid and the domain pattern is energetically favorable for films of any thickness. One can expect that this holds for the (111) tetragonal and (001) rhombohedral films. This supposition was justified by Romanov et al. (1998, 1999) who offered a treatment of the problem, which goes beyond the mean-strain approximation. Another interesting result obtained by these authors (Romanov et al., 1999) is that, in a certain range of parameters of the problem, the energetics of the domain pattern in the (111) tetragonal films allows two values of its period corresponding to stable and metastable domain structures.

It is important to note that the “purely elastic” analysis of the problem addressed above suffers from a limitation which can be crucial for the considered situation, namely the effect of the misfit strain on the order parameter is neglected. For the moment, in contrast to the case of the (001) tetragonal films, there is no theory for the (111) tetragonal and (001) rhombohedral films that would take into account this effect. However, it seems that there is at least one conclusion of the “purely mechanical” analysis, which can be revised by the analysis that takes into account the impact of misfit strain on the order parameter. Namely, it is the state of the films under high compressive strains (the case of large negative parent misfit strains). Let us explain this point for the case of (111) films made of material having the tetragonal phase in the bulk form. In this case, the “purely elastic” theory, assuming that the film is always in the tetragonal state, predicts that the multidomain state is energetically favorable. However, as seen from the phase diagram shown in Fig. 9.3.7, for negative values of the parent misfit strains, the

single-domain state of this system can be rhombohedral. This state can be more energetically favorable than multidomain tetragonal state, especially for large negative values of the parent misfit strain.

9.3.5 Domain Formation Driven by Elastic Effects: Theory vs. Experiment

In this section we discuss the available experimental data on ferroelectric domain patterns in thin films (see Sect. 9.2) in the context of existing theories (Sects. (9.3.1), (9.3.2), (9.3.3), and (9.3.4)). We will mainly address the data on the domain pattern in (001) perovskite films. We will cover the behavior of the domain fraction and period as functions of the temperature, material of the substrate, film thickness, and composition.

9.3.5.1 Domain Fraction of a/c -Pattern in (001) Tetragonal Perovskite Films as a Function of Temperature

The available experimental data on the temperature dependence of c -domain fraction, α_{eq} , in PbTiO_3 films show a decrease in α_{eq} when approaching the transition temperature. This is illustrated in Fig. 9.2.10 for the case of films deposited on MgO and KTaO_3 substrates. The thicknesses of these films are 200 and 250 nm, respectively. For such thicknesses dense a/c -domain patterns are expected. Thus, we will invoke the theories of the dense a/c -domain structure. Three of them are presently available: (i) purely elastic theory of the a/c -pattern (Roytburd, 1997; 1998a), (see Sect. 9.3.3), (ii) purely elastic theory of three-domain-state structures based on the a/c -patterns (see Sect. 9.3.3) (Roytburd, 1997; 1998a), (iii) theory of the a/c -pattern taking into account the stress-induced variation of the order parameter (Koukhar et al., 2001) (see Sect. 9.3.4.). The results of these theories for α_{eq} , Eqs. (9.3.82), (9.3.51), and 9.3.79), can be presented within a unified formula

$$\alpha_{\text{eq}} = 1 - A \left(\frac{-Q_{12}}{Q_{11} - Q_{12}} + \frac{\varepsilon_{\text{P}}}{(Q_{11} - Q_{12})P^2} \right), \quad (9.3.92)$$

where

$$A = 1 + \nu = 1 - \frac{s_{12}}{s_{11}}; \quad P = P_{\text{S}} \quad \text{for theory (i),} \quad (9.3.93)$$

$$A = 2; \quad P = P_{\text{S}} \quad \text{for theory (ii),} \quad (9.3.94)$$

and

$$A = 1 + \nu = 1 - \frac{s_{12}}{s_{11}}; \quad P = P_{\text{S}}^* \quad \text{for theory (iii).} \quad (9.3.95)$$

Here P_S and P_S^* are the spontaneous polarization in the bulk material and that calculated for the domain pattern taking into account the average stress in the film (given by Eq. (9.3.80)), respectively. The less known parameter among those entering Eq. (9.3.92) is the parent misfit strain, ε_P . It is controlled by the lattice mismatch between the film and substrate in the paraelectric phase, the dislocation-driven stress release, and the thermal expansions of the film and substrate. The aforementioned uncertainty of ε_P results from that of the scenario of the dislocation-assisted stress release. A detailed discussion of this problem can be found in a paper by Speck and Pompe (1994). In the following discussion, we will adopt a scenario, which is presently considered as most realistic, namely, that the dislocation-assisted stress release does not take place below the crystallization temperature of the film T_G . In this case, the parent misfit strain ε_P can be expressed in terms of the residual misfit strain at the crystallization temperature of the films, ε_r , and the *thermal strain* ε_{th} :

$$\varepsilon_P = \varepsilon_r + \varepsilon_{th}; \quad \varepsilon_{th} = (a_{TS} - a_{TF})(T - T_G). \quad (9.3.96)$$

where a_{TS} and a_{TF} are the thermal expansion coefficients of the substrate and film in the paraelectric phase, respectively. The residual misfit ε_r is controlled by the equilibrium concentration of misfit dislocations. Its equilibrium value, ε_{r0} , can be evaluated using Eqs. (9.3.15):

$$\varepsilon_{r0} = \varepsilon_{high} = \frac{a_S - a_C}{a_S} \quad \text{for } h < h_c, \quad (9.3.97a)$$

$$\varepsilon_{r0} = \varepsilon_{low} = \text{sign}(a_S - a_C) \frac{L(h)}{h} \quad \text{for } h > h_c, \quad (9.3.97b)$$

where a_S and a_C are the lattice constants of the substrate and film at T_G , respectively. The critical thickness of the misfit dislocations h_c and the weakly h -dependent parameter $L(h)$ are defined by Eqs. (9.3.11) and (9.3.16). For $h < h_c$, the equilibrium value of the residual misfit strain given by Eq. (9.3.97a) determines the real value of ε_r whereas, for $h > h_c$, the real value of ε_r should lie between ε_{high} and ε_{low} tending to ε_{low} in the ideal situation of the equilibrium density of misfit dislocations.

Now let us discuss the experimental data shown in Fig. 9.2.10 in terms of the results of the three theories presented above. As is clear from the inspection of Eqs. (9.3.92), (9.3.93), (9.3.94), and (9.3.95), in all three theories, an essential temperature dependence of α_{eq} can arise from temperature variations of the polarization P and parent misfit strain. Analysis of the material parameter of the PbTiO_3 and the substrates (MgO and KTaO_3) shows (see Table 9.3.1) that the thickness of the films (200 and 250 nm) is definitely greater than the critical thickness of the misfit dislocation formation h_c so that the dislocation-assisted stress-release mechanism is active. At the crystallization temperature, this mechanism can provide a release of misfit stress down to its equilibrium values

Table 9.3.1 Parameters of some crystalline substrates and the strain states of (001) PbTiO₃ epitaxial films on these substrates. ε_{MPT} means the non-relaxed value of the misfit strain ($\varepsilon_{\text{high}}$) of the PbTiO₃ film. The numbers in the parentheses show either the temperature or the film thickness

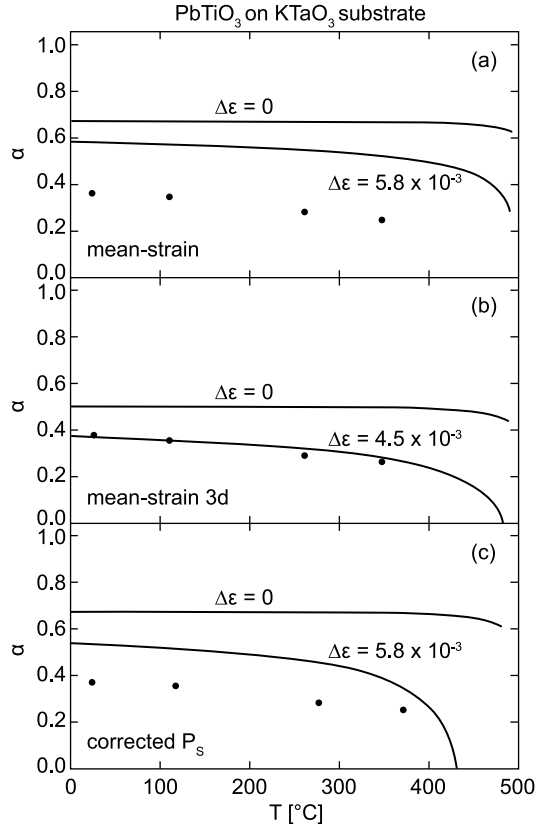
	$a_S, a_c, \text{\AA}$ (700°C)	$a_{\text{TS}}, a_{\text{TF}}$ $\times 10^6, \text{K}$	$\varepsilon_{\text{MPT}} \times 10^3$ (700°C)	$h_c, \text{\AA}$	$L, \text{\AA}$ (2000 \AA)	$\varepsilon_{r_0} \times 10^3$ (2000 \AA)	$\varepsilon_{\text{th}} \times 10^3$ (25°C)
MgO	4.251	13.4	64	5	1.7	0.8	-3.6
KTaO ₃	4.004	6.7	6.3	175	1.7	0.8	0.9
SrTiO ₃	3.934	11	-11	86	1.7	-0.8	-2.0
LaAlO ₃	3.821	11	-41	11	1.7	-0.8	-2.0
PbTiO ₃	3.979	8					

of 0.8×10^{-3} and 0.7×10^{-3} for the 200 and 250 nm thick films, respectively. Let us compare the data on the temperature dependence of α_{eq} shown in Fig. 9.2.10 with the predictions of the three theories on the assumption that, at T_G , the equilibrium concentration of misfit dislocations is reached whereas at lower temperatures only the thermal stress controls the parent misfit strain. This comparison is illustrated in Figs. 9.3.19 and 9.3.20. It is seen that, though the theories give a reasonable room temperature value (at least for MgO substrate) of the domain fraction, none of them is able to explain the temperature variation of α_{eq} . The theories yield more reasonable predictions if we assume that the stress release at T_G is not complete, i.e., that ε_r is somewhat larger than ε_{r_0} . In Figs. 9.3.19 and 9.3.20, we have plotted the predictions of the three theories for $\alpha_{\text{eq}}(T)$ with values of $\varepsilon_r = \varepsilon_{r_0} + \Delta\varepsilon$ (from the interval $\varepsilon_{\text{low}} - \varepsilon_{\text{high}}$) adjusted to have the best correspondence with the experiment. It is seen, first of all, that now all the theories give qualitatively correct trends. As for more quantitative comparison, in the case of films on KTaO₃, the three-domain-state model provides the best fit to the experimental data whereas, for the films on MgO, the theory taking into account the stress-induced variation of the order parameter seems to be the best. In both cases the best fit corresponds to a value of ε_r about 5×10^{-3} . Though, the body of the experimental data is not large enough for a thorough analysis one can conclude, from the above consideration, that the stress release in PbTiO₃ at T_G is not complete. A finite element analysis of the a/c -domain pattern in the PbTiO₃ on MgO system offered by Lee and coworkers (2001a) has led to the same conclusion. The analysis based on Eq. (9.3.92) also suggests that the temperature dependence of α_{eq} is stemming from that of the spontaneous polarization rather than from the temperature dependence of the thermal strain.

Concerning the theoretical predictions on the composition of the a/c -domain pattern the following remarks should be done.

- (i) The theory of Koukhar et al. (2001) should be considered as virtually exact with a reservation concerning the renormalization of the P^6 -terms (mentioned in Sect. 9.3.2). Far from the phase transition the prediction of this theory is very close to that of the Roytburd's theory of the a/c -pattern

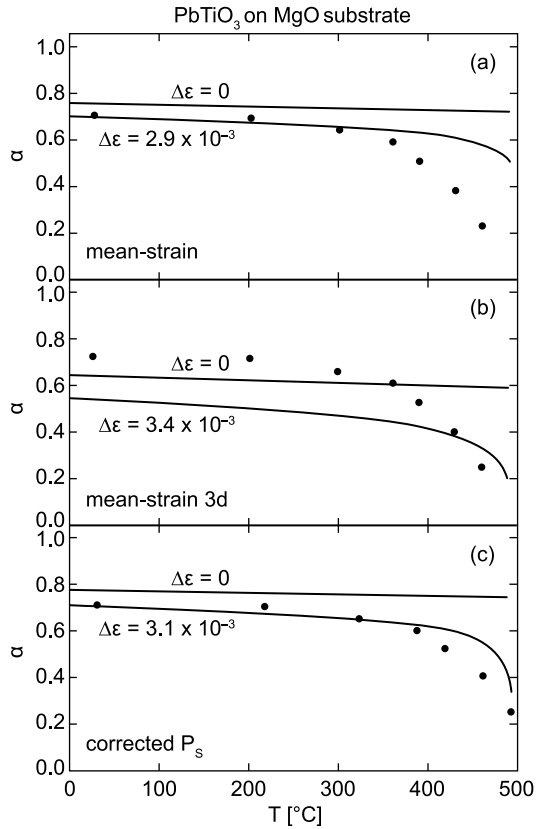
Fig. 9.3.19 Experimental data (points) (Kwak et al., 1992) on the temperature dependence of the fraction of c -domains, α , in a/c -domain patterns in (001) PbTiO_3 films on KTaO_3 substrates fitted to (a) the mean-strain theory with two domain states, (b) the mean-strain theory with three domain states, and (c) the mean-strain theory with two domain states and corrected value of the spontaneous polarization. (See the text.) Curves marked with $\Delta\varepsilon = 0$ are the results of the calculations performed for the equilibrium value of the residual misfit strain, ε_{r0} . The other curves are the results of the calculations performed for the values of the residual misfit strain, which are larger than ε_{r0} by values of $\Delta\varepsilon$ indicated in the graphs



(Roytburd 1997, 1998a). At room temperature, the prediction of these theories is a few percent close to each other as seen in Figs. 9.3.19 and 9.3.20. The reason for that is a closeness of values of P_s and P_s^* at room temperature.

- (ii) Using the diagram, Fig. 9.3.17a, developed by Koukhar et al. (2001) for (001) PbTiO_3 films, one can perform a further comparison of the theory to the experiment for the PbTiO_3 on MgO system. The best fit shown in Fig. 9.3.20c corresponds to the straight dashed line shown in this diagram. The cross-section of the diagram with this line predicts a change of the domain state as a function of the temperature, namely a transition from a/c - to a_1/a_2 -pattern at about 400°C . We have no experimental evidence concerning this transition. In the considered framework, the absence of the a/c - to a_1/a_2 -transition might be attributed to the persistence of the a/c -pattern as metastable (cf. diagram shown in Fig. 9.3.11).
- (iii) The available experimental data on $\alpha_{\text{eq}}(T)$ correspond to the case of the positive residual misfit strain at the crystallization temperature. All the above theories naturally explain the correlation between the positive sign of the residual strain and decreasing $\alpha_{\text{eq}}(T)$ with increasing temperature.

Fig. 9.3.20 Experimental data (*points*) (Lee and Baik, 1999) on the temperature dependence of the fraction of *c*-domains, α , in *a/c*-domain patterns in (001) PbTiO₃ films on MgO substrates fitted to (a) the mean-strain theory with two domain states, (b) the mean-strain theory with three domain states, (c) the mean-strain theory with two domain states and corrected value of the spontaneous polarization. (See the text.) Curves marked with $\Delta\varepsilon = 0$ are the results of the calculations performed for the equilibrium value of the residual misfit strain, ε_{r0} . The other curves are the results of the calculations performed for the values of the residual misfit strain, which are larger than ε_{r0} by values of $\Delta\varepsilon$ indicated in the graphs



The reason for this is that the sign in the second term (leading) in the parentheses in Eq. (9.3.92) is contorted by the sign of the residual strain. Similarly, these theories will predict an increasing temperature dependence of α_{eq} in the case of negative residual strain at the crystallization temperature (see Eq. (9.3.92)), which is the case of SrTiO₃ and LaAlO₃ substrates (see Table 9.3.1). Unfortunately, at present, there are no experimental data available to test this point.

On the lines of the above discussion one expects Eq. (9.3.92) to describe, at least qualitatively, the concentration dependence α_{eq} in PZT on MgO system shown in Fig. 9.2.11. However, assuming that, in PbTiO₃ and PZT, the residual stresses at T_G are of the same order of magnitude and taking into account the difference between the material parameters of these crystals, one cannot explain this dependence. At the same time, one readily checks that these theories provide a correct trend under the assumption that, in PZT, the relaxation of the residual stress at T_G is much smaller than that in PbTiO₃. This scenario is supported by the finite element analysis offered by Lee and coworkers (2001).

9.3.5.2 Thickness Dependence of the Domain Fraction of a/c -Pattern in (001) Tetragonal Perovskite Films

The available experimental data on the thickness dependence of domain pattern in (001) tetragonal perovskite film mainly cover PbTiO_3 and PZT films thicker than 15 nm. Using our estimates for the critical thickness h_0 as a fraction of the domain wall width (see Sect. 9.3.3.3) we conclude that the thicknesses of these films exceed h_0 by some two orders of magnitude. For such thicknesses, the domain pattern is expected to be dense so that we can apply the theory of the dense domain pattern to the analysis of the above data. Addressing the room temperature data we can neglect the effect of stress-induced variation of the order parameter and base our consideration on the mean-strain theory (see Sects. 9.3.4). Thus, combining Eqs. (9.3.63), (9.3.68) and using the relation $\phi = (\varepsilon_P - Q_{12}P_S^2)/(Q_{11} - Q_{12})P_S^2$, we arrive at the following expression for the thickness dependence of the c -domain fraction in the a/c -pattern

$$\alpha_{\text{eq}} = \frac{1}{2} + \left[\frac{1}{2} + \frac{(1+\nu)Q_{12}}{Q_{11} - Q_{12}} \left(1 - \frac{\varepsilon_P}{Q_{12}P_S^2} \right) \right] \frac{1}{1 - \sqrt{\frac{h_0}{h}}} + \frac{h_s}{h}. \quad (9.3.98)$$

To discuss the thickness dependence of α_{eq} one needs information on the thickness dependence of the parent misfit strain ε_P . In general, this dependence is controlled by the scenario of the dislocation-assisted stress release in the film. For the quantitative comparison of the theory with the experiment, we will adopt the already addressed above scenario, namely, that the dislocation-assisted stress release does not take place below the crystallization temperature of the film T_G whereas the dislocation density at this temperature is in equilibrium. Under these assumptions, using Eqs. (9.3.96) and (9.3.97b) we find the following thickness dependence of ε_P :

$$\varepsilon_P = \varepsilon_{\text{th}} + \text{sign}(a_S - a_c) \frac{L(h)}{h}, \quad L(h) = 0.24 \ln(0.7 \cdot h), \quad (9.3.99)$$

where h should be taken in Å. Combining Eqs. (9.3.98) and (9.3.99) we find

$$\alpha_{\text{eq}} = \frac{1}{2} + \left[\frac{1}{2} + \frac{(1+\nu)Q_{12}}{Q_{11} - Q_{12}} \left(1 - \frac{\varepsilon_{\text{th}}}{Q_{12}P_S^2} - \frac{h_r}{h} \right) \right] \frac{1}{1 - \sqrt{\frac{h_0}{h}}} + \frac{h_s}{h}, \quad (9.3.100)$$

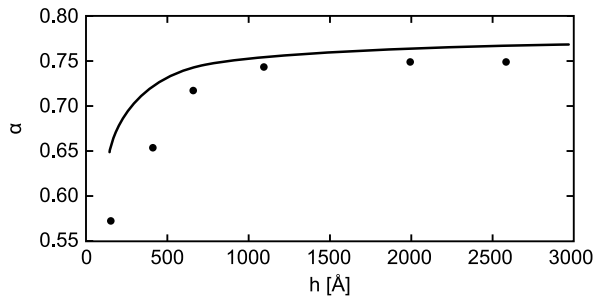
where

$$h_r = \text{sign}(a_S - a_c) \frac{L(h)}{Q_{12}P_S^2}. \quad (9.3.101)$$

From Eq. (9.3.100) we see that, in the above situation, the thickness dependence of α_{eq} is governed by three effects characterized by three spatial scales:

(i) the size effect related to the microstresses with the scale h_0 , (ii) the size effect related to the difference between the energies of the a - and c -domain/substrate interfaces with the scale h_S , and (iii) the thickness dependence of the equilibrium stress release with the scale $h_r = L/(Q_{12}P_S^2) \cong 150 \text{ \AA}$. Among these effects, the size effect related to the difference in the interface energies is the most difficult to evaluate quantitatively. However, based on a very rough estimate of $|h_S|$ as about one-tenth of the domain wall thickness (see Sect. 9.3.3.3) we conclude that this effect does not look essential for the considered systems. Neglecting this effect in Eq. (9.3.100) we arrive at an expression for the thickness dependence of α_{eq} , which contains only one not exactly known parameter h_0 . For $h_0 = 2 \text{ \AA}$, this expression reasonably imitates the data for the PbTiO₃ on MgO system as seen in Fig. 9.3.21. The used value of h_0 is consistent with its estimate as a fraction of the domain wall thickness. The simulated effect is mainly due to the thickness dependence of the residual strain at T_G slightly compensated by the size effect related to the microstresses. Of importance to notice is that the sense of the size effect, i.e., increasing or decreasing type of the predicted $\alpha_{eq}(h)$ dependence, is controlled by the sign of the residual strain, which is in turn controlled by that of the parent misfit strain.

Fig. 9.3.21 Experimental data (*points*) (Lee and Baik, 2000) on the film-thickness dependence of the fraction of c -domains, α , in a/c -domain patterns in (001) PbTiO₃ films on MgO substrates fitted to Eq. (9.3.100). See the text



Thus, the experimental $\alpha_{eq}(h)$ dependence in the PbTiO₃ on MgO system can be reasonably compared with the quantitative predictions of the theory assuming the equilibrium dislocation density at T_G . As for the experimental $\alpha_{eq}(h)$ dependences for PbTiO₃ (100) films deposited on other substrates (KTaO₃, SrTiO₃, and LaAlO₃; see Fig. 9.2.9b, c, and d), these occur to be too strong to be interpreted in terms of this equation. However, one may rationalize these experimental data assuming that the residual stress at T_G does not arrive at its equilibrium value given by Eq. (9.3.97b).

Let us do this using a more general relation, Eq. (9.3.98). In the case of non-equilibrium density of misfit dislocation, similar to the equilibrium situation, in thicker films the dislocation density is expected to be larger. In turn, this means that the thicker the film, the smaller the residual misfit strain. Taking this into account, one can rewrite the parenthesis in Eq. (9.3.98) in the form

$$\left(1 - \frac{\varepsilon_{th}}{Q_{12}P_S^2} - \frac{\varepsilon_r}{Q_{12}P_S^2}\right),$$

where ε_r is the residual misfit strain contorted by the non-equilibrium density of misfit dislocation. According to the above reasoning, $|\varepsilon_r|$ is a decreasing function of the film thickness. It is clear that this parenthesis will provide an increasing thickness dependence of α_{eq} , if $\varepsilon_r > 0$, and a decreasing dependence, if $\varepsilon_r < 0$. Using the information on the non-relaxed misfit strain given in Table 9.3.1, we find that the sense the $\alpha_{eq}(h)$ dependences shown in Fig. 9.2.9b, c, and d perfectly corresponds to the sign of ε_{MPT} , which obviously controls the sign of ε_r . A magnitude of the size effect in the case of KTaO_3 , SrTiO_3 , and LaAlO_3 substrates could be attributed to larger values of the residual misfit strains at T_G in these systems.

9.3.5.3 Periodicity of a/c -Patterns in (001) Tetragonal Perovskite Films

Images obtained with SEM, TEM, SFM, and other visualization techniques provided a wide body of information on the periodicity of the a/c -pattern in (001) tetragonal PbTiO_3 and PZT films (see Sect. 9.2.1). These data were obtained on films having the thicknesses large enough to apply the theory of dense a/c -pattern. Thus the result of the mean-strain theory for the domain period W , Eq. (9.3.57), can be used for the discussion of these experimental data. We will use this expression with $\nu = 0.3$ and $\xi = 0.27$, rewriting it in the form

$$W = 7.4\tau\sqrt{hh_{0a/c}},$$

$$\tau = \frac{0.25}{\alpha(1-\alpha)}, \quad (9.3.102)$$

$$h_{0a/c} = 5.6 \frac{\sigma_w}{E\varepsilon_T^2}. \quad (9.3.103)$$

Here parameter τ describes the effect of the c -domain fraction α on the domain period W . The characteristic length h_{0ac} for the a/c -domain pattern has been evaluated (see Eq. (9.3.71)) for PbTiO_3 films as a fraction of domain wall thickness that corresponds to a few angstroms at room temperature. One should mention that this estimate is very rough first of all because of the roughness of the available estimates for the surface energy of the domain wall σ_w . On the other hand, one may expect no essential difference between the values of h_{0ac} for PbTiO_3 and tetragonal PZT since the pronounced variation (between PbTiO_3 and PZT) of the tetragonality strain entering the estimate may be substantially compensated with the variation of σ_w .

Let us apply Eq. (9.3.102) to the analysis of the data on the periodicity of the a/c -domain pattern in PbTiO_3 and PZT listed in Table 9.3.2. In the same table we give the values of parameter $h_{0a/c}$, which is calculated from these data using Eq. (9.3.102). As seen from this table the estimated value of the characteristic

Table 9.3.2 The experimental data on a/c domain patterns in (001) PbTiO₃ epitaxial films on different substrates: h , film thickness, W , period of the pattern, α , fraction of c-domain, and $\tau = 1/[4\alpha(1 - \alpha)]$. The last column gives the values of the parameter $h_{0a/c}$ of the main strain theory calculated from these data using Eq. (9.3.103)

	h , nm	W , nm	α	τ	$h_{0a/c}$, Å
PbTiO ₃ /MgO [1]	790	50–200	0.8	1.6	0.2–4
PbTiO ₃ /MgO [2]	1200	80–300	0.7	1.2	0.7–10
PbTiO ₃ /KTaO ₃ [3]	200	40	0.3	1.2	1
PbTiO ₃ /LaAlO ₃ [4]	150	25–100	0.75	1.3	7–68
PZT(20/80)/SrTiO ₃ [5]	400	200	0.85	2	5
PZT(20/80)/SrTiO ₃ [6]	400	120–140	0.8	1.6	3–4
PZT(20/80)/SrTiO ₃ [7]	350	200–700	0.8	1.6	9–100

[1] Foster et al., 1995; [2] Surowiak et al., 1993; [3] Lee et al., 2001b; [4] Yen and Chen, 1999; [5] Alpay et al., 1999; [6] Ganpule et al., 2000a; [7] Nagarajan et al., 2001.

length of the $h_{0a/c}$ exhibits some three-orders-of-magnitude spread which by no means can be attributed to a variation of material parameters of the system like the degree of stoichiometry and/or composition. This clearly indicates that the theory of equilibrium ferroelastic domain pattern in thin films at least not always provides a reasonable description of the real experimental situation. The reason for this disparity is that the real domain pattern appears to be far from the equilibrium one, i.e., it does not correspond to the energy minimum of the system. Data corresponding to a situation which is very far from the equilibrium were reported by Nagarajan et al. (2001) (the last row in Table 9.3.2) where the authors observed enormous spread of the local periodicity of the pattern. Disregarding these data we however find that the data from the rest of the table correspond to a value of $h_{0a/c}$ that is about few angstroms; this is consistent in the order of magnitude with the theoretical estimate given above.

Comparing the data on the domain fraction α and domain period W discussed in this section one notices that the equilibrium theory of the domain pattern provides a better description for the latter than for the former. The reason for that is rather obvious. In thick enough films, the domain fraction is controlled by the energy of macrostresses, which is proportional to the film thickness h . At the same time the period is controlled by the balance between the energy of microstresses and the energy of the domain walls, resulting in a contribution to the energy proportional to \sqrt{h} . This energy is roughly $\sqrt{h/h_{0a/c}}$ times smaller than that controlling α . The implication is that the domain wall pinning (that prevents the domain pattern from reaching its equilibrium state) should affect the period stronger than the domain fraction. Since the pinning energy per wall is proportional to the wall area that is in turn proportional to h , in thicker films, one expects stronger deviations of the domain period from its equilibrium value.

9.3.5.4 Periodicity of Domain Patterns in (111) Tetragonal and (001) Rhombohedral Perovskite Films

Experimental data on the period of the domain patterns in (111) tetragonal and (001) rhombohedral perovskite films are available only for relatively thick films so that the result of mean-strain approach can be used of their interpretation.

For (111) tetragonal PZT (25/75) films, the data on domain wall spacing for 300–700 nm thick films were reported to be consistent with the square root law predicted by Eq. (9.3.90) (Zybill et al., 2000). The observed domain pattern was attributed to the type containing oblique domain walls (see Fig. 9.2.18c and d). For such pattern, Eqs. (9.3.90) and (9.3.91) can be rewritten (with $\omega_s = \varepsilon_T/\sqrt{3}$, $\sigma = \sqrt{3/2}\sigma_w$, $\nu = 0.3$, and $\zeta = 0.27$) as

$$W = 7.4\sqrt{hh_0}. \quad (9.3.104)$$

$$h_0 = 10.3 \frac{\sigma_w}{E \varepsilon_T^2}. \quad (9.3.105)$$

In terms of Eq. (9.3.104), the reported data yield a value of parameter h_0 of about 0.4 Å. Now, concluding from Eqs. (9.3.105) and (9.3.103) that $h_{0a/c} \approx 0.5h_0$, we can estimate $h_{0a/c} \approx 0.2$ Å. This value is some one order of magnitude smaller than the rough theoretical estimate. Comparing this value to the set of experimental estimates obtained for the data on the a/c -pattern (Table 9.3.2) we find it corresponding to the lower limit of the set.

The information on domain patterns in (001) rhombohedral perovskite films has been offered by Streiffer et al. (1998) for PZT (80/20) and (65/35). The data reported do not allow us to discuss the thickness dependence of the domain period. However, these data enable estimation of the parameter h_0 . For the structure with vertical domain walls (see Fig. 9.2.17) reported in this chapter, the basic Eqs. (9.3.90) and (9.3.91) can be rewritten as

$$W = 3\sqrt{hh_0}, \quad (9.3.106)$$

$$h_0 = 6.8 \frac{\sigma_w}{E \delta^2}, \quad (9.3.107)$$

where we have set $\zeta = 0.27(2 - \nu)/(1 - \nu)$, $\omega_s = \delta$, $\sigma = \sigma_w$, and $\nu = 0.3$. The data reported in this chapter (PZT 80/20, $h = 520$ nm, $W/2 = 80$ – 120 nm, and PZT (65/35), $h = 700$ nm, $W/2 = 50$ – 100 nm) yield, via Eq. (9.3.107), an estimate $h_0 \approx 50$ – 640 Å. Interpretation of this result is difficult because of the lack of the information of the wall energy for the rhombohedral phase. Assuming $\sigma_w \cong 10^{-2}$ J/m² Streiffer et al. (1998) found this estimate consistent with the theory. Indeed, with the experimental values $\delta \approx 0.005$ and $1/E = 7 \times 10^{-12}$ J/m³, Eq. (9.3.107) leads a theoretical estimate $h_0 \cong 200$ Å, which is consistent with the above experimental estimate. Comparing Eqs. (9.3.107) with (9.3.103) one can rationalize such large (compared to $h_{0a/c}$) value

of h_0 as owing to the smallness of shear deformation $\omega_s \approx \delta \approx 0.005$ in the rhombohedral case compared to that in the tetragonal case, $\omega_s \approx \epsilon_T \approx 0.06$.

9.4 Domain Pattern and Electrostatic Effects

As it was discussed in Chap. 5 the depolarizing fields created by the appearance of the spontaneous polarization at the phase transition lead, if not screened by mobile chargers, to splitting the ferroelectric crystal into domains. In the case of thin films, this effect is also expected. Here one can distinguish two situations different from that in a non-electroded slab of a bulk ferroelectric. First is the case of a ferroelectric film in a short-circuited capacitor. For a real ferroelectric thin film, the short-circuiting does not necessarily lead to screening of the depolarizing field because the ferroelectric/electrode interface often behaves as a thin dielectric layer (see Sect. 9.5.2 for more discussion of this point). This situation can be modeled by considering a short-circuited capacitor containing a ferroelectric/dielectric sandwich structure. The second situation is a ferroelectric film deposited onto insulating substrate having free surface exposed to a reactive atmosphere. In this case, the bound charge of the polarization at the free surface may be considered as screened by the free chargers provided by the reactive atmosphere. At the same time, the bound charges of the polarization at the ferroelectric/substrate interface may not be screened. In what follows we will discuss the theories covering these situations.

9.4.1 Equilibrium Domain Pattern in Ferroelectric/Dielectric Sandwich Structure

The problem of domain pattern formation in a capacitor containing a ferroelectric and electrode-adjacent passive layer(s) was address by Kopal et al. (1999) and by Bratkovsky and Levanyuk (2000a). Let us specify the mathematical formulation of the problem and briefly discuss the principal results obtained and the range of their applicability.

A 180° domain pattern is considered in a ferroelectric film, which is sandwiched between two dielectric layers and electrodes. The resulting capacitor structure is shown in Fig. 9.4.1. It is assumed that the energetically favorable domain pattern is

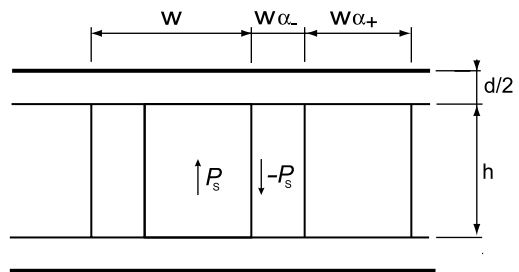


Fig. 9.4.1 Schematic cross-section of a capacitor where two dielectric layers separate a multidomain ferroelectric from two electrodes. The domain widths (W_+ and W_-) and the period of the c -domain pattern (W) are indicated

periodic. Its two parameters, the period W and asymmetry $A = \alpha_+ - \alpha_-$ where α_+ and α_- are the volume fractions of the positively and negatively poled domain, can be found minimizing the appropriate thermodynamic potential, which in this case is given by Eq. (8.2.13). In the “hard-ferroelectric” approximation where the displacement in both the ferroelectric and dielectric of the passive layer can be written as $D_i = P_{S_i} + \epsilon_0 \kappa_{ij} E_j$, this potential reads

$$G = \frac{1}{2} \int E_i (D_i - P_{S_i}) d^3x - q_1 \phi_1 - q_2 \phi_2. \quad (9.4.1)$$

where q 's and ϕ 's are the charges and potentials on the electrodes, respectively, and the integration is taken over the whole volume of the capacitor. In terms of the potential difference applied to the capacitor V and the distribution of the P_S -related bound charge density at the interfaces between the ferroelectric and the passive layers, $\sigma_f = \pm P_S$, G can be expressed as

$$G/S = \frac{1}{2S} \int \sigma_f \phi \, dS + \frac{1}{2} \sigma_e V, \quad (9.4.2)$$

where S is the area of the capacitor and σ_e is the charge of the capacitor; the integration is taken over the interfaces between the ferroelectric and the passive layers. The distribution of the electrostatic potential ϕ as well as the charge σ_e as functions of W and A can be found by solving the Laplace equation with the proper boundary conditions (see Sect. 5.2.). Then, the total thermodynamic potential of the system, G_{tot} (hereafter as a shorthand we will call it energy), can be found as a sum of the surface energy of the domain walls and the electrostatic energy, Eq. (9.4.2), calculated using the found expressions for ϕ and σ_e . The final forms of G_{tot} reads (Kopal et al., 1999; Bratkovsky and Levanyuk, 2000a; 2001c)

$$G_{\text{tot}}/S = \frac{2\sigma_W h}{W} + \frac{dh/\epsilon_0}{\kappa_d h + \kappa_c d} \left(\frac{P_N^2}{2} - \frac{V P_N \epsilon_0 \kappa_d}{d} \right) + P_S^2 \frac{4W}{\epsilon_0 \pi^3} \sum_{n=1}^{\infty} \frac{\sin^2 \left[n \frac{\pi}{2} \left(1 + \frac{P_N}{P_S} \right) \right]}{n^3 D_n}, \quad (9.4.3)$$

where

$$D_n = \kappa_d \coth \frac{n\pi d}{W} + \sqrt{\kappa_a \kappa_c} \coth \left(\sqrt{\frac{\kappa_a}{\kappa_c}} \frac{n\pi h}{W} \right). \quad (9.4.4)$$

Here $P_N = AP_S$ is the net spontaneous polarization of the ferroelectric; κ_a , κ_c , and κ_d are the in-plane and out-of-plane lattice permittivities of the ferroelectric films and that of the dielectric layer, respectively; σ_W is the surface energy of the domain wall; the contributions independent of the period and the asymmetry of the pattern are skipped over.²⁷ In Eq. (9.4.4), the first term gives the surface energy of the walls, the second one gives the electrostatic energy of the system calculated neglecting the effects of stray fields (inhomogeneity of the

²⁷ In the corresponding equation from the paper of Kopal et al. (1999), Eq. (2), there is a misprint: $V/2$ instead of V .

field in the plane of the capacitor), and the third term gives the energy of the stray fields. In the limit of infinitely thick dielectric layers ($d \rightarrow \infty$) with $\kappa_d = 1$ and at $V = 0$, the last two terms of Eq. (9.4.3) can be reduced to Eq. (5.2.16). It is expected since, in this limit, the treated problem becomes equivalent to that of the domain pattern in ferroelectric slab in vacuum treated in Sect. 5.2.

The net spontaneous polarization and the period of the pattern as a function of the applied voltage and the parameters of the system can be determined by minimizing the found expression of the energy of the system with respect to these variables. In general, these calculations can be performed only numerically. However, using analytical result available in several limiting cases, it is possible to trace the main trends of the behavior of the system and to distinguish its new features brought about by the presence of the dielectric layers.

Let us discuss the equilibrium domain pattern when the system is short-circuited and compare it with the classical results for a non-electroded ferroelectric slab. First of all, the presence of the passive layers and short-circuited electrodes ceases to influence the behavior of the system when the domain period is much smaller than the thickness of the passive layers ($W \ll d$) since in this case the stray fields of the pattern do not reach the electrodes. Thus, in this case, we arrive at a situation like in a non-electroded ferroelectric, which, for dense domain patterns (for $W \leq \sqrt{\kappa_a/\kappa_c}h$), corresponds to the classical result by Mitsui and Furuichi (1953). Accordingly, for $V = 0$ and $W \leq d$, $\sqrt{\kappa_a/\kappa_c}h$, the minimization of Eq. (9.4.1.3) yields a symmetric pattern with the distance between the walls:

$$W/2 = \sqrt{h_M h}, \tag{9.4.5}$$

where the characteristic length reads

$$h_M = 3.7\epsilon_0(\kappa_d + \sqrt{\kappa_a\kappa_c})\sigma_W/P_S^2. \tag{9.4.6}$$

One readily checks that at $\kappa_d = 1$, Eqs. (9.4.5) and (9.4.6) are identical to the results of Mitsui and Furuichi given by Eqs. (5.2.21) and (5.2.22).

The presence of the passive layers and the short-circuited electrodes becomes really essential when the thickness of the layers is much smaller than the period of the pattern ($d \ll W$). In this case the thickness dependence of the period essentially differs from that given by Eq. (9.4.5). In this limit for the dense domain pattern, strictly speaking at $W \leq \sqrt{\kappa_a/\kappa_c}h$, an analytical form of this dependence can be found for a special case where $\kappa_d = \sqrt{\kappa_a\kappa_c}$. It reads (Bratkovsky and Levanyuk, 2000a,b)

$$W/2 = 0.95d \exp\left(0.4 \frac{h_M h}{d^2}\right). \tag{9.4.7}$$

There is one more limiting case where an analytical solution can be readily found at $\kappa_d = \sqrt{\kappa_a\kappa_c}$, namely the situation where the passive layers are much thicker than the domain period ($W \ll d$) but where the domain pattern is not

dense ($W \gg h$). In this case, employing the symmetry of expression (9.4.4) with respect to swapping $d \leftrightarrow h\sqrt{\kappa_a/\kappa_c}$, we get the result by substitution $h\sqrt{\kappa_a/\kappa_c}$ for d in Eq. (9.4.7). This leads to the thickness dependence of the period for very thin films

$$W/2 = 0.95 h\sqrt{\kappa_a/\kappa_c} \exp\left(0.4 \frac{h_M \kappa_a}{h \kappa_c}\right), \quad (9.4.8)$$

which is similar to that found for very thin films in the case of the ferroelastic a_1/a_2 -domain pattern (cf. Eq. (9.3.78)).

The asymptotic thickness dependences of domain period given above provide a qualitative description of the evolution of the domain pattern in a wide thickness range, on condition that the thickness of the passive layers d is greater than the characteristic scale h_M . For this regime, such description is illustrated in Fig. (9.4.2)²⁸ for $d/h_M = 3$ and $\kappa_a = \kappa_c$. However, if this condition is not met, the range of applicability of the asymptotic relations Eqs. (9.4.5), (9.4.7), and (9.4.8) vanishes so that the domain pattern modeling can be performed only numerically. To the best of our knowledge, no simulation of this kind is available in the literature. Using Eq. (6.2.10c) for the wall surface energy we can get an estimate for the characteristic length h_M as being about the domain wall width t_W . Thus, in materials like PbTiO_3 or PZT at room temperature, one expects h_M to be of the order 1–3 nm. This means that the above analytical results can be applied to the situation where the passive layer is thicker than a few nanometers.

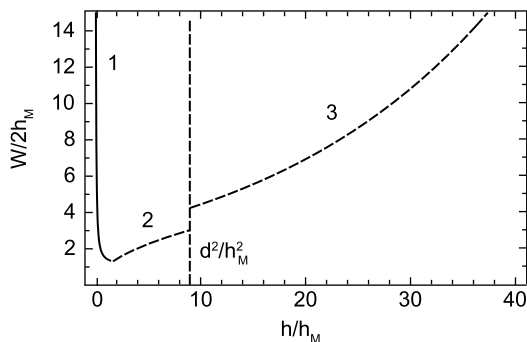


Fig. 9.4.2 Dependence of the period of a c -domain pattern on the thickness of the ferroelectric calculated for a dielectric/ferroelectric sandwich structure placed in a short-circuited capacitor (shown in Fig. 9.4.1). The segments of the curves marked with (1), (2), and (3) show the results of calculations according to asymptotic relations (9.4.8), (9.4.5), and (9.4.7), respectively. See the text

²⁸ The range of validity of the shown curve is actually limited by conditions $h > W$ for large h and $d > W$ for small h . For $h_M/d = 3$ and $\kappa_a = \kappa_c$, that gives the range of validity $0.2 < h/h_M < 45$.

9.4.2 Equilibrium Domain Pattern in Ferroelectric Films on Insulating Substrates

Consider the equilibrium domain pattern in a ferroelectric film deposited onto an insulating substrate and having the polarization bound charge screened at its free surface. As in the previous section we will be interested in a 180° domain pattern in a ferroelectric which is not too close to the phase transition so that the “hard-ferroelectric” approximation may be applicable. Though this problem is different from that addressed in the previous section, it can be formally treated using the results obtained for the latter. To do that, two points should be clarified. First, since the screened free surface of the film is equipotential, the equilibrium distribution of the polarization in it is identical to that in one half of the ferroelectric films of a double thickness but having the insulating substrate material at both interfaces (Streiffer et al., 2002). Thus, the problem is reduced to that for a ferroelectric slab immersed in an infinite volume of the dielectric material of the substrate. Second, if the total thickness of the dielectric d in the short-circuited capacitor containing two electrode-adjacent dielectric layers (see Fig. 9.4.1) formally tends to infinity, the screening effect of the electrodes vanishes so that one arrives at a problem of the domain pattern in a ferroelectric slab immersed in an infinite volume of the dielectric.

Taking into account the above arguments and using Eq. (9.4.3), the energy of the equilibrium domain pattern in the ferroelectric film of thickness h on an insulating substrate can be written

$$G_{\text{tot}}/S = \frac{4\sigma_W h}{W} + P_S^2 \frac{4W}{\varepsilon_0 \kappa_d \pi^3} \sum_{n=1,3,5,\dots}^{\infty} \frac{1}{n^3 \tilde{D}_n}, \quad (9.4.9)$$

where

$$\tilde{D}_n = 1 + \frac{\sqrt{\kappa_a \kappa_c}}{\kappa_d} \coth \left(\sqrt{\frac{\kappa_a}{\kappa_c}} \frac{2n\pi h}{W} \right) \quad (9.4.10)$$

and for the notations see the previous section.²⁹ The equilibrium domain period can be found by minimizing G_{tot} with respect to W . In the case of practical importance of a dense domain pattern ($W \leq \sqrt{\kappa_a/\kappa_c} h$), this leads to relations (9.4.5) and (9.4.6) where h should be replaced with $2h$. This gives

$$W = 5.4 \sqrt{\varepsilon_0 (\kappa_d + \sqrt{\kappa_a \kappa_c}) h \sigma_W / P_S^2}. \quad (9.4.11)$$

This theory was used by Streiffer and his coworkers (2002) for the interpretation of their data on a dense 180° domain pattern in PbTiO_3 films deposited on SrTiO_3 (see Sect. 9.2.1). In this work, using the material parameters of

²⁹ Equations (9.4.9) and (9.4.10) with $\kappa_d = 1$ become identical to those obtained by Kopal et al. (1997) for the problem of the domain pattern in a ferroelectric slab in vacuum (see Chap. 5).

PbTiO₃ and SrTiO₃ as well as the results of ab initio calculations for the wall energy σ_w (Meyer and Vanderbilt, 2002), the authors reduced Eq. (9.4.11) down to the relation $W = 3.2 h^{0.5}$ (W and h in nm), which was found in good agreement with their experimental data.

9.4.3 Limitations of Hard-Ferroelectric Approximation and Results Obtained Beyond This Approximation

The limitations of the hard-ferroelectric approximation have been already discussed in Sect. 5.2 for the case of a ferroelectric plate embedded in a dielectric medium (with the out-of-plane direction of the spontaneous polarization). Similar limitations apply to the results obtained in this approximation for a dielectric/ferroelectric/dielectric sandwich with the same orientation of the polarization.

An obvious problem appears in the case where the predicted domain period essentially exceeds the film thickness (wide domain pattern). In this case, the depolarizing field in the domains is very close to that in the single-domain film. Here, for the sandwich structure placed in a short-circuited capacitor, the depolarizing field leads to a shift of the Curie–Weiss temperature, T_0 , down by

$$\Delta T_0 = \frac{Cd}{\kappa_b d + \kappa_d h}, \quad (9.4.12)$$

where C and κ_b are the Curie–Weiss constant and the background permittivity of the ferroelectric, respectively; the rest of the notations are identical to those introduced above in this section. In the case of very thick passive layer ($d \rightarrow \infty$), Eq. (9.5.12) reduces to the results obtained for a ferroelectric slab embedded in a dielectric medium, Eq. (2.3.46). The derivation of Eq. (9.5.12) is similar to that of Eq. (2.3.46) (it can also be readily obtained from the theoretical results on ferroelectric/dielectric composites; see the paper by Sherman et al. (2006)). In view of possibly high values of C , such shift can be appreciable. For temperatures lower than $T_0 - \Delta T_0$, this shift will lead to a reduction of the value of the spontaneous polarization. In this case, results of the hard-ferroelectric approximation (e.g., (9.4.8) and (9.4.6)) still might be applicable though an additional check of this approach is needed. At the same time, for $T_0 > T > T_0 - \Delta T_0$, this shift means the suppression of the homogeneous ferroelectric state in the domains. This obviously implies that the results of the hard-ferroelectric approximation for wide domains (i.e., when $W \gg h$ is predicted) are invalid. In the above discussion it was implied that we are dealing with a proper ferroelectric. In the case of an improper ferroelectric, as was shown in Sect. 5.2, the depolarizing field does not destabilize the ferroelectric state but only reduces its spontaneous polarization. Thus, in improper ferroelectrics, all the results obtained above in this section, should hold, however, with modified (film-thickness dependent) values of the spontaneous polarization.

In principle, we can continue the discussion of shortcoming of the hard-ferroelectric approximation; however, we believe that it is more instructive to

discuss the approach, which goes beyond this approximation. A further progress in this matter is possible on the lines of the Landau theory, which incorporates the gradient terms (often called Ginzburg–Landau theory). We have used this theory in Chap. 6 for the description of structures of domain walls. Such approach in application to layered dielectric/ferroelectric/dielectric structures has been pioneered in the 1980s by Chensky and Tarasenko (1982). Recently, mainly motivated by the activity in ferroelectric thin films, further studies in this direction have been performed (Stephanovich et al., 2005; De Guerville et al., 2005; Bratkovsky and Levanyuk, 2006). The refusal to use the hard-ferroelectric approximation makes the mathematical treatment much more involved. Presentation of this treatment goes beyond the scope of the book. Below we restrict ourselves to the presentation of the mathematical formulation of the problem and highlight some of the results obtained.

Now the starting point of the theory is the thermodynamic potential of the system, which reads (cf. Eq. (9.4.1))

$$G = \int_{-h/2}^{h/2} \left[\frac{\alpha}{2} P^2 + \frac{\beta}{4} P^4 + \frac{\delta_{3333}}{2} \left(\frac{\partial P}{\partial z} \right)^2 + \frac{\delta_{1313}}{2} \left(\frac{\partial P}{\partial x} \right)^2 + \frac{\varepsilon_0 \kappa_b}{2} E_z^2 + \frac{\varepsilon_0 \kappa_a}{2} E_x^2 \right] dz dx$$

$$+ \varepsilon_0 \kappa_d \int_{h/2}^{h/2+d/2} E^2 dz dx - q_1 \varphi_1 - q_2 \varphi_2, \quad (9.4.13)$$

where $\alpha = (T - T_0)/(\varepsilon_0 C)$. Here the notation are the same as above in this section, κ_a is the in-plane value of the dielectric constant of the ferroelectric, δ 's are the proper components of the tensor of the correlation coefficients (cf. Eq. (6.2.46)). The Euler equation obtained by variation of this functional with respect to P should be solved together with the Maxwell equations

$$\operatorname{div} \mathbf{D} = 0 \quad \text{and} \quad \operatorname{curl} \mathbf{E} = 0, \quad (9.4.14)$$

where the electrical displacement in the ferroelectric is defined as

$$D_z = P + \varepsilon_0 \kappa_b E_z, \quad D_x = \varepsilon_0 \kappa_a E_x, \quad (9.4.15)$$

whereas in the dielectric layers

$$\mathbf{D} = \varepsilon_0 \kappa_d \mathbf{E}. \quad (9.4.16)$$

Here X -axis is set in the plane of the film and Z -axis normal to it.

De Guerville et al. (2005) have addressed the domain formation in the dielectric/ferroelectric/dielectric structure placed in a short-circuited capacitor and for the case where the domain wall spacing is smaller than the thicknesses of both the film and dead layer. The problem was actually equivalent to that in a ferroelectric plate embedded in a dielectric medium. The

numerical treatment showed that the period of the domain pattern is in a reasonable agreement with the results of the hard-ferroelectric approximation (Eqs. (9.4.5) and (9.4.6)) at any temperature (even close to the transition temperature). At the same time, it was found that the abrupt spatial distribution of the polarization (reminding that in the hard-ferroelectric approximation) occurs only for thick enough films or/and far enough from the transition temperature. In the opposite case, the simulations yielded smooth domain patterns (soft domains) where the wall spacing and width are comparable. Yet closer to the phase transition or/and for yet thinner films comes the paraelectric phase. Figure 9.4.3 illustrates this result.

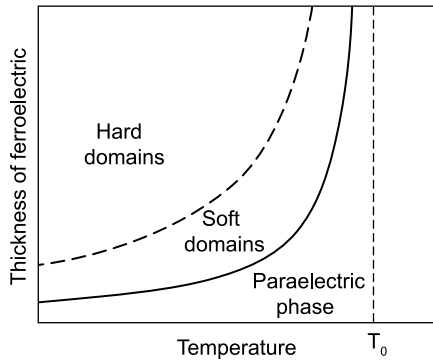


Fig. 9.4.3 Schematic of temperature–thickness diagram for the polarization state in a plate of a uniaxial ferroelectric embedded into a dielectric medium with the direction of the ferroelectric axis perpendicular to the plain of the plate. ‘Hard domains’ and ‘soft domains’ stand for a domain pattern where the wall thickness is much smaller than the period and that where these parameters are comparable, respectively. See the text. Reprinted with permission from De Guerville et al. (2005). Copyright (2005), Elsevier

The same theoretical framework was also used by Chensky and Tarasenko (1982) for testing the stability of the paraelectric state in the aforementioned system in the temperature interval $T_0 - \Delta T_0 < T < T_0$, where ΔT comes from Eq. (9.4.12). The stability was checked with respect to a “soft domain” pattern with

$$P = a \cos kx \cos qz. \quad (9.4.17)$$

Here a , k , and q are the constants. It was shown that the stability of the paraelectric state is controlled by the relation between ΔT_0 and a material-dependent parameter ΔT_{dom} : if $\Delta T_{\text{dom}} > \Delta T_0$, the paraelectric state in the sandwich structure is stable down to the transition into single-domain state at $T_S = T_0 - \Delta T_0$; in the opposite case, a transition into multidomain state takes place at

$$T_M(h) = T_0 - \Delta T_{\text{dom}}. \quad (9.4.18)$$

The period of the domain pattern was found to be close to the dependence given by Eq. (9.4.5) except for temperatures, which are very close to T_M .

In the case of a thin dead layer, i.e., at $h \gg d$ (the situation of interest for thin film ferroelectric capacitors), Chensky and Tarasenko (1982) found

$$\Delta T_{\text{dom}} = \frac{C}{h} \sqrt{\frac{12\varepsilon_0 \delta_{1313}}{\kappa_x}}, \quad (9.4.19)$$

whereas Eq. (9.4.12) can be simplified down to the form

$$\Delta T_0 = \frac{Cd}{\kappa_d h}. \quad (9.4.20)$$

Here it is instructive to mention that when the theory is applied to a ferroelectric thin film capacitor deposited, as usually, on a thick substrate, the transition temperature T_0 is that of the strained films, which can be substantially different from its value for the bulk material (see Sect. (9.3.2)).

It was also shown that, if $\Delta T_{\text{dom}} < \Delta T_0$, on further cooling below T_M the multinomial state remains the only possible (stable) one down to temperature

$$T_{\text{SS}}(h) = T_0 - 1.5\Delta T_0 + 0.5\Delta T_{\text{dom}}. \quad (9.4.21)$$

Below this temperature two states are possible—multidomain and single-domain, though the latter is less energetically favorable. Chensky and Tarasenko also made some predictions concerning the state of the system for temperatures below T_{SS} . Approximating the polarization pattern with its first harmonics, i.e., using ansatz (9.4.17), they showed that at temperatures below

$$T_{\text{SSS}}(h) = T_0 - 3\Delta T_0 + 2\Delta T_{\text{dom}} \quad (9.4.22)$$

the multi- and single-domain states are both possible but now the single-domain state has a lower energy.

The hierarchy of the critical temperatures, T_M , T_{SS} , and T_{SSS} for a given film thickness can be transformed into a hierarchy of the critical thicknesses at a given temperature T , h_M , h_{SS} , and h_{SSS} , which are the solutions of the equations $T_M(h) = T$, $T_{\text{SS}}(h) = T$, and $T_{\text{SSS}}(h) = T$, respectively. Thus, for $h < h_M$ the ferroelectric is in the paraelectric state, for $h_M < h < h_{\text{SS}}$ the ferroelectric is in a multidomain state, for $h_{\text{SS}} < h < h_{\text{SSS}}$ the ferroelectric can be in both multidomain and single-domain states, the latter being metastable, and for $h_{\text{SSS}} < h$ the ferroelectric can be again in both multi- and single-domain states, but with the former being metastable.

The Chensky–Tarasenko theory also enables a description of the state of the ferroelectric for the case where a fixed potential difference is kept between the plates of the capacitor.

The prediction of this theory should be taken with reservations because of two reasons: (i) the polarization profile in the domain pattern is described in the first harmonics approximation and (ii) the elastic effects are not taken into

account. The first issue is crucial for calculation of T_{SSS} : The result given by Eq. (9.4.22) is actually the upper bound for T_{SSS} . However, for a certain combination of the parameters of the system, it may serve a very rough estimate. The second issue may be of importance for calculations of T_{SS} (Pertsev and Kohlstedt, 2007) and T_{SSS} . This matter is presently under discussion (Pertsev and Kohlstedt, 2008; Bratkovsky and Levanyuk, 2008).

9.5 Switching and Polarization Hysteresis

The polarization response of ferroelectric thin films makes the most important characteristics of these from the application point of view. The small thickness of the films obviously enables the application of high electric fields to the material, which can promote an effective switching of the ferroelectric at relatively low applied voltages. However, already the first investigations of the ferroelectric thin film capacitors revealed that the switching behavior as well as the small-signal dielectric response of the films is not identical to those of the bulk materials of nominally the same compositions. For example, the films typically exhibit lower values of the relative permittivity and higher values of the coercive field. For the interpretation of these and other properties of ferroelectric thin films, a number of different models were suggested. The present section addresses typical features of the polarization response of ferroelectric thin films and the models which provide description of these features.

9.5.1 Pulse Switching

Experimental studies of the pulse switching kinetics of the ferroelectric thin films were mainly performed by using the classical transient current method and the poling back technique, which were already discussed in Sect. 7.4. The results obtained with these techniques are rather contradictory as well as their interpretation (see, e.g., Scott et al., 1988; Larsen et al., 1991; DeVilbiss and DeVilbiss, 1999; Seike et al., 2000; Song et al., 1997; Lohse et al., 2001; Tagantsev et al., 2002b). This is related, first, to the difference in real parameters of the materials, which in turn seem to be very processing dependent, second, to the way the raw data on switching current are analyzed and, third, to the width of the time interval monitored. The body of the available data will be summarized below in this section.

The polarization switching in 100–300 nm thick PZT and $\text{SrBi}_2\text{Ta}_2\text{O}_9$ films can be rather fast: For a switching voltage of a few volts, the switching times lay in nanosecond–sub-nanosecond range. Figures 9.5.1 and 7.4.3 show examples of switching curves. These curves were obtained by excluding the artifacts related to the RC parameter of the measuring setup. In the case of the curve shown in Fig. 9.5.1a (174 nm thick film of $\text{SrBi}_2\text{Ta}_2\text{O}_9$), the measured switching

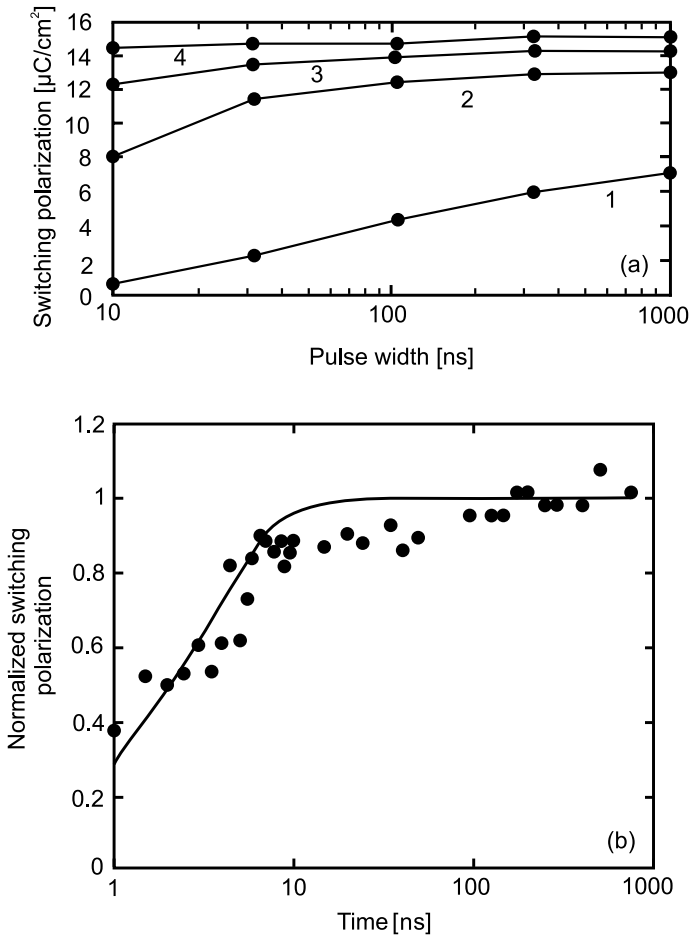


Fig. 9.5.1 Example of monitoring the pulse switching kinetics in $\text{SrBi}_2\text{Ta}_2\text{O}_9$ (a) and PZT (b) thin films. In (a), the voltage of the switching pulses for the curves are 1–1, 2–2, 3–3, and 4–7 V. After DeVilbiss and DeVilbiss (1999). In (b), the voltage of the switching pulses is 3 V. After Seike et al. (2000)

current density was checked to be independent of the capacitor area (DeVilbiss and DeVilbiss, 1999). The curve shown in Fig. 9.5.1b (250 nm thick film of PZT) was obtained measuring the reading signal of a 16 kbit memory cell matrix with a subtraction of the RC-controlled background current of the setup (Seike et al., 2000). The curve shown in Fig. 7.4.3 (135 nm thick film of modified PZT) was obtained using the poling back technique, the capacitor area independence of the results being checked (Tagantsev et al., 2002a,b).

The interpretation of switching behavior monitored in relatively narrow (typically two decades) time interval is usually based in the classical Kolmogorov–Avrami scenario using Eq. (7.7.24) or its modified versions. These data were found to

be in a reasonable agreement with this equation with the k parameter ranging from 1 to 2 corresponding to the situation of one- to two-dimensional domain growth from already existing nuclei (see, e.g., Seike et al., 2000). Better fits were obtained by using non-integer values of k or the hypothesis of a crossover between the two- and one-dimensional situations as shown in Fig. 8.7.9.

An analysis of the switching data in a wider time interval showed that the switching dynamics can be very far from that predicted by the Kolmogorov–Avrami scenario (Lohse et al., 2001; Tagantsev et al., 2002b). This can be clearly seen by comparing the switching curves shown in Fig. 7.4.3 to the results of modeling for the Kolmogorov–Avrami scenario shown Fig. 8.7.7b, namely the variation of the average slope of the experimental curves with changing the applied field cannot be reproduced by this scenario. On the level of Eq. (8.7.24) it is associated with the fact that, in this model, any variation of the applied field translates into a variation of parameter t_{sw} , which results only in a simple shift of the switching curves in semi-logarithmic scale. An alternation scenario assumes (Tagantsev et al., 2002b) that the switching kinetics of the film is controlled by the statistics of polarization reversal in quasi-independent regions of the films rather than by the statistics of the domain coalescence employed by the Kolmogorov–Avrami scenario. This alternative model, the so-called nucleation-limited switching model, is defined by the following assumptions:

- (i) The film is represented as an ensemble of elementary regions that switch independently.
- (ii) The switching of an elementary region occurs once a domain of reversed polarization is nucleated in the region.
- (iii) Time needed for switching of an elementary region is equal to the waiting time for the first nucleation, i.e., the time needed for filling the region with the expanding domain is neglected compared to the waiting time.
- (iv) The distribution of the waiting times for the ensemble of the elementary regions is smooth and exponentially broad, i.e., covering many decades.

This model results in a simple expression of the normalized switched polarization $q(t)$ (the fraction of the total switchable polarization that has been switched during the time t)

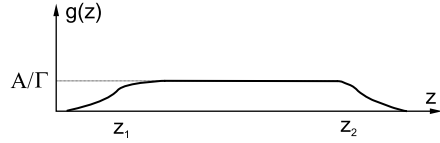
$$q(t) = \int_{-\infty}^{\log t} g(z) dz \quad (9.5.1)$$

in terms of the distribution function for the waiting times τ , $g(\log \tau)$, normalized in the logarithmic scale:

$$\int_{-\infty}^{\infty} g(z) dz = 1. \quad (9.5.2)$$

It was shown that the essential features of the switching dynamics monitored in a wide time interval (illustrated by Fig. 7.4.3) can be described in terms of this

Fig. 9.5.2 Spectrum of waiting times used in the nucleation-limited switching model



model with a simple shape of the spectrum $g(z)$ shown in Fig. 9.5.2. The spectrum is specified by three parameters: $z_1 = \log \tau_{\min}$ and $z_2 = \log \tau_{\max}$ —logarithms of the typical minimum and maximum times, τ_{\min} and τ_{\max} , and the decay constant Γ for the Lorentzian tails of the spectrum, where either $g(z) \propto ((z - z_1)^2 + \Gamma^2)^{-1}$ or $g(z) \propto ((z - z_2)^2 + \Gamma^2)^{-1}$. For this kind of spectrum, an explicit expression for the normalized switched polarization can be written as

$$\begin{aligned} q(t) &= A \left(\frac{\pi}{2} - \arctan \frac{z_1 - z_0}{\Gamma} \right) && \text{for } z_0 < z_1 \\ q(t) &= A \left(\frac{\pi}{2} + \frac{z_0 - z_1}{\Gamma} \right) && \text{for } z_1 < z_0 < z_2, \\ q(t) &= A \left(\frac{\pi}{2} + \frac{z_2 - z_1}{\Gamma} + \arctan \frac{z_0 - z_2}{\Gamma} \right) && \text{for } z_2 < z_0 \end{aligned} \quad (9.5.3)$$

where $A = \Gamma(z_2 - z_1 + \Gamma\pi)^{-1}$ and $z_0 = \log t$. A fit of switching curves Fig. 7.4.3 to Eq. (9.5.3) with z_1 and z_2 used as adjustable parameters and fixed Γ is shown in Fig. 9.5.3a. The parameters z_1 and z_2 (corresponding to this fit) plotted as functions of the switching voltage are shown in Fig. 9.5.3b. The typical maximal waiting time $\tau_{\max} = 10^{22}$ was found to follow an exponential field dependence

$$\tau_{\max} = \tau_0 e^{(E_0/E)^n}, \quad (9.5.4)$$

where $n = 1.5$, $\tau_0 = 10^{-13}$ s, and $E_0 = 770$ kV/cm. As mentioned by Tagantsev et al. (2002b) the fit given by Eq. (9.5.4) is not unique; however, physically, the ambiguity is not so large since the pre-exponential factor is expected to be of the order of the inverse of the soft-mode frequency ω_{SM} whereas the activation field E_0 should not be greater than the thermodynamic coercive field E_{crit} . For PZT at room temperature, these parameters are expected to be $\omega_{SM} \cong 10^{13} \text{ s}^{-1}$ and $E_{\text{crit}} = 0.5 - 1$ MV/cm. It is seen that the fitting parameters used meet these requirements.

For the moment, despite extensive efforts (see Sect. 8.7.2), there is no self-consistent theory of domain nucleation in ferroelectrics. For this reason, comparison of Eq. (9.5.4) with the results of existing theories is not instructive. However, the following remarks may be of interest. First of all, the clearly exponential field dependence of the upper edge of the spectrum of the waiting times, Eq. (9.5.4), is consistent with the expected activation nature of the phenomenon. On the other hand, Eq. (9.5.4) suggests that we are dealing with the activation energy for the nucleation, which is proportional to E^{-n} with $n = 1.5$. This dependence is comparable with the results of early theories on the

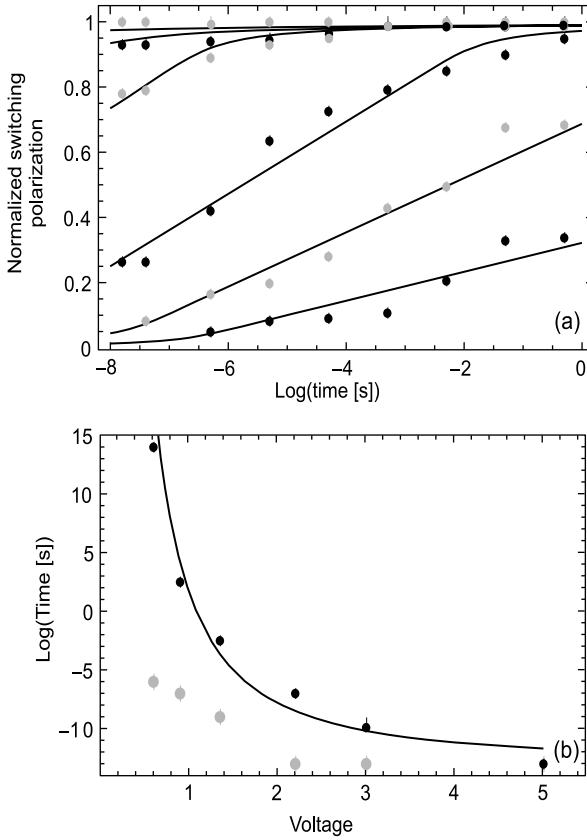


Fig. 9.5.3 (a) Fit of the switching curves for a PZT film shown in Fig. 7.4.3 using the prediction of the nucleation-limited switching model, Eq. (9.5.3). Experimental data from Fig. 7.4.3 for voltages of 0.6, 1.35, and 3 V are marked with *black dots*, the data for 0.9, 2.2, and 5 V are marked with *gray dots*. (b) Upper (*black dots*) and lower (*gray dots*) limits for the spectrum of waiting times for domain nucleation used for fitting curves in (a) as functions of the applied voltage. The *solid line* shows a fit of the experimental data for voltage dependence of the maximal waiting time to the function given by Eq. (9.5.4). After Tagantsev et al. (2002a,b)

activated polarization reversal, which give the functional dependence (9.5.4) but with $n = 1$ (cf. Eq. (8.4.10)) and $n = 2$ (Miller and Weinreich, 1960) and $n = 2.5$ (cf. Eqs. (8.7.2) and (8.7.4)).

The activation nature of the temperature dependences of the edges of the waiting time spectrum has also been checked by monitoring the switching kinetics in modified PZT films in the temperature range from -50 to $+90$ °C. It has been shown (Stolichov et al., 2004, 2005b) that, using the parameters of the waiting time spectrum determined at room temperature and the activation temperature dependence of τ_{\min} and τ_{\max} , the model gives good description of the switching kinetics in the whole temperature range.

A remark about the origin of the exponential broadness of spectrum of waiting times, which makes the main assumption of the model, should be made. As was discussed in Sect. 8.7.2, the energy barriers for the nucleation of reverse domains, U^* , when evaluated in terms the Landauer theory for an ideal crystal, are very large, making at least thousands of thermal energies kT for typical experimental situations. This implies that, in the ideal situation, the waiting times for the nucleation, which are inversely proportional to the Gibbs factor $\exp(-U^*/kT)$ are infinitely long. In a real situation, the nucleation barriers are believed to be reduced by the external factors (like defects or free carriers) by orders of magnitude from some thousands of thermal energies kT down to a few tens of kT . Thus, the resulting activation energy for the nucleation, U_r , actually represents the difference between two energies, which are orders of magnitude larger than this energy itself. This implies that small fluctuations of these two energies can lead to an essential spread of U_r . Since the waiting time is an exponential function of the activation energy, this spread should lead to an exponentially broad spectrum of waiting times. This reasoning is supported by the results obtained from the model of surface-stimulated domain nucleation addressed in Sect. 8.7.2. Here, the cancellation of two contributions to the nucleation barrier (the energy of the Landauer nucleus and that of coupling between the polarization and the electrode) is illustrated with the curve shown in Fig. 8.7.4. In the steep part of this curve (corresponding to a realistic regime of thermoactivation nucleation) small variations of the system parameters readily lead to order-of-magnitude variations of the activation barrier U_r .

Clearly, the nucleation-limited switching model represents a limiting case of the switching kinetics opposite to the Kolmogorov–Avrami model. However, this model seems to reproduce properly essential features of the switching kinetics in the case of the region-by-region switching scenario.

9.5.2 Ferroelectric Hysteresis Loops; Size Effects

As we have discussed in Chap. 8, in bulk ferroelectric samples, polarization-field (P – E) hysteresis loops are typically taken by using continuous (sinusoidal or triangular wave) driving voltage. In ferroelectric thin films this technique is rarely used. Usually, in the films, P – E hysteresis loops are monitored employing a set of pulses shown in Fig. 9.5.4. Voltage profiles of this kind are common in

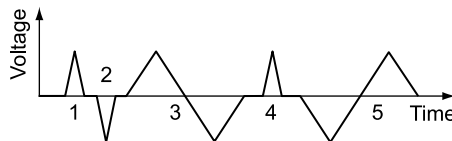


Fig. 9.5.4 Set of voltage pulse used for taking polarization hysteresis loops. Pulses 1, 2, and 4 prepare the ferroelectric in the positively or negatively poled state. Pulses 3 and 5 used for monitoring the loops starting from different initial states

commercially available testing setups produced by Radiant Technologies and aixACCT. A typical feature of P - E loops taken by using these voltage profiles is a gap between the points corresponding to the beginning and the end of the measuring cycle (shown in Fig. 9.5.5). The origin of this gap is a back-switching during the time when the sample stays in a poled state before the application of the next measuring profile. The loops obtained are characterized, in addition to the remanent polarization (P_r) and coercive field (E_c), also by switchable polarization (P_{sw}) and non-switchable polarization (P_{ns}) explained in Fig. 9.5.5. Typically, the loops are symmetrized along the P -axis, i.e., the absolute values of the polarization reached at the tips of the loop are set equal by adding a proper polarization offset. Interpretation of non-symmetrized P - E hysteresis loop is a difficult task easily affected by experimental artifacts; we will not discuss these kinds of loops in our book. The terminology introduced above is associated with the so-called pulse method of determination of the switching parameters of ferroelectric capacitors. In this method, voltage pulses are applied to the capacitor tested and P_{sw} and P_{ns} are obtained by the integration of the current response induced by these pulses. An alternative terminology exists where ferroelectric capacitors are tested with voltage steps. In this case, $P_{sw}^* = P_{sw} + (P_{max} - P_r)$ represents the switching polarization whereas $P_{ns}^* = P_{ns} + (P_{max} - P_r)$ the non-switching polarization. In this book we will use the pulse switching terminology. The description of real ferroelectric loops in the films also requires taking into account a possible voltage (field) offset of the loops. In this case, one distinguishes the positive and negative non-equal coercive fields, (E_c^+) and (E_c^-), as well as the positive and negative non-equal remanent polarizations (P_r^+) and (P_r^-).

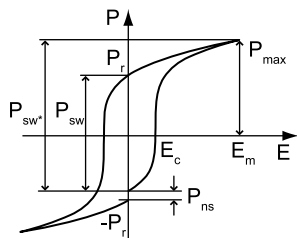


Fig. 9.5.5 Notations for parameters of a polarization hysteresis loop

Typically, a P - E hysteresis loop obtained from ferroelectric thin film capacitors has a shape similar to that of the loops obtained from the bulk ferroelectrics. In capacitors based on BaTiO_3 (Abe et al., 2000), PZT (Stolitchnov et al., 2000), and $\text{SrBi}_2\text{Ta}_2\text{O}_9$ films (Kalinin et al., 2004), well-shaped ferroelectric loops have been documented for the amplitudes of the driving voltage down to 1 V (see Fig. 9.5.6). Such small values are hardly attainable in capacitors containing bulk counterparts of these materials. However, comparing the values of the electric field needed for switching in bulk and thin film samples of the same material one comes across the opposite situation. Namely,

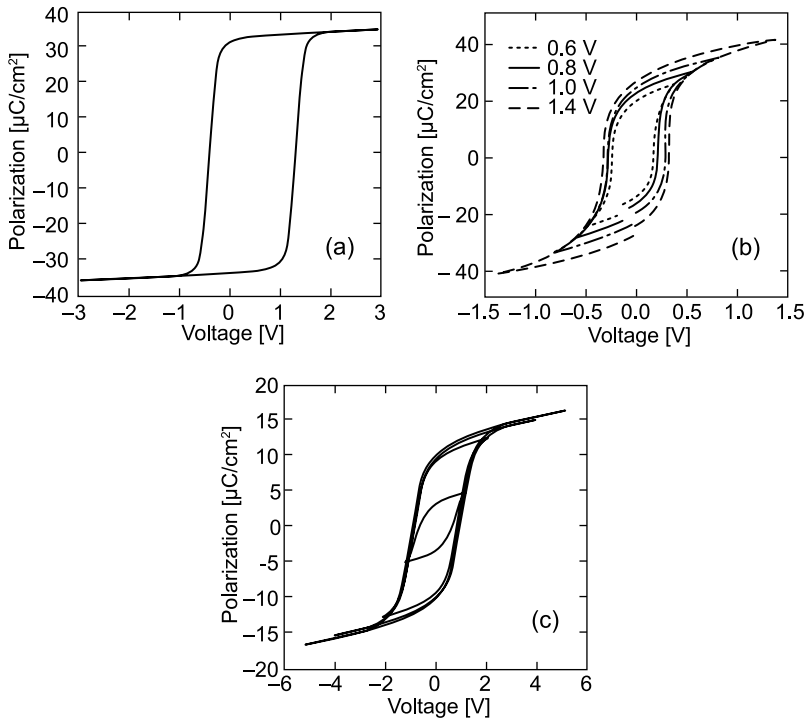


Fig. 9.5.6 Examples of polarization hysteresis loop of ferroelectric thin films: (a) 58 nm thick of BaTiO_3 . After Abe et al. (2000); (b) 100 nm thick $\text{Pb}(\text{Zr}_{0.45}\text{Ti}_{0.55})\text{O}_3$. After Stolichnov et al. (2000); (c) 180 nm thick $\text{SrBi}_2\text{Ta}_2\text{O}_9$. After Kalinin et al. (2004)

the switching in thin films requires much higher fields than in the bulk materials of similar compositions. This situation is illustrated in Fig. 9.5.7 where the $P-E$ loops taken from a 500 μm thick ceramic sample and from a thin film which is 0.5 μm thick; in both cases, the material is morphotropic boundary 2% Nb-doped PZT (Tagantsev, 1996). It is seen that the coercive field in the film is some 10 times larger than that in the bulk counterpart. In addition the loop itself is much more tilted in the case of the film. A systematic analysis of the switching data on PZT films with Pt electrodes revealed a decreasing thickness dependence of the coercive field consistent with the above observation (Haertling, 1997). Figure 9.5.8a illustrates this dependence. However, such dependence is not solely controlled by the ferroelectric material used in the thin film capacitor but rather by the combination of materials of the ferroelectric and electrodes. This is suggested by the results on PZT with conductive oxide electrodes (Cillessen et al., 1997) and on $\text{SrBi}_2\text{Ta}_2\text{O}_9$ capacitors with Pt electrodes (Zhu et al., 1998) presented in Fig. 9.5.8b, where actually no thickness dependence of the coercive field can be traced. An example of a strong increase in the coercive

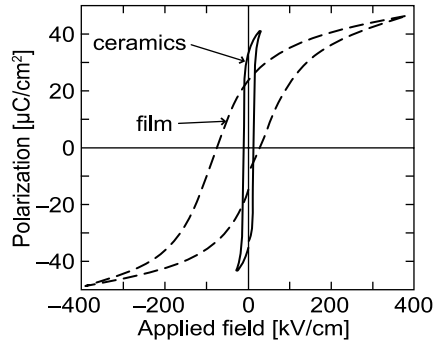


Fig. 9.5.7 Comparison of polarization hysteresis loop taken from a 500 μm thick ceramic sample and from a thin film which is 0.5 μm thick; in both cases, the material is morphotropic boundary 2% Nb-doped PZT. After Tagantsev (1996)

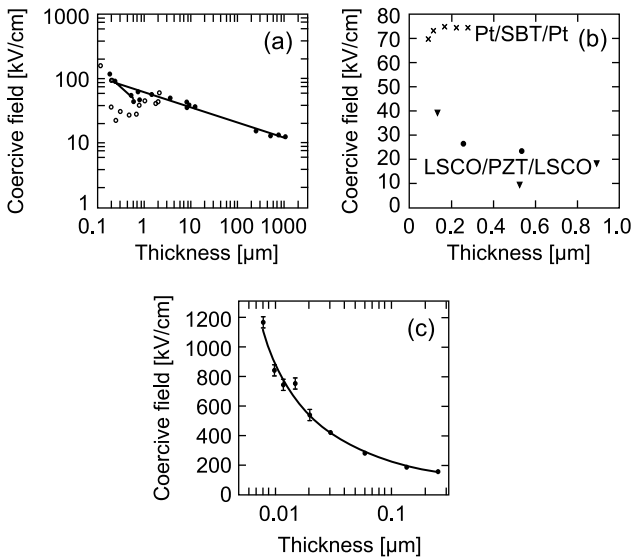


Fig. 9.5.8 Examples of thickness dependences of the coercive field in thin film capacitors. (a) Perovskite—Pt electrodes systems $\text{Pt}/(\text{Pb},\text{Li})(\text{Zr},\text{Ti})\text{O}_3/\text{Pt}$. After Haertling (1997). (b) Perovskite—oxide electrodes system $(\text{La}_{0.5}\text{Sr}_{0.5})\text{CoO}_3/\text{Pb}(\text{Zr}_{0.53}\text{Ti}_{0.47})\text{O}_3/(\text{La}_{0.5}\text{Sr}_{0.5})\text{CoO}_3$ (LSCO/PZT/LSCO). After Cillessen et al. (1997). Aurivillius structure—Pt electrode system $\text{Pt}/(\text{SrBi}_2\text{Ta}_2\text{O}_9)_{0.8}(\text{Bi}_3\text{TiNbO}_9)_{0.2}/\text{Pt}$ (Pt/SBT/Pt). After Zhu et al. (1998). (c) SrRuO_3 Pt-perovskite-oxide electrode system $\text{Pb}(\text{Zr}_{0.52}\text{Ti}_{0.48})\text{O}_3/\text{SrRuO}_3$. After Pertsev et al. (2003a)

field with decreasing thickness (up to its thermodynamic value) has been reported by Pertsev et al. (2003a) for PZT capacitors with bottom oxide and top Pt electrodes. The thickness dependence of the coercive field obtained in this work is shown in Fig. 9.5.8c.

Two possible sources of the above size effect on switching can be distinguished. First, the processing conditions for single crystals, ceramics, and thin films are different and they may not be identical for films of different thicknesses. For instance, typically, in thin films, the processing temperature is lower and there is a possibility for a substantial loss of a volatile component (Pb in the case of PZT). This can influence the composition and microstructure of the material and, in turn, its switching performance. Second, even if the composition and microstructure of the material are thickness independent, one can expect a thickness dependence of the switching behavior due to a number of physical size effects. These effects have been under consideration in the literature for some 50 years. In what follows we will discuss the ideas of these effects and the relevance of these ideas to experimental observations. We restrict ourselves to a discussion of the ideas that could account for mechanisms leading to the two aforementioned features of the loops in the films, namely high coercive field and strong tilt. These ideas are associated with the following issues:

1. Size of nucleus of the reverse domains.
2. Surface pinning of domain walls.
3. Semiconductor-depletion-assisted nucleation of reverse domains.
4. Surface non-switchable (passive) layer.

9.5.2.1 Size Effect on Nucleation of the Reverse Domains

The idea of a size effect related to the nucleation of reverse domains has been put forward by Janovec (1958) and by Kay and Dunn (1962). It is based on the nucleation theory of Landauer (1957) that we discussed in Sect. 8.7.2. This theory yields the relation between the length of the critical nucleus l^* and the applied field E :

$$l^* \propto E^{-3/2}. \quad (9.5.5)$$

(Equations 8.7.2 and 8.7.4 readily lead to Eq. (9.5.5).) Based on this relation, one formulates the following scenario for the size effect. The coercive field E_c is defined as the minimal field at which the critical nuclei can form. Any field that corresponds to the critical nucleus length, l^* , smaller than the film thickness, h , can produce critical nuclei. If the field corresponds to l^* greater than the film thickness, it cannot produce nuclei because their length would be larger than that of the film thickness. The implication is that the value of E_c can be estimated from the condition $l^* \cong h$. Thus, from Eq. (9.5.5), one finds the thickness dependence of the coercive field

$$E_c \propto h^{-2/3}. \quad (9.5.6)$$

Unfortunately, this idea encounters several problems, which impedes its application to real systems (Tagantsev, 1996). Here we mention only the most serious of these. As we showed in Sect. 8.7.2 the energy of critical nucleus in the Landauer theory is so high that the probability of the nucleation, even for

relatively high fields (typical to thin films), vanishes in the scale of the lifetime of the universe. This means that the outlined above size effect is irrelevant to the ferroelectric switching taking place on realistic time scales. However, one should mention that the very idea of this kind of size effect might be successfully employed in the case of a realistic nucleation mechanism.

9.5.2.2 Surface Pinning Size Effect

The idea that a surface contribution to the coercive force can result in a size effect for the coercive field has been discussed by several authors (Drougard and Landauer, 1959; Callaby, 1965; Lebedev and Sigov, 1994). The scenario based on this idea can be outlined as follows. One considers the switching from a state already containing domain walls that are perpendicular to the plane of the films. The defects are assumed to be the origin of the coercive force for the walls. The contributions of both surface and bulk defects are taken into account. For thin films, where the contribution of the surface pinning becomes comparable to that of the bulk one, a thickness dependence of the coercive force is expected. The coercive field is found from the following balance-of-force equation for the wall:

$$2P_S E_c S_W = f_b S_W + 2f_c L,$$

where S_W and L are the area of the wall and length of the crossing line between the wall and the film/electrode interface, respectively; f_b and f_c are the area density of the bulk coercive force and the linear density of the surface coercive force, respectively. Since $S_W = Lh$, the above balance-of-force equation immediately yields

$$E_c \propto 1 + h_{Leb}/h, \quad (9.5.7)$$

where $h_{Leb} = 2f_c/f_b$ is the characteristic length of the size effect.

The idea of this model does not encounter principal objections. As a problem with this approach one can indicate the lack of a reliable estimate of the surface pinning strength. Lebedev and Sigov (1994) have suggested the surface roughness to be a possible origin for the surface domain wall pinning and derived a relation between the amplitude of the random surface pinning potential and f_c .

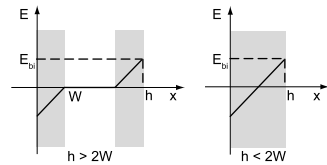
9.5.2.3 Depletion-Assisted Nucleation of Reverse Domains

The electrochemical interaction between the conductive electrodes and the electronic carriers of the ferroelectric may result in the so-called depletion effect, i.e., the removal of the carriers from narrow electrode-adjacent regions so that charged regions of bare impurities are formed near the electrodes. In the case of a wide gap and heavily compensated semiconductor, which is often the case for typical ferroelectrics, this built-in charge is related to deep trapping centers and oxygen vacancies (Brennan, 1995). It can be considered as immobile during electrical measurements at room temperature and homogeneous inside

the depletion layers (Simmons, 1971). The depletion phenomenon is characterized by the parameter W called *depletion layer width*, which is a function of the electrochemical parameters of the electrode/ferroelectric interface. If the film thickness h is larger than $2W$, the film will contain two space charge layers at the two electrodes and a neutral region in the middle. This is the case of *partial depletion*. If $h < 2W$, the film is homogeneously filled with space charge. This is the case of *full depletion*. A sketch of the distribution of the built-in electric field in a film subjected to the depletion effect is shown in Fig. 9.5.9. The absolute value of this field at the electrodes, E_{bi} , can be readily found (from the Poisson equation) in the following form (see, e.g., Tagantsev et al., 1994):

$$E_{bi} = \frac{eN_d}{\epsilon_0\kappa_f} W \quad \text{for } h > 2W, \quad E_{bi} = \frac{eN_d}{\epsilon_0\kappa_f} \frac{h}{2} \quad \text{for } h < 2W, \quad (9.5.8)$$

Fig. 9.5.9 Distribution of the built-in electric field in films with thicknesses larger than the double depletion width $2W$ (partial depletion) and smaller than $2W$ (full depletion)



where e and N_d are the charge of the doping centers and their concentration and κ_f is the lattice dielectric constant of the ferroelectric. Referring the reader to the original paper (Tagantsev et al., 1994) for a more detailed discussion we shall only outline the suggested mechanism of the thickness dependence of the coercive field E_c . Consider switching from the negatively poled single-domain state when a positive external field E is applied to the capacitor. The first step of the switching is the nucleation of reverse domains. Since for $E > 0$ the total (depletion + external) field reaches its maximum at one electrode (the right one in Fig. 9.5.9), the nucleation of positive domains will occur at this electrode. Let the nucleation threshold field be E_{cn} . Then, the condition for surface nucleation can be written as

$$E_{cn} = E + E_{bi}. \quad (9.5.9)$$

If the threshold field is much higher than the field required keeping the domain walls (created due to the nucleation) moving, then the nucleation is the bottleneck for switching, and the condition for nucleation (9.5.9) is also the condition for switching. One can thus find the coercive field from Eqs. (9.5.8) and (9.5.9) as

$$E_c = E_{cn} - Ah, \quad A = \frac{eN_d}{2\epsilon_0\kappa_f}; \quad \text{for } h < 2W. \quad (9.5.10)$$

For thicker films (with $h > 2W$), where the surface built-in field is thickness independent, one expects the coercive field to be thickness independent.

This mechanism can explain the thickness dependence of the coercive field in PZT films with Pt electrodes thinner than a few micrometers. In this interval, a pronounced thickness dependence of E_c is documented for $h < h_d = 0.5 \mu\text{m}$ with a typical slope $A = \frac{\partial E_c}{\partial h} \approx (0.15 - 0.25) \times 10^7 \text{ kV/cm}^2$ (Tagantsev et al., 1994). This corresponds to a concentration of once-ionized doping centers $N_d = \frac{2A\kappa_f \epsilon_0}{e} \approx (0.3 - 0.4) \times 10^{19} \text{ cm}^{-3}$ ($\kappa_f = 300$ was used as an estimate). On the other hand, in terms of this model, the appearance of the thickness dependence of E_c at $h \approx h_d = 0.5 \mu\text{m}$ implies the depletion layer width in the bulk material, W , to be about $h_d/2 = 0.25 \mu\text{m}$. Using the relation³⁰ $V_{bi} = AW^2$ (Tagantsev et al., 1994) and the above values of W and A , one can also evaluate the contact built-in potential $V_{bi} \cong 1 \text{ V}$. The estimates obtained for N_d , W , and V_{bi} are comparable with typical values of these parameters in perovskites (Scott et al., 1991; Waser and Klee, 1992; Brennan, 1992b). Thus, the suggested mechanism looks compatible with the semiconductor properties of perovskites.

9.5.2.4 Surface Passive Layer

A most obvious reason for the difference between the switching performance of ferroelectric thin films and that of their bulk counterpart of the same composition is the presence of a non-switching “passive” dielectric layer (or a layer with a reduced switching ability) between the ferroelectric and electrode of ferroelectric capacitors. The impact of such passive layers on the equilibrium domain pattern in thin films has been already addressed in Sect. 9.4.1. In the present section we will address the impact of such layers on switching in thin films. This problem has been approached in the literature for the past 50 years; however, certain misunderstanding of one essential issue of the problem has been persisting for a long time.

The commonly used approach to the influence of a passive layer on the polarization response of a ferroelectric capacitor is to consider it as in-series connection of a capacitor containing ferroelectric with that containing a dielectric. Clearly, this “in-series capacitors” model is an approximation, for example, it does not take into account the stray fields of the domain pattern of the ferroelectric. On the other hand, this model provides a clear and simple description of the basic features of the phenomenon. In this section, we discuss the effect of the passive layer of ferroelectric hysteresis employing the “in-series capacitors” model since more advanced considerations of the problem are not

³⁰ In this relation, following the original paper, we do not make any difference between the dielectric constant at the temperature of the electrochemical equilibrium (at which the depletion layer forms) and that at the measuring temperature (at which the trapped creates the built-in field). The incorporation of this difference in the theory will not affect the qualitative conclusions of the analysis. A more advance discussion of the depletion effect can be found in Subsect. 9.5.3.

presently available in the literature. In what follows, we overview the theory developed for the case where the passive layer is a perfect insulator layer (Miller et al., 1990; Brennan, 1992; Tagantsev et al., 1995a) as well as for the case where the layer is a dielectric with a threshold conduction (Cillessen et al., 1997; Tagantsev and Stolichnov, 1999).

The effects which are out of the reach of the “in-series capacitors” model will be discussed later in Sect. 9.6 where the problem of small-signal dielectric response of the capacitor containing a passive layer is addressed.

9.5.2.5 Insulating Passive Layer

The sandwich structure shown in Fig. 9.5.10 is considered. Neglecting the possible inhomogeneity of the electric field in the plane of the capacitor its switching behavior can be analyzed based on the condition of continuity of the normal component of the electric displacement and the equation for the potential drop across the system:

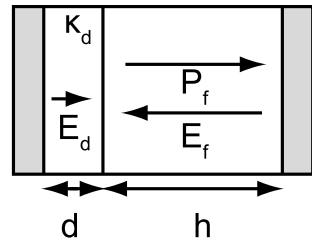


Fig. 9.5.10
 Electrode–passive
 layer–ferroelectric–electrode
 sandwich structure.
 Thickness of the passive
 layer is d , that of the
 ferroelectric is h

$$\begin{aligned} \epsilon_0 \kappa_d E_d &= \epsilon_0 E_f + P_f \\ d E_d + h E_f &= (d + h) E \end{aligned} \tag{9.5.11}$$

where E is the applied field; P_f and E_f are the average polarization and electric field in the ferroelectric, h being its thickness; E_d , d , and κ_d are the average field in the dielectric, its thickness, and its dielectric constant, respectively. For the case of a thin passive layer ($d \ll h$) we are interested in, Eq. (9.5.11) can be reduced to a set of simple equations relating the polarization and field in the ferroelectric to the field applied to the sandwich and the average polarization in it, P (i.e., the quantity that is actually measured). Neglecting, as usually, the difference between the polarization and displacement of the ferroelectric, these equations read

$$\begin{aligned} E_f &= E - \frac{d}{h} E_d, \\ E_d &= \frac{P_f}{\epsilon_0 \kappa_d}, \\ P &= P_f. \end{aligned} \tag{9.5.12}$$

Equations (9.5.12) enable calculations of the set of hysteresis loops $P(E, E_m)$ of the sandwich for different amplitudes of driving field E_m , if such a set, $P_f(E_f, E_{fm})$, is known for the ferroelectric (where E_{fm} is the amplitude of the field seen by the ferroelectric). The scheme of the calculations is as follows. To obtain the loops of the sandwich for a given value of E_m (say E_1) one, first, determines the amplitude of the driving field E_{fm} seen by the ferroelectric when the amplitude E_m of the driving field equals E_1 . This value of E_{fm} , which we denote as E_2 , can be found as a root of the equation

$$E_{fm} = E_1 - \frac{d}{\varepsilon_0 \kappa_d h} P_f(E_{fm}, E_{fm}). \quad (9.5.13)$$

Thus we find that the polarization and field in the ferroelectric during the cycling considered are related by the function $P_f = P_f(E_f, E_2)$ so that the loops exhibited by the sandwich can be generated using the equations

$$E_f = E - \frac{d}{\varepsilon_0 \kappa_d h} P_f(E_f, E_2), \quad (9.5.14)$$

$$P = P_f(E_f). \quad (9.5.15)$$

This approach was applied to modeling hysteresis loops of a sandwich containing ferroelectric films whose set of hysteresis loops was available from experiment. The results of such modeling (Tagantsev et al., 1995) are presented in Fig. 9.5.11a. Comparing the loop for the ferroelectric with those for the sandwich with different thicknesses of the passive layer, the following trends can be distinguished.³¹ An increase in the passive layer thickness (a decrease in the thickness of the ferroelectric) results in (i) an essential tilt of the loops, (ii) an essential reduction of the remanent polarization P_r , (iii) a certain reduction of the maximal polarization on the loop P_m , and (iv) a certain reduction of the coercive field E_c . Analytical treatment of the problem (Tagantsev et al., 1995) confirmed such observations. It was also analytically shown that, in the limit of high amplitudes of the driving field E_m (where the polarization loops seen by the ferroelectric become fully saturated), effects (iii) and (iv) disappear whereas effects (i) and (ii) hold. For the coercive field, this trend is illustrated in Fig. 9.5.11b. Referring the reader to the original paper (Tagantsev et al., 1995) for details of the analysis, we would like to comment here only two issues: the tilt of the loop and the behavior of E_c .

To characterize the tilt of the loop it is convenient to consider its slope at E_c , $\left. \frac{dP}{dE} \right|_{P=0}$, as a measure of the tilt. Using Eq. (9.5.12) this parameter can be readily related to the corresponding parameter of the loop of the ferroelectric $\left. \frac{dP_f}{dE_f} \right|_{P_f=0}$:

³¹ The gap seen on the calculated loops is an artifact of calculations which use an experimental set of loops with gaps (like shown in Fig. 9.5.6b).

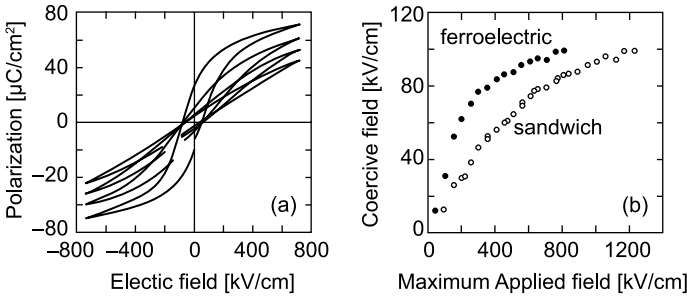


Fig. 9.5.11 (a) Hysteresis loop of a ferroelectric (the less tilted) and the calculated loops of the sandwich (ferroelectric/thin dielectric layer) for different values of $d/\kappa_d h = 0.003, 0.09, 0.018$ (the larger d , the larger the tilt). In the calculations, a set of hysteresis loops of the ferroelectric was used as its dielectric portrait. (b) The calculated dependence of the coercive field of the sandwich containing a ferroelectric (with $d/\kappa_d h = 0.01$) on the amplitude of the driving field compared to that of the ferroelectric. After Tagantsev et al. (1995a)

$$\left. \frac{dP}{dE} \right|_{P=0} = \left. \frac{dP_f}{dE_f} \right|_{P_f=0} + \frac{d}{\epsilon_0 \kappa_d}, \tag{9.5.16}$$

(with $h \gg d$) where one can easily recognize the formula for in-series connection of two capacitors applied to the considered structure.³² Equation (9.5.16) clearly explains the aforementioned relation between d (or h) and the tilt of the polarization loop of the sandwich.

The impact of the passive layer on the coercive field of the system illustrated in Fig. 9.5.11b is less evident than that in the case of the loop tilt. Actually, this result seems contradictory to the routine reasoning: “The coercive field is roughly the field needed to switch the ferroelectric. There is a drop of potential across the passive layer. Thus a higher voltage should be applied to the sandwich than to the bare ferroelectric to switch it. For this reason, one expects the coercive field to increase with increasing thickness of the passive layer.” We elucidate the origin of the effect illustrated in Fig. 9.5.11b by pointing out a drawback of the above reasoning. First, according to Eqs. (9.5.12), the drop of potential across the passive layer equals $Pd/\epsilon_0 \kappa_d$ so that at E_c (where $P = 0$) it vanishes to within the accuracy of our calculations. Thus, the fields seen by the ferroelectric and sandwich at E_c are the same. This means that, if the loop exhibited by the ferroelectric part of the sandwich is saturated (by “saturated” we mean the fact that P_f and E_c of the loop are virtually independent of driving field) then the coercive fields of the ferroelectric and sandwich are equal (cf. Fig. 9.5.11b). The case where the loop exhibited by the ferroelectric part

³² Here, it is worth to remind that, in general, the slope of the loop at coercivity is different from the differential susceptibility measured at this point since the latter is not influenced, in contrast to the slope, by the irreversible contribution to the polarization response.

of the sandwich is not saturated requires a more involved treatment which shows that, in this regime, E_c is a decreasing function of $d/\kappa_d h$. This behavior is related to the fact that the loop exhibited by the ferroelectric part of the sandwich is driven by a field whose amplitude is smaller than that of the field applied to the sandwich.

9.5.2.6 Passive Layer with Threshold Conduction

An estimate of the electric field acting in the passive layer E_d during switching in a capacitor containing a thin film of a conventional ferroelectric like PZT shows that it can be very large. For example, taking $P = 0.3 \text{ C/m}^2$ and the dielectric permittivity of the passive layer even as high as $\kappa_d = 100$, one finds $E_d = 3 \text{ MV/cm}$. This field is large enough to induce considerable charge injection across the layer. Thus, an adequate description of the switching in a ferroelectric capacitor may require taking into account this injection as well as the influence of the injected charge on the switching and on the injection itself (Cillessen et al., 1997; Tagantsev and Stolichnov, 1999). This phenomenon can be readily incorporated into the model considered above by taking into account (i) the free carrier transport across the layer, $J(E_d)$ being the current density across the layer, and (ii) the accumulation of these free carriers at the ferroelectric/dielectric interface, σ being the corresponding surface charge density. An essential feature brought about by the introduction of the injection in the model is an effective screening of ferroelectric polarization by the charge of accumulated carriers.

The switching behavior of the system is then described by a modified version of Eqs. (9.5.12) appended with the equation for the charge transport across the layer³³:

$$E_f = E - \frac{d}{h} E_d, \quad (9.5.17)$$

$$E_d = \frac{P_f - \sigma}{\epsilon_0 \kappa_d}, \quad (9.5.18)$$

$$P = P_f, \quad (9.5.19)$$

$$\frac{d\sigma}{dt} = J(E_d). \quad (9.5.20)$$

Here the screening effect of the charge at the ferroelectric/dielectric interface is clearly seen in Eq. (9.5.18). This screening results in some reduction of the field in the passive layer. According to Eq. (9.5.19), the total polarization of the sandwich is taken equal to the polarization of the ferroelectric layer P ;

³³ We remind that the situation of a thin passive layer is treated ($d \ll h$). This is taken into account in the following equations.

i.e., the contribution of the dielectric layer is neglected.³⁴ The complete description of the problem is given by Eqs. (9.5.17), (9.5.18), (9.5.19), and (9.5.20) appended with the specified dependences $J(E_d)$ and $P_f(E_f)$.

Following Tagantsev and Stolichnov (1999) we will discuss the impact of this kind of passive layer on the coercive field of the sandwich. For simplicity we consider the case of saturated loops, for which, in the previous model, E_c of the sandwich was found independent of the layer thickness and equal to the coercive field of the ferroelectric E_{c_0} . As for the $J(E_d)$ dependence, we assume it to be very steep and being characterized by a threshold field, E_{th} . In other words, in this model, if in the surface dielectric layer $E_d < E_{th}$, the layer behaves as an insulator whereas if $E_d > E_{th}$ the layer behaves as a nonlinear conductor maintaining E_d very close to E_{th} (slightly higher), irrespective of the passing current. This is a reasonable approximation for typical injection mechanisms in thin dielectric films.

The impact of this kind of passive layer on E_c can be readily elucidated from the following consideration. The behavior of the system differs depending on the relation between E_{th} and the maximal polarization P_m on the hysteresis loop. If $E_{th} > P_m/\varepsilon_0\kappa_d$, the field in the surface layer $E_d = P_f/\varepsilon_0\kappa_d$ (see Eq. (9.5.18) where σ is set to zero before the onset of injection) is always smaller than the injection threshold field so that the injection is off during the cycling and the surface layer behaves as an ideal insulator. In this case the model reduces to the insulating layer model treated above and we find no effect of the passive layer on the coercive field, i.e.,

$$E_c = E_{c_0}. \quad (9.5.21)$$

If $E_{th} < P_m/\varepsilon_0\kappa_d$, the field in the surface layer E_d will reach the threshold value E_{th} during cycling and the injection will be on during some phases of the switching cycle. This injection will bring some charge at the ferroelectric/dielectric interface, which, in turn, will affect the value of the coercive field of the sandwich E_c . It has been shown (Tagantsev and Stolichnov, 1999) that, for $\varepsilon_0\kappa_d E_{th} < P_m < 2\varepsilon_0\kappa_d E_{th}$,

$$E_c = E_{c_0} + \frac{d}{\varepsilon_0\kappa_d h} (P_m - \varepsilon_0\kappa_d E_{th}) \quad (9.5.22)$$

and, for $P_m > 2\varepsilon_0\kappa_d E_{th}$

³⁴ Note that, in this case, the total (measured) polarization of the system is not given by the charge on the electrode, which is equal to $P_f - \sigma$, since the variation of the latter is not fully controlled by the current in the external circuit. We remind that, in the used approximation where the difference between the polarization and the electrical displacement is neglected, the current in the external circuit is linked to the polarization by the relation $I_{ext} = A \cdot dP/dt$, where A is the electrode area.

$$E_c = E_{c0} + \frac{d}{h} E_{th}. \quad (9.5.23)$$

The physical difference between the regimes corresponding to Eqs. (9.5.22) and (9.5.23) is that, in the first case, the injection is on during some phases of the switching cycle but it is off at the coercive field point whereas, in the second case, the injection is also on at this point. It is seen from these equations that the injection implies a thickness dependence of the coercive field of the sandwich and, in the first regime, an additional dependence of it on P_m . These dependences are illustrated in Fig. 9.5.12a.

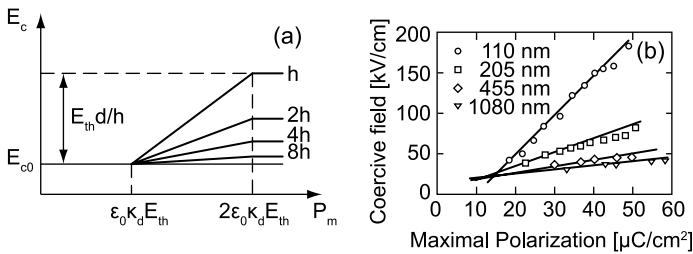


Fig. 9.5.12 (a) The coercive field, E_c , of thin ferroelectric films of different thicknesses plotted as a function of P_m —the maximal polarization on the P - E loop used for measuring E_c . (a) Results of modeling which take into account the charge injection across the dielectric layer. (b) Results of measurements on (111) highly textured $\text{PbZr}_{0.45}\text{Ti}_{0.55}\text{O}_3$ ferroelectric films with Pt electrodes. The film thicknesses are indicated in the graphs. After Tagantsev and Stolichnov (1999)

It is worth noting that there is a transparent physics behind the trends given by Eqs. (9.5.22) and (9.5.23). In the case where the injection is on at E_c , Eq. (9.5.23), the field in the passive layer is exactly known and equal to E_{th} so that this relation directly follows from a simple calculation of the voltage drop across the sandwich at coercivity: $hE_{c0} + dE_{th}$ (Cillessen et al., 1997). The trend given by relation (9.5.22), namely the increase in E_c with increasing P_m , can be understood from the following argument. At the tip of the loops (at $P = P_m$) the polarization is screened by a certain amount of charge at the ferroelectric/dielectric interface. When the applied field reduces from its maximum, this charge holds constant (as we would need a field in the opposite direction and above the threshold value in order to reverse the charge transport) up to the E_c point (since at E_c the injection is still off). At this point ($P = 0$), this charge is no longer compensated by the bound charge of the polarization and it creates a field that opposes polarization reversal, finally resulting in an increase in E_c . Since the screening charge increases with increasing P_m , E_c increases with P_m as well.

A remarkable feature of the theoretical results given by Eq. (9.5.22) is that its relevance to experimentally observed effects can be verified by analyzing a two-dimensional array of data: E_c as a function of the film thickness, h , and the maximal polarization, P_m . An example of such analysis for a Pt/PZT/Pt thin film capacitor is shown in Fig. 9.5.12b where it is seen that the experimental results reproduce fairly well the fan-like structure of the graph predicted by the model.

According to Tagantsev and Stolichnov (1999), apart from the description of the size effect in switching in a Pt/PZT/Pt system, the presented model also gives a possible explanation for the much smaller magnitude of this effect in Bi-containing films (Zhu et al., 1998) and oxide electrode systems (Cillessen et al., 1997) (see Fig. 9.5.8). In the first case, a smaller magnitude of the maximal ferroelectric polarization P_m in these materials can be a reason for the absence of nearby-electrode injection and, as a result, for the absence of the size effect on the coercive field (i.e., $P_m < E_{th}\epsilon_0\kappa_d$ in Fig. 9.5.12a). In the case of PZT with oxide electrodes, known for much higher leakage currents than those in the Pt/PZT/Pt system, one could expect a much stronger nearby-electrode injection. In terms of the model, this corresponds to small E_{th} and the regime of relatively large P_m (i.e., $P_m > 2E_{th}\epsilon_0\kappa_d$ in Fig. 9.5.12a). In this regime, the magnitude of the size effect is proportional to E_{th} and therefore small. In other words, this means that the injection actually short-circuits the nearby-electrode layer, so that the layer ceases to influence the switching.

9.5.3 Effects of Internal Bias and Imprint

Very often the switching characteristics of ferroelectric thin film capacitors are not symmetric with respect to the reversal of the applied voltage. In this case, one speaks about the presence of an *internal bias field* in the capacitor, which creates this asymmetry. Although the presentation of the electric field seen by the ferroelectric as the sum of the applied and internal bias field does not usually correspond to a real situation (as will become clear from the following discussion), we will be using the established term “internal bias” when speaking about the switching asymmetry, implying the ratio V_{off}/h where V_{off} is the voltage offset of the switching characteristics of the film and h is its thickness.

By the term internal bias field effects we mean two classes of phenomena: (i) *built-in internal bias field* development as a result of processing of the ferroelectric capacitor and (ii) internal bias field development in the ferroelectric capacitor as a result of keeping the capacitor in a poled state for some time (exposition time). The latter effect is customarily called *imprint*. During the exposition time the capacitor can also be treated with an electrical field, elevated temperature, or visible/UV light illumination. In the latter two situations one also uses the terms *thermal* and *optical imprints*, respectively.

In the present section, we first theoretically address the models for internal bias effects in ferroelectric thin films. These models are related to trapped (i.e., immobile on the time scale of the switching experiment) charge in the film, reorientation of polar defects in the bulk of the film, the poling effect of the ferroelectric/electrode interface, and the depletion effect. We will also theoretically address the imprint scenario related to charge transport in the vicinity of electrodes. We will end this section with a discussion of relevant experimental findings.

9.5.3.1 Voltage Offset Caused by Nearby-Electrode Trapped Charge

It is obvious that space charge asymmetrically trapped in the film should lead to some asymmetry of the ferroelectric switching. Typically, in thin films this charge is trapped close to the ferroelectric/electrode interfaces. In this case, the ferroelectric capacitor can be roughly modeled as the in-series connection of an ideal ferroelectric capacitor with another (surface) capacitor, having the thickness equal to the distance between the centroid of the trapped charge and the electrode, with the charge of the second capacitor being set equal to the total trapped charge. If we assume that due to the impact of the ferroelectric/electrode interface the surface capacitor is non-switchable, we arrive at the simple model for the internal bias field effect driven by the electric charge trapped at the ferroelectric/electrode interface. This model (where in addition the “material” of the surface capacitance is assumed to be nonpolar) has been used by Grossmann et al. (2002a,b) and by Tagantsev et al. (2004b) for the description of the imprint phenomenon. An electrostatically identical model has been already discussed in the previous section. This model contains a sandwich structure with a ferroelectric layer and a thin dielectric layer (passive layer) separated by the interface containing the trapped charge (see Fig. 9.5.10). The internal bias effect in this model is controlled by the relation between the voltage offset and the amount of the trapped charge. To obtain this relation, one starts from that for the total voltage drop across the system and from the equation for the jump of the electrical displacement at the ferroelectric/passive layer interface

$$V = hE_f + dE_d, \quad (9.5.24)$$

$$D_f - \sigma = \varepsilon_0 \kappa_d E_d \quad (9.5.25)$$

and an equation following from these:

$$D_f - \sigma = \varepsilon_0 \kappa_d \left(\frac{V}{d} - \frac{h}{d} E_f \right), \quad (9.5.26)$$

where V is the voltage applied to the capacitor; D_f and E_f are the electrical displacement and field in the ferroelectric, h being its thickness; E_d , d , and κ_d are

the field in the passive layer, its thickness, and dielectric permittivity, respectively. Here σ stands for the surface density of trapped charge at the ferroelectric/passive layer interface.

We define the voltage offset, V_{off} , as the difference in the applied voltages that produce the same switching in the cases of the charged and uncharged ferroelectric/passive layer interfaces. In terms of Eq. (9.5.26), “to produce the same switching” means to arrive at the same values of D_f and E_f . Following this definition and writing Eq. (9.5.26) for the capacitors with and without the trapped charge, we find from the difference between these two equations:

$$V_{\text{off}} = -\frac{d\sigma}{\epsilon_0\kappa_d}. \quad (9.5.27)$$

It is instructive to rewrite Eq. (9.5.26) in terms of V_{off} and of the voltage applied to the ferroelectric layer, $V_f = hE_f$:

$$V_f = V - V_{\text{off}} - \frac{dD_f}{\epsilon_0\kappa_d}. \quad (9.5.28)$$

This equation clearly illustrates the statement from the beginning of this section that the electric field seen by the ferroelectric is not simply the sum of the applied and the internal bias fields. Such presentation is valid only at $D_f = 0$, i.e., only at two points of the $P-E$ hysteresis loop. Otherwise, the depolarizing field (controlling the last term in Eq. (9.5.28)) also contributes to the difference between the applied field and that seen by the ferroelectric.

At this point it is important to mention that, in general, the voltage offset just calculated, V_{off} , can essentially differ from the voltage offset, $V_{\text{off-cr}}$, defined as the half-sum of the coercive voltages of the $P-E$ loop of the same capacitor. There are two reasons for that. First, if the ferroelectric loop is not saturated, in the presence of the internal bias, the degree of saturation at the tips of the loop is different from that observed in the absence of the internal bias. For this reason, the switching curves of the ferroelectric $D_f(E_f)$ may not be the same for these two cases. Hence Eq. (9.5.26) may lead no more to Eq. (9.5.27). Second, the measured $P-E$ loops are usually symmetrized with respect to the P -axis (see the beginning of Sect. 9.5.2); therefore in order to compare them to the experimental data, the calculated loops should also be symmetrized by introducing some polarization offset. This polarization offset will result in an additional voltage offset.

It is instructive to demonstrate the difference between $V_{\text{off-cr}}$ and V_{off} . In general, to calculate such difference is a complicated task. To give an idea about it, we will evaluate $V_{\text{off-cr}}$ in our model for the case of saturated $P-E$ loops in the hard-ferroelectric approximation, where it is set that

$$D_f = P_N + \kappa_f\epsilon_0 E_f. \quad (9.5.29)$$

Here P_N and κ_f are the domain contribution to polarization of the ferroelectric and the lattice contribution to its permittivity, respectively. In addition, close to the coercivity, we approximate the hysteresis loop of the ferroelectric as

$$D_f = \varepsilon_0 \kappa_{cr} (E_f - E_c), \quad (9.5.30)$$

where E_c is the coercive field of the ferroelectric and κ_{cr} is a constant controlling the slope of the loop at coercivity. Using Eq. (9.5.26) and the relation between the average displacement of the capacitor, D , and D_f , i.e.,

$$D = \frac{\varepsilon_0 \kappa_d E_d d + D_f h}{h + d} = D_f - \frac{\sigma d}{h + d}, \quad (9.5.31)$$

(derived with the aid of Eq. (9.5.25)), one readily finds for the polarization offset of the saturated loop (i.e., a loop with $P_N = \pm P_0$ at its tips)³⁵:

$$\Delta D = \frac{d\sigma}{h} \left(\frac{\kappa_f}{\kappa_d^*} - \frac{h}{d + h} \right), \quad (9.5.32)$$

where

$$\kappa_d^* = \kappa_d + \frac{d}{h} \kappa_f. \quad (9.5.33)$$

Using the above relations, one finds the values of the positive and negative coercive voltages of the symmetrized loop, V_+ and V_- , i.e., the values of the applied voltage at which the displacement of the system equals ΔD :

$$V_{\pm} = \pm h E_c + \left(\frac{h}{\kappa_{cr}} + \frac{d}{\kappa_d} \right) \left(\Delta D + \frac{\sigma d}{d + h} \right) - \frac{d\sigma}{\kappa_d}. \quad (9.5.34)$$

This leads to the final expression for the voltage offset of the symmetrized loop

$$V_{\text{off-cr}} \equiv \frac{V_+ + V_-}{2} = - \frac{d\sigma}{\varepsilon_0 \kappa_d^*} \left(1 - \frac{\kappa_f}{\kappa_{cr}} \right) = V_{\text{off}} \frac{1 - \frac{\kappa_f}{\kappa_{cr}}}{1 + \frac{d\kappa_f}{h\kappa_d}}. \quad (9.5.35)$$

The relation (9.5.35) suggests that $V_{\text{off-cr}}$ and V_{off} may essentially differ. In the case of a ferroelectric material with square loops (i.e., where $\kappa_f \ll \kappa_{cr}$) and for very thin passive layers (where $d \ll h\kappa_d/\kappa_f$) $V_{\text{off-cr}} \approx V_{\text{off}}$. On the other hand, for thicker passive layers where $d \geq h\kappa_d/\kappa_f$, $V_{\text{off-cr}}$ and V_{off} can differ dramatically in the values as well as in their functional dependence on the parameters of the problem. For instance, in the latter regime, V_{off} is

³⁵ As everywhere in this book we neglect the difference between the polarization and electric displacement of ferroelectric systems.

independent of the film thickness (see Eq. (9.5.27)) whereas $V_{\text{off-cr}}$ is strongly dependent on it.

The above consideration shows that the interpretation of experimental data on the internal field effects should be done with paying proper attention to the method of the evaluation of the internal bias.

9.5.3.2 Electrode-Adjacent Injection Model for Imprint

In thin ferroelectric films, as we have seen in Sects. 9.4 and 9.5, the presence of electrode-adjacent passive layer may be essential for various properties of the film. For the description of the impact of such a layer on ferroelectric domain patterns, on the coercive field of hysteresis loops, and on their tilt, the passive layer has been modeled as a thin dielectric layer between the ferroelectric and the electrode. A version of this model, which makes allowance for charge transport across the layer, is also appropriate for a mechanism for the internal field effect. Grossmann et al. (2002a,b) offered an imprint mechanism of this kind for ferroelectric thin film capacitors. The driving force of the mechanism can be explained as follows. In a capacitor with such a passive layer, at remanence (i.e., the capacitor is poled and then short-circuited), the bound charge of the remanent polarization is separated from the charge on the electrodes and, as a result, the layer is subjected to a very high electric field (see Sect. 9.5.2 for an estimate). This field can promote charge transfer from the electrode to the ferroelectric/passive layer interface. During further electrical cycling, the field in the passive layer will change its direction following the variation of polarization in the ferroelectric. Accordingly, the charge at the ferroelectric/dielectric interface will change in time, its evolution depending on the cycling regime. If the time elapsed while the capacitor is at remanence is comparable to the cycling period, a periodical variation of this charge with a vanishing average value is expected. This situation has been addressed in Sect. 9.5.2.6 where it has been shown that, in this regime, the loop remains symmetric. If, however, the time elapsed while the capacitor is at remanence is much greater than the cycling period, it is possible that the charge at the ferroelectric/dielectric interface is only slightly time dependent, having an appreciable average value (over the cycling period). This occurs if the charge accumulated at the interface is too large to be removed by the field in the layer during half the cycling period. The electric charge thus accumulated at the ferroelectric/passive layer interface will lead to the appearance of an internal bias field as described in the previous section.

In this model, the description of imprint requires, first, the calculations of the accumulated charge and second, finding the voltage offset by using the corresponding relations from the previous section. Under reasonable assumptions on the charge transport across the passive layer, one finds that the offset voltage is a logarithmic-type function of the time spent by the capacitor in the poled state (the exposition time), which agrees qualitatively with experimental observations (see Sect. 9.5.3.6). This logarithmic-type time dependence of the

voltage offset was demonstrated by Grossmann et al. (2002b) using numerical simulation and by Tagantsev et al. (2004b) using an analytical approach. Below we will address the analytical approach, mainly following the aforementioned paper.

First, we consider the situation where the capacitor is under open circuit conditions during the exposition time. Depending on the parameters of the system, the electrical conditions may alter some of the conclusions of our analysis. We will return to this point later on. In the model we are considering, the charge transport across the passive layer is fully described by Eqs. (9.5.24) and (9.5.25) and by the equation for the charge accumulation (9.5.20), where the hard-ferroelectric approximation (9.5.29) is adopted as the constitutive equation of the ferroelectric. We consider the situation where, originally, the ferroelectric is not poled, i.e., $P_N = 0$, and where, originally, the charge at the ferroelectric/passive layer interface is equal to zero, i.e., $\sigma = 0$. Then the ferroelectric is poled with a voltage pulse (i.e., we set $P_N = P_S$ and $V = 0$ just after application of the pulse) and left in this poled state. In the presence of the passive layer, the polarization of the ferroelectric will result in a depolarizing field in the ferroelectric film and in a field in the passive layer, which is much higher than the depolarizing one. The field in this layer will cause charge transport across it, resulting in the accumulation of the charge at the ferroelectric/passive layer interface. Let us calculate this charge, $\sigma(t, P_S)$, as a function of the exposition time, t , for the case of open electric circuit. The condition $P_N = P_S$ is assumed to hold at any t , which corresponds to the situation where the polarization relaxation rate is smaller than the rate of charge accumulation at the interface. A proper variable for the calculations is the field in the passive layer, E_d , which satisfies the relationships following from Eqs. (9.5.24), (9.5.25), (9.5.20), and (9.5.29):

$$\varepsilon_0 \kappa_d \frac{dE_d}{dt} = -J(E_d), \quad (9.5.36)$$

$$\sigma = -\kappa_d \varepsilon_0 [E_d(0) - E_d(t)], \quad (9.5.37)$$

$$E_d(0) = -\frac{P_S}{\varepsilon_0 \kappa_d^*}, \quad (9.5.38)$$

with κ_d^* defined by Eq. (9.5.33). Here, Eqs. (9.5.36) and (9.5.37) have been obtained using the open electric circuit conditions that in our model correspond to a time-independent electric displacement in the ferroelectric; Eq. (9.5.38) corresponds to the condition $V = 0$, which is valid just after the poling, i.e., at $t = 0$. Equations (9.5.36), (9.5.37), and (9.5.38) appended with the law for the charge transport across the passive layer $J(E)$ specify the mathematical problem. We will consider the situation where the charge transport across the passive layer can be described by an exponential equation, i.e., where $J(E)$ can be written as

$$J(E) = A \left(\frac{E}{E_{\text{th}}} \right)^\alpha \exp \left[\text{sign} \beta \left(\frac{E}{E_{\text{th}}} \right)^\beta \right]. \quad (9.5.39)$$

This situation covers the Pool–Frenkel, thermoionic (Schottky), and cold-field emission mechanisms, which are typical for dielectrics at high electric fields (O’Dwyer, 1973). By introducing a new variable³⁶

$$q = \exp \left[\text{sign} \beta \left(\frac{E_d}{E_{\text{th}}} \right)^\beta \right] \quad (9.5.40)$$

we can rewrite Eq. (9.5.36) (with $J(E)$ coming from Eq. (9.5.39)) as

$$\tau \frac{dq}{dt} = -|\ln q|^\gamma q^2, \quad (9.5.41)$$

where

$$\tau = \frac{\varepsilon_0 \kappa_d E_{\text{th}}}{|\beta| A} \quad \text{and} \quad \gamma = 1 + \frac{\alpha - 1}{\beta}. \quad (9.5.42)$$

In the case that we call “weak screening case,” an approximate analytic solution³⁷ to this equation is possible. In this case, where the conduction in the passive layer is truly exponential (i.e., $1/|\ln q| \ll 1$) and the polarization screening by the trapped charge is far from saturation (i.e., the current value of σ is much smaller than its value at the end of screening, which for the open circuit conditions equals $P_S \kappa_d / \kappa_d^*$), the solution to Eq. (9.5.5) to within the accuracy of small parameters $1/|\ln q|$ and $\kappa_d^* \sigma / (P_S \kappa_d)$ can be presented as (Tagantsev et al., 2004b)

$$\frac{q(0)}{q} = 1 + \frac{t}{\tau_0}, \quad (9.5.43)$$

where

$$\tau_0 = \frac{\tau}{q(0) |\ln q(0)|^\gamma} \quad (9.5.44)$$

³⁶ This analysis is related to the case of positive E_d ; in the general case, Eq. (9.5.39) should be taken with $|E_d|$ instead of E_d . This obviously does not affect the results of our analysis.

³⁷ This kind of solution is well known in the theory of transient currents in dielectrics (see, e.g., Baginskii and Kostsov, 1985; Lundstrom and Svensson, 1972).

and the initial value of q equals $q(0) = \exp\left[\text{sign}\beta\left(\frac{P_S}{\varepsilon_0\kappa_d^*E_{\text{th}}}\right)^\beta\right]$. Using Eqs. (9.5.37), (9.5.38), (9.5.43), and (9.5.44) we find the accumulated charge as a function of the exposition time and of other parameters of the problem:

$$\sigma = \frac{\varepsilon_0\kappa_d E_{\text{th}}}{|\beta|} \left(\frac{P_S}{\varepsilon_0\kappa_d^*E_{\text{th}}}\right)^{1-\beta} \ln(1 + t/\tau_0), \quad (9.5.45)$$

where

$$\tau_0 = \frac{\kappa_d}{\kappa_d^*} \frac{P_S}{|\beta|A} \left(\frac{\varepsilon_0\kappa_d^*E_{\text{th}}}{P_S}\right)^{\alpha+\beta} \exp\left[-\text{sign}\beta\left(\frac{P_S}{\varepsilon_0\kappa_d^*E_{\text{th}}}\right)^\beta\right]. \quad (9.5.46)$$

According to Eq. (9.5.27) this leads to the following expression for the voltage offset³⁸:

$$V_{\text{off}} = V_0 \ln(1 + t/\tau_0), \quad (9.5.47)$$

where

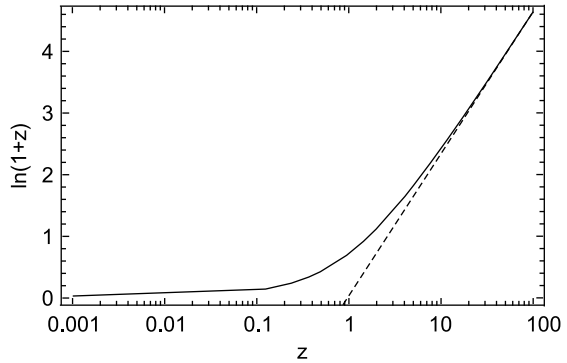
$$V_0 = \frac{dE_{\text{th}}}{|\beta|} \left(\frac{P_S}{\varepsilon_0\kappa_d^*E_{\text{th}}}\right)^{1-\beta}. \quad (9.5.48)$$

We therefore see that the exponential form of the conduction equation for the passive layer leads to a universal logarithmic-type time dependence for the voltage offset in the case of weak compensation of the depolarizing field by carrier transport across the passive layer. This dependence is illustrated in Fig. 9.5.13. The regime of weak compensation may be relevant to the real experimental situations since exponentially long times are required to pass from this regime to that of strong compensation. The explicit expression for the voltage offset, Eq. (9.5.47), is controlled only by two parameters, V_0 and τ_0 , which have the meaning of “logarithmic slope” in the regime of logarithmic charge relaxation and of the crossover time between the regimes of linear and logarithmic relaxations, respectively. Equations (9.5.46), (9.5.47), and (9.5.48) and the explicit expressions for the parameters entering these relations enable us to extract some clear predictions from the theory.

Imprint is a logarithmic function of time only in the limit of large times. In general, it is not linear in the semi-logarithmic scale. Its semi-logarithmic dependence might give the impression that the imprint accelerates with time.

³⁸ We neglect the sign in the expression for V_{off} since, in practice, the sign of the voltage applied to a capacitor is fixed by convention. For a given convention, the sign of V_{off} can be determined from simple electrostatic arguments.

Fig. 9.5.13 Electrode-adjacent injection model for imprint. Plot of Eq. (9.5.47), time dependence ($z = t/\tau_0$) of the normalize voltage offset V_{off}/V_0 in the case of weak compensation of the depolarizing field by carrier transport across the passive layer



In reality, the relaxation slows down with time (sublinear) and its apparent acceleration is an artifact of the semi-logarithmic scale.

Equations (9.5.46), (9.5.47), and (9.5.48) enable a description of the temperature dependence of the imprint in the cases of the Pool–Frenkel mechanism and of the thermoionic emission as well as of cold-field emission (O’Dwyer, 1973). In the case of the thermoionic emission and of the Pool–Frenkel mechanism $\beta = 1/2$ and

$$E_{\text{th}} = \frac{4\pi\epsilon_0\kappa_h(kT)^2}{be^3}, \tag{9.5.49}$$

where k is the Boltzmann constant, κ_h is the optical dielectric constant of the material, T is the temperature, e is the charge of the electron, and $b = 1$ for the thermoionic emission and $1 < b < 2$ for the Pool–Frenkel mechanism. For these mechanisms, the parameter α may acquire the values 1, 3/4, and 0, depending on the field interval. The factor A is basically an exponential function of the temperature

$$A \propto e^{-(\Phi/kT)}, \tag{9.5.50}$$

where Φ stands for the Pool–Frenkel or the interfacial Schottky activation barrier.

Using the above relations, for the situation where the charge transport across the passive layer is controlled by the thermoionic or Pool–Frenkel mechanisms, we find

$$V_0 = 2d\sqrt{\frac{P_S E_{\text{th}}}{\epsilon_0\kappa_d^*}} \propto dT\sqrt{\frac{P_S}{\kappa_d^*}}, \tag{9.5.51}$$

$$\ln \tau_0 = A_0 + \frac{\tilde{\Phi}}{kT}, \tag{9.5.52}$$

where A_0 is a weakly temperature-dependent constant and $\tilde{\Phi}$ is the activation barrier calculated with the field-induced reduction. From these relationships and Eq. (9.5.47) we conclude that, in this case where the charge transport is thermally activated, the temperature dependence of the imprint is very different for the regimes of linear and logarithmic charge relaxations. In the linear regime, i.e., at $t \ll \tau_0$, the temperature dependence of $V_{\text{off}} \propto V_0/\tau_0$ is exponential with the activation energy equal to that of the conduction mechanism responsible for charge transport across the passive layer. On the other hand, in the logarithmic regime, i.e., at $t \gg \tau_0$, the explicit temperature dependence of $V_{\text{off}} \propto V_0(\ln t - \ln \tau_0)$ is close to linear.

The results for the case of tunneling transport through the passive layer, where $\beta = -1$ and $\alpha = 2$ (O'Dwyer, 1973), can be obtained on the same line. However, in this case, $\gamma = 0$ and Eq. (9.5.43) provides an exact solution to Eq. (9.5.41) for an arbitrary degree of polarization screening. For the accumulated charge this solution gives

$$\sigma = P_S \frac{\kappa_d}{\kappa_d^*} \frac{\ln(1 + t/\tau_0)}{\ln(1 + t/\tau_0) + \frac{\varepsilon_0 \kappa_d^* E_{\text{th}}}{P_S}}. \quad (9.5.53)$$

In the case of weak screening this relation is consistent with Eqs. (9.5.45), (9.5.46), (9.5.47), and (9.5.48). It clearly shows that the approximate solution is justified at $\sigma \ll \kappa_d/\kappa_d^* P_S$.

The above analysis has treated the case of charge relaxation under open-circuited electric conditions for the external circuit. These conditions are consistent with the experimental situation at small times, since during the exposition time the capacitor is typically electrically disconnected from the rest of the circuit. However, at long enough times, the parasitic charge transport between the electrodes may become important shifting the situation close to the short-circuited electrical conditions. For this reason, it is instructive to evaluate the impact of the electrical conditions on the charge relaxation. An analysis similar to that given above readily shows that, under short-circuited conditions, the basic equations (9.5.36) and (9.5.37) should be modified by substitution of the permittivity of the passive layer κ_d with κ_d^* . The modified equations will still lead to Eq. (9.5.47), but Eqs. (9.5.46), (9.5.48), (9.5.51), and (9.5.53) should be replaced with their modified versions:

$$\tau_0 = \frac{P_S}{|\beta|A} \left(\frac{\varepsilon_0 \kappa_d^* E_{\text{th}}}{P_S} \right)^{\alpha+\beta} \exp \left[- \left(\frac{P_S}{\varepsilon_0 \kappa_d^* E_{\text{th}}} \right)^\beta \right], \quad (9.5.46a)$$

$$V_0 = \frac{\kappa_d^* d E_{\text{th}}}{\kappa_d |\beta|} \left(\frac{P_S}{\varepsilon_0 \kappa_d^* E_{\text{th}}} \right)^{1-\beta}, \quad (9.5.48a)$$

$$V_0 = 2d \frac{\kappa_d^*}{\kappa_d} \sqrt{\frac{P_S E_{th}}{\epsilon_0 \kappa_d^*}} \propto dT \sqrt{P_S \kappa_d^*}, \quad (9.5.51a)$$

$$\sigma = P_S \frac{\ln(1 + t/\tau_0)}{\ln(1 + t/\tau_0) + \frac{\epsilon_0 \kappa_d^* E_{th}}{P_S}}. \quad (9.5.53a)$$

It is clear that these modifications will not affect the principal conclusions obtained above; however, there may be some changes in the details when κ_d and κ_d^* are essentially different, i.e., when $d\kappa_f \gg h\kappa_d$. For instance, in this case, $V_0 \propto \sqrt{hd}$ under the open circuit situation, whereas $V_0 \propto \sqrt{d^3/h}$ under short-circuited conditions.

9.5.3.3 Poling Effect of Misfit Dislocations

A possible source of internal bias in ferroelectric thin film capacitors is the mechanical coupling between the ferroelectric material and the electrodes. The internal bias occurs when the atomic structure of the interface between the ferroelectric and the electrode favors a certain direction of polarization in the capacitor. Here we will discuss a simplest scenario of such effect, which is related to dislocation-assisted stress release in epitaxial films.

In epitaxial films at the ferroelectric/substrate (bottom electrode) interface, the lattice of the ferroelectric perfectly matches that of the substrate while the bulk lattice constants of the two materials are different. For this reason, just at the interface, the ferroelectric is always strained. As we discussed in Sect. 9.3.1, typically this strain leads to the appearance of misfit dislocations, and as a result the strain decays with the distance from the interface, creating a strain gradient. This strain gradient induces a linear polarization response via the flexoelectric effect (see, e.g., Tagantsev, 1991; Tagantsev, 1986a; Ma and Cross, 2001). However, in contrast to the piezoelectric effect,³⁹ the flexoelectric effect can control the sign of the ferroelectric polarization (poling effect). If this poling effect is large enough, an internal bias can appear in the capacitor. Let us evaluate the magnitude of this poling effect and the corresponding voltage offset.

Let the value of the in-plane lattice constant of the unstrained ferroelectric be a and that of the ferroelectric in the vicinity of the ferroelectric/substrate interface be $a_S > a$. In the case of cube-on-cube ferroelectric/substrate epitaxy, a_S is just the lattice parameter of the substrate (bottom electrode). The lattice constant of the ferroelectric in the “bulk” of the film, a_S^* , which lies between a and

³⁹ An important difference between the piezoelectric and flexoelectric effects is that the sign of the piezoelectric effect in ferroelectrics (with the rare exception for ferroelectrics with a piezoelectric paraelectric phase) is controlled by that of the ferroelectric polarization. For this reason, the strain can control (via the piezoelectric effect) only the spatial axis along which the ferroelectric polarization is directed, but not its sign.

a_S , is controlled by the density of misfit dislocations at the ferroelectric/substrate (bottom electrode), ρ . For simplicity we will treat the problem in terms of the stress release model already used in Sect. 9.3.1 (see Fig. 9.3.2), where the Burgers vector lies in the plane of the film. In this model, according to Eq. (9.3.8), the aforementioned parameters are related as

$$a_S^* = a_S(1 - a\rho). \quad (9.5.54)$$

Hence the variation of the lattice parameter of the ferroelectric from a_S to a_S^* takes place between the ferroelectric/substrate interface and the bulk. This variation takes place in a thin interfacial layer whose thickness is roughly equal to the inter-dislocation distance $1/\rho$. Thus, using Eq. (9.5.54), the out-of-plane component of the strain gradient near the ferroelectric/substrate interface can be evaluated as

$$\frac{\partial \varepsilon_{11}}{\partial x_3} \cong \left(\frac{a_S - a}{a} - \frac{a_S^* - a}{a} \right) / \rho^{-1} \approx \frac{1}{a_S} \varepsilon_M^{*2}, \quad (9.5.55)$$

where x_3 is the Cartesian coordinate normal to the plane of the film and $\varepsilon_M^* = \frac{a_S - a_S^*}{a}$ is the amount of strain released by the misfit dislocations. Depending on the film thickness and on the conditions of the strain relaxation in the film, ε_M^* varies between zero and the misfit strain $\varepsilon_M = \frac{a_S - a}{a}$.

The flexoelectric effect can be described as an additional term $\Delta F = g_{ijk}^{(0)} P_i \partial \varepsilon_{jk} / \partial x_l$ in the Landau free energy expansion (Tagantsev, 1991; 1986a). Being controlled by a fourth rank tensor it is allowed in materials of any symmetry. To assess the poling efficiency of this effect, we estimate the value of the effective electric field, $E_i^{\text{eff}} = -\partial(\Delta F) / \partial P_i$, which would produce the same polarization as the strain gradient. The information on the values of the flexoelectric tensor components $g_{ijkl}^{(0)}$ in ferroelectrics is very limited; however, an order-of-magnitude estimate compatible with experimental data for perovskites (Ma and Cross, 2001) is $|g_{ijkl}^{(0)}| \cong e / (4\pi \varepsilon_0 a)$, where e stands for the electron charge (Tagantsev, 1991; 1986a; Kogan, 1963). Using this estimate we evaluate the value of the out-of-plane component of the effective electric field generated by the strain gradient as⁴⁰

$$E^{\text{eff}} = g_{3311}^{(0)} (\partial \varepsilon_{xx} / \partial z + \partial \varepsilon_{yy} / \partial z) \cong \frac{2g_{3311}^{(0)}}{a} \varepsilon_M^{*2} \cong \frac{2e}{4\pi \varepsilon_0 a^2} \varepsilon_M^{*2} = 2E_{\text{at}} \varepsilon_M^{*2}, \quad (9.5.56)$$

where $E_{\text{at}} \approx 90 \text{ MV/cm}$ is the so-called typical atomic electric field. For epitaxial films, the misfit strain is typically about 1–5%. This gives an upper limit

⁴⁰ As everywhere in the book we consider all strains as small, thus here we neglect the difference between ε_M^{*2}/a_S and ε_M^{*2}/a .

estimate for the released misfit strain ϵ_M^* . Thus, according to Eq. (9.5.56), the strain gradient works as an electric field of some 20–500 kV/cm in an electrode-adjacent layer that is a few tens of lattice constant thick. It is clear that this effective electric field will impose some asymmetry on the switching behavior of the ferroelectric capacitor. Let us discuss this phenomenon in terms of a simple model offered by Abe and coworkers (Abe et al., 1997;2002), which is illustrated in Fig. 9.5.14. The model considers only two possible directions of polarization in the capacitor (“up” and “down”) and postulates that the strain gradient is large enough to block the polarization direction in a certain electrode-adjacent layer. Actually, the flexoelectric coupling is not the only mechanism that can block switching in the passive layer; direct “microscopic” coupling between the polarization and the dislocation can also contribute to this blocking. The presence of such non-switchable polar layer implies that one of the possible directions of polarization is preferable in the switchable part of the capacitor. In Fig. 9.5.14, this is the “up” direction. The state with the reverse polarization is energetically less favorable, because it contains a head-to-head polarization configuration at the boundary between the switchable and non-switchable parts of the capacitor. The energy of the electric field related to the bound charge at the head-to-head polarization junction will make the “down” state of polarization “energetically costly.” If this field is not compensated by free carriers, this state is metastable at best. However, if some free charge is accumulated at the interface between the switchable and non-switchable parts, the “down” state can be stabilized. Thus, we arrive at a model similar to that treated in the beginning of this section (see Eqs. (9.5.24), (9.5.25), (9.5.26), and (9.5.27)); the difference is that now the passive layer is polar and affected by the effective electric field induced by the strain gradient. These features can be readily

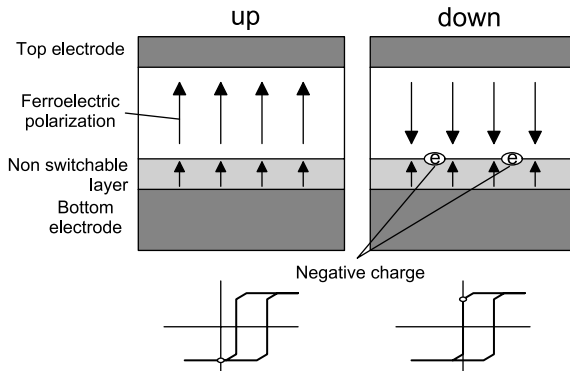


Fig. 9.5.14 The model devised by Abe and coworkers (1997, 2002) to explain the voltage offset of ferroelectric loops caused by the poling effect of the strain gradient at the ferroelectric/electrode interface. The hysteresis loop corresponding to the states “up” and “down” are schematically shown in “applied voltage”–“charge” coordinates. The top electrode is grounded and the voltage is applied to the bottom electrode

incorporated in the consideration by modifying Eqs. (9.5.25) and (9.5.26) as follows (note, Eq. (9.5.24) is still valid):

$$D_f - \sigma = \varepsilon_0 \kappa_d (E_d + E^{\text{eff}}) + P_{\text{LS}}, \quad (9.5.57)$$

$$D_f - \sigma - P_{\text{LS}} - \varepsilon_0 \kappa_d E^{\text{eff}} = \varepsilon_0 \kappa_d \left(\frac{V}{d} - \frac{h}{d} E_f \right), \quad (9.5.58)$$

where P_{LS} is the spontaneous polarization in the strain-graded layer, $d \cong \rho^{-1} \cong a/\varepsilon_{\text{M}}^*$ is its thickness, and the rest of the notations has been introduced above in this section. Similar to the derivation of Eq. (9.5.27), we obtain for the voltage offset in the modified model

$$V_{\text{off}} = -d \frac{P_{\text{LS}} + \varepsilon_0 \kappa_d E^{\text{eff}} + \sigma}{\varepsilon_0 \kappa_d}. \quad (9.5.59)$$

This equation has the same physical meaning as (9.5.27): The voltage offset is controlled by the immobile charge at the ferroelectric/dielectric interface. While in the case of Eq. (9.5.27) such charge was simply the trapped free charge σ , now it is the sum of the bound charge associated with the non-switchable surface layer and the trapped free charge.

For the model illustrated in Fig. 9.5.14, $P_{\text{LS}} = P_{\text{S}}$ and it is constant during the switching. To evaluate the voltage offset, information on the compensating free charge at the interface is needed. If the “up” state is held long enough, the compensation charge σ may reach a value of $-\varepsilon_0 \kappa_d E^{\text{eff}}$, which corresponds to full neutralization of the bound charge at the interface between the switchable and non-switchable parts of the ferroelectric. According to Eq. (9.5.59), this corresponds to

$$V_{\text{off}} = -d \frac{P_{\text{S}}}{\varepsilon_0 \kappa_d}. \quad (9.5.60)$$

If this screening is not full, then $-\varepsilon_0 \kappa_d E^{\text{eff}} < \sigma < 0$. According to Eq. (9.5.59) this will alter the estimate (9.5.60). However, the relative variation of this estimate due to incomplete screening will not exceed $\varepsilon_0 \kappa_d E^{\text{eff}}/P_{\text{S}}$, which is expected to be much smaller than unity except maybe for the situation occurring very close to the transition temperature. Thus, the estimate (9.5.60) should usually be valid for the “up” state.

As to the case of the “down” state, full screening of the bound charge requires the accumulation of a much larger amount of free charge at the interface between the switchable and non-switchable regions: $\sigma = -2P_{\text{S}} - \varepsilon_0 \kappa_d E^{\text{eff}}$. This corresponds to a voltage offset of the opposite sign:

$$V_{\text{off}} = d \frac{P_{\text{S}}}{\varepsilon_0 \kappa_d}. \quad (9.5.61)$$

In contrast to the “up” state, the degree of screening (i.e., the variation of the charge in the range⁴¹ $-2P_S - \varepsilon_0\kappa_d E^{\text{eff}} < \sigma < -\varepsilon_0\kappa_d E^{\text{eff}}$) may essentially affect this estimate leading to a wide widow for V_{off} :

$$-d \frac{P_S}{\varepsilon_0\kappa_d} < V_{\text{off}} < d \frac{P_S}{\varepsilon_0\kappa_d}. \quad (9.5.62)$$

Thus, for the “down” state, estimate (9.5.61) gives the upper limit for the possible positive offset. As clear from inequality (9.5.62), if for some reason the screening of the rather large bound charge at the interface between the switchable and non-switchable parts of the ferroelectric is not complete, smaller positive offsets and even some negative offsets may occur.

The present model enables us to estimate the upper limit for absolute value of the voltage offset induced by dislocation-assisted strain relaxation in epitaxial films. From Eqs. (9.5.60) and (9.5.61) and taking into account that $d \cong a/\varepsilon_M^*$ we find

$$|V_{\text{off}}| \cong \frac{1}{\varepsilon_M^*} \frac{aP_S}{\varepsilon_0\kappa_d}. \quad (9.5.63)$$

For realistic values of the parameters entering this estimate ($\varepsilon_M^* = 0.01$; $P_S = 0.25 \text{ C/m}^2$; $a = 0.4 \text{ nm}$; $\kappa_d = 150$) we find $|V_{\text{off}}| \cong 8 \text{ V}$.

Notice that, “surprisingly,” the model predicts $|V_{\text{off}}|$ to be inversely proportional to the dislocation-assisted strain release ε_M^* . It is instructive to comment on this point. First, the thickness of the strain-graded layer d (being inversely proportional to the misfit dislocation density) does go as $1/\varepsilon_M^*$. The voltage offset given by Eq. (9.5.63) is actually the product of d and the electric field induced by the spontaneous polarization in this layer, which is independent of d . Thus, here everything looks reasonable. Second, the very high values of $|V_{\text{off}}|$, which according to Eq. (9.5.63) should be generated by very small values of ε_M^* , are beyond the range of applicability of this model. The point is that, according to the model, the effective electric field in the strain-graded layer, E^{eff} , is proportional to ε_M^{*2} . This field is assumed to block the switching in this layer. It is clear that if ε_M^* is too small (which means small E^{eff}), the blocking effect of misfit dislocations may not be strong enough to prevent switching in the surface layer (because of small E^{eff}). In other words, for too small values of ε_M^* , the main assumption of the model that the switching in the surface layer is blocked ceases to hold.

All in all, the presence of misfit dislocations at the ferroelectric/electrode interface should lead to the internal bias field effect; however, the quantitative

⁴¹ The upper limit of this range correspond to the situation where, after full charge compensation in the ‘up’ state the sample is brought to the ‘down’ state without any redistribution of the free charge.

evaluation of this effect may require an analysis, which is more involved than that given above.

9.5.3.4 Voltage Offset Due to Reorientation of Random Field Defects

We have already discussed the interaction of the reorientable defects with domain walls in Sect. 8.5.4. Now we are interested in the internal bias effect associated with this kind of defects. The identification and investigation of this effect was pioneered by Carl and Härdtl (1978), who recognized it as the principal origin of the internal bias field in ferroelectric ceramics. Let us give a simple description of this effect.

In Sects. 6.4 and 8.5.4, we have considered, for simplicity, random field defects in the case of a uniaxial ferroelectric, where only two possible orientations of defects were possible. Now we consider a more general situation with multiple orientations of the polarization and defects, specifying the orientation of a defect with a unitary vector τ_i . In this case the contribution to the free energy density from the interaction of the defects with the homogeneous polarization in the sample, P_i , can be written in the following form:

$$\Delta F = -\frac{\gamma}{V_S} \sum \tau_i P_i, \quad (9.5.64)$$

where the summation is implied over the defects in the sample of the volume V_S . Here γ is the coupling constant. In the case of a uniaxial ferroelectric it can be linked via the relation $v = 2P\gamma$ to the interaction energy v (introduced in Sect. 6.4). Now the internal bias field created by the defects can be written as

$$E_i^{\text{bias}} = -\frac{\partial \Delta F}{\partial P_i} = \gamma n \langle \tau_i \rangle, \quad (9.5.65)$$

where n and $\langle \tau_i \rangle$ are the concentration of the reorientable defects and the average value of their τ_i vectors. In a poled sample, due to the defect-polarization coupling a preferable orientation of the defects occurs leading to $\langle \tau_i \rangle \neq 0$. According to Eq. (9.5.65), $\langle \tau_i \rangle \neq 0$ results in the appearance of internal bias field.

For the case of ferroelectric thin films, an essential issue is that the internal bias field is a bulk property of the sample, so that it is independent of the film thickness. That implies the offset voltage which is proportional to the film thickness h :

$$V_{\text{off}} = h\gamma n \langle \tau_i \rangle. \quad (9.5.66)$$

It is useful to underline that the electric field seen by the ferroelectric is just equal to the applied field whereas the voltage offset given by Eq. (9.5.66) is the result of poling effect of the oriented defects, which is not associated with the appearance of a real electric field. This situation is similar to the piezoelectric

effects where the poling effect of the strain is not associated with the appearance of a real electric field.

9.5.3.5 Voltage Offset Due to Depletion Effect

We have seen above in this section that the effect of semiconductor depletion may influence the switching behavior of ferroelectric thin films. The driving force of this phenomenon is the formation of electrode-adjacent regions of immobile space charge which produces a built-in electric field. Of importance is that this built-in field does not vary during switching. In the case where the electrochemical states of the two electrode-adjacent regions of the ferroelectric are not identical, an asymmetry in the switching process may occur. The relation between the asymmetry of the built-in electric field and that of the hysteresis loops is sensitive to the switching scenario. We will now discuss the case of the scenario addressed above in Sect. 9.5.2.3 where the electrode-adjacent nucleation of reverse domains is considered as the bottleneck of switching.

Let us start with the case of partial depletion. This is illustrated in Fig. 9.5.9 for the situation where the electrochemical states of the nearby-electrode regions of the ferroelectric are identical so that the depletion regions have the same thicknesses. If this is not the case, e.g., if the surface built-in potentials are different for the two ferroelectric/electrode interfaces, the depletion widths at the two electrodes will be different. We can relate the surface built-in potentials V_1 and V_2 to the W_1 and W_2 , of the depletion layers formed by these potentials (the suffix refers to the electrode considered) as follows⁴²:

$$V_1 = \frac{eN_d}{2\varepsilon_0\kappa_1} W_1^2, \quad V_2 = \frac{eN_d}{2\varepsilon_0\kappa_1} W_2^2, \quad (9.5.67)$$

where κ_1 is the dielectric constant of the ferroelectric at the temperature at which electrochemical equilibrium is reached at the electrodes; the rest of the notations are identical to those used in Sect. 9.5.2.3. Similar to Eq. (9.5.8), the built-in fields at the electrodes can also be found as

$$E_1 = \frac{eN_d}{\varepsilon_0\kappa_f} W_1, \quad E_2 = -\frac{eN_d}{\varepsilon_0\kappa_f} W_2, \quad (9.5.68)$$

where κ_f is the dielectric constant of the ferroelectric at the temperature at which the switching measurements are performed. According to the considered switching scenario, polarization reversal takes place once the electric field seen by the ferroelectric at its interface with an electrode (sum of the applied and built-in fields) reaches a critical value of E_{c_0} . Thus, the absolute values of both the positive and negative coercive fields of the system will always be

⁴² These relations follow from simple electrostatics on the standard assumption that the charge density in the depletion layers is homogeneous.

smaller than E_{c_0} , namely $E_{c_0} - |E_1|$ and $E_{c_0} - |E_2|$. Using Eqs. (9.5.67) and (9.5.68), we can evaluate the voltage offset of the polarization loop (non-symmetrized along the P -axis) via the half-sum of the coercive voltages. This half-sum gives

$$V_{\text{off}} = -h \frac{E_{c_0} - |E_1| - (E_{c_0} - |E_2|)}{2} = \frac{\kappa_1}{\kappa_f} (V_1 - V_2) \frac{h}{W_1 + W_2}; \quad h > W_1 + W_2, \quad (9.5.69)$$

where h is the film thickness. Here, the voltage offset is given for the case where the loop is monitored as a function of the potential difference between electrode “2” and electrode “1.”

The case of full depletion, i.e., where $h < W_1 + W_2$, can be treated similar to obtain the following expression for the voltage offset:

$$V_{\text{off}} = \frac{\kappa_1}{\kappa_f} (V_1 - V_2); \quad h < W_1 + W_2. \quad (9.5.70)$$

Thus, we see that the depletion effect may lead to a voltage offset in polarization loops. In the case of full depletion, it is equal to the difference between the built-in potentials (which are responsible for the formation of the depletion layers near the two electrodes) times the factor κ_1/κ_f . For films thicker than $W_1 + W_2$, the partial depletion occurs and the voltage offset becomes larger than $\kappa_1(V_1 - V_2)/\kappa_f$ and proportional to the film thickness. Considering that values in the range 1–2 V are a realistic estimate for these potentials, a voltage offset up to a few volts can be predicted by the depletion model. It is of interest to note that this model predicts a correlation between the thickness dependence of the coercive field (see Sect. 9.5.2) and of the “field offset” V_{off}/h : In the case of full depletion, both are thickness dependent, whereas they are thickness independent in the case of partial depletion.

It is instructive to consider the applicability of Eqs. (9.5.69) and (9.5.70). In general, the interfacial built-in potentials are fully controlled by the materials the ferroelectric and the electrode are made of. However, the potentials V_1 and V_2 introduced above can be identified with the aforementioned contact potentials with a reservation. Let us elucidate this issue for a situation often met experimentally. A ferroelectric film is deposited and crystallized onto a metallic bottom electrode (electrode “1”) at a rather high temperature, e.g., 650°C. Then a top electrode of the same metal (electrode “2”) is deposited at a much lower temperature, e.g., 200°C. Let the contact potential between the ferroelectric and the electrodes be V_0 . Formally, in this situation one might set $V_1 = V_2 = V_0$. In reality, the conditions for formation of depletion layers at the two electrodes are very different. For instance, one can expect that at 650°C electrochemical equilibrium (involving deep trapping levels) is reached at the electrode, whereas 200°C may be insufficient to reach this equilibrium. In such a situation, the depletion layer is formed only near the first electrode, so that according to the definition of V_1 and V_2 as *potentials responsible for the formation of the depletion*

layers in the capacitor, we should set $V_1 = V_0$ and $V_2 = 0$. We thus see that the difference between the contact potentials at the electrodes and the potentials V_1 and V_2 can be essential and the model can predict a nonzero voltage offset in the case where the materials of the two electrodes are the same.

9.5.3.6 Internal Bias Field and Imprint—Experimental Observations

A number of experimental techniques have been used for observation and characterization of internal bias field effects in ferroelectric thin films. The method mostly used for this purpose is to monitor the coercive voltages of electric-field-driven hysteresis loops of different parameters of the film, like polarization (Takayama and Tomita, 1989; Dimos et al., 1994), differential capacitance (Abe et al., 1997), or the longitudinal piezoelectric coefficient “ d_{33} ” (Kholkin et al., 1998; Alexe et al., 2001). In this method, the voltage offset, $V_{\text{off-cr}}$, is calculated as the half-sum of the measured coercive voltages (taken with their signs). This method is quite illustrative; however, it is not optimal for qualitative characterization of the phenomenon. Two of its drawbacks have been discussed in Sect. 9.5.3.1. First, relating the half-sum of the coercive voltages of a polarization loop with the real voltage offset V_{off} poses a serious problem. Second, for $P - E$ loops, the polarization offset is conventionally set at zero whereas, in the presence of internal bias, the switching driven with a “symmetric” ac field is intrinsically “asymmetric.” This artificial elimination of the polarization offset of the loop can bring about an additional spurious voltage offset which can be substantial. Although we have discussed these problems in detail only for the voltage offset mechanism related to trapped charge, it is clear that for any voltage offset mechanism there may be some difference between the real voltage offset and that calculated from the coercive voltages of the $P - E$ loop. For the case of “ d_{33} ”-loops, the situation may be even worse. If in a part of the film the polarization is frozen in one direction, whereas in the rest of the film the switching is “symmetric” but with a tilted loop, the resulting “ $d_{33} - E$ ” loop will exhibit a spurious voltage offset. From the point of view of memory applications (for which the imprint control is of primary importance), the hysteresis-loop-biased method discussed here is not really informative, since in these applications it is the fast pulse technique that is used rather than the relatively slow hysteresis technique.

The method of characterization of the internal field effects, which is the most common in memory applications of ferroelectric thin films, is the so-called PUND test proposed by Traynor et al. (1997). In this test, the tested capacitor is subjected to the sequence of voltage pulses shown in Fig. 9.5.15 and the charges, Q_P , Q_U , Q_N , and Q_D switched by pulses P, U, N, and D, respectively, are collected. In the case of a capacitor not affected by an internal bias field, $Q_P = Q_N > Q_U = Q_D$. If it is affected, the information on the internal bias field is provided by the difference between Q_P and Q_N . If the internal bias field is positive, the switching from the positively poled state to the negatively poled one will be less efficient than in the case of the opposite sense of switching,

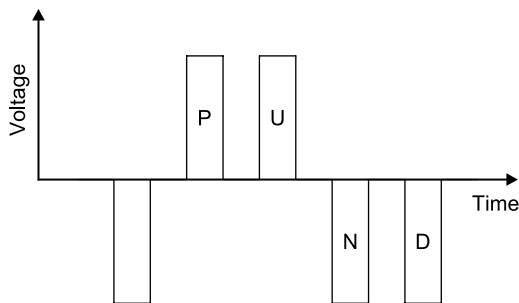
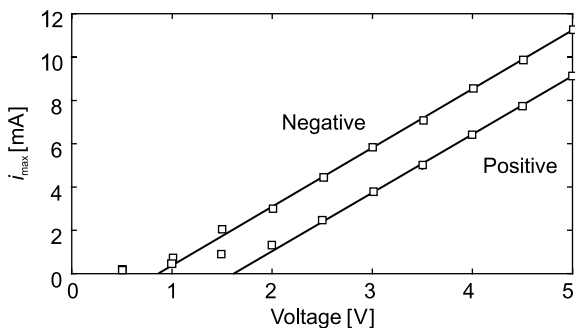


Fig. 9.5.15 The PUND method used for the characterization of internal field effects in ferroelectric capacitor systems. The capacitor is subjected to a sequence of positive P and U and negative N and D voltage pulses, and for each pulse ($i = P, U, N, D$), the switching charge Q_i is measured. The difference between Q_N and Q_P gives information about the sign of the internal bias field

resulting in $Q_P < Q_N$ and vice versa. The advantage of this method is that it directly evaluates the impact of the internal bias field on the charges Q_P and Q_N , which are used for reading the information bit stored in a memory capacitor. On the other hand, the value of the voltage offset is not directly given by this technique.

There are also methods that directly provide the value of the voltage offset for the pulse switching regime. The basic idea of these methods is to compare voltages applied to the capacitor that produce the same switching effects in the case where the internal bias field is directed along the applied field, against it, and when it is absent. This approach has been used by Abe et al. (2000) to evaluate the built-in internal bias in $BaTiO_3$ thin films by comparing the voltages which give the same values of the maximum switching current for each sense of switching. Figure 9.5.16 exemplifies this method. In this figure, the maximum switching current is plotted as a function of the amplitudes of applied positive and negative voltage pulses. The voltage shift between the curves, corresponding to two signs of the applied field, is about 0.9 V, which can be interpreted as the presence of a

Fig. 9.5.16 Pulses switching in a 58 nm thick film of $BaTiO_3$; polarization hysteresis loop taken from this film is shown in Fig. 9.5.6a. Maximum switching current vs. applied voltage for each sense (negative and positive) of voltage application. After Abe et al. (2000)



voltage offset $V_{\text{off}} = 0.45 \text{ V}$. This can be compared to the $P - E$ loop which is taken from the same film (shown Fig. 9.5.6a). The coercive voltages of this loop give a value of the voltage offset close to that determined from the data on switching currents. This may be expected, since the loop is saturated and quite rectangular.

A similar method based on this idea has been used by Tagantsev et al. (2004b) for imprint characterization. In this method, the charge obtained by switching against the internal bias field of the imprinted capacitor is compared to that of the nonimprinted capacitor. Then, the difference between these charges, ΔP , is converted into a voltage offset by using the voltage dependence of the switching charge for the nonimprinted capacitor. Figure 9.5.17 illustrates the application of this method to evaluate the dependence of imprint in PLZT film

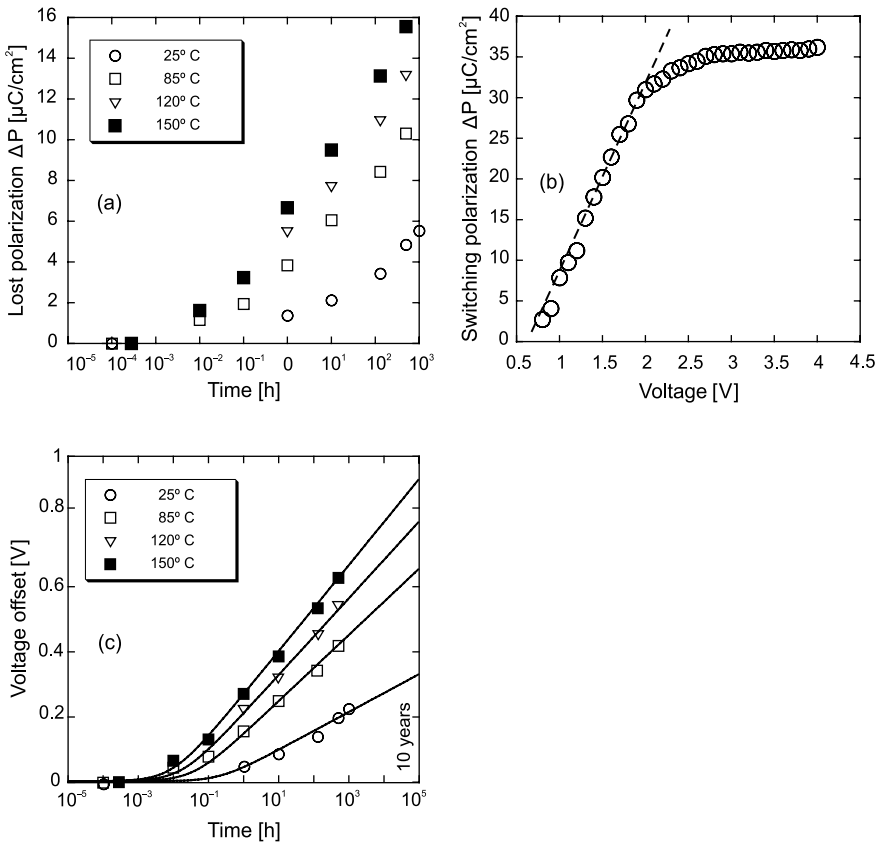


Fig. 9.5.17 Imprint in PLZT film capacitors: (a) difference between the switching charge of the imprinted and the nonimprinted capacitor, ΔP , as a function of exposition time for different exposition temperatures; (b) switching charge as a function of applied voltage for the nonimprinted capacitor; and (c) calculated voltage offset as a function of exposition time and exposition temperature. After Tagantsev et al. (2004b)

capacitors on the exposition time and temperature. Figure 9.5.17a shows the exposition time dependence of ΔP acquired at different exposition temperatures with voltage pulses of 1.8 V. Figure 9.5.17b shows the voltage dependence of the switching charge used for the data conversion. Because of the linear character of this curve below 2 V, for 1.8 V pulses, the conversion relation can be written as

$$V_{\text{off}} = A \cdot \Delta P \quad (9.5.71)$$

with $A = 0.041 \text{ V cm}^2/\mu\text{C}$. Finally Fig. 9.5.17c shows the determined dependence of V_{off} on the exposition time and temperature.

A feature of the voltage offset, which is often discussed in the literature, is its increasing dependence on the film thickness (Grossmann et al., 2002b; Dimos et al., 1994; Abe et al., 1997). Data illustrating this trend for built-in internal bias in BaTiO_3 films and for photoinduced imprint in PZT films are presented in Fig. 9.5.18. The interpretation of this trend still remains unclear. The point is that in all these papers the internal bias effect is attributed either to nearby-electrode charge trapping (Dimos et al., 1994; Grossmann et al., 2002b) or to the nearby-electrode strain gradient (Abe et al., 1997) mechanisms. At the same time, as shown above in this section, the strain gradient mechanism implies no explicit thickness dependence of the voltage offset, whereas the charge trapping mechanism predicts a certain thickness dependence of the voltage offset only in a rather special case⁴³ where $d/\kappa_d \gg h/\kappa_f$. (In this case, κ_d^* entering the expressions for the amplitude V_0 (cf. Eqs. (9.5.33), (9.5.47), (9.5.51), and (9.5.51a)) is inversely proportional to the film thickness. This leads to a thickness dependence of V_{off} , which however is not linear.) So, there seems to be a problem with the interpretation of this phenomenon in terms of the model used by these authors. This suggests that other voltage offset mechanisms (related to the depletion effect or reorientable defects) providing a linear thickness dependence of V_{off} (see discussion above in this section) may apply to these systems. Alternatively, an implicit thickness dependence of the voltage offset, e.g., through the remanent polarization, might give an explanation in terms of the interface-controlled mechanisms.

Experimental investigations of the built-in voltage offset in Pt/PZT/Pt thin film capacitors clearly reveal a composition dependence of this phenomenon; specifically, it was documented that the higher the titanium concentration, the stronger the built-in voltage offset (Kholkin et al., 1998; Lee et al., 1997a,b; Hiboux and Muralt, 2001). This effect is illustrated in Fig. 9.5.19a where the built-in field of sputtered 300 nm thick PZT films is plotted as a function of Zr content. This effect was equally reported for sputtered and

⁴³ In the paper by Dimos et al. (1994), a relation Eq. (1), which predicts a linear thickness dependence of V_{off} , was used in the discussion. This relation is valid only in the absence of charges on the electrodes. The formulae, taking into account these charges, Eqs. (9.5.27) and (9.5.35) of this book, do not predict such dependence.

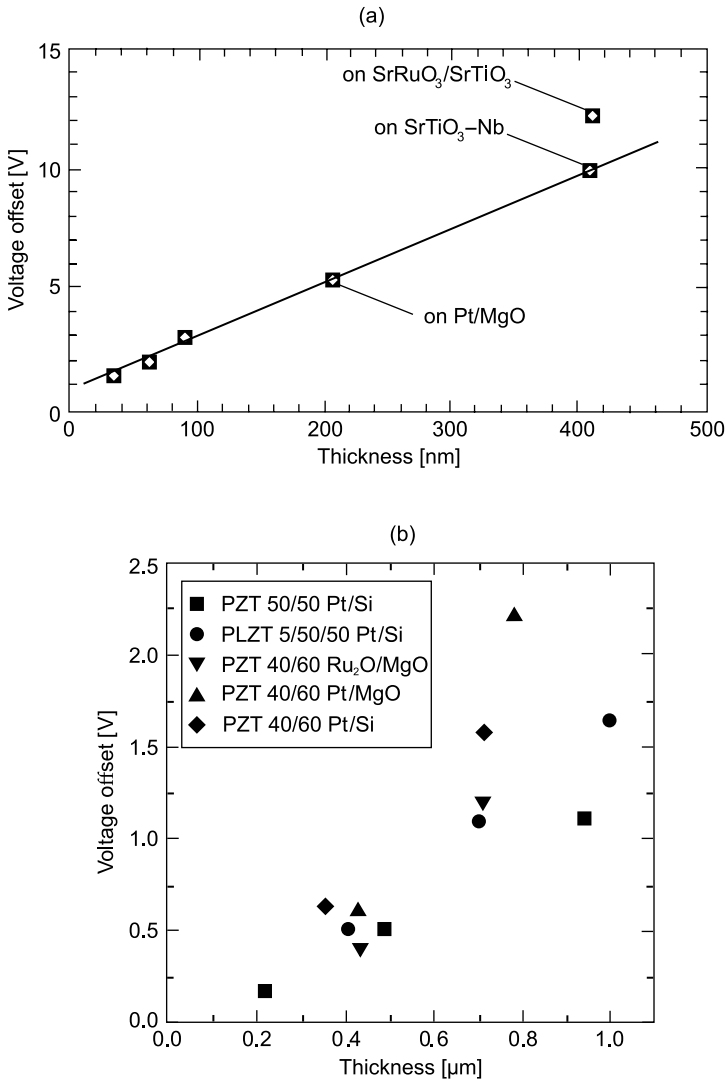


Fig. 9.5.18 Thickness dependence of the voltage offset measured (a) in BaTiO₃ films with built-in internal bias (after Abe et al., 1997) and (b) in PZT films with photoinduced imprint. Materials of the bottom electrodes and substrates are indicated. Materials of the top and bottom electrodes are identical. Reprinted with permission from Dimos et al. (1994). Copyright (1994), American Institute of Physics

sol-gel deposited films. The original voltage offset was found to be removable by annealing at 350–450 °C (Kholkin et al., 1998; Lee et al., 1997a; Hiboux, 2001). This is illustrated in Fig. 9.5.19b. Kholkin et al. have interpreted the annealing-assisted removal of the voltage offset in terms of the depletion-

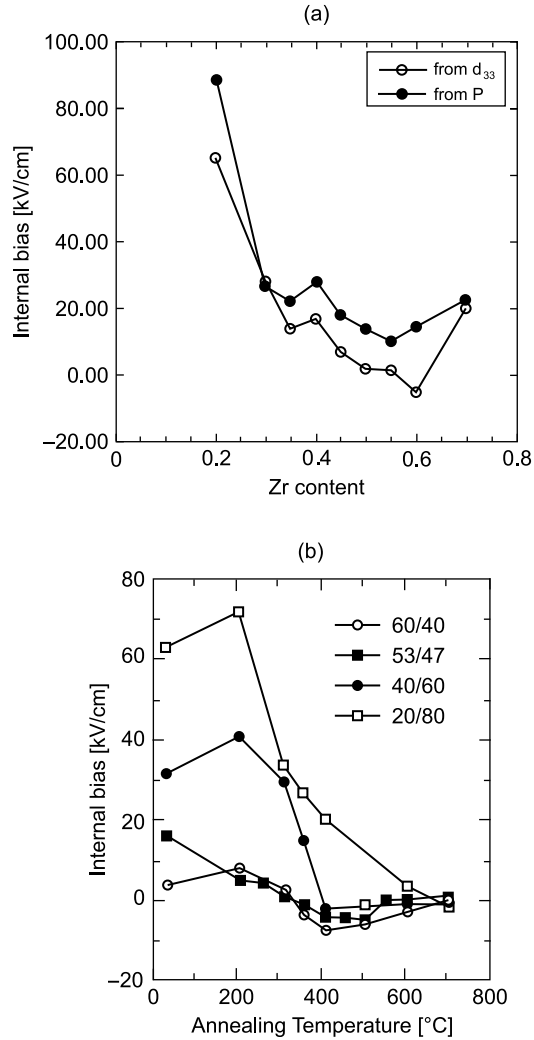


Fig. 9.5.19 (a) Effect of Zr/Ti ratio on the voltage offset evaluated from the piezoelectric and polarization loop measurements. After Hiboux and Murali (2001). (b) Effect of annealing at 350–450°C on the voltage offset for different values of the Zr/Ti ratio. After Lee et al. (1997a)

assisted scenario. In as-fabricated PZT capacitors, the Pt top electrode is deposited at room temperature, whereas the bottom electrode/PZT interface is exposed to 600–650°C for some 15–30 min. This creates an asymmetry in the depletion of electrons from deep trapping states in PZT. Specifically, no depletion at the top electrode in the as-fabricated capacitor is expected, because the room temperature is presumably too low to establish

electrochemical equilibrium near this electrode. In terms of the theoretical treatment given above in this section, this is equivalent to a difference in the built-in surface potentials in Eq. (9.5.69) and (9.5.70), which can lead to a built-in voltage offset. After the annealing, electrochemical equilibrium is expected to be established at the top electrode leading to the equilibration of the built-in surface potentials and suppression of the built-in voltage offset. The thickness dependence of the voltage offset reported by Kholkin et al. (1998) is qualitatively compatible with the theoretical predictions of Eqs. (9.5.69) and (9.5.70).

At this point it is instructive to draw the reader attention of to the difference between built-in internal field and built-in polarization. There are many ways of determining the former (as discussed above), while the latter can be practically determined only from pyroelectric (Takayama and Tomita, 1989) or piezoelectric measurements. It is typically evaluated from the d_{33} offset of the piezoelectric hysteresis loop (Kholkin et al., 1998). In principle, the behavior of the built-in internal field and of the built-in polarization may be very different, since the built-in polarization gives information both on the asymmetry of switching in the active part of the film and on the net polarization of the non-switchable (frozen) part of the film, whereas the built-in internal field gives information only on the former. A correlation between these parameters, e.g., as a function of the films composition, and their uncorrelated behavior have both been reported (Kholkin et al., 1998; Hiboux and Muralt, 2001).

The built-in internal field has been reported to be influenced by the value of the oxygen pressure maintained during cooling the films from the crystallization temperature down to room temperature (Lee et al., 1995a; Pike et al., 1995). This effect is illustrated in Fig. 9.5.20 where the voltage sift of the $P - E$ hysteresis loops as a function of oxygen pressure is shown for a

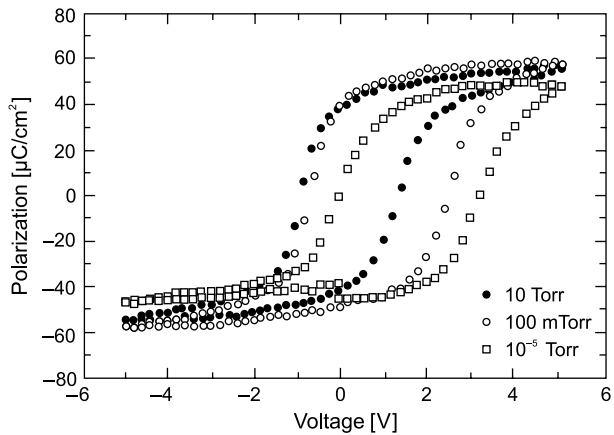
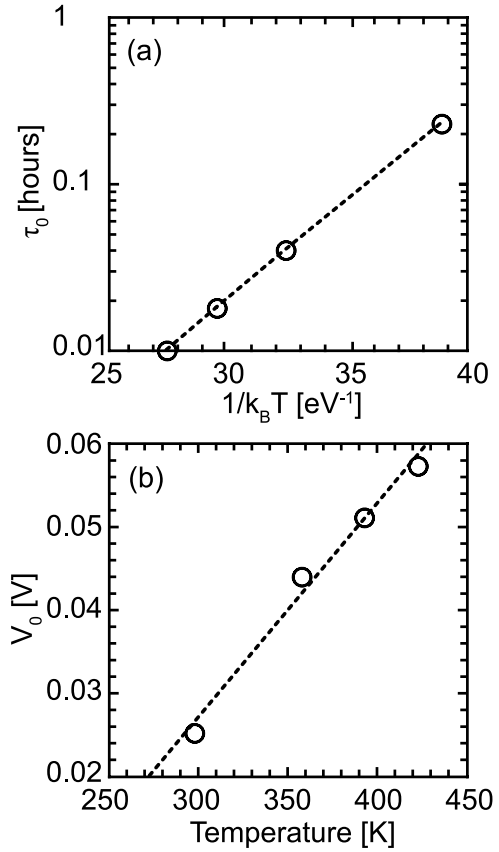


Fig. 9.5.20 Effect on the built-in internal field of the oxygen pressure at which a PZT capacitor with oxide electrodes was maintained during cooling. The voltage offset of the $P - E$ loop increases with decreasing oxygen pressure. After Lee et al. (1995a)

PZT capacitor with oxide electrodes. The authors attributed this effect to the coupling of the ferroelectric polarization with oxygen vacancies (the concentration of the latter is assumed to be correlated with the oxygen pressure maintained during cooling). Experimental data, which can also attest to the role of oxygen vacancies in the formation of built-in field in PZT thin films, have been reported on imprint in donor-doped (Nb, Ta, and W substitutions for Ti) films (Warren et al., 1995a). In this work, doping was found to reduce the thermally induced imprint. This reduction was connected to that of the oxygen vacancy concentration accompanying the doping (similar to the case of bulk PZT ceramics). Remarkably, in the same material, the authors found that UV light illumination-assisted (optical) imprint was virtually insensitive to this kind of doping. This suggests that electronic defects rather than oxygen vacancies are active in optical imprint. This observation, together with other observations from the literature, suggests that more than one imprint mechanism can be active in one material.

The dependence of the imprint-induced voltage offset on the exposition time has been found to be logarithmically slow. For an empirical fit of this dependence different single functions and combination of functions have been used,—for instance, a single logarithm function (Traynor et al., 1997), two logarithm functions with different parameters at small and large times (Schorn et al., 2003), and a stretched exponential function (Dimos et al., 1994). The experimental data on the exposition time and temperature dependence of the imprint-induced voltage offset in PZT films have been analyzed in terms of the electrode-adjacent trapping model discussed earlier in this section. Grossman et al. (2002b) performed numerical simulations in terms of this model assuming Pool–Frenkel emission (with activation barriers of 0.35 eV) to be the conduction mechanism in the nearby-electrode passive layer. The imprint data by Tagantsev et al. (2004b), already shown in 9.5.17c, have been fitted in terms of the analytical theory for the electrode-adjacent trapping model—Eqs. (9.5.47), (9.5.51), and (9.5.52),—for the case of thermoionic or Pool–Frenkel emission. A fit of the time dependence of the voltage offset is shown in Fig. 9.5.17c. The parameters of the theory, V_0 and τ_0 , determined from this fit, are plotted as functions of temperature in Fig. 9.5.21. It is seen that the theory provides a good description of the time dependence of imprint observed in this experiment. The theoretical predictions for the temperature dependence of V_0 and τ_0 are also in qualitative agreement with the trends observed experimentally: The experimentally determined value of τ_0 is an exponential function of temperature (with an activation energy of 0.27 eV), whereas V_0 is a linear function of temperature. However, it is clear that the theory is too rough to give a thorough quantitative description of the experimental observations. For example, the theory predicts no offset in the linear temperature dependence of V_0 when a substantial negative offset is seen in Fig. 9.5.21b.

Fig. 9.5.21 Temperature dependence of the parameters V_0 and τ_0 in the analytical theory for imprint due to electrode-adjacent charge trapping (see Eqs. (9.5.47), (9.5.51), and (9.5.52)). These parameters have been determined from the fit of the time dependence of the voltage offset shown in Fig. 9.5.17c. After Tagantsev et al. (2004b)



9.6 Small-Signal Response

In ferroelectric thin films, both intrinsic and extrinsic (domain) contributions to the dielectric permittivity are influenced by a number of factors which are of minor importance or absent in the case of bulk ferroelectrics such as small thickness, mechanical impact of the substrate/electrode interface, semiconductor ferroelectric/electrode phenomena, etc. In this section we will present the theoretical results related to these phenomena and compare these results with the available experimental data. In the following three sections we will address the effects related to the lattice contribution to the permittivity in the paraelectric phase. Further on we will discuss domain-related phenomena.

9.6.1 Intrinsic Contribution—Effect of Passive Layer

It is obvious that the dielectric response of a sandwich structure consisting of two, ferroelectric and dielectric, layers is sensitive to the presence of the dielectric layer. In terms of simple electrostatic consideration it is also clear that the out-of-plane and in-plane components of the effective permittivity of the system are differently affected by this layer since the first case corresponds to the “in-series” connection of the layers whereas, in the second case, it is the “parallel” connection. Such a consideration leads to well-known expressions for effective permittivity of the system κ_{eff} :

$$\frac{h+d}{\kappa_{\text{eff}}} = \frac{d}{\kappa_d} + \frac{h}{\kappa} \quad (9.6.1)$$

and

$$(h+d)\kappa_{\text{eff}} = d\kappa_d + h\kappa \quad (9.6.2)$$

for out-of-plane and in-plane case, respectively. Here h and d are the thicknesses of the ferroelectric and dielectric, κ and κ_d being their permittivities. These formulae are strictly applicable to the situation where the permittivity of the ferroelectric κ is controlled by the lattice contribution. In the case where the domain contribution to κ is essential, their application may be limited (see Sect. 9.6.5). In situations of practical interest, the dielectric has much smaller thickness and permittivity than the ferroelectric so that Eqs. (9.6.1) and (9.6.1.2) can be simplified down to the forms

$$\kappa_{\text{eff}}^{-1} = \kappa^{-1} + \frac{d}{h}\kappa_d^{-1}, \quad (9.6.3)$$

$$\kappa_{\text{eff}} = \kappa \left(\frac{h-d}{h} \right). \quad (9.6.4)$$

The relations given above may be relevant to the dielectric response of real ferroelectric thin films. Actually, a number of reasons may cause ferroelectric thin films to exhibit a dielectric response identical or similar to that of the sandwich structure discussed above. The simplest possibility is the presence of a secondary phase at the surface of the films. In addition, there exist two intrinsic reasons for this kind of dielectric behavior, which are related to surface-adjacent variation of the polarization (field induced or spontaneous) and to the charge distribution in the electrodes.

The charge distribution in the electrodes becomes important when the film is characterized by using a parallel plate capacitor. The origin of the phenomenon is the fact that the free charges in the electrode form a layer of finite thickness. For this reason, the gravity center of the charges in the electrode is separated by

some distance from the polarization bound charge in the ferroelectric. If the dielectric response of a film is monitored by using a parallel plate capacitor, the free charges in the electrode behave as a capacitor connected in series with the material of the films (Batra and Silverman, 1972; Tilley and Zeks, 1992). Treatment of the electron gas in the electrode in the Thomas–Fermi approximation (Ziman, 1972) shows that this capacitor has the capacitance per unit area of ϵ_0/l_s where l_s is the Thomas–Fermi screening length. This leads to an expression for the apparent out-of-plane dielectric permittivity of the film, which is similar to that given by Eq. (9.6.3):

$$\kappa_{\text{eff}}^{-1} = \kappa^{-1} + \frac{2l_s}{h}. \quad (9.6.5)$$

The impact of the surface-adjacent variation of the polarization (field-induced or spontaneous) on the effective permittivity of the film was first theoretically addressed by Kretschmer and Binder (1979). Below we will present the results of their theory for the paraelectric phase, which are generalized to the case of non-zero background dielectric susceptibility of the ferroelectric, $\kappa_b - 1$, which was ignored in their work.

The starting point of the model by Kretschmer and Binder is the assumption that the surface value of the polarization in a ferroelectric is not affected by the applied electric field as strongly as that in the bulk. This is consistent with the microscopic argument that the ferroelectric softness of the lattice is somehow suppressed near to the surface. The simplest modeling of this point can be performed in the framework of the continuous Landau theory for a situation where the polarization at the two surfaces of the film is completely blocked. The linear polarization response in this case can be described by using the following equation for the polarization in the film:

$$E = \alpha P - \delta \frac{\partial^2 P}{\partial x^2} \quad (9.6.6)$$

with the boundary conditions

$$P(0) = 0 \text{ and } P(h) = 0, \quad (9.6.7)$$

where the surfaces of the films are at $x = 0$ and $x = h$. Equation (9.6.6) is a literalized version of Eq. (8.4.24) written for the paraelectric phase.

In the case of the in-plane component of the effective permittivity of the system, which is typically monitored using the planar capacitor setup (with the gap between the electrodes g much greater than the film thickness) the expected inhomogeneity of polarization across the film is mainly transversal, which does not create a depolarizing field. Thus, the field E entering Eq. (9.6.6) is equal to the “applied field” $E_{\text{ext}} = V/g$, where V is the voltage applied to the gap. In this

case, the distribution of the polarization across the film can be readily found in the form

$$P(x) = \frac{E_{\text{ext}}}{\alpha} \left(1 - \frac{\cosh \frac{x-h/2}{\xi}}{\cosh \frac{h}{2\xi}} \right), \quad (9.6.8)$$

where

$$\xi = \sqrt{\frac{\delta}{\alpha}} \quad (9.6.9)$$

is the so-called correlation radius evaluated in the paraelectric phase. The physical meaning of this parameter was discussed above in Sect. 6.2, where it was introduced for the ferroelectric phase. Typically, ξ rarely exceeds a few nanometers. For the case of practical interest where $h \gg \xi$, Eq. (9.6.8) leads to the following value of the average polarization in the films:

$$\bar{P} = \frac{1}{h} \int_0^h P(x) dx = \frac{E_{\text{ext}}}{\alpha} \left(1 - \frac{2\xi}{h} \right). \quad (9.6.10)$$

This corresponds to an effective dielectric permittivity of the system:

$$\kappa_{\text{eff}} = \kappa \left(\frac{h - 2\xi}{h} \right). \quad (9.6.11)$$

This equation means that, effectively, in this case there are two layers of thickness ξ having the dielectric constant much smaller than κ so that they do not actually contribute to the polarization response. Alternatively, these layers can be considered as connected in parallel with a ferroelectric film of thickness $h - 2\xi$.

In the case of the out-of-plane component of the effective permittivity of the system, which corresponds to the situation of a parallel plate capacitor, the polarization is normal to the plane of the films and its variation is longitudinal, which *does create a depolarizing field*. This is a crucial difference compared to the previous case. The relation between the “applied field” $E_{\text{ext}} = V/h$ and the field seen by the ferroelectric can be found from the Poisson equation. Taking into account the background contribution to the displacement⁴⁴ $\varepsilon_0 \kappa_b E$ (where κ_b is the contribution to the electric permittivity from the nonferroelectric lattice modes of the crystal, typically $\kappa_b \ll \kappa$), the Poisson equation in our case is $d(\varepsilon_0 \kappa_b E + P)/dx = 0$ leading to the relationship

$$E = E_{\text{ext}} - \frac{1}{\varepsilon_0 \kappa_b} (P - \bar{P}). \quad (9.6.12)$$

⁴⁴ Making allowance for the background permittivity becomes often important when the depolarizing effect is involved, cf. Sects. 2.2.3 and 2.3.6.

Using this relationship, Eq. (9.6.6) can be rewritten as

$$E_{\text{ext}} - \alpha \bar{P} = \left(\alpha + \frac{1}{\epsilon_0 \kappa_b} \right) (P - \bar{P}) - \delta \frac{\partial^2 (P - \bar{P})}{\partial x^2}. \quad (9.6.13)$$

The solution to this equation that satisfies the boundary conditions Eq. (9.6.7) reads

$$P(x) = \frac{E_{\text{ext}}}{\alpha} \left(1 - \frac{\cosh \frac{x-h/2}{\xi_1}}{\cosh \frac{h}{2\xi_1}} \right) \frac{1}{1 + 2 \frac{\kappa}{\kappa_b} \frac{\xi_1}{h} \tanh \frac{h}{2\xi_1}}, \quad (9.6.14)$$

where $\xi_1 = \xi / \sqrt{1 + \kappa / \kappa_b} \approx \xi / \sqrt{\kappa / \kappa_b} = \sqrt{\kappa_b} \sqrt{\delta \epsilon_0}$ has the meaning of the scales on which, in this geometry, the polarization changes appreciably near the film surfaces. Note that ξ_1 is smaller than ξ so that, in any situation of practical interest, $\xi_1 / h < 1$. Under this conditions, Eq. (9.6.10) leads to the following expression for the effective dielectric permittivity of the film:

$$\kappa_{\text{eff}}^{-1} = \kappa^{-1} + \kappa_b^{-1} \frac{2\xi_1}{h}. \quad (9.6.15)$$

This relation corresponds to the in-series connection of the ferroelectric film with two dielectric layers of thickness ξ_1 and dielectric permittivity κ_b .

Thus we see that the surface region with partially suppressed dielectric response behaves as a passive layer; however, in contrast to a real dielectric layer its thickness is essentially different for in-plane and out-of-plane geometries.

The above theoretical treatment of the problem has been presented for the situation, where the polarization at the surfaces of the film is completely blocked (cf. Eq. (9.6.7)). The more general situation where the blocking is not complete can be simulated by using the mixed boundary conditions

$$P(0) - \lambda \frac{\partial P}{\partial x} \Big|_{x=0} = 0 \quad \text{and} \quad P(h) + \lambda \frac{\partial P}{\partial x} \Big|_{x=h} = 0. \quad (9.6.16)$$

These conditions interpolate the situation between blocked ($\lambda = 0$) and free ($\lambda \rightarrow \infty$) polarizations at the surfaces of the film. After this modification, the above results, Eqs. (9.6.11) and (9.6.15), still hold however but with the substitutions

$$\xi \Rightarrow \frac{\xi}{1 + \lambda / \xi} \quad \text{and} \quad \xi_1 \Rightarrow \frac{\xi_1}{1 + \lambda / \xi_1}. \quad (9.6.17)$$

Thus, as one can expect, the weakening of the surface blocking leads to a reduction of the effective passive layer thickness, the effect vanishing in the limit of free polarization at the film surface ($\lambda \rightarrow \infty$).

It is instructive to illustrate schematically the difference between the spatial distribution of the polarization for the “in-plane” and “out-of-plane” situations (Fig. 9.6.1). In the “in-plane” situation, where there is no depolarizing effect, the polarization reaches the bulk value E_{ext}/α (i.e., the value expected in the bulk sample for the same value of the applied field) exponentially fast. On the other hand, in the “out-of-plane” situation, due to depolarizing effects, the polarization changes yet faster with the distance from the electrode, but finally reaches a value which is smaller than E_{ext}/α . This figure also illustrates the geometrical meaning of parameter λ as the so-called extrapolation length.

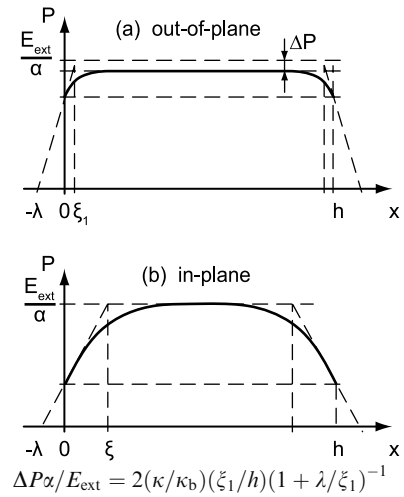


Fig. 9.6.1 Schematic distribution of polarization across a film of thickness h for the out-of-plane (a) and in-plane (b) cases.

All in all, the two models of interfacial polarization blocking predict an increasing thickness dependence of the effective dielectric permittivity of the films, see Eqs. (9.6.11) and (9.6.15).

Let us now address the applicability of these predictions to real experimental situations in $(\text{Ba,Sr})\text{TiO}_3$ films, the material for which the discussed size effect is of practical importance. To do so, some information on the correlation length ξ in the material is needed in addition to its known dielectric parameters. This information may be extracted from the data on dispersion of the soft-mode phonons. Based on the experimental data (Tagantsev et al., 2001a; Yamada et al., 1969) and neglecting the anisotropy of the correlation length, Tagantsev et al. (2003, 2005) have evaluated the temperature-independent parameter $\xi/\sqrt{\kappa} = \sqrt{\delta\epsilon_0}$ as 0.03 Å for BaTiO_3 and 0.08 Å for SrTiO_3 . For $\kappa = 1600$, this leads to the estimates for the correlation radius ξ as 1.2 Å for BaTiO_3 and 3.2 Å for SrTiO_3 . Using the recent data by Hlinka and Matron for BaTiO_3 (2006) given in Table 2.3.1, one finds a strong anisotropy and larger values of the parameter $\sqrt{\delta\epsilon_0} : \sqrt{\delta_{1111}\epsilon_0} \approx 0.7 \text{ \AA}$ and $\sqrt{\delta_{1212}\epsilon_0} \approx 0.1$. These values are

relevant to the longitudinal (out-of-plane geometry) and transverse (in-plane geometry) variations of the polarization, respectively. Though, these estimates are contradictory, these enable us to draw important conclusions about the applicability of the model.

- (i) For situations of practical interest, the expected thickness dependence of the in-plane component of the measured permittivity is very weak. According to Eq. (9.6.11) the expected relative correction to the bulk permittivity is about $2\xi/h$. For 200 nm thick films, this makes a 1% correction at most. However, this result may be taken only as a qualitative one since the theoretical situation corresponds to the limit of the range of applicability of the continuous theory; the latter is applicable if the typical scale of the polarization variation (ξ in this case) is substantially larger than the lattice constant of the material (4 Å in the case of (Ba,Sr)TiO₃), which is clearly not the case.
- (ii) For the out-of-plane component of the measured permittivity, a much stronger impact of the surface blocking of the polarization is found. According to Eq. (9.6.15), the expected relative correction to the bulk permittivity is about $2(\xi_1/h)(\kappa/\kappa_b)$, that is some $\sqrt{\kappa/\kappa_b}$ times larger than in the case of the in-plane component. On the other hand, assuming $\kappa_b \cong 10$, the scale $\xi_1 = \sqrt{\kappa_b} \sqrt{\delta \varepsilon_0}$ (i.e., 0.2–2 Å) is below the value of the lattice constant of the material, so that the use of this theoretical prediction, even as an order-of-magnitude estimate, can hardly be justified. Nevertheless, the physics standing behind Eq. (9.6.15), namely the in-series connection of the surface passive layer with the “bulk” ferroelectric part of the film, sounds reasonable. In this context, Eq. (9.6.15) might be used as a semi-empirical relation, ξ_1/κ_b being a fitting parameter. An analysis of the thickness dependence of the out-of-plane component of the dielectric constant in terms of Eq. (9.6.15), performed by Vendik and Zubko (2000) for (Ba,Sr)TiO₃ thin films, yields values of ξ_1/κ_b in the range 0.2–2.5 Å. Good examples of the experimental data on the thickness dependence of the out-of-plane permittivity of (Ba,Sr)TiO₃ thin films, which can be successfully fitted to Eq. (9.6.15), are shown in Fig. 9.6.2a and b (Streiffner et al., 1999; Basceri et al., 1997), in both cases ξ_1/κ_b being about 0.5 Å. In these papers, a convincing breakdown of this kind of data is presented.

Unlike the surface polarization blocking scenario, the mechanisms related to the free charge distribution in the electrodes stands on more solid grounds. The prediction of this mechanism, Eq. (9.6.5), which can be strictly justified mathematically (e.g., in terms of Thomas–Fermi approximation), is identical to the result for the out-of-plane permittivity of the ferroelectric/dielectric sandwich with $d/\kappa_d = 2l_s$. Experimental data (Vendik and Zubko, 2000) for (Ba,Sr)TiO₃ thin films place $d/2\kappa_d$ in the range 0.2–2.5 Å, which is comparable to typical values of the Thomas–Fermi screening length in metals $l_s \approx 0.5\text{Å}$.

One more useful qualitative conclusion can be drawn on the basis of the above modeling for the out-of-plane component of the permittivity. Namely, its thickness dependence may be sensitive to the electrode material since the

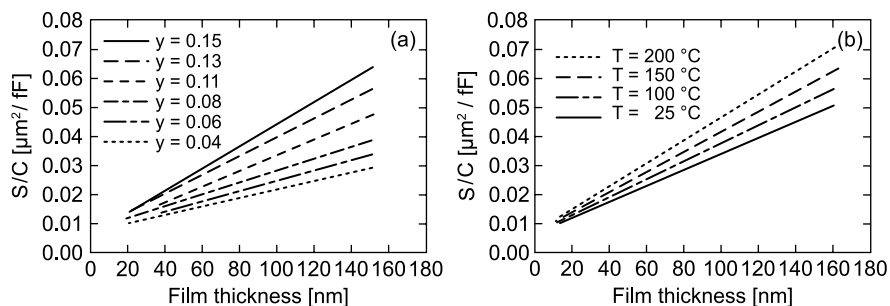


Fig. 9.6.2 (a) Film thickness dependences of the inverse zero-bias capacitance density of $\text{Ba}_{0.7}\text{Sr}_{0.3}\text{Ti}_{1+y}\text{O}_{3+z}$ film-based plate capacitors at different Ti contents y . Reprinted with permission from Streiffer et al. (1999). Copyright (1999), American Institute of Physics (Streiffer et al., 1999). (b) The inverse of the zero-bias capacitance density of $\text{Ba}_{0.7}\text{Sr}_{0.3}\text{TiO}_3$ film-based plate capacitors as a function of film thickness at different temperatures. Reprinted with permission from Basceri et al. (1997). Copyright (1997)

effective thickness of the surface dead layer is a function of the boundary conditions at the electrodes, which in turn may be dependent on the electrode material. Here a number of scenarios have been discussed in the literature.

First, it has been suggested by Vendik and Zubko (1997) that the surface blocking of polarization is much less pronounced in the case of a similarity between the ferroelectric and electrode, specifically, when the electrode is oxide and the ferroelectric is an oxide perovskite.

Other scenarios, by Tagantsev and Stolichnov (1999) and by Gerra et al. (2006), are explained as follows. The mechanisms of formation of effective passive layers (additional capacitors) at the ferroelectric/electrode interface discussed above (due to Thomas–Fermi screening length and the polarization variation at the interface) can be viewed more fully. The first mechanism is related to the fact that when free charges in the electrode approach the ferroelectric–electrode interface to screen the bound charge of the ferroelectric, they form a layer of finite thickness (Thomas–Fermi screening length). Therefore, the center of gravity of the free charges is displaced with respect to the interface, creating a double electric layer (capacitor). On the other hand, the polarization cannot drop abruptly in going from the ferroelectric to the metal (the effect which in continuous theory is described by Eq. (9.6.14)). For this reason, the center of gravity of the bound charge is shifted away from the metal, creating another capacitor. These two mechanisms, shown schematically in Fig. 9.6.3a, may act simultaneously as two back-to-back in-series capacitors. In an effort to improve the performance of ferroelectric thin film devices, it was found that the surface capacitor effect is much weaker when the electrodes are conductive metal oxides, such as RuO_2 , IrO_2 , or SrRuO_3 . Unlike the case of simple Pt electrodes, for such materials no additional surface capacitor has been revealed by dielectric measurements (Lee et al., 1995b). When looking for the

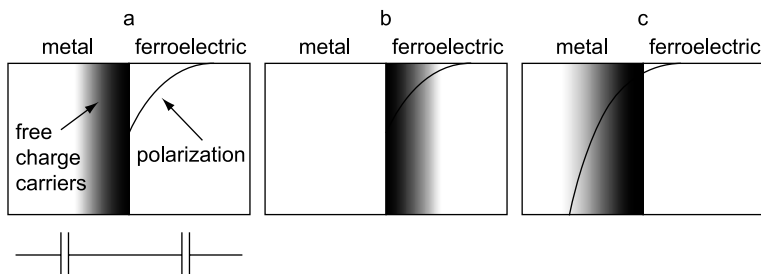


Fig. 9.6.3 The surface capacitor effect shown schematically. **(a)** A finite thickness of the bound charge associated with the variation of the polarization at the electrode and a finite thickness of the free charge in the electrode can be related to two capacitors connected in series with the ferroelectric. **(b)** Compensation of the bound charge by the presence of free charge carriers in the ferroelectric, for example, as a result of doping or contact phenomena. **(c)** Penetration of the ionic polarization into the metal, for example, as a result of the mechanical relaxation of the electrode ions in response to the ferroelectric distortion of the adjacent lattice. The gradient in *shading* represents the concentration of free charge carriers, while the *solid line* represents the absolute value of polarization

reason that makes the screening more efficient in the case of oxide electrode one distinguishes the following possibilities. One possibility (Tagantsev and Stolichnov, 1999) is an enhanced concentration of free charge carriers in the first few layers of the ferroelectric, for example, as a result of doping (Tagantsev and Stolichnov, 1999) or of contact phenomena (Ohtomo and Hwang, 2004). This possibility is schematically illustrated in Fig. 9.6.3b. We can say that in this case the free charges move to where the bound charges are situated, so as to screen them “in situ.” Here we are dealing with a kind of short-circuiting of the electrode-adjacent layer containing the polarization bound charge. The second possibility (Gerra et al., 2006) is the penetration of the bound polarization charges into the electrode. In the case of oxide electrodes, this is made feasible by their ionic structure. We can imagine that the ionic displacements that produce the polarization in the ferroelectric might continue for some distance into the metal oxide structure, leading again to in situ screening. This scenario is schematically illustrated in Fig. 9.6.3c. It is worthy of note that whichever the mechanism behind it, in situ screening can essentially cancel out the destructive effect of the additional surface capacitor, thus explaining the enhanced performance of oxide electrodes.

For the moment, there is neither experimental nor theoretical results supporting the short-circuiting scenario, while the results of *ab initio* modeling reported for $\text{SrRuO}_3/\text{BaTiO}_3/\text{SrRuO}_3$ stack by Gerra et al. (2006) demonstrated that the presentation of polarization into the electrode takes place in this system resulting an approximately two times increase in the parasitic capacitance associated with the electrode/ferroelectric interface.

This modeling supports the interpretation of the reduced size effect on permittivity in systems with oxide electrodes related to the penetration of

polarization into the oxide electrode. However, there is no consensus on this issue in the literature (see Stengel and Spaldin, 2006).

To conclude the discussion of passive layer effects, it is instructive to give a table (Table 9.6.1) for the thicknesses of a dielectric layers with $\kappa_d = 1$, producing the same effect as each of the passive layer mechanisms considered in this section.

Table 9.6.1 Thickness of a dielectric layer with $\kappa_d = 1$, which impacts the dielectric permittivity of the film identical to the effects listed in the first column

	In-plane permittivity	Out-of-plane permittivity
Real layer with $\kappa_d = 1$	d	d
Full surface blocking of polarization	ξ	$\xi_1/\kappa_b = \xi/\sqrt{\kappa\kappa_b}$
Partial surface blocking of polarization	$\frac{\xi}{1 + \lambda/\xi}$	$\frac{\xi_1/\kappa_b}{1 + \lambda/\xi_1}$
Electrode effect	–	l_s
Partial depletion effect, $h > 2W$	–	$h_d = \epsilon_0\beta\rho_0^2 W^3$
Full depletion effects, $h < 2W$	–	$h_d\left(\frac{h}{2W}\right)^3$

h , film thickness

d , thickness of the layer

ξ , correlation radius

κ and κ_b , permittivity and background permittivity of the ferroelectric

λ , extrapolation length for the polarization boundary conditions

l_s , Thomas–Fermi screening length

β , coefficient of the dielectric nonlinearity

ρ_0 , space charge density in the depletion layer

W , depletion layer width

9.6.2 Intrinsic Contribution—Depletion Effect

The impact of the depletion effect on the polarization response of ferroelectric thin films was already discussed in this chapter in the context of their switching behavior (Sects. 9.5.2 and 9.5.3). In this section we will address the impact of the built-in space charge induced by the depletion effect on the lattice contribution to the small-signal polarization response of a ferroelectric film in the paraelectric phase. We will consider the cases of full and partial depletion illustrated in Fig. 9.5.9. We will show that, for the small-signal response, the depletion effect manifestation is similar to that of a passive surface layer. This result is consistent with that obtained by Bratkovsky and Levanyuk (2000b), who first treated the problem for the case of full depletion.

The impact of the depletion space charge on the effective dielectric permittivity of a parallel plate capacitor containing a ferroelectric can be elucidated with the following simple arguments. The built-in depletion charge results in a certain built-in electric field which in turn creates a built-in x -dependent polarization $P_b(x)$, x being the coordinate normal to the plane of the films. For the dielectric response of the film, this implies a local, x -dependent permittivity.

Using the equation of state of the ferroelectric, $E = \alpha P + \beta P^3$, the out-of-plane component of the local permittivity can be written as⁴⁵

$$\kappa_{\text{loc}}(x) = \frac{1}{\varepsilon_0} \left(\frac{\partial E}{\partial P} \right)^{-1} \Bigg|_{P=P_b} = \frac{\varepsilon_0^{-1}}{\alpha + 3\beta P_b^2(x)}. \quad (9.6.18)$$

Taking into account the “in-series” geometry of the problem the effective dielectric constant of the system can be found by averaging $1/\kappa_{\text{loc}}(x)$ across the film thickness:

$$\frac{1}{\kappa_{\text{eff}}} = \frac{1}{h} \int_0^h \frac{dx}{\kappa_{\text{loc}}(x)} = \frac{1}{k} + \frac{3\beta\varepsilon_0}{h} \int_0^h P_b^2(x) dx, \quad (9.6.19)$$

where $\kappa = 1/\varepsilon_0\alpha$ is the relative permittivity of the ferroelectric. The exact value of $P_b(x)$ can be obtained from a rather cumbersome solution to the equation of state for the ferroelectric and the Poisson equation

$$\frac{d(\varepsilon_0\kappa_b E + P_b(x))}{dx} = \rho(x), \quad (9.6.20)$$

where $\rho(x)$ is the density of the built-in charge. This solution should also obey the condition

$$\int_0^h E dx = 0. \quad (9.6.21)$$

A good approximation for the built-in polarization can be readily obtained if, in Eq. (9.6.20), one neglects the term $\varepsilon_0\kappa_b E$. This approximation is justified by a large value of the dielectric permittivity of the ferroelectric (i.e., $\kappa \gg \kappa_b$). Then, Eqs. (9.6.20) and (9.6.21) yield

$$P_b(x) = (x - h/2)\rho_0 \quad (9.6.22)$$

for the full depletion case, where $h < 2W$, and

$$\begin{aligned} P_b(x) &= (x - W)\rho_0 & 0 < x < W \\ P_b(x) &= 0 & \text{for } W < x < h - W \\ P_b(x) &= (x - h + W)\rho_0 & h - W < x < h \end{aligned} \quad (9.6.23)$$

for the case of partial depletion, where $h > 2W$. Here $\rho_0 = eN_d$ is the space charge density in the depleted regions and W is the depletion layer width, e and

⁴⁵ Here, as mainly in this book, we neglect the difference between D and P in ferroelectrics.

N_d being the charge and the volume density of ionized impurities in the depletion regions.

Using this result for the built-in polarization and Eq. (9.6.19) we find that the depletion leads to a reduction of the effective dielectric permittivity of the film. In the cases of the partial and full depletion, one finds

$$\frac{1}{\kappa_{\text{eff}}} = \frac{1}{\kappa} + \frac{2\varepsilon_0\beta\rho_0^2 W^3}{h} \quad (9.6.24)$$

and

$$\frac{1}{\kappa_{\text{eff}}} = \frac{1}{\kappa} + \frac{\varepsilon_0\beta\rho_0^2 h^2}{4}, \quad (9.6.25)$$

respectively. Equations (9.6.24) and (9.6.25) imply that, for the effective dielectric permittivity of the film, the depletion effect is equivalent to the in-series connection of the ferroelectric with a linear capacitor. In the case of partial depletion, this capacitance is independent of film thickness, so that the film behaves like a film with a real passive layer, while in the case of full depletion, according to Eq. (9.6.25) this capacitance goes as h^{-3} . A comparison of the “passive layer” effect due to depletion with other passive layer effects is presented in Table 9.6.1.

It is instructive to evaluate the potential impact of depletion effect on permittivity. Numerically, it is not substantial; it is, however, comparable with that of the effective passive layers discussed in the previous section. For values of W and ρ_0 compatible with the data on ferroelectric perovskites with metallic electrodes, i.e., $W = 0.2 \mu\text{m}$, $\beta = 8 \times 10^9 \text{ JC}^{-4} \text{ m}^5$, and $\rho_0 \cong 1.6 \times 10^{-19} \times 10^{18} \text{ C/cm}^3 = 0.16 \text{ C/cm}^3$ (Tagantsev et al., 2003; Waser and Klee, 1992; Brennan, 1995; Tagantsev et al., 1994), one finds that, in the case of partial depletion (where $h > 2W$), a single depletion layer works as a dielectric layer with $\kappa_d = 1$ and thickness $h_d = \varepsilon_0\beta\rho_0^2 W^3 \approx 0.15 \text{ \AA}$. In the case of full depletion, the depletion effect on permittivity can be readily identified with a strong reduction of the effect with decreasing film thickness (see Eq. (9.6.25)). It is also worth mentioning that, as for any “in-series model,” the impact of depletion on the dielectric constant of a ferroelectric material in the paraelectric phase is formally equivalent to a lowering of its Curie–Weiss temperature (Bratkovsky and Levanyuk, 2000b).

9.6.3 Intrinsic Contribution—Strain Effect

As it was discussed in Sect. 9.3.2 the clamping of the in-plane lattice constant of a film deposited onto a substrate significantly influences the single-domain state

of the material. Specifically, the clamping modifies the temperatures of ferroelectric phase transitions, T_C , and the corresponding Curie–Weiss temperatures, T_0 . The result of importance for the dielectric permittivity in the paraelectric phase addressed this section is a linear dependence of T_0 on the parent misfit strain. This link will obviously lead to a modification of the value of the film permittivity and its temperature dependence. The latter effect is due to the temperature dependence of the parent misfit strain inevitable when the temperature expansion coefficients of the substrate and the film are different. Let us illustrate this phenomena with some relations for a most often addressed situation: (001) and (111) films of BaTiO₃-type ferroelectrics deposited onto a dissimilar substrate. We will address the case where the misfit strain is isotropic in the plane of the film, i.e., $\varepsilon_{P\alpha\beta} = \varepsilon_P \delta_{\alpha\beta}$. In this case, according to Pertsev et al. (1998) and Tagantsev et al. (2002a) (see also Eqs. (9.3.22) and (9.3.24)), the quadratic in polarization terms of the thermodynamic potential, which control the polarization response in question, reads

$$\Delta G = \frac{T - T_0 - A_{\text{in}}\varepsilon_P}{2\varepsilon_0 C} (P_1^2 + P_2^2) + \frac{T - T_0 - A_{\text{out}}\varepsilon_P}{2\varepsilon_0 C} P_3^2, \quad (9.6.26)$$

where, for the (001) films

$$A_{\text{in}} = 2\varepsilon_0 C \frac{Q_{11} + Q_{12}}{s_{11} + s_{12}}, \quad A_{\text{out}} = 2\varepsilon_0 C \frac{2Q_{12}}{s_{11} + s_{12}}, \quad (9.6.27)$$

and, for (111) films⁴⁶

$$A_{\text{in}} = 2\varepsilon_0 C \frac{4(Q_{11} + 2Q_{12} + Q_{44}/2)}{4s_{11} + 8s_{12} + s_{44}}, \quad A_{\text{out}} = 2\varepsilon_0 C \frac{4(Q_{11} + 2Q_{12} - Q_{44})}{4s_{11} + 8s_{12} + s_{44}}, \quad (9.6.28)$$

where P_3 , P_1 , and P_2 stand for the out-of-plane and two in-plane components of the polarization, respectively; the rest of notation is consistent with those used above in Sects. 2.3 and 9.3.2. The values of parameters A_{in} and A_{out} for some perovskite ferroelectrics are listed in Table 9.6.2.

The parameters given in the Table 9.6.2 clearly suggests that the polarization response of the strained films is anisotropic. Taking into account the temperature dependence of ε_P given by Eq. (9.3.28) one readily finds the Curie–Weiss temperatures, T_{in} , T_{out} , and the Curie–Weiss constants, C_{in} , C_{out} , for the in-plane and out-of-plane components of the permittivity, as (Streiffer et al., 1999; Pertsev et al., 1999a)

⁴⁶ The following relations correspond to those from paper by Tagantsev et al. (2002a) to within the difference in the definition of Q_{44} .

Table 9.6.2 Parameters controlling the impact of the misfit strain on the temperature anomaly of dielectric permittivity of typical ferroelectric films

	001		111	
	$A_{\text{in}}, 10^4 \text{ K}$	$A_{\text{out}}, 10^4 \text{ K}$	$A_{\text{in}}, 10^4 \text{ K}$	$A_{\text{out}}, 10^4 \text{ K}$
PbTiO ₃	3	-2.5	2.7	0.16
BaTiO ₃	3.6	-4.7	2.3	-0.32
SrTiO ₃	3	-1.5	1.8	1.2

The experimental data used for calculations are taken from the papers by Pertsev et al. (1998) and Uwe and Sakudo (1976) and from a reference book (Landolt-Börnstein, 1981). In the case of SrTiO₃, the whole set of data for Q 's is contradictory; a self-consistent subset of these data has been used in calculations. A discussion of the inaccuracy of evaluation of the strain effects on permittivity in SrTiO₃ can be found in the paper by Haeni et al. (2004).

$$C_{\text{in, out}} = \frac{C}{1 - A\Delta a} = C + \frac{A\Delta a}{1 - A\Delta a} C, \quad (9.6.29)$$

$$T_{\text{in, out}} = \frac{T_0 + A(\varepsilon_{\text{P}_0} - \Delta a T_G)}{1 - A\Delta a}, \quad (9.6.30)$$

where the corresponding value of A_{in} and A_{out} should be used for A , $\Delta a = a_{\text{TS}} - a_{\text{TF}}$ is the difference between the thermal expansion coefficient of the substrate and the ferroelectric, and ε_{P_0} is the misfit strain at the deposition temperature T_G . The equation for $T_{\text{in, out}}$ was obtained under the assumption that below T_G no dislocation-assisted release of the misfit strain takes place.

The effects predicted by Eqs. (9.6.29) and (9.6.30) may be appreciable. For realistic parameters of ferroelectric thin films one may expect $\Delta a = (2 - 6) \times 10^{-6}$, according to Table 9.6.2 and Eq. (9.6.29) this may lead up to a 30% modification of the Curie–Weiss constant.

The strain-induced changes of the Curie–Weiss temperatures can also be significant. In the case of ultrathin film (below 50 nm), the epitaxial misfit strain may achieve a value of one percent. This corresponds, according to Table 9.6.2 and Eq. (9.6.30), to a shift of T_0 up to $A\varepsilon_{\text{P}_0} \cong 500 \text{ K}$. In the opposite limiting case of rather thick films, where the strain release at the deposition temperature is very strong, ε_{P_0} is typically of secondary importance compared to the thermal strains. In this case, setting $\varepsilon_{\text{P}_0} = 0$ in Eq. (9.6.30) one gets an estimate

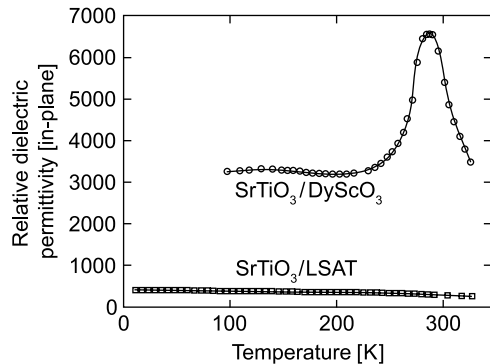
$$T_{\text{in, out}} \approx T_0 - \frac{A\Delta a}{1 - A\Delta a} (T_G - T_0). \quad (9.6.31)$$

This estimate corresponds to somehow smaller effects. However, according to it there may be combinations of material parameters providing a 100–200 K shift of the Curie–Weiss temperature.

The predictions of the theoretical approach overviewed above corroborates with experimental observation in perovskite thin films. A few examples are given below.

In the case of relatively thick films, the theory states (cf. Eqs. (9.6.29) and (9.6.31)) that the variation of the Curie–Weiss temperature and that of the Curie–Weiss constant are controlled by the sign of $A\Delta a/(1 - A\Delta a)$ (actually it is the sign of $A\Delta a$) and correlated: a decrease in T_0 implies an increase in C and vice versa. This kind of behavior was reported by Pertsev et al. (1999a) for BaTiO_3 and SrTiO_3 films deposited onto Si. The authors found the experimentally observed variation of T_{out} , and C_{out} to be in reasonable agreement with the theory presented above. In the case of an ultrathin (12 nm) film of BaTiO_3 deposited onto a compressive SrTiO_3 substrate, a 500 K increase in the transition temperature was documented from the out-of-plane dielectric testing of the material (Yoneda et al., 1998). The value of A_{out} corresponding to this situation, 4.7×10^4 K, leads to a shift of the Curie–Weiss temperature up for some 500 K for an in-plane strain of 1%. This value is comparable to the data on the in-plane lattice constant of the BaTiO_3 films reported in the same paper. A clear manifestation of the strain effects on the permittivity in films of SrTiO_3 has been reported by Haeni et al. (2004). They observed (see Fig. 9.6.4) a strong enhancement of the permittivity in the case of DyScO_3 substrate (with $\varepsilon_{\text{P}} = 0.008$ at room temperature) and a strong reduction of the permittivity in the case of $(\text{LaAlO}_3)_{0.29}(\text{SrAl}_{0.5}\text{Ta}_{0.5}\text{O}_3)_{0.71}$ substrate (with $\varepsilon_{\text{P}} = -0.009$ at room temperature). The variations of permittivity observed are compatible with the predictions of Eqs. (9.6.29) and (9.6.30). For example, according to these equations and Table 9.6.2, the misfit strain of $\varepsilon_{\text{P}} = 0.008$ should lead to a 240 K increase in the Curie–Weiss temperature whereas some 250 K increase has been observed.

Fig. 9.6.4 In-plane dielectric constant measured at a frequency of 10 GHz in 500 Å thick epitaxial (100) SrTiO_3 films deposited on (110) DyScO_3 and (100) $(\text{LaAlO}_3)_{0.29}(\text{SrAl}_{0.5}\text{Ta}_{0.5}\text{O}_3)_{0.71}$ substrates. See the text. After Haeni et al. (2004)



9.6.4 Extrinsic Contribution—Mechanical Effects

In this section we will address the dielectric response of equilibrium domain patterns of a ferroelectric film, which is determined by the mechanical coupling between the film and the substrate. Application of

an electric field to such pattern will modify it leading to a change of the net spontaneous polarization of the sample. To describe the corresponding dielectric response, one should relate this change to the value of the applied field. In this section we present a solution to this problem for the case of the a/c pattern in a (001) film of a BaTiO₃-type tetragonal ferroelectric (see Fig. 9.2.1) and will give some results for the a_1/a_2 -pattern. For more information on the problem we refer the reader to the comprehensive paper by Koukhar et al. (2001).

The main features of the phenomenon can be identified in terms of the simple mean-strain theory by Roytburd (see Sect. 9.3.3). We will start with the situation where the film is thick enough so that the domain pattern is dense and it is fully controlled by the energy of average mechanical strain in the system. Further on we will discuss the thickness effects. In this situation according to Eq. (9.3.40) the energy density of the a/c -pattern reads

$$\Phi_{\text{el}}(\alpha) = \alpha u_c + (1 - \alpha)u_a - \alpha(1 - \alpha)u_{\text{ac}}, \quad (9.6.32)$$

where α is the volume fraction of c -domains, u_c and u_a are the elastic energy densities of the c - and a -single-domain states, and u_{ac} is the energy density corresponding of the indirect long-range interaction between domains through the substrate. The energy u_{ac} serves as the driving force for the domain formation in the film. According to Eq. (9.3.41) u_{ac} can be found as a function of the tetragonality strain $\varepsilon_{\text{T}} \approx (c - a)/a$, the Poisson ratio ν , and the Young modulus E of the ferroelectric:

$$u_{\text{ac}} = \frac{1}{2} \frac{E\varepsilon_{\text{T}}^2}{1 - \nu^2}. \quad (9.6.33)$$

The rigidity (with respect to variations of α) of the equilibrium domain pattern that corresponds to the minimum of $\Phi_{\text{el}}(\alpha)$ is obviously proportional to this energy density so that the domain contribution to permittivity, κ_{ij}^{dom} , should be inversely proportional to it. The explicit expression for κ_{ij}^{dom} can be readily found as

$$\kappa_{ij}^{\text{dom}} = \frac{1}{\varepsilon_0} \frac{\partial P_i}{\partial E_j} = \frac{1}{\varepsilon_0} \frac{\partial \alpha}{\partial E_j} \Delta P_i = \frac{\Delta P_i \Delta P_j}{2\varepsilon_0 u_{\text{ac}}}. \quad (9.6.34)$$

Here $P_i = \alpha P_i^{(c)} + (1 - \alpha)P_i^{(a)}$ and $\Delta P_i = P_i^{(c)} - P_i^{(a)}$ with $P_i^{(c)}$ and $P_i^{(a)}$ being the vectors of the spontaneous polarization in c - and a -domains, respectively. To obtain the result given by Eq. (9.6.34), one first finds α as a function of the applied field E_i by minimizing the energy (9.6.32) appended with the term $-\mathbf{PE}$. Now, setting the polarization in the c - and a -domains as $(0 \ 0 \ P_S)$ and $(P_S \ 0 \ 0)$, respectively, we find for the matrix of κ_{ij}^{dom}

$$\kappa_{ij}^{\text{dom}} = \begin{pmatrix} A & 0 & A \\ 0 & 0 & 0 \\ A & 0 & A \end{pmatrix} A = \frac{(1 - v^2)P_S^2}{E\varepsilon_0\varepsilon_T^2}. \quad (9.6.35)$$

A few features of this result are worth commenting. First, as was first recognized by Pertsev with coworkers (1996), the contribution of this domain pattern to the permittivity is independent of the domain wall density (period of the pattern). This makes a striking difference with the case of domains in a mechanically free ferroelectric crystal where the motion of domain walls is controlled by local pinning forces, e.g., interaction with defects. In the latter case, the domain contribution to the permittivity is obviously proportional to the density of the domain walls in the sample. This difference corresponds to the difference in the type of the pinning forces: the local wall/defect coupling in the case of the crystal and the long-range mechanical interaction in the case of the film. Second, using the results of Landau theory for the parameters entering Eq. (9.6.35), one can show that the considered extrinsic contribution is proportional to the lattice part of the permittivity along the c -axis, κ_c , with a weakly temperature-dependent proportionality factor of the order of unity. In the framework of the Landau theory of the second-order phase transition, where $P_S^2 \propto 1/\kappa_c$ and $\varepsilon_T \propto P_S^2 \propto 1/\kappa_c$, the factor A/κ_c is just a numerical constant. This factor can be readily evaluated from the material parameters of the ferroelectric. At room temperature for PbTiO_3 , using the set of these parameters already used when obtaining the estimate for Eq. (9.3.71), we find $A/\kappa_c \approx 0.8$.

The results of the Roytburd's theory enable also assessing the thickness dependences of the contribution of the a/c -pattern to the permittivity of the film. The important result of the theory is that the indirect long-range interaction between domains through the substrate, which is responsible for the formation of the domain pattern, weakens on decreasing the film thickness. An important manifestation of this phenomena is the narrowing of the interval of existence of the a/c -variant on decreasing the films thickness as clearly seen in Fig. 9.3.11. The implication of this phenomenon for our problems is that the domain contribution to the permittivity should increase in decreasing film thickness. Quantitatively, this thickness effect (see Eq. (9.3.60)) is incorporated into the Roytburd's theory by substitution $u_{12} \left(1 - \sqrt{h_0/h}\right)$ for u_{12} where h_0 is the critical thickness defined by Eq. (9.3.56). For the domain contribution to permittivity, this translates into a $1/\left(1 - \sqrt{h_0/h}\right)$ times increase in κ_{ij}^{dom} . One should mention that the practical use of his result is very limited since the Roytburd's theory is strictly applicable at roughly $h > 30h_0$ so that only a very small ($< 2\%$) thickness-dependent variations of the κ_{ij}^{dom} is legible to be described by it. To check whether the expected trend can lead to significant increase on κ_{ij}^{dom} , a more involved mathematical analysis of the problem is needed. Such analysis has been offered by Pertsev with coworkers (1996).

They have shown that indeed a decrease in h can lead a substantial amplification of the domain contribution to the permittivity. Their calculations yielded a 100 times increase in κ_{ij}^{dom} in films of PbTiO_3 with $h \approx h_0$ and for a value of the relative coherence strain allowing the existence of the a/c -domain pattern for such small h . It is, however, worth mentioning that an experimental observation of this phenomenon seems to be a very difficult task because of a too small film thickness required: According to the estimates from Sect. 9.3.3, at $h \approx h_0$, the film should be thinner than the domain walls.

The above consideration can be readily extended to the case of the a_1/a_2 -pattern, which is possible in the same kind of epitaxial films (see Fig. 9.2.1). It leads to results qualitatively identical to those obtained for the a/c pattern. Specifically, now, using the results of Eqs. (9.3.46) and (9.3.47), we find

$$\kappa_{ij}^{\text{dom}} = \begin{pmatrix} A_a & A_a & 0 \\ A_a & A_a & 0 \\ 0 & 0 & 0 \end{pmatrix} \quad A_a = \frac{(1 + \nu)P_S^2}{2E\epsilon_0\epsilon_T^2} \quad (9.6.36)$$

instead of (9.6.35). Comparing (9.6.35) with (9.6.36) we see that the magnitude of the effect is a factor of $2(1 - \nu)$ smaller for the case of the a_1/a_2 -pattern. For the component κ_{11}^{dom} for PbTiO_3 , this makes a factor of about 1.4. Concerning the thickness effects, no results of more advanced calculations for the polarization response of the a_1/a_2 -pattern are presently available.

The results presented above were obtained in the approximation where a variation of the spontaneous polarization due to the average stress in the film was neglected. This effect was incorporated into the theory by Koukhar et al. (2001). The results obtained within this theory are illustrated in Fig. 9.6.5 where the lattice and domain contributions to the dielectric permittivity of a (001) PbTiO_3 epitaxial film are shown as functions of the parent misfit strain at room

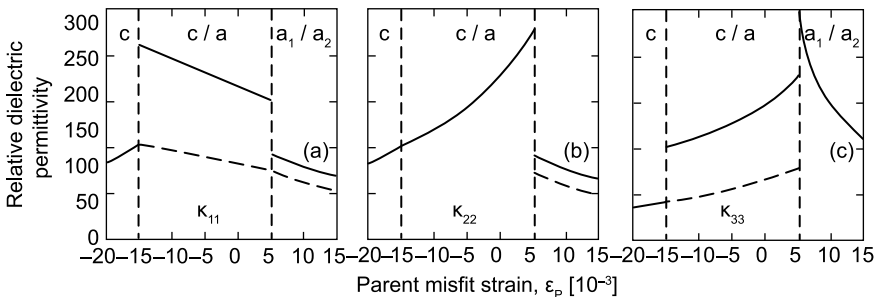


Fig. 9.6.5 Dependences of the relative permittivity of a (001) PbTiO_3 film on the parent misfit strain ϵ_p calculated for temperature of 25 °C. The dashed lines show the components of permittivity of PbTiO_3 films with pinned domain walls. In the intervals where no dashed lines are shown, the domain contributions are absent and the solid lines show the lattice contributions to the permittivity. After Koukhar et al. (2001)

temperature. Comparing the plots shown in this figure with the prediction of the simple theory (domain contributions evaluated above should be compared to the difference between the dashed and solid lines) we see that the mean-field approach provides a good approximation to the results of more exact theory by Koukhar et al.

9.6.5 Extrinsic Contribution—Electrostatic Effects

The extrinsic (domain) contribution to the dielectric permittivity of a ferroelectric thin film may be affected by electrostatic effects. This happens when the electric field in the film is not fully controlled by the potential difference between the electrodes of the capacitor but also is sensitive to variations of the domain pattern. This situation readily occurs when the ferroelectric capacitor contains a passive electrode-adjacent layer, so that the field in the ferroelectric differs from the applied one by the depolarizing field. A simple and general approach to this problem is to consider the ferroelectric and the passive layer as two capacitors connected in series. In the previous section, this approach was applied to the analysis of switching. Though simple and physically transparent, this approach is limited since it deals with values of the electric field and polarization averaged over the capacitor area. This description may not be adequate when the ferroelectric film contains an array of domains crossing the film from one electrode to the other (the so-called through domains). As was discussed in Sect. 9.4, an adequate description of this system requires taking into account not only the aforementioned average values of the electrical variables but also their stray components. In that Section, we have considered the theory of the equilibrium domain pattern in a ferroelectric capacitor containing passive electrode-adjacent layers and an array of “through” 180° domains (see Fig. 9.4.1) to reveal an important role of stray electric fields in this phenomenon. As was shown by Kopal et al. (1999) (see also later works by Bratkovsky and Levanyuk, 2000a and 2001c) stray fields can also essentially control the small-signal dielectric response of this system so that the simple in-series capacitors approach may readily fail in its original formulation. However, a further analysis of the problem by Mokry et al. (2004) showed that, for a typical experimental situation of dense domain patterns and a finite wall mobility, the in-series capacitors formula remains valid though with a modified value (i.e., different from the real value of the material) of the permittivity of the passive layer.

Let us consider the linear dielectric response of the aforementioned “passive layers” system (see Fig. 9.4.1). Specifically, following Mokry et al. (2004) we will address the situation of a non-poled domain pattern of period W , which however may be different from its equilibrium value. This is a reasonable approximation to a realistic situation in the system, since reaching the equilibrium domain configuration can easily be impeded by coupling of domains with crystalline defects in the ferroelectric. The out-of-plane component of the permittivity of the

ferroelectric itself $\kappa = \kappa_m + \kappa_c$ is equal to the sum of the intrinsic lattice contribution, κ_c , and the extrinsic of one, κ_m , which is associated with the domain wall motion controlled by coupling between the wall and crystalline defects (defect pinning). In a capacitor containing the ferroelectric and passive layers, there are three factors that govern the linear dielectric response: (i) the rigidity of the crystalline lattice, which controls the intrinsic contribution κ_c , (ii) the electrostatic energy of system, and (iii) the coupling of the domain walls with the imperfections of the system, which controls the extrinsic contribution κ_m . In terms of the thermodynamic potential, the description of the linear response requires taking into account only the terms linear and quadratic in the net spontaneous polarization of the ferroelectric

$$P_N = \alpha P_S - (1 - \alpha) P_S, \quad (9.6.37)$$

where α is the volume fraction of the positively poled domains in the pattern. (In the considered situation, α follows the variation of the applied field staying close to 1/2.) The part of this potential related to the electrostatic energy of system can readily be found by expanding in P_N the earlier obtained expression Eq. (9.4.3). This expansion yields

$$G_{el}/S = h \left(\frac{P_N^2}{2\varepsilon_0\kappa_{el}} - \frac{P_N V/h}{1 + \kappa_c d/(\kappa_d h)} \right), \quad (9.6.38)$$

where

$$\frac{1}{\kappa_{el}} = \frac{d}{\kappa_d h + \kappa_c d} + \frac{2W}{\pi h} \sum_{n=1}^{\infty} \frac{(-1)^n}{n D_n} \quad (9.6.39)$$

with D_n coming from Eq. (9.4.4); see for the rest of notations Sect. 9.4.1. Here the parameter $1/\kappa_{el}$ has the meaning of the contribution to the inverse dielectric susceptibility of the system, which is controlled by the electrostatic energy of the domain pattern.

The part of the thermodynamic potential of the system related to the domain wall pinning by defects can be presented in the following form:

$$G_m/S = \frac{h P_N^2}{2\varepsilon_0 \kappa_m}, \quad (9.6.40)$$

where κ_m is the extrinsic contribution to the permittivity of the ferroelectric itself already introduced. (Below we will justify this relation.) Thus, for the thermodynamic potential of the system associated with the domains we have

$$G_{tot}/S = h \left(\frac{P_N^2}{2\varepsilon_0 \kappa_w} - \frac{P_N V/h}{1 + \kappa_c d/(\kappa_d h)} \right), \quad (9.6.41)$$

where

$$1/\kappa_w = 1/\kappa_{el} + 1/\kappa_m. \quad (9.6.42)$$

The response of the net spontaneous polarization P_N to the voltage V applied to the capacitor can be found from the condition for the minimum of the thermodynamic potential G_{tot} :

$$\partial G_{tot}/\partial P_N = 0. \quad (9.6.43)$$

Now, the validity of Eq. (9.6.40) can be readily verified. In the absence of the passive layer ($d \rightarrow 0$) the restoring force associated with the electrostatic energy is expected to vanish ($1/\kappa_{el} \rightarrow 0$); this can be formally shown using Eqs. (9.6.39) and (9.4.4). Thus, from Eqs. (9.6.41), (9.6.42), and (9.6.43) we get $P_N = \varepsilon_0 \kappa_m V/h$ in accordance with the definition of κ_m .

To calculate the effective permittivity of the system, $\kappa_{eff} \equiv C(h+d)/\varepsilon_0 S$ where C is its capacitance, one uses Eqs. (9.6.38), (9.6.39), (9.6.40), (9.6.41), (9.6.42), and (9.6.43) and the relation

$$C/S = \frac{P_N/V + \varepsilon_0 \kappa_c}{1 + \kappa_c d/(\kappa_d h)} \quad (9.6.44)$$

that can be obtained from the Poisson equation (Kopal et al., 1999; Bratkovsky and Levanyuk, 2001c). Finally, Eqs. (9.6.38), (9.6.39), (9.6.40), (9.6.41), (9.6.42), (9.6.43), and (9.6.44) yield (Mokry et al., 2004)

$$\frac{h+d}{\kappa_{eff}} = \frac{h}{\kappa_c + \kappa_w} + \frac{d}{\kappa_d} \left[1 - \left(\frac{\kappa_w}{\kappa_c + \kappa_w} \right)^2 \frac{h}{h+h_c} \right], \quad (9.6.45)$$

where

$$h_c = \frac{d}{\kappa_w} \frac{\kappa_c^2}{\kappa_c + \kappa_w}. \quad (9.6.46)$$

Though formula (9.6.45) is similar to the in-series capacitors formula given by Eq. (9.6.1), the contribution of domain wall motion to the dielectric response of the system κ_w contains the function κ_{el} , which, in general, depends on the film thickness. Thus, in general, Eq. (9.6.45) can exhibit a thickness dependence of the effective permittivity qualitatively different from that of the in-series capacitors formula. However, in the case of practical interest, where the domain pattern is dense ($W < h$) and the passive layer is thin ($d < h$), this relation can be simplified down to the following form (Mokry et al., 2004), which we will refer to below as *dense pattern approximation*:

$$\frac{S\varepsilon_0}{C} \equiv \frac{h+d}{\kappa_{\text{eff}}} = \frac{h}{\kappa} + \frac{d}{\kappa_{\text{mod}}}, \quad (9.6.47)$$

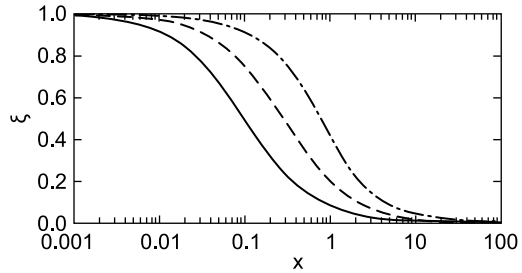
where

$$\kappa_{\text{mod}} = \frac{\kappa_d}{1 - (\kappa_m/\kappa)^2 \xi(2d/W)}, \quad (9.6.48)$$

$$\xi(\tau) = \frac{2\kappa_d}{\pi\tau} \sum_{n=1}^{\infty} \frac{(-1)^n/n}{\kappa_d \coth(n\pi\tau) + \sqrt{\kappa_c\kappa_a}}. \quad (9.6.49)$$

Here $\xi(\tau)$ is a function decreasing from 1 to 0 with increasing τ . The plots of this function for three sets of parameters of the problem are shown in Fig. 9.6.6.

Fig. 9.6.6 Function $\xi(x)$ given by Eq. (9.6.49) plotted for $\kappa_d = \sqrt{\kappa_c\kappa_a}$ (*dash-dotted line*), $\kappa_d = 0.3\sqrt{\kappa_c\kappa_a}$ (*dashed line*), and $\kappa_d = 0.1\sqrt{\kappa_c\kappa_a}$ (*solid line*). After Mokry et al. (2004)



Thus, one arrives at the simple in-series capacitors formula, Eq. (9.6.1), where, however, the real value of the passive layer permittivity κ_d is replaced by its apparent value κ_{mod} . The physical reason for the simplification of the model is the following. In the case of a dense domain pattern, the stray fields created by the periodic charge distribution at one electrode essentially decay with the distance from this electrode. For this reason, the distribution of the electric field in the vicinity of an electrode (closer to the electrode than W , which is $\ll h$) can be associated with a capacitor whose capacitance is independent of the film thickness. Thus, the film behaves as a ferroelectric capacitor corresponding to the “bulk” of the film connected in series with two capacitors which are associated with the distribution of the electric field in the vicinity of the electrodes.

Comparing the result obtained, Eq. (9.6.47), to the simple “in-series” formula, Eq. (9.6.1), we see that though the slope of the h dependence of the inverse capacitance is the same (the permittivity of the ferroelectric itself), in the polydomain case, the offset of this dependence brings information not only on the permittivity of the passive layer κ_d but also on the period of the domain pattern and the distribution of the dielectric response of the ferroelectric material itself between the intrinsic, κ_c , and extrinsic, κ_m , contributions.

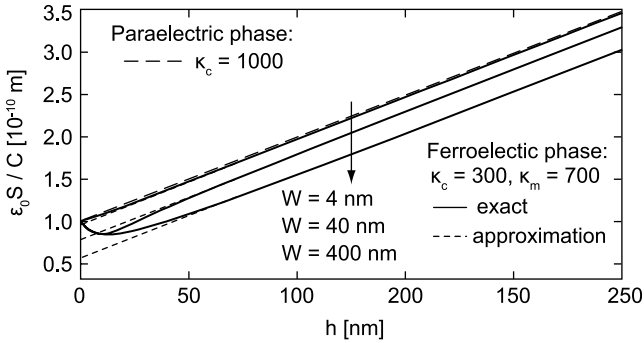


Fig. 9.6.7 Effect of domain period W on the offset of the film thickness (h) dependence of the factor S_{ϵ_0}/C for the model discussed in Sect. 9.6.5. The *dashed line* corresponds to the simple in-series capacitors formula, i.e., to Eq. (9.6.47) with $\kappa_{\text{mod}} = \kappa_d$; physically, this corresponds to the response in the paraelectric phase. The *thinner dashed lines* marked with “approximation” show the results obtained in the dense pattern approximation, i.e., using Eqs. (9.6.47), (9.6.48), and (9.6.49). The *solid lines* correspond to the exact formulae, i.e., to Eq. (9.6.45), (9.6.46), and (9.6.39). The calculations have been performed for $\kappa_d = 20$ and $d = 2 \text{ nm}$. After Mokry et al. (2004)

The effect of domain period on the offset of the h dependence of the inverse capacitance predicted by Eq. (9.6.47) is illustrated in Fig. 9.6.7. It is seen that, in the polydomain case, this offset can be substantially smaller than that predicted by the simple “in-series” formula (shown with dashed line). In this figure, the predictions of the dense pattern approximation, Eq. (9.6.47), are compared to those of the exact formula Eq. (9.6.45). We see that, for dense domain patterns, i.e., for $h > W$, the former provides a very good approximation.

The sensitivity of the extrapolated offset of the h dependence of the inverse capacitance to the distribution of the dielectric response of the ferroelectric material between the extrinsic and intrinsic contributions is illustrated in Fig. 9.6.8. It is seen that the effect can be appreciable.

Two qualitative predictions following from the results obtained above are worth mentioning. First, since $\xi(d/W) \rightarrow 0$ as $d/W \rightarrow \infty$, in the limit of a thick passive layer $d \gg W$, the dense pattern approximation, Eq. (9.6.47), reduces to the simple in-series capacitors formula with the true permittivity of the passive layer, Eq. (9.6.1), disregarding the other parameters of the system. For the special case of infinite domain wall mobility, i.e., in the limit $\kappa_m \rightarrow \infty$ (so that $\kappa \rightarrow \infty$), this result reduces to the relation $S_{\epsilon_0}/C = d/\kappa_d$ derived by⁴⁷ Kopal et al. (1999).

The second prediction relates to the situation where the domain period significantly exceeds the thickness of the passive layer, i.e., $W \gg d$. In this case, $\xi(d/W) \rightarrow 1$ so that Eqs. (9.6.47) and (9.6.48) can be simplified as

⁴⁷ This relation was also later obtained by Bratkovsky and Levanyuk (2000a). However, in this paper it was argued that it holds not only for $d \gg W$. This statement contradicts the results of detailed calculations given in the original paper by Kopal et al. (1999).

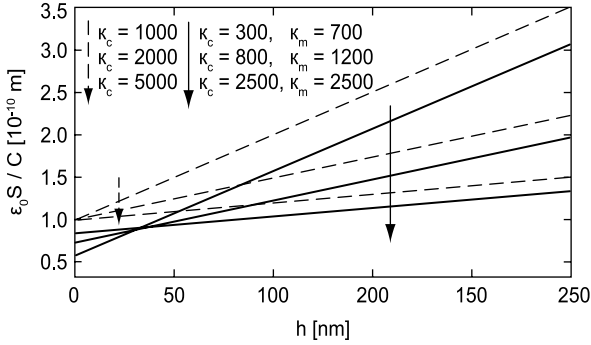


Fig. 9.6.8 Graph shows how the offset of the thickness dependence of the factor $S\varepsilon_0/C$ is affected by the distribution of the dielectric response of the ferroelectric $\kappa = \kappa_m + \kappa_c$ between the intrinsic κ_c and extrinsic κ_m contributions, for a dense domain pattern with $W = 400$ nm. The *dashed line* corresponds to the in-series capacitors formula, while the *solid line* to the dense pattern approximation. The calculations have been performed for $\kappa_d = 20$ and $d = 2$ nm. After Tagantsev and Gerra (2006)

$$\frac{h+d}{\kappa_{\text{eff}}} = \frac{h}{\kappa} + \frac{d}{\kappa_d} \left(1 - \frac{\kappa_m^2}{(\kappa_c + \kappa_m)^2} \right). \quad (9.6.50)$$

It is clear from this equation that when the dielectric response is dominated by the extrinsic contribution, i.e., $\kappa_m \gg \kappa_c$ so that $\kappa_m/(\kappa_m + \kappa_c) \rightarrow 1$, the “suppressive” effect of the passive layer drastically weakens.

This phenomenon can be rationalized as follows. The restoring force keeping the domain parent in the unpoled state is controlled by the electrostatic energy of the bound parent charges of the spontaneous polarization at the ferroelectric/passive interface, $U_{\text{el}}(\alpha)$. For the situation considered, i.e., for $h \gg d$, this energy is close to that of the electric field in the passive layer. Thus, it can be approximated as $U_{\text{el}}(\alpha) \propto \alpha \langle E_+^2 \rangle + (1 - \alpha) \langle E_-^2 \rangle$ where $\langle E_+^2 \rangle$ and $\langle E_-^2 \rangle$ are the average of the squares of the electric field in the segments of the passive layer contacting the ends of the positively and negatively poled domains. In the limit $W \gg d$, the absolute values E_+ and E_- are very close to $P_S/(\varepsilon_0 \kappa_d)$, except for small regions close to the domain walls and virtually independent of α . This implies $U_{\text{el}}(\alpha)$ independent of α in the limit $d/W \rightarrow 0$ and vanishing of the “suppressive” effect of the passive layer. In contrast in the opposite case $W \ll d$, $E_+ \approx E_- \approx P_N/(\varepsilon_0 \kappa_d)$, and $U_{\text{el}}(\alpha) \propto P_N^2 \propto (2\alpha - 1)^2$. Now it is this strong α dependence of $U_{\text{el}}(\alpha)$ that controls the “suppressive” effect of the passive layer leading to the “in-series” formula, Eq. (9.6.1).

Numerical simulations illustrating the reduction of the “suppressive” effect of the passive layer at $W \gg d$ can be found, for the case $\kappa_m/(\kappa_m + \kappa_c) = 1$, in the paper by Bratkovsky and Levanyuk (2001c).

A prediction of the theory that can be checked experimentally is the temperature dependence of the extrapolated offset of the $S\varepsilon_0/C$ vs. h dependence.

Namely, in films where the dielectric data in the paraelectric phase suggest the presence of a passive layer, in the ferroelectric phase, this offset may be essentially temperature dependent due to the expected temperature dependence of the ratio κ_m/κ_c . According to Mokry et al. (2004) the dielectric behavior of thin films of ferroelectric copolymer of vinylidene fluoride and tetrafluoroethylene might be interpreted in terms of this scenario.

The model discussed above has practical significance: On the one hand, it shows the possibility of justifying the classical “in-series” formula for the case of films with dense domain patterns (though with an effective permittivity of the passive layer); on the other hand, it reveals some non-trivial features of the system, such as the reduced “suppressive” action of the passive layer on the extrinsic contribution to the permittivity. At the same time, when using the results provided by this model one should recognize its limitations. Among these the most important seems to be the neglect of possible domain wall bending and that of possible impact of the charge transport across the passive layer, which has been discussed in Sects. 9.5.2 and 9.5.3.

9.7 Polarization Fatigue in Thin Ferroelectric Films

This section is devoted to the phenomenon of *polarization fatigue*, which consists of deterioration of switching ability of a ferroelectric capacitor after it has been subjected to multiple polarization reversals. This phenomenon is typically characterized by monitoring the switchable and non-switchable polarizations, P_{sw} and P_{ns} (see Sect. 9.5.2 for the definitions), as functions of the number of switching cycles N . Reduction of P_{sw} or $P_{sw} - P_{ns}$ with N is used to quantify the polarization fatigue of the capacitor.

From the point of view of classical physics of ferroelectrics, the polarization fatigue should not necessarily take place in ferroelectric capacitors. We mean that in terms of the classical switching scenario (nucleation of reverse domains, their forward growth, their sideways expansion, and merging) there is no principal limitation on the multiple repetition of the switching cycle. The fact that the polarization fatigue does often occur in real ferroelectric capacitors indicates that the switching cycling induces some modifications in the system, which are beyond the simple switching scenario. In very general terms, these modifications can be associated with creation of new imperfections in the system or/and a redistribution of those already existing in it. The polarization fatigue, then, can be viewed as a consequence of the “damage” imposed by these defects on the switching process in the ferroelectric. Thus, when exploring the phenomenon of polarization fatigue, we can distinguish two questions: (i) How does multiple electric stress of the capacitor lead to creation or redistribution of the imperfections? (ii) What are these imperfections and how do they affect the switching performance of the ferroelectric capacitor? In this section we will discuss these questions.

Most of the experimental and theoretical studies on polarization fatigue have been performed for ferroelectric-thin-film-based capacitors since they have been found suitable for memory applications based on the detection of the difference $P_{sw} - P_{ns}$. These studies led researchers to realize that it is a complicated phenomenon extremely sensitive to the materials of the ferroelectric and electrodes as well as to the conditions of polarization cycling (temperature, driving field amplitude, switching pulse length, etc.). In addition, the body of experimental data on polarization fatigue is very contradictory (see for review, Tagantsev et al., 2001b) strongly suggesting that this phenomenon is controlled by numerous mechanisms of different nature. At the moment of writing this book, though a certain progress in understanding of these mechanisms is available, one should recognize that this understanding is still limited. For this reason, a consistent overall picture of polarization fatigue in ferroelectric-thin film capacitors cannot be presented in this book. On the other hand, the ideas, approaches, and models developed in the field are worth the readers' attention. We will discuss these in the present section and support them with available experimental data on $\text{Pb}(\text{Zr},\text{Ti})\text{O}_3$ (PZT)-based thin films.

9.7.1 How Can Imperfections Influence Polarization Switching in Ferroelectric Capacitor?

Testing the switching performance of a ferroelectric capacitor, one typically monitors the switchable polarization, P_{sw} , which mainly controls the difference $P_{sw} - P_{ns}$ essential for the memory applications. In this section we will discuss how P_{sw} can be reduced by the imperfections appeared or redistributed in the ferroelectric capacitor during switching cycling. In answering this question, the following possibilities can be distinguished: (i) reduction of the measured polarization due to a decrease in the effective electrode area; (ii) reduction of the electric field seen by the ferroelectric; (iii) the polarization switching itself becomes more difficult. Let us consider these possibilities.

9.7.1.1 Reduction of the Effective Electrode Area

An increasing (with the number of switching cycles) fraction of the volume of a capacitor can cease to contribute to the total polarization response as a result of burning or delamination of the electrode(s) provoked by voltage cycling. Formally this process is equivalent to a reduction of the area of the ferroelectric capacitor. Monitoring the evolution of several parameters of the capacitor during fatigue cycling one can easily identify this mechanism. If this mechanism governs the fatigue, all of the polarization parameters of the P - E loop, e.g., P_r , P_{sw} , and P_{ns} (defined in Fig. 9.5.2) as well as the small signal dielectric constant

and the conduction of the sample should scale down by the same factor. Manifestations of this kind of mechanism have been demonstrated in PZT thin films (Johnson et al., 1990; Colla et al., 1998b) by analyzing a correlation between conduction, dielectric constant, and P_r .

Though this mechanism can be a reason for a reduction of switchable polarization of a ferroelectric capacitor, it can be typically eliminated by optimizing electrode deposition, so that it does not seem to be the matter of concern for practical applications of ferroelectric films.

9.7.1.2 Reduction of the Electrical Field Seen by Ferroelectric

If the switching cycling results in the appearance of a electrode-adjacent low dielectric constant or non-switchable layer (passive layer) in the ferroelectric capacitor, the field seen by the ferroelectric will be different from that applied. The appearance of such layer was put forward as a possible fatigue mechanism by Larsen et al. (1994). The description of the impact of the passive layer on the switching performance of a ferroelectric capacitor was discussed in Sect. 9.5.2 where two models were considered. In these models the passive layer was treated (i) either as absolutely insulating dielectric layer or (ii) as a dielectric layer with threshold conduction. According to the first model the growth of the passive layer will result in a reduction of remanent (and switchable polarization) and a tilt of polarization loop. These features are typical for the evolution of the hysteresis loop in fatigued capacitors (Paton et al., 1997; Pawlaczyk et al., 1995; Majumder et al., 1997; Al-Shareef et al., 1996). However, modeling the whole set of parameters of the hysteresis loop in terms of growing passive-layer mechanism has not been found in reasonable agreement with experimental observation (Tagantsev et al., 1995b). The description of switching in terms of the second model is focused on the behavior of coercive field of the polarization loop. According to this model, a growing passive layer should lead to an increase in the coercive field, which does not seem to be typical for polarization fatigue. Thus, for the moment, it is difficult to judge whether the growing passive-layer mechanism is relevant to the polarization fatigue taking place in ferroelectric thin films.

9.7.1.3 Mechanisms of Switching Modification

The third principal possibility for the reduction of switching polarization during switching cycling is related to a change in the switching process itself. The switching process can be divided into two stages: (i) nucleation of new (reverse) domains and (ii) growth of existing domains. As discussed in Sect. 8.7.2 the domain nucleation in defect-free ferroelectrics typically has too low probability to provide realistic switching rates. In real materials, the switching from a poled state should start either at sites where the activation energy of the new domain nucleation is locally reduced (due to defects or a special local electrode

geometry) or at residuals of the reverse domains, which have survived at the end of the polarization reversal due to a special environment. Both types of sites may play the role of *seeds* for the formation of new domains inside single-domain regions. In this context, the suppression of switching should be associated with blocking the growth of these seeds.

One may consider two ways this process can occur, corresponding to two basic mechanisms of switching suppression. These mechanisms can be summarized as follows. First, a seed gives a macroscopic domain whose boundaries are pinned (somehow immobilized). If this domain does not contain seeds of reverse domains, the area occupied by the domain does not contribute to switching anymore. This is the so-called “wall pinning” mechanism. Second, in a region of the film, all the seeds of domains with reverse polarization are inhibited (somehow made unable to produce macroscopic domains). As a result, this area ceases to contribute to switching. This is the scenario of the so-called “seed inhibition” mechanism. There exists also the third reason to make the switching more difficult, which is related to electrostatic effect of charges trapped at the ferroelectric/electrode interface. This can be called “local imprint” mechanism because it is conceptually close to that of imprint. Let us consider below these mechanisms.

9.7.1.4 Wall Pinning Mechanism

Under certain conditions, the wall pinning (immobilizing domain walls caused by their interaction with defects) results in suppression of the switching ability of a ferroelectric domain. These conditions are (A) all the walls surrounding the domain are immobilized and (B) the domain does not contain seeds for reverse domain formation. If condition (B) is not met, new mobile domain walls can appear to allow further switching. In this context, the fatigue is considered as a process of domain wall pinning by defects, density of which is great enough to satisfy the two aforementioned conditions. An essential feature of the fatigued state produced by this mechanism is a dense domain structure. According to condition (B) the fatigued state should be close to the “one domain per one seed” structure. The virgin and aforementioned fatigued states of the capacitor are schematically illustrated in Fig. 9.7.1a and b.

The nature of the pinning which contributes to this mechanism is believed to be the interaction between the bound charges on the domain walls and the mobile carriers (Warren et al., 1995b). The bound charges of the wall appear due to a local violation of the condition of wall electroneutrality, $\text{div}\vec{P} = 0$. These charges appear, for instance, on a 180° wall, which is not exactly parallel to the polarization direction in the domains (Fig. 9.7.1b). The electrostatic coupling between the bound charge of the wall and mobile carriers results in the formation of complexes, “wall + compensating charge.” This complex is immobilized if the carriers of the complex are trapped at deep levels in the forbidden gap of the ferroelectric. One should note that the wall pinning mechanism can also take place if non-charged defects migrate to walls and

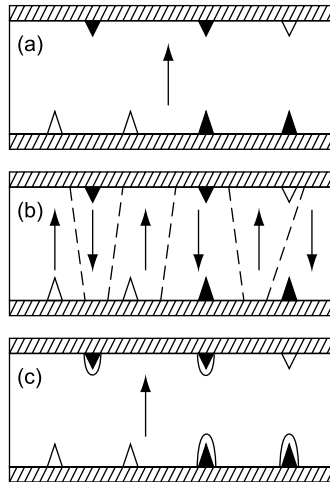


Fig. 9.7.1 Two scenarios of fatigue via modification of the switching process. (a) Schematic drawing of a section of a ferroelectric thin film capacitor in the virgin state. The electrodes are shown with *hatched pattern*. The active seeds of nucleation of new domains with the upward and downward directions of the polarization are shown with *open* and *filled triangles*, respectively. The *arrows* show the direction of the spontaneous polarization. (b) Schematic drawing of the same section in the state fatigued according to the “wall pinning” scenario. *Dashed lines* stand for domain walls. (c) Schematic drawing of the same section in the state fatigued according to the “seed inhibition” scenario. The *circled triangles* stand for the nucleation seeds which have become inactive. After Tagantsev et al. (2001b)

pin them. However, this mechanism is not usually discussed as less efficient compared to the first one.

This wall pinning mechanism for suppression of polarization reversal has been proposed by a group from Sandia National Laboratories (Warren et al., 1995b).

9.7.1.5 Seed Inhibition Mechanism

The alternative scenario for suppression of the polarization reversal is related to the first stage of switching—nucleation of reverse domains. The key difference between this scenario and that discussed above is that the switching ability of the seeds is now suppressed in the embryonic state before they create a macroscopic domain. The basic points of this scenario are as follows:

- (i) A ferroelectric film is divided into regions, which switch independently. This means that, in each region, the switching is provided by a finite number of seeds belonging to it.
- (ii) A given “independent” region of the film loses its ability to switch when all the nucleation seeds for one domain polarity are blocked in their embryonic state. This is schematically shown in Fig. 9.7.1c.

- (iii) The active seeds are located at the ferroelectric/electrode interfaces. There are the following reasons for this. First, near the interface, both the usually elevated defect density and the electrode roughness create conditions for formation of nucleation seeds. Second, as already discussed in Sect. 9.5.2, the electric field near the electrodes is expected to be different from the applied field by a value of the depletion-effect-induced built-in electric field that has different signs at the two electrodes. Thus, for each sense of switching, the most favorable conditions for the growth of the seeds take place near the electrodes, specifically, for one sense of switching, near one electrode and, for the other sense of switching, near the other. At the “favorable” electrode the applied field sums up with the built-in one.
- (iv) Fatigue is associated with blocking seeds by ionic or electronic defects accumulated near the interface. These can be created by charges injected from the electrode or the charges that can arrive from the bulk of the material as a result of electromigration during the electric stressing of the capacitor.

This, seed inhibition, mechanism for suppression of polarization reversal has been proposed by a group from Swiss Federal Institute of Technology (EPFL) (Colla et al., 1997).

9.7.1.6 Experimental Evidence for Wall Pinning and Seed Inhibition Mechanisms

Analysis of the macroscopic manifestations of these two mechanisms can readily reveal a common feature which is unfortunately shared with the passive layer scenario making identification of the mechanisms difficult. Namely, all three scenarios predict a tilt of polarization loop during fatigue cycling. This trend has been already discussed for the passive layer scenario. As for the other two scenarios it can be explained as follows. Fatigue usually occurs via an inhomogeneous (region-by-region) loss of the switching ability of the film. Thus, roughly, the integral loop of the sample corresponds to a weighted average of the original loop of the virgin sample (from working regions) and hysteresis-free response of the areas where the switching is blocked. Clearly, the obtained integral response yields a polarization loop more tilted than the original one. Thus, using only data on the loop tilt these three scenarios cannot be distinguished. However, as has been demonstrated by Klissurska et al. (1997), one can really distinguish between the passive layer scenario and the other two by monitoring a set of parameters of the polarization loop rather than just its tilt. To the best of our knowledge this method has not been applied for analysis of fatigue data.

An interesting approach has been proposed by Colla et al. (1998c) and Taylor et al. (1999) for experimental discrimination between the wall pinning and the seed inhibition mechanisms. It is based on salient features of these mechanisms listed below.

- (i) The key step of the wall pinning mechanisms is the migration of free carriers toward the bound charges of the domain walls. This process requires time so that the mechanism should be more efficient the longer the period of time during which the system is exposed to the charge migration. In other words, the slower the switching, the stronger the fatigue caused by the wall pinning mechanisms. No dependence of this type is expected for the seed inhibition mechanism.
- (ii) For the same reason, the fatigue associated with the pinning scenario should be very sensitive to the shape of the driving pulses. Rectangular pulses should produce less polarization degradation than those of the same length but triangular or of a rounded form. The most damaging should be pulses with a long plateau on the level of the coercive field since during this plateau the sample contains the maximum concentration of domain walls. However, no effect of this type is expected for the seed inhibition mechanism.
- (iii) The fatigued state created by the seed inhibition mechanism may contain relatively large single-domain regions corresponding to the regions of independent switching since one seed may be responsible for initiation of switching in a large region. In contrast, the fatigued state created by the wall pinning mechanism should contain a high concentration of domains with immobilized walls. In this case, in the poled state, the total area of domain walls of the fatigued material should be much greater than that of the virgin material. Though inefficient for switching, these walls should still contribute to the small-signal dielectric constant of the film. Thus, the polarization fatigue, if it follows the pinning scenario, should be accompanied by an increase in the small-signal dielectric permittivity measured in the poled state.
- (iv) The increase in the concentration of pinned domain walls in the sample corresponding to the wall pinning mechanism can also be detected by analyzing the behavior of constant α in the relation for nonlinear dielectric response in the case of Rayleigh-type dielectric response (see Eqs. (8.7.41) and (8.7.42)). This constant is conditioned by irreversible domain wall displacements and, if the population of pinned domain walls increases, α should increase as well.

Based on the features listed above several experimental tests have been performed.

A clear manifestation of the wall pinning mechanism can be revealed by using the sensitivity of this mechanism to the time during which the capacitor is in a state containing the maximum amount of the domain walls. That was done in fatigue experiments performed at a very slow cycling on relatively thick (1,400 nm) PZT films (Colla et al., 1998c). As shown in Fig. 9.7.2a, a variation of the profile of the fatiguing signal from rectangular to that with a plateau at the coercive field level dramatically changes the fatigue rate. The profile with the plateau corresponds to much longer time during which the capacitor is exposed to a field close to the coercive field, where the sample contains the maximal amount of the domain walls. The observed correlation between the profile of the driving field and the fatigue rate is consistent with the “wall pinning” mechanism.

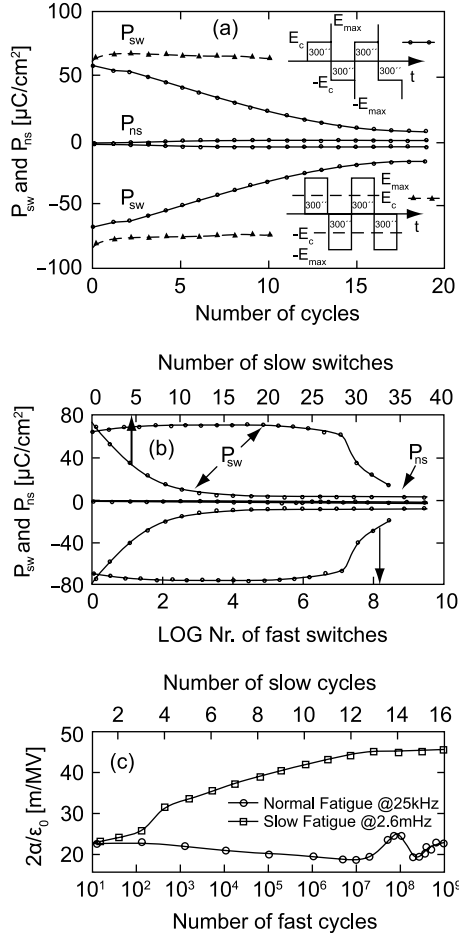


Fig. 9.7.2 (a) Suppression of switchable polarization by square ac pulses and by cycling with a long exposure at a field close to E_c . The pulse duration is 300 s. After Colla et al. (1998c). (b) Two types of suppression of switching polarization: by ac cycling at 30 kHz (*lower axis*; logarithmic scale (!)) and by slow cycling at 1.7 mHz, (*upper axis*; linear scale (!)). After Colla et al. (1998c). (c) Evolution of the Rayleigh coefficient α as a function of number of fast (*squares*) and slow (*circles*) switching cycles. After Taylor et al. (1999)

Another way to identify the “wall pinning” mechanism is to monitor increasing population of the pinned domain walls in the fatigued state. Features (iii) and (iv) from the above list can be employed for such monitoring. The corresponding tests have been performed on 1,400 nm thick PZT films. One has monitored the dielectric permittivity in the poled state, κ_p , during electrical stressing with a wave of triangular shape at a very low frequency (1.7 mHz) and with a square-wave profile at 30 kHz (Colla et al., 1998c). It was found that in the slow cycling case, the polarization degradation is very fast (see Fig. 9.7.2b)

and is accompanied by an increase in κ_p (about 15%). In the case of high-frequency cycling, the polarization degradation is much slower and is accompanied by a slight decrease in κ_p during the cycling. In identical experiments, one has also monitored the Rayleigh constant α . It was found (see Fig. 9.7.2c) that α is really sensitive to fatigue treatment (it increases during cycling) only in the case of very slow cycling (Taylor et al., 1999). These two experiments suggest that the mechanisms governing fatigue in the two considered regimes are very different and that the case of slow cycling is consistent with the wall pinning mechanism. In the case of high-frequency cycling, the fatigue was attributed to the seed inhibition mechanism (Colla et al., 1998c). However, one should note that this test does not provide enough information to distinguish between the seed inhibition mechanism and a formation of a switching-induced passive layer.

A fingerprint of the seed inhibition mechanism is the partition of fatigued films into large single-domain frozen areas. A micron-size pattern of this type has been observed (Colla et al., 1998c) by using scanning force microscopy. A more detailed discussion of investigations of polarization fatigue by means of scanning force microscopy will be given in Sect. 9.8.

It should be stressed that the clear evidence for the participation of the wall pinning mechanism in polarization fatigue discussed above has been obtained by using a rather special material (1,400 nm thick PZT film) and special conditions of fatigue (very slow cycling with a pulse shape different from rectangular). However, the cycling performed with a square-wave voltage profile does not seem to activate this mechanism. According to Tagantsev et al. (2001a,b), in “normally thin” (100–300 nm) PZT films, even the use of low frequencies and special fatiguing profiles does not activate the wall pinning mechanism. These authors also conclude that, though being an efficient tool of artificial polarization suppression (e.g., in experiment involving combined action of dc field, illumination, and heat treatment—see the paper by Warren et al. (1995b)) the wall pinning mechanism does not play any significant role in polarization fatigue in PZT films of thickness typically used for memory applications (100–300 nm). This conclusion, however, contradicts that drawn from the data reported by Ramesh et al. (1992) and Majumder et al. (1997). These authors observed a frequency dependence of fatigue of the type expected for the wall pinning mechanisms in relatively thin films.

9.7.1.7 Fatigue as “Local Imprint”

One should also mention one additional mechanism that may be responsible for making switching more difficult. The key point of this scenario is that the fatigue corresponds to the appearance of regions in the ferroelectric capacitor where the screening charge (which originally has been on the electrodes) has partially moved into the ferroelectric and trapped there (Shur et al., 2001a). This means that, on the local scale, this mechanism of fatigue is basically equivalent to the injection-assisted imprint mechanism (see Sect. 9.5.3). If the trapped fraction of

screening charge is large enough, both the wall motion and nucleation of reversed domains can be substantially impeded in the region. In simple words, one can say that in these regions the ferroelectric polarization are pinned by the attraction between the polarization bound charge and the trapped screening charge. On the scale of the whole capacitors, the difference between the fatigue and imprint scenarios is that, in the imprinted state, the whole capacitor is imprinted in the same direction, whereas in the fatigued sample, these directions are not the same in different parts of it. Due to this similarity the considered fatigue mechanism can be called “local imprint” mechanism. This mechanism enables rather simple modeling of the dielectric properties in the fatigue states so that its relevance to the degradation phenomena in real ferroelectric capacitors, in principle, can be reliably established. For the moment, we would like to point out only one evident macroscopic manifestation of this phenomenon. According to this mechanism, the fatigue state can be roughly represented as a parallel connection of three types of capacitors which exhibit (i) the virgin polarization loop, (ii) loops with a positive voltage offset, and (iii) loops with a negative voltage offset. It is easy to conclude that the integral loops of the capacitors should be somehow pinched. Thus, an expected manifestation of this mechanism is progressive pinching of the polarization loop during fatigue treatment. To the best of our knowledge, this trend has not been experimentally observed. The available to date experimental data are not enough to judge the relevance of this mechanism to fatigue in real ferroelectric thin films.

9.7.2 What Are These Imperfections and How Do They Affect the Switching Performance of Ferroelectric Capacitor?

All of the mechanisms previously discussed (except for the electrode-degradation mechanism) involve a variation in the density of imperfections of the ferroelectric itself. In the case of the wall pinning mechanism, we have considered electronic free carriers as the “working imperfections” that block domain wall motion. Conceptually similar domain blocking scenario has been modeled by Brennan et al. (1994) who considered oxygen vacancy redistribution toward head-to-head (tail-to-tail) domain configurations. For the functioning of the “passive layer” and “seed-inhibition” mechanisms, an increase in the defect concentration near the ferroelectric/electrode interface is required. Two hypotheses have been put forward to provide such increase. First, it was suggested that the switching cycling leads to redistribution of the oxygen vacancies existing in the ferroelectric (Yoo and Desu, 1992; Scott et al., 1991). Second, it was suggested that the cycling leads to creation of new defects due to electron injection from the electrodes (Mihara et al., 1994; Stolichnov et al., 2000; Tagantsev and Stolichnov, 1999; Du and Chen, 1998). Below we briefly discuss these hypotheses basically following the critical analysis offered by Tagantsev et al. (2001b).

9.7.2.1 Oxygen Vacancy Redistribution Mechanism

Oxygen vacancies are natural and the most mobile ionic defects of perovskite materials like PZT. For this reason, the redistribution of oxygen vacancies has been put forward by many authors as the driving force of polarization fatigue (Yoo and Desu, 1992; Scott et al., 1991). These authors suggested that the depletion-induced built-in electric field is responsible for the oxygen vacancy accumulation at the ferroelectric/electrode interface. Oxygen vacancies are often involved in the interpretation of experimental data on polarization fatigue in terms of a concept that can be called “oxygen vacancy hypothesis.” This hypothesis implies, first, that an increase in oxygen vacancy concentration is in general detrimental for switchable polarization and, second, that the driving electrical field is responsible for the redistribution of these species. In principle, being appended with the “passive layer” or “seed inhibition” scenario this hypothesis may make the driving force element for a fatigue mechanism. However, there is very limited experimental support for this hypothesis. The strongest indirect argument in favor of this hypothesis is related to the fatigue endurance of PZT-containing capacitors with electrodes made of conductive oxides (e.g., SrRuO₃, RuO₂, IrO₂), which was found much better than that of the PZT capacitors with metallic (e.g., Pt) electrodes (Bernstein et al., 1993; Auciello et al., 1995; Cross et al., 1998). By assuming that oxide electrodes represent an efficient sink for oxygen vacancies, Al-Shareef et al. (1996) explained the positive effect of the oxide electrodes on the fatigue endurance of PZT capacitors as a result of reduction of the oxygen vacancy concentration in the ferroelectric, thus supporting the oxygen vacancy hypothesis. At the same time, the rest of the experimental results relevant to this hypothesis do not clearly support it. For example, the data on the effect of donor and acceptor doping on polarization fatigue in PZT films are contradictory while, if the oxygen vacancy concentration were decisive for the fatigue endurance, donor doping would always slow down the fatigue rate and acceptor one would always accelerate it (a more detailed discussion of the experimental situation can be found in the paper by Tagantsev et al. (2001b)). The results of more direct investigation of the problem are also ambiguous. The work by Brazier et al. (1999) where a non-monotonical dependence of the fatigue endurance of PZT thin films on the partial oxygen pressure has been reported is to be mentioned. If just enhanced oxygen vacancy concentration were detrimental for polarization switching, this dependence would be monotonical. Another direct test for the “fatigue-oxygen vacancy migration” correlation has been performed by Schloss et al. (2002) who used O¹⁸ isotope tracer to monitor oxygen vacancy migration in PZT thin films during switching cycling. No clear correlation of this kind has been reported. All in all, it does not seem that an increased concentration of oxygen vacancies itself is sufficient for enhancement of polarization fatigue at least in PZT thin film capacitors. It is important to indicate that this conclusion does not exclude some correlation between the oxygen stoichiometry and the fatigue performance of PZT capacitors since these species

are strongly involved in the defect chemistry of the material whereas polarization fatigue, in general, is a defect-chemistry-related phenomenon.

9.7.2.2 Injection Mechanism

Free carriers injected from the electrodes into the ferroelectric film can be trapped at deep levels and immobilized producing charged defects. The resulting defects can make the driving force for phenomenological scenarios of fatigue discussed in the previous section. Specifically, these defects can participate either in the formation of a non-switching electrode-adjacent layer, in the inhibition of seeds of reverse domains, in bulk pinning of the domain walls, or finally, in the “local imprint” mechanism. The role of the injection in polarization fatigue has been pointed out by several authors (Scott et al., 1991; Mihara et al., 1994; Stolichnov et al., 2000; Tagantsev and Stolichnov, 1999; Du and Chen, 1998). The conclusion of Mihara et al. (1994) was based on a rather weak temperature dependence of the fatigue endurance of Pt/PZT/Pt capacitors. Du and Chen (1998) have demonstrated an improved fatigue endurance of PZT capacitors with Pt electrodes appended with a thin SiO₂ layer between PZT and the top electrode. They have interpreted this improvement as a result of suppression of the injection into the capacitor, the injection being considered as the driving force of fatigue.

When discussing the injection-assisted polarization fatigue one distinguishes the case of injection associated with the current passing through the ferroelectric capacitor and the case of the so-called nearby-electrode injection, where the injected chargers enter only a thin electrode-adjacent layer of the ferroelectric. According to Tagantsev et al. (2001b) the first case does not seem to be relevant, at least, to the real experimental situation in PZT thin film capacitors. As for the nearby-electrode injection, two ways to relate injection with polarization switching have been discussed (Tagantsev et al., 2001b). First, it was suggested that the charge injection is promoted by the elevated electrical field that accompanies the nucleation of reverse domains. Alternatively, the injection is viewed as induced by the elevated electrical field that develops in an effective low dielectric constant surface layer. This kind of injection has been addressed in Sect. 9.5.2, in the context of the size effect on switching. To date, the injection scenario of polarization fatigue has not been entitled to comprehensive theoretical treatment. Simple modeling of some relevant issues as well as some qualitative predictions of this fatigue scenario can be found in the paper by Tagantsev et al. (2001b).

9.7.3 Overall Picture of Polarization Fatigue in PZT Thin Films

In the previous section, we have classified and discussed the principal phenomenological scenarios of suppression of switching ability of ferroelectric thin films as well as the microscopic aspect of fatigue mechanisms in these systems. The obtained classification can be visualized as the scheme depicted in Fig. 9.7.3,

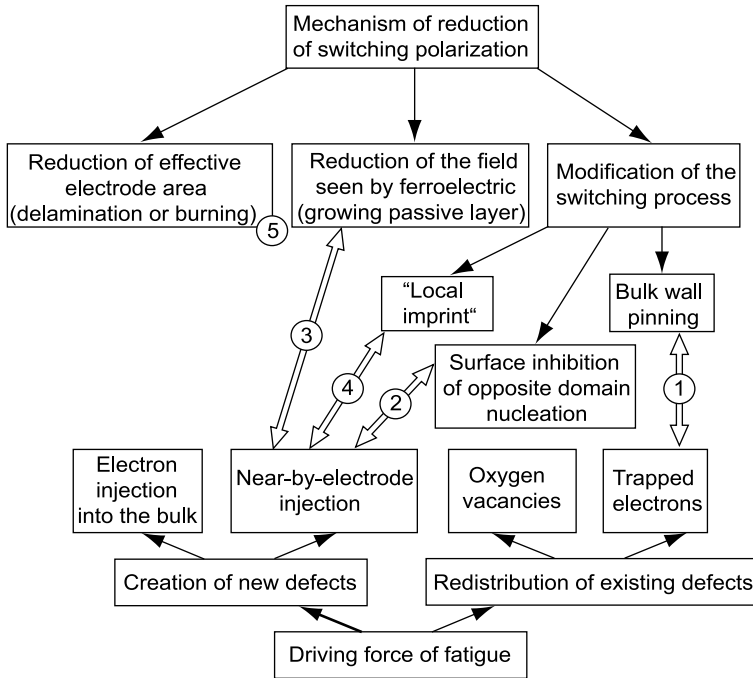


Fig. 9.7.3 The relationship between the phenomena associated with polarization fatigue according to different fatigue models. After Tagantsev et al. (2001b)

which has been offered by Tagantsev et al. (2001b). In this scheme, the numbers from 1 to 5 indicate the fatigue scenarios which, according to these authors, are most relevant to experimental situation in PZT thin films. These scenarios are

1. The bulk pinning of domain walls, which results in the formation of a domain structure where the individual domains do not contain active centers of reverse domain nucleation. The most probable driving force for this mechanism is the migration and trapping of free electronic carriers. The mechanism can be active in the suppression of switchable polarization for special types of cycling. However, for typical fatigue tests of PZT capacitors, it does not look to be of importance.
2. Inhibition of the seeds of reverse domain nucleation caused by the nearby-electrode injection is a good candidate for the fatigue mechanism in PZT thin films. Many features of the polarization fatigue can be explained in terms of this mechanism.
3. Formation of a passive surface layer that modifies the electric field seen by the ferroelectric film. The most probable driving force of this mechanism is the nearby-electrode injection of electrons. Some features of polarization fatigue can be interpreted in terms of this mechanism. However, no decisive experimental tests for this mechanism have been performed.

4. Nearby-electrode screening of ferroelectric polarization with low-mobility free carriers. Fatigued capacitors can be presented as a parallel connection of small regions where the polarization is strongly “imprinted”, the direction of blocked polarization being different in different regions. It is the so-called “local imprint” mechanism. No experimental evidence is available to support this mechanism.
5. An always-possible source of loss in switchable polarization during cycling is an effective reduction of the electrode area due to electrode burning or delamination. Usually one can cope with this problem by optimization of the processing so that this mechanism does not look to be a matter of real concern for memory applications.

A general remark concerning all listed scenarios can be made. Being physically substantially different, these scenarios, in principle, can be distinguished by their typical experimental manifestations. However, this distinction, as a rule, requires a complex study of the phenomena whereas monitoring a single property could be misleading. For instance, progressive tilt of polarization hysteresis loops is an evident manifestation of growing passive layer scenario (no. 3 in the list). However, taken alone this feature cannot be considered as a strong argument in its favor since scenario nos 1 and 2 can also manifest themselves in progressive tilt of the loops.

9.8 Scanning Force Microscopy Study of Polarization Reversal

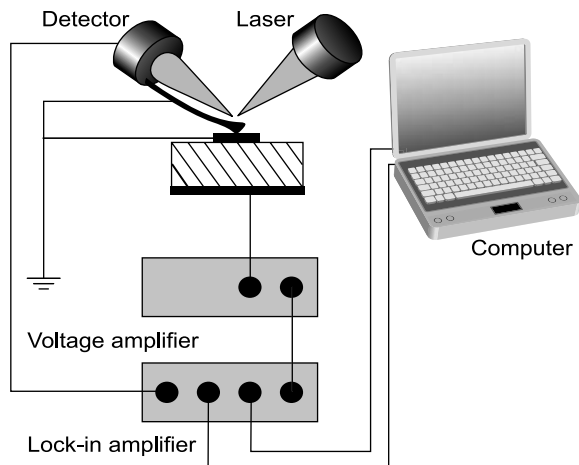
The Scanning force microscopy (SFM) as a tool for the investigation and control of ferroelectric domains was already discussed in Sect. 4.5. In ferroelectric thin films, this technique resulted in a real breakthrough providing an opportunity for nanoscale characterization and control of domain patterns. Some results obtained with SFM were already mentioned in present chapter when discussing the structures of “natural” domain patterns in the films. In this section we will discuss the applications of SFM to investigation of polarization reversal in ferroelectric thin films. The foregoing two sections are devoted to the results obtained using two modifications of the SFM technique, which are mainly used for this purpose.

The technique mostly used for investigation of domain dynamics in ferroelectric films is the traditional top-electrode-free piezoelectric force microscopy (PFM) which was already discussed in Sect. 4.5.8 as a technique for the characterization of bulk ferroelectric materials. In this technique, the voltage consisting of the quasistatic “poling” and ac “testing” components is applied to the sample through a metallized SFM tip. The amplitude of the former is much greater than that of the latter. The tip displacements at the ac frequency of the testing signal are detected. The role of the first component of the applied field is to modify the domain structure of the sample whereas the role of the second part is to monitor the local piezoelectric response in it by comparing the amplitude and the phase of the testing signal with those of the detected

mechanical response. In this technique, the electric field in the ferroelectric is strongly localized near the tip. This enables the domain manipulation and characterization down to the nanometer scale. At the same time, the switching conditions in the inhomogeneous field near the tip may be very different from those in parallel plate capacitors typically used in application of ferroelectric thin films. This is a serious drawback of this technique if one is interested in switching performance of ferroelectric thin film capacitors. Another problem with the top-electrode-free PFM is poor time resolution, since acquisition of an SFM image requires a time period of the order of minutes.

The second modification of SFM technique, which can be called “through-electrode” PFM, is free from some drawbacks of the top-electrode-free method. For the first time, this technique was used by Gruverman (Auciello et al., 1997) and later was extensively used by the EPFL group (Colla et al., 1998a; Hong et al., 1999b). The setup used in this method is schematically shown in Fig. 9.8.1. The external voltage (both switching and imaging components) can be applied either by using an additional conductor attached to the top electrode or directly through the conductive PFM tip. In both cases the piezoelectric displacement is probed locally by the SFM tip and the spatial distribution of the piezoelectric response is imaged through the top electrode. In such a configuration, a homogeneous electric field is generated throughout the ferroelectric film, which allows quantitative treatment of domain wall dynamics and investigation of polarization reversal mechanism in ferroelectric capacitors. Due to the reduced time constant, fast pulse switching and transient current measurements can be accomplished in submicron capacitors, thus making PFM suitable for memory device testing. However, the presence of the top electrode (typically at least 100 nm thick) lowers the lateral resolution of the technique compared to that of the electrode-free method. The through-electrode and electrode-free methods also differ in the information that they can provide on the distribution

Fig. 9.8.1 Schematic of a setup used for the “electrode through” PFM imaging. SFM tip and top electrode (shown in *black*) are grounded. The bottom electrode (shown in *black*) is used to apply an ac probing signal. The bottom electrode is also used to apply the controlling voltage that manipulate the domain state of the sample (shown in *hatched pattern*). The circuit for application of the controlling voltage is not shown



of the piezoelectric response across the film thickness: The electrode-free method senses the piezoelectric response averaged over some tip-adjacent region whereas the through-electrode method senses the response averaged over the whole film thickness.

The information on the local piezoelectric response obtained in both techniques is translated into that on the polarization state of the sample. As was discussed in Sect. 4.5.8, the sign of the local piezoelectric response (actually the phase difference between the testing voltage and the piezosignal) is interpreted as the sign of the spontaneous polarization in region tested for a given position of the tip. In thin films this interpretation holds as far as the tested region is single domain. If this region is polydomain, the sign of the piezoresponse is customarily interpreted as the sign of the net polarization averaged over the testing volume. In general, the correlation between the signs of the average piezoresponse and net polarization may not take place since, in general, on average nonpolar sample can be piezoelectric. In the case of switching dominated by the 180° polarization reversal (the situation typical for thin films), such correlation may be justified, however, with a reservation that the ac piezoelectric signal should be acquired in the absence of the poling voltage. This condition is clear in the context of Sect. 8.7.7 where was shown that, under a dc bias, even in 180° domain patterns, the changes of sign of the polarization and piezoelectric coefficient may take place at different values of the applied field. The interpretation of the amplitude of the local piezoelectric response is not always straightforward. In the case where the tested region near the tip is single domain, the amplitude brings information on the value and orientation of the spontaneous polarization and on the degree of mechanical clamping by the substrate. If this region is multidomain, the amplitude is also dependent on the fractions of different ferroelectric domain states in the region.

In what follows we will overview the results obtained by both PFM techniques and the traditional topographical scanning.

9.8.1 Top-Electrode-Free PFM

Most of SFM studies of the polarization reversal in ferroelectric thin films have been performed using the top-electrode-free PFM technique. The results obtained with this technique have provided new information on details of polarization reversal in these systems as well as direct experimental support for the knowledge already developed from indirect experiments and theories. Below we will discuss some of these results.

Domain wall mobility in very thin (30–80 nm) PZT (20/80 on $\text{SrTiO}_3\text{:Nb}$ electrode) films has been evaluated in the experiments performed by the group of Triscone (Tybell et al., 2002). In these studies, an SFM tip was, first, used to create a reverse domain near and under the tip by application of a voltage pulse. Then the size of the domain obtained was measured by PFM scanning

of the top surface of the film with ac voltage which was small enough not to distort the domain pattern created at the poling stage of the experiment. It was found that, in a few decades of the values, the wall velocity follows the “activation field dependence” $\exp(-E_0/E)$, shown in Fig. 9.8.2, with the activation field of the order of 20 MV/cm. Such a law has been known for domain wall motion in BaTiO₃ single crystal, through with some 10⁷ times smaller value of the activation field. In the case of BaTiO₃, this field dependence is consistent with the Miller–Weinreich theory (see Sect. 8.4.2) for the thermally activated motion of domain walls in the Peierls lattice potential. In the case of PZT film, the value of the activation field is too large to be interpreted in them of the Miller–Weinreich theory. The authors have attributed their observation to a manifestation of the defect-controlled creep motion of the domain wall (see Sect. 8.4.5).

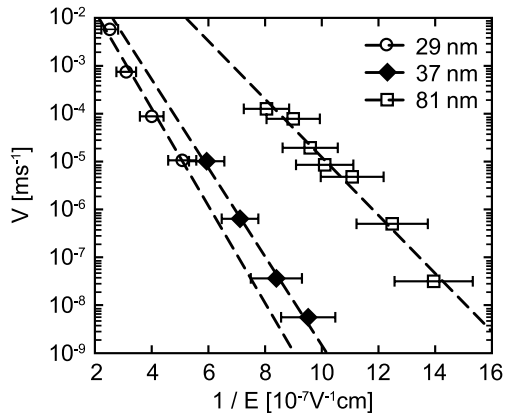


Fig. 9.8.2 The domain wall velocity in a PZT film as a function of the inverse of the applied field for films of different thicknesses. The velocity is evaluated from PFM data. After Tybell et al. (2002)

Useful information has been obtained on the interaction between the 180° domain walls, grain boundaries, and 90° domain walls. As clear from theoretical analysis given in Sect. 9.3, in thin films on a substrate, displacements of 90° (ferroelastic) domain walls are strongly limited by the clamping effect of the substrate. Thus, the switching is basically supported by the motion of 180° domain walls that travel in the film, in general, through a network of gain boundaries and 90° domain walls.

The poling/scanning technique described above enables the visualization of coupling between 180° domain walls and the grain boundaries. It has been often observed (see, e.g., Roelofs et al., 2000) that grain boundaries can stop the motion of 180° domain wall so that the grain and domain boundaries roughly coincide. However, as documented by Gruverman et al. (1998a) under appropriated applied field some propagation of a switching front through grain boundaries is also possible. This is illustrated in Fig. 9.8.3.

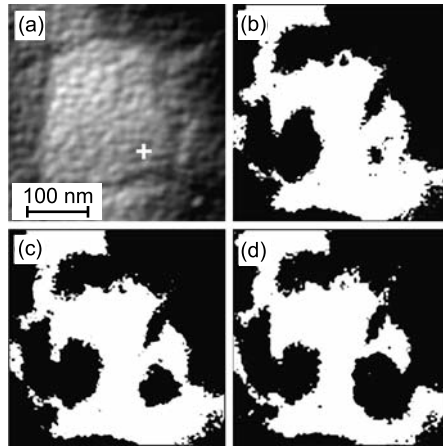


Fig. 9.8.3 Domain dynamics observed in a PZT 53/47 film. (a) Topographic image with the white cross indicating the tip position during dc voltage application. (b, c, d) Piezoresponse images showing domain sidewise growth and apparent domain expansion into a neighboring grain. (b) Original domain structure. (c, d) Domain structures after application of a 8 V pulse of different durations: (c) –50 ms and (d) –150 ms. After Gruverman et al. (1998a). Reprinted, with permission, from the *Annual Review of Materials Research* Volume 28 © 1998 by Annual Reviews. www.annualreviews.org

Interesting information on coupling between 180° and 90° domain walls has been obtained by Roelofs et al. (2002). In this work, (001) PZT (20/80) films on SrTiO_3 substrate with oxide bottom electrode have been characterized with PFM. The cross-hatched domain pattern of narrow a -domains embedded in a c -domain matrix, shown in Fig. 9.2.4, is typical for this kind of films. The film was switched from original negatively poled state to that positively poled by scanning with a voltage of -8 V by conductive SFM tip. The out-of-plane and in-plane PFM images shown in Fig. 9.8.4 were taken before and after switching. These images show that the switching of the out-of-plane component of the polarization in the c -domains (seen in the out-of-plane PFM image) is accompanied by that of the in-plane component of the a -domains (seen in the in-plane PFM image). The driving force of this correlated switching of c - and a -domains is the fact that the “head-to-head” and “tail-to-tail” 90° domain walls are charged and, for this reason, energetically unfavorable. As clear from Fig. 9.8.4, the polarization reversal only in c -domains (with the directions of the polarization in the a -domains kept unchanged) would lead to the creation of these energetically unfavorable situations. This coupling between 180° and 90° domain walls impacts motion of the former. It has been documented (Roelofs et al., 2002) that 90° domain walls represent an obstacle for motion of 180° walls. However these obstacles can be finally overcome with the walls. PFM experiments in these kinds of films have revealed other interesting features of

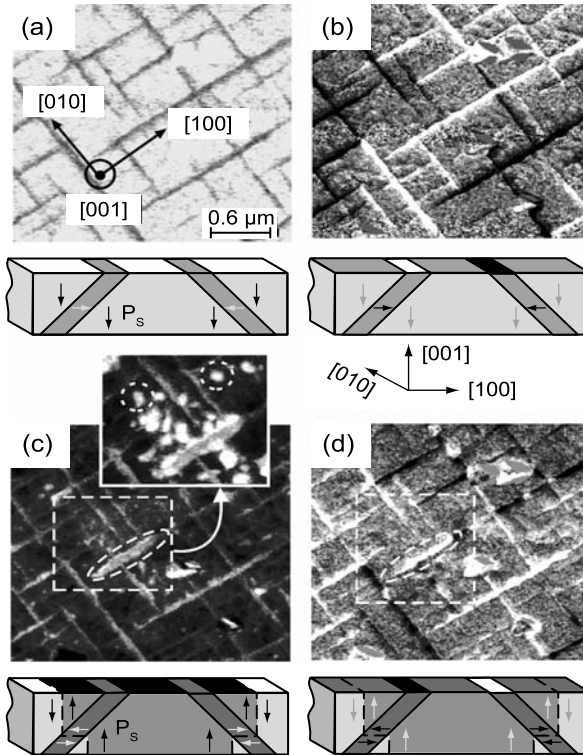


Fig. 9.8.4 Piezoresponse images of a polydomain PZT film in an as-grown state, (a) and (b), and after poling, (c) and (d). The “out-of-plane” PFM signals is shown in (a) and (c) whereas the “in-plane” signals in (b) and (d). Regions with *bright*, *dark*, and *intermediate* contrasts correspond to different orientations of the polarization in ferroelectric domains, as shown schematically in the sketches below the PFM images. Ellipse in (c) and (d) demonstrates a specific region, where the polarization orientation remains unchanged after poling. It is seen that the reverse of the contrast of *c*-domains (*dark* and *bright* in (a) to (c)) correlates with that of *a*-domains (*dark* and *bright* in (b) to (d)). Sketches below (c) and (d) show that the correlated switching of *a*- and *c*-domains ensures the electroneutrality of the domain walls separating them. The *inset* in (c) is an image taken later from the same area. It shows that it is from the non-switchable region that the polarization backswitching starts. Reprinted with permission from Roelofs et al. (2002). Copyright (2002), American Institute of Physics

the polarization reversal in these systems. Due to the presence of an internal bias field in these films, the positively poled state was found to be metastable exhibiting spontaneous backswitching. It was observed that this backswitching can start with the reverse domain nucleation at immobile 90° domain walls. PFM images (Ganpule et al., 2000a) illustrating this kind of nucleation and the initial growth of reverse domains are shown in Fig. 9.8.5.

As has been repeatedly indicated above in this chapter, ferroelastic domain pattern are mainly controlled by the clamping effect of the substrate. For this

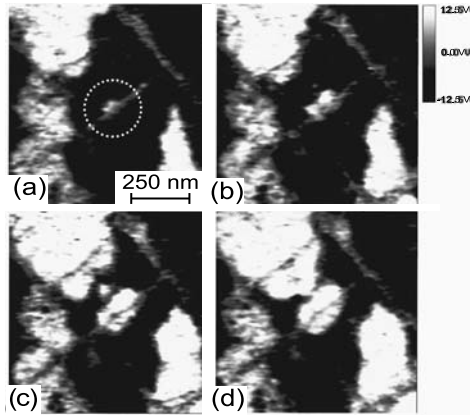


Fig. 9.8.5 PFM images of a region of a PTZ film scanned with tip biased at -10 V. The *black and white contrasts* correspond to *c*-domains (with the polarization normal to the plane of the film). The *grey contrast* corresponds to *a*-domains (with the in-plane orientations of the polarization). Figures (a), (b), (c), and (d) are recorded as functions of time of scan, (a) $-1,500$, (b) $-2,000$, (c) $-4,000$, and (d) $-4,500$ s. It is seen how a nucleus of reverse polarization appears at a narrow stripe of *a*-domain and subsequently grows. Reprinted with permission from Ganpule et al. (2000a). Copyright (2000), American Institute of Physics

reason one cannot expect any electric-field-driven global rearrangement of the ferroelastic domain pattern of the film since such rearrangement would lead to a strong increase in the elastic energy of the system. At the same time, in principle, local rearrangement of this kind may be possible. Another situation where 90° domain walls are less blocked by the clamping effect of the substrate occurs in islands of the film having dimensions comparable to its thickness. Both of these situations have been identified by using the PFM imaging.

Chen et al. (2004) has studied the polarization reversal in PZT (20/80) films with typical cross-hatched pattern shown in Fig. 9.2.4. It has been found that the polarization reversal in a *c*-domain induced by a voltage loaded SFM tip, which primarily results in formation of a cylindrical reverse *c*-domain, can also lead to the creation of new *a*-domains. Figure 9.8.6 shows the creation of one new *a*-domain. This phenomenon can be rationalized as follows. When the reverse cylindrical domain appeared is objected to the *electric field parallel to its polarization*, it cannot freely increase its height and shrink in width as being clamped in by the matrix which is not subjected to the electric field induced by the SFM tip. Thus, under the applied voltage the reverse domain is under an in-plane tensile stress. This stress can be released by formation of one or several *a*-domains around the reverse *c*-domain.⁴⁸ It is not a priori clear that the resulting structure will be energetically favorable since the appearance of the

⁴⁸ This effect is similar to the formation of *a*-domains in ferroelectric films under tensile misfit strain (c.f. Sect. 9.3.3)

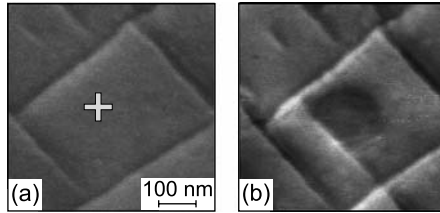


Fig. 9.8.6 (a) PFM domain structure image of the PZT film before local switching; (b) PFM image after a local switching with a -12 V pulse for 3 s applied at the point shown with the *cross*. Formation of a new *a*-domain at the border of the switched area is seen. Reprinted with permission from Chen et al. (2004). Copyright (2004), American Institute of Physics

a-domains would increase the energy of the system due to the misalignment of the polarization and field in the *a*-domains. An estimate of the energy balance in the system shows (Chen et al., 2004) that this phenomenon can be expected in PZT (20/80) films but not in films of PZT (50/50). This is compatible with the experimental PFM results on PZT (50/50) where the aforementioned formation of new *a*-domains has not been observed.

Electrode-free PFM studies provide conclusive evidence that, in islands of ferroelectric films having dimensions comparable to the film thickness, 90° domain walls do become mobile: They can appear and disappear during the polarization reversal and significantly contribute to the piezoelectric response of the film. Figure 9.8.7 shows the PFM images obtained by Nagarajan et al. (2003) from a $1 \mu\text{m}^2$ island of $1 \mu\text{m}$ thick PZT (20/80) film for the as deposited (a) and differently poled states (b, c, and d). Appreciable evolution of the 90° domain wall pattern is clearly seen in these images. The PFM obtained data by Buhlmann et al. (2002) shown in Fig. 9.8.8 document a tremendous increase in the piezoelectric response of islands of a 200 nm thick PZT (20/80) film obtained as a result of the decrease in their aspect ratios. This increase of some 300% cannot be interpreted in terms of the lattice contribution to the piezoresponse

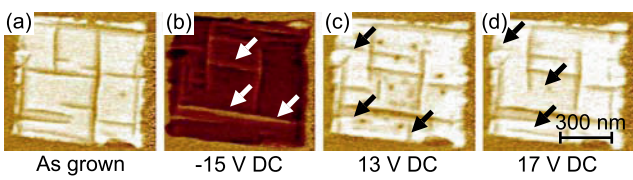
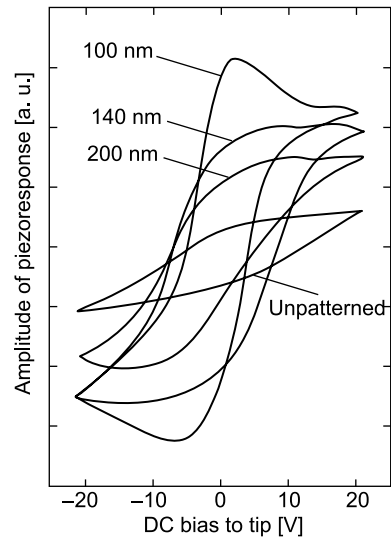


Fig. 9.8.7 The evolution of the ferroelastic domain structure as a function of applied electric field for a $1 \mu\text{m}^2$ island of a $1 \mu\text{m}$ thick PZT film. Piezoresponse images before and after application of various dc bias voltages (by scanning with a dc-biased SFM tip). The film mainly contains *c*-domains. *a*-domains are seen as *narrow straight stripes*. It is seen that the application of the field leads to appreciable modification of ferroelectric domain pattern. *Arrows* indicate the places where such modification can be seen. After Nagarajan et al. (2003)

Fig. 9.8.8 Piezoelectric hysteresis loops of a PZT film. The loops are taken with electrode-free PFM from the unpatterned film and from square-patterned islands with the lateral sizes from 100 to 200 nm (indicated in the figure). Reprinted with permission from Buhlmann et al. (2002). Copyright (2002), American Institute of Physics



clearly attesting to the contribution from displacements of ferroelastic walls which are less mechanically clamped in smaller islands.

PFM images enable characterization of the temporal evolution of reverse domains written with a voltage-loaded SFM tip. The written domains may be very stable. For PZT films thinner than 100 nm, at least several-day room temperature stability of written reverse domains has been reported by Hidaka et al. (1997) and by the group of Triscone (Tybell et al., 2002). It has been shown that poling pulses of 10–12 V and 50–100 μ s duration are sufficient for writing stable domains with the diameter about the film thickness. Another example of stable reverse domains has been documented by Gruverman and Tanaka (2001), for 200 nm thick $\text{SrBi}_2\text{Ta}_2\text{O}_9$ films on IrO_2 electrodes, though with a much longer writing time (8 V/1 s). At the same time, these authors have found that similar films but with Pt electrodes exhibit appreciable relaxation of reverse domains. The relaxation rate has been found to be strongly dependent on the width and the amplitude of the writing pulse as well as on the poling prehistory of the sample (a domain written for the second time at the same place is more stable). These dependences are illustrated in Figs. 9.8.9 and 9.8.10. The time dependence of the relaxation of SFM-written reverse domains has been found to follow dynamics that is clearly slower than exponential and can be fitted to logarithmic (Gruverman and Tanaka, 2001; Jo et al., 2000) or stretched exponential laws (Ganpule et al., 2000b; Fu et al., 2003).

It is generally accepted that the driving force of backswitching behind the domain relaxation is the built-in internal bias field. Actually any of the mechanisms of built-in internal bias field discussed earlier in this chapter may lead to backswitching in the film. The slow relaxation kinetics of reverse domains is attributed to various mechanisms such as a wide spectrum of relaxation times (Jo et al., 2000), a mechanism linked to a random-walk process (Gruverman

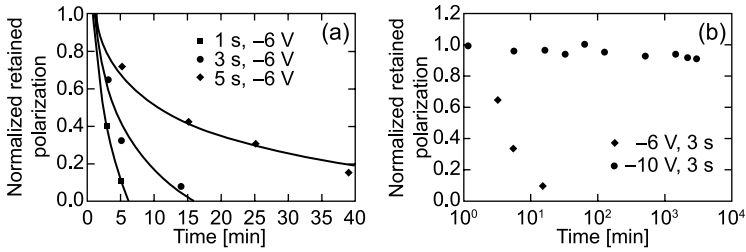


Fig. 9.8.9 Polarization retention in a SrBi₂Ta₂O₉ film with Pt bottom electrode. Normalized retained polarization was calculated as a ratio of domain area at a certain time to this domain initial area (approximately 1 min after the domain was written by voltage pulse application to a selected point, i.e., by immobile tip). **(a)** Dynamics of retention loss for different poling times. The poling voltage is -6 V. **(b)** Effect of the poling voltage on domain stability. The poling time is 3 s. Reprinted with permission from Gruverman and Tanaka (2001). Copyright (2001), American Institute of Physics

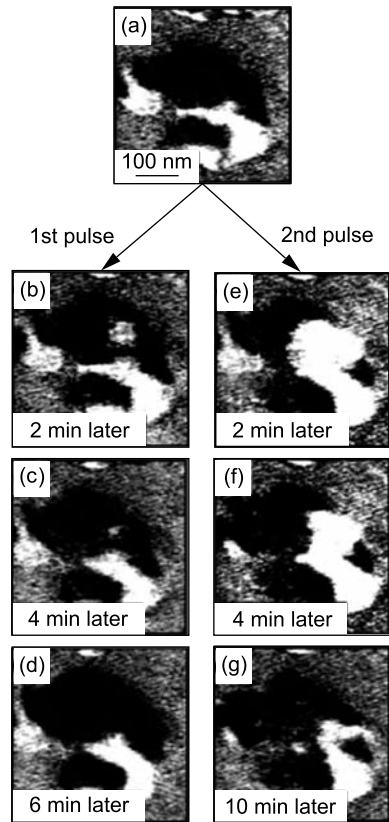


Fig. 9.8.10 Piezoresponse images of a SrBi₂Ta₂O₉ film with Pt bottom electrode illustrating the effect of switching prehistory on retention behavior. **(a)** As-grown domain structure. **(b)**, **(c)**, and **(d)** Retention loss after application of the first switching pulse of -6 V, 1 s; **(e)**, **(f)**, and **(g)** retention loss after application of the second but identical switching pulse. Reprinted with permission from Gruverman and Tanaka (2001). Copyright (2001), American Institute of Physics

et al., 1997) or a Kolmogorov–Avrami mechanism with the electric field seen by the domain walls corrected according to the fraction of the backswitched volume of the film (Ganpule et al., 2002). All in all, there are many scenarios for the relaxation of SFM-written domains discussed; however, the understanding of the problem developed so far is not sufficient to distinguish between them.

9.8.2 Through-Electrode PFM

The through-electrode PFM imaging enables getting information on the spatial distribution of polarization in ferroelectric capacitors. Here of interest is the information on polarization distribution during switching as well as in the fatigued and imprinted states.

A comprehensive study of polarization distribution during switching has been performed by Hong et al. (1999a) and Hong and Setter (2002). PFM images from PZT film-based capacitors were taken in the pulse mode, i.e., these were taken at zero bias after application of poling field pulses of different amplitudes, between the pulses the material being always set at the remanence. The analysis of the PFM images revealed an inhomogeneous (over the capacitor area) character of switching, which can be readily expected. As was pointed out by Hong et al. (1999b) and Hong and Setter (2002), another remarkable feature of the typical PFM images is that the switching is accompanied with essential reduction of the average amplitude of the local piezoelectric signal in a rather wide interval of the poling field. At the same time, the change of the average phase takes place in a rather narrow interval of the poling fields close to the coercive field. This behavior is illustrated in Fig. 9.8.11 for a 295 nm thick $\text{Pb}(\text{Zr}_{0.45}\text{Ti}_{0.55})\text{O}_3$ film of (111) orientation with 100 nm thick top electrode. The lateral resolution of this image is not better than 100 nm due to the electrode thickness. PFM images of higher resolution taken from similar films but with much thinner top electrode (it was polished down to 10–15 nm) obtained by Stolichnov et al. (2005a) (see Fig. 9.8.12) document the same behavior but at a smaller spatial scale: Though the amplitude in the major part of the area scanned is close to the saturation, apart from the clearly seen domain boundaries there are regions where the amplitude is essentially reduced.

Following Hong et al. (1999b) and Hong and Setter (2002), the aforementioned reduction of the amplitude of the PFM signal during polarization reversal can be readily discussed in terms of a simplified switching model where the polarization reversal is promoted with 180° switching with the direction of the polarization normal to the electrodes and the new domain always nucleates at the electrodes with domain walls which make small angles with the polarization direction.⁴⁹ In

⁴⁹ In (111) $\text{Pb}(\text{Zr}_{0.45}\text{Ti}_{0.55})\text{O}_3$ films discussed, the spontaneous polarization may not be directed normal to the electrodes so that the real situation may be more complicated than the considered model. However, this complication does not affect the qualitative conclusions of the consideration given below in the text.

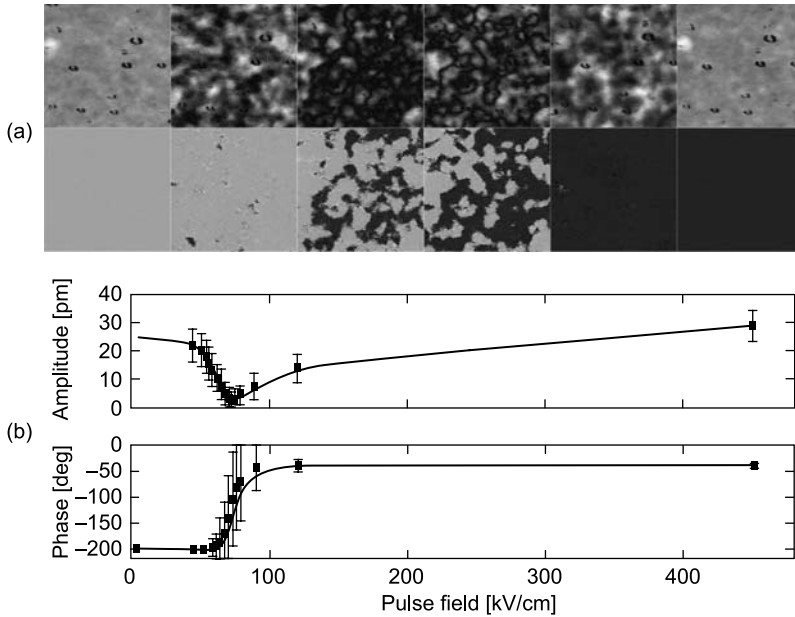
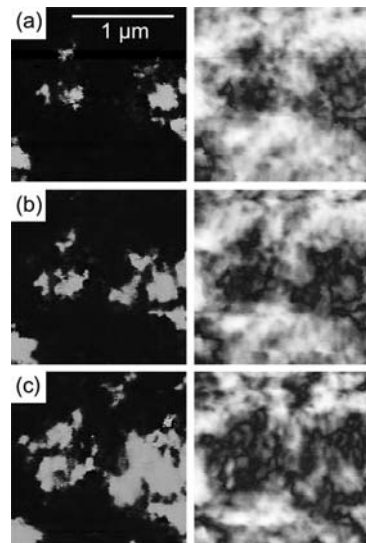


Fig. 9.8.11 (a) Through-electrode PFM images of an area of ferroelectric capacitor containing a PZT film; amplitude—above, phase—below. The images are taken after the application of voltage pulses of increasing amplitude (from left to right). The image size $10 \times 10 \mu\text{m}$. (b) The amplitude and phase of the PFM signal averaged over the images taken in the same experiment plotted as functions of the pulse amplitudes. (Sengbum Hong, private communication). It is seen in (a) and (b) that the phase switches in a narrower field interval than the amplitude

Fig. 9.8.12 Images of the phase (left) and amplitude (right) of the local piezoelectric response measured through a 10 nm thick top electrode of a Pt/PZT/Pt capacitor partially switched with voltage pulses of 1.2 (a), 1.6 (b), and 2 V (c). The lateral spatial resolution of about 20 nm is seen. In the amplitude image, thin dark stripes corresponding to the lowered amplitude at domain boundaries are seen. After Stolichnov et al. (2005a,b)



this framework, two basic scenarios can be distinguished. In the first, traditional scenario, the switching rate is limited by domain nucleation or/and domain wall side motion while the time of the forward growth of the nucleated domains is neglected. In this scenario, the domain pattern during switching should mainly consist of “through domain” as illustrated in Fig. 9.8.13a and b. We will call it *through scenario*. In the alternative scenario, the rate-limiting stage of switching is the forward growth of newly nucleated domains with “through domains” appearing only at the final stage of the polarization reversal. A polarization distribution across the film cross-section with a zigzag domain pattern, which is typical for intermediate stages of switching in this scenario, is schematically shown in Fig. 9.8.13c. We will call it *zigzag scenario*.

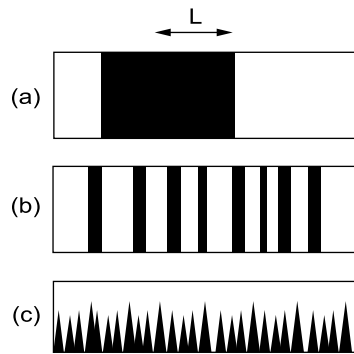


Fig. 9.8.13 Schematics of cross-section of a film containing 180° domains (shown in *black* and *white*) with the spontaneous polarization normal to its plane. L is the lateral spatial resolution of PFM. See the text

These scenarios can be readily distinguished using through-electrode PFM imaging if the image resolution L is better than the typical domain size (Fig. 9.8.13a). In this case, obviously, the through scenario corresponds to the amplitude of the piezoresponse, which basically stays during switching at its saturated (single domain) value, except the narrow vicinity of the domain walls. At the same time according to the zigzag scenario, a substantial reduction of the amplitude is possible in an appreciable interval of poling fields. Based on this reasoning Hong et al. (1999a,b) and Hong and Setter (2002) has interpreted their results (with an essential amplitude reduction) in terms of the zigzag scenario.

In the case where the typical domain size is smaller than the image resolution L illustrated in Fig. 9.8.13b, the above reasoning does not hold any more. In this case, the piezoelectric response is averaged over $L \times L$ area so that, in the through scenario, the amplitude can be significantly smaller than its single-domain value. Thus, if the polarization reversal occurs via the through scenario with the typical domain spacing smaller than the image resolution, a substantial reduction of amplitude of the piezoresponse will also be expected.

Finally we see that the PFM results just discussed above are consistent with both the zigzag scenario and the through scenario with narrow domains.

Distinction between these scenarios does not seem possible without additional experiments. Useful information can be provided by PFM images taken with different top-electrode thicknesses: In the through scenario, for thinner electrodes (better resolution) higher amplitudes of the piezoresponse are expected whereas, in zigzag scenario such dependence is not expected.

Another kind of inhomogeneity of the polarization reversal has been observed in small capacitors based on (111)-modified PZT films (Stolichnov et al., 2002a). It has been found that switching of the capacitor can be accompanied by backswitching of its central part, the phenomenon taking place for both direction of switching. PFM images documenting this phenomenon in $2 \times 3 \times 0.135 \mu\text{m}^3$ capacitors are shown in Fig. 9.8.14. The authors (Stolichnov et al., 2002a) did not observe this effect in capacitors of significantly smaller and larger areas; however, later the effect has been observed in smaller area capacitors as well (A. Gruverman, private communication). The interpretation of this phenomenon was based on the assumption that, first, the single-domain state map of PZT (111) film is similar to that PbTiO_3 (111) film shown in Fig. 9.3.7 and, second, the state of the film is close to the line of isomorphic phase transition. The main point of the interpretation is that the states of the central (more stressed) and outer (less stressed) parts of the capacitor correspond to the different sides of this transition line. It was shown that in this situation the antiparallel orientation of out-of-plane component of

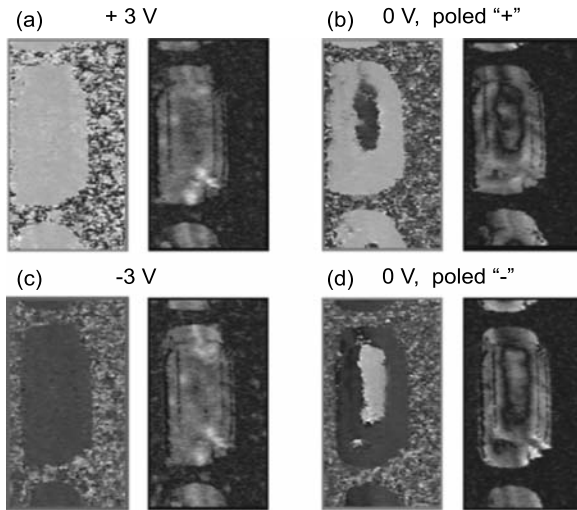


Fig. 9.8.14 Maps of the phase (*left*) and amplitude (*right*) of piezoelectric response of a capacitor $2 \times 3 \mu\text{m}$ containing a (111)-oriented PZT film. **(a)** Capacitor under dc a voltage of $+3 \text{ V}$ applied to the bottom electrode. **(b)** The same measurement repeated after the dc voltage has been switched off. **(c)** Capacitor under a dc voltage of -3 V . **(d)** The same measurement repeated after the dc voltage of -3 V dc has been switched off. After Stolichnov et al. (2002)

spontaneous polarization in the central and outer parts of the capacitor may be energetically favorable (Stolichnov et al., 2002a).

Through-electrode PFM studies also provide information on the state of ferroelectric capacitors prone to the polarization fatigue and on the imprint degradation in these systems. It has been found that these phenomena often occur inhomogeneously across the capacitor area. Gruverman et al. (2003) has evaluated the imprint in ferroelectric capacitors with (111)-modified PZT films to find that the central areas of them are stronger prone to imprint than those peripheral. Through-electrode PFM characterization of PZT by Colla et al. (1998a) has documented a “region-by-region” type of “polarization freezing” during fatigue testing of the capacitor. PFM images shown in Fig. 9.8.15 illustrate this type of evolution of the local polarization state of ferroelectric capacitor during a fatigue test.

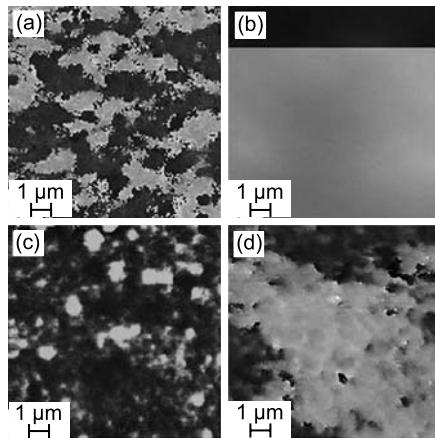


Fig. 9.8.15 Phase of “through–electrode” PFM images of a Pt/PZT/Pt capacitor: (a) “As-prepared” and (b) poled. The *bright* and *dark parts* of (b) were obtained by poling with opposite polarity of the applied field, positive and negative, respectively. Images (c) and (d) were taken from the same capacitor but after 10^5 and 10^7 switching cycles followed with negative poling, respectively. The *bright areas* in (c) and (d) represent the areas where the polarization cannot be switched. After Colla et al. (1998a)

9.9 Films of Proper Ferroelectric–Ferroelastics

The ferroelectric materials commonly used for thin film processing belong to the same ferroic class, the class of proper ferroelectrics–improper ferroelastics. In the previous sections of this chapter, we considered various properties of thin films of these materials. One of the conclusions that can be drawn from this consideration is that these properties are strongly affected by the mechanical coupling between the ferroelectric film and substrate. In this context, it is clear

that films of proper ferroelectrics–improper ferroelastics and that of proper ferroelectrics/ferroelastics can significantly differ in their dielectric, switching, and domain properties. The origin of this difference is the type of polarization–strain coupling in these materials: In the paraelectric phase of proper ferroelectrics/ferroelastics, the bilinear (piezoelectric) coupling between the polarization and strain takes place whereas in proper ferroelectrics–improper ferroelastics this coupling is absent. In this section we will discuss the properties of films of proper ferroelectrics/ferroelastics as they are predicted by the phenomenological theory. Since proper ferroelectrics–ferroelastics are very rare among ferroelectrics and no experimental information on the films of these materials is presently available, we will restrict ourselves to a consideration of one example of such a system. Specifically, we will consider ferroelectric properties of a film of a KDP-type material on a dissimilar substrate, the direction of the ferroelectric polarization being normal to the substrate plane. Films of this orientation are expected to be the most sensitive to the clamping effect of the substrate since, for this orientation, the ferroelectric polarization is always (at any temperature) coupled to the shear strain in the plane of the films, which in turn is fully clamped by the substrate. We will consider the problem of the phase transition into the single-domain ferroelectric state and the dielectric permittivity of the polydomain state of this system following the paper by Tagantsev (2005). Films of proper ferroelectrics/ferroelastics are also of interest from the point of view of the choice of the order parameter in Landau theory. We will comment on this issue at the end of this section.

The phase transition to the single-domain ferroelectric state can be approached in terms of Landau theory. According to the results obtained in this framework for proper ferroelectrics–improper ferroelastics (see Sect. 9.3.2) the Curie–Weiss temperature T_0 in the films may significantly differ from its value for the bulk material, the effect being driven by the electrostrictive coupling between the polarization and strain. The essential feature of this effect is that it vanishes if the parent misfit strain, $\varepsilon_{p\alpha\beta}$, is zero. Another manifestation of the electrostrictive coupling is a renormalization of the coefficient of the dielectric nonlinearity of the film, which may influence the order of the transition into the single-domain ferroelectric state. One can readily check that these effects hold for proper ferroelectrics–ferroelastics. However in the latter, there exist other effects related to the transition to the single-domain ferroelectric state. Namely, in proper ferroelectrics–ferroelastics, (i) the mechanical clamping imposed on the film by the substrate may lead to a shift of T_0 even at vanishing parent misfit strain, $\varepsilon_{p\alpha\beta} = 0$ and (ii) the component of parent misfit strain, which is linearly coupled with the polarization suppresses the phase transition in the film working like a dc electric field.

We evaluate these effects by using the Gibbs energy expansion for the KDP-type ferroelectrics given by Eq. (2.3.27) where we keep, apart from the out-of-plane component of the polarization P_3 , only one component of stress, which is linearly coupled with P_3 , i.e., the in-plane shear stress σ_6 . The rest of the terms will manifest itself in the effects which are common for proper

ferroelectrics–improper ferroelastics and proper ferroelectrics/ferroelastics and discussed in Sect. 9.3.2. Thus, we start from the expansion

$$\Phi = \Phi_o + \frac{\alpha_o}{2}(T - T_o)P_3^2 + \frac{\beta}{4}P_3^4 + \frac{\gamma}{6}P_3^6 - \frac{1}{2}s_{66}^P\sigma_6^2 - b_{36}P_3\sigma_6. \quad (9.9.1)$$

It leads us to the following equations of state of the film:

$$\varepsilon_6 = -\frac{\partial\Phi}{\partial\sigma_6} = s_{66}^P\sigma_6 + b_{36}P_3, \quad (9.9.2)$$

$$E_3 = \frac{\partial\Phi}{\partial P_3} = \alpha_o(T - T_o)P_3 + \beta P_3^3 + \gamma P_3^5 - b_{36}\sigma_6. \quad (9.9.3)$$

For a film deposited onto a substrate, the in-plane shear strain is controlled by the corresponding component of the parent misfit strain, i.e., $\varepsilon_6 = \varepsilon_{P6}$, so that, from Eqs. (9.9.2) and (9.9.3), we arrive at the equation for the polarization in the film:

$$E_3 + \frac{b_{36}}{s_{66}^P}\varepsilon_{P6} = \alpha_o(T - T_o + \delta T_o)P_3 + \beta P_3^3 + \gamma P_3^5, \quad (9.9.4)$$

$$\delta T_o = \frac{b_{36}^2}{\alpha_o s_{66}^P} = b_{36}^2 c_{66}^P \varepsilon_o C, \quad (9.9.5)$$

where $\alpha_o = 1/(\varepsilon_o C)$, $c_{66}^P = 1/s_{66}^P$, and C is the Curie–Weiss constant. We clearly see that the impact of ε_{P6} component of the parent misfit strain is identical to that of an electric field of $E_{\text{eff}} = b_{36}c_{66}^P\varepsilon_{P6}$ applied normally to the film. Thus, this component of the parent misfit strain leads to a poling of the film in the absence of the electric field. Experimentally, this will result in a smearing of the dielectric anomaly at the Curie–Weiss temperature. According to (9.9.4), the latter is also modified in the film. It is shifted down, the shift being independent of the value of the parent misfit strain, in contrast to the case of proper ferroelectrics–improper ferroelastics. The value of the shift is controlled by the coupling constant between the polarization and stress b_{36} and by the in-plane shear modulus of the ferroelectric c_{66}^P . As one could naturally expect, at $b_{36} \rightarrow 0$ or $c_{66}^P \rightarrow 0$, the mechanical clamping by the substrate ceases to influence the order parameter of the transition and δT_o vanishes.

It is instructive to estimate the size of aforementioned effects for KDP films of the considered orientation. Using the parameters of KDP crystals (Jona and Shirane, 1962), $b_{36} = 0.15 \text{ m}^2/\text{C}$, $c_{66}^P = 0.6 \times 10^{10} \text{ N/m}^2$, and $C = 3250 \text{ K}$, we find

$$\delta T_o \approx 4 \text{ K} \quad \text{and} \quad E_{\text{eff}} \approx 9\varepsilon_{P6} \text{ MV/cm}. \quad (9.9.6)$$

The predicted shift of the Curie–Weiss temperature in the KDP films is small, though it might be detected experimentally. The poling effect of the film/substrate lattice mismatch may occur only in the case of a low in-plane symmetry of the substrate, which can provide $\varepsilon_{p_6} \neq 0$. The size of this effect is difficult to evaluate since no information is available on the possible values of the in-plane shear component of the parent misfit strain in films of KDP-type ferroelectrics.

In the single-domain state, as is clear from Eq. (9.9.2), the ferroelectric film considered is stressed. The stress can be released by formation of a 180° domain pattern where the sign of the spontaneous deformation ε_{s_6} alternates. Elastically, such domain pattern is similar the a_1/a_2 domain pattern in tetragonal (001) perovskite films (see discussion in Sect. 9.3.3.) and it is more energetically favorable than the metastable single-domain state. However, the dielectric responses of these systems are quite different.

To illustrate this issue, we will consider the small-signal dielectric response of a defect-free KDP-type film so that the domain wall motion is not affected by the pinning caused by defects. We will do it for the situation where the domain pattern is in equilibrium and dense (film thickness is much greater than the domain period) and the substrate does not impose parent shear misfit strain on the film (i.e., $\varepsilon_6 = 0$), the situation similar to that addressed in Sect. 9.6.4 for films of a proper ferroelectric–improper ferroelastic. In this case, the domain states are “elastically equivalent” (like in the a_1/a_2 pattern) having the same volume fractions *in the absence of an electric field*. The application of the field changes these fractions; however, the condition $\varepsilon_6 = 0$ always holds on average (over the volume of the film), although the local value of the shear strain ε_6 alternates from domain to domain. Another essential feature of the system is that, because the domain pattern is dense, in the main part of the film (except a substrate-adjacent layer having thickness about the domain period) stress σ_6 can be treated as homogeneous. Using the above arguments and averaging Eq. (9.9.2), we readily find a relation

$$\sigma_6 = -c_{66}^P b_{36} \bar{P}_3 \quad (9.9.7)$$

between σ_6 and the average polarization:

$$\bar{P}_3 \equiv P_+(1/2 + \Delta) + P_-(1/2 - \Delta) = 2\Delta P_S + \frac{\delta P_+ + \delta P_-}{2}, \quad (9.9.8)$$

where $\delta P_+ = P_+ - P_S$ and $\delta P_- = P_- + P_S$. Here P_+ , P_- , and P_S are the polarization in the positively and negatively poled domains of the film, and the absolute value of the spontaneous polarization in the bulk and mechanically free material, respectively; Δ is the deviation of the fraction of the positively poled domains from $1/2$. Relation (9.9.7) substantially simplifies the calculation of the dielectric response of the system. In these calculations, first, we find the polarization in the domains, P_+ and P_- , and the average polarization \bar{P}_3 for given Δ and E_3 and, second, we determine Δ as a function of E_3 to finally arrive at \bar{P}_3 as a function of E_3 .

The polarization in domains of the dense pattern is controlled by Eq. (9.9.3) where the stress comes from Eq. (9.9.7). According to the latter, in the non-poled pattern (i.e., at $\bar{P}_3 = 0$) the domains are not stressed so that, in the absence of the field, their polarization equals $\pm P_S$. To find the deviations of the polarization in the domains from these values, δP_+ and δP_- , which are driven by the asymmetry of the pattern or/and applied field, Eq. (9.9.8) should be also take into account. Since we are interested in the small-signal response, i.e., $|\delta P_+|, |\delta P_-| \ll P_S$, we can linearize Eq. (9.9.3). Finally, from Eqs. (9.9.3), (9.9.7), and (9.9.8) we get

$$\delta P_+ \chi^{-1} + c_{66}^P b_{36}^2 \left(2\Delta P_S + \frac{\delta P_+ + \delta P_-}{2} \right) = E_3, \quad (9.9.9)$$

$$\delta P_- \chi^{-1} + c_{66}^P b_{36}^2 \left(2\Delta P_S + \frac{\delta P_+ + \delta P_-}{2} \right) = E_3, \quad (9.9.10)$$

for the positive and negative domains, respectively, where $\chi^{-1} = \alpha_0(T - T_0) + 3\beta P_S^2 + 5\gamma P_S^4$ is the lattice permittivity in the ferroelectric phase of the bulk material. Further, from Eqs. (9.9.9), (9.9.10), and (9.9.8) we readily obtain the polarization in the domains and the average polarization of the domain pattern at given values of E_3 and Δ :

$$\delta P_+ = \delta P_- = \frac{E_3 - 2\Delta P_S c_{66}^P b_{36}^2}{\chi^{-1} + c_{66}^P b_{36}^2}, \quad (9.9.11)$$

$$\bar{P}_3 = \frac{E_3 + 2\Delta P_S \chi^{-1}}{\chi^{-1} + c_{66}^P b_{36}^2}. \quad (9.9.12)$$

To obtain the asymmetry parameter Δ as a function of the field we will consider the average thermodynamic function of the film corresponding to the condition of fixed electric field \bar{G} :

$$\bar{G} \equiv \tilde{G}_+(1/2 + \Delta) + \tilde{G}_-(1/2 - \Delta), \quad (9.9.13)$$

where \tilde{G}_+ and \tilde{G}_- are the thermodynamic function (cf. Eq. (9.3.19))

$$\tilde{G} = \Phi + \varepsilon_1 \sigma_1 + \varepsilon_2 \sigma_2 + \varepsilon_6 \sigma_6 - P_3 E_3 \quad (9.9.14)$$

calculated for the two domain states in the film. Using Eqs. (9.9.7), (9.9.8), and (9.9.11), \bar{G} can be expressed in terms of Δ and E_3 as follows:

$$\bar{G} = \frac{2\chi^{-1} P_S}{\chi^{-1} + c_{66}^P b_{36}^2} [b_{36}^2 c_{66}^P P_S \Delta^2 - E_3 \Delta]. \quad (9.9.15)$$

Being interested in the small-signal response, we have kept in this expression only linear and quadratic terms in Δ . The minimization of this expression with respect to Δ gives Δ as a function of the field:

$$\Delta = \frac{E_3}{2P_S c_{66}^P b_{36}^2}. \tag{9.9.16}$$

Combining (9.9.12) and (9.9.16) we find for the dielectric susceptibility of the polydomain film

$$\chi_{\text{tot}} = \frac{\overline{P}_3}{E_3} = \frac{1}{c_{66}^P b_{36}^2}. \tag{9.9.17}$$

Interestingly, as seen from Eqs. (9.9.11) and (9.9.16), the polarization in the domains is not affected by the application of the electric field, since the dielectric response (from E_3) is exactly compensated by the piezoelectric response (from σ_6 via Δ), so that $\delta P_+ = \delta P_- = 0$.

Thus, we find that the susceptibility of the polydomain state of the film is independent of temperature. Using the material parameters of KDP given above, the corresponding value of the relative permittivity can be evaluated as $\chi_{\text{tot}}/\epsilon_0 \approx 840$. Not too close to the phase transition, this value substantially exceeds the lattice contribution to the permittivity in the bulk material. This situation significantly differs from that in the films of proper ferroelectric–improper ferroelastics addressed in Sect. 9.6.4. In the latter case, the domain and lattice contribution to the permittivity of the film were of the same order, having similar temperature dependences.

The results obtained above can be illustrated with the calculated temperature dependence of dielectric permittivity in the KDP film of the considered orientation, which is shown in Fig. 9.9.1. When plotting this curve, we used Eq. (9.9.4) for the paraelectric phase and Eq. (9.9.17) for the ferroelectric phase. In addition it was assumed that, in the film, the phase transition from the paraelectric to the ferroelectric polydomain state of the film takes place at T_{polyd} which is very close to the transition temperature in the bulk material, T_0 . This is justified

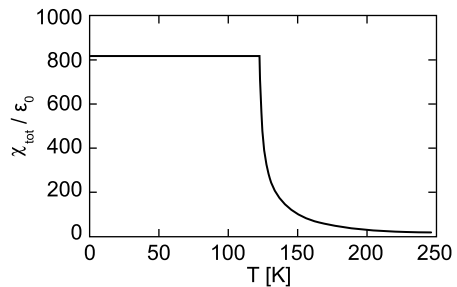


Fig. 9.9.1 Relative dielectric susceptibility of a ferroelectric/ferroelastic thin film with a dense domain pattern calculated for the parameters of KDP. After Tagantsev (2005)

for films which are thick enough. The point is as follows. In the dense domain pattern the material is on average non-stress; this favors the transition to the multidomain state at T_0 . However, the gain in the bulk energy of the ferroelectric state is opposed by the energy of the stray elastic field at the substrate/ferroelectric interface and the self-energy of the domain walls. The gain in the bulk energy is obviously proportional to the film thickness h whereas, as was discussed in Sect. 9.3.3, the optimized sum of the latter two contributions to the energy of the system is proportional to \sqrt{h} . Thus, the thicker the film, the more dominant the role of the bulk energy and, therefore the closer T_{polyd} to T_0 . For the moment, no quantitative theory, which could specify $T_0 - T_{\text{polyd}}$ vs. h dependence for KDP-type films is available in the literature. However, this difference can be roughly evaluated as (Tagantsev, 2005; Bratkovsky and Levanyuk, 2001a,b)

$$T_0 - T_{\text{polyd}} \cong \delta T_0 a / h \quad (9.9.18)$$

where δT_0 is coming from Eq. (9.9.5) and a is the atomic spacing in the material. This implies that, in realistically thick KDP films, the difference $T_0 - T_{\text{polyd}}$ is really small.

The result obtained above that the permittivity of polydomain proper ferroelectric–ferroelastic films is temperature independent (in contrast to a pronounced temperature dependence in films of proper ferroelectric–improper ferroelastics) can be readily elucidated at least not too close to the phase transition where the results of the Roytburd mean-strain theory are applicable. As clear from Sect. 9.6.4, the domain contribution to the dielectric constant from a ferroelastic domain pattern in a film clamped by a substrate is proportional to P_S^2 and inversely proportional to the spontaneous deformation squared. At the same time the spontaneous deformation is proportional to P_S in proper ferroelectric–ferroelastics and to P_S^2 in proper ferroelastics–improper ferroelastics. This implies the domain contribution to the permittivity, which is temperature independent in proper ferroelectric–ferroelastics whereas in proper ferroelastics–improper ferroelastics it goes as $1/P_S^2$.


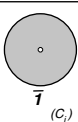
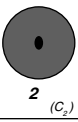
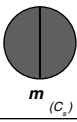
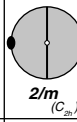
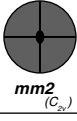

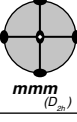
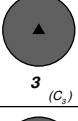
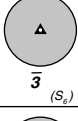
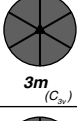
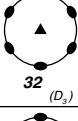
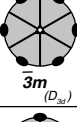
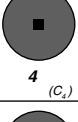
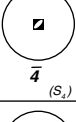

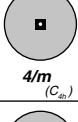
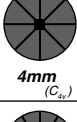


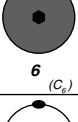
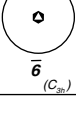
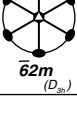
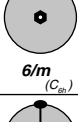
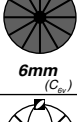
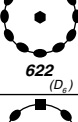
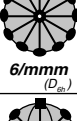
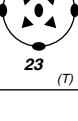
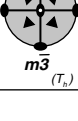
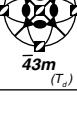
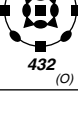
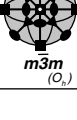
To conclude this section we would like to discuss one more remarkable feature of films of proper ferroelectric/ferroelastics. Namely, this system makes an exemplary case where the choice of the order parameter (between variables with the same transformation properties) is crucial. In the KDP-type materials, many features can be described equally well using either P_3 or ε_6 as the order parameter. In the above analysis we have used P_3 as the order parameter. Such choice corresponds to the case of KDP, the classical example of the system under consideration, where there is no freedom in choice between P_3 or ε_6 since with the strain as the order parameter one fails to explain the absence of the temperature anomaly of c_{66}^P , which is experimentally documented (Jona and Shirane, 1962). At the same time, in principle, one may address the same problem using ε_6 as the order parameter. Such analysis has been performed by Bratkovsky and Levanyuk (2001a,b) who have arrived at conclusions which are totally different from

those presented above. Specifically, their theory predicts absolute instability of the single-domain state (at any temperature) and suppression of the domain contribution to the dielectric permittivity (in the linear approximation). Here it is worth mentioning that some of the properties of the system considered may be rather insensitive to the order parameter choice. For example, though the aforementioned approach by Bratkovsky and Levanyuk is absolutely inapplicable to the description of the dielectric properties of KDP thin films, the description of the equilibrium domain pattern obtained within this approach makes a reasonable approximation.

Appendix A

32 Point Groups: Notations, Symmetry Elements, Crystalline Classes, Group Orders, Subgroups, and Supergroups

Table A.1 Stroganov's table for 32 point groups

Triclinic	 1 (C_1)			 $\bar{1}$ (C_1)			
Monoclinic	 2 (C_2)			 m (C_2)		 $2/m$ (C_{2h})	
Orthorhombic				 $mm2$ (C_{2v})	 222 (D_2)	 mmm (D_{2h})	
Trigonal	 3 (C_3)			 $\bar{3}$ (S_6)	 $3m$ (C_{3v})	 32 (D_3)	 $\bar{3}m$ (D_{3d})
Tetragonal	 4 (C_4)	 $\bar{4}$ (S_4)	 $\bar{4}2m$ (D_{2d})	 $4/m$ (C_{4h})	 $4mm$ (C_{4v})	 422 (D_4)	 $4/mmm$ (D_{4h})
Hexagonal	 6 (C_6)	 $\bar{6}$ (C_{3h})	 $\bar{6}2m$ (D_{3h})	 $6/m$ (C_{6h})	 $6mm$ (C_{6v})	 622 (D_6)	 $6/mmm$ (D_{6h})
Cubic	 23 (T)			 $m\bar{3}$ (T_d)	 $\bar{4}3m$ (T_d)	 432 (O)	 $m\bar{3}m$ (O_h)



 → polar
  → centrosymmetric

Table A.2 Group orders, subgroups, and supergroups among the 32 point groups

$m\bar{3}m$	48	*							
$\bar{4}3m$	24	× *							
432	24	× *							
$m\bar{3}$	24	× *							
23	12	××××*							
$6/mmm$	24		*						
$\bar{6}m2$	12		× *						
$6mm$	12		× *						
622	12		×× *						
$6/m$	12		× *						
$\bar{6}$	6		×× ×*						
6	6		× ×× × *						
$\bar{3}m$	12	×	×	*					
$3m$	6	××	×××	× *					
32	6	× ×	××× ×	× *					
$\bar{3}$	6	×× ×	× ×	× *					
3	3	×××××	×××××××	××××*					
$4/mmm$	16	×			*				
$\bar{4}2m$	8	××			× *				
$4mm$	8	×			× *				
422	8	× ×			× *				
$4/m$	8	×			× *				
$\bar{4}$	4	××			×× ×*				
4	4	× ×			× ××× *				
mmm	8	× ×	×		×	*			
$mm2$	4	×× ×	×××		×××	× *			
222	4	×××××	× ×		×× ×	× *			
$2/m$	4	× ×	× ×	×	× ×	×	*		
m	2	×× ×	××× ××	××	××× ×	××	× *		
2	2	×××××	××××× ×	× ×	×××××××	×××	× *		
$\bar{1}$	2	× ×	× ×	× ×	× ×	×	×	*	
1	1	×××××	×××××××	×××××	×××××××	×××	×××	× *	

The second column gives the order of the group. The asterisk at the top of each vertical column indicates the supergroup. The ×'s vertically below it indicate the subgroups which belong to this supergroup. Adapted from Bloss (1971).

Appendix B

Ferroc species

Table B.1 Ferroc species

1 Species no.	2 Species designation	3 n_F	4 q	5 q_P	6 q_ε	7 q_d	8 q_s	9
001	$m\bar{3}m - d - \bar{4}3m$	1	2	0	1	2	1	
002	$m\bar{3}m - 432$	1	2	0	1	0	1	$\varepsilon[V^2]$
003	$m\bar{3}m - m\bar{3}$	1	2	0	1	0	1	$\{V^2V^2\}$
004	$m\bar{3}m - d - 23$	1	4	0	1	2	1	RR
005	$m\bar{3}m - \varepsilon s - \bar{3}_{xyz}m_{\bar{xy}}$	4	4	0	4	0	4	
006	$m\bar{3}m - P\varepsilon ds - 3_{xyz}m_{\bar{xy}}$	4	8	8	4	8	4	
007	$m\bar{3}m - \varepsilon ds - 3_{xyz}2_{\bar{xy}}$	4	8	0	4	8	4	
008	$m\bar{3}m - \varepsilon s - \bar{3}_{xyz}$	4	8	0	4	0	8	
009	$m\bar{3}m - Pds - 3xyz$	4	16	8	4	16	8	RR
010	$m\bar{3}m - \varepsilon s - 4_z/m_x m_y m_z$	3	3	0	3	0	3	
011	$m\bar{3}m - \varepsilon ds - 4_z 2_{xy} m_x$	3	6	0	3	6	3	1
012	$m\bar{3}m - \varepsilon ds - 4_z 2_{xy} m_{xy}$	3	6	0	3	6	3	1
013	$m\bar{3}m - P\varepsilon ds - 4_z m_x m_{xy}$	3	6	6	3	6	3	
014	$m\bar{3}m - \varepsilon ds - 4_z 2_x 2_{xy}$	3	6	0	3	6	3	
015	$m\bar{3}m - \varepsilon s - 4_z/m_z$	3	6	0	3	0	6	
016	$m\bar{3}m - \varepsilon ds - \bar{4}$	3	12	0	3	12	6	RR
017	$m\bar{3}m - P\varepsilon ds - 4$	3	12	6	3	12	6	
018	$m\bar{3}m - \varepsilon s - m_x m_y m_z$	1	6	0	6	0	6	
019	$m\bar{3}m - \varepsilon s - m_{xy} m_{\bar{xy}} m_z$	3	6	0	6	0	6	
020	$m\bar{3}m - P\varepsilon ds - m_x m_y 2_z$	3	12	6	6	12	6	
021	$m\bar{3}m - P\varepsilon ds - m_{xy} m_{\bar{xy}} 2_z$	3	12	6	6	12	6	RR
022	$m\bar{3}m - P\varepsilon ds - m_{\bar{xy}} m_z 2_{xy}$	6	12	12	6	12	6	RR
023	$m\bar{3}m - \varepsilon ds - 2_x 2_y 2_z$	1	12	0	6	12	6	
024	$m\bar{3}m - \varepsilon ds - 2_{xy} 2_{\bar{xy}} 2_z$	3	12	0	6	12	6	RR
025	$m\bar{3}m - \varepsilon s - 2_{xy}/m_{xy}$	6	12	0	12	0	12	2 IRs
026	$m\bar{3}m - \varepsilon s - 2_z/m_z$	3	12	0	12	0	12	RR
027	$m\bar{3}m - P\varepsilon ds - m_z$	3	24	24	12	24	12	2 IRs
028	$m\bar{3}m - P\varepsilon ds - m_{xy}$	6	24	24	12	24	12	
029	$m\bar{3}m - P\varepsilon ds - 2_{xy}$	6	24	12	12	24	12	
030	$m\bar{3}m - P\varepsilon ds - 2_z$	3	24	6	12	24	12	RR
031	$m\bar{3}m - \varepsilon s - \bar{1}$	1	24	0	24	0	24	2 IRs
032	$m\bar{3}m - P\varepsilon ds - 1$	1	48	48	24	24	24	2 IRs

Table B.1 (continued)

1 Species no.	2 Species designation	3 n_F	4 q	5 q_P	6 q_ε	7 q_d	8 q_s	9
033	$\bar{4}3m - 23$	1	2	0	1	1	1	$\varepsilon[V^2]$
034	$\bar{4}3m - P\varepsilon ds - 3_{xyz}m_{\bar{x}y}$	4	4	4	4	4	4	
035	$\bar{4}3m - P\varepsilon ds - 3_{xyz}$	4	8	4	4	4	8	
036	$\bar{4}3m - \varepsilon ds - \bar{4}_z 2_x m_{xy}$	3	3	0	3	3	3	
037	$\bar{4}3m - \varepsilon ds - \bar{4}_z$	3	6	0	3	6	6	
038	$\bar{4}3m - P\varepsilon ds - m_{xy}m_{\bar{x}y}2_z$	3	6	6	6	6	6	
039	$\bar{4}3m - \varepsilon ds - 222$	1	6	0	6	6	6	
040	$\bar{4}3m - P\varepsilon ds - m_{xy}$	6	12	12	12	12	12	2 IRs
041	$\bar{4}3m - P\varepsilon ds - 2_z$	3	12	6	12	12	12	RR
042	$\bar{4}3m - P\varepsilon ds - 1$	1	24	24	24	24	24	2 IRs
043	$432-d-23$	1	2	0	1	2	1	
044	$432 - \varepsilon ds - 3_{xyz}2_{\bar{x}y}$	4	4	0	4	4	4	
045	$432 - P\varepsilon ds - 3_{xyz}$	4	8	8	4	8	8	
046	$432 - \varepsilon ds - 4_z 2_x 2_{xy}$	3	3	0	3	3	3	
047	$432 - P\varepsilon ds - 4_z$	3	6	6	3	6	6	
048	$432 - \varepsilon ds - 2_x 2_y 2_z$	1	6	0	6	6	6	
049	$432 - \varepsilon ds - 2_{xy} 2_{\bar{x}y} 2_z$	3	6	0	6	6	6	
050	$432 - P\varepsilon ds - 2_{xy}$	6	12	12	12	12	12	
051	$432 - P\varepsilon ds - 2_z$	3	12	6	12	12	12	RR
052	$432 - P\varepsilon ds - 1$	1	24	24	24	24	24	2 IRs
053	$m\bar{3} - d - 23$	1	2	0	1	2	1	
054	$m\bar{3} - \varepsilon s - \bar{3}_{xyz}$	4	4	0	4	0	4	
055	$m\bar{3} - P\varepsilon ds - 3_{xyz}$	4	8	8	4	8	4	
056	$m\bar{3} - \varepsilon s - mmm$	1	3	0	3	0	3	
057	$m\bar{3} - P\varepsilon ds - m_x m_y 2_z$	3	6	6	3	6	3	
058	$m\bar{3} - \varepsilon ds - 1$	1	6	0	3	6	3	
059	$m\bar{3} - \varepsilon s - 2_z/m_z$	3	6	0	6	0	6	
060	$m\bar{3} - P\varepsilon ds - m_z$	3	12	12	6	12	6	
061	$m\bar{3} - P\varepsilon ds - 2_z$	3	12	6	6	12	6	RR
062	$m\bar{3} - s - \bar{1}$	1	12	0	12	0	12	
063	$m\bar{3} - P\varepsilon ds - 1$	1	24	24	12	24	12	
064	$23 - P\varepsilon ds - 3_{xyz}$	4	4	4	4	4	4	
065	$23 - \varepsilon ds - 222$	1	3	0	3	3	3	
066	$23 - P\varepsilon ds - 2$	3	6	6	6	6	6	
067	$23 - P\varepsilon ds - 1$	1	12	12	12	12	12	
068	$6/mmm - d - \bar{6}_z m_y 2_x$	1	2	0	1	2	1	
	$6/mmm - d - \bar{6}_z m_x 2_y$							
069	$6/mmm - Pd - 6mm$	1	2	2	1	2	1	
070	$6/mmm - d - 622$	1	2	0	1	2	1	
071	$6/mmm - 6/m$	1	2	0	1	2	1	$\varepsilon V[V^2]$
072	$6/mmm - d - \bar{6}$	1	4	0	1	4	1	RR
073	$6/mmm - Pd - 6$	1	4	2	1	4	1	RR
074	$6/mmm - s - \bar{3}_z m_x$	1	2	0	1	2	2	
	$6/mmm - s - \bar{3}_z m_y$							
075	$6/mmm - Pd - 3_z m_x$	1	4	2	1	4	2	RR
	$6/mmm - Pd - 3_z m_y$							

Table B.1 (continued)

1 Species no.	2 Species designation	3 n_F	4 q	5 q_P	6 q_ε	7 q_d	8 q_s	9
076	$6/mmm - ds - 3_2 2_x$ $6/mmm - ds - 3_2 2_y$	1	4	0	1	4	2	RR
077	$6/mmm - s - \bar{3}$	1	4	0	1	0	4	RR
078	$6/mmm - Pds - 3$	1	8	2	1	8	4	RR
079	$6/mmm - \varepsilon s - m_x m_y m_z$	3	3	0	3	3	3	
080	$6/mmm - P\varepsilon ds - m_x m_y 2_z$	3	6	2	3	6	3	
081	$6/mmm - P\varepsilon ds - m_x m_z 2_y$ $6/mmm - P\varepsilon ds - m_y m_z 2_x$	3	6	6	3	6	3	
082	$6/mmm - \varepsilon ds - 222$	3	6	0	3	6	3	
083	$6/mmm - \varepsilon s - 2_x/m_x$ $6/mmm - \varepsilon s - 2_y/m_y$	3	6	0	6	0	6	
084	$6/mmm - \varepsilon s - 2_z/m_z$	1	6	0	6	0	6	
085	$6/mmm - P\varepsilon ds - m_x$ $6/mmm - P\varepsilon ds - m_y$	3	12	12	6	12	6	RR
086	$6/mmm - P\varepsilon ds - m_z$	1	12	12	6	12	6	
087	$6/mmm - P\varepsilon ds - 2_x$ $6/mmm - P\varepsilon ds - 2_y$	3	12	6	6	12	6	RR
088	$6/mmm - P\varepsilon ds - 2_z$	1	12	2	6	12	6	
089	$6/mmm - s - \bar{1}$	1	12	0	12	0	12	
090	$6/mmm - P\varepsilon ds - 1$	1	24	24	12	24	12	RR
091	$\bar{6}m2 - d - \bar{6}$	1	2	0	1	2	1	
092	$\bar{6}m2 - Pds - 3m$	1	2	2	1	2	2	
093	$\bar{6}m2 - ds - 32$	1	2	0	1	2	2	
094	$\bar{6}m2 - Pds - 3$	1	4	2	1	4	4	RR
095	$\bar{6}m2 - P\varepsilon ds - m_x m_z 2_y$	3	3	3	3	3	3	
096	$\bar{6}m2 - P\varepsilon ds - m_z$	1	6	6	6	6	6	
097	$\bar{6}m2 - P\varepsilon ds - m_x$	3	6	6	6	6	6	
098	$\bar{6}m2 - P\varepsilon ds - 2y$	3	6	3	6	6	6	
099	$\bar{6}m2 - P\varepsilon ds - 1$	1	12	12	12	12	12	
100	$6mm - d - 6$	1	2	1	1	2	1	
101	$6mm - ds - 3_2 m_x$ $6mm - ds - 3_2 m_y$	1	2	1	1	2	2	
102	$6mm - ds - 3$	1	4	1	1	4	4	RR
103	$6mm - \varepsilon ds - m_x m_y 2_z$	3	3	1	3	3	3	
104	$6mm - P\varepsilon ds - m_x$ $6mm - P\varepsilon ds - m_y$	3	6	6	6	6	6	
105	$6mm - \varepsilon ds - 2_z$	1	6	1	6	6	6	
106	$6mm - P\varepsilon ds - 1$	1	12	12	12	12	12	
107	$622 - Pd - 6$	1	2	2	1	2	1	
108	$622 - ds - 3_2 2_x$ $622 - ds - 3_2 2_y$	1	2	0	1	2	2	
109	$622 - Pds - 3$	1	4	2	1	4	4	RR
110	$622 - \varepsilon ds - 2_x 2_y 2_z$	3	3	0	3	3	3	
111	$622 - P\varepsilon ds - 2_x$ $622 - P\varepsilon ds - 2_y$	3	6	6	6	6	6	
112	$622 - P\varepsilon ds - 2_z$	1	6	2	6	6	6	

Table B.1 (continued)

1 Species no.	2 Species designation	3 n_F	4 q	5 q_P	6 q_ε	7 q_d	8 q_s	9
113	$622-P\epsilon ds-1$	1	12	12	12	12	12	
114	$6/m-d-\bar{6}$	1	2	0	1	2	1	
115	$6/m-Pd-6$	1	2	2	1	2	1	
116	$6/m-s-\bar{3}$	1	2	0	1	0	2	
117	$6/m-Pds-3$	1	4	2	1	4	2	RR
118	$6/m-\varepsilon s-2/m$	1	3	0	3	0	3	
119	$6/m-P\epsilon ds-m$	1	6	6	3	6	3	
120	$6/m-P\epsilon ds-2$	1	6	2	3	6	3	
121	$6/m-\varepsilon s-\bar{1}$	1	6	0	6	0	6	
122	$6/m-P\epsilon ds-1$	1	12	12	6	12	12	RR
123	$\bar{6}-Pds-3$	1	2	2	1	2	2	
124	$\bar{6}-P\epsilon ds-m$	1	3	3	3	3	3	
125	$\bar{6}-P\epsilon ds-1$	1	6	6	6	6	6	
126	$6-ds-3$	1	2	1	1	2	2	
127	$6-\varepsilon ds-2$	1	3	1	3	3	3	
128	$6-P\epsilon ds-1$	1	6	6	6	6	6	
129	$\bar{3}m-Pd-3m$	1	2	2	1	2	1	
130	$\bar{3}m-d-32$	1	2	0	1	2	1	
131	$\bar{3}m-s-\bar{3}$	1	2	0	1	0	2	
132	$\bar{3}m-Pds-3$	1	4	2	1	4	2	RR
133	$\bar{3}m-\varepsilon s-2/m$	3	3	0	3	0	3	
134	$\bar{3}m-P\epsilon ds-m$	3	6	6	3	6	3	
135	$\bar{3}m-P\epsilon ds-2$	3	6	6	3	6	3	
136	$\bar{3}m-\varepsilon s-\bar{1}$	1	6	0	6	0	6	
137	$\bar{3}m-P\epsilon ds-1$	1	12	12	6	12	6	
138	$3m-ds-3$	1	2	1	1	2	2	
139	$3m-P\epsilon ds-m$	3	3	3	3	3	3	
140	$3m-P\epsilon ds-1$	1	6	6	6	6	6	
141	$32-Pds-3$	1	2	2	1	2	2	
142	$32-P\epsilon ds-2$	3	3	3	3	3	3	
143	$32-P\epsilon ds-1$	1	6	6	6	6	6	
144	$\bar{3}-Pd-3$	1	2	2	1	2	1	
145	$\bar{3}-\varepsilon s-\bar{1}$	1	3	0	3	0	3	
146	$\bar{3}-P\epsilon ds-1$	1	6	6	3	6	3	
147	$3-P\epsilon ds-1$	1	3	3	3	3	3	
148	$4/mmm-d-\bar{4}_z2_xm_{xy}$	1	2	0	1	2	1	
	$4/mmm-d-\bar{4}_z2_{xy}m_x$							
149	$4/mmm-Pd-4mm$	1	2	2	1	2	1	
150	$4/mmm-d-422$	1	2	0	1	2	1	
151	$4/mmm-s-4/m$	1	2	0	1	0	2	
152	$4/mmm-ds-\bar{4}$	1	4	0	1	4	2	RR
153	$4/mmm-Pds-4$	1	4	2	1	4	2	RR
154	$4/mmm-\varepsilon s-m_xm_y m_z$	1	2	0	2	0	2	
	$4/mmm-\varepsilon s-m_{xy}m_{\bar{xy}}m_z$							
155	$4/mmm-P\epsilon ds-m_y m_z 2_x$	2	4	4	2	4	2	
	$4/mmm-P\epsilon ds-m_{\bar{xy}}m_z 2_{xy}$							

Table B.1 (continued)

1 Species no.	2 Species designation	3 n_F	4 q	5 q_P	6 q_ε	7 q_d	8 q_s	9
156	$4/mmm-P\epsilon ds-m_x m_y 2_z$ $4/mmm-P\epsilon ds-m_{xy} m_{\bar{xy}} 2_z$	1	4	2	2	4	2	RR
157	$4/mmm-\epsilon ds-2_x 2_y 2_z$ $4/mmm-\epsilon ds-2_{xy} 2_{\bar{xy}} 2_z$	1	4	0	2	4	2	RR
158	$4/mmm-\epsilon s-2_x/m_x$ $4/mmm-\epsilon s-2_{xy}/m_{xy}$	2	4	0	4	0	4	
159	$4/mmm-\epsilon s-2_z/m_z$	1	4	0	4	0	4	RR
160	$4/mmm-P\epsilon ds-m_x$ $4/mmm-P\epsilon ds-m_{xy}$	2	8	8	4	8	4	RR
161	$4/mmm-P\epsilon ds-m_z$	1	8	8	4	8	4	
162	$4/mmm-P\epsilon ds-2_x$ $4/mmm-P\epsilon ds-2_{xy}$	2	8	4	4	8	4	RR RR
163	$4/mmm-P\epsilon ds-2_z$	1	8	2	4	8	4	RR
164	$4/mmm-\epsilon s-\bar{1}$	1	8	0	8	0	8	
165	$4/mmm-P\epsilon ds-1$	1	16	16	8	16	8	RR
166	$\bar{4}2m-ds-4$	1	2	0	1	2	2	
167	$\bar{4}2m-P\epsilon ds-mm2$	1	2	2	2	2	2	
168	$\bar{4}2m-\epsilon ds-222$	1	2	0	2	2	2	
169	$\bar{4}2m-P\epsilon ds-m_{xy}$	2	4	4	4	4	4	
170	$\bar{4}2m-P\epsilon ds-2_x$	2	4	4	4	4	4	
171	$\bar{4}2m-P\epsilon ds-2_z$	1	4	2	4	4	4	RR
172	$\bar{4}2m-P\epsilon ds-1$	1	8	8	8	8	8	
173	$4mm-ds-4$	1	2	1	1	2	2	
174	$4mm-\epsilon ds-m_x m_y 2_z$ $4mm-\epsilon ds-m_{xy} m_{\bar{xy}} 2_z$	1	2	1	2	2	2	
175	$4mm-P\epsilon ds-m_x$ $4mm-P\epsilon ds-m_{xy}$	2	4	4	4	4	4	
176	$4mm-\epsilon ds-2$	1	4	1	4	4	4	RR
177	$4mm-P\epsilon ds-1$	1	8	8	8	8	8	
178	$422-Pds-4$	1	2	2	1	2	2	
179	$422-\epsilon ds-2_x 2_y 2_z$ $422-\epsilon ds-2_{xy} 2_{\bar{xy}} 2_z$	1	2	0	2	2	2	
180	$422-P\epsilon ds-2_x$ $422-P\epsilon ds-2_{xy}$	2	4	4	4	4	4	
181	$422-P\epsilon ds-2_z$	1	4	2	4	4	4	RR
182	$422-P\epsilon ds-1$	1	8	8	8	8	8	
183	$4/m-d-4$	1	2	0	1	2	1	
184	$4/m-Pd-4$	1	2	2	1	2	1	
185	$4/m-\epsilon s-2/m$	1	2	0	2	0	2	
186	$4/m-P\epsilon ds-m$	1	4	4	2	4	2	
187	$4/m-P\epsilon ds-2$	1	4	2	2	4	2	RR
188	$4/m-\epsilon s-\bar{1}$	1	4	0	4	0	4	
189	$4/m-P\epsilon ds-1$	1	8	8	4	8	4	RR
190	$\bar{4}-P\epsilon ds-2$	1	2	2	2	2	2	
191	$\bar{4}-P\epsilon ds-1$	1	4	4	4	4	4	
192	$4-\epsilon ds-2$	1	2	1	2	2	2	

Table B.1 (continued)

1 Species no.	2 Species designation	3 n_F	4 q	5 q_P	6 q_ε	7 q_d	8 q_s	9
193	$4-P\epsilon ds-1$	1	4	4	4	4	4	
194	$mmm-Pd-m_x m_y 2z$ $mmm-Pd-m_x m_z 2y$ $mmm-Pd-m_y m_z 2x$	1	2	2	1	2	1	
195	$mmm-d-222$	1	2	0	1	2	1	
196	$mmm-\epsilon s-2_x/m_z$ $mmm-\epsilon s-2_y/m_y$ $mmm-\epsilon s-2_z/m_x$	1	2	0	2	0	2	
197	$mmm-P\epsilon ds-m_x$ $mmm-P\epsilon ds-m_y$ $mmm-P\epsilon ds-m_z$	1	4	4	2	4	2	RR
198	$mmm-P\epsilon ds-2_x$ $mmm-P\epsilon ds-2_y$ $mmm-P\epsilon ds-2_z$	1	4	2	2	4	2	RR
199	$mmm-\epsilon s-\bar{1}$	1	4	0	4	0	4	RR
200	$mmm-P\epsilon ds-1$	1	8	8	4	8	4	RR
201	$mm2-P\epsilon ds-m_x$ $mm2-P\epsilon ds-m_y$	1	2	2	2	2	2	
202	$mm2-\epsilon ds-2$	1	2	1	2	2	2	
203	$mm2-P\epsilon ds-1$	1	4	4	4	4	4	RR
204	$222-P\epsilon ds-2_x$ $222-P\epsilon ds-2_y$ $222-P\epsilon ds-2_z$	1	2	2	2	2	2	
205	$222-P\epsilon ds-1$	1	4	4	4	4	4	RR
206	$2/m-Pd-m$	1	2	2	1	2	1	
207	$2/m-Pd-2$	1	2	2	1	2	1	
208	$2/m-\epsilon s-\bar{1}$	1	2	0	2	0	2	
209	$2/m-P\epsilon ds-1$	1	4	4	2	4	2	RR
210	$m-P\epsilon ds-1$	1	2	2	2	2	2	
211	$2-P\epsilon ds-1$	1	2	2	2	2	2	
212	$\bar{1}-Pd-1$	1	2	2	1	2	1	

Column 1: sequential number of the species. *Column 2:* symbol of the species. *Column 3:* number of equivalent subgroups F . *Column 4:* total number of domain states. *Column 5:* number of ferroelectric domain states. Here 0 means that F is nonpolar while 1 means that F is pyroelectric with only one orientation of P_S (or better to say, of the pyroelectric coefficient). *Column 6:* number of ferroelastic domain states. Number 1 means that F is nonferroelastic. *Column 7:* number q_d of domain states differing in the piezoelectric tensor or, more generally, in the tensor of symmetry $V[V^2]$ or $[V^2]V$. Here number 0 means that F is not piezoelectric while 1 means that F is piezoelectric but has no new components of the appropriate tensor. *Column 8:* number of ferrobielastic domain states. Here 1 means that the compliance matrix has no new components in the distorted phase. *Column 9:* the lowest order tensor in which some domain states are distinguished for higher order ferroics; symbols “2 IRs” and “RR” indicate that the transition is induced by two different irreducible representations or by a reducible representation, respectively

Appendix C

Phase Transitions into Ferroelectric Phases

Table C.1 Phase transitions into ferroelectric phases

1 Species no.	2 Species designation	3 q	4 Data on polarization	5 qp	6 Data on strain	7 q_ε	8 Shuvalov's symbol
Cubic parent phase							
006	$m\bar{3}m - P\epsilon ds - 3_{xyz}m_{xy}$	8	$P_x = P_y = P_z$	8	$\delta\epsilon_{xx}, \delta\epsilon_{xx}, \delta\epsilon_{xx}, \delta\epsilon_{xx}, 0, 0, 0$	4	$m\bar{3}m(4)D3F3m =$
009	$m\bar{3}m - P\epsilon ds - 3_{xyz}$	16	$[P_x = P_y = P_z]$	8	$\delta\epsilon_{xx}, \delta\epsilon_{xx}, \delta\epsilon_{xx}, \delta\epsilon_{xx}, \delta\epsilon_{yz}, \delta\epsilon_{yz}, \delta\epsilon_{yz}, \delta\epsilon_{yz}$	4	$*m\bar{3}m(4)D3F3 =$
013	$m\bar{3}m - P\epsilon ds - 4_2m_xm_{xy}$	6	P_z	6	$\delta\epsilon_{xx}, \delta\epsilon_{xx}, \delta\epsilon_{zz}, 0, 0, 0$	3	$m\bar{3}m(3)D4F4mm =$
017	$m\bar{3}m - P\epsilon ds - 4_2$	12	$[P_z]$	6	$\delta\epsilon_{xx}, \delta\epsilon_{xx}, \delta\epsilon_{zz}, 0, 0, 0$	3	$*m\bar{3}m(3)D4F4 =$
020	$m\bar{3}m - P\epsilon ds - m_xm_y2_z$	12	$[P_z]$	6	$\delta\epsilon_{xx}, \delta\epsilon_{xx}, \delta\epsilon_{yz}, \delta\epsilon_{yz}, 0, 0, 0$	6	$*m\bar{3}m(3)D2Fmm2\neq$
021	$m\bar{3}m - P\epsilon ds - m_{xy}m_{xy}2_z$	12	$[P_z]$	6	$\delta\epsilon_{xx}, \delta\epsilon_{xx}, \delta\epsilon_{zz}, 0, 0, \epsilon_{xy}$	6	$*m\bar{3}m(3)D2Fmm2\neq$
022	$m\bar{3}m - P\epsilon ds - m_{xy}m_z2_{xy}$	12	$P_x = P_y (P_x = P_y)$	12	$\delta\epsilon_{xx}, \delta\epsilon_{xx}, \delta\epsilon_{zz}, 0, 0, \epsilon_{xy}$	6	$m\bar{3}m(6)D2Fmm2 =$
027	$m\bar{3}m - P\epsilon ds - m_z$	24	$P_x, P_y (P_x, P_y)$	24	$\delta\epsilon_{xx}, \delta\epsilon_{yy}, \delta\epsilon_{zz}, 0, 0, \epsilon_{xy}$	12	$m\bar{3}m(12)A4Fm =$
028	$m\bar{3}m - P\epsilon ds - m_{xy}$	24	$P_x = -P_y, P_z$	24	$\delta\epsilon_{xx}, \delta\epsilon_{xx}, \delta\epsilon_{zz}, \delta\epsilon_{yz}, -\delta\epsilon_{yz}, \epsilon_{xy}$	12	$m\bar{3}m(12)A^*2Fm =$
029	$m\bar{3}m - P\epsilon ds - 2_{xy}$	24	$(P_y = P_x)$	12	$\delta\epsilon_{xx}, \delta\epsilon_{xx}, \delta\epsilon_{zz}, \delta\epsilon_{yz}, -\delta\epsilon_{yz}, \epsilon_{xy}$	12	$*m\bar{3}m(3)D2F2\neq$
030	$\bar{3}m - P\epsilon ds - 2_z$	24	$[P_z]$	6	$\delta\epsilon_{xx}, \delta\epsilon_{yy}, \delta\epsilon_{zz}, 0, 0, \epsilon_{xy}$	12	$*m\bar{3}m(3)D4F2\neq$
032	$m\bar{3}m - P\epsilon ds - 1$	48	$P_x, P_y, P_z (P_x, P_y, P_z)$	48	$\delta\epsilon_{xx}, \delta\epsilon_{yy}, \delta\epsilon_{zz}, \delta\epsilon_{yz}, \delta\epsilon_{yz}, \epsilon_{xy}$	24	$*m\bar{3}m(24)A1F1 =$
034	$3m - P\epsilon ds - 3_{xyz}m_{xy}$	4	$P_x = P_y = P_z$	4	$\delta\epsilon_{xx}, \delta\epsilon_{xx}, \delta\epsilon_{xx}, \delta\epsilon_{yz}, \delta\epsilon_{yz}, \delta\epsilon_{yz}$	4	$\bar{4}3m(4/2)D3F3m$
035	$\bar{4}3m - P\epsilon ds - 3_{xyz}m_{xy}$	8	$(P_x = P_y = P_z)$	4	$\delta\epsilon_{xx}, \delta\epsilon_{xx}, \delta\epsilon_{xx}, \delta\epsilon_{yz}, \delta\epsilon_{yz}, \delta\epsilon_{yz}$	4	$*\bar{4}3m(4/2)D3F3$
038	$\bar{4}3m - P\epsilon ds - m_{xy}m_{xy}2_z$	6	P_z	6	$\delta\epsilon_{xx}, \delta\epsilon_{xx}, \delta\epsilon_{zz}, 0, 0, \epsilon_{xy}$	6	$\bar{4}3m(3)D4Fmm2\neq$
040	$\bar{4}3m - P\epsilon ds - m_{xy}$	12	$P_x = P_y, P_z (P_x = P_y, P_z)$	12	$\delta\epsilon_{xx}, \delta\epsilon_{xx}, \delta\epsilon_{zz}, \delta\epsilon_{yz}, -\delta\epsilon_{yz}, \epsilon_{xy}$	12	$\bar{4}3m(12/2)AmFm$
041	$\bar{4}3m - P\epsilon ds - 2_z$	12	$[P_z]$	6	$\delta\epsilon_{xx}, \delta\epsilon_{yy}, \delta\epsilon_{zz}, 0, 0, \epsilon_{xy}$	12	$*\bar{4}3m(6/2)D4F2$

Table C.1 (continued)

1 Species no.	2 Species designation	3 q	4 Data on polarization	5 q_P	6 Data on strain	7 q_ϵ	8 Shuvalov's symbol
042	$\bar{4}3m - P\epsilon ds - 1$	24	P_x, P_y, P_z (P_x, P_y, P_z)	24	$\delta\epsilon_{xx}, \delta\epsilon_{yy}, \delta\epsilon_{zz}, \epsilon_{yz}, \epsilon_{zx}, \epsilon_{xy}$	24	$\bar{4}3m(24/2)A1F1$
045	$432 - P\epsilon ds - 3_{xyz}$	8	$P_x = P_y = P_z$	8	$\delta\epsilon_{xx}, \delta\epsilon_{xx}, \delta\epsilon_{xx}\epsilon_{yz}, \epsilon_{yz}, \epsilon_{yz}$	4	$432(4)D3F3 =$
047	$432 - P\epsilon ds - 4_z$	6	P_z	6	$\delta\epsilon_{xx}, \delta\epsilon_{xx}, \delta\epsilon_{zz}, 0, 0, 0$	3	$432(3)D4F4 =$
050	$432 - P\epsilon ds - 2_{xy}$	12	$P_x = P_y$ ($P_x = P_y$)	12	$\delta\epsilon_{xx}, \delta\epsilon_{xx}, \delta\epsilon_{zz}, \epsilon_{yz}, -\epsilon_{yz}, \epsilon_{xy}$	12	$432(6)D2F2 \neq$
051	$432 - P\epsilon ds - 2_z$	12	$[P_z]$	6	$\delta\epsilon_{xx}, \delta\epsilon_{yy}, \delta\epsilon_{zz}, 0, 0, \epsilon_{xy}$	12	$*432(3)D2F2 \neq$
052	$432 - P\epsilon ds - 1$	24	P_x, P_y, P_z (P_x, P_y, P_z)	24	$\delta\epsilon_{xx}, \delta\epsilon_{yy}, \delta\epsilon_{zz}, \epsilon_{yz}, \epsilon_{zx}, \epsilon_{xy}$	24	$432(24/2)A1F1$
055	$m\bar{3} - P\epsilon ds - 3_{xyz}$	8	$P_x = P_y = P_z$	8	$\delta\epsilon_{11}, \delta\epsilon_{11}, \delta\epsilon_{11}, \epsilon_{23}, \epsilon_{23}, \epsilon_{23}$	4	$m\bar{3}(4)D3F3 =$
057	$m\bar{3} - P\epsilon ds - m_x m_y 2_z$	6	P_z	6	$\delta\epsilon_{11}, \delta\epsilon_{22}, \delta\epsilon_{33}, 0, 0, 0$	3	$m\bar{3}(3)DmFmm2 =$
060	$m\bar{3} - P\epsilon ds - m_z$	12	P_x, P_y	12	$\delta\epsilon_{11}, \delta\epsilon_{22}, \delta\epsilon_{33}, 0, 0, \epsilon_{12}$	6	$m\bar{3}(6)AmFm =$
061	$m\bar{3} - P\epsilon ds - 2_z$	12	$[P_z]$	6	$\delta\epsilon_{11}, \delta\epsilon_{22}, \delta\epsilon_{33}, 0, 0, \epsilon_{12}$	6	$*m\bar{3}(3)D2F2 \neq$
063	$m\bar{3} - P\epsilon ds - 1$	24	P_x, P_y, P_z	24	$\delta\epsilon_{11}, \delta\epsilon_{22}, \delta\epsilon_{33}, \epsilon_{23}, \epsilon_{31}, \epsilon_{12}$	12	$m\bar{3}(12)A1F1 =$
064	$23 - P\epsilon ds - 3_{xyz}$	4	$P_x = P_y = P_z$	4	$\delta\epsilon_{11}, \delta\epsilon_{11}, \delta\epsilon_{11}, \epsilon_{23}, \epsilon_{23}, \epsilon_{23}$	4	$23(4/2)D3F3$
066	$23 - P\epsilon ds - 2_z$	6	P_z	6	$\delta\epsilon_{11}, \delta\epsilon_{22}, \delta\epsilon_{33}, 0, 0, \epsilon_{12}$	6	$23(3)D2F2 \neq$
067	$23 - P\epsilon ds - 1$	12	P_x, P_y, P_z	12	$\delta\epsilon_{11}, \delta\epsilon_{22}, \delta\epsilon_{33}, \epsilon_{23}, \epsilon_{31}, \epsilon_{12}$	12	$23(12/2)A1F1$
Hexagonal and trigonal parent phases							
069	$6/mmm - Pd - 6mm$	2	P_z	2	$\delta\epsilon_{xx}, \delta\epsilon_{xx}, \delta\epsilon_{zz}, 0, 0, 0$	1	$6/mmm(1)$ $D6F6mm =$
073	$6/mmm - Pd - 6$	4	$[P_z]$	2	$\delta\epsilon_{xx}, \delta\epsilon_{xx}, \delta\epsilon_{zz}, 0, 0, 0$	1	$*6/mmm(1)D6F6 =$
075	$6/mmm - Pds - 3_z m_x$	4	$[P_z]$	2	$\delta\epsilon_{xx}, \delta\epsilon_{xx}, \delta\epsilon_{zz}, 0, 0, 0$	1	$*6/mmm(1)$ $D6F3m =$
078	$6/mmm - Pds - 3 m_y$	8	$[P_z]$	2	$\delta\epsilon_{xx}, \delta\epsilon_{xx}, \delta\epsilon_{zz}, 0, 0, 0$	1	$*6/mmm(1)D6F3 =$
080	$6/mmm - Peds - m_x m_y 2_z$	6	(P_z)	6	$\delta\epsilon_{xx}, \delta\epsilon_{yy}, \delta\epsilon_{zz}, 0, 0, 0$	3	$*6/mmm(3)$ $D6Fmm2 =$
081	$6/mmm - Peds - m_x m_y 2_y$	6	P_y	6	$\delta\epsilon_{xx}, \delta\epsilon_{yy}, \delta\epsilon_{zz}, 0, 0, 0$	3	$6/mmm(3)$ $D2Fmm2 =$

Table C.1 (continued)

1 Species no.	2 Species designation	3 q	4 Data on polarization	5 q_P	6 Data on strain	7 q_ϵ	8 Shuvalov's symbol
085	$6/mmm-P\epsilon ds-m_y m_z^2 x$ $6/mmm-P\epsilon ds-m_x$ $6/mmm-P\epsilon ds-m_y$	12	P_x $[P_y, P_z]$ $[P_x, P_z]$	12	$\delta\epsilon_{xx}, \delta\epsilon_{yy}, \delta\epsilon_{zz}, 0, 0, 0$ $\delta\epsilon_{xx}, \delta\epsilon_{yy}, \delta\epsilon_{zz}, \epsilon_{yz}, 0, 0$ $\delta\epsilon_{xx}, \delta\epsilon_{yy}, \delta\epsilon_{zz}, -\sqrt{3}\epsilon_{zx}$ $\epsilon_{zx}(\sqrt{3}/2)(\delta\epsilon_{xx}-\delta\epsilon_{yy})$	6	$6/mmm(6)A6Fm =$
086	$6/mmm-P\epsilon ds-m_z$	12	P_x, P_y	12	$\delta\epsilon_{xx}, \delta\epsilon_{yy}, \delta\epsilon_{zz}, 0, 0, \epsilon_{xy}$	6	$6/mmm(6)A6Fm =$
087	$6/mmm-P\epsilon ds-2_x$ $6/mmm-P\epsilon ds-2_y$	12	$[P_x]$ $[P_y]$	6	$\delta\epsilon_{xx}, \delta\epsilon_{yy}, \delta\epsilon_{zz}, \epsilon_{yz}, 0, 0$ $\delta\epsilon_{xx}, \delta\epsilon_{yy}, \delta\epsilon_{zz}, -\sqrt{3}\epsilon_{zx}, \epsilon_{zx}$ $(\sqrt{3}/2)(\delta\epsilon_{xx}-\delta\epsilon_{yy})$	6	$*6/mmm(3)D2F2$
088	$6/mmm-P\epsilon ds-2_z$	12	(P_z)	2	$\delta\epsilon_{xx}, \delta\epsilon_{yy}, \delta\epsilon_{zz}, 0, 0, \epsilon_{xy}$	6	$*6/mmmD2_z Fnm2 \neq$
090	$6/mmm-P\epsilon ds-1$	24	$[P_x, P_y, P_z]$	24	$\delta\epsilon_{xx}, \delta\epsilon_{yy}, \delta\epsilon_{zz}, \epsilon_{yz}, \epsilon_{zx}, \epsilon_{xy}$	12	$6/mmm(12)A1F1 =$
092	$6m2-P\epsilon ds-3m$	2	P_z	2	$\delta\epsilon_{xx}, \delta\epsilon_{yy}, \delta\epsilon_{zz}, 0, 0, 0$	1	$*6m2(1)D6F3m =$
094	$6m2-P\epsilon ds-3$	4	$[P_z]$	2	$\delta\epsilon_{xx}, \delta\epsilon_{yy}, \delta\epsilon_{zz}, 0, 0, 0$	1	$6m2(1)D6F3 =$
095	$6m2-P\epsilon ds-m_y m_z^2 x$	3	P_x	3	$\delta\epsilon_{xx}, \delta\epsilon_{yy}, \delta\epsilon_{zz}, 0, 0, 0$ $(\sqrt{3}/2)(\delta\epsilon_{xx}-\delta\epsilon_{yy})$	3	$*6m2(3/2)D2Fnm2$
096	$6m2-P\epsilon ds-m_z$	6	P_x, P_y	6	$\delta\epsilon_{xx}, \delta\epsilon_{yy}, \delta\epsilon_{zz}, 0, 0, \epsilon_{xy}$	6	$6m2(6/2)A6Fm$
097	$6m2-P\epsilon ds-m_x$	6	(P_y, P_z)	6	$\delta\epsilon_{xx}, \delta\epsilon_{yy}, \delta\epsilon_{zz}, \epsilon_{yz}, 0, 0$	6	$6m2(6/2)Am_x Fm$
098	$6m2-P\epsilon ds-2_x$	6	(P_y)	3	$\delta\epsilon_{xx}, \delta\epsilon_{yy}, \delta\epsilon_{zz}, \sqrt{3}\epsilon_{zx}, \epsilon_{zx} (\sqrt{3}/2)$ $(\delta\epsilon_{xx}-\delta\epsilon_{yy})$	6	$*6m2(12/2)A1F1$
099	$6m2-P\epsilon ds-1$	12	(P_x, P_y, P_z)	12	$\delta\epsilon_{xx}, \delta\epsilon_{yy}, \delta\epsilon_{zz}, \epsilon_{yz}, \epsilon_{zx}, \epsilon_{xy}$	12	$6m2(12/2)A1F1$
104	$6mm-P\epsilon ds-m_y$ $6mm-P\epsilon ds-m_x$	6	$P_y, \delta P_z$ $P_x, \delta P_z$	6	$\delta\epsilon_{xx}, \delta\epsilon_{yy}, \delta\epsilon_{zz}, \epsilon_{yz}, 0, 0$ $\delta\epsilon_{xx}, \delta\epsilon_{yy}, \delta\epsilon_{zz}, -\sqrt{3}\epsilon_{zx}, \epsilon_{zx}$ $(\sqrt{3}/22)(\delta\epsilon_{xx}-\delta\epsilon_{yy})$	6	$6mm(6/2)AmFm$
106	$6mm-P\epsilon ds-1$	12	$P_x, P_y, \delta P_z$	12	$\delta\epsilon_{xx}, \delta\epsilon_{yy}, \delta\epsilon_{zz}, \epsilon_{yz}, \epsilon_{zx}, \epsilon_{xy}$	12	$6mm(12/2)A1F1$
107	$622-Pd-6$	2	P_z	2	$\delta\epsilon_{xx}, \delta\epsilon_{yy}, \delta\epsilon_{zz}, 0, 0, 0$	1	$622(1)D6F6 \parallel$
109	$622-P\epsilon ds-3$	4	$[P_z]$	2	$\delta\epsilon_{xx}, \delta\epsilon_{yy}, \delta\epsilon_{zz}, 0, 0, 0$	1	$*622(12)D6F3 =$
111	$622-P\epsilon ds-2_x$ $622-P\epsilon ds-2_y$	6	P_x P_y	6	$\delta\epsilon_{xx}, \delta\epsilon_{yy}, \delta\epsilon_{zz}, -\sqrt{3}\epsilon_{zx}, \epsilon_{zx}$ $(\sqrt{3}/2)(\delta\epsilon_{xx}-\delta\epsilon_{yy})$	6	$622(3)D2F2 \neq$

Table C.1 (continued)

1 Species no.	2 Species designation	3 q	4 Data on polarization	5 qp	6 Data on strain	7 q_e	8 Shuvalov's symbol
112	$622-Peds-2_z$	2	(P_z)	2	$\delta\epsilon_{xx}, \delta\epsilon_{yy}, \delta\epsilon_{zz}, 0, 0, \epsilon_{xy}$	6	$*622(1)D6F2\neq$
113	$622-Peds-1$	12	$P_x, P_y, (P_z)$	12	$\delta\epsilon_{xx}, \delta\epsilon_{yy}, \delta\epsilon_{zz}, \epsilon_{yz}, \epsilon_{zx}, \epsilon_{xy}$	12	$622(1/2)A1F1$
115	$6/m-Pd-6$	2	P_z	2	$\delta\epsilon_{xx}, \delta\epsilon_{zz}, \delta\epsilon_{zz}, 0, 0, 0$	1	$6/m(1)D6F6 =$
117	$6/m-Pds-3$	4	$[P_z]$	2	$\delta\epsilon_{xx}, \delta\epsilon_{xx}, \delta\epsilon_{zz}, 0, 0, 0$	1	$*6/mD6F3 =$
119	$6/m-Peds-m$	6	P_x, P_y	6	$\delta\epsilon_{xx}, \delta\epsilon_{yy}, \delta\epsilon_{zz}, 0, 0, \epsilon_{xy}$	3	$6/m(3)A6Fm =$
120	$6/m-Peds-2$	6	(P_z)	2	$\delta\epsilon_{xx}, \delta\epsilon_{yy}, \delta\epsilon_{zz}, \epsilon_{yz}, \epsilon_{zx}, \epsilon_{xy}$	3	$*6/m(1)D6F2$
122	$6/m-Peds-1$	12	$[P_x, P_y, P_z]$	12	$\delta\epsilon_{xx}, \delta\epsilon_{yy}, \delta\epsilon_{zz}, \epsilon_{yz}, \epsilon_{zx}, \epsilon_{xy}$	6	$6/m(6)A1F1 =$
123	$\bar{6}-Pds-3$	2	P_z	2	$\delta\epsilon_{xx}, \delta\epsilon_{xx}, \delta\epsilon_{zz}, 0, 0, 0$	1	$\bar{6}(1)D6F3 =$
124	$\bar{6}-Peds-m$	3	P_x, P_y	3	$\delta\epsilon_{xx}, \delta\epsilon_{yy}, \delta\epsilon_{zz}, 0, 0, \epsilon_{xy}$	3	$\bar{6}(3/2)A6Fm$
125	$\bar{6}-Peds-1$	6	(P_x, P_y, P_z)	6	$\delta\epsilon_{xx}, \delta\epsilon_{yy}, \delta\epsilon_{zz}, \epsilon_{yz}, \epsilon_{zx}, \epsilon_{xy}$	6	$\bar{6}(6/2)A1F1$
128	$6-Peds-1$	6	$P_x, P_y, \delta P_z$	6	$\delta\epsilon_{xx}, \delta\epsilon_{yy}, \delta\epsilon_{zz}, \epsilon_{yz}, \epsilon_{zx}, \epsilon_{xy}$	6	$\bar{6}(6/2)A1F1$
129	$\bar{3}m-Pd-3m$	2	P_z	2	$\delta\epsilon_{xx}, \delta\epsilon_{xx}, \delta\epsilon_{zz}, 0, 0, 0$	1	$\bar{3}m(1)D\bar{3}F3m =$
132	$\bar{3}m-Pds-3m$	4	$[P_z]$	2	$\delta\epsilon_{xx}, \delta\epsilon_{xx}, \delta\epsilon_{zz}, 0, 0, 0$	1	$*\bar{3}m(1)D\bar{3}F3 =$
134	$\bar{3}m-Peds-m_x$	6	$P_y, (P_z)$	6	$\delta\epsilon_{xx}, \delta\epsilon_{xx}, \delta\epsilon_{zz}, \epsilon_{yz}, 0, 0$	3	$\bar{3}m(3)AmFm =$
135	$\bar{3}m-Peds-2_x$	6	P_x	6	$\delta\epsilon_{xx}, \delta\epsilon_{xx}, \delta\epsilon_{zz}, \epsilon_{yz}, 0, 0$	3	$\bar{3}m(3)DmF2 =$
137	$\bar{3}m-Peds-1$	12	$P_x, P_y, (P_z)$	12	$\delta\epsilon_{xx}, \delta\epsilon_{yy}, \delta\epsilon_{zz}, \epsilon_{yz}, \epsilon_{zx}, \epsilon_{xy}$	6	$\bar{3}m(6)A1F1 =$
139	$\bar{3}m-Peds-m_x$	3	$P_y, \delta P_z$	3	$\delta\epsilon_{xx}, \delta\epsilon_{xx}, \delta\epsilon_{zz}, \epsilon_{yz}, 0, 0$	3	$\bar{3}m(3/2)AmFm$
140	$\bar{3}m-Peds-1$	6	$P_x, P_y, \delta P_z$	6	$\delta\epsilon_{xx}, \delta\epsilon_{yy}, \delta\epsilon_{zz}, \epsilon_{yz}, \epsilon_{zx}, \epsilon_{xy}$	6	$\bar{3}m(6/2)A1F1$
141	$32-Pds-3$	2	P_z	2	$\delta\epsilon_{xx}, \delta\epsilon_{xx}, \delta\epsilon_{zz}, 0, 0, 0$	1	$32(1)D3F3 =$
142	$32-Peds-2_x$	3	P_x	3	$\delta\epsilon_{xx}, \delta\epsilon_{xx}, \delta\epsilon_{zz}, \epsilon_{yz}, 0, 0$	3	$32(3/2)D2F2$
143	$32-Peds-1$	6	$P_x, P_y, (P_z)$	6	$\delta\epsilon_{xx}, \delta\epsilon_{yy}, \delta\epsilon_{zz}, \epsilon_{yz}, \epsilon_{zx}, \epsilon_{xy}$	6	$32(6/2)A1F1$
144	$\bar{3}-Pd-3$	2	P_z	2	$\delta\epsilon_{xx}, \delta\epsilon_{xx}, \delta\epsilon_{zz}, 0, 0, 0$	1	$\bar{3}(1)D3F3 =$
146	$\bar{3}-Peds-1$	6	$P_x, P_y, (P_z)$	6	$\delta\epsilon_{xx}, \delta\epsilon_{yy}, \delta\epsilon_{zz}, \epsilon_{yz}, \epsilon_{zx}, \epsilon_{xy}$	3	$\bar{3}(3)A1F1 =$
147	$\bar{3}-Peds-1$	3	P_x, P_y	3	$\delta\epsilon_{xx}, \delta\epsilon_{yy}, \delta\epsilon_{zz}, \epsilon_{yz}, \epsilon_{zx}, \epsilon_{xy}$	3	$\bar{3}(3/2)A1F1$

Table C.1 (continued)

1 Species no.	2 Species designation	3 q	4 Data on polarization	5 q_p	6 Data on strain	7 q_e	8 Shuvalov's symbol
Tetragonal parent phase							
149	$4/mmm-Pd-4mm$	2	P_z	2	$\delta\epsilon_{xx}, \delta\epsilon_{yy}, \delta\epsilon_{zz}, 0, 0, 0$	1	$4/mmm(1)D4F4mm =$
153	$4/mmm-Pds-4$	4	$[P_z]$	2	$\delta\epsilon_{xx}, \delta\epsilon_{yy}, \delta\epsilon_{zz}, 0, 0, 0$	1	$*4/mmm(1)D4F4 =$
155	$4/mmm-Peds-m_y m_z 2_x$	4	P_x	4	$\delta\epsilon_{xx}, \delta\epsilon_{yy}, \delta\epsilon_{zz}, 0, 0, 0$	2	$4/mmm(2)D2Fmm2 =$
156	$4/mmm-Peds-m_x m_z 2_{xy}$	4	$P_x = P_y$	2	$\delta\epsilon_{xx}, \delta\epsilon_{yy}, \delta\epsilon_{zz}, 0, 0, \epsilon_{xy}$	2	$*4/mmm(2)D4Fmm2 \neq$
	$[P_z]$		$\delta\epsilon_{xx}, \delta\epsilon_{yy}, \delta\epsilon_{zz}, 0, 0, \epsilon_{xy}$				
160	$4/mmm-Peds-m_x$	8	$[P_x, P_z]$	8	$\delta\epsilon_{xx}, \delta\epsilon_{yy}, \delta\epsilon_{zz}, \epsilon_{yz}, \epsilon_{yz}, 0, 0$	4	$*4/mmm(4)A2Fm =$
161	$4/mmm-Peds-m_{xy}$	8	$[P_x = P_y, P_z]$	8	$\delta\epsilon_{xx}, \delta\epsilon_{yy}, \delta\epsilon_{zz}, \epsilon_{yz}, -\epsilon_{yz}, \epsilon_{xy}$	4	$4/mmm(4)A4Fm =$
			P_x, P_y		$\delta\epsilon_{xx}, \delta\epsilon_{yy}, \delta\epsilon_{zz}, 0, 0, \epsilon_{xy}$		
162	$4/mmm-Peds-2_x$	8	$[P_x]$	4	$\delta\epsilon_{xx}, \delta\epsilon_{yy}, \delta\epsilon_{zz}, \epsilon_{yz}, 0, 0$	4	$*4/mmm(2)D4F2$
163	$4/mmm-Peds-2_{xy}$	8	$[P_x = P_y]$	2	$\delta\epsilon_{xx}, \delta\epsilon_{yy}, \delta\epsilon_{zz}, \epsilon_{yz}, -\epsilon_{yz}, \epsilon_{xy}$	4	$*4/mmm(1)D4F2$
			$[P_z]$		$\delta\epsilon_{xx}, \delta\epsilon_{yy}, \delta\epsilon_{zz}, 0, 0, \epsilon_{xy}$		
165	$4/mmm-Peds-2_z$	16	$[P_x, P_y, P_z]$	16	$\delta\epsilon_{xx}, \delta\epsilon_{yy}, \delta\epsilon_{zz}, \epsilon_{yz}, \epsilon_{yz}, \epsilon_{zx}, \epsilon_{xy}$	8	$4/mmm(8)A1F1 =$
167	$\bar{4}2m-Peds-nm2$	2	P_z	2	$\delta\epsilon_{xx}, \delta\epsilon_{yy}, \delta\epsilon_{zz}, 0, 0, \epsilon_{xy}$	2	$\bar{4}2m(1)D4Fmm2 \neq$
169	$\bar{4}2m-Peds-m_{xy}$	4	$P_x = P_y, P_z$	4	$\delta\epsilon_{xx}, \delta\epsilon_{yy}, \delta\epsilon_{zz}, \epsilon_{yz}, -\epsilon_{yz}, \epsilon_{xy}$	4	$\bar{4}2m(4/2)AmFm$
170	$\bar{4}2m-Peds-2_x$	4	P_x	4	$\delta\epsilon_{xx}, \delta\epsilon_{yy}, \delta\epsilon_{zz}, \epsilon_{yz}, 0, 0$	4	$\bar{4}2m(2)D2F2 \neq$
171	$\bar{4}2m-Peds-2_z$	4	$[P_z]$	2	$\delta\epsilon_{xx}, \delta\epsilon_{yy}, \delta\epsilon_{zz}, 0, 0, \epsilon_{xy}$	4	$*\bar{4}2m(1)D4F2$
172	$\bar{4}2m-Peds-1$	8	$P_x, P_y, (P_z)$	8	$\delta\epsilon_{xx}, \delta\epsilon_{yy}, \delta\epsilon_{zz}, \epsilon_{yz}, \epsilon_{zx}, \epsilon_{xy}$	8	$\bar{4}2m(8/2)A1F1$
175	$4mm-Peds-m_x$	4	$P_y, \delta P_z$	4	$\delta\epsilon_{xx}, \delta\epsilon_{yy}, \delta\epsilon_{zz}, \epsilon_{yz}, 0, 0$	4	$4mm(4/2)AmFm$
177	$4mm-Peds-m_{xy}$	8	$P_x = P_y, \delta P_z$	8	$\delta\epsilon_{xx}, \delta\epsilon_{yy}, \delta\epsilon_{zz}, \epsilon_{yz}, -\epsilon_{yz}, \epsilon_{xy}$	8	$4mm(8/2)A1F1$
			$P_x, P_y, \delta P_z$		$\delta\epsilon_{xx}, \delta\epsilon_{yy}, \delta\epsilon_{zz}, \epsilon_{yz}, \epsilon_{zx}, \epsilon_{xy}$		
178	$422-Pds-4$	2	P_z	2	$\delta\epsilon_{xx}, \delta\epsilon_{yy}, \delta\epsilon_{zz}, \epsilon_{yz}, \epsilon_{zx}, \epsilon_{xy}$	1	$422(1)D4F4 =$
180	$422-Peds-2_x$	4	P_x	4	$\delta\epsilon_{xx}, \delta\epsilon_{yy}, \delta\epsilon_{zz}, \epsilon_{yz}, 0, 0$	4	$422(2)D2F2 \neq$
			$P_x = P_y$	$\delta\epsilon_{xx}, \delta\epsilon_{yy}, \delta\epsilon_{zz}, \epsilon_{yz}, \epsilon_{yz}, 0, 0$			
181	$422-Peds-2_{xy}$	4	$[P_z]$	2	$\delta\epsilon_{xx}, \delta\epsilon_{yy}, \delta\epsilon_{zz}, \epsilon_{yz}, -\epsilon_{yz}, \epsilon_{xy}$	4	$*422(1)D4F3 \neq$
182	$422-Peds-2_z$	8	$P_x, P_y, (P_z)$	8	$\delta\epsilon_{xx}, \delta\epsilon_{yy}, \delta\epsilon_{zz}, \epsilon_{yz}, \epsilon_{yz}, \epsilon_{zx}, \epsilon_{xy}$	8	$422(8/2)A1F1$

Table C.1 (continued)

1 Species no.	2 Species designation	3 q	4 Data on polarization	5 q_p	6 Data on strain	7 q_ϵ	8 Shuvalov's symbol
184	$4/m-Pd-4$	2	P_z	2	$\delta\epsilon_{xx}, \delta\epsilon_{yy}, \delta\epsilon_{zz}, 0, 0, 0$	1	$4/m(1)D4F4 =$
186	$4/m-Peds-m$	4	P_x, P_y	4	$\delta\epsilon_{xx}, \delta\epsilon_{yy}, \delta\epsilon_{zz}, 0, 0, \epsilon_{xy}$	2	$4/m(2)A4Fm =$
187	$4/m-Peds-2$	4	$[P_z]$		$\delta\epsilon_{xx}, \delta\epsilon_{yy}, \delta\epsilon_{zz}, 0, 0, \epsilon_{xy}$	2	$*4/m(1)D4F2 \neq$
189	$4/m-Peds-1$	8	$[P_x, P_y, P_z]$	8	$\delta\epsilon_{xx}, \delta\epsilon_{yy}, \delta\epsilon_{zz}, \epsilon_{yz}, \epsilon_{zx}, \epsilon_{xy}$	4	$4/m(4)A1F1 =$
190	$4-Peds-2$	2	P_z	2	$\delta\epsilon_{xx}, \delta\epsilon_{yy}, \delta\epsilon_{zz}, 0, 0, \epsilon_{xy}$	2	$4(1)D4F2$
191	$4-Peds-1$	4	$P_x, P_y, (P_z)$	4	$\delta\epsilon_{xx}, \delta\epsilon_{yy}, \delta\epsilon_{zz}, \epsilon_{yz}, \epsilon_{zx}, \epsilon_{xy}$	4	$4(4/2)A1F1$
193	$4-Peds-1$	4	$P_x, P_y, \delta P_z$	4	$\delta\epsilon_{xx}, \delta\epsilon_{yy}, \delta\epsilon_{zz}, \epsilon_{yz}, \epsilon_{zx}, \epsilon_{xy}$	4	$4(4/2)A1F1$
Orthorhombic parent phase							
194	$mmm-Pd-m_x m_y 2_z$	2	P_z	2	$\delta\epsilon_{xx}, \delta\epsilon_{yy}, \delta\epsilon_{zz}, 0, 0, 0$	1	$mmm(1)D2Fmm2 =$
	$mmm-Pd-m_x m_y 2_y$		P_y		$\delta\epsilon_{xx}, \delta\epsilon_{yy}, \delta\epsilon_{zz}, 0, 0, 0$		
	$mmm-Pd-m_y m_x 2_x$		P_x		$\delta\epsilon_{xx}, \delta\epsilon_{yy}, \delta\epsilon_{zz}, 0, 0, 0$		
197	$mmm-Peds-m_x$	4	$[P_y, P_z]$	4	$\delta\epsilon_{xx}, \delta\epsilon_{yy}, \delta\epsilon_{zz}, \epsilon_{yz}, 0, 0$	2	$mmm(2)AmFm =$
	$mmm-Peds-m_y$		$[P_x, P_z]$		$\delta\epsilon_{xx}, \delta\epsilon_{yy}, \delta\epsilon_{zz}, 0, \epsilon_{zx}, 0$		
	$mmm-Peds-m_z$		$[P_x, P_y]$		$\delta\epsilon_{xx}, \delta\epsilon_{yy}, \delta\epsilon_{zz}, 0, 0, \epsilon_{xy}$		
198	$mmm-Peds-2_x$	4	$[P_x]$	2	$\delta\epsilon_{xx}, \delta\epsilon_{yy}, \delta\epsilon_{zz}, \epsilon_{yz}, 0, 0$	2	$*mmm(1)D2F2 \neq$
	$mmm-Peds-2_y$		$[P_y]$		$\delta\epsilon_{xx}, \delta\epsilon_{yy}, \delta\epsilon_{zz}, 0, \epsilon_{zx}, 0$		
	$mmm-Peds-2_z$		$[P_z]$		$\delta\epsilon_{xx}, \delta\epsilon_{yy}, \delta\epsilon_{zz}, 0, 0, \epsilon_{xy}$		
200	$mmm-Peds-1$	8	$[P_x, P_y, P_z]$	8	$\delta\epsilon_{xx}, \delta\epsilon_{yy}, \delta\epsilon_{zz}, \epsilon_{yz}, \epsilon_{zx}, \epsilon_{xy}$	4	$mmm(4)A1F1 =$
201	$mm2-Peds-m_x$	2	$P_y, \delta P_z$	2	$\delta\epsilon_{xx}, \delta\epsilon_{yy}, \delta\epsilon_{zz}, \epsilon_{yz}, 0, 0$	2	$mm2(2/2)AmFm$
	$mm2-Peds-m_y$		$P_x, \delta P_z$		$\delta\epsilon_{xx}, \delta\epsilon_{yy}, \delta\epsilon_{zz}, 0, \epsilon_{zx}, 0$		
203	$mm2-Peds-1$	4	$[P_x]_x, \delta P_z$	4	$\delta\epsilon_{xx}, \delta\epsilon_{yy}, \delta\epsilon_{zz}, \epsilon_{yz}, \epsilon_{zx}, \epsilon_{xy}$	4	$mm2(4/2)A1F1$
204	$222-Peds-2_x$	2	P_x	2	$\delta\epsilon_{xx}, \delta\epsilon_{yy}, \delta\epsilon_{zz}, \epsilon_{yz}, 0, 0$	2	$*222(1)D2F2 \neq$
	$222-Peds-2_y$		P_y		$\delta\epsilon_{xx}, \delta\epsilon_{yy}, \delta\epsilon_{zz}, 0, \epsilon_{zx}, 0$		
	$222-Peds-2_z$		P_z		$\delta\epsilon_{xx}, \delta\epsilon_{yy}, \delta\epsilon_{zz}, 0, 0, \epsilon_{xy}$		
205	$222-Peds-1$	4	$[P_x, P_y, P_z]$	4	$\delta\epsilon_{xx}, \delta\epsilon_{yy}, \delta\epsilon_{zz}, \epsilon_{yz}, \epsilon_{zx}, \epsilon_{xy}$	4	$222(2/2)A1F1$

Table C.1 (continued)

1 Species no.	2 Species designation	3 q	4 Data on polarization	5 q_P	6 Data on strain	7 q_ϵ	8 Shuvalov's symbol
monoclinic parent phase							
206	$2/m-Pd-m$	2	P_x, P_y	2	$\delta\epsilon_{xvs}, \delta\epsilon_{yjs}, \delta\epsilon_{zsz}, 0, 0, \delta\epsilon_{xy}$	1	$*2/m(1)AmFm =$
207	$2/m-Pd-2$	2	P_z	2	$\delta\epsilon_{xvs}, \delta\epsilon_{yjs}, \delta\epsilon_{zsz}, 0, 0, \delta\epsilon_{xy}$	1	$2/m(1)D2F2 =$
209	$2/m-P\epsilon ds-1$	4	$[P_x, P_y, P_z]$	4	$\delta\epsilon_{xvs}, \delta\epsilon_{yjs}, \delta\epsilon_{zsz}, \epsilon_{yz}, \epsilon_{zx}, \delta\epsilon_{xy}$	2	$2/m(2)A1F1 =$
210	$m-P\epsilon ds-1$	2	P_z	2	$\delta\epsilon_{xvs}, \delta\epsilon_{yjs}, \delta\epsilon_{zsz}, \epsilon_{yz}, \epsilon_{zx}, \delta\epsilon_{xy}$	2	$m(2/2)A1F1$
211	$2-P\epsilon ds-1$	2	P_x, P_y	2	$\delta\epsilon_{xvs}, \delta\epsilon_{yjs}, \delta\epsilon_{zsz}, \epsilon_{yz}, \epsilon_{zx}, \delta\epsilon_{xy}$	2	$2(2/2)A1F1$
Triclinic parent phase							
212	$\bar{1}-Pd-1$	1	P_x, P_y, P_z	2	$\delta\epsilon_{xvs}, \delta\epsilon_{yjs}, \delta\epsilon_{zsz}, \delta\epsilon_{yjs}, \delta\epsilon_{zsz}, \delta\epsilon_{xy}$	1	$\bar{1}(1)A1F1 =$

Column 1: sequential number of the species. *Column 2:* symbol of the species. *Column 3:* total number of domain states. *Column 4:* nonzero components of polarization in the phase F , specified for the subgroup orientation shown in the symbol. δP_k , change of polarization component which was already permitted by symmetry in the parent phase; P_k , new component of spontaneous polarization. P_k without brackets—"proper" component of polarization (assuming no unit-cell multiplication), i.e., P_k serves as the order parameter. P_k in brackets—"improper" polarization component, arising as a secondary effect. Two lines are given in the table if both proper and improper scenarios can be responsible for the development of polarization. The distinction between (P_k) and [P_k]—see text in Sect. 2.1.9. *Column 5:* number of ferroelectric domain states. *Column 6:* strain components (in the coordinate system of G) compatible with the symmetry of the phase F . If the component is "symmetry breaking" (not allowed in G), it is written as ϵ_{kl} . If it is already allowed in G , it has the prefix δ . (Remark: two components $\delta\epsilon_{kl}, \delta\epsilon_{lm}$ compatible with the symmetry of G , which are equal in G , may become different in the phase F . It is then the difference $\delta\epsilon_{kl} - \delta\epsilon_{lm}$ between them which 'breaks' the symmetry.) *Column 7:* number of ferroelastic domain states. Number 1 means that F is nonferroelastic. *Column 8:* Shuvalov's symbol. *Top of each section:* strain components compatible with the symmetry of the parent phase, in the sequence $\delta\epsilon_{xvs}, \delta\epsilon_{yjs}, \delta\epsilon_{zsz}, \delta\epsilon_{yjs}, \delta\epsilon_{zsz}, \delta\epsilon_{xy}$.

Appendix D

Spontaneous Polarization, Spontaneous Strain, and Orientation of Domain Walls in Ferroic Species

In the tables of this appendix, one finds the information on the spontaneous polarization, spontaneous strain, and orientation of domain walls (DW) in all ferroic species. These tables are compiled by Dr. J. Erhart based on his paper (2004) with corrections.

Table D.1 gives the general information on the ferroic domain states, types of the domain wall separating them, and the number of the table (from Tables D.2, D.3, D.4, D.5, D.6, D.7, D.8, D.9, D.10, D.11, D.12, D.13, D.14, D.15, D.16, D.17, D.18, D.19, D.20, D.21, D.22, D.23, D.24, D.25, D.26, D.27, D.28, D.29, and D.30) containing the detailed information for a given species. The table number applies to the species of the same line and all following ones until a new table number appears. Tables D.2, D.3, D.4, D.5, D.6, D.7, D.8, D.9, D.10, D.11, D.12, D.13, D.14, D.15, D.16, D.17, D.18, D.19, D.20, D.21, D.22, D.23, D.24, D.25, D.26, D.27, D.28, D.29, and D.30 give the wall orientations in the case where these are conditioned by the mechanical effects, i.e. in the case of W_∞ walls no information on the wall orientation is given. The wall orientation is specified with the components of its normal vector expressed in orthogonal or hexagonal basis (standard crystallographic coordinate choice). The coordinate system is adopted the same as in parent phase. In the titles of Tables D.2, D.3, D.4, D.5, D.6, D.7, D.8, D.9, D.10, D.11, D.12, D.13, D.14, D.15, D.16, D.17, D.18, D.19, D.20, D.21, D.22, D.23, D.24, D.25, D.26, D.27, D.28, D.29, and D.30, the change of the crystalline class at the phase transitions addressed in the table is indicated.

Table D.1 General information on domain states and types of the domain wall

1 Species no.	2 Species designation	3 q_ϵ	4 q_P	5 Domain wall pairs Charge/neutrality of domain walls	6 Table no.
212	$\bar{1} \rightarrow 1$	1	2	$W_\infty^N - W_\infty^C$	D.2
207	$2/m \rightarrow 2$	1	2	$W_\infty^N - W_\infty^C$	D.9
206	$2/m \rightarrow m$	1	2	$W_\infty^N - W_\infty^C$	
211	$2 \rightarrow 1$	2	2	$W_f^N - S^C$	D.3
210	$m \rightarrow 1$	2	2	$W_f^C - S^N$	
209	$2/m \rightarrow 1$	2	4	$W_f^{N,C} - S^{C,N}$	
208	$2/m \rightarrow \bar{1}$	2	0	$W_f - S$	
194	$mmm \rightarrow mm2$	1	2	$W_\infty^N - W_\infty^C$	D.21
197	$mmm \rightarrow m_x$	2	4	$W_f^{N,C} - W_f^{C,N}$	D.10

Table D.1 (continued)

1 Species no.	2 Species designation	3 q_ε	4 q_p	5 Domain wall pairs Charge/neutrality of domain walls	6 Table no.
198	$mmm \rightarrow 2_x$	2	2	$W_f^N - W_f^N$	
196	$mmm \rightarrow 2_x/m_x$	2	0	$W_f - W_f$	
201	$mm2 \rightarrow m_x$	2	2	$W_f^N - W_f^C$	
204	$222 \rightarrow 2_x$	2	2	$W_f^N - W_f^N$	
202	$mm2 \rightarrow 2_z$	2	1	$W_f^N - W_f^N$	D.11
200	$mmm \rightarrow 1$	4	8	$W_f^{N,C} - S^{C,N}$	D.4
199	$mmm \rightarrow \bar{1}$	4	0	$W_f - S$	
203	$mm2 \rightarrow 1$	4	4	$W_f^N - S^C, W_f^C - S^N$	
205	$222 \rightarrow 1$	4	4	$W_f^N - S^C$	
149	$4/mmm \rightarrow 4mm$	1	2	$W_\infty^N - W_\infty^C$	D.28
153	$4/mmm \rightarrow 4$	1	2	$W_\infty^N - W_\infty^C$	
184	$4/m \rightarrow 4$	1	2	$W_\infty^N - W_\infty^C$	
178	$422 \rightarrow 4$	1	2	$W_\infty^N - W_\infty^C$	
154	$4/mmm \rightarrow m_x m_y m_z$	2	0	$W_f - W_f$	D.22
155	$4/mmm \rightarrow 2_x m_y m_z$	2	4	$W_f^{N,C} - W_f^{C,N}$	
156	$4/mmm \rightarrow m_x m_y 2_z$	2	2	$W_f^N - W_f^N$	
157	$4/mmm \rightarrow 2_x 2_y 2_z$	2	0	$W_f - W_f$	
168	$\bar{4}2m \rightarrow 2_x 2_y 2_z$	2	0	$W_f - W_f$	
174	$4mm \rightarrow m_x m_y 2_z$	2	1	$W_f^N - W_f^N$	
179	$422 \rightarrow 2_x 2_y 2_z$	2	0	$W_f - W_f$	
167	$\bar{4}2m \rightarrow m_{xy} m_{\bar{xy}} 2_z$	2	2	$W_f^N - W_f^N$	D.23
162	$4/mmm \rightarrow 2_x$	3	4	$W_f^N - W_f^N, W_f^{N,C} - S^{C,N}$	D.12
160	$4/mmm \rightarrow m_x$	3	8	$W_f^{N,C} - W_f^{C,N}, W_f^{N,C} - S^{C,N}$	
158	$4/mmm \rightarrow 2_x/m_x$	3	0	$W_f - W_f, W_f - S$	
170	$\bar{4}2m \rightarrow 2_x$	3	4	$W_f^N - W_f^N, W_f^C - S^N$	
175	$4mm \rightarrow m_x$	3	4	$W_f^N - W_f^C, W_f^C - S^N$	
180	$422 \rightarrow 2_x$	3	4	$W_f^N - W_f^N, W_f^N - S^C$	
163	$4/mmm \rightarrow 2_z$	4	2	$W_f^N - W_f^N, S^N - S^N$	D.13
161	$4/mmm \rightarrow m_z$	4	8	$W_f^{N,C} - W_f^{C,N}, S^* - S^*$	
159	$4/mmm \rightarrow 2_z/m_z$	4	0	$W_f - W_f, S - S$	
171	$\bar{4}2m \rightarrow 2_z$	4	2	$W_f^N - W_f^N, S^N - S^N$	
176	$4mm \rightarrow 2_z$	4	1	$W_f^N - W_f^N, S^N - S^N$	
181	$422 \rightarrow 2_z$	4	2	$W_f^N - W_f^N, S^N - S^N$	
187	$4/m \rightarrow 2_z$	2	2	$S^N - S^N$	
186	$4/m \rightarrow m_z$	2	4	$S^* - S^*$	
185	$4/m \rightarrow 2_z/m_z$	2	0	$S - S$	
190	$\bar{4} \rightarrow 2_z$	2	2	$S^N - S^N$	
192	$4 \rightarrow 2_z$	2	1	$S^N - S^N$	
169	$\bar{4}2m \rightarrow m_{xy}$	4	4	$W_f^N - W_f^C, W_f^N - S^{pC}$	D.14
165	$4/mmm \rightarrow 1$	8	16	$R, W_f^{N,C} - S^{C,N}$	D.5
164	$4/mmm \rightarrow \bar{1}$	8	0	$R, W_f - S$	
172	$\bar{4}2m \rightarrow 1$	8	8	$R, W_f^N - S^C, W_f^C - S^N$	
177	$4mm \rightarrow 1$	8	8	$R, W_f^N - S^C, W_f^C - S^N$	
182	$422 \rightarrow 1$	8	8	$R, W_f^N - S^C$	
189	$4/m \rightarrow 1$	4	8	$R, W_f^{N,C} - S^{C,N}$	

Table D.1 (continued)

1 Species no.	2 Species designation	3 q_ε	4 q_p	5 Domain wall pairs Charge/neutrality of domain walls	6 Table no.
188	$4/m \rightarrow \bar{1}$	4	0	$R, W_f - S$	
191	$\bar{4} \rightarrow 1$	4	4	$R, W_f^N - S^C$	
193	$4 \rightarrow 1$	4	4	$R, W_f^N - S^C$	
129	$\bar{3}m \rightarrow 3m$	1	2	$W_\infty^N - W_\infty^C$	D.28
132	$\bar{3}m \rightarrow 3$	1	2	$W_\infty^N - W_\infty^C$	
141	$32 \rightarrow 3$	1	2	$W_\infty^N - W_\infty^C$	
144	$\bar{3} \rightarrow 3$	1	2	$W_\infty^N - W_\infty^C$	
134	$\bar{3}m \rightarrow m_x$	3	6	$W_f^{N,C} - S^{C,N}$	D.15
135	$\bar{3}m \rightarrow 2_x$	3	6	$W_f^{N,C} - S^{C,N}$	
133	$\bar{3}m \rightarrow 2_x/m_x$	3	0	$W_f - S$	
139	$3m \rightarrow m_x$	3	3	$W_f^C - S^N$	
142	$32 \rightarrow 2_x$	3	3	$W_f^N - S^C$	
137	$\bar{3}m \rightarrow 1$	6	12	$R, W_f^{N,C} - S^{C,N}$	D.6
136	$\bar{3}m \rightarrow \bar{1}$	6	0	$R, W_f - S$	
140	$3m \rightarrow 1$	6	6	$R, W_f^C - S^N$	
143	$32 \rightarrow 1$	6	6	$R, W_f^N - S^C$	
145	$\bar{3} \rightarrow \bar{1}$	3	0	R	
146	$\bar{3} \rightarrow 1$	3	6	R	
147	$3 \rightarrow 1$	3	3	R	
69	$6/mmm \rightarrow 6mm$	1	2	$W_\infty^N - W_\infty^C$	D.28
73	$6/mmm \rightarrow 6$	1	2	$W_\infty^N - W_\infty^C$	
107	$622 \rightarrow 6$	1	2	$W_\infty^N - W_\infty^C$	
115	$6/m \rightarrow 6$	1	2	$W_\infty^N - W_\infty^C$	
75	$6/mmm \rightarrow 3_2m_x$	1	2	$W_\infty^N - W_\infty^C$	D.28
78	$6/mmm \rightarrow 3$	1	2	$W_\infty^N - W_\infty^C$	
92	$\bar{6}m2 \rightarrow 3_2m_x$	1	2	$W_\infty^N - W_\infty^C$	
94	$\bar{6}m2 \rightarrow 3$	1	2	$W_\infty^N - W_\infty^C$	
109	$622 \rightarrow 3$	1	2	$W_\infty^N - W_\infty^C$	
123	$\bar{6} \rightarrow 3$	1	2	$W_\infty^N - W_\infty^C$	
117	$6/m \rightarrow 3$	1	2	$W_\infty^N - W_\infty^C$	
79	$6/mmm \rightarrow m_xm_y m_z$	3	0	$W_f - W_f$	D.24
80	$6/mmm \rightarrow m_xm_y 2_z$	3	2	$W_f^N - W_f^N$	
81	$6/mmm \rightarrow 2_xm_y m_z$	3	6	$W_f^{N,C} - W_f^{C,N}$	
82	$6/mmm \rightarrow 2_x 2_y 2_z$	3	0	$W_f - W_f$	
95	$\bar{6}m2 \rightarrow m_x 2_y m_z$	3	3	$W_f^N - W_f^C$	
103	$6mm \rightarrow m_x m_y 2_z$	3	1	$W_f^N - W_f^N$	
110	$622 \rightarrow 2_x 2_y 2_z$	3	0	$W_f - W_f$	
87	$6/mmm \rightarrow 2_x$	6	6	$W_f^N - W_f^N, W_f^{N,C} - S^{C,N}$	D.16
85	$6/mmm \rightarrow m_x$	6	12	$W_f^{N,C} - W_f^{C,N}, W_f^{N,C} - S^{C,N}$	
83	$6/mmm \rightarrow 2_x/m_x$	6	0	$W_f - W_f, W_f - S$	
97	$\bar{6}m2 \rightarrow m_x$	6	6	$W_f^N - W_f^C, W_f^N - S^C, W_f^C - S^N$	
104	$6mm \rightarrow m_x$	6	6	$W_f^N - W_f^C, W_f^C - S^N$	
111	$622 \rightarrow 2_x$	6	6	$W_f^N - W_f^N, W_f^N - S^C$	
88	$6/mmm \rightarrow 2_z$	6	2	$W_f^N - W_f^N, S^N - S^N$	D.17
86	$6/mmm \rightarrow m_z$	6	12	$W_f^{N,C} - W_f^{C,N}, S^* - S^*$	

Table D.1 (continued)

1 Species no.	2 Species designation	3 q_ε	4 q_p	5 Domain wall pairs Charge/neutrality of domain walls	6 Table no.
84	$6/mmm \rightarrow 2_z/m_z$	6	0	$W_f - W_f, S - S$	
96	$\bar{6}m2 \rightarrow m_z$	6	6	$W_f^N - W_f^C, S^* - S^*$	
105	$6mm \rightarrow 2_z$	6	1	$W_f^N - W_f^N, S^N - S^N$	
112	$622 \rightarrow 2_z$	6	2	$W_f^N - W_f^N, S^N - S^N$	
120	$6/m \rightarrow 2_z$	3	2	$S^N - S^N$	
119	$6/m \rightarrow m_z$	3	6	$S^* - S^*$	
118	$6/m \rightarrow 2_z/m_z$	3	0	$S - S$	
124	$\bar{6} \rightarrow m_z$	3	3	$S^* - S^*$	
127	$6 \rightarrow 2_z$	3	1	$S^N - S^N$	
98	$\bar{6}m2 \rightarrow 2_y$	6	3	$W_f^N - W_f^N, W_f^N - S^C, W_f^C - S^N$	D.18
90	$6/mmm \rightarrow 1$	12	24	$R, W_f^{N,C} - S^{C,N}$	D.7
89	$6/mmm \rightarrow \bar{1}$	12	0	$R, W_f - S$	
99	$\bar{6}m2 \rightarrow 1$	12	12	$R, W_f^N - S^C, W_f^C - S^N$	
106	$6mm \rightarrow 1$	12	12	$R, W_f^N - S^C, W_f^C - S^N$	
113	$622 \rightarrow 1$	12	12	$R, W_f^N - S^C$	
122	$6/m \rightarrow 1$	6	12	$R, W_f^{N,C} - S^{C,N}$	
121	$6/m \rightarrow \bar{1}$	6	0	$R, W_f - S$	
125	$\bar{6} \rightarrow 1$	6	6	$R, W_f^C - S^N$	
128	$6 \rightarrow 1$	6	6	$R, W_f^N - S^C$	
5	$m\bar{3}m \rightarrow \bar{3}_{xyz}m_{\bar{x}y}$	4	0	$W_f - W_f$	D.30
6	$m\bar{3}m \rightarrow 3_{xyz}m_{\bar{x}y}$	4	8	$W_f^{N,C} - W_f^{C,N}$	
7	$m\bar{3}m \rightarrow 3_{xyz}2_{\bar{x}y}$	4	0	$W_f - W_f$	
8	$m\bar{3}m \rightarrow \bar{3}_{xyz}$	4	0	$W_f - W_f$	
9	$m\bar{3}m \rightarrow 3_{xyz}$	4	8	$W_f^{N,C} - W_f^{C,N}$	
34	$43m \rightarrow 3_{xyz}m_{\bar{x}y}$	4	4	$W_f^N - W_f^C$	
35	$\bar{4}3m \rightarrow 3_{xyz}$	4	4	$W_f^N - W_f^C$	
44	$432 \rightarrow 3_{xyz}2_{\bar{x}y}$	4	0	$W_f - W_f$	
45	$432 \rightarrow 3_{xyz}$	4	8	$W_f^{N,C} - W_f^{C,N}$	
54	$m\bar{3} \rightarrow \bar{3}_{xyz}$	4	0	$W_f - W_f$	
55	$m\bar{3} \rightarrow 3_{xyz}$	4	8	$W_f^{N,C} - W_f^{C,N}$	
64	$23 \rightarrow 3_{xyz}$	4	4	$W_f^N - W_f^C$	
10	$m\bar{3}m \rightarrow 4_z/m_z m_x m_y$	3	0	$W_f - W_f$	D.29
13	$m\bar{3}m \rightarrow 4_z m_x m_{xy}$	3	6	$W_f^{N,C} - W_f^{C,N}$	
11	$m\bar{3}m \rightarrow \bar{4}_z 2_{xy} m_x$	3	0	$W_f - W_f$	
12	$m\bar{3}m \rightarrow \bar{4}_z 2_x m_{xy}$	3	0	$W_f - W_f$	
14	$m\bar{3}m \rightarrow 4_z 2_x 2_{xy}$	3	0	$W_f - W_f$	
15	$m\bar{3}m \rightarrow 4_z/m_z$	3	0	$W_f - W_f$	
16	$m\bar{3}m \rightarrow \bar{4}$	3	0	$W_f - W_f$	
17	$m\bar{3}m \rightarrow 4$	3	6	$W_f^{N,C} - W_f^{C,N}$	
36	$43m \rightarrow \bar{4}_z 2_x m_{xy}$	3	0	$W_f - W_f$	
37	$\bar{4}3m \rightarrow 4$	3	0	$W_f - W_f$	
46	$432 \rightarrow 4_z 2_x 2_{xy}$	3	0	$W_f - W_f$	
47	$432 \rightarrow 4$	3	6	$W_f^{N,C} - W_f^{C,N}$	
18	$m\bar{3}m \rightarrow m_x m_y m_z$	6	0	$R, W_f - W_f$	D.25
20	$m\bar{3}m \rightarrow m_x m_y 2_z$	6	6	$R, W_f^N - W_f^N, W_f^{N,C} - W_f^{C,N}$	

Table D.1 (continued)

1 Species no.	2 Species designation	3 q_ε	4 q_p	5 Domain wall pairs Charge/neutrality of domain walls	6 Table no.
23	$m\bar{3}m \rightarrow 2_x 2_y 2_z$	6	0	$R, W_f - W_f$	
39	$\bar{4}3m \rightarrow 222$	6	0	$R, W_f - W_f$	
48	$432 \rightarrow 2_x 2_y 2_z$	6	0	$R, W_f - W_f$	
56	$m\bar{3} \rightarrow mmm$	3	0	R	
57	$m\bar{3} \rightarrow m_x m_y 2_z$	3	6	R	
58	$m\bar{3} \rightarrow 222$	3	0	R	
65	$23 \rightarrow 222$	3	0	R	
21	$m\bar{3}m \rightarrow m_{xy} m_{\bar{xy}} 2_z$	6	6	$W_f^N - W_f^N, W_f^{N,C} - S^{C,N}$	D.26
19	$m\bar{3}m \rightarrow m_{xy} m_{\bar{xy}} m_z$	6	0	$W_f - W_f, W_f - S$	
24	$m\bar{3}m \rightarrow 2_{xy} 2_{\bar{xy}} 2_z$	6	0	$W_f - W_f, W_f - S$	
49	$432 \rightarrow 2_{xy} 2_{\bar{xy}} 2_z$	6	0	$W_f - W_f, W_f - S$	
22	$m\bar{3}m \rightarrow 2_{xy} m_{\bar{xy}} m_z$	6	12	$W_f^{N,C} - W_f^{C,N}, W_f^{N,C} - S^{C,N}$	D.27
38	$\bar{4}3m \rightarrow m_{xy} m_{\bar{xy}} 2_z$	6	6	$W_f^N - W_f^N, W_f^C - S^N$	
29	$m\bar{3}m \rightarrow 2_{xy}$	12	12	$R, W_f^N - W_f^N, W_f^{N,C} - S^{C,N}$	D.19
28	$m\bar{3}m \rightarrow m_{xy}$	12	24	$R, W_f^{N,C} - W_f^{C,N}, W_f^{N,C} - S^{C,N}$	
25	$m\bar{3}m \rightarrow 2_{xy}/m_{xy}$	12	0	$R, W_f - W_f, W_f - S$	
40	$\bar{4}3m \rightarrow m_{xy}$	12	12	$R, W_f^N - W_f^C, W_f^N - S^C, W_f^C - S^N$	
50	$432 \rightarrow 2_{xy}$	12	12	$R, W_f^N - W_f^N, W_f^N - S^C$	
30	$m\bar{3}m \rightarrow 2_z$	12	6	$R, W_f^N - W_f^N, W_f^{N,C} - S^{C,N}, S^N - S^N$	D.20
27	$m\bar{3}m \rightarrow m_z$	12	24	$R, W_f^{N,C} - W_f^{C,N}, W_f^{N,C} - S^{C,N}, S^* - S^*$	
26	$m\bar{3}m \rightarrow 2_z/m_z$	12	0	$R, W_f - W_f, W_f - S, S - S$	
41	$\bar{4}3m \rightarrow 2_z$	12	6	$R, W_f^N - W_f^N, W_f^C - S^N, S^N - S^N$	
51	$432 \rightarrow 2_z$	12	6	$R, W_f^N - W_f^N, W_f^N - S^C, S^N - S^N$	
61	$m\bar{3} \rightarrow 2_z$	6	6	$R, W_f^N - W_f^N$	
60	$m\bar{3} \rightarrow m_z$	6	12	$R, W_f^{N,C} - W_f^{C,N}$	
59	$m\bar{3} \rightarrow 2_z/m_z$	6	0	$R, W_f - W_f$	
66	$23 \rightarrow 2_z$	6	6	$R, W_f^N - W_f^N$	
32	$m\bar{3}m \rightarrow 1$	24	48	$R, W_f^{N,C} - S^{C,N}$	D.8
31	$m\bar{3}m \rightarrow \bar{1}$	24	0	$R, W_f - S$	
42	$\bar{4}3m \rightarrow 1$	24	24	$R, W_f^N - S^C, W_f^C - S^N$	
52	$432 \rightarrow 1$	24	24	$R, W_f^N - S^C$	
63	$m\bar{3} \rightarrow 1$	12	24	$R, W_f^{N,C} - S^{C,N}$	
62	$m\bar{3} \rightarrow \bar{1}$	12	0	$R, W_f - S$	
67	$23 \rightarrow 1$	12	12	$R, W_f^N - S^C$	
1	$m\bar{3}m \rightarrow \bar{4}3m$	1	0		
2	$m\bar{3}m \rightarrow 432$	1	0		
3	$m\bar{3}m \rightarrow m\bar{3}$	1	0		
4	$m\bar{3}m \rightarrow 23$	1	0		
33	$\bar{4}3m \rightarrow 23$	1	0		
43	$432 \rightarrow 23$	1	0		
53	$m\bar{3} \rightarrow 23$	1	0		
68	$6/mmm \rightarrow \bar{6}_z m_y 2_x$	1	0		
70	$6/mmm \rightarrow 622$	1	0		

Table D.1 (continued)

1 Species no.	2 Species designation	3 q_ε	4 q_p	5 Domain wall pairs Charge/neutrality of domain walls	6 Table no.
71	$6/mmm \rightarrow 6/m$	1	0		
72	$6/mmm \rightarrow \bar{6}$	1	0		
74	$6/mmm \rightarrow \bar{3}_z m_x$	1	0		
76	$6/mmm \rightarrow 3_z 2_x$	1	0		
77	$6/mmm \rightarrow \bar{3}$	1	0		
91	$\bar{6}m2 \rightarrow \bar{6}$	1	0		
93	$\bar{6}m2 \rightarrow 32$	1	0		
108	$622 \rightarrow 3_z 2_x$	1	0		
114	$6/m \rightarrow 6$	1	0		
116	$6/m \rightarrow \bar{3}$	1	0		
130	$\bar{3}m \rightarrow 32$	1	0		
131	$\bar{3}m \rightarrow \bar{3}$	1	0		
148	$4/mmm \rightarrow \bar{4}_z 2_x m_{xy}$	1	0		
150	$4/mmm \rightarrow 422$	1	0		
151	$4/mmm \rightarrow 4/m$	1	0		
152	$4/mmm \rightarrow \bar{4}$	1	0		
166	$\bar{4}2m \rightarrow \bar{4}$	1	0		
183	$4/m \rightarrow \bar{4}$	1	0		
195	$mmm \rightarrow 222$	1	0		
100	$6mm \rightarrow 6$	1	1		
101	$6mm \rightarrow 3_z m_x$	1	1		
102	$6mm \rightarrow 3$	1	1		
126	$6 \rightarrow 3$	1	1		
138	$3m \rightarrow 3$	1	1		
173	$4mm \rightarrow 4$	1	1		

Column 1: sequential number of the species. *Column 2:* symbol of the species. *Column 3:* number of ferroelastic domain states. *Column 4:* number of ferroelectric domain states. *Column 5:* type of permissible pairs of domain walls (domain wall orientation symbols: W_∞ -arbitrary, W_f -fixed, S -dependent on spontaneous strains, R -no walls). Charge/neutrality of ferroelectric domain walls is labeled by superscript C, N, respectively For centrosymmetric parent phases both superscripts are used in some cases, i.e. the same domain wall is either charged or neutral according to the choice of spontaneous polarization pair (antiparallel spontaneous polarizations are allowed in such species). When the charge/neutrality of a domain wall depends on the specific values of spontaneous strains, it is labeled by superscript*. *Column 6:* number of the table containing the detailed information on domain states and orientations of domain walls for given species. The table number applies to the species of the same line and all following ones until a new table number appears. *The last 34 rows:* species belonging to high-order ferroics where the domain states are distinguishable neither by spontaneous polarization nor by spontaneous strain. Here, the domain walls are of W_∞ type and electroneutral for any orientation.

Table D.2 Triclinic to triclinic

Species strains	$\bar{1} \rightarrow 1$ polarizations
1 $\begin{pmatrix} \varepsilon_1 & \varepsilon_2 & \varepsilon_3 \\ \varepsilon_4 & \varepsilon_5 & \varepsilon_6 \end{pmatrix}$	$(P_1 \ P_2 \ P_3)$ $(-P_1 \ -P_2 \ -P_3)$

Table D.3 Monoclinic to triclinic

All species	$m \rightarrow 1$	$2/m \rightarrow 1$ $2/m \rightarrow \bar{1}(P=0)$ $2 \rightarrow 1$ (upper polarizations only)
strains	polarizations	polarizations
1 $\begin{pmatrix} \varepsilon_1 & \varepsilon_2 & \varepsilon_3 \\ \varepsilon_4 & \varepsilon_5 & \varepsilon_6 \end{pmatrix}$	$(P_1 \ P_2 \ P_3)$	$(P_1 \ P_2 \ P_3)$ $(-P_1 \ -P_2 \ -P_3)$
2 $\begin{pmatrix} \varepsilon_1 & \varepsilon_2 & \varepsilon_3 \\ -\varepsilon_4 & \varepsilon_5 & -\varepsilon_6 \end{pmatrix}$	$(P_1 \ -P_2 \ P_3)$	$(-P_1 \ P_2 \ -P_3)$ $(P_1 \ -P_2 \ P_3)$
S	1	2
1	N/A	$(010)^N$ $(10a)^C$
2	$(010)^C$ $(10a)^N$	N/A

$a = \varepsilon_4/\varepsilon_6$

Table D.4 Orthorhombic to triclinic

All species	$mmm \rightarrow 1$ $mmm \rightarrow \bar{1}(P=0)$	$mm2 \rightarrow 1$	$222 \rightarrow 1$
strains	polarizations	polarizations	polarizations
1 $\begin{pmatrix} \varepsilon_1 & \varepsilon_2 & \varepsilon_3 \\ \varepsilon_4 & \varepsilon_5 & \varepsilon_6 \end{pmatrix}$	$(P_1 \ P_2 \ P_3)$ $(-P_1 \ -P_2 \ -P_3)$	$(P_1 \ P_2 \ P_3)$	$(P_1 \ P_2 \ P_3)$
2 $\begin{pmatrix} \varepsilon_1 & \varepsilon_2 & \varepsilon_3 \\ \varepsilon_4 & -\varepsilon_5 & -\varepsilon_6 \end{pmatrix}$	$(-P_1 \ P_2 \ P_3)$ $(P_1 \ -P_2 \ -P_3)$	$(-P_1 \ P_2 \ P_3)$	$(P_1 \ -P_2 \ -P_3)$
3 $\begin{pmatrix} \varepsilon_1 & \varepsilon_2 & \varepsilon_3 \\ -\varepsilon_4 & \varepsilon_5 & -\varepsilon_6 \end{pmatrix}$	$(P_1 \ -P_2 \ P_3)$ $(-P_1 \ P_2 \ -P_3)$	$(P_1 \ -P_2 \ P_3)$	$(-P_1 \ P_2 \ -P_3)$
4 $\begin{pmatrix} \varepsilon_1 & \varepsilon_2 & \varepsilon_3 \\ -\varepsilon_4 & -\varepsilon_5 & \varepsilon_6 \end{pmatrix}$	$(P_1 \ P_2 \ -P_3)$ $(-P_1 \ -P_2 \ P_3)$	$(-P_1 \ -P_2 \ P_3)$	$(-P_1 \ -P_2 \ P_3)$

Table D.4 (continued) $mmm \rightarrow 1, mmm \rightarrow \bar{1} (P = 0)$ (above diagonal) $mm2 \rightarrow 1$ (below diagonal)

S	1	2	3	4
1	N/A	$(100)^C$ $(01a)^N$	$(010)^C$ $(10b)^N$ $(001)^N$	$(001)^C$ $(1c0)^N$ $(010)^N$
2	$(100)^C$ $(01a)^N$	N/A	$(1\bar{c}0)^C$	$(10\bar{b})^C$ $(100)^N$
3	$(010)^C$ $(10b)^N$	$(001)^N$ $(1\bar{c}0)^C$	N/A	$(01\bar{a})^C$
4	$(001)^N$ $(1c0)^C$	$(010)^C$ $(10\bar{b})^N$	$(100)^C$ $(01\bar{a})^N$	N/A

 $222 \rightarrow 1$

S	1	2	3	4
1	N/A	$(100)^N$ $(01a)^C$	$(010)^N$ $(10b)^C$ $(001)^N$	$(001)^N$ $(1c0)^C$ $(010)^N$
2		N/A	$(1\bar{c}0)^C$	$(10\bar{b})^C$ $(100)^N$
3			N/A	$(01\bar{a})^C$
4				N/A

$$a = \varepsilon_5/\varepsilon_6, b = \varepsilon_4/\varepsilon_6, c = \varepsilon_4/\varepsilon_5$$

Table D.5 Tetragonal to triclinic

All species strains	422 \rightarrow 1		$\bar{4}2m \rightarrow 1$		4/mmm \rightarrow 1, 4/mmm \rightarrow $\bar{1}(P=0)$ 4/m \rightarrow 1, 4/m \rightarrow $\bar{1}(P=0)$ (strains 1-4 only)	
	4 \rightarrow $\bar{1}$ (strains 1-4 only)	4mm \rightarrow 1	4 \rightarrow $\bar{1}$ (strains 1-4 only)	$\bar{4}2m \rightarrow 1$	4/mmm \rightarrow 1, 4/mmm \rightarrow $\bar{1}(P=0)$	4/m \rightarrow 1, 4/m \rightarrow $\bar{1}(P=0)$ (strains 1-4 only)
	polarizations	polarizations	polarizations	polarizations	polarizations	polarizations
1 $\begin{pmatrix} \epsilon_1 & \epsilon_2 & \epsilon_3 \\ \epsilon_4 & \epsilon_5 & \epsilon_6 \end{pmatrix}$	$(P_1 \ P_2 \ P_3)$	$(P_1 \ P_2 \ P_3)$	$(P_1 \ P_2 \ P_3)$	$(P_1 \ P_2 \ P_3)$	$(P_1 \ P_2 \ P_3)$	$(P_1 \ P_2 \ P_3)$
2 $\begin{pmatrix} \epsilon_2 & \epsilon_1 & \epsilon_3 \\ \epsilon_5 & -\epsilon_4 & -\epsilon_6 \end{pmatrix}$	$(-P_2 \ P_1 \ P_3)$	$(-P_2 \ P_1 \ P_3)$	$(-P_2 \ P_1 \ P_3)$	$(P_2 \ -P_1 \ -P_3)$	$(-P_1 \ -P_2 \ -P_3)$	$(-P_1 \ -P_2 \ -P_3)$
3 $\begin{pmatrix} \epsilon_1 & \epsilon_2 & \epsilon_3 \\ -\epsilon_4 & -\epsilon_5 & \epsilon_6 \end{pmatrix}$	$(-P_1 \ -P_2 \ P_3)$	$(-P_1 \ -P_2 \ P_3)$	$(-P_1 \ -P_2 \ P_3)$	$(-P_1 \ -P_2 \ P_3)$	$(-P_1 \ -P_2 \ P_3)$	$(-P_1 \ -P_2 \ P_3)$
4 $\begin{pmatrix} \epsilon_2 & \epsilon_1 & \epsilon_3 \\ -\epsilon_5 & \epsilon_4 & -\epsilon_6 \end{pmatrix}$	$(P_2 \ -P_1 \ P_3)$	$(P_2 \ -P_1 \ P_3)$	$(P_2 \ -P_1 \ P_3)$	$(-P_2 \ P_1 \ -P_3)$	$(P_2 \ -P_1 \ P_3)$	$(P_2 \ -P_1 \ P_3)$
5 $\begin{pmatrix} \epsilon_1 & \epsilon_2 & \epsilon_3 \\ \epsilon_4 & -\epsilon_5 & -\epsilon_6 \end{pmatrix}$	$(P_1 \ -P_2 \ -P_3)$	$(-P_1 \ P_2 \ P_3)$	$(P_1 \ -P_2 \ -P_3)$	$(P_1 \ -P_2 \ -P_3)$	$(-P_1 \ P_2 \ P_3)$	$(-P_1 \ P_2 \ P_3)$
6 $\begin{pmatrix} \epsilon_1 & \epsilon_2 & \epsilon_3 \\ -\epsilon_4 & \epsilon_5 & -\epsilon_6 \end{pmatrix}$	$(-P_1 \ P_2 \ -P_3)$	$(P_1 \ -P_2 \ P_3)$	$(-P_1 \ P_2 \ -P_3)$	$(-P_1 \ P_2 \ -P_3)$	$(P_1 \ -P_2 \ P_3)$	$(P_1 \ -P_2 \ P_3)$
7 $\begin{pmatrix} \epsilon_2 & \epsilon_1 & \epsilon_3 \\ -\epsilon_5 & -\epsilon_4 & \epsilon_6 \end{pmatrix}$	$(P_2 \ P_1 \ -P_3)$	$(-P_2 \ -P_1 \ P_3)$	$(P_2 \ P_1 \ -P_3)$	$(-P_2 \ -P_1 \ P_3)$	$(-P_2 \ -P_1 \ P_3)$	$(-P_2 \ -P_1 \ P_3)$
8 $\begin{pmatrix} \epsilon_2 & \epsilon_1 & \epsilon_3 \\ \epsilon_5 & \epsilon_4 & \epsilon_6 \end{pmatrix}$	$(-P_2 \ -P_1 \ -P_3)$	$(P_2 \ P_1 \ P_3)$	$(-P_2 \ -P_1 \ -P_3)$	$(P_2 \ P_1 \ P_3)$	$(P_2 \ P_1 \ P_3)$	$(-P_2 \ -P_1 \ -P_3)$

Table D.5 (continued)

S	1	2	3	4	5	6	7	8
	422 → 1 (all eight strains), 4 → 1 (strains 1-4 only) (above diagonal)							
	42m → 1 (all eight strains), 4 → 1 (strains 1-4 only) (below diagonal)							
1	N/A	R	(001) ^N (1a0) ^C	R	(100) ^N (01b) ^C	(010) ^N (10c) ^C	(110) ^N (11d ₊) ^C	(110) ^N (11d ₋) ^C
2	R	N/A	R	(001) ^N (a10) ^C	(110) ^N (11d ₋) ^C	(110) ^N (11d ₊) ^C	(010) ^N (10b) ^C	(100) ^N (01c) ^C
3	(001) ^N (1a0) ^C	R	N/A	R	(010) ^N (10c) ^C	(100) ^N (01b) ^C	(110) ^N (11d ₋) ^C	(110) ^N (11d ₊) ^C
4	R	(001) ^N (a10) ^C	R	N/A	(110) ^N (11d ₊) ^C	(110) ^N (11d ₋) ^C	(100) ^N (01c) ^C	(010) ^N (10b) ^C
5	(100) ^N (01b) ^C	(110) ^C (11d ₋) ^N	(010) ^N (10c) ^C	(110) ^C (11d ₊) ^N	N/A	(001) ^N (1a0) ^C	R	R
6	(010) ^N (10c) ^C	(110) ^C (11d ₊) ^N	(100) ^N (01b) ^C	(110) ^C (11d ₋) ^N	(001) ^N (1a0) ^C	N/A	R	R
7	(110) ^C (11d ₊) ^N	(010) ^N (10b) ^C	(110) ^C (11d ₋) ^N	(100) ^N (01c) ^C	R	R	N/A	(001) ^N (a10) ^C
8	(110) ^C (11d ₋) ^N	(100) ^N (01c) ^C	(110) ^C (11d ₊) ^N	(010) ^N (10b) ^C	R	R	(001) ^N (a10) ^C	N/A

Table D.5 (continued)

	1	2	3	4	5	6	7	8
$4/mmm \rightarrow \bar{1}(P=0), 4/mmm \rightarrow 1, 4mm \rightarrow 1$ (all eight strains),								
$4/m \rightarrow \bar{1}(P=0), 4/m \rightarrow 1$ (strains 1-4 only)								
S	1	2	3	4	5	6	7	8
1	N/A	R	$(001)^N$ $(1a0)^C$	R	$(100)^C$ $(01b)^N$	$(010)^C$ $(10c)^N$	$(110)^C$ $(1\bar{1}\bar{d}_+)^N$	$(110)^C$ $(11d_-)^N$
2		N/A	R	$(001)^N$ $(\bar{a}10)^C$	$(110)^C$ $(1\bar{1}\bar{d}_-)^N$	$(110)^C$ $(11\bar{d}_+)^N$	$(010)^C$ $(40b)^N$	$(100)^C$ $(01c)^N$
3			N/A	R	$(010)^C$ $(10c)^N$	$(100)^C$ $(01b)^N$	$(110)^C$ $(11\bar{d}_-)^N$	$(110)^C$ $(11d_+)^N$
4				N/A	$(110)^C$ $(11d_+)^N$	$(110)^C$ $(11d_-)^N$	$(100)^C$ $(01\bar{c})^N$	$(010)^C$ $(10b)^N$
5					N/A	$(001)^N$ $(1a0)^C$	R	R
6						N/A	R	R
7							N/A	$(001)^N$ $(a10)^C$
8								N/A

$$a = \epsilon_4/\epsilon_5, b = \epsilon_5/\epsilon_6, c = \epsilon_4/\epsilon_6, d_{\pm} = (\epsilon_5 \pm \epsilon_4)/(\epsilon_2 - \epsilon_1)$$

Table D.6 Trigonal to triclinic

All species strains	$\bar{3}2 \rightarrow 1$	$\bar{3}m \rightarrow \bar{1}(P=0)$	$\bar{3}m \rightarrow 1$	$\bar{3}m \rightarrow 1$	$\bar{3}m \rightarrow 1$
	$\bar{3} \rightarrow \bar{1}, \bar{3} \rightarrow \bar{1}(P=0)$	(strains 1-3 only)	(strains 1-3 only)	(strains 1-3 only)	(strains 1-3 only)
	polarizations	polarizations	polarizations	polarizations	polarizations
1	$\begin{pmatrix} \varepsilon_1 & \varepsilon_2 & \varepsilon_3 \\ \varepsilon_4 & \varepsilon_5 & \varepsilon_6 \end{pmatrix}$	$(P_1 \ P_2 \ P_3)$	$(P_1 \ P_2 \ P_3)$	$(P_1 \ P_2 \ P_3)$	$(P_1 \ P_2 \ P_3)$
2	$\begin{pmatrix} \varepsilon_1^+ & \varepsilon_2^- & \varepsilon_3 \\ \varepsilon_4^- & \varepsilon_5^- & \varepsilon_6^- \end{pmatrix}$	$(-P_1^+ \ P_2^- \ P_3)$	$(-P_1^+ \ P_2^- \ P_3)$	$(-P_1^+ \ P_2^- \ P_3)$	$(-P_1^+ \ P_2^- \ P_3)$
3	$\begin{pmatrix} \varepsilon_1^- & \varepsilon_2^+ & \varepsilon_3 \\ -\varepsilon_4^+ & -\varepsilon_5^+ & \varepsilon_6^+ \end{pmatrix}$	$(-P_1^- \ -P_2^+ \ P_3)$	$(-P_1^- \ -P_2^+ \ P_3)$	$(-P_1^- \ -P_2^+ \ P_3)$	$(-P_1^- \ -P_2^+ \ P_3)$
4	$\begin{pmatrix} \varepsilon_1 & \varepsilon_2 & \varepsilon_3 \\ \varepsilon_4 & -\varepsilon_5 & -\varepsilon_6 \end{pmatrix}$	$(P_1 \ -P_2 \ -P_3)$	$(-P_1 \ P_2 \ P_3)$	$(-P_1 \ P_2 \ P_3)$	$(P_1 \ -P_2 \ -P_3)$
5	$\begin{pmatrix} \varepsilon_1^- & \varepsilon_2^+ & \varepsilon_3 \\ -\varepsilon_4^+ & \varepsilon_5^+ & -\varepsilon_6^- \end{pmatrix}$	$(-P_1^- \ P_2^+ \ -P_3)$	$(P_1^- \ -P_2^+ \ P_3)$	$(P_1^- \ -P_2^+ \ P_3)$	$(-P_1^- \ P_2^+ \ -P_3)$
6	$\begin{pmatrix} \varepsilon_1^+ & \varepsilon_2^- & \varepsilon_3 \\ \varepsilon_4^- & -\varepsilon_5^- & -\varepsilon_6^- \end{pmatrix}$	$(-P_1^+ \ -P_2^- \ -P_3)$	$(P_1^+ \ P_2^- \ P_3)$	$(P_1^+ \ P_2^- \ P_3)$	$(-P_1^+ \ -P_2^- \ -P_3)$

$$\varepsilon_1^+ = (1/4)(\varepsilon_1 \pm \sqrt{3}\varepsilon_6 + 3\varepsilon_2), \varepsilon_2^+ = (1/4)(3\varepsilon_1 \pm \sqrt{3}\varepsilon_6 + \varepsilon_2), \varepsilon_6^+ = (1/2)(\pm\sqrt{3}\varepsilon_1 - \varepsilon_6 \mp \sqrt{3}\varepsilon_2),$$

$$\varepsilon_5^+ = (1/2)(\pm\varepsilon_5 - \sqrt{3}\varepsilon_4), \varepsilon_4^+ = (1/2)(\sqrt{3}\varepsilon_5 \pm \varepsilon_4), P_1^+ = (1/2)(P_1 \pm \sqrt{3}P_2), P_2^+ = (1/2)(\sqrt{3}P_1 \pm P_2)$$

Table D.6 (continued)

$\bar{3}m \rightarrow 1, \bar{3}m \rightarrow \bar{1}(P=0), 32 \rightarrow 1$ (all six strains),
 $\bar{3} \rightarrow \bar{1}(P=0), \bar{3} \rightarrow 1, \bar{3} \rightarrow 1$ (strains 1–3 only) (above diagonal)
 $3m \rightarrow 1$ (below diagonal)

S	1	2	3	4	5	6
1	N/A	R	R	$(2\bar{1}\bar{1}0)^N$	$(1\bar{1}20)^N$	$(1\bar{1}20)^N$
2	R	N/A	R	$(01\bar{1}a)^C$ $(1\bar{1}20)^N$ $(1\bar{1}0c_-)^C$	$(\bar{1}10c_+)^C$ $(1\bar{1}20)^N$ $(10\bar{1}\bar{a})^C$	$(\bar{1}01c_-)^C$ $(2\bar{1}\bar{1}0)^N$ $(01\bar{1}b_+)^C$
3	R	R	N/A	$(1\bar{1}20)^N$ $(10\bar{1}c_+)^C$	$(2\bar{1}\bar{1}0)^N$ $(01\bar{1}b_-)^C$	$(1\bar{1}20)^N$ $(\bar{1}10\bar{a})^C$
4	$(2\bar{1}\bar{1}0)^C$ $(01\bar{1}a)^N$ $(1\bar{1}20)^C$	$(1\bar{1}20)^C$ $(1\bar{1}0c_-)^N$ $(1\bar{1}20)^C$	$(1\bar{1}20)^C$ $(10\bar{1}c_+)^N$ $(2\bar{1}\bar{1}0)^C$	N/A	R	R
5	$(\bar{1}10c_+)^N$ $(1\bar{1}20)^C$	$(10\bar{1}\bar{a})^N$ $(2\bar{1}\bar{1}0)^C$	$(01\bar{1}b_-)^N$ $(1\bar{1}20)^C$	R	N/A	R
6	$(1\bar{1}20)^C$ $(101c_-)^N$	$(2\bar{1}\bar{1}0)^C$ $(01\bar{1}b_+)^N$	$(1\bar{1}20)^C$ $(1\bar{1}20)^C$ $(\bar{1}10\bar{a})^N$	R	R	N/A

$$a = \sqrt{3}(\epsilon_s/\epsilon_0), b_{\pm} = 2\sqrt{3}(\epsilon_s \pm \sqrt{3}\epsilon_4)/[\pm\sqrt{3}(\epsilon_1 - \epsilon_2) + \epsilon_6], c_{\pm} = \mp(1/2)b_{\pm}$$

Table D.7 Hexagonal to triclinic species

All species	$6/mmm \rightarrow 1$		polarizations	polarizations	polarizations
	$622 \rightarrow 1$	$6/mmm \rightarrow \bar{1} (P=0)$			
	$6/m \rightarrow 1, 6/m \rightarrow \bar{1} (P=0)$ (strains 1-6 only)	$6/m \rightarrow 1, 6/m \rightarrow \bar{1} (P=0)$ (strains 1-6 only)			
	$6 \rightarrow 1$ (upper polarizations only, strains 1-6 only)	$6 \rightarrow 1$ (strains 1-6 only)			
strains	strains	strains	strains	strains	strains
1	$\begin{pmatrix} \varepsilon_1 & \varepsilon_2 & \varepsilon_3 \\ \varepsilon_4 & \varepsilon_5 & \varepsilon_6 \end{pmatrix}$	$\begin{pmatrix} P_1 & P_2 & P_3 \\ -P_1 & -P_2 & -P_3 \end{pmatrix}$	$\begin{pmatrix} P_1 & P_2 & P_3 \end{pmatrix}$	$\begin{pmatrix} P_1 & P_2 & P_3 \end{pmatrix}$	$\begin{pmatrix} P_1 & P_2 & P_3 \end{pmatrix}$
2	$\begin{pmatrix} \varepsilon_1^+ & \varepsilon_2^+ & \varepsilon_3 \\ \varepsilon_4^+ & \varepsilon_5^+ & \varepsilon_6 \end{pmatrix}$	$\begin{pmatrix} P_1^+ & P_2^+ & P_3 \\ -P_1^+ & -P_2^+ & -P_3 \end{pmatrix}$	$\begin{pmatrix} P_1^+ & P_2^+ & P_3 \end{pmatrix}$	$\begin{pmatrix} P_1^+ & P_2^+ & P_3 \end{pmatrix}$	$\begin{pmatrix} -P_1^+ & -P_2^+ & -P_3 \end{pmatrix}$
3	$\begin{pmatrix} \varepsilon_1^+ & \varepsilon_2^- & \varepsilon_3 \\ \varepsilon_4^+ & \varepsilon_5^- & \varepsilon_6 \end{pmatrix}$	$\begin{pmatrix} P_1^+ & P_2^- & P_3 \\ -P_1^+ & -P_2^- & -P_3 \end{pmatrix}$	$\begin{pmatrix} -P_1^+ & P_2^- & P_3 \end{pmatrix}$	$\begin{pmatrix} -P_1^+ & P_2^- & P_3 \end{pmatrix}$	$\begin{pmatrix} -P_1^+ & P_2^- & P_3 \end{pmatrix}$
4	$\begin{pmatrix} \varepsilon_1 & \varepsilon_2 & \varepsilon_3 \\ -\varepsilon_4 & -\varepsilon_5 & \varepsilon_6 \end{pmatrix}$	$\begin{pmatrix} P_1 & P_2 & -P_3 \\ -P_1 & -P_2 & P_3 \end{pmatrix}$	$\begin{pmatrix} P_1 & P_2 & P_3 \end{pmatrix}$	$\begin{pmatrix} P_1 & P_2 & P_3 \end{pmatrix}$	$\begin{pmatrix} P_1 & P_2 & -P_3 \end{pmatrix}$
5	$\begin{pmatrix} \varepsilon_1^- & \varepsilon_2^+ & \varepsilon_3 \\ -\varepsilon_4^+ & -\varepsilon_5^- & \varepsilon_6 \end{pmatrix}$	$\begin{pmatrix} P_1^- & P_2^+ & P_3 \\ -P_1^- & -P_2^+ & -P_3 \end{pmatrix}$	$\begin{pmatrix} -P_1^- & -P_2^+ & P_3 \end{pmatrix}$	$\begin{pmatrix} -P_1^- & -P_2^+ & P_3 \end{pmatrix}$	$\begin{pmatrix} -P_1^- & -P_2^+ & P_3 \end{pmatrix}$
6	$\begin{pmatrix} \varepsilon_1^+ & \varepsilon_2^- & \varepsilon_3 \\ -\varepsilon_4^+ & -\varepsilon_5^- & -\varepsilon_6 \end{pmatrix}$	$\begin{pmatrix} P_1^+ & P_2^- & P_3 \\ -P_1^+ & -P_2^- & -P_3 \end{pmatrix}$	$\begin{pmatrix} P_1^+ & -P_2^- & P_3 \end{pmatrix}$	$\begin{pmatrix} P_1^+ & -P_2^- & P_3 \end{pmatrix}$	$\begin{pmatrix} -P_1^+ & P_2^- & -P_3 \end{pmatrix}$
7	$\begin{pmatrix} \varepsilon_1 & \varepsilon_2 & \varepsilon_3 \\ \varepsilon_4 & -\varepsilon_5 & -\varepsilon_6 \end{pmatrix}$	$\begin{pmatrix} P_1 & -P_2 & -P_3 \\ -P_1 & P_2 & P_3 \end{pmatrix}$	$\begin{pmatrix} P_1 & P_2 & P_3 \end{pmatrix}$	$\begin{pmatrix} -P_1 & P_2 & P_3 \end{pmatrix}$	$\begin{pmatrix} -P_1 & P_2 & P_3 \end{pmatrix}$
8	$\begin{pmatrix} \varepsilon_1^- & \varepsilon_2^+ & \varepsilon_3 \\ \varepsilon_4^- & -\varepsilon_5^+ & -\varepsilon_6 \end{pmatrix}$	$\begin{pmatrix} P_1^- & P_2^+ & -P_3 \\ -P_1^- & -P_2^+ & P_3 \end{pmatrix}$	$\begin{pmatrix} P_1^- & P_2^+ & P_3 \end{pmatrix}$	$\begin{pmatrix} -P_1^- & P_2^+ & P_3 \end{pmatrix}$	$\begin{pmatrix} P_1^- & -P_2^+ & -P_3 \end{pmatrix}$
9	$\begin{pmatrix} \varepsilon_1^+ & \varepsilon_2^- & \varepsilon_3 \\ \varepsilon_4^+ & -\varepsilon_5^- & -\varepsilon_6 \end{pmatrix}$	$\begin{pmatrix} P_1^+ & P_2^- & -P_3 \\ -P_1^+ & -P_2^- & P_3 \end{pmatrix}$	$\begin{pmatrix} P_1^+ & P_2^- & P_3 \end{pmatrix}$	$\begin{pmatrix} P_1^+ & P_2^- & P_3 \end{pmatrix}$	$\begin{pmatrix} P_1^+ & P_2^- & P_3 \end{pmatrix}$
10	$\begin{pmatrix} \varepsilon_1 & \varepsilon_2 & \varepsilon_3 \\ -\varepsilon_4 & \varepsilon_5 & -\varepsilon_6 \end{pmatrix}$	$\begin{pmatrix} P_1 & -P_2 & P_3 \\ -P_1 & P_2 & -P_3 \end{pmatrix}$	$\begin{pmatrix} P_1 & -P_2 & P_3 \end{pmatrix}$	$\begin{pmatrix} P_1 & -P_2 & P_3 \end{pmatrix}$	$\begin{pmatrix} -P_1 & P_2 & -P_3 \end{pmatrix}$
11	$\begin{pmatrix} \varepsilon_1^- & \varepsilon_2^+ & \varepsilon_3 \\ -\varepsilon_4^+ & \varepsilon_5^+ & -\varepsilon_6 \end{pmatrix}$	$\begin{pmatrix} P_1^- & P_2^+ & -P_3 \\ -P_1^- & -P_2^+ & P_3 \end{pmatrix}$	$\begin{pmatrix} P_1^- & -P_2^+ & P_3 \end{pmatrix}$	$\begin{pmatrix} P_1^- & -P_2^+ & P_3 \end{pmatrix}$	$\begin{pmatrix} P_1^- & -P_2^+ & P_3 \end{pmatrix}$
12	$\begin{pmatrix} \varepsilon_1^+ & \varepsilon_2^- & \varepsilon_3 \\ -\varepsilon_4^+ & \varepsilon_5^- & -\varepsilon_6 \end{pmatrix}$	$\begin{pmatrix} P_1^+ & P_2^- & -P_3 \\ -P_1^+ & -P_2^- & P_3 \end{pmatrix}$	$\begin{pmatrix} -P_1^+ & -P_2^- & P_3 \end{pmatrix}$	$\begin{pmatrix} -P_1^+ & -P_2^- & P_3 \end{pmatrix}$	$\begin{pmatrix} P_1^+ & P_2^- & -P_3 \end{pmatrix}$

$$\begin{aligned} \varepsilon_1^+ &= (1/4)(\varepsilon_1 + \sqrt{3}\varepsilon_4 + 3\varepsilon_2), \varepsilon_2^+ = (1/4)(3\varepsilon_1 + \sqrt{3}\varepsilon_6 + \varepsilon_2), \varepsilon_3^+ = (1/2)(\pm\sqrt{3}\varepsilon_1 - \varepsilon_6 \mp \sqrt{3}\varepsilon_2), \\ \varepsilon_4^+ &= (1/2)(\pm\varepsilon_5 - \sqrt{3}\varepsilon_4), \varepsilon_5^+ = (1/2)(\sqrt{3}\varepsilon_5 \pm \varepsilon_4), \varepsilon_6^+ = (1/2)(P_1 \pm \sqrt{3}P_2), P_2^+ = (1/2)(\sqrt{3}P_1 \pm P_2) \end{aligned}$$

Table D.7 (continued)

$\bar{6}/m\bar{m}m \rightarrow \bar{1} (P=0)$, $\bar{6}/m\bar{m}m \rightarrow 1$ (all 12 strains), $\bar{6}/m \rightarrow \bar{1} (P=0)$, $\bar{6}/m \rightarrow 1$, $\bar{6} \rightarrow \bar{1}$ (strains 1–6 only) (above diagonal)
 $\bar{6}m2 \rightarrow 1$ (all 12 strains), $\bar{6} \rightarrow \bar{1}$ (strains 1–6 only) (below diagonal)

S	1	2	3	4	5	6	7	8	9	10	11	12
1	N/A	R	R	(0001) ^N (2a ₊ a ₋ 0) ^C	R	R	($\bar{2}110$) ^N (011c) ^C	(1100) ^N (112d ₋) ^C	(1210) ^N (101e ₋) ^C	(0110) ^N (211b) ^C	(1120) ^N (110e ₊) ^C	(1010) ^N (121d ₊) ^C
2	R	N/A	R	R	(0001) ^N (2g ₊ h ₊ 0) ^C	R	(1010) ^N (121d ₋) ^C	(2110) ^N (011e ₋) ^C	(1100) ^N (112b) ^C	(1210) ^N (101e ₊) ^C	(0110) ^N (211d ₊) ^C	(1120) ^N (110c) ^C
3	R	R	N/A	R	R	(0001) ^N (2h ₋ g ₋ 0) ^C	(1120) ^N (110e ₋) ^C	(1010) ^N (121b) ^C	(2110) ^N (011e ₊) ^C	(1100) ^N (112d ₊) ^C	(1210) ^N (101e) ^C	(0110) ^N (211d ₋) ^C
4	(0001) ^C (2a ₊ a ₋ 0) ^N	R	R	R	R	R	(0110) ^N (211b) ^C	(1120) ^N (110e ₊) ^C	(1010) ^N (121d ₊) ^C	(2110) ^N (011c) ^C	(1100) ^N (112d ₋) ^C	(1210) ^N (101e ₋) ^C
5	R	(0001) ^C (2g ₊ h ₊ 0) ^N	R	R	N/A	R	(1210) ^N (101e ₊) ^C	(0110) ^N (211d ₊) ^C	(1120) ^N (110c) ^C	(1010) ^N (121d ₋) ^C	(2110) ^N (011e ₋) ^C	(1100) ^N (112b) ^C
6	R	R	(0001) ^C (2h ₋ g ₋ 0) ^N	R	R	N/A	(1100) ^N (112d ₊) ^C	(1210) ^N (101c) ^C	(0110) ^N (211d ₋) ^C	(1120) ^N (110e ₋) ^C	(1010) ^N (121b) ^C	(2110) ^N (011e ₊) ^C
7	($\bar{2}110$) ^C (011c) ^N	(1010) ^N (121d ₋) ^C	(1120) ^C (110e ₋) ^N	(1100) ^N (211b) ^C	(1210) ^C (101e ₊) ^N	(1100) ^N (112d ₊) ^C	N/A	R	R	(0001) ^N (2a ₋ a ₊ 0) ^C	R	R
8	(1100) ^N (112d ₋) ^C	($\bar{2}110$) ^C (011e ₋) ^N	(1120) ^C (110e ₊) ^N	(1120) ^C (110e ₊) ^N	(1120) ^C (110e ₊) ^N	(1210) ^C (101c) ^N	R	N/A	R	R	(0001) ^N (2h ₊ g ₊ 0) ^C	R
9	(1210) ^C (101e ₋) ^N	(1100) ^N (112b) ^C	(2110) ^C (011e ₊) ^N	(1010) ^N (121d ₊) ^C	(1120) ^C (110c) ^N	(0110) ^N (211d ₋) ^C	R	R	N/A	R	R	(0001) ^N (2g ₋ h ₋ 0) ^C
10	(0110) ^N (211b) ^C	(1210) ^C (101e ₊) ^N	(1100) ^N (112d ₊) ^C	(1120) ^C (110e ₋) ^N	(1120) ^C (110e ₋) ^N	(1120) ^C (110e ₋) ^N	(0001) ^C (2a ₋ a ₊ 0) ^N	R	R	N/A	R	R
11	(1120) ^C (110e ₊) ^N	(0110) ^N (211d ₊) ^C	(1210) ^C (101e ₋) ^N	(1100) ^N (112d ₋) ^C	(1120) ^C (110c) ^N	(1010) ^N (121b) ^C	R	(0001) ^C (2h ₊ g ₊ 0) ^N	R	R	N/A	R
12	(1010) ^N (121d ₊) ^C	(1120) ^C (110e ₋) ^N	(0110) ^N (211d ₋) ^C	(1210) ^C (101e ₋) ^N	(1100) ^N (112b) ^C	(2110) ^C (011e ₊) ^N	R	R	(0001) ^C (2g ₋ h ₋ 0) ^N	R	R	N/A

Table D.7 (continued)

$6mm \rightarrow 1$	1	2	3	4	5	6	7	8	9	10	11	12
1	N/A	R	R	$(0001)^N$ $(2a_+a_-0)^C$	R	R	$(2\bar{1}10)^C$ $(0\bar{1}1c)^N$	$(\bar{1}100)^C$ $(112d_-)^N$	$(1210)^C$ $(10\bar{1}e_-)^N$	$(0\bar{1}10)^C$ $(2\bar{1}\bar{1}b)^N$	$(1120)^C$ $(1\bar{1}0e_+)^N$	$(10\bar{1}0)^C$ $(12\bar{1}d_+)^N$
2	N/A	R	R	$(0001)^N$ $(2g_+h_+0)^C$	R	R	$(10\bar{1}0)^C$ $(12\bar{1}d_-)^N$	$(2\bar{1}\bar{1}0)^C$ $(0\bar{1}\bar{1}e_-)^N$	$(1100)^C$ $(112b)^N$	$(1210)^C$ $(10\bar{1}e_+)^N$	$(0\bar{1}\bar{1}0)^C$ $(2\bar{1}\bar{1}d_+)^N$	$(1120)^C$ $(1\bar{1}0\bar{e})^N$
3	N/A	R	R	R	$(0001)^N$ $(2h_-g_-0)^C$	R	$(1120)^C$ $(1\bar{1}0\bar{e}_-)^N$	$(10\bar{1}0)^C$ $(12\bar{1}b)^N$	$(2\bar{1}\bar{1}0)^C$ $(0\bar{1}\bar{1}e_+)^N$	$(1100)^C$ $(112d_+)^N$	$(1210)^C$ $(10\bar{1}\bar{e})^N$	$(0\bar{1}\bar{1}0)^C$ $(2\bar{1}\bar{1}d_-)^N$
4	N/A	R	R	N/A	R	R	$(0\bar{1}\bar{1}0)^C$ $(2\bar{1}\bar{1}b)^N$	$(1120)^C$ $(1\bar{1}0\bar{e}_+)^N$	$(10\bar{1}0)^C$ $(12\bar{1}d_+)^N$	$(2\bar{1}\bar{1}0)^C$ $(0\bar{1}\bar{1}\bar{e})^N$	$(1100)^C$ $(112\bar{d}_-)^N$	$(1210)^C$ $(10\bar{1}\bar{e}_-)^N$
5	N/A	R	R	N/A	R	R	$(12\bar{1}0)^C$ $(10\bar{1}\bar{e}_+)^N$	$(0\bar{1}\bar{1}0)^C$ $(2\bar{1}\bar{1}d_+)^N$	$(1120)^C$ $(1\bar{1}0c)^N$	$(10\bar{1}0)^C$ $(12\bar{1}d_-)^N$	$(2\bar{1}\bar{1}0)^C$ $(0\bar{1}\bar{1}\bar{e}_-)^N$	$(1100)^C$ $(112b)^N$
6	N/A	R	R	N/A	R	R	$(1100)^C$ $(112d_+)^N$	$(1210)^C$ $(10\bar{1}c)^N$	$(0\bar{1}\bar{1}0)^C$ $(2\bar{1}\bar{1}d_-)^N$	$(1120)^C$ $(1\bar{1}0e_-)^N$	$(10\bar{1}0)^C$ $(121b)^N$	$(2\bar{1}\bar{1}0)^C$ $(0\bar{1}\bar{1}\bar{e}_+)^N$
7	N/A	R	R	N/A	R	R	N/A	R	R	$(0001)^N$ $(2a_-a_+0)^C$	R	R
8	N/A	R	R	N/A	R	R	N/A	R	R	R	$(0001)^N$ $(2h_+g_+0)^C$	R
9	N/A	R	R	N/A	R	R	N/A	R	R	R	R	$(0001)^N$ $(2g_-h_-0)^C$
10	N/A	R	R	N/A	R	R	N/A	R	R	R	R	R
11	N/A	R	R	N/A	R	R	N/A	R	R	R	R	R
12	N/A	R	R	N/A	R	R	N/A	R	R	R	R	N/A

$a_{\pm} = -1 \pm \sqrt{3}(\epsilon_4/\epsilon_5)$, $b = 3(\epsilon_4/\epsilon_6)$, $c = \sqrt{3}(\epsilon_5/\epsilon_6)$, $d_{\pm} = \sqrt{3}(\sqrt{3}\epsilon_5 \pm \epsilon_4)/[\epsilon_1 - \epsilon_2 \mp (1/\sqrt{3})\epsilon_6]$, $e_{\pm} = (\epsilon_5 \pm \sqrt{3}\epsilon_4)/[\epsilon_1 - \epsilon_2 \pm (1/\sqrt{3})\epsilon_6]$, $g_{\pm} = 2(\epsilon_5 \pm (\epsilon_5 \mp \sqrt{3}\epsilon_4))/(\epsilon_5 \mp \sqrt{3}\epsilon_4)$, $h_{\pm} = -4\epsilon_5/(\epsilon_5 \mp \sqrt{3}\epsilon_4)$

Table D.8 Cubic to triclinic

All species strains	432 → 1		m3m → 1, m3m → 1 (P = 0)	
	23 → 1 (strains 1–12 only)	polarizations	m3 → 1	m3 → 1 (P = 0) (strains 1–12 only)
1	$\begin{pmatrix} \epsilon_1 & \epsilon_2 & \epsilon_3 \\ \epsilon_4 & \epsilon_5 & \epsilon_6 \end{pmatrix}$	$\begin{pmatrix} P_1 & P_2 & P_3 \end{pmatrix}$	$\begin{pmatrix} P_1 & P_2 & P_3 \end{pmatrix}$	$\begin{pmatrix} P_1 & P_2 & P_3 \end{pmatrix}$
2	$\begin{pmatrix} \epsilon_1 & \epsilon_2 & \epsilon_3 \\ -\epsilon_4 & -\epsilon_5 & \epsilon_6 \end{pmatrix}$	$\begin{pmatrix} -P_1 & -P_2 & P_3 \end{pmatrix}$	$\begin{pmatrix} -P_1 & -P_2 & P_3 \end{pmatrix}$	$\begin{pmatrix} -P_1 & -P_2 & -P_3 \end{pmatrix}$
3	$\begin{pmatrix} \epsilon_1 & \epsilon_2 & \epsilon_3 \\ \epsilon_4 & -\epsilon_5 & -\epsilon_6 \end{pmatrix}$	$\begin{pmatrix} P_1 & -P_2 & -P_3 \end{pmatrix}$	$\begin{pmatrix} P_1 & -P_2 & -P_3 \end{pmatrix}$	$\begin{pmatrix} P_1 & P_2 & -P_3 \end{pmatrix}$
4	$\begin{pmatrix} \epsilon_1 & \epsilon_2 & \epsilon_3 \\ -\epsilon_4 & \epsilon_5 & -\epsilon_6 \end{pmatrix}$	$\begin{pmatrix} -P_1 & P_2 & -P_3 \end{pmatrix}$	$\begin{pmatrix} -P_1 & P_2 & -P_3 \end{pmatrix}$	$\begin{pmatrix} -P_1 & P_2 & P_3 \end{pmatrix}$
5	$\begin{pmatrix} \epsilon_3 & \epsilon_1 & \epsilon_2 \\ \epsilon_6 & \epsilon_4 & \epsilon_5 \end{pmatrix}$	$\begin{pmatrix} P_3 & P_1 & P_2 \end{pmatrix}$	$\begin{pmatrix} P_3 & P_1 & P_2 \end{pmatrix}$	$\begin{pmatrix} P_3 & P_1 & P_2 \end{pmatrix}$
6	$\begin{pmatrix} \epsilon_2 & \epsilon_3 & \epsilon_1 \\ \epsilon_5 & \epsilon_6 & \epsilon_4 \end{pmatrix}$	$\begin{pmatrix} P_2 & P_3 & P_1 \end{pmatrix}$	$\begin{pmatrix} P_2 & P_3 & P_1 \end{pmatrix}$	$\begin{pmatrix} -P_2 & -P_3 & -P_1 \end{pmatrix}$
7	$\begin{pmatrix} \epsilon_3 & \epsilon_1 & \epsilon_2 \\ -\epsilon_6 & -\epsilon_4 & \epsilon_5 \end{pmatrix}$	$\begin{pmatrix} -P_3 & -P_1 & P_2 \end{pmatrix}$	$\begin{pmatrix} -P_3 & -P_1 & P_2 \end{pmatrix}$	$\begin{pmatrix} -P_3 & -P_1 & P_2 \end{pmatrix}$
8	$\begin{pmatrix} \epsilon_2 & \epsilon_3 & \epsilon_1 \\ -\epsilon_5 & -\epsilon_6 & \epsilon_4 \end{pmatrix}$	$\begin{pmatrix} -P_2 & -P_3 & P_1 \end{pmatrix}$	$\begin{pmatrix} -P_2 & -P_3 & P_1 \end{pmatrix}$	$\begin{pmatrix} P_3 & P_1 & -P_2 \end{pmatrix}$
9	$\begin{pmatrix} \epsilon_3 & \epsilon_1 & \epsilon_2 \\ \epsilon_6 & -\epsilon_4 & -\epsilon_5 \end{pmatrix}$	$\begin{pmatrix} P_3 & -P_1 & -P_2 \end{pmatrix}$	$\begin{pmatrix} P_3 & -P_1 & -P_2 \end{pmatrix}$	$\begin{pmatrix} -P_2 & -P_3 & P_1 \end{pmatrix}$
10	$\begin{pmatrix} \epsilon_2 & \epsilon_3 & \epsilon_1 \\ \epsilon_5 & -\epsilon_6 & -\epsilon_4 \end{pmatrix}$	$\begin{pmatrix} P_2 & -P_3 & -P_1 \end{pmatrix}$	$\begin{pmatrix} P_2 & -P_3 & -P_1 \end{pmatrix}$	$\begin{pmatrix} P_3 & -P_1 & -P_2 \end{pmatrix}$
11	$\begin{pmatrix} \epsilon_3 & \epsilon_1 & \epsilon_2 \\ -\epsilon_6 & \epsilon_4 & -\epsilon_5 \end{pmatrix}$	$\begin{pmatrix} -P_3 & P_1 & -P_2 \end{pmatrix}$	$\begin{pmatrix} -P_3 & P_1 & -P_2 \end{pmatrix}$	$\begin{pmatrix} P_2 & -P_3 & P_1 \end{pmatrix}$
12	$\begin{pmatrix} \epsilon_2 & \epsilon_3 & \epsilon_1 \\ -\epsilon_5 & \epsilon_6 & -\epsilon_4 \end{pmatrix}$	$\begin{pmatrix} -P_2 & P_3 & -P_1 \end{pmatrix}$	$\begin{pmatrix} -P_2 & P_3 & -P_1 \end{pmatrix}$	$\begin{pmatrix} -P_2 & P_3 & -P_1 \end{pmatrix}$

Table D.8 (continued)

All species strains	432 \rightarrow 1		$m\bar{3}m \rightarrow 1, m\bar{3}m \rightarrow \bar{1}(P=0)$	
	$2\bar{3} \rightarrow \bar{1}$ (strains 1–12 only)	polarizations	$\bar{4}3m \rightarrow 1$	$m\bar{3} \rightarrow \bar{1}, m\bar{3} \rightarrow \bar{1}(P=0)$ (strains 1–12 only)
13	$\begin{pmatrix} \epsilon_2 & \epsilon_1 & \epsilon_3 \\ \epsilon_5 & -\epsilon_4 & -\epsilon_6 \end{pmatrix}$	$(-P_2 \ P_1 \ P_3)$	$(P_2 \ -P_1 \ -P_3)$	$(-P_2 \ P_1 \ P_3)$
14	$\begin{pmatrix} \epsilon_2 & \epsilon_1 & \epsilon_3 \\ -\epsilon_5 & \epsilon_4 & -\epsilon_6 \end{pmatrix}$	$(P_2 \ -P_1 \ P_3)$	$(-P_2 \ P_1 \ -P_3)$	$(P_2 \ -P_1 \ -P_3)$
15	$\begin{pmatrix} \epsilon_1 & \epsilon_3 & \epsilon_2 \\ -\epsilon_4 & \epsilon_6 & -\epsilon_5 \end{pmatrix}$	$(P_1 \ -P_3 \ P_2)$	$(-P_1 \ P_3 \ -P_2)$	$(P_1 \ -P_3 \ P_2)$
16	$\begin{pmatrix} \epsilon_1 & \epsilon_3 & \epsilon_2 \\ -\epsilon_4 & -\epsilon_6 & \epsilon_5 \end{pmatrix}$	$(P_1 \ P_3 \ -P_2)$	$(-P_1 \ -P_3 \ P_2)$	$(P_1 \ P_3 \ -P_2)$
17	$\begin{pmatrix} \epsilon_3 & \epsilon_2 & \epsilon_1 \\ \epsilon_6 & -\epsilon_5 & -\epsilon_4 \end{pmatrix}$	$(-P_3 \ P_2 \ P_1)$	$(P_3 \ -P_2 \ -P_1)$	$(-P_3 \ P_2 \ P_1)$
18	$\begin{pmatrix} \epsilon_3 & \epsilon_2 & \epsilon_1 \\ -\epsilon_6 & -\epsilon_5 & \epsilon_4 \end{pmatrix}$	$(P_3 \ P_2 \ -P_1)$	$(-P_3 \ -P_2 \ P_1)$	$(P_3 \ P_2 \ -P_1)$
19	$\begin{pmatrix} \epsilon_2 & \epsilon_1 & \epsilon_3 \\ -\epsilon_5 & -\epsilon_4 & \epsilon_6 \end{pmatrix}$	$(P_2 \ P_1 \ -P_3)$	$(-P_2 \ -P_1 \ P_3)$	$(P_2 \ P_1 \ -P_3)$
20	$\begin{pmatrix} \epsilon_2 & \epsilon_1 & \epsilon_3 \\ \epsilon_5 & \epsilon_4 & \epsilon_6 \end{pmatrix}$	$(-P_2 \ -P_1 \ -P_3)$	$(P_2 \ P_1 \ P_3)$	$(-P_2 \ -P_1 \ -P_3)$
21	$\begin{pmatrix} \epsilon_1 & \epsilon_3 & \epsilon_2 \\ \epsilon_4 & -\epsilon_6 & -\epsilon_5 \end{pmatrix}$	$(-P_1 \ P_3 \ P_2)$	$(P_1 \ -P_3 \ -P_2)$	$(-P_1 \ P_3 \ P_2)$
22	$\begin{pmatrix} \epsilon_3 & \epsilon_2 & \epsilon_1 \\ -\epsilon_6 & \epsilon_5 & -\epsilon_4 \end{pmatrix}$	$(P_3 \ -P_2 \ P_1)$	$(-P_3 \ P_2 \ -P_1)$	$(P_3 \ -P_2 \ P_1)$
23	$\begin{pmatrix} \epsilon_3 & \epsilon_2 & \epsilon_1 \\ \epsilon_6 & \epsilon_5 & \epsilon_4 \end{pmatrix}$	$(-P_3 \ -P_2 \ -P_1)$	$(P_3 \ P_2 \ P_1)$	$(-P_3 \ -P_2 \ -P_1)$

Table D.8 (continued)

432 \rightarrow 1, $m\bar{3}m \rightarrow$ 1, $m\bar{3}m \rightarrow \bar{1}(P=0)$ (all 24 strains), $23 \rightarrow 1$, $m\bar{3} \rightarrow 1$, $m\bar{3} \rightarrow \bar{1}(P=0)$ (strains 1–12 only) (above diagonal)
 43m \rightarrow 1 (below diagonal)

S	1	2	3	4	5	6	7	8	9	10	11	12
1	N/A	$(001)^N$ $(1\bar{b}0)^C$	$(100)^N$ $(01c)^C$	$(010)^N$ $(10a)^C$	R	R	R	R	R	R	R	R
2	$(001)^N$ $(1\bar{b}0)^C$	N/A	$(010)^N$ $(10\bar{a})^C$	$(100)^N$ $(01\bar{c})^C$	R	R	R	R	R	R	R	R
3	$(100)^N$ $(01c)^C$	$(010)^N$ $(10\bar{a})^C$	N/A	$(001)^N$ $(1\bar{b}0)^C$	R	R	R	R	R	R	R	R
4	$(010)^N$ $(10a)^C$	$(100)^N$ $(01\bar{c})^C$	$(001)^N$ $(1\bar{b}0)^C$	N/A	R	R	R	R	R	R	R	R
5	R	R	R	R	N/A	R	$(001)^N$ $(a10)^C$	R	$(100)^N$ $(01b)^C$	R	$(010)^N$ $(c01)^C$	R
6	R	R	R	R	R	N/A	R	$(001)^N$ $(1c0)^C$	R	$(100)^N$ $(0a1)^C$	R	$(010)^N$ $(b01)^C$
7	R	R	R	R	$(001)^N$ $(a10)^C$	R	N/A	R	$(010)^N$ $(c01)^C$	R	$(100)^N$ $(01b)^C$	R
8	R	R	R	R	R	$(001)^N$ $(1c0)^C$	R	N/A	R	$(010)^N$ $(b01)^C$	R	$(100)^N$ $(0a1)^C$
9	R	R	R	R	$(100)^N$ $(01b)^C$	R	$(010)^N$ $(c01)^C$	R	N/A	R	$(001)^N$ $(a10)^C$	R
10	R	R	R	R	R	$(100)^N$ $(0a1)^C$	R	$(010)^N$ $(b01)^C$	R	N/A	R	$(001)^N$ $(1c0)^C$
11	R	R	R	R	$(010)^N$ $(c01)^C$	R	$(100)^N$ $(01b)^C$	R	$(001)^N$ $(a10)^C$	R	N/A	R
12	R	R	R	R	R	$(010)^N$ $(b01)^C$	R	$(100)^N$ $(0a1)^C$	R	$(001)^N$ $(1c0)^C$	R	N/A

Table D.8 (continued)

S	13	14	15	16	17	18	19	20	21	22	23	24
1	R	R	R	R	R	R	$(110)^N$ $(1\bar{1}d_+)^C$	$(1\bar{1}0)^N$ $(11d_-)^C$	$(011)^N$ $(\bar{f}_+1\bar{1})^C$	$(101)^N$ $(1\bar{e}_+1)^C$	$(101)^N$ $(1\bar{e}_-1)^C$	$(01\bar{1})^N$ $(\bar{f}_-11)^C$
2	R	R	$(01\bar{1})^N$ $(\bar{f}_+11)^C$	$(011)^N$ $(\bar{f}_-1\bar{1})^C$	$(10\bar{1})^N$ $(1\bar{e}_+1)^C$	$(101)^N$ $(1\bar{e}_-1)^C$	$(1\bar{1}0)^N$ $(11d_-)^C$	$(110)^N$ $(11d_+)^C$	R	R	R	R
3	$(110)^N$ $(1\bar{1}\bar{d}_-)^C$	$(1\bar{1}0)^N$ $(11d_+)^C$	R	R	$(101)^N$ $(1e_+1)^C$	$(10\bar{1})^N$ $(1e_+1)^C$	R	R	$(01\bar{1})^N$ $(\bar{f}_-11)^C$	R	R	$(011)^N$ $(\bar{f}_+1\bar{1})^C$
4	$(1\bar{1}0)^N$ $(11\bar{d}_+)^C$	$(110)^N$ $(1\bar{1}d_+)^C$	$(011)^N$ $(\bar{f}_-1\bar{1})^C$	$(01\bar{1})^N$ $(\bar{f}_+11)^C$	R	R	R	R	R	$(10\bar{1})^N$ $(1e_-1)^C$	$(101)^N$ $(1e_+1)^C$	R
5	R	$(101)^N$ $(1\bar{f}_+1)^C$	R	$(110)^N$ $(1\bar{1}e_+)^C$	$(011)^N$ $(\bar{d}_+1\bar{1})^C$	R	R	$(10\bar{1})^N$ $(1\bar{f}_-1)^C$	R	R	$(01\bar{1})^N$ $(\bar{d}_-11)^C$	$(1\bar{1}0)^N$ $(11\bar{e}_-)^C$
6	$(011)^N$ $(e_+1\bar{1})^C$	R	$(101)^N$ $(1d_+1)^C$	R	R	$(110)^N$ $(1\bar{1}\bar{f}_+)^C$	R	$(01\bar{1})^N$ $(\bar{e}_-11)^C$	R	R	$(1\bar{1}0)^N$ $(1\bar{1}\bar{f}_-)^C$	$(101)^N$ $(1d_-1)^C$
7	$(10\bar{1})^N$ $(1\bar{f}_+1)^C$	R	R	$(1\bar{1}0)^N$ $(11e_-)^C$	R	$(011)^N$ $(\bar{d}_-1\bar{1})^C$	$(101)^N$ $(1\bar{f}_-1)^C$	R	R	$(01\bar{1})^N$ $(\bar{d}_+11)^C$	R	$(110)^N$ $(11\bar{e}_+)^C$
8	R	$(01\bar{1})^N$ $(e_+11)^C$	R	$(101)^N$ $(1d_-1)^C$	R	$(1\bar{1}0)^N$ $(11\bar{f}_-)^C$	$(011)^N$ $(\bar{e}_-1\bar{1})^C$	R	$(101)^N$ $(1d_+1)^C$	R	$(110)^N$ $(1\bar{1}\bar{f}_+)^C$	R
9	$(101)^N$ $(1\bar{f}_+1)^C$	R	$(1\bar{1}0)^N$ $(11\bar{e}_+)^C$	R	$(01\bar{1})^N$ $(d_+11)^C$	R	$(10\bar{1})^N$ $(1\bar{f}_+1)^C$	R	$(110)^N$ $(11\bar{e}_-)^C$	R	$(011)^N$ $(d_+11)^C$	R
10	$(01\bar{1})^N$ $(e_-11)^C$	R	R	$(101)^N$ $(1d_+1)^C$	$(110)^N$ $(1\bar{1}\bar{f}_-)^C$	R	R	$(011)^N$ $(\bar{e}_+1\bar{1})^C$	$(101)^N$ $(1d_-1)^C$	$(1\bar{1}0)^N$ $(11\bar{f}_+)^C$	R	R
11	R	$(10\bar{1})^N$ $(1\bar{f}_-1)^C$	$(110)^N$ $(1\bar{1}\bar{e}_-)^C$	R	R	$(01\bar{1})^N$ $(d_+11)^C$	R	$(101)^N$ $(1\bar{f}_+1)^C$	R	$(110)^N$ $(011)^N$ $(d_-11)^C$	R	R
12	R	$(011)^N$ $(e_-11)^C$	$(101)^N$ $(1d_-1)^C$	R	$(1\bar{1}0)^N$ $(1\bar{1}\bar{f}_+)^C$	R	$(01\bar{1})^N$ $(\bar{e}_+11)^C$	R	R	$(110)^N$ $(1\bar{1}\bar{f}_-)^C$	R	$(101)^N$ $(1d_+1)^C$

Table D.8 (continued)

S	1	2	3	4	5	6	7	8	9	10	11	12
13	R	R	$(110)^C$ $(1\bar{1}d_+)^N$	$(110)^C$ $(11d_+)^N$	R	$(011)^C$ $(e_+1\bar{1})^N$	$(101)^C$ $(1f_+1)^N$	R	$(101)^C$ $(1f_+1)^N$	$(011)^C$ $(e_-1\bar{1})^N$	R	R
14	R	R	$(110)^C$ $(11d_+)^N$	$(110)^C$ $(1\bar{1}d_-)^N$	$(101)^C$ $(1f_+1)^N$	R	R	$(01\bar{1})^C$ $(e_+1\bar{1})^N$	R	R	$(10\bar{1})^C$ $(1f_-1)^N$	$(011)^C$ $(e_-1\bar{1})^N$
15	R	$(01\bar{1})^C$ $(f_+1\bar{1})^N$	R	$(011)^C$ $(f_-1\bar{1})^N$	R	$(101)^C$ $(1d_+1)^N$	R	R	$(110)^C$ $(11e_+)^N$	R	$(110)^C$ $(11e_-)^N$	$(10\bar{1})^C$ $(1d_-1)^N$
16	R	$(011)^C$ $(f_-1\bar{1})^N$	R	$(01\bar{1})^C$ $(f_+1\bar{1})^N$	$(110)^C$ $(11e_+)^N$	R	$(110)^C$ $(11e_-)^N$	$(101)^C$ $(1d_-1)^N$	R	$(10\bar{1})^C$ $(1d_+1)^N$	R	R
17	R	$(10\bar{1})^C$ $(1e_-1)^N$	$(101)^C$ $(1e_-1)^N$	R	$(011)^C$ $(d_+1\bar{1})^N$	R	R	R	$(01\bar{1})^C$ $(d_+1\bar{1})^N$	$(110)^C$ $(11f_-)^N$	R	$(110)^C$ $(11f_+)^N$
18	R	$(101)^C$ $(1e_-1)^N$	$(10\bar{1})^C$ $(1e_+1)^N$	R	R	$(110)^C$ $(11f_+)^N$	$(011)^C$ $(d_-1\bar{1})^N$	$(110)^C$ $(11f_-)^N$	R	R	$(01\bar{1})^C$ $(d_+1\bar{1})^N$	R
19	$(110)^C$ $(1\bar{1}d_+)^N$	$(110)^C$ $(11d_+)^N$	R	R	R	R	$(101)^C$ $(1f_-1)^N$	$(011)^C$ $(e_-1\bar{1})^N$	$(10\bar{1})^C$ $(1f_+1)^N$	R	R	$(01\bar{1})^C$ $(e_+1\bar{1})^N$
20	$(110)^C$ $(11d_-)^N$	$(110)^C$ $(1\bar{1}d_+)^N$	R	R	$(10\bar{1})^C$ $(1f_-1)^N$	$(01\bar{1})^C$ $(e_-1\bar{1})^N$	R	R	R	$(011)^C$ $(e_+1\bar{1})^N$	$(101)^C$ $(1f_+1)^N$	R
21	$(011)^C$ $(f_+1\bar{1})^N$	R	$(01\bar{1})^C$ $(f_-1\bar{1})^N$	R	R	R	R	$(10\bar{1})^C$ $(1d_+1)^N$	$(110)^C$ $(11e_+)^N$	$(101)^C$ $(1d_-1)^N$	$(110)^C$ $(11e_-)^N$	R
22	$(101)^C$ $(1e_+1)^N$	R	R	$(10\bar{1})^C$ $(1e_-1)^N$	R	R	$(01\bar{1})^C$ $(d_+1\bar{1})^N$	R	R	$(110)^C$ $(11f_+)^N$	$(110)^C$ $(11f_-)^N$	$(110)^C$ $(11f_+)^N$
23	$(10\bar{1})^C$ $(1e_-1)^N$	R	R	$(101)^C$ $(1e_+1)^N$	$(01\bar{1})^C$ $(d_-1\bar{1})^N$	$(110)^C$ $(11f_-)^N$	R	$(110)^C$ $(11f_+)^N$	$(011)^C$ $(d_+1\bar{1})^N$	R	R	R
24	$(01\bar{1})^C$ $(f_-1\bar{1})^N$	R	$(011)^C$ $(f_+1\bar{1})^N$	R	$(110)^C$ $(11e_-)^N$	$(10\bar{1})^C$ $(1d_-1)^N$	$(110)^C$ $(11e_+)^N$	R	R	R	R	$(101)^C$ $(1d_+1)^N$

Table D.8 (continued)

S	13	14	15	16	17	18	19	20	21	22	23	24
13	N/A	$(001)^N$ $(b10)^C$	R	R	R	R	$(010)^N$ $(10\bar{c})^C$	$(100)^N$ $(01a)^C$	R	R	R	R
14	$(001)^N$ $(b10)^C$	N/A	R	R	R	R	$(100)^N$ $(01\bar{a})^C$	$(010)^N$ $(10c)^C$	R	R	R	R
15	R	R	N/A	$(100)^N$ $(0\bar{a}1)^C$	R	R	R	R	$(001)^N$ $(1\bar{a}0)^C$	R	R	$(010)^N$ $(10b)^C$
16	R	R	$(100)^N$ $(0\bar{a}1)^C$	N/A	R	R	R	R	$(010)^N$ $(10b)^C$	R	R	$(001)^N$ $(1a0)^C$
17	R	R	R	R	N/A	$(010)^N$ $(\bar{a}01)^C$	R	R	R	$(001)^N$ $(\bar{c}10)^C$	$(100)^N$ $(0b1)^C$	R
18	R	R	R	R	$(010)^N$ $(\bar{a}01)^C$	N/A	R	R	R	$(100)^N$ $(0b1)^C$	$(001)^N$ $(c10)^C$	R
19	$(010)^N$ $(10\bar{c})^C$	$(100)^N$ $(01\bar{a})^C$	R	R	R	R	N/A	$(001)^N$ $(b10)^C$	R	R	R	R
20	$(100)^N$ $(01a)^C$	$(010)^N$ $(10c)^C$	R	R	R	R	$(001)^N$ $(b10)^C$	N/A	R	R	R	R
21	R	R	$(001)^N$ $(1\bar{a}0)^C$	$(010)^N$ $(10b)^C$	R	R	R	R	N/A	R	R	$(100)^N$ $(0c1)^C$
22	R	R	R	R	$(001)^N$ $(\bar{c}10)^C$	$(100)^N$ $(0b1)^C$	R	R	R	N/A	$(010)^N$ $(a01)^C$	R
23	R	R	R	R	$(100)^N$ $(0b1)^C$	$(001)^N$ $(c10)^C$	R	R	R	$(010)^N$ $(a01)^C$	N/A	R
24	R	R	$(010)^N$ $(10b)^C$	$(001)^N$ $(1a0)^C$	R	R	R	R	$(100)^N$ $(0c1)^C$	R	R	N/A

$$a = \varepsilon_4/\varepsilon_6, b = \varepsilon_4/\varepsilon_5, c = \varepsilon_5/\varepsilon_6, d_{\pm} = (\varepsilon_4 \pm \varepsilon_5)/[2(\varepsilon_2 - \varepsilon_1)], e_{\pm} = (\varepsilon_6 \pm \varepsilon_4)/[2(\varepsilon_3 - \varepsilon_1)], f_{\pm} = (\varepsilon_6 \pm \varepsilon_5)/[2(\varepsilon_3 - \varepsilon_2)]$$

Table D.9 Monoclinic to monoclinic

All species	$2/m \rightarrow m$	$2/m \rightarrow 2$
strains	polarizations	polarizations
1	$(P_1 \ 0 \ P_3)$	$(0 \ P_2 \ 0)$
	$(-P_1 \ 0 \ -P_3)$	$(0 \ -P_2 \ 0)$
	$\begin{pmatrix} \varepsilon_1 & \varepsilon_2 & \varepsilon_3 \\ 0 & \varepsilon_5 & 0 \end{pmatrix}$	

Table D.10 Orthorhombic to monoclinic

All species	$mmm \rightarrow m_x$ $mm2 \rightarrow m_x$ (upper polarizations only)	$mmm \rightarrow 2_x$ $mmm \rightarrow 2_x/m_x(P=0)$ $222 \rightarrow 2_x$ (upper polarizations only)
strains	polarizations	polarizations
1	$(0 \ P_2 \ P_3)$	$(P_1 \ 0 \ 0)$
	$(0 \ -P_2 \ -P_3)$	$(-P_1 \ 0 \ 0)$
2	$(0 \ -P_2 \ P_3)$	$(-P_1 \ 0 \ 0)$
	$(0 \ P_2 \ -P_3)$	$(P_1 \ 0 \ 0)$
	$\begin{pmatrix} \varepsilon_1 & \varepsilon_2 & \varepsilon_3 \\ \varepsilon_4 & 0 & 0 \end{pmatrix}$	
	$\begin{pmatrix} \varepsilon_1 & \varepsilon_2 & \varepsilon_3 \\ -\varepsilon_4 & 0 & 0 \end{pmatrix}$	
S	1	2
1	N/A	$(010)^C$ $(001)^N$
2	$(010)^N$ $(001)^N$	N/A

Table D.11 Orthorhombic to monoclinic

Species	$mm2 \rightarrow 2_z$
strains	polarization
1	$(0 \ 0 \ P_3)$
	$\begin{pmatrix} \varepsilon_1 & \varepsilon_2 & \varepsilon_3 \\ 0 & 0 & \varepsilon_6 \end{pmatrix}$
2	$(0 \ 0 \ P_3)$
	$\begin{pmatrix} \varepsilon_1 & \varepsilon_2 & \varepsilon_3 \\ 0 & 0 & -\varepsilon_6 \end{pmatrix}$
S	1
1	N/A
	$(100)^N$ $(010)^N$
2	N/A

Table D.12 Tetragonal to monoclinic

All species	$4/mmm \rightarrow 2_x$ $4/mmm \rightarrow 2_x/m_x (P=0)$ $422 \rightarrow 2_x$ (upper polarizations only)			
	$4mm \rightarrow m_x$	$422 \rightarrow 2_x$ (upper polarizations only)	$\bar{4}2m \rightarrow 2_x$	$4/mmm \rightarrow m_x$
strains	polarizations	polarizations	polarizations	polarizations
1 $\begin{pmatrix} \varepsilon_1 & \varepsilon_2 & \varepsilon_3 \\ \varepsilon_4 & 0 & 0 \end{pmatrix}$	$(0 \ P_2 \ P_3)$	$(P_1 \ 0 \ 0)$ $(-P_1 \ 0 \ 0)$	$(P_1 \ 0 \ 0)$	$(0 \ P_2 \ P_3)$ $(0 \ -P_2 \ -P_3)$
2 $\begin{pmatrix} \varepsilon_2 & \varepsilon_1 & \varepsilon_3 \\ 0 & -\varepsilon_4 & 0 \end{pmatrix}$	$(-P_2 \ 0 \ P_3)$	$(0 \ P_1 \ 0)$ $(0 \ -P_1 \ 0)$	$(0 \ -P_1 \ 0)$	$(-P_2 \ 0 \ P_3)$ $(P_2 \ 0 \ -P_3)$
3 $\begin{pmatrix} \varepsilon_1 & \varepsilon_2 & \varepsilon_3 \\ -\varepsilon_4 & 0 & 0 \end{pmatrix}$	$(0 \ -P_2 \ P_3)$	$(-P_1 \ 0 \ 0)$ $(P_1 \ 0 \ 0)$	$(-P_1 \ 0 \ 0)$	$(0 \ -P_2 \ P_3)$ $(0 \ P_2 \ -P_3)$
4 $\begin{pmatrix} \varepsilon_2 & \varepsilon_1 & \varepsilon_3 \\ 0 & \varepsilon_4 & 0 \end{pmatrix}$	$(P_2 \ 0 \ P_3)$	$(0 \ -P_1 \ 0)$ $(0 \ P_1 \ 0)$	$(0 \ P_1 \ 0)$	$(P_2 \ 0 \ P_3)$ $(-P_2 \ 0 \ -P_3)$

 $4mm \rightarrow m_x; 4/mmm \rightarrow m_x$ (above diagonal) $4/mmm \rightarrow 2_x, 4/mmm \rightarrow 2_x/m_x (P=0), 422 \rightarrow 2_x$ (below diagonal)

S	1	2	3	4
1	N/A	$(110)^C$ $(\bar{1}\bar{1}\bar{a})^N$	$(010)^C$ $(001)^N$	$(\bar{1}\bar{1}0)^C$ $(11a)^N$
2	$(110)^N$ $(\bar{1}\bar{1}\bar{a})^C$	N/A	$(\bar{1}\bar{1}0)^C$ $(11\bar{a})^N$	$(100)^C$ $(001)^N$
3	$(010)^N$ $(001)^N$	$(\bar{1}\bar{1}0)^N$ $(11\bar{a})^C$	N/A	$(110)^C$ $(\bar{1}\bar{1}\bar{a})^N$
4	$(\bar{1}\bar{1}0)^N$ $(11a)^C$	$(100)^N$ $(001)^N$	$(110)^N$ $(\bar{1}\bar{1}\bar{a})^C$	N/A

 $\bar{4}2m \rightarrow 2_x$.

S	1	2	3	4
1	N/A	$(110)^C$ $(\bar{1}\bar{1}\bar{a})^N$	$(010)^N$ $(001)^N$	$(\bar{1}\bar{1}0)^C$ $(11a)^N$
2		N/A	$(\bar{1}\bar{1}0)^C$ $(11\bar{a})^N$	$(100)^N$ $(001)^N$
3			N/A	$(110)^C$ $(\bar{1}\bar{1}\bar{a})^N$
4				N/A

$$\bar{a} = \varepsilon_4 / (\varepsilon_2 - \varepsilon_1)$$

Table D.13 (continued)

S	1	2	3	4
	$4/nmm \rightarrow 2_z, 4/nmm \rightarrow 2_z/m_z (P=0), 4mm \rightarrow 2_z, \bar{4}2m \rightarrow 2_z, 422 \rightarrow 2_z$ (all four strains), $4/m \rightarrow 2_z, 4 \rightarrow 2_z, \bar{4} \rightarrow 2_z$ (strains 1 and 2 only) (above diagonal)			
	$4/nmm \rightarrow m_z$ (all four strains), $4/m \rightarrow m_z, 4/m \rightarrow 2_z/m_z (P=0)$ (strains 1 and 2 only) (below diagonal)			
1	N/A	$(1\bar{a}_+0)^N$ $(1\bar{a}_-0)^N$	$(100)^N$ $(010)^N$	$(110)^N$ $(\bar{1}\bar{1}0)^N$
2	$(1\bar{a}_+0)^*$ $(1\bar{a}_-0)^*$	N/A	$(110)^N$ $(\bar{1}\bar{1}0)^N$	$(100)^N$ $(010)^N$
3	$(100)^N$ $(010)^C$	$(110)^N$ $(\bar{1}\bar{1}0)^C$	N/A	$(1a_+0)^N$ $(1a_-0)^N$
4	$(110)^N$ $(\bar{1}\bar{1}0)^C$	$(100)^C$ $(010)^N$	$(1a_+0)^*$ $(1a_-0)^*$	N/A

$$a_{\pm} = (p \pm \sqrt{p^2 + 4})/2, p = 2\epsilon_6/(\epsilon_2 - \epsilon_1)$$

*N neutrality or charge of DW depends on the values of strain components and Ps

Table D.14 Tetragonal to monoclinic

Species	$\bar{4}2m \rightarrow m_{xy}$			
strains	polarizations			
1	$\begin{pmatrix} \varepsilon_1 & \varepsilon_1 & \varepsilon_3 \\ -\varepsilon_5 & \varepsilon_5 & \varepsilon_6 \end{pmatrix}$			$(P_1 \ -P_1 \ P_3)$
2	$\begin{pmatrix} \varepsilon_1 & \varepsilon_1 & \varepsilon_3 \\ \varepsilon_5 & \varepsilon_5 & -\varepsilon_6 \end{pmatrix}$			$(-P_1 \ -P_1 \ -P_3)$
3	$\begin{pmatrix} \varepsilon_1 & \varepsilon_1 & \varepsilon_3 \\ \varepsilon_5 & -\varepsilon_5 & \varepsilon_6 \end{pmatrix}$			$(-P_1 \ P_1 \ P_3)$
4	$\begin{pmatrix} \varepsilon_1 & \varepsilon_1 & \varepsilon_3 \\ -\varepsilon_5 & -\varepsilon_5 & -\varepsilon_6 \end{pmatrix}$			$(P_1 \ P_1 \ -P_3)$

S	1	2	3	4
1	N/A	$(010)^N$ $(10\bar{a})^C$	$(001)^N$ $(\bar{1}10)^C$	$(100)^N$ $(01a)^C$
2		N/A	$(100)^N$ $(01\bar{a})^C$	$(001)^N$ $(110)^C$
3			N/A	$(010)^N$ $(10a)^C$
4				N/A

$a = \varepsilon_5/\varepsilon_6$

Table D.15 Trigonal to monoclinic

All species	$\bar{3}m \rightarrow 2_x \bar{3}m \rightarrow 2_x/m_x (P = 0)$ $32 \rightarrow 2_x$ (upper polarizations only)	$\bar{3}m \rightarrow m_x$ $3m \rightarrow m_x$ (upper polarizations only)	
strains	polarizations	polarizations	
1	$\begin{pmatrix} \varepsilon_1 & \varepsilon_2 & \varepsilon_3 \\ \varepsilon_4 & 0 & 0 \end{pmatrix}$	$(P_1 \ 0 \ 0)$ $(-P_1 \ 0 \ 0)$	$(0 \ P_2 \ P_3)$ $(0 \ -P_2 \ -P_3)$
2	$\begin{pmatrix} \varepsilon'_1 & \varepsilon'_2 & \varepsilon'_3 \\ -\varepsilon_4 & -\varepsilon_5 & -\varepsilon_6 \end{pmatrix}$	$(-P'_1 \ P''_1 \ 0)$ $(P'_1 \ -P''_1 \ 0)$	$(-P'_2 \ -P''_2 \ P_3)$ $(P'_2 \ P''_2 \ -P_3)$
3	$\begin{pmatrix} \varepsilon'_1 & \varepsilon'_2 & \varepsilon'_3 \\ -\varepsilon_4 & \varepsilon_5 & \varepsilon_6 \end{pmatrix}$	$(-P'_1 \ -P''_1 \ 0)$ $(P'_1 \ P''_1 \ 0)$	$(P'_2 \ -P''_2 \ P_3)$ $(-P'_2 \ P''_2 \ -P_3)$

$\varepsilon'_1 = (1/4)(\varepsilon_1 + 3\varepsilon_2), \varepsilon'_2 = (1/4)(3\varepsilon_1 + \varepsilon_2), \varepsilon'_3 = (\sqrt{3}/2)(\varepsilon_1 - \varepsilon_2), \varepsilon'_5 = (\sqrt{3}/2)\varepsilon_4, \varepsilon'_4 = (1/2)\varepsilon_4$
 $P'_1 = (1/2)P_1, P''_1 = (\sqrt{3}/2)P_1, P'_2 = (\sqrt{3}/2)P_2, P''_2 = (1/2)P_2$

Table D.15 (continued)

$\bar{3}m \rightarrow 2_x, \bar{3}m \rightarrow 2_x/m_x (P = 0), 32 \rightarrow 2_x$ (above diagonal)

$\bar{3}m \rightarrow m_x, 3m \rightarrow m_x$ (below diagonal)

S	1	2	3
1	N/A	$(1\bar{1}\bar{2}0)^N$ $(1\bar{1}0a)^C$	$(\bar{1}2\bar{1}0)^N$ $(10\bar{1}a)^C$
2	$(11\bar{2}0)^C$ $(1\bar{1}0a)^N$	N/A	$(2\bar{1}\bar{1}0)^N$ $(01\bar{1}a)^C$
3	$(1\bar{2}10)^C$ $(10\bar{1}a)^N$	$(2\bar{1}\bar{1}0)^C$ $(01\bar{1}a)^N$	N/A

$$a = -\sqrt{3}\varepsilon_4/(\varepsilon_2 - \varepsilon_1)$$

Table D.16 Hexagonal to monoclinic

All species	$6/mmm \rightarrow 2_x$ 622 $\rightarrow 2_x$ (upper polarizations only)	$6/mmm \rightarrow m_x$ 6mm $\rightarrow m_x$ (upper polarizations only)	$\bar{6}m2 \rightarrow m_x$
	$6/mmm \rightarrow 2_x/m_x (P = 0)$	polarizations	
strains	polarizations	polarizations	polarizations
1 $\begin{pmatrix} \varepsilon_1 & \varepsilon_2 & \varepsilon_3 \\ \varepsilon_4 & 0 & 0 \end{pmatrix}$	$(P_1 \ 0 \ 0)$ $(-P_1 \ 0 \ 0)$	$(0 \ P_2 \ P_3)$ $(0 \ -P_2 \ -P_3)$	$(0 \ P_2 \ P_3)$
2 $\begin{pmatrix} \varepsilon'_1 & \varepsilon'_2 & \varepsilon'_3 \\ \varepsilon'_4 & \varepsilon'_5 & \varepsilon'_6 \end{pmatrix}$	$(P'_1 \ P'_1 \ 0)$ $(-P'_1 \ -P'_1 \ 0)$	$(-P'_2 \ P'_2 \ P_3)$ $(P'_2 \ -P'_2 \ -P_3)$	$(P'_2 \ -P'_2 \ -P_3)$
3 $\begin{pmatrix} \varepsilon'_1 & \varepsilon'_2 & \varepsilon'_3 \\ -\varepsilon'_4 & \varepsilon'_5 & -\varepsilon'_6 \end{pmatrix}$	$(-P'_1 \ P'_1 \ 0)$ $(P'_1 \ -P'_1 \ 0)$	$(-P'_2 \ -P'_2 \ P_3)$ $(P'_2 \ P'_2 \ -P_3)$	$(-P'_2 \ -P'_2 \ P_3)$
4 $\begin{pmatrix} \varepsilon_1 & \varepsilon_2 & \varepsilon_3 \\ -\varepsilon_4 & 0 & 0 \end{pmatrix}$	$(-P_1 \ 0 \ 0)$ $(P_1 \ 0 \ 0)$	$(0 \ -P_2 \ P_3)$ $(0 \ P_2 \ -P_3)$	$(0 \ P_2 \ -P_3)$
5 $\begin{pmatrix} \varepsilon'_1 & \varepsilon'_2 & \varepsilon'_3 \\ -\varepsilon'_4 & -\varepsilon'_5 & \varepsilon'_6 \end{pmatrix}$	$(-P'_1 \ -P'_1 \ 0)$ $(P'_1 \ P'_1 \ 0)$	$(P'_2 \ -P'_2 \ P_3)$ $(-P'_2 \ P'_2 \ -P_3)$	$(P'_2 \ -P'_2 \ P_3)$
6 $\begin{pmatrix} \varepsilon'_1 & \varepsilon'_2 & \varepsilon'_3 \\ \varepsilon'_4 & -\varepsilon'_5 & -\varepsilon'_6 \end{pmatrix}$	$(P'_1 \ -P'_1 \ 0)$ $(-P'_1 \ P'_1 \ 0)$	$(P'_2 \ P'_2 \ P_3)$ $(-P'_2 \ -P'_2 \ -P_3)$	$(-P'_2 \ -P'_2 \ -P_3)$

$$\varepsilon'_1 = (1/4)(\varepsilon_1 + 3\varepsilon_2), \varepsilon'_2 = (1/4)(3\varepsilon_1 + \varepsilon_2), \varepsilon'_6 = (\sqrt{3}/2)(\varepsilon_1 - \varepsilon_2), \varepsilon'_5 = -(\sqrt{3}/2)\varepsilon_4, \varepsilon'_4 = (1/2)\varepsilon_4$$

$$P'_1 = (1/2)P_1, P'_1 = (\sqrt{3}/2)P_1, P'_2 = (1/2)P_2, P'_2 = (\sqrt{3}/2)P_2$$

$6/mmm \rightarrow 2_x, 6/mmm \rightarrow 2_x/m_x (P = 0), 622 \rightarrow 2_x$ (above diagonal)

$6/mmm \rightarrow m_x, 6mm \rightarrow m_x$ (below diagonal)

S	1	2	3	4	5	6
1	N/A	$(10\bar{1}0)^N$ $(12\bar{1}\bar{a})^C$	$(11\bar{2}0)^N$ $(1\bar{1}0\bar{a})^C$	$(01\bar{1}0)^N$ $(0001)^N$	$(\bar{1}210)^N$ $(10\bar{1}a)^C$	$(1\bar{1}00)^N$ $(11\bar{2}a)^C$
2	$(10\bar{1}0)^C$ $(12\bar{1}\bar{a})^N$	N/A	$(01\bar{1}0)^N$ $(2\bar{1}\bar{1}\bar{a})^C$	$(\bar{1}210)^N$ $(10\bar{1}\bar{a})^C$	$(0001)^N$ $(1\bar{1}00)^N$	$(2\bar{1}\bar{1}0)^N$ $(01\bar{1}a)^C$
3	$(11\bar{2}0)^C$ $(1\bar{1}0\bar{a})^N$	$(01\bar{1}0)^C$ $(2\bar{1}\bar{1}\bar{a})^N$	N/A	$(1\bar{1}00)^N$ $(11\bar{2}\bar{a})^C$	$(2\bar{1}\bar{1}0)^N$ $(01\bar{1}a)^C$	$(0001)^N$ $(10\bar{1}0)^N$
4	$(01\bar{1}0)^C$ $(0001)^N$	$(\bar{1}210)^C$ $(10\bar{1}\bar{a})^N$	$(1\bar{1}00)^C$ $(11\bar{2}\bar{a})^N$	N/A	$(10\bar{1}0)^N$ $(12\bar{1}a)^C$	$(11\bar{2}0)^N$ $(1\bar{1}0a)^C$
5	$(\bar{1}210)^C$ $(10\bar{1}a)^N$	$(0001)^N$ $(1\bar{1}00)^C$	$(2\bar{1}\bar{1}0)^C$ $(01\bar{1}\bar{a})^N$	$(10\bar{1}0)^C$ $(12\bar{1}a)^N$	N/A	$(01\bar{1}0)^N$ $(2\bar{1}\bar{1}a)^C$
6	$(1\bar{1}00)^C$ $(11\bar{2}a)^N$	$(2\bar{1}\bar{1}0)^C$ $(01\bar{1}\bar{a})^N$	$(0001)^N$ $(10\bar{1}0)^C$	$(11\bar{2}0)^C$ $(1\bar{1}0a)^N$	$(01\bar{1}0)^C$ $(2\bar{1}\bar{1}a)^N$	N/A

Table D.16 (continued)

$\bar{6}m2 \rightarrow m_x$						
S	1	2	3	4	5	6
1	N/A	$(10\bar{1}0)^N$	$(11\bar{2}0)^C$	$(01\bar{1}0)^N$	$(1\bar{2}10)^C$	$(1\bar{1}00)^N$
2		$(1\bar{2}1\bar{a})^C$	$(1\bar{1}0\bar{a})^N$	$(0001)^C$	$(10\bar{1}a)^N$	$(11\bar{2}a)^C$
3		N/A	$(01\bar{1}0)^N$	$(1\bar{2}10)^C$	$(0001)^C$	$(2\bar{1}\bar{1}0)^C$
4			$(2\bar{1}\bar{1}\bar{a})^C$	$(10\bar{1}\bar{a})^N$	$(1\bar{1}00)^N$	$(01\bar{1}a)^N$
5			N/A	$(1\bar{1}00)^N$	$(2\bar{1}\bar{1}0)^C$	$(0001)^C$
6				$(11\bar{2}\bar{a})^C$	$(01\bar{1}\bar{a})^N$	$(10\bar{1}0)^N$
				N/A	$l(10\bar{1}0)^N$	$(11\bar{2}0)^C$
					$(1\bar{2}1a)^C$	$(1\bar{1}0a)^N$
					N/A	$(01\bar{1}0)^N$
						$(2\bar{1}\bar{1}a)^C$
						N/A

$$a = \varepsilon_4 / (\varepsilon_2 - \varepsilon_1)$$

Table D.17 Hexagonal to monoclinic

All species straips	$622 \rightarrow 2_z$		$6/mmm \rightarrow 2_z/m_z (P=0)$		$6/mmm \rightarrow m_z 6/m \rightarrow m_z$		$6mm \rightarrow 2_z$	
	$6 \rightarrow 2_z$ (straips 1-3 only)	$6/m \rightarrow 2_z/m_z (P=0)$ (straips 1-3 only)	polarizations	polarizations	(straips 1-3 only)	(straips 1-3 only)	polarizations	polarizations
1	$\begin{pmatrix} \varepsilon_1 & \varepsilon_2 & \varepsilon_3 \\ 0 & 0 & \varepsilon_6 \end{pmatrix}$	$\begin{pmatrix} 0 & 0 & P_3 \\ 0 & 0 & -P_3 \end{pmatrix}$	$\begin{pmatrix} 0 & 0 & P_3 \\ 0 & 0 & -P_3 \end{pmatrix}$	$\begin{pmatrix} P_1 & P_2 & 0 \\ -P_1 & -P_2 & 0 \end{pmatrix}$	$\begin{pmatrix} P_1 & P_2 & 0 \\ -P_1 & -P_2 & 0 \end{pmatrix}$	$\begin{pmatrix} 0 & 0 & P_3 \\ 0 & 0 & P_3 \end{pmatrix}$	$\begin{pmatrix} P_1 & P_2 & 0 \\ -P_1 & -P_2 & 0 \end{pmatrix}$	$\begin{pmatrix} 0 & 0 & P_3 \\ 0 & 0 & P_3 \end{pmatrix}$
2	$\begin{pmatrix} \varepsilon_1^- & \varepsilon_2^+ & \varepsilon_3 \\ 0 & 0 & \varepsilon_6^+ \end{pmatrix}$	$\begin{pmatrix} 0 & 0 & P_3 \\ 0 & 0 & -P_3 \end{pmatrix}$	$\begin{pmatrix} 0 & 0 & P_3 \\ 0 & 0 & -P_3 \end{pmatrix}$	$\begin{pmatrix} P_1^- & P_2^+ & 0 \\ -P_1^- & -P_2^+ & 0 \end{pmatrix}$	$\begin{pmatrix} P_1^- & P_2^+ & 0 \\ -P_1^- & -P_2^+ & 0 \end{pmatrix}$	$\begin{pmatrix} 0 & 0 & P_3 \\ 0 & 0 & P_3 \end{pmatrix}$	$\begin{pmatrix} P_1^- & P_2^+ & 0 \\ -P_1^- & -P_2^+ & 0 \end{pmatrix}$	$\begin{pmatrix} 0 & 0 & P_3 \\ 0 & 0 & P_3 \end{pmatrix}$
3	$\begin{pmatrix} \varepsilon_1^+ & \varepsilon_2^- & \varepsilon_3 \\ 0 & 0 & \varepsilon_6^- \end{pmatrix}$	$\begin{pmatrix} 0 & 0 & P_3 \\ 0 & 0 & -P_3 \end{pmatrix}$	$\begin{pmatrix} 0 & 0 & P_3 \\ 0 & 0 & -P_3 \end{pmatrix}$	$\begin{pmatrix} P_1^+ & P_2^- & 0 \\ -P_1^+ & -P_2^- & 0 \end{pmatrix}$	$\begin{pmatrix} P_1^+ & P_2^- & 0 \\ -P_1^+ & -P_2^- & 0 \end{pmatrix}$	$\begin{pmatrix} 0 & 0 & P_3 \\ 0 & 0 & P_3 \end{pmatrix}$	$\begin{pmatrix} P_1^+ & P_2^- & 0 \\ -P_1^+ & -P_2^- & 0 \end{pmatrix}$	$\begin{pmatrix} 0 & 0 & P_3 \\ 0 & 0 & P_3 \end{pmatrix}$
4	$\begin{pmatrix} \varepsilon_1^- & \varepsilon_2^+ & \varepsilon_3 \\ 0 & 0 & -\varepsilon_6^+ \end{pmatrix}$	$\begin{pmatrix} 0 & 0 & -P_3 \\ 0 & 0 & P_3 \end{pmatrix}$	$\begin{pmatrix} 0 & 0 & -P_3 \\ 0 & 0 & P_3 \end{pmatrix}$	$\begin{pmatrix} P_1^- & -P_2^+ & 0 \\ -P_1^- & P_2^+ & 0 \end{pmatrix}$	$\begin{pmatrix} P_1^- & -P_2^+ & 0 \\ -P_1^- & P_2^+ & 0 \end{pmatrix}$	$\begin{pmatrix} 0 & 0 & P_3 \\ 0 & 0 & P_3 \end{pmatrix}$	$\begin{pmatrix} P_1^- & -P_2^+ & 0 \\ -P_1^- & P_2^+ & 0 \end{pmatrix}$	$\begin{pmatrix} 0 & 0 & P_3 \\ 0 & 0 & P_3 \end{pmatrix}$
5	$\begin{pmatrix} \varepsilon_1^+ & \varepsilon_2^- & \varepsilon_3 \\ 0 & 0 & -\varepsilon_6^- \end{pmatrix}$	$\begin{pmatrix} 0 & 0 & -P_3 \\ 0 & 0 & P_3 \end{pmatrix}$	$\begin{pmatrix} 0 & 0 & -P_3 \\ 0 & 0 & P_3 \end{pmatrix}$	$\begin{pmatrix} P_1^+ & -P_2^- & 0 \\ -P_1^+ & P_2^- & 0 \end{pmatrix}$	$\begin{pmatrix} P_1^+ & -P_2^- & 0 \\ -P_1^+ & P_2^- & 0 \end{pmatrix}$	$\begin{pmatrix} 0 & 0 & P_3 \\ 0 & 0 & P_3 \end{pmatrix}$	$\begin{pmatrix} P_1^+ & -P_2^- & 0 \\ -P_1^+ & P_2^- & 0 \end{pmatrix}$	$\begin{pmatrix} 0 & 0 & P_3 \\ 0 & 0 & P_3 \end{pmatrix}$
6	$\begin{pmatrix} \varepsilon_1 & \varepsilon_2 & \varepsilon_3 \\ 0 & 0 & -\varepsilon_6 \end{pmatrix}$	$\begin{pmatrix} 0 & 0 & -P_3 \\ 0 & 0 & P_3 \end{pmatrix}$	$\begin{pmatrix} 0 & 0 & -P_3 \\ 0 & 0 & P_3 \end{pmatrix}$	$\begin{pmatrix} P_1 & -P_2 & 0 \\ -P_1 & P_2 & 0 \end{pmatrix}$	$\begin{pmatrix} P_1 & -P_2 & 0 \\ -P_1 & P_2 & 0 \end{pmatrix}$	$\begin{pmatrix} 0 & 0 & P_3 \\ 0 & 0 & P_3 \end{pmatrix}$	$\begin{pmatrix} P_1 & -P_2 & 0 \\ -P_1 & P_2 & 0 \end{pmatrix}$	$\begin{pmatrix} 0 & 0 & P_3 \\ 0 & 0 & P_3 \end{pmatrix}$

$$P_1^\pm = (1/2)(P_1 \pm \sqrt{3}P_2), P_2^\pm = (1/2)(\sqrt{3}P_1 \pm P_2), \varepsilon_1^\pm = (1/4)(\varepsilon_1 \pm \sqrt{3}\varepsilon_6 + 3\varepsilon_2), \varepsilon_2^\pm = (1/4)(3\varepsilon_1 \pm \sqrt{3}\varepsilon_6 + \varepsilon_2), \varepsilon_6^\pm = (1/2)(\pm\sqrt{3}\varepsilon_1 - \varepsilon_6 \mp \sqrt{3}\varepsilon_2)$$

Table D.17 (continued)

$6/mmm \rightarrow 2_z/m_z (P=0)$, $622 \rightarrow 2_z$, $6/mmm \rightarrow 2_z$, $6mm \rightarrow 2_z$ (all six strains),
 $6/m \rightarrow 2_z/m_z (P=0)$, $6 \rightarrow 2_z$, $6/m \rightarrow 2_z$ (strains 1-3 only) (above diagonal)

$6/mmm \rightarrow m_z$ (all six strains), $6/m \rightarrow m_z$, $6 \rightarrow m_z$ (strains 1-3 only) (below diagonal)

S	1	2	3	4	5	6
1	N/A	$(2k_+l_+0)^N$ $(2k_-l_-0)^N$	$(2m_+n_+0)^N$ $(2m_-n_-0)^N$	$(1\bar{1}00)^N$ $(11\bar{2}0)^N$	$(10\bar{1}0)^N$ $(1210)^N$	$(2\bar{1}\bar{1}0)^N$ $(01\bar{1}0)^N$
2	$(2k_+l_+0)^*$ $(2k_-l_-0)^*$	N/A	$(2p_+q_+0)^N$ $(2p_-q_-0)^N$	$(2\bar{1}\bar{1}0)^N$ $(01\bar{1}0)^N$	$(11\bar{2}0)^N$ $(1100)^N$	$(1210)^N$ $(10\bar{1}0)^N$
3	$(2m_+n_+0)^*$ $(2m_-n_-0)^*$	$(2p_+q_+0)^*$ $(2p_-q_-0)^*$	N/A	$(10\bar{1}0)^N$ $(1210)^N$	$(2\bar{1}\bar{1}0)^N$ $(01\bar{1}0)^N$	$(11\bar{2}0)^N$ $(1100)^N$
4	$(1100)^N$ $(11\bar{2}0)^C$	$(2\bar{1}\bar{1}0)^N$ $(01\bar{1}0)^C$	$(10\bar{1}0)^N$ $(1210)^C$	N/A	$(2q_+p_+0)^N$ $(2q_-p_-0)^N$	$(2l_+k_+0)^N$ $(2l_-k_-0)^N$
5	$(10\bar{1}0)^C$ $(1210)^N$	$(11\bar{2}0)^C$ $(1100)^N$	$(2\bar{1}\bar{1}0)^N$ $(01\bar{1}0)^C$	$(2q_+p_+0)^*$ $(2q_-p_-0)^*$	N/A	$(2n_+m_+0)^N$ $(2n_-m_-0)^N$
6	$(2\bar{1}\bar{1}0)^N$ $(01\bar{1}0)^C$	$(1210)^C$ $(10\bar{1}0)^N$	$(11\bar{2}0)^N$ $(1100)^C$	$(2l_+k_+0)^*$ $(2l_-k_-0)^*$	$(2n_+m_+0)^*$ $(2n_-m_-0)^*$	N/A

Table D.17 (continued)

$\bar{\delta}m_2 \rightarrow m_z$	1	2	3	4	5	6
1	N/A	$(2k_+l_0)^*$ $(2k_-l_0)^*$	$(2m_+n_0)^*$ $(2m_-n_0)^*$	$(1\bar{1}00)^N$ $(11\bar{2}0)^C$	$(10\bar{1}0)^N$ $(1\bar{2}10)^C$	$(2\bar{1}\bar{1}0)^C$ $(01\bar{1}0)^N$
2	N/A	N/A	$(2p_+q_0)^*$ $(2p_-q_0)^*$	$(2\bar{1}\bar{1}0)^C$ $(01\bar{1}0)^N$	$(11\bar{2}0)^C$ $(1\bar{1}00)^N$	$(1\bar{2}10)^C$ $(10\bar{1}0)^N$
3			N/A	$(10\bar{1}0)^N$ $(1\bar{2}10)^C$	$(2\bar{1}\bar{1}0)^C$ $(01\bar{1}0)^N$	$(11\bar{2}0)^C$ $(1\bar{1}00)^N$
4				N/A	$(2q_+p_0)^*$ $(2q_-p_0)^*$	$(2l_+k_0)^*$ $(2l_-k_0)^*$
5					N/A	$(2n_+m_0)^*$ $(2n_-m_0)^*$
6						N/A

*Neutrality/charge of DW depends on the values of spontaneous strain/polarization

$$k_{\pm} = 2[\varepsilon_6 - \sqrt{3}(\varepsilon_1 - \varepsilon_2) \mp \sqrt{3}\sqrt{(\varepsilon_1 - \varepsilon_2)^2 + \varepsilon_6^2}]/[\varepsilon_6 + \sqrt{3}(\varepsilon_1 - \varepsilon_2)],$$

$$l_{\pm} = 2[-2\varepsilon_6 \pm \sqrt{3}\sqrt{(\varepsilon_1 - \varepsilon_2)^2 + \varepsilon_6^2}]/[\varepsilon_6 + \sqrt{3}(\varepsilon_1 - \varepsilon_2)]$$

$$m_{\pm} = 2[2\varepsilon_6 \pm \sqrt{3}\sqrt{(\varepsilon_1 - \varepsilon_2)^2 + \varepsilon_6^2}]/[-\varepsilon_6 + \sqrt{3}(\varepsilon_1 - \varepsilon_2)],$$

$$n_{\pm} = 2[-\varepsilon_6 - \sqrt{3}(\varepsilon_1 - \varepsilon_2) \mp \sqrt{3}\sqrt{(\varepsilon_1 - \varepsilon_2)^2 + \varepsilon_6^2}]/[-\varepsilon_6 + \sqrt{3}(\varepsilon_1 - \varepsilon_2)]$$

$$p_{\pm} = 2[-\varepsilon_6 - \sqrt{3}(\varepsilon_1 - \varepsilon_2) \mp \sqrt{3}\sqrt{(\varepsilon_1 - \varepsilon_2)^2 + \varepsilon_6^2}]/\varepsilon_6,$$

$$q_{\pm} = 2[-\varepsilon_6 + \sqrt{3}(\varepsilon_1 - \varepsilon_2) \pm \sqrt{3}\sqrt{(\varepsilon_1 - \varepsilon_2)^2 + \varepsilon_6^2}]/\varepsilon_6$$

Table D.18 Hexagonal to monoclinic

Species		$\bar{6}m2 \rightarrow 2_y$
strains		polarizations
1	$\begin{pmatrix} \varepsilon_1 & \varepsilon_2 & \varepsilon_3 \\ 0 & \varepsilon_5 & 0 \end{pmatrix}$	$(0 \ P_2 \ 0)$
2	$\begin{pmatrix} \varepsilon'_1 & \varepsilon'_2 & \varepsilon'_3 \\ \varepsilon_4 & \varepsilon_5 & \varepsilon_6 \end{pmatrix}$	$(P'_2 \ -P'_2 \ 0)$
3	$\begin{pmatrix} \varepsilon'_1 & \varepsilon'_2 & \varepsilon'_3 \\ \varepsilon_4 & -\varepsilon_5 & -\varepsilon_6 \end{pmatrix}$	$(-P'_2 \ -P'_2 \ 0)$
4	$\begin{pmatrix} \varepsilon_1 & \varepsilon_2 & \varepsilon_3 \\ 0 & -\varepsilon_5 & 0 \end{pmatrix}$	$(0 \ P_2 \ 0)$
5	$\begin{pmatrix} \varepsilon'_1 & \varepsilon'_2 & \varepsilon'_3 \\ -\varepsilon_4 & -\varepsilon_5 & \varepsilon_6 \end{pmatrix}$	$(P'_2 \ -P'_2 \ 0)$
6	$\begin{pmatrix} \varepsilon'_1 & \varepsilon'_2 & \varepsilon'_3 \\ -\varepsilon_4 & \varepsilon_5 & -\varepsilon_6 \end{pmatrix}$	$(-P'_2 \ -P'_2 \ 0)$

$$\varepsilon'_1 = (1/4)(\varepsilon_1 + 3\varepsilon_2), \varepsilon'_2 = (1/4)(3\varepsilon_1 + \varepsilon_2), \varepsilon'_3 = (\sqrt{3}/2)(\varepsilon_1 - \varepsilon_2),$$

$$\varepsilon'_5 = (1/2)\varepsilon_5, \varepsilon'_4 = (\sqrt{3}/2)\varepsilon_5$$

$$P'_2 = (1/2)P_2, P'_2 = (\sqrt{3}/2)P_2$$

S	1	2	3	4	5	6
1	N/A	$(10\bar{1}\bar{a})^N$ $(1\bar{2}10)^C$	$(11\bar{2}\bar{b})^C$ $(1\bar{1}00)^N$	$(2\bar{1}\bar{1}0)^N$ $(0001)^N$	$(1\bar{2}1\bar{b})^C$ $(10\bar{1}0)^N$	$(1\bar{1}0\bar{a})^N$ $(11\bar{2}0)^C$
2		N/A	$(01\bar{1}\bar{a})^N$ $(2\bar{1}\bar{1}0)^C$	$(1\bar{2}1\bar{b})^C$ $(10\bar{1}0)^N$	$(0001)^N$ $(11\bar{2}0)^N$	$(2\bar{1}\bar{1}\bar{b})^C$ $(01\bar{1}0)^N$
3			N/A	$(1\bar{1}0a)^N$ $(11\bar{2}0)^C$	$(2\bar{1}\bar{1}b)^C$ $(01\bar{1}0)^N$	$(0001)^N$ $(1\bar{2}10)^N$
4				N/A	$(10\bar{1}a)^N$ $(1\bar{2}10)^C$	$(11\bar{2}b)^C$ $(1\bar{1}00)^N$
5					N/A	$(01\bar{1}a)^N$ $(2\bar{1}\bar{1}0)^C$
6						N/A

$$a = \varepsilon_5 / (\varepsilon_2 - \varepsilon_1), b = 3a$$

Table D.19 Cubic to monoclinic

All species strains	$m\bar{3}m \rightarrow m_{xy}$		$m\bar{3}m \rightarrow 2_{xy}/m_{xy} (P=0)$	
	$4\bar{3}m \rightarrow m_{xy}$ (upper polarizations only)	polarizations	$432 \rightarrow 2_{xy}$ (upper polarizations only)	polarizations
1	$\begin{pmatrix} \epsilon_1 & \epsilon_1 & \epsilon_3 \\ -\epsilon_5 & \epsilon_5 & \epsilon_6 \end{pmatrix}$	$\begin{pmatrix} P_1 & -P_1 & P_3 \\ -P_1 & P_1 & -P_3 \end{pmatrix}$	$\begin{pmatrix} P_1 & P_1 & 0 \\ -P_1 & -P_1 & 0 \end{pmatrix}$	$\begin{pmatrix} P_1 & P_1 & 0 \\ -P_1 & -P_1 & 0 \end{pmatrix}$
2	$\begin{pmatrix} \epsilon_1 & \epsilon_1 & \epsilon_3 \\ \epsilon_5 & \epsilon_5 & -\epsilon_6 \end{pmatrix}$	$\begin{pmatrix} -P_1 & -P_1 & -P_3 \\ P_1 & P_1 & P_3 \end{pmatrix}$	$\begin{pmatrix} -P_1 & P_1 & 0 \\ P_1 & -P_1 & 0 \end{pmatrix}$	$\begin{pmatrix} -P_1 & P_1 & 0 \\ P_1 & -P_1 & 0 \end{pmatrix}$
3	$\begin{pmatrix} \epsilon_1 & \epsilon_1 & \epsilon_3 \\ \epsilon_5 & -\epsilon_5 & \epsilon_6 \end{pmatrix}$	$\begin{pmatrix} -P_1 & P_1 & P_3 \\ P_1 & -P_1 & -P_3 \end{pmatrix}$	$\begin{pmatrix} -P_1 & -P_1 & 0 \\ P_1 & P_1 & 0 \end{pmatrix}$	$\begin{pmatrix} -P_1 & -P_1 & 0 \\ P_1 & P_1 & 0 \end{pmatrix}$
4	$\begin{pmatrix} \epsilon_1 & \epsilon_1 & \epsilon_3 \\ -\epsilon_5 & -\epsilon_5 & -\epsilon_6 \end{pmatrix}$	$\begin{pmatrix} P_1 & P_1 & -P_3 \\ -P_1 & -P_1 & P_3 \end{pmatrix}$	$\begin{pmatrix} P_1 & -P_1 & 0 \\ -P_1 & P_1 & 0 \end{pmatrix}$	$\begin{pmatrix} P_1 & -P_1 & 0 \\ -P_1 & P_1 & 0 \end{pmatrix}$
5	$\begin{pmatrix} \epsilon_1 & \epsilon_3 & \epsilon_1 \\ \epsilon_5 & \epsilon_6 & -\epsilon_5 \end{pmatrix}$	$\begin{pmatrix} -P_1 & P_3 & P_1 \\ P_1 & -P_3 & -P_1 \end{pmatrix}$	$\begin{pmatrix} P_1 & 0 & P_1 \\ -P_1 & 0 & -P_1 \end{pmatrix}$	$\begin{pmatrix} P_1 & 0 & P_1 \\ -P_1 & 0 & -P_1 \end{pmatrix}$
6	$\begin{pmatrix} \epsilon_1 & \epsilon_3 & \epsilon_1 \\ \epsilon_5 & -\epsilon_6 & \epsilon_5 \end{pmatrix}$	$\begin{pmatrix} -P_1 & -P_3 & -P_1 \\ P_1 & P_3 & P_1 \end{pmatrix}$	$\begin{pmatrix} P_1 & 0 & -P_1 \\ -P_1 & 0 & P_1 \end{pmatrix}$	$\begin{pmatrix} P_1 & 0 & -P_1 \\ -P_1 & 0 & P_1 \end{pmatrix}$
7	$\begin{pmatrix} \epsilon_3 & \epsilon_1 & \epsilon_1 \\ \epsilon_6 & -\epsilon_5 & \epsilon_5 \end{pmatrix}$	$\begin{pmatrix} P_3 & P_1 & -P_1 \\ -P_3 & -P_1 & P_1 \end{pmatrix}$	$\begin{pmatrix} 0 & P_1 & P_1 \\ 0 & -P_1 & -P_1 \end{pmatrix}$	$\begin{pmatrix} 0 & P_1 & P_1 \\ 0 & -P_1 & -P_1 \end{pmatrix}$
8	$\begin{pmatrix} \epsilon_3 & \epsilon_1 & \epsilon_1 \\ -\epsilon_6 & -\epsilon_5 & -\epsilon_5 \end{pmatrix}$	$\begin{pmatrix} -P_3 & P_1 & P_1 \\ P_3 & -P_1 & -P_1 \end{pmatrix}$	$\begin{pmatrix} 0 & P_1 & -P_1 \\ 0 & -P_1 & P_1 \end{pmatrix}$	$\begin{pmatrix} 0 & P_1 & -P_1 \\ 0 & -P_1 & P_1 \end{pmatrix}$
9	$\begin{pmatrix} \epsilon_1 & \epsilon_3 & \epsilon_1 \\ -\epsilon_5 & -\epsilon_6 & -\epsilon_5 \end{pmatrix}$	$\begin{pmatrix} P_1 & -P_3 & P_1 \\ -P_1 & P_3 & -P_1 \end{pmatrix}$	$\begin{pmatrix} -P_1 & 0 & P_1 \\ P_1 & 0 & -P_1 \end{pmatrix}$	$\begin{pmatrix} -P_1 & 0 & P_1 \\ P_1 & 0 & -P_1 \end{pmatrix}$
10	$\begin{pmatrix} \epsilon_1 & \epsilon_3 & \epsilon_1 \\ -\epsilon_5 & \epsilon_6 & \epsilon_5 \end{pmatrix}$	$\begin{pmatrix} P_1 & P_3 & -P_1 \\ -P_1 & -P_3 & P_1 \end{pmatrix}$	$\begin{pmatrix} -P_1 & 0 & -P_1 \\ P_1 & 0 & P_1 \end{pmatrix}$	$\begin{pmatrix} -P_1 & 0 & -P_1 \\ P_1 & 0 & P_1 \end{pmatrix}$
11	$\begin{pmatrix} \epsilon_3 & \epsilon_1 & \epsilon_1 \\ -\epsilon_6 & \epsilon_5 & \epsilon_5 \end{pmatrix}$	$\begin{pmatrix} -P_3 & -P_1 & -P_1 \\ P_3 & P_1 & P_1 \end{pmatrix}$	$\begin{pmatrix} 0 & -P_1 & P_1 \\ 0 & P_1 & -P_1 \end{pmatrix}$	$\begin{pmatrix} 0 & -P_1 & P_1 \\ 0 & P_1 & -P_1 \end{pmatrix}$
12	$\begin{pmatrix} \epsilon_3 & \epsilon_1 & \epsilon_1 \\ \epsilon_6 & \epsilon_5 & -\epsilon_5 \end{pmatrix}$	$\begin{pmatrix} P_3 & -P_1 & P_1 \\ -P_3 & P_1 & -P_1 \end{pmatrix}$	$\begin{pmatrix} 0 & -P_1 & -P_1 \\ 0 & P_1 & P_1 \end{pmatrix}$	$\begin{pmatrix} 0 & -P_1 & -P_1 \\ 0 & P_1 & P_1 \end{pmatrix}$

Table D.19 (continued)
 $\bar{m}\bar{3}m \rightarrow m_{xy}, \bar{4}3m \rightarrow m_{xy}$ (above diagonal)
 $\bar{m}\bar{3}m \rightarrow 2_{xy}, \bar{m}\bar{3}m \rightarrow 2_{xy}/m_{xy} (P=0), \bar{4}32 \rightarrow 2_{xy}$ (below diagonal)

S	1	2	3	4	5	6	7	8	9	10	11	12
1	N/A	$(010)^N$ $(10\bar{a})^C$	$(001)^N$ $(1\bar{1}0)^C$	$(100)^N$ $(01a)^C$	R	R	R	R	$(011)^C$ $(\bar{c}1\bar{1})^N$	$(01\bar{1})^C$ $(b11)^N$	$(101)^C$ $(1\bar{b}1)^N$	$(101)^C$ $(1\bar{c}1)^N$
2	$(010)^N$ $(10\bar{a})^C$	N/A	$(100)^N$ $(01\bar{a})^C$	$(001)^N$ $(110)^C$	$(011)^C$ $(b11)^N$	$(01\bar{1})^C$ $(c11)^N$	R	R	R	R	$(10\bar{1})^C$ $(1c1)^N$	$(101)^C$ $(1c1)^N$
3	$(001)^N$ $(110)^N$	$(100)^N$ $(01\bar{a})^C$	N/A	$(010)^N$ $(10a)^C$	$(011)^C$ $(\bar{c}11)^N$	$(01\bar{1})^C$ $(b11)^N$	$(10\bar{1})^C$ $(1b1)^N$	$(101)^C$ $(1\bar{c}1)^N$	R	R	R	R
4	$(100)^N$ $(01a)^C$	$(001)^N$ $(110)^N$	$(010)^N$ $(10a)^C$	N/A	R	R	$(101)^C$ $(1c1)^N$	$(10\bar{1})^C$ $(b11)^N$	$(011)^C$ $(b11)^N$	$(01\bar{1})^C$ $(c11)^N$	R	R
5	R	$(011)^N$ $(b11)^C$	$(01\bar{1})^N$ $(\bar{c}11)^C$	R	N/A	$(100)^N$ $(0a\bar{1})^C$	R	$(110)^C$ $(11\bar{c})^N$	$(001)^N$ $(1a0)^C$	$(010)^N$ $(101)^C$	R	$(110)^C$ $(11b)^N$
6	R	$(01\bar{1})^N$ $(c11)^C$	$(011)^N$ $(b11)^C$	R	$(100)^N$ $(0a\bar{1})^C$	N/A	$(110)^C$ $(11b)^N$	R	$(010)^N$ $(101)^C$	$(001)^N$ $(1a0)^C$	$(110)^C$ $(11c)^N$	R
7	R	R	$(10\bar{1})^N$ $(1b1)^C$	$(101)^N$ $(1c1)^C$	R	$(110)^N$ $(11b)^C$	N/A	$(010)^N$ $(a01)^C$	R	$(110)^C$ $(11c)^N$	$(001)^N$ $(a10)^C$	$(100)^N$ $(011)^C$
8	R	R	$(101)^N$ $(1c1)^C$	$(10\bar{1})^N$ $(1b1)^C$	$(110)^N$ $(11c)^C$	R	$(010)^N$ $(a01)^C$	N/A	$(110)^C$ $(11b)^N$	R	$(100)^N$ $(011)^C$	$(001)^N$ $(a10)^C$
9	$(011)^N$ $(\bar{c}11)^C$	R	R	$(01\bar{1})^N$ $(b11)^C$	$(001)^N$ $(1a0)^C$	$(010)^N$ $(101)^N$	R	$(110)^N$ $(11b)^C$	N/A	$(100)^N$ $(0a1)^C$	R	$(110)^C$ $(11c)^N$
10	$(01\bar{1})^N$ $(b11)^C$	R	R	$(011)^N$ $(c11)^C$	$(010)^N$ $(1a0)^C$	$(001)^N$ $(1a0)^C$	$(110)^N$ $(11c)^C$	R	$(100)^N$ $(0a1)^C$	N/A	$(110)^C$ $(11b)^N$	R
11	$(101)^N$ $(1b1)^C$	$(10\bar{1})^N$ $(1c1)^C$	R	R	R	$(110)^N$ $(11c)^C$	$(001)^N$ $(a10)^C$	$(100)^N$ $(011)^N$	R	$(110)^N$ $(11b)^C$	N/A	$(010)^N$ $(a01)^C$
12	$(10\bar{1})^N$ $(1c1)^C$	$(101)^N$ $(1b1)^C$	R	R	$(110)^N$ $(11b)^C$	R	$(100)^N$ $(011)^N$	$(001)^N$ $(a10)^C$	$(110)^N$ $(11c)^C$	R	$(010)^N$ $(a01)^C$	N/A

$a = \epsilon_5/\epsilon_6, b = (\epsilon_6 - \epsilon_5)/(\epsilon_3 - \epsilon_1), c = (\epsilon_6 + \epsilon_5)/(\epsilon_3 - \epsilon_1)$

Table D.20 Cubic to monoclinic species

All species	$m\bar{3}m \rightarrow 2_z m\bar{3}m \rightarrow 2_z/m_z (P=0)$ 432 $\rightarrow 2_z$ (upper polarizations only) strains 1–6 only for following species:		$m\bar{3}m \rightarrow m_2, m\bar{3} \rightarrow m_2$ (strains 1–6 only)
	strains	polarizations	
1	$\begin{pmatrix} \varepsilon_1 & \varepsilon_2 & \varepsilon_3 \\ 0 & 0 & \varepsilon_6 \end{pmatrix}$	$\begin{pmatrix} 0 & 0 & P_3 \\ 0 & 0 & -P_3 \end{pmatrix}$	$\begin{pmatrix} P_1 & P_2 & 0 \\ -P_1 & -P_2 & 0 \end{pmatrix}$
2	$\begin{pmatrix} \varepsilon_3 & \varepsilon_1 & \varepsilon_2 \\ \varepsilon_6 & 0 & 0 \end{pmatrix}$	$\begin{pmatrix} P_3 & 0 & 0 \\ -P_3 & 0 & 0 \end{pmatrix}$	$\begin{pmatrix} 0 & P_1 & P_2 \\ 0 & -P_1 & -P_2 \end{pmatrix}$
3	$\begin{pmatrix} \varepsilon_2 & \varepsilon_3 & \varepsilon_1 \\ 0 & \varepsilon_6 & 0 \end{pmatrix}$	$\begin{pmatrix} 0 & P_3 & 0 \\ 0 & -P_3 & 0 \end{pmatrix}$	$\begin{pmatrix} P_2 & 0 & P_1 \\ -P_2 & 0 & -P_1 \end{pmatrix}$
4	$\begin{pmatrix} \varepsilon_1 & \varepsilon_2 & \varepsilon_3 \\ 0 & 0 & -\varepsilon_6 \end{pmatrix}$	$\begin{pmatrix} 0 & 0 & -P_3 \\ 0 & 0 & P_3 \end{pmatrix}$	$\begin{pmatrix} P_1 & -P_2 & 0 \\ -P_1 & P_2 & 0 \end{pmatrix}$
5	$\begin{pmatrix} \varepsilon_3 & \varepsilon_1 & \varepsilon_2 \\ -\varepsilon_6 & 0 & 0 \end{pmatrix}$	$\begin{pmatrix} -P_3 & 0 & 0 \\ P_3 & 0 & 0 \end{pmatrix}$	$\begin{pmatrix} 0 & P_1 & -P_2 \\ 0 & -P_1 & P_2 \end{pmatrix}$
6	$\begin{pmatrix} \varepsilon_2 & \varepsilon_3 & \varepsilon_1 \\ 0 & -\varepsilon_6 & 0 \end{pmatrix}$	$\begin{pmatrix} P_3 & 0 & 0 \\ 0 & -P_3 & 0 \end{pmatrix}$	$\begin{pmatrix} 0 & -P_1 & P_2 \\ P_2 & 0 & -P_1 \end{pmatrix}$
7	$\begin{pmatrix} \varepsilon_2 & \varepsilon_1 & \varepsilon_3 \\ -\varepsilon_6 & 0 & 0 \end{pmatrix}$	$\begin{pmatrix} 0 & 0 & P_3 \\ 0 & 0 & -P_3 \end{pmatrix}$	$\begin{pmatrix} -P_2 & P_1 & 0 \\ P_2 & -P_1 & 0 \end{pmatrix}$
8	$\begin{pmatrix} \varepsilon_2 & \varepsilon_1 & \varepsilon_3 \\ \varepsilon_6 & 0 & 0 \end{pmatrix}$	$\begin{pmatrix} 0 & 0 & -P_3 \\ 0 & 0 & P_3 \end{pmatrix}$	$\begin{pmatrix} P_2 & P_1 & 0 \\ -P_2 & -P_1 & 0 \end{pmatrix}$
9	$\begin{pmatrix} \varepsilon_1 & \varepsilon_3 & \varepsilon_2 \\ 0 & \varepsilon_6 & 0 \end{pmatrix}$	$\begin{pmatrix} 0 & -P_3 & 0 \\ 0 & P_3 & 0 \end{pmatrix}$	$\begin{pmatrix} P_1 & 0 & P_2 \\ -P_1 & 0 & -P_2 \end{pmatrix}$
10	$\begin{pmatrix} \varepsilon_3 & \varepsilon_2 & \varepsilon_1 \\ \varepsilon_6 & 0 & 0 \end{pmatrix}$	$\begin{pmatrix} -P_3 & 0 & 0 \\ P_3 & 0 & 0 \end{pmatrix}$	$\begin{pmatrix} -P_1 & 0 & -P_2 \\ 0 & P_2 & P_1 \end{pmatrix}$
11	$\begin{pmatrix} \varepsilon_1 & \varepsilon_3 & \varepsilon_2 \\ 0 & -\varepsilon_6 & 0 \end{pmatrix}$	$\begin{pmatrix} 0 & P_3 & 0 \\ 0 & -P_3 & 0 \end{pmatrix}$	$\begin{pmatrix} 0 & -P_2 & -P_1 \\ P_1 & 0 & -P_2 \end{pmatrix}$
12	$\begin{pmatrix} \varepsilon_3 & \varepsilon_2 & \varepsilon_1 \\ -\varepsilon_6 & 0 & 0 \end{pmatrix}$	$\begin{pmatrix} P_3 & 0 & 0 \\ -P_3 & 0 & 0 \end{pmatrix}$	$\begin{pmatrix} -P_1 & 0 & P_2 \\ 0 & P_2 & -P_1 \end{pmatrix}$

Table D.20 (continued)
 $\bar{4}3m \rightarrow 2_z$ (above diagonal)
 $m\bar{3}m \rightarrow 2_z, m\bar{3}m \rightarrow 2_z/m_z (P=0), 432 \rightarrow 2_z$ (all 12 strains), $m\bar{3} \rightarrow 2_z, m\bar{3} \rightarrow 2_z/m_z (P=0), 23 \rightarrow 2_z$ (strains 1-6 only) (below diagonal)

S	1	2	3	4	5	6	7	8	9	10	11	12
1	N/A	R	R	$(100)^N$ $(010)^N$	R	R	$(1\bar{z}+0)^N$ $(1\bar{z}-0)^N$	$(1\bar{1}0)^N$ $(110)^N$	$(01\bar{1})^C$ $(\bar{c}11)^N$	$(10\bar{1})^C$ $(1d\bar{1})^N$	$(011)^C$ $(\bar{c}11)^N$	$(101)^C$ $(1d\bar{1})^N$
2	R	N/A	R	R	$(010)^N$ $(001)^N$	R	$(101)^C$ $(1c\bar{1})^N$	$(10\bar{1})^C$ $(1\bar{c}1)^N$	$(1\bar{1}0)^C$ $(11d)^N$	$(011)^N$ $(01\bar{1})^N$	$(110)^C$ $(11d)^N$	$(01z_+)^N$ $(01z_-)^N$
3	R	R	N/A	R	R	$(100)^N$ $(001)^N$	$(011)^C$ $(d11)^N$	$(01\bar{1})^C$ $(d11)^N$	$(10\bar{1})^N$ $(101)^N$	$(1\bar{1}0)^C$ $(11\bar{c})^N$	$(10z_+)^N$ $(10z_-)^N$	$(110)^C$ $(11\bar{c})^N$
4	$(100)^N$ $(010)^N$	R	R	N/A	R	R	$(1\bar{1}0)^N$ $(110)^N$	$(1z_+0)^N$ $(1z_-0)^N$	$(011)^C$ $(c11)^N$	$(101)^C$ $(1d\bar{1})^N$	$(01\bar{1})^C$ $(c11)^N$	$(10\bar{1})^C$ $(1d\bar{1})^N$
5	R	$(010)^N$ $(001)^N$	R	R	N/A	R	$(10\bar{1})^C$ $(1c\bar{1})^N$	$(101)^C$ $(1\bar{c}1)^N$	$(110)^C$ $(1\bar{1}d)^N$	$(01z_+)^N$ $(01z_-)^N$	$(1\bar{1}0)^C$ $(11d)^N$	$(011)^N$ $(01\bar{1})^N$
6	R	R	$(100)^N$ $(001)^N$	R	R	N/A	$(01\bar{1})^C$ $(d11)^N$	$(011)^C$ $(d11)^N$	$(10z_+)^N$ $(10z_-)^N$	$(110)^C$ $(11c)^N$	$(10\bar{1})^N$ $(101)^N$	$(110)^C$ $(11c)^N$
7	$(1z_+0)^N$ $(1z_-0)^N$	$(101)^N$ $(1c\bar{1})^C$	$(011)^N$ $(d11)^C$	$(1\bar{1}0)^N$ $(110)^N$	$(10\bar{1})^N$ $(1c1)^C$	$(01\bar{1})^N$ $(d11)^C$	N/A	$(100)^N$ $(010)^N$	R	R	R	R
8	$(1\bar{1}0)^N$ $(110)^N$	$(10\bar{1})^N$ $(1c\bar{1})^C$	$(01\bar{1})^N$ $(d11)^C$	$(1z_+0)^N$ $(1z_-0)^N$	$(101)^N$ $(1\bar{c}1)^C$	$(011)^N$ $(d11)^C$	$(100)^N$ $(010)^N$	N/A	R	R	R	R
9	$(01\bar{1})^N$ $(\bar{c}11)^C$	$(1\bar{1}0)^N$ $(11d)^C$	$(10\bar{1})^N$ $(101)^N$	$(011)^N$ $(c11)^C$	$(110)^N$ $(11d)^C$	$(10z_+)^N$ $(10z_-)^N$	R	R	N/A	R	$(100)^N$ $(001)^N$	R
10	$(10\bar{1})^N$ $(1d\bar{1})^C$	$(011)^N$ $(011)^C$	$(1\bar{1}0)^N$ $(11\bar{c})^C$	$(101)^N$ $(1d\bar{1})^C$	$(01z_+)^N$ $(01z_-)^N$	$(110)^N$ $(11c)^C$	R	R	R	N/A	R	$(010)^N$ $(001)^N$
11	$(011)^N$ $(\bar{c}11)^C$	$(110)^N$ $(11d)^C$	$(10z_+)^N$ $(10z_-)^N$	$(01\bar{1})^N$ $(c11)^C$	$(1\bar{1}0)^N$ $(11d)^C$	$(10\bar{1})^N$ $(101)^N$	R	R	$(100)^N$ $(001)^N$	R	N/A	R
12	$(101)^N$ $(1d\bar{1})^C$	$(01z_+)^N$ $(01z_-)^N$	$(110)^N$ $(11\bar{c})^C$	$(10\bar{1})^N$ $(1d\bar{1})^C$	$(01\bar{1})^N$ $(011)^N$	$(110)^N$ $(11c)^C$	R	R	R	R	R	N/A

Table D.20 (continued)

$m\bar{3}m \rightarrow m_z$ (all 12 strains), $m\bar{3} \rightarrow m_z$ (strains 1–6 only)	1	2	3	4	5	6	7	8	9	10	11	12
1	N/A	R	R	$(100)^N$ $(010)^C$	R	R	$(1\bar{z}_+)^C$ $(1\bar{z}_-)^C$	$(1\bar{1}0)^C$ $(110)^N$	$(011)^C$ $(\bar{c}11)^N$	$(101)^C$ $(1\bar{d}1)^N$	$(011)^C$ $(\bar{c}11)^N$	$(101)^C$ $(1\bar{d}1)^N$
2	N/A	R	R	$(010)^N$ $(001)^C$	R	R	$(101)^C$ $(1\bar{c}1)^N$	$(101)^C$ $(1\bar{c}1)^N$	$(1\bar{1}0)^C$ $(11\bar{d})^N$	$(011)^N$ $(011)^C$	$(110)^N$ $(1\bar{1}d)^C$	$(01\bar{z}_+)^*$ $(01\bar{z}_-)^*$
3	N/A	R	R	$(100)^N$ $(001)^C$	R	R	$(011)^N$ $(\bar{d}11)^C$	$(011)^C$ $(\bar{d}11)^N$	$(101)^C$ (101)	$(1\bar{1}0)^C$ $(11\bar{c})^N$	$(10z_+)^*$ $(10z_-)^*$	(110) $(11\bar{c})$
4	N/A	R	R	N/A	R	R	$(1\bar{1}0)^C$ $(110)^N$	$(1z_+0)^*$ $(1z_-0)^*$	(011) $(c11)$	$(101)^N$ $(1\bar{d}1)^C$	$(01\bar{1})^C$ $(c11)^N$	$(101)^N$ $(1\bar{d}1)^C$
5	N/A	R	R	N/A	R	R	$(101)^C$ $(1c1)^N$	$(101)^C$ $(1\bar{c}1)^N$	$(110)^N$ $(1\bar{1}d)^C$	$(01z_+)^*$ $(01z_-)^*$	$(1\bar{1}0)^C$ $(11d)^N$	$(01\bar{1})^C$ (011)
6	N/A	R	R	N/A	R	R	$(011)^N$ $(\bar{d}11)^C$	$(011)^C$ $(\bar{d}11)^N$	$(10z_+)^*$ $(10z_-)^*$	(110) $(11c)$	$(101)^N$ $(101)^C$	$(1\bar{1}0)^C$ $(11c)^N$
7	N/A	R	R	N/A	R	R	N/A	$(100)^C$ $(010)^N$	R	R	R	R
8	N/A	R	R	N/A	R	R	N/A	N/A	R	R	R	R
9	N/A	R	R	N/A	R	R	N/A	N/A	R	R	R	R
10	N/A	R	R	N/A	R	R	N/A	N/A	R	R	R	R
11	N/A	R	R	N/A	R	R	N/A	N/A	R	R	R	R
12	N/A	R	R	N/A	R	R	N/A	N/A	R	R	R	R

$a = \varepsilon_2 - \varepsilon_1$, $b = -2\varepsilon_6$, $c = \varepsilon_6/(\varepsilon_3 - \varepsilon_2)$, $d = \varepsilon_6/(\varepsilon_3 - \varepsilon_1)$, $z_{\pm} = (-b \pm \sqrt{b^2 + 4a^2})/2a$

*Neutrality/charge of DW depends on the values of spontaneous strain/polarization

Table D.21 Orthorhombic to orthorhombic

Species		$mmm \rightarrow m_x m_y 2_z$
strains		polarizations
1	$\begin{pmatrix} \varepsilon_1 & \varepsilon_2 & \varepsilon_3 \\ 0 & 0 & 0 \end{pmatrix}$	$\begin{pmatrix} 0 & 0 & P_3 \\ 0 & 0 & -P_3 \end{pmatrix}$

Table D.22 Tetragonal to orthorhombic

Species	$4mm \rightarrow m_x m_y 2_z$	$4/mmm \rightarrow m_x m_y 2_z$	$4/mmm \rightarrow 2_x 2_y 2_z$	$4/mmm \rightarrow m_x m_y m_z$
strains	polarizations	polarizations	polarizations	polarizations
1	$\begin{pmatrix} \varepsilon_1 & \varepsilon_2 & \varepsilon_3 \\ 0 & 0 & 0 \end{pmatrix}$	$\begin{pmatrix} 0 & 0 & P_3 \\ 0 & 0 & -P_3 \end{pmatrix}$	$\begin{pmatrix} 0 & 0 & P_3 \\ 0 & 0 & -P_3 \end{pmatrix}$	$\begin{pmatrix} P_1 & 0 & 0 \\ -P_1 & 0 & 0 \end{pmatrix}$
2	$\begin{pmatrix} \varepsilon_2 & \varepsilon_1 & \varepsilon_3 \\ 0 & 0 & 0 \end{pmatrix}$	$\begin{pmatrix} 0 & 0 & P_3 \\ 0 & 0 & -P_3 \end{pmatrix}$	$\begin{pmatrix} 0 & 0 & -P_3 \\ 0 & 0 & P_3 \end{pmatrix}$	$\begin{pmatrix} 0 & -P_1 & 0 \\ 0 & P_1 & 0 \end{pmatrix}$

$4mm \rightarrow m_x m_y 2_z$, $422 \rightarrow 2_x 2_y 2_z (P = 0)$; $4/mmm \rightarrow m_x m_y 2_z$, $4/mmm \rightarrow 2_x 2_y 2_z (P = 0)$,
 $\bar{4}2m \rightarrow 2_x 2_y 2_z (P = 0)$ (above diagonal)
 $4/mmm \rightarrow m_x m_y m_z (P = 0)$, $4/mmm \rightarrow 2_x m_y m_z$ (below diagonal)

S	1	2
1	N/A	$\begin{pmatrix} (110)^N \\ (\bar{1}\bar{1}0)^N \end{pmatrix}$
2	$\begin{pmatrix} (110)^C \\ (\bar{1}\bar{1}0)^N \end{pmatrix}$	N/A

Table D.23 Tetragonal to orthorhombic

Species		$\bar{4}2m \rightarrow m_x m_y m_z 2_z$
strains		polarizations
1	$\begin{pmatrix} \varepsilon_1 & \varepsilon_1 & \varepsilon_3 \\ 0 & 0 & \varepsilon_6 \end{pmatrix}$	$\begin{pmatrix} 0 & 0 & P_3 \end{pmatrix}$
2	$\begin{pmatrix} \varepsilon_1 & \varepsilon_1 & \varepsilon_3 \\ 0 & 0 & -\varepsilon_6 \end{pmatrix}$	$\begin{pmatrix} 0 & 0 & -P_3 \end{pmatrix}$

S	1	2
1	N/A	$\begin{pmatrix} (100)^N \\ (010)^N \end{pmatrix}$
2		N/A

Table D.24 Hexagonal to orthorhombic

All species	$\bar{6}m2 \rightarrow m_x 2_y m_z$ $622 \rightarrow 2_x 2_y 2_z (P=0)$ $6/mmm \rightarrow m_x m_y m_z (P=0)$ $6/mmm \rightarrow 2_x 2_y 2_z (P=0)$	$6/mmm \rightarrow 2_x m_y m_z$	$6/mmm \rightarrow m_x m_y 2_z$ $6mm \rightarrow m_x m_y 2_z$ (upper polarizations only)	
strains	polarizations	polarizations	polarizations	
1	$\begin{pmatrix} \varepsilon_1 & \varepsilon_2 & \varepsilon_3 \\ 0 & 0 & 0 \end{pmatrix}$	$(0 \ P_2 \ 0)$	$\begin{pmatrix} P_1 & 0 & 0 \\ -P_1 & 0 & 0 \end{pmatrix}$	$\begin{pmatrix} 0 & 0 & P_3 \\ 0 & 0 & -P_3 \end{pmatrix}$
2	$\begin{pmatrix} \varepsilon'_1 & \varepsilon'_2 & \varepsilon_3 \\ 0 & 0 & \varepsilon'_6 \end{pmatrix}$	$(-P''_2 \ P'_2 \ 0)$	$\begin{pmatrix} P'_1 & P''_1 & 0 \\ -P'_1 & -P''_1 & 0 \end{pmatrix}$	$\begin{pmatrix} 0 & 0 & P_3 \\ 0 & 0 & -P_3 \end{pmatrix}$
3	$\begin{pmatrix} \varepsilon'_1 & \varepsilon'_2 & \varepsilon_3 \\ 0 & 0 & -\varepsilon'_6 \end{pmatrix}$	$(-P''_2 \ -P'_2 \ P_3)$	$\begin{pmatrix} -P'_1 & P''_1 & 0 \\ P'_1 & -P''_1 & 0 \end{pmatrix}$	$\begin{pmatrix} 0 & 0 & P_3 \\ 0 & 0 & -P_3 \end{pmatrix}$

$$\varepsilon'_1 = (1/4)(\varepsilon_1 + 3\varepsilon_2), \varepsilon'_2 = (1/4)(3\varepsilon_1 + \varepsilon_2), \varepsilon'_6 = (\sqrt{3}/2)(\varepsilon_1 - \varepsilon_2)$$

$$P'_1 = (1/2)P_1, P''_1 = (\sqrt{3}/2)P_1, P'_2 = (1/2)P_2, P''_2 = (\sqrt{3}/2)P_2$$

$6/mmm \rightarrow m_x m_y m_z (P=0)$, $6/mmm \rightarrow 2_x 2_y 2_z (P=0)$, $\bar{6}m2 \rightarrow m_x 2_y m_z, 622 \rightarrow 222 (P=0)$
(above diagonal); $6/mmm \rightarrow 2_x m_y m_z$ (below diagonal)

S	1	2	3
1	N/A	$(10\bar{1}0)^C$ $(1\bar{2}10)^N$	$(11\bar{2}0)^C$ $(1\bar{1}00)^N$
2	$(10\bar{1}0)^N$ $(1\bar{2}10)^C$	N/A	$(01\bar{1}0)^C$ $(2\bar{1}\bar{1}0)^N$
3	$(11\bar{2}0)^N$ $(1\bar{1}00)^C$	$(01\bar{1}0)^N$ $(2\bar{1}\bar{1}0)^C$	N/A

$6/mmm \rightarrow m_x m_y 2_z, 6mm \rightarrow m_x m_y 2_z$

S	1	2	3
1	N/A	$(10\bar{1}0)^N$ $(1\bar{2}10)^N$	$(11\bar{2}0)^N$ $(1\bar{1}00)^N$
2		N/A	$(01\bar{1}0)^N$ $(2\bar{1}\bar{1}0)^N$
3			N/A

Table D.25 Cubic to orthorhombic

		$m\bar{3}m \rightarrow m_x m_y 2_z, m\bar{3}m \rightarrow 2_x 2_y 2_z (P = 0)$		$m\bar{3}m \rightarrow m_x m_y m_z (P = 0),$		
		$432 \rightarrow 2_x 2_y 2_z (P = 0)$				
		$43m \rightarrow 222 (P = 0)$		Strains 1–3 only for following species:		
		$23 \rightarrow 222 (P = 0), m\bar{3} \rightarrow mmm (P = 0)$				
All species		$m\bar{3} \rightarrow 222 (P = 0), m\bar{3} \rightarrow m_x m_y 2_z$				
strains		polarizations				
1	$\begin{pmatrix} \varepsilon_1 & \varepsilon_2 & \varepsilon_3 \\ 0 & 0 & 0 \end{pmatrix}$	$\begin{pmatrix} 0 & 0 & P_3 \\ 0 & 0 & -P_3 \end{pmatrix}$				
2	$\begin{pmatrix} \varepsilon_3 & \varepsilon_1 & \varepsilon_2 \\ 0 & 0 & 0 \end{pmatrix}$	$\begin{pmatrix} P_3 & 0 & 0 \\ -P_3 & 0 & 0 \end{pmatrix}$				
3	$\begin{pmatrix} \varepsilon_2 & \varepsilon_3 & \varepsilon_1 \\ 0 & 0 & 0 \end{pmatrix}$	$\begin{pmatrix} 0 & P_3 & 0 \\ 0 & -P_3 & 0 \end{pmatrix}$				
4	$\begin{pmatrix} \varepsilon_2 & \varepsilon_1 & \varepsilon_3 \\ 0 & 0 & 0 \end{pmatrix}$	$\begin{pmatrix} 0 & 0 & P_3 \\ 0 & 0 & -P_3 \end{pmatrix}$				
5	$\begin{pmatrix} \varepsilon_3 & \varepsilon_2 & \varepsilon_1 \\ 0 & 0 & 0 \end{pmatrix}$	$\begin{pmatrix} -P_3 & 0 & 0 \\ P_3 & 0 & 0 \end{pmatrix}$				
6	$\begin{pmatrix} \varepsilon_1 & \varepsilon_3 & \varepsilon_2 \\ 0 & 0 & 0 \end{pmatrix}$	$\begin{pmatrix} 0 & -P_3 & 0 \\ 0 & P_3 & 0 \end{pmatrix}$				
		$m\bar{3}m \rightarrow m_x m_y m_z (P = 0), m\bar{3}m \rightarrow m_x m_y 2_z, m\bar{3}m \rightarrow 2_x 2_y 2_z (P = 0), 432 \rightarrow 222 (P = 0),$		$43m \rightarrow 222 (P = 0)$ (all six strains), $m\bar{3} \rightarrow m_x m_y 2_z, 23 \rightarrow 222 (P = 0), m\bar{3} \rightarrow mmm (P = 0),$		
		$m\bar{3} \rightarrow 222 (P = 0)$ (strains 1–3 only)				
S	1	2	3	4	5	6
1	N/A	R	R	$(1\bar{1}0)^N$ $(110)^N$	$(10\bar{1})^N$ $(101)^C$	$(01\bar{1})^N$ $(011)^C$
2		N/A	R	$(10\bar{1})^C$ $(101)^N$	$(01\bar{1})^N$ $(011)^N$	$(1\bar{1}0)^N$ $(110)^C$
3			N/A	$(01\bar{1})^C$ $(011)^N$	$(1\bar{1}0)^N$ $(110)^C$	$(10\bar{1})^N$ $(101)^N$
4				N/A	R	R
5					N/A	R
6						N/A

Table D.26 Cubic to orthorhombic

		$m\bar{3}m \rightarrow m_{xy} m_{xy} m_z (P = 0)$	
		$m\bar{3}m \rightarrow m_{xy} m_{xy} 2_z$	
		$m\bar{3}m \rightarrow 2_{xy} 2_{xy} 2_z (P = 0)$ upper symmetry operations only for	
All species		$432 \rightarrow 2_{xy} 2_{xy} 2_z (P = 0)$	
strains		polarizations	
1	$\begin{pmatrix} \varepsilon_1 & \varepsilon_1 & \varepsilon_3 \\ 0 & 0 & \varepsilon_6 \end{pmatrix}$	$\begin{pmatrix} 0 & 0 & P_3 \\ 0 & 0 & -P_3 \end{pmatrix}$	
2	$\begin{pmatrix} \varepsilon_1 & \varepsilon_1 & \varepsilon_3 \\ 0 & 0 & -\varepsilon_6 \end{pmatrix}$	$\begin{pmatrix} P_3 & 0 & 0 \\ -P_3 & 0 & 0 \end{pmatrix}$	

Table D.26 (continued)

All species		$m\bar{3}m \rightarrow m_{xy}m_{\bar{xy}}m_z (P = 0)$ $m\bar{3}m \rightarrow m_{xy}m_{\bar{xy}}2_z$ $m\bar{3}m \rightarrow 2_{xy}2_{\bar{xy}}2_z (P = 0)$ upper symmetry operations only for $432 \rightarrow 2_{xy}2_{\bar{xy}}2_z (P = 0)$	
strains		polarizations	
3	$\begin{pmatrix} \varepsilon_1 & \varepsilon_3 & \varepsilon_1 \\ 0 & \varepsilon_6 & 0 \end{pmatrix}$	$(0 \ P_3 \ 0)$	$(0 \ -P_3 \ 0)$
4	$\begin{pmatrix} \varepsilon_3 & \varepsilon_1 & \varepsilon_1 \\ -\varepsilon_6 & 0 & 0 \end{pmatrix}$	$(0 \ 0 \ P_3)$	$(0 \ 0 \ -P_3)$
5	$\begin{pmatrix} \varepsilon_3 & \varepsilon_1 & \varepsilon_1 \\ \varepsilon_6 & 0 & 0 \end{pmatrix}$	$(-P_3 \ 0 \ 0)$	$(P_3 \ 0 \ 0)$
6	$\begin{pmatrix} \varepsilon_1 & \varepsilon_3 & \varepsilon_1 \\ 0 & -\varepsilon_6 & 0 \end{pmatrix}$	$(0 \ -P_3 \ 0)$	$(0 \ P_3 \ 0)$

S	1	2	3	4	5	6
1	N/A	$(100)^N$ $(010)^N$	$(01\bar{1})^N$ $(\bar{a}11)^C$	$(101)^N$ $(1\bar{a}\bar{1})^C$	$(10\bar{1})^C$ $(1\bar{a}\bar{1})^N$	$(011)^N$ $(\bar{a}\bar{1}\bar{1})^C$
2		N/A	$(011)^C$ $(a1\bar{1})^N$	$(10\bar{1})^C$ $(1a1)^N$	$(101)^N$ $(1a\bar{1})^C$	$(01\bar{1})^C$ $(a11)^N$
3			N/A	$(110)^C$ $(1\bar{1}\bar{a})^N$	$(1\bar{1}0)^N$ $(11\bar{a})^C$	$(100)^N$ $(001)^N$
4				N/A	$(010)^N$ $(001)^N$	$(1\bar{1}0)^C$ $(11a)^N$
5					N/A	$(110)^N$ $(\bar{1}\bar{1}\bar{a})^C$
6						N/A

$$a = \frac{\varepsilon_6}{\varepsilon_3 - \varepsilon_1}$$

Table D.27 Cubic to orthorhombic

All species		$43m \rightarrow m_{xy}m_{\bar{xy}}2_z$	$m\bar{3}m \rightarrow 2_{xy}m_{\bar{xy}}m_z$
strains		polarizations	polarizations
1	$\begin{pmatrix} \varepsilon_1 & \varepsilon_1 & \varepsilon_3 \\ 0 & 0 & \varepsilon_6 \end{pmatrix}$	$(0 \ 0 \ P_3)$	$(P_1 \ P_1 \ 0)$ $(-P_1 \ -P_1 \ 0)$
2	$\begin{pmatrix} \varepsilon_3 & \varepsilon_1 & \varepsilon_1 \\ \varepsilon_6 & 0 & 0 \end{pmatrix}$	$(P_3 \ 0 \ 0)$	$(0 \ P_1 \ P_1)$ $(0 \ -P_1 \ -P_1)$
3	$\begin{pmatrix} \varepsilon_1 & \varepsilon_3 & \varepsilon_1 \\ 0 & \varepsilon_6 & 0 \end{pmatrix}$	$(0 \ P_3 \ 0)$	$(P_1 \ 0 \ P_1)$ $(-P_1 \ 0 \ -P_1)$
4	$\begin{pmatrix} \varepsilon_1 & \varepsilon_1 & \varepsilon_3 \\ 0 & 0 & -\varepsilon_6 \end{pmatrix}$	$(0 \ 0 \ -P_3)$	$(-P_1 \ P_1 \ 0)$ $(P_1 \ -P_1 \ 0)$
5	$\begin{pmatrix} \varepsilon_3 & \varepsilon_1 & \varepsilon_1 \\ -\varepsilon_6 & 0 & 0 \end{pmatrix}$	$(-P_3 \ 0 \ 0)$	$(0 \ P_1 \ -P_1)$ $(0 \ -P_1 \ P_1)$
6	$\begin{pmatrix} \varepsilon_1 & \varepsilon_3 & \varepsilon_1 \\ 0 & -\varepsilon_6 & 0 \end{pmatrix}$	$(0 \ -P_3 \ 0)$	$(P_1 \ 0 \ -P_1)$ $(-P_1 \ 0 \ P_1)$

Table D.27 (continued)

S	1	2	3	4	5	6
1	N/A	$(10\bar{1})^C$ $(1\bar{a}1)^N$	$(01\bar{1})^C$ $(\bar{a}11)^N$	$(100)^C$ $(010)^N$	$(101)^C$ $(1\bar{a}\bar{1})^N$	$(011)^C$ $(\bar{a}1\bar{1})^N$
2	$(10\bar{1})^C$ $(1\bar{a}1)^N$	N/A	$(1\bar{1}0)^C$ $(11\bar{a})^N$	$(101)^C$ $(1a\bar{1})^N$	$(010)^N$ $(001)^C$	$(110)^N$ $(1\bar{1}a)^C$
3	$(01\bar{1})^C$ $(\bar{a}11)^N$	$(1\bar{1}0)^C$ $(11\bar{a})^N$	N/A	$(011)^N$ $(a1\bar{1})^C$	$(110)^N$ $(1\bar{1}\bar{a})^C$	$(100)^N$ $(001)^C$
4	$(100)^N$ $(010)^N$	$(101)^C$ $(1a\bar{1})^N$	$(011)^C$ $(a1\bar{1})^N$	N/A	$(10\bar{1})^C$ $(1a1)^N$	$(01\bar{1})^N$ $(a11)^C$
5	$(101)^C$ $(1\bar{a}\bar{1})^N$	$(010)^N$ $(001)^N$	$(110)^C$ $(1\bar{1}\bar{a})^N$	$(10\bar{1})^C$ $(1a1)^N$	N/A	$(1\bar{1}0)^C$ $(11a)^N$
6	$(011)^C$ $(\bar{a}1\bar{1})^N$	$(110)^C$ $(1\bar{1}a)^N$	$(100)^N$ $(001)^N$	$(01\bar{1})^C$ $(a11)^N$	$(1\bar{1}0)^C$ $(11a)^N$	N/A

$$a = \varepsilon_6 / (\varepsilon_3 - \varepsilon_1)$$

Table D.28 Tetragonal to tetragonal, trigonal to trigonal, hexagonal to trigonal, and hexagonal to hexagonal. Structure of tensor components is the same in all species listed, but the coordinate system is chosen for parent phase of each species

				$6/mmm \rightarrow 3_2m_x$	
				$6/mmm \rightarrow 3$	
		$4/mmm \rightarrow 4$	$\bar{3}m \rightarrow 3$	$6/m \rightarrow 3$	$6/mmm \rightarrow 6mm$
		$4/mmm \rightarrow 4mm$	$3m \rightarrow 3m$	$6m2 \rightarrow 3_2m_x$	$6/mmm \rightarrow 6$
		$4/m \rightarrow 4$	$\bar{3} \rightarrow 3$	$\bar{6}m2 \rightarrow 3\bar{6} \rightarrow 3$	$6/m \rightarrow 6$
All species		$422 \rightarrow 4$	$32 \rightarrow 3$	$622 \rightarrow 3$	$622 \rightarrow 6$
strains	polarizations	polarizations	polarizations	polarizations	polarizations
1	$\begin{pmatrix} \varepsilon_1 & \varepsilon_1 & \varepsilon_3 \\ 0 & 0 & 0 \end{pmatrix}$	$\begin{pmatrix} 0 & 0 & P_3 \\ 0 & 0 & -P_3 \end{pmatrix}$			

Table D.29 Cubic to tetragonal

		$m\bar{3}m \rightarrow 4_2m_xm_{xy}$	
		$m\bar{3}m \rightarrow 4_22_xm_{xy}(P=0)$	
		$m\bar{3}m \rightarrow 4_22_{xy}m_x(P=0)$	
		$m\bar{3}m \rightarrow 4_22_x2_{xy}(P=0)$	$432 \rightarrow 4$
		$m\bar{3}m \rightarrow 4(P=0)$	$43m \rightarrow 4_22_xm_{xy}(P=0)$
		$m\bar{3}m \rightarrow 4m\bar{3}m \rightarrow 4_2/m_2m_xm_y(P=0)$	$43m \rightarrow 4(P=0)$
All species		$m\bar{3}m \rightarrow 4_2/m_2(P=0)$	$432 \rightarrow 4_22_x2_{xy}(P=0)$
strains	polarizations	polarizations	polarizations
1	$\begin{pmatrix} \varepsilon_1 & \varepsilon_1 & \varepsilon_3 \\ 0 & 0 & 0 \end{pmatrix}$	$\begin{pmatrix} 0 & 0 & P_3 \\ 0 & 0 & -P_3 \end{pmatrix}$	$\begin{pmatrix} 0 & 0 & P_3 \\ 0 & 0 & -P_3 \end{pmatrix}$
2	$\begin{pmatrix} \varepsilon_3 & \varepsilon_1 & \varepsilon_1 \\ 0 & 0 & 0 \end{pmatrix}$	$\begin{pmatrix} P_3 & 0 & 0 \\ -P_3 & 0 & 0 \end{pmatrix}$	$\begin{pmatrix} P_3 & 0 & 0 \\ -P_3 & 0 & 0 \end{pmatrix}$
3	$\begin{pmatrix} \varepsilon_1 & \varepsilon_3 & \varepsilon_1 \\ 0 & 0 & 0 \end{pmatrix}$	$\begin{pmatrix} 0 & P_3 & 0 \\ 0 & -P_3 & 0 \end{pmatrix}$	$\begin{pmatrix} 0 & P_3 & 0 \\ 0 & -P_3 & 0 \end{pmatrix}$

Table D.29 (continued)

S	1	2	3
1	N/A	$(10\bar{1})^C$ $(101)^N$	$(011)^N$ $(01\bar{1})^C$
2		N/A	$(110)^N$ $(1\bar{1}0)^C$
3			N/A

Table D.30 Cubic to trigonal species

All species	$m\bar{3}m \rightarrow 3_{xyz}m_{\bar{x}y}$	$432 \rightarrow 3_{xyz}2_{\bar{x}y} (P=0)$	$\bar{4}3m \rightarrow 3_{xyz}m_{\bar{x}y}$	$m\bar{3} \rightarrow 3_{xyz} m\bar{3} \rightarrow \bar{3}_{xyz} (P=0)$	$23 \rightarrow 3_{xyz}$ (upper polarizations only)
	$m\bar{3}m \rightarrow 3_{xyz}m_{\bar{x}y}$	$432 \rightarrow 3_{xyz}2_{\bar{x}y} (P=0)$	$\bar{4}3m \rightarrow 3_{xyz}m_{\bar{x}y}$	$m\bar{3} \rightarrow 3_{xyz} m\bar{3} \rightarrow \bar{3}_{xyz} (P=0)$	$23 \rightarrow 3_{xyz}$ (upper polarizations only)
strains	polarizations	polarizations	polarizations	polarizations	polarizations
1	$\begin{pmatrix} \varepsilon_1 & \varepsilon_1 & \varepsilon_1 \\ \varepsilon_6 & \varepsilon_6 & \varepsilon_6 \end{pmatrix}$	$\begin{pmatrix} P_1 & P_1 & P_1 \\ -P_1 & -P_1 & -P_1 \end{pmatrix}$	$\begin{pmatrix} P_1 & P_1 & P_1 \\ -P_1 & -P_1 & -P_1 \end{pmatrix}$	$\begin{pmatrix} P_1 & P_1 & P_1 \\ -P_1 & -P_1 & -P_1 \end{pmatrix}$	$\begin{pmatrix} P_1 & P_1 & P_1 \\ -P_1 & -P_1 & -P_1 \end{pmatrix}$
2	$\begin{pmatrix} \varepsilon_1 & \varepsilon_1 & \varepsilon_1 \\ \varepsilon_6 & -\varepsilon_6 & -\varepsilon_6 \end{pmatrix}$	$\begin{pmatrix} -P_1 & P_1 & P_1 \\ P_1 & -P_1 & -P_1 \end{pmatrix}$	$\begin{pmatrix} -P_1 & P_1 & P_1 \\ P_1 & -P_1 & -P_1 \end{pmatrix}$	$\begin{pmatrix} P_1 & -P_1 & -P_1 \\ -P_1 & P_1 & P_1 \end{pmatrix}$	$\begin{pmatrix} P_1 & -P_1 & -P_1 \\ -P_1 & P_1 & P_1 \end{pmatrix}$
3	$\begin{pmatrix} \varepsilon_1 & \varepsilon_1 & \varepsilon_1 \\ -\varepsilon_6 & -\varepsilon_6 & \varepsilon_6 \end{pmatrix}$	$\begin{pmatrix} -P_1 & -P_1 & P_1 \\ P_1 & P_1 & -P_1 \end{pmatrix}$	$\begin{pmatrix} -P_1 & -P_1 & P_1 \\ P_1 & P_1 & -P_1 \end{pmatrix}$	$\begin{pmatrix} -P_1 & -P_1 & P_1 \\ P_1 & P_1 & -P_1 \end{pmatrix}$	$\begin{pmatrix} -P_1 & -P_1 & P_1 \\ P_1 & P_1 & -P_1 \end{pmatrix}$
4	$\begin{pmatrix} \varepsilon_1 & \varepsilon_1 & \varepsilon_1 \\ -\varepsilon_6 & \varepsilon_6 & -\varepsilon_6 \end{pmatrix}$	$\begin{pmatrix} P_1 & -P_1 & P_1 \\ -P_1 & P_1 & -P_1 \end{pmatrix}$	$\begin{pmatrix} P_1 & -P_1 & P_1 \\ -P_1 & P_1 & -P_1 \end{pmatrix}$	$\begin{pmatrix} -P_1 & P_1 & -P_1 \\ P_1 & -P_1 & P_1 \end{pmatrix}$	$\begin{pmatrix} -P_1 & P_1 & -P_1 \\ P_1 & -P_1 & P_1 \end{pmatrix}$

Table D.30 (continued)
 $m\bar{3}m \rightarrow \bar{3}_{xyz}m_{xy}(P=0)$, $m\bar{3}m \rightarrow 3_{xyz}m_{xy}$, $m\bar{3}m \rightarrow 3_{xyz}2_{xy}(P=0)$, $m\bar{3}m \rightarrow \bar{3}_{xyz}(P=0)$, $m\bar{3}m \rightarrow 3_{xyz}$; $432 \rightarrow 3_{xyz}2_{xy}(P=0)$,
 $432 \rightarrow 3_{xyz}$ (above diagonal); $43m \rightarrow 3_{xyz}m_{xy}$, $43m \rightarrow 3_{xyz}$; $m\bar{3} \rightarrow 3_{xyz}$, $m\bar{3} \rightarrow \bar{3}_{xyz}(P=0)$, $m\bar{3} \rightarrow 3_{xyz}$, $23 \rightarrow 3_{xyz}$ (below diagonal)

S	1	2	3	4
1	N/A	(100) ^C (011) ^N	(001) ^N (110) ^C	(010) ^C (101) ^N
2	(100) ^N (011) ^C	N/A	(010) ^C (101) ^N	(001) ^N (110) ^C
3	(001) ^N (110) ^C	(010) ^N (101) ^C	N/A	(100) ^C (011) ^N
4	(010) ^N (101) ^C	(001) ^N (110) ^C	(100) ^N (011) ^C	N/A

Appendix E

Piezoelectric Coefficients in Ferroelectric Phases of BaTiO₃-Type Perovskites

Tables of this appendix give the d-piezoelectric coefficients in ferroelectric phases of BaTiO₃-type perovskites calculated as a result of linearization of the electrostrictive equation. Rows stand for domain states (DS) represented in Fig. 2.3.5. Piezoelectric coefficients are related to the cubic coordinate system. The meaning of symbols a, b, c, d, and e in each phase is shown below each table.

Table E.1 Tetragonal phase (species $m\bar{3}m-4mm$)

DS	P_S	d_{11}	d_{12}	d_{13}	d_{15}	d_{16}	d_{21}	d_{22}	d_{23}	d_{24}	d_{26}	d_{31}	d_{32}	d_{33}	d_{34}	d_{35}
1	100	c	b	b	0	0	0	0	0	0	a	0	0	0	0	a
2	$\bar{1}00$	-b	-c	-b	0	0	0	0	0	0	-a	0	0	0	0	-a
3	010	0	0	0	0	a	b	c	b	0	0	0	0	0	a	0
4	0 $\bar{1}0$	0	0	0	0	-a	-b	-c	-b	0	0	0	0	0	-a	0
5	001	0	0	0	a	0	0	0	0	a	0	b	b	c	0	0
6	00 $\bar{1}$	0	0	0	-a	0	0	0	0	-a	0	-b	-b	-c	0	0

- a = $2Q_{44}P_S\chi_{33}$
- b = $2Q_{12}P_S\chi_{11}$
- c = $2Q_{11}P_S\chi_{11}$

Components of the permittivity correspond to the matrix of permittivity for DS-1 given below

$$\begin{pmatrix} \chi_{11} & & \\ & \chi_{33} & \\ & & \chi_{33} \end{pmatrix}$$

Table E.2 Orthorhombic phase (species $m\bar{3}m-mm2$)

DS	P_S	d_{11}	d_{12}	d_{13}	d_{15}	d_{16}	d_{21}	d_{22}	d_{23}	d_{24}	d_{26}	d_{31}	d_{32}	d_{33}	d_{34}	d_{35}
1	$\bar{1}10$	d	c	b	0	e	c	d	b	0	e	0	0	0	a	a
2	$\bar{1}\bar{1}0$	-d	-c	-b	0	-e	-c	-d	-b	0	-e	0	0	0	-a	-a
3	$\bar{1}\bar{1}0$	d	c	b	0	-e	-c	-d	-b	0	e	0	0	0	-a	a
4	$\bar{1}10$	-d	-c	-b	0	e	c	D	b	0	-e	0	0	0	a	-a
5	011	0	0	0	a	a	b	D	c	e	0	b	c	d	e	0
6	0 $\bar{1}\bar{1}$	0	0	0	-a	-a	-b	-d	-c	-e	0	-b	-c	-d	-e	0
7	01 $\bar{1}$	0	0	0	-a	a	b	D	c	-e	0	-b	-c	-d	e	0
8	10 $\bar{1}$	0	0	0	a	-a	-b	-d	-c	e	0	b	c	d	-e	0
9	101	d	b	c	e	0	0	0	0	a	a	c	b	d	0	e
10	$\bar{1}0\bar{1}$	-d	-b	-c	-e	0	0	0	0	-a	-a	-c	-b	-d	0	-e
11	$\bar{1}01$	-d	-b	-c	e	0	0	0	0	a	-a	c	b	d	0	-e
12	10 $\bar{1}$	d	b	c	-e	0	0	0	0	-a	a	-c	-b	-d	0	e

$$a = \sqrt{2} Q_{44} P_S \chi_{11}$$

$$b = \sqrt{2} Q_{12} P_S (\chi_{33} + \chi_{23})$$

$$c = \sqrt{2} P_S (Q_{12} \chi_{33} + Q_{11} \chi_{23})$$

$$d = \sqrt{2} P_S (Q_{11} \chi_{33} + Q_{12} \chi_{23})$$

$$e = \sqrt{2} Q_{44} P_S (\chi_{33} + \chi_{23})$$

Components of the permittivity correspond to the matrix of permittivity for DS-5 given below

$$\begin{pmatrix} \chi_{11} & & & \\ & \chi_{33} & \chi_{33} & \\ & \chi_{33} & \chi_{33} & \\ & & & \chi_{33} \end{pmatrix}$$

Table E.3 Rhombohedral phase (species $m\bar{3}m-3m$)

DS	P_S	d_{11}	d_{12}	d_{13}	d_{14}	d_{15}	d_{16}	d_{21}	d_{22}	d_{23}	d_{24}	d_{25}	d_{26}	d_{31}	d_{32}	d_{33}	d_{34}	d_{35}	d_{36}	
1	111	a	b	b	d	c	c	B	a	b	c	d	c	b	b	a	c	c	c	d
2	$\bar{1}\bar{1}\bar{1}$	-a	b	-b	-d	-c	-c	-b	-a	-b	-c	-d	-c	-b	-b	-a	-c	-c	-c	-d
3	11 $\bar{1}$	a	b	b	-d	-c	c	B	a	b	-c	-d	c	-b	-b	-a	c	c	c	-d
4	$\bar{1}\bar{1}\bar{1}$	-a	-b	-b	d	c	-c	-b	-a	-b	c	d	-c	b	b	a	-c	-c	-c	d
5	11 $\bar{1}$	a	b	b	-d	c	-c	-b	-a	-b	c	-d	c	b	b	a	-c	c	c	-d
6	$\bar{1}\bar{1}\bar{1}$	-a	-b	-b	d	-c	c	B	a	b	-c	d	-c	-b	-b	-a	c	-c	-c	d
7	11 $\bar{1}$	-a	-b	-b	-d	c	c	B	a	b	c	-d	-c	b	b	a	c	c	-c	-d
8	$\bar{1}\bar{1}\bar{1}$	a	b	b	d	-c	-c	-b	-a	-b	-c	d	c	-b	-b	-a	-c	-c	c	d

$$a = (2/\sqrt{3}) P_S (Q_{11} \chi_{11} + 2Q_{12} \chi_{12})$$

$$b = (2/\sqrt{3}) P_S [(Q_{12} \chi_{11} + (Q_{12} + Q_{11}) \chi_{12})]$$

$$c = (2/\sqrt{3}) P_S Q_{44} (\chi_{11} + \chi_{12})$$

$$d = (4/\sqrt{3}) P_S Q_{44} \chi_{12}$$

Components of the permittivity correspond to the matrix of permittivity for DS-1 given below

$$\begin{pmatrix} \chi_{11} & \chi_{12} & \chi_{12} \\ \chi_{12} & \chi_{11} & \chi_{12} \\ \chi_{12} & \chi_{12} & \chi_{11} \end{pmatrix}$$

Appendix F

Tensors: Properties and Notations

Transformation Laws for Tensors

Transformation law for a second-rank tensor:

$$T'_{ip} = a_{ij}a_{pq}T_{jq}.$$

Transformation law for an n th-rank tensor:

$$M'_{\frac{ij\dots pt}{n}} = \frac{a_{ii'}a_{jj'}\dots a_{pp'}a_{tt'}}{n} M_{\frac{ij\dots pt}{n}}.$$

Here n under the lines indicate the number of a 's in the product or total number of suffices. Summation over repeated (dummy) suffices from 1 to 3 is implied (Einstein convention). The tensor in the original orthogonal reference frame ($X_1 X_2 X_3$) is written without the prime. The tensor in the transformed orthogonal reference frame ($X'_1 X'_2 X'_3$) is written with the prime. The table of the direction cosines for transformation of the reference frame ($X_1 X_2 X_3$) \Rightarrow ($X'_1 X'_2 X'_3$) is denoted as

$$a_{ij} = \cos(X'_i \wedge X_j).$$

Transformation law for an n th-rank pseudotensor:

$$M'_{\frac{ij\dots pt}{n}} = \frac{a_{ii'}a_{jj'}\dots a_{pp'}a_{tt'}}{n} M_{\frac{ij\dots pt}{n}} \det(a)$$

Voigt Notations for Tensors

Stress vector: $\sigma_n = (\sigma_{11} \ \sigma_{22} \ \sigma_{33} \ \sigma_{23} \ \sigma_{13} \ \sigma_{12})$

Strain vector: $\varepsilon_n = (\varepsilon_{11} \ \varepsilon_{22} \ \varepsilon_{33} \ 2\varepsilon_{23} \ 2\varepsilon_{13} \ 2\varepsilon_{12})$

Hook's law: $\sigma_n = s_{nm}\varepsilon_m$ and $\varepsilon_n = s_{nm}\sigma_m$ with the summation over dummy suffices: $n, m = 1 - 6$.

Stiffness and compliance symmetric matrices:

$$c_{mn} = \begin{pmatrix} c_{1111} & c_{1122} & c_{1131} & c_{1123} & c_{1113} & c_{1112} \\ & c_{2222} & c_{2233} & c_{2223} & c_{2213} & c_{2212} \\ & & c_{3333} & c_{3323} & c_{3313} & c_{3312} \\ & & & c_{2323} & c_{2313} & c_{2312} \\ & & & & c_{1313} & c_{1312} \\ & & & & & c_{1212} \end{pmatrix},$$

$$s_{mn} = \begin{pmatrix} s_{1111} & s_{1122} & s_{1131} & 2s_{1123} & 2s_{1113} & 2s_{1112} \\ & s_{2222} & s_{2233} & 2s_{2223} & 2s_{2213} & 2s_{2212} \\ & & s_{3333} & 2s_{3323} & 2s_{3313} & 2s_{3312} \\ & & & 4s_{2323} & 4s_{2313} & 4s_{2312} \\ & & & & 4s_{1313} & 4s_{1312} \\ & & & & & 4s_{1212} \end{pmatrix}.$$

Direct and converse piezoelectric effects: $P_i = d_{in}\sigma_n$ and $\varepsilon_n = d_{in}E_i$, with the summation over dummy suffices: $n = 1 - 6$, $i = 1 - 3$.

Matrix of piezoelectric d -coefficients:

$$d_{in} = \begin{pmatrix} d_{111} & d_{122} & d_{133} & 2d_{123} & 2d_{113} & 2d_{112} \\ d_{211} & d_{222} & d_{233} & 2d_{223} & 2d_{213} & 2d_{212} \\ d_{311} & d_{322} & d_{333} & 2d_{323} & 2d_{313} & 2d_{312} \end{pmatrix}.$$

Notation for Symmetry of Tensors

$[V^2]$ – symmetric second-rank tensor: $q_{ij} = q_{ji}$.

$\{V^2\}$ – antisymmetric second-rank tensor: $q_{ij} = -q_{ji}$.

V^2 – second-rank tensor.

$\varepsilon[V^2]$ – symmetric second-rank pseudotensor: $q_{ij} = q_{ji}$.

$\varepsilon\{V^2\}$ – antisymmetric second-rank pseudotensor: $q_{ij} = -q_{ji}$.

εV^2 – second-rank pseudotensor.

$[V^3]$ – third-rank tensor symmetric with respect to all indices.

$V[V^2]$ – third-rank tensor symmetric with respect to two indices: $q_{ijk} = q_{ikj}$.

$\{V^2\}V$ – third-rank tensor antisymmetric with respect to two indices:

$$q_{ijk} = -q_{jik}.$$

V^3 – third-rank tensor.

$\varepsilon V[V^2]$ – third-rank pseudotensor symmetric with respect to two indices:

$$q_{ijk} = q_{ikj}.$$

$\varepsilon\{V^2\}V$ – third-rank pseudotensor antisymmetric with respect to two indices: $q_{ijk} = -q_{jik}$.

- $[V^4]$ – fourth-rank tensor symmetric with respect to all indices.
 $V[V^3]$ – fourth-rank tensor symmetric with respect to the last three indices.
 $[[V^2]^2]$ – fourth-rank tensor symmetric with respect to two pairs of indices under permutations: $q_{ijkl} = q_{jikl} = q_{ijlk} = q_{klij}$.
 $[(V^2)]^2$ – fourth-rank tensor symmetric with respect to the permutations of the pairs of indices: $q_{ijkl} = q_{klij}$.
 $\{V^2 V^2\}$ – fourth-rank tensor antisymmetric with respect to the permutations of the pairs of indices: $q_{ijkl} = -q_{klij}$.
 $[V^2]V^2$ – fourth-rank tensor symmetric with respect to two indices: $q_{ijkl} = q_{jikl}$.
 V^4 – fourth-rank tensor.

References

- Abboud, B., Le Bihan, R., Michelet, A., M'Bama, F., Hilczer, B., *Ferroelectrics* **140**, 45 (1993)
- Abe, R., *J. Phys. Soc. Jpn.* **13**, 244 (1958)
- Abe, R., *Jpn. J. Appl. Phys.* **3**, 243 (1964)
- Abe, K., *J. Phys. Soc. Jpn.* **56**, 757 (1987)
- Abe, K., Komatsu, S., Yanase, N., Sano, K., Kawakubo, T., *Jpn. J. Appl. Phys.* **36**, 5846 (1997)
- Abe, K., Yanase, N., Kawakubo, T., *Jpn. J. Appl. Phys.* **39**, 4059 (2000)
- Abe, K., Yanase, N., Yasamoto, T., Kawakubo, T., *J. Appl. Phys.* **91**, 323 (2002)
- Abplanalp, M., Eng, L.M., Günter, P., *Appl. Phys. A* **66**, S231 (1998)
- Afonikova, N.S., Shmyt'ko, I.M., Shekhtman, V.Sh., *Izvestiya Akad. Nauk SSSR, ser. fiz.* **43**, 1611 (1979)
- Afonikova, N.S., Borovikov, V.V., Shmyt'ko, I.M., *Sov. Phys. Solid State* **29**, 462 (1987)
- Agranovich, V.M., Ginzburg, V.L., *Crystal Optics with Accounting for Spatial Dispersion and the Theory of Excitons*. Nauka, Moscow (1979)
- Agronin, A., Rosenwaks, Y., Rosenman, G., *Appl. Phys. Lett.* **85**, 452 (2004)
- Ahluwalia, R., Cao, W., *Ferroelectrics* **251**, 191 (2001)
- Ahluwalia, R., Cao, W., *J. Appl. Phys.* **93**, 537 (2003)
- Ahn, C.H., Tybell, T., Antognazza, L., Char, K., Hammond, R.H., Beasley, M.R., Fischer, O., Triscone, J.-M., *Science* **276**, 1100 (1997)
- Aizu, K., *Phys. Rev.* **140**, A590 (1965)
- Aizu, K., *Phys. Rev.* **146**, 423 (1966)
- Aizu, K., *J. Phys. Soc. Jpn.* **27**, 387 (1969)
- Aizu, K., *J. Phys. Soc. Jpn.* **28**, 706 (1970a)
- Aizu, K., *Phys. Rev. B* **2**, 754 (1970b)
- Aizu, K., *J. Phys. Soc. Jpn.* **32**, 1287 (1972)
- Aizu, K., *J. Phys. Soc. Jpn.* **35**, 180 (1973a)
- Aizu, K., *J. Phys. Soc. Jpn.* **34**, 121 (1973b)
- Akaba, N., Suzuki, S., Takagi, M., *J. Phys. Soc. Jpn.* **46**, 1583 (1979)
- Akbaz, M.A., Davies, P.K., *J. Am. Ceram. Soc.* **80**, 2933 (1997)
- Aknazarov, S.Kh., Shabel'nikov, L.G., Shekhtman, V.Sh., *Sov. Phys. Solid State* **17**, 16 (1975)
- Al-Shareef, H.N., Tuttle, B.A., Warren, W.L., Headley, T.J., Dimos, D., Voigt, J.A., Nasby, R.D., *J. Appl. Phys.* **79**, 1013 (1996)
- Aleshko-Ozhevskij, O.P., *Ferroelectrics* **48**, 157 (1983)
- Aleshko-Ozhevskij, O.P., Bowen, D.K., Davies, S.T., *Ferroelectrics* **62**, 53 (1985)
- Alexe, M., Gruverman, A. (eds.): *Ferroelectrics at Nanoscale: Scanning Probe Microscopy Approach*. Springer, New York (2004)
- Alexe, M., Harnagea, C., Hesse, D., Gösele, U., *Appl. Phys. Lett.* **79**, 242 (2001)
- Alpay, S.P., Prakash, A.S., Aggarwal, S., Ramesh, R., Roytburd, A.L., Shuk, P., Greenblatt, M., Polydomain structure of epitaxial PbTiO₃ films on MgO, in *Ferroelectric Thin Films*

- VI, edited by Treece, R.E., Jones, R.E., Foster, C.M., Desu, S.B., Yoo, I.K. (Mater. Res. Soc. Symp. Proc. **Volume 493**, p. 111, Warrendale, PA, 1998)
- Alpay, S.P., Nagarajan, V., Bendersky, L.A., Vaudin, M.D., Aggarwal, S., Ramesh, R., Roytburd, A.L., J., Appl. Phys. **85**, 3271 (1999)
- Alpay, S.P., Roytburd, A.L., J. Appl. Phys. **83**, 4714 (1998)
- Amin, A., Newnham, R.E., Phys. Stat. Sol. (a) **61**, 215 (1980)
- Anderson, J.R., Brady, G.W., Merz, W.J., Remeika, J.P., J. Appl. Phys. **26**, 1387 (1955)
- Anderson, T.L., Newnham, R.E., Cross, L.E., Laughner, J.W., Phys. Stat. Sol. (a) **37**, 235 (1976)
- Andrews, S.R., Cowley, R.A., J. Phys. C Solid State Phys. **19**, 615 (1986)
- Anisimova, V.N., Filippov, M.N., Shuvalov, L.A., JETP Lett. **40**, 873 (1984)
- Antoshin, M.K., Spivak, G.V., Izvestiya Akad. Nauk SSSR, ser. fiz. **36**, 1901 (1972)
- Aoyama, J., Suzuki, S., Takagi, M., J. Phys. Soc. Jpn. **61**, 3613 (1992)
- Aristov, V.V., Kokhanchik, L.S., Meyer, K.-P., Blumtritt, H., Phys. Stat. Sol. (a) **78**, 229 (1983)
- Aristov, V.V., Kokhanchik, L.S., Voronovskii, Yu.I., Phys. Stat. Sol. (a) **86**, 133 (1984)
- Arlt, G., J. Mater. Sci. **25**, 2655 (1990)
- Arlt, G., Sasko, P., J. Appl. Phys. **51**, 4956 (1980)
- Auciello, O., Gifford, K.D., Lichtenwalner, D.J., Dat, R., Al-Shareef, H.N., Bellur, K.R., Kingon, A., Integr. Ferroelectr. **6**, 173 (1995)
- Auciello, O., Gruverman, A., Tokumoto, H., Integr. Ferroelectr. **15**, 107 (1997)
- Avakyants, L.P., Kiselev, D.F., Chervyakov, A.V., Sov. Phys. Solid State **138**, 138 (1985)
- Averty, D., Le Bihan, R., Ferroelectrics **140**, 17 (1993)
- Avrami, M., J. Chem. Phys. **8**, 212 (1940)
- Ayroles, R., Torres, J., Aubree, J., Roucau, C., Tanaka, M., Appl. Phys. Lett. **34**, 4 (1979)
- Baginskii, I.L., Kostsov, E.G., Phys. Stat. Sol. **91**, 705 (1985)
- Bah, I.S., Balyunis, L.E., Topolov, V.Yu., Fesenko, O.E., Ferroelectrics **152**, 237 (1994)
- Balagurov, A.M., Beskrovnyi, A.I., Datt, I.D., Shuvalov, L.A., Schagina, N.M., Kristallografiya **31**, 1087 (1986)
- Balashova, E.V., Tagantsev, A.K., Phys. Rev. B **48**, 9979 (1993)
- Balyunis, L.E., Topolov, V.Yu., Bah, I.S., Turik, A.V., J. Phys. Condens. Matter **5**, 1419 (1993)
- Barad, Y., Lettieri, J., Theis, C.D., Schlom, D.G., Gopalan, V., J. Appl. Phys. **89**, 1387 (2001)
- Barkla, H.M., Finlayson, D.M., Philos. Mag. **44**, 109 (1953)
- Barkley, J.R., Jeitschko, W., J. Appl. Phys. **44**, 938 (1973)
- Baron, C., Cheng, H., Gupta, M.C., Appl. Phys. Lett. **68**, 481 (1996)
- Barrett, R.C., Quate, C.F., J. Appl. Phys. **70**, 2725 (1991)
- Barsch, G.R., Krumhansl, J.A., Phys. Rev. Lett. **53**, 1069 (1984)
- Bartich, A.T., Wouters, D.J., Maes, H.E., Ricketts, J.T., Waser, R., J. Appl. Phys. **89**, 3420 (2001)
- Basceri, C., Streiffer, S.K., Kingon, A.I., Waser, R., J. Appl. Phys. **82**, 2497 (1997a)
- Basceri, C., Streiffer, S.K., Kingon, A.I., Waser, R., J. Appl. Phys. **82**, 2505 (1997b)
- Bastie, P.M., Bornarel, J., J. Phys. C Solid State Phys. **12**, 1785 (1979)
- Bastie, P., Bornarel, J., Lajzerowicz, J., Schneider, J.R., Ferroelectrics **14**, 587 (1976)
- Bastie, P., Bornarel, J., Dolino, G., Vallade, M., Ferroelectrics **26**, 789 (1980)
- Batra, I.P., Silverman, B.D., Solid State Commun. **11**, 291 (1972)
- Bell, A.J., Cross, L.E., Ferroelectrics **59**, 197 (1984)
- Bernstein, S., Wong, T., Kisler, Y., Tustison, R., J. Mater. Res. **8**, 12 (1993)
- Bertagnolli, E., Kittinger, E., Tichy, J., J. Appl. Phys. **50**, 6267 (1979)
- Betzig, E., Trautman, J.K., Science **257**, 189 (1992)
- Beudon, D., Le Bihan, R., Jpn. J. Appl. Phys. Suppl. **24-2**, 548 (1985)
- Beudon, D., Le Bihan, R., Lompere, P., Godefroy, G., Ferroelectrics **81**, 111 (1988)
- Bhalla, A., Cross, L.E., J. Mater. Sci. Lett. **12**, 2346 (1977)
- Bhalla, A.S., Cross, L.E., Ferroelectrics **36**, 403 (1981)
- Bhide, V.G., Bapat, N.J., J. Appl. Phys. **34**, 181 (1963)
- Bhide, V.G., Chilmulgund, N.D., Indian J. Pure Appl. Phys. **3**, 253 (1965)

- Biedrzycki, K., Hajir, D., Le Bihan, R., *Ferroelectrics* **140**, 253 (1993)
- Bierlein, J.D., Ahmed, F., *Appl. Phys. Lett.* **51**, 1322 (1987)
- Biletskii, I.N., Vlokh, R.O., Otko, A.I., Shopa, Y.I., *Ukrainskii Fizicheskii Zhurnal* **33**, 689 (1988)
- Binggeli, B., Fatuzzo, E., *J. Appl. Phys.* **36**, 1431 (1965)
- Bittel, H., Müser, H.E., Berndes, G., *Untersuchungen über ferroelektrische Domänenwände und Nachwirkungserscheinungen*. Westdeutscher Verlag, Köln und Opladen (1968)
- Bjorkstam, J.L., Oettel, R.E., *Proceedings of the International Meeting on Ferroelectricity*, Prague 1966, vol. II, p. 91 (1966)
- Bjorkstam, J.L., Oettel, R.E., *Phys. Rev.* **159**, 427 (1967)
- Blank, H., Amelinckx, S., *Appl. Phys. Lett.* **2**, 140 (1963)
- Blatter, G., Feigelman, M.V., Geshkenbein, V.B., Larkin, A.I., Vinokur, V.M., *Rev. Mod. Phys.* **66**, 1125 (1994)
- Blinov, L.M., Barberi, R., Palto, S.P., *J. Appl. Phys.* **89**, 3960 (2001)
- Blistanov, A.A., Geras'kin, V.V., Stepanova, A.V., Puchkova, M.V., Sorokin, N.G., *Sov. Phys. Solid State* **26**, 684 (1984)
- Bloss, F.D., *An Introduction to the Methods of Optical Crystallography*. Holt, Rinehart and Winston, New York (1961)
- Bloss, F.D., *Crystallography and Crystal Chemistry: An Introduction*. Holt, New York (1971)
- Bluhm, H., Schwarz, U.D., Meyer, K.-P., Wiesendanger, R., *Appl. Phys. A* **61**, 525 (1995)
- Bluhm, H., Wiesendanger, R., Meyer, K.-P., *J. Vac. Sci. Technol. B* **14**, 1180 (1996)
- Bluhm, H., Wadas, A., Wiesendanger, R., Roshko, A., Aust, J.A., Nam, D., *Appl. Phys. Lett.* **71**, 146 (1997)
- Bluhm, H., Schwarz, U.D., Wiesendanger, R., *Phys. Rev. B* **57**, 161 (1998)
- Blumberg, H., Kürsten, H.D., *Kristall und Technik* **14**, 985 (1979)
- Blushakova, N.N., Nekrasova, G.M., Rudyak, V.M., *Ferroelectrics* **97**, 227 (1989)
- Bond, W.L., *Zeitschrift für Kristallographie* **99**, 488 (1938)
- Bonnell, D.A. (ed.): *Scanning Probe Microscopy and Spectroscopy: Theory, Techniques, and Applications*. John Wiley & Sons (2000)
- Bornarel, J., *J. Appl. Phys.* **43**, 845 (1972)
- Bornarel, J., *Ferroelectrics* **9**, 197 (1975)
- Bornarel, J., *Ferroelectrics* **71**, 255 (1987)
- Bornarel, J., *Phase Transitions* **34**, 147 (1991)
- Bornarel, J., *Ferroelectrics* **172**, 53 (1995)
- Bornarel, J., Bastie, P., *J. Phys. C Solid State Phys.* **13**, 5843 (1980)
- Bornarel, J., Cach, R., *J. Phys. Condens. Matter* **5**, 2977 (1993)
- Bornarel, J., Lajzerowicz, J., *J. Appl. Phys.* **39**, 4339 (1968)
- Bornarel, J., Lajzerowicz, J., *J. Phys. Soc. Jpn. Suppl.* **28**, 360 (1970)
- Bornarel, J., Lajzerowicz, J., *J. Phys. Colloq. C2* **33 Suppl. 4**, C2-153 (1972a)
- Bornarel, J., Lajzerowicz, J., *Ferroelectrics* **4**, 177 (1972b)
- Bornarel, J., Legrand, J.F., *Ferroelectrics* **39**, 1127 (1981)
- Bornarel, J., Fousek, J., Glogarová, M., *Czech. J. Phys. B* **22**, 864 (1972)
- Bornarel, P., Fousková, A., Guyon, P., Lajzerowicz, J., *Proceedings of the International Meeting on Ferroelectricity*, Prague 1966, vol. II, p. 81 (1966)
- Bornarel, J., Cach, R., Kvitek, Z., *Ferroelectrics* **236**, 117 (2000)
- Borodina, V.A., Kuznetsov, V.G., *Izvestiya Akad. Nauk SSSR, ser. fiz.* **48**, 1146 (1984)
- Boser, O., *J. Appl. Phys.* **62**, 1344 (1987)
- Boulestix, C., Yangui, B., Ben Salem, M., Manolikas, C., Amelinckx, S., *J. Phys. Paris* **47**, 461 (1986)
- Bradt, R.C., Ansell, G.S., *J. Appl. Phys.* **38**, 5407 (1967)
- Bradt, R.C., Ansell, G.S., *IEEE Trans. Electron. Devices* **16**, 594 (1969)
- Bratkovsky, A.M., Levanyuk, A.P., *Phys. Rev. Lett.* **84**, 3177 (2000a)
- Bratkovsky, A.M., Levanyuk, A.P., *Phys. Rev. B* **61**, 15042 (2000b)

- Bratkovsky, A.M., Levanyuk, A.P., *Phys. Rev. Lett.* **86**, 3642 (2001a)
- Bratkovsky, A.M., Levanyuk, A.P., *Phys. Rev. B* **64**, 134107 (2001b)
- Bratkovsky, A.M., Levanyuk, A.P., *Phys. Rev. B* **63**, 132103 (2001c)
- Bratkovsky, A.M., Levanyuk, A.P., *Appl. Phys. Lett.* **89**, 253108 (2006)
- Bratkovsky, A.M., Levanyuk, A.P., *Phys. Rev. Lett.* **100**, 149701 (2008)
- Bratkovsky, A.M., Marais, S.C., Heine, V., Salje, E.K.H., *J. Phys. Condens. Matter* **6**, 3679 (1994)
- Braun, T., Kleemann, W., Dec, J., Thomas, P.A., *Phys. Rev. Lett.* **94**, 117601 (2005)
- Brazier, M., Mansour, S., McElfresh, M., *Appl. Phys. Lett.* **74**, 4032 (1999)
- Brazovskii, S., Nattermann, T., *Adv. Phys.* **53**, 177 (2004)
- Brennan, C.J., *Ferroelectrics* **132**, 245 (1992a)
- Brennan, C.J., *Integr. Ferroelectr.* **2**, 73 (1992b)
- Brennan, C.J., *Integr. Ferroelectr.* **7**, 93 (1995)
- Brezina, B., Fotcenkov, A.A., *Czech. J. Phys. B* **14**, 21 (1964)
- Brezina, B., Havránková, M., *Cryst. Res. Technol.* **20**, 787 (1985)
- Brezina, B., Fousek, J., Glanc, A., *Czech. J. Phys. B* **11**, 595 (1961)
- Brennan, C.J., Parrella, R.D., Larsen, D.E., *Ferroelectrics* **151**, 33 (1994)
- Brixner, L.H., Bierstedt, P.E., Jaep, W.F., Barkley, J.R., *Mater. Res. Bull.* **8**, 497 (1973)
- Bruce, D.A., *J. Phys. C Solid State Phys.* **14**, 5195 (1981)
- Buhlmann, S., Dwir, B., Baborowski, J., Muralt, P., *Appl. Phys. Lett.* **80**, 3195 (2002)
- Bulaevskii, L.N., *Sov. Phys. Solid State* **5**, 2329 (1964)
- Bulaevskii, L.N., Ginzburg, V.L., *Sov. Phys. JETP* **18**, 530 (1964)
- Bulaevskii, L.N., Vekhter, B.G., *Sov. Phys. JETP* **64**, 851 (1986)
- Bullbich, A.A., Gufan, Yu.M., *Ferroelectrics* **98**, 277 (1989)
- Bune, A.V., Fridkin, V.M., Ducharme, S., Blinov, L.M., Palto, S.P., Sorokin, A.V., Yudin, S.G., Zlatkin, A., *Nature* **391**, 874 (1998)
- Burfoot, J.C., *Proc. Phys. Soc.* **73**, 641 (1959)
- Burfoot, J.C., Latham, R.V., *Br. J. Appl. Phys.* **14**, 933 (1963)
- Burfoot, J.C., Taylor, G.W., *Polar Dielectrics and their Applications*. The Macmillan Press Ltd., London (1979)
- Bursill, L.A., Peng, J.L., *Nature* **311**, 550 (1984)
- Bursill, L.A., Peng J.L., *Ferroelectrics* **70**, 191 (1986)
- Bursill, L.A., Peng J.L., Feng, D., *Philos. Mag.A* **48**, 953 (1983)
- Bursill, L.A., Lin, P.J., "High resolution electron microscopy of electronic ceramic material" in *Electronic Ceramic Materials*, edited by Nowotny, J. (Trans-Tech Publications, pp. 421–460, 1992)
- Burtsev, E.V., Chervonobrodov, S.P., *Ferroelectrics* **45**, 97 (1982)
- Busch, G., Scherrer, P., *Naturwissenschaften* **23**, 737 (1935)
- Bush, A.A., Venevtsev, Yu.N., *Fizika tverdogo tela* **28**, 1970 (1986)
- Cady, W.G., *Piezoelectricity*. McGraw-Hill, New York (1946)
- Cahn, R.W., *Adv. Phys.* **3**, 363 (1954)
- Cahn, J.W., *Acta Metallur.* **8**, 554 (1960)
- Callaby, D.R., *J. Appl. Phys.* **36**, 2751 (1965)
- Callaby, D.R., *J. Appl. Phys.* **38**, 431 (1967)
- Cameron, D.P., *IBM J. Res. Develop.* **1**, 2 (1957)
- Campbell, D.S., *J. Electron. Control* **3**, 330 (1957)
- Campbell, D.S., *Philos. Mag.* **7**, 1157 (1962)
- Cantoni, M., Bharadwaja, S., Gentil, S., Setter, N., *J. Appl. Phys.* **96**, 3870 (2004)
- Cao, W., Barsch, G.R., *Phys. Rev. B* **41**, 4334 (1990)
- Cao, W., Cross, L.E., *Phys. Rev. B* **44**, 5 (1991)
- Cao, W., Cross, L.E., *Ferroelectrics* **157**, 19 (1994)
- Cao, W., Randall, C., *Solid State Commun.* **86**, 435 (1993)
- Cao, W., Barsch, G.R., Krumhansl, J.A., *Phys. Rev. B* **42**, 6396 (1990)
- Cao, W., Tavener, S., Xie, S., *J. Appl. Phys.* **86**, 5739 (1999)

- Capelle, B., Malgrange, C., *J. Appl. Phys.* **53**, 6762 (1982)
- Capelle, B., Epelboin, Y., Malgrange, C., *J. Appl. Phys.* **53**, 6767 (1982)
- Carl, K., Härdtl, K.H., *Ferroelectrics* **17**, 473 (1978)
- Castellanos-Guzmán, A.G., Campa-Molina, J., Reyes-Gomez, J., *Ferroelectrics* **172**, 151 (1995)
- Cáslavský, J., Polcarová, M., *Czech. J. Phys. B* **14**, 454 (1964)
- Cáslavský, J., Polcarová, M., *Czech. J. Phys. B* **15**, 372 (1965)
- Chabin, M., Ildefonse, J.P., Gilletta, F., *Ferroelectrics* **13**, 333 (1976)
- Chabin, M., Gilletta, F., Ildefonse, J.P., *J. Appl. Cryst.* **10**, 247 (1977)
- Chaikin, P.M., Lubensky, T.C.: *Principles of Condensed Matter Physics*. Cambridge University Press (1995)
- Chakrabarti, B.K., Acharyya, M., *Rev. Mod. Phys.* **71**, 847 (1999)
- Chaudhari, R.M., Krishnakumar, R., *Ferroelectrics* **97**, 255 (1989)
- Chen, J., Zhou, Q., Hong, J.-F., Wang, W.-S., Ming, N.-B., Feng, D., Fang, C.-G., *J. Appl. Phys.* **66**, 336 (1989)
- Chen, L., Ouyang, J., Ganpule, C.S., Nagarajan, V., Ramesh, R., Roytburd, A.L., *Appl. Phys. Lett.* **84**, 254 (2004)
- Chenskii, E.V., *Fizika tverdogo tela* **14**, 2241 (1972)
- Chenskii, E.V., Tarasenko, V.V., *Zh. Eksp. Teor. Fiz.* **83**, 1089 (1982)
- Chensky, E.V., Tarasenko, V.V., *Sov. Phys. JETP* **56**, 521 (1982)
- Chervonobrodov, S.P., Roytburd, A.L., *Ferroelectrics* **83**, 109 (1988)
- Cho, Y., Ohara, K., *Appl. Phys. Lett.* **79**, 3842 (2001)
- Cho, Y., Atsumi, S., Nakamura, K., *Jpn. J. Appl. Phys.* **36**, 3152 (1997a)
- Cho, Y., Kiriwara, A., Saeki, T., *Jpn. J. Appl. Phys.* **36**, 360 (1997b)
- Cho, Y., Kazuta, S., Matsuura, K., *Appl. Phys. Lett.* **75**, 2833 (1999)
- Cho, Y., Fujimoto, K., Hiranaga, Y., Wagatsuma, Y., Onoe, A., Terabe, K., Kitamura, K., *Appl. Phys. Lett.* **81**, 4401 (2002)
- Choi, W.K., Choi, S.K., Lee, H.M., *J. Korean Phys. Soc.* **32**, S1694 (1998)
- Chrosch, J., Salje, E.K.H., *Physica C* **225**, 111 (1994)
- Chrosch, J., Salje, E.K.H., *J. Appl. Phys.* **85**, 722 (1999)
- Chynoweth, A.G., *Phys. Rev.* **102**, 705 (1956)
- Chynoweth, A.G., *Phys. Rev.* **110**, 1316 (1958)
- Chynoweth, A.G., *Phys. Rev.* **113**, 159 (1959)
- Chynoweth, A.G., *Phys. Rev.* **117**, 1235 (1960)
- Chynoweth, A.G., Abel, J.L., *J. Appl. Phys.* **30**, 1615 (1959a)
- Chynoweth, A.G., Abel, J.L., *J. Appl. Phys.* **30**, 1073 (1959b)
- Chynoweth, A.G., Feldmann, W.L., *J. Phys. Chem. Solids* **15**, 225 (1960)
- Cillessen, J.F.M., Prins, M.W.J., Wolf, R.M., *J. Appl. Phys.* **81**, 2777 (1977)
- Clay, W., Evans, B.J., Latham, R.V., *J. Phys. D Appl. Phys.* **7**, 1291 (1974)
- Colla, E.L., Hong, S., Taylor, D.V., Tagantsev, A.K., Setter, N., *Appl. Phys. Lett.* **72**, 2763 (1998a)
- Colla, E.L., Tagantsev, A.K., Taylor, D., Kholkin, A.L., *J. Korean Phys. Soc. (Proc. Suppl.)* **32**, S1353 (1998b)
- Colla, E.L., Tagantsev, A.K., Taylor, D.V., Kholkin, A.L., *Integr. Ferroelectr.* **18**, 19 (1997)
- Colla, E.L., Taylor, D.V., Tagantsev, A.K., Setter, N., *Appl. Phys. Lett.* **72**, 2478 (1998c)
- Collins, M.A., Blumen, A., Currie, J.F., Ross, J., *Phys. Rev. B* **19**, 3630 (1979)
- Conti, S., Salje, E.K.H., *J. Phys. Condens. Matter* **13**, L847 (2001)
- Cook Jr., W.R., *J. Am. Ceram. Soc.* **39**, 17 (1956)
- Correia, A., Massanell, J., Garcia, N., Levanyuk, A.P., Zlatkin, A., Przeslawski, J., *Appl. Phys. Lett.* **68**, 2796 (1996)
- Courtens, E., *Phys. Rev. B* **33**, 2975 (1986)
- Cowley, J.M.: *Diffraction Physics*. North-Holland, Amsterdam (1975)
- Cowley, R.A., Axe, J.D., Iizumi, M., *Phys. Rev. Lett.* **36**, 806 (1976)
- Cross, L.E., Bhalla, A., *Phys. Stat. Sol. (a)* **48**, 431 (1978)

- Cross, L.E., Cline, T.W., *Ferroelectrics* **11**, 333 (1976)
- Cross, L.E., Nicholson, B.J., *Philos. Mag.* **46**, 453 (1955)
- Cross, L.E., Fousková, A., Cummins, S.E., *Phys. Rev. Lett.* **21**, 812 (1968)
- Cross, J., Fujiki, M., Tsukada, M., Kotaka, Y., Goto, Y., *Integr. Ferroelectr.* **21**, 263 (1998)
- Cudney, R.S., Fousek, J., Zgonik, M., Günter, P., Garrett, M.H., Rytz, D., *Ferroelectrics* **157**, 45 (1994)
- Cudney, R.S., Garces-Chavez, V., Negrete-Regagnon, P., *Opt. Lett.* **22**, 439 (1997)
- Cummins, H.Z., *Phys. Rep.* **185**, 211 (1990)
- Cummins, S.E., Cross, L.E., *Appl. Phys. Lett.* **10**, 14 (1967)
- Cummins, S.E., Cross, L.E., *J. Appl. Phys.* **39**, 2268 (1968)
- Dabrowska, K., Daszczyńska, W., Jaskiewicz, A., *Acta Phys. Pol. A* **51**, 539 (1977)
- Damjanovic, D.: Hysteresis in piezoelectric and ferroelectric materials, in *Science of Hysteresis*, edited by Bertotti, G., Mayergoyz, I., pp. 337–465, Elsevier, Oxford (2005)
- Darinskii, B.M., Fedosov, V.N., *Sov. Phys. Solid State* **13**, 17 (1971)
- Darinskii, B.M., Lazarev, A.P., Sidorkin, A.S., *Fizika tverdogo tela* **31**, 287 (1989a)
- Darinskii, B.M., Sidorkin, A.S., Lazarev, A.P., *Ferroelectrics* **98**, 245 (1989b)
- Darinskii, B.M., Lazarev, A.P., Sidorkin, A.S., *Kristallografiya* **36**, 757 (1991)
- David, W.I.F., Wood, I.G., *J. Phys. C Solid State Phys.* **16**, 5149 (1983)
- De Guerville, F., Luk'yanchuk, I., Lahoche, L., El Marssi, M., *Mater. Sci. Eng. B Solid State Mater. r Adv. Technol.* **120**, 16 (2005)
- De Wainer, L.S., De Dussel, H.L., De Benyacar, A.R., *Thin Solid Films* **69**, 351 (1980)
- Dec, J., *Ferroelectrics* **81**, 123 (1988)
- Dec, J., *Phase Transitions* **45**, 35 (1993)
- Dec, J., Kwapulinski, J., *J. Phys. Condens. Matter* **1**, 3389 (1989)
- Dec, J., Kleemann, W., Itoh, M., *Ferroelectrics* **298**, 163 (2004)
- Dennis, M.D., Bradt, R.C., *J. Appl. Phys.* **45**, 1931 (1974)
- Desu, S.B., Dudekevich, V.P., Dudkevich, P.V., Zakharchenko, I.N., Kushlyan, G.L.: Thermodynamics of epitaxial ferroelectric films, in *Epitaxial Oxide Thin Films II*, edited by Speck, J.S., Fork, D.K., Wolf, R.M., Shiosaki, T. (*Mater. Res. Soc. Symp. Proc. Volume 401*, p. 1995, Warrendale, PA, 1996)
- DeVilbiss, A.D., DeVilbiss, A.J., *Integr. Ferroelectr.* **26**, 285 (1999)
- Devonshire, A.F., *Philos. Mag.* **40**, 1040 (1949)
- Devonshire, A.F., *Philos. Mag.* **42**, 1065 (1951)
- Diamant, H., Drenck, K., Pepinsky, R., *Rev. Sci. Instrum.* **28**, 30 (1957)
- DiDomenico Jr., M., Wemple, S.H., *Phys. Rev.* **155**, 539 (1967)
- Dimos, D., Warren, W.L., Sinclair, M.B., Tuttle, B.A., Schwartz, R.W., *J. Appl. Phys.* **76**, 4305 (1994)
- Distler, G.I., Konstantinova, V.P., Gerasimov, Yu.M., Tolmacheva, G.A., *Pis'ma v ZhETF* **6**, 868 (1967)
- Distler, G.I., Konstantinova, V.P., Gerasimov, Y.M., Tolmacheva, G.A., *Nature* **218**, 762 (1968)
- Dolino, G., *Phys. Rev. B* **6**, 4025 (1972)
- Dolino, G., *Appl. Phys. Lett.* **22**, 123 (1973)
- Dolino, G., *Rev. Phys. Appl.* **10**, 433 (1975)
- Dolino, G., Lajzerowicz, J., Vallade, M., *Solid State Commun.* **7**, 1005 (1969)
- Dolino, G., Lajzerowicz, J., Vallade, M., *Phys. Rev. B* **2**, 2194 (1970)
- Dolino, G., Bachheimer, J.P., Vallade, M., *Appl. Phys. Lett.* **22**, 623 (1973)
- Domanski, S., *Proc. Phys. Soc. (London)* **B72**, 306 (1958)
- Dontsova, L.I., Popov, E.S., *Izvestiya Akad. Nauk SSSR, ser. fiz.* **39**, 854 (1975)
- Dontsova, L.I., Popov, E.S., Shil'nikov, A.V., Bulatova, L.G., Tikhomirova, N.A., Shuvalov, L.A., *Kristallografiya* **26**, 758 (1981)
- Dontsova, L.I., Bulatova, L.G., Popov, E.S., Shil'nikov, A.V., Chebotarev, A.A., Tikhomirova, N.A., Baranov, A.I., Shuvalov, L.A., *Kristallografiya* **27**, 305 (1982)

- Dontzova, L.I., Tikhomirova, N.A., Shuvalov, L.A., *Ferroelectrics* **97**, 87 (1989)
- Dontsova, L.I., Tikhomirova, N.A., Bulatova, L.G., Korina, R.V., *Kristallografiya* **33**, 450 (1988)
- Dontsova, L.I., Tikhomirova, N.A., Shuvalov, L.A., *Kristallografiya* **39**, 158 (1994)
- Dougherty, J.P., Sawaguchi, E., Cross, L.E., *Appl. Phys. Lett.* **20**, 364 (1972)
- Drougard, M.E., Landauer, R., *J. Appl. Phys.* **30**, 1663 (1959)
- Drougard, M.E., Young, D.R., *Phys. Rev.* **94**, 1561 (1954)
- Drougard, M.E., Funk, H.L., Young, D.R., *J. Appl. Phys.* **25**, 1166 (1954)
- Du, X., Chen, I.-W., *J. Appl. Phys.* **83**, 7789 (1998)
- Ducharme, S., Bune, A., Fridkin, V., Blinov, L., Palto, S., Petukhova, N., Yudin, S., *Ferroelectrics* **202**, 29 (1997)
- Dudnik, E.F., Shuvalov, L.A., *Ferroelectrics* **98**, 207 (1989)
- Dudnik, E.F., Sushko, S.A., Kiosse, G.A., Malinovskiy, T.I., *Ferroelectrics* **48**, 149 (1983)
- Duiker, H.M., Beale, P.D., *Phys. Rev.* **41**, 490 (1990)
- Dvorak, V., *J. Phys. Soc. Jpn. Suppl.* **28**, 252 (1970)
- Dvorak, V., *Phys. Stat. Sol. (b)* **45**, 147 (1971)
- Dvorak, V., *J. Phys. Paris* **33**, C2-89 (1972)
- Dvorak, V., *Ferroelectrics* **7**, 1 (1974)
- Dvorak, V., Janovec, V., *Jpn. J. Appl. Phys.* **4**, 400 (1965)
- Dvorak, V., Malek, Z., Mastner, J., Janovec, V., Glanc, A., *J. Appl. Phys.* **35**, 1875 (1964)
- Eisner, J., *Ferroelectrics* **8**, 621 (1974)
- Eknadosyants, E.I., Borodin, V.Z., Piralova, A.T., Boldyreva, Z.P., Proskuryakov, B.F., Biryukova, T.V., *Sov. Phys. Crystallogr.* **23**, 218 (1978)
- Eknadosyants, E.I., Pinskaya, A.N., Borodin, V.Z., *Sov. Phys. Crystallogr.* **32**, 613 (1987)
- Eknadosyants, E.I., Borodin, V.Z., Smotrakov, V.G., Eremkin, V.V., Pinskaya, A.N., *Ferroelectrics* **111**, 283 (1990)
- Eknadosyants, E.I., Borodin, V.Z., Pinskaya, A.N., Eremkin, V.V., Smotrakov, V.G., *Crystallogr. Rep.* **42**, 1029 (1997)
- Eng, L.M., *Nanotechnology* **10**, 405 (1999)
- Eng, L.M., Güntherodt, H.-J., *Ferroelectrics* **236**, 35 (2000)
- Eng, L.M., Friedrich, M., Fousek, J., Günter, P., *J. Vac. Sci. Technol. B* **14**, 1191 (1996)
- Eng, L.M., Fousek, J., Günter, P., *Ferroelectrics* **191**, 211 (1997)
- Eng, L.M., Bammerlin, M., Loppacher, Ch., Guggisberg, M., Bennewitz, R., Lüthi, R., Meyer, E., Güntherodt, H.-J., *Appl. Surf. Sci.* **140**, 253 (1999a)
- Eng, L.M., Bammerlin, M., Loppacher, Ch., Guggisberg, M., Bennewitz, R., Lüthi, R., Meyer, E., Huser, Th., Heinzelman, H., Güntherodt, H.-J., *Ferroelectrics* **222**, 153 (1999b)
- Eng, L.M., Bammerlin, M., Loppacher, Ch., Guggisberg, M., Meyer, E., Güntherodt, H.-J., *Surf. Interface Anal.* **27**, 422 (1999c)
- Eng, L.M., Güntherodt, H.-J., Schneider, G.A., Köpke, U., Munoz Saldana, J., *Appl. Phys. Lett.* **74**, 233 (1999d)
- English, F.L., *J. Appl. Phys.* **39**, 2302 (1968a)
- English, F.L., *J. Appl. Phys.* **39**, 128 (1968b)
- Erhart, J., *Phase Transitions* **77**, 989 (2004)
- Errandonea, G., *Ferroelectrics* **36**, 423 (1981)
- Esayan, S.Kh., Lemanov, V.V., Smolenskii, G.A., *Sov. Phys. Dokl.* **19**, 393 (1974)
- Fally, M., Fuih, A., Müller, V., *Phys. Rev. B* **64**, 026101 (2001)
- Fatuzzo, E., *J. Appl. Phys.* **32**, 1571 (1961)
- Fatuzzo, E., *Phys. Rev.* **127**, 1999 (1962)
- Fatuzzo, E., Merz, W.J., *Phys. Rev.* **116**, 61 (1959)
- Fatuzzo, E., Merz, W.J., *Ferroelectricity*. North-Holland, Amsterdam (1966)
- Fedorenko, A.A., Mueller, V., Stepanow, S., *Phys. Rev. B* **70**, 134301 (2004)
- Fedosov, V.N., Sidorkin, A.S., *Fizika tverdogo tela* **19**, 1322 (1977)
- Feisst, A., Koidl, P., *Appl. Phys. Lett.* **47**, 1125 (1985)

- Fesenko, O.E., Smotrakov, V.G., *Ferroelectrics* **12**, 211 (1976)
- Fesenko, E.G., Gavrilyatchenko, V.G., Martinenko, M.A., Semenchov, A.F., *Ferroelectrics* **6**, 61 (1973)
- Fesenko, E.G., Martynenko, M.A., Gavrilyatchenko, V.G., Semenchov, A.F., *Izvestiya Akad. Nauk SSSR, ser. fiz.* **39**, 762 (1975)
- Fesenko, E.G., Gavrilyatchenko, V.G., Semenchov, A.F., Yufatova, S.M., *Ferroelectrics* **63**, 289 (1985)
- Fesenko, E.G., Gavrilyachenko, V.G., Semenchov, A.F., *Domain Structure of Multiaxial Ferroelectric Crystals (in Russian)*. Publishing House of the Rostov University, Rostov on Don (1990)
- Flack, H.D., *Acta Cryst.* **A 43**, 564 (1987)
- Flippen, R.B., *J. Appl. Phys.* **46**, 1068 (1975)
- Floquet, N., Valot, C.M., Mesnier, M.T., Niepce, J.C., Normand, L., Thorel, A., Kilaas, R., *J. Phys.* III **7**, 1105 (1997)
- Foeth, M., Sfera, A., Stadelmann, P., Buffat, P.-A., *J. Electron Microsc.* **48**, 717 (1999a)
- Foeth, M., Stadelmann, P., Buffat, P.-A., *Ultramicroscopy* **75**, 203 (1999b)
- Foeth, M., Stadelmann, P., Robert, M., *Phys. A –Stat. Mech Appl.* **373**, 439 (2007)
- Fomichev, N.N., *Izvestiya Akad. Nauk SSSR, ser. fiz.* **29**, 962 (1965)
- Forsbergh Jr., P.W., *Phys. Rev.* **76**, 1187 (1949)
- Foster, C.M., Li, M.B.Z., Miller, D., Baldo, P.M., Rehn, L.E., Bai, G.R., Guo, D., You, H., Merkle, K.L., *J. Appl. Phys.* **78**, 2607 (1995)
- Foster, C.M., Bai, G.-R., Csencsit, R., Vetrone, J., Jammy, R., Wills, L.A., Carr, E., Amano, J., *J. Appl. Phys.* **81**, 2349 (1997)
- Fousek, J., *Proceedings of the European Meeting on Ferroelectricity, Saarbrücken 1969*, p. 147 (1970)
- Fousek, J., *Czech. J. Phys.* **B 21**, 955 (1971)
- Fousek, J., *Proceedings of the International Symposium on the Applications of Ferroelectrics, Washington 1994*, p. 171 (1994)
- Fousek, J., *J. Appl. Phys.* **36**, 588 (1965a)
- Fousek, J., *Czech. J. Phys.* **B 15**, 412 (1965b)
- Fousek, J., *Jpn. J. Appl. Phys.* **6**, 950 (1967)
- Fousek, J., Brezina, B., *Czech. J. Phys.* **B 10**, 511 (1960)
- Fousek, J., Brezina, B., *Czech. J. Phys.* **B 11**, 344 (1961)
- Fousek, J., Brezina, B., *J. Phys. Soc. Jpn.* **19**, 830 (1964)
- Fousek, J., Janousek, V., *Phys. Stat. Sol.* **13**, 195 (1966)
- Fousek, J., Janovec, V., *J. Appl. Phys.* **40**, 135 (1969)
- Fousek, J., Janovec, V., *J. Phys. Soc. Jpn. Suppl.* **28**, 380 (1970)
- Fousek, J., Petzelt, J., *Phys. Stat. Sol. (a)* **55**, 11 (1979)
- Fousek, J., Safrankova, M., *Jpn. J. Appl. Phys.* **4**, 403 (1965)
- Fousek, J., Safrankova, M., *Proceedings of the International Meeting on Ferroelectricity, Prague 1966, vol. II*, p. 59 (1966)
- Fousek, J., Safrankova, M., Kaczer, J., *Appl. Phys. Lett.* **8**, 192 (1966)
- Fousek, J., Glogarová, M., Kursten, H.D., *Ferroelectrics* **11**, 469 (1976)
- Fousek, J., Günter, P., Hagenbucher, J.J., Plesko, S., Smutny, F., *Ferroelectrics* **25**, 351 (1980)
- Fousková, A., *J. Phys. Soc. Jpn.* **20**, 1625 (1965)
- Fousková, A., Fousek, J., *Phys. Stat. Sol. (a)* **32**, 213 (1975)
- Fousková, A., Janousek, V., *J. Phys. Soc. Jpn.* **20**, 1619 (1965)
- Fouskova, A., Guyon, P., Lajzerowicz, J., *C. R. Acad. Sci. Paris* **262**, 907 (1966)
- Franke, K., Besold, J., Haessler, W., Seegebarth, C., *Surf. Sci. Lett.* **302**, L283 (1994)
- Fu, D.S., Suzuki, K., Kato, K., Suzuki, H., *Appl. Phys. Lett.* **82**, 2130 (2003)
- Fuchs, E., Liesk, W., *J. Phys. Chem. Solids* **25**, 845 (1964)
- Fujimoto, M., Sinha, B.V., *Ferroelectrics* **46**, 227 (1983)
- Furuhata, Y., *J. Phys. Soc. Jpn. Suppl.* **28**, 425 (1970)

- Furuhata, Y., Toriyama, K., Appl. Phys. Lett. **23**, 361 (1973)
- Gadkari, S.C., Sabharwal, S.C., Ghosh, B., Indian J. Pure Appl. Phys. **24**, 289 (1986)
- Galiyarova, N.M., Dontsova, L., Ferroelectrics **222**, 269 (1999)
- Galtsev, V.V., Nedostup, N.A., Ivanov, N.R., Tikhomirova, N.A., Ferroelectrics **111**, 217 (1990)
- Gan, Q., Wasa, K., Eom, C.B., Mater. Sci. Eng. B **56**, 204 (1998)
- Ganpule, C.S., Nagarajan, V., Li, H., Ogale, A.S., Steinhauer, D.E., Aggarwal, S., Williams, E., Wolf, P.D., Appl. Phys. Lett. **77**, 292 (2000a)
- Ganpule, C.S., Nagarajan, V., Ogale, S.B., Roytburd, A.L., Williams, E.D., Appl. Phys. Lett. **77**, 3275 (2000b)
- Ganpule, C.S., Nagarajan, V., Hill, B.K., Roytburd, A.L., Williams, E.D., Alpay, S.P., Roelofs, A., Waser, R., Eng, L.M., J. Appl. Phys. **91**, 1477 (2002)
- Gao, C., Duewer, F., Lu, Y., Xiang, X.-D., Appl. Phys. Lett. **73**, 1146 (1998)
- Gentner, J.O., Gerthsen, P., Schmidt, N.A., Send, R.E., J. Appl. Phys. **49**, 4485 (1978)
- Gerra, G., Tagantsev, A.K., Setter, N., Phys. Rev. Lett. **94**, 107602 (2005)
- Gerra, G., Tagantsev, A.K., Setter, N., Parlinski, K., Phys. Rev. Lett. **96**, 107603 (2006)
- Gilletta, F., Phys. Stat. Sol. (a) **11**, 721 (1972)
- Gladkii, V.V., Magataev, V.K., Sidnenko, E.V., Ferroelectrics **5**, 107 (1973)
- Glanc, A., Málek, Z., Mastner, J., Novák, M., Strajblová, J., J. Appl. Phys. **35**, 1870 (1964)
- Glazer, A.M., Groves, P., Smith, D.T., J. Phys. E Sci. Instrum. **17**, 95 (1984)
- Glogarová, M.: Anchoring of MBBA liquid crystal on ferroelectric triglycine sulphate, in Advances in Liquid Crystals and Applications, edited by Bata, L., pp. 1107–1113, Pergamon Press, Akademiai Kiado, Oxford, Budapest (1980)
- Glogarová, M., J. Phys. Paris **42**, 1569 (1981)
- Glogarová, M., Fousek, J., Phys. Stat. Sol. (a) **15**, 579 (1972)
- Glogarová, M., Janovec, V., Tikhomirova, N.A., J. Phys. Paris suppl. **40**, Colloque C3, C3–502 (1979)
- Glushkov, V.F., Magataev, V.K., Svinarev, V.V., Von Cieminski, J., Shuvalov, L.A., Sov. Phys. Crystallogr. **32**, 416 (1987)
- Gonzales, G., Serna, J., Ferroelectrics **54**, 305 (1984)
- Gopalan, V., Gupta, M.C., Ferroelectrics **198**, 49 (1997)
- Gopalan, V., Raj, R., Appl. Phys. Lett. **68**, 1323 (1996)
- Gopalan, V., Raj, R., J. Appl. Phys. **81**, 865 (1997)
- Gopalan, V., Mitchell, T.E., Furukawa, Y., Kitamura, K., Appl. Phys. Lett. **72**, 1981 (1998)
- Goulpeau, L., Phys. Stat. Sol. **32**, K1 (1969)
- Grabar, A.A., Bercha, A.I., Simchera, V.Yu., Stoika, I.M., Ferroelectrics **202**, 211 (1997)
- Grandet, G., Le Bihan, R., Derrien, J., Pilorget, L., Ferroelectrics **39**, 1225 (1981)
- Gränicher, H., Müller, K.A., Mater. Res. Bull. **6**, 977 (1971)
- Grekov, A.A., Adonin, A.A., Protsenko, N.P., Ferroelectrics **13**, 483 (1976)
- Gridnev, S.A., Shuvalov, L.A., Ferroelectrics **48**, 113 (1983)
- Gridnev, S.A., Kudryash, V.I., Shuvalov, L.A., Izvestiya Akad. Nauk SSSR, ser. fiz. **43**, 1718 (1979)
- Gridnev, S.A., Kudryash, V.I., Prasolov, B.N., Dybov, V.T., Ferroelectrics **111**, 233 (1990)
- Grossmann, M., Bolten, D., Lohse, O., Boettger, U., Waser, R., Tiedke, S., Appl. Phys. Lett. **77**, 3830 (2000)
- Grossmann, M., Lohse, O., Bolten, D., Boettger, U., Schneller, T., Waser, R., J. Appl. Phys. **92**, 2680 (2002a)
- Grossmann, M., Lohse, O., Bolten, D., Boettger, U., Waser, R., J. Appl. Phys. **92**, 2688 (2002b)
- Grubsky, V., MacCormack, S., Feinberg, J., Opt. Lett. **21**, 6 (1996)
- Gruverman, A., Ikeda, Y., Jpn. J. Appl. Phys. **37**, L939 (1998)

- Gruverman, A., Tanaka, M., *J. Appl. Phys.* **89**, 1836 (2001)
- Gruverman, A., Auciello, O., Tokumoto, H., *J. Vac. Sci. Technol. B* **14**, 602 (1996)
- Gruverman, A., Tokumoto, H., Prakash, A.S., Aggarwal, S., Yang, B., Wuttig, M., Ramesh, R., Auciello, O., Venkatesan, T., *Appl. Phys. Lett.* **71**, 3492 (1997a)
- Gruverman, A.L., Hatano, J., Tokumoto, H., *Jpn. J. Appl. Phys.* **36**, 2207 (1997b)
- Gruverman, A., Auciello, O., Tokumoto, H., *Annu. Rev. Mater. Sci.* **28**, 101 (1998a)
- Gruverman, A., Auciello, O., Tokumoto, H., *Integr. Ferroelectr.* **19**, 49 (1998b)
- Gruverman, A., Rodriguez, B.J., Kingon, A.I., Nemanich, R.J., Cross, J.S., Tsukada, M., *Appl. Phys. Lett.* **82**, 3071 (2003)
- Gupta, M.C., Risk, W.P., Nutt, A.C.G., Lau, S.D., *Appl. Phys. Lett.* **63**, 1167 (1993)
- Guymont, M., *Phys. Rev. B* **24**, 2647 (1981)
- Guymont, M., *Acta Cryst. A* **47**, 559 (1991)
- Guyon, P., Lajzerowicz, J., *Phys. Stat. Sol.* **16**, 525 (1966)
- Günter, P., Huignard, J.-P. (eds.): *Photorefractive Materials and their Applications*. Springer-Verlag, Berlin (1988)
- Güthner, P., Dransfeld, K., *Appl. Phys. Lett.* **61**, 1137 (1992)
- Ha, D.-H., Kim, J.-J., *Jpn. J. Appl. Phys. Suppl.* **24-2**, 556 (1985)
- Hadni, A., *Proceedings of the Symposium on Submillimeter Waves, Polytech. Inst., Brooklyn 1970*, p. 251 (1970)
- Hadni, A., *Ferroelectrics* **140**, 25 (1993)
- Hadni, A., Thomas, R., *Phys. Stat. Sol. (a)* **31**, 71 (1975)
- Hadni, A., Thomas, R., *Ferroelectrics* **11**, 493 (1976)
- Hadni, A., Henninger, Y., Thomas, R., Schumachen, P., *J. Phys. Paris* **26**, 345 (1965)
- Hadni, A., Lambert, J.P., Pradhan, M.M., Thomas, R., *Infrared Phys.* **13**, 305 (1973)
- Hadni, A., Bassia, J.M., Gerbaux, X., Thomas, R., *Appl. Opt.* **15**, 2150 (1976)
- Hadni, A., Thomas, R., Ungar, S., Gerbaux, X., *Ferroelectrics* **47**, 201 (1983)
- Haeni, J.H., Irvin, P., Chang, W., Uecker, R., Reiche, P., Li, Y.L., Choudhury, S., Tian, W., Hawley, M.E., Craigo, B., Tagantsev, A.K., Pan, X.Q., Streiffner, S.K., Chen, L.Q., Kirchofer, S.W., Levy, J., Schlom, D.G., *Nature* **430**, 758 (2004)
- Haertling, G.H., *Integr. Ferroelectr.* **14**, 219 (1997)
- Hagemann, H.-J., *J. Phys. C Solid State Phys.* **11**, 3333 (1978)
- Hamano, K., Zhang, J., Abe, K., Mitsui, T., Sakata, H., Ema, K., *Ferroelectrics* **172**, 165 (1995)
- Hamano, K., Zhang, J., Abe, K., Mitsui, T., Sakata, H., Ema, K., *J. Phys. Soc. Jpn.* **65**, 142 (1996)
- Hamazaki, S.I., Shimizu, F., Kojima, S., Takashige, M., *J. Korean Phys. Soc. (Proc. Suppl.)* **29**, S503 (1996)
- Hamazaki, S.I., Tashiro, N., Fukurai, Y., Shimizu, F., Takashige, M., Kojima, S., *Ferroelectrics* **219**, 183 (1998)
- Hartmann, E., Windsch, W., *Phys. Stat. Sol. (a)* **13**, 119 (1972)
- Hashimoto, S., Orihara, H., Ishibashi, Y., *J. Phys. Soc. Jpn.* **63**, 1601 (1994)
- Hatano, J., Le Bihan, R., *Ferroelectrics* **111**, 223 (1990)
- Hatano, J., Suda, F., Futama, H., *Jpn. J. Appl. Phys.* **12**, 1644 (1973)
- Hatano, J., Suda, F., Futama, H., *J. Phys. Soc. Jpn.* **41**, 188 (1976)
- Hatano, J., Suda, F., Futama, H., *J. Phys. Soc. Jpn.* **43**, 1933 (1977)
- Hatano, J., Suda, F., Futama, H., *Ferroelectrics* **20**, 265 (1978)
- Hatano, J., Kume, N., Kubota, K., Tsukamoto, T., Futama, H., Gesi, K., *Jpn. J. Appl. Phys. Suppl.* **24-2**, 844 (1985a)
- Hatano, J., Suda, F., Aikawa, F., Futama, H., Szczesniak, L., Hilczer, B., *Ferroelectrics* **63**, 69 (1985b)
- Hatano, J., Le Bihan, R., Aikawa, F., Mbama, F., *Ferroelectrics* **106**, 33 (1990a)
- Hatano, J., Rafii, N., Robert, M.-C., Le Bihan, R., *Ferroelectrics* **106**, 39 (1990b)

- Hatano, J., Watanabe, T., Le Bihan, R., *Ferroelectrics* **126**, 311 (1992)
- Haun, M.J., Furman, E., Jang, S.J., McKinstry, H.A., Cross, L.E., *J. Appl. Phys.* **62**, 3331 (1987)
- Hayashi, M., *Memoirs of the Faculty of Engineering, Nagoya University* **24**, 216 (1972a)
- Hayashi, M., *J. Phys. Soc. Jpn.* **33**, 616 (1972b)
- Hayashi, M., *J. Phys. Soc. Jpn.* **34**, 1240 (1973)
- Hayashi, M., Mishima, H., *Jpn. J. Appl. Phys.* **8**, 968 (1969)
- Heimann, B., *Principles of chemical etching – the art and science of etching crystals.*, in *Crystals*, vol. 8, edited by J. Grabmaier, Springer Verlag, Berlin (1982)
- Heising, R.A., *Quartz Crystals for Electrical Circuits*. D. Van Nostrand, New York (1947)
- Hetzler, U., Würfel, P., *Ferroelectrics* **20**, 275 (1978)
- Hiboux, S., Ph.D. Thesis, Swiss Federal Institute of Technology (EPFL), (2001)
- Hiboux, S., Muralt, P., *Integr. Ferroelectr.* **36**, 83 (2001)
- Hiboux, S., Muralt, P., Maeder, T., *J. Mater. Res.* **14**, 4307 (1999)
- Hidaka, T., Maruyama, T., Saitoh, M., Mikoshiba, N., Shimizu, M., Shiosaki, T., Wills, L.A., Hikes, R., Dicarolis, S.A., Amano, J., *Appl. Phys. Lett.* **68**, 2358 (1996)
- Hidaka, T., Maruyama, T., Sakai, I., Saitoh, M., Wills, L.A., Hikes, R., Dicarolis, S.A., Amano, J., Foster, C.M., *Integr. Ferroelectr.* **17**, 319 (1997)
- Hilczer, B., Meyer, K.-P., Pawlaczyk, C., Szczesniak, L., *Phys. Stat. Sol. (a)* **28**, K101 (1975)
- Hilczer, B., Pawlaczyk, C., Szczesniak, L., Meyer, K.-P., Scholz, R., *Mater. Sci.* **7**, 427 (1981)
- Hilczer, B., Szczesniak, L., Meyer, K.-P., *Ferroelectrics* **97**, 59 (1989)
- Hirano, T., Kawai, H., Suzuki, H., Kaneko, S., Wada, T., *Ferroelectrics* **231**, 211 (1999)
- Hlinka, J., *Ferroelectrics* **375**, 132 (2008)
- Hlinka, J., Marton, P., *Phys. Rev. B* **74**, 104104 (2006)
- Holakovskiy, J., *Phys. Stat. Sol. (b)* **56**, 615 (1973)
- Holec, D., Zhang, Y., Rao, D.V.S., Kappers, M.J., McAleese, C., Humphreys, C.J., *J. Appl. Phys.* **104**, 123514 (2008)
- Hong, S. (ed.): *Nanoscale Phenomena in Ferroelectric Thin Films*. Springer-Verlag, New York (2004)
- Hong, S., Setter, N., *Appl. Phys. Lett.* **81**, 3437 (2002)
- Hong, J.W., Kahng, D.S., Shin, J.C., Kim, H.J., Khim, Z.G., *J. Vac. Sci. Technol. B* **16**, 2942 (1998a)
- Hong, J.W., Noh, K.H., Park, S., *Phys. Rev. B* **58**, 5078 (1998b)
- Hong, J.W., Park, S.-I., Khim, Z.G., *Rev. Sci. Instrum.* **70**, 1735 (1999a)
- Hong, S., Colla, E.L., Kim, E., Taylor, D.V., Tagantsev, A.K., Muralt, P., No, K., Setter, N., *J. Appl. Phys.* **86**, 607 (1999b)
- Hooton, J.A., Merz, W.J., *Phys. Rev.* **98**, 409 (1955)
- Hoshino, S., Mitsui, T., Jona, F., Pepinsky, R., *Phys. Rev.* **107**, 1255 (1957)
- Houé, M., Townsend, P.D., *J. Phys. D Appl. Phys.* **28**, 1747 (1995)
- Hsu, W.-Y., Raj, R., *Appl. Phys. Lett.* **67**, 3733 (1995)
- Hu, Y.H., Chan, H.M., Wen, Z.X., Harmer, M.P., *J. Am. Ceram. Soc.* **69**, 594 (1986)
- Hu, Z.W., Jiang, S.S., Huang, P.Q., Huang, X.R., Feng, D., Wang, J.Y., Li, L.X., *Appl. Phys. Lett.* **64**, 55 (1994)
- Huang, X.R., Hu, Z.W., Jiang, S.S., Jiang, J.H., Tian, Y.L., Han, Y., Wang, J.Y., *J. Appl. Phys.* **75**, 7756 (1994a)
- Huang, X.R., Jiang, S.S., Hu, Z.W., Xu, X.Y., Zeng, W., Jiang, J.H., Wang, J.Y., Feng, D., *Phys. Rev. B* **50**, 13149 (1994b)
- Huang, X.R., Jiang, S.S., Hu, X.B., Xu, X.Y., Zeng, W., Feng, D., Wang, J.Y., *Phys. Rev. B* **52**, 9932 (1995)
- Huang, Y.N., Li, X., Ding, Y., Wang, Y.N., Shen, H.M., Zhang, Z.F., Fang, C.S., Zhuo, S.H., Fung, P.C.W., *Phys. Rev. B* **55**, 16159 (1997)
- Hubert, C., Levy, J., *Appl. Phys. Lett.* **73**, 3229 (1998)

- Hubert, C., Levy, J., Carter, A.C., Chang, W., Kiechoefer, S.W., Horwitz, J.S., Chrisey, D.B., Appl. Phys. Lett. **71**, 3353 (1997)
- Huibregtse, E.J., Young, D.R., Phys. Rev. **103**, 1705 (1956)
- Husimi, K., J. Phys. Soc. Jpn. **15**, 731 (1960)
- Igras, E., Kristallografiya **4**, 121 (1959)
- Imry, Y., Ma, S., Phys. Rev. Lett. **35**, 1399 (1975)
- Indenbom, V.L., Sov. Phys. Crystallogr. **5**, 106 (1960)
- Indenbom, V.L., Bull. Acad. Sci. USSR **43**, 69 (1979)
- Ishibashi, Y., Dvorak, V., J. Phys. Soc. Jpn. **41**, 1650 (1976)
- Ishibashi, Y., Iwata, M., Jpn. J. Appl. Phys. **38**, 800 (1999)
- Ishibashi, Y., Takagi, Y., J. Phys. Soc. Jpn. **31**, 506 (1971)
- Ishigame, Y., Sahara, T., Nishihara, H., Opt. Lett. **16**, 375 (1991)
- Ishihara, S., Ye, Z.G., Rabe, H., Rivera, J.-P., Kubel, F., Schmid, H., Ferroelectrics **140**, 53 (1993)
- Ishizuka, K., Uyeda, N., Acta Cryst. A **33**, 740 (1977)
- Ivanov, N.R., Tikhomirova, N.A., Ginzberg, A.V., Chumakova, S.P., Ferroelectr.s Lett. **15**, 127 (1993)
- Ivanov, N.R., Tikhomirova, N.A., Ginzberg, A.V., Chumakova, S.P., Eknadiosyants, E.I., Borodin, V.Z., Pinskaya, A.N., Babanskikh, V.A., D'yakov, V.A., Crystallogr. Rep. **39**, 593 (1994)
- Iwasaki, H., Miyazawa, S., Koizumi, H., Sugii, K., Niizeki, N., J. Appl. Cryst. **43**, 4907 (1972)
- Jaffe, B., Cook Jr., W.R., Jaffe, H.: Piezoelectric Ceramics. Academic Press, London (1971)
- Janovec, V., Czech. J. Phys. **8**, 3 (1958)
- Janovec, V., Czech. J. Phys. **9**, 468 (1959)
- Janovec, V., Czech. J. Phys. **B 22**, 974 (1972)
- Janovec, V., Ferroelectrics **12**, 43 (1976)
- Janovec, V., Brezina, B., Glanc, A., Czech. J. Phys. **B 10**, 690 (1960)
- Janovec, V., Dvorak, V., Petzelt, J., Czech. J. Phys. **B 25**, 1362 (1975)
- Janovec, V., Schranz, W., Warhanek, H., Zikmund, Z., Ferroelectrics **98**, 171 (1989)
- Janovec, V., Richterová, L., Litvin, D.B., Ferroelectrics **140**, 95 (1993)
- Janta, J., J. Phys. Soc. Jpn. **28 Suppl.**, 340 (1970)
- Janta, J., Ferroelectrics **2**, 299 (1971)
- Jaskiewicz, A., Przeslawski, J., Phys. Stat. Sol. (a) **56**, 365 (1979)
- Jex, H., Müllner, M., Tietze, H., Lehner, N., Wilson, S., Phys. Rev. B **26**, 2539 (1982)
- Jiang, S.S., Hu, Z.W., Yang, P., Feng, D., Ferroelectrics **140**, 71 (1993)
- Jiang, B., Lee, J.C., Zurcher, P., Jones, J.R.E., Integr. Ferroelectr. **16**, 199 (1997)
- Jiang, F., Kojima, S., Yang, Y., Yin, Q., Ferroelectrics **222**, 237 (1999)
- Jo, W., Kim, D.C., Hong, J.W., Appl. Phys. Lett. **76**, 390 (2000)
- Johnson, D.J., Amm, D.T., Griswold, E., Sreenivas, K., Yi, G., Sayer, M.: Measuring fatigue in PZT thin films, in Ferroelectric Thin Films, edited by Kingon, A.I., Myers, E.R. (Mater. Res. Soc. Symp. Proc. **Volume 200**, p. 289, Warrendale, PA, 1990)
- Jona, F., Shirane, G., Ferroelectric Crystals. Pergamon Press, Oxford (1962)
- Jona, F., Shirane, G., Pepinsky, R., Phys. Rev. **97**, 1584 (1955)
- Jonscher, A.K., Universal Relaxation Law. Chelsea Dielectrics Press, London (1996)
- Jun, C., Wang, W.-S., Qi, L., Duan, F., Cryst. Res. Technol. **23**, 747 (1988)
- Kadlec, F., Petzelt, J., Zelezny, V., Volkov, A.A., Solid State Commun. **94**, 725 (1995)
- Kahmann, F., Matull, R., Rupp, R.A., Seglins, J., Europhys. Lett. **13**, 405 (1990)
- Kahmann, F., Matull, R., Rupp, R.A., Seglins, J., Phase Transitions **40**, 171 (1992)
- Kahmann, F., Matull, R., Rupp, R.A., Seglins, J., Ferroelectrics **151**, 139 (1994)
- Kaiser, D.L., Vaudin, M.D., Rotter, L.D., Wang, Z.L., Cline, J.P., Hwang, C.S., Marinenko, R.B., Gillen, J.G., Appl. Phys. Lett. **66**, 2801 (1995)
- Kalinin, S.V., Bonnell, D.A., Phys. Rev. B **63**, 125411 (2001a)
- Kalinin, S.V., Bonnell, D.A., Appl. Phys. Lett. **78**, 1116 (2001b)
- Kalinin, S.V., Gruverman, A. (eds.): Scanning Probe Microscopy of Electrical and Electro-mechanical Phenomena at the Nanoscale. Springer, New York (2006)

- Kalinin, S.V., Gruverman, A., Bonnell, D.A., *Appl. Phys. Lett.* **85**, 795 (2004)
- Kalinin, S.V., Johnson, C.Y., Bonnell, D.A., *J. Appl. Phys.* **91**, 3816 (2002)
- Kamentsev, V.P., Rudyak, V.M., *Izvestiya Akad. Nauk SSSR, ser. fiz.* **48**, 1204 (1984)
- Kang, Y.M., Baik, S., *J. Appl. Phys.* **82**, 2532 (1997)
- Kardar, M., *J. Appl. Phys.* **61**, 3601 (1987)
- Karpov, A.I., Poplavko, Yu.M., *Izvestiya Akad. Nauk SSSR, ser. fiz.* **48**, 1193 (1984)
- Kawata, H., Suzuki, S., Takagi, M., *J. Phys. Soc. Jpn.* **50**, 3398 (1981)
- Kay, H.F., Dunn, J.W., *Philos. Mag.* **7**, 2027 (1962)
- Kholkin, A.L., Brooks, K.G., Taylor, D.V., Hiboux, S., Setter, N., *Integr. Ferroelectr.* **22**, 525 (1998)
- Kholodenko, L.P., *Sov. Phys. Solid State* **3**, 2284 (1962)
- Kinase, W., Takahasi, H., *J. Phys. Soc. Jpn.* **12**, 464 (1957)
- Kinase, W., Okayama, H., Yoshikawa, A., Taguchi, N., *J. Phys. Soc. Jpn.* **28**, **Suppl.**, 383 (1970)
- Kirpichnikova, L.F., Shuvalov, L.A., Urusovskaya, A.A., Ivanov, N.R., Kiosse, G.A., *Ferroelectrics* **140**, 1 (1993)
- Kirpichnikova, L.F., Urusovskaya, A.A., Dolbinina, V.V., *Ferroelectrics* **172**, 133 (1995)
- Kitamura, K., Furukawa, Y., Niwa, K., Gopalan, V., Mitchell, T.E., *Appl. Phys. Lett.* **73**, 3073 (1998)
- Kittel, C., *Phys. Rev.* **82**, 729 (1951)
- Kittel, C., *Solid State Commun.* **10**, 119 (1972)
- Klapper, H., *Prog. Cryst. Growth Charact.* **14**, 367 (1987)
- Klassen-Neklyudova, M.V., *Mechanical Twinning of Crystals. Consultants Bureau, New York* (1964)
- Kleemann, W., Dec, J., Prosandeev, S.A., Braun, T., Thomas, P.A., *Ferroelectrics* **334**, 3 (2006)
- Klissurska, R., Tagantsev, A.K., Brooks, K.G., Setter, N., *J. Am. Ceram. Soc.* **80**, 336 (1997)
- Kliya, M.O., Lyachovitskaya, V.A., *J. Phys. Soc. Jpn. Suppl.* **28**, 217 (1970a)
- Kliya, M.O., Lyachovitskaya, V.A., *Sov. Phys. Crystallogr.* **15**, 59 (1970b)
- Kobayashi, J., *Phys. Stat. Sol.* **21**, 151 (1967)
- Kobayashi, J., *Phase Transitions* **36**, 95 (1991)
- Kobayashi, J., Yamada, N., Nakamura, T., *Phys. Rev. Lett.* **11**, 410 (1963)
- Kobayashi, J., Someya, T., Furuhashi, Y., *Phys. Lett. A* **38**, 309 (1972)
- Kobzareva, S.A., Distler, G.I., Konstantinova, V.P., *Sov. Phys. Crystallogr.* **15**, 431 (1970)
- Kogan, S.M., *Sov. Phys. Solid State* **5**, 2069 (1963)
- Kojima, S., *Jpn. J. Appl. Phys. Suppl.* **23-1**, 203 (1983)
- Kojima, S., *Ferroelectrics* **93**, 279 (1989)
- Kokhanchik, L.S., *Izvestiya Akad. Nauk SSSR, ser. fiz.* **57**, 62 (1993)
- Kolmogorov, A.N., *Izv. Acad. Nauk; Ser. Math.* **3**, 355 (1937)
- Kolomeisky, E.B., Levanyuk, A.P., Sigov, A.S., *Ferroelectrics* **104**, 195 (1990)
- Komukae, M., Tanaka, M., Osaka, T., Makita, Y., Kozawa, K., Uchida, T., *J. Phys. Soc. Jpn.* **59**, 197 (1990)
- Konstantinova, V.P., *Kristallografiya* **7**, 748 (1962)
- Konstantinova, V.P., Stankovskaya, Ya., *Sov. Phys. Crystallogr.* **15**, 325 (1970)
- Konstantinova, V.P., Stankovska, I., *Sov. Phys. Crystallogr.* **16**, 123 (1971)
- Konstantinova, V.P., Tikhomirova, N.A., Glogarová, M., *Ferroelectrics* **20**, 259 (1978)
- Kopal, A., Bahník, T., Fousek, J., *Ferroelectrics* **202**, 267 (1997)
- Kopal, A., Mokry, P., Fousek, J., Bahník, T., *Ferroelectrics* **223**, 127 (1999)
- Koptsik, V.A., Toshev, S.D., *Izvestiya Akad. Nauk SSSR, ser. fiz.* **29**, 956 (1965)
- Koralewski, M., Szafranski, M., *Ferroelectrics* **97**, 233 (1989)
- Koukhar, V.G., Pertsev, N.A., Waser, R., *Phys. Rev. B* **64**, 214103 (2001)
- Koukhar, V.G., Pertsev, N.A., Kohlstedt, H., Waser, R., *Phys. Rev. B* **73**, 214103 (2006)
- Kovalevich, V.I., Shuvalov, L.A., Volk, T.R., *Phys. Stat. Sol. (a)* **45**, 249 (1978)
- Krainyuk, G.G., Nosenko, A.E., Otko, A.I., *Ferroelectrics* **48**, 175 (1983a)

- Krainyuk, G.G., Otko, A.I., Nosenko, A.E., *Izvestiya Akad. Nauk SSSR, ser. fiz.* **47**, 758 (1983b)
- Krainyuk, G.G., Otko, A.I., Nosenko, A.E., *Bull. Acad. Sci. USSR* **47**, 132 (1983c)
- Krajewski, T., Jaroszyk, F., *Acta Phys. Polon. A* **43**, 845 (1973)
- Kretschmer, R., Binder, K., *Phys. Rev. B* **20**, 1065 (1979)
- Kronmüller, H., *Z. Angew. Physik* **30**, 9 (1970)
- Kroupa, J., Fousek, J., Fousková, A., Petzelt, J., Pavel, M., Kamba, S., Fuith, A., Warhanek, H., *Ferroelectrics* **87**, 121 (1988)
- Krug, R., Würfel, P., Ruppel, W., *Ferroelectrics* **139**, 17 (1993a)
- Krug, R., Würfel, P., Ruppel, W., *Appl. Opt.* **32**, 6458 (1993b)
- Kubel, F., Schmid, H., *Ferroelectrics* **129**, 101 (1992)
- Kudryash, V.I., Prasolov, B.N., Fedosyuk, R.M., *Izvestiya Akad. Nauk SSSR, ser. fiz.* **53**, 1410 (1989)
- Kudzin, A.Yu., Guskina, L.G., Petrushkevich, I.S., *Fizika tverdogo tela* **6**, 92 (1964)
- Kugel, V.D., Rosenman, G., *Appl. Phys. Lett.* **68**, 2813 (1996)
- Kugel, V.D., Rosenman, G., Shur, D., *J. Phys. D Appl. Phys.* **28**, 2360 (1995)
- Kukushkin, S.A., Osipov, A.V., *Phys. Rev. B* **65**, 174101 (2002)
- Kulcsar, F., *J. Am. Ceram. Soc.* **39**, 13 (1956)
- Kumada, A., *Phys. Lett.* **30A**, 186 (1969)
- Kumada, A., *J. Jpn. Soc. Appl. Phys. Suppl.* **39**, 258 (1970)
- Kumada, A., Yumoto, H., Ashida, S., *J. Phys. Soc. Jpn. Suppl.* **28**, 351 (1970)
- Kuramoto, K., *J. Phys. Soc. Jpn.* **56**, 1859 (1987)
- Kuroda, A., Kurimura, S., Uesu, Y., *Appl. Phys. Lett.* **69**, 1565 (1996)
- Kvitek, Z., Bornarel, J., *Ferroelectrics* **172**, 271 (1995)
- Kvitek, Z., Bornarel, J., *Ferroelectrics* **190**, 31 (1997)
- Kwak, B.S., Erbil, A., Wilkens, B.J., Budai, J.D., Chisholm, M.F., Boatner, L.A., *Phys. Rev. Lett.* **68**, 3733 (1992)
- Kwak, B.S., Erbil, A., Budai, J.D., Chisholm, M.F., Boatner, L.A., Wilkens, B.J., *Phys. Rev. B* **49**, 14865 (1994)
- Laikhtman, B.D., *Sov. Phys. Solid State* **15**, 62 (1973)
- Laikhtman, B.D., Petrov, V.Yu., *Sov. Phys. JETP* **46**, 628 (1977a)
- Laikhtman, B.D., Petrov, V.Yu., *Fizika tverdogo tela* **19**, 1512 (1977b)
- Laikhtman, B.D., Tagantsev, A.K., *Sov. Phys. Solid State* **17**, 1127 (1975)
- Lajzerowicz, J., *Ferroelectrics* **24**, 179 (1980)
- Lajzerowicz, J., *Ferroelectrics* **35**, 219 (1981)
- Lajzerowicz, J., Niez, J.J., *J. Phys. Lett. Paris* **40**, L-165 (1979)
- Landauer, R., *J. Appl. Phys.* **28**, 227 (1957)
- Landauer, R., Young, D.R., Drougard, M.E., *J. Appl. Phys.* **27**, 752 (1956)
- Landolt-Börnstein, *Numerical Data and Functional Relationships in Science and Technology*, New Series vol. III/3. Springer, New York (1969)
- Landolt-Börnstein, *Numerical Data and Functional Relationships in Science and Technology*, New Series vol. III/9. Springer, New York (1975)
- Landolt-Börnstein, *Numerical Data and Functional Relationships in Science and Technology*, New Series vol. III/16a. Springer, New York (1981)
- Landolt-Börnstein, *Numerical Data and Functional Relationships in Science and Technology*, New Series vol. III/16b. Springer, New York (1982)
- Landolt-Börnstein, *Numerical Data and Functional Relationships in Science and Technology*, New Series vol. III/28b. Springer, New York (1990a)
- Landolt-Börnstein, *Numerical Data and Functional Relationships in Science and Technology*, New Series vol. III/28a. Springer, New York (1990b)
- Lang, A.R., *Appl. Phys. Lett.* **7**, 168 (1965)
- Larkin, A.I., Ovchinnikov, Y.N., *J. Low Temp. Phys.* **34**, 409 (1979)

- Larsen, P.K., Kampschoer, G.L.M., Ulenaers, M.J.E., Spierings, A.C.M., Cuppens, R., Appl. Phys. Lett. **59**, 611 (1991)
- Larsen, P.K., Dormans, G.J.M., Taylor, D.J., Van Veldhoven, P.J., J. Appl. Phys. **76**, 2405 (1994)
- Latham, R.V., Br. J. Appl. Phys. **18**, 1383 (1967)
- Laughner, J.W., Newnham, R.E., Cross, L.E., Phys. Stat. Sol. (a) **56**, K83 (1979)
- Laughner, J.W., Wadhawan, V.K., Newnham, R.E., Ferroelectrics **36**, 439 (1981)
- Laurell, F., Roelofs, M.G., Bindloss, W., Hsiung, H., Suna, A., Bierlein, J.D., J. Appl. Phys. **71**, 4664 (1992)
- Lawless, W.N., Phys. Rev. **175**, 619 (1968)
- Lawless, W.N., Ferroelectrics **73**, 395 (1987)
- Lawless, W.N., Fousek, J., J. Phys. Soc. Jpn. **28**, 419 (1970)
- Le Bihan, R., Ferroelectrics **97**, 19 (1989)
- Le Bihan, R., Ferroelectrics **111**, (1990)
- Le Bihan, R., Abboud, B., Ferroelectrics **92**, 375 (1989)
- Le Bihan, R., Chartier, J.L., Proceedings of the Seventh International Vacuum Congress and Third International Conference on Solid Surfaces, Vienna 1977, 2647 (1977)
- Le Bihan, R., Maussion, M., C. R. Acad. Sci. Paris **272B**, 1010 (1971)
- Le Bihan, R., Maussion, M., Ferroelectrics **7**, 307 (1974)
- Le Bihan, R., Sella, C., J. Phys. Soc. Jpn. **28 Suppl.**, 377 (1970)
- Le Bihan, R., Chartier, J.L., Jean, L., Ferroelectrics **17**, 429 (1977)
- Le Bihan, R., Maussion, M., Marbeuf, Ph., Ferroelectrics **22**, 827 (1978)
- Le Bihan, R., Boudjema, E.H., Hilzler, B., Szczesniak, L., Mayer, C.-P., Ferroelectrics **55**, 189 (1984)
- Le Bihan, R., Averty, D., Pain, D., Ferroelectrics **172**, 181 (1995)
- Lebedev, N.I., Sigov, A.S., Integr. Ferroelectr. **4**, 21 (1994)
- Lee, K.S., Baik, S., J. Appl. Phys. **85**, 1995 (1999)
- Lee, K.S., Baik, S., J. Appl. Phys. **87**, 8035 (2000)
- Lee, J.-H., Nakamura, T., Takashige, M., Jpn. J. Appl. Phys. **23**, 378 (1984)
- Lee, J., Ramesh, R., Keramidis, V.G., Warren, W.L., Pike, G.E., Evans, J.T., Appl. Phys. Lett. **66**, 1337 (1995a)
- Lee, J.J., Thio, C.L., Desu, S.B., J. Appl. Phys. **78**, 5073 (1995b)
- Lee, E.G., Wouters, D.J., Willems, G., Maes, H.E., Appl. Phys. Lett. **70**, 2404 (1997a)
- Lee, K.S., Kang, Y.M., Baik, S., Integr. Ferroelectr. **14**, 43 (1997b)
- Lee, K., Lee, K.S., Baik, S., J. Appl. Phys. **90**, 6327 (2001a)
- Lee, K.S., Choi, J.H., Lee, J.Y., Baik, S., J. Appl. Phys. **90**, 4095 (2001b)
- Lee, W.T., Salje, E.K.H., Bismayer, U., J. Phys. Condens. Matter **14**, 7901 (2002)
- Lee, W.T., Salje, E.K.H., Bismayer, U., J. Appl. Phys. **93**, 9890 (2003)
- Lehnen, P., Dec, J., Kleemann, W., J. Phys. D Appl. Phys. **33**, 1932 (2000)
- Lejcek, L., Czech. J. Phys. B **33**, 447 (1983)
- Levanyuk, A.P., Sigov, A.S., Defects and Structural Phase Transitions. Gordon and Breach, New York (1988)
- Levanyuk, A.P., Sannikov, D.G., Zh. Eksp. Teor. Fiz. **55**, 256 (1968)
- Levy, J., Hubert, C., Trivelli, A., J. Chem. Phys. **112**, 7848 (2000)
- Li, Z., Foster, C.M., Dai, X.-H., Xu, X.-Z., Chan, S.-K., Lam, D.J., J. Appl. Phys. **71**, 4481 (1992)
- Li, Y.L., Hu, S.Y., Liu, Z.K., Chen, L.Q., Appl. Phys. Lett. **78**, 3878 (2001)
- Li, Y.L., Hu, S.Y., Liu, Z.K., Chen, L.Q., Acta Mater. **50**, 395 (2002)
- Li, Y.L., Choudhury, S., Liu, Z.K., Chen, L.Q., Appl. Phys. Lett. **83**, 1608 (2003)
- Li, Y.L., Cross, L.E., Chen, L.Q., J. Appl. Phys. **98**, 64101 (2005)
- Lian, L., Chong, T.C., Kumagai, H., Hirano, M., Taijing, L., Ng, S.C., J. Appl. Phys. **80**, 376 (1996)
- Liao, J., Yang, Y., Hui, S.X., Luo, H.S., Yin, Q.R., Ferroelectrics **231**, 55 (1999a)

- Liao, J., Yang, Y., Jiang, X.P., Hui, S.X., Yin, Q.R., *Mater. Lett.* **39**, 335 (1999b)
- Lim, A.R., Jeong, S.-Y., *Solid State Commun.* **110**, 131 (1999)
- Lim, A.R., Choh, S.H., Jang, M.S., *J. Phys. Condens. Matter* **1**, 1571 (1989)
- Lim, A.R., Choh, S.H., Jang, M.S., *J. Phys. Condens. Matter* **7**, 7309 (1995)
- Lin, C.H., Yen, B.M., Batzer, R.S., Chen, H., *Ferroelectrics* **221**, 237 (1999)
- Lin, P.J., Bursill, L.A., *Phil. Mag. A* **48**, 251 (1983)
- Lines, M.E., Glass, A.M., *Principles and Applications of Ferroelectrics and Related Materials*. Clarendon Press, Oxford (1977)
- Little, E.A., *Phys. Rev.* **98**, 978 (1955)
- Litvin, D.B., Janovec, V., *Ferroelectrics* **191**, 9 (1997)
- Logé, R.E., Suo, Z., *Acta Mater.* **44**, 3429 (1996)
- Lohse, O., Grossmann, M., Boettger, U., Boltzen, D., Waser, R., *J. Appl. Phys.* **89**, 2332 (2001)
- Lopez Rodriguez, V., Gonzales Ibeas, J., *Ferroelectrics* **6**, 203 (1973)
- Love, E.A.H., *A Treatise on the Mathematical Theory of Elasticity*. Dover, New York (1944)
- Lu, Y., Wei, T., Duewer, F., Lu, Y., Ming, N., Schultz, P.G., Xiang, X.-D., *Science* **276**, 2004 (1997)
- Luh, Y.S., Feigelson, R.S., Fejer, M.M., Byer, R.L., *J. Cryst. Growth* **78**, 135 (1986)
- Lundstrom, K.I., Svensson, C.M., *IEEE Trans. Electron Devices* **ED 19**, 826 (1972)
- Luo, E.Z., Xie, Z., Xu, J.B., Wilson, I.H., Zhao, L.H., *Phys. Rev. B* **61**, 203 (2000)
- Lüthi, R., Haefke, H., Grütter, P., Güntherodt, H.-J., *Surf. Sci. Lett.* **285**, L498 (1993a)
- Lüthi, R., Haefke, H., Meyer, K.-P., Meyer, E., Howald, L., Güntherodt, H.-J., *J. Appl. Phys.* **74**, 7461 (1993b)
- Lüthi, R., Haefke, H., Gutmannsbauer, W., Meyer, E., Howald, L., Güntherodt, H.-J., *J. Vac. Sci. Technol. B* **12**, 2451 (1994a)
- Lüthi, R., Meyer, E., Howald, L., Haefke, H., Anselmetti, D., Dreier, M., Ruetschi, M., Bonner, T., Overney, R.M., Frommer, J., Güntherodt, H.-J., *J. Vac. Sci. Technol.* **12**, 1673 (1994b)
- Lyuksyutov, I.F., Nattermann, T., Pokrovsky, V., *Phys. Rev. B* **59**, 4260 (1999)
- Ma, W., Cross, L.E., *Appl. Phys. Lett.* **79**, 4420 (2001)
- Maffit, K.N., *J. Appl. Phys.* **39**, 3878 (1968)
- Magataev, V.K., Gladkii, V.V., Zheludev, I.S., *Izvestija AN SSSR, ser. fiz.* **39**, 778 (1975)
- Maier, I.O., Sokolov, A.I., Tagantsev, A.K., *Sov. Phys. Solid State* **22**, 892 (1980)
- Majumder, S.B., Mohapatra, Y.N., Agrawal, D.C., *Appl. Phys. Lett.* **70**, 138 (1997)
- Makio, S., Nitanda, F., Ito, K., Sato, M., *Appl. Phys. Lett.* **61**, 3077 (1992)
- Malek, Z., Mastner, J., Hrdlicka, J., Janta, J., *Solid State Electron.* **7**, 655 (1964)
- Manolikas, C., Amelinckx, S., *Phys. Stat. Sol. (a)* **60**, 167 (1980a)
- Manolikas, C., Amelinckx, S., *Phys. Stat. Sol. (a)* **60**, 607 (1980b)
- Marchenko, V.I., *Zh. Eksp. Teor. Fiz.* **77**, 2419 (1979)
- Martin, Y., Williams, C.C., Wickramasinghe, H.K., *J. Appl. Phys.* **61**, 4723 (1987)
- Martin, Y., Abraham, D.W., Wickramasinghe, H.K., *Appl. Phys. Lett.* **52**, 1103 (1988)
- Martinez, J.L., Gonzalo, J.A., *Ferroelectrics* **44**, 5 (1982)
- Maruyama, T., Saitoh, M., Sakai, I., Hikada, T., Yano, Y., Noguchi, T., *Appl. Phys. Lett.* **73**, 3524 (1998)
- Marvan, M., *Czech. J. Phys. B* **19**, 482 (1969)
- Matthews, J.W., Blakeslee, A.E., *J. Cryst. Growth* **27**, 118 (1974)
- Matthias, B., von Hippel, A., *Phys. Rev.* **73**, 1378 (1948)
- Matyjasek, K., Jakubas, R., *Ferroelectrics* **190**, 25 (1997)
- Mauguin, C., *Bull. Soc. Fr. Minér.* **34**, 71 (1911)
- Maussion, M., Le Bihan, R., *Ferroelectrics* **13**, 465 (1976)
- Maussion, M., Polomska, M., Le Bihan, R., *Ferroelectr. Lett.* **6**, 41 (1986)
- Mayergoyz, I.D., *Mathematical Models of Hysteresis*. Springer Verlag, New York, Berlin (1991)
- McLaren, A.C., Phakey, P.P., *Phys. Stat. Sol.* **31**, 723 (1969)
- Meeks, S.W., Auld, B.A., *Appl. Phys. Lett.* **47**, 102 (1985)

- Megaw, H.D.: *Ferroelectricity in Crystals*. Methuen, London (1957)
- Meleshina, V.A., *Kristallografiya* **9**, 381 (1964)
- Meleshina, V.A., *J. Phys. Soc. Jpn. Suppl.* **28**, 357 (1970)
- Meleshina, V.A., *Sov. Phys. Crystallogr.* **16**, 471 (1971)
- Meleshina, V.A., Indenbom, V.L., Bagdasarov, Kh.S., Pelkhovskaya, T.M., *Sov. Phys. Crystallogr.* **18**, 764 (1974)
- Merz, W.J., *Phys. Rev.* **88**, 421 (1952)
- Merz, W.J., *Phys. Rev.* **91**, 513 (1953)
- Merz, W.J., *Phys. Rev.* **95**, 690 (1954)
- Merz, W.J., *J. Appl. Phys.* **27**, 938 (1956)
- Metrat, G., *Ferroelectrics* **26**, 801 (1980)
- Meyer, K.-P., *Veröffentlichungen 12. Tagung Elektronenmikroskopie, Dresden 1988*, 491 (1988)
- Meyer, B., Vanderbilt, D., *Phys. Rev. B* **65**, 104111 (2002)
- Meyerhofer, D., *Phys. Rev.* **112**, 413 (1958)
- Miga, S., Dec, J., Pawelczyk, M., *J. Phys. Condens. Matter* **8**, 8413 (1996)
- Mihara, T., Watanabe, H., Araujo, C.A.P.d., *Jpn. J. Appl. Phys.* **33**, 3996 (1994)
- Miller, R.C., *Phys. Rev.* **111**, 736 (1958)
- Miller, R.C., Savage, A., *Phys. Rev.* **112**, 755 (1958)
- Miller, R.C., Savage, A., *Phys. Rev. Lett.* **2**, 294 (1959a)
- Miller, R.C., Savage, A., *Phys. Rev.* **115**, 1176 (1959b)
- Miller, R.C., Savage, A., *J. Appl. Phys.* **31**, 662 (1959c)
- Miller, R.C., Savage, A., *J. Appl. Phys.* **32**, 714 (1961)
- Miller, R.C., Weinreich, G., *Phys. Rev.* **117**, 1460 (1960)
- Miller, S.L., Nasby, R.D., Schwank, J.R., Rodgers, M.S., Dressendorfer, P.V., *J. Appl. Phys.* **68**, 6463 (1990)
- Ming, N.-B., Hong, J.-F., Feng, D., *J. Mater. Sci.* **17**, 1663 (1982)
- Mitsui, T., Furuichi, J., *Phys. Rev.* **90**, 193 (1953)
- Mitsui, T., Furuichi, J., *Phys. Rev.* **95**, 558 (1954)
- Mochizuki, J., Futama, H., *J. Phys. Soc. Jpn.* **23**, 127 (1967)
- Mohler, E., Pitka, R., *Solid State Commun.* **14**, 791 (1974)
- Mokry, P., Tagantsev, A.K., Setter, N., *Phys. Rev. B* **70**, 172107 (2004)
- Mokry, P., Tagantsev, A.K., Fousek, J., *Phys. Rev. B* **75**, 094110 (2007)
- Molotskii, M., *Philos. Mag. Lett.* **83**, 763 (2003a)
- Molotskii, M., *J. Appl. Phys.* **93**, 6234 (2003b)
- Molotskii, M., Kris, R., Rosenman, G., *J. Appl. Phys.* **88**, 5318 (2000)
- Molotskii, M., Agronin, A., Urenski, P., Shvebelman, M., Rosenman, G., Rosenwaks, Y., *Phys. Rev. Lett.* **90**, 107601 (2003)
- Moon, E.Y., Choh, S.H., Park, Y.H., Yeom, H.Y., Jang, M.S., *J. Phys. C Solid State Phys.* **20**, 1867 (1987)
- Moravec, F., Konstantinova, V.P., *Kristallografiya* **13**, 284 (1968)
- Mulvihill, M.L., Cross, L.E., Cao, W., Uchino, K., *J. Am. Ceram. Soc.* **80**, 1462 (1997)
- Munoz Saldana, J., Schneider, G.A., Eng, L.M., *Surf. Sci.* **480**, L402 (2001)
- Müller, K.A., Berlinger, W., *Solid State Commun.* **8**, 549 (1970)
- Müser, H.E., Kuhn, W., Albers, J., *Phys. Stat. Sol. (a)* **49**, 51 (1978)
- Nagarajan, V., Jenkins, I.G., Alpay, S.P., Li, H., Aggarwal, S., Salamanca-Riba, L., Ramesh, R., *J. Appl. Phys.* **86**, 595 (1999)
- Nagarajan, V., Ganpule, C.S., Li, H., Salamanca-Riba, L., Roytburd, A.L., Williams, E.D., Ramesh, R., *Appl. Phys. Lett.* **79**, 2805 (2001)
- Nagarajan, V., Roytburd, A., Stanishevsky, A., Prasertchoung, S., Zhao, T., Chen, L., Melngailis, J., Auciello, O., Ramesh, R., *Nat. Mater.* **2**, 43 (2003)
- Nakamura, T., *J. Phys. Soc. Jpn.* **8**, 1379 (1960)
- Nakamura, K., *Jpn. J. Appl. Phys.* **31 Suppl.** **31-1**, 9 (1991)
- Nakamura, T., Nakamura, H., *Jpn. J. Appl. Phys.* **1**, 253 (1962)

- Nakamura, K., Tourlog, A., *Appl. Phys. Lett.* **63**, 2065 (1993)
- Nakamura, T., Ogihara, H., Kobayashi, J., *J. Phys. Soc. Jpn.* **18**, 1716 (1963)
- Nakamura, E., Sato, H., Motegi, H., *J. Phys. Soc. Jpn.* **47**, 1567 (1979)
- Nakamura, E., Ushio, S., Abe, K., *J. Phys. Soc. Jpn.* **53**, 403 (1984)
- Nakamura, E., Kuramoto, K., Deguchi, K., Hayashi, K., *Ferroelectrics* **98**, 51 (1989)
- Nakatani, N., *J. Phys. Soc. Jpn.* **32**, 1556 (1972)
- Nakatani, N., *Jpn. J. Appl. Phys.* **12**, 1723 (1973)
- Nakatani, N., *J. Phys. Soc. Jpn.* **39**, 741 (1975)
- Nakatani, N., *Jpn. J. Appl. Phys.* **18**, 491 (1979)
- Nakatani, N., *Jpn. J. Appl. Phys.* **24**, L528 (1985)
- Nakatani, N., *Ferroelectrics* **97**, 127 (1989a)
- Nakatani, N., *Jpn. J. Appl. Phys.* **28 Suppl.** **28–2**, 143 (1989b)
- Nakatani, N., *Jpn. J. Appl. Phys.* **30**, 1024 (1991a)
- Nakatani, N., *Jpn. J. Appl. Phys.* **30**, 3445 (1991b)
- Nakatani, N., Hirota, M., *Jpn. J. Appl. Phys.* **20**, 2281 (1981)
- Nanamatsu, S., Kimura, M., Doi, K., Matsushita, S., Yamada, N., *Ferroelectrics* **8**, 511 (1974)
- Nassau, K., Levinstein, H.J., Loiacono, G.M., *Appl. Phys. Lett.* **6**, 228 (1965)
- Nattermann, T., *J. Phys. C Solid State Phys.* **16**, 4125 (1983)
- Nattermann, T., Shapir, Y., Vilfan, I., *Phys. Rev. B* **42**, 8577 (1990)
- Nattermann, T., Pokrovsky, V., Vinokur, V.M., *Phys. Rev. Lett.* **87**, 197005 (2001)
- Nechaev, V.N., Roshchupkin, A.M., *Fizika tverdogo tela* **30**, 2286 (1988)
- Nechaev, V.N., Roshchupkin, A.M., *Fizika tverdogo tela* **31**, 243 (1989)
- Nettleton, R.E., *J. Appl. Phys.* **38**, 2775 (1967)
- Newnham, R.E., Cross, L.E., *Mater. Res. Bull.* **9**, 927 (1974a)
- Newnham, R.E., Cross, L.E., *Mater. Res. Bull.* **9**, 1021 (1974b)
- Newton, R.R., Ahearn, A.J., McKay, K.G., *Phys. Rev.* **75**, 103 (1949)
- Néel, L., *Cah. Phys.* **12**, 1 (1942)
- Niizeki, N., Hasegawa, M., *J. Phys. Soc. Jpn.* **19**, 550 (1964)
- Niizeki, N., Yamada, T., Toyoda, H., *Jpn. J. Appl. Phys.* **6**, 318 (1967)
- Nomura, S., Asao, Y., Sawada, S., *J. Phys. Soc. Jpn.* **16**, 917 (1961)
- Nonnenmacher, M., O'Boyle, M.P., Wickramasinghe, H.K., *Appl. Phys. Lett.* **58**, 2921 (1991)
- Novák, M., Hrdlicka, J., *Czech. J. Phys. B* **18**, 122 (1968)
- Novak, J., Salje, E.K.H., *J. Phys. Condens. Matter* **10**, L359 (1998)
- Nutt, A.C.G., Gopalan, V., Gupta, M.C., *Appl. Phys. Lett.* **60**, 2828 (1992)
- Nye, J.F., *Physical Properties of Crystals*. Clarendon Press, Oxford (1992)
- O'Dwyer, J.J., *The Theory of Electrical Conduction and Breakdown in Solid Dielectrics*. Clarendon Press, Oxford (1973)
- O'Keefe, M.A., Hetherington, C.J.D., Wang, Y.C., Nelson, E.C., Turner, J.H., Kisielowski, E.C., Malm, J.-O., Mueller, R., Ringnald, J., Pan, M., Thust, A., *Ultramicroscopy* **89**, 215 (2001)
- Odagawa, H., Cho, Y., *Ferroelectrics* **251**, 29 (2001)
- Odagawa, H., Cho, Y., *Appl. Phys. Lett.* **80**, 2159 (2002)
- Ogawa, T., Senda, A., Kasanami, T., *Jpn. J. Appl. Phys.* **30**, 2145 (1991)
- Oh, K.-Y., Uchino, K., Cross, L.E., *J. Am. Ceram. Soc.* **77**, 2809 (1994)
- Ohgami, J., Sugawara, Y., Morita, S., Nakamura, E., Ozaki, T., *Jpn. J. Appl. Phys.* **35**, 2734 (1996)
- Ohtomo, A., Hwang, H.Y., *Nature* **427**, 423 (2004)
- Okada, K., Suzuki, I., Sugie, H., *J. Phys. Soc. Jpn. Suppl.* **49**, 178 (1980)
- Oleinik, A.S., Bokov, V.A., *Sov. Phys. Solid State* **17**, 560 (1975)
- Orihara, H., Hashimoto, S., Ishibashi, Y., *J. Phys. Soc. Jpn.* **63**, 1031 (1994)
- Orlik, X.K., Labardi, M., Allegrini, M., *Appl. Phys. Lett.* **77**, 2042 (2000)
- Otko, A.I., Stasyuk, I.V., *Ferroelectrics* **172**, 207 (1995)

- Otko, A.I., Nesterenko, N.M., Krainyuk, G.G., Nosenko, A.E., *Ferroelectrics* **48**, 143 (1983)
- Otko, A.I., Nosenko, A.E., Sol'skii, I.M., Burak, Y.V., *Fizika tverdogo tela* **31**, 42 (1989)
- Otko, A.I., Nosenko, A.E., Volk, T.R., Shuvalov, L.A., *Ferroelectrics* **145**, 163 (1993a)
- Otko, A.I., Zapart, W., Zapart, M.B., Kapustianik, V.B., Kuznir, O., *Ferroelectrics* **141**, 43 (1993b)
- Otko, A.I., Nosenko, A.E., Gumennyi, R.M., Stasyuk, I.V., Solskii, I.M., *Ferroelectrics* **191**, 159 (1997)
- Otto, T., Grafström, S., Chaib, H., Eng, L.M., *Appl. Phys. Lett.* **84**, 1168 (2004)
- Ozaki, T., *Ferroelectrics* **172**, 65 (1995)
- Ozaki, T., Fuji, K., Aoyagi, S., *J. Appl. Phys.* **80**, 1697 (1996)
- Ozaki, T., Ohgami, J., *J. Phys. Condens. Matter* **7**, 1711 (1995)
- Ozaki, T., Senju, T., Nakamura, E., *J. Phys. Soc. Jpn.* **62**, 3027 (1993)
- Ozaki, T., Kitamura, T., Ohgami, J., Nakamura, E., *Ferroelectrics* **157**, 87 (1994)
- Ozaki, T., Amau, T., Kawata, H., Mizung, K., Mori, K., *J. Phys. Soc. Jpn.* **66**, 479 (1997)
- Padilla, J., Zhong, W., Vanderbilt, D., *Phys. Rev. B* **53**, R5969 (1996)
- Pakulski, G., Breczewski, T., Mroz, B., Krajewski, T., *Ferroelectrics* **74**, 375 (1987)
- Pakulski, G., Mroz, B., Krajewski, T., *Ferroelectrics* **48**, 259 (1983)
- Pan, W., Zhang, Q., Bhalla, A.S., Cross, L.E., *J. Am. Ceram. Soc.* **71**, C-302 (1988)
- Park, Y., *Solid State Commun.* **113**, 379 (2000)
- Park, B.M., Chung, S.J., *J. Am. Ceram. Soc.* **77**, 3193 (1994)
- Park, B.M., Park, H.M., Chung, S.J., *J. Korean Phys. Soc. (Proc. Suppl.)* **32**, S752 (1998)
- Parpia, D.Y., *Philos. Mag. A* **46**, 691 (1982a)
- Parpia, D.Y., *Philos. Mag. A* **45**, 593 (1982b)
- Paruch, P., Giamarchi, T., Triscone, J.M., *Phys. Rev. Lett.* **94**, 197601 (2005)
- Paruch, P., Giamarchi, T., Tybell, T., Triscone, J.-M., *J. Appl. Phys.* **100**, 051608 (2006)
- Pastrnak, J., Cross, L.E., *Phys. Stat. Sol. (b)* **44**, 313 (1971)
- Paton, E., Brazier, M., Mansour, S., Bement, A., *Integr. Ferroelectr.* **18**, 29 (1997)
- Pawlaczyk, C., Tagantsev, A.K., Brooks, K., Reaney, I.M., Klissurska, R., Setter, N., *Integr. Ferroelectr.* **8**, 293 (1995)
- Payne, M.C., Teter, M.P., Allan, D.C., Arias, T.A., Joannopoulos, J.D., *Rev. Mod. Phys.* **64**, 1045 (1992)
- Pearson, G.L., Feldmann, W.L., *Phys. Chem. Solids* **9**, 28 (1959)
- Peercy, P.S., Samara, G.A., *Phys. Rev. B* **8**, 2033 (1973)
- Pendergrass, L.L., *J. Appl. Phys.* **62**, 231 (1987)
- Peng, J.-L., Bursill, L.A., *Philos. Mag. A* **45**, 911 (1982)
- People, R., Bean, J.C., *Appl. Phys. Lett.* **47**, 322 (1985)
- Perez, R., Toribio, E., Gorri, J.A., Benadero, L., *Ferroelectrics* **74**, 3 (1987)
- Petroff, J.F., *Phys. Stat. Sol.* **31**, 285 (1969)
- Pertsev, N.A., Arlt, G., *J. Appl. Phys.* **74**, 4105 (1993)
- Pertsev, N.A., Kohlstedt, H., *Phys. Rev. Lett.* **98**, 257603 (2007)
- Pertsev, N.A., Kohlstedt, H., *Phys. Rev. Lett.* **100**, 149702 (2008)
- Pertsev, N.A., Koukhar, V.G., *Phys. Rev. Lett.* **84**, 3722 (2000)
- Pertsev, N.A., Zembilgotov, A.G., *J. Appl. Phys.* **78**, 6170 (1995)
- Pertsev, N.A., Arlt, G., Zembilgotov, A.G., *Phys. Rev. Lett.* **76**, 1364 (1996)
- Pertsev, N.A., Zembilgotov, A.G., Tagantsev, A.K., *Phys. Rev. Lett.* **80**, 1988 (1998)
- Pertsev, N.A., Zembilgotov, A.G., Hoffmann, S., Waser, R., Tagantsev, A.K., *J. Appl. Phys.* **85**, 1698 (1999a)
- Pertsev, N.A., Zembilgotov, A.G., Tagantsev, A.K., *Ferroelectrics* **223**, 79 (1999b)
- Pertsev, N.A., Tagantsev, A.K., Setter, N., *Phys. Rev. B* **61**, R825 (2000)
- Pertsev, N.A., Tagantsev, A.K., Setter, N., *Phys. Rev. B* **65**, 219901 (2002)
- Pertsev, N.A., Contreras, J.R., Kukhar, V.G., Hermanns, B., Kohlstedt, H., Waser, R., *Appl. Phys. Lett.* **83**, 3356 (2003a)

- Pertsev, N.A., Koukhar, V.G., Kohlstedt, H., Waser, R., *Phys. Rev. B* **67**, 054107 (2003b)
- Petzelt, J., Grigas, J., Mayerova, I., *Ferroelectrics* **6**, 225 (1974)
- Peuzin, J.C., Tasson, M., *Phys. Stat. Sol. (a)* **37**, 119 (1976)
- Pike, G.E., Warren, W.L., Dimos, D., Tuttle, B.A., Ramesh, R., Lee, J., Keramidis, V.G., Evans, J.T., *Appl. Phys. Lett.* **66**, 484 (1995)
- Pique, J.P., Dolino, G., Vallade, M., *J. Phys. Paris* **38**, 1527 (1977)
- Polcarová, M., Brádler, J., Janta, J., *Phys. Stat. Sol. (a)* **2**, K137 (1970)
- Polomska, M., Jakubas, R., *Ferroelectrics* **106**, 57 (1990)
- Pompe, W., Gong, X., Suo, Z., Speck, J.S., *J. Appl. Phys.* **74**, 6012 (1993)
- Pouget, J., Maugin, G.A., *Phys. Lett.* **109A**, 389 (1985)
- Poykko, S., Chadi, D.J., *Appl. Phys. Lett.* **75**, 2830 (1999)
- Pradhan, M.M., Garg, R.K., Arora, M., *Ferroelectrics* **56**, 251 (1984)
- Prasad, V.C.S., Subbarao, E.C., *Ferroelectrics* **15**, 143 (1977)
- Preisach, F., *Z. Phys.* **94**, 277 (1935)
- Pulvari, C.F., Kuebler, W., *J. Appl. Phys.* **29**, 1315 (1958a)
- Pulvari, C.F., Kuebler, W., *J. Appl. Phys.* **29**, 1742 (1958b)
- Putnis, A., Salje, E., *Phase Transitions* **48**, 85 (1994)
- Rabe, H., Burkhardt, E., Rivera, J.-P., Schmid, H., Walker, E., Sadowski, W., Karkut, M.G., Antognazza, J.-M., Triscone, J.-M., Fischer, O., *Ferroelectrics* **92**, 129 (1989)
- Rabe, H., Rivera, J.-P., Burkhardt, E., Schmid, H., *Sci. Tech. Inform.* **10**, 174 (1993)
- Rabe, H., Rivera, J.-P., Schmid, H., Chaminade, J.-P., Nganga, L., *Mat. Sci. Eng.* **B5**, 243 (1990)
- Rabe, K.A., Ahn, C.H., Triscone, J.M. (eds.): *Physics of Ferroelectrics: A Modern Perspective*. Springer, Berlin, Heidelberg, New York (2007)
- Ramesh, R., Chan, W.K., Wilkens, B., Sands, T., Tarascon, J.M., Keramidis, V.G., *Integr. Ferroelectr.* **1**, 1 (1992)
- Rao, C.N.R., Rao, K.J.: *Phase Transitions in Solids*. McGraw-Hill, New York (1978)
- Rapoport, S.L., Dontsova, L.I., *Sov. Phys. Crystallogr.* **15**, 327 (1970)
- Ratcliffe, P.J., *Phys. Stat. Sol. (a)* **70**, 211 (1982)
- Ravi, R., Sangunni, K.S., Narayanan, P.S., *J. Phys. E Sci. Instrum.* **13**, 585 (1980)
- Ravikumar, V., Rodrigues, R.P., Dravid, V.P., *J. Am. Ceram. Soc.* **80**, 1117 (1997)
- Rayleigh, L., *Philos. Mag.* **23**, 225 (1887)
- Resta, R., *Rev. Mod. Phys.* **66**, 899 (1994)
- Rivera, J.-P., *Ferroelectrics* **141**, 159 (1993)
- Robert, M.C., Lefaucheux, F., *J. Cryst. Growth* **65**, 637 (1983)
- Robert, G., Damjanovic, D., Setter, N., Turik, A.V., *J. Appl. Phys.* **89**, 5067 (2001)
- Robinson, G.Y., White, R.M., *Appl. Phys. Lett.* **10**, 320 (1967)
- Roelofs, A., Böttger, U., Waser, R., Schlaphof, F., Trogisch, S., Eng, L.M., *Appl. Phys. Lett.* **77**, 3444 (2000)
- Roelofs, A., Pertsev, N.A., Waser, R., Schlaphof, F., Eng, L.M., Ganpule, C., Nagarajan, V., Ramesh, R., *Appl. Phys. Lett.* **80**, 1424 (2002)
- Roetschi, H., *J. Sci. Instrum.* **39**, 152 (1962)
- Roitburd, A.L., *Sov. Phys. Dokl.* **16**, 305 (1971)
- Roitburd, A.L., *Phys. Stat. Sol. (a)* **37**, 329 (1976)
- Romanov, A.E., Pompe, W., Speck, J.S., *J. Appl. Phys.* **79**, 4037 (1996)
- Romanov, A.E., Lefevre, M.J., Speck, J.S., Pompe, W., Streiffner, S.K., Foster, C.M., *J. Appl. Phys.* **83**, 2754 (1998)
- Romanov, A.E., Vojta, A., Pompe, W., Lefevre, M.J., Speck, J.S., *Phys. Stat. Sol. (a)* **172**, 225 (1999)
- Rosenman, G., *Ferroelectrics* **141**, 95 (1993)
- Rosenman, G., Kugel, V.D., *Ferroelectrics* **157**, 105 (1994)
- Rosenman, G., Kugel, V.D., Shur, D., *Ferroelectrics* **172**, 7 (1995)
- Rosenman, G., Rez, I., *J. Appl. Phys.* **73**, 1904 (1993)

- Roytburd, A.L., Elastic domains in ferroelectric epitaxial films., in *Thin films Ferroelectric Material and Devices*, edited by Ramesh, R., Kluwer Academic Publishers, Boston/Dordrecht/London (1997)
- Roytburd, A.L., *J. Appl. Phys.* **83**, 228 (1998a)
- Roytburd, A.L., *J. Appl. Phys.* **83**, 239 (1998b)
- Roytburd, A.L., Alpay, S.P., Bendersky, L.A., Nagarajan, V., Ramesh, R., *J. Appl. Phys.* **89**, 553 (2001)
- Rudiyak, V.M., Kudzin, A.Y., Panchenk, T., *Sov. Phys. Solid State* **14**, 2112 (1973)
- Rychetsky, I., *Ferroelectrics* **172**, 105 (1995)
- Rychetsky, I., Schranz, W., *J. Phys. Condens. Matter* **5**, 1455 (1993)
- Rychetsky, I., Schranz, W., *J. Phys. Condens. Matter* **6**, 11159 (1994)
- Rychetsky, I., Schranz, W., Zielinski, P., *Ferroelectrics* **126**, 383 (1992)
- Safránková, M., *Czech. J. Phys. B* **20**, 797 (1970a)
- Safránková, M., *Proceedings of the European Meeting on Ferroelectricity, Saarbruecken 1969*, p. 231 (1970b)
- Safrankova, M., Fousek, J., Kaczer, J., *Proceedings of the International Meeting on Ferroelectricity, Prague 1966*, p. 51 (1966)
- Safrankova, M., Fousek, J., Kizhaev, S.A., *Czech. J. Phys. B* **17**, 559 (1967)
- Sakata, H., Hamano, K., *J. Phys. Soc. Jpn.* **61**, 3786 (1992)
- Sakata, H., Hamano, K., *Ferroelectrics* **140**, 169 (1993)
- Salje, E.K.H.: *Phase Transitions in Ferroelastic and Co-elastic Crystals*. Cambridge University Press, Cambridge (1990)
- Salje, E.K.H., *Phase Transitions* **55**, 37 (1995)
- Salje, E., Chrosch, J., *Ferroelectrics* **183**, 85 (1996)
- Salje, E., Hoppmann, G., *Mater. Res. Bull.* **11**, 1545 (1976)
- Salomon, R.E., *Ferroelectrics* **33**, 185 (1981)
- Sannikov, D.G., *Sov. Phys. JETP* **14**, 98 (1962)
- Sapriel, J., *Phys. Rev. B* **12**, 5128 (1975)
- Saurenbach, F., Terris, B.D., *Appl. Phys. Lett.* **56**, 1703 (1990)
- Savage, A., Miller, R.C., *J. Appl. Phys.* **31**, 1546 (1960)
- Sawada, A., Abe, R., *Jpn. J. Appl. Phys.* **5**, 401 (1966)
- Sawada, A., Abe, R., *Jpn. J. Appl. Phys.* **6**, 699 (1967)
- Sawyer, C.B., Tower, C.H., *Phys. Rev.* **35**, 269 (1930)
- Scherf, Ch., Hahn, Th., Heger, G., Becker, R.A., Wunderlich, W., Klapper, H., *Ferroelectrics* **191**, 171 (1997)
- Schlenker, M., Baruchel, J., *Ferroelectrics* **162**, 299 (1994)
- Schloss, L.F., McIntyre, P.C., Hendrix, B.C., Bilodeau, S.M., Roeder, J.F., Gilbert, S.R., *Appl. Phys. Lett.* **81**, 3218 (2002)
- Schmid, H., *Rost Kristallov* **7**, 32 (1967)
- Schmid, H., Polarized light microscopy (PLM) of ferroelectric and ferroelastic domains in transmitted and reflected light, in *Ferroelectric Ceramics*, edited by Setter, N., Colla, E., pp. 107–126, Birkhäuser Verlag, Basel (1993)
- Schmidt, V.H., Parker, R.S., *J. Phys. Colloq. C2* **33**, 109 (1972)
- Schmidt, G., Borchardt, G., Von Cieminski, J., Grützmänn, D., Purinsch, E., Isupov, V.A., *Ferroelectrics* **42**, 3 (1982)
- Schmid, H., Burkhardt, E., Walker, E., Brixel, W., Clin, M., Rivera, J.-P., Jorda, J.-L., Francois, M., Yvon, K., *Z. Phys. B Condens. Matter* **72**, 305 (1988a)
- Schmid, H., Rivera, J.-P., Clin, M., Williams, A., Burkhardt, E., *Physica C* **153–155**, 1748 (1988b)
- Schmahl, W.W., Putnis, A., Salje, E., Freeman, P., Graeme-Barber, A., Jones, R., Singh, K. K., Blunt, J., Edwards, P.P., Loram, J., Mirza, K., *Philos. Mag.Lett.* **60**, 241 (1989)
- Schorn, P., Ellerkmann, U., Bolten, D., Boettger, U., Waser, R., *Integr. Ferroelectr.* **53**, 361 (2003)
- Schranz, W., *Phase Transitions* **51**, 1 (1994)

- Schranz, W., Rychetsky, I., *J. Phys. Condens. Matter* **5**, 3871 (1993)
- Schranz, W., Streuselberger, T., Fuith, A., Warhanek, H., Götzinger, M., *Ferroelectrics* **88**, 139 (1988)
- Schranz, W., Rychetsky, I., Warhanek, H., *Ferroelectrics* **141**, 61 (1993)
- Scott, J.F., Araujo, C.A.P.d., Melnick, B.M., McMillan, L.D., Zuleeg, R., *J. Appl. Phys.* **70**, 382 (1991)
- Scott, J.F., Kammerdiner, L., Parris, M., Traynor, S., Ottenbacher, V., Shawabkeh, A., Oliver, W.F., *J. Appl. Phys.* **64**, 787 (1988)
- Scott, J.F., Araujo, C.A.P.d., McMillan, L.D., *Ferroelectric thin films and thin film devices*, in *Ferroelectric Ceramics*, edited by Setter, N., Colla, E., pp. 185–211, Birkhäuser Verlag, Basel (1993)
- Seifert, A., Lange, F.F., Speck, J.S., *J. Mater. Res.* **10**, 680 (1995)
- Seike, A., Amanuma, K., Kobayashi, S., Tatsumi, T., Koike, H., Hada, H., *J. Appl. Phys.* **88**, 3445 (2000)
- Selyuk, B.V., *Kristallografiya* **16**, 356 (1971)
- Sessler, G.M., Broadhurst, M.G., Davis, G.T., Gross, B., Mascarenhas, S., van Turnhout, J., West, J.E., *Electrets*. Springer-Verlag, Berlin (1980)
- Setter, N., Damjanovic, D., Eng, L., Fox, G., Gevorgian, S., Hong, S., Kingon, A., Kohlstedt, H., Park, N.Y., Stephenson, G.B., Stolichnov, I., Tagantsev, A.K., Taylor, D.V., Yamada, T., Streiffer, S., *J. Appl. Phys.* **100**, 51606 (2006)
- Shakmanov, V.V., Spivak, G.V., *Sov. Phys. Solid State* **10**, 802 (1968)
- Shapiro, S.M., Gammon, R.W., Cummins, H.Z., *Appl. Phys. Lett.* **10**, 113 (1966)
- Shekhtman, V.Sh., Shabel'nikov, L.G., Shmyt'ko, I.M., Aknazarov, S.Kh., *Sov. Phys. Solid State* **14**, 2690 (1973)
- Shenyavskaya, L.A., Distler, G.I., *Fizika tverdogo tela* **18**, 1451 (1976)
- Shepherd, I.W., Barkley, J.R., *Solid State Commun.* **10**, 123 (1972)
- Sherman, V.O., Tagantsev, A.K., Setter, N., Iddles, D., Price, T., *J. Appl. Phys.* **99**, 074104 (2006)
- Shiau, S.M., Anderson, T.L., Newnham, R.E., Cross, L.E., *Mater. Res. Bull.* **19**, 831 (1984)
- Shil'nikov, A.V., Nesterov, V.N., Pozdnyakov, A.P., Fedorikhin, V.A., Shuvalov, L.A., *Ferroelectrics* **222**, 317 (1999a)
- Shil'nikov, A.V., Pozdnyakov, A.P., Nesterov, V.N., Fedorikhin, V.A., Uzakov, R.E., *Ferroelectrics* **223**, 149 (1999b)
- Shiojiri, M., Isshiki, T., Saijo, H., Tsujikura, M., Nakada, A., Nakano, Y., Ikeda, M., Nomura, T., *Phys. Stat. Sol. (a)* **129**, 353 (1992)
- Shur, V.Ya., Letuchev, V.V., Popov, Yu.A., *Sov. Phys. Solid State* **24**, 1957 (1982)
- Shur, V.Ya., Letuchev, V.V., Ovechkina, I.V., *Fizika tverdogo tela* **26**, 3474 (1984a)
- Shur, V.Ya., Letuchev, V.V., Rumyantsev, E.L., *Sov. Phys. Solid State* **26**, 1521 (1984b)
- Shur, V.Ya., Letuchev, V.V., Rumyantsev, E.L., Charikova, T.B., *Zhurnal Tekhnicheskoi Fiziki* **55**, 1666 (1985a)
- Shur, V.Ya., Letuchev, V.V., Rumyantsev, E.L., Ovechkina, I.V., *Fizika tverdogo tela* **27**, 1585 (1985b)
- Shur, V.Ya., Letuchev, V.V., Rumyantsev, E.L., Ovechkina, I.V., *Fizika tverdogo tela* **27**, 1232 (1985c)
- Shur, V.Ya., Popov, Yu.A., Rumyantsev, E.L., Subbotin, A.L., Vshivkova, V.V., *Izvestiya Akad. Nauk SSSR, ser. fiz.* **49**, 1860 (1985d)
- Shur, V.Ya., Gruverman, A.L., Korovina, N.V., Orlova, M.E., Sherstovinoval, L.V., *Fizika tverdogo tela* **30**, 299 (1988)
- Shur, V.Y., Gruverman, A.L., Letuchev, V.V., Rumyantsev, E.L., Subbotin, A.L., *Ferroelectrics* **98**, 29 (1989a)
- Shur, V.Ya., Kuminov, V.P., Gruverman, A.L., Kopylova, E.B., *Izvestiya Akad. Nauk SSSR, ser. fiz.* **53**, 1403 (1989b)
- Shur, V.Ya., Gruverman, A.L., Kuminov, V.P., Tonkachyova, N.A., *Ferroelectrics* **111**, 197 (1990)

- Shur, V.Ya., Gruverman, A.L., Ponomarev, N.Y., Tonkachyova, N.A., *Ferroelectrics* **126**, 371 (1992)
- Shur, V.Ya., Rumyantsev, E.L., Subbotin, A.L., *Ferroelectrics* **140**, 305 (1993a)
- Shur, V.Ya., Subbotin, A.L., Kuminov, V.P., *Ferroelectrics* **140**, 101 (1993b)
- Shur, V., Rumyantsev, E., Makarov, S., *J. Appl. Phys.* **84**, 445 (1998)
- Shur, V., Rumyantsev, E., Batchko, R., Miller, G., Fejer, M., Byer, R., *Ferroelectrics* **221**, 157 (1999)
- Shur, V.Ya., Rumyantsev, E.L., Nikolaeva, E.V., Shishkin, E.I., *Appl. Phys. Lett.* **77**, 3636 (2000a)
- Shur, V.Ya., Rumyantsev, E.L., Nikolaeva, E.V., Shishkin, E.I., Fursov, D.V., Batchko, R., G., Eyress, L.A., Fejer, M.M., Byer, R.L., *Appl. Phys. Lett.* **76**, 143 (2000b)
- Shur, V.Y., Rumyantsev, E.L., Nikolaeva, E.V., Shishkin, E.I., Baturin, I.S., *J. Appl. Phys.* **90**, 6312 (2001a)
- Shur, V.Ya., Nikolaeva, E.V., Shishkin, E.I., Kozhevnikov, V.L., Chernykh, A.P., Terabe, K., Kitamura, K., *Appl. Phys. Lett.* **79**, 3146 (2001b)
- Shur, V.Ya., Nikolaeva, E.V., Shishkin, E.I., Chernykh, A.P., Terabe, K., Kitamura, K., Ito, H., Nakamura, K., *Ferroelectrics* **269**, 195 (2002)
- Shuvalov, L.A., *Izvestiya Akad. Nauk SSSR, ser. fiz.* **24**, 1416 (1960)
- Shuvalov, L.A., Ivanov, N.R., *Kristallografiya* **9**, 363 (1964)
- Shuvalov, L.A., *J. Phys. Soc. Jpn. Suppl.* **28**, 38 (1970)
- Shuvalov, L.A. (ed.): *Modern Crystallography IV*. Springer-Verlag, Berlin (1988)
- Shuvalov, L.A., Gridnev, S.A., Kudryash, V.I., Prasolov, B.N., *Phys. Stat. Sol. (a)* **83**, 131 (1984)
- Shuvalov, L.A., Dudnik, E.F., Nepochatenko, V.A., Vagin, S.V., *Izvestiya Akad. Nauk SSSR, ser. fiz.* **49**, 297 (1985a)
- Shuvalov, L.A., Dudnik, E.F., Vagin, S.V., *Ferroelectrics* **65**, 143 (1985b)
- Shuvalov, L.A., Dudnik, E.F., Pozdnev, V.G., *Izvestiya Akad. Nauk SSSR, ser. fiz.* **51**, 2119 (1987)
- Sidorkin, A.S., *Ferroelectrics* **150**, 313 (1993)
- Sidorkin, A.S.: *Domain Structure in Ferroelectrics and Related Materials*. International Science Publishing, Cambridge (2006)
- Simmons, J.G., *J. Phys. Chem. Solids* **32**, 2581 (1971)
- Sinha, J.K., *J. Sci. Instrum.* **42**, 696 (1965)
- Sinyakov, E.V., Duda, V.M., Dudnik, E.F., Yakunin, S.I., *Sov. Phys. Solid State* **13**, 2149 (1972)
- Sirotnin, Y.I., Shaskol'skaya, M.P., *Foundations of Crystal Physics*. Nauka, Moscow (1979)
- Skliar, A., Rosenman, G., Lereah, Y., Angert, N., Tseitlin, M., Roth, M., *Ferroelectrics* **191**, 187 (1997)
- Slater, J.S., *Phys. Rev.* **78**, 748 (1950)
- Smolenskii, G.A., Bokov, V.A., Isupov, V.A., Krainik, N.N., Pasyukov, R.E., Sokolov, A.I., *Ferroelectrics and Related Materials*. Gordon and Breach, New York (1984)
- Smolyaninov, I.I., Lee, C.H., Davis, C.C., *Appl. Phys. Lett.* **74**, 1942 (1999)
- Smolyaninov, I.I., Liang, H.Y., Lee, C.H., Davis, C.C., Nagarajan, V., Ramesh, R., *J. Microsc.* **202**, 250 (2001)
- Sogr, A.A., *Ferroelectrics* **97**, 47 (1989)
- Sogr, A.A., Kopylova, I.B., *Ferroelectrics* **172**, 217 (1995)
- Sogr, A.A., Kopylova, I.B., *Ferroelectrics* **191**, 193 (1996)
- Someya, T., Azumi, T., Kobayashi, J., *J. Phys. Soc. Jpn. Suppl.* **28**, 374 (1970)
- Song, T.K., Aggarwal, S., Prakash, A.S., Yang, B., Ramesh, R., *Appl. Phys. Lett.* **71**, 2211 (1997)
- Sonin, E.B., Tagantsev, A.K., *Zh. Eksp. Teor. Fiz.* **94**, 315 (1988)
- Sonin, E.B., Tagantsev, A.K., *Ferroelectrics* **98**, 291 (1989)
- Speck, J.S., Pompe, W., *J. Appl. Phys.* **76**, 466 (1994)

- Spivak, G.V., Igras, Ye., Zheludev, I.S., *Doklady Akad. Nauk SSSR* **122**, 54 (1958)
- Spivak, G.V., Igras, E., Pryamkova, I.A., Zheludev, I.S., *Sov. Phys. Crystallogr.* **4**, 115 (1959)
- Spycher, R., Buffat, P.A., Stadelmann, P., *Helv. Phys. Acta* **60**, 804 (1987)
- Srikant, V., Tarsa, E.J., Clarke, D.R., Speck, J.S., *J. Appl. Phys.* **77**, 1517 (1995)
- Stadler, H.L., *J. Appl. Phys.* **34**, 570 (1963)
- Stadler, H.L., *J. Appl. Phys.* **37**, 1947 (1966)
- Stadler, H.L., Zachmanidis, P.J., *J. Appl. Phys.* **34**, 3255 (1963)
- Stadler, H.L., Zachmanidis, P.J., *J. Appl. Phys.* **35**, 2625 (1964a)
- Stadler, H.L., Zachmanidis, P.J., *J. Appl. Phys.* **35**, 2895 (1964b)
- Stankowska, J., Czarnecka, A., *Ferroelectrics* **98**, 95 (1989)
- Stasyuk, I.V., Pavlenko, N., Polomska, M., *Phase Transitions* **62**, 167 (1997)
- Steinhauer, D.E., Anlage, S.M., *J. Appl. Phys.* **89**, 2314 (2001)
- Steinhauer, D.E., Vlahacos, C.P., Wellstood, F.C., Anlage, S.M., Canedy, C., Ramesh, R., Stanishevsky, A., Melngailis, J., *Appl. Phys. Lett.* **75**, 3180 (1999)
- Stemmer, S., Streiffer, S.K., Ernst, F., Rühle, M., *Philos. Mag.A* **71**, 713 (1995)
- Stengel, M., Spaldin, N.A., *Nature* **443**, 679 (2006)
- Stephanovich, V.A., Lukyanchuk, I.A., Lahoche, L., Marssi, M.E., *Phys. Rev. Lett.* **94**, 047601 (2005)
- Stern, E.A., *Phys. Rev. Lett.* **93**, 037601 (2004)
- Stern, J.E., Terris, B.D., Mamin, H.J., Rugar, D., *Appl. Phys. Lett.* **53**, 2717 (1988)
- Stolichnov, I., Tagantsev, A.K., Colla, E., Gentil, S., Hiboux, S., Baborowski, J., Muralt, P., Setter, N., *J. Appl. Phys.* **88**, 2154 (2000)
- Stolichnov, I., Colla, E., Tagantsev, A., Bharadwaja, S.N., Hong, S., Setter, N., Cross, J.S., Tsukada, M., *Appl. Phys. Lett.* **80**, 4804 (2002a)
- Stolichnov, I., Colla, E., Tagantsev, A.K., Bharadwaja, S.N., Hong, S., Setter, N., Cross, J.S., Tsukada, M.: Direct nanoscale observation of size effects on polarization instability in Pb(Zr,Ti)O₃ film capacitors, in *Ferroelectric Thin Films X*, edited by Gilbert, S.R., Miyasaka, Y., Wouters, D., Trolier-McKinstry, S., Streiffer, S.K. (Mater. Res. Soc. Symp. Proc. **Volume 688**, p. 235, Warrendale, PA, 2002b)
- Stolichnov, I., Tagantsev, A.K., Setter, N.: Polarization reversal model and prediction of temperature-dependent switching of ferroelectric capacitors, in *Ferroelectric Thin Films XII*, edited by Hoffmann-Eifert, S., Funakubo, H., Kingon, A.I., Koutzaroff, I., Joshi, V. (Mater. Res. Soc. Symp. Proc. **Volume 784**, p. 441, Warrendale, PA, 2004)
- Stolichnov, I., Malin, L., Colla, E., Tagantsev, A.K., Setter, N., *Appl. Phys. Lett.* **86**, 012902 (2005a)
- Stolichnov, I., Tagantsev, A.K., Colla, E., Setter, N., Cross, J.S., *J. Appl. Phys.* **98**, 084106 (2005b)
- Streiffer, S.K., Parker, C.B., Romanov, A.E., Lefevre, M.J., Zhao, L., Speck, J.S., Pompe, W., Foster, C.M., Bai, G.R., *J. Appl. Phys.* **83**, 2742 (1998)
- Streiffer, S.K., Basceri, C., Parker, C.B., Lash, S.E., Kingon, A.I., *J. Appl. Phys.* **86**, 4565 (1999)
- Streiffer, S.K., Eastman, J.A., Fong, D.D., Thompson, C., Munkholm, A., Ramana Murty, M.V., Auciello, O., Bai, G.R., Stephenson, G.B., *Phys. Rev. Lett.* **89**, 67601 (2002)
- Strukov, B.A., Toshev, S.D., *Sov. Phys. Crystallogr.* **9**, 349 (1964)
- Strukov, B.A., Meleshina, V.A., Kalinin, V.I., Taraskin, S.A., *Kristallografiya* **17**, 1166 (1972a)
- Strukov, B.A., Velichko, I.A., Baddur, A., Koptsik, V.A., *Fizika tverdogo tela* **14**, 1034 (1972b)
- Strukov, B.A., Taraskin, S.A., Meleshina, V.A., Belugina, N.V., Yurin, V.A., *Ferroelectrics* **22**, 727 (1978)
- Strukov, B.A., Levanyuk, A.P.: *Ferroelectric Phenomena in Crystals*. Springer, Berlin (1998)
- Sturman, B.I., Fridkin, V.M.: *The Photovoltaic and Photorefractive effects in Noncentrosymmetric Materials*. Gordon and Breach Science Publishers, Philadelphia (1992)
- Suda, F., *J. Phys. Soc. Jpn.* **47**, 1556 (1979)
- Suda, F., Hatano, J., Futama, H., *J. Phys. Soc. Jpn.* **45**, 916 (1978a)
- Suda, F., Hatano, J., Futama, H., *J. Phys. Soc. Jpn.* **44**, 244 (1978b)

- Surowiak, Z., Dec, J., Skulski, R., Fesenko, E.G., Gavrilyatchenko, V.G., Semenchov, A.F., *Ferroelectrics* **20**, 277 (1978)
- Surowiak, Z., Mukhortov, V.M., Dudkevich, V.P., *Ferroelectrics* **139**, 1 (1993)
- Suzuki, K., *Solid State Commun.* **11**, 937 (1972)
- Suzuki, I., Ishibashi, Y., *Ferroelectrics* **64**, 181 (1985)
- Suzuki, S., Takagi, M., *J. Phys. Soc. Jpn.* **30**, 188 (1971)
- Suzuki, S., Takagi, M., *J. Phys. Soc. Jpn.* **32**, 1302 (1972)
- Sviridov, E.V., Alyoshin, V.A., Mukhortov, V.M., Golovko, Yu.I., Dudkevich, V.P., Fesenko, E.G., *Ferroelectrics* **56**, 149 (1984)
- Sviridov, E., Alyoshin, V., Golovko, Y., Zakharchenko, I., Mukhortov, V., Dudkevich, V., *Ferroelectrics* **128**, 1 (1992)
- Szczesniak, L., Szczepanska, L., *Ferroelectrics* **111**, 167 (1990)
- Szczesniak, L., Sliwa, M., Hilczer, B., Meyer, K.-P., Margraf, R., *Kristall und Technik* **11**, 1189 (1976)
- Szczesniak, L., Meyer, K.-P., Blumtritt, H., Hilczer, B., Le Bihan, R., Boudjema, E.H., *Phys. Stat. Sol. (a)* **88**, 93 (1985)
- Szczesniak, L., Meyer, K.-P., Hilczer, B., *Ferroelectrics* **81**, 139 (1988)
- Szczesniak, L., Hilczer, B., Meyer, K.-P., *Ferroelectrics* **172**, 227 (1995)
- Tabarez-Muñoz, C., Rivera, J.-P., Bezinges, A., Monnier, A., Schmid, H., *Jpn. J. Appl. Phys. Suppl.* **24-2**, 1051 (1985)
- Tagantsev, A.K., *Phys. Rev. B* **34**, 5883 (1986a)
- Tagantsev, A.K., *JETP Lett.* **45**, 447 (1986b)
- Tagantsev, A.K., *Sov. Ph. Usp.* **30**, 588 (1987)
- Tagantsev, A.K., *Ferroelectrics* **79**, 57 (1988)
- Tagantsev, A.K., *Phase Transitions* **35**, 119 (1991)
- Tagantsev, A.K., *Phys. Rev. Lett.* **69**, 2760 (1993)
- Tagantsev, A.K., *Ferroelectrics* **184**, 79 (1996)
- Tagantsev, A.K., *Phys. Rev. Lett.* **94**, 247603 (2005)
- Tagantsev, A.K., Fousek, J., *Ferroelectrics* **221**, 193 (1999)
- Tagantsev, A.K., Gerra, G., *J. Appl. Phys.* **100**, 051607 (2006)
- Tagantsev, A.K., Sonin, E.B., *Ferroelectrics* **98**, 297 (1989)
- Tagantsev, A.K., Siny, I.G., Prokhorova, S.D., *Izvestiya Akad. Nauk SSSR, ser. fiz.* **51**, 2082 (1987)
- Tagantsev, A.K., Pawlaczyk, C., Brooks, K., Setter, N., *Integr. Ferroelectr.* **4**, 1 (1994)
- Tagantsev, A.K., Landivar, M., Colla, E., Setter, N., *J. Appl. Phys.* **78**, 2623 (1995a)
- Tagantsev, A.K., Pawlaczyk, C., Brooks, K., Landivar, M., Colla, E., Setter, N., *Integr. Ferroelectr.* **6**, 309 (1995b)
- Tagantsev, A.K., Stolichnov, I.A., *Appl. Phys. Lett.* **74**, 1326 (1999)
- Tagantsev, A.K., Courtens, E., Arzel, L., *Phys. Rev. B* **64**, 224107 (2001a)
- Tagantsev, A.K., Stolichnov, I., Colla, E.L., Setter, N., *J. Appl. Phys.* **90**, 1387 (2001b)
- Tagantsev, A.K., Pertsev, N.A., Muralt, P., Setter, N., *Phys. Rev. B* **65**, 012104 (2002a)
- Tagantsev, A.K., Stolichnov, I., Setter, N., Cross, J.S., Tsukada, M., *Phys. Rev. B* **66**, 214109 (2002b)
- Tagantsev, A.K., Sherman, V.O., Astafiev, K.F., Venkatesh, J., Setter, N., *J. Electroceramics* **11**, 5 (2003)
- Tagantsev, A.K., Muralt, P., Fousek, J.: Shape of piezoelectric hysteresis loop for non-ferroelastic switching, in *Ferroelectric Thin Films XII*, edited by Hoffmann-Eifert, S., Funakubo, H., Kingon, A.I., Koutsaroff, I., Joshi, V. (Mater. Res. Soc. Symp. Proc. **Volume 784**, p. 517, Warrendale, PA, 2004a)
- Tagantsev, A.K., Stolichnov, I., Setter, N., Cross, J.S., *J. Appl. Phys.* **96**, 6616 (2004b)
- Tagantsev, A.K., Sherman, V.O., Astafiev, K.F., Venkatesh, J., Setter, N., *J. Electroceramics* **14**, 199 (2005)

- Takagi, M., Suzuki, S., Proceedings of the Sixth International Congress for Electron Microscopy, Kyoto 1966. vol. 1, 623 (1966)
- Takagi, M., Suzuki, S., *J. Phys. Soc. Jpn.* **63**, 1580 (1994)
- Takagi, M., Suzuki, S., Tanaka, K., *J. Phys. Soc. Jpn.* **23**, 134 (1967)
- Takagi, M., Akaba, N., Suzuki, S., *J. Phys. Soc. Jpn.* **46**, 1811 (1979)
- Tanaka, M., Honjo, G., *J. Phys. Soc. Jpn.* **19**, 954 (1964)
- Takahashi, K., Takagi, M., *J. Phys. Soc. Jpn.* **44**, 1266 (1978a)
- Takahashi, K., Takagi, M., *J. Phys. Soc. Jpn.* **44**, 1664 (1978b)
- Takayama, R., Tomita, Y., *J. Appl. Phys.* **65**, 1666 (1989)
- Takashige, M., Fukurai, N., Hamazaki, S.I., Shimizu, F., *J. Korean Phys. Soc. (Proc. Suppl.)* **32**, S721 (1998)
- Takashige, M., Hamazaki, S., Takahashi, Y., Shimizu, F., *Ferroelectrics* **240**, 93 (2000)
- Tanaka, M., Honjo, G., *J. Phys. Soc. Jpn.* **19**, 954 (1964)
- Tanaka, M., Saito, R., Tsuzuki, K., *Jpn. J. Appl. Phys.* **21**, 291 (1982)
- Taylor, G.W., *Australian J. of Physics* **15**, 549 (1962)
- Taylor, G.W., *IEEE Trans. Electron. Comput.* **EC-14**, 881 (1965)
- Taylor, G.W., *J. Appl. Phys.* **37**, 593 (1966)
- Taylor, D.V., Damjanovic, D., Colla, E., Setter, N., *Ferroelectrics* **225**, 91 (1999)
- Terris, B.D., Stern, J.E., Rugar, D., Mamin, H.J., *Phys. Rev. Lett.* **63**, 2669 (1989)
- Terris, B.D., Stern, J.E., Rugar, D., Mamin, H.J., *J. Vac. Sci. Technol.* **A8**, 374 (1990)
- Theis, C.D., Schlom, D.G., *J. Mater. Res.* **12**, 1297 (1997)
- Tietze, H., Müllner, M., Jex, H., *Phys. Stat. Sol. (a)* **66**, 239 (1981)
- Tikhomirov, O.A., *J. Appl. Phys.* **80**, 2358 (1996)
- Tikhomirova, N.A., Dontsova, L.I., Pikin, S.A., Ginzberg, A.V., Adomenas, P.V., *Sov. Phys. Crystallogr.* **23**, 701 (1978)
- Tikhomirova, N.A., Dontsova, L.I., Pikin, S.A., Shuvalov, L.A., *JETP Lett.* **29**, 37 (1979)
- Tikhomirova, N.A., Pikin, S.A., Shuvalov, L.A., Dontsova, L.I., Popov, E.S., Shilnikov, A.V., Bulatova, L.G., *Ferroelectrics* **29**, 145 (1980a)
- Tikhomirova, N.A., Shuvalov, L.A., Baranov, A.I., Karasev, A.R., Dontsova, L.I., Popov, E.S., Shilnikov, A.V., Bulatova, L.G., *Ferroelectrics* **29**, 51 (1980b)
- Tikhomirova, N.A., Dontsova, L.I., Pikin, S.A., Shuvalov, L.A., *Kristallografiya* **30**, 734 (1985a)
- Tikhomirova, N.A., Ginzberg, A.V., Dontsova, L.I., Pikin, S.A., Shuvalov, L.A., *Kristallografiya* **30**, 330 (1985b)
- Tikhomirova, N.A., Shuvalov, L.A., Dontsova, L.I., *Ferroelectrics* **70**, 1 (1986a)
- Tikhomirova, N.A., Shuvalov, L.A., Dontsova, L.I., Bulatova, L.G., Potikha, L.Z., *Sov. Phys. Crystallogr.* **31**, 682 (1986b)
- Tikhomirova, N.A., Adomenas, P.V., Volnyanskii, M.D., Ginzberg, A.V., *Sov. Phys. Crystallogr.* **36**, 853 (1991a)
- Tikhomirova, N.A., Ginzberg, A.V., Chumakova, S.P., Volnyanskii, M.D., Polomska, M., Adomenas, P.V., *Ferroelectrics Letters* **13**, 81 (1991b)
- Tikhomirov, O., Red'kin, B., Trivelli, A., Levy, J., *J. Appl. Phys.* **87**, 1932 (2000)
- Tilley, D.R., Zeks, B., *Ferroelectrics* **134**, 313 (1992)
- Tomaszewski, P.E., *Phase Transitions* **38**, 221 (1992a)
- Tomaszewski, P.E., *Phase Transitions* **38**, 127 (1992b)
- Tolédano, P., Dmitriev, V., *Ferroelectrics* **191**, 85 (1997)
- Tolédano, P., Tolédano, J.-C., *Phys. Rev. B* **25**, 1946 (1982)
- Toledano, J.C., Toledano, P.: *The Landau theory of phase transitions*. World Scientific, Singapore (1988)
- Tomek, J., Janovec, V., Fousek, J., Zikmund, Z., *Ferroelectrics* **20**, 253 (1978)
- Tomita, N., Orihara, H., Ishibashi, Y., *J. Phys. Soc. Jpn.* **58**, 1190 (1989)
- Tonkov, E.Y.: *High Pressure Phase Transformations*. Gordon and Breach, Philadelphia (1992)

- Toshev, S., Proceedings of the International Meeting on Ferroelectricity, Prague 1996, V.II, 31 (1966)
- Toshev, S.D., Sov. Phys. Crystallogr. **8**, 87 (1963a)
- Toshev, S.D., Sov. Phys. Crystallogr. **8**, 541 (1963b)
- Toyoda, H., Waku, S., Hirabayashi, H., J. Phys. Soc. Jpn. **14**, 1003 (1959)
- Tran, C.D., Gerbaux, X., Hadni, A., Ferroelectrics **33**, 31 (1981)
- Traynor, S., Hadnagy, T., Kammerdiner, L., Integr. Ferroelectr. **16**, 63 (1997)
- Tsai, F., Khiznichenko, V., Cowley, J.M., Ultramicroscopy **45**, 55 (1992)
- Tsao, J.K.: Materials Fundamentals for Molecular Beam Epitaxy. Academic, New York (1993)
- Tsunekawa, S., Takei, H., J. Phys. Soc. Jpn. **40**, 1523 (1976)
- Tsukamoto, T., Hatano, J., Futama, H., J. Phys. Soc. Jpn. Suppl. B **49**, 155 (1980)
- Tsukamoto, T., Hatano, J., Futama, H., J. Phys. Soc. Jpn. **51**, 3948 (1982)
- Tsukamoto, T., Hatano, J., Futama, H., J. Phys. Soc. Jpn. **53**, 838 (1984)
- Tsunekawa, S., Fukuda, T., Ozaki, T., Yoneda, Y., Okabe, T., Terauchi, H., J. Appl. Phys. **84**, 999 (1998)
- Tsunekawa, S., Ichikawa, J., Nagata, H., Applied Surface Science **137**, 61 (1999)
- Tsunekawa, S., Fukuda, T., Ozaki, T., Yoneda, Y., Terauchi, H., Appl. Phys. Lett. **71**, 1486 (1997)
- Turik, A.V., Sov. Phys. Solid State **5**, 885 (1963)
- Turik, A.V., Sov. Phys. Solid State **5**, 2141 (1964)
- Turik, A.V., Sov. Phys. Solid State **12**, 688 (1970)
- Tybell, T., Paruch, P., Giamarchi, T., Triscone, J.-M., Phys. Rev. Lett. **89**, 97601 (2002)
- Tylczynski, Z., Acta Phys. Polon. **A 51**, 865 (1977)
- Ubbelohde, A.R., Woodward, I., Nature **156**, 20 (1945)
- Uchida, N., Ikeda, T., Jpn. J. Appl. Phys. **4**, 867 (1965)
- Ujma, Z., Dmytrov, D., Handerek, J., Ferroelectrics **81**, 107 (1988)
- Ungar, S., Hadni, A., Thomas, R., Strimer, P., Ferroelectrics **33**, 43 (1981)
- Unruh, H.-G., Z. Angew. Physik **16**, 315 (1963)
- Unruh, H.G., Phys. kondens. Materie **4**, 275 (1965)
- Usher, T.D., Poole, J.C.P., Farach, H.A., Ferroelectrics **110**, 67 (1990)
- Uwe, H., Sakudo, T., Physical Review B **13**, 271 (1976)
- Vagin, S.V., Dudnik, E.F., Izvestiya Akad. Nauk SSSR, ser. fiz. **47**, 500 (1983)
- Vagin, S.V., Dudnik, E.F., Sinyakov, E.V., Izvestiya Akad. Nauk SSSR, ser. fiz. **43**, 1735 (1979)
- Vaks, V.G.: Introduction to the Microscopic Theory of Ferroelectrics (in Russian). Nauka, Moscow (1973)
- Valasek, J., Phys. Rev. **17**, 475 (1921)
- Vendik, O.G., Zubko, S.P., J. Appl. Phys. **82**, 4475 (1997)
- Vendik, O.G., Zubko, S.P., J. Appl. Phys. **88**, 5343 (2000)
- Verwerft, M., Van Tendeloo, G., Van Landuyt, J., Amelinckx, S., Ferroelectrics **97**, 5 (1989)
- Vlasko-Vlasov, V.K., Indenbom, M.V., Ossipyan, Yu.A., Physica C **153-155**, 1677 (1988)
- Vlokh, R.O., Vlokh, O.V., Kabelka, H., Warhanek, H., Ferroelectrics **190**, 89 (1997)
- Vlokh, R., Uesu, Y., Yamada, Y., Skab, I., Vlokh, O., J. Phys. Soc. Jpn. **67**, 3335 (1998)
- Volk, T., Woehlecke, M., Lithium Niobate. Defects, Photorefraction and Ferroelectric Switching. Springer Series in Materials Science (2008)
- von Cieminski, J., Schmidt, G., Ferroelectrics **81**, 233 (1988)
- von Cieminski, J., Kleint, C., Beige, H., Höche, R., Ferroelectrics **109**, 95 (1990)
- von Hippel, A., Rev. Mod. Phys. **22**, 221 (1950)
- Vysochanskii, Yu.M., Maior, M.M., Perechinskii, S.I., Tikhomirova, N.A., Sov. Phys. Crystallogr. **37**, 90 (1992)
- Wadhawan, V.K.: Introduction to Ferroic Materials. Gordon and Breach Science Publishers, The Netherlands (2000)

- Wadhawan, V.K., *Phase Transitions* **3**, 3 (1982)
- Wadhawan, V.K., *Phase Transitions* **9**, 297 (1987)
- Wahlstrom, E.E.: *Optical Crystallography*. 5th edn. John Wiley, New York (1979)
- Wang, B., Xiao, Z., *J. Appl. Phys.* **88**, 1464 (2000)
- Wang, S., Dudley, M., Cheng, L.K., Bierlein, J.D., Bindloss, W.: Imaging of ferroelectric domains in KTiOPO_4 single crystals by synchrotron X-ray topography, in *Ferroelectric Thin Films III*, edited by Myers, E.R., Tuttle, B.A., Desu, S.B., Larsen, P.K. (Mater. Res. Soc. Symp. Proc. **Volume 310**, p. 29, Warrendale, PA, 1993)
- Wang, Y.G., Zhong, W.L., Zhang, P.L., *Phys. Rev. B* **51**, 5311 (1995)
- Wang, Y.G., Dec, J., Kleemann, W., *J. Appl. Phys.* **84**, 6795 (1998)
- Wang, R., Zhu, Y., Shapiro, S.M., *Phys. Rev. B* **61**, 8814 (2000a)
- Wang, Y.-G., Kleemann, W., Woike, T., Pankrath, R., *Phys. Rev. B* **61**, 3333 (2000b)
- Wang, Y.L., Tagantsev, A.K., Damjanovic, D., Setter, N., Yamarkin, V.K., Sokolov, A.I., *Phys. Rev. B* **73**, 132103 (2006)
- Wang, Y.L., Tagantsev, A.K., Damjanovic, D., Setter, N., *Appl. Phys. Lett.* **91**, 62905 (2007a)
- Wang, Y.L., Tagantsev, A.K., Damjanovic, D., Setter, N., Yamarkin, V.K., Sokolov, A.I., Lukyanchuk, I.A., *J. Appl. Phys.* **101**, 104115 (2007b)
- Warren, W.L., Dimos, D., *Appl. Phys. Lett.* **64**, 866 (1994)
- Warren, W.L., Dimos, D., Pike, G.E., Tuttle, B.A., Raymond, M.V., Ramesh, R., Evans, J.T., *Appl. Phys. Lett.* **67**, 866 (1995a)
- Warren, W.L., Dimos, D., Tuttle, B.A., Pike, G.E., Schwartz, R.W., Clew, P.J., McIntyre, D. C., *J. Appl. Phys.* **77**, 6695 (1995b)
- Waser, R., Klee, M., *Integr. Ferroelectr.* **2**, 23 (1992)
- Weber, H.P., Tofield, B.C., Liao, P.F., *Phys. Rev. B* **11**, 1152 (1975)
- Wechsler, M.S., Lieberman, D.S., Read, T.A., *Trans. Amer. Inst. Mining Met. Engrs.* **197**, 1503 (1953)
- Weidmann, E.J., Anderson, J.C., *Thin Solid Films* **7**, 27 (1971)
- Weinmann, D., Vogt, H., *Phys. Stat. Sol. (a)* **23**, 463 (1974)
- Wemple, S.H., DiDomenico, M.Jr., Camlibel, I., *Appl. Phys. Lett.* **12**, 209 (1968)
- Wicker, A., Lotz, B., Wittmann, J.C., Legrand, J.F., *Polymer Commun.* **30**, 251 (1989)
- Wicker, A., Legrand, J.F., Lotz, B., Wittmann, J.C., *Ferroelectrics* **106**, 51 (1990)
- Wieder, H.H., *J. Appl. Phys.* **28**, 367 (1957)
- Wiesendanger, E., *Czech. J. Phys.* **B 23**, 91 (1973)
- Willard, G.W.: Use of the Etch Technique For Determining Orientation and Twinning in Quartz Crystals. In *Quartz Crystals For Electrical Circuits*, edited by Heising, R.A., pp. 164–204, D.Van Nostrand Co., New York (1947)
- Williams, D.B., Carter, C.B.: *Transmission Electron Microscopy*. Plenum Press, New York, (2004)
- Wood, E.A., Miller, R.C., Remeika, J.P., *Acta Cryst.* **15**, 1273 (1962)
- Wooster, W.A., Wooster, N., *Nature* **157**, 405 (1946)
- Wruck, B., Salje, E.K.H., Zhang, M., Abraham, T., Bismayer, U., *Phase Transitions* **48**, 135 (1994)
- Xu, Y.: *Ferroelectric Materials and their Applications*. North-Holland, Amsterdam (1991)
- Yakunin, S.I., Shakmanov, V.V., Spivak, G.V., Vasil'eva, N.V., *Sov. Phys. Solid State* **14**, 310 (1972)
- Yamada, Y., Shirane, G., Linz, A., *Phys. Rev.* **177**, 848 (1969)
- Yamada, M., Nada, N., Saitoh, M., Watanabe, K., *Appl. Phys. Lett.* **62**, 435 (1993)
- Yamamoto, T., *Jpn. J. Appl. Phys.* **35**, 5104 (1996)
- Yamamoto, N., Yagi, K., Honjo, G., *Phys. Stat. Sol. (a)* **42**, 257 (1977a)
- Yamamoto, N., Yagi, K., Honjo, G., *Phys. Stat. Sol. (a)* **44**, 147 (1977b)
- Yang, T.J., Mohideen, U., Gupta, M.C., *Appl. Phys. Lett.* **71**, 1960 (1997)
- Yang, T.J., Gopalan, V., Swart, P.J., Mohideen, U., *Phys. Rev. Lett.* **82**, 4106 (1999)
- Yen, B.M., Chen, H., *J. Appl. Phys.* **85**, 853 (1999)

- Yin, Q.R., Yang, Y., Zhang, B.Y., Luo, H.S., Yin, Z.W., *J. Korean Phys. Soc. (Proc. Suppl.)* **32**, S719 (1998)
- Yin, Q.R., Liao, J., Zhang, B.Y., Yang, Y., Hang, F.M., *Ferroelectrics* **231**, 11 (1999)
- Yokota, S., *J. Phys. Soc. Jpn.* **51**, 1884 (1982)
- Yoneda, Y., Okabe, T., Sakaue, K., Terauchi, H., *J. Appl. Phys.* **83**, 2458 (1998)
- Yoo, I., Desu, S., *Phys. Stat. Sol. (a)* **133**, 565 (1992)
- Yudin, S.P., Panchenko, T.V., Kudzin, A.Yu., *Ferroelectrics* **18**, 45 (1978)
- Zapart, M.B., Snoeck, E., Saint-Gregoire, P., *Ferroelectrics* **191**, 179 (1997)
- Zavala, G., Fendler, J.H., Trolrier McKinstry, S., *J. Appl. Phys.* **81**, 7480 (1997)
- Zen'iti, K., Husimi, K., Kataoka, K., *J. Phys. Soc. Jpn.* **13**, 661 (1958)
- Zeyen, C.M.E., Meister, H., *Ferroelectrics* **14**, 731 (1976)
- Zhang, L., Ren, X., *Phys. Rev. B* **73**, 094121 (2006)
- Zhang, L.X., Ren, X., *Phys. Rev. B* **71**, 174108 (2005)
- Zhang, X., Hashimoto, T., Joy, D.C., *Appl. Phys. Lett.* **60**, 784 (1992)
- Zhang, X., Joy, D.C., Zhang, Y., Hashimoto, T., Allard, L., Nolan, T.A., *Ultramicroscopy* **51**, 21 (1993)
- Zhang, X., Joy, D.C., Allard, L.F., Nolan, T.A., *Ferroelectrics* **157**, 159 (1994)
- Zhang, B.Y., Jiang, F.M., Yang, Y., Yin, Q.R., *Ferroelectr. Lett.* **22**, 21 (1996)
- Zhao, J., Yang, P., Jiang, S., Jiang, X., Jiang, J., Xian, D., Geng, Z., Zou, Q., *Appl. Phys. Lett.* **59**, 1952 (1991)
- Zhirnov, V.A., *Zh. Eksp. Teor. Fiz.* **35**, 1175 (1958)
- Zhelnova, O., Fesenko, O., *Sov. Phys. Solid State* **27**, 4 (1985)
- Zheludev, I.S., Shuvalov, L.A., *Kristallografiya* **1**, 681 (1956)
- Zheludev, I.S., Shuvalov, L.A., *Kristallografiya* **4**, 459 (1959)
- Zhong, W., Vanderbilt, D., Rabe, K.M., *Phys. Rev. B* **52**, 6301 (1995)
- Zhu, S., Cao, W., *Phys. Rev. Lett.* **79**, 2558 (1998)
- Zhu, Y.M., Suenaga, M., *Philos. Mag. A* **66**, 457 (1992)
- Zhu, J., Zhang, X., Zhu, Y., Desu, S.B., *J. Appl. Phys.* **83**, 1610 (1998)
- Zikmund, Z., *Czech. J. Phys. B* **34**, 932 (1984)
- Zikmund, Z., Fousek, J., *Ferroelectrics* **79**, 73 (1988)
- Zikmund, Z., Fousek, J., *Phys. Stat. Sol. (a)* **112**, 625 (1989)
- Ziman, J.M.: *Principles of the Theory of Solids*. Cambridge University Press, London (1972)
- Zurbuchen, M.A., Asayama, G., Schlom, D.G., *Phys. Rev. Lett.* **88**, 107601 (2002)
- Zvereva, O.V., Minizon, Yu.M., Smol'skii, I.L., *Kristallografiya* **37**, 778 (1992)
- Zwicker, B., Scherrer, P., *Helv. Phys. Acta* **17**, 346 (1944)
- Zybill, C.E., Boubekour, H., Radojkovic, P., Schwartzkopff, M., Hartmann, E., Koch, F., Gross, G., Rezek, B., Bruchhaus, R., Wersing, W.: Domain Structure of poled ferroelectric (111) PZT ($\text{PbTi}_{0.75}\text{Zr}_{0.25}\text{O}_3$) Films, in *Ferroelectric Thin Films VII*, edited by Jones, R.E., Schwartz, R.W., Summerfelt, S., Yoo, I.K. (Mater. Res. Soc. Symp. Proc. **Volume 541**, p. 449, Warrendale, PA, 1999)
- Zybill, C.E., Li, B., Koch, F., Graf, T., *Phys. Stat. Sol. (a)* **177**, 303 (2000)

Index

A

A_1/a_2 -pattern, 525f, 533, 536, 575, 579, 585, 587–588, 592, 668, 670
 A_1/a_2 -variant, 524–525, 565–566, 570–572, 575, 579, 584
Ab initio calculations, 317, 319, 604
A/c- pattern, 532–533, 569, 572, 589, 591–592, 594–598, 668–669
Activated regime, 392–403, 418, 425, 427, 455, 457
Activation
 energy, 372, 394, 453, 454f–455f, 464, 611, 613, 636, 652, 679
 field, 372, 397–403, 417, 430, 433, 439f, 442, 611, 693
A-domains, 123, 130, 152, 154–155, 158–160, 254, 259, 263–264, 389, 524, 527–529, 532, 563–565, 571, 575, 668, 694–697
AFM, 143, 203
AgCl, 135–136, 186, 274, 288
AgNbO₃, 286
Aizu strain, 25–28, 65, 68, 78
 α -alanine, 127, 442, 513
AlPO₄, 114t, 267
Ambivalent pair, 53, 57
Ammonium chloride, 112t, 350
Anisotropy of the wall velocity, 369, 417
Antiferrodistortive, 15
Antiphase boundaries, 126t–127t, 129, 240–241, 261, 311, 313–314, 322
A-SNOM, 201, 290
Aurivillius phase, 544
Average spontaneous strain, 223, 262

B

Ba₂NaNb₃O₁₅, 285
Backscattered electrons, 183–184

Backswitching, 333, 340, 345, 375–376, 383, 414, 435, 476–477, 480, 614, 695, 698, 703
(Ba,Pb)TiO₃, 285
Barium titanate, *see* BaTiO₃
Barkhausen pulses, 169, 389, 434–435
(Ba,Sr)TiO₃, *see* BST
BaTiO₃, 6, 13–14, 24, 39, 47, 59–60, 62, 66, 68, 70–71, 75, 93–97, 112t, 114t, 123–125, 128–132, 136, 152, 155–156, 159–160, 165, 167, 174, 178, 181–183, 193, 195–196, 199, 201, 203–205, 211, 214, 223–224, 227, 253, 255–260, 262, 275t, 281, 283, 285, 300, 307, 309–310, 313, 315–317, 319, 322, 336, 338, 341, 343, 345, 349, 360–371, 378–380, 386–394, 397–402, 410, 412, 417, 430–438, 441–442, 456, 467, 484, 486, 488–492, 497–498, 512–514, 518, 521–524, 532–534, 545, 554, 556, 558–560, 575, 580–582, 585, 614–615, 646, 649, 658, 661, 665, 667, 693, 774–780
Beam coupling topography, 180–181
Bending contribution, 498–502
Bi₄Ti₃O₁₂, 58, 116t, 126t, 169, 204, 522–523, 542–543
BiVO₄, 116t, 237, 313
Bloch line, 312
Bloch wall, 272, 300
Branching, 218, 219f, 231
Brazilian twins, 266
Bright field image, 188–190
BST, 524
Burgers vector, 240, 250, 550–551, 638

C

C₉H₁₈NO, 116t, 385
Ca₂Sr(C₂H₃COO)₆, 132

- CCD camera, 163, 180, 187
 CCD microscope, 163, 169
 $\text{Cd}_2(\text{NH}_4)_2(\text{SO}_4)_3$, 113t, 263
 $\text{Cd}_3(\text{PO}_4)_3\text{Cl}$, 113t, 356
 C-domains, 130, 149, 152–154, 157, 159–160,
 254, 258, 263–264, 488–489, 525,
 527–528, 530–535, 546, 563, 565,
 569–571, 575–577, 580–582, 589,
 591–597, 599, 602, 668, 670, 694–697
 $(\text{CH}_3\text{NH}_3)_5\text{Bi}_2\text{Br}_{11}$, 117t, 142, 376
 Charge injection, 624, 626f, 688
 Checkerboard pattern, 124, 260
 Circular domains, 233, 416–417
 Circulation line, 312
 Clamping approximation, 68, 164, 167, 169,
 237, 243, 261
 Clapping angle, 66–68, 164, 167–169, 173,
 221t, 249, 528
 Coercive field, 85, 89, 92, 157, 295, 333, 337,
 339, 348, 356, 358, 406, 408–410,
 432–434, 438–440, 443, 447–449,
 451–452, 454–456, 466, 468, 476–477,
 480, 484, 488, 498, 504, 512, 522, 608,
 611, 614–620, 622–627, 630–631,
 643–644, 679, 683, 700
 Cole-Cole plot, 503–507, 510
 Compatibility condition, 62–63, 68–69, 189,
 208, 221–223, 238, 241, 243, 262, 264,
 267, 353, 382
 Compensation by free charges, 255
 Composition, 2, 5, 11, 66, 72, 111, 236, 268,
 391, 443–445, 530, 589, 591, 597, 617,
 620, 648, 651
 Conditions of mechanical compatibility, 301,
 305, 311, 382, 524
 Confocal scanning optical microscopy, 201
 Contact mode, 149, 151f
 Correlation
 coefficient, 220, 287f, 292, 308, 605
 energy, 292, 294, 303, 305, 307, 310–311
 length, 293–294, 296, 306, 658
 radius, 293, 656, 658, 662
 Creep, 321, 354, 418–429, 507–508,
 510–511, 693
 exponent, 425–426, 428–429
 Critical nucleus, 395–396, 398, 400–401, 451,
 453, 456–457, 617
 Critical thickness, 214, 548, 550–551, 559,
 573, 575, 585, 587–588, 590, 594,
 607, 669
 Crystal family, 20, 50
 Crystallization temperature, 522, 546, 582,
 590, 592–594, 651
 CsCuCl_3 , 58, 113t, 350
 CsH_2PO_4 , 118t, 196–197
 CsHSeO_4 , 76, 116t
 CSOM, *see* Confocal scanning optical
 microscopy
 CsPbCl_3 , 112t, 205
 Curie-Weiss constants, 84, 102–105, 217,
 604, 665–667, 706
 Curie-Weiss temperatures, 104, 296,
 556–557, 604, 664–667, 705–707
 A/c- variant, 524–528, 564, 566, 569,
 575–583, 669
 Czochralski-grown crystals, 260
- D**
 Dark field imaging, 187–190, 285–286
 Dauphiné twinning, 265, 350
 Dauphiné twins, 46, 73, 123, 174, 177, 196,
 266–267
 Dead layer, 605, 607, 660
 Debye relaxation, 487
 Debye screening length, 220, 309, 414
 Decoration technique, 8, 131–142, 228, 230,
 234, 361, 370, 372
 Defect-stimulated nucleation, 452
 Degeneracy factor, 39, 46
 Degenerate domain states, 38
 Delamination, 678, 690
 Dense domain pattern, 210, 213, 217–218,
 240, 263, 267, 489, 516, 560, 573,
 579–580, 584–585, 594, 601, 603, 671,
 674–677, 709f, 710
 Depinning, 418–419, 422–424, 428, 500,
 504, 513
 Depletion layer, 619–620, 643–644,
 662–664
 Depolarization energy, 208, 211–212, 215,
 226, 228, 256, 326–327, 395–396, 422,
 425–426, 457, 482–483
 Depolarizing field, 104, 199, 209, 211, 217,
 219–220, 226, 231, 257, 262, 284, 326,
 359, 367, 376, 412–414, 451, 456, 482,
 516, 559, 561, 599, 604, 629, 632,
 634–635, 655–656, 671
 Dielectric permittivity
 background, 103, 104–105, 217
 Diffusion of free carriers, 374
 Dinamical contrast, 281
 Dip technique, 123, 125, 128
 Dislocation, 25, 39
 density, 547–550, 552
 DKDP, 246, 251, 252f, 280, 291, 446

Domain

- coalescence, 353, 363, 457–459, 464, 610
- contribution, 447, 464, 471, 479, 484–485, 491, 630, 654, 668–671, 710–711
- freezing, 447–448, 505, 511–514
- nucleation, 122, 183, 430, 441f, 449, 451–457, 611–613, 679, 689, 695, 702
- pair, 52–60, 62–64, 66–69, 74, 77t, 95, 99, 123, 125t, 129, 162, 164, 167, 171, 175, 183, 197, 236, 254, 256, 260, 262–263, 266, 278, 291, 311, 315, 370, 388–389, 542–543
- period, 210, 217, 219–220, 560–562, 567–568, 572, 577, 579, 584, 586–587, 596–604, 675, 707
- wall thickness, 190, 196, 205, 218, 272–273, 280f, 281, 284–287, 291, 293, 314–315, 535, 573, 595–596
- 90° domain walls, 152, 191, 192f, 199, 259–260, 273, 283f, 285f, 285–286, 287f, 307, 309f, 386, 435, 515, 541, 543f, 544, 693–697
- Double hysteresis loops, 87, 334, 336, 436–437
- Dynamic transition, 470
- DyScO₃, 667f

E

- EBBA, 138, 140
- Effective dimension of the wall, 324
- Effective Hamiltonian, 317, 319
- Effective interface dimension, 505
- Effective mass, 496–498, 515–516, 518
- EFM, 143–147, 149, 622
- Elastic anisotropy, 303, 562, 574
- Elastic Green functions, 560, 575
- Elasto-optics, 173–174, 266
- Electrical conductivity, 128, 185, 256–257, 336, 361, 374
- Electrocaloric effect, 485–488
- Electrolyte electrodes, 362
- Electron
 - emission effect, 204
 - holography, 275t, 283–285, 291
 - mirror microscopy, 182, 193–194
- Electro-optics, 173–175
- Emission
 - cold-field, 635
- Emission of the acoustic waves, 516
- EPR, 204–205
- Equilibrium residual misfit strain, 548
- Equitranslational transitions, 43

- Etchant, 58, 123, 125, 127t, 128–129, 241f
- Etch hillocks, 122
- Etching rates, 122–123, 125, 127t, 129
- Etch pits, 122–123, 126t–127t
- Euler equation, 293, 297, 301, 314, 404, 605
- Ewald sphere, 187–188
- Extrapolation length, 658, 662
- Extrinsic contribution, 481, 483–490, 502, 504–506, 508, 513, 667–677

F

- Ferrobielastic switching, 266, 350
- Ferroelectric, 356
- Ferroelastic
 - domain pairs, 53–58, 62–63, 66, 69, 74, 129, 162, 164, 171, 183, 197
 - domain states, 4f, 45, 47, 50–51, 53, 68, 76, 94–95, 125, 162, 164, 205, 222, 235–243, 262, 443, 527, 552–553
 - loops, 345, 348
- Ferroelastoelectrics, 29, 31, 35–36, 44, 47, 58, 90, 92, 99, 123, 195, 208, 265–267, 349–350, 356
- Ferroelectric breakdown, 481–483
- Ferroelectric/electrode interface, 104, 410–414, 452–453, 456, 458, 599, 628, 639, 641, 643, 660, 680, 682, 686–687
- Ferroic, 1, 3, 5–107, 109–121, 123, 129, 143, 161, 164–166, 170–172, 193–195, 197, 203–208, 220–225, 247, 253, 255, 262, 266, 268, 271–274, 279, 285, 288, 291–293, 296, 305, 310, 313, 315, 319–322, 328, 349, 351, 353–358, 361, 382, 391–392, 418–419, 430, 521, 548, 560, 574, 704, 713, 728–770
- Fictitious dislocations, 560, 573, 575
- Flexible defects, 419, 427–428
- Flexoelectric coupling, 304, 639
- Flexoelectric effect, 304, 318, 559, 637–638
- Forsbergh pattern, 260f
- Forward growth, 353, 378, 430, 441, 445–446, 483, 677, 702
- Free-charge density, 211, 359
- Frequency dependence of the polarization loop, 468
- Frequency modulation, 144
- Friction force, 143, 150–151, 159, 409, 515
- Frozen disorder, 419, 421
- Frozen polarization, 480–481
- Full ferroelectric, 39, 51
- Fused quartz, 532

G

- GaAs, 532
 Gadolinium molybdate, *see* GMO
 GASH, 19, 114t, 132–133, 135–136, 145, 150–153, 185–186, 234–235, 289, 361, 372
 GdDy(MoO₄)₃, 195, 282
 GdF₃, 136, 288
 Gibbs energy, 82–84, 86, 89, 91, 93–94, 96, 307, 355, 359, 705
 GMO, 6–8, 30–31, 34–35, 74–75, 97–99, 116t, 126t, 136, 169, 193, 203, 214, 240–241, 247, 253, 261, 273, 276t, 278, 282–283, 288, 311, 314, 383–385, 410, 414
 Gold electrodes, 365
 Growth dimensions, 442, 447
 Growth pyramids, 225–226, 228, 234, 255
 Guanidinium uranyl sulphate trihydrate, *see* GASH
 Gyration tensor, 170–172

H

- Hard-ferroelectric approximation, 217–219, 359, 482, 600, 603–608, 629, 632
 Head-to-head, 60, 71–72, 233, 255, 258–259, 358–359, 413–414, 446, 639, 686, 694
 HF, 123–128, 136
 Hg₂Br₂, 115t, 313–314
 High resolution transmission electron microscopy, 187, 191–193, 285
 HNO₃, 118, 126–128
 H₃PO₄, 118t, 124, 125t–127t
 HRTEM, *see* High resolution transmission electron microscopy
 Hysteresis loop, 6–9, 19, 85, 87, 253, 331–340, 344–351, 368, 375, 387, 431–439, 442–444, 447, 450, 455, 466–471, 475–480, 613–653

I

- Illumination, 131, 163, 169, 180, 187, 189, 199, 360, 375, 435, 627, 652, 685
 Imprint, 427, 627–628, 631, 634–636, 645, 647–649, 652–653, 680, 685–686, 688, 690, 700, 704
 Improper ferroelectrics, 34, 38–39, 46–48, 60, 81, 97–99, 210, 214, 217–218, 240, 263, 296, 310, 414, 604

- Injection, 624–627, 631, 635, 685–686, 688–689
 Injection model for imprint, 631–637
 Internal bias, 333, 336, 442, 627–629, 631, 637, 641–642, 645–649, 695, 698
 Intrinsic contribution, 483, 501, 654, 662–664, 672, 675
 Inverse exponential law, 368–369, 371–372, 376, 378–379
 IrO₂, 541, 687, 698
 Irreducible representation, 44, 46, 48, 720

J

- Jonscher universal relaxation law, 505

K

- K₂Cd₂(SO₄)₃, 113t, 264
 K₂NaAlF₆, 356
 K₂ZnCl₄, 142
 KAlSi₃O₈, 268
 KCl, 123
 KD₂PO₄, 116t, 276t, 279, 391
 KDP, 30–31, 35, 68, 74, 91–92, 97, 99–100, 105, 116t, 137, 169, 203–204, 214, 224, 235, 239, 245–253, 276t, 279–280, 315, 384–385, 388–391, 403, 446–448, 462, 488, 511–513, 705–707, 709–711
 KFe(MoO₄)₂, 115t, 242, 244, 346, 348
 KH₃(SeO₃)₂, 7, 117t, 348
 Kinematical contrast, 281
 KIn(WO₄)₂, 115t, 244
 Kittel-Mitsui-Furuichi, 210
 KNbO₃, 75–76, 112t, 126t, 179, 193, 197, 224, 253, 261, 276, 285, 523, 542–543
 Kolmogorov-Avrami, 442, 447, 459, 462, 464, 466, 468, 492, 610, 613, 700
 KPFM, 143
 KSc(MoO₄)₂, 115t, 205
 KSCN, 115t, 237–240, 313–314
 KTaO₃, 253, 524–525, 530–532, 589–592, 596
 K(Ta,Nb)O₃, 257
 KTiOPO₄, 117t, 127t, 134, 141, 174, 186, 197, 199, 505–506

L

- (La AlO₃)_{0.29} (SrAlO₃)_{0.71}, 667
 LaAlO₃, 152–153, 280, 291, 524, 530–531, 591, 593, 595
 Lagbeinites, 168
 Lamella domain patents, 249

- Lamellar twins, 1
 LaNbO₄, 116t, 345
 Landauer theory, 451–452, 613, 617
 Landau theory, 11, 34, 44, 61, 81, 100–101, 105, 107, 310, 404, 440, 456, 476–477, 496, 498, 514f, 544, 554, 560, 580, 605, 655, 669, 705
 LaP₅O₁₄, 117t, 235–236
 LAS, 113t, 135–136
 Laser tomography, 203
 Lateral piezoresponse, 159–160
 Lead germanate, 58, 72–73, 114t, 126, 131, 172, 214, 233, 275, 291, 328, 361, 365, 374–375, 382–384
 Left coset, 41–43, 45
 Lens-shaped domains, 218, 238–240, 373
 Lenticular domains, 226–227, 381, 417
 LFM, 143, 150–151
 Li₂Ge₇O₁₅, 105, 107, 113t, 139
 LiCl, 362, 380, 436
 LiCsO₄, 345–346
 LiH₃(SeO₃)₂, 118t, 141, 492
 LiNbO₃, 8–9, 72, 114t, 126t, 128, 131, 152, 155, 174, 179, 185–186, 201, 203–204, 443–446, 483
 Linear dichroism, 172
 Linear wall, 298, 311, 503
 LiNH₄SO₄, 113t, 282
 Liquid crystal, 131–132, 137–142, 225, 228, 361, 372–373
 Liquid electrode, 177, 338, 362, 365–369, 379, 381, 436
 LiTaO₃, 70, 72, 114t, 126, 186, 201–202, 204, 275t, 285, 290f, 443–446
 Lithium niobate, *see* LiNbO₃
 Logarithmic charge relaxation, 634, 636
- M**
 MASD, 113t, 262
 Matthews-Blakeslee criterion, 548
 Maximum polar subgroups, 33, 48
 MBBA, 138, 140–141
 Mean strain approach, 560, 562, 573–578, 581–582, 586–588, 598
 Mechanical twinning, 2
 Mercury, 115t, 128, 226, 371
 Mg₃B₇O₁₃Cl, 75, 113t
 MgO, 125t, 445f, 524, 527–534, 542, 582, 590–593, 595
 Micro-Raman spectroscopy, 205
 Microstresses, 561, 566–570, 575–576, 595
 Miller-Weinreich theory, 394–397, 417, 693
- Minor species, 45–46
 Misfit dislocations, 522, 544–545, 547–548, 552, 559, 582, 590–591, 595–596, 637–638, 641
 Misfit strain, 544–548, 550–554, 556–559, 563–567, 574, 580–582, 585, 587–596, 638–639, 665–667, 670, 696, 705–707
 Mixed boundary conditions, 657
 Mobility law, 366, 383–385, 390, 405–406, 408–410, 412, 415, 427–428, 502–503, 507
 Monte-Carlo simulations, 319
 Morphic birefringence, 28, 166
 Morphic components, 165, 356
 Morphotropic phase boundaries, 65, 451, 455
 Multiaxial ferroelectrics, 51, 59, 208, 253, 260, 307
- N**
 NaNbO₃, 75, 78–80, 253, 261
 NaNO₂, 14–15, 117t, 127t, 129, 134, 138, 141–142, 178, 185, 196, 199, 274t, 281–282, 288, 306
 Natural spontaneous strains, 20–28, 50, 65, 90, 165, 222, 237, 545, 585
 NdP₅O₁₄, 74, 75, 117t, 131, 197, 203–204, 235–236
 Near-field scanning optical microscopy, 201
 Needle-like domains, 389–391, 445
 Néel type structure, 313
 Nematic liquid crystal, *see* NLC
 (NH₂CH₂COOH)₃·H₂SO₄, *see* TGS
 (NH₄)₂BeF₄, 117t, 137
 (NH₄)₂SO₄, 113t, 127t
 (NH₄)₃H(SO₄)₂, 205
 NH₄Cl, 74, 112t, 173
 NH₄LiSO₄, 135
 NLC, 137–142, 373–374
 NMR, 205, 237
 Non-activated regime, 392, 394, 402–410, 425
 Nondestructive visualization, 157
 Nonferroics, 16
 Nonlinear dielectric constant, 154
 Non-linear dielectric response, 153–155, 359, 683
 Nucleation
 barrier, 454, 455f, 457, 613
 problem, 396, 451, 456
 rate, 395, 397–401, 404, 442, 451–452, 455, 461, 464, 466, 468–469, 494
 time, 461

- Nucleation-limited-switching model, 610–613
- Nuclei of reverse domains, 353, 449
- O**
- Oernstein-Zernicke function, 294
- Optical activity, 57–58, 119t, 161, 170–172, 233, 361, 375
- Optical impermeability, 163, 166
- Optical indicatrix, 162–163, 174, 235
- Order-disorder, 13, 14, 105, 237–238, 268
- Order-parameter vortex, 312
- Orientational domain states, 39–40, 42, 46, 48, 237, 249
- Oxide electrode, 615–616, 627, 651–652, 661–662, 687
- Oxygen vacancies, 437, 618, 652, 686–687
- Oxygen vacancy, 322, 437, 652, 686–687
- P**
- Parent misfit strain, 545, 547, 554, 556–559, 580–582, 585, 588–591, 594–595, 665, 670, 705–707
- Partial ferroelastic, 39, 51, 57–58, 95, 253
- Partial ferroelectric, 39, 47
- Partial switching, 121, 344, 369, 371, 441, 470, 473, 477–481
- Passive layer, 247, 484, 599–602, 604, 617, 620–626, 628–636, 639, 664, 671–677, 682
- $\text{Pb}_3(\text{PO}_4)_2$, 6, 114t, 222, 242–244, 277, 313, 348
- $\text{Pb}_3(\text{P}_x\text{V}_{1-x}\text{O}_4)_2$, 348
- $\text{Pb}_3(\text{VO}_4)_2$, 114t, 244–245
- $\text{Pb}_3\text{Ge}_3\text{O}_{11}$, *see* Lead germanate
- PbCl_2 , 136
- $\text{Pb}(\text{Fe}_{1/2}\text{Nb}_{1/2})\text{O}_3$, 505–506
- $(\text{Pb},\text{La})\text{TiO}_3$, *see* PLT
- PbTiO_3 , 66, 94, 96, 112t, 125t, 152–153, 159–160, 189–190, 223, 257–259, 285–287, 523–525, 527–532, 551, 558–559, 572–573, 590–597, 602, 669, 703
- PbZrO_3 , 15, 46, 78–80, 112t, 125t, 253, 261
- $\text{Pb}(\text{Zr},\text{Ti})\text{O}_3$, *see* PZT
- Peierls barrier, 317–318, 394–395, 398, 402–403, 516, 518
- Peierls potential, 321, 323, 392, 425, 490–493, 496–498, 502
- Penetration twins, 1–2
- Permissible wall, 62–64, 66–68, 74, 80, 243, 250, 254, 262–264, 315
- Permittivity, 7, 9, 28, 47, 61, 103–105, 134, 165–166, 170, 210, 212, 217, 263, 295–296, 326, 334, 387, 406, 417, 455, 482, 484–497, 501–514, 653–659, 662–675, 705, 709–771
- PFM, 143, 150, 158–161, 328, 691–698, 700–704
- Phase
- coexistence, 87–88
 - distorted, 485
 - field calculations, 560, 582, 584–585
 - high symmetry, 13, 17, 268, 529
 - high temperature, 13, 110, 139, 266, 546, 552, 644
 - incommensurate, 10, 109–110, 120, 265, 267
 - low symmetry, 13, 18, 20, 22, 25, 38, 40, 92, 240, 269, 544, 584
 - low temperature, 13, 58, 110, 135, 163, 205, 247, 253, 260, 270, 296, 304, 345, 513, 522, 546
 - matching, 177–178
 - transformation, 3–4, 6, 15, 20, 52, 88, 110, 165, 268, 442, 457
 - transition in the wall structure, 312
- Piezoelectric clamping, 485, 488–490
- Piezoelectric force microscopy, *see* PFM
- Piezoelectric hysteresis loops, 475–481, 698
- Pinning, 157, 231, 309, 321, 354, 371, 418–429, 500–502, 507–509, 597, 617–618, 669, 680–689, 707
- Pinning pressure, 418–428
- Pinning of wall by charged defects, 309
- PLT, 524, 531–532
- PLZT, 336–337, 647
- Polarization fatigue, 677–690, 704
- Polarization reversal, 6–9, 58, 71, 141–142, 153, 183, 262, 333, 340, 349, 363–364, 382, 404–406, 443, 449–450, 468, 481–483, 610, 626, 677, 680–682, 690–704
- Polarizing microscope, 75, 137, 170, 172, 233, 243–244, 255–256, 360–361, 369, 375, 389
- Poling back technique, 341–342, 608–609
- Prefractals, 215, 248
- Preisach model, 472, 474–475
- Pressure acting on a wall, 357–358
- Primary ferroics, 28–29
- Proper ferroelastics, 34, 235, 364, 704–706, 709–710

- Proper ferroelectrics, 34, 39, 42, 47–48,
50, 60, 98–100, 105, 107, 170,
210–211, 217–218, 414, 604,
704–706, 710
- Protonic conductivity, 338
- Prototypic, 13, 557
- Pseudo-proper ferroelectrics, 217
- Pt, 112t, 126t–127t, 171, 204, 308–309, 374,
541, 615–616, 626–627, 648, 650,
687–688, 698–699, 701, 704, 778
- PUND test, 645
- Pyroelectric coefficient, 17–21, 30, 45, 48, 84,
175, 197, 199, 331, 486, 720
- Pyroelectric probe technique, 199, 361, 371
- PZT, 146, 152–153, 156–158, 201, 342,
358, 451, 453, 455, 465, 529–531,
539–542, 593–594, 596–598, 611–612,
614–617, 620, 627, 648–652, 678–679,
684–685, 687–689, 697–698, 700–701,
703–704
- Q**
- Quartz, 2, 46, 58, 73, 114t, 123, 172, 174, 177,
195–196, 265–267, 349–350
- R**
- Random bond, 321–322, 325, 419, 499, 502
- Random field, 321–322, 499, 508, 642–643
- Rayleigh constant, 685
- Rayleigh loops, 470–475
- RbCaF₃, 205
- RB defect, 321–322, 325, 329, 427, 429
- RbH₂PO₄, 116t, 391
- R-cases, 64
- Real and imaginary parts of the
susceptibility, 485
- Relative coherency strain, 546, 563, 565, 567,
569, 571, 576–577, 581–582
- Remeika method, 193, 255–256, 365
- Reorientable defects, 642, 648
- Residual misfit strain, 548, 590, 592–593,
595–596
- Retardation effects, 376–377
- RF defect, 321–322, 324–326, 419–420,
427–428, 437, 443
- Rochelle Salt, 31, 118t–119t, 133, 161,
168, 213–214, 224, 241–242,
332, 335–336, 348, 360, 363,
382–384, 511
- Rotational wall, 300, 311
- Roughening, 319–329, 498
- Roughness exponent, 321, 323–325,
327–328, 425, 509–510
- Rub technique, 125
- RuO₂, 660, 687
- S**
- SAED, *see* Selected area electron diffraction
- Sample surface, 5, 121, 124, 137, 141–143,
147, 149, 154, 156, 158, 162,
182–183, 185, 199–201, 203, 205, 210,
218, 254, 258, 284, 288–289, 315, 344,
360, 481
- Sawyer-Tower circuit, 332–333, 336, 432
- SBN, 115t, 157
- SbSI, 71, 126, 134
- Scanning acoustic microscopy, 203
- Scanning electron acoustic microscopy, 203
- Scanning force microscopy, *see* SFM
- Scanning nonlinear dielectric microscopy,
143, 153, 524, 533
- Screening, 102, 140, 143, 147, 219–220, 231,
309, 359, 412–414, 554, 599, 603, 624,
626, 633, 636, 640–641, 655, 659–662,
685–686, 690
- Secondary electrons, 183–186
- Secondary ferroics, 29, 31
- Secondary order parameter, 38
- Second optical harmonics, *see* SH
- Seed inhibition, 680–683, 685–687
- Selected area electron diffraction,
187–191, 539
- Selective crystallization, 134
- SFM, 142–144, 146, 150–153, 160–161, 231,
236, 288–289, 481–483, 524, 526–527,
530, 533, 541, 544, 596, 690–692, 694,
696–698
- SH, 176–179
- Short-circuited capacitor, 209, 554, 599,
602–605
- Size effects, 422, 569, 571, 613–627
- Slater model, 315–317, 319
- Sliding regime, 508, 510
- Sn₂P₂S₆, 118, 142, 182
- SNDM, 143, 150, 153–155, 524
- SNOM, *see* Near-field scanning optical
microscopy
- Soft domains, 606
- Spectrum of waiting times, 455,
611–613
- Spinodal decomposition, 247, 268
- Spinodals, 449
- Spontaneous birefringence, 28, 165–166,
168, 170, 174

- Spontaneous polarization, 7–8, 16–18, 21, 33, 35, 38, 47–48, 50–51, 59, 83–84, 89–90, 94, 99–100, 102, 104–107, 119t, 143, 146–147, 154–157, 184, 189–190, 210–211, 284, 295, 311, 318, 322, 326–327, 340–341, 351–352, 386, 388, 402, 436–437, 449, 481, 515–517, 536, 538, 559, 584–585, 590–593, 600, 641, 668, 670, 673, 707, 727
- Spontaneous strain, 8, 20–28, 47, 50–51, 62–63, 68, 76, 78, 90–91, 130, 165–166, 168, 221–223, 236–237, 240, 243, 257, 262, 270, 280, 311, 322, 343, 364, 536, 545, 585–586
- Square-root thickness dependence, 562
- Square-shaped domain, 364–365, 380
- $\text{Sr}_{0.61}\text{Ba}_{0.39}\text{Nb}_2\text{O}_6$, *see* SBN
- $\text{SrBi}_2\text{Ta}_2\text{O}_9$, 51, 116t, 522–523, 544, 608–609, 614–616, 698–699
- SrRuO_3 , 539, 616, 661
- SrTiO_3 , 112t, 253, 261, 303, 313, 505, 522, 524, 526, 529–531, 533–535, 542–543, 557, 591, 593, 595–597, 603, 658, 666–667, 694
- S-SNOM, 201–202, 290
- SSPM, 143, 147–149
- Stochastic regime, 508
- Stoichiometric, 443–445
- Strain gradient, 268, 304, 559, 637–639, 648
- Stress-free walls, 62–63
- Stress release, 522, 538, 544–553, 564–565, 575, 590–591, 594–595, 637–638
- Stroboscopic illumination, 163, 169, 360, 375
- Strong pinning, 419–423, 426–428, 500–501, 509
- Suborientational domains, 68–69
- Substrate, 129, 131–132, 135–137, 152–153, 315, 484, 521–522, 524–535, 538, 542, 544–576, 579–593, 603, 637–638, 649, 653, 664–669, 692–696, 704–707, 710
- Super-ionic conduction, 505
- Surface boundary conditions, 373
- Surface layer, 1, 154, 184, 226, 228, 232, 256, 260, 275, 338, 365, 367, 370, 373, 376, 411–413, 434, 625, 640–641, 662, 688–689
- Surface-stimulated domain nucleation, 613
- S walls, 63, 65, 68, 75–80, 237, 243–245, 260, 311, 353
- Swiss cheese technique, 181–182
- Switching current, 340–341, 343, 349, 361–363, 365, 372–373, 378–379, 389, 434, 443–447, 465–466, 492–496, 646–647
- Switching regime, 429, 441, 504, 510–511, 646
- Switching time, 8, 341–343, 348, 373–374, 379, 430–431, 441, 447, 608
- Symmetry breaking strain, 23, 90
- T**
- T*-effect, 343–344
- Tail-to-tail, 72, 255, 686, 694
- Tanane, 30, 116t, 385–386
- TANDEL effect, 339–340
- Tanh-type solution, 293, 298–299, 302
- Temperature
- autostabilization, 339
 - gradient, 72, 199, 223, 233, 247, 251–252, 255, 257–258
 - hysteresis, 88
- Tertiary ferroics, 29, 356
- Tetragonality
- ratio, 546, 563
 - strain, 546, 586, 596, 668
- TGFB, 118t–119t, 137, 233, 438–442, 462–463
- TGS, 6, 70–73, 88–90, 118t, 125–128, 131–142, 145, 150–153, 177–178, 183–186, 197, 199–200, 202–204, 224–233, 253, 256, 274, 281–282, 288–290, 295, 305–306, 335, 339–340, 343, 349, 355, 358, 361, 364, 370–374, 378, 381, 410, 415, 417, 438–443, 446–448, 467, 470, 488, 492, 495, 505–506, 512–513
- TGSe, 118t–119t, 227, 233, 306, 381, 415, 417
- Thermal expansion, 11, 27, 90, 532, 552, 554, 559, 586, 590, 666
- Thermal fluctuations, 236, 272, 292, 294, 322, 325, 392, 394, 404, 418–419, 424, 427, 457, 490, 497
- Thermally activated regime, 13, 391, 394, 418, 422–423, 425, 427–428, 455–457, 461, 490, 636, 693
- Thermodynamic coercive field, 85, 89, 92, 295, 356, 406, 408–410, 434, 440, 448–449, 451–452, 466, 476–477, 611
- Thiourea, 117t–118t, 133, 137, 282
- Thomas-Fermi screening length, 655, 659–660, 662
- Threshold conduction, 621, 624–627, 679

- Through domains, 353, 441, 449, 460, 462, 467, 483, 671, 702
- Time of thermal relaxation, 486
- Topological defects, 312, 320, 418, 421
- Top-seeded solution growth, 255
- Transformation twins, 3, 75
- Transient current method, 341–342, 608
- Transition
 - displacive, 13
 - distortive, 11–13, 43
 - ferrodistortive, 14–15
 - reconstructive, 11–12, 41
- Translational domain states, 39–41, 44, 69
- Transmission electron microscopy, 121, 182, 186–193, 268, 283, 285–287, 524
- Tricritical point, 82, 294, 296
- Triferroelastic, 119t, 356
- Triglycine sulphate, *see* TGS
- Triple hysteresis loops, 437
- Turmaline, 172
- Tweed patterns, 267–270
- Twin boundary, 2, 5
- Twin components, 1–3
- Twinning complex, 52–53, 57, 64
- Twinning dislocations, 250, 391
- Twinning operation, 1, 52–53, 57–58, 64, 66, 164, 166, 168, 170, 173, 255
- Two – beam diffraction conditions, 189–190, 285
- Two-dimensional nucleation, 398–400, 442
- U**
- Uniaxial ferroelectrics, 51, 225–235, 374, 443, 558
- UV light illumination, 627, 652
- V**
- Velocity anisotropy, 373, 379
- Vertical piezoresponse, 158–160
- Vicinal substrate, 529
- Virtual ground, 333
- Voltage offset, 442–444, 627–632, 634–635, 637, 639–653, 686
- W**
- Waiting time for nucleation, 464
- Wall mobility, 85, 228, 366, 383, 393–394, 397–408, 411, 415, 502–503, 675, 692
- 90° wall motion, 360
- Wandering exponent, *see* Roughness exponent
- Weak beam dark field image, 187–190, 285–286
- Weak ferroelectricity, 100–107
- Weak pinning, 421–426, 428–429, 507–509
- Wedge-shaped domains, 74–75, 131, 236, 254, 382, 386, 388–391
- Wedge-type domains, 430
- W_f walls, 68, 74–78, 80, 237, 240, 243–244, 260–262
- WO₃, 115t, 183
- X**
- X-ray
 - diffraction, 23–24, 88, 175, 194, 205, 237, 247, 249, 266, 268, 277, 280
 - diffractometry, 280
 - scattering, 276, 278, 280, 535
 - topography, 70, 121, 194–196, 236, 255, 266, 274–275, 277, 281–282, 291
- Y**
- YBa₂Cu₃O_{7-x}, 172, 270, 280, 286
- Z**
- Zig-zag domain wall pattern, 256
- Zig-zag shape, 374